

NASA SP-106

N67-15884

# The Dynamic Behavior of Liquids in Moving Containers

With Applications to Space Vehicle Technology

*Edited by*  
H. Norman Abramson

Prepared under contract no. NASr-94(07)  
by the Southwest Research Institute for the  
National Aeronautics and Space Administration



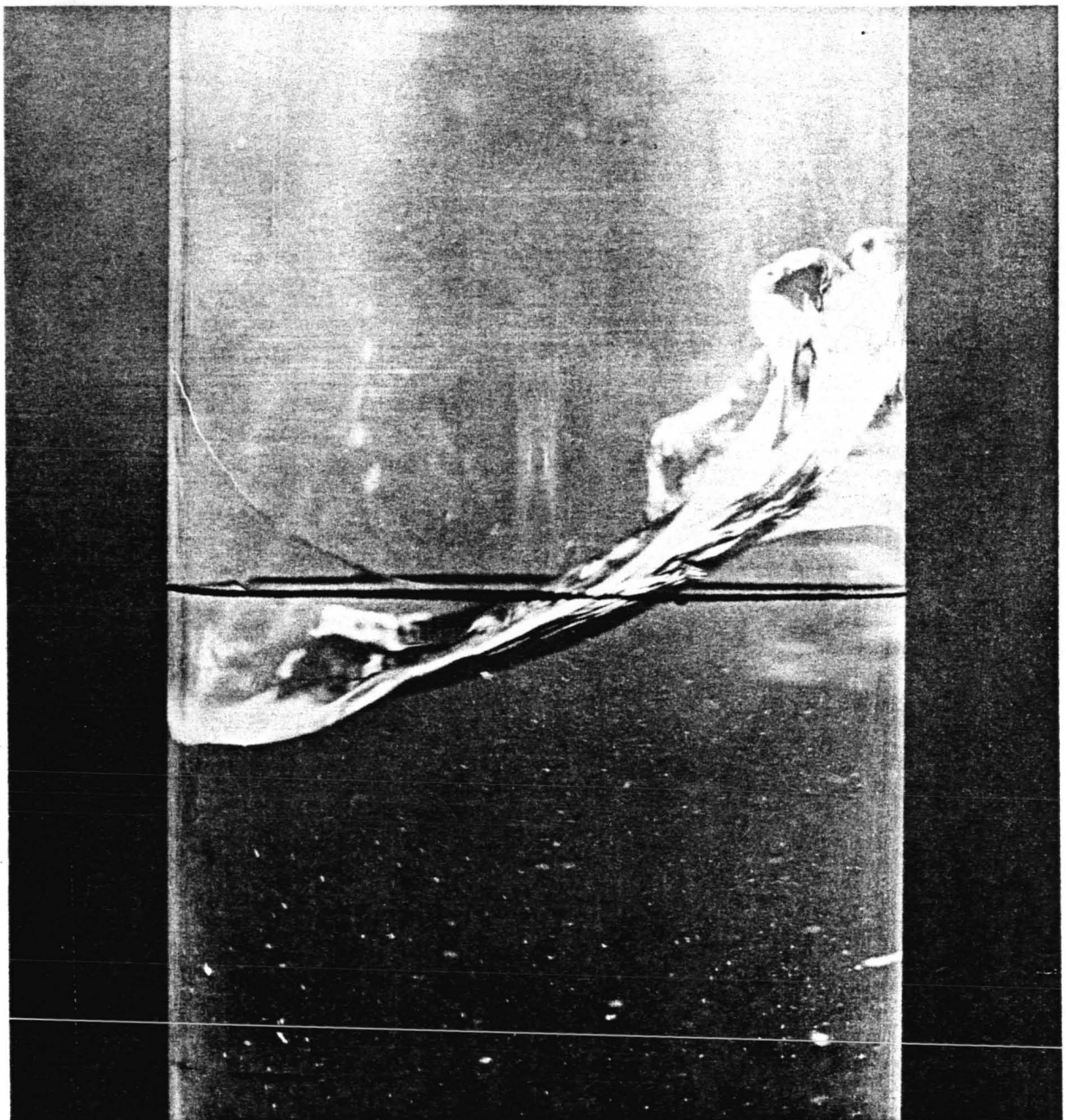
REPRODUCED BY  
**NATIONAL TECHNICAL  
INFORMATION SERVICE**  
U.S. DEPARTMENT OF COMMERCE  
SPRINGFIELD, VA. 22161

Scientific and Technical Information Division  
1966  
NATIONAL AERONAUTICS AND SPACE ADMINISTRATION  
Washington, D.C.

464

**NOTICE**

THIS DOCUMENT HAS BEEN REPRODUCED  
FROM THE BEST COPY FURNISHED US BY  
THE SPONSORING AGENCY. ALTHOUGH IT  
IS RECOGNIZED THAT CERTAIN PORTIONS  
ARE ILLEGIBLE, IT IS BEING RELEASED  
IN THE INTEREST OF MAKING AVAILABLE  
AS MUCH INFORMATION AS POSSIBLE.



**Large amplitude liquid motion in a cylindrical container**

## **Foreword**

Approximately 90 percent of all the scientists and engineers who ever pushed a stylus, quill, or pen since the beginning of mankind are alive and productive today. Moreover, the number is increasing at a rapid rate. It is no wonder that we feel a rapid surge in the number of papers and reports that are finding their way into the literature. As an example, the total number of abstracts of papers published in the NASA serial document entitled "Scientific and Technical Aerospace Reports" for the first 3 months of 1963 was 2840, whereas for the same period 2 years later in 1965 the number swelled to 6338. As a result, today's research scientist or engineer finds he is spending increasingly more time reviewing the reports of others in order to remain abreast of the state of the art in his chosen endeavor. To lighten this burden, it becomes almost a necessity to collect periodically the material in a given area, and to try to single out the significant and present it in an orderly fashion as a summary document. In this form, the state of the art becomes readily apparent. Additional benefits accrue by uncovering gaps in the knowledge in some areas, while at the same time indicating areas where the coverage has been excessive and requires deemphasis.

In view of the many uses afforded by such a document, it is felt that one of the most important functions of a research organization is to determine where and when such summaries are required, and to see that they find their way into print. The following work on liquid behavior in moving containers, through the excellent efforts of its editor and the other contributors, is considered to have met the requirements for a summary document of this nature.

DOUGLAS MICHEL  
*Space Vehicle Structure Programs*  
*Office of Advanced Research and Technology, NASA*

## **Editor's Preface**

The dynamic behavior of liquids in moving containers is a fascinating subject that has attracted the attention of geophysicists and seismologists, engineers, mathematicians, and other scientific workers for a period of many years. With the development of space technology as an active program of hardware development and testing and widespread laboratory research, it was perhaps to have been expected that the motions of propellants and other liquids contained in launch vehicles and spacecraft would be of great interest. It has turned out, in fact, that in many cases this problem has exerted a very great influence on both design details and concepts. It is therefore the purpose of this monograph to present a rather comprehensive view of the general subject as it specifically relates to space technology applications.

General technical direction for the organization and production of this volume was vested in an Advisory Committee consisting of Douglas Michel of the NASA Office of Advanced Research and Technology as chairman, George W. Brooks of the NASA Langley Research Center, Helmut F. Bauer of the Georgia Institute of Technology, and myself. Obviously, however, responsibility for the accuracy of technical details within each chapter resides with the individual authors. It was my challenging and yet rewarding task to attempt to provide a unifying influence in the welding together of the various contributions. Many staff members of Southwest Research Institute gave generously of their efforts and talents in the production of this volume; I specifically wish to acknowledge, both for myself and all of the authors, our appreciation to Emil Gavlick for supervision of the production and editing of the final draft copy, and to Victor Hernandez and James Stevens for preparing all of the illustrations.

H. NORMAN ABRAMSON  
*Department of Mechanical Sciences  
Southwest Research Institute*

---

**Preceding page blank**

## Contributors

- H. NORMAN ABRAMSON**  
*Director, Department of Mechanical Sciences  
Southwest Research Institute*
- HELMUT F. BAUER**  
*Professor of Engineering Mechanics  
Georgia Institute of Technology*
- GEORGE W. BROOKS**  
*Assistant Chief, Dynamic Loads Division  
Langley Research Center, NASA*
- WEN-HWA CHU**  
*Senior Research Engineer  
Department of Mechanical Sciences  
Southwest Research Institute*
- JOHN F. DALZELL**  
*Senior Research Engineer  
Department of Mechanical Sciences  
Southwest Research Institute*
- FRANKLIN T. DODGE**  
*Senior Research Engineer  
Department of Mechanical Sciences  
Southwest Research Institute*
- DANIEL D. KANA**  
*Senior Research Engineer  
Department of Mechanical Sciences  
Southwest Research Institute*
- WILLIAM C. REYNOLDS**  
*Associate Professor of Mechanical Engineering  
Stanford University*
- HUGH M. SATTERLEE**  
*Staff Engineer  
Lockheed Missiles & Space Co.*
- SANDOR SILVERMAN**  
*Research Engineer  
Department of Mechanical Sciences  
Southwest Research Institute*

# Contents

CHAPTER	PAGE
1 INTRODUCTION..... H. Norman Abramson	1
2 LATERAL SLOSHING IN MOVING CONTAINERS..... Sandor Silverman and H. Norman Abramson	13
3 NONLINEAR EFFECTS IN LATERAL SLOSHING..... H. Norman Abramson, Wen-Hwa Chu, and Franklin T. Dodge	79
4 DAMPING OF LIQUID MOTIONS AND LATERAL SLOSHING..... Sandor Silverman and H. Norman Abramson	105
5 SIMULATION AND EXPERIMENTAL TECHNIQUES..... <i>Part I: Simulation of Liquid Sloshing</i> ..... John F. Dalzell <i>Part II: Experimental Techniques and Apparatus</i> ..... George W. Brooks	145 145 170
6 ANALYTICAL REPRESENTATION OF LATERAL SLOSHING BY EQUIVALENT MECHANICAL MODELS..... Franklin T. Dodge	199
7 VEHICLE STABILITY AND CONTROL..... Helmut F. Bauer	225
8 VERTICAL EXCITATION OF PROPELLANT TANKS..... Franklin T. Dodge	269
9 INTERACTION BETWEEN LIQUID PROPELLANTS AND THE ELASTIC STRUCTURE..... Daniel D. Kana	303
10 SPECIAL TOPICS..... <i>Part I: Liquid Impact on Tank Bulkheads</i> ..... John F. Dalzell <i>Part II: Liquid Rotation and Vortexing During Draining</i> ..... Franklin T. Dodge <i>Part III: Longitudinal Oscillations of Flight Vehicles</i> ..... Daniel D. Kana	353 353 373 378
11 LIQUID PROPELLANT BEHAVIOR AT LOW AND ZERO g..... William C. Reynolds and Hugh M. Satterlee	387
APPENDIX—PHYSICAL PROPERTIES OF SELECTED LIQUIDS .....	441
AUTHOR INDEX.....	451
SUBJECT INDEX .....	455

## CONVERSION FACTORS

$$t_c = (5/9)(t_f - 32^\circ)$$

$$t_k = t_c + 273 = (5/9)(t_f + 459.4)$$

$t_c$  = temperature,  $^{\circ}\text{C}$

$t_f$  = temperature,  $^{\circ}\text{F}$

$t_k$  = temperature,  $^{\circ}\text{K}$

$$\begin{aligned} 1 \text{ poise} &= 5.8016 \times 10^{-7} \text{ lb}_{\text{force}} \text{ hr}/\text{ft}^2 = 1.4504 \times 10^{-5} \text{ lb}_{\text{force}} \text{ sec/in.}^2 \\ &= 1.0197 \times 10^{-3} \text{ gram}_{\text{force}} \text{ sec/cm}^2 = 1 \text{ gram}_{\text{mass}}/\text{cm sec} \end{aligned}$$

$$1 \text{ centimeter} = 0.3937 \text{ inch} = 0.03281 \text{ foot}$$

$$1 \text{ centimeter}^2 = 0.1550 \text{ inch squared} = 1.0764 \times 10^{-3} \text{ foot squared}$$

$$1 \text{ dyne} = 0.2248 \times 10^{-5} \text{ lb}_{\text{force}}$$

$$1 \text{ dyne} = 10^{-5} \text{ newton}$$

$$1 \text{ dyne} = 1.02 \times 10^{-6} \text{ kilogram}_{\text{force}}$$

$$1 \text{ dyne/centimeter} = 0.5710 \times 10^{-6} \text{ lb}_{\text{force}}/\text{inch}$$

$$\begin{aligned} 1 \text{ atmosphere (standard)} &= 14.7 \text{ lb}_{\text{force}}/\text{in.}^2 = 1.013 \times 10^6 \text{ dynes/cm}^2 \\ &= 2116 \text{ lb}_{\text{force}}/\text{ft}^2 \\ &= 76.0 \text{ centimeters of mercury} \end{aligned}$$

## **Introduction**

***H. Norman Abramson***

### **1.1 THE DYNAMIC BEHAVIOR OF LIQUIDS IN MOVING CONTAINERS**

It is common everyday knowledge to each of us that any small container filled with liquid must be moved or carried very carefully to avoid spills. Experience has taught us that the unrestrained free surface of the liquid has an alarming propensity to undergo rather large excursions, for even very small motions of the container, and that one has to adjust very carefully the frequency of the container motion to avoid this sloshing of the liquid. Drinking coffee while riding on a train can be a frustrating experience, since the soft springs of most railroad cars designed for passenger comfort result in motions with frequencies distressingly close to those of the coffee.

Similar phenomena surround us at almost every turn, arising from the accoutrements of our modern technology and civilization as well as from nature, herself. Obviously, almost any moving vehicle provides a prime example wherein the response of a contained liquid may be of concern: (a) aircraft and rocket fuel tanks; (b) cargo, ballast, or fuel tanks of large ships; (c) fuel or cargo tanks of automotive vehicles; (d) railroad tank cars, etc. On a much larger scale, one should not omit from consideration the oscillations of water in lakes and harbors occurring as the result of earthquakes.

While it is the primary concern of this monograph to deal with this general subject as it applies to rockets and spacecraft, we would be remiss indeed to neglect some mention of these other applications. On the other hand, rather comprehensive reference lists have already been published on several occasions (refs. 1.1 through 1.4), and, therefore, we wish

to point out here only representative examples of some of the important technical areas that have been investigated, other than those that pertain specifically to space technology.

The motions of water in lakes and harbors have interested geophysicists and engineers for many years, from the viewpoints of tidal oscillations, seiches induced in harbors by storms in the open sea, and earthquake disturbances. The first two of these constitute a classical problem for which a large body of analytical solutions has been developed (refs. 1.5 through 1.7). A fine example of the application of such techniques to problems of engineering significance is that of the critical design of the Mulberry harbors for the Normandy invasion of World War II (ref. 1.8). Seismologists have been particularly interested not only in the liquid motion but in the forces produced by them on containing structures (refs. 1.9 through 1.14). The recent catastrophe of Longarone, Italy (October 9, 1963), in which landslides into the contained lake induced such violent sloshing motions of the water that, even though the dam structure itself did not fail, the overspilling water resulted in almost total destruction of the village and loss of life, represents yet another stark example of the real significance of these problems.

Oceangoing vessels are, of course, subject to rather violent sea conditions at times, resulting in fairly large amplitudes of pitching, heaving, rolling, and other motions. The response of liquids contained in cargo, ballast, or fuel tanks has therefore often been of concern, although the problem is usually alleviated to a large extent by the ship's master operating with tanks as nearly completely empty or completely full as he can arrange. On the other hand, the

stabilization of ships in roll by means of passively acting partially full tank systems has proved quite effective in many instances, even though the optimum design of such tanks is as yet an uncertain art (refs. 1.15 and 1.16).

In similar fashion, the motions of liquids in automotive, or rail vehicle, cargo or fuel tanks have at times been of concern. Usually, however, in these cases the volume and weight of the contained liquid has been sufficiently small compared with vehicle weight that the forces produced are of little consequence, such that even very crude and simple baffles have served to suppress the liquid motion sufficiently. An interesting case in point, however, is that the fuel tanks of all racing cars in the Indianapolis 500 of 1965 contained hollow plastic ball-like devices ("wiffle" balls) intended to prevent fuel sloshing.

Aircraft certainly constitute a class of vehicles in which one would anticipate that liquid response in fuel tanks might be a significant problem. Indeed, such is the case, although the earliest occurrence of such problems arose not just of itself, but through coupling with other well-known aircraft dynamic problems. The first was probably that of sloshing in wing fuel tanks coupling with the wing vibration modes so as to modify seriously the flutter characteristics (ref. 1.17); the second was probably that of the overall effect of fuel sloshing on aircraft dynamic stability (ref. 1.18). For aircraft such as the supersonic transport, in which a large portion of the takeoff gross weight may be in fuel, this problem could be of governing importance to many aspects of the design.

Perhaps just two more examples, this time from particularly military applications, may serve to round out this brief survey of liquid response problems which precedes our primary area of application to space technology. One of these concerns the flight characteristics of a spin-stabilized projectile having a liquid core (refs. 1.19 and 1.20). In fact, it has been found that the motions of the contained liquid may couple with the natural nutational mode of motion of the projectile so as to cause actual flight instabilities. The entire question of liquid behavior in spinning tanks (refs. 1.21 and 1.22)

is a very interesting one which, unfortunately, we shall not be able to discuss in any detail in this monograph. The other problem relates to explosion effects on liquid-filled tanks (ref. 1.23). In the case of nuclear detonations, of course, the loading on the tank may result from either the airblast or the ground shock, the latter case being somewhat related to the problem of earthquake excitation mentioned previously.

### 1.2 PROPELLANT SLOSHING IN LAUNCH VEHICLES

Turning our attention now to those aspects of the general problem that are of most direct importance to space technology, consider the large liquid-filled boost or launch vehicle. Such devices have an enormous percentage of their initial weight as fuel and consequently the dynamic forces resulting from the motions of these large liquid masses could be very substantial, even beyond the capabilities of the control system to counteract them or the structure to resist them. The important thing to realize, however, is that we are dealing with a fairly complex dynamical system and must therefore be especially aware of the possibility of coupling between various of its components. Thus, the control system natural frequencies, the elastic body frequencies, and the fuel-slosh frequencies must all be fairly widely separated; unfortunately, this is not always the case. Table 1.1 gives data for several representative vehicles, from which one can see that the various frequencies are indeed not always widely separated.

If the dominant fuel-slosh frequencies are close to any of the control system frequencies, an instability in the flight characteristics can result; while if the fuel-slosh frequencies are close to the elastic body bending frequencies, a large amplitude dynamic response problem may arise. In any case, the governing design problem is that of stability and control, so that one must also carefully consider the location and configuration of the propellant tanks and the characteristics of the control sensing elements (ref. 1.24).

Saturn I provides us with a clear example of an actual in-flight stability problem arising as a

TABLE 1.1.—*Characteristics of Some Representative Launch Vehicles*

Vehicle	Length, m	Diameter, m	Thrust, kp	Range, n. mi.	Control frequency, cps	Fundamental slosh frequency at liftoff, cps	Fundamental bending frequency at liftoff, cps	Important missions
Redstone.....	21	1.78	32 000	200	0.5	0.8	10-12	Exploration.
Redstone-Mercury	25	1.78	32 000	200	.5	.8	10	Suborbital manned flights.
Jupiter.....	20	2.65	68 000	1500	.4	.6	9	Reentry, recovery of monkeys Able and Baker.
Juno II.....	25	2.65	68 000	-----	.4	.6	8	Moon try, Sun orbit.
Saturn I.....	60	6.5	685 000	-----	.3	.45	2	Manned space flight.
Saturn V.....	130	10	$3.4 \times 10^4$	-----	.16	<sup>a</sup> 0.3-0.4	1	Manned space flight.

<sup>a</sup> Large slosh masses in unfavorable locations.<sup>b</sup> Exceptionally large slosh masses because of the large tank diameter.

consequence of fuel slosh (ref. 1.25). This vehicle, it may be recalled, is unusual by virtue of its clustered-tank configuration: A single large cylindrical tank, surrounded by a cluster of eight smaller cylindrical tanks (this is but one of several types of segmented or compartmented tank designs, as shown in fig. 1.1). Figure 1.2 shows a representation of two of the many telemetry records, taken during an early flight (1961), the upper one being the liquid-slosh amplitude in one of the outer LOX tanks and the lower one being the vehicle angular velocity in roll. The early parts of these records, say up to some time just under 100 seconds, are more or less random and of relatively small amplitude. At a flight time of about 100 seconds, however, the amplitudes of both the slosh motion and the roll velocity build up rapidly, with a fairly discrete frequency, for 10 seconds or so, and then begin to decay. The cause of these observed oscillations was attributed to a phase lag in the filter network of the roll control loop that exhibited itself near the frequency of the first rotational sloshing mode of this vehicle. At this particular time in the flight, the liquid level in the tank had dropped to the extent that the baffles provided for the purpose of suppressing sloshing motions were no longer effective and hence the damping of the propellant motions was very low. As the flight continued, the propellant

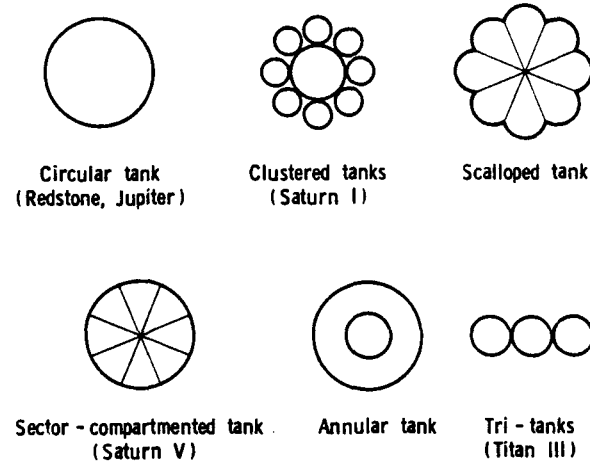


FIGURE 1.1.—Typical launch vehicle tank configurations.

level lowered even farther, to the extent that the slosh masses became quite small and a change in phasing of the liquid motions in the various outer tanks occurred, so that the oscillatory motions then began to damp out. Fortunately, this problem occurred late in the thrust portion of the flight so that the oscillations could not achieve dangerous levels before the propellant tanks became virtually exhausted; even so, there was a premature engine shutdown on this flight, which could have been caused by this oscillatory condition. Certainly, had this situation arisen early in the flight, the consequences might have been severe.

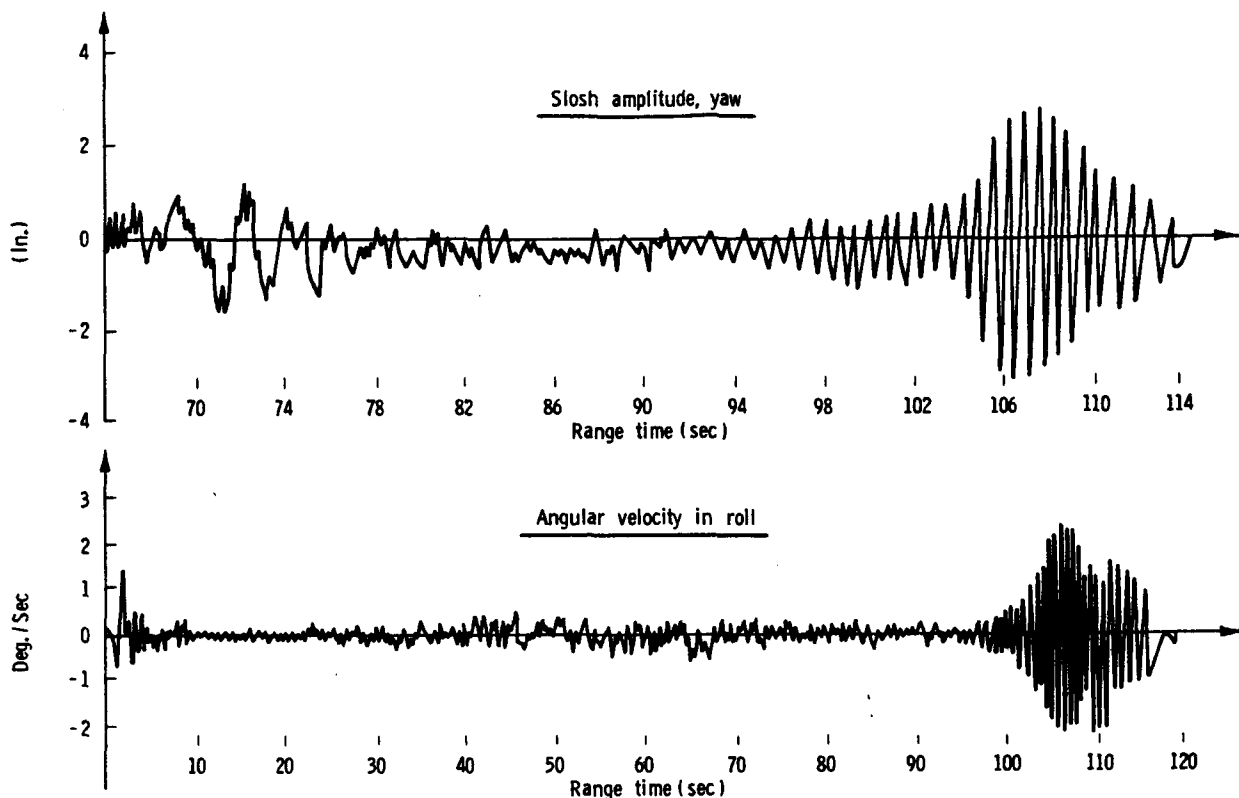


FIGURE 1.2.—Saturn I fuel slosh instability during flight (ref. 1.25).

Of course, as is evident from this discussion, because of the consumption of propellants during flight, significant changes in the various frequencies take place rather rapidly. An idea of these changes may be gained from figure 1.3, which compares behavior in circular and scalloped tanks (ref. 1.26). There are, in fact, many interesting features to these curves, and hence we shall return to them very shortly for some additional discussion.

Generally speaking, we have seen that sloshing of the liquid propellants may interact with both the control system dynamics and the elastic vehicle structural dynamics, each of which may also couple with the other. The liquid-sloshing frequencies are often closer to the rigid body control frequencies than to the elastic body frequencies (see table 1.1) and therefore might ordinarily be the more important problem area; however, the liquid system is subject to some degree of control and, hence, the interaction between the elastic structure and the control system may become

more important. Such control of the liquid dynamic behavior is generally accomplished either by the introduction of various arrangements of baffles intended to provide an adequate degree of damping in the liquid system (fig. 1.4), or by modifying the tank geometry in such a way as to change drastically the liquid frequencies.

In order to examine in further detail the various aspects of this quite complex problem, it should be noted first (from table 1.1) that both the liquid-slosh frequencies and the elastic-body-bending frequencies decrease with increasing tank diameter. Now, we have already seen that for large circular tank vehicles such as Saturn I, the slosh frequencies are so low as to couple with the rigid-body motions; this is seen clearly in the left side of figure 1.3. Successful flight would depend, in this case, upon the provision of adequate damping in the propellant tanks, probably by the use of various arrangements of baffles. Compartmentation, or subdivision, of the tank (fig. 1.1) has a very

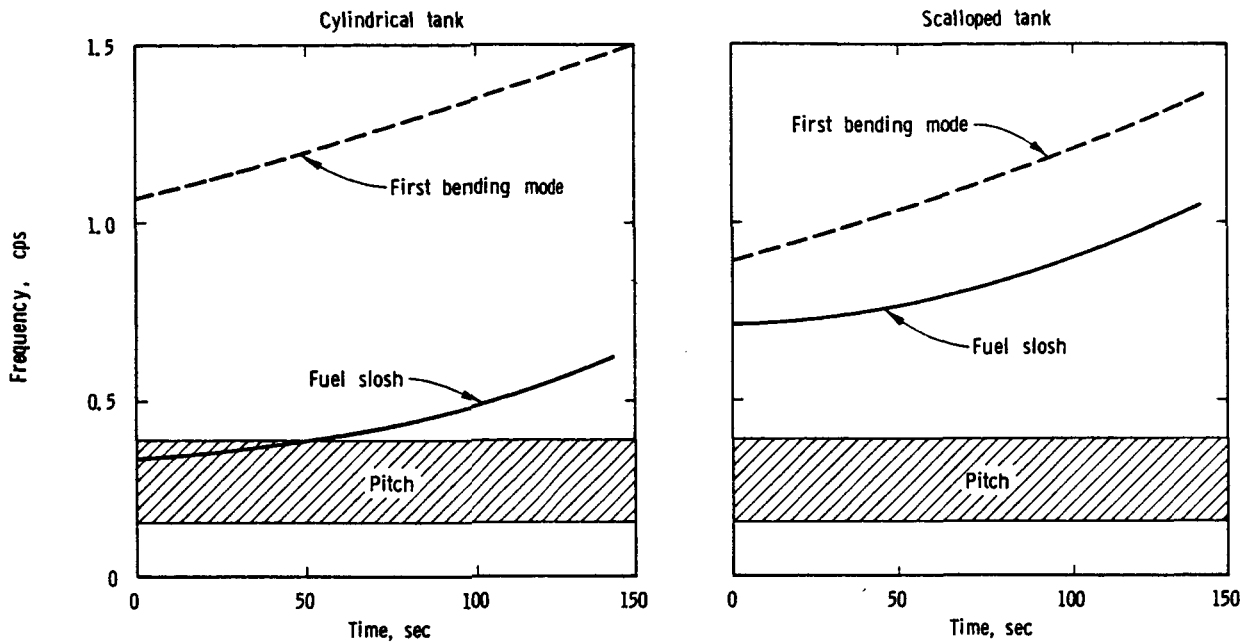


FIGURE 1.3.—Variation of vehicle frequencies with flight time (ref. 1.26).

marked effect in *increasing* the propellant slosh frequencies and, therefore, would appear to be an ideal method of avoiding coupling with the rigid-body motions; the right side of figure 1.3 clearly shows this effect. Unfortunately, however, this solution is not as simple as it seems, for the compartmented tanks usually have substantially reduced elastic bending frequencies (these decreases would probably also cause some changes in the control system design, so that the effects of such changes are by no means isolated unto themselves but form a loop), as compared with the circular tank, and, therefore, coupling between the propellant sloshing and elastic modes may result in large dynamic responses; again, this is indicated in the right side of figure 1.3. There is still another complication that enters this discussion when sector-compartmented tanks are considered: While the lowest slosh frequency is substantially raised by compartmentation, in the sector tank new slosh frequencies are introduced that are not widely spaced, so that the possibility of coupling with the elastic modes may be greatly enhanced.

The question of relative advantages of circular-versus-compartmented-tank configurations is one that has no simple answer. Aside

even from considerations of slosh characteristics and elastic bending frequencies discussed above, one should recognize that the compartmented tank would probably be lighter in weight than its equivalent circular tank (taking into account the weight of baffling required in the latter), but it would probably be considerably more expensive to fabricate.

### 1.3 PROPELLANT MOTIONS IN SPACE VEHICLES

The previous discussion has centered around what might be considered a typical case of liquid propellant sloshing in a large cylindrical tank, the liquid motions being described as arising essentially from lateral motions of the tank. Further considerations of such lateral sloshing are primarily involved with other tank geometries, such as those shown in figure 1.5, which represent only a very few possibilities. Obviously, it is of interest to know the propellant (or other liquid) slosh characteristics in these various kinds of tanks, and in various orientations.

The excitations or tank motions that may lead to propellant sloshing are also quite varied, encompassing a wide system of directions, amplitudes, and frequencies. Thus, the

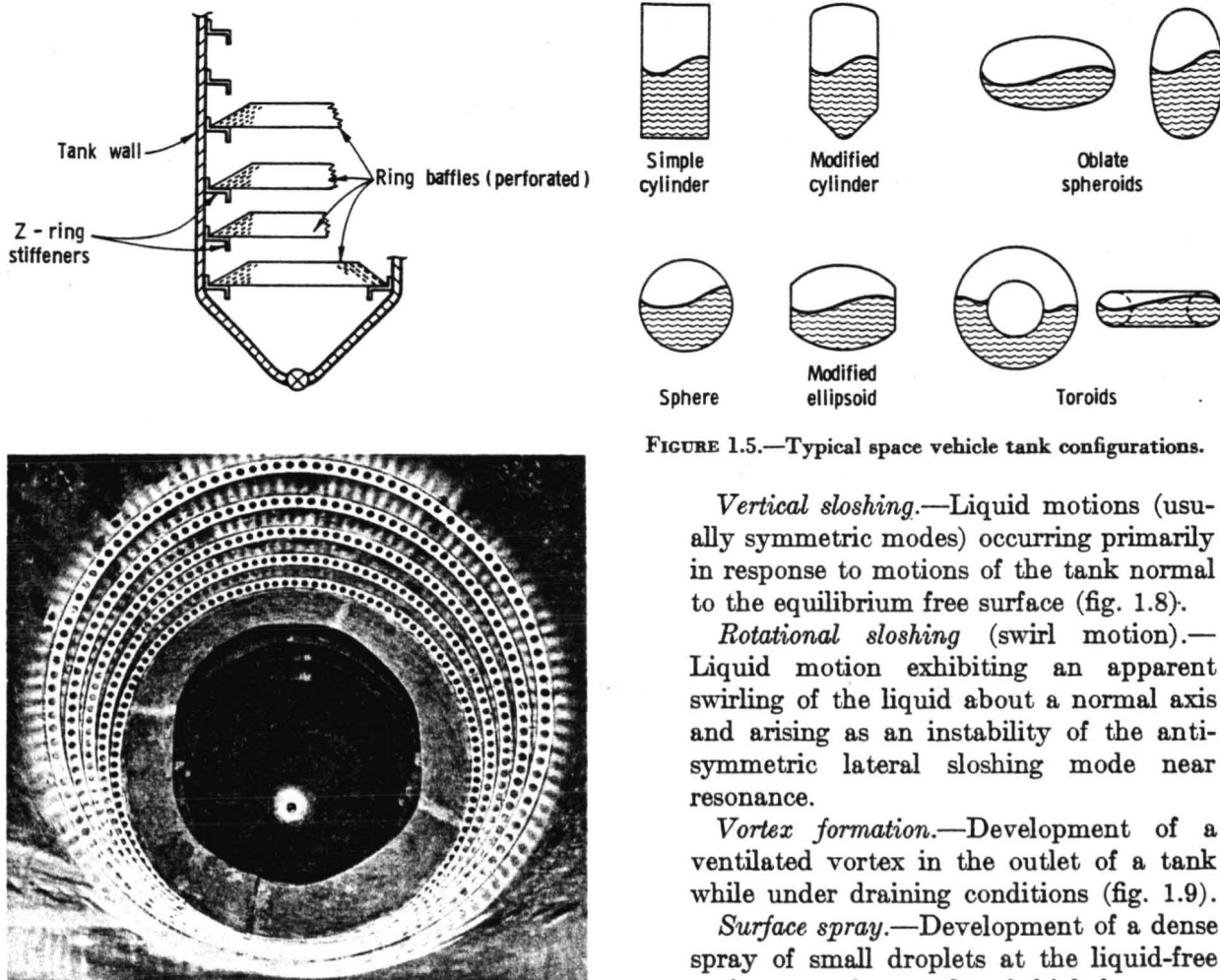


FIGURE 1.4.—Truncated-cone-type ring baffles for suppression of lateral sloshing.

contained liquids can be expected to respond in a variety of ways and, in fact, do exhibit an amazing number of kinds of motions of varying complexity, none of them really simple and all of them difficult to predict and understand (refs. 1.3, 1.4, and 1.27 through 1.30), although not all are of great importance in actual space vehicles. Without going into detail at this time, perhaps it is worthwhile to mention just a few of these:

*Lateral sloshing.*—This is the type of liquid motion (essentially antisymmetric modes) under discussion, occurring primarily in response to translational or pitching motions of the tank (figs. 1.6 and 1.7).

FIGURE 1.5.—Typical space vehicle tank configurations.

*Vertical sloshing.*—Liquid motions (usually symmetric modes) occurring primarily in response to motions of the tank normal to the equilibrium free surface (fig. 1.8).

*Rotational sloshing (swirl motion).*—Liquid motion exhibiting an apparent swirling of the liquid about a normal axis and arising as an instability of the anti-symmetric lateral sloshing mode near resonance.

*Vortex formation.*—Development of a ventilated vortex in the outlet of a tank while under draining conditions (fig. 1.9).

*Surface spray.*—Development of a dense spray of small droplets at the liquid-free surface as the result of high-frequency rigid-body excitation of the tank, or elastic vibrations (fig. 1.10).

*Dome impact.*—Liquid in a partially filled tank, under conditions of abrupt thrust cutoff while in the atmosphere, may impact against the opposing tank bulkhead.

*Low gravity phenomena.*—Under conditions of very low gravity (orbital or interplanetary flight), the liquid behavior is governed primarily by surface tension (and viscous) forces rather than by inertial forces and may be oriented randomly within the tank, depending essentially upon wetting characteristics on the tank wall.

*Docking impact.*—Liquid impact upon a tank bulkhead arising from docking, or other maneuvers in space flight, when the liquid is initially controlled by low gravity conditions.

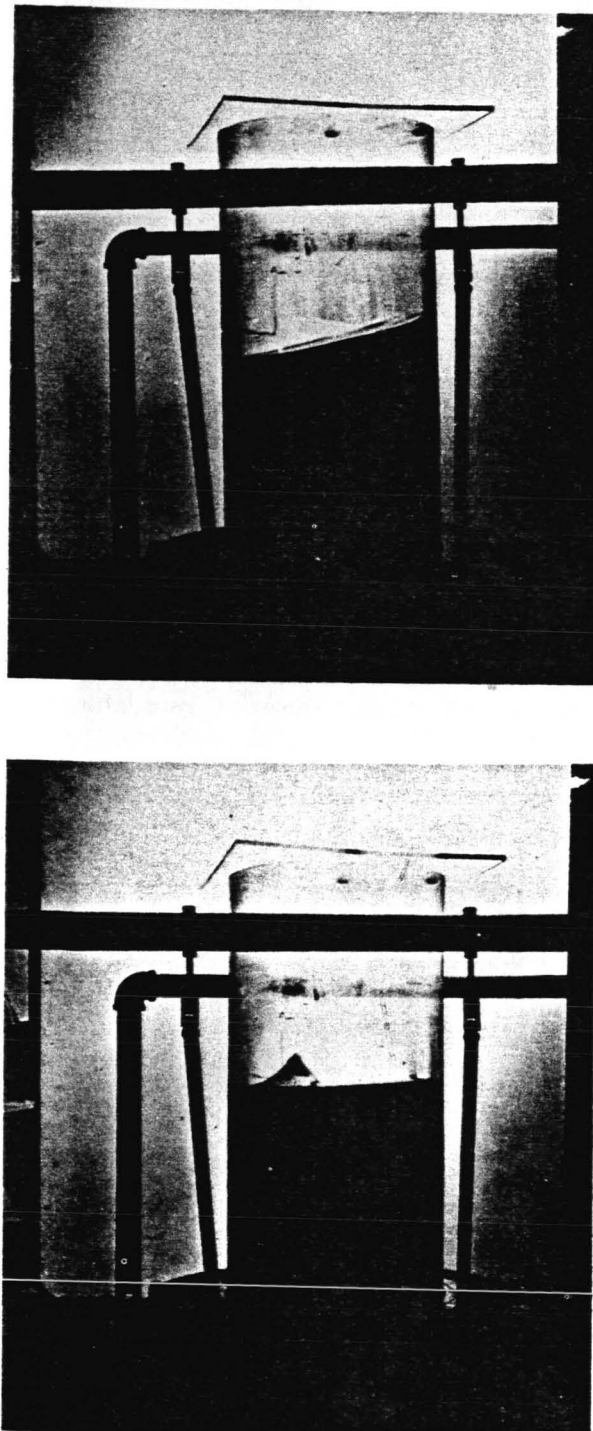


**FIGURE 1.6.**—First two free surface modes of liquid motion in an upright circular cylindrical tank.

The designer must, for each type of liquid motion, understand its behavior and characteristics sufficiently well to analyze its possible

229-648 O--67---2

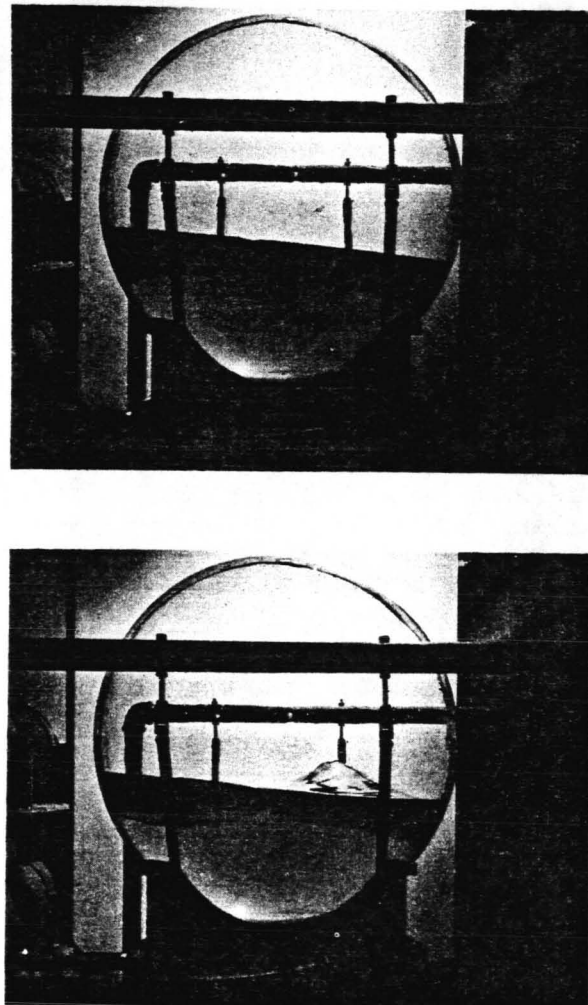


**FIGURE 1.7.**—First two free surface modes of liquid motion in a spherical tank.

interactions with other components of the dynamic system and to provide adequate remedial measures. For each type of tank configuration, orientation, and excitation, the designer requires, among other things, knowledge relating to (a) liquid natural frequencies and mode shapes, (b) forced response characteristics, (c) damping with and without baffles or other suppression devices, and (d) simulation techniques. We shall therefore discuss these various topics in some detail in the following chapters.

#### 1.4 SCOPE OF THE MONOGRAPH

This monograph attempts to present a rather comprehensive view of the general subject, and

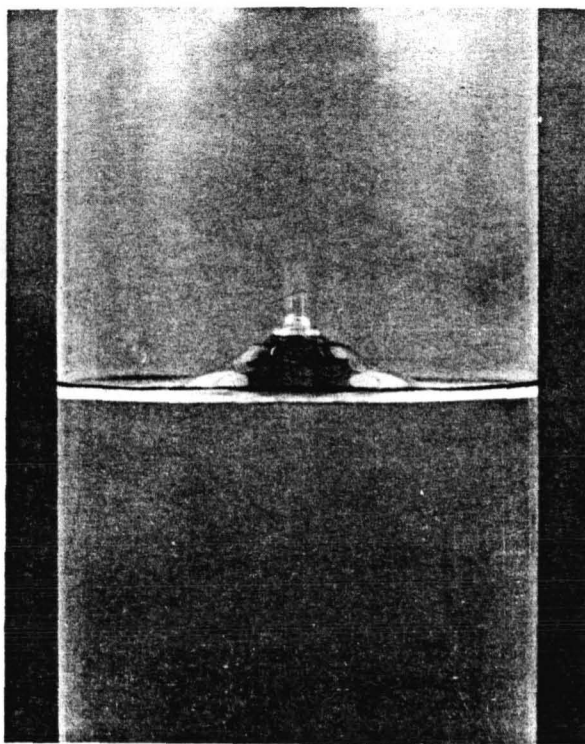


FIGURE 1.8.—Symmetric free surface mode of liquid motion resulting from vertical excitation.

while it is doubtful that any single presentation could be of equal value to students, researchers, analysts, and designers alike, it may be that each of these will at least find here significant quantities of helpful information. Each of the following chapters therefore discusses in detail one or more aspects of the general problem we have outlined in sketchy fashion in this introduction.

Each chapter attempts to give an integrated view of theoretical and experimental data on the particular subject at hand, with some concentration on the presentation of results rather than on the details of procedures; however, general methods of analysis have been outlined where it was felt that these have reasonably wide application, are relatively little known, or may be necessary to have at hand for proper application of the final results of data that are cited. A list of references is also given in each chapter, although, again, no claim is made for completeness. In this connection, it should be remarked that no special effort was made to cite

technical literature other than that readily available in the English language.

The characteristics of lateral sloshing behavior, primarily liquid frequencies, mode shapes, and forced response characteristics, for various container configurations are presented in some detail in chapter 2. The basic elements of the underlying hydrodynamic theory are presented, followed by analytical relationships and calculated and experimental data for a wide variety of cases. Only rigid tanks are considered.

The nonlinear effects rising inherently from particular tank geometries (primarily in the compartmented tank), or as a consequence of large amplitudes of excitation, or from instabilities in the large amplitude motions near resonance (rotational sloshing), are discussed in chapter 3. The first of these, especially, may have important implications for design.

Chapter 4 presents a large quantity of experimental data gained primarily from laboratory investigations of damping characteristics in lateral sloshing in rigid tanks. First, consideration is given to the simple viscous damping effects in various tanks and, second, to the effectiveness of different types of suppression devices. Such devices may take a wide variety of forms, ranging from floating objects and systems which follow the free surface to many types of fixed baffle configurations.

Because so much of our presently available knowledge on this general subject comes as a result of extensive laboratory investigations, the subjects of simulation and experimental techniques are discussed in detail in chapter 5. The subject of similitude by use of small models based on dimensional analysis is presented in some detail, and in rather general terms, which can then be specialized to specific cases. Physical properties of various propellants and other commonly used liquids, as well as a wide variety of potentially useful model liquids, are tabulated in the appendix.

With the force and moment response of the liquid under various conditions of lateral sloshing in rigid tanks fairly well defined in these early chapters, the question then arises of integrating this knowledge into analyses of the overall system dynamic behavior. This is usu-

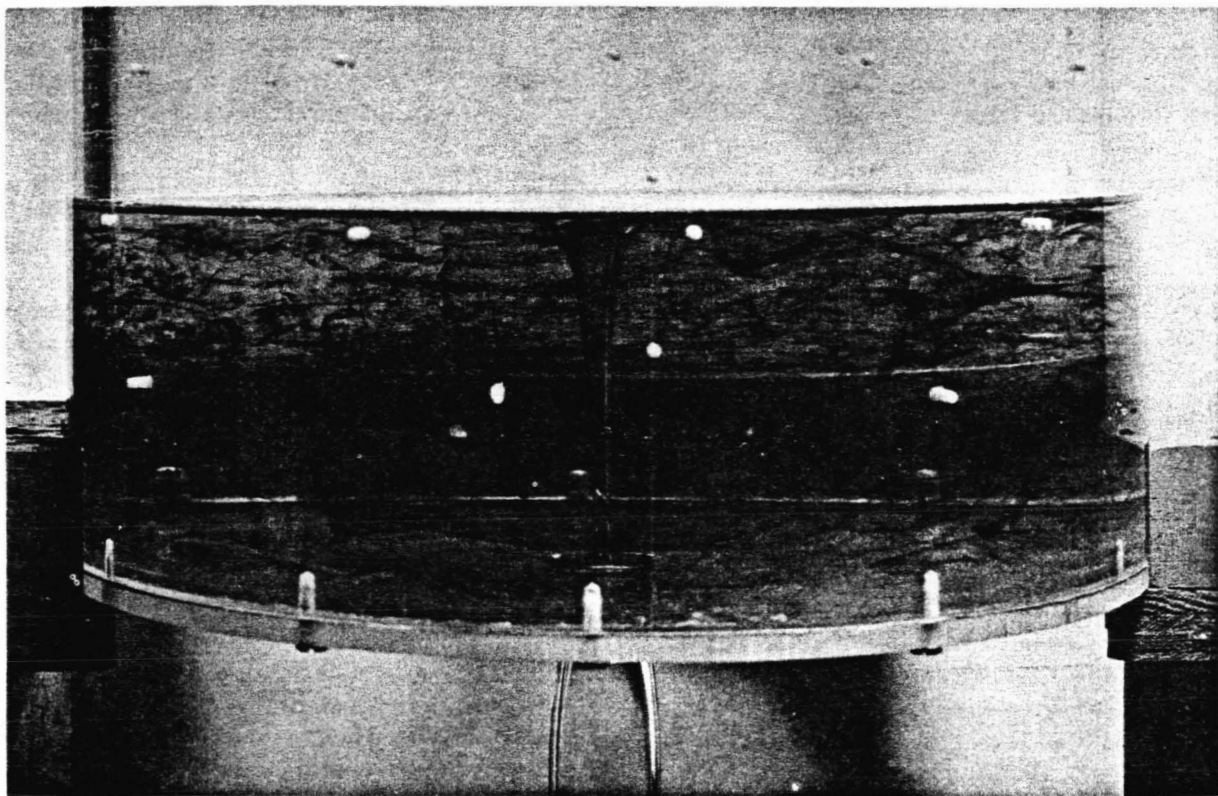


FIGURE 1.9.—Vortex formed during gravity draining of a tank.

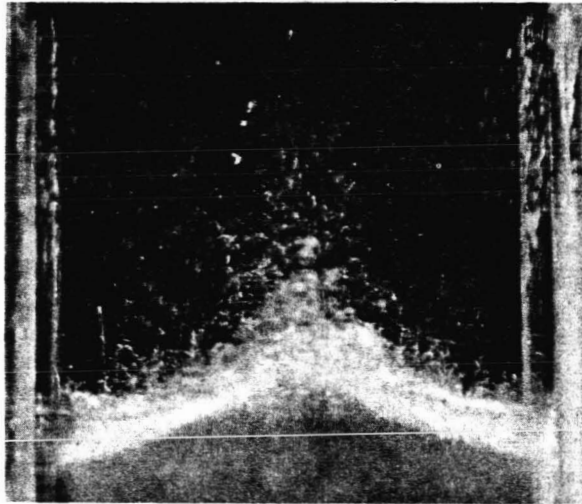


FIGURE 1.10.—Surface spray resulting from high frequency vertical excitation.

ally accomplished by first devising appropriate equivalent (mathematical) mechanical models composed of sets of simple spring-mass-dashpot (or pendulum) elements, which can then be

combined with similar representations for other dynamic components of the vehicle, and then the overall system dynamic behavior can be analyzed by analog or digital techniques. Various types of equivalent mechanical models are derived and discussed in chapter 6, including both very simple and relatively complex ones. The general subject of vehicle stability and control is then treated in chapter 7, demonstrating how various of the analyses and data are integrated; elastic body effects, however, are not yet included.

The various, and interesting, aspects of liquid behavior in response to vertical excitations of the tank are discussed in chapter 8. The first topic is that of subharmonic response (i.e., liquid response with a frequency *less* than that of the excitation) of the liquid surface to fairly low frequency excitations, with detailed comparisons made between theory and the results of laboratory experiments. The second topic relates to liquid spray formed at the free surface because of relatively high frequency

excitation; the third topic relates to certain interesting aspects of bubble dynamics and cavitation that have been observed in laboratory studies.

Chapter 9 now brings into focus some of the effects rising from the elasticity of the containers. The first point of discussion is that of the influence of the liquid in modifying the vibration characteristics of the elastic shell, without considering any significant coupling and primarily as a result only of the added mass. Both bending- and breathing-type vibrations are considered. Next, the coupled problem is considered and interesting forms of liquid response induced by tank wall elastic vibrations (observed in the laboratory) are discussed. The influence of the elastic bottom of the tank, with regard to the vertical sloshing problems discussed in chapter 8, is then discussed. Finally, the effects of body-bending flexibility on the general problem of vehicle stability and control, for which the rigid-body case was presented in chapter 7, are outlined.

Three interesting but unrelated topics that seem to warrant some presentation, although slightly apart from the bulk of the material presented in this monograph, are collected together in chapter 10. The problem of dome impact is presented first, and while such a

problem actually arose during one phase of development of the Redstone missile, the importance of this problem in launch-abort situations and the closely related one of orbital maneuvering and docking is not yet fully established. Vortex formation is an interesting phenomenon, but one which can be suppressed quite simply in most cases by baffling the tank outlets, and is therefore discussed only briefly. The Titan II launch vehicle, in the early stages of its flight test program, exhibited rather severe longitudinal oscillations of the entire system, now often called "pogo" oscillations. The liquid systems and the elastic structure were quite well coupled and, together with the combustion system, formed a closed loop. While not solely a problem of liquid dynamic response, it was felt that the phenomenon was of sufficient importance to warrant a brief presentation.

The various complex and important behavior of liquids under conditions of low and zero gravity are discussed in detail in chapter 11, the concluding chapter of this monograph. Means of simulating such behavior in laboratory experiments are especially treated in some detail, as are the various techniques for controlling the location and orientation of liquids within tanks subject to the weightless condition of the space environment.

#### REFERENCES

- 1.1. SLOANE, MARGARET N.: The Dynamics of the Sloshing Phenomenon (a Literature Survey). Rept. GM-60-5111-5, Space Technology Laboratories, Inc., Apr. 1960.
- 1.2. COOPER, R. M.: Dynamics of Liquids in Moving Containers. *ARS J.*, vol. 30, Aug. 1960, pp. 725-729.
- 1.3. ABRAMSON, H. NORMAN: Dynamic Behavior of Liquids in Moving Containers. *Appl. Mech. Revs.*, vol. 16, No. 7, July 1963, pp. 501-506.
- 1.4. ABRAMSON, H. NORMAN: Some Current Aspects of the Dynamic Behavior of Liquids in Rocket Propellant Tanks. *Applied Mechanics Surveys*, Spartan Books, Inc., Washington, D.C., 1966.
- 1.5. LAMB, H.: *Hydrodynamics*. Sixth ed. Dover Publications, New York, 1945.
- 1.6. GOLDSBOROUGH, G. R.: The Tidal Oscillations in an Elliptic Basin of Variable Depth. *Proc. Roy. Soc. (London)*, A, 130, 1930, pp. 157-167.
- 1.7. VANONI, V. A.; AND CARR, J. H.: Harbor Surging. *Proc. First Conf. Coastal Engineering*, Long Beach, Calif., 1951, pp. 60-68.
- 1.8. PENNEY, W. G.; AND PRICE, A. T.: Some Gravity Wave Problems in the Motion of Perfect Fluids. Part II. Finite Periodic Stationary Gravity Waves in a Perfect Liquid. *Phil. Trans. Roy. Soc. London*, A, 244, 1952, p. 254.
- 1.9. WESTERGAARD, H. M.: Water Pressure on Dams During Earthquakes. *Trans. Am. Soc. Civil Engineers*, vol. 98, 1933, pp. 418-472.
- 1.10. JACOBSEN, L. S.: Impulsive Hydrodynamics of Fluid Inside a Cylindrical Tank and of Fluid Surrounding a Cylindrical Pier. *Bull. Seism. Soc. Am.*, vol. 39, 1949, pp. 189-204.
- 1.11. WERNER, P. W.; AND SUNDQUIST, K. J.: On Hydrodynamic Earthquake Effects. *Trans. Am. Geophysical Union*, vol. 30, no. 5, Oct. 1949, pp. 636-657.

- 1.12. JACOBSEN, L. S.; AND AYRE, R. S.: Hydrodynamic Experiments With Rigid Cylindrical Tanks Subjected to Transient Motions. *Bull. Seism. Soc. Am.*, vol. 41, 1951, pp. 313-346.
- 1.13. HOUSNER, G. W.: Dynamic Pressures on Accelerated Fluid Containers. *Bull. Seism. Soc. Am.*, vol. 47, 1957, pp. 15-35.
- 1.14. CLOUGH, R. W.: Effects of Earthquakes on Underwater Structures. *Proc. Second World Conf. Earthquake Engineering*, Japan, 1960, pp. 815-831.
- 1.15. BLAGOVESHCHENSKY, S. N.: Theory of Ship Motions. English ed. Dover Publications, New York, 1962.
- 1.16. VASTA, J.; GIDDINGS, A. J.; TAPLIN, A.; AND STILLWELL, J. J.: Roll Stabilization by Means of Passive Tanks. *Trans. SNAME*, vol. 69, 1961, pp. 411-460.
- 1.17. SEWALL, J. L.: An Experimental and Theoretical Study of the Effect of Fuel on Pitching-Translation Flutter. *NACA TN 4166*, Dec. 1957.
- 1.18. GRAHAM, E. W.; AND RODRIGUEZ, A. M.: The Characteristics of Fuel Motion Which Affect Airplane Dynamics. *J. Appl. Mech.*, vol. 19, Sept. 1952, pp. 381-388.
- 1.19. STEWARTSON, K.: On the Stability of a Spinning Top Containing Liquid. *J. Fluid Mech.*, vol. 5, part 4, 1959.
- 1.20. SCOTT, W. E.: The Free Flight Stability of a Liquid Filled, Spinning Shell. *BRL Repts. 1120, 1135, 1233*, Aberdeen Proving Ground, Md.
- 1.21. MILES, J. W.: Free Surface Oscillations in a Rotating Liquid. *Journal of Physics of Fluids*, vol. 2, no. 3, May-June 1959, pp. 297-305.
- 1.22. WINCH, D. M.: An Investigation of the Liquid Level at the Wall of a Spinning Tank. *NASA TN D-1536*, Aug. 1962.
- 1.23. BARON, M. L.; AND BLEICH, H.: The Dynamic Analysis of Empty and Partially Full Cylindrical Tanks, Part II—Analysis of Uplift and Structural Damage. *DASA Rept. 1123B*, Sept. 1959.
- 1.24. GEISSLER, E. D.: Problems of Attitude Stabilization of Large Guided Missiles. *Aerospace Engineering*, vol. 19, Oct. 1960, pp. 24-29, 68-71.
- 1.25. Saturn SA-1 Flight Evaluation. *Rept. MPR-SAT-WF-61-8*, NASA MSFC, Dec. 1961.
- 1.26. BISPLINGHOFF, RAYMOND L.; AND MICHEL, DOUGLAS: Some Structural Dynamic Problems of Space Vehicles. *Japan Society of Aeronautical and Space Sciences*, Tokyo, Nov. 1963.
- 1.27. ABRAMSON, H. NORMAN: Amazing Motions of Liquid Propellants. *Astronautics*, vol. 6, Mar. 1961, pp. 35-37.
- 1.28. ABRAMSON, H. NORMAN: Liquid Dynamic Behavior in Rocket Propellant Tanks. *Proc. ONR/AIA Symposium on Structural Dynamics of High Speed Flight* (Los Angeles), Apr. 1961, pp. 287-318.
- 1.29. MOISEYEV, N. N.; MYSHKIS, A. D.; AND PETROV, A. A.: On the Problems of Hydrodynamics in Cosmonautics. *XVth International Astronautical Congress* (Warsaw), Sept. 1964.
- 1.30. GLUCK, D. F.; AND GILLE, J. P.: Fluid Mechanics of Zero-G Propellant Transfer in Spacecraft Propulsion Systems. *ASME Journal of Engineering for Industry*, Feb. 1965, pp. 1-7.

# Lateral Sloshing in Moving Containers

*Sandor Silverman and H. Norman Abramson*

## 2.1 MATHEMATICAL BACKGROUND

We have discussed in chapter 1 how lateral sloshing of propellants or other liquids may be induced in a rocket or space vehicle and why it is of importance. We shall present, in this chapter, theoretical and experimental results pertaining to undamped liquid sloshing behavior in rigid containers. Obviously, any attempt to repeat details of the mathematical developments leading to these results would be far too voluminous to permit incorporation in a monograph of this type. Further, while the detailed manipulations for any specific tank geometry are quite tedious, the principal mathematical problem of finding a solution to the boundary-value problem for Laplace's equation is straightforward and relatively well known. The natural frequencies, mode shapes, potential functions, free surface displacements, and forces and moments are given for a variety of container geometries. In the case of forced motion, the forcing function is assumed to be of the form  $e^{i\omega t}$ . Solutions for arbitrary tank motions may be obtained from harmonic solutions by using Fourier series or Fourier integral techniques, and while some analyses of liquid behavior in containers subjected to impulsive motion have been performed (see ref. 2.1 for specific references), they are not of governing importance for this monograph.

During sloshing in a cylindrical container, the lower part of the liquid performs oscillations as though it were a rigid body and only the liquid in the vicinity of the free surface moves independently; as the frequency of oscillation of the free surface increases, the motion penetrates less deeply into the liquid. For liquid depth to diameter  $h/d > 1$ , the liquid natural frequencies may be considered to be independent of the

liquid depth, as will be shown later. For containers of symmetric cross section, the frequencies of primary interest are the lowest few corresponding to the first few antisymmetric mode shapes. It is intuitively clear that the symmetric liquid mode shapes do not cause any resultant lateral forces and moments to act on the container; they can, however, couple with the elastic container and lead to other interesting aspects of the overall problem. (This general subject will be discussed in detail in ch. 8.) In the case of a circular cylindrical tank, the orthogonality condition for trigonometric functions insures that antisymmetric motion is the only class of motion which contributes to the net horizontal force and moment exerted by the liquid on the container (refs. 2.1 and 2.2).

Several methods have been employed to minimize the effects of liquid motion. Baffles of various configurations have been devised which add a small amount of damping to the system and mainly affect the magnitude of the slosh forces and the amplitude of the liquid motion. (See ch. 4.) If a shift in the range of the fluid natural frequencies is desired, a more effective method is to divide the tank into subtanks by means of radial or concentric walls, which has led to interest in the ring sector tank and its variations (sec. 2.3). Bauer (refs. 2.3 to 2.5) has shown theoretically that compartmentation of a cylindrical tank into sectors has the effect of raising the first natural frequency and lowering the second so that these two frequencies are not widely separated, as has been confirmed experimentally (refs. 2.6 to 2.8). These experiments have also indicated that: (a) radial compartmentation with solid walls does not reduce the slosh forces as much as do ordinary ring baffles, and (b) there is a marked

dependence of liquid natural frequency on excitation amplitude. (Such nonlinear effects will be discussed in more detail in ch. 3.)

The cylindrical tank with an annular cross section has also been investigated theoretically in reference 2.2, but experimental verification of this theory is not yet available. The attractiveness of this tank configuration resides in the wide separation between frequencies of the inner and outer compartments and in the fact that phasing of the liquid motions between the two compartments results in a lower total force.

Eulitz (refs. 2.9 and 2.10) has suggested that sloshing be avoided by using an experimentally based analytical method. Virtually countless other schemes for the suppression of sloshing have been proposed at one time or another, but we shall not recount them here.

In general, very good agreement between theory and experimental observations has been obtained for lateral sloshing. Wall-pressure distributions have been obtained from sloshing experiments with rigid model cylindrical tanks having flat bottoms (ref. 2.11), and it has been found that the total force and moment obtained by integration of the pressure distributions are in good agreement with theory. Sloshing behavior in tanks with conical bottoms can be represented by sloshing behavior in a tank with an equivalent flat bottom (based on equal liquid volumes); this conclusion appears to be valid at least through the second mode and possibly through the third, and implies that a similar technique may be applied (with caution) to tanks of other bottom geometries (ref. 2.12).

A few general theoretical analyses for predicting natural frequencies of fluids in containers of various shapes are available (refs. 2.13 and 2.14). Lamb (ref. 2.13) discusses the elliptic canal in section 291, the parabolic container in section 193 (tidal wave theory), and the 45° conical canal in section 258. Troesch (ref. 2.14) discusses the conical tank and the hyperboloid, and also presents graphs of container cross sections which were obtained using an inverse technique. It is interesting to note that Troesch found that the fundamental frequency for a container which looks very much like a cone differs from that of a cone by 25 percent, indicating that the eigenvalue can

be quite sensitive to changes in container shapes. Somewhat different results are indicated in reference 2.15 for a cylindrical container with elliptical cross section, in which it was determined that the effect of small tank ellipticity on the natural frequencies is small. It is seen from this discussion that it is difficult to draw general conclusions about the behavior of liquids in containers. Further references on containers of various shapes are given in references 2.1 and 2.16.

### Basic Theory: Assumptions

An "exact" solution to the general problem of fluid oscillations in a moving container is extremely difficult. The simplifying assumptions that are generally employed in such a theoretical analysis and which are employed in this chapter are as follows (some of these will be relaxed in following chapters):

Rigid tank	Irrotational flow field
Nonviscous fluid	Homogeneous fluid
Incompressible fluid	No sinks or sources
Small displacements, velocities, and slopes of the liquid-free sur- face	

Since the question of interaction between the liquid and the elastic tank is an exceedingly complex one, we shall assume for present purposes that the tank is rigid. (Interaction problems will be discussed in ch. 9.) For unbaffled tanks of relatively large proportions, the viscous forces of the fuel may be neglected as being small compared to other forces, which is a very accurate assumption except in a small region near the boundary. The assumption that the fluid is incompressible seems to be generally valid for the fuels and liquids in current use.

The liquid free surface displacements, slopes, and velocities are assumed small, which linearizes the boundary conditions at the free surface. Some discussion of the significance of the linearization of the boundary condition is given in references 2.13 and 2.17. Briefly, two non-linear boundary conditions must be satisfied at the free surface; by employing the above-mentioned assumption, these two conditions are linearized and combined to give only a single condition.

The assumption of irrotational flow is compatible with the assumption of zero viscosity since, as is well known, motion in a nonviscous fluid which is irrotational at one instant always remains irrotational (ref. 2.17). This assumption, along with the linearized boundary conditions, yields a theory which can be employed for the analysis of several practical container geometries.

The assumption of no sinks or sources, keeping in mind the assumed incompressibility of the liquid, requires that the liquid volume be constant; therefore, for example, the theory may not be valid for a rapidly draining tank. This is discussed further in chapter 10.

### Basic Theory: Analysis

It will be found convenient in this chapter to employ either rectangular or circular cylindrical coordinates located at various points in the container. Unless otherwise stated, the coordinates will be located on the undisturbed liquid surface, with the  $x$  and  $y$  axes in the plane of the surface and the  $z$  coordinate normal to the surface. The assumption of irrotational flow insures the existence of a single-valued velocity potential  $\Phi(x, y, z, t)$  in any simply connected region, from which the velocity field can be derived by taking the gradient (it should be noted that some authors prefer to define the velocity as the negative of  $\nabla\Phi$ )

$$\vec{V} = \nabla\Phi \quad (2.1)$$

or in terms of the components of the velocity vector,  $V$  (in rectangular coordinates)

$$u = \frac{\partial\Phi}{\partial x}, \quad v = \frac{\partial\Phi}{\partial y}, \quad w = \frac{\partial\Phi}{\partial z} \quad (2.2)$$

The vector statement of Newton's second law of motion for a particle in a nonviscous fluid is

$$-\frac{1}{\rho}\nabla p + \vec{F}_B = \vec{A} \quad (2.3)$$

where  $\rho$  is the mass density,  $p$  is the intensity of normal pressures,  $F_B$  is the body force vector, and  $A$  the acceleration vector. By noting the fact that

$$\frac{d(\cdot)}{dt} = u \frac{\partial(\cdot)}{\partial x} + v \frac{\partial(\cdot)}{\partial y} + w \frac{\partial(\cdot)}{\partial z} + \frac{\partial(\cdot)}{\partial t} \quad (2.4)$$

the above equations may be rewritten

$$\begin{aligned} \frac{\partial u}{\partial t} + u \frac{\partial u}{\partial x} + v \frac{\partial u}{\partial y} + w \frac{\partial u}{\partial z} &= -\frac{1}{\rho} \frac{\partial p}{\partial x} \\ \frac{\partial v}{\partial t} + u \frac{\partial v}{\partial x} + v \frac{\partial v}{\partial y} + w \frac{\partial v}{\partial z} &= -\frac{1}{\rho} \frac{\partial p}{\partial y} \\ \frac{\partial w}{\partial t} + u \frac{\partial w}{\partial x} + v \frac{\partial w}{\partial y} + w \frac{\partial w}{\partial z} &= -\frac{1}{\rho} \frac{\partial p}{\partial z} - A \end{aligned} \quad (2.5)$$

where it has been assumed that the only body force present is due to the acceleration field. The continuity of the fluid (mass conservation law) must be preserved. Enforcing this requirement, and noting the assumption of incompressibility, we have

$$\nabla \cdot V = 0 \quad (2.6)$$

Equations (2.5) and (2.6) are sufficient, once appropriate initial and boundary conditions are imposed, to determine the velocity components  $u$ ,  $v$ , and  $w$  and the pressure,  $p$ , uniquely.

Substituting equation (2.1) into equation (2.6), it is seen that  $\Phi$  must satisfy the Laplace equation:

$$\nabla^2 \Phi = \frac{\partial^2 \Phi}{\partial x^2} + \frac{\partial^2 \Phi}{\partial y^2} + \frac{\partial^2 \Phi}{\partial z^2} = 0 \quad (2.7)$$

where  $\nabla^2$  is given in the above equation in rectangular coordinates.

By noting that the flow is irrotational and  $\rho = \text{constant}$ , the equations of motion (2.5) may be integrated and then linearized to obtain Bernoulli's law (the integration function is absorbed in the definition of  $\Phi$  with no loss in generality, cf. ref. 2.17)

$$\frac{\partial \Phi}{\partial t} + \frac{1}{\rho} p + gz = 0 \quad (2.8)$$

where the acceleration field has been specialized to that of gravitation. Thus,  $\Phi$  is determined from equation (2.7) and appropriate boundary conditions, the velocity components from equation (2.1), and the pressure distribution from equation (2.8). The free surface displacement is obtained from equation (2.10) to be derived below (the pressure at the free surface is usually considered to be zero), while the forces and moments acting on the container may be found

by appropriate integrations of the pressure. (See, for example, sec. 2.3.)

It is often convenient to write the velocity potential as the sum of the potential of the container motion,  $\phi_c$ , and the potential of the liquid moving relative to the container,  $\Phi_1$ . That is

$$\Phi = \phi_c + \Phi_1$$

If the container is stationary,  $\phi_c = 0$ , while if the container is in motion  $\phi_c$  can be found by integrating the equation

$$\nabla \phi_c = V \text{ (container)} \rightarrow$$

and the constant of integration may be taken as zero, since it can be absorbed in  $\Phi_1$ . The potential  $\phi_c$  is independent of container geometry and has been evaluated for roll, pitch, and translational motion of the container (ref. 2.18). It should be noted that  $\phi_c$  satisfies the Laplace equation for pitch and translation, but not for roll motions of the container. In this latter case, the sum of  $\phi_c + \Phi_1$  is made to satisfy the Laplace equation by making  $\Phi_1$  the solution of a Poisson equation.

A complete discussion of the derivation of the above equations may be found in references 2.17 and 2.19. Reference 2.17 should also be consulted for an excellent discussion of the boundary conditions which are simply stated in linearized form below.

At the container walls

$$\frac{\partial \Phi}{\partial n} = v_n \quad (2.9)$$

where  $\partial/\partial n$  denotes differentiation in the direction normal to the surface of a rigid body in contact with the fluid, and  $v_n$  is the common velocity of the fluid and boundary surface in the direction normal to the surface. Imposing Bernoulli's law and the condition that the fluid particles must stay on the surface, and then linearizing the results, leads to the equations describing the free surface

$$\begin{aligned} \frac{\partial \Phi}{\partial t} + g\delta &= -\frac{1}{\rho} p_0 \\ \frac{\partial \delta}{\partial t} - \frac{\partial \Phi}{\partial z} &= 0 \end{aligned} \quad (2.10)$$

where  $z = \delta(x, y, t)$  is the equation of the free surface, and  $p_0(x, y, t)$  is the surface pressure.

By eliminating  $\delta$  between these two relations, a single equation for  $\Phi$  is obtained as

$$\frac{\partial^2 \Phi}{\partial t^2} + g \frac{\partial \Phi}{\partial z} = -\frac{1}{\rho} \frac{\partial p_0}{\partial t} \quad (2.11a)$$

For most cases, it is assumed that  $p_0 = \text{constant}$ , so that

$$\frac{\partial^2 \Phi}{\partial t^2} + g \frac{\partial \Phi}{\partial z} = 0 \quad (2.11b)$$

In the case of pitching motions of an accelerating vehicle, the free surface condition is (ref. 2.20)

$$\rho \frac{\partial^2 \Phi_1}{\partial t^2} + \rho A_r \frac{\partial \Phi_1}{\partial z} + \rho A_r x \frac{\partial \theta_y}{\partial t} - \rho A_r y \frac{\partial \theta_x}{\partial t} = 0 \quad (2.12)$$

where  $\theta_x$  and  $\theta_y$  are the pitch angles about the  $x$  and  $y$  axes as shown in figure 2.1,  $A$  is the total acceleration in the  $z$  direction,  $A_r$  is the acceleration in the  $z$  direction due to thrust, and  $A = A_r + g$ . For a ground test, the acceleration of the vehicle due to thrust is zero so that  $A_r = 0$ ,  $A = g$ . For pitching motions during launch, the effect of the gravitational field may be neglected so that the body force is due entirely to the thrust and the inertia force due to gravity and the body force due to gravity cancel each other; therefore,  $g = 0$  and  $A = A_r$ . For oscillations given by  $\theta_y = |\theta_y| e^{i\omega t}$ ,  $\theta_x = |\theta_x| e^{i\omega t}$ , the free surface condition given above may be simplified by the transformation

$$\Phi_1 = \phi_2 + \phi_3 + A_r x \left( \frac{-\theta_y}{i\omega} \right) + A_r y \left( \frac{\theta_x}{i\omega} \right)$$

where  $\phi_2$  and  $\phi_3$  satisfy the free surface condition

$$\frac{\partial^2 \phi}{\partial t^2} + A \frac{\partial \phi}{\partial z} = 0$$

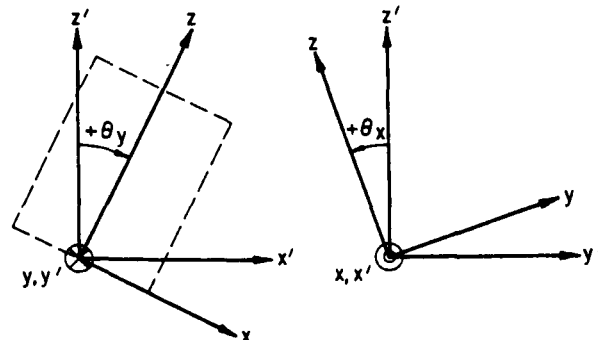


FIGURE 2.1.—Coordinates for accelerating tank.

For the case of no pitching motion, equation (2.12) reduces to

$$\frac{\partial^2 \phi_1}{\partial t^2} + A \frac{\partial \phi_1}{\partial z} = 0$$

which is equivalent to equation (2.11b).

The foregoing linear boundary value problem is generally solved by employing the classical method of separation of variables, and much information concerning the behavior of liquids in moving containers has been obtained for several practical container geometries, including the compartmented cylindrical tank.

In addition to the technique of separation of variables, several other methods have been employed to analyze lateral sloshing of liquids in containers. Budiansky (ref. 2.21) used a sophisticated integral equation technique to find the natural frequencies and slosh forces in the cases of a half full, and nearly full spherical container and a circular canal filled to an arbitrary depth. Lawrence, Wang, and Reddy (ref. 2.22) have shown that the problem of finding a velocity potential  $\Phi$  which satisfies the equations (2.7), (2.9), and (2.11b) ( $v_n=0$  in eq. (2.9)) is equivalent to finding a velocity potential which makes an integral an extremum. This conclusion is significant in that not only is the governing differential equation automatically satisfied, but all necessary boundary conditions are also. The velocity potential may be obtained approximately by employing the Rayleigh-Ritz technique. This technique has been used rather extensively (refs. 2.22 to 2.25). Troesch (ref. 2.14) employed an inverse technique to find the natural frequencies and obtained results for several interesting geometries; he also gave an interesting discussion of the relationship between container geometry and liquid natural frequencies. It was shown, for example, that if two containers have the same free surface and if one is completely contained in the other, then the smaller container possesses the smaller eigenvalue. Ehrlich (ref. 2.26) investigated the finite difference technique applied to obtaining the fundamental frequency in axisymmetric fluid-filled containers of arbitrary bottom geometry.

## 2.2 RECTANGULAR TANK

### Natural Frequencies

The mode shapes and frequencies in a rectangular tank (see fig. 2.2) are given by Lamb (ref. 2.13, sec. 257)

$$\delta = \sum_{m=0}^{\infty} \sum_{n=0}^{\infty} A_{mn} \cos \left[ \frac{m\pi}{a} \left( x + \frac{a}{2} \right) \right] \times \cos \left[ \frac{n\pi}{b} \left( y + \frac{b}{2} \right) \right] \quad (2.13a)$$

$$\omega_{mn}^2 = gk \tanh(kh) \quad (2.13b)$$

where

$$k^2 = \pi^2 \left( \frac{m^2}{a^2} + \frac{n^2}{b^2} \right)$$

$m, n$  are integers ranging from 0 to  $\infty$ , and  $\delta$  is the elevation of the liquid above the reference level  $z=h/2$ . If  $a > b$ , the lowest frequency of interest is obtained by letting  $m=1, n=0$

$$\omega_{10}^2 = \frac{g\pi}{a} \tanh \left( \pi \frac{h}{a} \right) \quad (2.13c)$$

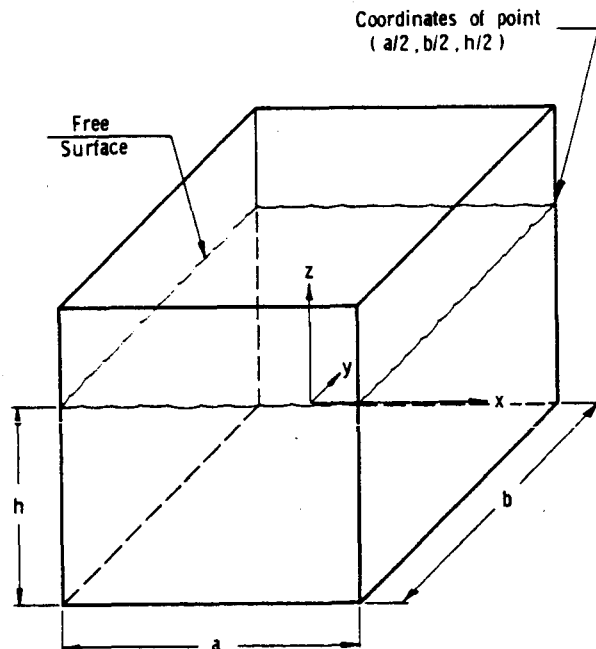


FIGURE 2.2.—Coordinate system and tank geometry for rectangular tank.

The higher frequencies may be obtained from equation (2.13b) once the dimensions  $a$  and  $b$  are known. If  $kh$  is small, equation (2.13b) may be approximated by

$$\omega_{mn}^2 = k^2 gh \quad (2.13d)$$

Eide (ref. 2.27) has presented the results of an analytical investigation of the problem of the variation of pitch motion of a vehicle under low inertial forces due to fuel sloshing in a rectangular tank. He assumed that the forces due to thrust, rotation, and capillary action are of the same order of magnitude, and that they are all much greater than the Coriolis force, and then determined the velocity potential and frequency of the free surface oscillation generated by an impulsive torque. The equations of motion derived for the rotation of a vehicle containing a large amount of liquid were then investigated to determine the general behavior of the vehicle and the stability of the free surface motion. Because of the specific

application of this analysis to low gravity problems, it will be discussed further in chapter 11.

### Forced Oscillations

The response of a fluid to simple harmonic motions of the tank in translation, pitching, and yawing is given in reference 2.28. This paper is a condensation of reference 2.29, which contains a more detailed discussion, in addition to the solution of arbitrary tank motions through the use of Laplace transforms. The assumptions listed in section 2.1 are employed, with the additional condition that the angle of container rotation during pitch is small.

#### Horizontal Motion Parallel to $x$ -Axis

The velocity potential, the horizontal force on the container in the  $x$ -direction, and the moment acting on the container about the  $y$  axis (positive moments are given by the "right-hand" sign convention) for a displacement of the container given by  $x(t) = x_0 \sin(\Omega t)$  are as follows:

$$\Phi = +x_0 \Omega \cos \Omega t \left\{ x + \sum_{n=0}^{\infty} (-1)^n \frac{4a}{\pi^2(2n+1)^2} \left( \frac{\Omega^2}{\omega_n^2 - \Omega^2} \right) \times \frac{\sin \left[ (2n+1) \frac{\pi}{a} x \right] \cosh \left[ (2n+1) \frac{\pi}{a} \left( z + \frac{h}{2} \right) \right]}{\cosh \left[ (2n+1) \pi \frac{h}{a} \right]} \right\} \quad (2.14a)$$

$$\frac{F_H}{W_F} = \frac{x_0}{h} f^2 \sin \Omega t \left\{ 1 + \sum_{n=0}^{\infty} \frac{8 \tanh [(2n+1)\pi r_1]}{\pi^3 (2n+1)^3 r_1} \frac{1}{\left( \frac{f_n}{f} \right)^2 - 1} \right\} \quad (2.14b)$$

$$\frac{M_y}{W_F h} = \frac{x_0}{h} f^2 \sin \Omega t \left\{ \frac{1}{12r_1^2} + \sum_{n=0}^{\infty} \frac{8 \tanh [(2n+1)\pi r_1]}{\pi^3 (2n+1)^3 r_1} \left( \frac{1}{2} - \frac{\tanh \left[ (2n+1) \frac{\pi}{2} r_1 \right]}{(2n+1) \frac{\pi}{2} r_1} + \frac{1}{f_n^2} \right) \frac{1}{\left( \frac{f_n}{f} \right)^2 - 1} \right\} \quad (2.14c)$$

where now

$$\omega_n^2 = (2n+1) \frac{\pi g}{a} \tanh \left[ (2n+1) \frac{\pi h}{a} \right]$$

$$r_1 = h/a$$

$$f^2 = \frac{h}{g} \Omega^2$$

$$f_n^2 = (h/g) \omega_n^2$$

$$W_F = \rho g h a b \text{ (total weight of liquid)} = g M_F$$

#### Pitching About $y$ -Axis

The velocity potential, horizontal force in the  $x$ -direction, and moment acting on the container about the  $y$ -axis, for an angular displacement of the tank walls in pitch given by  $\theta(t) = \theta_0 \sin \Omega t$ , are as follows:

$$\Phi = +\theta_0 \Omega \cos \Omega t \left\{ \sum_{n=0}^{\infty} (-1)^n \frac{4}{\pi^3 (2n+1)^3} \left( \frac{h^2 \sin \left[ (2n+1) \frac{\pi}{h} z \right] \sinh \left[ (2n+1) \frac{\pi}{h} x \right]}{\cosh \left[ (2n+1) \frac{\pi a}{2h} \right]} \right. \right. \\ \left. \left. + \frac{a^2 \sin \left[ (2n+1) \frac{\pi}{a} x \right] \cosh \left[ (2n+1) \frac{\pi}{a} \left( z - \frac{h}{2} \right) \right]}{\sinh \left[ (2n+1) \frac{\pi}{a} h \right]} \right) \right. \\ \left. + \sum_{n=0}^{\infty} (-1)^n \frac{4a}{\pi^2 (2n+1)^2} \left( \frac{\Omega^2}{\omega_n^2 - \Omega^2} \right) \left( \frac{h}{2} - \frac{2a \tanh \left[ (2n+1) \frac{\pi h}{2a} \right]}{\pi (2n+1)} + \frac{g}{\omega_n^2} \right) \right. \\ \left. \times \frac{\sin \left[ (2n+1) \frac{\pi}{a} x \right] \cosh \left[ (2n+1) \frac{\pi}{a} \left( z + \frac{h}{2} \right) \right]}{\cosh \left[ (2n+1) \frac{\pi h}{a} \right]} \right\} \quad (2.15a)$$

$$\frac{F_H}{W_r} = \theta_0 f^2 \sin \Omega t \left\{ \frac{1}{12r_1^2} + \sum_{n=0}^{\infty} \frac{8 \tanh \left[ (2n+1)\pi r_1 \right]}{\pi^3 (2n+1)^3 r_1} \left( \frac{1}{2} - \frac{\tanh \left[ (2n+1) \frac{\pi}{2} r_1 \right]}{(2n+1) \frac{\pi}{2} r_1} + \frac{1}{f_n^2} \right) \frac{1}{\left( \frac{f_n}{f} \right)^2 - 1} \right\} \quad (2.15b)$$

$$\frac{M_y}{W_r h} = \theta_0 f^2 \sin \Omega t \left\{ \frac{I_{r_y}}{M_r h^2} + \frac{1}{12 f^2 r_1^2} + 2 \sum_{n=0}^{\infty} \frac{8 \tanh \left[ (2n+1)\pi r_1 \right]}{\pi^3 (2n+1)^3 r_1} \right. \\ \left. \times \left( \frac{1}{2} - \frac{\tanh \left[ (2n+1) \frac{\pi}{2} r_1 \right]}{(2n+1) \frac{\pi}{2} r_1} + \frac{1}{2f_n^2} \right) \frac{1}{f_n^2} + \sum_{n=0}^{\infty} \frac{8 \tanh \left[ (2n+1)\pi r_1 \right]}{\pi^3 (2n+1)^3 r_1} \right. \\ \left. \times \left( \frac{1}{2} - \frac{\tanh \left[ (2n+1) \frac{\pi}{2} r_1 \right]}{(2n+1) \frac{\pi}{2} r_1} + \frac{1}{f_n^2} \right)^2 \frac{1}{\left( \frac{f_n}{f} \right)^2 - 1} \right\} \quad (2.15c)$$

where  $I_{r_y}$  is the effective moment of inertia of the fluid about the  $y$ -axis (moment of inertia with the free surface fixed).

#### *Yawing About z-Axis*

The velocity potential and the moment acting

---

on the container about the  $z$ -axis (there are no resultant horizontal forces), for an angular displacement of the tank walls in yaw given by  $\phi(t) = \phi_0 \sin \Omega t$ , are as follows:

$$\begin{aligned}
 \Phi = -\phi_0 \Omega \cos \Omega t & \left\{ \sum_{n=0}^{\infty} (-1)^n \frac{4}{\pi^3 (2n+1)^3} \left[ \frac{b^2 \sin \left[ (2n+1) \frac{\pi}{b} y \right] \sinh \left[ (2n+1) \frac{\pi}{b} x \right]}{\cosh \left[ (2n+1) \frac{\pi a}{2b} \right]} \right. \right. \\
 & \left. \left. - \frac{a^2 \sin \left[ (2n+1) \frac{\pi}{a} x \right] \sinh \left[ (2n+1) \frac{\pi}{a} y \right]}{\cosh \left[ (2n+1) \frac{\pi b}{2a} \right]} \right] \right\} + \sum_{m=0}^{\infty} \sum_{n=0}^{\infty} (-1)^{m+n} \left( \frac{\Omega^2}{\omega_{mn}^2 - \Omega^2} \right) \\
 & \times \frac{16ab[b^2(2n+1)^2 - a^2(2m+1)^2] \operatorname{sech} \left[ \frac{\pi h}{ab} \sqrt{b^2(2n+1)^2 + a^2(2m+1)^2} \right]}{\pi^4 (2m+1)^2 (2n+1)^2 [b^2(2n+1)^2 + a^2(2m+1)^2]} \\
 & \times \left. \sin \left[ (2n+1) \frac{\pi}{a} x \right] \sin \left[ (2m+1) \frac{\pi}{b} y \right] \cosh \left[ \frac{\pi}{ab} \sqrt{b^2(2n+1)^2 + a^2(2m+1)^2} \left( z + \frac{h}{2} \right) \right] \right\} \\
 & \quad (2.16a)
 \end{aligned}$$

where the resonant frequencies  $\omega_{mn}$  are given by

$$\omega_{mn}^2 = g \frac{\pi}{ab} \sqrt{b^2(2n+1)^2 + a^2(2m+1)^2} \tanh \left[ \frac{\pi h}{ab} \sqrt{b^2(2n+1)^2 + a^2(2m+1)^2} \right] \quad (2.16b)$$

$$\begin{aligned}
 M_z = \phi_0 \Omega^2 \sin \Omega t & \left\{ \frac{32\rho h}{\pi^5} \sum_{n=0}^{\infty} \frac{1}{(2n+1)^5} \left[ a^4 \tanh \left[ (2n+1) \frac{\pi b}{2a} \right] \right. \right. \\
 & \left. \left. + b^4 \tanh \left[ (2n+1) \frac{\pi a}{2b} \right] \right] - \frac{1}{12} \rho abh(a^2 + b^2) \right. \\
 & \left. + \sum_{m=0}^{\infty} \sum_{n=0}^{\infty} \frac{\omega_{mn}}{g} \frac{64\rho a^3 b^3 [b^2(2n+1)^2 - a^2(2m+1)^2]^2}{\pi^8 [b^2(2n+1)^2 + a^2(2m+1)^2]^2 (2m+1)^4 (2n+1)^4} \left( \frac{\Omega^2}{\omega_{mn}^2 - \Omega^2} \right) \right\} \quad (2.16c)
 \end{aligned}$$

### 2.3 CIRCULAR CYLINDRICAL TANK

The upright cylindrical container of circular cross section is obviously of considerable importance for our discussion here because of its relationship to the configuration of large boost vehicles. Indeed, this tank geometry is perhaps the most important of all, and, fortunately, the analysis of lateral liquid sloshing is not especially difficult. However, because of the frequent necessity to reduce sloshing masses or to shift the liquid natural frequencies, subdivision of such containers into compartments by either radial or concentric walls is relatively

common practice, so that the basic simple geometry transforms into other more complex forms. For purposes of our presentation here, it is somewhat advantageous to begin with the most general compartmented tank, the ring sector, and then present results for other configurations as special cases. It is interesting to note that the solution to the shallow water (tidal) oscillations of a liquid in a ring sector tank was suggested by Lamb (ref. 2.13, art. 191) and that the natural frequencies for tidal oscillations of a fluid in a sector tank were obtained by Rayleigh (ref. 2.30, art. 339).

### Ring Sector Compartmented Tank

This configuration is not only of practical importance, but from the analysis of liquid sloshing in this type tank, the behavior of liquids in all cylindrical tanks composed of radial and circular walls may be obtained by appropriate selection of the geometric variables. For purposes of review, the procedures employed to obtain the natural frequencies and to solve the problem of lateral sloshing of a liquid in a ring sector tank induced by translational motion of the container will be outlined first, following closely the discussion of reference 2.3. Results for other types of container motion (refs. 2.3, 2.19, and 2.31) are also then given. It should be noted that the theoretical results presented are valid for a single sector tank. To use the results for compartmented cylindrical tanks, one must superimpose the effects of all the compartments. For example, the contribution to the total force in the  $x$ -direction of all eight compartments has been accounted for in the theoretical curves presented in figure 2.8.

#### Free Oscillations

The geometry of the tank and coordinates are shown in figure 2.3. The flow field of a liquid with free surface in a cylindrical container of ring sector cross section with vertex angle  $2\pi\alpha$

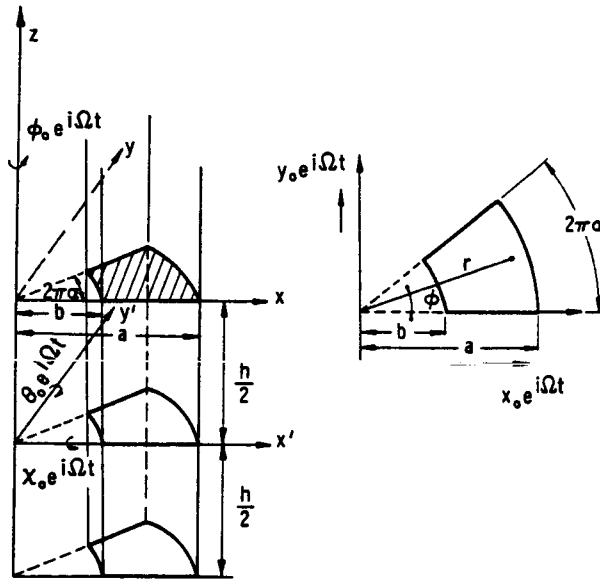


FIGURE 2.3.—Coordinate system and tank geometry for ring sector tank (ref. 2.3).

and a flat bottom is obtained from the solution to the Laplace equation  $\nabla^2\Phi_1=0$  with the boundary conditions

$$\frac{\partial\Phi_1}{\partial z}=0 \quad \text{at the tank bottom } z=-h \quad (2.17a)$$

$$\frac{\partial\Phi_1}{\partial r}=0 \quad \text{at the circular cylindrical tank walls } r=a, b \quad (2.17b)$$

$$\frac{1}{r} \frac{\partial\Phi_1}{\partial\phi}=0 \quad \text{at the sector walls } \phi=0, 2\pi\alpha \quad (2.17c)$$

$$\frac{\partial^2\Phi_1}{\partial t^2}+g \frac{\partial\Phi_1}{\partial z}=0 \quad \text{at the free surface } z=0 \quad (2.17d)$$

Assuming a product solution of the form

$$\Phi_1(r, \phi, z, t)=e^{i\omega t}R(r)G(\phi)Z(z)$$

and substituting into the Laplace equation, the following expression for  $\Phi_1$  is obtained

$$\begin{aligned} \Phi_1=e^{i\omega t}\{ & C_1 \cos\nu\phi+C_2 \sin\nu\phi \}[\{ C_3 \cosh\lambda z \\ & +C_4 \sinh\lambda z \} \{ C_5 J_\nu(\lambda r)+C_6 Y_\nu(\lambda r) \} \\ & +\{ C_7 z+C_8 \} \{ C_9 r^\nu+C_{10} r^{-\nu} \}] \end{aligned} \quad (2.18a)$$

where  $\nu$  and  $\lambda$  are constants and  $J_\nu(\lambda r)$  and  $Y_\nu(\lambda r)$  are Bessel functions of the first and second kinds of order  $\nu$ . Care must be taken in the choice of the "separation" constants  $\nu$  and  $\lambda$ , and their signs, to insure that the mathematical solutions actually describe the physical problem. The velocity potential which satisfies the boundary conditions at the container walls (eqs. (2.17b) and (2.17c)) is

$$\Phi_1(r, \phi, z, t)=\sum_m \sum_n A_{mn} e^{i\omega_{mn}t} \cos\left(\frac{m}{2\alpha}\phi\right)$$

$$\times \frac{\cosh\left[\xi_{mn}\left(\frac{z+h}{a}+\frac{h}{a}\right)\right]}{\cosh\left[\xi_{mn}\frac{h}{a}\right]} C_{m/2\alpha}\left(\xi_{mn}\frac{r}{a}\right) \quad (2.18b)$$

where

$$\begin{aligned} C_{m/2\alpha}\left(\xi_{mn}\frac{r}{a}\right) \equiv C(\sigma) = & J_{m/2\alpha}(\sigma)Y'_{m/2\alpha}(\xi_{mn}) \\ -J'_{m/2\alpha}(\xi_{mn})Y_{m/2\alpha}(\sigma) \end{aligned} \quad (2.18c)$$

The values  $\xi_{mn}$  are the positive roots of the equation<sup>1</sup>

$$\Delta_{m/2\alpha} = J'_{m/2\alpha}(\xi) Y'_{m/2\alpha}(k\xi) \\ - J'_{m/2\alpha}(k\xi) Y'_{m/2\alpha}(\xi) = 0 \quad (2.18d)$$

and  $k = b/a$  is the diameter ratio of the inner and outer tank walls. The unknown constants  $A_{mn}$  can be obtained from the initial conditions. The equation for the eigenvalues of the liquid is obtained from the free surface condition, equation (2.17d)

$$\omega_{mn}^2 = \omega^2 = \frac{g}{a} \xi_{mn} \tanh\left(\xi_{mn} \frac{h}{a}\right) \quad m, n = 0, 1, \dots \quad (2.19)$$

<sup>1</sup> The roots of this determinant are plotted in fig. 2.4, and tabulated in table 2.1, as a function of  $k$  for the special case of  $m/2\alpha=1$ . Further discussion on the roots of this determinant may be found in ref. 2.2, while extensive tables and graphs of  $\Delta_{m/2\alpha}(\xi)=0$  are presented in ref. 2.32.

It is seen that the frequencies of the liquid decrease with liquid depth and with increasing tank radius. For a given tank size, the possibility of shifting the frequencies is expressed by

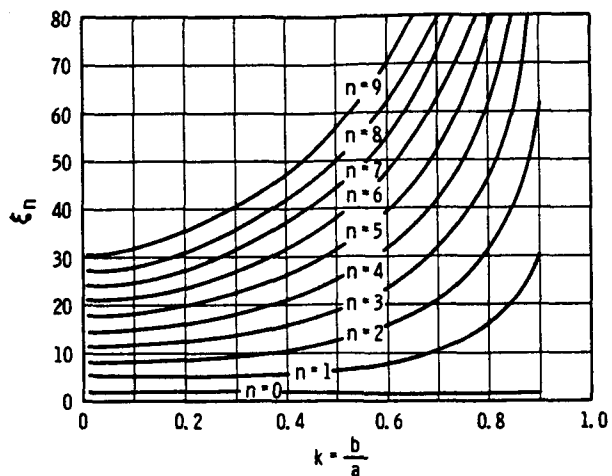


FIGURE 2.4.—Roots of  $\Delta_1(\xi)=0$  versus parameter  $k$  (ref. 2.2).

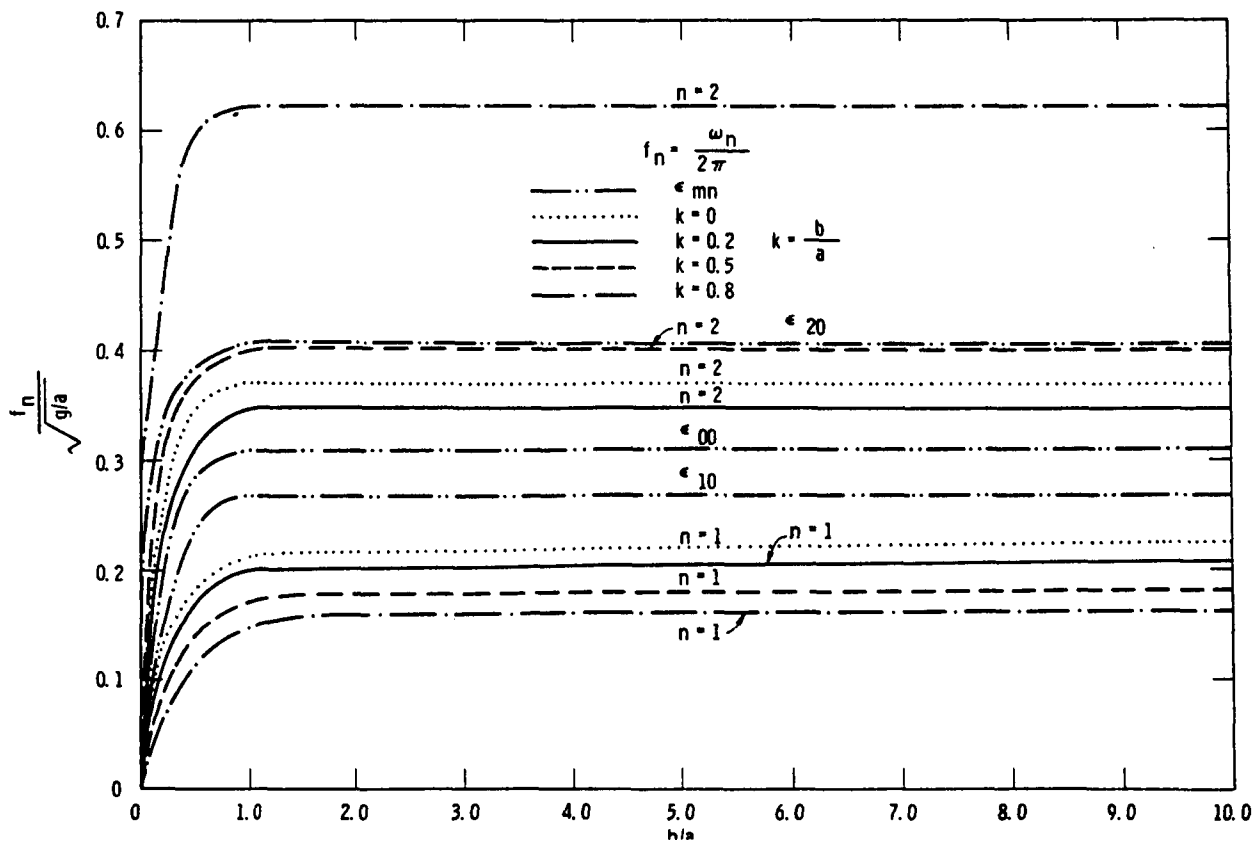


FIGURE 2.5.—Natural frequency parameter for containers of circular, annular, and quarter-circular cross section (ref. 2.3).

TABLE 2.1.—Roots of the Determinant  $\Delta_{m/2\alpha}(\xi)=0$ , Eq. (2.18d)[ $m/2\alpha=1$ ]

$n \setminus k$	0.01	0.1	0.2	0.3	0.4	0.5	0.6	0.7	0.8	0.9
0.....	1. 84080	1. 80347	1. 70512	1. 58207	1. 46179	1. 35468	1. 26209	1. 18238	1. 11338	1. 05312
1.....	5. 32913	5. 13714	4. 96086	5. 13742	5. 65919	6. 56494	8. 04111	10. 59188	15. 77812	31. 44697
2.....	8. 53050	8. 19917	8. 43307	9. 30835	10. 68335	12. 70657	15. 80132	21. 00412	31. 45132	62. 84810
3.....	11. 69512	11. 35879	12. 16501	13. 68367	15. 84811	18. 94268	23. 62394	31. 45577	47. 15038	94. 26451
4.....	14. 84607	14. 63436	15. 99324	18. 11588	21. 04879	25. 20249	31. 46329	41. 91895	62. 85103	125. 67496
5.....	17. 98982	17. 98642	19. 86163	22. 57071	26. 26408	31. 47214	39. 30762	52. 38450	78. 55486	157. 08804
6.....	21. 12895	21. 38369	23. 75018	27. 03693	31. 48593	37. 74587	47. 15522	62. 85225	94. 26013	188. 50221
7.....	24. 26472	24. 80814	27. 64977	31. 50921	36. 71185	44. 02232	55. 00467	73. 32123	109. 96622	219. 91695
8.....	27. 39787	28. 24974	31. 55634	35. 98546	41. 94030	50. 30046	62. 85525	83. 79098	125. 67278	251. 33201
9.....	30. 52885	31. 70269	35. 46753	40. 46433	47. 17043	56. 57973	70. 70660	94. 26122	141. 37967	282. 74731

$\xi_{mn}$ . For large values of  $h/a$  (i.e.,  $h/a > 1$ ), the approximation

$$\omega^2 = \frac{g}{a} \xi_{mn}$$

is accurate. Figure 2.5 gives the natural frequencies for fluids in containers of circular, annular, and quarter-circular ( $90^\circ$  sector) cross section.

#### Translational Forced Oscillations

For forced excitation  $x=x_0 e^{i\Omega t}$  normal to the container wall (see fig. 2.3), the boundary conditions are:

$$\left. \begin{array}{l} \frac{\partial \Phi}{\partial r} = i\Omega x_0 e^{i\Omega t} \cos \phi \quad \text{at the circular} \\ \text{cylindrical tank walls } r=a, b \\ \frac{\partial \Phi}{\partial z}=0 \quad \text{at the bottom of the} \\ \text{container } z=-h \\ \frac{1}{r} \frac{\partial \Phi}{\partial \phi}=0 \quad \text{at the sector wall } \phi=0 \\ \frac{1}{r} \frac{\partial \Phi}{\partial \phi} = -i\Omega x_0 e^{i\Omega t} \sin 2\pi\alpha \quad \text{at the} \\ \text{sector wall } \phi=2\pi\alpha \\ \frac{\partial^2 \Phi}{\partial t^2} + g \frac{\partial \Phi}{\partial t} = 0 \quad \text{at the free surface} \\ z=0 \end{array} \right\} \quad (2.20)$$

By extracting the container motion

$$\Phi = \{\Phi_1 + i\Omega x_0 r \cos \phi\} e^{i\Omega t}$$

boundary conditions for the disturbance poten-

tial, which are homogeneous at the container walls, are obtained as

$$\left. \begin{array}{l} \frac{\partial \Phi_1}{\partial r}=0 \quad \text{for } r=a, b \\ \frac{\partial \Phi_1}{\partial z}=0 \quad \text{for } z=-h \\ \frac{1}{r} \frac{\partial \Phi_1}{\partial \phi}=0 \quad \text{for } \phi=0, 2\pi\alpha \\ g \frac{\partial \Phi_1}{\partial z} - \Omega^2 \Phi_1 = i\Omega^3 x_0 r \cos \phi \quad \text{for } z=0 \end{array} \right\} \quad (2.21)$$

and therefore the disturbance potential  $\Phi_1(r, \phi, z)$  which satisfies the Laplace equation has the same form as equation (2.18b). Omitting the double summation and indices and introducing the abbreviations

$$\bar{\phi} = \frac{m}{2\alpha} \phi, \zeta = \xi_{mn} \frac{z}{a}, \sigma = \xi_{mn} \frac{r}{a} \text{ and } \kappa = \xi_{mn} \frac{h}{a}$$

the disturbance potential is

$$\Phi_1(r, \phi, z) = A \cos \bar{\phi} C(\sigma) \frac{\cosh(\kappa + \zeta)}{\cosh \kappa}$$

To determine the unknown coefficients  $A_{mn}$ , from the condition of the free fluid surface the right-hand side of this boundary condition has to be expanded into a series where  $\cos \phi$  is represented as the Fourier series

$$\cos \phi = \sum_{m=0}^{\infty} a_m \cos \bar{\phi} \quad (2.22a)$$

with

$$a_0 = \frac{\sin \bar{\alpha}}{\bar{\alpha}}, \quad a_m = \frac{2\bar{\alpha}(-1)^{m+1} \sin \bar{\alpha}}{(m^2\pi^2 - \bar{\alpha}^2)}, \quad (\bar{\alpha} = 2\pi\alpha)$$

The function  $r$  is represented as a Bessel series

$$r = \sum_{n=0}^{\infty} b_{mn} C(\sigma)$$

where

$$\begin{aligned} b_{mn} &= \frac{a \int_{k\xi_{mn}}^{\xi_{mn}} \sigma^2 C(\sigma) d\sigma}{\xi_{mn} \int_{k\xi_{mn}}^{\xi_{mn}} \sigma C^2(\sigma) d\sigma} \\ &= \frac{2aN_2(\xi_{mn})}{\left[ \frac{4}{\pi^2 \xi_{mn}^2} - k^2 C^2(k\xi_{mn}) \right] - \frac{m^2}{4\alpha^2 \xi_{mn}^2} \left[ \frac{4}{\pi^2 \xi_{mn}^2} - C^2(k\xi_{mn}) \right]} \quad (2.22b) \end{aligned}$$

The coefficients  $A_{mn}$  become

$$A_{mn} = \frac{i\Omega a_m b_{mn} x_0 \eta^2}{(1-\eta^2)} \quad (2.22c)$$

where  $\eta = \Omega/\omega$  is the ratio of the exciting frequency to the natural frequency. The velocity potential  $\Phi$  for translational container excitation in  $x$ -direction is then

$$\begin{aligned} \Phi(r, \phi, z, t) &= i\Omega x_0 e^{i\Omega t} \left\{ r \cos \phi \right. \\ &\quad \left. + \frac{a_m b_{mn} C(\sigma) \eta^2 \cosh(\kappa + \zeta)}{(1-\eta^2) \cosh \kappa} \cos \bar{\phi} \right\} \quad (2.23) \end{aligned}$$

The first term (potential of the rigid body) satisfies the boundary conditions at the tank walls, while the second part (disturbance potential) vanishes at the tank walls. The free surface condition is satisfied by both parts of the formula. The free surface displacement, the pressure and velocity distribution, as well as the forces and moments of the liquid, can be determined from the potential by differentiations and integrations with respect to the time and spatial coordinates.

The surface displacement of the propellant, which is measured from the undisturbed position of the liquid, may be obtained from equation (2.10), with  $p_0$  equal zero

$$\delta = \frac{\Omega^2}{g} x_0 e^{i\Omega t} \left\{ r \cos \phi + \frac{a_m b_{mn} C(\sigma) \eta^2}{(1-\eta^2)} \cos \bar{\phi} \right\} \quad (2.24)$$

and the pressure at depth  $(-z)$  is obtained from equation (2.8) as

$$\begin{aligned} p &= -\rho \frac{\partial \Phi}{\partial t} - g\rho z = \rho \Omega^2 x_0 e^{i\Omega t} \left[ r \cos \phi \right. \\ &\quad \left. + \frac{a_m b_{mn} \eta^2 \cosh(\kappa + \zeta) C(\sigma) \cos \bar{\phi}}{(1-\eta^2) \cosh \kappa} \right] - \rho g z \quad (2.25) \end{aligned}$$

At the outer container wall,  $r=a$ , the function  $C(\sigma) = (2/\pi \xi_{mn})$ , while at the inner container wall,  $r=b$ , the function  $C(\sigma)$  has a value  $C(k\xi_{mn})$ . At the sector walls  $\phi=0, \phi=\bar{\alpha}$ , the cosine assumes the value 1 and  $(-1)^m$ , respectively. The pressure distribution at the tank bottom is obtained from equation (2.25) with  $z=-h$  ( $\zeta=-\kappa$ ).

By integration of the appropriate components of the pressure distribution, the liquid forces and moments can be obtained. The resulting force in the  $x$ -direction is therefore

$$\begin{aligned} F_x &= \int_0^{\bar{\alpha}} \int_{-h}^0 (ap_a - bp_b) \cos \phi d\phi dz \\ &\quad - \int_b^a \int_{-h}^0 p_{\phi=0} \sin \bar{\alpha} dr dz \end{aligned}$$

Here the first integral represents a contribution of the pressure distribution at the circular container walls, and the second integral stems from the pressure distribution at the sector walls. With the mass of the liquid  $M_F = \rho \pi a^2 h \alpha (1-k^2)$ , the fluid force becomes

$$\begin{aligned} F_x &= M_F \Omega^2 x_0 e^{i\Omega t} \left[ 1 + 2 \frac{(-1)^{m+1} a_m b_{mn} \sin \bar{\alpha} \eta^2 \tanh \kappa}{\bar{\alpha} a (1-k^2) (1-\eta^2)} \right. \\ &\quad \times \left. \left\{ N_0(\xi_{mn}) + \frac{\bar{\alpha}^2}{(\pi^2 m^2 - \bar{\alpha}^2)} \left[ \frac{2}{\pi \xi_{mn}} - k C(k\xi_{mn}) \right] \right\} \right] \quad (2.26a) \end{aligned}$$

The force component in the  $y$ -direction is governed by

$$\begin{aligned} F_y &= \int_0^{\bar{\alpha}} \int_{-h}^0 (ap_a - bp_b) \sin \phi d\phi dz \\ &\quad + \int_b^a \int_{-h}^0 p_{\phi=0} \cos \bar{\alpha} dr dz - \int_b^a \int_{-h}^0 p_{\phi=0} dr dz \end{aligned}$$

which then leads to

$$F_y = -2M_p \Omega^2 x_0 e^{i\Omega t} \frac{a_m b_{mn} \eta^2 [1 - (-1)^m \cos \bar{\alpha}] \tanh \kappa}{-a \bar{\alpha} (1 - k^2) (1 - \eta^2) \kappa} \times \left\{ N_0(\xi_{mn}) + \frac{\bar{\alpha}^2}{(\pi^2 m^2 - \bar{\alpha}^2)} \left[ \frac{2}{\pi \xi_{mn}} - k C(k \xi_{mn}) \right] \right\} \quad (2.26b)$$

Here (see appendix A)

$$N_0(\xi_{mn}) = \frac{1}{\xi_{mn}} \int_{k \xi_{mn}}^{\xi_{mn}} C(\sigma) d\sigma$$

The first term,  $M_p \Omega^2 x_0 e^{i\Omega t}$ , in equation (2.26a) represents the inertial force of the liquid (that is, the force that would be produced by an equal volume of solidified liquid). The fluid moments  $M_y$  and  $M_z$  with respect to the point  $(0, 0, -h/2)$  are given by

$$M_y = \int_0^{\bar{\alpha}} \int_{-h}^0 (ap_a - bp_b) \left( \frac{h}{2} + z \right) \cos \phi d\phi dz + \int_0^{\bar{\alpha}} \int_b^a p_{z=-h} r^2 \cos \phi d\phi dr - \int_b^a \int_{-h}^0 p_{\phi=\alpha} \sin \alpha \left( \frac{h}{2} + z \right) dr dz$$


---

and

$$M_z = - \int_0^{\bar{\alpha}} \int_{-h}^0 (ap_a - bp_b) \left( \frac{h}{2} + z \right) \sin \phi d\phi dz - \int_0^{\bar{\alpha}} \int_b^a p_{z=-h} r^2 \sin \phi d\phi dr + \int_b^a \int_{-h}^0 \left( \frac{h}{2} + z \right) p_{\phi=\alpha} dr dz - \int_b^a \int_{-h}^0 \left( \frac{h}{2} + z \right) p_{\phi=\alpha} \cos \alpha dr dz$$

$M_y$  is the moment about an axis passing through point  $(0, 0, -h/2)$  parallel to the  $y$ -axis while  $M_z$  is the moment about an axis parallel to the  $z$ -axis through the same point. In these formulas, the first integral again represents the contribution of the pressure distribution at the circular cylindrical tank walls. The second integral is the contribution of the bottom pressure, while the remaining integrals represent the pressure contribution at the sector walls to the moment. After the integration has been performed, the moments of the liquid are

$$M_y = M_p \Omega^2 a x_0 e^{i\Omega t} \left[ \frac{1+k^2}{4h/a} \left( 1 + \frac{\sin \bar{\alpha} \cos \bar{\alpha}}{\bar{\alpha}} \right) + \frac{\sin \bar{\alpha}}{\bar{\alpha}} \frac{(-1)^{m+1} a_m b_{mn} \eta^2}{\alpha (1-\eta^2) (1-k^2) \xi_{mn}} \left\{ \left[ \tanh \kappa + \frac{2}{\kappa} \left( \frac{1}{\cosh \kappa} - 1 \right) \right] \left[ N_0(\xi_{mn}) + \frac{\bar{\alpha}^2}{(\pi^2 m^2 - \bar{\alpha}^2) \kappa} \left[ \frac{2}{\pi \xi_{mn}} - k C(k \xi_{mn}) \right] \right] + \frac{2 \bar{\alpha}^2 \xi_{mn}^2 N_2(\xi_{mn})}{(\pi^2 m^2 - \bar{\alpha}^2) \kappa \cosh \kappa} \right\} \right] + \frac{2 M_p g a}{3} \frac{(1-k^3)}{(1-k^2)} \frac{\sin \bar{\alpha}}{\bar{\alpha}} \quad (2.26c)$$

$$M_z = -M_p \Omega^2 a x_0 e^{i\Omega t} \left[ \frac{(1+k^2)}{4h/a} \frac{\sin^2 \bar{\alpha}}{\bar{\alpha}} - \frac{1}{\bar{\alpha}} \frac{a_m b_{mn} [1 - (-1)^m \cos \bar{\alpha}] \eta^2}{(1-\eta^2) (1-k^2) \xi_{mn} \alpha} \left\{ \left[ \tanh \kappa + \frac{2}{\kappa} \left( \frac{1}{\cosh \kappa} - 1 \right) \right] \left[ N_0(\xi_{mn}) + \frac{\bar{\alpha}^2}{(\pi^2 m^2 - \bar{\alpha}^2) \kappa} \left[ \frac{2}{\pi \xi_{mn}} - k C(k \xi_{mn}) \right] \right] + \frac{2 \bar{\alpha}^2 \xi_{mn}^2 N_2(\xi_{mn})}{(\pi^2 m^2 - \bar{\alpha}^2) \kappa \cosh \kappa} \right\} \right] - \frac{2 M_p g a}{3} \frac{(1-k^3)}{(1-k^2)} \frac{(1-\cos \bar{\alpha})}{\bar{\alpha}} \quad (2.26d)$$


---

where

$$N_2(\xi_{mn}) = \frac{1}{\xi_{mn}^3} \int_{k \xi_{mn}}^{\xi_{mn}} \sigma^2 C(\sigma) d\sigma$$

Since the reference axis does not pass through the center of gravity of the undisturbed liquid, the last term in the moment formula represents the static moment of the liquid.

The velocity distribution in the radial, angular, and axial directions are

$$u_r = \frac{\partial \Phi}{\partial r} = -i\Omega x_0 e^{i\Omega t} \left[ \cos \phi + \frac{a_m b_{mn} \eta^2 \xi_{mn} \cosh(\kappa + \zeta)}{(1 - \eta^2)a \cosh \kappa} C'(\sigma) \cos \bar{\phi} \right] \quad (2.27a)$$

$$u_\phi = \frac{1}{r} \frac{\partial \Phi}{\partial \phi} = -i\Omega x_0 e^{i\Omega t} \left[ \sin \phi + \frac{a_m b_{mn} \eta^2 (m/2\alpha) \cosh(\kappa + \zeta)}{r(1 - \eta^2)a \cosh \kappa} C(\sigma) \sin \bar{\phi} \right] \quad (2.27b)$$

$$w = \frac{\partial \Phi}{\partial z} = i\Omega x_0 e^{i\Omega t} \frac{a_m b_{mn} \eta^2 \xi_{mn} \sinh(\kappa + \zeta)}{a(1 - \eta^2) \cosh \kappa} C(\sigma) \cos \bar{\phi} \quad (2.27c)$$

In these equations for pressure, forces, moments, and velocity distributions of the liquid, the term for the solidified liquid is represented as a single term and not as a series. This results in a faster convergence of the solution. The velocity distributions in the container are obtained by omitting the first term in the braces; that is, omitting the term  $\cos \phi$  for the radial velocity component of  $u_r$  and  $\sin \phi$  for the angular component of  $u_\phi$ .

General notes pertaining to translational oscillations:

- (1) The results for container motion  $y = y_0 e^{i\Omega t}$  are given in appendix A (also see fig. 2.3).
- (2) The following definitions are applicable in appendix A:

$\ln$  natural logarithm

$\Gamma$  the gamma function

$\psi$  the derivative of the logarithm of the gamma function, that is,

$$\psi = \frac{d}{dz} [\ln \Gamma(z)] = -\gamma + (z-1) \sum_{\lambda=0}^{\infty} \frac{1}{(1+\lambda)(z+\lambda)}$$

where  $\gamma = 0.5772$  is the Euler constant.

- (3) It should be noted that, because of singularities that occur in the velocity potential, the results contained in this section are not valid for  $\alpha = \frac{1}{4}$  and  $\alpha = \frac{3}{4}$ . For these two cases, special modifications must be made to form admissible functions.

#### Rotational Forced Oscillations

Liquid behavior induced by pitching- and roll-type motions of the container is described by the equations given in appendix B.

In this table  $\theta_0$ ,  $x_0$ , and  $\phi_0$  are the rotational amplitudes about the  $y$ ,  $x$ , and  $z$  axes. Note:

- (1) The equations for the pitch-type motions,  $\theta_0$  and  $x_0$  are valid for a coordinate system with its origin located midway between the tank bottom and the undisturbed fluid surface, on the vertex axis of the tank. (See fig. 2.3,  $x'$ ,  $y'$ ,  $z'$  coordinates.)
- (2) The equations for the roll motions,  $\phi_0$ , are valid for a coordinate system with its origin located in the undisturbed free surface.
- (3) To obtain the displacements of the free surface in tank-fixed coordinates, subtract that resulting from container motion from that of the space-fixed system. Thus,

$$\delta^* = \delta - \left\{ \begin{array}{l} (r \cos \phi) \theta_0 e^{i\Omega t} \\ (r \sin \phi) x_0 e^{i\Omega t} \end{array} \right\}$$

- (4) The quantities  $C_m$  are defined in appendix A.
- (5) The forces given in appendix B are with respect to the space-fixed (inertial) coordinate system.
- (6) In appendix B (rotational excitation) the terms in the upper portion of the brackets correspond to the motion  $\theta = \theta_0 e^{i\Omega t}$ , while those in the lower portion correspond to  $x = x_0 e^{i\Omega t}$ .

#### Forced Oscillations Resulting From Tank Bending

Bauer (refs. 2.31 and 2.33) has solved the problem of liquid sloshing in a ring sector tank resulting from a prescribed bending-type motion of the tank walls. That is, given a motion of the walls of the form  $x_0(z)e^{i\Omega t}$  or

$y_0(z)e^{i\Omega t}$  (see fig. 2.6), he obtained equations for the velocity potential, liquid free surface displacements, pressures, forces, moments, and velocity distribution, as given in the following. Note there is assumed to be no interaction between the container and fluid. (Interactions between the moving liquid and the elastic container will be studied in ch. 9.)

The velocity potential is (the first term within the brackets corresponds to the motion  $x_0e^{i\Omega t}$  and the second term to  $y_0e^{i\Omega t}$ ):

$$\Phi(r, \phi, z, t) = e^{i\Omega t} \left[ \left\{ i\Omega x_0(z)r \cos \phi \right\} + \sum_{m=0}^{\infty} \sum_{n=0}^{\infty} A_{mn}(z) C_{m/2\alpha} \left( \xi_{mn} \frac{r}{a} \right) \cos \left( \frac{m}{2\alpha} \phi \right) \right] \quad (2.28a)$$

where

$$A_{mn}(z) = \frac{i\Omega ab_{mn} \left\{ \frac{a_m}{c_m} \right\} \eta^2}{\xi_{mn} \cosh \left( \xi_{mn} \frac{h}{a} \right) (1 - \eta^2)} \left[ \sinh \left( \xi_{mn} \frac{z}{a} \right) + \frac{\xi_{mn} g}{a\Omega^2} \cosh \left( \xi_{mn} \frac{z}{a} \right) \right] \left[ \left\{ \begin{array}{l} x'_0(-h) \\ y'_0(-h) \end{array} \right\} + \int_{-h}^z \left\{ \begin{array}{l} x''_0(\xi) \\ y''_0(\xi) \end{array} \right\} \cosh \left[ \xi_{mn} \left( \frac{\xi+h}{a} \right) \right] d\xi \right] \\ + \cosh \left[ \xi_{mn} \left( \frac{z+h}{a} \right) \right] \left[ \int_z^0 \left\{ \begin{array}{l} x''_0(\xi) \\ y''_0(\xi) \end{array} \right\} \cosh \left[ \xi_{mn} \left( \frac{\xi+h}{a} \right) \right] d\xi \right] \\ \times \left[ \sinh \left( \xi_{mn} \frac{z}{a} \right) + \frac{\xi_{mn} g}{a\Omega^2} \cosh \left( \xi_{mn} \frac{z}{a} \right) \right] \quad (2.28b)$$

and primes denote differentiation with respect to  $z$ . All other quantities have been previously defined.

The surface displacement of the liquid measured from the undisturbed position is

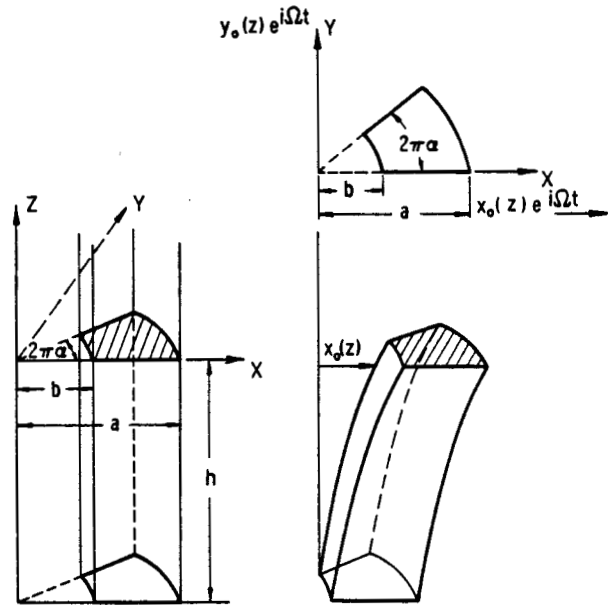


FIGURE 2.6.—Coordinate system and tank geometry for bending excitation (ref. 2.31).

$$\delta = \frac{\Omega^2}{g} e^{i\Omega t} \left[ \left\{ \begin{array}{l} x_0(0)r \cos \phi \\ y_0(0)r \sin \phi \end{array} \right\} + \sum_{m=0}^{\infty} \sum_{n=0}^{\infty} A_{mn}(0) C_{m/2\alpha} \left( \xi_{mn} \frac{r}{a} \right) \cos \left( \frac{m}{2\alpha} \phi \right) \right] \quad (2.29)$$

The pressure at depth ( $-z$ ) is

$$p = -\rho \frac{\partial \phi}{\partial t} - g\rho z = \rho\Omega^2 e^{i\Omega t} \left[ \left\{ \begin{array}{l} x_0(z)r \cos \phi \\ y_0(z)r \sin \phi \end{array} \right\} + \sum_{m=0}^{\infty} \sum_{n=0}^{\infty} A_{mn}(z) C_{m/2\alpha} \left( \xi_{mn} \frac{r}{a} \right) \cos \left( \frac{m}{2\alpha} \phi \right) \right] - \rho g z \quad (2.30)$$

The liquid forces in the  $x$  and  $y$  directions are

$$F_x = M_F \Omega^2 e^{i\Omega t} \left[ \left\{ \begin{array}{l} \frac{1}{h} \int_{-h}^0 x_0(z) dz \\ 0 \end{array} \right\} + \sum_{m=0}^{\infty} \sum_{n=0}^{\infty} \frac{(-1)^{m+1} \sin 2\pi\alpha}{i\Omega\pi\alpha ah(1-k^2)} \int_{-h}^0 A_{mn}(z) dz \right. \\ \left. \times \left( \frac{4\alpha^2}{m^2 - 4\alpha^2} \left[ \frac{2}{\pi\xi_{mn}} - k C_{m/2\alpha}(k\xi_{mn}) \right] + N_0(\xi_{mn}) \right) \right] \quad (2.31a)$$

$$F_x = M_F \Omega^2 e^{i\Omega t} \left[ \left\{ \begin{array}{l} 0 \\ \frac{1}{h} \int_{-h}^0 y_0(z) dz \end{array} \right\} + \sum_{m=0}^{\infty} \sum_{n=0}^{\infty} \frac{i[1-(-1)^m \cos 2\pi\alpha]}{2\pi\alpha ah(1-k^2)} \int_{-h}^0 A_{mn}(z) dz \right. \\ \left. \times \left( \frac{4\alpha^2}{(m^2-4\alpha^2)} \left[ \frac{2}{\pi\xi_{mn}} - kC_{m/2\alpha}(k\xi_{mn}) \right] + N_0(\xi_{mn}) \right) \right] \quad (2.31b)$$

The term  $\frac{M_F}{h} \Omega^2 e^{i\Omega t} \int_{-h}^0 x_0(z) dz$  in front of the double summation in  $F_x$  represents the inertial force; i.e., the force that would be produced by an equal volume of solidified liquid.

The liquid moments with respect to the point  $(0, 0, -h/2)$  are

$$M_y = M_F \Omega^2 e^{i\Omega t} \left[ \left\{ \begin{array}{l} \frac{1}{h} \int_{-h}^0 \left( \frac{h}{2} + z \right) x_0(z) dz + \frac{a^2 x_0(-h)(1+k^2)}{4h} \left( 1 + \frac{\sin 2\pi\alpha \cos 2\pi\alpha}{2\pi\alpha} \right) \\ 0 + \frac{a^2 y_0(-h)(1+k^2)}{4h} \frac{\sin^2 2\pi\alpha}{2\pi\alpha} \end{array} \right\} \right. \\ \left. + \sum_{n=0}^{\infty} \sum_{m=0}^{\infty} \frac{(-1)^{m+1} \sin 2\pi\alpha}{i\Omega\pi\alpha ah(1-k^2)} \left\{ \frac{4\alpha^2 a^2}{(m^2-4\alpha^2)} N_2(\xi_{mn}) A_{mn}(-h) + \left[ \frac{4\alpha^2}{(m^2-4\alpha^2)} \left[ \frac{2}{\pi\xi_{mn}} - kC_{m/2\alpha}(k\xi_{mn}) \right] \right. \right. \right. \\ \left. \left. \left. + N_0(\xi_{mn}) \right] \int_{-h}^0 \left( \frac{h}{2} + z \right) A_{mn}(z) dz \right\} \right] + M_F g \frac{a}{3} \frac{\sin 2\pi\alpha}{\pi\alpha} \frac{(1+k+k^2)}{(1+k)} \quad (2.32a)$$

$$M_z = M_F \Omega^2 e^{i\Omega t} \left[ \left\{ \begin{array}{l} \frac{a^2(1+k^2)x_0(-h)}{4h} \frac{\sin^2 2\pi\alpha}{2\pi\alpha} \\ \frac{1}{h} \int_{-h}^0 \left( \frac{h}{2} + z \right) y_0(z) dz + \frac{a^2(1+k^2)y_0(-h)}{4h} \left( 1 - \frac{\sin 2\pi\alpha \cos 2\pi\alpha}{2\pi\alpha} \right) \end{array} \right\} \right. \\ \left. + \sum_{n=0}^{\infty} \sum_{m=0}^{\infty} \frac{i[1-(-1)^m \cos 2\pi\alpha]}{\Omega a \pi \alpha h (1-k^2)} \left\{ \frac{4\alpha^2 a^2}{(m^2-4\alpha^2)} A_{mn}(-h) N_2(\xi_{mn}) \right. \right. \\ \left. \left. + \left[ \frac{4\alpha^2}{m^2-4\alpha^2} \left[ \frac{2}{\pi\xi_{mn}} - kC_{m/2\alpha}(k\xi_{mn}) \right] + N_0(\xi_{mn}) \right] \int_{-h}^0 \left( \frac{h}{2} + z \right) A_{mn}(z) dz \right\} \right] \\ + M_F g \frac{a}{3} \frac{[1-\cos 2\pi\alpha]}{\pi\alpha} \frac{(1+k+k^2)}{(1+k)} \quad (2.32b)$$

The first integrals in equations (2.32) represent the contribution of the pressure distribution from the circular walls. The second integral is the contribution of the pressure at the tank bottom, while the remaining integrals can be identified as the contribution to the moment from the pressure distribution at the tank sector walls. The last term in these equations represents the moment of the undisturbed liquid about the point  $(0, 0, -h/2)$ .

The velocity distribution is given as

$$u_r = e^{i\Omega t} \left[ \left\{ \begin{array}{l} i\Omega x_0(z) \cos\phi \\ i\Omega y_0(z) \sin\phi \end{array} \right\} + \sum_{n=0}^{\infty} \sum_{m=0}^{\infty} A_{mn}(z) \cos\left(\frac{m}{2\alpha}\phi\right) \frac{\xi_{mn}}{a} C'_{m/2\alpha}\left(\xi_{mn}, \frac{r}{a}\right) \right] \quad (2.33a)$$

$$u_\phi = -e^{i\Omega t} \left[ \left\{ \begin{array}{l} i\Omega x_0(z) \sin \phi \\ -i\Omega y_0(z) \cos \phi \end{array} \right\} + \sum_{n=0}^{\infty} \sum_{m=0}^{\infty} A_{mn}(z) \sin \left( \frac{m}{2\alpha} \phi \right) \frac{m}{2\alpha r} C_{m/2\alpha} \left( \xi_{mn} \frac{r}{a} \right) \right] \quad (2.33b)$$

$$w = e^{i\Omega t} \left[ \left\{ \begin{array}{l} i\Omega r x'_0(z) \cos \phi \\ i\Omega r y'_0(z) \sin \phi \end{array} \right\} + \sum_{n=0}^{\infty} \sum_{m=0}^{\infty} A'_{mn}(z) \cos \left( \frac{m}{2\alpha} \phi \right) C_{m/2\alpha} \left( \xi_{mn} \frac{r}{a} \right) \right] \quad (2.33c)$$

The velocity distribution in the tank is obtained by omitting the first term in  $u_r$  and  $u_\phi$ ; these terms represent the tank motion.

Solutions for the special cases of bending of sector, annular, and circular tanks are given in the following paragraphs of this chapter.

### Circular Sector Compartmented Tank

The solution of the hydrodynamic problem for cylindrical containers of sector cross section may be obtained from the more general solutions presented in the preceding paragraphs by allowing the diameter ratio  $b/a$  to approach zero. The determinant  $\Delta_{m/2\alpha}(\xi) = 0$  then reduces to  $J'_{m/2\alpha}(\xi) = 0$ , the zeros of which are denoted as  $\epsilon_{mn}$ . The expansion functions  $C(\sigma)$  simplify to  $J_{m/2\alpha} \left( \epsilon_{mn} \frac{r}{a} \right)$ .

### 45° Sector Tank

Bauer (ref. 2.5) determined the velocity potentials and the natural frequencies corresponding to translation, pitch, yaw, and roll

$$\Phi(r, \phi, z, t) = i\Omega \phi_0 e^{i\Omega t} a^2 \left\{ \left( \frac{r}{a} \right)^2 \left( \phi - \frac{\pi}{8} \right) + \frac{2 \cos(8m-4)\phi}{(2m-1)[4(2m-1)^2-1]\pi} \right\} \left\{ \left( \frac{r}{a} \right)^{8m-4} - \frac{1}{2} \left( \frac{r}{a} \right)^2 \frac{1}{(2m-1)} \right\} + \frac{2[f_{2m-1,n} - 2(2m-1)e_{2m-1,n}]\eta^{*2} J_{8m-4}(\sigma^*) \cosh(\xi^* + \kappa^*)}{\pi(2m-1)[4(2m-1)^2-1](1-\eta^{*2}) \cosh \kappa^*} \cos(8m-4)\phi \quad (2.34c)$$

In these equations, various quantities are employed as follows:

$$\xi = \epsilon_{mn} \frac{z}{a}, \sigma = \epsilon_{mn} \frac{r}{a}, \kappa = \epsilon_{mn} \frac{h}{a}, J(\sigma) = J_{4m} \left( \epsilon_{mn} \frac{r}{a} \right),$$

$$a_0 = \frac{2(2)^{1/2}}{\pi}, a_m = \frac{4(-1)^{m+1}(2)^{1/2}}{\pi(16m^2-1)}, c_0 = \frac{2}{\pi} [2 - (2)^{1/2}]$$

$$c_m = \frac{4[(-1)^m(2)^{1/2}-2]}{\pi(16m^2-1)}, \eta = \frac{\Omega}{\omega_{mn}}, \gamma = g \frac{\epsilon_{mn}}{a\Omega^2}$$

$$b_{mn} = \frac{4\alpha\epsilon_{mn}(16m^2-1)}{(\epsilon_{mn}^2 - 16m^2)J_{4m}^2(\epsilon_{mn})} \sum_{\mu=0}^{\infty} \frac{J_{4m+2\mu+1}(\epsilon_{mn})}{(4m+2\mu+3)(4m+2\mu-1)}$$

$$A_{mn} = \frac{ab_{mn}\eta^2}{\epsilon_{mn}(1-\eta^2) \cosh \kappa} \left[ 2 \sinh \left( \frac{\kappa}{4} \right) - \left( \frac{\kappa}{2} + \gamma \right) \cosh \left( \frac{\kappa}{2} \right) \right] \left\{ \begin{array}{l} a_m \\ c_m \end{array} \right\}$$

motions of a 45° sector tank, as summarized below.

For translation in the  $x$ - and  $y$ -directions, with excitations of the forms  $x_0 e^{i\Omega t}$  and  $y_0 e^{i\Omega t}$

$$\Phi(r, \phi, z, t) = i\Omega e^{i\Omega t} \left[ \left\{ \begin{array}{l} x_0 r \cos \phi \\ y_0 r \sin \phi \end{array} \right\} + \left\{ \begin{array}{l} a_m x_0 \\ c_m y_0 \end{array} \right\} \frac{\eta^2 b_{mn} J(\sigma) \cosh(\xi + \kappa)}{(1-\eta^2) \cosh \kappa} \cos 4m\phi \right] \quad (2.34a)$$

For pitching and yawing motions about the  $x$  and  $y$  axes,  $x_0 e^{i\Omega t}$  and  $\theta_0 e^{i\Omega t}$ :

$$\Phi(r, \phi, z, t) = i\Omega e^{i\Omega t} \left[ \left\{ \begin{array}{l} x_0 r z \cos \phi \\ y_0 r z \sin \phi \end{array} \right\} - \left\{ \begin{array}{l} \theta_0 \\ x_0 \end{array} \right\} [A_{mn} \cosh \xi + B_{mn} \sinh \xi] J(\sigma) \cos 4m\phi \right] \quad (2.34b)$$

For roll excitation about the  $z$  axis, with excitation  $\phi_0 e^{i\Omega t}$ :

$$B_{mn} = \frac{ab_{mn}\eta^2}{\epsilon_{mn}(1-\eta^2)\cosh \kappa} \left[ \left( 3\gamma - \frac{\kappa}{2} \right) \sinh \left( \frac{\kappa}{2} \right) - 2 \cosh \left( \frac{\kappa}{2} \right) \right] \left\{ \frac{a_m}{c_m} \right\}$$

$$f_{2m-1,n} = \frac{8(2m-1)}{[\bar{\epsilon}_{mn}^2 - 16(2m-1)^2]J_{8m-4}(\bar{\epsilon}_{mn})}$$

$$\epsilon_{2m-1,n} = \frac{4\bar{\epsilon}_{mn}(2m-1)(4m-3)(4m-1)}{[\bar{\epsilon}_{mn}^2 - 16(2m-1)^2]J_{8m-4}^2(\bar{\epsilon}_{mn})} \sum_{\mu=0}^{\infty} \frac{[8m+2\mu-3]J_{8m+2\mu-3}(\bar{\epsilon}_{mn})}{(4m+\mu-3)(4m+\mu-2)(4m+\mu-1)(4m+\mu)}$$

where  $\bar{\epsilon}$  are the roots of  $J'_{8m-4}(\bar{\epsilon})=0$  and  $J(\sigma^*) \equiv J_{8m-4}[\epsilon(r/a)]$ . Further, the quantities  $\xi^*$ ,  $\sigma^*$ ,  $\eta^*$ , and  $\kappa^*$  are defined by

$$\xi^* = \xi_{2m-1,n} \frac{z}{a} \quad \kappa^* = \xi_{2m-1,n} \frac{h}{a}$$

$$\sigma^* = \xi_{2m-1,n} \frac{r}{a} \quad \eta^* = \frac{\Omega}{\omega_{2m-1,n}}$$

The natural frequencies are obtained from the equation

$$\omega_{mn}^2 = \omega^2 = \frac{g}{a} \epsilon_{mn} \tanh \left( \epsilon_{mn} \frac{h}{a} \right) \quad m, n = 0, 1, 2, \dots \quad (2.35)$$

where the values  $\epsilon_{mn}$  are the positive roots of  $J'_{4m}(\epsilon)=0$ . Figure 2.7 shows the natural frequencies ( $f_{mn} = \frac{\omega_{mn}}{2\pi}$ ) as a function of liquid depth; the roots  $\epsilon_{mn}$  are given in table 2.2.

Figures 2.8 and 2.9 show, respectively, the force in the  $x$ -direction corresponding to excitation in that direction and the moment about the  $z$ -axis corresponding to roll motion, as a function of the forcing frequency.

Experimental data on force response in  $45^\circ$  sector tanks in translation have been obtained and compared with these theoretical predictions (refs. 2.6 to 2.8). Figure 2.8 shows relatively good correlations in the magnitude of the force response except, of course, in the immediate vicinity of the first mode resonance. On the other hand, there are marked differences in the experimental and theoretically predicted resonant frequencies, with the former always less than the latter. This "softening" characteristic is a consequence of the essentially nonlinear behavior of compartmented tanks and therefore is primarily dependent upon excitation amplitude, as can be seen in figure 2.10. (Such nonlinear effects, essentially dependent upon geometry, will be discussed in more detail in ch. 3.)

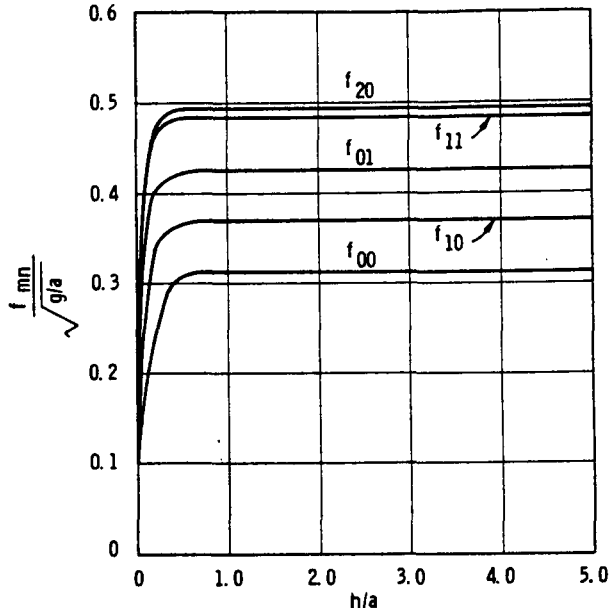


FIGURE 2.7.—Natural frequency parameter for  $45^\circ$  sector tank (ref. 2.5).

### 90° Sector Tank

Bauer (refs. 2.3 and 2.4) has also obtained theoretical results for predicting the behavior of a liquid in a  $90^\circ$  sector (quarter) cylindrical tank both by solving the hydrodynamic equations (ref. 2.4) and by considering this configuration as a special case of the ring sector tank (ref. 2.3). The forces and moments due to translational, pitching, and roll excitations will be summarized in the following.

The velocity potential for translational excitation in the  $x$ -direction ( $x_0 e^{i\Omega t}$ ) is

$$\Phi(r, \phi, z, t) = i\Omega x_0 e^{i\Omega t} \left\{ r \cos \phi + \frac{a_m b_{mn} \cos 2m\phi \cosh(\kappa + \xi) J_{2m}(\sigma) \eta^2}{(1 - \eta^2) \cosh \kappa} \right\} \quad (2.36a)$$

where

$$a_0 = -\frac{2}{\pi}, \quad a_m = \frac{(-1)^{m+1}}{\pi \left( m^2 - \frac{1}{4} \right)}$$

$$b_{mn} = \frac{16a\epsilon_{mn} \left( m^2 - \frac{1}{4} \right)}{(\epsilon_{mn}^2 - 4m^2) J_{2m}^2(\epsilon_{mn})} \times \sum_{\mu=0}^{\infty} \frac{J_{2m+2\mu+1}(\epsilon_{mn})}{(2m+2\mu-1)(2m+2\mu+3)}$$

$\epsilon_{mn}$  are the roots of the equation

$$J'_{2m}(\epsilon_{mn}) = 0$$

and the definitions of  $\eta$ ,  $\kappa$ , and  $\zeta$  as given in equation (2.21) are valid if  $\xi_{mn}$  is replaced by  $\epsilon_{mn}$ .

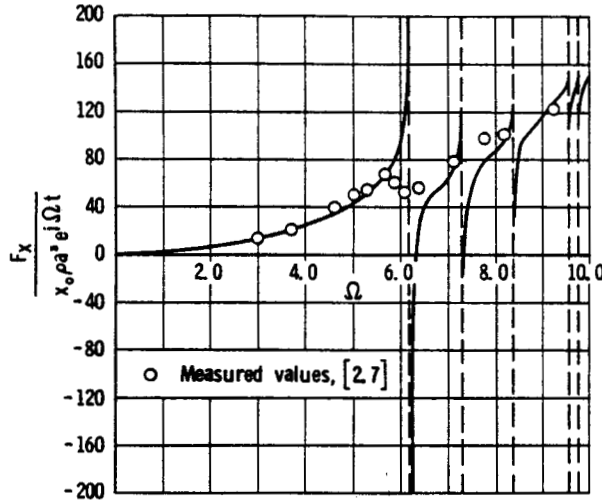


FIGURE 2.8.—Magnification factor for  $x$  component of liquid force for excitation in  $x$  direction in  $45^\circ$  sector tank (ref. 2.5).

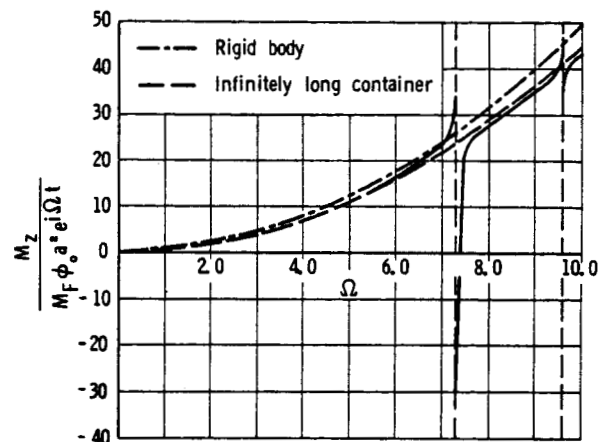


FIGURE 2.9.—Magnification factor for liquid moment  $M_z$  for roll excitation in  $45^\circ$  sector tank (ref. 2.5).

The natural frequencies may be obtained from the equation

$$\omega_{mn}^2 = \frac{g}{a} \epsilon_{mn} \tanh \left( \epsilon_{mn} \frac{h}{a} \right) \quad (2.36b)$$

and are shown graphically in figure 2.5, while the roots  $\epsilon_{mn}$  are given in table 2.2.

Equations for the free surface displacements, forces and moments [with respect to the point  $(0, 0, -h/2)$ ] are given in detail in appendix C. The forces and moments are plotted against excitation frequency in figures 2.11 and 2.12. In appendix C, the first term in  $F_x$  corresponds to the inertial force of the liquid (fig. 2.11), the last term in the moment expressions correspond to the static moment, and the terms

TABLE 2.2.—Roots of  $J'_{\frac{m}{2\alpha}}(\xi_{mn}) = 0$

[Refs. 2.4 and 2.8]

$n$	$\frac{m}{2\alpha}$	0	1	2	3	4	5	6	7	8	10	12	14	16	18
0.....	3.832	1.841	3.054	4.201	5.318	6.416	7.501	8.578	9.647	11.716	13.821	15.917	18.104	20.189	
1.....	7.016	5.331	6.706	8.015	9.282	10.520	11.735	12.932	14.116	16.448	18.745	21.015	23.264	25.495	
2.....	10.173	8.536	9.909	11.346	12.682	13.987	15.268	16.529	17.774	20.223	22.629	25.002	27.347	29.670	
3.....	13.324	11.708	13.170	14.586	15.964	17.313	18.637	19.942	21.226	23.761	26.246	28.694	31.112	33.504	
4.....	16.471	14.864	16.348	17.789	19.196	20.576	21.932	23.268	24.587	27.182	29.729	32.237	34.712	37.160	
5.....	19.616	18.016	19.513	20.973	22.401	23.804	25.184	26.545	27.889	30.535	33.131	35.889	38.212	40.707	
6.....	22.760	21.164	22.672	24.145	25.590	27.010	28.410	29.791	31.155	33.842	36.481	39.079	41.643	44.178	
7.....	25.904	24.312	25.826	27.310	28.768	30.203	31.618	33.015	34.397	37.118	39.792	42.428	45.052	47.595	
8.....	29.047	27.488	28.978	30.470	31.930	33.385	34.831	36.224	37.620	40.371	43.075	45.740	48.371	50.971	
9.....	32.189	30.602	32.127	33.627	35.104	36.561	38.000	39.422	40.830	43.607	46.338	49.030	51.687	54.315	

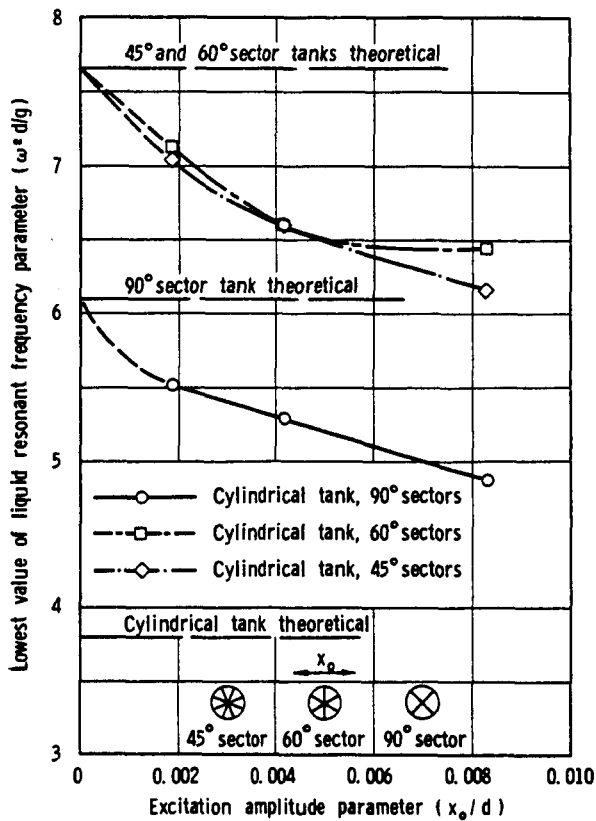


FIGURE 2.10.—Effect of excitation amplitude on the lowest resonant frequency for 45°, 60°, and 90° sector tanks (ref. 2.8).

$L_0$  and  $L_2$  are defined by

$$L_0 = \frac{2}{\epsilon_{mn}} \sum_{\mu=0}^{\infty} J_{2m+2\mu+1}(\epsilon_{mn})$$

$$L_2 = \frac{2(4m^2-1)}{\epsilon_{mn}} \sum_{\mu=0}^{\infty} \frac{J_{2m+2\mu+1}(\epsilon_{mn})}{(2m+2\mu-1)(2m+2\mu+3)}$$

As in the case of the 45° sector tank, measured force response (refs. 2.6 and 2.8) is in relatively good agreement with theory, but measured resonant frequencies are substantially less than predicted. The variation of frequency with excitation amplitude for the 90° sector tank is also shown in figure 2.10. Note again the relative values of frequencies for sector tanks of various vertex angles (compare with fig. 2.5). In addition, it should be noted that the ordinates (magnification functions) of the figures in this chapter have the units of 1/sec<sup>2</sup>.

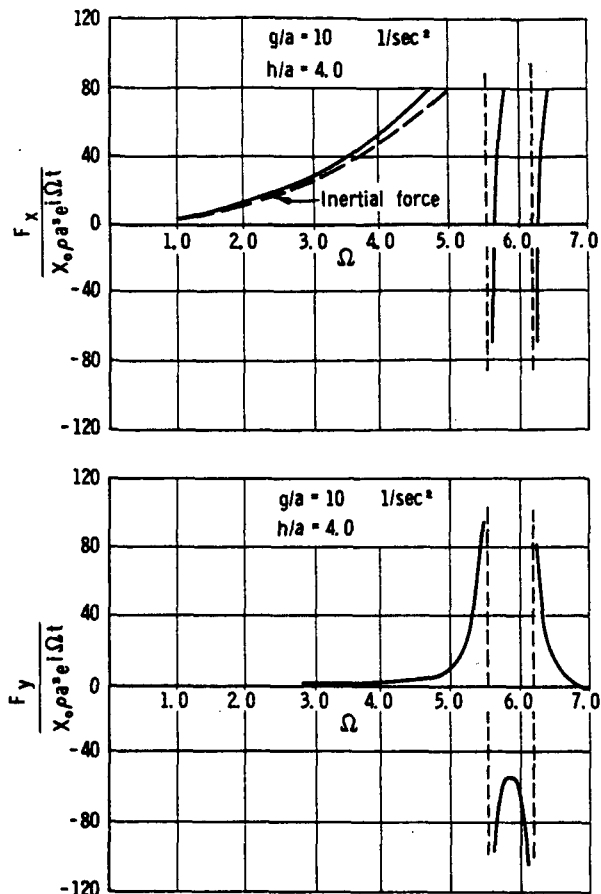


FIGURE 2.11.—Magnification factor of liquid force in a 90° sector cylindrical tank (excitation along  $x$  axis) (ref. 2.3).

The velocity potential for rotational oscillations about the  $y$ -axis excited by  $\theta_0 e^{i\Omega t}$  is

$$\Phi(r, \phi, z, t) = -i\Omega\theta_0 e^{i\Omega t} \{ r_2 \cos \phi - [A_{mn} \cosh \xi + B_{mn} \sinh \xi] J_{2m}(\sigma) \cos 2m\phi \} \quad (2.36c)$$

where  $A_{mn}$  and  $B_{mn}$  are given in appendix B, providing that appropriate values of  $a_m$  and  $b_{mn}$  are used<sup>2</sup> and that  $\xi_{mn}$  is replaced by  $\epsilon_{mn}$ . The free surface displacements, forces and moments are given in appendix C, while the liquid force is plotted versus excitation frequency in figure 2.13. The wave forms of the free surface at times before and after the first

<sup>2</sup> See eqs. (2.22) for definitions of  $a_m$  and  $b_{mn}$ .

and second natural frequencies are shown in figure 2.14.

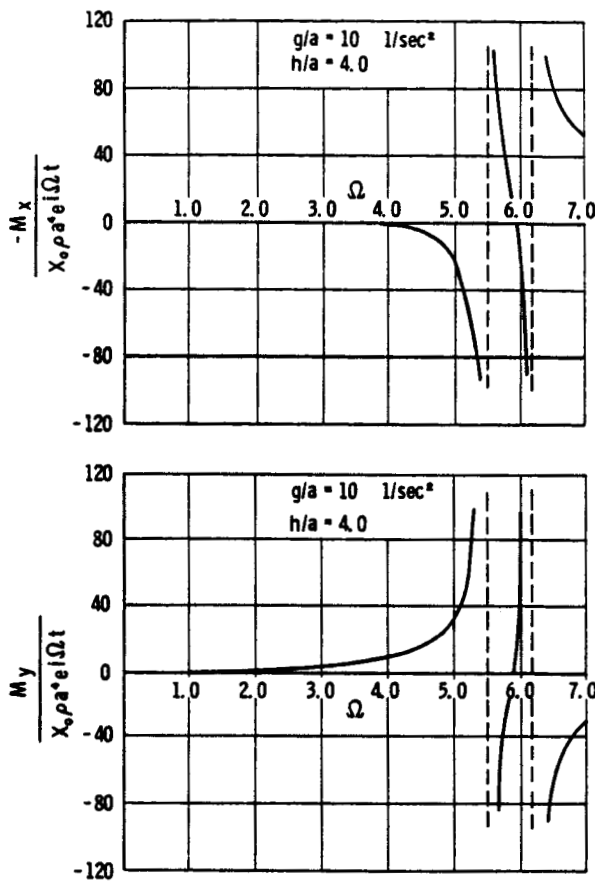


FIGURE 2.12.—Magnification factor of liquid moment in a 90° sector cylindrical tank (excitation along  $x$  axis) (ref. 2.3).

For roll oscillations of the container excited by  $\phi = \phi_0 e^{i\Omega t}$ , the velocity potential is

$$\begin{aligned} \Phi(r, \phi, z, t) = & i\Omega\phi_0 e^{i\Omega t} \left\{ r^2 \left( \phi - \frac{\pi}{r} \right) \right. \\ & + \frac{2a^2 \cos[(4m-2)\phi]}{\pi(2m-1)[(2m-1)^2-1]} \left[ \left( \frac{r}{a} \right)^{4m-2} - \frac{(r/a)^2}{(2m-1)} \right] + \frac{2a^2}{\pi} \left( \frac{r}{a} \right)^2 \left[ \ln \left( \frac{r}{a} \right) + \frac{1}{2} \right] \cos 2\phi \\ & + \frac{2a^2}{\pi} \frac{[f_{2m-1,n} - e_{2m-1,n}(2m-1)]\eta^{*2} J_{4m-2}(\sigma^*)}{(2m-1)[(2m-1)^2-1](1-\eta^{*2}) \cosh \kappa^*} \cosh(\kappa^* + \zeta^*) \cos(4m-2)\phi \\ & \left. + \frac{a^2 (2f_n - e_n) \cosh(\kappa_1^* + \zeta_1^*) \eta_1^{*2} J_2(\sigma_1^*) \cos 2\phi}{\pi (1-\eta_1^{*2}) \cosh \kappa_1^*} \right\} \quad (2.37) \end{aligned}$$

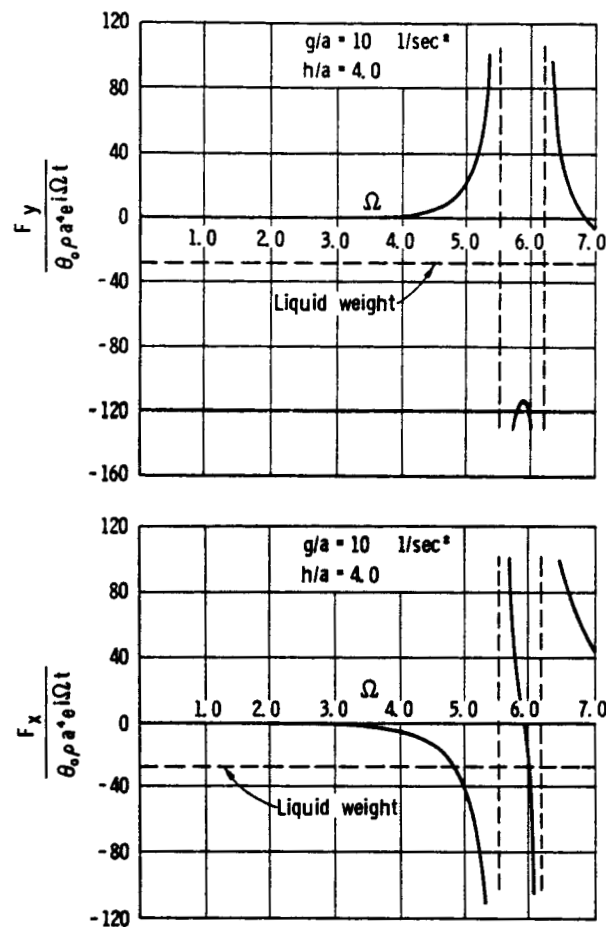


FIGURE 2.13.—Magnification factor of liquid force in a 90° sector cylindrical tank (rotational excitation about  $y$  axis) (ref. 2.3).

where

$$f_n = -\frac{8}{(\bar{\epsilon}_n^2 - 4) J_2^2(\bar{\epsilon}_n)} \sum_{\mu=0}^{\infty} \frac{J_{2\mu+1}(\bar{\epsilon}_n)}{(\mu+1)(\mu+3)}$$

$$\epsilon_n = \frac{4}{(\bar{\epsilon}_n^2 - 4) J_2(\bar{\epsilon}_n)}$$

$$f_{2m-1,n} = \frac{4(2m-1)}{[\bar{\epsilon}_{2m-1,n}^2 - 4(2m-1)^2] J_{4m-2}(\bar{\epsilon}_{2m-1,n})}$$

$$\epsilon_{2m-1,n} = \frac{2m\bar{\epsilon}_{2m-1,n}(2m-1)}{(m-1)[\bar{\epsilon}_{2m-1,n}^2 - 4(2m-1)^2] J_{4m-2}^2(\bar{\epsilon}_{2m-1,n})} \sum_{\mu=0}^{\infty} \frac{(4m+2\mu-1) J_{4m+2\mu-1}(\bar{\epsilon}_{2m-1,n})}{(2m+2\mu-2)(2m+2\mu-1)(2m+\mu)(2m+\mu+1)}$$

and the quantities  $\kappa_1^*, \sigma_1^*, \eta_1^*, \xi_1^*, \kappa^*, \sigma^*, \eta^*$ , and  $\xi^*$  are defined in appendix C. The values  $\bar{\epsilon}_n$  are the roots of the equation  $J'_2(\bar{\epsilon}_n) = 0$  while the values  $\bar{\epsilon}_{2m-1,n}$  are solutions of the equation  $J'_{4m-2}(\bar{\epsilon}_{2m-1,n}) = 0$ . Figures 2.15 to 2.17 illustrate the magnification factors for the forces and moments of the liquid, while explicit expressions for free surface displacements, forces, and moments are given in appendix C. The values of  $L_0$ ,  $L_1$ , and  $L_2$  associated with roll motions (these are different for translational motions) are

$$L_0 = \frac{2}{\bar{\epsilon}_{2m-1,n}} \sum_{\mu=0}^{\infty} J_{4m+2\mu-1}(\bar{\epsilon}_{2m-1,n})$$

$$L_1 = \frac{2m-1}{\bar{\epsilon}_{2m-1,n}} \sum_{\mu=0}^{\infty} \frac{(4m+2\mu-1) J_{4m+2\mu-1}(\bar{\epsilon}_{2m-1,n})}{(2m+\mu-1)(2m+\mu)}$$

$$L_2 = \frac{2(4m-1)(4m-3)}{\bar{\epsilon}_{2m-1,n}} \sum_{\mu=0}^{\infty} \frac{J_{4m+2\mu-1}(\bar{\epsilon}_{2m-1,n})}{(4m+2\mu+1)(4m+2\mu-3)}$$

#### General Sector Tank

The case of a sector tank with an arbitrary vertex angle is discussed in references 2.3 and 2.31. The results for translational, rotational, roll and bending oscillations are given in appendixes D and E. The following points should be noted in connection with these tables:

- (1) The quantities  $a_m$ ,  $b_{mn}$ , and  $c_m$  are given in equations (2.22) and appendix A. The terms  $b_{mn}$  may be simplified to

$$b_{mn} = \frac{a \int_0^{\epsilon_{mn}} \rho^2 J(\rho) d\rho}{\epsilon_{mn} \int_0^{\epsilon_{mn}} \rho J^2(\rho) d\rho}$$

$$= 2a \frac{\frac{\Gamma(m/4\alpha + 3/2)}{\Gamma(m/4\alpha - 1/2)} \sum_{\mu=0}^{\infty} \frac{(m/2\alpha + 2\mu + 1) \Gamma(m/4\alpha + \mu - 1/2)}{\Gamma(m/4\alpha + \mu + 5/2)} J_{m/2\alpha + 2\mu + 1}(\epsilon_{mn})}{\epsilon_{mn} (1 - m^2/4\alpha^2 \epsilon_{mn}^2) J_{m/2\alpha}^2(\epsilon_{mn})} \quad m, n = 0, 1, 2, \dots$$

- (2) The determinant  $\Delta_{m/2\alpha} = 0$  reduces to  $J'_{m/2\alpha}(\xi) = 0$ , the zeros of which are denoted by  $\epsilon_{mn}$ ; the roots may be obtained from table 2.2.
- (3) The functions  $C(\sigma)$  simplify to the Bessel functions  $J_{m/2\alpha}\left(\epsilon_{mn} \frac{r}{a}\right)$ .

Liquid natural frequencies for the  $60^\circ$  sector tank have been determined experimentally (ref. 2.8) and therefore are also shown in figure 2.10.

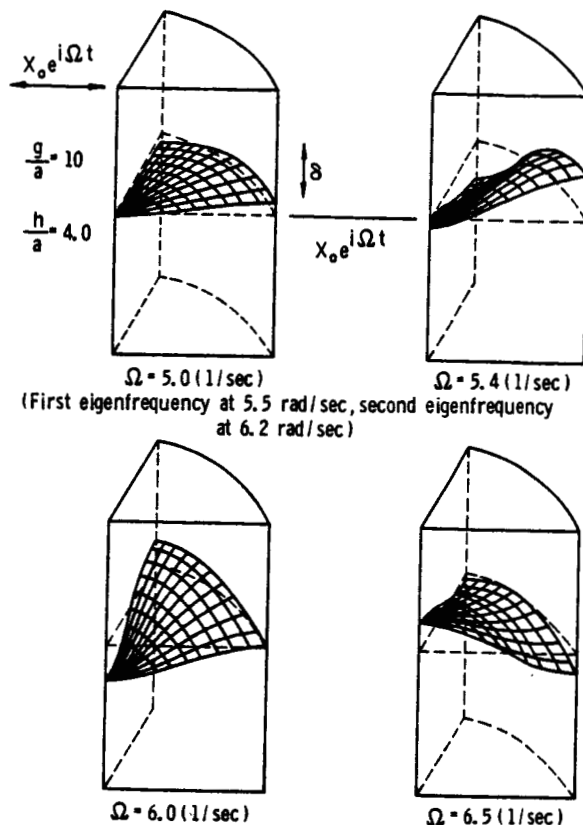


FIGURE 2.14.—Wave form of the liquid free surface in a circular quarter tank (ref. 2.3).

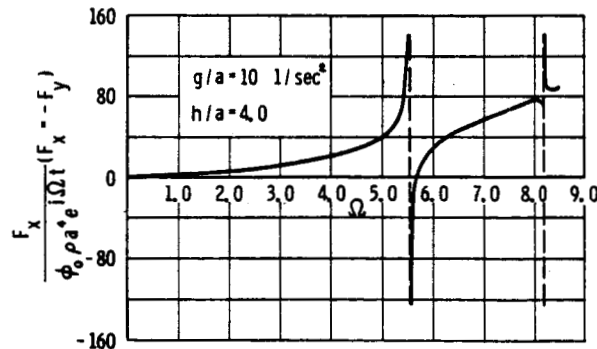


FIGURE 2.15.—Magnification factor of liquid force in a 90° sector cylindrical tank (roll excitation about z axis) (ref. 2.3).

#### Ring-Compartmented (Annular) Tank

Perhaps it is worthwhile to mention here, once again, the essential characteristics of compartmented tanks that lead to their study. If one wishes to avoid coupling between various components of a dynamical system, an effective

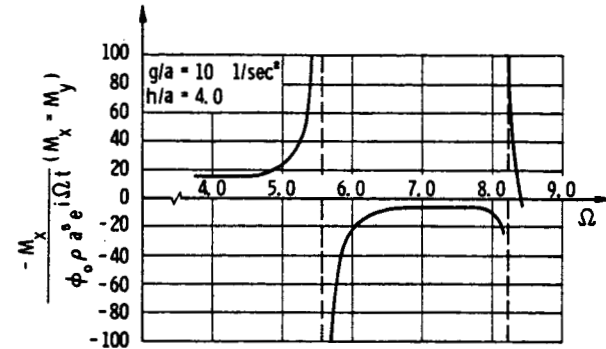


FIGURE 2.16.—Magnification factor of liquid moment in a 90° sector cylindrical tank (roll excitation about z axis) (ref. 2.3).

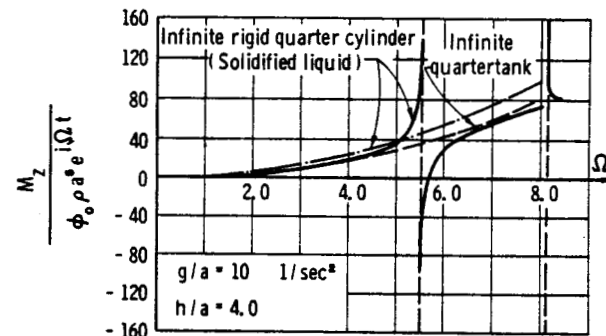


FIGURE 2.17.—Magnification factor of liquid moment in a 90° sector cylindrical tank (roll excitation about z axis) (ref. 2.3).

procedure to employ is often that of modifying one component in such a way that its natural frequencies are shifted appreciably. In the case of a liquid-filled tank, of course, compartmentation is the means of shifting the liquid frequencies, as may be seen in figures 2.5 and 2.10. Figure 2.5, especially, shows that sector compartmentation does indeed have the effect of increasing the frequency of the lowest mode in the uncompartmented tank, but also introduces additional modes with frequencies that are relatively closely spaced. On the other hand, compartmentation by annular ring has the effect of decreasing the frequency of the lowest mode while introducing additional modes that are relatively widely spaced.

The annular tank has been considered theoretically in references 2.2 and 2.34. Equations for the liquid natural frequencies, free surface displacements, forces and moments induced by

free, translational, pitching, and bending type oscillations have been derived and extensive plots presented in reference 2.2. The methods employed are again similar to those outlined in earlier portions of this chapter, with the results presented below. The velocity potential for a liquid in a ring tank subjected to arbitrary pitching and translational motion has also been derived in reference 2.34, although the fluid forces and moments were calculated only for those special cases of a circular cylindrical tank.

#### Free Oscillations

The origin of the coordinate system is located at the center of the plane of the undisturbed free surface with the  $z$ -axis pointing out of the liquid (fig. 2.18). For free oscillations, the velocity potential is

$$\Phi(r, \phi, z, t) = e^{i\Omega t} \left\{ (\bar{C}_{nm} \sin m\phi + \bar{D}_{nm} \cos m\phi) \frac{\cosh \left[ \xi_{nm} \left( \frac{h}{a} + \frac{z}{a} \right) \right] C_m \left( \xi_{nm} \frac{r}{a} \right)}{\cosh \left( \xi_{nm} \frac{h}{a} \right) Y'_m(\xi_{nm})} \right\} \quad (2.38)$$

where  $\bar{C}_{nm}$  and  $\bar{D}_{nm}$  are to be determined from the initial conditions,  $\xi_{nm}$  are the positive roots of equation (2.18d) for the case  $2\alpha=1$ , the  $C_m \left( \xi_{nm} \frac{r}{a} \right)$  are defined by equation (2.18c) for the case  $2\alpha=1$ , and  $k=b/a$  is the diameter ratio of the inner and outer tank walls. The roots of the equation  $\Delta_m=0$  for  $m=1$  are tabulated for various values of  $k$  in table 2.1 and plotted in figure 2.4. The natural frequencies are obtained from the relation

$$\omega_{nm}^2 = \frac{g}{a} \xi_{nm} \tanh \left( \xi_{nm} \frac{h}{a} \right) \quad (2.39)$$

and are shown in figure 2.5 for tank diameter ratios of 0.2, 0.5, and 0.8 as a function of the liquid height. The frequencies of the cylindrical inner tank are also shown for comparison. The tank configuration having a ratio of  $k$  between 0.5 and 0.7 would appear to offer the

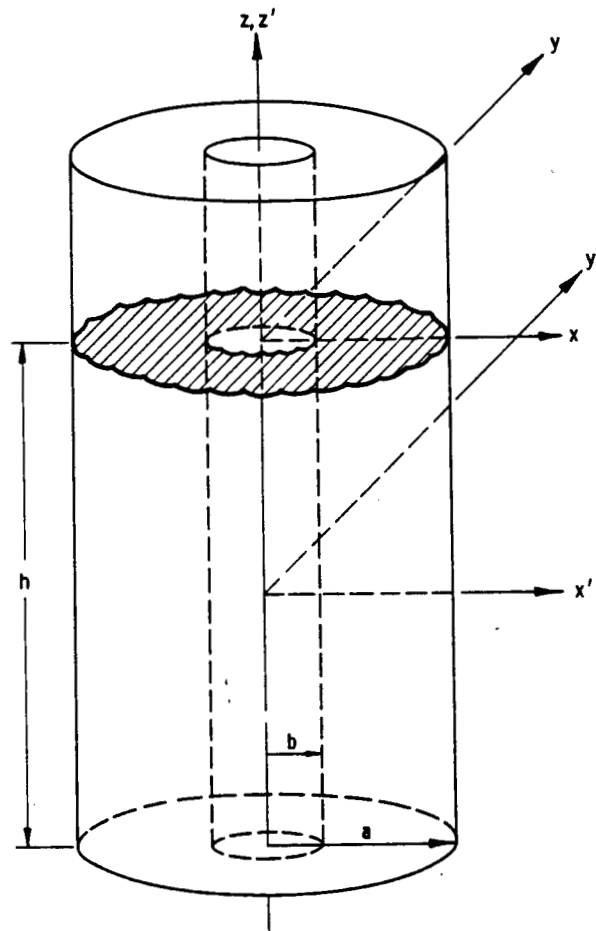


FIGURE 2.18.—Circular cylindrical ring (annular) tank.

most promise of phasing the liquid motions of the inner and outer tank such that some slosh force cancellation is obtained. Such cancellation is promoted by the fact that for this range of  $k$ , the liquid masses in the two tanks are approximately equal.

The free surface displacements, measured from the undisturbed surface, and the pressure at depth ( $-z$ ) are

$$\begin{aligned} \delta(r, \phi, t) &= -\frac{1}{g} \left( \frac{\partial \Phi}{\partial t} \right)_{z=0} \\ &= -\frac{1}{g} \sum_{m=0}^{\infty} \sum_{n=0}^{\infty} \omega_{nm} [\bar{C}_{nm} \sin m\phi \\ &\quad + \bar{D}_{nm} \cos m\phi] \frac{C_m \left( \xi_{nm} \frac{r}{a} \right)}{Y'_m(\xi_{nm})} e^{i\omega_{nm} t} \quad (2.40a) \end{aligned}$$

$$p = -i\rho \sum_{n=0}^{\infty} \sum_{m=0}^{\infty} \omega_{nm} \{ \bar{C}_{nm} \sin m\phi + \bar{D}_{nm} \cos m\phi \}$$

$$\times \frac{\cosh \left[ \frac{\xi_{nm}}{a}(z+h) \right] C_m \left( \xi_{nm} \frac{r}{a} \right)}{\cosh \left( \xi_{nm} \frac{h}{a} \right) Y'_m(\xi_{nm})} e^{i\omega_{nm} t} - \rho g z$$
(2.40b)

As a matter of general interest, the three lowest liquid free surface modes are shown in figure 2.19 for  $k=0.3$ . The displacements are normalized to unity at the outer tank wall, and  $n$  indicates the mode number.

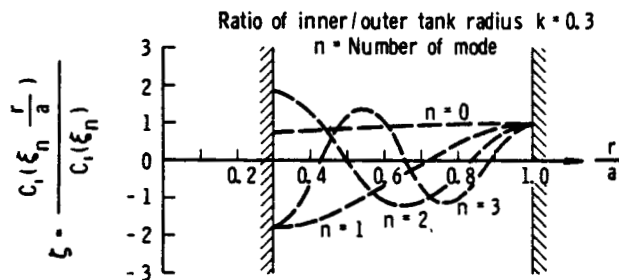


FIGURE 2.19.—Free surface modes for free oscillation in a ring tank,  $k=0.3$ ,  $n=0$  to 3 (ref. 2.2).

The slosh forces and moments acting on the container caused by the free liquid oscillations may be obtained by integration of the pressure distribution. Thus

$$F_z = -\frac{iM_F}{a} \sum_{n=0}^{\infty} \frac{\omega_{n1} \bar{D}_{n1}}{Y'_1(\xi_{n1})} \frac{\tanh \left( \xi_{n1} \frac{h}{a} \right)}{\left( \xi_{n1} \frac{h}{a} \right)}$$

$$\times \left[ \frac{2}{\pi \xi_{n1}} - k C_1(k \xi_{n1}) \right] \frac{e^{i\omega_{n1} t}}{(1-k^2)} \quad (2.41a)$$

$$F_x = -\frac{iM_F}{a} \sum_{n=0}^{\infty} \frac{\omega_{n1} \bar{C}_{n1}}{Y'_1(\xi_{n1})} \frac{\tanh \left( \xi_{n1} \frac{h}{a} \right)}{\left( \xi_{n1} \frac{h}{a} \right)}$$

$$\times \left[ \frac{2}{\pi \xi_{n1}} - k C_1(k \xi_{n1}) \right] \frac{e^{i\omega_{n1} t}}{(1-k^2)} \quad (2.41b)$$

The moments about the center of gravity of the liquid are

$$M_y = -iM_F \sum_{n=0}^{\infty} \frac{\omega_{n1} \bar{D}_{n1} e^{i\omega_{n1} t}}{\xi_{n1} Y'_1(\xi_{n1}) (1-k^2)}$$

$$\times \left[ \frac{2}{\pi \xi_{n1}} - k C_1(k \xi_{n1}) \right] \left[ \frac{1}{2} \tanh \left( \xi_{n1} \frac{h}{a} \right) \right.$$

$$\left. + \frac{1}{\left( \xi_{n1} \frac{h}{a} \right)} \left( \frac{2}{\cosh \left( \xi_{n1} \frac{h}{a} \right)} - 1 \right) \right] \quad (2.42a)$$

$$M_x = -iM_F \sum_{n=0}^{\infty} \frac{\omega_{n1} \bar{C}_{n1} e^{i\omega_{n1} t}}{\xi_{n1} Y'_1(\xi_{n1}) (1-k^2)}$$

$$\times \left[ \frac{2}{\pi \xi_{n1}} - k C_1(k \xi_{n1}) \right] \left[ \frac{1}{2} \tanh \left( \xi_{n1} \frac{h}{a} \right) \right.$$

$$\left. + \frac{1}{\left( \xi_{n1} \frac{h}{a} \right)} \left( \frac{2}{\cosh \left( \xi_{n1} \frac{h}{a} \right)} - 1 \right) \right] \quad (2.42b)$$

It should be noted that only the modes  $m=1, 3, 5, \dots$  contribute to the forces and moments. The velocity distribution in the tank is

$$u_r = \sum_{n=0}^{\infty} \sum_{m=0}^{\infty} \frac{\xi_{nm}}{a} [\bar{C}_{nm} \sin m\phi + \bar{D}_{nm} \cos m\phi]$$

$$\times \frac{\cosh \left[ \frac{\xi_{nm}}{a}(z+h) \right] C'_m \left( \xi_{nm} \frac{r}{a} \right)}{\cosh \left( \xi_{nm} \frac{h}{a} \right) Y'_m(\xi_{nm})} e^{i\omega_{nm} t} \quad (2.43a)$$

$$u_\phi = \frac{1}{r} \sum_{n=0}^{\infty} \sum_{m=0}^{\infty} m [\bar{C}_{nm} \cos m\phi - \bar{D}_{nm} \sin m\phi] \\ \times \frac{\cosh \left[ \frac{\xi_{nm}}{a} (z+h) \right] C_m \left( \xi_{nm} \frac{r}{a} \right) e^{iu_{nm} t}}{\cosh \left( \xi_{nm} \frac{h}{a} \right) Y'_m(\xi_{nm})} \quad (2.43b)$$

$$w = \sum_{n=0}^{\infty} \sum_{m=0}^{\infty} \frac{\xi_{nm}}{a} [\bar{C}_{nm} \sin m\phi + \bar{D}_{nm} \cos m\phi] \\ \times \frac{\sinh \left[ \frac{\xi_{nm}}{a} (z+h) \right] C_m \left( \xi_{nm} \frac{r}{a} \right) e^{iu_{nm} t}}{\cosh \left( \xi_{nm} \frac{h}{a} \right) Y'_m(\xi_{nm})} \quad (2.43c)$$

#### Translational Forced Oscillations

For forced translational oscillations of the form  $x_0 e^{i\Omega t}$ , the velocity potential is given by

$$\Phi(r, \phi, z, t) = i\Omega x_0 e^{i\Omega t} a \cos \phi \\ \times \left[ \frac{r}{a} + \sum_{n=0}^{\infty} \frac{\bar{A}_n \cosh \left[ \frac{\xi_{n1}}{a} (z+h) \right]}{\left( \frac{\omega_{n1}^2}{\Omega^2} - 1 \right) \cosh \left( \xi_{n1} \frac{h}{a} \right)} C_1 \left( \xi_{n1} \frac{r}{a} \right) \right] \quad (2.44)$$

where

$$\bar{A}_n = 2 \frac{\left[ \frac{2}{\pi \xi_{n1}} - k C_1(k \xi_{n1}) \right]}{\frac{4}{\pi^2 \xi_{n1}^2} (\xi_{n1}^2 - 1) + C_1^2(k \xi_{n1}) (1 - k^2 \xi_{n1}^2)}$$

The wave form of the free fluid surface, measured from the undisturbed fluid level, and the pressure distribution in the tank at depth ( $-z$ ) are

$$\delta(r, \phi, t) = \frac{\Omega^2}{(g/a)} x_0 e^{i\Omega t} \cos \phi \\ \times \left[ \frac{r}{a} + \sum_{n=0}^{\infty} \frac{\bar{A}_n C_1 \left( \xi_{n1} \frac{r}{a} \right)}{\left( \frac{\omega_{n1}^2}{\Omega^2} - 1 \right)} \right] \quad (2.45a)$$

and forces and moments are plotted versus excitation frequency for  $k=0.5$  and  $0.9$  in figures 2.20 and 2.21. The velocity distributions are given by

$$p = \rho \Omega^2 x_0 e^{i\Omega t} a \cos \phi \\ \times \left[ \frac{r}{a} + \sum_{n=0}^{\infty} \frac{\bar{A}_n \cosh \left[ \frac{\xi_{n1}}{a} (z+h) \right]}{\left( \frac{\omega_{n1}^2}{\Omega^2} - 1 \right) \cosh \left( \xi_{n1} \frac{h}{a} \right)} C_1 \left( \xi_{n1} \frac{r}{a} \right) \right] - \rho g z \quad (2.45b)$$

The free surface displacements for various values of  $k$  and  $h/a$  have been calculated and are plotted in reference 2.2.

The fluid forces and moments (with respect to the center of gravity of the undisturbed fluid and positive according to the "right-hand" rule) are given by the equations

$$F_x = M_F \Omega^2 x_0 e^{i\Omega t} \left[ 1 + \sum_{n=0}^{\infty} \frac{\bar{A}_n \left[ \frac{2}{\pi \xi_{n1}} - k C_1(k \xi_{n1}) \right]}{\left( \frac{\omega_{n1}^2}{\Omega^2} - 1 \right) (1 - k^2)} \right. \\ \left. \times \frac{\tanh \left( \xi_{n1} \frac{h}{a} \right)}{\left( \xi_{n1} \frac{h}{a} \right)} \right] \quad (2.46a)$$

$$F_y = 0 \quad (2.46b)$$

$$M_y = M_F \Omega^2 x_0 e^{i\Omega t} a \left[ \frac{1+k^2}{4h/a} \right. \\ \left. + \sum_{n=0}^{\infty} \frac{\bar{A}_n \left[ \frac{2}{\pi \xi_{n1}} - k C_1(k \xi_{n1}) \right]}{2\xi_{n1}(1-k^2) \left( \frac{\omega_{n1}^2}{\Omega^2} - 1 \right)} \left[ \tanh \left( \xi_{n1} \frac{h}{a} \right) \right. \right. \\ \left. \left. + \frac{2}{\left( \xi_{n1} \frac{h}{a} \right)} \left[ \frac{2}{\cosh \left( \xi_{n1} \frac{h}{a} \right)} - 1 \right] \right] \right] \quad (2.46c)$$

$$M_x = 0 \quad (2.46d)$$

$$u_r = i\Omega x_0 e^{i\Omega t} \cos \phi \left\{ 1 + \sum_{n=0}^{\infty} \frac{\bar{A}_n \xi_n \cosh \left[ \frac{\xi_n}{a} (z+h) \right]}{\left( \frac{\omega_n^2}{\Omega^2} - 1 \right) \cosh \left( \xi_n \frac{h}{a} \right)} C'_1 \left( \xi_n \frac{r}{a} \right) \right\} \quad (2.47a)$$

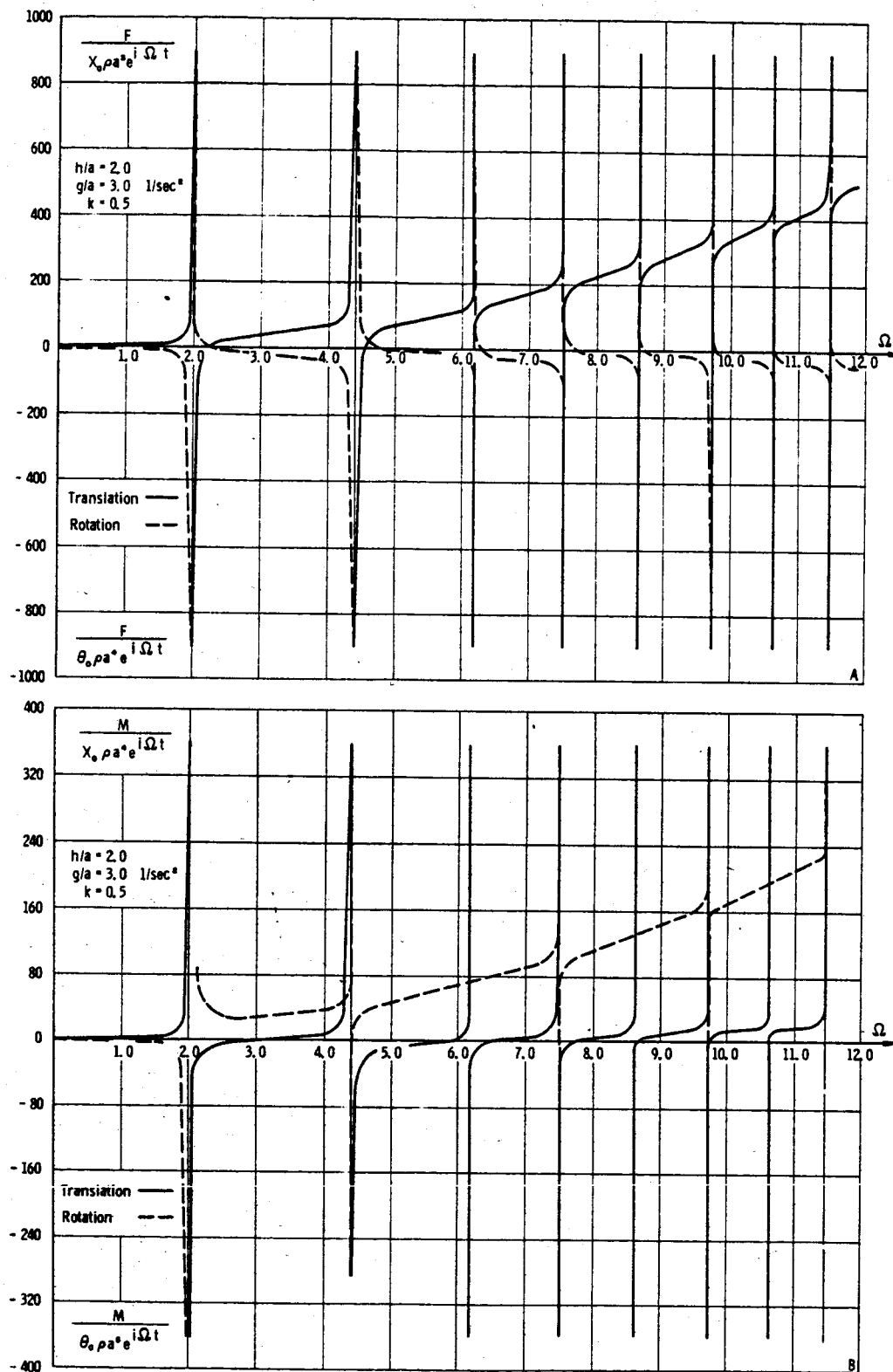


FIGURE 2.20.—Liquid force and moment in a ring tank ( $k=0.5$ ) resulting from translation and pitching excitation (ref. 2.2).

229-648 O-67-4

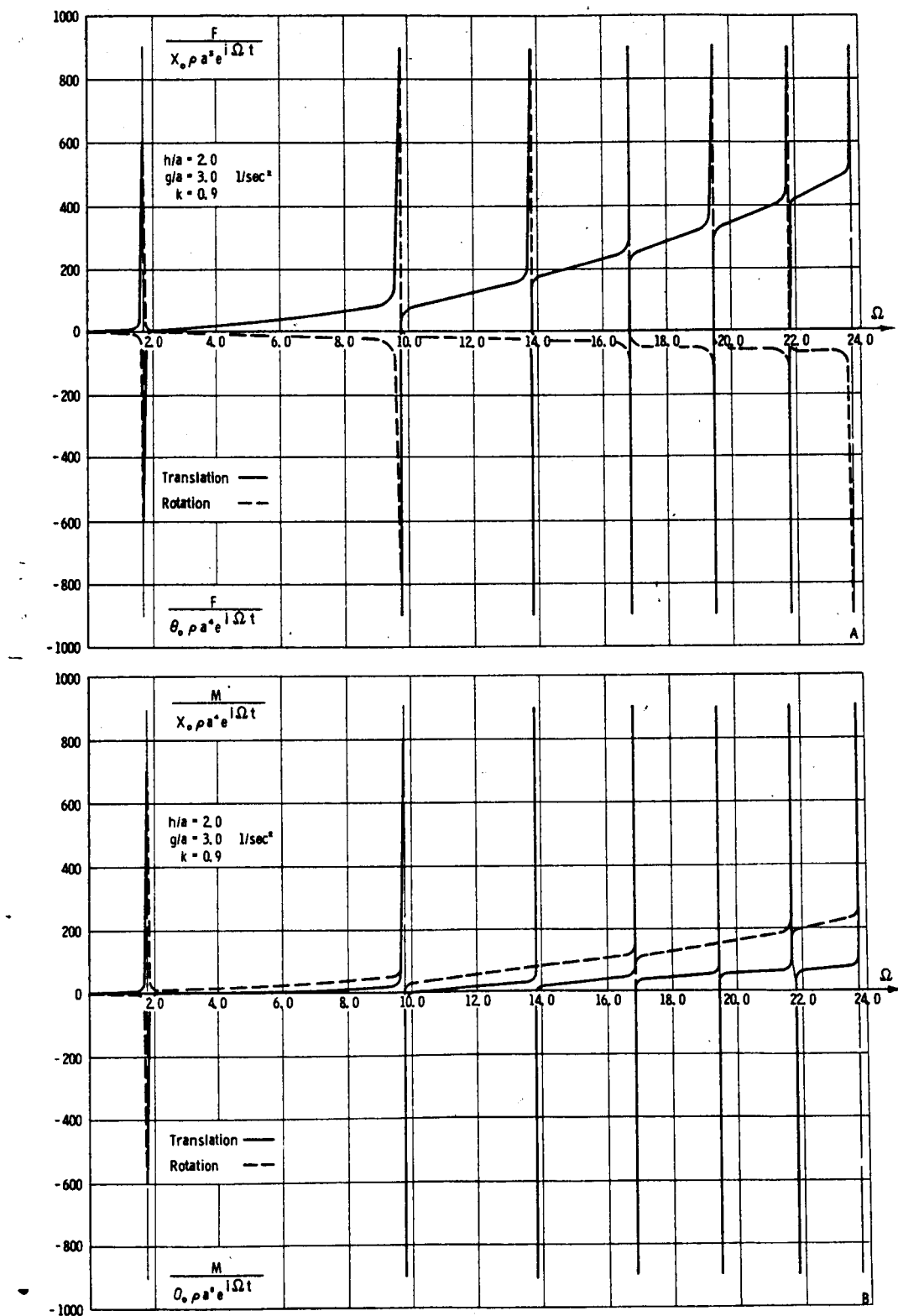


FIGURE 2.21.—Liquid force and moment in a ring tank ( $k=0.9$ ) resulting from translation and rotational excitation (ref. 2.2).

$$u_\phi = i\Omega x_0 e^{i\Omega t} \sin \phi \left\{ 1 + \frac{1}{\left(\frac{r}{a}\right)} \sum_{n=0}^{\infty} \frac{\bar{A}_n \cosh \left[ \frac{\xi_n}{a} (z+h) \right]}{\left( \frac{\omega_n^2}{\Omega^2} - 1 \right) \cosh \left( \xi_n \frac{h}{a} \right)} C_1 \left( \xi_n \frac{r}{a} \right) \right\} \quad (2.47b)$$

$$w = i\Omega x_0 e^{i\Omega t} \cos \phi \sum_{n=0}^{\infty} \frac{\bar{A}_n \xi_n \sinh \left[ \frac{\xi_n}{a} (z+h) \right]}{\left( \frac{\omega_n^2}{\Omega^2} - 1 \right) \cosh \left( \xi_n \frac{h}{a} \right)} C_1 \left( \xi_n \frac{r}{a} \right) \quad (2.47c)$$

The velocity distribution in the tank is obtained from equations (2.47) leaving out the terms "unity" in the parentheses, since these represent the tank motion.

#### *Rotational Forced Oscillations*

The velocity potential for a liquid in response to small forced rotational oscillations  $\theta_0 e^{i\Omega t}$  about an axis through the center of gravity of the undisturbed fluid is

$$\Phi(r, \phi, z, t) = i\Omega \theta_0 e^{i\Omega t} a^2 \cos \phi \left\{ \frac{z}{a} \frac{r}{a} + \sum_{n=0}^{\infty} \frac{\bar{A}_n C_1 \left( \xi_n \frac{r}{a} \right)}{\left( \frac{\omega_n^2}{\Omega^2} - 1 \right) \cosh \left( \xi_n \frac{h}{a} \right)} \left[ \left( \frac{g}{a\Omega^2} + \frac{1}{2} \frac{h}{a} \right) \cosh \left[ \frac{\xi_n}{a} \left( \frac{h}{2} + z \right) \right] \right. \right. \\ \left. \left. - \frac{4g}{a\Omega^2} \sinh \left( \xi_n \frac{z}{a} \right) \sinh \left( \frac{\xi_n}{2} \frac{h}{a} \right) - \frac{2}{\xi_n} \sinh \left[ \frac{\xi_n}{a} \left( \frac{h}{2} - z \right) \right] \right] \right\} \quad (2.48)$$

where the coordinates are located at the center of gravity of the liquid ( $x'$ ,  $y'$ ,  $z'$  coordinates of fig. 2.18).

The wave form  $\delta$  of the free fluid surface measured in the inertial system is

$$\delta(r, \phi, t) = -\Omega^2 \theta_0 e^{i\Omega t} a \cos \phi \left\{ \frac{\frac{1}{2} \left( \frac{h}{a} \right) \left( \frac{r}{a} \right)}{\left( \frac{g}{a} \right)} + \sum_{n=0}^{\infty} \frac{\bar{A}_n C_1 \left( \xi_n \frac{r}{a} \right)}{\left( \frac{\omega_n^2}{\Omega^2} - 1 \right)} \left[ \frac{h/2a}{g/a} - \frac{1}{\Omega^2} + \frac{2}{\Omega^2 \cosh \left( \xi_n \frac{h}{a} \right)} \right] \right\} \quad (2.49)$$

The free fluid surface displacement in the tank is  $\delta^* = \delta - \theta_0 e^{i\Omega t} r \cos \phi$ . The pressure distribution in the tank at a depth  $z$  is

$$p = -\rho \Omega^2 \theta_0 e^{i\Omega t} a^2 \cos \phi \left\{ \frac{z}{a} \frac{r}{a} + \sum_{n=0}^{\infty} \frac{\bar{A}_n C_1 \left( \xi_n \frac{r}{a} \right)}{\left( \frac{\omega_n^2}{\Omega^2} - 1 \right) \cosh \left( \xi_n \frac{h}{a} \right)} \left[ \left( \frac{g}{a\Omega^2} + \frac{1}{2} \frac{h}{a} \right) \cosh \left[ \frac{\xi_n}{a} \left( \frac{h}{2} + z \right) \right] \right. \right. \\ \left. \left. - \frac{4g}{a\Omega^2} \sinh \left( \xi_n \frac{z}{a} \right) \sinh \left( \frac{\xi_n}{2} \frac{h}{a} \right) - \frac{2}{\xi_n} \sinh \left[ \frac{\xi_n}{a} \left( \frac{h}{2} - z \right) \right] \right] \right\} + \rho g \left[ \frac{h}{2} - z - r \theta_0 e^{i\Omega t} \cos \phi \right] \quad (2.50)$$

The fluid forces and moments are given by

$$F_x = -M_F g \theta_0 e^{i\Omega t} - M_F \Omega^2 \theta_0 e^{i\Omega t} \sum_{n=0}^{\infty} \frac{\bar{A}_n \left[ \frac{2}{\xi_n} - k C_1(k \xi_n) \right]}{\left( \frac{\omega_n^2}{\Omega^2} - 1 \right) (1 - k^2) \xi_n} \left[ \left( \frac{g}{a \Omega^2} + \frac{1}{2} \right) \tanh \left( \xi_n \frac{h}{a} \right) + \frac{2}{\left( \xi_n \frac{h}{a} \right)} \left( \frac{2}{\cosh \left( \xi_n \frac{h}{a} \right)} - 1 \right) \right] \quad (2.51a)$$

$$F_y = 0 \quad (2.51b)$$

where the first term is the component due to the gravitational force, and

$$M_y = -M_F g \theta_0 e^{i\Omega t} \frac{a(1+k^2)}{\frac{4h}{a}} - M_F \Omega^2 \theta_0 e^{i\Omega t} a^2 \left\{ \frac{1}{12} \left( \frac{h}{a} \right)^2 - \frac{1}{8} (1+k^2) + \sum_{n=0}^{\infty} \frac{\bar{A}_n \left[ \frac{2}{\pi \xi_n} - k C_1(k \xi_n) \right]}{\left( \frac{\omega_n^2}{\Omega^2} - 1 \right) (1 - k^2) \xi_n} \left[ \left( \frac{1}{4} \frac{h}{a} - \frac{3g}{2a \Omega^2} - \frac{4}{\xi_n} \frac{h}{a} \right) \tanh \left( \xi_n \frac{h}{a} \right) + \frac{1}{\xi_n \cosh \left( \xi_n \frac{h}{a} \right)} \left( 2 - \frac{4g}{a \Omega^2} \frac{1}{h} \right) + \left( \frac{5g}{a \Omega^2} \frac{1}{\xi_n} \frac{h}{a} + \frac{1}{2 \xi_n} \right) \right] \right\} \quad (2.51c)$$

$$M_z = 0 \quad (2.51d)$$

Figure 2.21 also shows, as an example, the forces and moments resulting from rotational excitation, plotted versus frequency for  $k=0.9$ .

The velocity components are

$$u_r = i \Omega \theta_0 e^{i\Omega t} a \cos \phi \left\{ \frac{z}{a} + \sum_{n=0}^{\infty} \frac{\bar{A}_n \xi_n C_1 \left( \xi_n \frac{r}{a} \right)}{\left( \frac{\omega_n^2}{\Omega^2} - 1 \right) \cosh \left( \xi_n \frac{r}{a} \right)} \left[ \left( \frac{g}{a \Omega^2} + \frac{1}{2} \frac{h}{a} \right) \cosh \left[ \frac{\xi_n}{a} \left( z + \frac{h}{2} \right) \right] - \frac{4g}{a \Omega^2} \sinh \left( \xi_n \frac{z}{a} \right) \sinh \left( \frac{\xi_n h}{2a} \right) - \frac{2}{\xi_n} \sinh \left[ \frac{\xi_n}{a} \left( \frac{h}{2} - z \right) \right] \right] \right\} \quad (2.52a)$$

$$u_\phi = i \Omega \theta_0 e^{i\Omega t} a \sin \phi \left\{ \frac{z}{a} + \frac{1}{(r/a)} \sum_{n=0}^{\infty} \frac{\bar{A}_n C_1 \left( \xi_n \frac{r}{a} \right)}{\left( \frac{\omega_n^2}{\Omega^2} - 1 \right) \cosh \left( \xi_n \frac{h}{a} \right)} \left[ \left( \frac{g}{a \Omega^2} + \frac{1}{2} \frac{h}{a} \right) \cosh \left[ \frac{\xi_n}{a} \left( z + \frac{h}{2} \right) \right] - \frac{4g}{a \Omega^2} \sinh \left( \xi_n \frac{z}{a} \right) \sinh \left( \frac{\xi_n h}{2a} \right) - \frac{2}{\xi_n} \sinh \left[ \frac{\xi_n}{a} \left( \frac{h}{2} - z \right) \right] \right] \right\} \quad (2.52b)$$

$$w = i\Omega\theta_0 e^{i\Omega t} a \cos \phi \left\{ \frac{r}{a} - 2 \frac{r}{a} - \sum_{n=0}^{\infty} \frac{\bar{A}_n \xi_n C_1 \left( \frac{\xi_n r}{a} \right)}{\left( \frac{\omega_n^2}{\Omega^2} - 1 \right) \cosh \left( \frac{\xi_n h}{a} \right)} \left[ \left( \frac{g}{a\Omega^2} + \frac{1}{2} \frac{h}{a} \right) \sinh \left[ \frac{\xi_n}{2} \left( z + \frac{h}{2} \right) \right] \right. \right. \\ \left. \left. - \frac{4g}{a\Omega^2} \sinh \left( \frac{\xi_n h}{2} \right) \cosh \left( \xi_n \frac{z}{a} \right) + \frac{2}{\xi_n} \cosh \left[ \frac{\xi_n}{a} \left( \frac{h}{2} - z \right) \right] \right] \right\} \quad (2.52c)$$

The velocity distribution in the tank is obtained by omitting the terms  $z/a$  in  $u$ , and  $u_\phi$  and  $r/a$  in  $w$ , since these represent the tank motion.

#### Forced Oscillations Resulting From Tank Bending

The origin of the coordinate system is taken in the center of the plane of the undisturbed fluid surface and the  $z$ -axis is pointing out of the liquid. The tank walls  $r=a, b$  are assumed to have a bending-type motion in the direction of the  $x$ -axis with an amplitude  $x_0(z)e^{i\Omega t}$ . Analytical results obtained from the solution to this problem (refs. 2.31 and 2.33) are given as follows.

The velocity potential is

$$\Phi(r, \phi, z, t) = i\Omega e^{i\Omega t} a \cos \phi \left\{ \frac{r}{a} x_0(z) + \sum_{n=0}^{\infty} \frac{\bar{A}_n C_1 \left( \frac{1}{a} \xi_n r \right)}{\frac{1}{a} \xi_n \cosh \left( \frac{1}{a} \xi_n h \right) (\omega_n^2 - \Omega^2)} \left[ \left\{ \Omega^2 \sinh \left( \frac{1}{a} \xi_n z \right) \right. \right. \right. \\ \left. \left. + \frac{1}{a} \xi_n g \cosh \left( \frac{1}{a} \xi_n z \right) \right\} \left\{ x'_0(-h) + \int_{-h}^z x''_0(\xi) \cosh \left[ \frac{1}{a} \xi_n (\xi + h) \right] d\xi \right\} \right. \\ \left. + \cosh \left[ \frac{1}{a} \xi_n (z + h) \right] \left\{ \int_z^0 x''_0(\xi) \left[ \Omega^2 \sinh \left( \frac{1}{a} \xi_n \xi \right) \right. \right. \right. \\ \left. \left. + \frac{1}{a} \xi_n g \cosh \left( \frac{1}{a} \xi_n \xi \right) \right] d\xi + \frac{1}{a} \xi_n [\Omega^2 x_0(0) - g x'_0(0)] \right\} \right] \right\} \quad (2.53)$$

where  $\bar{A}_n$  is given by equation (2.44) and prime denotes differentiation with respect to  $z$ . The free surface displacements measured from the undisturbed surface are

$$\delta = \frac{\Omega^2 e^{i\Omega t} \cos \phi}{(g/a)} \left\{ \frac{r}{a} x_0(0) + \sum_{n=0}^{\infty} \frac{\bar{A}_n C_1 \left( \frac{1}{a} \xi_n r \right)}{\frac{1}{a} \xi_n \cosh \left( \frac{1}{a} \xi_n h \right) (\omega_n^2 - \Omega^2)} \left[ \frac{1}{a} \xi_n g \left\{ x'_0(-h) \right. \right. \right. \\ \left. \left. + \int_{-h}^0 x''_0(\xi) \cosh \left[ \frac{1}{a} \xi_n (\xi + h) \right] d\xi \right\} + \frac{1}{a} \xi_n [\Omega^2 x_0(0) - g x'_0(0)] \cosh \left( \frac{1}{a} \xi_n h \right) \right] \right\} \quad (2.54)$$

The pressure distribution in the tank is

$$\begin{aligned}
 p = & \rho \Omega^2 e^{i\Omega t} a \cos \phi \left\{ \frac{r}{a} x_0(z) + \sum_{n=0}^{\infty} \frac{\bar{A}_n C_1 \left( \frac{1}{a} \xi_n r \right)}{\frac{1}{a} \xi_n \cosh \left( \frac{1}{a} \xi_n h \right) (\omega_n^2 - \Omega^2)} \left[ \left\{ \Omega^2 \sinh \left( \frac{1}{a} \xi_n \right) \right. \right. \right. \right. \\
 & \left. \left. \left. \left. + \frac{1}{a} \xi_n g \cosh \left( \frac{1}{a} \xi_n z \right) \right\} \left\{ x'_0(-h) + \int_{-h}^z x''_0(\xi) \cosh \left[ \frac{1}{a} \xi_n (\xi + h) \right] d\xi \right\} \right. \right. \\
 & \left. \left. \left. \left. + \cosh \left[ \frac{1}{a} \xi_n (z + h) \right] \left\{ \int_z^0 x''_0(\xi) \left[ \Omega^2 \sinh \left( \frac{1}{a} \xi_n \xi \right) \right. \right. \right. \right. \right. \\
 & \left. \left. \left. \left. \left. \left. + \frac{1}{a} \xi_n g \cosh \left( \frac{1}{a} \xi_n \xi \right) \right] d\xi + \frac{1}{a} \xi_n [\Omega^2 x_0(0) - g x'_0(0)] \right\} \right] \right\} - \rho g z \quad (2.55)
 \end{aligned}$$

$$\begin{aligned}
 F_z = & M_p \Omega^2 e^{i\Omega t} \left\{ \frac{1}{h} \int_{-h}^0 x_0(z) dz + \sum_{n=0}^{\infty} \frac{\bar{A}_n \frac{2}{\pi \xi_n} - k C_1(k \xi_n)}{\frac{1}{a} \xi_n h \cosh \left( \frac{1}{a} \xi_n h \right) (\omega_n^2 - \Omega^2)(1 - k^2)} \right. \\
 & \times \left[ x'_0(-h) \left\{ \frac{\Omega^2}{\frac{1}{a} \xi_n} \left( 1 - \cosh \left( \frac{1}{a} \xi_n h \right) \right) + g \sinh \left( \frac{1}{a} \xi_n h \right) \right\} + \int_{-h}^0 \left\{ \Omega^2 \sinh \left( \frac{1}{a} \xi_n z \right) \right. \right. \\
 & \left. \left. + \frac{1}{a} \xi_n g \cosh \left( \frac{1}{a} \xi_n z \right) \right\} \int_{-h}^z x''_0(\xi) \cosh \left[ \frac{1}{a} \xi_n (\xi + h) \right] d\xi dz + [\Omega^2 x_0(0) - g x'_0(0)] \sinh \left( \frac{1}{a} \xi_n h \right) \right. \\
 & \left. \left. + \int_{-h}^0 \cosh \left[ \frac{1}{a} \xi_n (z + h) \right] \int_z^0 x''_0(\xi) \left[ \Omega^2 \sinh \left( \frac{1}{a} \xi_n \xi \right) + \frac{1}{a} \xi_n g \cosh \left( \frac{1}{a} \xi_n \xi \right) \right] d\xi dz \right] \right\} \quad (2.56a)
 \end{aligned}$$

$$F_r = 0 \quad (2.56b)$$

The moment of the fluid referred to the position of the undisturbed center of gravity of the liquid is

$$\begin{aligned}
 M_y = M_F a^2 \Omega^2 e^{i\Omega t} & \left\{ \frac{(1+k^2)x_0(-h)}{4h} + \frac{1}{a^2} \int_{-h}^0 \left( \frac{1}{2} + \frac{z}{h} \right) x_0(z) dz \right. \\
 & + \sum_{n=0}^{\infty} \frac{\bar{A}_n \left[ \frac{2}{\pi \xi_n} - k C_1(k \xi_n) \right]}{\frac{1}{a} \xi_n h a^2 \cosh \left( \frac{1}{a} \xi_n h \right) (\omega_n^2 - \Omega^2)(1-k^2)} \left[ x'_0(-h) \left\{ \left( \frac{h \Omega^2}{2 \frac{1}{a} \xi_n} - \frac{g}{\frac{1}{a} \xi_n} \right) \right. \right. \\
 & \left. \left. + \left( \frac{h \Omega^2}{2 \frac{1}{a} \xi_n} + \frac{2g}{\frac{1}{a} \xi_n} \right) \cosh \left( \frac{1}{a} \xi_n h \right) - \left( \frac{2 \Omega^2}{\left( \frac{1}{a} \xi_n \right)^2} + \frac{gh}{2} \right) \sinh \left( \frac{1}{a} \xi_n h \right) \right\} \right. \\
 & + \frac{\Omega^2}{\left( \frac{1}{a} \xi_n \right)^2} \int_{-h}^0 x''_0(\xi) \sinh \left( \frac{1}{a} \xi_n \xi \right) d\xi + \frac{g}{\frac{1}{a} \xi_n} \int_{-h}^0 x''_0(\xi) \cosh \left( \frac{1}{a} \xi_n \xi \right) d\xi \\
 & + \frac{h \Omega^2}{2} \int_{-h}^0 \sinh \left( \frac{1}{a} \xi_n z \right) \int_{-h}^z x''_0(\xi) \cosh \left[ \frac{1}{a} \xi_n (\xi + h) \right] d\xi dz \\
 & + \frac{\frac{1}{a} \xi_n g h}{2} \int_{-h}^0 \cosh \left( \frac{1}{a} \xi_n z \right) \int_{-h}^z x''_0(\xi) \cosh \left[ \frac{1}{a} \xi_n (\xi + h) \right] d\xi dz \\
 & + \frac{h \Omega^2}{2} \int_{-h}^0 \cosh \left[ \frac{1}{a} \xi_n (z + h) \right] \int_z^0 x''_0(\xi) \sinh \left( \frac{1}{a} \xi_n \xi \right) d\xi dz \\
 & + \frac{h \frac{1}{a} \xi_n g}{2} \int_{-h}^0 \cosh \left[ \frac{1}{a} \xi_n (z + h) \right] \int_z^0 x''_0(\xi) \cosh \left( \frac{1}{a} \xi_n \xi \right) d\xi dz \\
 & + \Omega^2 \int_{-h}^0 z \sinh \left( \frac{1}{a} \xi_n z \right) \int_{-h}^z x''_0(\xi) \cosh \left[ \frac{1}{a} \xi_n (\xi + h) \right] d\xi dz \\
 & + \frac{1}{a} \xi_n g \int_{-h}^0 z \cosh \left( \frac{1}{a} \xi_n z \right) \int_{-h}^z x''_0(\xi) \cosh \left[ \frac{1}{a} \xi_n (\xi + h) \right] d\xi dz \\
 & + \Omega^2 \int_{-h}^0 z \cosh \left[ \frac{1}{a} \xi_n (z + h) \right] \int_z^0 x''_0(\xi) \sinh \left( \frac{1}{a} \xi_n \xi \right) d\xi dz \\
 & + \frac{1}{a} \xi_n g \int_{-h}^0 z \cosh \left[ \frac{1}{a} \xi_n (z + h) \right] \int_z^0 x''_0(\xi) \cosh \left( \frac{1}{a} \xi_n \xi \right) d\xi dz \\
 & \left. \left. \left. - [\Omega^2 x_0(0) - g x'_0(0)] \left\{ \frac{\cosh \left( \frac{1}{a} \xi_n h \right)}{\frac{1}{a} \xi_n} - \frac{2}{\frac{1}{a} \xi_n} - \frac{h}{2} \sinh \left( \frac{1}{a} \xi_n h \right) \right\} \right] \right] \quad (2.56c)
 \end{aligned}$$

$$M_z = 0 \quad (2.56d)$$

The velocity components are

$$u_r = i\Omega e^{i\Omega t} a \cos \phi \left\{ \frac{x_0(z)}{a} + \sum_{n=0}^{\infty} \frac{\bar{A}_n C_1 \left( \frac{1}{a} \xi_n r \right)}{\cosh \left( \frac{1}{a} \xi_n h \right) (\omega_n^2 - \Omega^2)} \left[ \begin{aligned} & \left\{ \Omega^2 \sinh \left( \frac{1}{a} \xi_n z \right) \right. \\ & \left. + \frac{1}{a} \xi_n g \cosh \left( \frac{1}{a} \xi_n z \right) \right\} \left\{ x'_0(-h) + \int_{-h}^z x''_0(\xi) \cosh \left[ \frac{1}{a} \xi_n (\xi+h) \right] d\xi \right\} \\ & + \cosh \left[ \frac{1}{a} \xi_n (z+h) \right] \left\{ \int_z^0 x''_0(\xi) \left[ \Omega^2 \sinh \left( \frac{1}{a} \xi_n \xi \right) \right. \right. \\ & \left. \left. + \frac{1}{a} \xi_n g \cosh \left( \frac{1}{a} \xi_n \xi \right) \right] d\xi + \frac{1}{a} \xi_n [\Omega^2 x_0(0) - g x'_0(0)] \right\} \end{aligned} \right] \right\} \quad (2.57a)$$

$$u_\phi = i\Omega e^{i\Omega t} a \sin \phi \left\{ \frac{x_0(z)}{a} + \frac{1}{r} \sum_{n=0}^{\infty} \frac{\bar{A}_n C_1 \left( \frac{1}{a} \xi_n r \right)}{\frac{1}{a} \xi_n \cosh \left( \frac{1}{a} \xi_n h \right) (\omega_n^2 - \Omega^2)} \left[ \begin{aligned} & \left\{ \Omega^2 \sinh \left( \frac{1}{a} \xi_n z \right) \right. \\ & \left. + \frac{1}{a} \xi_n g \cosh \left( \frac{1}{a} \xi_n z \right) \right\} \left\{ x'_0(-h) + \int_{-h}^z x''_0(\xi) \cosh \left[ \frac{1}{a} \xi_n (\xi+h) \right] d\xi \right\} \\ & + \cosh \left[ \frac{1}{a} \xi_n (z+h) \right] \left\{ \int_z^0 x''_0(\xi) \left[ \Omega^2 \sinh \left( \frac{1}{a} \xi_n \xi \right) \right. \right. \\ & \left. \left. + \frac{1}{a} \xi_n g \cosh \left( \frac{1}{a} \xi_n \xi \right) \right] d\xi + \frac{1}{a} \xi_n [\Omega^2 x_0(0) - g x'_0(0)] \right\} \right] \end{aligned} \right\} \quad (2.57b)$$

$$w = i\Omega e^{i\Omega t} a \cos \phi \left\{ \frac{r}{a} x'_0(z) + \sum_{n=0}^{\infty} \frac{\bar{A}_n C_1 \left( \frac{1}{a} \xi_n r \right)}{\frac{1}{a} \xi_n \cosh \left( \frac{1}{a} \xi_n h \right) (\omega_n^2 - \Omega^2)} \left[ \begin{aligned} & \left\{ \Omega^2 \frac{1}{a} \xi_n \cosh \left( \frac{1}{a} \xi_n z \right) \right. \\ & \left. + \left( \frac{1}{a} \xi_n \right)^2 g \sinh \left( \frac{1}{a} \xi_n z \right) \right\} \left\{ x'_0(-h) + \int_{-h}^z x''_0(\xi) \cosh \left[ \frac{1}{a} \xi_n (\xi+h) \right] d\xi \right\} \\ & + \frac{1}{a} \xi_n \sinh \left[ \frac{1}{a} \xi_n (z+h) \right] \left\{ \int_z^0 x''_0(\xi) \left[ \Omega^2 \sinh \left( \frac{1}{a} \xi_n \xi \right) \right. \right. \\ & \left. \left. + \frac{1}{a} \xi_n g \cosh \left( \frac{1}{a} \xi_n \xi \right) \right] d\xi + \frac{1}{a} \xi_n [\Omega^2 x_0(0) - g x'_0(0)] \right\} \right] \end{aligned} \right\} \quad (2.57c)$$

For  $z_0 = \text{constant}$ , all of these results transform into the results of the translational oscillations in  $x$ -direction of the rigid tank.

### Circular Uncompartmented Tank

#### General Discussion

We turn our attention now to the simple case of the cylindrical tank of circular cross section, uncompartmented either by annular or radial walls. The problem of lateral liquid sloshing in such a tank may be obtained, of course, from the general solutions for the ring sector tank given earlier, or from direct analysis. The latter is perhaps well exemplified by Kachigan and Schmitt (refs. 2.35 to 2.37) who employed Laplace transform techniques to determine the liquid response induced by arbitrary translational and pitching motions of the tank. Also, the early work of Miles (ref. 2.38) should be noted, especially as he considered the more general formulation of the problem for a slightly viscous liquid with time-varying depth in a cylindrical tank of arbitrary cross section. Of course, nearly all of the work of Bauer described earlier in this chapter was specialized by him to this particular case (refs. 2.2, 2.3, 2.19, and 2.39). The behavior of liquid in a tank subjected to harmonic translational excitation in two orthogonal directions has also been treated by Bauer (ref. 2.40).

Extensive experimental investigations (refs. 2.11, 2.12, and 2.41 to 2.44) have confirmed these various theoretical analyses. Good correlation has been obtained not only for frequencies and free surface displacement but for pressure distributions and force and moment response. While theoretical analyses had shown that the influence of the flat tank bottom is significant only for liquid depths less than, say, one tank radius (see fig. 2.5), and this also is substantiated by the experimental data, the influence of a spherical or conical bottom is less well defined (see also sec. 2.6 for liquid behavior in conical tanks). Figure 2.22 shows experimentally determined values of liquid natural frequency versus liquid depth in a cylindrical tank with a spherical bottom (ref. 2.43). An experimental evaluation of the effects of a conical bottom was made in reference 2.12, with the interesting result

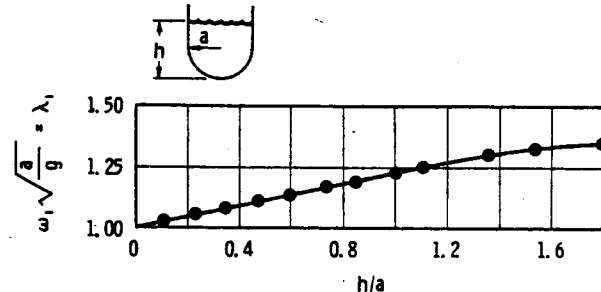


FIGURE 2.22.—Experimentally determined natural frequency of a fluid in a circular cylindrical tank with a spherical bottom (ref. 2.43).

that the conical bottom could be replaced by an equivalent flat bottom (based on liquid volumes) for estimating both liquid frequencies and forces, and this appears to be valid at least through the second liquid mode, and possibly the third, for fluid depths as low as  $h/d=1/4$ .

The effects of ellipticity of the cross section were investigated theoretically by Chu (ref. 2.15), who was seeking some insight into the effect of small out of roundness on the behavior of liquids in circular tanks. It was determined that the liquid natural frequencies were only slightly modified by the distortion of the cross section, but that entirely new modes (and hence frequencies) were introduced that have no counterpart in the perfectly circular tank. Somewhat similar results were obtained experimentally in a study of liquid motions in oblate spheroidal tanks (ref. 2.45) (see also section 2.7) in that it was found that, for ellipsoidal tanks oriented such that the free surface cross section is elliptical, a normal mode of liquid motion occurs which does not exist when the tank is oriented such that the free surface cross section is circular.

The previous discussion has been confined to *upright* circular cylinders; however, the behavior of a liquid in a circular canal (see fig. 2.23) has also been investigated, both theoretically and experimentally (refs. 2.13 (sec. 259), 2.21, and 2.44). Since symmetrical modes of oscillation are not induced by transverse motion of the canal, attention is restricted to the antisymmetric modes. Rotation of the canal about its center produces no sloshing nor, by symmetry, does vertical tank motion produce horizontal slosh forces. All pressures are in

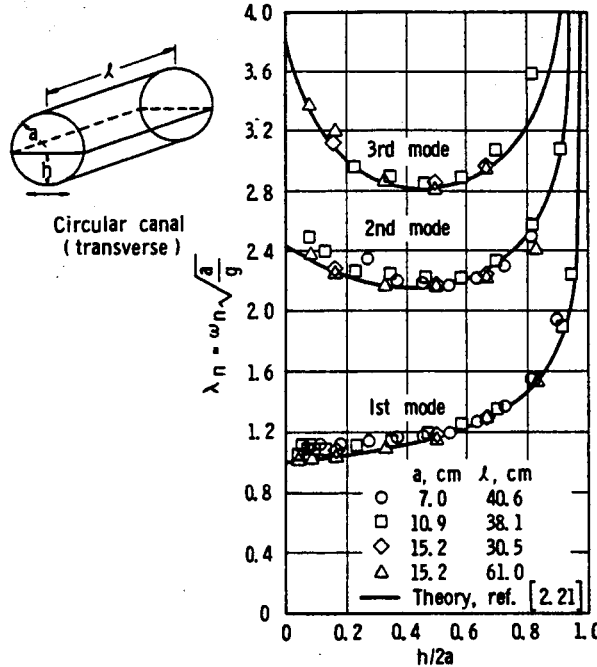


FIGURE 2.23.—Variation of liquid natural frequency parameter with depth for transverse modes in a circular canal (ref. 2.44).

the radial direction and, therefore, the slosh forces acting upon the container pass through the center of the section. Some numerical and experimental results are presented in figures 2.23 and 2.24 (refer to ref. 2.21 for the general theory of sloshing in circular canals). It is seen from figure 2.23 that good agreement is obtained between theory and experiment for transverse oscillations. The experimental results given in figure 2.24 indicate that the frequency parameter for the longitudinal modes in a circular canal are essentially independent of tank geometry (there is no theory available for predicting the frequencies for this orientation).

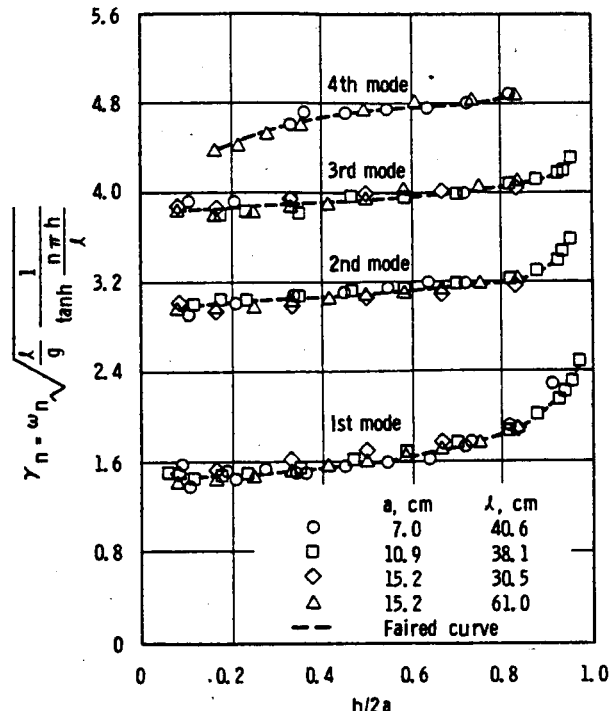


FIGURE 2.24.—Variation of liquid natural frequency parameter with depth for longitudinal modes in a circular canal (ref. 2.44).

#### Forced Oscillations

For translational and rotational oscillations of the form  $x_0 e^{i\Omega t}$  and  $\theta_0 e^{i\Omega t}$ , the velocity potentials given earlier in this section reduce to (see ref. 2.3 for mathematical details)

$$\Phi(r, \phi, z, t) = i\Omega x_0 e^{i\Omega t} a \cos \phi \left\{ \frac{r}{a} + \frac{2J_1\left(\epsilon_n \frac{r}{a}\right) \cosh\left[\epsilon_n \left(\frac{z}{a} + \frac{h}{a}\right)\right]}{(\epsilon_n^2 - 1)J_1(\epsilon_n) \cosh\left(\epsilon_n \frac{h}{a}\right) \left(\frac{\omega_n^2}{\Omega^2} - 1\right)} \right\} \quad (2.58a)$$

$$\Phi(r, \phi, z, t) = -i\Omega\theta_0 e^{i\Omega t} a^2 \cos \phi \left\{ \frac{r}{a} \frac{z}{a} + \frac{2J_1\left(\epsilon_n \frac{r}{a}\right)\left(\frac{\Omega^2}{\omega_n^2}\right)}{\epsilon_n(\epsilon_n^2 - 1)J_1(\epsilon_n) \cosh\left(\epsilon_n \frac{h}{a}\right)\left(1 - \frac{\Omega^2}{\omega_n^2}\right)} \left[ \left(\gamma + \frac{\epsilon_n h}{2a}\right) \cosh\left(\frac{\epsilon_n h}{2a} + \frac{\epsilon_n z}{a}\right) \right. \right. \\ \left. \left. - 4\gamma \sinh\left(\frac{\epsilon_n h}{2a}\right) \sinh\left(\epsilon_n \frac{z}{a}\right) - 2 \sinh\left(\frac{\epsilon_n h}{2a} - \frac{\epsilon_n z}{a}\right) \right] \right\} \quad (2.58b)$$

where  $\epsilon_n$  are the roots of the equation  $J'_1(\epsilon_n) = 0$  and the natural frequencies  $\omega_n$  are given by

$$\omega_n^2 = \frac{g}{a} \epsilon_n \tanh\left(\epsilon_n \frac{h}{a}\right) \quad (2.58c)$$

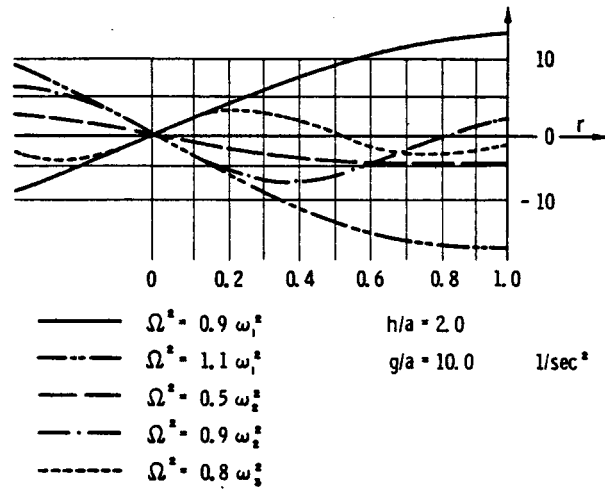
The first few roots of  $J'_1(\epsilon_n) = 0$  are as given in table 2.2, and the lowest two natural frequencies are plotted in figure 2.5 as a function of  $h/a$ . Appendix F gives the equations for free surface displacements, forces, and moments for both types of excitation, and these results are shown typically in figures 2.25 to 2.27.

The solution of the problem of sloshing in a circular cylindrical tank resulting from prescribed bending type oscillations of the tank walls (ref. 2.31) may also be obtained from the more general solution presented earlier in this section; equations for the velocity potential, free surface displacements, forces, and moments are therefore given in appendix G.

#### 2.4 SPHERICAL TANK

Spherical tanks, because of their high volume-to-weight ratio and obvious structural advantages, are very often employed in space vehicles. Unfortunately, however, the theoretical analysis of liquid oscillations in such a container is a problem of considerable mathematical complexity so that a number of investigations employing various approximation techniques have been undertaken. Budiansky (ref. 2.21) employed a sophisticated integral equation technique and obtained liquid natural frequencies and forces for the cases of the half-full and the nearly-full tank. These results, together with the solution for the nearly empty tank and the known behavior of the circular canal, were used to calculate approximately the liquid behavior for arbitrary depth. McCarty and Stephens (ref. 2.44) obtained

#### (A) Translation



#### (B) Rotation

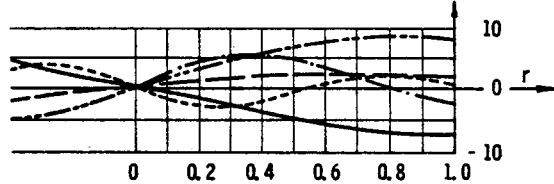


FIGURE 2.25.—Free surface displacement for various excitation frequency ratios in a circular cylindrical container (ref. 2.3).

experimental frequencies which agreed well with the theory of reference 2.21. (Additional frequency data were obtained for the sphere in connection with a study of spheroids (ref. 2.45), but not compared with theory.) Riley and Trembach (ref. 2.23) used the variational technique presented in references 2.14 and 2.22 to calculate frequencies, with good agreement also being obtained with these theoretical and experimental results. A finite difference numerical scheme was also successfully applied to the spherical tank (ref. 2.26). Stofan and Armstead (ref. 2.46) also employed the theory of

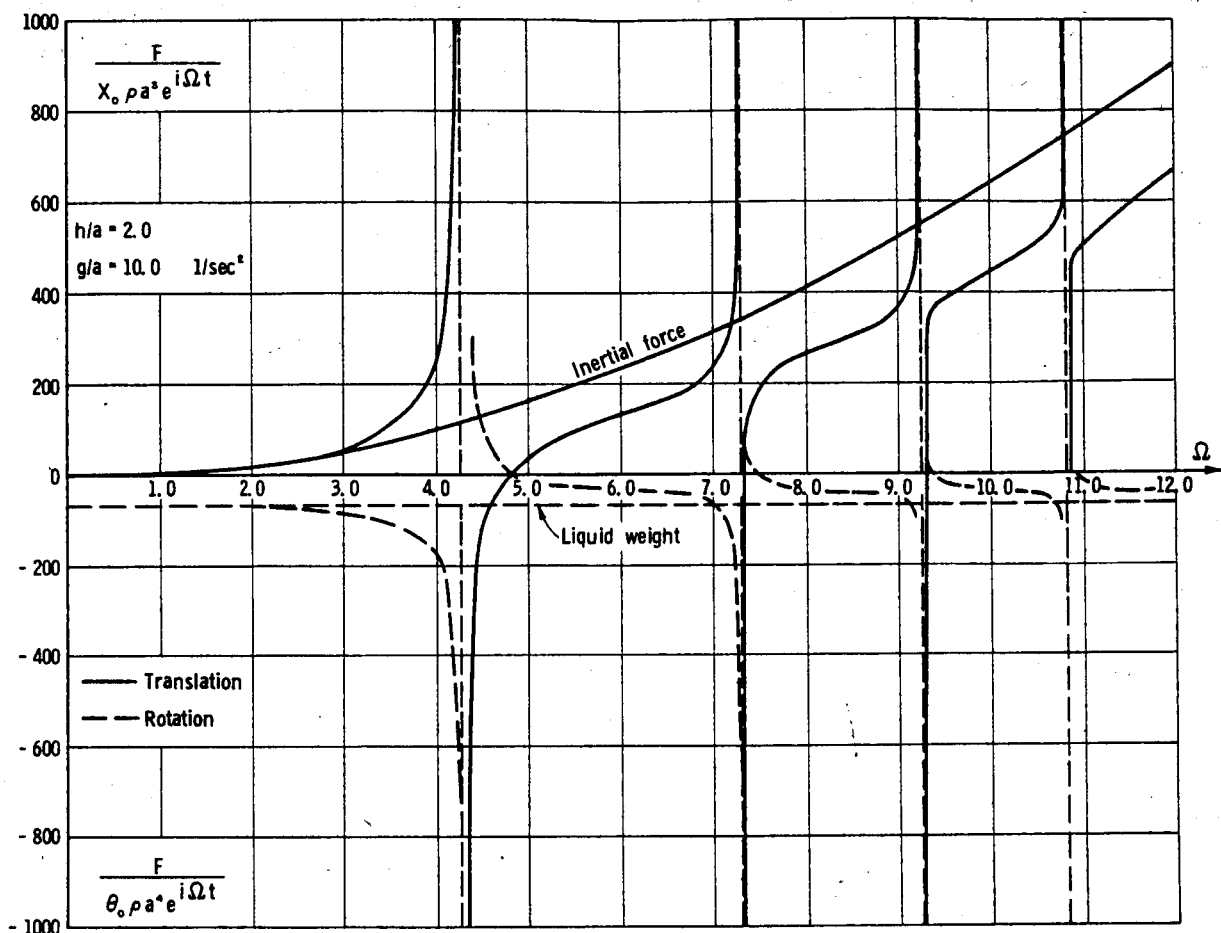


FIGURE 2.26.—Magnification function of the liquid force in a circular cylindrical container (ref. 2.3).

reference 2.21, but with an approximation technique for the kernel function; the frequencies and slosh forces calculated by this method were again in good agreement with experimental data, the slosh forces increasing with liquid depth to a maximum which occurs at the fundamental frequency for the half-full condition. Chu (ref. 2.47) developed a numerical procedure to determine the kernel function, which is related to the Neumann function on the boundary, and then utilized the method of reference 2.21 to calculate the liquid natural frequencies and the constants required to evaluate the force response. The method is general and may be applied to the tanks filled to an arbitrary depth. Extensive experiments, involving measurements of liquid frequencies, wall pressure distributions, slosh forces, etc., have also been carried out by Abramson, et al.

(refs. 2.48 and 2.49). Comparisons between these various calculated and measured frequencies, for various modes, are given in figure 2.28. The experimental data on frequencies for a sphere given in reference 2.45 also agree very well with all of the data given in this figure.

Experimental data for the fundamental liquid frequency in a spherical tank has also been reported in reference 2.43, together with relevant empirical equations, as shown in figure 2.29. The empirical equations, valid for certain ranges of the liquid depth parameter  $h/R$ , are

$$\lambda_1 = \frac{\sqrt{(1.84)^2 - \left(1.46 - \frac{h}{R}\right)^2} - 0.56}{\sqrt{2} \frac{h}{R} - \left(\frac{h}{R}\right)^2} \quad \left(0.1 < \frac{h}{R} < 1.0\right) \quad (2.59a)$$

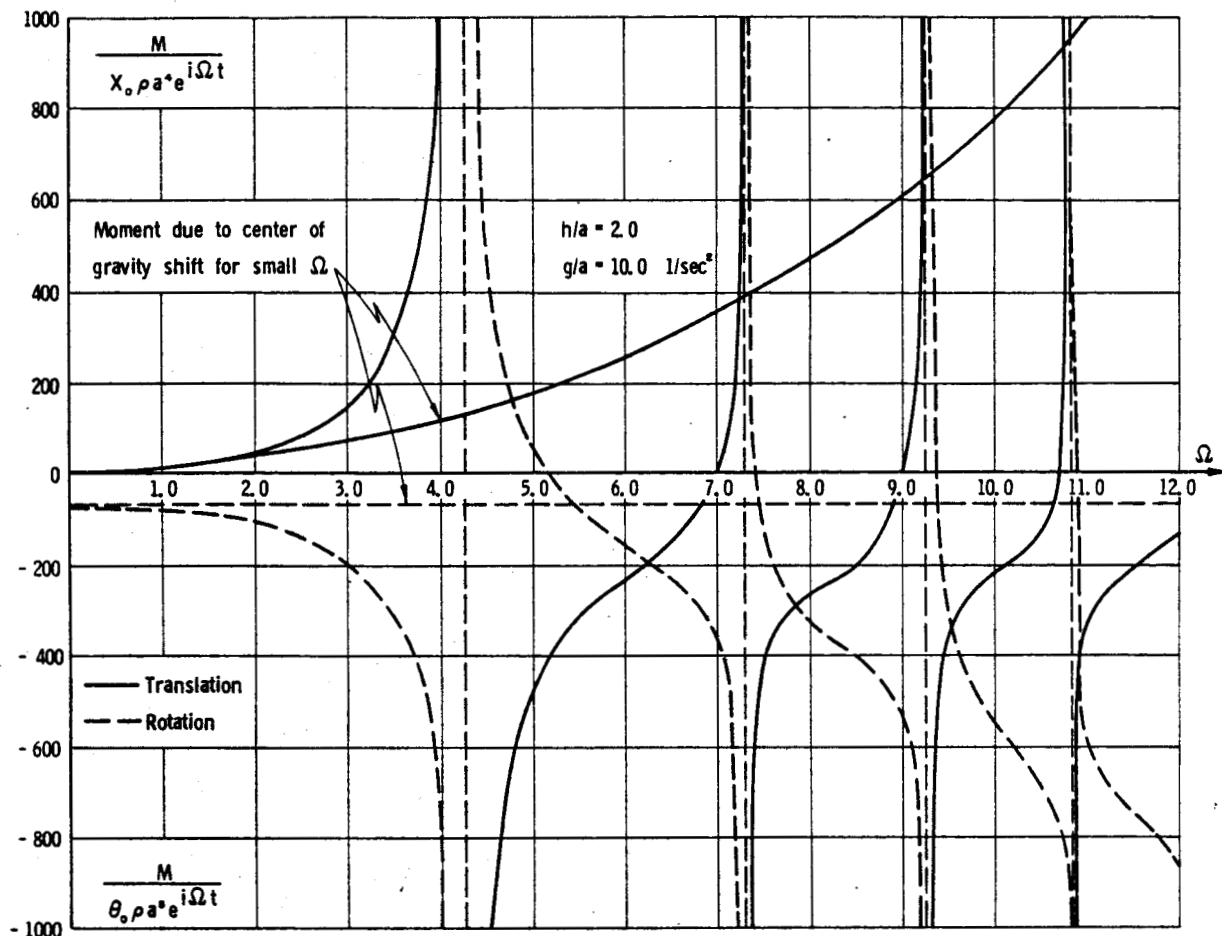


FIGURE 2.27.—Magnification function of the liquid moment in a circular cylindrical container (ref. 2.3).

$$\lambda_i = \frac{\sqrt{(1.84)^2 - \left(1.97 - \frac{h}{R}\right)^2} - 0.34}{\sqrt{2} \frac{h}{R} - \left(\frac{h}{R}\right)^2} \quad \left(1.0 < \frac{h}{R} < 2.0\right) \quad (2.59b)$$

or, more generally,

$$\lambda_i = \frac{C_1}{\sqrt{2} \frac{h}{R} - \left(\frac{h}{R}\right)^2} \quad \left(0.1 < \frac{h}{R} < 2.0\right) \quad (2.59c)$$

and the value of  $C_1$  is also given in figure 2.29 (for very small liquid depths  $h/R \leq 0.1$ , the liquid frequency can be obtained from the experimental data for a cylindrical tank with a spherical bottom given in fig. 2.22). In these equations

$$\lambda_i = \omega_i \sqrt{\frac{R}{g}}$$

Rattayya (ref. 2.25) also employed the variational technique of references 2.14 and 2.22 to obtain natural frequencies and slosh forces for liquid in an ellipsoidal tank, with the spherical tank as a special case. An empirical equation for the fundamental liquid frequency in the spherical tank was then developed in the form

$$\lambda_i^2 = \frac{1}{3} \frac{240 - 220 \frac{h}{R} + 72 \left(\frac{h}{R}\right)^2 - 9 \left(\frac{h}{R}\right)^3}{80 - 100 \frac{h}{R} + 44 \left(\frac{h}{R}\right)^2 - 9 \left(\frac{h}{R}\right)^3 + \left(\frac{h}{R}\right)^4} \times \sin \left[ \frac{\pi}{4} \left(2 - \frac{h}{R}\right) \left(1 + \frac{h}{3R}\right) \right] \quad (2.60)$$

Various of these values for the lowest liquid frequency are compared in table 2.3.

Therefore, the fundamental liquid frequency may be obtained with about equal accuracy

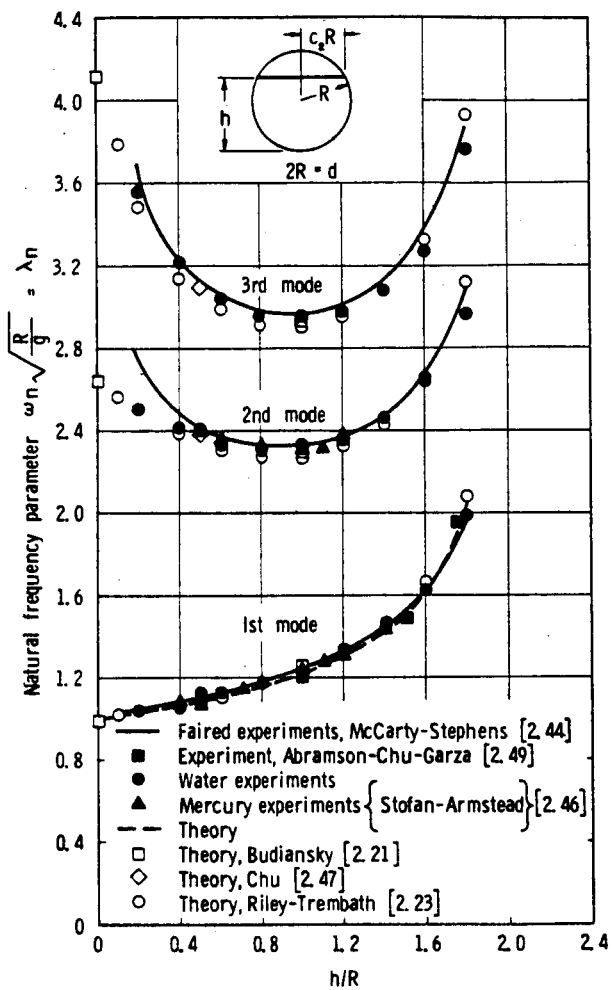


FIGURE 2.28.—Liquid natural frequency variation with depth in a spherical tank—comparisons of various theories and experimental data.

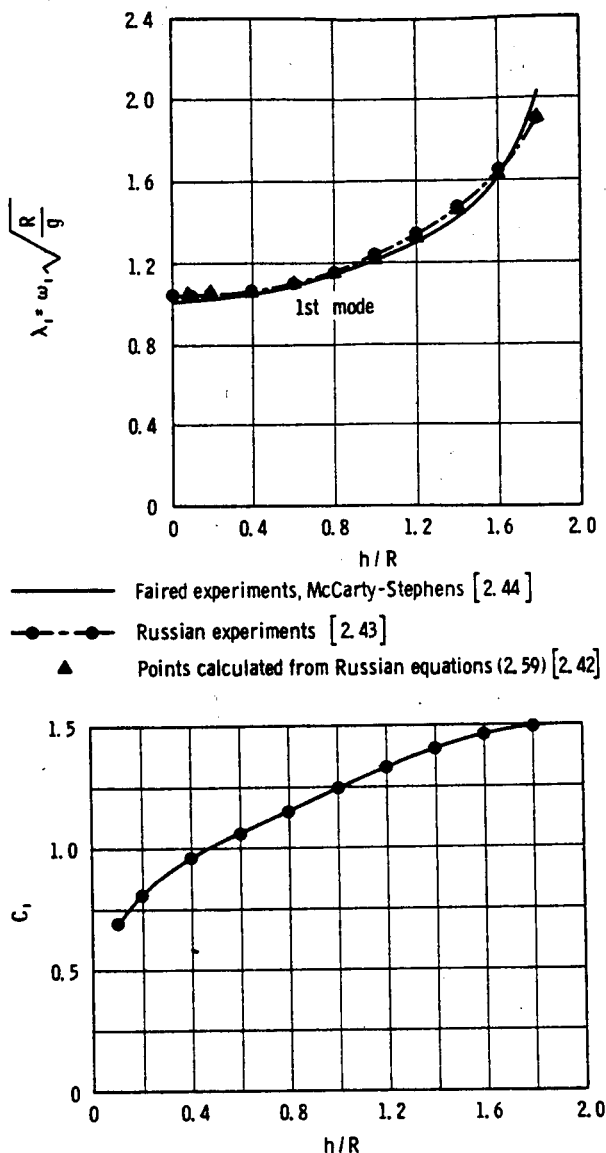


FIGURE 2.29.—Lowest liquid natural frequency variation with depth in a spherical tank—comparison of empirical equations and experimental data (ref. 2.43).

TABLE 2.3.—Comparison of Liquid Natural Frequency  $\lambda_1$  for a Spherical Tank

$\frac{h}{R}$	Mikishev (ref. 2.43)			Chu (ref. 2.47)	Budiansky (ref. 2.21)	Rattayya (ref. 2.25) (eq. (60))	Experiment (fig. 2.28)
	Eq. (59a)	Eq. (59b)	Fig. 2.22				
0.05			1.02				1.01
0.50	1.09			1.10	• 1.00	1.01	1.08
1.00	1.22	1.22			• 1.06	1.10	1.22
1.8		1.92			1.25	1.22	2.03
					• 2.04	1.83	

\*Obtained from fig. 9 of ref. 2.21.

(except for large depths) from equation (2.59) or (2.60) or read directly from figure 2.28. The liquid frequencies corresponding to the second and third modes may also be obtained from the data given in figure 2.28. The slosh forces as a function of liquid height may be obtained from the equations

$$\frac{d^2}{dt^2}(\delta_n) + \omega_n \delta_n = -\lambda_n^2 c_2 \frac{D_n}{E_n} \frac{d^2(U)}{dt^2} \quad (2.61a)$$

$$F_s = -M_p \frac{d^2}{dt^2}(U) - \pi \rho (c_2 R)^3 \sum_{n=1}^{\infty} D_n \frac{d^2}{dt^2}(\delta_n) \quad (2.61b)$$

where

$\delta_n$  = slosh height at the wall associated with the  $n$ th mode

$F_s$  = resulting slosh force acting through the center

$c_2$  = geometric parameter related to the fluid height shown in figure 2.28

$R$  = radius of the sphere

$U$  = transverse displacement of the container

$D_n, E_n$  = coefficients obtained from figure 2.30

The slosh force parameters  $D_n$  and  $E_n$  may be obtained from either reference 2.21 or 2.46 with about equal accuracy; the results from reference 2.21 are presented here (fig. 2.30).

Measurements of liquid force response (refs. 2.48 and 2.49) have revealed some interesting effects, especially as regards the influence of excitation amplitude in partially filled tanks and the liquid behavior in nearly full tanks. (These effects, which are essentially nonlinear in character, will be discussed in more detail in ch. 3.) Figure 2.31 shows some experimental data on liquid force response (ref. 2.49) compared with theory (ref. 2.21). There is obviously some significant effect of excitation amplitude (even granting some unreliability in the experimental data), especially as regards a noticeable frequency shift and generally better overall agreement for the smaller value of excitation amplitude. Figure 2.32 shows the strong effect of geometry in the nearly full spherical tank by virtually suppressing the liquid force response, with a strong secondary effect of excitation amplitude. Some further comparisons of force response in a quarter-

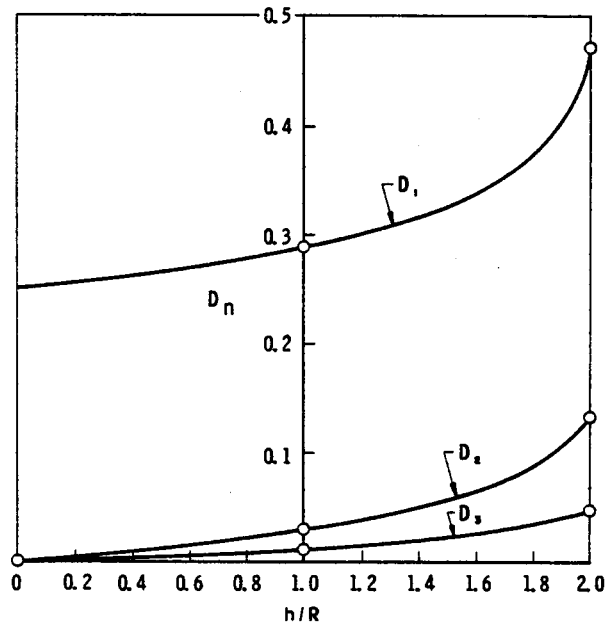
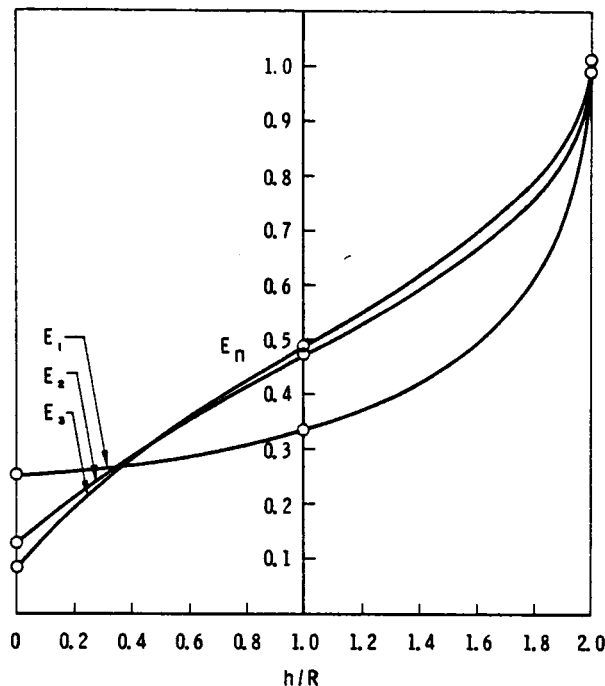


FIGURE 2.30.—Modal parameters  $D_n$  and  $E_n$  for determining force response in a sphere (ref. 2.21).

full tank are made by Chu (ref. 2.47), again with reasonable agreement.

Sumner and Stofan (ref. 2.50) also carried out an extensive investigation into the effects of (a) excitation amplitude, (b) tank size, and (c) liquid kinematic viscosity on the slosh

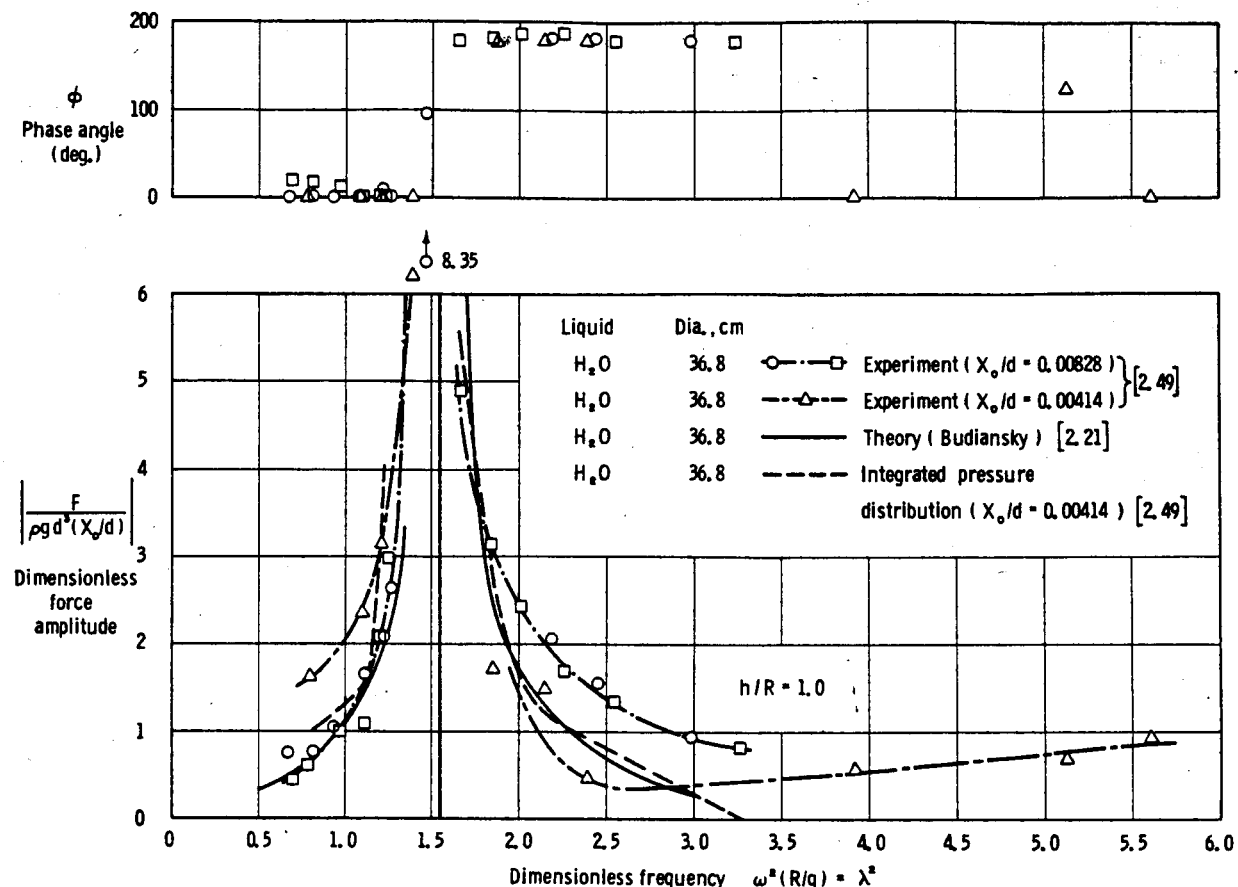


FIGURE 2.31.—Liquid total force response in a half-full spherical tank (ref. 2.49).

force corresponding to the lowest natural frequency (first mode) in a half-full tank. Figure 2.33 shows some typical results for constant excitation amplitude and variable liquid viscosity, while figure 2.34 shows the effects of varying excitation amplitude. It is seen from these data that, in general, the first-mode slosh force parameter increases with increasing excitation amplitude and with decreasing viscosity.

## 2.5 TOROIDAL TANK

The toroidal tank, because of packaging requirements, has been considered for storage of propellants and liquids for life-support systems. There is no theoretical analysis available for predicting the behavior of liquids in such tanks, and only limited experimental investigations have been reported (refs. 2.51 and 2.52).

There are available, however, certain empirical formulas and experimental results from these studies which predict with fair accuracy the natural frequencies and which have established principal trends in the liquid behavior. The effect of excitation amplitude on the frequencies and forces, however, was not investigated, nor were the experimental data successful in establishing the manner in which slosh forces vary with tank geometry and orientation. (See fig. 2.35.)

To simplify the analysis of liquid frequencies in the various container orientations, the toroid is "divided" into the regions shown in figure 2.35. This reduces the problem of predicting the liquid frequencies for any fluid depth to that of predicting the frequencies for depths in only certain regions, which can be done in each region by reference to an "analogous" container. Thus, the success in obtain-

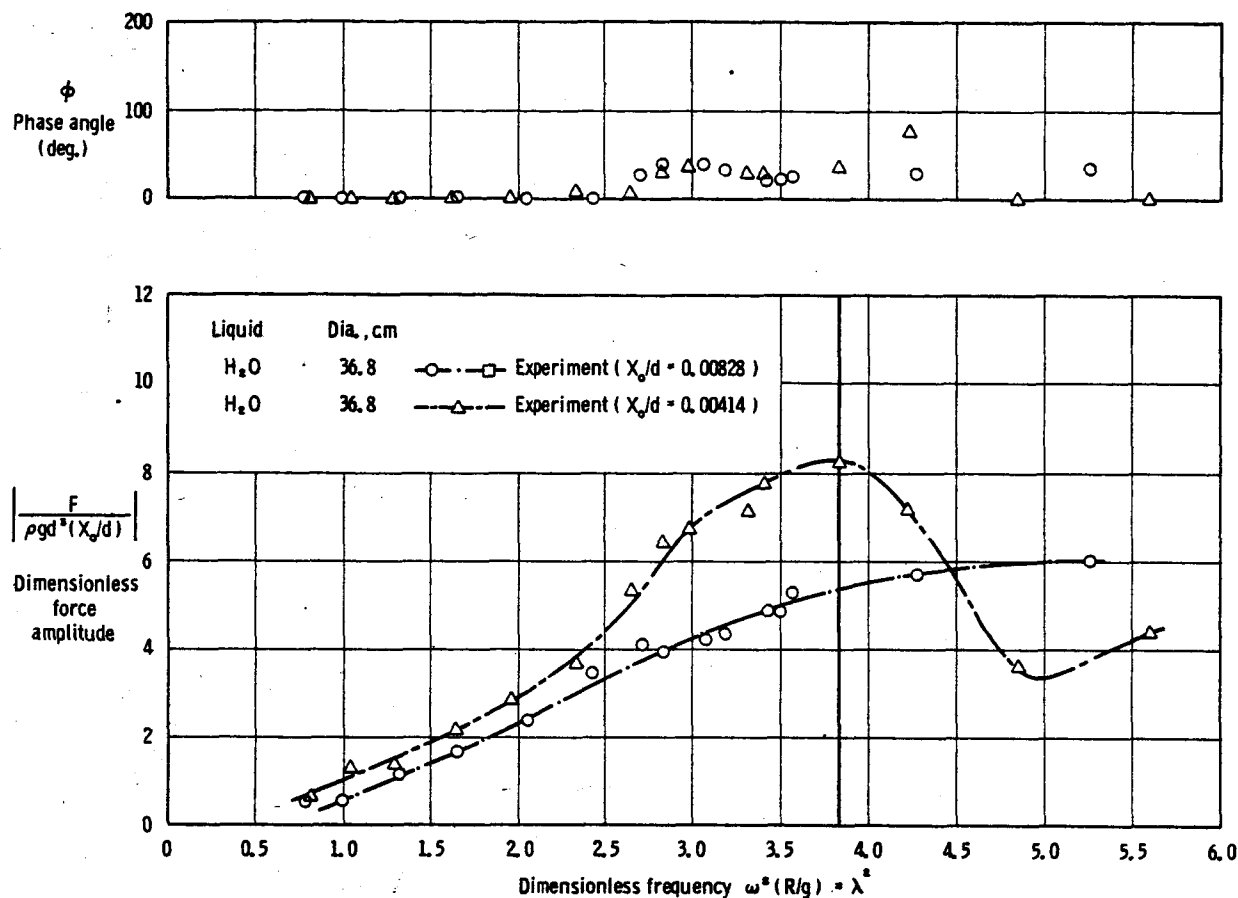


FIGURE 2.32.—Liquid total force response in a nearly full spherical tank (ref. 2.49).

ing a frequency parameter independent of tank size and geometry depends upon the accuracy of the analogy. The experimental results obtained in references 2.51 and 2.52 for each container orientation are discussed below, and the frequency parameters investigated for each orientation are summarized in table 2.4.

#### Horizontal Excitation

For this orientation, the liquid natural frequencies for an arbitrary liquid depth may be approximated by analogy with a ring tank in the form

$$\omega_n = \sqrt{\frac{g}{r_0}} \xi_n \tanh \frac{h_c}{r_0} \xi_n \quad (2.62)$$

where  $\xi_n$  are the roots of equation (2.18d) if  $m/2\alpha$  is set equal to unity and  $k$  is replaced by  $r_i/r_0$ ,  $h_c$  is the height of liquid in a ring tank required to produce a volume of liquid equal

to that contained in the toroid, and  $r_i$  and  $r_0$  are the inner and outer radii, respectively, of the liquid surface. Figure 2.36 indicates the generally good agreement obtained between frequencies calculated from this equation and those obtained experimentally. The liquid surface forms of the contained liquid for the first and second frequencies are also shown in the figure. In general, it is noted that—

- (a) A decrease in the liquid depth ratio results in a decrease of both the first and second natural frequencies.
- (b) For constant minor radius, an increase in the major radius results in a decrease in both the first and second natural frequencies.

The problem of determining the fluid forces in terms of tank geometry and liquid depth has not been resolved. It has been noted, however, from the typical data of figure 2.37, that

TABLE 2.4.—Summary of Nondimensional Frequency Parameters for Liquids in Toroidal Tanks  
[Ref. 2.51]

Orientation	Region	Mode	Parameter	Analogy
Horizontal.....	All.....	All.....	$\lambda_n = \omega_n \sqrt{\frac{r_0}{g} \frac{1}{\epsilon_n} \frac{1}{\tanh(\frac{h_c}{r_0} \epsilon_n)}}$	Annular circular cylinder
Vertical transverse.....	A, C.....	All.....	$\sigma_n = \omega_n \sqrt{\frac{r}{g}}$	Sphere of radius $r$
	B.....	All.....	$\sigma_n = \omega_n \sqrt{\frac{r}{g}}$	Circular cylinder of radius $r$
Vertical longitudinal.....	A, C.....	First.....	$\Psi_1 = \omega_1 \sqrt{\frac{R+r}{g}} \sqrt{\frac{\sin \phi}{\phi}}$	Simple pendulum
		All $n > 1$ .....	$\Psi_n = \omega_n \sqrt{\frac{R+r}{g}}$	Sphere of radius $R+r$
	B.....	First.....	$\Psi_1 = \omega_1 \sqrt{\frac{R}{g}} \sqrt{\frac{\theta}{\sin \theta}}$	Circular-arc tube
		All $n > 1$ .....	$\Psi_n = \omega_n \sqrt{\frac{r}{g} \frac{1}{\epsilon_{n-1}}}$	Circular cylinder of radius $r$

\* For convenience, values of  $\epsilon_n$  are listed as follows:  $\epsilon_1 = 1.841$ ;  $\epsilon_2 = 5.331$ ;  $\epsilon_3 = 8.536$ ;  $\epsilon_4 = 11.706$ ;  $\omega_n$ , experimentally determined natural frequency.

the maximum slosh force corresponds *not* to the lowest liquid mode, but rather to the second mode, except possibly for small values of the ratio of major to minor tank radii. The maximum slosh force in the first mode appears to occur at a liquid-depth ratio of about three-quarters, while in the second mode it appears to occur at a liquid-depth ratio of about one-half.

#### Transverse Excitation

For this orientation of the container, and in all three regions, A, B, C, the frequency parameter  $\sigma_n = \omega_n \sqrt{\frac{r}{g}}$  (where  $r$  is the minor radius of the toroid, fig. 2.35) can be obtained from the experimental results shown in figure 2.38. No data are available for liquid forces due to sloshing in this orientation.

#### Longitudinal Excitation

For this orientation of the container, the liquid frequency parameter can be defined variously for each region. In regions A and C, we have (ref. 2.51)

$$\psi_1 = \omega_1 \sqrt{\frac{R+r \sin \phi}{g \phi}} \quad \text{for the first frequency} \quad (2.63a)$$

and

$$\psi_n = \omega_n \sqrt{\frac{R+r}{g}} \quad \text{for higher frequencies} \quad (2.63b)$$

In region B, the relations are

$$\psi_1 = \omega_1 \sqrt{\frac{R}{g \sin \theta}} \quad \text{for the first frequency} \quad (2.63c)$$

and

$$\psi_n = \omega_n \sqrt{\frac{R}{g} \frac{1}{\epsilon_{n-1}}} \quad \text{for higher frequencies} \quad (2.63d)$$

The values for  $\psi_n$  in the foregoing equations may be obtained from the experimental results shown in figure 2.39. It should be noted that the approximations  $\psi_1$  (region A)  $\approx 1.0$  and  $\psi_n$  (region B)  $\approx 1.0$  are reasonable. It appears that: in region A, frequencies higher than the second are strongly dependent upon the ratio of major to minor radius; in region B, all frequencies are independent of the ratio of radii; in region C, all frequencies are dependent on the ratio of the radii and the tank size. The effects of tank size are, however, isolated.

## 2.6 CONICAL TANKS

The natural frequencies of liquids in conical containers have been investigated from a num-

ber of viewpoints (refs. 2.12, 2.14, 2.22, 2.24, 2.43, and 2.53).

A variational procedure was employed by Lawrence et al. (ref. 2.22) to obtain the natural frequencies of fluids in tanks ranging in geometry from shallow to deep. Plots of frequency versus depth for the cases of liquid modes with one and three nodal diameters ( $s=1, 3$ ) are given in figure 2.40.

Frequencies were determined experimentally (ref. 2.43) for cones of very small semivertex angles narrowing both upward and downward. An empirical relationship for frequency determined from this data is

$$\omega^2 \frac{r_0}{g} = 1.84 C_s^2 \quad (2.64)$$

where  $C_s$  is plotted in figure 2.41. It is noted that small angles correspond to large values of  $h_0/r_0$ , and thus it is difficult to obtain good correlation with the results presented in figure

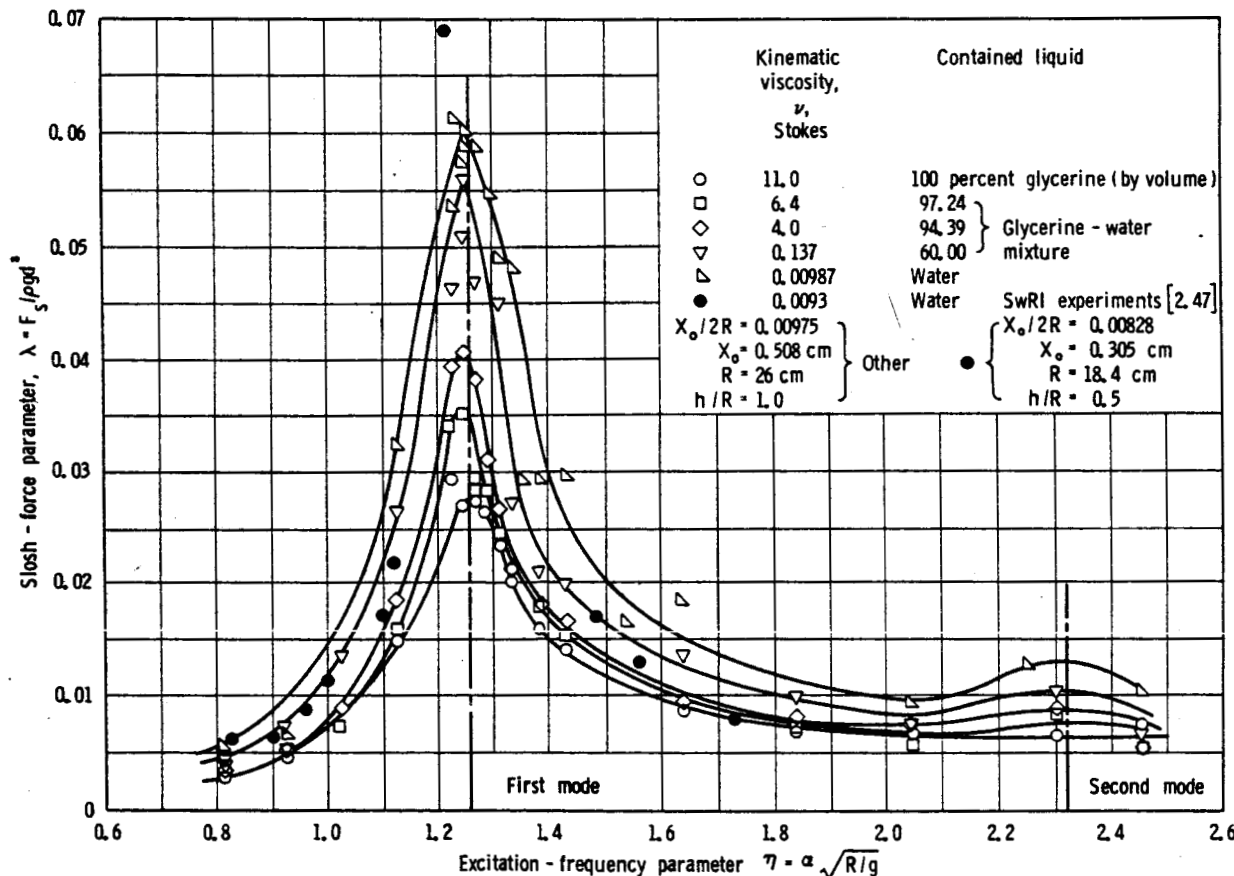


FIGURE 2.33.—Effect of kinematic viscosity on slosh-force parameter in a spherical tank (ref. 2.50).

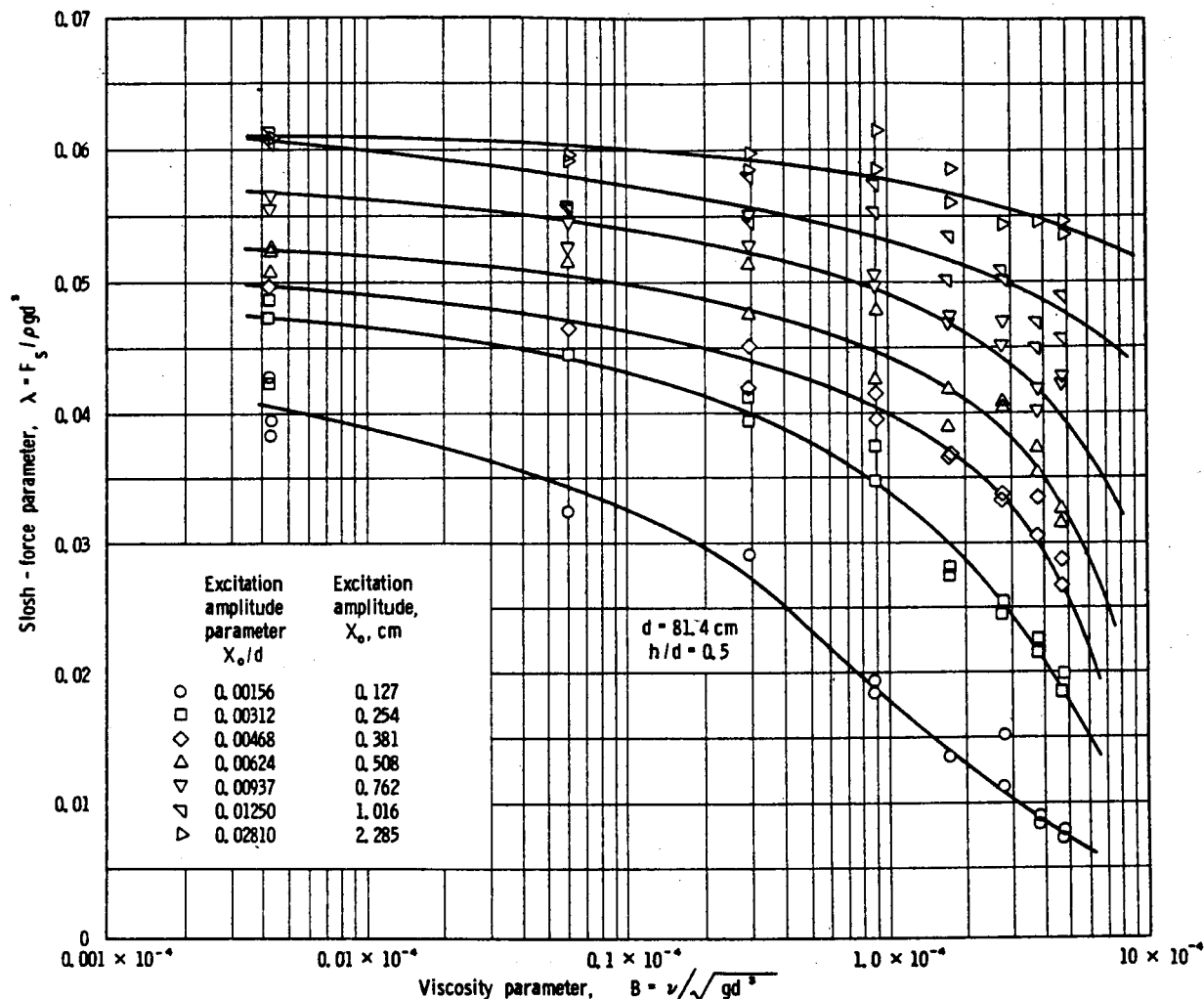


FIGURE 2.34.—First-mode slosh-force parameter as a function of viscosity parameter in a spherical tank (ref. 2.50).

2.40. Equation (2.64) is valid for  $h/r_0 > 2.75$  and for liquid oscillation amplitudes (measured at the wall) of less than about  $0.01 r_0$ . An analytical formulation of the problem of sloshing in a cone of small semivertex angle narrowing both upward and downward were later given in reference 2.24, along with comparisons between the solution of reference 2.22 and the experimental results given in reference 2.43.

Abramson and Ransleben (ref. 2.12) also obtained experimental results for liquid sloshing in cylindrical tanks having conical bottoms. These data were found to be in good agreement with the theoretical force response calculated by assuming the tank to be an "equivalent" flat-bottomed cylindrical tank. The equivalence, based upon equal liquid

volumes, appears to be valid down to liquid depths of about  $h_0/R = 0.50$ , and at least through the second mode (and possibly the third). Good agreement was also obtained for natural frequencies, supporting similar conclusions that had been arrived at analytically (ref. 2.22).

## 2.7 OBLATE SPHEROIDAL TANK

The natural frequencies of liquids in oblate spheroidal tanks have been investigated both experimentally (ref. 2.45) and theoretically (ref. 2.25). Empirical equations and experimental results obtained in the investigation of reference 2.45 will be reviewed in this section, including some of the effects of tank orientation (fig. 2.42), ellipticity and size, and fluid height.

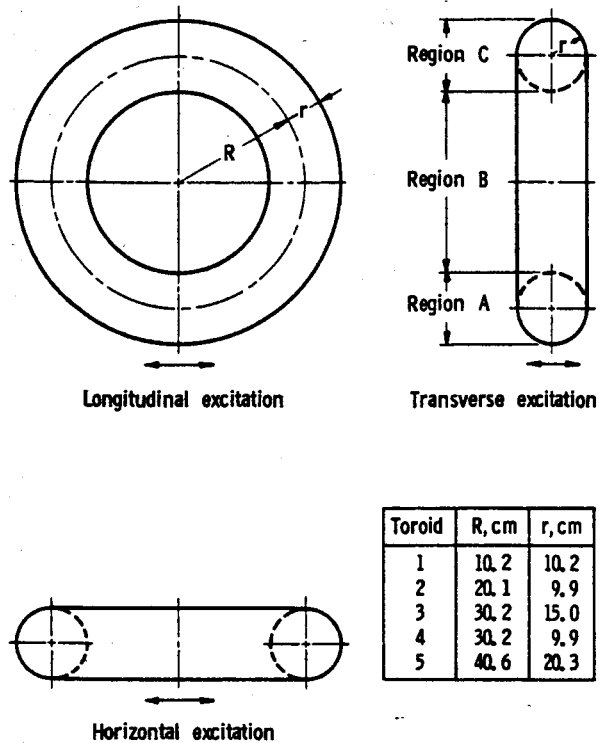


FIGURE 2.35.—Sketch showing orientation of toroidal tank and dimensions of test configurations (ref. 2.51).

It should be noted that the frequency parameters selected are not unique; several parameters were investigated in reference 2.45, and those yielding the best results were selected for presentation. As was the case with toroidal containers discussed in section 2.5, the parameters investigated were based upon fluid behavior in analogous containers and, therefore, the development of a valid frequency parameter independent of tank size and geometry is dependent upon the accuracy of the analogy.

Recently, the natural frequencies and mode shapes of liquids oscillating in horizontally oriented (see fig. 2.42) oblate spheroidal tanks have been calculated using variational techniques (ref. 2.25). The fluid forces and moments due to the liquid oscillating in one of its natural modes are given along with an equivalent mechanical model. (See ch. 6.) Numerical results obtained for the fundamental frequency in the special case of a spherical tank have already been given in section 2.4 (eq. (2.60)).

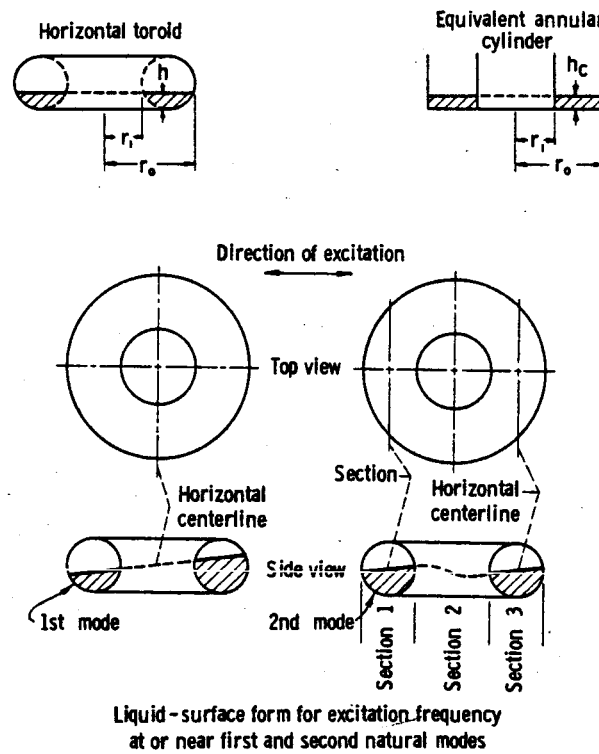
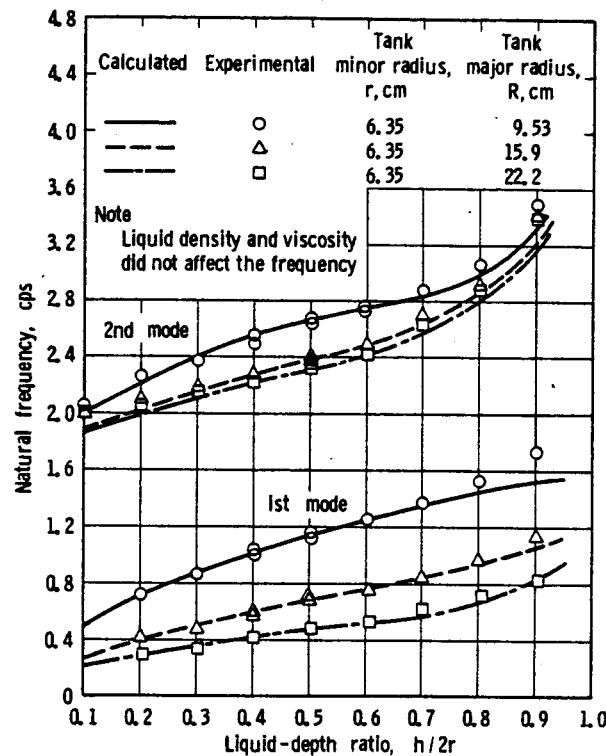


FIGURE 2.36.—Calculated and experimental values of the first two natural frequencies for horizontal orientation of toroid (after ref. 2.52).

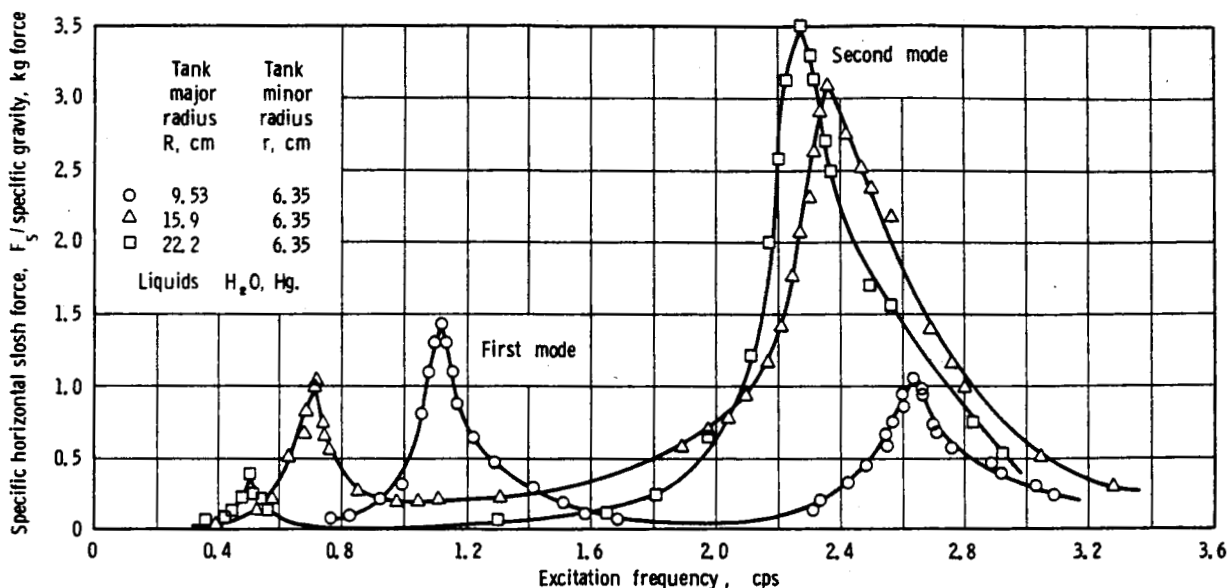


FIGURE 2.37.—First- and second-mode slosh forces for horizontal orientation of toroid at liquid depth ratio of 0.5 (after ref. 2.52).

### Horizontal Excitation

Theoretically calculated (ref. 2.25) natural frequencies for three different tank geometries in the horizontal orientation, as a function of liquid depth, are shown in figure 2.43.

The experimental study (ref. 2.45) showed that an empirical equation for the liquid natural frequencies of the form

$$\omega_n = \sqrt{\frac{g}{r} \epsilon_n \tanh\left(\frac{h_c}{r} \epsilon_n\right)} \quad (2.65a)$$

where  $h_c = \frac{1}{3} \frac{h(3b-h)}{2b-h}$  and  $\epsilon_n$  is the  $n$ th root of  $J'_1(\epsilon_n) = 0$ , gave quite good results (the poorest results occurred for the nearly full tank in the lowest liquid mode). The basis of this equation is that of the natural frequencies of liquid contained in an upright cylinder having a radius  $r$  equal to that of the liquid surface and a volume equal to the volume of liquid contained in the spheroid.

A comparison of these two sets of frequency data, for the three lowest liquid modes, is made in figure 2.44.

### Longitudinal and Transverse Excitations

Empirical equations for the liquid modes in containers with longitudinal and transverse

orientations were developed (ref. 2.45) by analogy with liquid frequencies in elliptic cylinders in the form

Longitudinal:

$$\omega_{n,l} = \sqrt{\frac{g}{r} k_{l,n} \tanh\left(\frac{h_c}{r} k_{l,n}\right)} \quad (2.65b)$$

Transverse:

$$\omega_{n,t} = \sqrt{\frac{g}{r} k_{t,n} \tanh\left(\frac{h_c}{r} k_{t,n}\right)} \quad (2.65c)$$

where  $r$  is the radius of the free surface (fig. 2.42) and

$$h_c = \frac{h}{6} \left(1 + \frac{4a-h}{2a-h}\right)$$

The parameters  $k_{l,n}$  and  $k_{t,n}$  are proportional to the positive parametric zeros of the first derivatives of the Mathieu function (these functions appear in the analysis of the elliptic cylinder (ref. 2.15)), and approximate values for the first mode ( $n=1$ ) are given in figure 2.45. By comparing these empirical equations with experimental data, it was found that they are essentially independent of both tank size and eccentricity, but that the ratio of experimentally determined to calculated frequency was different from unity.

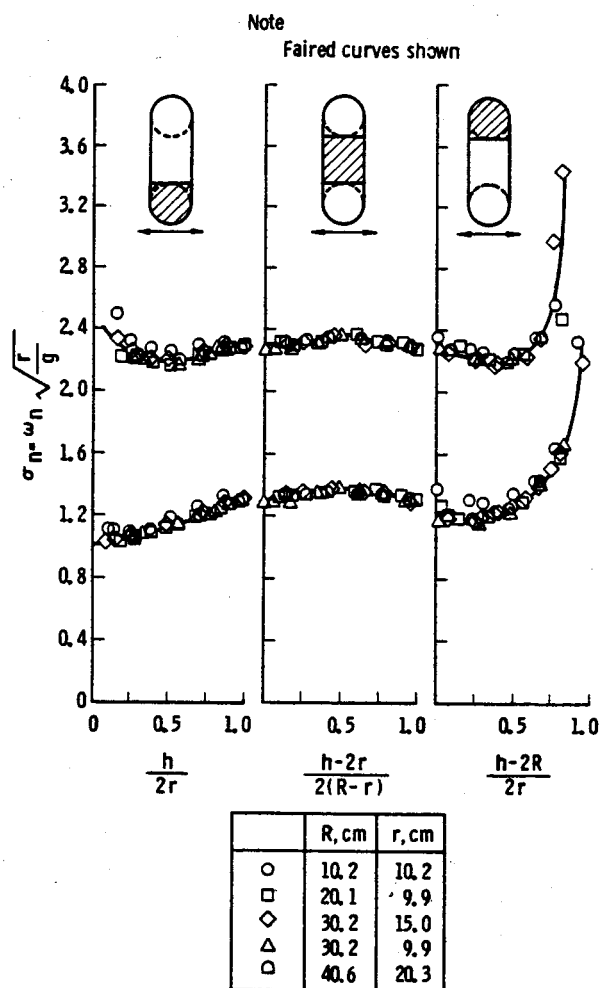


FIGURE 2.38.—Variation of liquid frequency parameter with depth for transverse modes of vertical toroidal tanks (ref. 2.51).

Actual experimental data for liquid frequencies in the longitudinal and transverse orientation are given as a function of liquid depth in figures 2.46 and 2.47. The curves shown are, of course, only faired through the data. It should be carefully noted that the "second" mode for a spherical tank (fig. 2.28) corresponds to the "third" modes of figures 2.46 and 2.47 and that the "second" modes of these figures have no counterpart in figure 2.28; this arises from the fact that new modes of oscillation occur when the planform of the liquid free surface is elliptical, as noted previously (see also ref. 2.15). These data indicate that, for a given eccentricity, the values of the

frequency parameter may be approximated by a single curve for a given modal number.

## 2.8 CONCLUDING REMARKS

From the results presented in the foregoing sections of this chapter, it should be evident that a great deal of information is readily available concerning the general subject of lateral sloshing of liquids in moving containers. For the simplest case of an upright cylinder of circular cross section, a very complete background of theory and experiment exists for virtually every aspect of the liquid behavior and its reaction on the tank. This is true even for the relatively more complex cases where the circular cross section is compartmented into rings or sectors by annular or radial walls. Virtually the same statement can be made for the rectangular tank, but for other and more difficult configurations our detailed knowledge is considerably diminished.

The cylindrical container of rectangular, circular, or elliptical cross section can, of course, be analyzed exactly on the basis of classical hydrodynamic theory. For other geometries, however, recourse has to be made to numerical solutions (ref. 2.26) or to other approximate techniques. The variational methods especially have proven to be quite useful in a variety of cases (refs. 2.14, 2.22, and 2.25), but there is no one method of analysis that is universally valid.

While we have considered various modes of excitation of these different containers and orientations, coupling arising from more than one excitation has largely been ignored. One formulation of rather general applicability has just become available (ref. 2.54), involving tanks of arbitrary shape moving with six degrees of freedom. Calculations have been carried out for tanks of spheroidal and toroidal configuration (ref. 2.55). One analysis involving coupled translational motion in two orthogonal motions has been mentioned earlier in this chapter (ref. 2.40); another study considered coupled translation and pitch (ref. 2.56).

The significant effects of nonlinearities of various types have been referred to, but this detailed consideration deferred to chapter 3.

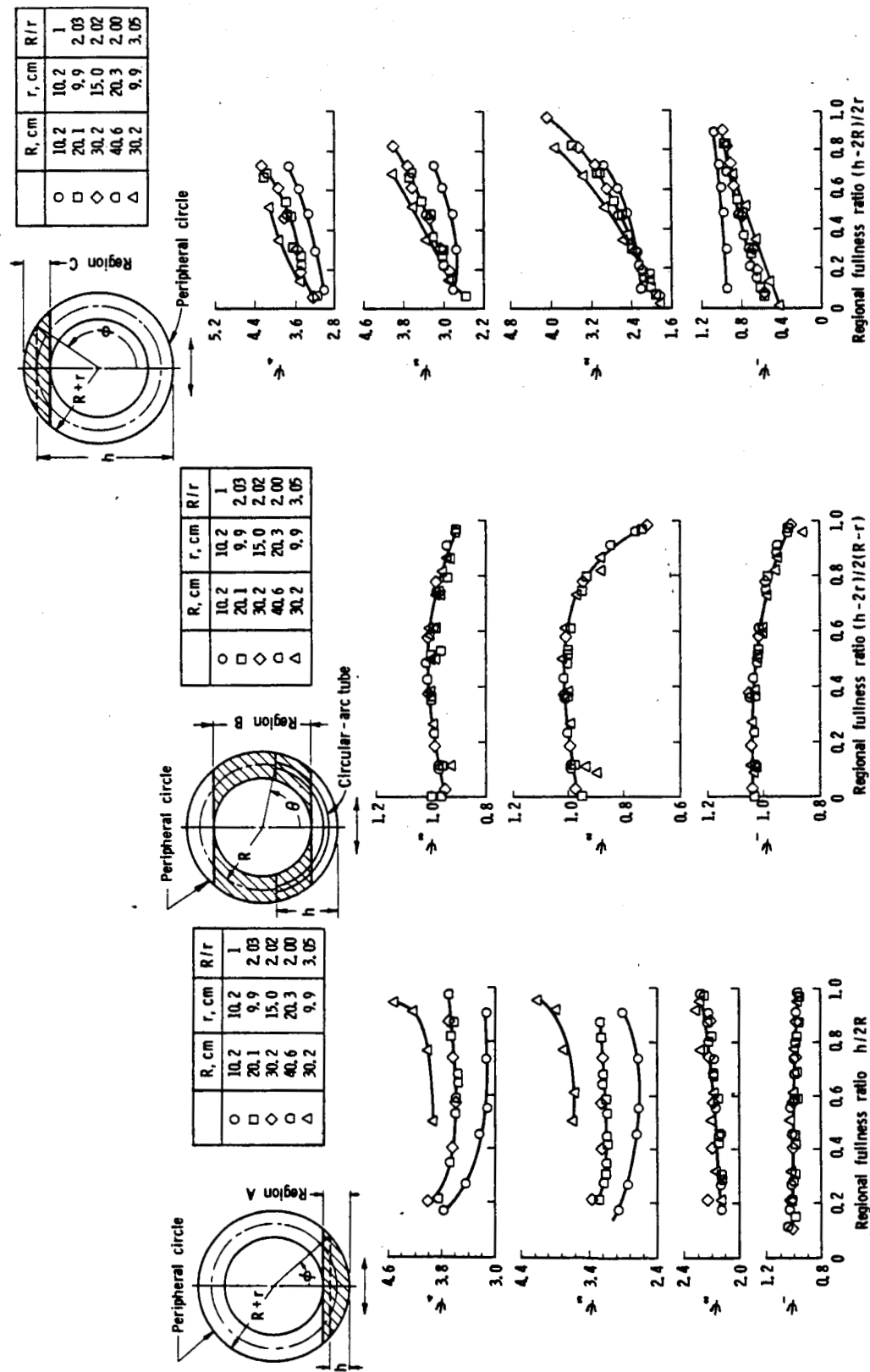


FIGURE 2.39.—Variation of liquid frequency parameters with depth for longitudinal modes of vertical toroidal tank (ref. 2.51).

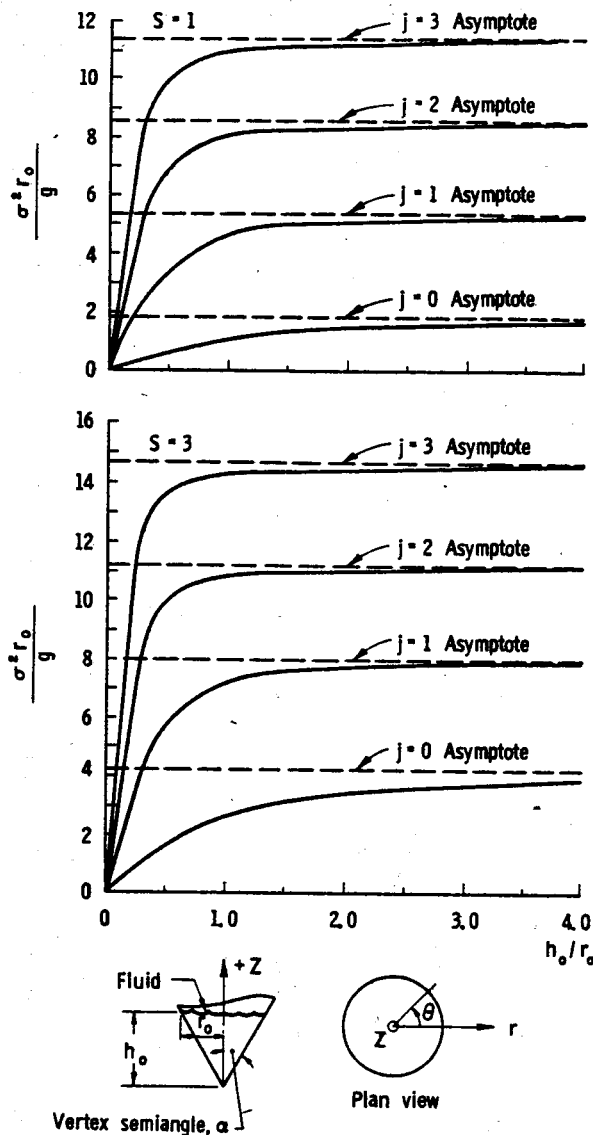


FIGURE 2.40.—Frequency versus depth for a conical tank (ref. 2.22).

Similarly, the very important question of suppression of lateral sloshing by mechanical baffles or other devices will be treated in chapter 4. And finally, the very important problem of simplified representation of lateral

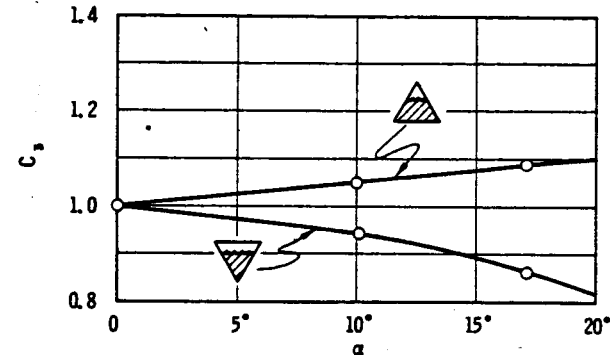


FIGURE 2.41.—Experimentally determined frequency parameter for conical tanks of small vertex angle (ref. 2.43).

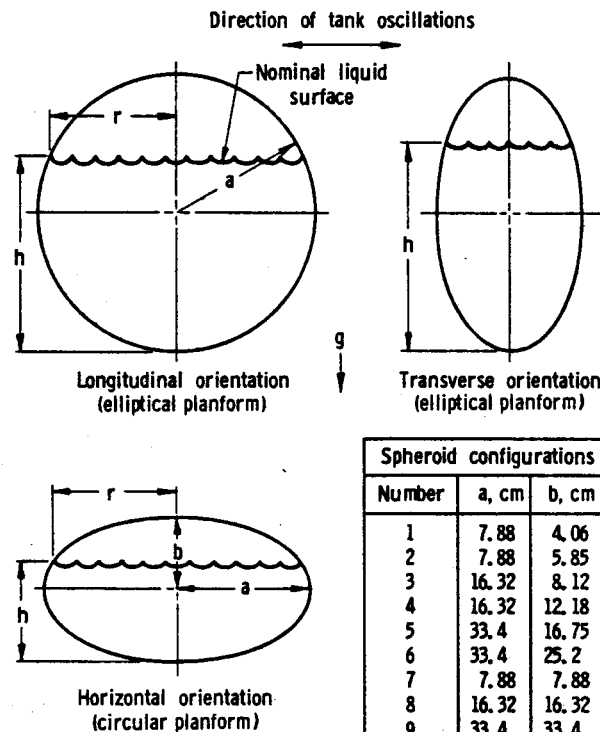


FIGURE 2.42.—Orientations and dimensions of spheroidal tanks studied in reference 2.45.

sloshing forces and moments under various circumstances will be discussed in chapter 6.

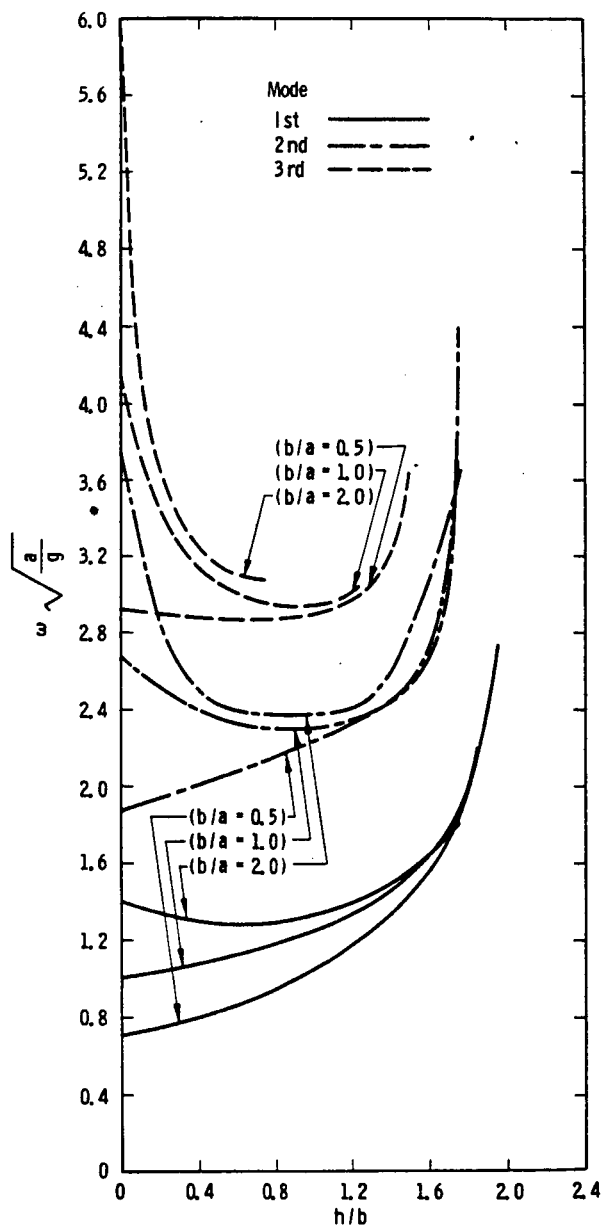


FIGURE 2.43.—Variation of slosh frequency with liquid depth in oblate spheroidal tanks (ref. 2.25).

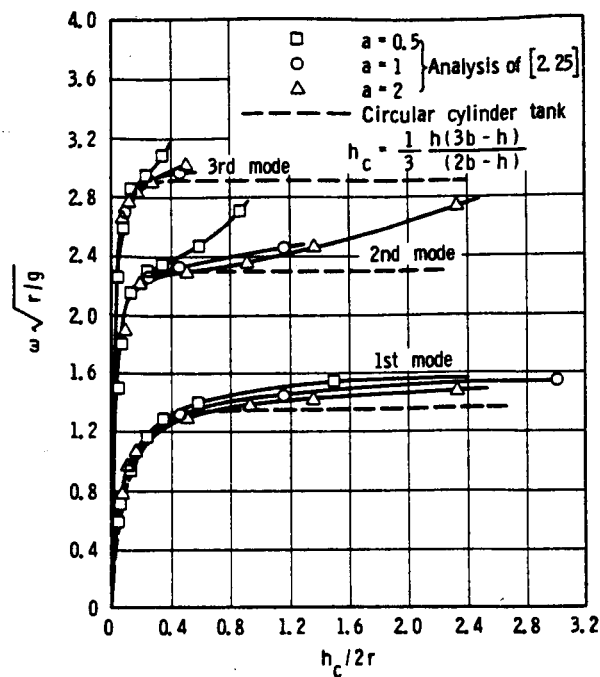


FIGURE 2.44.—Comparison of liquid frequency parameter with cylindrical tank solution in spheroidal tanks (ref. 2.25).

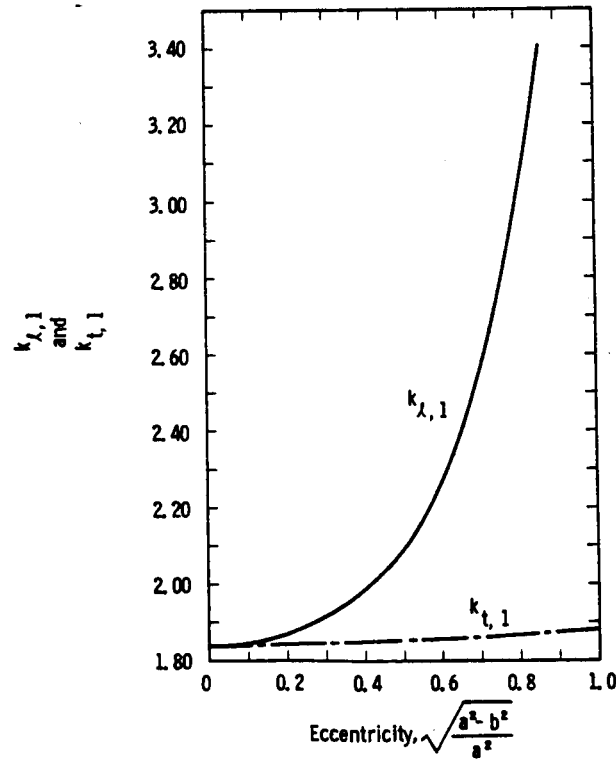


FIGURE 2.45.—Variation of parameters  $k_{t,1}$  and  $k_{\lambda,1}$  with eccentricity (ref. 2.45).

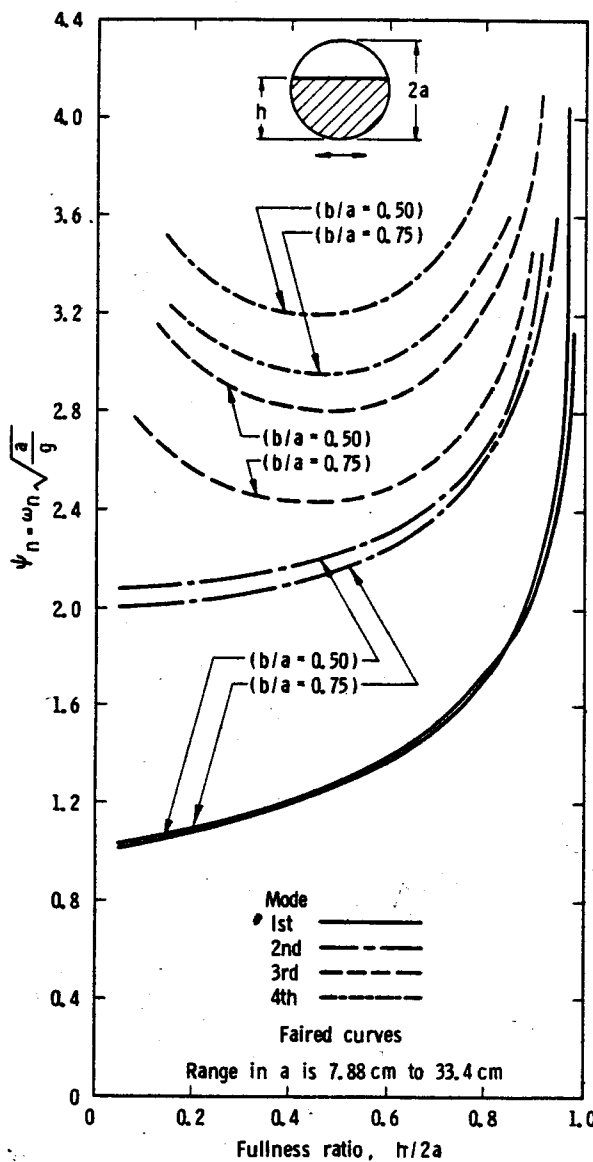


FIGURE 2.46.—Variation of frequency parameter with fullness ratio for liquid in spheroids with longitudinal orientation (after ref. 2.45).

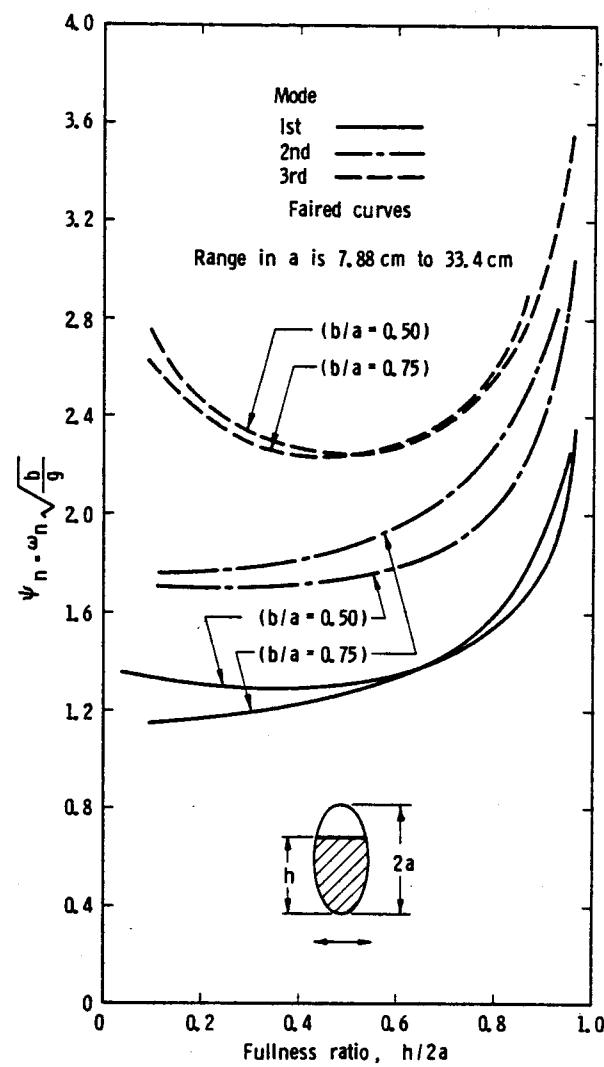


FIGURE 2.47.—Variation of frequency parameter with fullness ratio for liquids in spheroids with transverse orientation (after ref. 2.45).

#### REFERENCES

- 2.1. COOPER, R. M.: Dynamics of Liquids in Moving Containers. *ARS J.*, vol. 30, no. 8, Aug. 1960, pp. 725-729.
- 2.2. BAUER, HELMUT F.: Theory of the Fluid Oscillations in a Circular Cylindrical Ring Tank Partially Filled With Liquid. *NASA TN D-557*, 1960.
- 2.3. BAUER, HELMUT F.: Fluid Oscillations in the Containers of a Space Vehicle and Their Influence Upon Stability. *NASA TR R-187*, 1964.
- 2.4. BAUER, HELMUT F.: Liquid Sloshing in a Cylindrical Quarter Tank. *AIAA J.*, vol. 1, no. 11, Nov. 1963, pp. 2601-2606.
- 2.5. BAUER, HELMUT F.: Theory of Liquid Sloshing in a 45° Sector Compartmented Cylindrical Tank. *AIAA J.*, vol. 2, no. 4, Apr. 1964, pp. 768-770.
- 2.6. ABRAMSON, H. NORMAN; GARZA, LUIS R.; AND KANA, DANIEL D.: Liquid Sloshing in Compartmented Cylindrical Tanks. *ARS J.*, vol. 32, no. 6, June 1962, pp. 978-980.

- 2.7. ABRAMSON, H. NORMAN; CHU, WEN-HWA; AND GARZA, LUIS R.: Liquid Sloshing in 45° Sector Compartment Cylindrical Tanks. TR No. 3, Contr. NAS 8-1555, Southwest Research Institute, Nov. 1962.
- 2.8. ABRAMSON, H. NORMAN; AND GARZA, LUIS R.: Some Measurements of Liquid Frequencies and Damping in Compartmented Cylindrical Tanks. AIAA J. Spacecraft Rockets, vol. 2, no. 3, May-June 1965, pp. 453-455.
- 2.9. EULITZ, WERNER R.: Analysis and Control of Liquid Propellant Sloshing During Missile Flight. MTP-P and VE-P-61-22, NASA-MSFC, Dec. 1961.
- 2.10. EULITZ, WERNER R.: Practical Consequences of Liquid Propellant Slosh Characteristics Derived by Nomographic Methods. MTP-P and VE-P-63-7, NASA-MSFC, Oct. 1963.
- 2.11. ABRAMSON, H. NORMAN; AND RANSLEBEN, GUIDO E., JR.: Wall Pressure Distributions During Sloshing in Rigid Tanks. ARS J., vol. 31, no. 4, Apr. 1961, pp. 545-547.
- 2.12. ABRAMSON, H. NORMAN; AND RANSLEBEN, GUIDO E., JR.: Some Comparisons of Sloshing Behavior in Cylindrical Tanks With Flat and Conical Bottoms. ARS J., vol. 31, no. 4, Apr. 1961, pp. 542-544.
- 2.13. LAMB, H.: Hydrodynamics. Sixth ed., Dover Publ., 1945.
- 2.14. TROESCH, B. ANDREAS: Free Oscillations of a Fluid in a Container. In: Boundary Problems in Differential Equations (Rudolph E. Langer, ed.), Univ. of Wisconsin Press, 1960.
- 2.15. CHU, WEN-HWA: Sloshing of Liquids in Cylindrical Tanks of Elliptical Cross Section. ARS J., vol. 30, no. 4, Apr. 1960, pp. 360-363.
- 2.16. ABRAMSON, H. N.: Dynamic Behavior of Liquids in Moving Containers. Appl. Mech. Rev., vol. 16, no. 7, July 1963, pp. 501-506.
- 2.17. STOKER, J. J.: Water Waves. Interscience Publishers, Inc., New York, 1957.
- 2.18. ROBERTS, J. R.; BASURTO, E. R.; AND CHEN, P. Y.: Slash Design Handbook I. NASA CR-406, 1966.
- 2.19. BAUER, HELMUT F.: Theory of Fluid Oscillations in Partially Filled Cylindrical Containers. MTP-AERO-62-1, NASA-MSFC, Jan. 1962.
- 2.20. CHU, WEN-HWA: Free Surface Condition for Sloshing Resulting From Pitching and Some Corrections. ARS J., no. 11, Nov. 1960, pp. 1090-1094.
- 2.21. BUDIANSKY, BERNARD: Sloshing of Liquids in Circular Canals and Spherical Tanks. J. Aerospace Sci., vol. 27, no. 3, Mar. 1960, pp. 161-173.
- 2.22. LAWRENCE, H. R.; WANG, C. J.; AND REDDY, R. B.: Variational Solution of Fuel Sloshing Modes. Jet Propulsion, vol. 28, no. 11, Nov. 1958, pp. 729-736.
- 2.23. RILEY, JAMES D.; AND TREMBATH, N. W.: Sloshing of Liquids in Spherical Tanks. J. Aerospace Sci., vol. 28, no. 3, Mar. 1961, pp. 245-246.
- 2.24. DOKUCHAEV, L. V.: On the Solution of a Boundary Value Problem on the Sloshing of a Liquid in Conical Cavities. PMM, vol. 28, no. 1, 1964, pp. 151-154.
- 2.25. RATTAYYA, JASTI V.: Sloshing of Liquids in Axisymmetric Ellipsoidal Tanks. AIAA Paper No. 65-114, presented at the AIAA 2nd Aerospace Science Meeting, New York, N.Y., Jan. 25-27, 1965.
- 2.26. EHRLICH, L. W.; RILEY, J. D.; STRANGE, W. G.; AND TROESCH, B. A.: Finite-Difference Techniques for a Boundary Problem With an Eigenvalue in a Boundary Condition. J. Soc. Industr. Appl. Math., vol. 9, no. 1, Mar. 1961, pp. 149-164.
- 2.27. EIDE, DONALD G.: Preliminary Analysis of Variation of Pitch Motion of a Vehicle in a Space Environment Due to Fuel Sloshing in a Rectangular Tank. NASA TN D-2336, 1964.
- 2.28. GRAHAM, E. W.; AND RODRIGUEZ, A. M.: The Characteristics of Fuel Motion Which Affect Airplane Dynamics. J. Appl. Mech., vol. 19, no. 3, Sept. 1952, pp. 381-388.
- 2.29. GRAHAM, E. W.; AND RODRIGUEZ, A. M.: The Characteristics of Fuel Motion Which Affect Airplane Dynamics. Douglas Aircraft Co. Rept. No. SM-14212, Nov. 27, 1951.
- 2.30. RAYLEIGH, J. W. S.: The Theory of Sound. Vol. II. Dover Publ., 1945.
- 2.31. BAUER, HELMUT F.: Theory of Liquid Sloshing in Compartmented Cylindrical Tanks Due to Bending Excitation. MTP-AERO-62-61, NASA-MSFC, July 1962.
- 2.32. BAUER, H. F.: Tables and Graphs of Zeros of Cross Product Bessel Functions. MTP-AERO-63-50, NASA-MSFC, June 1963.
- 2.33. BAUER, HELMUT F.: Theory of Liquid Sloshing in Compartmented Cylindrical Tanks Due to Bending Excitation. AIAA J., vol. 1, no. 7, July 1963, pp. 1590-1596.
- 2.34. OKHOTSIMSKII, D. E.: Theory of the Motion of a Body With Cavities Partly Filled With a Liquid. NASA TT F-33, May 1960. Translated from Prikladnaia Matematika i Mekhanika, vol. 20, no. 1, Jan.-Feb. 1956.
- 2.35. KACHIGAN, K.: Forced Oscillations of a Fluid in a Cylindrical Tank. ZU-7-046 (Contract AF04(645)-4), Convair Astronautics, Oct. 1955.
- 2.36. SCHMITT, ALFRED F.: Forced Oscillations of a Fluid in a Cylindrical Tank Undergoing Both Translation and Rotation. ZU-7-069 (Contract AF04(645)-4), Convair Astronautics, Oct. 1956.
- 2.37. ARMSTRONG, G. L.; AND KACHIGAN, K.: Propellant Sloshing. Section 14.14/15, pp. 14-

- 14 to 14-27. In Handbook of Astronautical Engineering (Koelle, H. H., ed.), McGraw-Hill, 1961.
- 2.38. MILES, JOHN W.: On the Sloshing of Liquid in a Cylindrical Tank. Rept. No. AM6-5, The Ramo-Wooldridge Corp., Guided Missile Research Div., GM-TR-18, Apr. 1956.
- 2.39. BAUER, HELMUT F.: Fluid Oscillations in a Circular Cylindrical Tank. Tech. Rept. No. DA-TR-1-58, Army Ballistic Missile Agency, Apr. 1958. (Available from DDC; AD-160 272.)
- 2.40. BAUER, HELMUT F.: Fluid Oscillations of a Circular Cylindrical Tank Performing Lissajous-Oscillations. DA TR No. 2-58, ABMA, Apr. 1958.
- 2.41. ABRAMSON, H. NORMAN; AND RANSLEBEN, GUIDO E., JR.: Simulation of Fuel Sloshing Characteristics in Missile Tanks by Use of Small Models. ARS J., vol. 30, no. 7, July 1960, pp. 603-612.
- 2.42. ABRAMSON, H. NORMAN; AND RANSLEBEN, GUIDO E., JR.: Liquid Sloshing in Rigid Cylindrical Tanks Undergoing Pitching Motion. TR No. 11, Contract DA-23-072-ORD-1251, Southwest Research Institute, May 1961.
- 2.43. MIKISHEV, G. N.; AND DOROZHIN, N. YA.: An Experimental Investigation of Free Oscillations of a Liquid in Containers (in Russian). Izv. Akad. Nauk SSSR, Otd. Tekh. Nauk, Mekh. i Mashinostr., No. 4, pp. 48-53, July/Aug. 1961. Translated into English by D. Kana, Southwest Research Institute, June 30, 1963.
- 2.44. McCARTY, JOHN LOCKE; AND STEPHENS, DAVID G.: Investigation of the Natural Frequencies of Fluids in Spherical and Cylindrical Tanks. NASA TN D-252, 1960.
- 2.45. LEONARD, H. WAYNE; AND WALTON, WILLIAM C., JR.: An Investigation of the Natural Frequencies and Mode Shapes of Liquids in Oblate Spheroidal Tanks. NASA TN D-904, 1961.
- 2.46. STOFAN, ANDREW J.; AND ARMSTEAD, ALFRED L.: Analytical and Experimental Investigation of Forces and Frequencies Resulting From Liquid Sloshing in a Spherical Tank. NASA TN D-1281, 1962.
- 2.47. CHU, WEN-HWA: Fuel Sloshing in a Spherical Tank Filled to an Arbitrary Depth. AIAA J., vol. 2, no. 11, Nov. 1964, pp. 1972-1979.
- 2.48. ABRAMSON, H. N.; CHU, W.-H.; AND GARZA, L. R.: Liquid Sloshing in Spherical Tanks. TR No. 2, Contract NAS8-1555, Southwest Research Institute, Mar. 1962.
- 2.49. ABRAMSON, H. NORMAN; CHU, WEN-HWA; AND GARZA, LUIS R.: Liquid Sloshing in Spherical Tanks. AIAA J., vol. 1, no. 2, Feb. 1963, pp. 384-389.
- 2.50. SUMNER, IRVING E.; AND STOFAN, ANDREW J.: An Experimental Investigation of the Viscous Damping of Liquid Sloshing in Spherical Tanks. NASA TN D-1991, 1963.
- 2.51. MCCARTY, JOHN LOCKE; LEONARD, H. WAYNE; AND WALTON, WILLIAM C., JR.: Experimental Investigation of the Natural Frequencies of Liquids in Toroidal Tanks. NASA TN D-531, 1960.
- 2.52. SUMNER, IRVING E.: Preliminary Experimental Investigation of Frequencies and Forces Resulting From Liquid Sloshing in Toroidal Tanks. NASA TN D-1709, 1963.
- 2.53. LEVIN, E.: Oscillations of a Fluid in a Rectilinear Conical Container. AIAA J., vol. 1, no. 6, June 1963, p. 1447.
- 2.54. LOMEN, D. O.: Liquid Propellant Sloshing in Mobile Tanks of Arbitrary Shape. NASA CR-222, 1965.
- 2.55. LOMEN, D. O.: Digital Analysis of Liquid Propellant Sloshing in Mobile Tanks With Rotational Symmetry. NASA CR-230, 1965.
- 2.56. STEPHENS, DAVID G.; AND LEONARD, H. WAYNE: The Coupled Dynamic Response of a Tank Partially Filled With a Liquid and Undergoing Free and Forced Planar Oscillations. NASA TN D-1945, 1963.

## PRINCIPAL NOTATIONS

*A*=acceleration field  
*a*, *b*=tank dimensions  
*d*=diameter  
*e*=2.71828  
*F*=force  
*g*=gravitational acceleration  
*h*=liquid depth  
*I<sub>r</sub>*=total moment of inertia of liquid  
*i*= $\sqrt{-1}$   
*J<sub>v</sub>( )*=Bessel function of first kind of order *v*

*ln*=natural logarithm  
*M*=moment  
*M<sub>f</sub>*=total mass of liquid  
*N<sub>s</sub>(ξ<sub>m</sub>)*=integral defined in appendix A  
*p*=normal pressure  
*r*=radial coordinate, also radius of the free surface  
*R*=tank radius, sphere  
*t*=time  
*u*, *v*, *w*=rectangular velocity components

$u_r, u_\phi, w$ =cylindrical velocity components

$v$ =velocity

$W_F$ =total weight of liquid

$x, y, z$ =rectangular coordinate axes

$Y_r(\cdot)$ =Bessel function of second kind of order  $r$

$\alpha$ =vertex angle of sector tank; semi-vertex angle of conical tank

$\bar{\alpha}=2\pi\alpha$

$\Gamma$ =gamma function

$\delta$ =displacement of liquid free surface from equilibrium position with respect to space coordinate

$\delta^*$ =displacement with respect to coordinate fixed to tank

$$\zeta = \xi_m \frac{z}{a}$$

$$\zeta^* = \xi_{2m-1,n} \frac{z}{a}$$

$$\zeta_1^* = \xi_{2m-1,n} \frac{z}{a}$$

$$\eta = \frac{\Omega}{\omega_m}$$

$$\eta^* = \frac{\Omega}{\omega_{2m-1,n}}$$

$$\eta_1^* = \frac{\Omega}{\omega_{2m-1,n}}$$

$\theta$ =angular coordinate

$$\kappa = \xi_m \frac{h}{a}$$

$$\kappa^* = \xi_{2m-1,n} \frac{h}{a}$$

$$\kappa_1^* = \xi_{2m-1,n} \frac{h}{a}$$

$\nu$ =kinematic viscosity

$\rho$ =liquid mass density

$$\sigma = \xi_m \frac{r}{a}$$

$$\sigma^* = \xi_{2m-1,n} \frac{r}{a}$$

$$\sigma_1^* = \xi_{2m-1,n} \frac{r}{a}$$

$\Phi$ =velocity potential function

$\phi$ =angular coordinate

$$\bar{\phi} = \frac{m}{2\alpha} \phi$$

$\Omega$ =excitation frequency

$\omega$ =natural circular frequency

$\nabla$ =vector operator

$\rightarrow$ =indicates vector quantity

#### Subscripts:

$n$ =normal

$T$ =thrust

$H$ =horizontal

## APPENDIX A.—Cylindrical Tank With Ring Sector Cross Section, Excitation in y Direction

[Ref. 2.3]

$$\Phi(r, \phi, z, t) = i\Omega r_0 e^{i\frac{\pi}{2}kz} \left\{ r \sin \phi + \frac{c_m b_{mn} k^2 \cosh(kr + \xi)}{(1 - \eta^2) \cosh k} C(r) \cos \phi \right\}$$

$$\text{where } c_0 = \frac{1 - \cos \bar{\alpha}}{\bar{\alpha}} \quad c_m = \frac{2\bar{\alpha}(-1)^m \cos \bar{\alpha} - 1}{(\bar{m}^2 - \bar{\alpha}^2)}$$

The velocity distribution is obtained from Eqs. (2.27b) by substituting  $y_0$  for  $x_0$  and  $c_m$  for  $a_m$  in the double series. Also, in Eq. (2.27a)  $\cos \phi$  must be replaced by  $\sin \phi$  and in Eq. (2.27b)  $\sin \phi$  by  $-\cos \phi$ .

$$F_x = M_p \Omega^2 r_0 e^{i\frac{\pi}{2}kz} \frac{(-1)^{m+1} c_m b_{mn}^2 \sin \bar{\alpha} \tanh k}{\pi \alpha(1 - k^2)(1 - \eta^2) \kappa} \left\{ \frac{2}{\pi^2 m^2 - \bar{\alpha}^2} \left[ \frac{2}{\pi^2 \xi_{mn}} - k C_m (\xi_{mn}) \right] + N_d(\xi_{mn}) \right\}$$

$$F_y = M_p \Omega^2 r_0 e^{i\frac{\pi}{2}kz} \left\{ 1 - \frac{2c_m b_{mn} \eta^2 (1 - (-1)^m \cos \bar{\alpha})}{\pi \alpha(1 - k^2)(1 - \eta^2)} \frac{\tanh \kappa}{\kappa} \left( \frac{\bar{\alpha}^2}{m^2 - \bar{\alpha}^2} \left[ \frac{2}{\pi^2 \xi_{mn}} - k C_m (\xi_{mn}) \right] + N_d(\xi_{mn}) \right) \right\}$$

$$M_x = M_p \Omega^2 r_0 e^{i\frac{\pi}{2}kz} \left\{ \frac{(1 + k^2)}{4 \frac{\pi}{2}} \left( 1 + \frac{\sin \bar{\alpha}}{2} \cos \bar{\alpha} \right) - \frac{1}{\pi \alpha} \frac{\sin b_{mn}(1 - (-1)^m \cos \bar{\alpha}) \eta^2}{(1 - k^2)\xi_{mn}(1 - \eta^2)} \left( \tanh \kappa + \frac{2}{\kappa} \left( \frac{1}{\cosh \kappa} - 1 \right) \right) \right\} \left[ \frac{\bar{\alpha}^2}{m^2 - \bar{\alpha}^2} \left( \frac{2}{\pi^2 \xi_{mn}} - k C_m (\xi_{mn}) + N_d(\xi_{mn}) \right) + \frac{2\bar{\alpha}^2}{(\bar{m}^2 - \bar{\alpha}^2) \kappa} \frac{N_d(\xi_{mn})}{\cosh \kappa} \right] + 2M_p F_x \frac{\bar{\alpha}}{3} \frac{\sin \bar{\alpha}}{(1 - k^2)}$$

$$M_y = M_p \Omega^2 r_0 e^{i\frac{\pi}{2}kz} \left\{ \frac{(1 + k^2)}{4 \frac{\pi}{2}} \frac{\sin^2 \bar{\alpha}}{\pi \alpha} + \frac{\sin \bar{\alpha}}{\pi \alpha} \frac{(-1)^{m+1} c_m b_{mn} \eta^2}{(1 - k^2)\xi_{mn}(1 - \eta^2)} \left( \left[ \tanh \kappa + \frac{2}{\kappa} \left( \frac{1}{\cosh \kappa} - 1 \right) \right] \left[ \frac{\bar{\alpha}^2}{m^2 - \bar{\alpha}^2} \left( \frac{2}{\pi^2 \xi_{mn}} - k C_m (\xi_{mn}) + N_d(\xi_{mn}) \right) + \frac{2\bar{\alpha}^2}{(\bar{m}^2 - \bar{\alpha}^2) \kappa} \frac{N_d(\xi_{mn})}{\cosh \kappa} \right] + 2M_p F_y \frac{\bar{\alpha}}{3} \frac{\sin \bar{\alpha}}{(1 - k^2)} \right) \right\}$$

$$N_d(\xi_{mn}) = \frac{1}{\kappa + 1} \int_0^\infty r^k C_m \frac{(\xi_{mn})}{2\alpha} dr = -\frac{1}{\kappa + 1} \int_{\xi_{mn}}^{\xi_{mn}} r^k C_m \frac{(s)}{2\alpha} ds = \frac{\Gamma(m + \frac{k}{2} + \frac{1}{2})}{\xi_{mn} \Gamma(\frac{m}{2\alpha} - \frac{k}{2} + \frac{1}{2})} \sum_{\mu=0}^{\infty} \frac{\left( \frac{m}{2\alpha} + 2\mu + 1 \right) \Gamma\left( \frac{m}{2\alpha} - \frac{k}{2} + \frac{1}{2} + \mu \right)}{\Gamma\left( \frac{m}{2\alpha} + 2\mu + 1 \right) \Gamma\left( \frac{m}{2\alpha} + 2\mu + \frac{3}{2} + \mu \right)} \left[ \frac{j_m}{2\alpha} + 2\mu + 1 \left( \xi_{mn} \right) - k \Gamma \frac{m}{2\alpha} + 2\mu + 1 \left( \xi_{mn} \right) + j_m \frac{(\xi_{mn})}{2\alpha} \right] + j_m \frac{(\xi_{mn})}{2\alpha} \left\{ \frac{\left( \frac{m}{2\alpha} - 1 \right)}{2} \left( \frac{m}{2\alpha} - \mu - 1 \right) : \frac{2\mu - \frac{m}{2\alpha}}{\xi_{mn}} \left( 1 - k^{k+2\mu} - \frac{m}{2\alpha} + 1 \right) \right\}$$

$$+ \frac{2}{\pi} \sum_{\mu=0}^{\infty} \frac{(-1) \xi_{mn}^{2\mu + \frac{m}{2\alpha}} \left( 1 - k^{2\mu + \frac{m}{2\alpha}} - 1 \right)}{2\mu + \frac{m}{2\alpha} \mu! \left( \mu + \frac{m}{2\alpha} \right) \left( \mu + 2\mu + 1 \right)^2} + \frac{2\kappa + 1}{\pi} \sum_{\mu=0}^{\infty} \frac{(-1)^{\mu} \frac{m}{2\alpha} + 2\mu}{2\mu + \frac{m}{2\alpha} \mu! \left( \mu + \frac{m}{2\alpha} \right) \left( \mu + 2\mu + 1 \right)} \left[ \mu \left( \frac{\xi_{mn}}{2} \right) - \frac{1}{2} \psi(\mu + 1) - \frac{1}{2} \psi\left(\mu + \frac{m}{2\alpha} + 1\right) \right]$$

$$- \frac{2}{\pi} \sum_{\mu=0}^{\infty} \frac{(-1)^{\mu} \xi_{mn}^{2\mu + \frac{m}{2\alpha}}}{2\mu + \frac{m}{2\alpha} \mu! \left( \mu + \frac{m}{2\alpha} \right) \left( \mu + 2\mu + \frac{m}{2\alpha} + 1 \right)} \left\{ \mu \left( \frac{\xi_{mn}}{2} \right) - \frac{1}{2} \psi(\mu + 1) - \frac{1}{2} \psi\left(\mu + \frac{m}{2\alpha} + 1\right) \right\}$$

**APPENDIX B.—Cylindrical Tank With Ring Sector Cross Section, Excitation About y Axis and Roll.**  
**Excitation**

[Ref. 2.3]

$q(r, \phi, z, t) = \Omega_0 e^{j\Omega t} \left\{ \begin{array}{l} \theta_0 \\ \lambda_0 \end{array} \right\} \left[ \begin{array}{l} -r \sin \phi \\ -r \sin \phi \end{array} \right] + (A \cosh k_z + B \sinh k_z) C(r) \cos \phi$ $\theta_{mn} = \left( \frac{\lambda m n \pi^2}{k_m (1 - k_z^2) \cosh k_z} \right) \left[ \frac{1}{2} \sinh \left( \frac{k_z}{2} \right) - \left( \frac{k_z}{2} + \frac{\pi}{2} \right) \cosh \left( \frac{k_z}{2} \right) \right] \left\{ \begin{array}{l} \theta_m \\ \lambda_m \end{array} \right\}$ $B_{mn} = \left( \frac{\lambda m n \pi^2}{k_m (1 - k_z^2) \cosh k_z} \right) \left[ \left( \frac{3\pi}{2} - \frac{\pi}{2} \right) \sinh \left( \frac{k_z}{2} \right) - 2 \cosh \left( \frac{k_z}{2} \right) \right] \left\{ \begin{array}{l} \theta_m \\ \lambda_m \end{array} \right\}$
<p><b>Excitation About y Axis</b>  <math>\theta(t) = \theta_0 e^{j\Omega t}</math>      and x Axis  <math>x(t) = x_0 e^{j\Omega t}</math></p> $F_y = -M_p g \left\{ \begin{array}{l} \theta_0 \\ \lambda_0 \end{array} \right\} e^{j\Omega t} - 4 M_p \Omega^2 \left\{ \begin{array}{l} \theta_0 \\ \lambda_0 \end{array} \right\} e^{j\Omega t} \frac{\lambda_m n \sinh \left( \frac{k_z}{2} \right) (1 - (-1)^m \cos k_z)}{n(1 - k_z^2) k_z} \left[ N_0 (t_{mn}) + \frac{\pi^2}{(m^2 - n^2)} \left( \frac{2}{\sqrt{k_m n}} - k C_{\frac{m}{n}} (t_{mn}) \right) \right]$ $M_y = -\frac{M_p g \Omega^2 k_m (1 + k_z^2)}{4 k_z} \left\{ \begin{array}{l} \theta_0 \\ \lambda_0 \end{array} \right\} \frac{1 + \sinh \frac{k_z}{2} \cos \frac{k_z}{2}}{\sin \frac{k_z}{2}} + M_p \Omega^2 \left\{ \begin{array}{l} \theta_0 \\ \lambda_0 \end{array} \right\} e^{j\Omega t} \left[ \left\{ \begin{array}{l} \frac{(1+k_z^2)}{k_z} \left( 1 + \sinh \frac{k_z}{2} \cos \frac{k_z}{2} \right) - \frac{1}{12} \left( \frac{k_z}{2} \right)^2 \\ \frac{(1+k_z^2)}{k_z} \sinh \frac{k_z}{2} \end{array} \right\} + \frac{2(-1)^m \sinh \frac{k_z}{2}}{k_z \sinh k_m (1 - k_z^2)} \left[ B_{mn} \left\{ \cosh \left( \frac{k_z}{2} \right) - \frac{2}{k} \sinh \left( \frac{k_z}{2} \right) \right\} \right. \right. \\ \left. \left. + \frac{\pi^2}{(m^2 - n^2)} \left( \frac{2}{\sqrt{k_m n}} - k C_{\frac{m}{n}} (t_{mn}) \right) + N_0 (t_{mn}) \right] + \frac{8^2 k_m^2 N_0 (t_{mn})}{(m^2 - n^2) k_z} \left\{ A_{mn} \cosh \left( \frac{k_z}{2} \right) - B_{mn} \sinh \left( \frac{k_z}{2} \right) \right\} \right] + 2 M_p g \frac{\pi}{2} \frac{\sinh \frac{k_z}{2} \left( 1 - k_z^2 \right)}{(1 - k_z^2)}$ $M_x = -\frac{M_p g \Omega^2 k_m (1 + k_z^2)}{4 k_z} \left\{ \begin{array}{l} \theta_0 \\ \lambda_0 \end{array} \right\} \frac{\sinh \frac{k_z}{2}}{\left( 1 - \sinh \frac{k_z}{2} \cos \frac{k_z}{2} \right)} - M_p \Omega^2 \left\{ \begin{array}{l} \theta_0 \\ \lambda_0 \end{array} \right\} e^{j\Omega t} \left[ \left\{ \begin{array}{l} \frac{(1+k_z^2)}{k_z} \frac{\sinh^2 \frac{k_z}{2}}{k_z} \\ \frac{(1+k_z^2)}{k_z} \left( 1 - \sinh \frac{k_z}{2} \cos \frac{k_z}{2} \right) - \frac{1}{12} \left( \frac{k_z}{2} \right)^2 \end{array} \right\} - \frac{2(-1)^m \sinh \frac{k_z}{2} \cos k_z}{k_z \sinh k_m (1 - k_z^2)} \left[ B_{mn} \left\{ \cosh \left( \frac{k_z}{2} \right) - \frac{2}{k} \sinh \left( \frac{k_z}{2} \right) \right\} \right] \right. \\ \left. - 2 M_p g \frac{\pi}{2} \frac{\left( 1 - \cos k_z \right) \left( 1 - k_z^2 \right)}{(1 - k_z^2)} \right]$
$q(r, \phi, z, t) = \Omega_0 e^{j\Omega t} \left\{ \begin{array}{l} \theta_0 \\ \lambda_0 \end{array} \right\} \left[ \left( \frac{z}{r} \right)^2 (r - r_0) + \frac{N_0 (t_{mn})^2 \cos k_z}{r(2m-1)(r^2(2m-1)^2 - k_z^2)} \left[ \left( \frac{z}{r} \right)^2 \left( 1 - \frac{2m-1}{2r} + 2 \right) - \left( \frac{z}{r} \right)^2 \left( \frac{2m-1}{2r} - \frac{2m-1}{2r} \right) \frac{2m-1}{2r} \right] \right. \\ \left. + \frac{8k^2 C_{\frac{m}{n}} (t_{mn})^2 \sinh \left( \frac{k_z}{2} \right) \cos \frac{k_z}{2}}{r(2m-1)(r^2(2m-1)^2 - k_z^2)(1 - \eta^2 k_z^2) \cos k_z} \left[ \frac{2m-1, n \left( \frac{2m-1}{2r} + 2 \right) - q_{2m-1, n} \left( \frac{2m-1}{2r} - \frac{2m-1}{2r} \right) \frac{2m-1}{2r}}{\left( 1 - \frac{2m-1}{2r} \right)} - \frac{(2m-1)}{2r} q_{2m-1, n} \right] \right]$ $\left\{ \begin{array}{l} x_r \\ y_r \end{array} \right\} = M_p \Omega^2 k_0 e^{j\Omega t} \left\{ \begin{array}{l} \left( \frac{1-k_z^2}{1+k_z^2} \right) \left\{ \frac{2}{k_z} \sinh \frac{k_z}{2} + 2 \left( \frac{\sinh k_z - 1}{k_z} \right) \right\} + \frac{16k \sinh \frac{k_z}{2}}{k_z} \\ \left( \frac{2}{k_z} \sinh \frac{k_z}{2} - \frac{2}{k_z} \left( 1 + \cos k_z \right) \right) - \frac{16k (1 + \cos k_z)}{k_z} \end{array} \right\} \frac{1}{(2m-1)(Gm-1)^2 k_z^2 - k_z^2 (1 - k_z^2)} \left[ \frac{\pi^2}{(4m-1)^2 k_z^2 - k_z^2} \right]$ $+ \frac{16k^2}{(1 - k_z^2)} \left\{ \left( \frac{2m-1}{2r} - 1 \right) \left( 1 - \frac{2m-1}{2r} + 1 \right) \left( 1 - \frac{2m-1}{2r} + 2 \right) + \left( \frac{2m-1}{2r} + 1 \right) \left( \frac{2m-1}{2r} - k \right) \left( k - \frac{2m-1}{2r} \right) \right\} \frac{4k(1 - k_z^2)}{k_z(2m-1)} \\ + \frac{16k \left\{ \sin \frac{k_z}{2} \right\}}{(1 + \cos k_z)} \frac{\eta^2 \tanh k_z \left[ \frac{\pi^2}{(2(2m-1))^2 - k_z^2} \left( \frac{2}{\sqrt{k_{2m-1, n}}} - k C_{\frac{m}{n}} (k_{2m-1, n}) \right) + N_0 \right]}{k_{2m-1, n}(r^2(2m-1) - k_z^2)(1 - \eta^2 k_z^2)} \left[ \frac{t_{2m-1, n} \left( \frac{2m-1}{2r} + 2 \right) - q_{2m-1, n} \left( \frac{2m-1}{2r} - \frac{2m-1}{2r} \right) \frac{2m-1}{2r}}{1 - k_z^2} - \frac{(2m-1)}{4r} q_{2m-1, n} \right]$ <p><b>Roll Excitation</b>  <math>\dot{\theta}(t) = \theta_0 e^{j\Omega t}</math></p> $\left\{ \begin{array}{l} M_x \\ M_y \end{array} \right\} = M_p \Omega^2 k_0 e^{j\Omega t} \left[ 2 \left( \frac{1}{2} \frac{1 - k_z^2}{1 + k_z^2} \frac{\sinh k_z + 2 \frac{\sinh k_z - 1}{k_z}}{2 \frac{\sinh k_z}{k_z} - (1 + \cos k_z)} \right) + \frac{165}{\pi} \left\{ \begin{array}{l} \sin \frac{k_z}{2} \\ \cos \frac{k_z}{2} \end{array} \right\} \frac{1}{(2m-1)((2m-1)^2 k_z^2 - k_z^2)} \left[ \frac{\pi^2}{(2(2m-1))^2 - k_z^2} \right] \right]$ $+ \frac{\left( \frac{2m-1}{2r} + 2 \right) \left( 1 - \frac{2m-1}{2r} + 3 \right) \left( \frac{2m-1}{2r} + 2 \right) + \left( \frac{2m-1}{2r} + 1 \right) \left( \frac{2m-1}{2r} - k \right) \left( k - \frac{2m-1}{2r} \right)}{1 - k_z^2} \left[ \frac{4k(1 - k_z^2)}{k_z(2m-1)} \right] + \frac{4k \left\{ \begin{array}{l} \sin \frac{k_z}{2} \\ \cos \frac{k_z}{2} \end{array} \right\}}{1 + \cos k_z}$ $+ \eta^2 k^2 \left[ \frac{t_{2m-1, n} \left( \frac{2m-1}{2r} + 2 \right) - q_{2m-1, n} \left( \frac{2m-1}{2r} - \frac{2m-1}{2r} \right) \frac{2m-1}{2r}}{1 - k_z^2} - \frac{(2m-1)}{4r} q_{2m-1, n} \right] \left\{ \left[ \tanh k_z + \frac{\pi^2}{k_z^2} \left( \frac{1}{\cosh k_z} - 1 \right) \right] \left[ \frac{\pi^2}{(4(2m-1))^2 - k_z^2} \right] \right. \\ \left. + \left( \frac{2}{k_z} - k C_{\frac{m}{n}} (t_{mn}) \right) + N_0 (t_{mn}) \right] + \frac{k^2}{-k^2(2m-1)^2 + k_z^2} \frac{2k^2 t_{2m-1, n} N_0 (t_{mn})}{k^2 \cosh k_z} \right\} + 8 M_p g \frac{\pi}{2} \frac{1 - k_z^2}{1 - k_z^2} \left\{ \begin{array}{l} \sin \frac{k_z}{2} \\ \cos \frac{k_z}{2} \end{array} \right\}$ $M_z = M_p \Omega^2 k_0 e^{j\Omega t} \left\{ \begin{array}{l} 1 + k_z^2 + \frac{2k^2}{k_z^2} \frac{1}{(1 - k_z^2)(2m-1)(2m-1)^2 k_z^2 - k_z^2 (1 - k_z^2)} \left[ \frac{a(1 - k_z^2)}{(2m-1)} + \frac{\left( \frac{2m-1}{2r} + 2 \right)^2 \left( \frac{2m-1}{2r} - 2 \right)^2}{k_z^2} \right] \\ + \frac{32k}{\pi} \frac{N_0 (t_{mn})}{\eta^2} \frac{\tanh k_z \eta^2}{(2m-1)((2m-1)^2 k_z^2 - k_z^2)(1 - \eta^2 k_z^2)} \left[ \frac{t_{2m-1, n} \left( \frac{2m-1}{2r} + 2 \right) - q_{2m-1, n} \left( \frac{2m-1}{2r} - \frac{2m-1}{2r} \right) \frac{2m-1}{2r}}{1 - k_z^2} - \frac{(2m-1)}{4r} q_{2m-1, n} \right] \right\}$

## APPENDIX B.—Concluded

Notes	$\xi^a = \xi_{2m-1, n} \frac{x}{a}$	$\eta^a = \xi_{2m+1, n} \frac{x}{a}$
	$\alpha^a = \xi_{2m-1, n} \frac{h}{a}$	$\frac{\pi}{2} + \frac{2m+1}{2a} \phi$
	$\gamma^a = \frac{\Omega}{\omega_{2m-1, n}}$	$\bar{\gamma} = \frac{h}{a^2} \xi_{mn}$
	$C(\rho \phi) = C_{\frac{2m-1}{2a}} \left( \xi_{2m-1, n} \frac{x}{a} \right)$ and $\int_{\xi_{2m-1, n}}^{\xi_{2m-1, n}} \rho \phi C(\rho \phi) d\rho = 1^a$	
	$\xi_{2m-1, n} = \xi_{2m-1, n}^2 \int_{\xi_{2m-1, n}}^{\xi_{2m-1, n}} \rho \phi^2 C(\rho \phi) d\rho / 1^a$	
	$\eta_{2m-1, n} = \xi_{2m-1, n}^2 \int_{\xi_{2m-1, n}}^{\xi_{2m-1, n}} \frac{C(\rho \phi)}{\rho} \frac{d\rho^a}{\rho} / 1^a$	
	$\xi_{2m-1, n} = \xi_{2m-1, n}^2 \int_{\xi_{2m-1, n}}^{\xi_{2m-1, n}} \frac{2m+1}{2a} C(\rho \phi) d\rho / 1^a$	
	$\eta_{2m-1, n} = \xi_{2m-1, n}^2 \int_{\xi_{2m-1, n}}^{\xi_{2m-1, n}} \rho \phi \left( 1 - \frac{2m+1}{2a} \right) C(\rho \phi) d\rho / 1^a$	

The "double signs," i.e., "+" indicates that the "+" corresponds to  $F_x$  and the "-" to  $F_y$ . Similarly for expressions for  $M_x$  and  $M_y$ .

## APPENDIX C.—Circular Cylindrical Quarter (90° Sector) Tank

[Ref. 2.3]

$b = \frac{x_0 \Omega^2 e^{i\theta}}{g/a} \left[ \frac{1}{a} \cos \phi + \frac{a m b_{mn} n^2 J_{2m}(\epsilon) \cos 2m\phi}{a(1 - \eta^2)} \right]$  $F_x = M_F \Omega^2 x_0 e^{i\theta R} \left[ 1 + \frac{4n^2}{\pi a} \frac{(-1)^{m+1} a_m b_{mn} \tanh \kappa}{(1 - \eta^2)\kappa} \left\{ \frac{J_{2m}(\epsilon_{mn})}{(4m^2 - 1)} + L_d(\epsilon_{mn}) \right\} \right]$  <b>Excitation in the x Direction</b> $x(t) = x_0 e^{i\theta R}$ $F_y = M_F \Omega^2 x_0 e^{i\theta R} \frac{4a_m b_{mn} n^2 \tanh \kappa}{\pi a(1 - \eta^2)} \left\{ \frac{J_{2m}(\epsilon_{mn})}{(4m^2 - 1)} + L_d(\epsilon_{mn}) \right\}$ $M_x = -M_F \Omega^2 a x_0 e^{i\theta R} \left[ \frac{1}{\pi h/a} - \frac{2}{\pi} \frac{a_m b_{mn} n^2}{a_m m(1 - \eta^2)} \left\{ \frac{J_{2m}(\epsilon_{mn})}{(4m^2 - 1)} + L_d(\epsilon_{mn}) \right\} \right] \left[ \tanh \kappa + \frac{2}{\kappa} \left( \frac{1}{\cosh \kappa} - 1 \right) \right] + \frac{2\varepsilon_{mn}^2 L_d(\epsilon_{mn})}{(4m^2 - 1)\kappa \cosh \kappa} \left\{ \frac{4M_F g^2}{3\pi} \right\}$ $M_y = M_F \Omega^2 a x_0 e^{i\theta R} \left[ \frac{1}{4h/a} + \frac{2}{\pi} \frac{(-1)^{m+1} a_m b_{mn} n^2}{a_m m(1 - \eta^2)} \left\{ \frac{J_{2m}(\epsilon_{mn})}{(4m^2 - 1)} + L_d(\epsilon_{mn}) \right\} \right] \left[ \tanh \kappa + \frac{2}{\kappa} \left( \frac{1}{\cosh \kappa} - 1 \right) \right] + \frac{2\varepsilon_{mn}^2 L_d(\epsilon_{mn})}{(4m^2 - 1)\kappa \cosh \kappa} \left\{ \frac{4M_F g^2}{3\pi} \right\}$  $b = -\frac{a \Omega^2 \theta}{g/a} \left\{ \frac{h}{2a} \cos \phi - \left[ A_{mn} \cosh \left( \frac{\kappa}{2} \right) + B_{mn} \sinh \left( \frac{\kappa}{2} \right) \right] J_{2m}(\epsilon) \cosh 2m\phi \right\}$ $F_x = -M_F \theta_0 e^{i\theta R} + \frac{8M_F a \theta^2}{\pi} \theta_0 e^{i\theta R} \frac{(-1)^{m+1} A_{mn} \sinh \left( \frac{\kappa}{2} \right)}{\kappa} \left[ \frac{J_{2m}(\epsilon_{mn})}{(4m^2 - 1)} + L_d(\epsilon_{mn}) \right]$ $F_y = -M_F \theta_0 e^{i\theta R} - \frac{8M_F a \theta^2}{\pi} \theta_0 e^{i\theta R} \frac{A_{mn} \sinh \left( \frac{\kappa}{2} \right)}{\kappa} \left[ \frac{J_{2m}(\epsilon_{mn})}{(4m^2 - 1)} + L_d(\epsilon_{mn}) \right]$ <b>Rotational Excitation</b> $\theta(t) = \theta_0 e^{i\theta R}$ $M_x = + \frac{M_F g a \theta_0 e^{i\theta R}}{2\pi(h/a)} - M_F a^2 \Omega^2 \theta_0 e^{i\theta R} \left\{ \frac{1}{4\pi} - \frac{4}{\pi \epsilon_{mn}} \left[ B_{mn} \left\{ \cosh \left( \frac{\kappa}{2} \right) - \frac{2}{\kappa} \sinh \left( \frac{\kappa}{2} \right) \right\} \right] \right\} \left\{ \frac{J_{2m}(\epsilon_{mn})}{(4m^2 - 1)} + L_d(\epsilon_{mn}) \right\} + \frac{L_d(\epsilon_{mn}) \kappa^2}{(4m^2 - 1)\kappa} \left\{ A_{mn} \cosh \frac{\kappa}{2} - B_{mn} \sinh \left( \frac{\kappa}{2} \right) \right\} \left\{ \frac{4M_F g a}{4\pi} \right\} - \frac{4M_F g a}{4\pi}$ $M_y = + \frac{M_F g a \theta_0 e^{i\theta R}}{4h/a} + M_F a^2 \Omega^2 \theta_0 e^{i\theta R} \left\{ \frac{1}{8} - \frac{1}{\pi \epsilon_{mn}} \left[ B_{mn} \left\{ \cosh \left( \frac{\kappa}{2} \right) - \frac{2}{\kappa} \sinh \left( \frac{\kappa}{2} \right) \right\} \right] \right\} \left\{ \frac{J_{2m}(\epsilon_{mn})}{(4m^2 - 1)} + L_d(\epsilon_{mn}) \right\} + \frac{L_d(\epsilon_{mn}) \kappa^2}{(4m^2 - 1)\kappa} \left\{ A_{mn} \cosh \left( \frac{\kappa}{2} \right) - B_{mn} \sinh \left( \frac{\kappa}{2} \right) \right\} \left\{ \frac{4M_F g a}{4\pi} \right\} + \frac{4M_F g a}{4\pi}$
--

$\delta = \frac{\Phi_0 e^{i\Omega t} \omega_0^2}{g/a} \left\{ \left( \frac{z}{a} \right)^2 \left( \phi - \frac{\pi}{4} \right) + \frac{2}{a} \left( \frac{z}{a} \right)^2 \left[ L_0 \left( \frac{z}{a} \right) + \frac{1}{2} \right] \cos 2\phi + \frac{2}{a} \left[ L_0 \left( \frac{z}{a} \right)^2 - \frac{(r/a)^2 - (r/a)}{(2m-1)^2 - 1} \right] \right\} + \frac{\eta^{*2}}{a} \frac{(2f_n - e_n) L_0(\eta)}{(1 - \eta^2)} \cos 2\phi + \frac{2}{a}$ $+ \frac{(2m-1, n) \cdot (2m-1, n)^T \omega_0^2 \eta^{*2} \cos (4m-2)\phi}{(2m-1)(2m-1)^2 - 1} \left\{ \begin{aligned} F_x &= M_F \Omega^2 \omega_0^2 i R \left[ \frac{2}{3} - \frac{4}{\pi} + \frac{16}{9a^2} + \frac{8}{\pi^2} \left( \frac{1}{4m-1} - \frac{1}{3} \left( \frac{1}{2m-1} \right) \right) \right] + \frac{1}{8\pi d(2m-1)^2} \left( \frac{1}{2m-1} \right)^2 \left[ \frac{1}{3} L_0(\bar{e}_n) + L_0 d(\bar{e}_n) \right] + \frac{8}{\pi^2 a} \\ &\quad \cdot \frac{\left[ \frac{(2m-1, n) - \phi_{2m-1, n}}{2m-1, n(2m-1)^2 - 1} \right] \tanh \kappa^*}{\epsilon_{2m-1, n}(2m-1)^2 - \eta^2} \left[ \frac{1}{4} \left( \frac{4m-2(\epsilon_{2m-1, n})^2}{(2m-1)^2 - \frac{1}{4}} \right) + L_0 d(\epsilon_{2m-1, n}) \right] \end{aligned} \right\} - F_y \\ M_x &= M_F \Omega^2 \omega_0^2 i R \left\{ \begin{aligned} &\frac{1}{5} \frac{1}{a} \left( 1 - \frac{4}{\pi} \right) + \frac{4}{2\pi^2 a} + \frac{12}{\pi a^2} \left[ \frac{1}{4} \left( \frac{2m-1}{(2m-1)^2 - \frac{1}{4}} \right) \left( 2m-1 \right) \left[ 2m + \frac{1}{2} \right] \left( 2m-1 \right)^2 - 1 \right] \left[ (2m-1)^2 - \frac{1}{4} \right] \\ &\quad + \frac{2}{3} \frac{\bar{e}_n^2 L_2(\bar{e}_n)}{\kappa_1^2 \coth \kappa_1^2} + \frac{4}{\pi^2} \frac{\left[ \frac{(2m-1, n)}{2m-1} - \phi_{2m-1, n} \right] \eta^{*2}}{\left( (2m-1)^2 - 1 \right) \epsilon_{2m-1, n(1 - \eta^2)}} \left[ \tanh \kappa^* + \frac{2}{\kappa^2} \left( \frac{1}{\cosh(\kappa^2)} - 1 \right) \right] \end{aligned} \right\} + \frac{\frac{2}{\pi^2} \frac{(2f_n - e_n) \tanh(\kappa^2)}{\kappa_1^2 (1 - \eta^2)} \left[ \tanh(\kappa^2) + \frac{2}{\kappa^2} \left( \frac{1}{\cosh(\kappa^2)} - 1 \right) \right] \left[ L_0(\bar{e}_n) + \frac{1}{2} L_0 d(\bar{e}_n) \right]}{2 \left( (2m-1)^2 - \frac{1}{4} \right) (\kappa^2) \cosh(\kappa^2)} \\ M_z &= M_F \Omega^2 \omega_0^2 i R \left\{ \begin{aligned} &\frac{1}{2} - \frac{4}{\pi^2} \frac{1}{4m^2(2m-1)^2 - 1} \epsilon_{2m-1, n(1 - \eta^2)} \\ &\quad + \frac{8}{\pi^2} \frac{(2f_n - e_n) \tanh(\kappa^2) L_0(\bar{e}_n) \eta^{*2}}{\kappa_1^2 (1 - \eta^2)} \cdot \frac{16}{\pi^2} \frac{\left[ \frac{1}{2m-1} f_{2m-1, n} \epsilon_{2m-1, n} \eta^{*2} \tanh(\kappa^2) \right]}{\left( (2m-1)^2 - 1 \right) (\kappa^2) (1 - \eta^2)} \end{aligned} \right\} \end{aligned} \right\} \end{math> $	<p><b>Roll Excitation</b></p> $\phi(t) = \Phi_0 e^{i\Omega t}$ $\eta^* = \epsilon_{2m-1, n} \frac{h}{a}$ $\kappa^* = \epsilon_{2m-1, n} \frac{\pi}{a}$ $\sigma = \epsilon \min \frac{\pi}{a}$ $\eta = \frac{\Omega}{\omega_{mn}}$ $\eta_1^* = \bar{e}_{2m-1, n} \frac{\pi}{a}$ $\kappa_1^* = \bar{e}_{2m-1, n} \frac{\pi}{a}$ <p><b>Note</b></p> $\eta^* = \epsilon_{2m-1, n} \frac{h}{a}$ $\kappa^* = \epsilon_{2m-1, n} \frac{\pi}{a}$ $\sigma = \epsilon \min \frac{\pi}{a}$ $\eta = \frac{\Omega}{\omega_{mn}}$ $\eta_1^* = \bar{e}_{2m-1, n} \frac{\pi}{a}$ $\kappa_1^* = \bar{e}_{2m-1, n} \frac{\pi}{a}$ <p>See appropriate article for definitions of <math>L_0</math>, <math>L_1</math>, <math>L_2</math>.</p>
---	---

## APPENDIX D.—Circular Cylindrical Sector Tank

[Ref. 2.3]

$\bullet = \left\{ \begin{matrix} \text{Re}_0 \\ \text{Im}_0 \end{matrix} \right\} e^{i\theta} \left[ \begin{matrix} r \cos \phi \\ r \sin \phi \end{matrix} \right] + \frac{b_{mn} \eta^2}{(1 - \eta^2)} \left[ \begin{matrix} a_m \\ c_m \end{matrix} \right] \cos(\bar{\kappa}t) \frac{\cosh(\bar{\kappa}z)}{\cosh \bar{\kappa}} J(\sigma)$	$F_x = M_F \Omega^2 e^{i\theta} \left[ \begin{matrix} x_0 \\ y_0 \end{matrix} \right] \left[ 0 + \frac{2 \sin \bar{\alpha}}{\bar{\alpha}a} \frac{b_{mn} \eta^2}{(1 - \eta^2)} \left\{ \begin{matrix} a_m \\ c_m \end{matrix} \right\} (-1)^{m+1} \frac{\tanh \bar{\kappa}}{\bar{\kappa}} \left[ \frac{\bar{\alpha}^2}{(r^2 m^2 - \bar{\alpha}^2)} J(\epsilon_{mn}) + L_o(\epsilon_{mn}) \right] \right]$
$F_y = M_F \Omega^2 e^{i\theta} \left[ \begin{matrix} x_0 \\ y_0 \end{matrix} \right] \left[ 0 - \frac{2}{\bar{\alpha}a} \frac{b_{mn} \eta^2}{(1 - \eta^2)} \left\{ \begin{matrix} a_m \\ c_m \end{matrix} \right\} (1 - (-1)^m \cos \bar{\alpha}) \frac{\tanh \bar{\kappa}}{\bar{\kappa}} \left[ \frac{\bar{\alpha}^2}{(r^2 m^2 - \bar{\alpha}^2)} J(\epsilon_{mn}) + L_o(\epsilon_{mn}) \right] \right]$	$M_x = -M_F \Omega^2 e^{i\theta} \left[ \begin{matrix} x_0 \\ y_0 \end{matrix} \right] \left[ \left\{ \begin{matrix} \frac{1}{4h/a} & \frac{2\pi \ln^2 \bar{\alpha}}{\bar{\alpha}} \\ \frac{1}{4h/a} & \left( 1 - \frac{\sin \bar{\alpha} \cos \bar{\alpha}}{\bar{\alpha}} \right) \end{matrix} \right\} (1 - (-1)^m \cos \bar{\alpha}) \left\{ \begin{matrix} \frac{\bar{\alpha}^2}{(r^2 m^2 - \bar{\alpha}^2)} J(\epsilon_{mn}) + L_o(\epsilon_{mn}) \left[ \tanh \bar{\kappa} + \frac{2}{\bar{\kappa}} \left( \frac{1}{\cosh \bar{\kappa}} - 1 \right) \right] \right\} \right]$
$M_y = M_F \Omega^2 e^{i\theta} \left[ \begin{matrix} x_0 \\ y_0 \end{matrix} \right] \left[ \left\{ \begin{matrix} \frac{4}{h/a} & \left( 1 + \frac{\sin \bar{\alpha} \cos \bar{\alpha}}{\bar{\alpha}} \right) \\ \frac{4}{h/a} & \frac{\sin^2 \bar{\alpha}}{\bar{\alpha}} \end{matrix} \right\} + \frac{\sin \bar{\alpha}}{\bar{\alpha}a} \frac{(-1)^{m+1}}{(1 - \eta^2)} \frac{b_{mn} \eta^2}{c_m} \left\{ \begin{matrix} a_m \\ c_m \end{matrix} \right\} \left\{ \begin{matrix} \frac{\bar{\alpha}^2}{(r^2 m^2 - \bar{\alpha}^2)} J(\epsilon_{mn}) + L_o(\epsilon_{mn}) \\ \tanh \bar{\kappa} + \frac{2}{\bar{\kappa}} \left( \frac{1}{\cosh \bar{\kappa}} - 1 \right) \end{matrix} \right\} \right]$	$M_y = M_F \Omega^2 e^{i\theta} \left[ \begin{matrix} x_0 \\ y_0 \end{matrix} \right] \left[ \left\{ \begin{matrix} \frac{4}{h/a} & \left( 1 + \frac{\sin \bar{\alpha} \cos \bar{\alpha}}{\bar{\alpha}} \right) \\ \frac{4}{h/a} & \frac{\sin^2 \bar{\alpha}}{\bar{\alpha}} \end{matrix} \right\} + \frac{\sin \bar{\alpha}}{\bar{\alpha}a} \frac{(-1)^{m+1}}{(1 - \eta^2)} \frac{b_{mn} \eta^2}{c_m} \left\{ \begin{matrix} a_m \\ c_m \end{matrix} \right\} \left\{ \begin{matrix} \frac{\bar{\alpha}^2}{(r^2 m^2 - \bar{\alpha}^2)} J(\epsilon_{mn}) + L_o(\epsilon_{mn}) \\ \tanh \bar{\kappa} + \frac{2}{\bar{\kappa}} \left( \frac{1}{\cosh \bar{\kappa}} - 1 \right) \end{matrix} \right\} \right]$
$F_x = -M_F \Omega^2 e^{i\theta} \left[ \begin{matrix} x_0 \\ y_0 \end{matrix} \right] \left[ \left\{ \begin{matrix} \frac{2\pi \zeta_{mn}}{(r^2 m^2 - \bar{\alpha}^2)} & \frac{L_o(\epsilon_{mn})}{\cosh \bar{\kappa}} \\ \frac{2\pi \zeta_{mn}}{(r^2 m^2 - \bar{\alpha}^2)} & \frac{L_o(\epsilon_{mn})}{\cosh \bar{\kappa}} \end{matrix} \right\} - 2M_F \bar{s} \frac{\bar{s}}{3} \frac{(1 - \cos \bar{\alpha})}{\bar{\alpha}} \right]$	$F_y = -M_F \Omega^2 e^{i\theta} \left[ \begin{matrix} x_0 \\ y_0 \end{matrix} \right] \left[ \left\{ \begin{matrix} \frac{2\pi \zeta_{mn}}{(r^2 m^2 - \bar{\alpha}^2)} & \frac{L_o(\epsilon_{mn})}{\cosh \bar{\kappa}} \\ \frac{2\pi \zeta_{mn}}{(r^2 m^2 - \bar{\alpha}^2)} & \frac{L_o(\epsilon_{mn})}{\cosh \bar{\kappa}} \end{matrix} \right\} + 2M_F \bar{s} \frac{\bar{s}}{3} \frac{\sin \bar{\alpha}}{\bar{\alpha}} \right]$
$\bullet = (r, \phi, z, t) = - \left\{ \begin{matrix} \text{Re}_0 \\ \text{Im}_0 \end{matrix} \right\} e^{i\theta} \left[ \begin{matrix} r \cos \phi \\ r \sin \phi \end{matrix} \right] - \left\{ \begin{matrix} A_{mn} \cosh(\bar{\kappa}z) \\ B_{mn} \sinh(\bar{\kappa}z) \end{matrix} \right\} \cos \bar{\kappa} J(\sigma)$	$F_x = -M_F \Omega^2 \left\{ \begin{matrix} \theta_0 e^{i\theta} \\ 0 \end{matrix} \right\} + M_F \Omega^2 e^{i\theta} \left[ \begin{matrix} \theta_0 \\ x_0 \end{matrix} \right] \frac{4 \sinh \left( \frac{\bar{\kappa}}{2} \right) (-1)^{m+1} A_{mn} \sin \bar{\alpha}}{\kappa \bar{\alpha} a} \left[ \frac{\bar{\alpha}^2}{(r^2 m^2 - \bar{\alpha}^2)} J(\epsilon_{mn}) + L_o(\epsilon_{mn}) \right]$
$F_y = -M_F \Omega^2 \left\{ \begin{matrix} \theta_0 e^{i\theta} \\ x_0 \end{matrix} \right\} - M_F \Omega^2 e^{i\theta} \left[ \begin{matrix} \theta_0 \\ x_0 \end{matrix} \right] \frac{4 \sinh \left( \frac{\bar{\kappa}}{2} \right) A_{mn}}{\kappa \bar{\alpha} a} \left[ (1 - (-1)^m \cos \bar{\alpha}) \left[ \frac{\bar{\alpha}^2}{(r^2 m^2 - \bar{\alpha}^2)} J(\epsilon_{mn}) + L_o(\epsilon_{mn}) \right] \right]$	$M_x = \frac{M_F \left( \frac{h}{a} \right) \Omega^2 a^2}{(4h/a)} \left\{ \begin{matrix} \theta_0 \\ x_0 \end{matrix} \right\} \left[ \begin{matrix} \frac{1}{\bar{\alpha}} \frac{\sin^2 \bar{\alpha}}{\bar{\alpha}} \\ \frac{1}{\bar{\alpha}} \left( 1 - \frac{\sin \bar{\alpha} \cos \bar{\alpha}}{\bar{\alpha}} \right) \end{matrix} \right] - M_F \Omega^2 e^{i\theta} \left[ \begin{matrix} \theta_0 \\ x_0 \end{matrix} \right] \left[ \begin{matrix} \frac{1}{\bar{\alpha}} \frac{\sin^2 \bar{\alpha}}{\bar{\alpha}} \\ \frac{1}{\bar{\alpha}} \left( 1 - \frac{\sin \bar{\alpha} \cos \bar{\alpha}}{\bar{\alpha}} \right) \end{matrix} \right] - \frac{2(1 - (-1)^m \cos \bar{\alpha})}{a^2 \bar{\alpha} m n} \left[ B_{mn} \left\{ \cosh \left( \frac{\bar{\kappa}}{2} \right) - \frac{2}{\bar{\kappa}} \sinh \left( \frac{\bar{\kappa}}{2} \right) \right\} \right] \left\{ \frac{\bar{\alpha}^2}{(r^2 m^2 - \bar{\alpha}^2)} J(\epsilon_{mn}) \right\}$
$M_y = - \frac{M_F \left( \frac{h}{a} \right) \Omega^2 a^2}{(4h/a)} \left\{ \begin{matrix} \theta_0 \\ x_0 \end{matrix} \right\} + L_o(\epsilon_{mn}) \left[ \begin{matrix} \bar{\alpha}^2 L_o(\epsilon_{mn}) k^2 m n \\ \kappa (r^2 m^2 - \bar{\alpha}^2) \end{matrix} \right] + M_F \Omega^2 2\eta^2 e^{i\theta} \left[ \begin{matrix} \theta_0 \\ x_0 \end{matrix} \right] \left[ \begin{matrix} \frac{1}{8} \left( 1 + \frac{\sin \bar{\alpha} \cos \bar{\alpha}}{\bar{\alpha}} \right) - \frac{1}{12} \left( \frac{h}{a} \right)^2 \\ \frac{1}{8} \sin^2 \bar{\alpha} \end{matrix} \right] + \frac{2(-1)^{m+1}}{a^2 \bar{\alpha} m n} \sin \bar{\alpha} \left[ B_{mn} \left\{ \cosh \left( \frac{\bar{\kappa}}{2} \right) - \frac{2}{\bar{\kappa}} \sinh \left( \frac{\bar{\kappa}}{2} \right) \right\} \right] \left\{ \frac{\bar{\alpha}^2}{(r^2 m^2 - \bar{\alpha}^2)} J(\epsilon_{mn}) \right\}$	$+ L_o(\epsilon_{mn}) \left[ \begin{matrix} \bar{\alpha}^2 L_o(\epsilon_{mn}) k^2 m n \\ \kappa (r^2 m^2 - \bar{\alpha}^2) \end{matrix} \right] + 2M_F \bar{s} \frac{\bar{s}}{3} \frac{\sin \bar{\alpha}}{\bar{\alpha}}$

Excitation  
About Y Axis  
 $\theta(t) = \theta_0 e^{i\theta}$   
and X Axis  
 $x(t) = x_0 e^{i\theta}$

$\Psi(r, \phi, z, t) = M_F \epsilon_0 e^{i\Omega_a t} \left\{ \frac{r^2}{a^2} (\phi - \eta a) + \frac{8\bar{a}^2}{\pi} \frac{\cos \bar{\phi}}{(2m-1)(2n-1)(2\bar{a}^2 - 4\bar{a}^2)} \left[ \left( \frac{r}{a} \right)^2 - \frac{4a}{(2m-1)} \left( \frac{r}{a} \right)^2 \right] + \frac{4\bar{a}}{(2m-1)^2 \pi^2 - 4\bar{a}^2} \frac{\cosh(\zeta \phi + \kappa \theta) \cos \phi}{(1 - n^2) \cosh \kappa \theta} \right\}$ $\left\{ \begin{array}{l} F_x \\ F_y \end{array} \right\} = M_F r^2 \epsilon_0 \Omega^2 k_a^2 \left[ \begin{array}{l} \frac{2 \cos \bar{\phi}}{\bar{a}} - 2 + \frac{2}{3} \sin \bar{\phi} \\ \frac{2 \sin \bar{\phi}}{\bar{a}} - \frac{2}{3} (1 + \cos \bar{\phi}) \end{array} \right] - \frac{16\bar{a} \sin \bar{\phi}}{\pi} \left\{ \begin{array}{l} 2a/(2m+2n-1) - 4a/(2m-1) \\ (2m-1)(2m-1)^2 \bar{a}^2 - \bar{a}^2 \end{array} \right\} + \frac{(2m-1)^2 (2m-1)^2 \bar{a}^2}{(2m-1)^2 (2m-1)^2 \bar{a}^2 - \bar{a}^2} \left[ (2m-1) + 4a \right] \right\} * \frac{8 \sin \bar{\phi}}{(n/a)}$ $\left[ \frac{4a}{(2m-1)} f_{2m-1, n} e^{2m-1, n} \tanh \kappa \theta \eta^2 \left[ \frac{8\bar{a}^2}{\pi} f_{2m-1, n} (\epsilon_{2m-1, n}^2 - 4\bar{a}^2) \right] + L_d (\epsilon_{2m-1, n}) \right]$ $\epsilon_{2m-1, n} \left[ (2m-1)^2 \bar{a}^2 - 4\bar{a}^2 \right] (1 - \eta^2)$ $\left[ \frac{1}{5h/a} \left[ 1 + \cos \bar{\phi} - \frac{2 \sin \bar{\phi}}{\bar{a}} \right] \right] + \frac{48\bar{a}^2}{5\pi^2 (h/a)} \frac{\bar{a}^2 \sin \bar{\phi} ((2m-1) - 4a)}{(2m-1)^2 \bar{a}^2 - \bar{a}^2} ((2m-1) + 6a) (2m-1)^2$ $\left\{ \begin{array}{l} M_x \\ M_y \end{array} \right\} = M_F r^2 \epsilon_0 \Omega^2 k_a^2 \left[ \begin{array}{l} \frac{1}{5h/a} \left[ 1 + \cos \bar{\phi} - \frac{2 \sin \bar{\phi}}{\bar{a}} \right] \\ \frac{1}{5h/a} \left( \sin \bar{\phi} + \frac{2 \cos \bar{\phi} - 2}{\bar{a}} \right) \end{array} \right] + \frac{48\bar{a}^2}{5\pi^2 (h/a)} \frac{\bar{a}^2 \sin \bar{\phi} ((2m-1) - 4a)}{(2m-1)^2 \bar{a}^2 - \bar{a}^2} ((2m-1) + 6a) (2m-1)^2$ $\left. \begin{array}{l} + \frac{4}{a^2} \left[ \frac{4a}{(2m-1)} f_{2m-1, n} e^{2m-1, n} \right] \sin \bar{\phi} \\ + \frac{-2\bar{a}^2 e_{2m-1, n}^2 f_{2m-1, n}}{(2m-1)^2 \bar{a}^2 - \bar{a}^2} (1 + \cos \bar{\phi}) \end{array} \right] + \left\{ \begin{array}{l} L_d (\epsilon_{2m-1, n}) + \frac{2}{\kappa^2} \left( \frac{1}{\cosh \kappa \theta} - 1 \right) \\ L_d (\epsilon_{2m-1, n}) + \frac{(2m-1)^2 \bar{a}^2 - \bar{a}^2}{(2m-1)^2 \bar{a}^2 - \bar{a}^2} f_{2m-1, n} e^{2m-1, n} \end{array} \right\}$ $M_z = M_F r^2 \epsilon_0 \Omega^2 k_a^2 \left[ \frac{1}{2} - \frac{16\bar{a}^2}{\pi^2} \frac{1}{(2m-1)^2 ((2m-1)\bar{a}^2 + 2a)^2} - 16 \frac{4a}{(2m-1)^2 \pi^2 - 4\bar{a}^2} (1 - \eta^2) \kappa \theta \right]$	<p style="text-align: center;">Roll Excitation <math>\Phi(t) = \Phi_0 e^{i\Omega_a t}</math></p> $L_d(\epsilon_{mn}) = \frac{2}{\epsilon_{mn}} \sum_{\mu=0}^{\infty} J_{2\mu} + \frac{m}{2a} + 1 \quad (\epsilon_{mn} (\operatorname{Re} \frac{m}{2a} > -1))$ $L_1(\epsilon_{2m-1, n}) = \frac{2m-1}{i \cos 2m-1, n} \sum_{\mu=0}^{\infty} \frac{\left( \frac{2m-1}{2a} + 2\mu + 1 \right)}{\left( \frac{2m-1}{4a} + \mu \right) \left( \frac{2m-1}{4a} + \mu + 1 \right)} \frac{J_{2\mu+1}}{4a} + 2\mu + 1 \quad (\epsilon_{2m-1, n})$ $L_2(\epsilon_{mn}) = \frac{\Gamma \left( \frac{m}{4a} + \frac{3}{2} \right)}{\epsilon_{mn} \Gamma \left( \frac{m}{4a} - \frac{1}{2} \right)} \sum_{\mu=0}^{\infty} \frac{\left( \frac{m}{2a} + 2\mu + 1 \right) \Gamma \left( \frac{m}{4a} + \mu + \frac{1}{2} \right)}{\Gamma \left( \frac{m}{4a} + \mu + \frac{5}{2} \right)} J_{2\mu+1} + \epsilon_{mn}$ $\eta^2 = \frac{\Omega}{\omega_{2m-1, n}} \quad ; \quad \epsilon \Phi = \epsilon_{2m-1, n} \frac{z}{a} \quad ; \quad \kappa \Phi = \kappa_{2m-1, n} \frac{h}{a} \quad ; \quad \sigma \Phi = \sigma_{2m-1, n} \frac{h}{a}$ <p style="text-align: center;">Notes</p>
--	---

**APPENDIX E.—Oscillations Resulting From Bending-Type Displacements in Circular Sector Tank  $x(z, t) = x_0(z)e^{i\omega t}$** 

[The notation used is defined in section, "Bending Type Oscillations"; see appendix D for definitions of  $L_0$  and  $L_1$ ; ref. 2.3]

$$\begin{aligned} \delta &= \frac{\Omega^2 \sin \alpha}{g} \left[ \begin{cases} r x_0(0) \cos \phi \\ r y_0(0) \sin \phi \end{cases} \right] + \sum_{m=0}^{\infty} \sum_{n=0}^{\infty} A_{mn}(0) J \frac{m}{2a} \left( \epsilon_{mn} \frac{\pi}{a} \right) \cos \left( \frac{m}{2a} \phi \right) \\ F_x &= M_F \Omega^2 e^{i\Omega t} \left[ \frac{1}{h} \int_{-h}^0 \left\{ \begin{array}{l} x_0(z) \\ 0 \end{array} \right\} dz + \sum_{n=1}^{\infty} \sum_{m=0}^{\infty} (-1)^{m+1} \frac{\sin 2\pi n}{i\Omega n a h} \left[ \frac{-4a^2}{(m^2 - 4a^2)} J \frac{m}{2a} (\epsilon_{mn}) + L_0(\epsilon_{mn}) \right] \int_{-h}^0 A_{mn}(z) dz \right] \\ F_y &= M_F \Omega^2 e^{i\Omega t} \left[ \frac{1}{h} \int_{-h}^0 \left\{ \begin{array}{l} 0 \\ y_0(z) \end{array} \right\} dz + \sum_{n=1}^{\infty} \sum_{m=0}^{\infty} \frac{(-1)^m \cos 2\pi n - 1}{i\Omega n a} \left[ \frac{1}{h} \int_{-h}^0 A_{mn}(z) dz \left[ \frac{4a^2}{(m^2 - 4a^2)} J \frac{m}{2a} (\epsilon_{mn}) + L_0(\epsilon_{mn}) \right] \right] \right] \\ M_x &= -M_F \Omega^2 e^{i\Omega t} \left[ \frac{x d(-h)a^2}{4h} \frac{\sin^2 2\pi a}{2\pi a} \left( 1 - \frac{\sin 2\pi a \cos 2\pi a}{2\pi a} \right) + \frac{1}{h} \int_{-h}^0 \left( \frac{h}{2} + z \right) y_0(z) dz \right] + \sum_{n=1}^{\infty} \sum_{m=0}^{\infty} \frac{(-1)^m \cos 2\pi a - 1}{i\Omega n a h} \left[ \frac{-4a^2 a^2}{(m^2 - 4a^2)} A_{mn}(-h) L_2(\epsilon_{mn}) + \left( \frac{4a^2}{(m^2 - 4a^2)} J \frac{m}{2a} \right) A_{mn}(-h) \right. \\ &\quad \left. + L_0(\epsilon_{mn}) \int_{-h}^0 \left( \frac{h}{2} + z \right) A_{mn}(z) dz \right] - M_F g \frac{a}{3} \frac{[1 - \cos 2\pi a]}{\pi a} \\ M_y &= M_F \Omega^2 e^{i\Omega t} \left[ \begin{cases} -\frac{1}{h} \int_{-h}^0 \left( \frac{h}{2} + z \right) x_0(z) dz + \frac{x d(-h)a^2}{4h} \left( 1 + \frac{\sin 2\pi a \cos 2\pi a}{2\pi a} \right) \\ 0 + \frac{y d(-h)a^2}{4h} \frac{\sin 2\pi a}{2\pi a} \end{cases} \right] + \sum_{n=1}^{\infty} \sum_{m=0}^{\infty} \frac{(-1)^{m+1} \sin 2\pi n}{i\Omega n a h} \left( \frac{4a^2 a^2 L_2(\epsilon_{mn})}{(m^2 - 4a^2)} A_{mn}(-h) + \left[ \frac{4a^2}{(m^2 - 4a^2)} J \frac{m}{2a} \right] A_{mn}(-h) \right. \\ &\quad \left. + L_0(\epsilon_{mn}) \int_{-h}^0 \left( \frac{h}{2} + z \right) A_{mn}(z) dz \right) + M_F g \frac{a}{3} \frac{\sin 2\pi a}{\pi a} \end{aligned}$$

**Notes:** (1) The notation used is defined in Section 2.31, "Bending Type Oscillations."

(2) See Table 2.6 for definitions of  $L_0$  and  $L_1$ .

## APPENDIX F.—Circular Cylindrical Tank

 $\{\gamma = 0.5772157 \text{ is the Euler number; ref. 23}\}$ 

$\delta = \frac{\Omega^2}{g/a} x_0 e^{i\Omega t} \cos \phi \left\{ \frac{r}{a} + 2 \frac{J_1(\epsilon_n \frac{r}{a})}{(\epsilon_n^2 - 1) J_1(\epsilon_n) \left( \frac{\omega_n}{\Omega^2} - 1 \right)} \right\}$ $F_x = M_F \Omega^2 x_0 e^{i\Omega t} \left\{ 1 + 2 \frac{\tanh \epsilon_n \frac{h}{a}}{\epsilon_n \frac{h}{a} (\epsilon_n^2 - 1) \left( \frac{\omega_n}{\Omega^2} - 1 \right)} \right\}$ $M_y = M_F \Omega^2 z_0 e^{i\Omega t} \left\{ \frac{1}{4h/a} + 2 \frac{\frac{1}{\epsilon_n h} \left( \frac{2}{\cosh \epsilon_n \frac{h}{a}} - 1 \right) + \frac{1}{2} \tanh \epsilon_n \frac{h}{a}}{\epsilon_n (\epsilon_n^2 - 1) \left( \frac{\omega_n}{\Omega^2} - 1 \right)} \right\}$	$\delta = -\Omega^2 z_0 \theta_0 e^{i\Omega t} \cos \phi \left\{ \frac{1}{2} \frac{h r}{a^2} + 2 \frac{J_1(\epsilon_n \frac{r}{a})}{(\epsilon_n^2 - 1) J_1(\epsilon_n) \left( \frac{\omega_n}{\Omega^2} - 1 \right)} \left[ \frac{2}{\Omega^2 \cosh \epsilon_n \frac{h}{a}} + \frac{1}{2} \frac{h}{a} - \frac{1}{\Omega^2} \right] \right\}$ $F_x = -M_F g f_0 e^{i\Omega t} - 2M_F \Omega^2 \theta_0 e^{i\Omega t} \frac{\frac{2}{\epsilon_n h} \left( \frac{1}{\cosh \epsilon_n \frac{h}{a}} - 1 \right) + \left( \frac{\gamma}{\epsilon_n h} + \frac{1}{2} \right) \tanh \epsilon_n \frac{h}{a}}{\epsilon_n (\epsilon_n^2 - 1) \left( \frac{\omega_n}{\Omega^2} - 1 \right)}$ $M_y = -\frac{M_F g a \theta_0 e^{i\Omega t}}{4h/a} - M_F \Omega^2 a^2 \theta_0 e^{i\Omega t} \left\{ \frac{1}{12} \left( \frac{h}{a} \right)^2 - \frac{1}{8} + \frac{2}{\epsilon_n (\epsilon_n^2 - 1) \left( \frac{\omega_n}{\Omega^2} - 1 \right)} \left[ \left( 2 - \frac{4\gamma}{\epsilon_n a} \right) \frac{1}{\epsilon_n \cosh \epsilon_n \frac{h}{a}} + \frac{1}{\epsilon_n} \left( \frac{5\gamma}{\epsilon_n h} + \frac{1}{2} \right) + \frac{1}{\epsilon_n} \left( \frac{\epsilon_n a}{4} - \frac{3\gamma}{2} \right) \tanh \epsilon_n \frac{h}{a} \right] \right\}$
--	---

 $\gamma = .5772157 \text{ is the Euler number.}$

**APPENDIX G.—Oscillations Resulting From Bending-Type Displacements in Circular Cylindrical Tank  $x(z, t) = x_0(z)e^{i\omega t}$**

[Ref. 2.31]

$$\begin{aligned}
 \eta(r, \phi, z, t) &= \Omega^2 e^{i\omega t} x_0(z) \cos \left\{ \frac{r}{a} x_0'(z) + 2 \sum_{n=1}^{\infty} \frac{j_1(\epsilon_n \frac{r}{a}) \eta^2}{(r^2 - 1) J_1(\epsilon_n h)} \left[ \sinh \left( \epsilon_n \frac{z}{a} \right) + \frac{\epsilon_n \Omega^2}{a^2} \cosh \left( \epsilon_n \frac{z}{a} \right) (1 - \eta^2) \right] \right\} \\
 &\quad + \cosh \left[ \frac{\epsilon_n}{a} (z + h) \right] \left( \int_z^0 x_0''(z) \left[ \sinh \left( \epsilon_n \frac{z}{a} \right) + \frac{\epsilon_n \Omega^2}{a^2} \cosh \left( \epsilon_n \frac{z}{a} \right) \right] dz + \frac{\epsilon_n}{a} \left[ x_0'(0) - \frac{\Omega^2}{a^2} x_0''(0) \right] \right) \Bigg\} \\
 b &= \frac{\Omega^2 \cos \phi e^{i\omega t}}{8} \left\{ \frac{r}{a} x_0'(0) + 2 \sum_{n=1}^{\infty} \frac{j_1(\epsilon_n \frac{r}{a}) \eta^2}{(r^2 - 1) J_1(\epsilon_n) \left( \frac{\epsilon_n}{a} \right) \cosh \left( \epsilon_n \frac{h}{a} \right) (1 - \eta^2)} \left[ \frac{\epsilon_n \Omega^2}{a^2} \left( x_0'(h) + \int_h^0 x_0''(z) \cosh \left[ \frac{\epsilon_n}{a} (z + h) \right] dz \right) + \frac{\epsilon_n}{a} \cosh \left( \frac{\epsilon_n h}{a} \right) \left[ x_0'(0) - \frac{\Omega^2}{a^2} x_0''(0) \right] \right] \right\} \\
 F_x &= M_p \Omega^2 e^{i\omega t} \left\{ \frac{1}{h} \int_{-h}^0 x_0'(z) dz + 2 \sum_{n=1}^{\infty} \frac{n^2}{(\epsilon_n^2 - 1) \left( \epsilon_n \frac{h}{a} \right) \cosh \left( \epsilon_n \frac{h}{a} \right) (1 - \eta^2)} \left[ x_0'(h) \left( \frac{a}{\epsilon_n} [1 - \cosh \left( \frac{\epsilon_n h}{a} \right)] \right) + \frac{\Omega^2}{a^2} \sinh \left( \frac{\epsilon_n h}{a} \right) + \int_{-h}^0 \left( \sinh \left( \frac{\epsilon_n z}{a} \right) + \frac{\epsilon_n \Omega^2}{a^2} \cosh \left( \frac{\epsilon_n z}{a} \right) \right) dz \right] \right. \\
 &\quad \left. + \left[ x_0'(0) - \frac{\Omega^2}{a^2} x_0''(0) \right] \sinh \left( \frac{\epsilon_n h}{a} \right) + \int_{-h}^0 \cosh \left[ \frac{\epsilon_n}{a} (z + h) \right] \int_z^0 x_0''(z) \left[ \sinh \left( \frac{\epsilon_n}{a} z \right) + \frac{\epsilon_n \Omega^2}{a^2} \cosh \left( \frac{\epsilon_n}{a} z \right) \right] dz dz \right\} \\
 F_y &= 0 \quad M_x = 0 \\
 M_y &= M_p \frac{2\epsilon_n^2 \Omega^2}{a^2} e^{i\omega t} \left\{ \frac{x_0'(h)}{4h} + \frac{1}{a^2} \int_{-h}^0 \left( \frac{1}{2} + \frac{z}{h} \right) x_0(z) dz + 2 \sum_{n=1}^{\infty} \frac{\eta^2}{(\epsilon_n^2 - 1) \left( \epsilon_n^2 - 1 \right)} \left[ x_0'(h) \left( 1 - \eta^2 \right) \right] \right. \\
 &\quad \left. + \frac{\Omega^2}{\epsilon_n^2 - 1} \int_{-h}^0 x_0''(z) \sinh \left( \frac{\epsilon_n}{a} z \right) dz + \frac{\Omega^2}{\epsilon_n^2} \int_{-h}^0 x_0''(z) \cosh \left( \frac{\epsilon_n}{a} z \right) dz + \frac{h}{2} \int_{-h}^0 \left[ \sinh \left( \frac{\epsilon_n}{a} z \right) \int_z^0 x_0''(t) \cosh \left[ \frac{\epsilon_n}{a} (t + h) \right] dt \right] dz + \frac{\epsilon_n \Omega^2}{2a^2} \int_{-h}^0 \left[ \cosh \left( \frac{\epsilon_n}{a} z \right) \int_z^0 x_0''(t) \cosh \left[ \frac{\epsilon_n}{a} (t + h) \right] dt \right] dz \right. \\
 &\quad \left. + \frac{h}{2} \int_{-h}^0 \left[ \cosh \left[ \frac{\epsilon_n}{a} (z + h) \right] \int_z^0 x_0''(t) \sinh \left( \frac{\epsilon_n}{a} t \right) dt \right] dz + \frac{\epsilon_n \Omega^2}{2a^2} \int_{-h}^0 \left[ \cosh \left[ \frac{\epsilon_n}{a} (z + h) \right] \int_z^0 x_0''(t) \cosh \left( \frac{\epsilon_n}{a} t \right) dt \right] dz + \int_{-h}^0 \left[ z \sinh \left( \frac{\epsilon_n}{a} z \right) \int_z^0 x_0''(t) \cosh \left[ \frac{\epsilon_n}{a} (t + h) \right] dt \right] dz \right. \\
 &\quad \left. + \frac{\epsilon_n \Omega^2}{a^2} \int_{-h}^0 \left[ z \cosh \left( \frac{\epsilon_n}{a} z \right) \int_z^0 x_0''(t) \cosh \left[ \frac{\epsilon_n}{a} (t + h) \right] dt \right] dz + \int_{-h}^0 \left[ z \cosh \left[ \frac{\epsilon_n}{a} (z + h) \right] \int_z^0 x_0''(t) \sinh \left( \frac{\epsilon_n}{a} t \right) dt \right] dz + \frac{\epsilon_n \Omega^2}{a^2} \int_{-h}^0 \left[ z \cosh \left[ \frac{\epsilon_n}{a} (z + h) \right] \int_z^0 x_0''(t) \cosh \left[ \frac{\epsilon_n}{a} t \right] dt \right] dz \right. \\
 &\quad \left. - \left( x_0'(0) - \frac{\Omega^2 x_0''(0)}{a^2} \right) \frac{\cosh \left( \frac{\epsilon_n}{a} h \right)}{\frac{\epsilon_n}{a}} - \frac{2a}{\epsilon_n} \cdot \frac{h}{2} \sinh \left( \frac{\epsilon_n}{a} h \right) \right\}
 \end{aligned}$$

## Nonlinear Effects in Lateral Sloshing

*H. Norman Abramson, Wen-Hwa Chu, and Franklin T. Dodge*

### 3.1 INTRODUCTION

The preceding chapter presented the basic background of technology associated with lateral sloshing in rocket propellant tanks, as derived and obtained from linearized hydrodynamic theory. It should be readily apparent, however, that in actuality nonlinear effects will be present and will even, at times, govern the character of the liquid motions (fig. 3.1). Such nonlinear effects might be described in terms of three classes: (a) those which arise primarily as a consequence of the geometry of the container and are apparent even for rather small amplitudes of excitation and liquid response, (b) those which arise primarily as a consequence of large amplitude excitation and response, and (c) those which involve essentially different forms of liquid behavior produced by coupling or instabilities of various of the lateral sloshing modes. On the other hand, nonlinearities produced by the introduction of large damping into the system, as by baffles or other mechanical devices, are not included within the present discussion but will be treated in the following chapter. The nonlinear aspects of liquid motions resulting from excitation normal to the liquid free surface are, of course, also not included within the present discussion but will be treated in detail in chapter 8.

### 3.2 NONLINEAR EFFECTS ARISING FROM TANK GEOMETRY

#### Compartmented Cylindrical Tanks

The theory of lateral sloshing in circular cylindrical compartmented tanks, as outlined in chapter 2, was developed in rather straightforward fashion from the linearized hydrodynamic equations. The earliest experimental

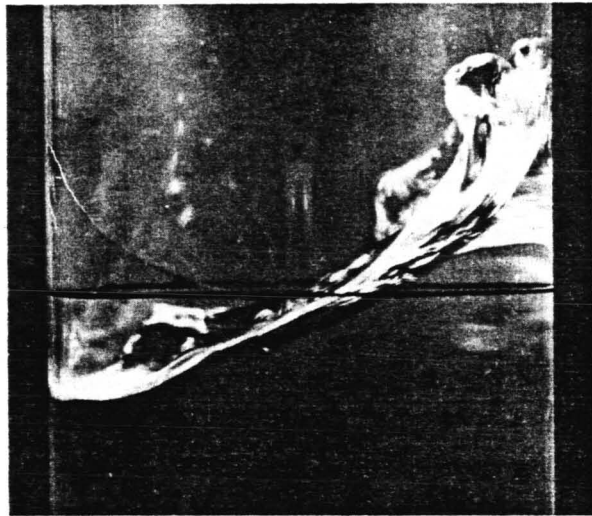


FIGURE 3.1.—Large amplitude breaking wave during lateral sloshing near first-mode resonance.

studies, however, failed to yield very good agreement between measured and predicted liquid frequencies (ref. 3.1), the measured frequencies always being somewhat low. Later measurements revealed (refs. 3.2 and 3.3) the strong dependence of the liquid frequencies on excitation amplitude and indicated agreement with the theoretical values for vanishingly small excitation amplitudes. This general effect is shown in figure 3.2 for 45°, 60°, and 90° sector configurations, the direction of excitation in each case being a bisector of one of the compartments.

Such nonlinear effects, in this instance consisting of a "softening" frequency characteristic, arise essentially from the tank geometry. The continuity of flow toward the center of the tank dictates a higher surface elevation than that of an uncompartmented tank because of

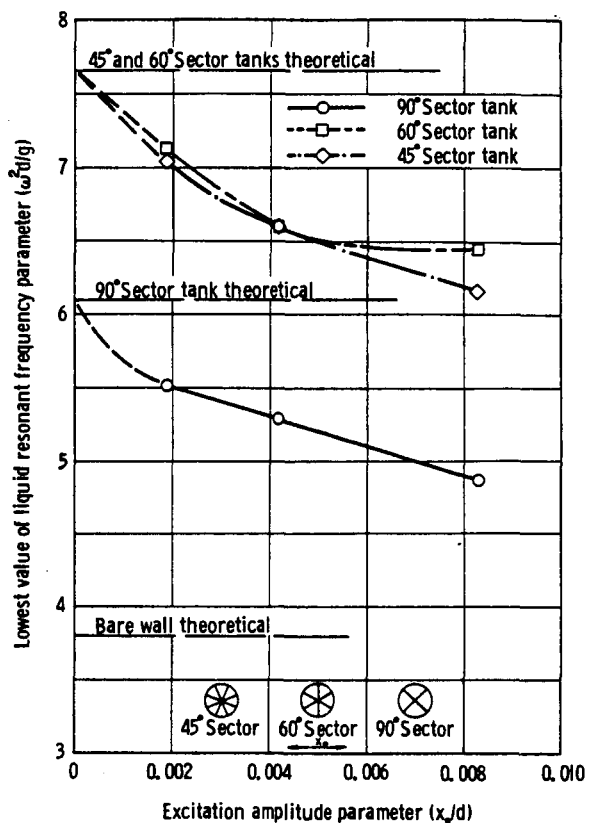


FIGURE 3.2.—Effect of excitation amplitude on the lowest liquid resonant frequency for 45°, 60°, and 90° sector tanks (ref. 3.3).

the decreasing area of the cross section (neglecting variations in radial velocity), and hence a marked change in liquid frequency.

Further, and dramatic, changes in the liquid frequencies take place when the walls of the sectors are perforated. By plotting the lower liquid frequency against an equivalent Reynolds number based upon perforation hole size and excitation amplitude, as in figure 3.3, it is readily apparent that two frequencies are possible for each tank. The higher frequency, corresponding to the lowest values of the equivalent Reynolds number, is essentially as described above for solid sector walls. However, as the equivalent Reynolds number becomes larger, corresponding essentially to increasing perforation hole size, the liquid frequency decreases very rapidly to that corresponding to the uncompartmented tank. The transition zone depends upon a number of factors, but it

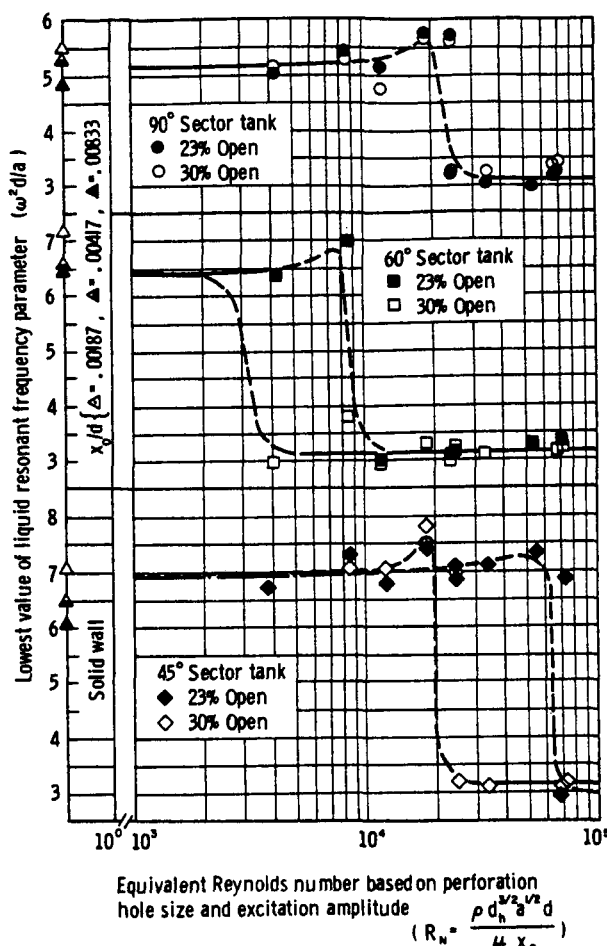


FIGURE 3.3.—Variation in lowest liquid resonant frequency with equivalent Reynolds number for 45°, 60°, and 90° perforated sector tanks (ref. 3.3).

appears that the percent of perforation may be one of the most important of them. In any event, it is immediately apparent that the shift in liquid frequencies provided by compartmentation can easily be negated by overzealous attempts to introduce damping or decrease structural weight by perforation.

The force response in a 90° sector cylindrical tank, as a function of excitation amplitude, is also of considerable interest and has also been explored experimentally (ref. 3.4). The data shown in figure 3.4 were obtained by slowly sweeping frequency with constant excitation amplitude, as is customary when exploring the jump phenomenon in a nonlinear system (refs. 3.5 and 3.6). As we know from the theoretical

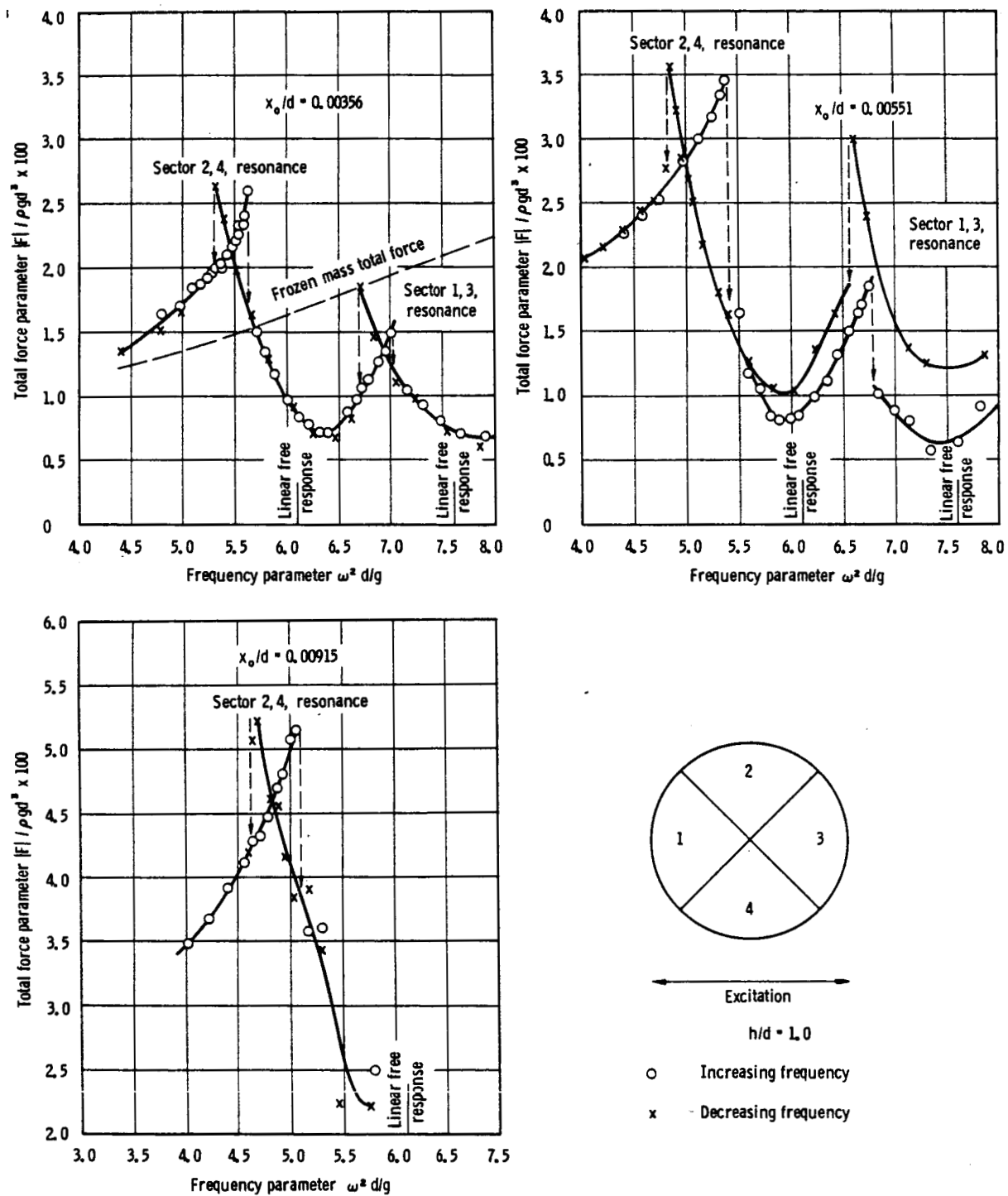


FIGURE 3.4.—Nonlinear liquid force response in 90° sector tank (ref. 3.4).

analysis of chapter 2, sector-compartmented tanks exhibit liquid resonances in sets, corresponding to the orientation of the various

sectors with respect to the direction to the excitation. Thus, the forced response curves should also exhibit resonant peaks in corre-

sponding sets (two peaks for the 90° sector tank), and the nonlinearities already discussed should lead to amplitude jumps near these resonant peaks. Looking at the data of figure 3.4, however, reveals the interesting feature that the double jumps occurring at each resonant peak are both downward (from higher to lower amplitudes). This arises, of course, from the fact that the data represent the total force response of all four sectors, even though only two of these are near resonance, and as a result the customary response picture is somewhat altered. (The nonlinear force response in an uncompartimented circular cylindrical tank will be discussed in detail later in this chapter (sec. 3.3).) Figure 3.4 (upper left plate) also shows the total force response of an equivalent "frozen" liquid mass; in this instance, the phasing of the forces produced by the various sectors at the higher frequencies tends to cancel and produce an even lower total force than does the equivalent frozen mass.

#### Spherical Tanks

Nonlinear effects in spherical tanks have not been investigated to any appreciable extent. However, even a cursory examination of the geometry leads to the conclusion that the strong boundary curvatures will appreciably modify lateral sloshing characteristics: for mean liquid depths less than one radius, the expanding volume would tend to suppress motions of the liquid free surface, while for liquid depths more than one radius the contracting volume could tend to induce breaking waves. The experimental data first available for relatively small excitation amplitudes (ref. 3.7) would tend to substantiate such beliefs, although they are not nearly so evident as in the case of the compartmented cylindrical tank.

Of course, as excitation amplitude is increased, the nonlinear characteristics of the response rapidly become dominant (ref. 3.4). This will be discussed in more detail in section 3.3.

#### Other Tank Configurations

The circular cylindrical tank does not appear to exhibit any particularly significant nonlinear effect in lateral sloshing as a consequence of geometry. Of course, as excitation amplitude

is increased such effects do appear, much as they are emphasized in the spherical tank. A similar statement could therefore probably be made regarding almost any other tank configuration. Basically, however, the fact is that for more unusual geometries (ellipsoidal, toroidal, etc.), experimental investigations up till now have centered about frequency determinations from free vibrations, so that nonlinearities of the type discussed so far in this chapter are not readily discernible. It is clear that the sector tank is somewhat unique in this respect.

Perhaps passing mention should be made of one special case associated with the rectangular tank. A rectangular tank of high aspect ratio, pitching about a transverse axis, and filled with liquid to only a shallow depth possesses strong nonlinear response characteristics for even extremely small excitation amplitudes (i.e., small pitch angles). This arises, obviously, from "piling up" of the liquid at one end of the long tank. At larger angles of excitation, and particularly in the presence of baffles, the response becomes even more strongly nonlinear; traveling waves have even been observed under such conditions (ref. 3.8), but these may be more the product of interference effects.

### 3.3 LARGE AMPLITUDE MOTIONS

#### Basic Equations

Several analytical theories have been developed for large amplitude lateral sloshing in rectangular or circular cylindrical containers. (See, for example, refs. 3.9 through 3.17.) We shall outline various of these in the present section, making such comparisons with experimental data as are available, and begin with a statement of relevant boundary conditions.

The liquid contained in the rocket tank is assumed to be incompressible and its motion irrotational; thus, there is a velocity potential  $\phi$  governed by the Laplace equation

$$\nabla^2 \phi = 0 \quad (3.1)$$

and the following well-known boundary conditions:

- (1) The relative normal velocity on the wetted wall,  $\Sigma$ , is zero; i.e.

$$\frac{\partial \phi}{\partial n} = v_n \quad \text{on } \Sigma \quad (3.2)$$

where  $\frac{\partial \phi}{\partial n}$  is the velocity of the liquid normal to the wall and  $v_n$  is the local normal velocity of the wetted boundaries.

- (2) The free surface at  $z=\xi(x, y)$  is subjected to a dynamic condition on pressure,  $p$ , and a kinematic condition on free surface elevation  $\xi$ . The dynamic condition is

$$p - p_0 = -\rho \left[ \frac{\partial \phi}{\partial t} + g\xi + \frac{1}{2} (\nabla \phi) \cdot (\nabla \phi) \right] = 0 \quad (3.3)$$

where the ullage pressure  $p_0$  is often taken as zero for simplicity. The kinematic condition, in rectangular coordinates, is (on  $z=\xi$ )

$$\frac{\partial \xi}{\partial t} = \frac{\partial \phi}{\partial z} - \frac{\partial \phi}{\partial x} \frac{\partial \xi}{\partial x} - \frac{\partial \phi}{\partial y} \frac{\partial \xi}{\partial y} \quad (3.4)$$

It is noted that the gradient of  $\phi$  yields the positive velocity vector  $\vec{q}$  of the fluid; that is,  $\nabla \phi = \vec{q}$ .

### Moiseyev's General Theory (ref. 3.9)

#### Free Vibrations of the Liquid

Let  $\psi(x, y)$  be a characteristic function (normal mode function). It satisfies the following conditions

$$(1) \quad \nabla^2 \psi = 0 \quad (3.4a)$$

$$(2) \quad \frac{\partial \psi}{\partial n} = 0 \text{ on the wetted wall} \quad (3.4b)$$

$$(3) \quad \frac{\partial \psi}{\partial n} = \lambda \psi \text{ on the free surface} \quad (3.4c)$$

That is,  $\lambda$  and  $\psi$  are the characteristic numbers and functions of the integral equation

$$\psi(x, y, 0) = \lambda \int_s H(x, y, 0; x', y', 0) \psi(x', y', 0) ds \quad (3.5)$$

where  $H$  is the Neumann function (Green's function of the second kind)<sup>1</sup> containing a unit

<sup>1</sup> A method of constructing the Neumann function numerically for a spherical bowl has been demonstrated in ref. 3.18.

sink. Also

$$\psi(x, y, z) = \lambda \int_s H(x, y, z; x', y', 0) \psi(x', y', 0) ds \quad (3.6)$$

so that the  $n$ th characteristic function and number can be computed from

$$\begin{aligned} \left\{ \psi_n(x, y, 0) \right\} &= \lambda_n \int_s \left\{ H(x, y, 0; x', y', 0) \right\} \\ &\quad \times \psi(x', y', 0) ds \end{aligned} \quad (3.7)$$

Let  $\phi_n^{(0)}$ ,  $\xi_n^{(0)}$  be the velocity potential and the free surface elevation of the  $n$ th mode of free vibration of infinitesimally small amplitude; then

$$\xi_n^{(0)} = \psi_n(x, y, 0) \sin(\sigma_n t) \quad (3.8a)$$

$$\phi_n^{(0)} = \frac{\sigma_n}{\lambda_n} \psi_n(x, y, z) \cos(\sigma_n t) \quad (3.8b)$$

The square of the frequency of the  $n$ th free vibration is

$$\sigma_n^2 = g \lambda_n \quad (3.9)$$

The mathematical problem formulated in the beginning of this section has been solved by Moiseyev (ref. 3.9), who used a method of expansion into a power series of an unknown parameter  $\epsilon$ ; i.e.

$$\phi = \epsilon \sum_{n=0}^{\infty} \phi_n \epsilon^n \quad (3.10)$$

$$\xi = \epsilon \sum_{n=0}^{\infty} \xi_n \epsilon^n \quad (3.11)$$

One expects that the period of the free vibration will be affected by the wave amplitude when the amplitude is allowed to have a finite magnitude. Thus, in order to introduce an amplitude dependent period into the theory automatically, it is assumed that the dimensionless time can be expressed as

$$\tau = \frac{t}{1 + \sum h_n \epsilon^n} \sigma_m \quad (3.12)$$

where the  $h_n$  are to be determined. (The liquid motions are assumed to occur in the vicinity of the  $m$ th linear mode.)

The free surface boundary conditions are to be satisfied at  $z=\xi(x, y)$ ; but  $\xi$ , from equation (3.11), is still unknown. In order to satisfy the free surface conditions at  $z=0$ , and thus circumvent this difficulty,  $\phi$  is expanded in a Taylor's series; that is, the  $k$ th term of the potential is written as

$$\phi_k = \sum_{n=1}^{\infty} f_{nk} \psi_n(x, y, z) \quad (3.13)$$

where  $f_{nk}$  are unknown functions of time.

By equating the terms of equal powers of  $\epsilon$  in the dynamic and kinematic free surface conditions, a system of equations can be obtained and then solved in succession. The zeroth approximation [ $n=0$  in equation (3.10)] works out to be

$$\left( \frac{\partial^2 \phi_0}{\partial \tau^2} + \frac{1}{\sigma_m^2} g \frac{\partial \phi_0}{\partial z} \right)_{z=0} = 0 \quad \text{for } k=0 \quad (3.14)$$

It can be shown from equations (3.7) that

$$\left( \frac{\partial \phi_0}{\partial z} \right)_{z=0} = \frac{\sigma_n^2}{g} \psi_n$$

Thus, by substituting equations (3.13) into (3.14a), one finds that

$$f''_{n0} + \frac{\sigma_n^2}{\sigma_m^2} f_{n0} = 0 \quad (3.15)$$

Consequently, if  $\sigma_n/\sigma_m$  is not an integer, the unique solution of equation (3.15) having a period of  $2\pi$  is

$$f_{n0} = 0 \text{ for } n \neq m; f_{m0} = C \cos \tau \quad (3.16)$$

where  $C$  is an arbitrary constant. It is more convenient to write  $C = ag/\sigma_m$  where  $a$  is arbitrary; thus, the zeroth order potential is

$$\phi_0 = \frac{ag}{\sigma_m} \psi_m \cos \tau$$

which is just the potential for free linear vibrations in the  $m$ th mode.

The first approximation ( $n=1$  in eq. (3.10)) is

$$\begin{aligned} \left( \frac{\partial^2 \phi_1}{\partial \tau^2} + \frac{1}{\sigma_m^2} g \frac{\partial \phi_1}{\partial z} \right)_{z=0} &= -\frac{h_1}{\sigma_m} ag \cos \tau \psi_m(x, y, 0) \\ &\quad + a^2 \sin 2\tau F_1^{(2)}(x, y) \end{aligned}$$

for  $k=1$ .  $F_1^{(2)}(x, y)$  is a function only of the zeroth approximation; it may be rewritten in a more convenient form by expanding it in a series of the characteristic functions:

$$F_1^{(2)}(x, y) = \sum b_{n1}^{(2)} \psi_n(x, y, 0)$$

Then the following system of equations arises for the determination of  $f_{n1}$

$$f''_{n1} + \frac{\sigma_n^2}{\sigma_m^2} f_{n1} = a^2 b_{n1}^{(2)} \sin 2\tau \quad (n \neq m)$$

$$f''_{m1} + f_{m1} = -\frac{h_1}{\sigma_m} ag \cos \tau + a^2 b_{m1}^{(2)} \sin 2\tau$$

In order to obtain periodic solutions, it is necessary and sufficient that resonance does not occur, and thus  $h_1=0$ . Hence, it can be seen from equation (3.12) that to the first approximation the period of the vibration does not depend on the amplitude. Also, all the  $f_{n1}$  may be computed from the preceding equation, since all of the  $b_{n1}^{(2)}$  are known; hence, the velocity potential can be determined completely.

By following the same procedure, the  $k$ th approximation is found to be

$$\left( \frac{\partial^2 \phi_k}{\partial \tau^2} + \frac{1}{\sigma_m^2} g \frac{\partial \phi_k}{\partial z} \right)_{z=0} = -\frac{h_k}{\sigma_m} ag \cos \tau \psi_m(x, y, 0)$$

$$+ a^2 \sum_{l=2}^{k+1} F_k^{(l)}(x, y) \sin l\tau \quad l=2, 4, 6, \dots$$

for  $k$  even, and

$$\left( \frac{\partial^2 \phi_k}{\partial \tau^2} + \frac{1}{\sigma_m^2} g \frac{\partial \phi_k}{\partial z} \right)_{z=0} = -\frac{h_k}{\sigma_m} ag \cos \tau \psi_m(x, y, 0)$$

$$+ a^2 \sum_{l=1}^{k+1} F_k^{(l)}(x, y) \cos l\tau \quad l=1, 3, 5, \dots$$

for  $k$  odd. All of the  $F_k^{(l)}$  are known in terms of lower order approximations, but, as before, it is convenient to write them as

$$F_k^{(l)} = \sum_{n=1}^{\infty} b_{nk}^{(l)} \psi_n(x, y, 0)$$

Then, the two equations preceding the  $F_k^{(l)}$  equation reduce to

$$f''_{nk} + \frac{\sigma_n^2}{\sigma_m^2} f_{nk} = a^2 \sum_l b_{nk}^{(l)} \begin{cases} \sin l\tau \\ \cos l\tau \end{cases}, n \neq m$$

$$f''_{mk} + f_{mk} = -\frac{h_k}{\sigma_m} ag \cos \tau + a^2 \sum_l b_{mk}^{(l)} \begin{cases} \sin l\tau \\ \cos l\tau \end{cases}$$

where the sine corresponds to the odd and the cosine to the even values of  $k$ , and at the same time the index  $l$  takes on even or odd values, respectively.

It is necessary and sufficient that resonance does not occur in order to insure that the two preceding equations possess periodic solutions; thus,

$$h_k = 0 \quad \text{for } k \text{ odd}$$

$$h_k = \frac{b_{km}^{(0)} a}{g} \quad \text{for } k \text{ even} \quad (3.17)$$

Using these solutions, the velocity potential and the free surface shape can be easily computed. If  $a$  is set equal to unity, the latter takes the form

$$\zeta = \epsilon \psi_m(x, y, 0) \sin \frac{\sigma_m t}{1 + h_2 \epsilon^2 + \dots} + \epsilon^2 (\dots) + \dots \quad (3.18)$$

Note that the frequency is a function of amplitude; that is,

$$\sigma_m^* = \frac{\sigma_m}{1 + h_2 \epsilon^2 + h_4 \epsilon^4 + \dots} \quad (3.19)$$

and that periodic vibrations with an arbitrary amplitude lying inside the circle of convergence of equation (3.18) are possible.

This theory, as Moiseyev pointed out, has a number of shortcomings. In particular, the procedure is possible only when  $\sigma_n/\sigma_m$  is not an integer for  $n \neq m$ . Also, the amplitude of the wave approaches its limiting value very rapidly and then the wave disintegrates. Thus, it seems that either a linear theory or a theory taking into account the energy dissipation in wave disintegration is needed. Nonetheless, it is impossible to conduct an analysis of resonance phenomena in a liquid with only a linear theory so that a nonlinear theory can be justified on these grounds. In order to determine the liquid response near resonance, it is necessary that the liquid be excited at the proper frequency; the forced response of the fluid must then be calculated. This is done in the next subsection.

#### Forced Vibrations of the Liquid

The potential  $\phi$  for forced vibrations can be constructed by adding a complementary solution  $\phi_c$  to a particular solution  $\phi_p$ , which satisfies the Laplace equation and the boundary condition on the wetted walls.  $\phi_c$  satisfies the Laplace equation and the homogeneous boundary conditions in terms of  $\psi_n$ . The nonlinear free surface conditions are satisfied by the sum of  $\phi_c$  and  $\phi_p$ , and can be put in the following forms

$$\left[ \frac{\partial \phi_c}{\partial t} + g \zeta + \frac{1}{2} (\nabla \phi_c)^2 \right]_{z=0} = \tilde{U}_1(t; \phi_c, \phi_p) = U_1(x, y, t) \quad (3.20a)^2$$

$$\left[ \frac{\partial \zeta}{\partial t} - \frac{\partial \phi_c}{\partial z} \right]_{z=0} = \tilde{U}_2(\zeta; \phi_c, \phi_p) = U_2(x, y, t) \quad (3.20b)^2$$

For simplicity, instead of a complete Fourier series in  $t$ , assume

$$U_1 = \frac{\mu}{\omega} \sin(\omega t) f(x, y) \quad (3.21)$$

where  $\mu$  is a parameter specifying the amplitude of the excitation.

The problem is to find periodic solutions of this system having a period of  $2\pi/\omega$ . However, the problem is not unique; that is, there can exist solutions that reduce to the solution of the free vibrations as  $\mu \rightarrow 0$ , or that reduce to a trivial solution as  $\mu \rightarrow 0$ . The latter solution was selected by Moiseyev.

The vibrations far away from resonance can be constructed in a manner similar to that used in the previous subsection; that is, it is assumed that

$$\phi_c = \sum_{n=1}^{\infty} \phi_n \mu^n \quad (3.22a)$$

$$\zeta = \sum_{n=1}^{\infty} \zeta_n \mu^n \quad (3.22b)$$

The amplitude-dependent period of the forced vibrations is equal to the given period of the excitation force; thus, the amplitude should be determined from the relation

---

<sup>2</sup>  $\tilde{U}_1$ ,  $\tilde{U}_2$  are functions of the derivatives of  $\phi_c$ ,  $\phi_p$ , and  $\zeta$ , but can be treated as functions of  $x$ ,  $y$ ,  $t$ , in the power series method.

$$T(\epsilon) = \frac{2\pi}{\omega} \quad (3.23)$$

From equations (3.19) and (3.23), the amplitude  $\epsilon$  thus is given by

$$\frac{\sigma_m - \omega}{\omega} = \epsilon^2 h_2 + \epsilon^4 h_4 + \dots \quad (3.24)$$

By following the same reasoning as before, one finds, for example, that

$$\phi_1 = \sum_{n=1}^{\infty} \frac{C_n \psi_n(x, y, z)}{\sigma_n^2 - \omega^2} \cos(\omega t) \quad (3.25)$$

where  $f(x, y)$  in equation (3.21) has been written as  $f(x, y) = \Sigma C_n \psi_n(x, y)$ .

Near resonance, the solution (eq. (3.25)) cannot be used. The method used here by Moiseyev is to consider the detuning  $\omega^2 - \sigma^2$  as small. In other words, it is assumed that near resonance

$$\omega^2 = \sigma_m^2 + \mu\alpha \quad (3.26a)$$

or

$$\alpha = \frac{\omega^2 - \sigma_m^2}{\mu} \quad (3.26b)$$

with  $\alpha$  a parameter. Thus, from equation (3.9), one finds that

$$g = \frac{\omega^2}{\lambda_m} - \mu \frac{\alpha}{\lambda_m} \quad (3.27)$$

Near resonance the series expansion for  $\phi$  should be expressed in the parameter  $\mu^{a/b}$  where now the ratio  $a/b$  may take on other than integral values. Since the forcing function is proportional to  $\mu$ , the power method should start from a fraction  $a/b < 1$ , i.e.,  $b = n_1 a$ ,  $n_1$  being an integer. However, it can be shown that no periodic solutions exist unless  $n_1 = 3$ .

Carrying out the analysis for  $n_1 = 3$ , one finds that if

$$\phi_c = \sum_{n=1}^{\infty} \phi_n \mu^{1/3n} \quad (3.28a)$$

and

$$\zeta = \sum_{n=1}^{\infty} \zeta_n \mu^{1/3n} \quad (3.28b)$$

then the approximate equations are

$$\frac{\partial \phi_1}{\partial t} + \frac{\omega^2}{\lambda_m} \zeta_1 = 0 \quad (3.29)$$

$$\frac{\partial \zeta_1}{\partial t} = \frac{\partial \phi_1}{\partial z} \quad (3.30)$$

$$\frac{\partial \phi_2}{\partial t} + \frac{\omega^2}{\lambda_m} \zeta_2 = A_1 \quad (3.31)$$

$$\frac{\partial \zeta_2}{\partial t} = \frac{\partial \phi_2}{\partial z} + B_1 \quad (3.32)$$

$$\frac{\partial \phi_3}{\partial t} + \frac{\omega^2}{\lambda_m} \zeta_3 = A_2 + \frac{f(x, y)}{\omega} \sin(\omega t) \quad (3.33)$$

$$\frac{\partial \zeta_3}{\partial t} = \frac{\partial \phi_3}{\partial z} + B_2 \quad (3.34)$$

where

$$A_1 = -\frac{\partial}{\partial t} \left( \zeta_1 \frac{\partial \phi_1}{\partial z} \right) - \frac{1}{2} (\nabla \phi_1)^2 \quad (3.35a)$$

$$A_2 = -\frac{\partial}{\partial t} \left( \zeta_1 \frac{\partial \phi_2}{\partial z} + \zeta_1^2 \frac{\partial^2 \phi_1}{\partial z^2} + \zeta_2 \frac{\partial \phi_1}{\partial z} \right) \\ - \nabla \phi_1 \left( \zeta_1 \frac{\partial}{\partial z} \nabla \phi_1 + \nabla \phi_2 \right) \quad (3.35b)$$

...

and

$$B_1 = -\frac{\partial \zeta_1}{\partial z} \frac{\partial \phi_1}{\partial z} + \zeta_1 \frac{\partial^2 \phi_1}{\partial z^2} \quad (3.36a)$$

$$B_2 = -\frac{\partial \zeta_1}{\partial x} \left( \frac{\partial \phi_2}{\partial x} + \zeta_1 \frac{\partial \phi_1}{\partial x} \right) - \frac{\partial \zeta_2}{\partial x} \frac{\partial \phi_1}{\partial x} \\ + \zeta_1 \frac{\partial^2 \phi_2}{\partial z^2} + \zeta_2 \frac{\partial^2 \phi_1}{\partial z^2} \quad (3.36b)$$

...

From equations (3.32a) and (3.32b), it can be seen that the first approximation is

$$\frac{\partial^2 \phi_1}{\partial t^2} + \frac{\omega^2}{\lambda_m} \frac{\partial \phi_1}{\partial z} = 0 \quad (3.37)$$

As before, it is assumed that

$$\phi_k = \sum_n f_{nk} \psi_n(x, y, z) \quad (3.38)$$

Hence, the "unique" periodic solution of equation (3.37) is

$$f_{n1} = 0 \quad \text{for} \quad n \neq m \quad (3.39a)$$

$$f_{m1} = M \sin(\omega t) + N \cos(\omega t) \quad (3.39b)$$

where  $M$  and  $N$  are constants to be determined from the third pair of equations by requiring that the resultant of all the resonance terms be zero.

Likewise, the second pair of equations results in

$$f_{m2} = M_1 \sin(\omega t) + N_1 \cos(\omega t) \\ + \text{second harmonics} \quad (3.40)$$

where  $M_1$  and  $N_1$  are constants similarly determined by the periodic requirement of the fourth approximation, which is the solution of the fourth pair of equations.

Thus, the solution near resonance can be computed to any degree of approximation. However, the details of its computation are very complex and so are not given in full here; the interested reader is referred to Moiseyev's original paper.

#### Penney and Price Theory for Finite Stationary Oscillations in a Rectangular Tank (ref. 3.11)

Although the theory of finite traveling waves has been known since the late-19th century, it has only been recently that standing waves of finite amplitude have been examined. Perhaps the first such theory is that due to Penney and Price (ref. 3.11), who have worked out the wave shape to the fifth power in the predominant amplitude.

One of Penney and Price's main conclusions is that the wave frequency is a function of its amplitude. In order to see how this result was derived, and to present an example of Moiseyev's general theory, Penney and Price's method will be given here in detail.

Only two-dimensional waves are considered, so that the appropriate solution of Laplace's equation for waves in an infinitely deep tank is

$$\Phi = \sum_{n=0}^{\infty} \bar{a}_n(t) e^{\frac{2n\pi z}{L}} \cos \frac{2n\pi}{L} x \quad (3.41)$$

where the  $z$  axis is positive upward with its origin at the undisturbed free surface, and the flow is independent of  $y$ . The boundary conditions that equation (3.41) satisfies are

$$\frac{\partial \Phi}{\partial z} = 0 \quad \text{at } z = -\infty$$

$$\frac{\partial \Phi}{\partial x} = 0 \quad \text{at } x = \pm \frac{L}{2}$$

Thus the nonlinear boundary conditions remain to be satisfied.

By assuming that the waves cannot exceed a certain maximum amplitude, the equation of the deformed free surface can be written as<sup>3</sup>

$$Z = \frac{1}{2} \bar{a}_0(t) + \sum_{n=1}^{\infty} \bar{a}_n(t) \cos \frac{2n\pi}{L} x \quad (3.42)$$

The algebraic labor is reduced by writing all equations in nondimensional form. All the lengths are multiplied by  $2\pi/L$  and the time by  $(2\pi g/L)^{1/2}$ . The nondimensional potential and wave form are then

$$\phi = \sum_{n=0}^{\infty} a_n e^{nx} \cos nx$$

$$\xi = \frac{1}{2} a_0 + \sum_{n=0}^{\infty} a_n \cos nx = \frac{1}{2} \sum_{n=-\infty}^{\infty} a_n e^{inx}$$

where  $a_{-n} = a_n$ . (The nondimensional form of  $x$  and  $z$  is still  $x$  and  $z$ .)

It is convenient first to work out simplified expressions for such factors as  $(\xi)^2$ ,  $(\xi)^3$ , and so forth. Now if

$$y = \frac{1}{2} \sum_{n=-\infty}^{\infty} b_n e^{inx}$$

then

$$\begin{aligned} \xi^2 &= \frac{1}{4} \sum_{m=-\infty}^{\infty} \sum_{n=-\infty}^{\infty} a_m b_n e^{i(m+n)x} \\ &= \frac{1}{4} \sum_{s=-\infty}^{\infty} \left( \sum_{m=-\infty}^{\infty} a_m b_{s-m} \right) e^{isx} \end{aligned}$$

so that

$$\xi^2 = \frac{1}{4} \sum_{s=-\infty}^{\infty} S_s e^{isx} \quad (3.43a)$$

where

$$S_s = \sum_{m=-\infty}^{\infty} a_m a_{s-m} \quad (3.43b)$$

Now let

$$\xi^N = \frac{1}{2^N} \sum_{s=-\infty}^{\infty} S_N(s) e^{isx} \quad (3.44)$$

<sup>3</sup>The coefficient  $\bar{a}_0$  is, of course, zero, since  $Z=0$  locates the mean level of the free surface, but it is retained here since doing so greatly simplifies the algebra.

or, in another form,

$$\zeta^N = \zeta \zeta^{N-1} = \frac{1}{2^N} \sum_{s=-\infty}^{\infty} \sum_{m=-\infty}^{\infty} a_m S_{N-1}(s-m) e^{isz} \quad (3.45)$$

From equations (3.44) and (3.45), it follows that

$$S_N(s) = \sum_{m=-\infty}^{\infty} a_m S_{N-1}(s-m) \quad (3.46)$$

so that by continued application

$$S_N(s) = \sum_{m_1=-\infty}^{\infty} \sum_{m_2=-\infty}^{\infty} \dots [a_{m_1} a_{m_2} \dots a_{s-m_1-m_2-\dots}] \quad (3.47)$$

It will be observed that  $S_0(0)=1$ ,  $S_0(s)=0$  for  $s \neq 0$ ,  $S_1(s)=a_s$  for all  $s$  and  $S_N(s)=S_N(-s)$ . Now one can write

$$e^{\tilde{\lambda}t} = \sum_{N=0}^{\infty} \frac{\tilde{\lambda}^N}{N!} \zeta^N = \sum_{N=0}^{\infty} \frac{\tilde{\lambda}^N}{N!} \left[ \frac{1}{2^N} \sum_{s=-\infty}^{\infty} S_N(s) e^{isz} \right] = \sum_{s=-\infty}^{\infty} E(\tilde{\lambda}, s) e^{isz} \quad (3.48)$$

where

$$E(\tilde{\lambda}, s) = E(\tilde{\lambda}, -s) = \sum_{N=0}^{\infty} \frac{\tilde{\lambda}^N}{2^N N!} S_N(s) \quad (3.49)$$

Finally, each term in equation (3.41a) can be evaluated for  $z=\zeta$ :

$$\begin{aligned} e^{\tilde{\lambda}t} \cos(\tilde{\mu}x) &= \frac{1}{2} \sum_{s=-\infty}^{\infty} E(\tilde{\lambda}, s) e^{is(s+\tilde{\mu})x} + \frac{1}{2} \sum_{s=-\infty}^{\infty} E(\tilde{\lambda}, s) e^{is(s-\tilde{\mu})x} \\ &= \frac{1}{2} \sum_{s=-\infty}^{\infty} [E(\tilde{\lambda}, s-\tilde{\mu}) + E(\tilde{\lambda}, s+\tilde{\mu})] e^{isz} \\ &= E(\tilde{\lambda}, \tilde{\mu}) + \sum_{s=1}^{\infty} \cos(sx) \{ E(\tilde{\lambda}, s-\tilde{\mu}) + E(\tilde{\lambda}, s+\tilde{\mu}) \} \end{aligned} \quad (3.50)$$

With these preliminary mathematics the coefficients  $\alpha_n$  and  $a_n$  can be conveniently determined from the free surface dynamic and kinematic conditions. The dynamic free surface condition requires at  $z=Z$  that the pressure be zero; that is, it is required that

$$\left\{ g_Z + \frac{\partial \Phi}{\partial t} + \frac{1}{2} \left[ \left( \frac{\partial \Phi}{\partial x} \right)^2 + \left( \frac{\partial \Phi}{\partial z} \right)^2 \right] \right\}_{z=z} = 0$$

which in dimensionless form is

$$\begin{aligned} \zeta + \sum_{n=0}^{\infty} \dot{\alpha}_n e^{nt} \cos nx \\ + \frac{1}{2} \sum_{m=1}^{\infty} \sum_{n=1}^{\infty} m n \alpha_m \alpha_n e^{(m+n)t} \cos(m-n)x = 0 \end{aligned} \quad (3.51)$$

The kinematic condition requires that

$$\left[ \frac{\partial f}{\partial t} + \frac{\partial \Phi}{\partial x} \frac{\partial f}{\partial x} + \frac{\partial \Phi}{\partial z} \frac{\partial f}{\partial z} \right]_{z=z(x,t)-z} = 0 \quad \text{on } z=Z \quad (3.52a)$$

or, in dimensionless form,

$$\begin{aligned} \left[ \frac{1}{2} \dot{a}_0 + \sum_{n=1}^{\infty} \dot{\alpha}_n \cos(nx) \right] \\ + \left[ \sum_{n=1}^{\infty} \alpha_n e^{nt} (-n) \sin(nx) \right] \\ \times \left[ \sum_{n=1}^{\infty} a_n(t) (-n) \sin(nx) \right] \\ - \left[ \sum_{n=1}^{\infty} \alpha_n e^{nt} (n) \cos(nx) \right] = 0 \end{aligned} \quad (3.52b)$$

By using the previously defined expressions for  $E(\tilde{\lambda}, s)$ , equation (3.51) can be written as

$$\frac{1}{2} \dot{a}_0 + \sum_{n=1}^{\infty} a_n \cos nx + \dot{\alpha}_0 + \sum_{n=1}^{\infty} \dot{\alpha}_n \left\{ E(n, n) + \sum_{l=1}^{\infty} \cos lx [E(n, l-n) + E(n, l+n)] \right\} + \frac{1}{2} \sum_{m=1}^{\infty} \sum_{n=1}^{\infty} m n \alpha_m \alpha_n \left\{ E(m+n, m-n) + \sum_{l=1}^{\infty} \cos lx [E(m+n, l-m+n) + E(m+n, s+m-n)] \right\} = 0 \quad (3.53)$$

and equation (3.52b) as

$$\frac{1}{2} \ddot{a}_0 + \sum_{m=1}^{\infty} \dot{\alpha}_m \cos mx + \frac{1}{2} \sum_{m=1}^{\infty} \sum_{n=1}^{\infty} m n \alpha_m \alpha_n \left\{ E(n, m-n) - E(n, m+n) + \sum_{l=1}^{\infty} \cos lx [E(n, l-m+n) + E(n, l+m-n) - E(n, l-m-n) - E(n, l+m+n)] \right\} - \sum_{n=1}^{\infty} n \alpha_n \left\{ E(n, n) + \sum_{l=1}^{\infty} \cos lx [E(n, l-n) + E(n, l+n)] \right\} = 0 \quad (3.54)$$

Since equations (3.53) and (3.54) are true for all  $x$ , it follows that the coefficient of each harmonic in the equations should be identically zero; thus,

$$-\frac{1}{2} \dot{a}_0 = \dot{\alpha}_0 + \sum_{n=1}^{\infty} \dot{\alpha}_n E(n, n) + \frac{1}{2} \sum_{m=1}^{\infty} \sum_{n=1}^{\infty} m n \alpha_m \alpha_n E(m+n, m-n) \quad (3.55a)$$

and

$$-a_s = \sum_{n=1}^{\infty} \dot{\alpha}_n [E(n, s-n) + E(n, s+n)] + \frac{1}{2} \sum_{m=1}^{\infty} \sum_{n=1}^{\infty} m n \alpha_m \alpha_n [E(m+n, s-m-n) + E(m+n, s+m-n)] \quad (3.55b)$$

where  $S$  is a positive integer. Also, from equation (3.54)

$$-\frac{1}{2} \ddot{a}_0 = \frac{1}{2} \sum_{m=1}^{\infty} \sum_{n=1}^{\infty} m n \alpha_m \alpha_n [E(n, m-n) - E(n, m+n)] - \sum_{n=1}^{\infty} n \alpha_n E(n, n) \quad (3.56a)$$

and

$$-\dot{a}_s = \frac{1}{2} \sum_{m=1}^{\infty} \sum_{n=1}^{\infty} m n \alpha_m \alpha_n [E(n, s-m+n) + E(n, s+m-n) - E(n, s-m-n) - E(n, s+m-n)] - \sum_{n=1}^{\infty} n \alpha_n [E(n, s-n) + E(n, s+n)] \quad (3.56b)$$

This system of infinitely many first order differential equations is to be solved by the method of finite term approximations to the infinite series. (As a check on the algebra, the time derivative  $\dot{a}_0$  of the constant liquid depth should be zero in equation (3.56a).) Note that equation (3.55a) can be regarded as an equation to determine  $\alpha_0$  in terms of the other  $\alpha_s$ ; but  $\alpha_0$  corresponds to the arbitrary time function in Bernoulli's equation and is only needed when computing the pressure.

To obtain an analytical solution, the coefficients  $a_s$  and  $\alpha_s$  are expressed in terms of integral powers of a parameter  $\epsilon$ . The  $a_s$  are assumed to be of order  $\epsilon$ , and  $\alpha_s$  to be of the same or higher order; this assumption can be justified by a critical examination of equations (3.55b) and (3.56b).

Equations for  $a_s$  and  $\alpha_s$  to the fifth order in  $\epsilon$  are given below. The equation for the constant term in the wave shape is

$$-a_0 = 0 = 2\dot{\alpha}_0 + \dot{\alpha}_1 \left( a_1 + \frac{1}{2} a_1 a_2 + \frac{1}{8} a_1^3 \right) + \dot{\alpha}_2 (a_1^2 + 2a_2) + \alpha_1^2 - a_1^2 \alpha_1^2 + 6a_1 \alpha_1 \alpha_2 + 4\alpha_2^2 \quad (3.57)$$

This equation can be used to calculate  $\alpha_0$  once the other  $\alpha_s$  and  $a_s$  have been computed.

The coefficient of the fundamental term in the amplitude must satisfy two equations derived from equations (3.55b) and (3.56b):

$$\begin{aligned} -a_1 &= \dot{\alpha}_1 \left( 1 + \frac{3}{8} a_1^2 + \frac{1}{2} a_2 + \frac{1}{4} a_1 a_3 + \frac{5}{192} a_1^4 \right) + \dot{\alpha}_2 a_1 \\ &\quad + \alpha_1^2 \left( a_1 + a_1 a_2 + \frac{1}{2} a_1^3 \right) + 2\dot{\alpha}_1 \dot{\alpha}_2 \quad (3.58) \end{aligned}$$

and

$$\begin{aligned} \dot{a}_1 &= \alpha_1 \left( 1 + \frac{1}{8} a_1^2 - \frac{1}{2} a_2 + \frac{1}{192} a_1^4 \right. \\ &\quad \left. - \frac{1}{4} a_1 a_3 + \frac{1}{4} a_2^2 \right) + \alpha_2 a_1 \quad (3.59)^* \end{aligned}$$

The equations for the second harmonics are

$$\begin{aligned} -a_2 &= \dot{\alpha}_1 \left( \frac{1}{2} a_1 + \frac{1}{2} a_1 a_2 + \frac{1}{2} a_3 + \frac{1}{12} a_1^3 \right) + \dot{\alpha}_2 (1 + a_1^2) \\ &\quad + \frac{3}{2} \dot{\alpha}_3 + \alpha_1^2 \left( a_2 + \frac{1}{2} a_1^2 \right) - 3\alpha_1 \alpha_2 a_1 - 3\alpha_1 \alpha_3 \\ \dot{a}_2 &= \alpha_1 \left( a_1 + \frac{1}{12} a_1^2 - a_3 \right) + \alpha_2 (2 + 2a_1^2) + 3\alpha_3 a_1 \end{aligned}$$

The equations for the third harmonic are

$$\begin{aligned} -a_3 &= \dot{\alpha}_1 \left( \frac{1}{2} a_2 + \frac{1}{8} a_1^2 + \frac{5}{384} a_1^4 + \frac{1}{8} a_2^2 + \frac{3}{12} a_1^2 a_2 \right. \\ &\quad \left. + \frac{1}{2} a_1 a_3 + \frac{1}{2} a_4 \right) + \dot{\alpha}_2 a_1 + \dot{\alpha}_3 + \alpha_1^2 \left( a_3 + a_1 a_2 + \frac{1}{6} a_1^3 \right) \\ \dot{a}_3 &= \alpha_1 \left( \frac{3}{8} a_1^2 + \frac{3}{2} a_2 + \frac{3}{128} a_1^4 + \frac{3}{16} a_1^2 a_2 \right. \\ &\quad \left. - \frac{3}{8} a_2^2 - \frac{3}{2} a_4 \right) - 3\alpha_3 a_1 - 3\alpha_4 \end{aligned}$$

The equations for the fourth harmonic are

$$\begin{aligned} -a_4 &= \dot{\alpha}_1 \left( \frac{1}{2} a_3 + \frac{1}{4} a_1 a_2 + \frac{1}{48} a_1^3 \right) + \dot{\alpha}_2 \left( a_2 + \frac{1}{2} a_1^3 \right) \\ &\quad + \frac{3}{2} \dot{\alpha}_3 a_1 + \dot{\alpha}_4 \\ \dot{a}_4 &= \alpha_1 \left( \frac{1}{12} a_1^3 + a_1 a_2 + 2a_3 \right) + \alpha_2 \left( 2a_1^2 + 4a_3 \right) \\ &\quad + 6\alpha_3 a_1 + 4\alpha_4 \end{aligned}$$

\* As mentioned previously,  $\dot{a}_0 = 0$ .

The equations for the fifth harmonic are

$$\begin{aligned} -a_5 &= \dot{\alpha}_1 \left( \frac{1}{2} a_4 + \frac{1}{8} a_2^2 + \frac{1}{4} a_1 a_3 \right. \\ &\quad \left. + \frac{1}{16} a_1^2 a_2 + \frac{1}{384} a_1^4 \right) + \dot{\alpha}_5 \\ \dot{a}_5 &= \alpha_1 \left( \frac{5}{384} a_1^4 + \frac{5}{16} a_1^2 a_2 + \frac{5}{8} a_2^2 + \frac{5}{4} a_1 a_3 + \frac{5}{2} a_4 \right) + 5\alpha_5 \end{aligned}$$

For very small oscillations, these equations reduce to

$$-a_s = \dot{\alpha}_s \quad (3.60a)$$

$$\dot{a}_s = s\alpha_s \quad (3.60b)$$

which have as a solution

$$a_s = \epsilon_s \cos(t\sqrt{s} + \sigma_s) \quad (3.61a)$$

where  $\epsilon_s$  and  $\sigma_s$  are arbitrary constants. Thus, the first-order surface elevation becomes

$$\zeta = \sum_{s=1}^{\infty} \epsilon_s \sin(t\sqrt{s} + \sigma_s) \cos(sx) \quad (3.61b)$$

Consequently, the free surface oscillations will not be strictly periodic in time unless  $\epsilon_s = 0$  except for those cases when  $s = n^2$ ,  $n$  an integer.

In order to pose a definite physical problem, Penney and Price studied those oscillations that reduce to a single harmonic term when the amplitude is made small. In particular, attention was centered on those oscillations which tend to

$$\zeta = \epsilon \cos x \sin t \quad (3.62)$$

as  $\zeta$  tends to zero.

By using equation (3.62), the nonlinear equations (3.58) to (3.59) can be solved to higher order, more exact approximations.

The second-order equations give a better approximation to the wave shape than do the first-order ones, as will be seen. They are

$$\left. \begin{aligned} -a_1 &= \dot{\alpha}_1 \text{ and } \dot{a}_1 = \alpha_1 \\ -a_2 &= \dot{\alpha}_2 + \frac{1}{2} \alpha_1 a_1 \text{ and } \dot{a}_2 = 2\alpha_2 + a_1 \alpha_1 \\ -a_s &= \dot{\alpha}_s \text{ and } \dot{a}_s = -s\alpha_s \quad (s > 2) \end{aligned} \right\} \quad (3.63)$$

Thus

$$\alpha_1 = \epsilon \sin t \text{ and } \alpha_1 = \epsilon \cos t \quad (3.64)$$

For strictly periodic motion  $\alpha_2 = 0$  in order to avoid a frequency  $\sqrt{2}$  times the fundamental frequency. If this is the case, then

$$\alpha_2 = \frac{1}{2} \epsilon^2 \sin^2 t = \frac{1}{4} \epsilon^2 (1 - \cos 2t) \quad (3.65)$$

Similarly,  $\alpha_3$  and  $\alpha_4$  are zero to the second order. Thus, the natural frequency of the waves is unchanged to the second order.

The second-order approximation can be substituted into the third-order terms for the third approximation; thus,

$$\ddot{\alpha}_1 + \alpha_1 = 4\dot{\alpha}_1 \alpha_1 - \alpha_1^3 \quad (3.66)$$

The third-order periodic solution that reduces to  $\alpha_1 = \epsilon \cos t$  is

$$\begin{aligned} \alpha_1 &= \epsilon \cos \left( \sqrt{1 - \frac{1}{4} \epsilon^2} t \right) \\ &\quad + \frac{5}{32} \epsilon^3 \cos \left( 3\sqrt{1 - \frac{1}{4} \epsilon^2} t \right) \end{aligned} \quad (3.67)$$

Also,  $\alpha_2 = 0$ ,  $\alpha_3 = 0$  to the third order. It follows that  $\alpha_3$ ,  $\alpha_4$ ,  $\alpha_5$  are all of fourth or higher order. Thus, in the third-order approximation the frequency of the waves depends on their amplitude.

Similarly, to the fourth-order approximation  $\alpha_1$  is still given by equation (3.67) and

$$\begin{aligned} \alpha_2 &= \frac{3}{112} \epsilon^4 \sin \left( \sqrt{1 - \frac{1}{4} \epsilon^2} 4t \right) \\ &\quad - \frac{1}{8} \epsilon^4 \sin \left( \sqrt{1 - \frac{1}{4} \epsilon^2} 2t \right) \end{aligned} \quad (3.68)$$

To the fifth order

$$\begin{aligned} \alpha_1 &= \epsilon \cos(\sigma t) + \left( \frac{5}{32} \epsilon^3 - \frac{535}{7168} \epsilon^5 \right) \cos(3\sigma t) \\ &\quad + \frac{283}{7186} \epsilon^5 \cos(5\sigma t) \end{aligned} \quad (3.69)$$

where

$$\sigma = \left( 1 - \frac{1}{4} \epsilon^2 - \frac{13}{128} \epsilon^4 \right)^{1/2} \quad (3.70)$$

<sup>5</sup> There are no fifth-order terms in  $a$ , or  $\dot{a}$ , when  $s$  is even.

and

$$\begin{aligned} \alpha_3 &= \frac{1}{96} \epsilon^5 \cos(\sigma t) + \frac{1}{64} \epsilon^5 \cos(3\sigma t) \\ &\quad - \frac{7}{2112} \epsilon^5 \cos(5\sigma t) \end{aligned} \quad (3.71a)$$

$$\begin{aligned} \alpha_5 &= -\frac{15}{1024} \epsilon^5 \cos(\sigma t) - \frac{45}{2048} \epsilon^5 \cos(3\sigma t) \\ &\quad + \frac{3}{2048} \epsilon^5 \cos(5\sigma t) \end{aligned} \quad (3.71b)$$

The corresponding free surface shape is given by

$$\begin{aligned} \alpha_1 &= \left( \epsilon + \frac{3}{32} \epsilon^3 - \frac{137}{3072} \epsilon^5 \right) \sin(\sigma t) \\ &\quad + \left( \frac{1}{16} \epsilon^3 - \frac{11}{5376} \epsilon^5 \right) \sin(3\sigma t) \\ &\quad + \frac{163}{21504} \epsilon^5 \sin(5\sigma t) \end{aligned} \quad (3.72a)$$

$$\begin{aligned} \alpha_2 &= \frac{1}{4} \epsilon^2 + \frac{1}{6} \epsilon^4 - \left( \frac{1}{4} \epsilon^2 - \frac{25}{192} \epsilon^4 \right) \cos(2\sigma t) \\ &\quad - \frac{67}{1344} \epsilon^4 \cos(4\sigma t) \end{aligned} \quad (3.72b)$$

$$\begin{aligned} \alpha_3 &= \left( \frac{9}{32} \epsilon^3 - \frac{1}{256} \epsilon^5 \right) \sin(\sigma t) \\ &\quad - \left( \frac{3}{32} \epsilon^3 - \frac{2195}{14336} \epsilon^5 \right) \sin(3\sigma t) \\ &\quad - \frac{16365}{473088} \epsilon^5 \sin(5\sigma t) \end{aligned} \quad (3.72c)$$

$$\alpha_4 = \frac{1}{8} \epsilon^4 - \frac{1}{6} \epsilon^4 \cos(2\sigma t) + \frac{1}{24} \epsilon^4 \cos(4\sigma t) \quad (3.72d)$$

$$\begin{aligned} \alpha_5 &= \frac{145}{768} \epsilon^5 \sin(\sigma t) - \frac{515}{3072} \epsilon^5 \sin(3\sigma t) \\ &\quad + \frac{85}{3072} \epsilon^5 \sin(5\sigma t) \end{aligned} \quad (3.72e)$$

with  $\sigma$  defined by equation (3.70).

The fifth-order wave shape can be examined easily for  $\sigma t = (n + \frac{1}{2})\pi$ , where  $n$  is an integer, since at these times the water is momentarily at rest and the wave everywhere reaches its maximum amplitude. The wave shape is

$$\begin{aligned} \zeta &= \left( \epsilon + \frac{1}{32} \epsilon^3 - \frac{47}{1344} \epsilon^5 \right) \cos x \\ &\quad + \left( \frac{1}{2} \epsilon^2 - \frac{79}{672} \epsilon^4 \right) \cos 2x + \left( \frac{3}{8} \epsilon^3 - \frac{12563}{59136} \epsilon^5 \right) \cos 3x \\ &\quad + \frac{1}{3} \epsilon^4 \cos 4x + \frac{295}{768} \epsilon^5 \cos 5x \end{aligned} \quad (3.73)$$

A closer examination shows that there is no point on the surface which is always at rest, that is, there are no true nodes; moreover, the free surface is never perfectly flat. The frequency of the wave as a function of its amplitude is given by equation (3.70)

$$\sigma = \left( 1 - \frac{1}{4} \epsilon^2 - \frac{13}{128} \epsilon^4 \right)^{1/2} \quad (3.74)$$

so that it may be seen that a finite amplitude wave in an infinitely deep tank is a nonlinear softening dynamic system.

Penney and Price also worked out the limiting condition on the maximum amplitude of the wave.

If the ullage or the atmospheric pressure is nearly zero, and the surface tension (excluding low gravity cases) is also nearly zero, then one may assume both are zero to obtain a simplified criterion of instability. Consider an element of volume of liquid on the free surface as a particle, then the only vertical forces are those due to vertical pressure gradient,  $\frac{\partial p}{\partial z} dx dy dz$ , the body force,  $\rho g dz dy dx$ , and the inertial force,  $-\frac{\partial w}{\partial t}$ . Thus, the balance of forces yields

$$\frac{\partial p}{\partial z} + \rho g + \rho \frac{\partial w}{\partial t} = 0 \quad (3.75)$$

on the free surface particle.

Since the value of  $p_0$  is practically zero,  $\frac{\partial p}{\partial z}$  must be nearly negative or zero. Therefore, equation (3.75) leads to the following approximate upper bound for stability

$$\frac{\partial w}{\partial t} + g \geq 0 \quad \text{or} \quad -\frac{\partial w}{\partial t} \leq g \quad (3.76)$$

which states that the downward acceleration  $\frac{\partial w}{\partial t}$  must be less than the gravitational acceleration,  $g$ .

The slope of the sharp crest of the limiting wave form can also be calculated. Along the free surface (of constant pressure)

$$\left( \frac{\partial^2 p}{\partial x^2} \right)_\pm (dx)^2 + 2 \left( \frac{\partial^2 p}{\partial x \partial z} \right)_\pm dx dz + \left( \frac{\partial^2 p}{\partial z^2} \right)_\pm (dz)^2 = 0 \quad (3.77a, b)$$

At the instant that the limiting wave form is

reached, the velocity  $q$  is zero and the pressure satisfies the Laplace equation at the tip of the crest. Then

$$\left( \frac{\partial^2 p}{\partial z^2} \right)_\pm = - \left( \frac{\partial^2 p}{\partial x^2} \right)_\pm$$

Also, by symmetry

$$\left( \frac{\partial^2 p}{\partial x \partial z} \right)_+ = - \left( \frac{\partial^2 p}{\partial x \partial z} \right)_-$$

Adding equation (3.77a) to equation (3.77b) yields

$$\left[ \left( \frac{\partial^2 p}{\partial x^2} \right)_+ + \left( \frac{\partial^2 p}{\partial x^2} \right)_- \right] [(dx)^2 - (dz)^2] = 0 \quad (3.78)$$

In general, the first bracket is nonzero, then  $dx = \pm dz$  or

$$\frac{dz}{dx} = \pm 1 \quad (3.79)^*$$

at the tip. Thus, the angle enclosed by the crest of the limiting wave form for the stationary wave is  $90^\circ$  in contrast to  $120^\circ$  for the progressive wave.

To check the limiting form of the stationary waves, Taylor (ref. 3.12) has shown that the fifth-order approximation is in good agreement with his experiments, except near the tip of the crest (fig. 3.5).

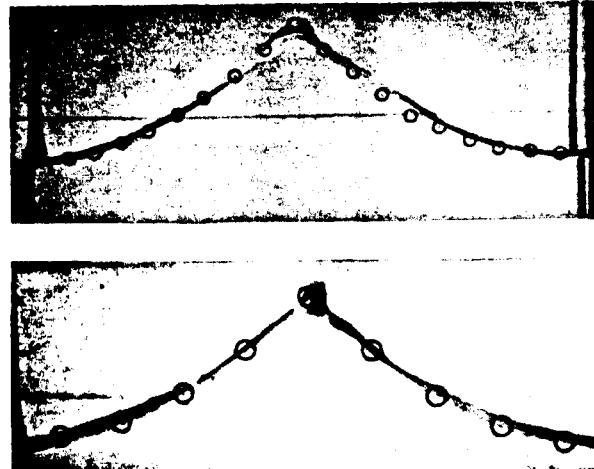


FIGURE 3.5.—Large amplitude stationary wave showing agreement with Penney and Price theory (ref. 3.11).

\* The same configuration results if a smooth curve was assumed. In that case, the symmetry condition demands  $\frac{\partial^2 p}{\partial x \partial z} = 0$ .

The perturbation method has also been applied by Tadjbakhsh and Keller (ref. 3.13) to standing surface waves of finite amplitude in rectangular tanks of finite depth. The solution is obtained to the third order of the amplitude of the linearized surface wave motion. An interesting result was observed to the effect that there is a depth about 0.17 of the wavelength above which the frequency is softening and below which the frequency is hardening, neglecting effects of the third and higher order terms. For brevity, this phenomenon is called "frequency reversal" and has been confirmed experimentally (ref. 3.14).

The critical depth of frequency reversal estimated by Fultz from his experiments is not accurate enough to modify the theoretical predicted value of 0.17.

The perturbation method was again employed by Verma and Keller (ref. 3.15) to three-dimensional waves, the results being similar to those for the two-dimensional waves.

Bauer (ref. 3.16) has extended the basic Penney and Price theory to forced oscillations of the rectangular tank. He considers the

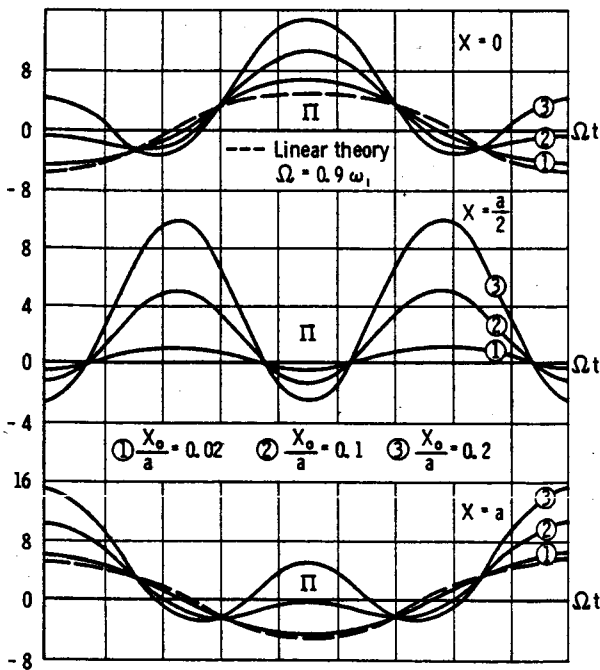


FIGURE 3.6.—Liquid free surface displacements in an infinite rectangular tank under forced oscillation near harmonic resonance for various excitation amplitudes (ref. 3.16).

two-dimensional problem (infinite length tank) with a finite depth of fluid, and carries out the equation to the third order. In this way, Bauer is able to derive a response that includes superharmonic terms in the free surface motions. Figure 3.6 shows the liquid free surface height versus time, for excitation frequency close to the harmonic resonance ( $\Omega = 0.9 \omega_1$ ). The top part of the figure shows the liquid height at the left wall of the tank ( $x=0$ ), the middle part of the figure the liquid height at the center of the tank ( $x=a/2$ ), and the lower part of the figure the liquid height at the right wall of the tank ( $x=a$ ). In each case, the dashed curve represents the result obtained from linear theory (always zero for  $x=a/2$ ), while the curves 1, 2, 3 represent results for varying excitation amplitudes ( $x_0 = 0.02 a$ ,  $x_0 = 0.1 a$ ,  $x_0 = 0.2 a$ , respectively). The nonlinear effects show up strongly with increasing excitation amplitude. Similar results are shown in figure 3.7 for an excitation frequency close to the superharmonic resonance ( $\Omega = \frac{1}{2} \omega_2$ ).

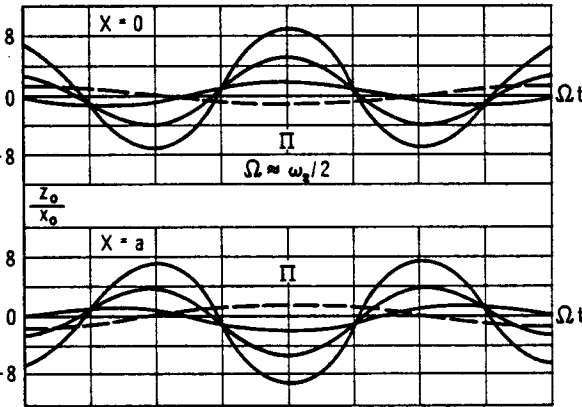


FIGURE 3.7.—Liquid free surface displacements in an infinite rectangular tank under forced oscillation near superharmonic resonance for various excitation amplitudes (ref. 3.16).

#### Extended Hutton Theory for Nonlinear Liquid Motions in a Cylindrical Tank (ref. 3.4)

For a circular cylindrical tank undergoing transverse oscillations, Hutton (ref. 3.19) assumed that the velocity potential of the disturbance can be approximated by the following form:

$$\begin{aligned}\tilde{\phi} = & \epsilon^{1/3}[\psi_1(r, \tau) \cos(\omega t) + \chi_1(r, \tau) \sin(\omega t)] \\ & + \epsilon^{2/3}[\psi_0(r, \tau) + \psi_2(r, \tau) \cos(2\omega t) \\ & + \chi_2(r, \tau) \sin(2\omega t)] + \epsilon[\psi_3(r, \tau) \cos(3\omega t) \\ & + \chi_3(r, \tau) \sin(3\omega t)] \quad (3.80)\end{aligned}$$

where

$t$ =time

$\tau = \frac{1}{2}\epsilon^{2/3}(\omega t)$ ; see equation (3.82)

$\omega$ =frequency

$\epsilon_0$ =tank displacement amplitude

$$\epsilon = \omega \epsilon_0 \quad (3.80a)$$

$$\begin{aligned}\psi_1 = & [f_1(\tau) \cos \theta + f_3(\tau) \sin \theta] J_1(\lambda_{11} r) \\ & \times \frac{\cosh [\lambda_{11}(z+h)]}{\cosh (\lambda_{11} h)} \quad (3.80b)\end{aligned}$$

$$\begin{aligned}\chi_1 = & [f_2(\tau) \cos \theta + f_4(\tau) \sin \theta] J_1(\lambda_{11} r) \\ & \times \frac{\cosh [\lambda_{11}(z+h)]}{\cosh (\lambda_{11} h)} \quad (3.80c)\end{aligned}$$

$$\psi_0 = \text{Constant (ref. 3.10, p. 30)} \quad (3.80d)$$

$$\begin{aligned}\psi_2 = & \sum_{n=1}^N \hat{A}_{0n} J_0(\lambda_{0n} r) \frac{\cosh [\lambda_{0n}(z+h)]}{\cosh (\lambda_{0n} h)} \\ & + \sum_{n=1}^N [\hat{A}_{2n} \cos(2\theta) + \hat{B}_{2n} \sin(2\theta)] J_2 \\ & \times (\lambda_{2n} r) \frac{\cosh [\lambda_{2n}(z+h)]}{\cosh (\lambda_{2n} h)} \quad (3.80e)\end{aligned}$$

$$\begin{aligned}\chi_2 = & \sum_{n=1}^N \hat{C}_{0n} J_0(\lambda_{0n} r) \frac{\cosh [\lambda_{0n}(z+h)]}{\cosh (\lambda_{0n} h)} \\ & + \sum_{n=0}^N [\hat{C}_{2n} \cos(2\theta) + \hat{D}_{2n} \sin(2\theta)] J_2 \\ & \times (\lambda_{2n} r) \frac{\cosh [\lambda_{2n}(z+h)]}{\cosh (\lambda_{2n} h)} \quad (3.80f)\end{aligned}$$

It is noted that  $N=5$  was used and  $\lambda_{0n}$ ,  $\lambda_{2n}$ ,  $\lambda_{11}$  are defined by

$$J'_0(\lambda_{0n} a) = 0, J'_2(\lambda_{2n} a) = 0, J'_1(\lambda_{11} a) = 0 \quad (3.80g)$$

$\psi_3$  and  $\chi_3$  are neglected with the third harmonics of order  $\epsilon$ .

The velocity potential is

$$\phi = \dot{x}_b r \cos \theta + \tilde{\phi} \quad (3.81)$$

where  $x_b$ =tank displacement. The form of the disturbance potential  $\tilde{\phi}$  in terms of  $J_m(\lambda_{mn} r)$   $\cosh [\lambda_{mn}(z+h)] \left\{ \begin{array}{l} \sin(m\theta) \\ \cos(m\theta) \end{array} \right\}$  satisfies the Laplace equation for inviscid irrotational flow as well as the velocity potential. The coefficients are to be determined by a combined nonlinear free surface condition, to the third order.

First, by the method of expansion into the small parameter  $\epsilon$ , the coefficient of  $\epsilon^{1/3}$ ,  $\epsilon^{2/3}$ ,  $\epsilon$  must vanish for all times. In doing so, the transformations

$$\tau = \frac{1}{2} \epsilon^{2/3} \omega t \text{ and } p_{11}^2 = \omega^2 (1 - \nu \epsilon^{2/3}) \quad (3.82)$$

are introduced.

For the  $\epsilon^{1/3}$  term to vanish, the conditions are satisfied by the assumed form of  $\psi_1$  and  $\chi_1$ . The  $\epsilon^{2/3}$  term contains only the constant term and the second harmonics. There were three resultant equations which are satisfied by the Galerkin method (or in this case the Fourier-Bessel technique) with the assumed forms of  $\psi_0$ ,  $\psi_2$ ,  $\chi_2$ . This determines  $\hat{B}_{2n}$ ,  $\hat{A}_{0n}$ ,  $\hat{A}_{2n}$ ,  $\hat{C}_{0n}$ ,  $\hat{C}_{2n}$ ,  $\hat{D}_{2n}$  in terms of  $f_i$ . It is noted that the equation resulting from terms independent of time is satisfied by  $\psi_0=\text{constant}$  and that the remaining two equations yield six equations from their components in  $J_0$ ,  $J_2 \cos(2\theta)$ ,  $J_2 \sin(2\theta)$ . In the  $\epsilon$  term, however, only the two first harmonic terms were assumed to vanish, treating time derivatives temporarily as constants. The  $J_1 \sin \theta$  and the  $J_1 \cos \theta$  components yield a set of four first-order nonlinear differential equations governing  $f_i$  ( $i=1, 2, 3, 4$ ); namely,

$$\begin{aligned}\frac{df_1}{d\tau} = & -\nu f_2 - K_1 f_2 (f_1^2 + f_2^2 + f_3^2 + f_4^2) \\ & + K_2 f_3 (f_2 f_3 - f_1 f_4) \quad (3.83a)\end{aligned}$$

$$\begin{aligned}\frac{df_2}{d\tau} = & F_1 + \nu f_1 (f_1^2 + f_2^2 + f_3^2 + f_4^2) + K_2 f_4 (f_2 f_3 - f_1 f_4) \quad (3.83b)\end{aligned}$$

$$\begin{aligned}\frac{df_3}{d\tau} = & -\nu f_4 (f_1^2 + f_2^2 + f_3^2 + f_4^2) - K_2 f_1 (f_2 f_3 - f_1 f_4) \quad (3.83c)\end{aligned}$$

$$\frac{df_4}{d\tau} = \nu f_3(f_1^2 + f_2^2 + f_3^2 + f_4^2) - K_2 f_2(f_2 f_3 - f_1 f_4) \quad (3.83d)$$

where  $K_1, K_2, F_1$  are constants (given in ref. 3.19). The values of  $K_1$  and  $K_2$  depend on many integrals which have been tabulated in reference 3.19 with some uncertain errors.<sup>7</sup>

The planar motion is given by the solution

$$f_1 = \gamma, f_2 = f_3 = f_4 = 0$$

and  $\gamma$  is governed by a cubic equation

$$K_1 \gamma^2 + F_1 \frac{1}{\gamma} + \nu = 0 \quad (3.84)$$

Near the first natural frequency, the instability of the planar motion is known to exist. The mathematical formulation of stability was to introduce a small disturbance  $c_1 e^{\lambda t}$  to the corresponding steady-state amplitude,  $f_1^{(0)}$  and then determine whether the initial disturbance grows or decays. If  $\lambda$  is positive, the amplitude of the disturbance grows and the motion is unstable. If  $\lambda$  is negative, then the motion is stable. These unstable liquid free surface

<sup>7</sup> In ref. 3.17 the values for  $I_{n1}^*$  are values of  $I_{n1}^*/\lambda_{11}^2$ ;  $K_0$  is the value of  $K_0/\lambda_{11}^2$ , according to communications with R. E. Hutton.

where

$$\begin{aligned} F_1 &= \left[ \int_{-h}^0 \int_0^{2\pi} p a \cos \theta d\theta dz \right]_{r=s} = \\ &- \rho a \left\{ -\epsilon^{1/3} \omega \sin(\omega t) \frac{4\pi \sinh(\lambda_{11} h)}{\lambda_{11}} + \frac{\epsilon}{2a^2} [\sin(\omega t) + \sin(3\omega t)] \right. \\ &\times \sum_{n=1}^{\infty} \frac{\pi}{2} A_n \frac{N_n}{(\lambda_{11}^2 - \lambda_{2n}^2)} [\lambda_{11} \sinh(\lambda_{11} h) \cosh(\lambda_{2n} h) \\ &- \lambda_{2n} \cosh(\lambda_{11} h) \sinh(\lambda_{2n} h)] + \frac{\epsilon}{2} [\sin(\omega t) + \sin(3\omega t)] \\ &\times \sum_{n=1}^{\infty} \frac{\pi}{2} A_n \left[ \frac{2M_n}{(\lambda_{11}^2 - \lambda_{0n}^2)} [\lambda_{11} \cosh(\lambda_{11} h) \sinh(\lambda_{0n} h) \right. \\ &- \lambda_{0n} \sinh(\lambda_{11} h) \cosh(\lambda_{0n} h)] + \frac{N_n}{(\lambda_{11}^2 - \lambda_{2n}^2)} [\lambda_{11} \cosh(\lambda_{11} h) \right. \\ &\times \sinh(\lambda_{2n} h) - \lambda_{2n} \sinh(\lambda_{11} h) \cosh(\lambda_{2n} h)] \left. \right] - \epsilon \omega a \pi h \sin(\omega t) \} \quad (3.86a) \end{aligned}$$

motions are now customarily referred to as "swirl," and will be discussed in the following section of this chapter.

Now, in order to determine the liquid force on the tank (ref. 3.4), the pressure is given by Bernoulli's equation in terms of the disturbance potential, as

$$p = -\rho \left\{ \frac{\partial \tilde{\phi}}{\partial t} + gz + \frac{1}{2} (\nabla \tilde{\phi} \cdot \nabla \tilde{\phi}) + \ddot{x}_1 r \cos \theta + f(t) \right\} + p_0 \quad (3.85)$$

where an arbitrary function of time  $f(t)$  can be absorbed into  $\partial \tilde{\phi}/\partial t$  through a redefinition of  $\tilde{\phi}$ .

The  $x$ -force on the tank is given by

$$F_x = \left[ \int_{-h}^0 \int_0^{2\pi} p a \cos \theta d\theta dx \right]_{r=s}$$

where  $\eta$  is the free surface elevation,  $a$  is the radius of the rigid tank, and  $h$  is the (initial) liquid depth.  $F_x$  can be evaluated to the third order, consistent with Hutton's theory (ref. 3.19), except for the contributions due to  $\psi_3$  and  $x_3$  which were not originally derived. Thus,

$$F_x \approx F_1 + F_2, \quad (3.86)$$

and

$$\begin{aligned}
 F_2 &= \left[ \int_0^n \int_0^{2\pi} p a \cos \theta dz \right]_{r=a} \\
 &= - \int_0^{2\pi} a \left[ \eta p(a, \theta, 0) + \frac{\eta^2}{2} p_z(a, \theta, 0) + O(\eta^4) \right] \cos \theta d\theta \\
 &\approx - \int_0^{2\pi} \left[ \frac{-p^2(a, \theta, 0)}{p_z(a, \theta, 0)} + \frac{1}{2} \frac{p^2(a, \theta, 0)}{p_z(a, \theta, 0)} \right] a \cos \theta d\theta \\
 &= \int_0^{2\pi} \frac{1}{2} \frac{p^2}{p_z} a \cos \theta d\theta \\
 &= \frac{1}{2} \frac{\rho a}{g} \pi \epsilon \left\{ \frac{3}{4} \frac{\omega^3}{g} \sin^3(\omega t) [\gamma J_1(\lambda_{11}a)]^3 \lambda_{11} \tanh(\lambda_{11}h) \right. \\
 &\quad - 4\omega^2 \sin(\omega t) \cos(2\omega t) \gamma J_1(\lambda_{11}a) \left[ \sum_{n=1}^{\infty} \hat{C}_{0n} J_0(\lambda_{0n}a) \right. \\
 &\quad \left. + \frac{1}{2} \sum_{n=1}^{\infty} \hat{C}_{2n} J_2(\lambda_{2n}a) \right] - \left[ \frac{\omega}{a^2} \frac{\sin(\omega t)}{4} \left( \frac{1+\cos(2\omega t)}{2} \right) [\gamma J_1(\lambda_{11}a)]^3 \right] \\
 &\quad \left. - \left[ \frac{3}{4} \omega \sin(\omega t) \left( \frac{1+\cos(2\omega t)}{2} \right) \right] [\gamma J_1(\lambda_{11}a)]^3 [\lambda_{11} \tanh(\lambda_{11}a)]^2 \right\} \quad (3.86b)^8
 \end{aligned}$$

where

$$M_z = \hat{C}_{0n} \frac{\lambda_{0n} J_0(\lambda_{0n}a)}{\cosh(\lambda_{0n}h)} \quad (3.87a)$$

$$N_\theta = -2 \frac{\hat{C}_{2n} J_2(\lambda_{2n}a)}{\cosh(\lambda_{2n}h)} \quad (3.87b)$$

$$N_z = \lambda_{2n} \frac{\hat{C}_{2n} J_2(\lambda_{2n}a)}{\cosh(\lambda_{2n}h)} \quad (3.87c)$$

$$A = \frac{\gamma J_1(\lambda_{11}a)}{\cosh(\lambda_{11}h)} \quad (3.87d)$$

$$A_\theta = -A \quad (3.87e)$$

$$A_z = \lambda_{11} A \quad (3.87f)$$

$$\hat{C}_{0n} = -\frac{\gamma^2}{2} \Omega_{0n} \quad (3.87g)$$

$$\hat{C}_{2n} = -\frac{\gamma^2}{2} \Omega_{2n} \quad (3.87h)$$

$\Omega_{0n}$ ,  $\Omega_{2n}$  are given by Hutton (ref. 3.19).  $\gamma$  is the amplitude of the steady-state part of  $f_1$ , and is governed by a cubic equation de-

\* The relation  $\eta \approx \frac{-p(r, \theta, 0)}{p_z(r, \theta, 0)}$  has been utilized in deriving  $F_2$ .

pending on the motion being planar or non-planar.<sup>9</sup>

A nonlinear theory essentially equivalent to that of Hutton has been derived by Rogge and Weiss (refs. 3.20 and 3.21).

Experimental studies of large amplitude liquid motions in tanks of circular cross section (cylindrical and spherical) are difficult because of the occurrence of swirl modes near the liquid natural frequencies, as mentioned previously and as will be discussed in more detail in the next section. Recourse has therefore been made to the installation of vertical splitter plates parallel to the direction of excitation to suppress rotational motions and thus the onset of swirl. Data obtained from such experimental studies (ref. 3.4) will be summarized in the following section.

A typical liquid *displacement* response curve for low excitation amplitude is shown in figure 3.8. The nonlinear softening characteristic jump phenomenon is clearly demonstrated. Total *force* response data (in the direction of excitation) are shown in figure 3.9 for several values of excitation amplitude. All these data

<sup>9</sup> Through private communications with R. E. Hutton, it was learned that  $I_{0n}^*$  in the expressions for  $\hat{G}_1$  and  $\hat{G}_2$  should be replaced by  $I_{0n}^*/\lambda_{11}^2$ , in order to calculate  $\gamma$  correctly.

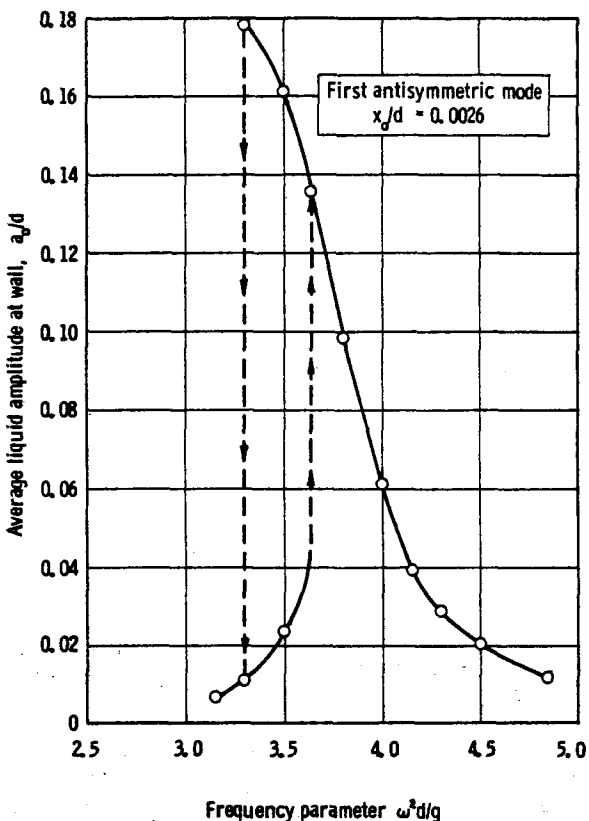


FIGURE 3.8.—Liquid free surface response in half-cylindrical tank demonstrating nonlinear characteristics (ref. 3.4).

were obtained by varying frequency while maintaining constant excitation amplitude; the sweep in frequency was made by first starting at a very low value and slowly increasing until substantially above first-mode resonance, and then sweeping back down to low values. This procedure revealed jump phenomena very clearly. The nonlinear softening characteristic of the response curves of figure 3.9 is quite evident.

The experimentally determined total force data are also compared directly in figure 3.9 with calculations from extensions of the analysis of Hutton, as presented earlier in this section. This theory is basically one of third order, but even then accounts for only certain elements of the nonlinear aspects of the problem; nevertheless, the theory is quite complex in its analytical details, and consequently good agreement with experimental data at and beyond resonance is hardly to be expected. If one

were to require the development of an improved theory, the choice between recommending a "better" third-order theory, or a similar fifth-order theory would not be an easy one. In any event, it may be noted from figure 3.9 that the agreement between theory and experiment for the in-phase branches is rather good, for all four values of excitation amplitude. The agreement is not so good for the out-of-phase branches. In the vicinity of resonance, the theory departs rather widely from the experimental values and, generally, does not give a good value for the frequency at which the jump occurs.

#### Experimental Data for Nonlinear Liquid Motions in a Spherical Tank (ref. 3.4)

As in the case of the circular cylindrical tank, it was found necessary to install a vertical splitter plate in the spherical tank (parallel to the direction of excitation) in order to suppress the liquid swirl mode. Resulting total force response data (amplitude only) for a half-full tank are shown in figure 3.10. Here again, the response is seen to possess a nonlinear softening characteristic, which is quite sensitive to excitation amplitude, as had been intimated some time ago (ref. 3.7). However, the response curves are not very well defined in the areas of the jumps, as compared with those of the cylindrical tank, probably as a consequence of the increased tendency of breaking waves to form because of the curvature at the mean liquid level (breaking wave would not occur in the cylindrical tank at an equivalent wave amplitude). The breaking waves certainly have some tendency to modify the normal instability process in the region of the jump frequencies; nevertheless, the jump behavior has been approximately delineated in figure 3.10 by the dashed lines.

#### 3.4 SWIRL MOTION (ROTARY SLOSHING)

##### General Description of the Liquid Motion

Many different experimental studies concerned with lateral sloshing have revealed an interesting type of liquid instability occurring very close to the lowest liquid resonant fre-

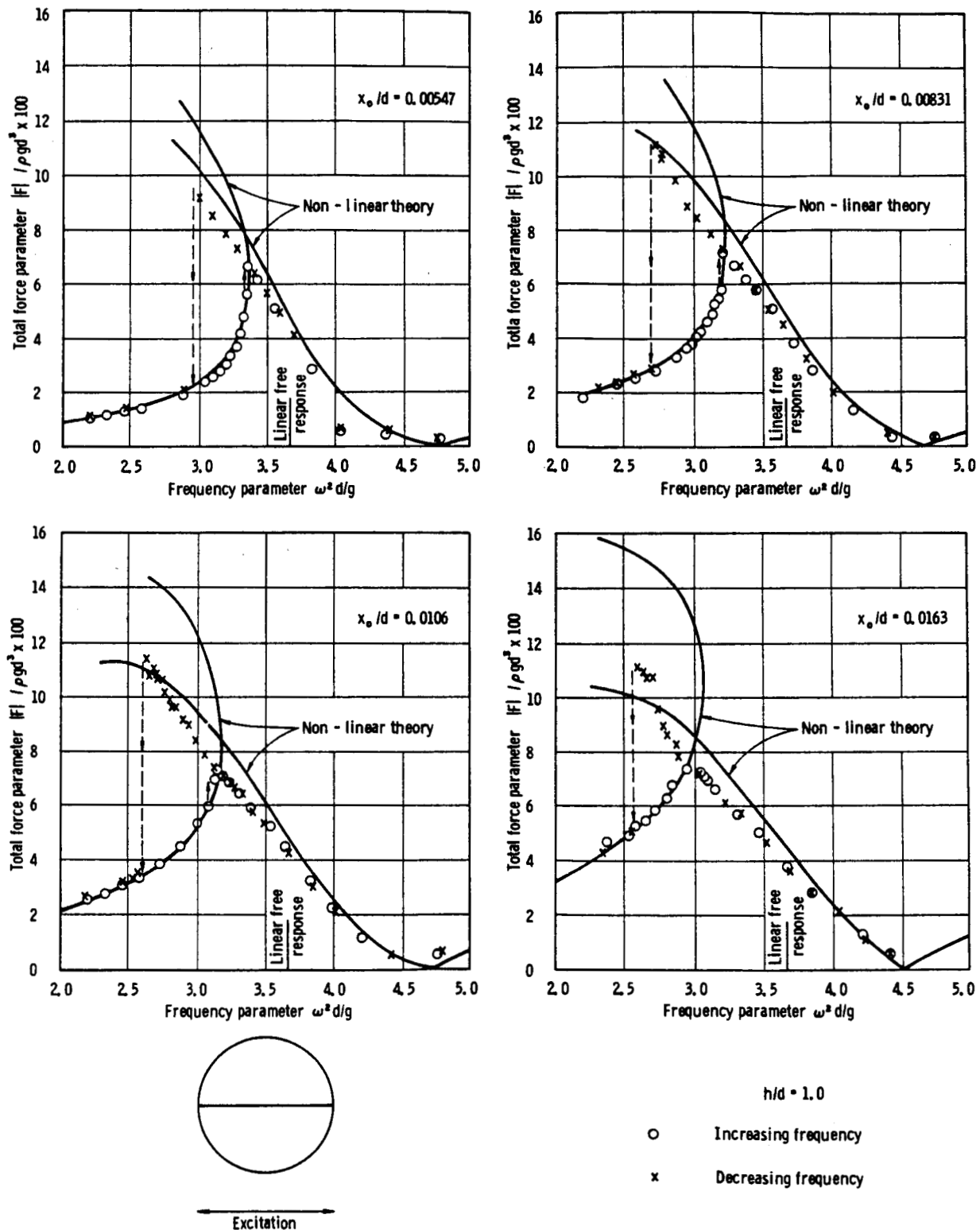


FIGURE 3.9.—Amplitude of liquid force response in half-cylindrical tank for various excitation amplitudes (ref. 3.4).

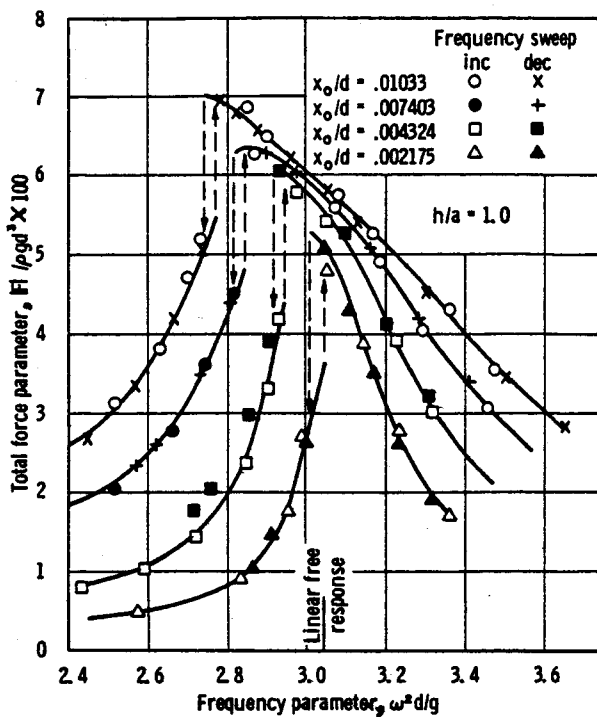


FIGURE 3.10.—Amplitude of liquid force response in spherical tank for various excitation amplitudes (ref. 3.4).

quency (refs. 3.22 and 3.23). The essential features of this complex liquid motion can be described qualitatively as an apparent "rotation" of the liquid about the vertical axis of symmetry of the tank, superimposed on the normal sloshing motion (ref. 3.23). The motion is even more complicated as a type of "beating" also seems to exist; the first antisymmetric liquid-sloshing mode first begins to transform itself into a rotational motion increasing in angular velocity in, say, the counterclockwise direction, which reaches a maximum and then decreases essentially to zero and then reverses and increases in angular velocity in the clockwise direction, and so on alternately. The frequency of rotation is less than that of the surface wave motion and therefore the liquid appears to undergo a vertical up-and-down motion as it rotates about the tank axis; the rotational frequency about this up-and-down axis is about the same as that of the wave motion. The liquid free surface, at least at relatively low excitation amplitudes, is essentially plane, and it is the apparent rotation of

this inclined plane about a vertical axis that we are attempting to describe. This phenomenon almost invariably occurs in laboratory tests at frequencies in the immediate neighborhood of one of the resonances of the normal sloshing modes, as mentioned above, and occurs whether the liquid has any initial gross rotation or not; the rotational mode can, however, be initiated at any excitation frequency by introducing some disturbance which provides a substantial initial rotation to the fluid.

### Theoretical Analyses

An attempt at providing an analytical description of this type of liquid motion was first made on the basis of the behavior of an equivalent linear conical pendulum (ref. 3.22). This theory was able to predict the general character of the stability boundaries, as shown in figure

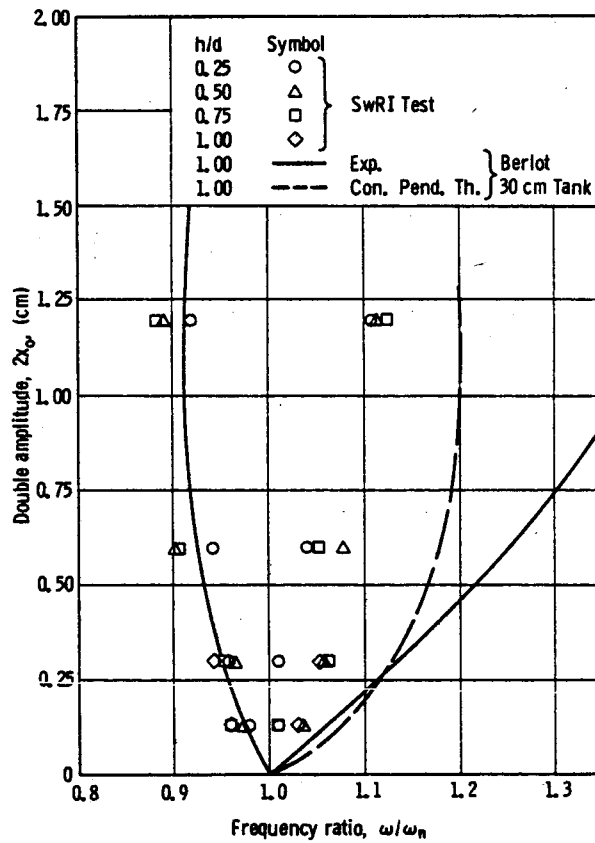


FIGURE 3.11.—Comparison of experimental data with theoretical stability boundaries for rotational liquid motion near first-mode resonance under transverse excitation (ref. 3.23).

3.11, although other features of the motion could not be explained; obviously, the phenomenon involves essentially nonlinear effects. An extension of the theory of the conical pendulum to include third-order terms in the amplitude soon became available (ref. 3.24), which then led directly to the desired nonlinear theory of liquid motion (refs. 3.19 and 3.25).<sup>10</sup> The nonlinear analysis shows three types of liquid motion to occur: normal planar motion, stable nonlinear (rotary) motion, and unstable (swirling) motion. These are in excellent agreement with the observed behavior (refs. 3.4, 3.19, 3.22, and 3.23). The theory also demonstrates that the rotational mode of liquid motion arises as a consequence of a nonlinear coupling between liquid motion parallel and perpendicular to the plane of excitation, and that this coupling takes place through the free surface waves.

The essential results from Hutton's theory (ref. 3.19) can be stated fairly simply by reference to the equations (3.83), which govern the coefficients of an approximate solution for nonlinear liquid motions near first-mode resonance. These equations are nonlinear and possess a nonplanar swirl motion solution as well as the usual planar motion solution. For swirl motion

$$f_1 = \gamma, f_2 = 0, f_3 = 0, f_4^2 = \gamma^2 + \frac{F_1}{K_1} \gamma^{-1} \quad (3.88)$$

The amplitude  $\gamma$  is again determined by a cubic equation; that is,

$$\nu = -\frac{K_1}{K_2} F_1 \gamma^{-1} + (K_2 - K_1) \gamma^2 \quad (3.89)$$

In order that  $f_4$  be real and nonzero, it is necessary that

$$\gamma^2 + \frac{F_1}{K_2} \gamma^{-1} > 0$$

The approximate steady-state solution then takes the form:

<sup>10</sup> This is essentially the theory as presented earlier in this chapter. An equivalent analysis has also been developed elsewhere (refs. 3.20 and 3.21).

$$\begin{aligned} \tilde{\phi} &= \epsilon^{1/3} \{ f_1 \cos \theta \cos (\omega t) + f_4 \sin \theta \sin (\omega t) \} J_1(\lambda_{11} r) \\ &\quad \times \frac{\cosh [\lambda_{11}(z+h)]}{\cosh (\lambda_{11} h)} + O(\epsilon^{2/3}) \\ &= \epsilon^{1/3} \left\{ \left[ \frac{f_1 + f_4}{2} \cos (\theta - \omega t) + \frac{f_1 - f_4}{2} \cos (\theta + \omega t) \right] \right. \\ &\quad \left. \times J_1(\lambda_{11} r) \frac{\cosh [\lambda_{11}(z+h)]}{\cosh (\lambda_{11} h)} \right\} + O(\epsilon^{2/3}) \end{aligned} \quad (3.90)$$

The swirl motions predicted are not simple rotary motions unless  $|f_4| \approx |f_1|$  and the higher order terms are negligible. The instability itself then leads to more complex modes of liquid motion, as described earlier.

### Experimental Data

Figure 3.12 shows some comparison between test data and the predicted stable and unstable planar and nonplanar regions. The predicted boundaries of the instability region agree closely with experimental data for small values of  $\epsilon$ . Poorer agreement for the non-

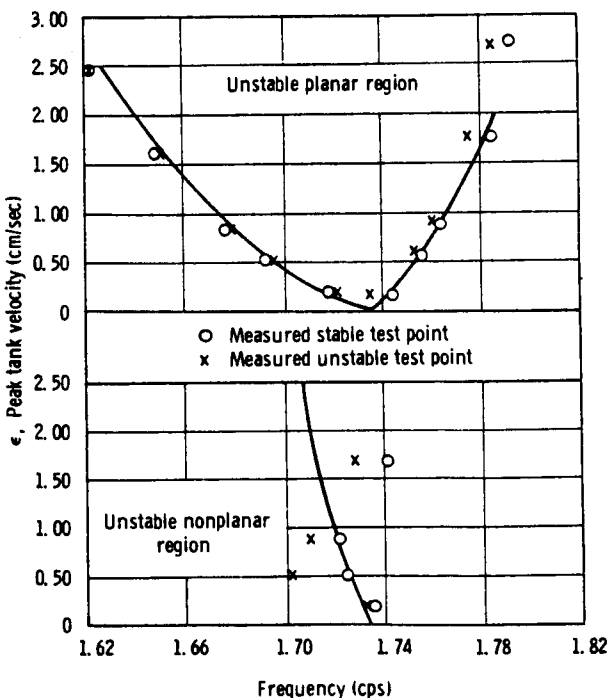


FIGURE 3.12.—Comparison of theoretical and experimental instability regions for nonplanar sloshing (ref. 3.19).

planar motion stability boundary is not surprising because of the difficulty in precisely determining this behavior; as the frequency is decreased, the transition is gradual from the steady-state harmonic nonplanar motion to the nonharmonic nonplanar motion existing in the instability region.

Some interesting experimental information on swirl motion was also obtained during a study of nonlinear lateral sloshing at large excitation amplitudes (ref. 3.4), as shown in figure 3.13. Most of the data shown in figure 3.13 were obtained by maintaining constant excitation amplitude while varying excitation frequency. At first, data were taken only for liquid motions arising basically from the first antisymmetric slosh mode, with no swirl occurring. Subsequently, the boundary of the swirl region was defined experimentally by maintaining constant excitation frequency and slowly increasing excitation amplitude until the swirl motion began to appear. The onset of swirl could be determined relatively precisely not only by visual observation but by the appearance of a significant force normal to the direction of excitation on the oscilloscope output. The swirl boundary thus obtained is shown in figure 3.13. It should be noted that this boundary is dependent upon both excitation frequency and amplitude, since in certain instances it was found that large amplitude breaking waves could be produced without

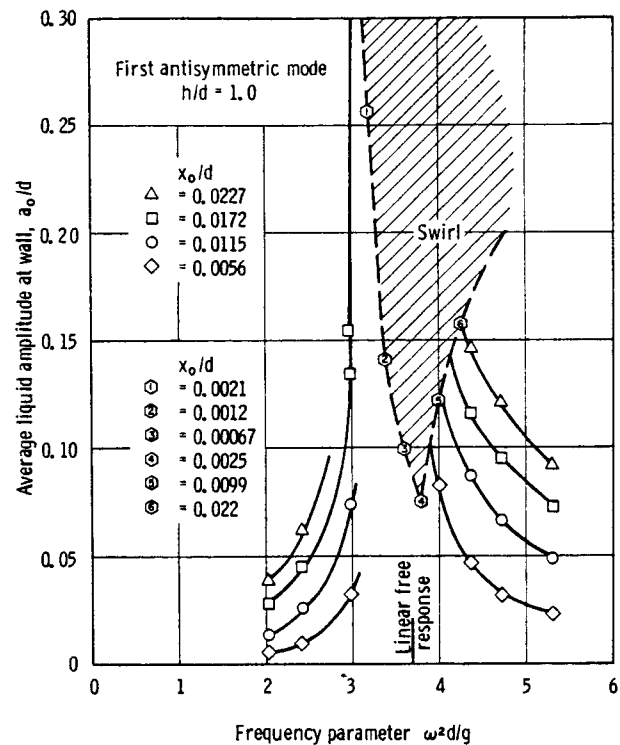


FIGURE 3.13.—Liquid free surface response in circular cylindrical tank showing swirl region (ref. 3.4).

swirl. In addition, it should be noted that within the swirl region the motion of the liquid has a phase angle of near  $90^\circ$  with respect to the input displacement. The data presented here are intended primarily to show the essential effects of increasing excitation amplitudes.

#### REFERENCES

- 3.1. ABRAMSON, H. N.; GARZA, L. R.; AND KANA, D. D.: Some Notes on Liquid Sloshing in Compartmented Cylindrical Tanks. *ARS J.*, vol. 32, no. 6, June 1962, pp. 978-980.
- 3.2. ABRAMSON, H. N.; CHU, W. H.; AND GARZA, L. R.: Liquid Sloshing in  $45^\circ$  Sector Compartmented Cylindrical Tanks. Tech. Rept. No. 3, Contract NAS8-1555, SwRI, Nov. 1962.
- 3.3. ABRAMSON, H. N.; AND GARZA, L. R.: Some Measurements of Liquid Frequencies and Damping in Compartmented Cylindrical Tanks. *AIAA J. Spacecraft Rockets*, vol. 2, no. 3, May-June 1965, pp. 453-455.
- 3.4. ABRAMSON, H. N.; CHU, W. H.; AND KANA, D. D.: Some Studies of Nonlinear Lateral Sloshing in Rigid Containers. *J. Appl. Mech.*, Dec. 1966.
- 3.5. STOKER, J. J.: Nonlinear Vibrations. Interscience Publishers, Inc., New York, 1950 (3d printing, 1957).
- 3.6. ABRAMSON, H. N.: Nonlinear Vibrations. Ch. 4, *Handbook of Shock and Vibration Control*. McGraw-Hill Book Co., 1961.
- 3.7. ABRAMSON, H. N.; CHU, W. H.; AND GARZA, L. R.: Liquid Sloshing in Spherical Tanks. *AIAA J.*, vol. 1, no. 2, Feb. 1963, pp. 384-389.
- 3.8. DALZELL, J. F.; CHU, W. H.; AND MODISSETTE, J. E.: Studies of Ship Roll Stabilization Tanks. Tech. Rept. no. 1, Contract N0NR 3926(00), Southwest Research Institute, Aug. 1964.
- 3.9. MOISEYEV, N. N.: On the Theory of Nonlinear Vibrations of a Liquid of Finite Volume. *Appl. Math. Mech. (PMM)*, vol. 22, no. 5, 1958, pp. 860-870.
- 3.10. NARIMANOV, G. S.: Concerning the Motion of a Container Partially Filled With a Liquid Taking Into Account Large Motions of the Latter (in Russian). *Appl. Math. Mech. (PMM)*, vol. 21, no. 4, 1957. Also available as a Space

- Technology Laboratories, Inc., Translation STL-T-Ru-18.
- 3.11. PENNEY, W. G.; AND PRICE, A. T.: Some Gravity Wave Problems in the Motion of Perfect Liquids. *Phil. Trans. Roy. Soc. (London)*, vol. A244, no. 254, 1952.
- 3.12. TAYLOR, G. I.: An Experimental Study of Standing Waves. *Proc. Roy. Soc. (London)*, vol. A218, 1952, pp. 44-59.
- 3.13. TADJBAKHSI, I.; AND KELLER, J. B.: Standing Waves of Finite Amplitude. *J. Fluid Mech.*, vol. 8, no. 3, July 1960, pp. 443-451.
- 3.14. FULTZ, D.: An Experimental Note on Finite Amplitude Standing Gravity Waves. *J. Fluid Mech.*, vol. 13, no. 2, June 1962, pp. 193-213.
- 3.15. VERMA, G. R.; AND KELLER, J. B.: Three-Dimensional Standing Surface Waves of Finite Amplitude. *Phys. Fluids*, vol. 5, no. 1, Jan. 1962, pp. 52-56.
- 3.16. BAUER, H. F.: Nonlinear Propellant Sloshing in a Rectangular Container of Infinite Length. North American Aviation, Inc., S&ID Report, SID 64-1593, 1964.
- 3.17. GAILLARD, P.: Theoretical and Experimental Research of Nonlinear Oscillations of Liquids in Containers and Channels of Constant Depth (in French). *Publ. Sci. Tech. Minist. l'Air*, France, no. 412, 1963.
- 3.18. CHU, W. H.: Liquid Sloshing in a Spherical Tank Filled to an Arbitrary Depth. *AIAA J.*, vol. 2, no. 11, Nov. 1964, pp. 1972-1979.
- 3.19. HUTTON, R. E.: An Investigation of Resonant, Nonlinear Nonplanar Free Surface Oscillations of a Fluid. *NASA TN D-1870*, 1963.
- 3.20. ROGGE, T. R.; AND WEISS, H. J.: An Approximate Nonlinear Analysis of the Stability of Sloshing Modes Under Translational and Rotational Excitations. *NASA CR-220*, 1965.
- 3.21. WEISS, H. J.; AND ROGGE, T. R.: A Nonlinear Analysis for Sloshing Forces and Moments on a Cylindrical Tank. *NASA CR-221*, 1965.
- 3.22. BERLOT, R. R.: Production of Rotation in a Confined Liquid Through Translational Motion of the Boundaries. *J. Appl. Mech.*, vol. 26, no. 4, Dec. 1959, pp. 513-516.
- 3.23. ABRAMSON, H. NORMAN; CHU, WEN-HWA; GARZA, LUIS R.; AND RANSLEBEN, GUIDO E., JR.: Some Studies of Liquid Rotation and Vortexing in Rocket Propellant Tanks. *NASA TN D-1212*, 1962.
- 3.24. MILES, J. W.: Stability of Forced Oscillations of a Spherical Pendulum. *Quart. Appl. Math.*, vol. 20, no. 1, Apr. 1962, pp. 21-32.
- 3.25. HUTTON, R. E.: Fluid Particle Motion During Rotary Sloshing. *J. Appl. Mech.*, vol. 31, no. 1, Mar. 1964, pp. 123-130.

#### PRINCIPAL NOTATIONS

- $a$ =an arbitrary constant or effective gravitational acceleration
- $C_n$ =the  $n$ th constant in equation (3.25)
- $d$ =diameter of the tank
- $F$ =force exerted on the tank by the fluid
- $f(x, y)$ =a function defined by equation (3.21)
- $f_{nk}$ =defined in equation (3.13)
- $g$ =gravitational acceleration
- $h_n$ =the  $n$ th coefficient defined by equation (3.12)
- $H$ =Neumann function
- $h$ =maximum depth of the liquid at rest
- $n$ =outer normal to the boundaries or an integer
- $p_{mn}$ =natural frequency of the  $m$ th sloshing mode
- $p_0$ =ullage pressure
- $p$ =pressure
- $r, \theta, z$ =cylindrical coordinates
- $\vec{q}$ =velocity vector of the fluid

- $S$ =the free surface when the liquid is stationary
- $s$ =the distance measured along the free surface
- $T$ =the period of vibrations
- $t$ =time
- $U_1, U_2$ =functions of  $(t, x, \text{ and } y)$
- $U$ =same as  $x_0$
- $v_n$ =local normal velocity of the wall
- $x, y, z$ =rectangular coordinates with positive  $z$  upward
- $x_0$ =amplitude of excitational displacement
- $\epsilon$ =a parameter related to the non-dimensional amplitude of the surface elevation
- $\zeta$ =free surface elevation
- $\lambda$ =characteristic number
- $\lambda_n$ = $n$ th characteristic number
- $\tilde{\lambda}$ =wavelength
- $\mu$ =a parameter related to the amplitude of excitation
- $\tilde{\mu}$ =a constant, see equation (3.50)

$\nu$ =transformed frequency, see equation (3.89)  
 $\rho$ =density of the fluid  
 $\Sigma$ =the wetted wall or the summation sign  
 $\Sigma_1$ =the moving part of the wetted wall  
 $\sigma$ =see equation (3.70)  
 $\sigma_n$ =the frequency of the  $n$ th free vibration  
 $\tau$ =a nondimensional time defined by equation (3.12)  
 $\phi$ =velocity potential  
 $\psi(x, y, 0)$ =characteristic function  
 $\psi_n(x, y, 0)$ = $n$ th characteristic function

$\psi(x, y, z)$ =function defined by equation (3.6)  
 $\omega$ =frequency of tank motion  
 $\omega_n$ = $n$ th natural frequency  
 $\frac{D}{Dt}$ =Stokes derivative

*Superscripts:*

$( )''$ =the second derivative of  $( )$  with respect to nondimensional time  
 $( )'$ =derivative of  $( )$  with respect to time  
 $( )^*$ =nondimensionalized quantities  
 $( )^{(0)}$ =steady-state value of  $( )$  unless otherwise specified

## Damping of Liquid Motions and Lateral Sloshing

*Sandor Silverman and H. Norman Abramson*

### 4.1 INTRODUCTION

Propellant sloshing is a potential source of disturbance which may be critical to the stability or structural integrity of space vehicles, as large forces and moments may be produced by the propellant oscillating at one of its fundamental frequencies in a partially filled tank. Since the liquid oscillatory frequency may nearly coincide with either the fundamental elastic body bending frequency or the dynamic control frequency of the vehicle at some time of the powered phase of the flight, the slosh forces could interact with the structure or control system. This could cause a failure of structural components within the vehicle or excessive deviation from its planned flight path. It is therefore necessary to consider means of providing adequate damping of the liquid motions and slosh forces and to develop methods for accounting for such damping in analyses made of vehicle performance.

Linear damping is usually introduced into the vehicle dynamic analysis through the resonance terms of the equations governing a mechanical model representation of the liquid forces and moments. This is done under the assumption that the behavior of the liquid oscillating in its fundamental mode is analogous to the behavior of a linear, viscously damped single degree-of-freedom system. (See chapters 6 and 7 for the development of such mechanical models.) The analysis then yields the amount of damping required for vehicle stability. One of the main problems which remains is to predict the amount of damping present in a given tank configuration.

The results of some of the numerous investigations in the field of liquid damping in rigid containers will be presented and dis-

cussed in this chapter. Unfortunately, the problem is essentially nonlinear and therefore few theories are available for predicting damping (refs. 4.1 through 4.5). Our principal knowledge of damping characteristics is the result of extensive experimental studies.

#### On Damping

The term "damping" is generally employed to describe the fact that some energy dissipation always occurs during fluid oscillations. By far the most comprehensive discussion of damping effects in propellant sloshing is contained in reference 4.6.

If there is no energy input to a system that is oscillating in one of its natural modes, the amplitude of successive oscillations decreases as a result of energy dissipation. This decreasing amplitude can be described by the logarithmic decrement, defined as

$$\delta = \ln \frac{\text{Maximum amplitude of any oscillation}}{\text{Maximum amplitude 1 cycle later}} \quad (4.1)$$

For a linear system, in which the restoring force is proportional to the amplitude of the displacement (measured from rest position), the total energy of oscillation at the peak amplitude of any cycle is proportional to the square of this amplitude. The logarithmic decrement can therefore also be written as

$$\delta = \ln \left( \frac{\text{Energy of motion of 1 cycle}}{\text{Energy of motion 1 cycle later}} \right)^{1/2} \quad (4.2)$$

In terms of the energy decrement per cycle  $\Delta E$  and the total energy of motion  $E$ , equation (4.2) can be reduced to

$$\delta \approx \frac{\Delta E}{2E} \ll 1 \quad (4.3)$$

Damping, whatever its nature, can be represented by an equivalent viscous damping in which the damping force opposing the motion is equal to a damping factor multiplied by the velocity of the oscillating component of the system. The ratio of the actual damping,  $c$ , to the critical damping,  $c_c$ , is denoted as  $\gamma$  and it can be shown (ref. 4.7) that, for small values of  $\gamma$

$$\delta = 2\pi\gamma = 2\pi \frac{c}{c_c} \quad (4.4)$$

The damping ratio  $\gamma$  may also be expressed in terms of energy by substituting equation (4.3) into equation (4.4)

$$\gamma = \frac{1}{4\pi} \frac{\Delta E}{E} \quad (4.5)$$

The damping ratio in the form used by Miles (ref. 4.2) in the theory of ring damping<sup>1</sup> in a circular tank is

$$\gamma = -\frac{\overline{dE}}{2\omega E} \quad (4.6)$$

where  $\overline{dE}/dt$  is the mean rate of energy dissipation over a cycle of period  $2\pi/\omega$  and  $\omega$  is the angular frequency of oscillation.

Several experimental techniques have been employed to obtain the damping factor and are outlined on the following pages.

(1) *Ring force method*.—A direct measurement of the force required to anchor the ring baffle to the tank wall is made. The wave amplitude is measured so that the total energy of motion and the wave velocity can be calculated from classical theory. The component of the ring force that is  $180^\circ$  out of phase with the vertical wave velocity at the ring position gives a measure of energy dissipation, while the dissipation per cycle compared with the total energy of motion determines the damping rate.

<sup>1</sup> One of the principal means of increasing the damping in a liquid propellant tank of cylindrical geometry is obviously that of introducing baffles in the form of thin rings attached normal to the tank wall. These and other types of baffles will be discussed in detail later.

(2) *The drive force method*.—A platform, upon which the tank is located, is driven at constant excitation amplitude and frequency. The force in the drive link, the amplitude of the platform motion, and the amplitude of the wave motion are recorded. The energy input required to maintain steady-state oscillations is the same as the energy dissipated. That component of the drive force that is in phase with the tank velocity delivers energy to the system at the same rate as the dissipation. It is the amount of this input per cycle compared with the total energy of motion, as measured by the wave amplitude, that determines the damping rate.

(3) *The wave (or force) amplitude response method*.—The wave (or force) amplitude as a function of drive frequency is determined for constant drive amplitude. The bandwidth technique (see refs. 4.7 and 4.8) is then applied to these response data to obtain the damping ratio  $\gamma$ . The relationship thus obtained is

$$\gamma = \frac{1}{2} \frac{\Delta\Omega}{\Omega_r} \left[ \left( \frac{z_{\max}}{z_1} \right)^2 - 1 \right]^{-1/2} \quad (4.7a)$$

where  $\Omega$  is the excitation frequency and  $z$  is the wave (or force) amplitude. A typical response curve is illustrated in figure 4.1. In practice, the ratio  $z_{\max}/z_1 = 2/\sqrt{2}$  is often used and thus equation (4.7a) simplifies to

$$\gamma = \frac{1}{2} \frac{\Delta\Omega}{\Omega_r} \quad (4.7b)$$

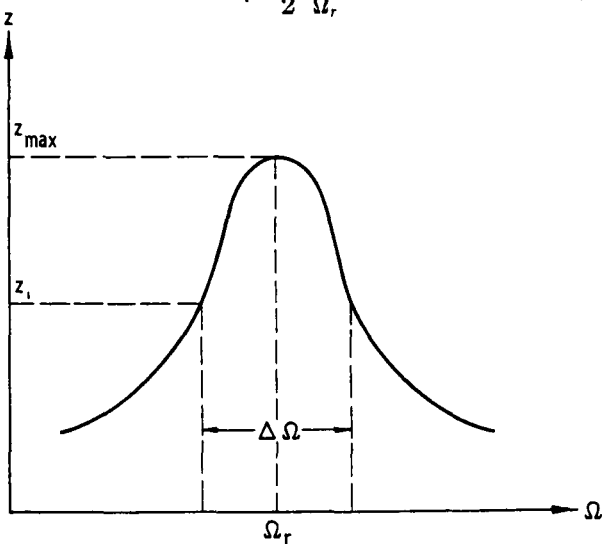


FIGURE 4.1.—Typical wave amplitude response curve.

A comprehensive discussion of the whole field of resonance testing is contained in references 4.9 and 4.10; included is a critical discussion of the bandwidth technique. It should be noted that this technique gives reliable results only if the natural frequencies are not close and the damping is not large. Also, the speed of the frequency sweep and the magnitude of the excitation amplitude may affect the results.

(4) *The wave amplitude decay method.*—The rate of decay of the free surface displacement after cessation of tank motion is measured. With zero input, the decreasing energy of motion as evidenced by the decreasing wave height is a result of the energy dissipated by the damping mechanism. The logarithmic decrement of successive wave heights may be calculated from these measurements and then the damping ratio is obtained from equation (4.4).

(5) *Anchor force decay method.*—The rate of decay of the peak force in the tank anchor is measured after the tank motion is suddenly stopped. The logarithmic decrement is then obtained from successive peak values and the damping ratio  $\gamma$  is obtained from equation (4.4).

The relationship between the damping factors calculated by the above methods cannot be stated easily unless the liquid dynamic behavior is essentially linear. The mechanisms which produce energy dissipation are thought to be known qualitatively, but only a few have been described quantitatively. The damping may be caused by the free surface boundary layer (see ref. 4.4), fluid viscosity, turbulence, boundary layer friction, and interchange of energy between different sloshing modes. In practical applications, of course, none of the previously described methods accounts for all the energy dissipated. The degree of nonlinearity of the system is significant in determining the amount of energy neglected by the various methods. If the system behaves linearly and the damping is small, then the relationships between the energy, logarithmic decrement, and damping ratio as expressed by equations (4.1) through (4.7) are valid.

Caution is especially required when considering the damping of fluid forces caused by oscillations of a tank of unsymmetric geometry. It is conceivable that the damping of

these forces may be quite dependent upon the direction in which the forces are measured and the technique used to measure the damping. Reduction of force amplitudes in multiple connected tanks (such as partitioned tanks) may be the result of phasing of the liquid motions rather than energy dissipation. Therefore, the designer must specify exactly what he is interested in—damping of fluid motions or damping of tank forces.

In table 4.1, and in figure 4.2, experimentally determined damping values for an annular ring baffle in a cylindrical tank with a flat bottom are given as a function of free surface wave amplitude. The values as obtained by the five experimental methods outlined above are compared, together with theoretical curves calculated for conditions conforming most closely to the assumptions of Miles' ring damping theory (ref. 4.2). (See sec. 4.5 of this chapter for a detailed discussion of ring damping from the viewpoints of both theory and experiment.) Experimental damping data for a single-ring baffle are compared in figure 4.3 with the damping factor as calculated from the ring damping theory (ref. 4.11).

### On Damping Investigations

Viscous damping alone, with particular reference to liquids in moving tanks, has been investigated from several viewpoints (refs. 4.12 through 4.15) demonstrating that the significant variables are liquid height, liquid kinematic viscosity, and tank size. Theoretically based equations which predict the damping factor as a function of these variables are modified with the aid of experimental data. In certain situations, it may be feasible to rely entirely upon viscous damping of the fluid to suppress the liquid motions.

The damping effectiveness of movable or floating devices has been studied on many occasions (refs. 4.16 through 4.22), but generally with the conclusion that while floating or movable-lid-type devices may damp liquid motions substantially, they also involve rather significant weight penalties.

Recently, additional interest has developed in positive expulsion bags and diaphragms (refs.

TABLE 4.1.—*Damping Ratios for an Annular Ring in a Cylindrical Tank*(Ring position  $(h-d)/R = 2.11$ ; ring-width parameter  $C = 0.235$ ;  $R = 15.1$  cm; test liquid-water)

[Ref. 4.6]

Method of damping measurement	$\frac{d_s}{R} = 0.168$		$\frac{d_s}{R} = 0.253$		$\frac{d_s}{R} = 0.505$	
	$\bar{z}/R$	$\gamma$	$\bar{z}/R$	$\gamma$	$\bar{z}/R$	$\gamma$
Ring force	0.050	0.019	0.15	0.026	0.19	0.0085
	.082	.024	.12	.027	.17	.0071
	.11	.027	.11	.026	.16	.0075
	.090	.023			.14	.0064
	.064	.024			.13	.0061
Drive force	.050	.029	.15	.027	.19	.012
	.082	.025	.12	.031	.17	.0093
	.11	.026	.11	.031	.16	.0091
	.090	.021			.14	.0094
	.064	.027			.13	.0079
Wave amplitude response	.28	.18	.23	.040	.21	.023
	.28	.18	.23	.042	.21	.024
Wave amplitude decay	.044	.020	.052	.016	.032	.0055
	.029	.015	.040	.014	.023	.0052
	.042	.026	.031	.013	.017	.0052
	.024	.019	.022	.010	.013	.0044
	.015	.014	.017	.0090	.034	.0065
	.036	.030	.051	.012	.028	.0047
	.027	.030	.039	.012	.024	.0044
	.017	.021	.026	.015	.021	.0047
	.012	.019	.020	.011		
	.0085	.017	.015	.0087		
	.0060	.015				
	.042	.017	.052	.025	.032	.0079
	.024	.017	.040	.016	.023	.0059
	.015	.012	.031	.014	.017	.0047
Anehor force decay	.036	.026	.022	.011	.013	.0039
	.027	.020	.051	.022	.034	.0062
	.017	.022	.039	.015	.028	.0052
	.012	.015	.026	.011	.024	.0058
	.0085	.014	.020	.010	.021	.0041
	.0060	.014	.015	.010		

4.16 and 4.17) because of their possible application to the problem of propellant transfer under weightless conditions. Experiments indicate that a major factor affecting liquid damping is the thickness of the membrane, since the amount of damping increases (as does the first natural frequency) with increasing thickness. Damping due to these devices has generally been found to be extremely high.

The major effort devoted to damping of liquid motion has been on investigating the damping due to various types of fixed baffles. This is

for a good reason—they provide large damping for relatively low weight, without other major drawbacks. These fixed baffles may be classified into nonring type and ring type. The non-ring type includes partitions and cruciforms (these are physically located in the same manner as a stringer), while the ring type includes both symmetrical rings and asymmetrical ring segments. In order to save weight, all of these various baffles are often perforated. It has been found that, within certain limits on the percent of area removed by perforation and

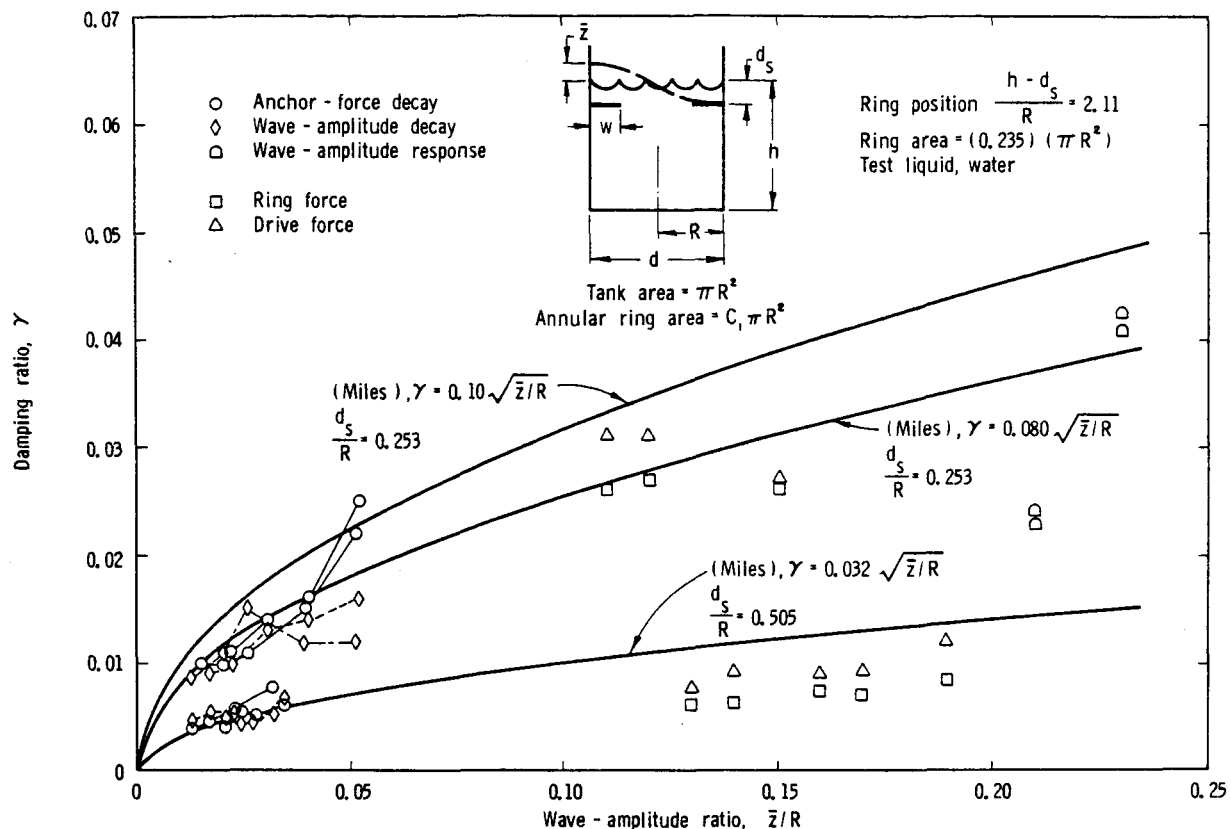


FIGURE 4.2.—Damping ratios for an annular ring in a cylindrical tank as obtained by various methods (ref. 4.6).

their diameter, a significant weight saving can be realized without loss of damping effectiveness or reduction in the resonant frequency. The effectiveness of rigid-type baffles depends largely upon the location of the baffle with respect to the liquid free surface and on the baffle geometry.

Baffles which have a tendency to transfer the first-mode sloshing into a rotary motion have been briefly investigated in references 4.23 and 4.24. Ring baffles having double spirals with opposite directions of rotation appear to be more desirable than single spirals, but the latter, along with swirl plates, induce the problem of liquid swirl.<sup>2</sup>

#### 4.2 VISCOUS DAMPING IN TANKS OF VARIOUS GEOMETRY

##### Circular Cylindrical Tank

At least three extensive experimental investigations have been carried out on viscous damping

<sup>2</sup> This phenomenon was mentioned in ch. 2 and discussed in more detail in ch. 3.

ing in circular cylinders (refs. 4.3, 4.4, and 4.15). The effects on damping of the liquid depth, liquid amplitude, kinematic viscosity, and surface tension were specifically investigated in reference 4.15, and an empirical relationship for calculating the damping coefficient was obtained in the form<sup>3</sup>

$$\delta = 4.98\nu^{1/2}R^{-3/4}g^{-1/4} \times \left[ 1 + \frac{0.318}{\sinh(1.84\frac{h}{R})} \left( \frac{1 - \frac{h}{R}}{\cosh(1.84\frac{h}{R})} + 1 \right) \right] \quad (4.8a)$$

where  $\nu$  is the kinematic viscosity,  $R$  is the tank radius,  $g$  is the acceleration of gravity,  $h$  is the liquid depth, and  $\delta$  is the logarithmic decrement

<sup>3</sup> It is not clear from the text (ref. 4.15) whether this equation was obtained from an examination of the experimental data or was obtained by using experimental data to modify equations which appear in a mentioned but unreferenced report of work by Rabinovich.

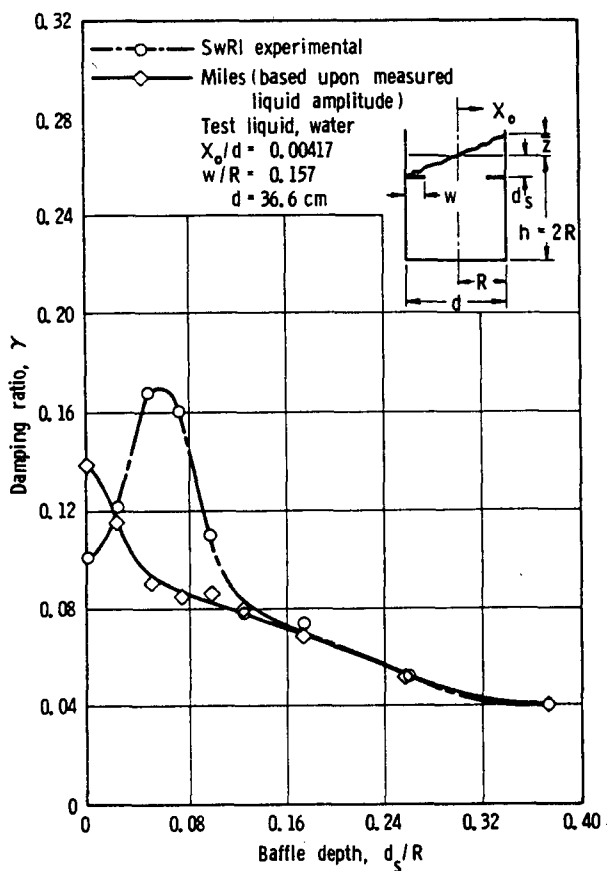


FIGURE 4.3.—Comparison of theory and experiment for damping provided by a flat solid-ring baffle as a function of baffle depth (ref. 4.11).

of the amplitude of the free surface oscillations. For large depths,  $h/R > 1.0$ , equation (4.8a) may be approximated by

$$\delta = 4.98\nu^{1/2}R^{-3/4}g^{-1/4} \quad (4.8b)$$

Employing two cylindrical tanks of different diameters (20 centimeters and 51.8 centimeters) and selecting liquids with different surface tensions  $\tau$  (but with identical kinematic viscosity  $\nu$ ), the effect of surface tension on the damping was investigated. It was concluded that, at least for small tanks, surface tension can significantly affect the damping coefficient, as shown in figure 4.4.

Damping in a cylindrical cavity with a spherical bottom was also determined experimentally, leading to an empirical equation for the damping coefficient in the form

$$\delta = C_2(4.98\nu^{1/2}R^{-3/4}g^{-1/4}) \quad (4.9)$$

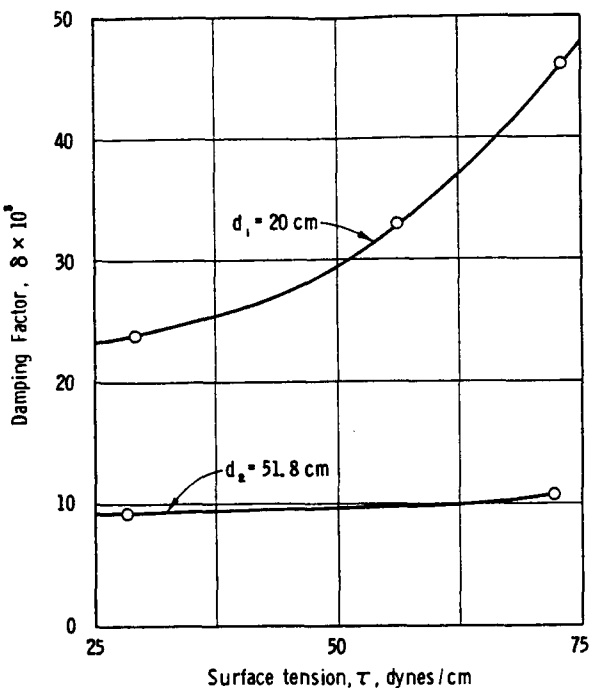


FIGURE 4.4.—The effect of surface tension on viscous damping in a cylindrical tank (ref. 4.15).

where  $C_2$  is given in figure 4.5 as a function of liquid depth. This equation reduces to equation (4.8b) for large liquid depths ( $h/R > 1.0$ ).

It was also determined from these experiments (ref. 4.15) that liquid amplitudes measured at the wall less than  $0.1R$  had no effect on the damping. This is in agreement with other studies (ref. 4.13) where no relation was found to exist between damping and liquid amplitude for a range of amplitudes at least up to  $0.05R$ .

Apparently unaware of the earlier Russian work discussed above (ref. 4.15), a similarly extensive experimental investigation was carried out by Stephens, et al. (ref. 4.13). The effects on damping of the liquid depth, efflux rate, liquid amplitude, kinematic viscosity, and tank size were investigated, and a damping factor was employed which is very similar (but not equivalent) to that given by equation (4.8a).<sup>4</sup>

$$\delta = K\nu^{1/2}R^{-3/4}g^{-1/4} \tanh\left(1.84\frac{h}{R}\right) \times \left[1 + 2\left(1 - \frac{h}{R}\right) \operatorname{csch}\left(3.68\frac{h}{R}\right)\right] \quad (4.10a)$$

<sup>4</sup> This equation was obtained independently by others (refs. 4.3 and 4.4).

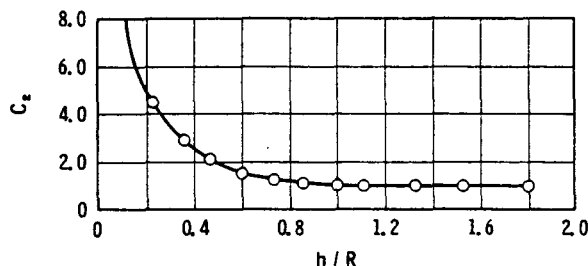


FIGURE 4.5.—Viscous damping coefficient for liquid in a cylindrical tank with a spherical bottom (ref. 4.15).

The theoretical value of  $K$  given by Miles (ref. 4.3) of  $K=0.56\times 2\pi$  differs from the value determined by these experiments of  $K=5.23$ . For large depths ( $h/R>1$ ), equation (4.10a) reduces to

$$\delta=5.23\nu^{1/2}R^{-3/4}g^{-1/4} \quad (4.10b)$$

This equation, as well as equation (4.8b) are plotted in figure 4.6, from which it is seen that either equations (4.8) or (4.10) may be used to obtain results which contain discrepancies of no more than the same order as the experimental scatter.

Some investigation was also made (ref. 4.13) to determine the effect of efflux rate on damping of the free surface displacements; no significant effect was observed for a range of efflux rates which caused surface velocities between 9.27 cm/sec and 0.266 cm/sec. It is of interest to note that two theories have been presented to predict the relationship between "damping" and tank drainage (refs. 4.1 and 4.5) and have been thoroughly discussed in reference 4.25. Except for a single term, which can generally be neglected as being small, the two theories are equivalent. It was concluded that the damping of the amplitude of the free surface displacements of a liquid during tank draining is a small positive quantity.

#### Oblate Spheroidal Tank

A limited experimental investigation has been conducted (ref. 4.12) to determine the damping of the fundamental antisymmetric mode of oscillation of water in an oblate spheroid. The damping factor was defined in the form

$$\delta=\frac{1}{n}\ln\frac{M_0}{M_n}$$

Data point	Tank radius, cm	Kinematic viscosity, stokes	Test liquid, [reference]
1	15.2	0.836	SAE 10-W oil [4.13]
2	3.8	0.00929	Water [4.4]
3	15.2	0.023	Kerosene [4.4]
4	7.6	0.00929	Water [4.4]
5	15.2	0.00929	Water [4.13]
6	38.1	0.023	Kerosene [4.13]
7	38.1	0.00929	Water [4.13]
8	45.7	0.00929	Water [4.13]
9	152.5	0.00929	Unpublished Convair / Astronautics data

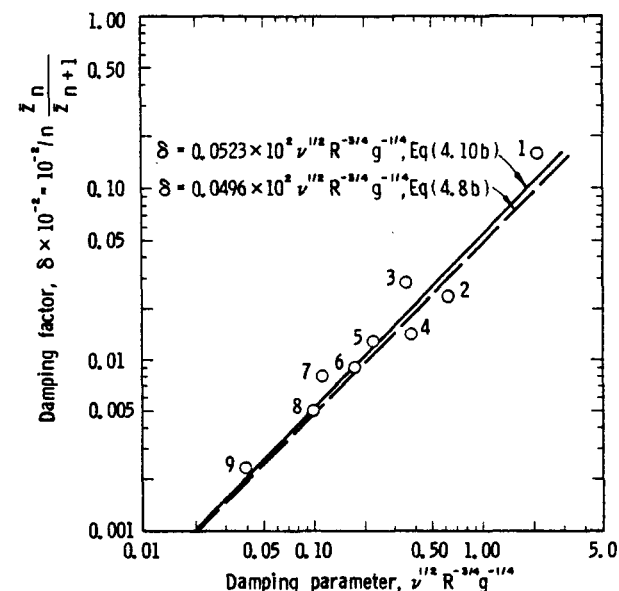


FIGURE 4.6.—Damping-viscosity-tank size relationships for liquid in a cylindrical tank (after ref. 4.13).

where  $M_0$  is the amplitude of a selected initial moment and  $M_n$  is the amplitude of the moment after  $n$  cycles of fluid oscillation. This damping factor, as a function of liquid depth, is given in figure 4.7. The increase in damping at the low liquid depths and the increase at large depths may be attributed to the shape of the container with respect to the shape of the free surface.

#### Spherical Tank

The damping characteristics of liquids in spherical tanks have also been investigated experimentally (refs. 4.14 and 4.15). The effects of kinematic viscosity, tank size, and excitation amplitude on the damping of the first-mode slosh forces were reported in refer-

ence 4.14. The liquid depth was held constant at  $h/R=1.0$ , since the maximum slosh forces in a spherical tank occur at the first natural frequency for this depth (ref. 4.26), and an empirical relationship was obtained in the form

$$\delta_N = 0.131 B^{0.359} \quad \text{for } \frac{h}{R} = 1.0 \quad (4.11a)$$

where

$$B = \frac{10^4}{2\sqrt{2}} \nu R^{-3/2} g^{-1/2}$$

The damping factor was defined by

$$\delta = \ln \frac{F_n}{F_{n+1}}$$

where  $F$  is slosh force and  $n$  indicates the cycle number. It is interesting to note that liquid swirl was never observed for those liquids having kinematic viscosities greater than approximately 0.929 stokes. The experimental data and the faired curve given by equation (4.11a) are shown in figure 4.8.

In an independent study (ref. 4.15), damping coefficients were also obtained as a function of liquid kinematic viscosity, the gravitational acceleration, tank radius, and liquid depth. The damping ratio was defined as the logarithmic decrement of the amplitude of the free surface displacements, leading to the empirical relationship

$$\delta_R = 0.08347 C_3 B^{1/2} \equiv C_3 (4.96 \nu^{1/2} R^{-3/4} g^{-1/4}) \quad (4.11b)$$

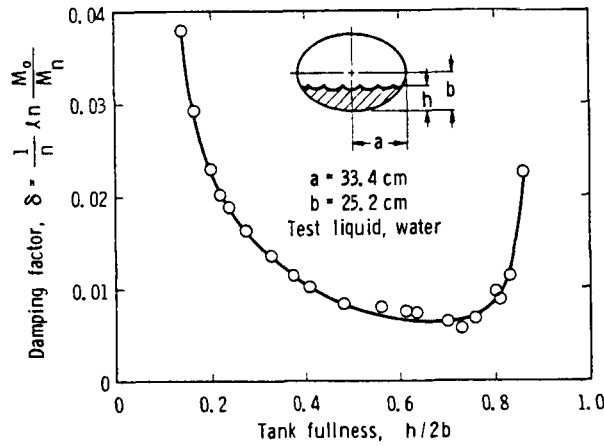


FIGURE 4.7.—Variation of damping factor with tank fullness for oblate spheroidal tank (ref 4.12).

where  $C_3$  is given as a function of  $h/R$  in figure 4.9 and  $B$  is defined in equation (4.11a). The following empirical relationships were also obtained:

$$\delta_R = 0.08347 B^{1/2} \left( \frac{R}{h} \right) \quad 0.1R \leq h \leq R \quad (4.12a)$$

$$\delta_R = 0.08347 B^{1/2} \frac{1 + 0.46 \left( 2 - \frac{h}{R} \right)}{1.46 \left( 2 - \frac{h}{R} \right)} \quad h \geq R \quad (4.12b)$$

For  $h/R < 0.1$ , equation (4.9) should be employed.

It is of interest to compare the damping factors given by equations (4.11) and (4.12) for the special case of the half-full tank. For this case,  $C_3=1.0$  and the relationship between  $\delta_R$  and  $\delta_N$  is found to be

$$\delta_N = 0.131 \left( \frac{\delta_R}{0.08347} \right)^{0.718} \quad (4.12c)$$

In general, these damping factors are not equivalent; the discrepancies may be seen in table 4.2 where the damping factors are given for water in spherical tanks of radius 15.25 centimeters and 30.5 centimeters (both references employed water to establish their equations and both employed small test tanks with radii varying from about 12.2 centimeters to 40.6 centimeters). This discrepancy may be partly explained on the basis that the relationship between the decay of the amplitude of the free surface displacements and the decay of the slosh forces is apparently nonlinear. As was discussed in chapter 3, nonlinear behavior is typical of liquid dynamics in spherical tanks.

TABLE 4.2.—Comparison of Damping Factors Given by Equations (4.11a) and (4.11b)

$R$ , cm	$\delta_N$ (eq. (4.11a))	$\delta_R$ (eq. (4.11b))	$\delta_N/\delta_R$ (eq. (4.12c))
15.25	0.031	0.011	2.61
30.5	.021	.0066	3.21

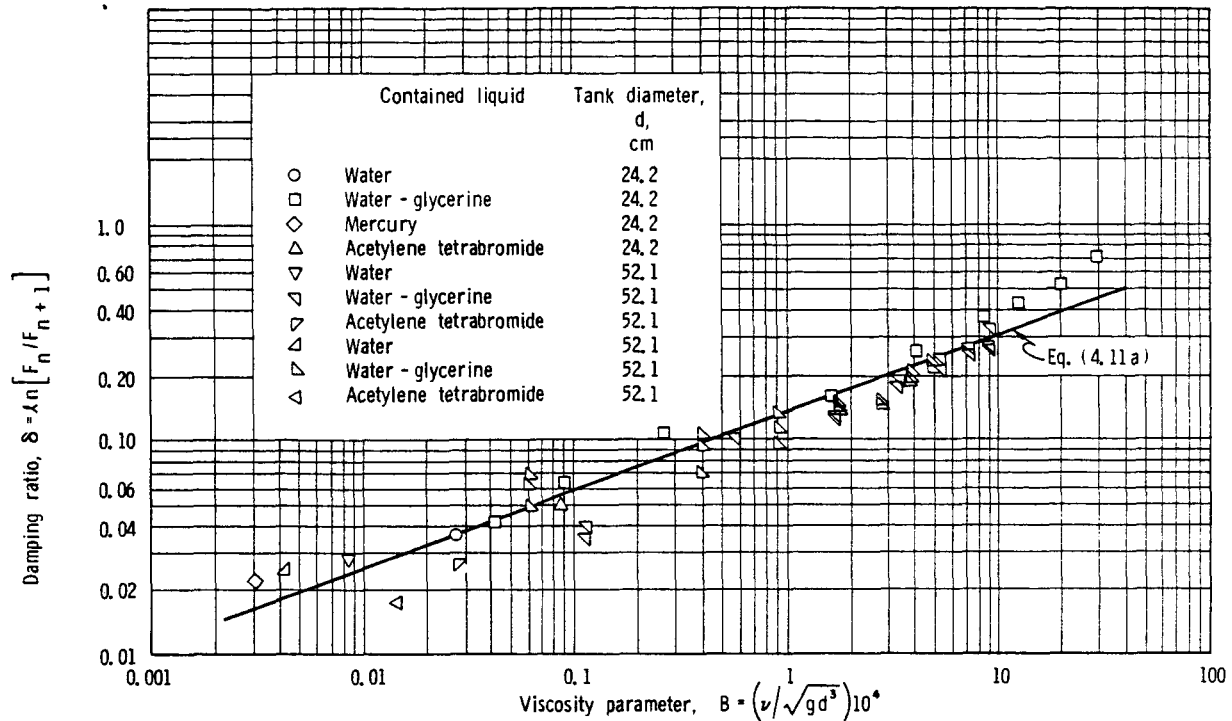


FIGURE 4.8.—Average first-mode damping ratio as a function of viscosity parameter for liquid in a spherical tank (ref. 4.14).

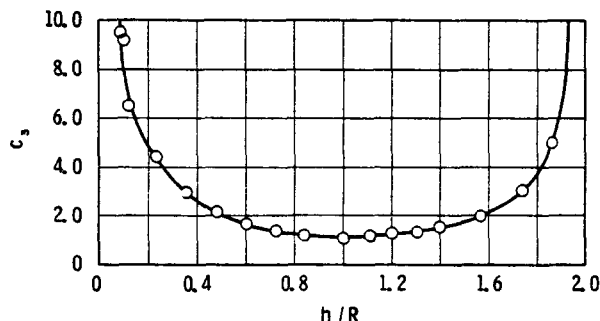


FIGURE 4.9.—Viscous damping coefficient for liquid in a spherical tank (ref. 4.15).

In reference 4.14 the damping coefficient  $\delta_N$  was observed to be independent of the excitation amplitude; in reference 4.15 the damping coefficient  $\delta_R$  was observed to be independent of liquid free surface amplitude up to amplitudes of  $0.1R$  measured at the tank wall.

#### Conical Tank

Damping of liquid motions in conical cavities narrowing upward and downward was also in-

vestigated experimentally in reference 4.15. The empirical viscous damping relationship

$$\delta = 4.964 C_4 C_5^{-1/2} \nu^{1/2} r_0^{-3/4} g^{-1/4} \quad \frac{h}{r_0} > 1.0 \quad (4.13)$$

was obtained, where  $C_4$  and  $C_5$  are given in figure 4.10 as functions of the cone semivertex angle,  $\alpha$ , for cones narrowing upward and downward, and  $r_0$  the radius of the free surface. This equation was found to be valid for  $h/r_0 > 1.0$ , and for liquid free surface displacements at the tank wall less than about  $0.01r_0$ . For amplitudes, measured at the wall, greater than  $0.01r_0$  and cone angles  $\alpha > 10^\circ$ , the damping coefficient depends upon the amplitude of the free surface displacements. For example, it was found that in a tank with a semivertex angle of  $17^\circ$ , and an amplitude of  $0.1r_0$ , the damping coefficient increases by a factor of 2. Again, damping was defined as the logarithmic decrement of the amplitude of the free surface displacements.

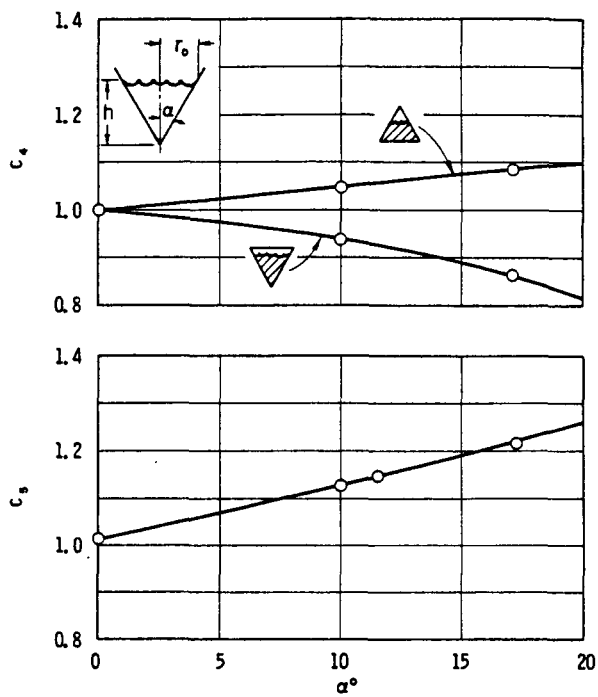


FIGURE 4.10.—Viscous damping coefficients for liquid in a conical tank (ref. 4.15).

### Toroidal Tank

A limited amount of data was obtained in reference 4.27 on viscous damping of acetylene tetrabromide in horizontally oriented toroidal tanks, with typical results shown in figure 4.11. The damping ratio tended: (1) to be independent of the tank's major radius, and (2) to decrease to a minimum value at the liquid depth ratio for which the specific slosh forces are a maximum. The damping ratio was defined by

$$\delta = \ln \frac{F_n}{F_{n+1}}$$

where  $F$  is the slosh force and  $n$  indicates the cycle of liquid oscillation. Since liquid dynamic behavior in toroidal tanks is extremely complicated (see ch. 2), the data shown in figure 4.11 should be applied to other conditions or tank orientations very cautiously.

### 4.3 DAMPING BY MOVABLE OR LIQUID SURFACE DEVICES

The necessity of damping the forces and moments produced by the sloshing liquid leads

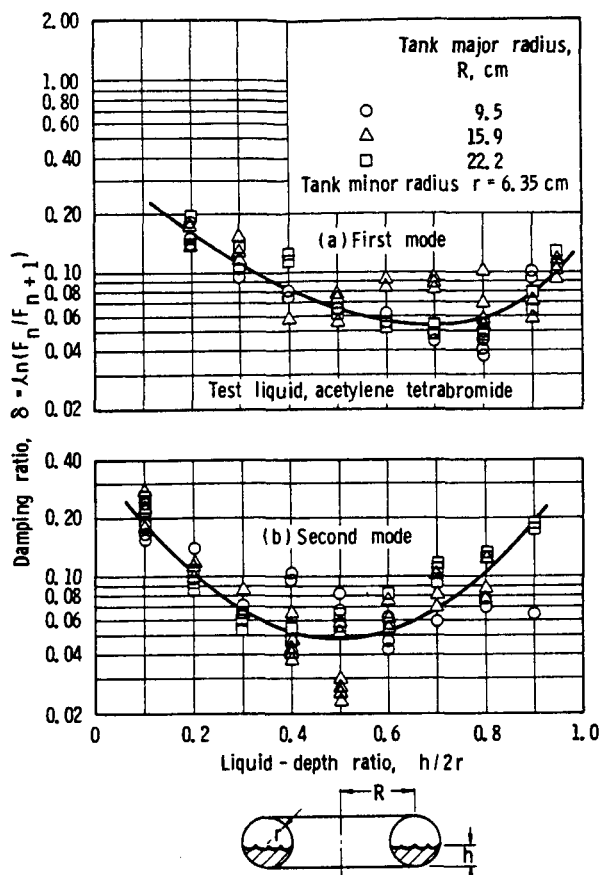


FIGURE 4.11.—Effect of liquid depth ratio on the damping ratio for acetylene tetrabromide in a toroidal tank (ref. 4.27).

one immediately to the concept of suppressing the motions of the liquid free surface. In principle, this can be accomplished by some type of rigid lid or cover which adjusts itself to the continual reduction in liquid height, or by some type of floating device that can absorb at least a portion of the energy of the moving liquid. Both of these types of devices will be discussed in the present section of this chapter, while various types of fixed slosh suppression devices (baffles) will be discussed in following sections.

### Floating Lids or Mats

The floating-lid type of liquid suppression device has been studied by Abramson and Ransleben (ref. 4.20). Experiments were conducted in circular cylindrical tanks having conical bottoms; rigid lids or covers were constructed of solid plates with diameters of 99,

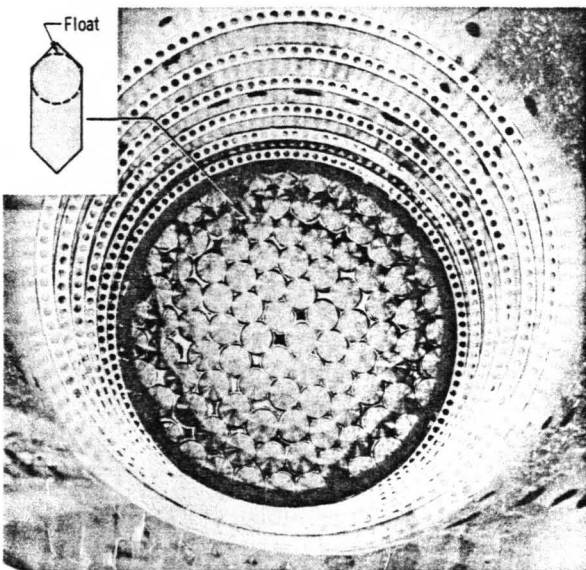


FIGURE 4.12.—Floating can slosh suppression device.

85, and 67 percent of the tank diameter. Other variables investigated were liquid density and viscosity (three liquids were used), excitation amplitude, and excitation frequency. It was concluded that: (1) the floating-lid-type device having a diameter of 85 percent or more of the tank diameter provides very high force damping,<sup>5</sup> (2) the peak force response increases with increasing values of the ratio  $\rho/\nu$ , and (3) the forces acting directly on the lids<sup>6</sup> appeared to be rather large so that significant weight penalties may be involved with the use of such devices. Of course, in actual practice, the inner tank wall of a propellant tank is generally a complex arrangement of stringers, stiffeners, other structural elements, plumbing, and so forth, so that a lid diameter of the order of 85 percent to 90 percent may be difficult to achieve unless the tank is a very large one.

Eulitz (ref. 4.18) also studied the possibility of employing a porous layer of material (commercially available coco-fiber mat) on the liquid surface, similar to the rigid lid discussed above. Aluminum spheres were embedded in this

<sup>5</sup> The damping factor was not explicitly calculated, this conclusion being reached by observation and comparison of the force response curves.

<sup>6</sup> Forces were actually measured by means of special dynamometer linkages.

material to obtain necessary buoyancy. While this technique was rather effective in suppressing liquid motions, difficulties were encountered in practical applications by virtue of the mat "hanging-up" and not remaining on the liquid surface.

#### Floating Cans

Floating devices, aptly described as "floating cans" (see fig. 4.12), were also proposed by Eulitz (ref. 4.18), and later investigated in detail by Abramson and Ransleben (refs. 4.19 and 4.21). These devices were fabricated of thin perforated material, employing a hollow sphere for buoyancy. The damping of liquid-slosh forces was fairly effective only when the cans were packed closely, but even so was less than could be obtained from fixed baffles (ref. 4.19).

#### Expulsion Bags and Diaphragms

Positive expulsion bags and diaphragms of elastomeric materials have been considered for the purpose of liquid transfer in a low gravity environment (ch. 11). The slosh force damping produced by these devices has been investigated by Stofan (refs. 4.16 and 4.17). The variables considered were tank size, diaphragm and bag thickness, and excitation amplitude. Since a slosh force parameter was used which is independent of liquid density and since maximum slosh forces in a spherical tank occur for the half-full tank, the liquid density and depth of fluid in the tank were considered only briefly. Slosh forces in a  $\frac{1}{4}$ -full spherical tank were investigated employing two liquids: mercury (ref. 4.16) and acetylene tetrabromide (ref. 4.17).

In general, it was found that significant damping of the force response was obtained, but was strongly dependent upon the diaphragm thickness. The second-mode force peak and liquid swirl were completely suppressed. The force parameter also increased with increasing excitation amplitude and appeared to increase with decreasing tank size. It should also be noted that as the diaphragm thickness increased, the peak slosh forces occurred at succeedingly higher values of excitation frequency.

The force damping data (the damping ratio was defined as  $\delta = \ln \frac{F_n}{F_{n+1}}$ ) exhibited considerable scatter (fig. 4.13). In general, the damping ratio increased with increasing diaphragm thickness and excitation amplitude (fig. 4.14) and decreasing tank diameter. Some effect of excitation frequency on the damping was observed in the 81.4-centimeter-diameter tank. Expulsion bags appeared to perform similarly to the diaphragms (fig. 4.14).

#### 4.4 DAMPING BY FIXED BAFFLES: NONRING TYPE

An almost bewildering array of baffle types and arrangements, all with the common feature of being fixed in location within the container, have been proposed. Basically, all these may be categorized as being generally of the form of annular rings or not. The present section is confined to the latter.

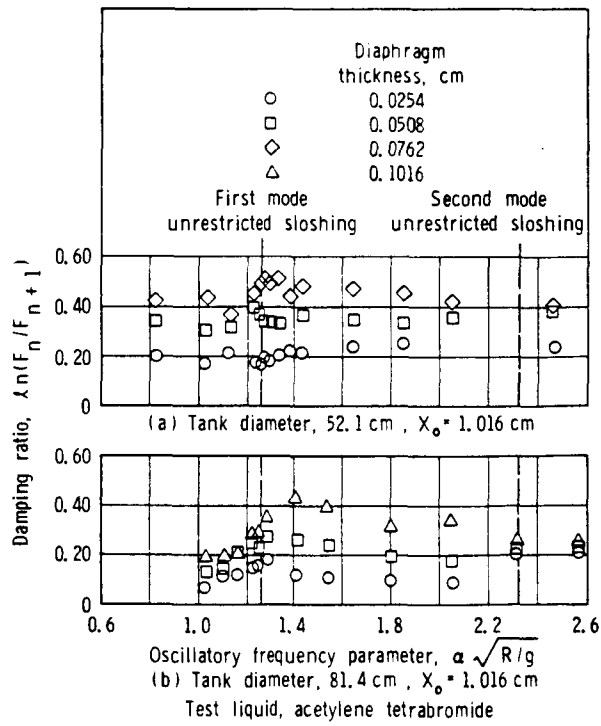


FIGURE 4.13.—Effect of diaphragm thickness on damping ratio for constant excitation amplitude (ref. 4.17).

#### Cruciform Baffles

Damping produced by cruciform baffles (fig. 4.15) has been investigated in references 4.12, 4.28, and 4.29. These baffles are located physically in the same manner as a stringer, so that for the circular cylinder there is the advantage of damping being independent of liquid depth; for the spheroid and the sphere, of course, damping is not independent of depth. The disadvantage of this configuration is that it provides only a relatively small amount of damping.

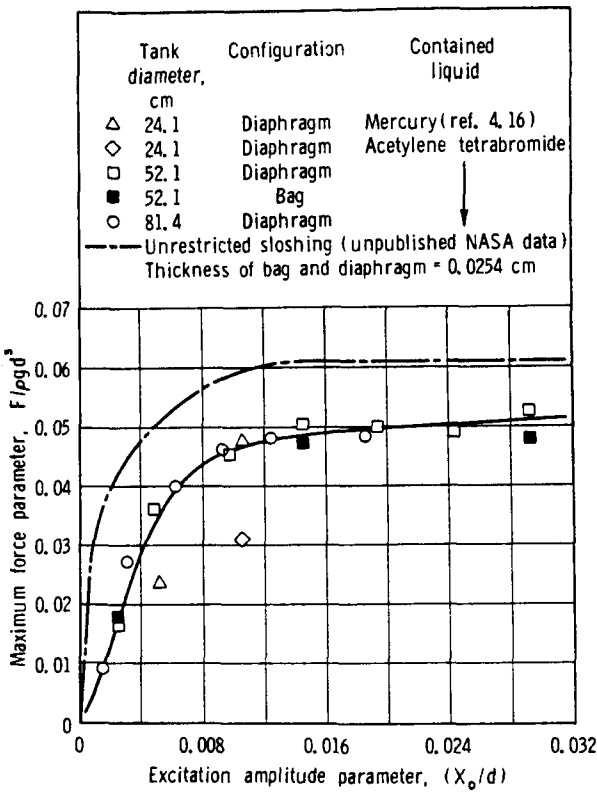


FIGURE 4.14.—Effect of excitation amplitude parameter on maximum force parameter (ref. 4.17).

Table 4.3 shows damping factors in a circular cylinder tank with cruciform baffles oriented 45° and 90° to the direction of excitation (ref. 4.28). Figure 4.16 shows the variation of damping with liquid depth for an oblate spheroid; the damping increases with decreasing depth.

Damping provided by cruciform (vertical configuration) baffles in a sphere (fig. 4.17) has been investigated in reference 4.29. By

TABLE 4.3.—*Damping Ratios for Cruciform Baffles in a Cylindrical Tank*

[Ref. 4.28]

Orientation, deg (fig. 4.15)	$\frac{w}{R}$	$\delta = \frac{1}{n} \ln \frac{M_0}{M_n}$
45	0.169	0.07
	.337	.169
90	.169	.072
	.337	.156

rotating figure 4.17 by 90°, the symmetry of the sphere yields a completely different baffle arrangement (horizontal configuration). Force response curves for both baffle arrangements are shown in figure 4.18, compared with similar data for the unbaffled tank.<sup>7</sup> Note that the horizontal configuration of the baffles gives vastly more reduction in slosh force than does the cruciform arrangement.

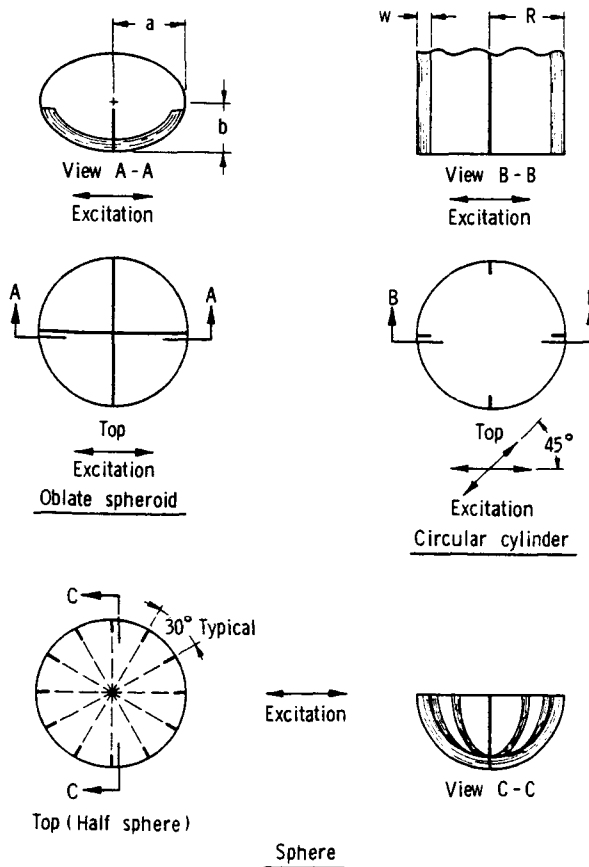


FIGURE 4.15.—Cruciform baffle configurations.

### Sector Compartmented Tanks

As discussed in detail (ch. 2), a very much used tank configuration is the circular cylinder compartmented into sectors by means of radial walls.<sup>8</sup> Of course, the principal reason for employing partitions is to shift the liquid resonant frequencies into a more desirable range, while perforations are introduced for weight reduction and only secondarily to reduce the amplitude of the liquid oscillations.<sup>9</sup> It is thus seen that perforation must add damping without lowering the resonant frequencies, or else the underlying reason for employing the partitions is defeated. The effects of sector wall perforation on the resonant frequencies and damping ratio as functions of excitation amplitude and frequency, percent and size of hole perforations, and liquid density and viscosity have been investigated experimentally (refs. 4.30 through 4.32). Damping factors were obtained from the force response curves by employing the bandwidth technique. The direction of translation with respect to the sector walls is as indicated in figure 2.10 of chapter 2, and size and liquid depth were generally held constant at  $d=36.6$  centimeters and  $h/2R=1.0$  (water).

### Liquid Resonant Frequencies

The variation of liquid resonant frequency with perforation size, excitation amplitude, and liquid density and viscosity has been described for a given percentage opening and tank size in terms of an "equivalent Reynolds number" parameter, as shown in figure 4.19. This representation seems about as effective as any, in view of the overall complexity of the data. The most important feature of these curves, obviously, is the large decrease in resonant frequency with increasing perforation hole size and percent open area. Clearly, the desired upward shift in frequencies to be obtained by

<sup>7</sup> These data are also compared with the response calculated for the cruciform (vertical configuration) baffle case by an equivalent mechanical model theory (ref. 4.29) (see also ch. 6). This theory, being completely linear, does not provide very good predictions.

<sup>8</sup> See ch. 3 for a discussion of significant nonlinear effects in compartmented tanks.

<sup>9</sup> Recall that reduction in total force response in compartmented tanks may occur as the result of phasing between sectors. (See chs. 2 and 3.)

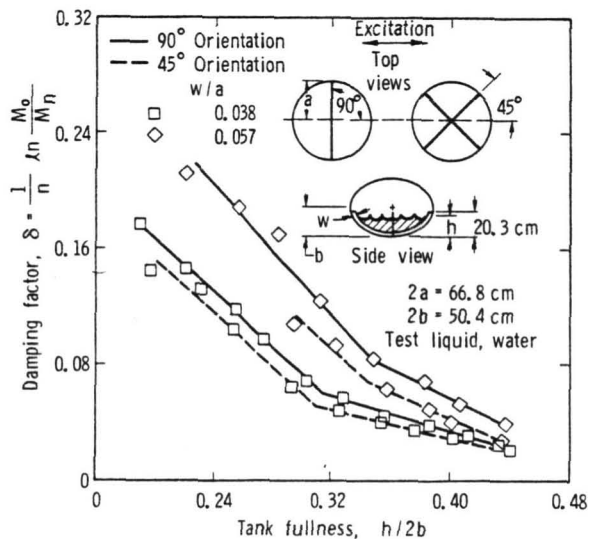


FIGURE 4.16.—Variation of damping factor with tank fullness for cruciform baffles in an oblate spheroid (ref. 4.12).

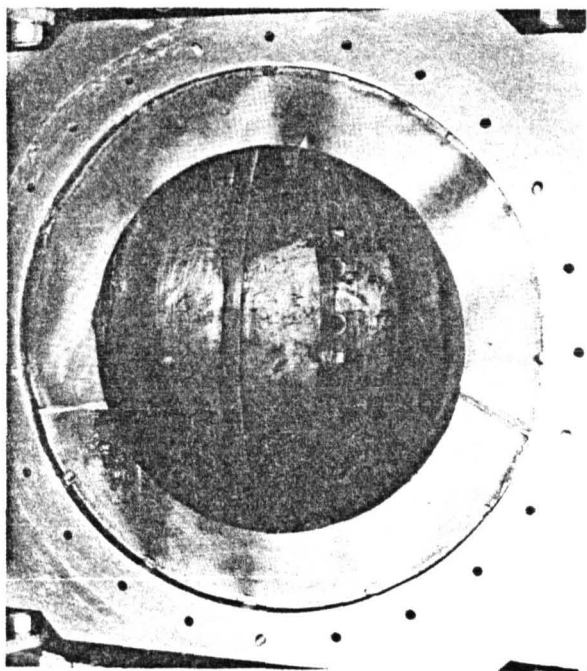


FIGURE 4.17.—Vertical (cruciform) baffle arrangement in spherical tank (ref. 4.29).

compartmentation can be completely nullified by overzealous attempts at weight saving by perforation. The precise nature and definition of the transition between the two frequency branches involves a complex interaction between various of the parameters.

#### Liquid Damping

The damping at the resonant frequency for the 90°, 60°, or 45° solid wall tanks is low, averaging approximately 0.04. However, at frequencies below the resonant value, the liquid sloshing is effectively damped. The experimental data (ref. 4.32) showed that perforated sectors with less than 10 percent open area will increase the damping ratio to approximately 0.1 while maintaining a liquid resonant frequency corresponding to a solid wall compartmented tank. For partitions with open areas greater than 10 percent, the damping produced is greater than 0.10, but the corresponding liquid resonant frequencies approach that of an uncompartmented cylindrical tank. The liquid viscosity and excitation amplitude have as large an effect on the liquid damping ratios as do the perforation hole size and percent of open area, and as much as all of these factors have on the liquid resonant frequencies.

Attempts to present the damping ratios versus Reynolds number, or other various parameters which include the factors affecting the damping, failed to yield an effective picture of these complex data. The best that could be done is something such as that shown in figure 4.20, which is a three-dimensional plot of the damping ratio versus the dimensionless resonant frequency parameter,  $\omega^2 d/g$ , and the percentage of open sector area for a 45° sectored tank. The results presented (ref. 4.33) are for three values of  $x_0/d$ , with water and methylene chloride as the test liquids. Maximum damping is produced for sectors with open areas of 16 to 23 percent. However, the excitation amplitude must be quite large to maintain the resonant frequency corresponding to solid sector walls. Additional tests with sectors of smaller hole diameter ratios ( $d_h/d = 0.00139$  and 0.00278) and open areas up to 23 percent increased the damping ratios to an average value of 0.15 while maintaining a frequency corresponding to the solid wall sector tank. Above 23 percent open area, the results become inconsistent in frequency and damping ratio.

Test results for 60° and 90° tanks with  $d_h/d = 0.0056$  are also available (ref. 4.33). For the 60-percent sector tank, increased damping

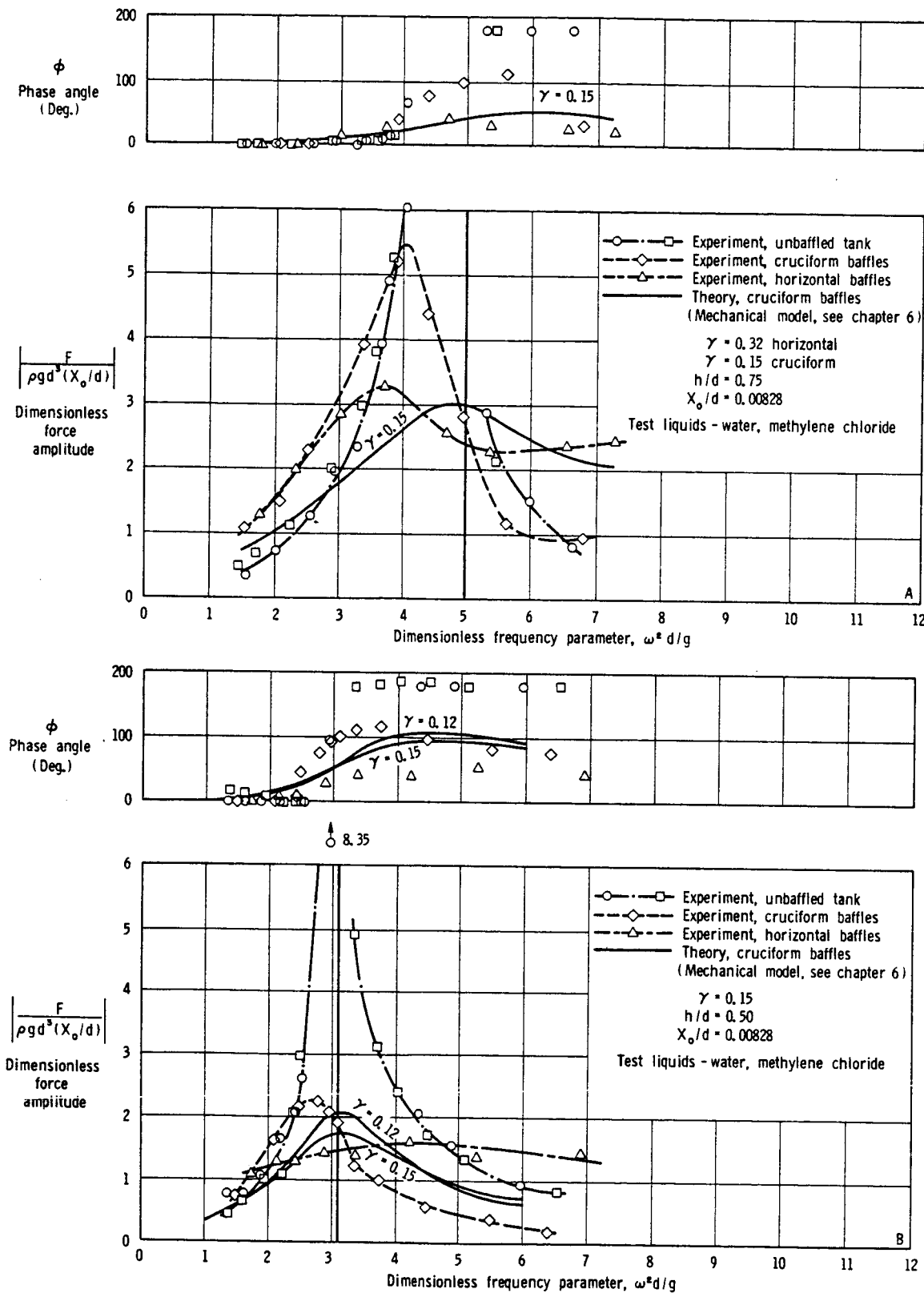


FIGURE 4.18.—Liquid force response in a baffled spherical tank (ref. 4.29).

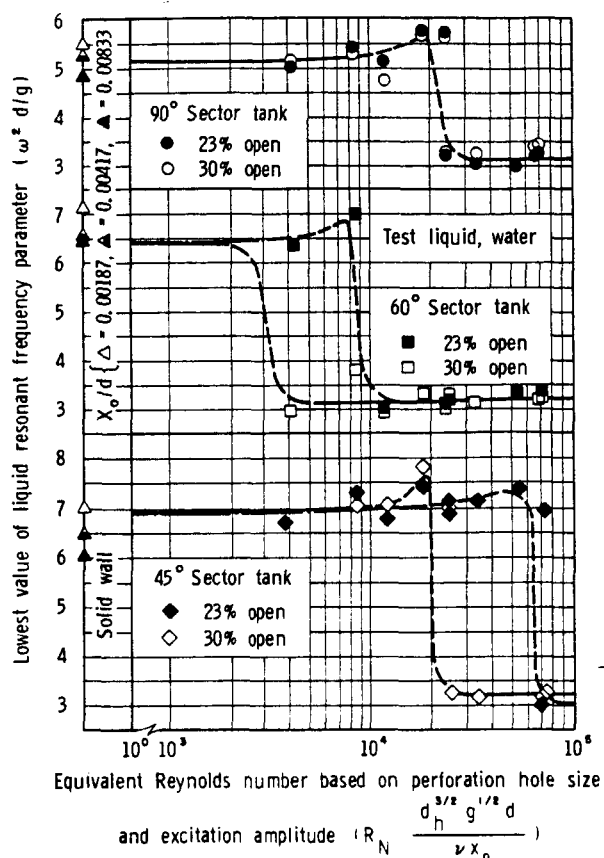


FIGURE 4.19.—Variation in lowest liquid resonant frequency for 90°, 60°, 45° sector tanks with equivalent Reynolds number (ref. 4.32).

ratios at frequencies corresponding to the solid sector wall exist only for open areas between 8 and 16 percent open area, depending on the excitation amplitude. Additional tests with  $d_h/d=0.00139$  and  $0.00278$  yielded mean damping ratios of approximately 0.12 at 16 percent to 23 percent open sector area, depending on excitation amplitude. The smaller open area corresponds to the lower excitation amplitudes. In the 90° tank, sectors with  $d_h/d=0.0056$  lose their compartmentation effect at small excitation amplitudes; however, tests with sector walls having  $d_h/d=0.00139$  and  $0.00278$  and up to 30 percent open area produced mean damping ratios of 0.12 at frequencies corresponding to the solid sector wall for  $x_0/d=0.00417$  and  $0.00833$ . Tests at  $x_0/d<0.00417$  with  $d_h/d=0.00139$  gave results similar to the solid sector. The results for  $d_h/d=0.00279$  were inconclusive,

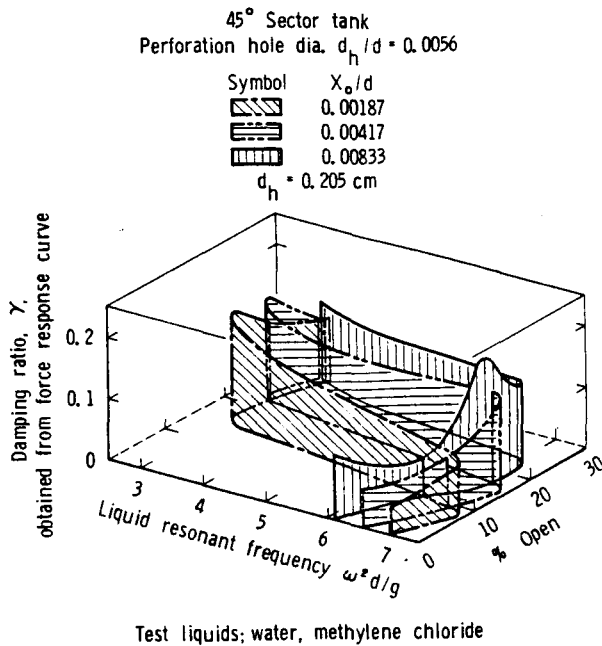


FIGURE 4.20.—Variation in damping ratio for 45° sector tank (ref. 4.33).

and no consistent damping ratios or resonant frequencies could be obtained.

#### Asymmetrical Plate Segment Baffles

Baffles having the form of a segment of a circular plate, and mounted normal to the wall in a circular cylindrical tank, have been investigated in references 4.23, 4.34, and 4.35. Experiments conducted in reference 4.23 indicated that these baffles could possibly provide large values of damping by transferring energy from the first mode of liquid oscillation into a high frequency checkerboard mode. Subsequent experiments carried out in reference 4.34 indicated that one particular asymmetric baffle arrangement provided more damping than did one particular ring baffle. (The areas of the two types of baffles were equivalent and they were equal to 16 percent of the cross-sectional area of the tank.) Somewhat contrasting results were obtained by Garza (ref. 4.35), who found that a particular ring baffle provided greater damping than did a particular asymmetric baffle at baffle depths from  $d_s/R=0$ , to  $d_s/R=0.12$  and approximately the same amount of damping at greater depths. In the latter experiments, the baffle area was 28 percent of

the tank cross-sectional area; the experimental results obtained are shown in figure 4.21. These contrasting results are not contradictory because of the different baffle areas involved; however, they do indicate clearly the need for further experiments before asymmetric baffles can be recommended for use in design.

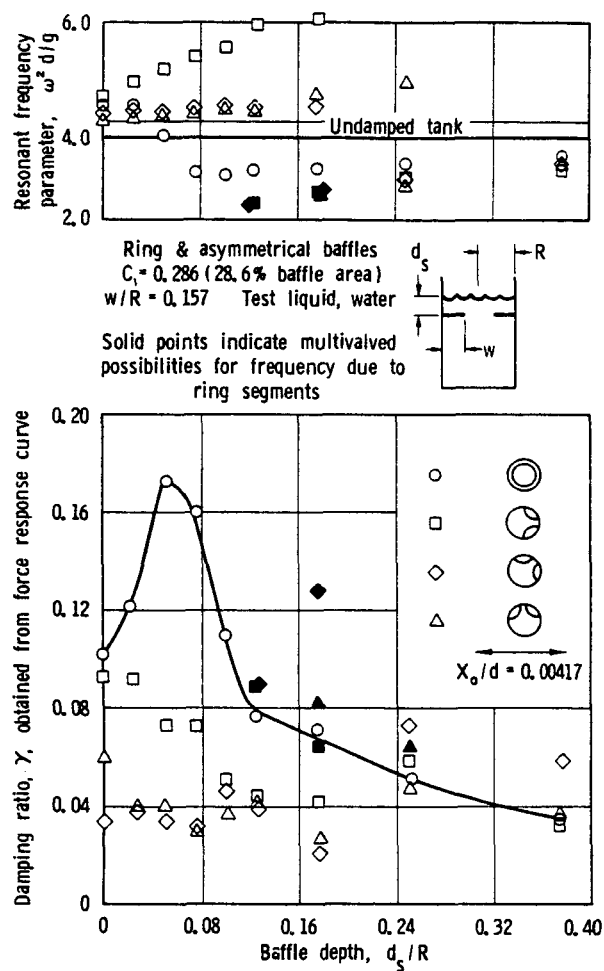


FIGURE 4.21.—Liquid resonant frequencies and damping ratios for ring and asymmetrical baffled cylindrical tanks (ref. 4.35).

#### 4.5 DAMPING BY FIXED BAFFLES: RING TYPE

##### Introduction

Symmetrical ring baffles, often perforated to save weight, are commonly used in rockets and spacecraft to reduce the effects of propellant sloshing. The damping of liquid motions in cylindrical tanks by ring baffles has

been studied experimentally in quite some detail and, to some extent, theoretically as well. As we discussed early in this chapter, Miles (ref. 4.2) using data based upon reference 4.36 succeeded in obtaining an analytical expression for the free surface damping produced by a solid ring baffle. The range of validity of Miles' theory was later extended (ref. 4.6). Bauer (ref. 4.37) modified Miles' results to account for the fact that part of the baffle may emerge from the liquid during a slosh cycle. The damping caused by the ring baffle breaking through the free liquid surface, though, is not accounted for (fig. 4.22). Experiments (refs. 4.6 and 4.11) have indicated, as we saw in figure 4.3, that for a certain baffle and tank geometry, this damping can be considerably larger than that predicted by Miles. For greater baffle depths, the theoretical predictions are generally quite good.

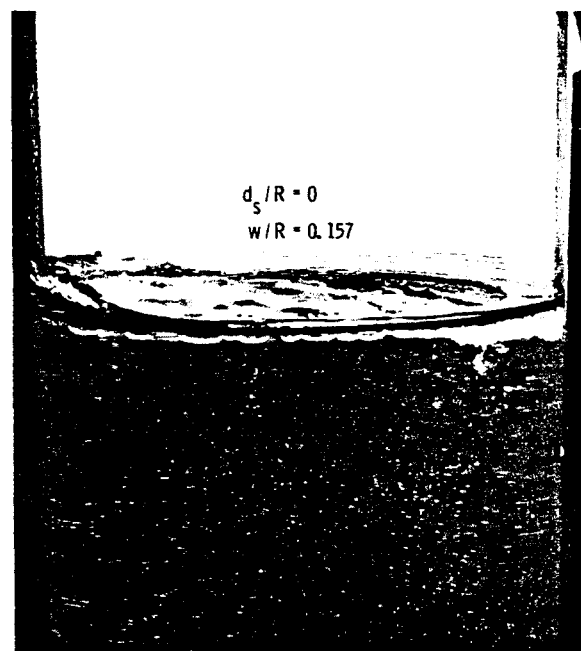


FIGURE 4.22.—Interaction between a flat solid-ring baffle and the liquid free surface at shallow liquid depth (ref. 4.38).

A great variety of modifications to the basic flat, solid annular ring baffle can easily be envisioned, some of which are sketched in figure 4.23. Generally, it appears that anything that is done to reduce the sharpness of

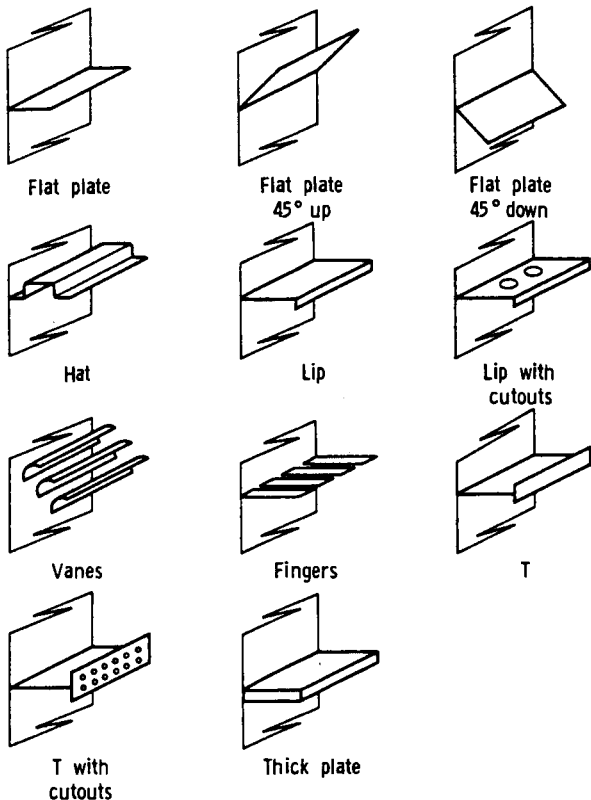


FIGURE 4.23.—Ring baffle configurations (ref. 4.23).

the edge plate (lip, sandwich, *T*, etc.) reduces the baffle effectiveness. Rings with radial clearance, conic sections (perforated and unperforated), and cruciforms in spheroidal tanks have all been investigated (ref. 4.28). Nearly all of these experiments have indicated the superiority of flat ring baffles in providing a great deal of damping for relatively small weight penalties. We shall therefore devote considerable discussion to these within the following pages.

#### Ring Damping in Cylindrical Tanks—Theory

The damping of liquid free surface oscillations in a circular cylindrical tank by a flat solid ring baffle has been predicted theoretically, as we have already noted, by Miles (ref. 4.2). The theory has been extended by O'Neill (ref. 4.6) and modified by Bauer (ref. 4.37).

The liquid, oscillating in its fundamental mode, produces a wave having its maximum amplitude at the wall. The direction of flow in the vicinity of the wall is essentially vertical,

and thus normal to an annular ring located a small distance below the free surface. Energy dissipation results from wave motion being opposed by the ring pressure  $\frac{\rho v^2}{2} C_D$ , where  $v$  is the local wave velocity producing the pressure and  $C_D$  is the local drag coefficient. It is then shown (ref. 4.2) that the damping ratio for ring damping in a circular cylindrical tank can be expressed by

$$\gamma = 0.473 e^{-5.52 \frac{d_s}{R}} C_1 \left( \frac{\bar{z}}{R} \right) C_D \quad (4.14)$$

where  $d_s$ ,  $c$ , and  $\bar{z}$  are related to tanks geometry and are shown in figure 4.2. This relationship is based upon the assumptions: (1) the fluid is oscillating in its fundamental mode and linearized potential theory accurately describes the flow except in a small region near the ring; (2) the local flow in the region of the ring is unaffected by the free surface or the tank bottom; (3) the circular frequency is accurately approximated by the potential flow solution for the undamped circular frequency (see ch. 2); and (4) the drag coefficient is independent of the angular coordinate. Assumptions (1) and (2) require that

$$C_1 \ll 1, \quad h - d_s > w, \quad h - d_s > \bar{z}$$

while assumption (3) requires that the damping be moderately small.

An expression for the drag coefficient, based upon certain experimental data (ref. 4.36), was presented by Miles as

$$C_D = 15 \left( \frac{U_m T}{D} \right)^{-1/2}, \quad 2 < \frac{U_m T}{D} < 20$$

where  $U_m$  is the timewise maximum velocity,  $T$  the period, and  $D$  the plate width. For large liquid depths,  $h/2R > 1$ , and for the dominant sloshing mode in a cylindrical tank, the above expression for  $C_D$  can be rewritten (employing the present notation) as

$$C_D = 15 \left[ \frac{2\pi}{C_1} e^{-1.84 \frac{d_s}{R}} \left( \frac{\bar{z}}{R} \right) \right]^{-1/2} \quad (4.15)$$

Substitution of equation (4.15) into equation (4.14) yields the damping ratio

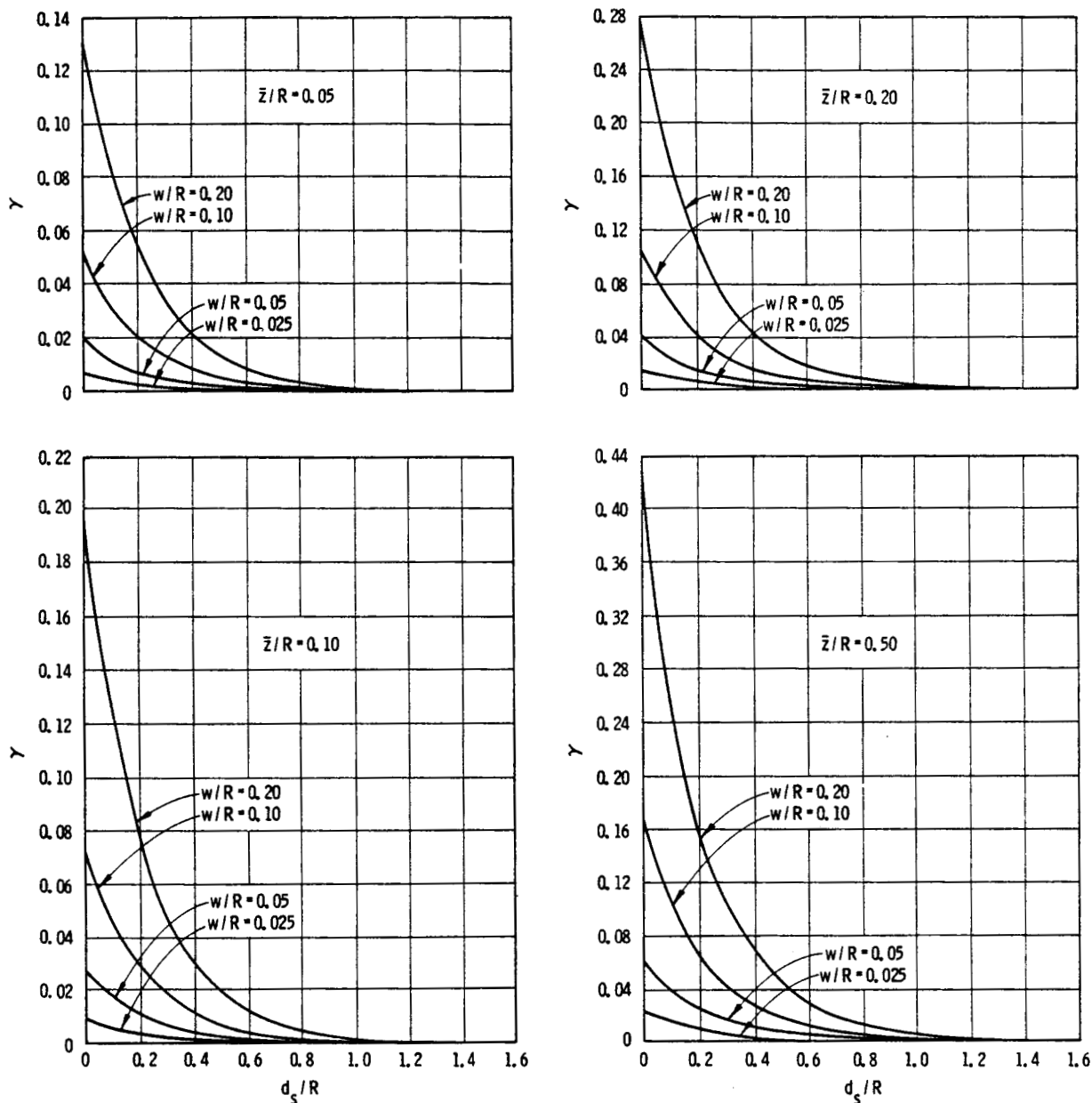


FIGURE 4.24.—Damping factor as a function of baffle depth calculated from Miles' theory (after ref. 4.37).

$$\gamma = 2.83 e^{-4.6 \frac{d_s}{R}} C_1^{3/2} \left( \frac{\bar{z}}{R} \right)^{1/2} \quad (4.16)$$

It should be noted that the damping decreases exponentially with increasing  $d_s/R$ . Calculated curves of damping factor versus baffle depth for various liquid amplitudes and with baffle width as a parameter are shown in figure 4.24.

Two significant contributions relative to equation (4.16) have been made in reference 4.6. First, the dimensionless force parameter  $F/\rho g R^3$  was introduced<sup>10</sup> and the maximum value of this parameter was related to  $\bar{z}$  by

<sup>10</sup> This force parameter is based upon the similitude theory presented in ref. 4.19, and is generally employed as it is often easier to measure than is the liquid amplitude.

employing linearized potential theory. For liquid oscillations in the fundamental mode in a deep tank, the relationship is

$$\left(\frac{F}{\rho ngR^3}\right)_{\max} = 1.71 \left(\frac{\bar{z}}{R}\right)$$

where  $ng$  is the acceleration along the tank axis. Substituting this into equation (4.16) yields

$$\gamma = 2.16 e^{-4.60 \frac{d_s}{R}} C_1^{3/2} \left(\frac{F}{\rho ngR^3}\right)_{\max}^{1/2} \quad (4.17)$$

Either equation (4.16) or (4.17) may be used to calculate the damping ratio. The advantage in using equation (4.17) is that no visual observation of the sloshing liquid itself, but only the force, is required. The second significant contribution is the extension of the range of validity of equations (4.16) and (4.17) through experimental observations. It was indicated that these equations may be employed for any value of  $\frac{\bar{z}}{R}$  or  $\left(\frac{F}{\rho ngR^3}\right)$  pertinent and reasonable for ring damping in propellant tanks, for any ring submergence  $\frac{d_s}{R} \geq 0$ , and for ring widths corresponding to  $C_1 < 0.25$ .

The data did have considerable scatter, but most of the damping ratios fell within  $\pm 30$  percent of the predicted values.

It should be noted that Bauer (ref. 4.37) has developed extensive plots from Miles' theory

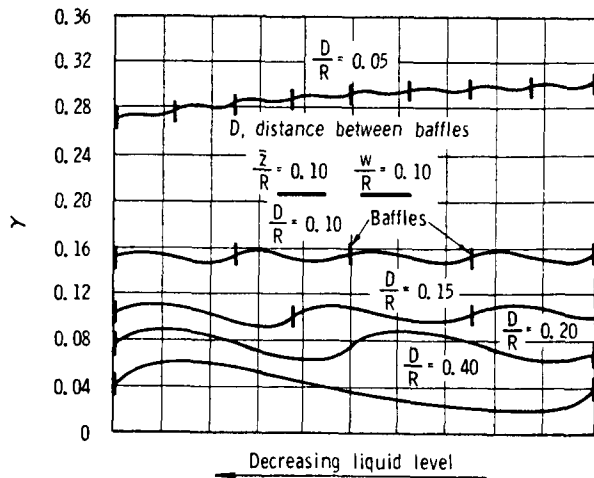


FIGURE 4.25.—Damping factor for a series of ring baffles calculated from Miles' theory (ref. 4.37).

showing the damping ratio for various values of baffle depth, baffle width, liquid amplitude, and baffle location. (See fig. 4.24.) He also computed the damping ratio as a function of liquid depth in a tank having a number of ring baffles, as shown typically in figure 4.25. The figure shows the effects of various baffle spacing and is based on 10 baffles above and 10 below the undisturbed liquid free surface.

As we discussed earlier, Bauer (ref. 4.37) also attempted to account for the condition during sloshing where part of the baffle emerges from the liquid. The effect is shown in figure 4.26 and can be compared directly with Miles' result from figure 4.24 (see also fig. 4.3).

#### Ring Damping in Cylindrical Tanks—Experiment

Damping produced by ring baffles in cylindrical tanks has been investigated extensively in a number of the references already cited in this chapter as well as in reference 4.38. Most of these studies have indicated that: (1) the flat ring baffle is a very effective damping device, and (2) the damping ratio is approximately independent of the mode of excitation (pitching or translation).

The experiments of O'Neill (ref. 4.6), as discussed previously, have extended the validity of the range of the ring damping theory of Miles and have compared various methods of obtaining the damping factor. Abramson and

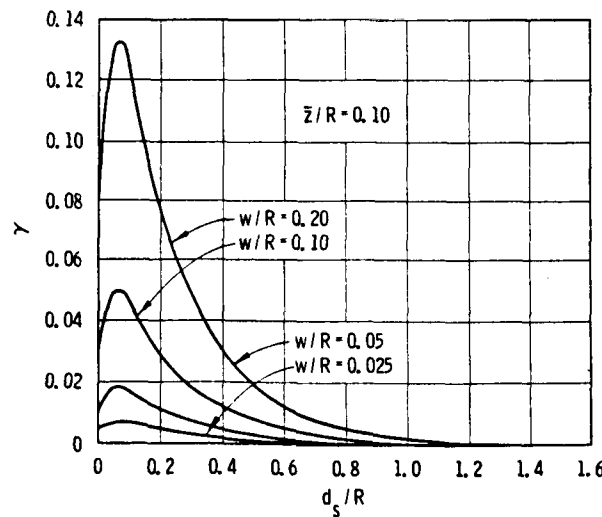


FIGURE 4.26.—Damping factor as a function of baffle depth calculated from Bauer's theory (ref. 4.37).

Garza (ref. 4.11) and Stephens (ref. 4.28) have investigated in detail various geometrical parameters and their effects on liquid resonant frequency and damping ratio. We shall present and discuss various of these results in the following paragraphs.

#### Liquid Resonant Frequency

The presence of a baffle obviously modifies the liquid resonant frequency, especially when it is located near the liquid surface (ref. 4.28). Figure 4.27 shows this effect, with baffle width as a parameter, for a single flat solid ring baffle. For perforated baffles, the frequency becomes dependent upon both the perforation hole size and the percent open (ref. 4.11), as can be seen in figures 4.28 and 4.29. (Solid ring baffle data are also included in these figures, for comparison; the effects of baffle width are given in fig. 4.27.) All of these experimental data show, generally, that the liquid resonant frequency is a maximum for a baffle located at the liquid free surface, decreases to a minimum at a baffle depth near  $d_s/R=0.10$ , and then increases gradually with increasing  $d_s/R$  until the

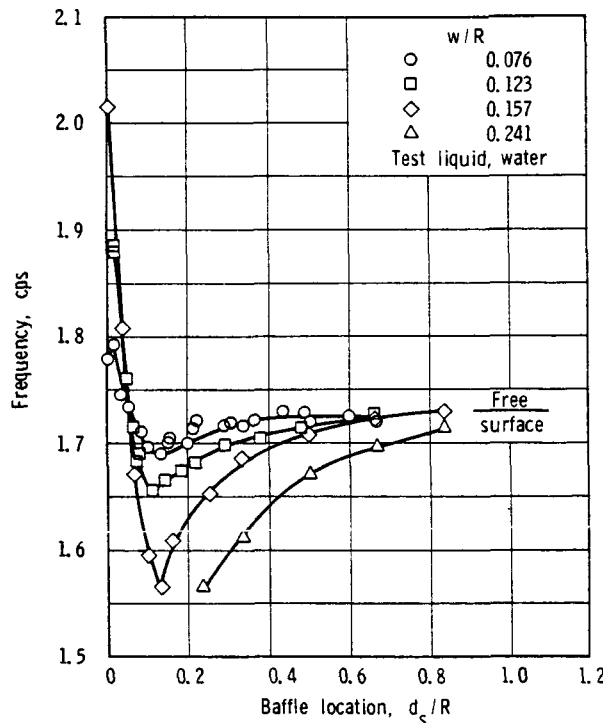


FIGURE 4.27.—Variation in liquid resonant frequency with baffle location (ref. 4.28).

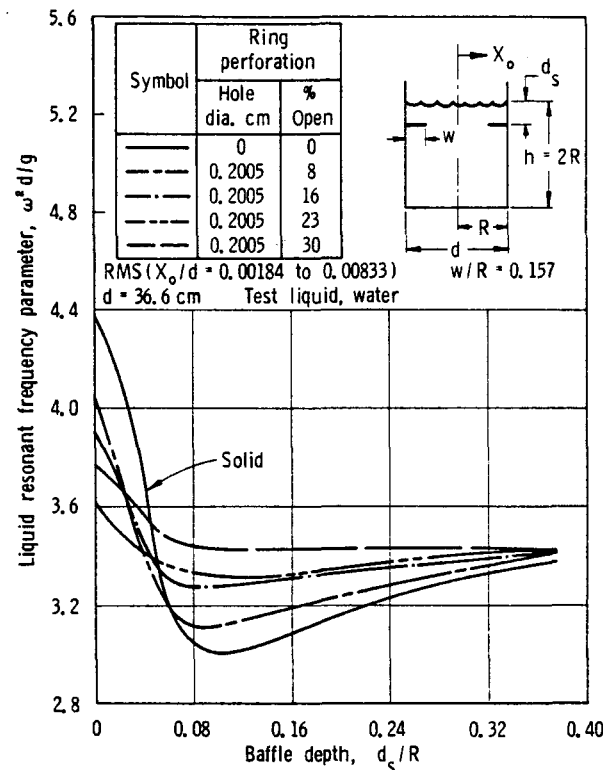


FIGURE 4.28.—Effect of percent perforation on liquid resonant frequencies as a function of baffle depth (ref. 4.11).

first liquid resonant frequency of an unbaffled tank is reached. For baffle depths greater than  $d_s/R=0.06$ , it may be observed that for 0.201-centimeter-diameter hole perforations the frequency increases with increasing percent of hole perforations; the frequency also increases with perforation hole size for a given percentage perforated area. Since the excitation amplitude significantly affects the frequency, measurements were made for various values ranging from  $0.00184 \leq x_0/d \leq 0.00823$  and then the data presented in terms of rms values.

For design purposes, the axial spacing between each of a series of ring baffles should be less than about  $d_s/R=0.08$ . This configuration yields the highest possible resonant frequency which can be maintained with a given baffle system. This effect is shown in figure 4.30 for two ring baffles.

#### Liquid Damping

The damping ratio for flat single-ring baffles is quite dependent upon excitation amplitude,

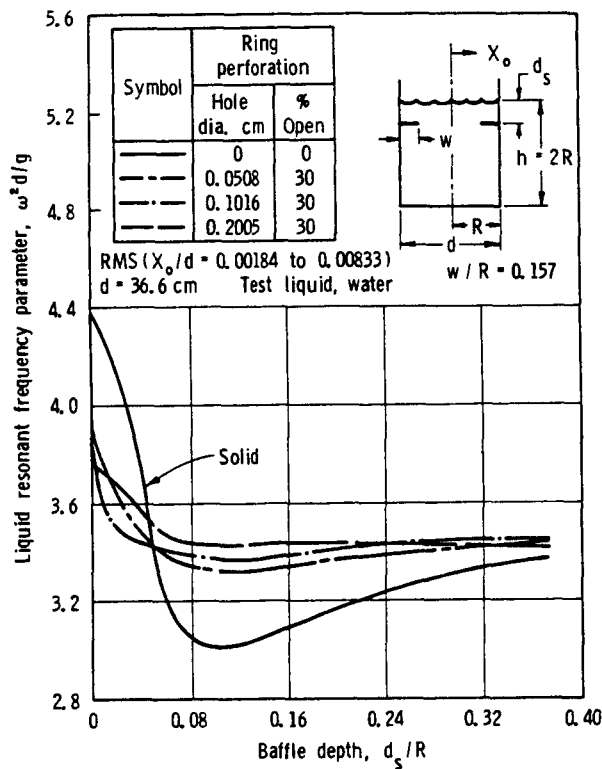


FIGURE 4.29.—Effect of perforation hole size on liquid resonant frequencies as a function of baffle depth (ref. 4.11).

as shown in figure 4.31, so that the various data will again be presented in terms of rms values. Figures 4.32 and 4.33 show the effects of percent perforation and hole size on damping factor, while figure 4.34 again shows the effect of baffle width, for solid ring baffles.

We have already discussed in detail the correlation with theory, as shown in figure 4.3, and, therefore, shall avoid repetition in this section.

The effects of liquid kinematic viscosity on the resonant frequency and damping ratio were not considered in these experiments (ref. 4.11); however, if the trends established in cylindrical tanks having perforated partitions (sec. 4.4) can be used as crude criteria, then it may turn out that the effects of kinematic viscosity are significant for perforated ring baffles.

Tests were also conducted with two solid ring baffles in the tank to determine the effects on damping—one baffle being placed above and one below the liquid surface, the

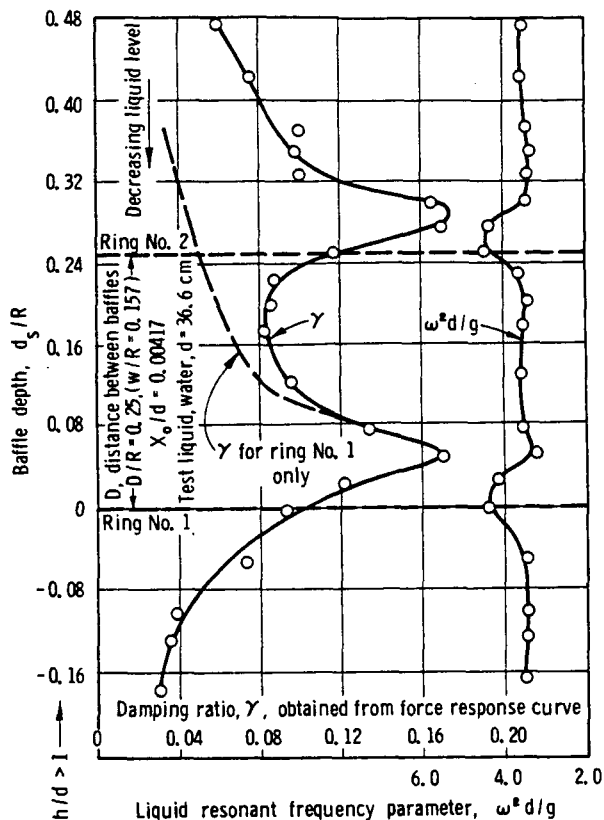


FIGURE 4.30.—Effects of double rings as a function of baffle depth (ref. 4.38).

results being shown in figure 4.30. These data indicate that the baffle above the surface is effective only if its distance from the free surface is less than about  $d_s/R = 0.125$ , while the submerged baffle is effective from about  $d_s/R = 0$  to  $d_s/R = 0.375$ . Tests of this nature are useful to designers in that they indicate the baffle spacing corresponding to some minimum acceptable damping ratio.

#### Conical-Section Baffles

The perforated conical ring baffles have also been investigated sufficiently to warrant some brief presentation of data within this section. Figure 4.35 shows the variation in damping factor as a function of baffle location, with baffle width as a parameter; one set of data for the inverted baffle is also included. Data for two perforated baffles (50 percent open) are shown in figure 4.36. These data would seem to indicate trends and values quite similar to those obtained for the flat rings.

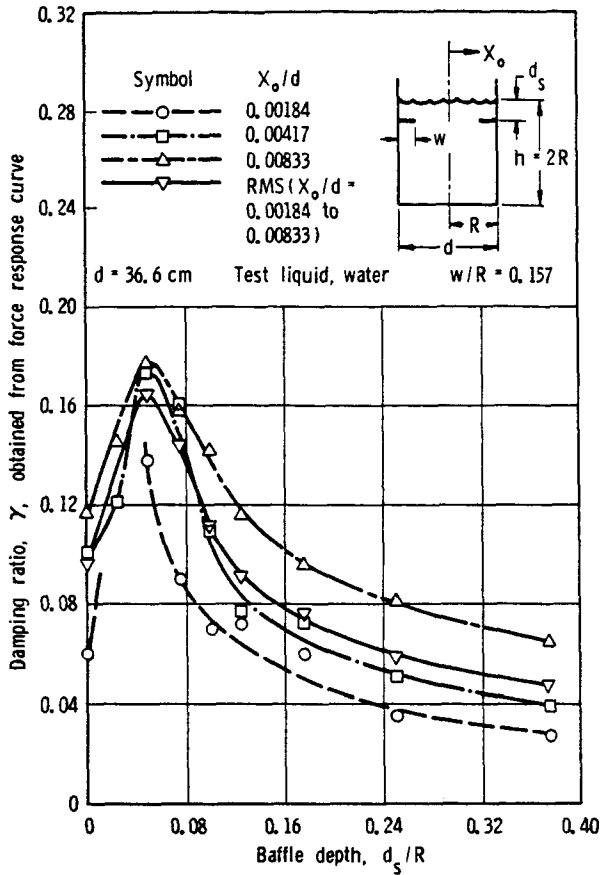


FIGURE 4.31.—Effect of excitation amplitude on damping effectiveness of a solid flat ring baffle as a function of baffle depth (ref. 4.38).

Conical-section perforated-ring baffles were also studied experimentally in the laboratory, with relation to simulation of a specific full-scale vehicle (ref. 19). (This study also included floating can devices, as discussed in sec. 4.3.) Figure 4.37 shows force response curves, comparing the full-scale prototype and model data, while figure 4.38 shows the variation of damping factor with an equivalent Reynolds number parameter, of the type mentioned previously. In this latter figure, data on floating cans (independent of liquid depth since they are surface devices) are also included.

#### Loads on Rigid Flat Ring Baffles

Some early data on baffle loads were given by Armstrong and Kachigan (ref. 4.39). The dynamic pressure at any point on the baffle resulting from liquid sloshing in its funda-

mental mode in a cylindrical tank is given by

$$\frac{p}{\theta_1 R \rho \cos \theta} = \frac{2ng}{(\epsilon_1^2 - 1)} \frac{J_1\left(\epsilon_1 \frac{r}{R}\right)}{J_1(\epsilon_1)} e^{-\epsilon_1 \frac{d_s}{R}}, \quad a_0 \leq r \leq R \quad (4.18)$$

where  $p$  is the pressure,  $\epsilon_1 = 1.84$  is the first root of  $J'_1(\epsilon) = 0$ , and  $d_s$ ,  $a_0$ ,  $r$ ,  $R$ ,  $\theta$ ,  $\theta_1$  are related to tank geometry and coordinates as shown in figure 4.39. It is seen that the pressure distribution varies with the cosine  $\theta$  around the circumference of the baffle and varies only slightly with the coordinate  $r$  for values of  $w/R$  generally employed in practice. The total moment  $M_b$  acting to overturn the baffle

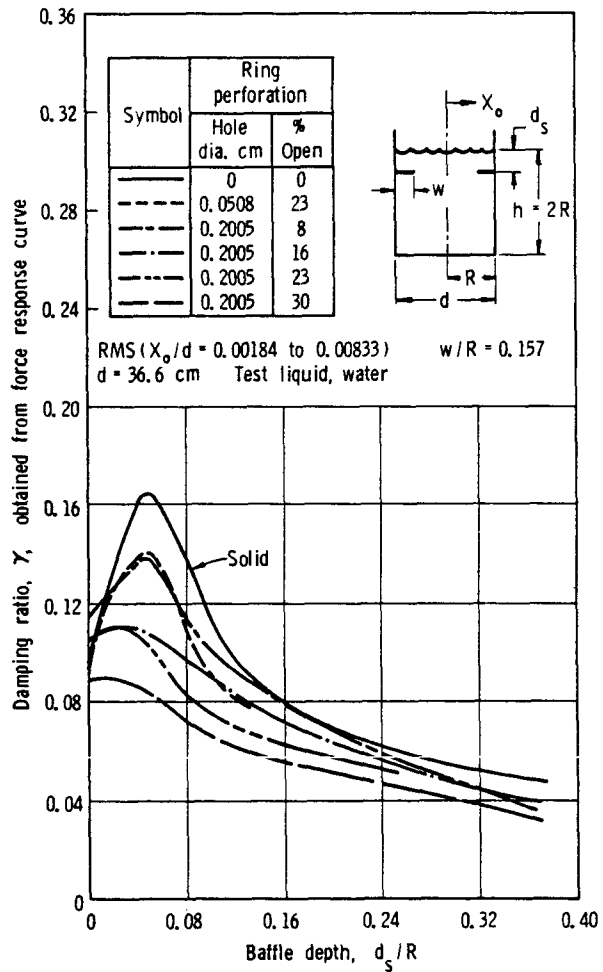


FIGURE 4.32.—Effect of percent perforation on damping effectiveness as a function of baffle depth (ref. 4.11).

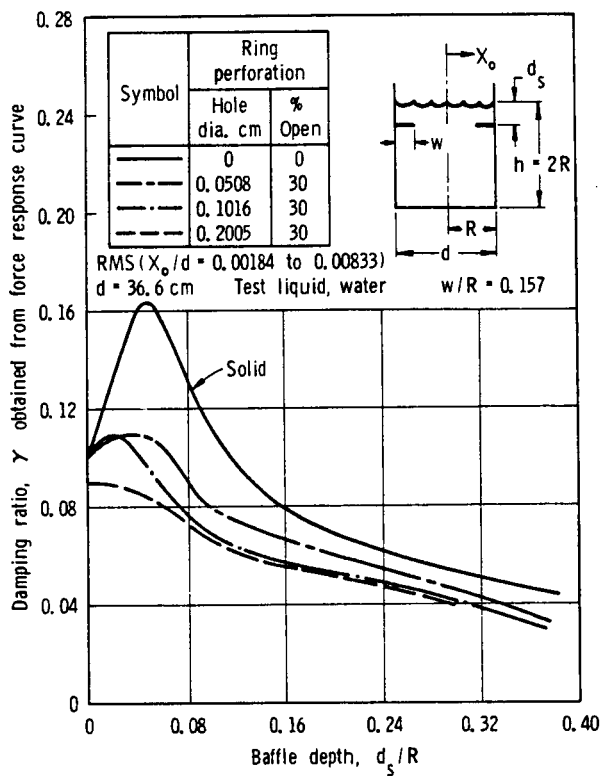


FIGURE 4.33.—Effect of perforation hole size on damping effectiveness as a function of baffle depth (ref. 4.11).

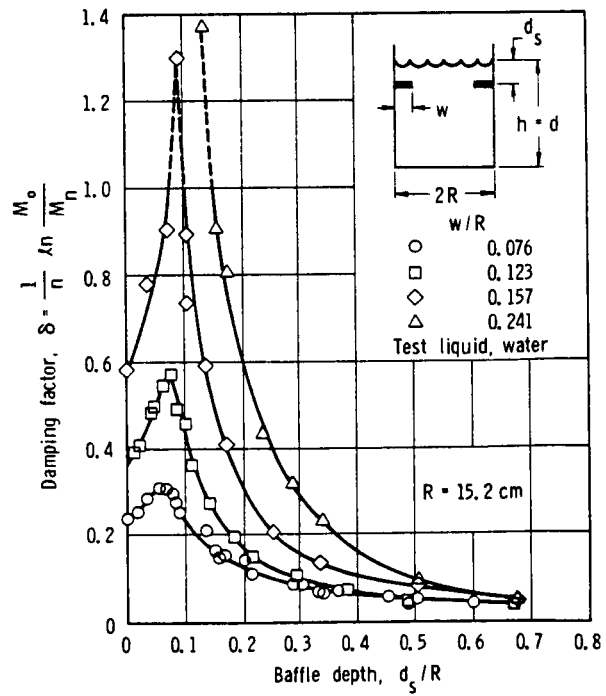


FIGURE 4.34.—Variation in damping factor with baffle location for solid baffles (ref. 4.28).

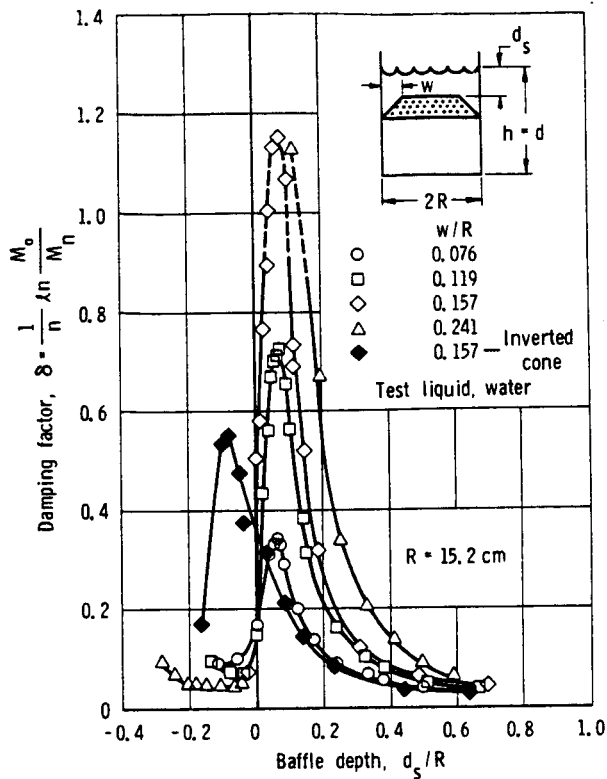


FIGURE 4.35.—Variation in damping factor with baffle location for solid conical-section baffles (ref. 4.28).

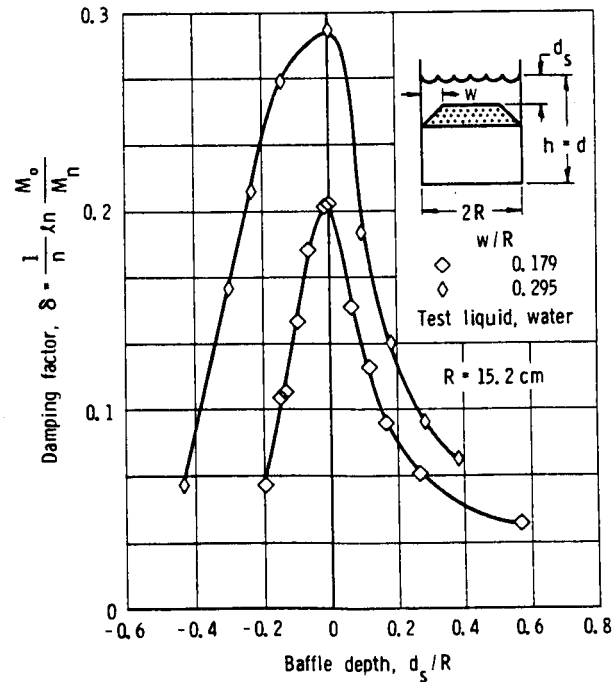


FIGURE 4.36.—Variation in damping factor with baffle location for perforated conical-section baffles (ref. 4.28).

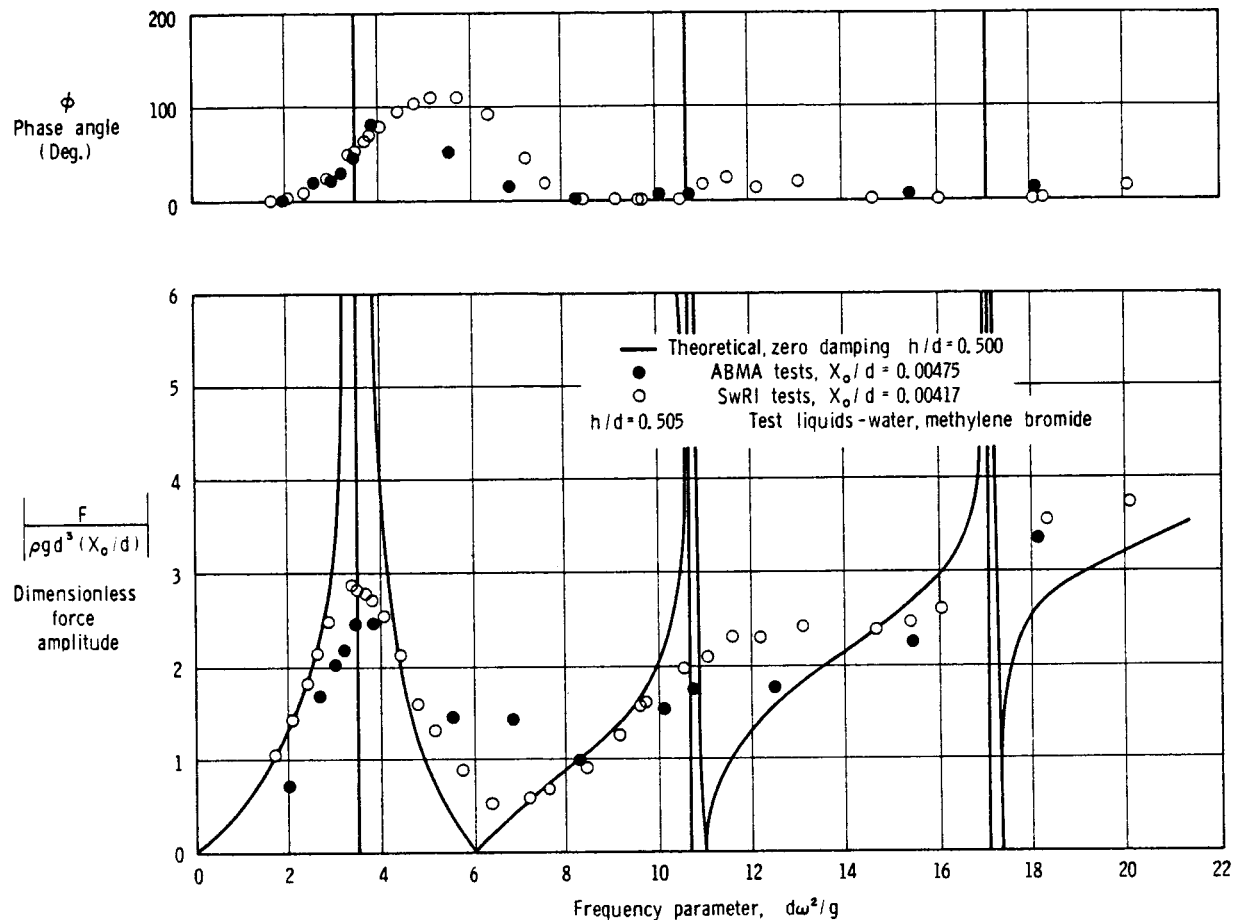


FIGURE 4.37.—Comparison of model and ABMA full-scale tests of force response in a tank with conical rings (ref. 4.19).

is obtained by integration of this pressure distribution over the baffle. Thus

$$\frac{M_b}{\theta_1 R^4 \rho} = \frac{\pi n g e^{-\epsilon_1 \frac{d_s}{R}}}{4} \left[ 1 - \frac{a_0}{R} \frac{J_1 \left( \epsilon_1 \frac{a_0}{R} \right)}{J_1(\epsilon_1)} + \left( \frac{a_0}{R} \right)^2 \epsilon_1 \frac{J'_1 \left( \epsilon_1 \frac{a_0}{R} \right)}{J_1(\epsilon_1)} \right] \quad (4.19a)$$

It can readily be determined by integration of the force per unit length of baffle over the circumference of the baffle that

$$M_b = \pi \bar{R}^2 F_b \quad (4.19b)$$

and that the total force  $F$  acting on one-half the

baffle is therefore

$$F = 2F_b \bar{R} = \frac{2M_b}{\pi \bar{R}} \quad (4.19c)$$

Figure 4.40 shows a plot of the left-hand side of equation (4.19a) as a function of  $d_s/R$  for various values of  $a_0/R$ , valid for fluid depths  $h/R > 1$ . For lower depths, a correction factor  $CF$  is given as

$$CF = \frac{e^{\epsilon_1 \frac{d_s}{R}}}{\cosh \left( \epsilon_1 \frac{d_s}{R} \right) + \sinh \left( \epsilon_1 \frac{d_s}{R} \right) \tanh \left( \epsilon_1 \frac{d_s}{R} \right)} \quad (4.20a)$$

to be applied such that

$$M_b (\text{true}) = M_b [\text{eq. (4.19a)}] \times CF \quad (4.20b)$$

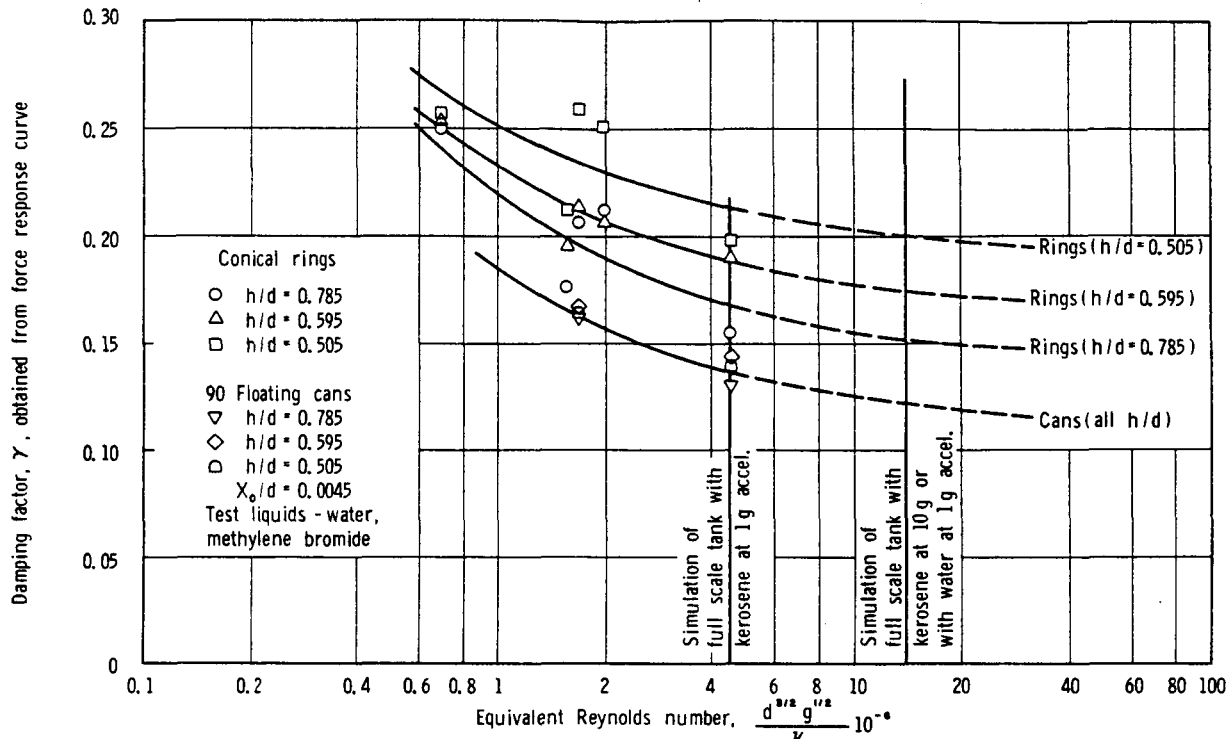


FIGURE 4.38.—Variation of damping factor with equivalent Reynolds number for conical-section rings and floating cans (ref. 4.19).

Figure 4.41 shows a comparison of theory and experiment for the force on a ring baffle; the agreement is quite good.

Another theoretical analysis of baffle loads was carried out by Liu (ref. 4.40). He employed conformal mapping to transform the baffle and tank wall into a simple plane for which a solution to Bernoulli's equation can readily be obtained, and then having the velocity and pressure distribution on the baffle in the transformed plane, the inverse transformation yielding the solution in the physical plane. The final result for the pressure on the baffle takes the form

$$p = (2\rho\omega)\bar{z}\omega\rho^{-3.68}\frac{d}{\bar{d}}\sqrt{1-(y/w)^2} \sin \omega t \cos \theta \quad (4.21)$$

where  $y$  is the coordinate in the radial direction measured inward from the tank wall.

Figure 4.42 shows a comparison of pressures on baffles as computed from equation (4.21) and as measured by Garza (ref. 4.41), for  $\theta=0^\circ$  with solid rings. For  $\theta=30^\circ$  and  $60^\circ$ ,

Garza found some slight reduction in the pressures and a general but slight flattening of the curves. The experimental data are generally slightly higher than are the calculated values. Figure 4.43 compares the experimental force data with the predictions of both theories. Except for very shallow baffle depths, the theoretical predictions appear to bracket the measured values. Garza also investigated (ref. 4.41) the effects of baffle perforation, employing about the same range of parameters utilized in previous studies of baffle characteristics (ref. 4.11). Both increasing perforation hole size and percent perforation resulted in reductions in the force acting on the baffle up to as much as 25 to 30 percent.

### Ring Damping in Spheroidal Tanks

#### Oblate Spheroids

The performance of ring baffles in an oblate spheroidal tank has been investigated in reference 4.12. The variables considered were

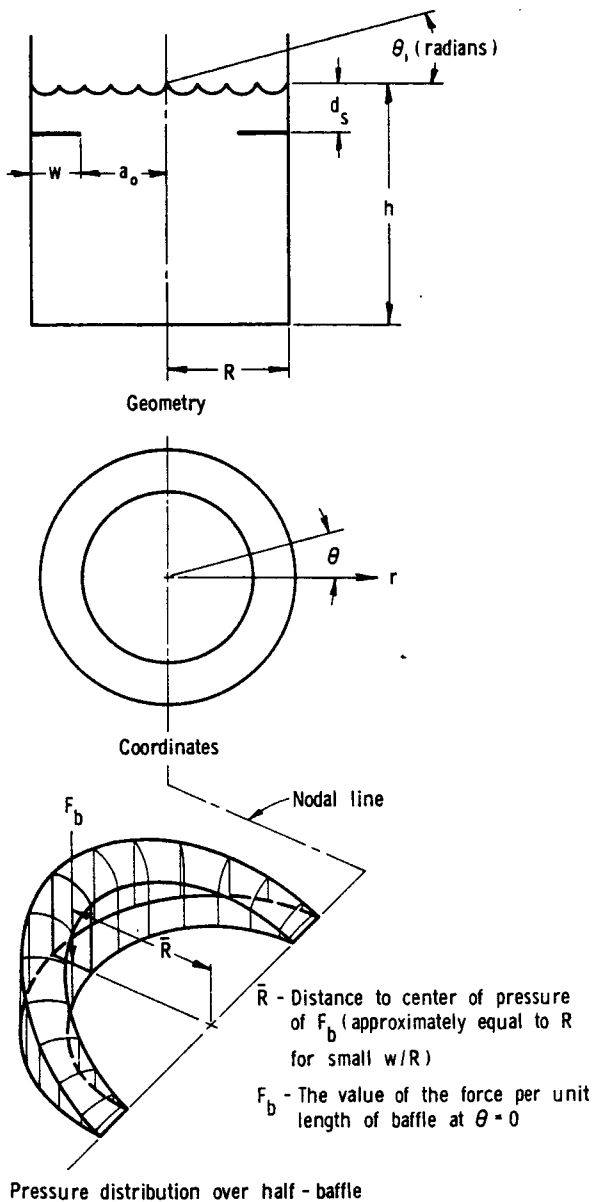


FIGURE 4.39.—Geometry, coordinates, and pressure distribution for ring pressure calculations.

the baffle submergence, tank fullness, baffle width, amplitude of the free surface displacements, and liquid kinematic viscosity. The variation of the liquid natural frequency with liquid depth and baffle location was also determined. The tank orientation is as shown in figure 4.44 and the damping factor was defined by

$$\delta = \frac{1}{n} \ln \frac{M_0}{M_n}$$

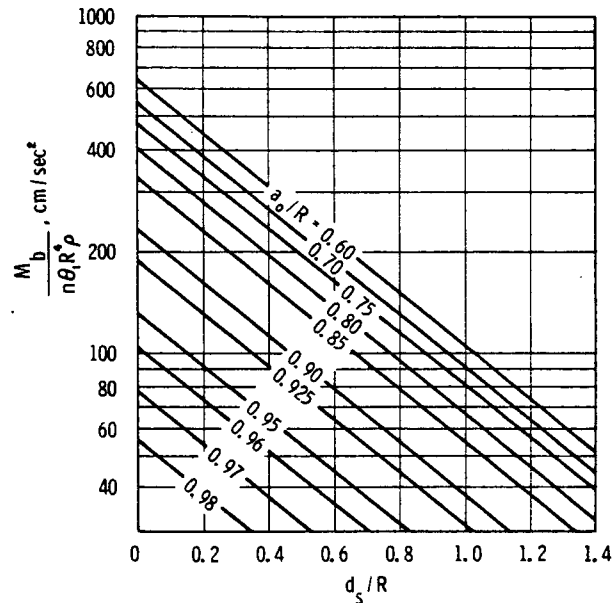


FIGURE 4.40.—Moments acting on an annular ring baffle as a function of baffle depth and width (ref. 4.39).

The variation of the damping factor with tank fullness for ring baffles of various widths is shown in figure 4.44. It is seen that the damping increases with baffle width, and also with tank fullness until a maximum value is reached when the liquid level is approximately at the baffle and then decreases with increasing fullness. The maximum damping also increases as  $h_B$  (fig. 4.44) is reduced. As the baffle is moved up, above the liquid free surface, the damping factor curve becomes much sharper with about the same maximum value. A comparison of damping factor obtained in both ring baffled and unbaffled tanks is shown in figure 4.45. The rather strong variation of damping with the free surface displacement  $\bar{z}$  (measured at the wall) is shown in figure 4.46, for a constant baffle width.

#### Spherical Tanks

Ring damping in spherical tanks has been investigated in references 4.29 and 4.42. The baffles used in reference 4.29 were perforated with 23 percent open area, a hole diameter of 0.02 inch, and a width ratio of  $w/R=0.285$ ; the configuration is shown in figure 4.17. (This has been referred to earlier in this section as the cruciform or vertical arrangement; rotation of

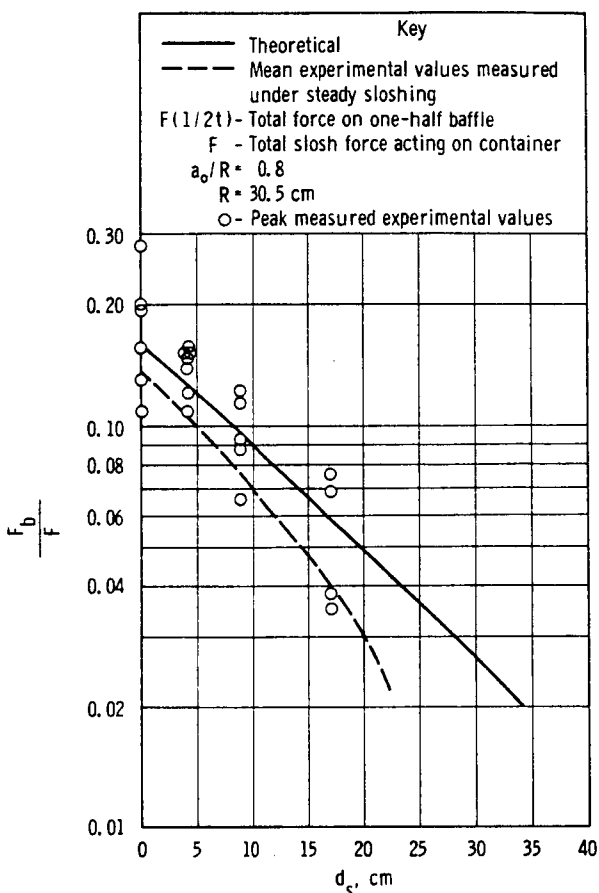


FIGURE 4.41.—Comparison of theory and experiment for forces acting on an annular-ring baffle (ref. 4.39).

the figure by  $90^\circ$  gives the horizontal arrangement.) The total force response and the damping factors obtained from force response data by means of the bandwidth technique are shown in figure 4.18. It is seen from these data that while the baffles lowered the fundamental frequency, they provided considerable damping over that of an unbaffled tank. It also appears that the horizontal baffle configuration provides greater damping than does the cruciform configuration.

Sumner (ref. 4.42) also considered the performance of annular ring baffles in spherical tanks containing water (fig. 4.47). (Note that this baffle arrangement is entirely different from either of those considered by Abramson (ref. 4.29) and mentioned in the preceding

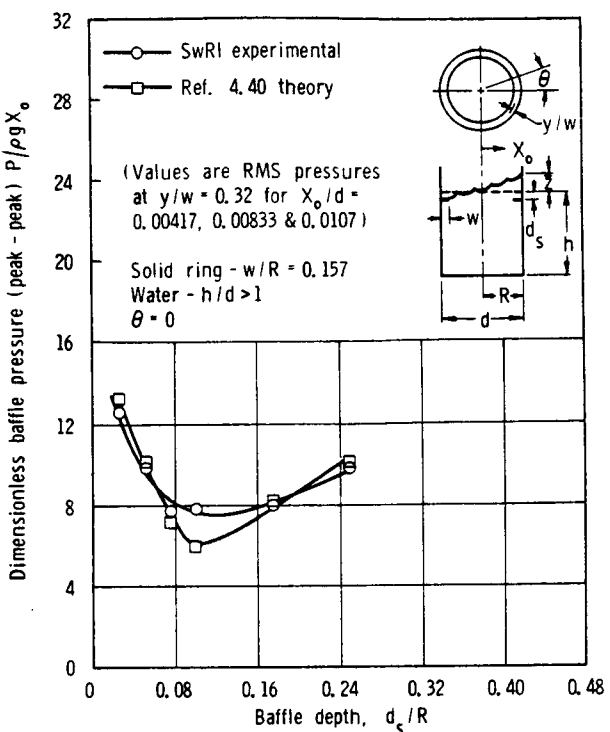


FIGURE 4.42.—Comparison of theoretical and experimental pressures on a solid-ring baffle (ref. 4.41).

paragraph.) The effects of several baffle variables on the liquid resonant frequency, force response, and damping factor [defined by  $\delta = \ln \left( \frac{F_n}{F_{n+1}} \right)$ ] were investigated. As also indicated by the earlier experiments (ref. 4.29), the dynamic behavior of liquids in spherical tanks is relatively nonlinear and complex, thus imposing some difficulties in presentation of data.

The liquid resonant frequency increases with increasing liquid depth and increasing baffle width, as shown in figure 4.48. A sharp increase in this frequency occurs for liquid levels at or slightly above the baffle; further increase in depth then results in a sharp decrease in the frequency. This rapid variation is believed to be caused by the baffle effectively changing the tank geometry. Figure 4.49 compares relative data for single-ring and three-ring configurations, for a single baffle width.

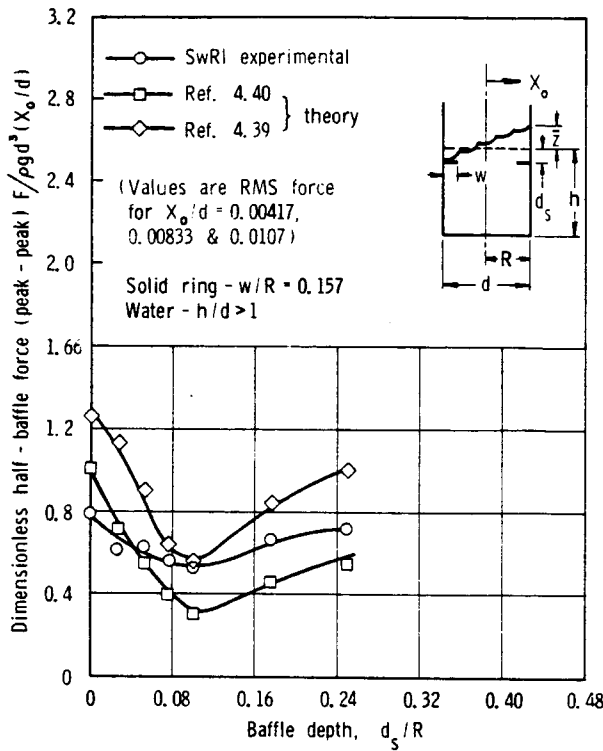


FIGURE 4.43.—Comparison of theoretical and experimental forces on a solid-ring baffle (ref. 4.41).

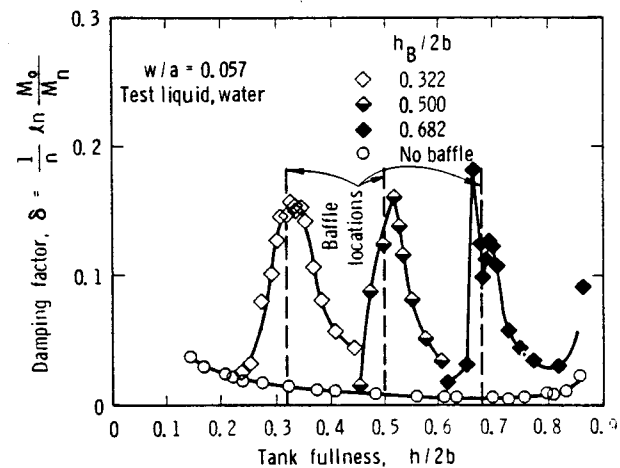


FIGURE 4.45.—Variation of damping with tank fullness for oblate spheroidal tanks with and without ring baffles (ref. 4.12).

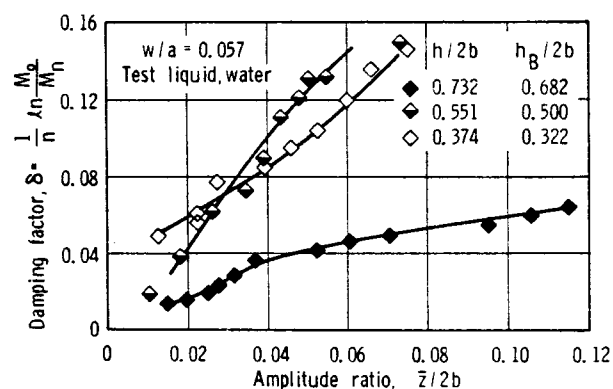


FIGURE 4.46.—Variation of damping factor with slosh amplitude ratio for oblate spheroidal tanks with ring baffles (ref. 4.12).

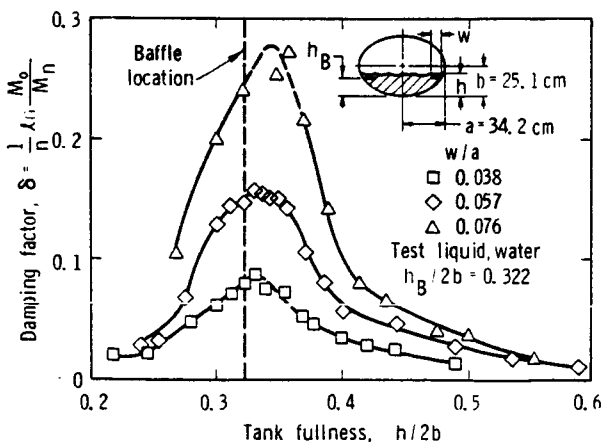


FIGURE 4.44.—Variation of damping factor with tank fullness for ring baffles in oblate spheroidal tanks (ref. 4.12).

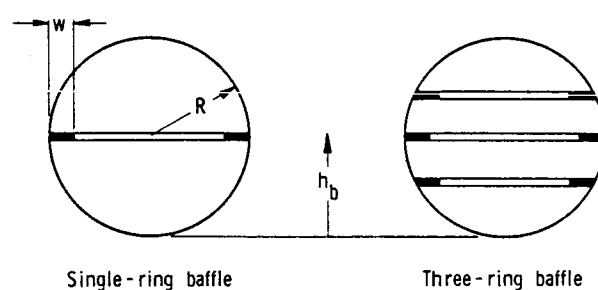


FIGURE 4.47.—Annular ring baffles in a spherical tank.

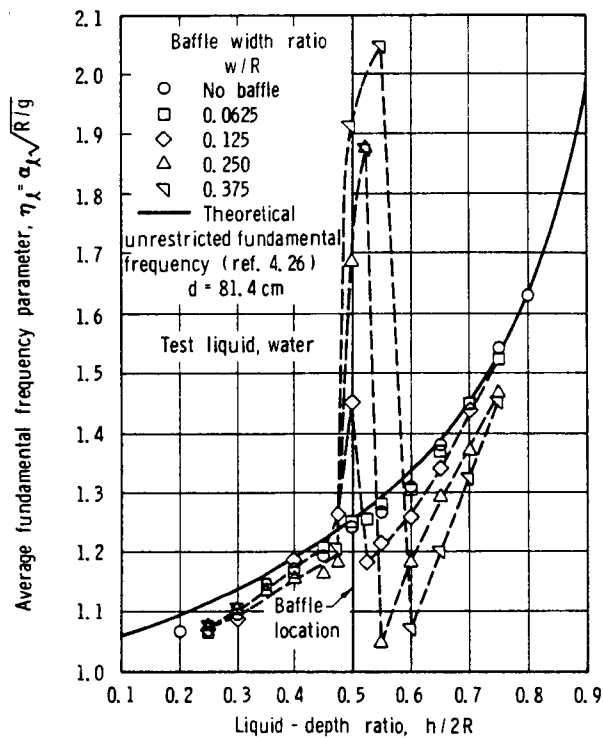


FIGURE 4.48.—Variation of fundamental frequency parameter with liquid depth ratio for rigid single-ring baffles in a spherical tank (ref. 4.42).

The slosh forces vary with excitation frequency and reach a maximum at approximately the liquid resonant frequency, increasing with increasing excitation amplitude and decreasing baffle width, as shown in figures 4.50 and 4.51; the variation with liquid depth may be seen in figure 4.52. In general, it was found that, for this series of experiments, the optimum baffle width, from considerations of slosh suppression characteristics and baffle weight, corresponded to  $w/R = 0.125$ . Also, for each baffle configuration, the slosh forces were most effectively suppressed when the liquid free surface was at or slightly above the baffle so that the baffle remained completely submerged during the liquid oscillations. The rigid baffles were ineffective in reducing the slosh forces for liquid levels more than  $0.30R$  to  $0.40R$  above and below the baffle location. The rigid, three-ring baffle configuration effectively suppressed the slosh forces for all liquid depths tested.

The effect of excitation frequency, liquid depth, and baffle width on damping ratio may be seen in figures 4.53 through 4.56, the first two for a single-ring arrangement and the last two for a three-ring arrangement. The maximum value of the damping obtained by varying the excitation frequency and holding constant the other variables is denoted as the first-mode damping ratio. Maximum damping was generally obtained when the liquid depth was approximately at the baffle. These rigid baffles provided high damping when the liquid surface was less than  $0.1R$  below and  $0.5R$  above the baffle. The three-ring baffle configuration provided damping ratios greater than 0.1 through a range of liquid depths  $0.25 \leq h/d \leq 0.80$ .

### Flexible Baffles

All the foregoing considerations of damping by fixed baffles have referred to rigid solid or perforated baffles. A number of studies, however, suggested that flexible baffles may offer substantial advantages in terms of both increased damping effectiveness and reduced baffle weight (refs. 4.28 and 4.42). An investi-

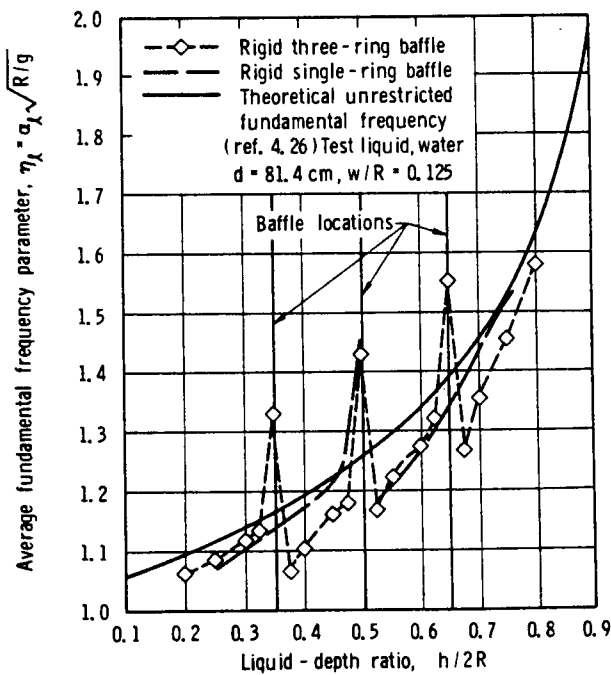


FIGURE 4.49.—Variation of average fundamental frequency parameter with liquid depth ratio for a rigid three-ring baffle in a spherical tank (ref. 4.42).

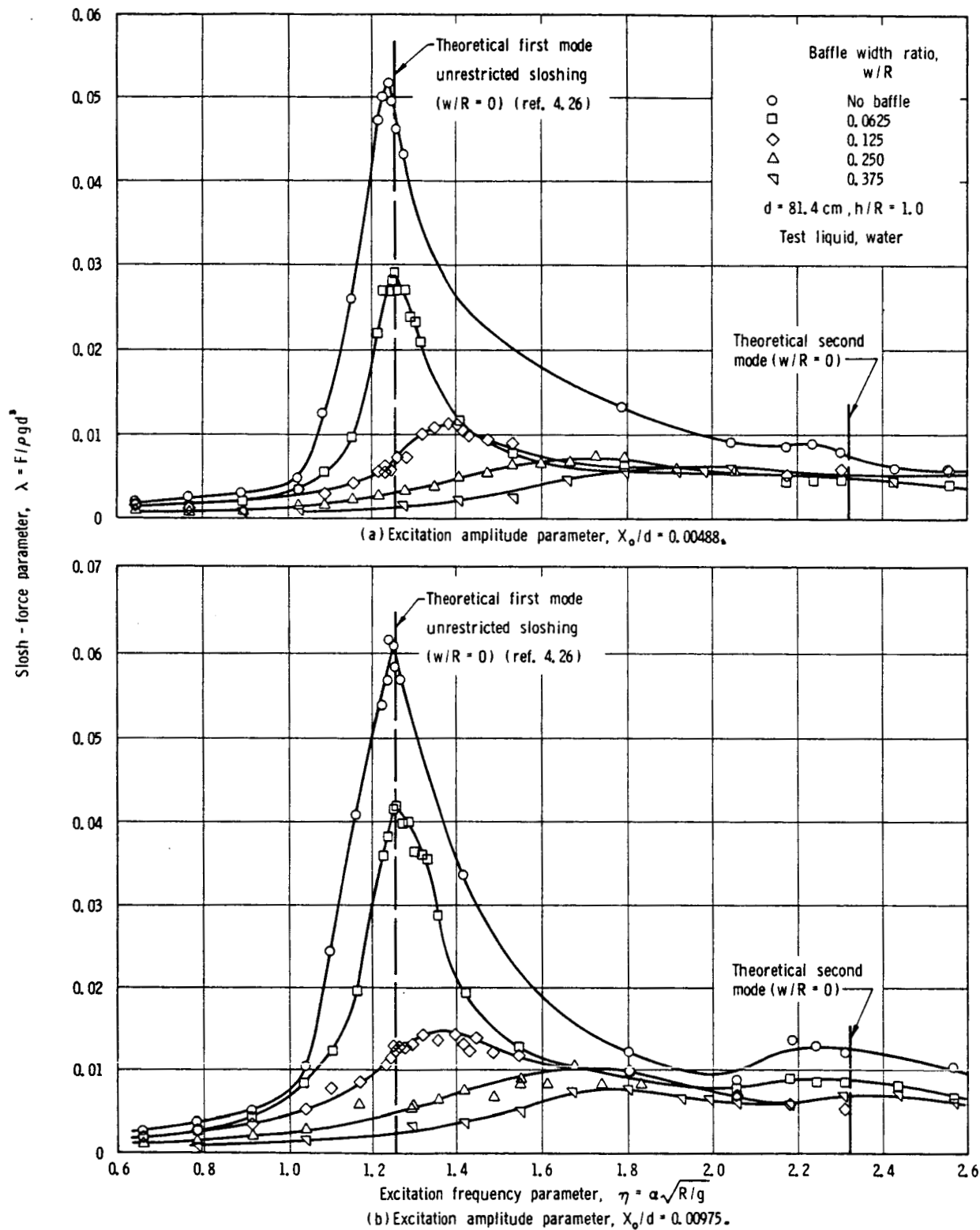


FIGURE 4.50.—Slosh-force parameter as a function of excitation frequency parameter for rigid single-ring baffles in a spherical tank (ref. 4.42).

gation of flexible baffles was therefore undertaken and reported by Stephens (ref. 4.43). The various baffle configurations examined by Stephens are shown in figure 4.57. Of these, the elastic cantilever configuration was so far superior in its high damping and very low weight characteristics (quite thin and flexible materials were considered, down to 0.0051-cm-thick Mylar) that most effort was devoted to it. The mechanism of energy dissipation is involved with the formation of a strong vortex in the liquid as it flows past the baffle.

Two nondimensional parameters were found to be of importance, as shown in figure 4.58. The first involves the periodicity of the liquid and the second the baffle flexibility. The effect of baffle flexibility is shown in figure 4.59, with liquid period as a parameter. The magnitude of the relative damping is greater than unity over all of the range of baffle flexibility shown, but decreases rapidly as flexibility increases to the point at which the baffle offers no resistance to the flow.

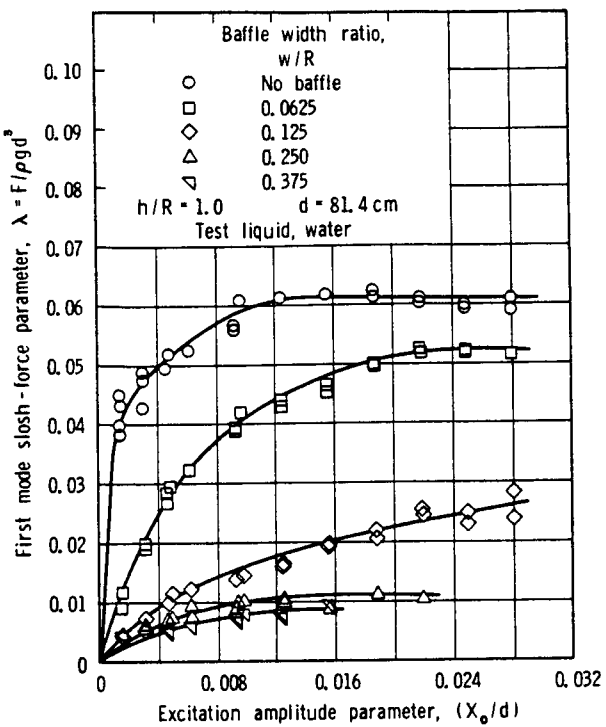


FIGURE 4.51.—Variation of first-mode slosh-force parameter with excitation amplitude parameter for rigid single-ring baffles in a spherical tank (ref. 4.42).

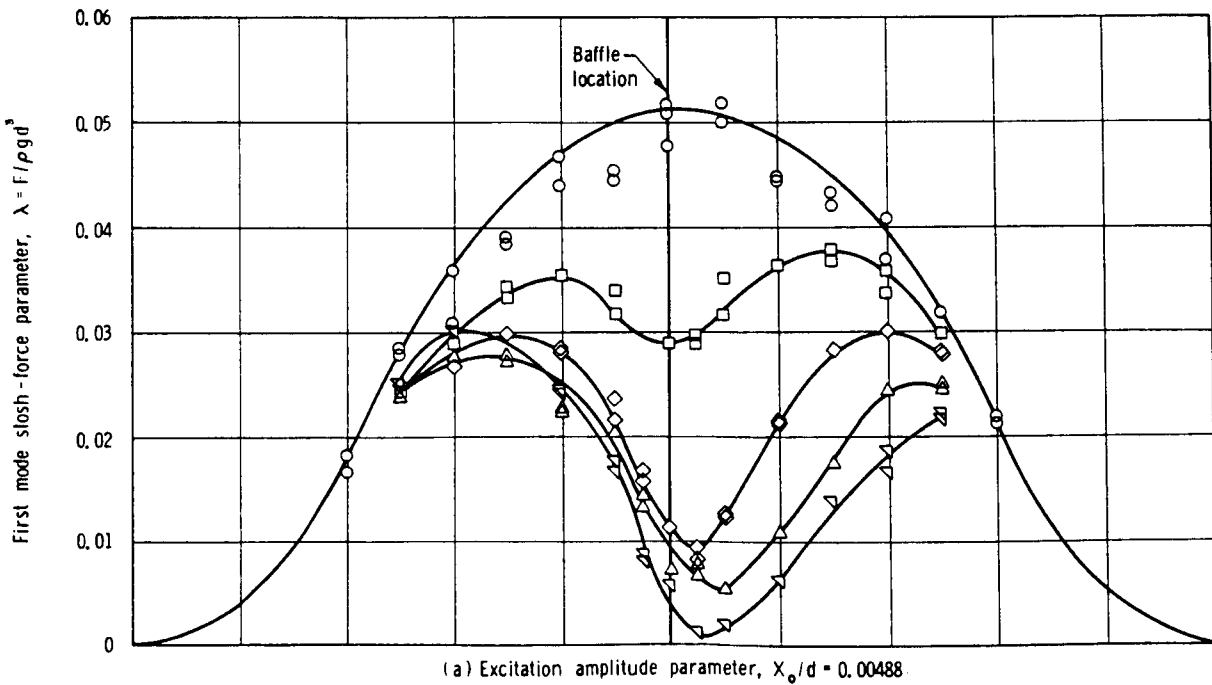


FIGURE 4.52.—Variation of first-mode slosh-force parameter with liquid depth ratio for rigid single-ring baffles in a spherical tank (ref. 4.42).

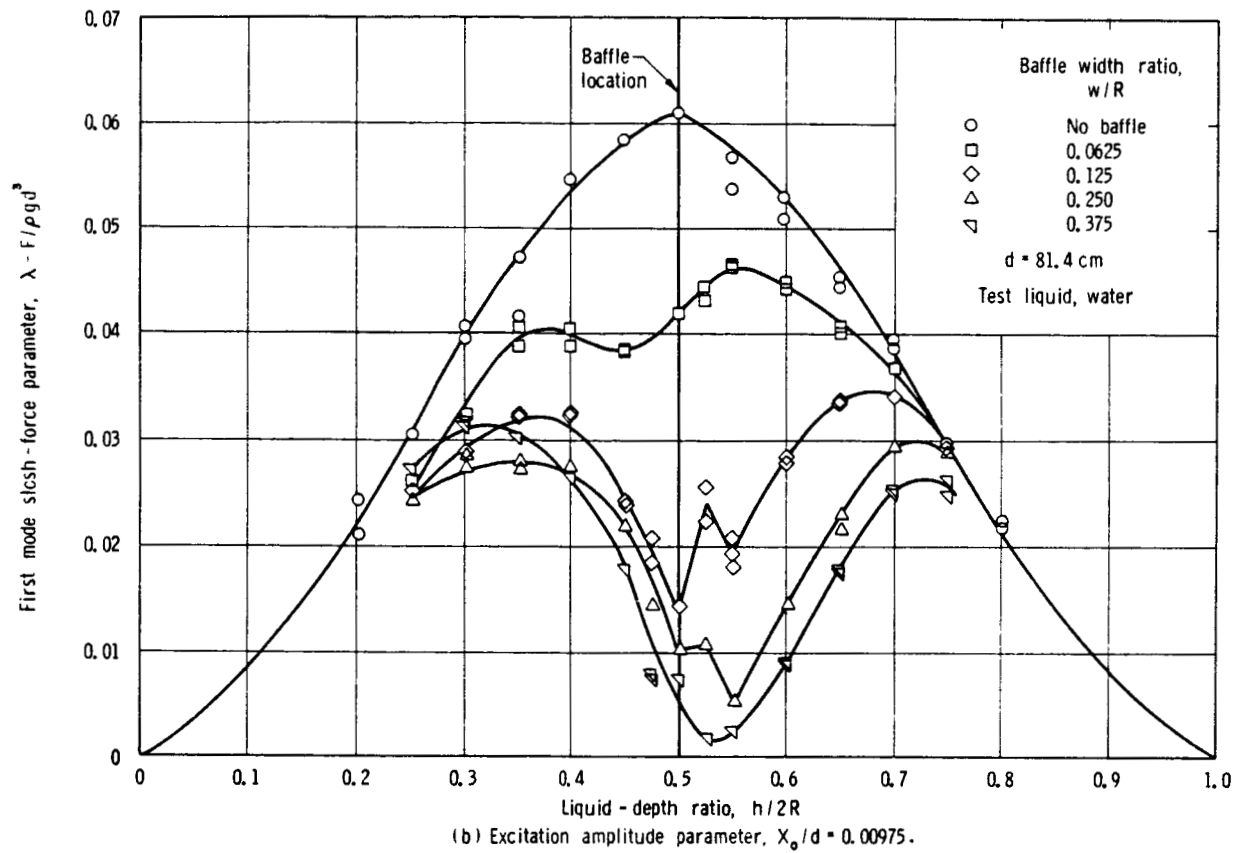


FIGURE 4.52.—Concluded.

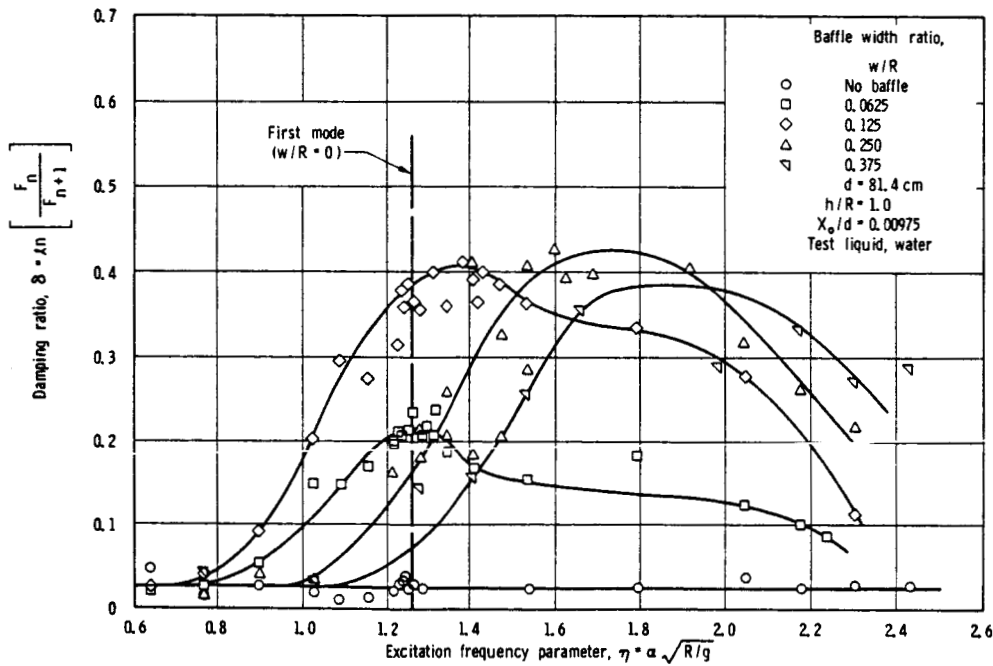


FIGURE 4.53.—Damping ratio as a function of excitation frequency parameter for rigid single-ring baffles in a spherical tank (ref. 4.42).

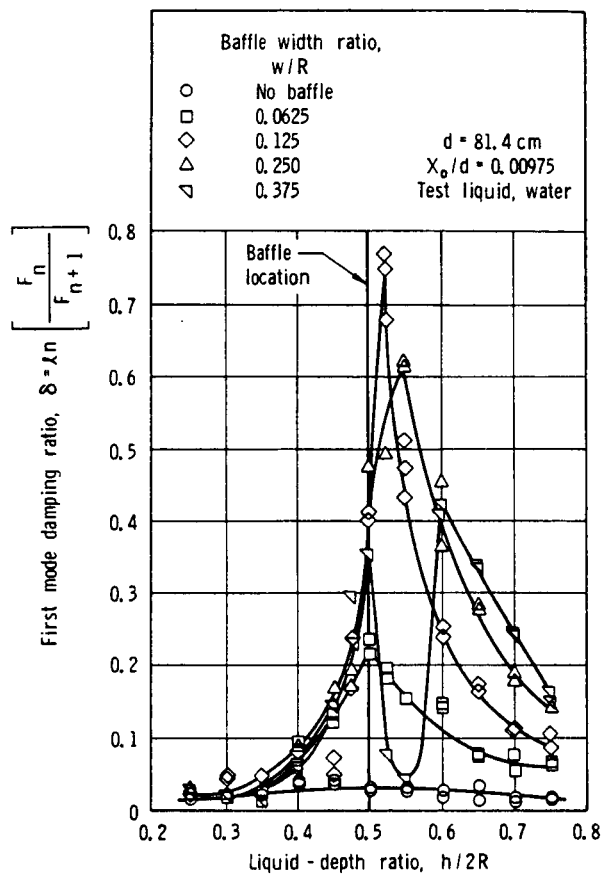


FIGURE 4.54.—Variation of first-mode damping ratio with liquid depth ratio for rigid single-ring baffles in a spherical tank (ref. 4.42).

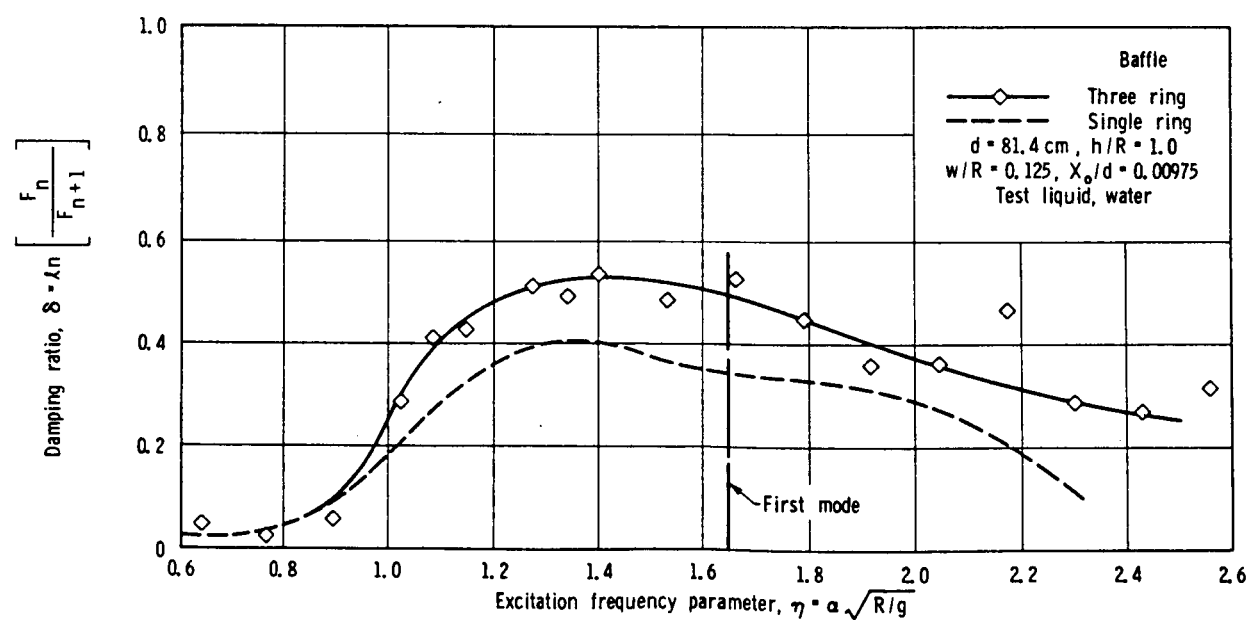


FIGURE 4.55.—Damping ratio as a function of excitation frequency parameter for rigid three-ring baffle in a spherical tank (ref. 4.42).

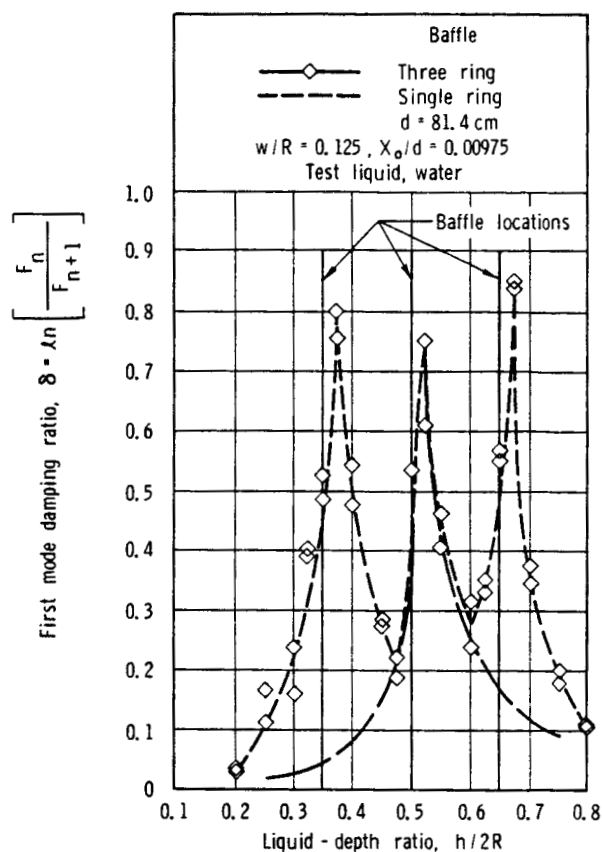


FIGURE 4.56.—Variation of first-mode damping ratio with liquid depth ratio for rigid three-ring baffles in a spherical tank (ref. 4.42).

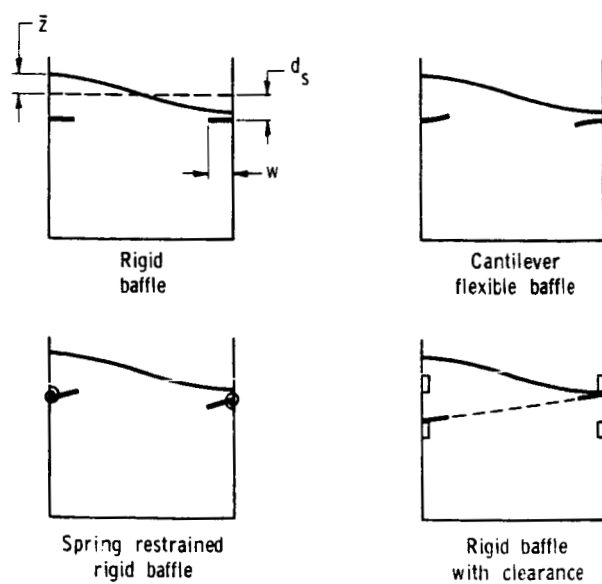
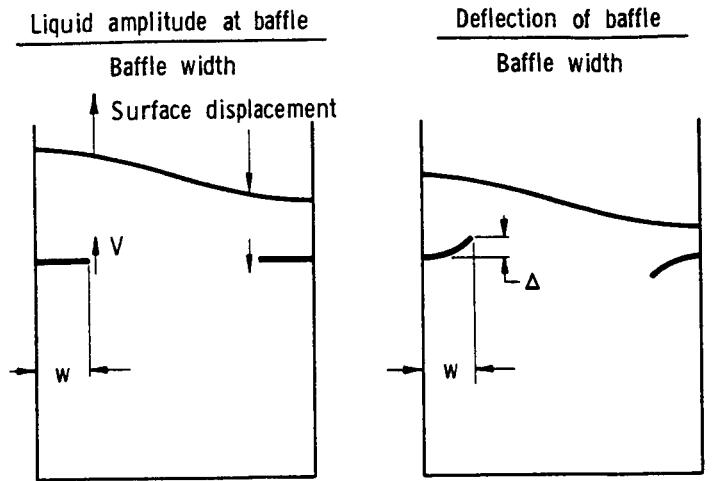


FIGURE 4.57.—Flexible or movable baffle configurations.



$$P = VT/w$$

V - Maximum fluid velocity  
at baffle location.

T - Period of the liquid  
oscillation.

$$F = \left(\frac{w}{t}\right)^3 (1 - \mu^2) \frac{\rho w^2}{E T^2}$$

$\mu, E, t$  - Poisson's ratio, modulus of  
elasticity, and thickness of  
the baffle material.

$\rho$  - Fluid density.

FIGURE 4.58.—Governing nondimensional  
parameters for flexible baffles.

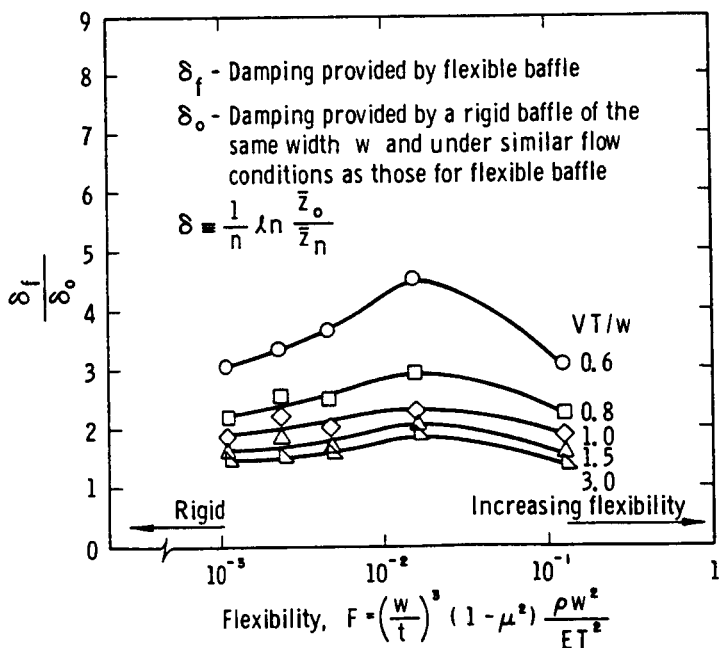


FIGURE 4.59.—Effect of baffle flexibility on  
relative damping (ref. 4.43).

## REFERENCES

- 4.1. MILES, J. W.: Note on the Damping of Free-Surface Oscillations Due to Drainage. Rept. No. TDR-930 (2270-20) TN-1, Aerospace Corp., El Segundo, Calif., Sept. 1961.
- 4.2. MILES, J. W.: Ring Damping of Free Surface Oscillations in a Circular Tank. *J. Appl. Mech.*, vol. 25, no. 2, June 1958, pp. 274-276.
- 4.3. MILES, J. W.: On the Sloshing of Liquid in a Cylindrical Tank. Rept. No. AM6-5, GM-TR-18, The Ramo-Wooldridge Corp., Guided Missile Research Div., Apr. 1956.
- 4.4. CASE, K. M.; AND PARKINSON, W. C.: Damping of Surface Waves in an Incompressible Liquid. *J. Fluid Mech.*, vol. 2, part 2, Mar. 1957, pp. 172-184.
- 4.5. NELSON, ROBERT H., JR.: The Sloshing of a Fluid Draining From a Flexible Tank. Ph. D. thesis, MIT, 1960.
- 4.6. O'NEILL, J. P.: Final Report on an Experimental Investigation of Sloshing. STL/TR-59-0000-09960, Space Tech. Labs., Inc. Available from DDC, AD-238107, Mar. 1960.
- 4.7. SCANLAN, ROBERT H.; AND ROSENBAUM, ROBERT: Introduction to the Study of Aircraft Vibration and Flutter. Macmillan Co., 1960, pp. 72-88.
- 4.8. GAUZY, H.: Measurement of Inertia and Structural Damping. Ch. 3 in Manual on Aeroelasticity, vol. IV. North Atlantic Treaty Organization, Advisory Group for Aeronautical Research and Development.
- 4.9. BISHOP, R. E. D.; AND GLADWELL, G. M. L.: An Investigation Into the Theory of Resonance Testing. *Phil. Trans. Roy. Soc. London, Ser. A*, vol. 255, no. 1055, Jan. 17, 1963, pp. 241-280.
- 4.10. GLADWELL, G. M. L.: A Refined Estimate of the Damping Coefficient. *J. Roy. Aeron. Soc.*, vol. 66, Feb. 1962, p. 125.
- 4.11. ABRAMSON, H. NORMAN; AND GARZA, LUIS R.: Some Measurements of the Effects of Ring Baffles in Cylindrical Tanks. *J. Spacecraft Rockets*, vol. 1, no. 5, Sept.-Oct. 1964, pp. 560-562.
- 4.12. STEPHENS, DAVID G.; LEONARD, H. WAYNE; AND SILVEIRA, MILTON A.: An Experimental Investigation of the Damping of Liquid Oscillations in an Oblate Spheroidal Tank With and Without Baffles. NASA TN D-808, 1961.
- 4.13. STEPHENS, DAVID G.; LEONARD, H. WAYNE; AND PERRY, TOM W.: Investigation of the Damping of Liquids in Right-Circular Cylindrical Tanks, Including the Effects of a Time-Variant Liquid Depth. NASA TN D-1367, 1962.
- 4.14. SUMNER, IRVING E.; AND STOFAN, ANDREW J.: An Experimental Investigation of Viscous Damping of Liquid Sloshing in Spherical Tanks. NASA TN D-1991, 1963.
- 4.15. MIKISHEV, G. N.; AND DOROZHKIN, N. YA.: An Experimental Investigation of Free Oscillations of a Liquid in Containers (in Russian). *Izv. Akad. Nauk SSSR, Otd. Tekh. Nauk, Mekh. i Mashinostr.*, no. 4, July/Aug. 1961, pp. 48-83. Transl. into English by D. Kana, Southwest Research Institute, June 30, 1963.
- 4.16. STOFAN, ANDREW J.; AND PAVLI, ALBERT J.: Experimental Damping of Liquid Oscillations in a Spherical Tank by Positive-Expulsion Bags and Diaphragms. NASA TN D-1311, 1962.
- 4.17. STOFAN, ANDREW J.; AND SUMNER, IRVING E.: Experimental Investigation of the Slosh-Damping Effectiveness of Positive-Expulsion Bags and Diaphragms in Spherical Tanks. NASA TN D-1712, 1963.
- 4.18. EULITZ, WERNER: A Can-Type Device Derived From Basic Slosh Studies. Rept. No. DSD-TR-4-58, Dev. Operations Div., ABMA, Redstone Arsenal, Ala., Aug. 1958. Available from DDC, AD-203348.
- 4.19. ABRAMSON, H. NORMAN; AND RANSLEBEN, GUIDO E., JR.: Simulation of Fuel Sloshing Characteristics in Missile Tanks by Use of Small Models. *ARS J.*, vol. 30, no. 7, July 1960, pp. 603-612.
- 4.20. ABRAMSON, H. NORMAN; AND RANSLEBEN, GUIDO E., JR.: Some Studies of a Floating Lid Type Device for Suppression of Liquid Sloshing in Rigid Cylindrical Tanks. TR No. 10, Contract DA-23-072-ORD-1251, Southwest Research Institute, May 1961.
- 4.21. ABRAMSON, H. NORMAN; AND RANSLEBEN, GUIDO E., JR.: Liquid Sloshing in Rigid Cylindrical Tanks Undergoing Pitching Motion. TR No. 11, Contract DA-23-072-ORD-1251, Southwest Research Institute, May 1961.
- 4.22. BAUER, HELMUT F.: Fluid Oscillations in the Containers of a Space Vehicle and Their Influence Upon Stability. NASA TR R-187, 1964.
- 4.23. COLE, HENRY A.; AND GAMBUCCI, BRUNO J.: Measured Two-Dimensional Damping Effectiveness of Fuel Sloshing Baffles Applied to Ring Baffles in Cylindrical Tanks. NASA TN D-694, 1961.
- 4.24. HOWELL, E.; AND EHLER, F. G.: Experimental Investigation of the Influence of Mechanical Baffles on the Fundamental Sloshing Mode of Water in a Cylindrical Tank. Rept. No.

- GM-TR-69, Space Tech. Labs., Inc., July 6, 1956.
- 4.25. LINDHOLM, ULRIC S.; KANA, DANIEL D.; CHU, WEN-HWA; AND ABRAMSON, H. NORMAN: Research in Liquid Dynamics in Missile Fuel Tanks. Quarterly Prog. Rept. No. 7, Contract No. NASw-2, Southwest Research Institute, Jan. 1, 1962.
- 4.26. STOFAN, ANDREW J.; AND ARMSTEAD, ALFRED L.: Analytical and Experimental Investigation of Forces and Frequencies Resulting From Liquid Sloshing in a Spherical Tank. NASA TN D-1281, 1962.
- 4.27. SUMNER, IRVING E.: Preliminary Experimental Investigation of Frequencies and Forces Resulting From Liquid Sloshing in Toroidal Tanks. NASA TN D-1709, 1963.
- 4.28. SILVEIRA, MILTON A.; STEPHENS, DAVID G.; AND LEONARD, H. WAYNE: Damping of Liquid Oscillations in Cylindrical Tanks With Various Baffles. NASA TN D-715, 1961.
- 4.29. ABRAMSON, H. NORMAN; CHU, WEN-HWA; AND GARZA, LUIS R.: Liquid Sloshing in Spherical Tanks. AIAA J., vol. 1, no. 2, Feb. 1963, pp. 384-389.
- 4.30. ABRAMSON, H. NORMAN; GARZA, LUIS R.; AND KANA, DANIEL D.: Liquid Sloshing in Compartmented Cylindrical Tanks. ARS J., vol. 32, no. 6, June 1962, pp. 978-980.
- 4.31. ABRAMSON, H. NORMAN; CHU, WEN-HWA; AND GARZA, LUIS R.: Liquid Sloshing in 45° Sector Compartmented Cylindrical Tanks. TR No. 3, Contract NAS8-1555, Southwest Research Institute, Nov. 1, 1962.
- 4.32. ABRAMSON, H. N.; AND GARZA, L. R.: Some Measurements of Liquid Frequencies and Damping in Compartmented Cylindrical Tanks. AIAA J. Spacecraft Rockets, vol. 2, no. 3, May-June 1965, pp. 453-455.
- 4.33. GARZA, LUIS R.: Measurements of Liquid Natural Frequencies and Damping in Compartmented Cylindrical Tanks. TR No. 8, Con-
- tract NAS8-1555, Southwest Research Institute, Feb. 1964.
- 4.34. COLE, HENRY A.; AND GAMBUCCI, BRUNO J.: Tests of an Asymmetrical Baffle for Fuel-Sloshing Suppression. NASA TN D-1036, 1961.
- 4.35. GARZA, LUIS R.: A Brief Comparison of Ring and Asymmetrical Baffle Characteristics. NASA CR-51373, 1963.
- 4.36. KEULEGAN, G. H.; AND CARPENTER, L. H.: Forces on Cylinders and Plates in an Oscillating Fluid. National Bureau of Standards Report 4821, Washington, D.C., Sept. 5, 1956.
- 4.37. BAUER, HELMUT F.: The Damping Factor Provided by Flat Annular Ring Baffles for Free-Fluid Surface Oscillations. MTP-AERO-62-81, NASA-MSFC, 1962.
- 4.38. ABRAMSON, H. NORMAN; AND GARZA, LUIS R.: Some Measurements of the Effects of Ring Baffles in Cylindrical Tanks. AIAA J. Spacecraft Rockets, vol. 1, no. 5, Sept.-Oct. 1964, pp. 560-562.
- 4.39. ARMSTRONG, G. L.; AND KACHIGAN, K.: Stability and Control. Ch. 14, in Handbook of Astronautical Engineering (H. H. Koelle, editor-in-chief), McGraw-Hill, 1961, pp. 14-25—14-27.
- 4.40. LIU, F. C.: Pressure on Baffle Rings Due to Fuel Sloshing in a Cylindrical Tank. R-AERO-4-64, NASA-MSFC, Jan. 17, 1964.
- 4.41. GARZA, L. R.: Theoretical and Experimental Pressures and Forces on a Ring Baffle Under Sloshing Conditions. AIAA J., Spacecraft Rockets, vol. 3, no. 2, Feb. 1966, pp. 276-278.
- 4.42. SUMNER, IRVING E.: Experimental Investigation of Slosh-Suppression Effectiveness of Annular-Ring Baffles in Spherical Tanks. NASA TN D-2519, 1964.
- 4.43. STEPHENS, DAVID G.: Flexible Baffles for Slosh Damping. AIAA J., Spacecraft Rockets, vol. 3, no. 5, May 1966, pp. 765-766.

## PRINCIPAL NOTATIONS

$a, b$ =tank dimensions for an oblate spheroid  
 $a_0$ =inside radius of the baffle  
 $d$ =tank diameter  
 $d_b$ =diameter of perforations of perforated baffle  
 $d_s$ =baffle depth below the free surface  
 $E$ =energy of motion, modulus of elasticity in tension and compression  
 $F$ =force  
 $g$ =gravitational acceleration  
 $h$ =liquid depth  
 $\ln$ =natural logarithm  
 $M$ =moment  
 $ng$ =axial acceleration of the tank  
 $p$ =pressure on the baffle

$R$ =tank radius  
 $r_0$ =radius of the free surface  
 $r, \theta, z$ =cylindrical coordinates  
 $w$ =baffle width  
 $x_0$ =excitation amplitude  
 $z$ =amplitude of liquid displacement from undisturbed surface measured at the wall  
 $\alpha$ =cone semivertex angle  
 $\gamma$ =ratio of actual to critical damping  
 $\delta$ =logarithmic decrement  
 $\nu$ =liquid kinematic viscosity  
 $\rho$ =liquid mass density  
 $\Omega$ =excitation frequency  
 $\omega$ =circular frequency of liquid oscillations

## Simulation and Experimental Techniques

### Part I. Simulation of Liquid Sloshing

*John F. Dalzell*

#### 5.1 INTRODUCTION

There is considerable justification, both technical and economic, for modeling sloshing phenomena in the laboratory. The model is almost always small relative to the prototype and thus costs little to build, compared to the prototype, and usually proportionately less to modify. At times models add certainty to an analytical approach, and in other cases provide the physical insight required to formulate analytical approaches. Small-scale modeling has become an essential complement to theoretical studies and full-scale observations of the behavior of fuel in the tanks of booster rockets and spacecraft.

The initial design of simulation experiments has much in common with the design of the final product in that it is usually impossible or impractical to satisfy simultaneously every aspect of the ideal goals of the design. Consequently, the most important part of an experimental design is the judgment of the designer as to which parameters, fluid properties, and system variables are important and which are not. In all cases, theory and previous experimental observations are combined in this judgment to the extent possible. However, if the simulation is necessary at all, some aspects of the underlying theory must be speculative, unconfirmed, missing, or perhaps too difficult to evaluate. The methods implied by the theory of similitude and dimensional analysis afford the designer of experiments a unifying tool which will ordinarily reduce the number of variables in the problem and systematize the requirements of the simulation. These methods,

however, do not remove the requirements for good judgment, since there is no one path to follow in their application to a given problem. An extensive modern literature on similitude and dimensional analysis is available. References 5.1 through 5.3 are examples of general texts, while references 5.4 through 5.6 are examples of textbooks containing treatments oriented toward fluid dynamics (this list is by no means exhaustive).

#### 5.2 REVIEW OF DIMENSIONAL ANALYSIS AS CUSTOMARILY APPLIED TO SIMULATION

Any physical measurement has two general characteristics: qualitative and quantitative. The qualitative characteristics serve to identify the class of quantities with which the measurement is to be associated and are called the dimensions of the quantity measured. The quantitative part of the measurement involves a number and an arbitrary standard of comparison called a unit (the measurement; "3 in." has dimensions of length and units of inches). Insofar as Newtonian mechanics is concerned, the four dimensional categories of Force,  $F$ ; Mass,  $M$ ; Length,  $L$ ; and Time,  $T$ , are related through the second law of motion

$$F = Ma \quad (5.1)$$

or dimensionally:

$$F \doteq M L T^{-2} \quad (5.2)$$

(where the symbol ( $\doteq$ ) denotes dimensional but not necessarily numerical equivalence) so

that any one of the four may be defined in terms of the other three. It is convenient and traditional to regard three of these four categories as independent, basic dimensions. In many analyses, force, length, and time are considered basic—in as many others, mass, length, and time are taken. The choice is a matter of convenience, though the *M-L-T* system has been most often used in sloshing simulation analyses. For problems involving heat or electricity, additional basic quantities (temperature,  $\theta$ ; quantity of heat,  $H$ ; charge,  $Q$ ; etc.) are often considered as basic dimensions. With conventional measuring techniques, the dimensions of any mechanical quantity may be expressed as a product of integral powers of the basic dimensions.

The methods of dimensional analysis are built on the principle of dimensional homogeneity (an equation expressing a physical relationship between quantities must be dimensionally homogeneous). The formal methods were probably started by Lord Rayleigh (ref. 5.7) and improved upon by Buckingham (ref. 5.8) with a broad generalization known as the  $\pi$ -theorem. The  $\pi$ -theorem, in general terms, states that the number of dimensionless and independent quantities required to express a relationship among the variables in any phenomenon is equal to the number of quantities involved, minus the number of independent dimensions in which those quantities may be measured. These dimensionless quantities are commonly called “ $\pi$ -terms,” and the only restriction on them is that they be dimensionless and independent.

There are a variety of methods in common use for deriving valid sets of  $\pi$ -terms from a given list of variables (one or more dependent) and parameters. A commonly accepted formal procedure which insures independence is as follows, given a list of  $n$  variables ( $\alpha_1, \alpha_2, \dots, \alpha_n$ ) containing  $m$  fundamental dimensions.

The conceptual functional relationship of the  $n$  variables may be written:

$$f(\alpha_1, \alpha_2, \dots, \alpha_n) = 0 \quad (5.3)$$

It is desired to form a function of  $\pi$ -terms

which is an equally valid representation of the phenomenon

$$F(\pi_1, \pi_2, \dots, \pi_{n-m}) = 0 \quad (5.4)$$

Each  $\pi$ -term must have the form

$$\pi = (\alpha_1^{x_1})(\alpha_2^{x_2}) \dots (\alpha_k^{x_k}) \dots (\alpha_n^{x_n}) \quad (5.5)$$

where the  $x_k$  are to be determined. Each  $\alpha_k$  is dimensionally

$$\alpha_k = (D_1^{a_{1k}})(D_2^{a_{2k}}) \dots (D_j^{a_{jk}}) \dots (D_m^{a_{mk}}) \quad (5.6)$$

(where the  $D_i$  denote the  $m$  fundamental dimensions,  $L, T, M, \theta$ , etc.). Thus the general  $\pi$ -term is dimensionally

$$\begin{aligned} \pi = & [D_1^{a_{11}} D_2^{a_{21}} \dots D_m^{a_{m1}}]^{x_1} [D_1^{a_{12}} D_2^{a_{22}} \dots D_m^{a_{m2}}]^{x_2} \\ & \dots [D_1^{a_{1k}} \dots D_j^{a_{jk}} \dots D_m^{a_{mk}}]^{x_k} \\ & \dots [D_1^{a_{1n}} D_2^{a_{2n}} \dots D_m^{a_{mn}}]^{x_n} \end{aligned} \quad (5.7)$$

If  $\pi$  is to be dimensionless, the combined exponent on each of the dimensions  $D_i$  must be zero. Thus, for  $j=1, 2, \dots, m$ ,

$$\sum_{k=1}^n a_{jk} x_k = 0 \quad (5.8)$$

Since equation (5.8) represents a system of  $m$  linear algebraic equations in  $n$  unknowns (the  $x_k$ ), it is possible, generally, to solve this system of equations for the first  $m$  values of  $x_k$  in terms of linear combinations of the remaining  $n-m$  unknown exponents. This general solution may be written for  $k=1, 2, \dots, m$ :

$$x_k = \sum_{p=m+1}^n c_{pk} x_p \quad (5.9)$$

where the  $c_{pk}$  are functions of the  $a_{jk}$  and are calculable in general, if the determinant of the coefficients  $a_{jk}$  ( $j=1, 2, \dots, m; k=1, 2, \dots, m$ ) is nonzero. If the original list of variables contains each of the basic dimensions in more than one variable, and if the basic dimensions do not always occur in the same combination in the dimensional representation of the variables, it will be possible to make a choice of  $m$  of the unknown exponents  $x_k$  such that the

solution, equation (5.9), is possible. The  $x_p$  in equation (5.9) are arbitrary. Thus, there are an unlimited number of solutions for the set of exponents,  $x_k$ , ( $k=1, 2 \dots m$ ), since the set of exponents,  $x_p$ , ( $p=m+1, \dots n$ ), may be chosen in an unlimited number of ways. Thus, it is possible to form a solution by setting  $x_{m+1}$  equal to unity and all the other  $x_p$  to zero. This process can be repeated by setting each of the  $x_p$  equal to unity in turn. The result is  $n-m$  sets of solutions for the exponents  $x_k$ , ( $k=1, 2, \dots m$ ), as follows:

$$\left. \begin{array}{ll} [x_k]_1 = c_{m+1, k} & k=1, 2, \dots, m \\ [x_k]_2 = c_{m+2, k} & k=1, 2, \dots, m \\ \dots & \dots \\ [x_k]_{n-m} = c_{n, k} & k=1, 2, \dots, m \end{array} \right\} \quad (5.10)$$

The theory of linear equations states that there are  $n-m$  linearly independent solutions to equation (5.9). The  $n-m$  sets of solutions shown in equations (5.10) constitute  $n-m$  such linearly independent sets of solutions, probably the simplest set. If a member of this set (eqs. (5.10)) is replaced by itself multiplied by any number other than zero, the resulting set remains a linearly independent one. Similarly any member of the set of solutions (eqs. (5.10)) may be replaced by its sum with any or all of the other members of the set with the same result.

The general  $\pi$ -term may be written by substituting equation (5.9) into equation (5.5)

In this expression, the subscript  $i$  has been added to denote  $n-m$  particular choices of the arbitrary exponents  $x_k$ . Equations (5.10) show that one permissible choice for these exponents yields the  $n-m$  bracketed terms in equation (5.11) for the  $n-m$  independent  $\pi$ -terms. Other choices for the arbitrary exponents are just as valid so long as the set of  $x_k$  chosen will

result in  $n-m$  linearly independent solutions of equation (5.9).

It is evident from the form of equation (5.11) and the conditions on the linearly independent solutions of equation (5.9) that so long as replacement operations are carried out one at a time:

- (1) Any member of a valid set of  $\pi$ -terms may be replaced by itself raised to any (non-zero) power; and

- (2) Any member of a valid set of  $\pi$ -terms may be replaced by itself raised to any nonzero power and multiplied by any or all of the other members of the set, each raised to any power.

In general, while two analysts performing a systematic dimensional analysis of the same set of variables may come up with valid sets of  $\pi$ -terms having different form, they must each have the same number of terms, and it will be possible to transform the results of the first analyst into those of the second; in other words, the formal methods of dimensional analysis imply that alternative solutions for a valid set of  $\pi$ -terms are not independent, and hence no one of them can be expected to contain any essential information not common to the others.

There are some obvious restrictions on the nature of the set of  $m$  variables chosen to be repeating in equation (5.11). The dimensions of these variables must include all the,  $m$ , fundamental dimensions,  $D_j$ , at least once. Also, no two of these repeating variables can have the same dimensional form nor should it be possible to form a dimensionless group from these variables alone (these are the primary conditions for a solution for the  $c_{pk}$  coefficients). An additional consideration is that if only one variable,  $\alpha_k$ , has the basic dimension  $D$ , in its dimensional form, then the conceptual functional relationship between the variables and parameters (eq. (5.3)) cannot be dimensionally homogeneous, the variable is either not important or some additional parameter is missing from the original list.

Since most engineers are accustomed to forming dimensionless numbers by inspection and to manipulating ratios, a method of performing dimensional analyses by inspection is attractive. Equation (5.11) suggests a

systematic way in which valid sets of  $\pi$ -terms may be easily formed by inspection. After forming the initial list of variables, and writing down their dimensional form, a subset of  $m$  variables satisfying the conditions above is picked for the set of repeating variables. The product of all of these  $m$  variables with each of the nonrepeating variables is formed,  $n-m$  products in all, and proper exponents assigned to the repeating variables by inspection so that the product is dimensionless.

### 5.3 APPLICATION OF DIMENSIONAL ANALYSIS TO SIMULATION

When simulation is the object of the analysis, the conceptual functional relationship between the  $\pi$ -terms is used in the sense that a complete function

$$F(\pi_1, \pi_2, \dots, \pi_{n-m}) = 0 \quad (5.4)$$

applies to a system of any size. Consequently, if all the  $n-m$  dimensionless  $\pi$ -terms are held the same in model and prototype, the simulation is assumed to be correct. If one or more of the implied equalities is not met in the simulation, the simulation is "out of scale" with respect to the  $\pi$ -terms involved. If one of the particular variables is a source of scaling difficulty, the set of  $\pi$ -terms should probably be manipulated so that this variable appears in only one term. In this respect, the ambiguity of the dimensional analysis is useful, since the experimental designer can insure that the dependent variable, or a highly controllable or primary independent variable, is included in only the most convenient  $\pi$ -term(s), thus automatically insuring a consistent nondimensional method of presenting results.

It is usually the case that the analyst cannot tell at the outset what final form the  $\pi$ -terms should have. This, like the form of the function under investigation, must be revealed either by analysis or by experiment. In any event, the analyst is closer to his goal after dimensional analysis than before, even though the final and best grouping of variables is to be determined.

It is often the case that simulation cannot be obtained unless the effects of one or more

variables of possible importance are neglected. In this situation, it is common to conduct a series of special experiments wherein the offending parameter is varied as much as feasible to assess its importance or to develop an extrapolation method.

In many cases in the literature, the  $\pi$ -terms resulting from a dimensional analysis are transformed into a ratio notation for convenience in experimental design. Under the modeling assumption in a previous paragraph, each  $\pi$ -term for the prototype may be formally equated to the corresponding  $\pi$ -term for the model

$$(\pi_i)_M = (\pi_i)_F \quad (5.12)$$

where the subscripts  $M$  and  $F$  denote model and prototype values, respectively. Letting

$$\pi_i = (\alpha_1)^{v_{1i}} (\alpha_2)^{v_{2i}} \dots (\alpha_k)^{v_{ki}}$$

substitution yields

$$\begin{aligned} &[(\alpha_1)^{v_{1i}} (\alpha_2)^{v_{2i}} \dots (\alpha_k)^{v_{ki}}]_M \\ &= [(\alpha_1)^{v_{1i}} (\alpha_2)^{v_{2i}} \dots (\alpha_k)^{v_{ki}}]_F \end{aligned} \quad (5.13)$$

The dimensions of the variables  $\alpha_k$  do not change between model and prototype, but only their magnitudes; consequently, the subscripts apply only to the magnitudes of the  $\alpha_k$  and equation (5.13) may be transposed and simplified to

$$1 = \left[ \frac{(\alpha_1)_M}{(\alpha_1)_F} \right]^{v_{1i}} \left[ \frac{(\alpha_2)_M}{(\alpha_2)_F} \right]^{v_{2i}} \dots \left[ \frac{(\alpha_k)_M}{(\alpha_k)_F} \right]^{v_{ki}} \quad (5.14)$$

Introducing the notations

$$\pi_i' = \frac{(\pi_i)_M}{(\pi_i)_F}$$

and

$$(\alpha_k)' = \frac{(\alpha_k)_M}{(\alpha_k)_F} \quad (5.15)$$

we have

$$1 = \pi_i' = [(\alpha_1)'^{v_{1i}} (\alpha_2)'^{v_{2i}} \dots (\alpha_k)'^{v_{ki}}] \quad (5.16)$$

Since the form of  $\pi_i'$  is exactly the same as that of  $\pi_i$ , a set of  $n-m$  equations, which must be satisfied in the simulation, may be formed from the set of  $n-m$   $\pi$ -terms by substituting for each variable in the  $\pi$ -term the ratio between its magnitude in the model and its magnitude in the prototype, and equating the result to unity. It is evident that these simulation equations may be manipulated in exactly the same way as the original  $\pi$ -terms; that is, any one of the  $n-m$  equations may be raised to any power or can be replaced by its product with any one or all of the other simulation equations.

#### 5.4 SIMULATION ANALYSIS FOR LIQUID SLOSHING

Simulation analyses are implicit or explicit in virtually every experimental report cited in the present volume, though there are few references devoted wholly to this subject. Perhaps the most detailed exposition is that of Sandorff (ref. 5.9), who considers the simulation of a compressible, viscous fluid in an elastic tank and gives experimental design examples as well as some properties of typical model and prototype fluids, and of some typical structural materials. As has been noted, different analysts will often derive slightly different similarity parameters even when the initial assumptions are the same, and will almost certainly arrive at different results when the initial assumptions differ. For their purposes, Abramson and Ransleben (ref. 5.10) consider an incompressible, viscid fluid in a rigid tank with some different criteria resulting than those of Sandorff. Similarly, Epperson, Brown, and Abramson (ref. 5.11) considered a rigid tank containing an incompressible viscid fluid and an incompressible gas with the fluid-gas interface having the property of surface tension and, as would be expected, arrive at some still different criteria.

In simulation analyses for the fuel sloshing problem, thermodynamic effects, and so forth, are usually omitted from consideration. Because fuel sloshing is a dynamic mechanical problem, the basic dimensions involved are either mass, length, and time or force, length,

and time, and Newton's second law holds. Consequently the  $\pi$ -theorem says that there will be three fewer  $\pi$ -terms than variables, whatever the nature of the assumptions regarding the importance of particular fluid properties, etc., made by the analyst.

For present purposes, it is convenient to attempt to unify the treatments of the authors cited above by a parallel analysis. For these purposes, the method outlined in section 5.2 will be followed as it has the advantage that if the repeating variables are selected and consistently used to form  $\pi$ -terms, a valid set is automatically insured.

In support of what may be criticized as an arbitrary selection of these repeating variables, it may be remarked that the physical system under consideration consists of a solid (though possibly elastic) tank which is filled with two fluids of sufficiently different densities and sufficiently insoluble in each other that a well-defined free surface can exist. This system is subjected to various accelerations, both rapidly varying and slowly varying, which cause fluid motion and a deformation of the free surface, thus giving rise to forces or pressures on the tank which interest the rocket or spacecraft designer, and which in almost all of the sloshing simulation studies to date have been the dependent variables of the problem. With the exception of very low gravity problems, the presence of a gravitational field of some sort is the most important constraint on the configuration of the fluids and plays a vital part in the results of theoretical fluid dynamics, which are covered at length elsewhere in this monograph. Additionally, forces or pressures resulting from these theoretical analyses are directly proportional to the mass densities of the fluids.

It is not unnatural then to choose as a repeating variable some characteristic length describing the size of the tank, say the diameter,  $D$ . One of the slowly varying acceleration components,  $a$ , which might correspond to the acceleration of gravity in the laboratory and to gravitational plus a constant thrust-induced acceleration in the prototype may be selected as a second, and the mass density of the more

dense of the two fluids in the tank can be selected as a third repeating variable:

<i>Repeating variable</i>	<i>Symbol</i>	<i>Dimension</i>
Characteristic diameter.....	<i>D</i>	<i>L</i>
Acceleration (linear).....	<i>a</i>	<i>LT<sup>-2</sup></i>
Liquid mass density.....	<i>ρ</i>	<i>ML<sup>-3</sup></i>

It can be seen that no nondimensional ratio can be formed from these three variables and that all basic dimensions are represented.

The remaining variables of potential interest may be classified as follows:

- (1) Geometrical
- (2) Kinematic requirements, primary independent variables
- (3) Mass density requirements
- (4) Dependent variables, forces, pressures, response parameters
- (5) Properties of structural materials
- (6) Dynamic properties of fluids
- (7) Interfacial effects

Consideration of variables in the first four groups will yield dimensionless parameters of the type which result naturally in treatments of the rigid body and incompressible inviscid hydrodynamic aspects of the fuel-sloshing problem. Elasticity and/or plasticity of the tank is introduced in the fifth group, and the remaining two groups introduce fluid properties other than mass density.

### Geometrical Considerations

If the three repeating variables chosen in the preceding paragraph are used to form a  $\pi$ -term with any additional variable having only the dimension of length, the exponents assigned mass density and acceleration must be zero, and there results the ratio of the new variable with the characteristic diameter, *D*. Consequently, if *n* linear dimensions, *b<sub>i</sub>*, in addition to *D*, are required to fully describe the tank

$$\pi_i = \frac{b_i}{D} \quad i=1, 2, \dots, n \quad (5.17)$$

In ratio notation

$$\pi'_i = \frac{(b_r)_i}{D_r} = 1 \quad i=1, 2, \dots, n$$

or

$$D_r = (b_r)_i \quad i=1, 2, \dots, n \quad (5.18)$$

Equations (5.17) and (5.18) are simply formal representations of the notion of strict geometrical similarity expressly implied in every engineering drawing. A similarity analysis for a practical fluid dynamic or structural problem will always result in strict geometrical similarity.

Thus, several trivial  $\pi$ -terms useful for manipulative purposes can be written as:

<i>Geometric variable</i>	<i><math>\pi</math>-term</i>
Any length, <i>b</i> .....	$\pi_1 = b/D$
Any angle, $\beta$ .....	$\pi_2 = \beta$
Any area, <i>A</i> .....	$\pi_3 = A/D^2$
Any volume, <i>V</i> .....	$\pi_4 = V/D^3$
Any area moment of inertia, <i>A<sub>2</sub></i> .....	$\pi_5 = A_2/D^4$
Any volume moment of inertia, <i>V<sub>2</sub></i> .....	$\pi_6 = V_2/D^5$

(5.19)

These results apply to any length variables pertaining to the configuration of the fluid, and in the strict sense to the thicknesses, and so forth, of structural elements.

Deviations from strict geometric similarity to simplify the model must be justified on grounds other than those of the similarity analysis. The only class of fluid dynamic problems where strict geometric similarity of the fluid boundaries is not maintained is that of the study of flow in rivers, harbors, and dams. There has yet been no justification advanced for deviations from strict geometric similarity in the fuel-sloshing problem, and none are generally made as far as the fluid boundary conditions are concerned.

Geometrical considerations pose no conceptual difficulty in any simulation, but often pose practical fabrication problems which may severely limit the experimental design. All the previously cited authors (refs. 5.9 through 5.11) have employed rather strict geometric similarity for the fluid boundary conditions in their analyses and usually single out one or more geometric variables of particular importance (such as the static liquid depth) which are formally included in the similarity specifications.

### Kinematic Requirements

In general there is some characteristic time associated with the sloshing problem. This

can be a natural period of some liquid free surface mode, the duration of an excitation transient, etc. If a particular characteristic time is denoted by  $\tau$ , and a  $\pi$ -term is formed with the chosen repeating variables

$$\pi_7 = \tau \sqrt{a/D}$$

or

$$\pi_7 = \frac{\tau^2 a}{D} \quad (5.20)$$

These are the forms derived and used in previous studies (refs. 5.9 through 5.12). If frequency,  $\omega$ , is conceptually more meaningful

$$\pi_8 = \omega \sqrt{D/a}$$

or

$$\pi_8 = \omega^2 \frac{D}{a} \quad (5.21)$$

The latter form of equation (5.21) has been extensively used as the independent frequency parameter in reporting slosh-force response data. In most dynamic problems, the number of frequency or time parameters is nearly as great as that of the length parameters. Including these other conceptual times or frequencies results in additional  $\pi$ -terms similar to equations (5.20) and 5.21), and these may be reduced to ratios of times or frequencies, as

$$\begin{aligned} \pi_9 &= \tau_i/\tau & (\tau_i = \text{any other time parameter}) \\ \pi_{10} &= \omega_i/\omega & (\omega_i = \text{any other frequency parameter}) \end{aligned} \quad (5.22)$$

A great variety of kinematic variables are of potential interest in the fuel-sloshing problem. It can be seen that the magnitude of any other acceleration,  $\ddot{x}$ , impressed upon the tank system results in

$$\pi_{11} = \ddot{x}/a \quad (5.23)$$

Any impressed velocity considered  $\dot{x}$ , results in

$$\pi_{12} = \dot{x}/\sqrt{aD} \quad (5.24)$$

Equation (5.24) is a general form of the familiar Froude number. Equations (5.20) through (5.24) are perfectly consistent with time-dependent impressed motions which have geometrically similar magnitudes in model and

prototype at the corresponding times defined by equation (5.20). Similar results to equations (5.23) and (5.24) obtain for angular velocities and accelerations:

$$\pi_{13} = \dot{\beta} \sqrt{D/a} \quad (5.25)$$

(for any angular velocity  $\dot{\beta}$ )

$$\pi_{14} = \ddot{\beta} D/a \quad (5.26)$$

(for any angular acceleration  $\ddot{\beta}$ ). Basically, the simulation analysis implies a uniform distortion of the time scale in accordance with maintaining equation (5.20) (or a variant) the same in model and prototype. Because this analysis presumes that a linear acceleration,  $a$ , is of prime importance, this parameter appears in every kinematic  $\pi$ -term. So long as a body force affects the fluid dynamics of the problem (in the laboratory or in the prototype), the acceleration parameter cannot be neglected and will materially affect what type of simulation is possible.

The analyses of references 5.9 through 5.11 are of this type and each contains the same essential specifications for kinematic similarity.

### Mass Density Requirements

In general, the fuel-sloshing problem has elements which are solid, liquid, and gaseous. Each of these elements has a mass density. Consequently, consideration of the mass density of the gas and the tank structure as additional parameters of interest results in

$$\pi_{15} = \rho_{\text{gas}}/\rho \quad (5.27)$$

$$\pi_{16} = \rho_{\text{solid}}/\rho \quad (5.28)$$

(where  $\rho$  is the previously chosen liquid density). In words, the ratios of the densities of liquid, solid, and gas must be the same in the model as in the prototype, though nothing is revealed thus far about the relative magnitudes of mass density between model and prototype. One sloshing simulation study (ref. 5.11) considered the gas density, where exactly the above relations were found. For the most part, the density of the gas is neglected as being of very small magnitude relative to the density of the

liquid (implicit in refs. 5.9 and 5.10) and this assumption is apparently borne out by experiment, at least in the normal fuel-sloshing problem. Specification of mass density of the solids in fixed ratio to the liquid density will satisfy the requirements of rigid body dynamics. For example, if the mass density of floating-can slosh-suppression devices (see ch. 4) bears the same ratio to that of the liquid in model and in prototype, geometrically similar cans will float on the surface of the liquid at scaled drafts. The mass density of the tank is quite properly neglected in reference 5.10, since the tank was assumed rigid and the interest was wholly in the fluid dynamics involved, all experimental results being independent of or corrected for the rigid body dynamics of the tank.

For reasons which will be apparent in a later section, Sandorff (ref. 5.9) considered the tank wall mass per unit area or, in other words, justified a departure from strict structural geometric similarity in combination with consideration of solid mass density.

#### Dependent Variables, Forces, Pressures, Response Parameters

The most common quantities of interest in sloshing simulation have been the net dynamic forces,  $F$ , and moments,  $\bar{M}$ , exerted by the liquid on the tank:

$$\pi_{17} = F/\rho a D^3 \quad (5.29)$$

$$\pi_{18} = \bar{M}/\rho a D^4 \quad (5.30)$$

Similarly, for pressure  $P$

$$\pi_{19} = P/\rho a D \quad (5.31)$$

When fluid elevations,  $\xi$ , velocities,  $\dot{\xi}$ , and accelerations,  $\ddot{\xi}$ , in response to tank motion are of interest, the resulting  $\pi$ -terms have exactly the same form as the corresponding kinematic parameters:

$$\pi_{20} = \xi/D \quad (5.32)$$

$$\pi_{21} = \dot{\xi}/\sqrt{a D} \quad (5.33)$$

$$\pi_{22} = \ddot{\xi}/a \quad (5.34)$$

Actually, the force or pressure variables might under some circumstances be the independent

variables and the tank motion the dependent variables. The form of the immediately preceding nondimensional parameters is the same as that of Sandorff (ref. 5.9). In reference 5.10 and elsewhere, slosh-force amplitude response,  $|F|$ , is sometimes presented as

$$\frac{|F|}{\rho a D^3 (x_0/D)}$$

(where  $x_0$  is the tank excitation amplitude). Essentially this is the replacement of  $\pi_{17}$  by  $\pi_{17}/\pi_1$  and implies that the slosh-force response and the tank excitation are related by a linear differential equation.

#### Summary of Inertial and Mechanical Scaling

The usual sloshing simulation problem involves measuring one or all of the dependent variables when the tank is given an acceleration as a function of time. It can be noted that some of the parameters derived in the last four subsections are redundant, and are related to one another in quite ordinary mechanical ways. Certain other sets of parameters are of potential use as consistent nondimensional ways of presenting experimental results. Yet other parameters are useful for the manipulation of the form of the remaining parameters.

Though such lists of  $\pi$ -terms as have been developed in the preceding paragraphs are not uncommon results of dimensional analysis, the restrictions on experimental design which have been imposed thus far in the analysis are very few. The most important relation developed between model and prototype quantities to this point is equation (5.20), which can be written in ratio notation as

$$\pi_r' = \tau_r^2 a_r / D_r = 1 \quad (5.35)$$

or

$$\tau_r^2 = D_r / a_r$$

This result means that if all the important variables pertaining to the problem have been outlined in the preceding sections, a model of any geometric scale,  $D_r$ , can be used in a 1 g acceleration field by varying the time scale,  $\tau_r$ . This relation fixes the time scale if the geometric scale,  $D_r$ , is determined from other considerations.

No restrictions have been placed upon the geometric scale,  $D_r$ , or upon the mass density scale,  $\rho_r$ , thus far. It has been assumed that the acceleration scale,  $a_r$ , is fixed by the respective acceleration fields encountered by model and prototype. In many problems, practical fabrication problems control the geometric scale ratio, and, in some instances, the implied compression or expansion of the model time scale, equation (5.35), may not be feasible or economic.

Given that the acceleration scale is important in any given simulation, and that the time scale does not impose really serious limitations on the experimental designer, approximate simulation plots showing permissible geometric scale ratios,  $D_r$ , as a function of the required acceleration scale ratio,  $a_r$ , are useful in showing the types of simulations which can be achieved. The corresponding simulation plot for the analysis to this point is devoid of restrictions, but no material properties have been introduced into the analysis thus far. It is the question of exactly what construction materials and fluids should be used in the model that introduce serious restrictions on what can be done. These questions will be taken up in the next sections with the implied understanding that all the nondimensional parameters developed in the preceding sections will hold.

### Structural Material Properties

Chapter 9 of this monograph may be referred to for a more detailed account of the importance of dynamic interaction between the sloshing fluid and the elastic deformations of the containing structure. Thus far in the similitude analysis, only the density of a geometrically similar structure has been considered. When the elastic properties of the material are described by Young's modulus,  $E$ , and Poisson's ratio,  $\bar{\nu}$ ,

$$\pi_{23} = E/\rho a D \quad (5.36)$$

$$\pi_{24} = \bar{\nu} \quad (5.37)$$

for stress,  $\bar{\sigma}$ , and strain,  $\epsilon$ , we have

$$\pi_{25} = \bar{\sigma}/\rho a D \quad (5.38)$$

$$\pi_{26} = \epsilon \quad (5.39)$$

The preceding  $\pi$ -terms in conjunction with those in the previous section define a "replica" structural tank model whose dynamic deflections will be geometrically similar to those of the prototype at corresponding times defined by equation (5.20). To illustrate this notion, the theoretical frequencies of the natural modes of vibration of plates may be written as

$$W^2 = \frac{E}{\rho_r (1 - \bar{\nu}^2) t_p^2} \times (\text{a nondimensional function of plate geometry}) \quad (5.40)$$

( $t_p$  denotes plate thickness). If the ratio of natural frequencies of a plate in the replica model to the corresponding plate in the prototype is taken, we have

$$(W_r)^2 = \frac{E_r}{\rho_r} \frac{(1 - \bar{\nu}^2)_{\text{prototype}}}{(1 - \bar{\nu}^2)_{\text{model}}} \frac{1}{(t_p)^2} \quad (5.41)$$

If  $\pi_{24}$  is the same in model and prototype,  $\pi_{18}$  is satisfied and if  $E_r$  is written from equation (5.36)

$$E_r = \rho_r a_r D_r \quad (5.42)$$

then

$$(W_r)^2 = a_r / D_r \quad (5.43)$$

Equation (5.43) is exactly the same as the frequency ratio required by equation (5.21).

The ratio expression (5.42) provides a means of evaluating what sort of simulation might be feasible for replica structural modeling using dissimilar structural materials (ref. 5.13) with simultaneous satisfaction of inertial scaling, and this expression has been partially plotted in figure 5.1 as lines of  $D_r$  vs.  $a_r$  for values of the composite ratio  $E_r/\rho_r$ . The ratio  $E/\rho$  for any material actually used in the structure of a booster rocket or spacecraft is likely to be somewhere near maximum for known materials because of the premium placed on unnecessary weight and, consequently, the composite ratio,  $E_r/\rho_r$ , will probably not have a value exceeding 1.0, whatever the choice of model materials. If the weak, heavy composites now under development (ref. 5.13) are included, model materials might be available to provide a minimum value of  $E_r/\rho_r$  of about 0.01. Thus the simulation plot (fig. 5.1) is divided into a band bounded by the lines:  $E_r/\rho_r = 1$  and 0.01 in

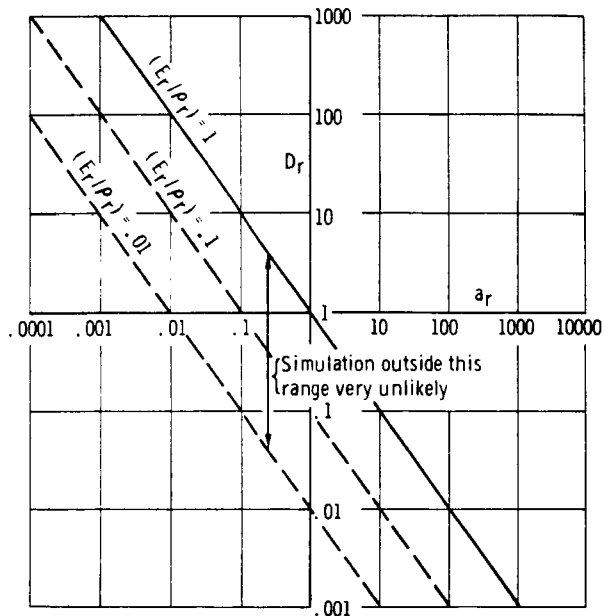


FIGURE 5.1.—Approximate simulation ranges—replica model of elastic tank, inertial scaling of fluid dynamics only.

which simulation under the stated assumptions may be feasible; far outside this band, simulation is highly unlikely.

If simulation of the plastic behavior of the material is attempted (yield strength,  $\sigma_y$ , for example):

$$\pi_{27} = \sigma_y / \rho a D \quad (5.44)$$

Equation (5.44) is of the same form as equation (5.42), and much the same arguments apply to the feasible range of  $[(\sigma_y)/\rho]$  as applied to that for  $E_r/\rho_r$ . Consequently, figure 5.1 will roughly apply to this case also.

There appears to be little hope for this type of simulation in the low gravity case if the laboratory is at 1 g ( $a_r > 100$ ), at least not with any reasonable geometric scales. There is potential in the case that the prototype is in a relatively high acceleration field and the model is at 1 g, especially if the model can be as large as or slightly larger than the prototype.

On the whole, replica modeling of structure is expensive and sometimes impossible. (See the further discussion of replica modeling in pt. II of this chapter.) An alternate approach is developed by Sandorff (ref. 5.9). This ap-

proach still involves strict geometric similarity insofar as the fluid boundaries are concerned, but involves relaxation of structural geometric similarity so that the structural portion of the model is "adequate" for purposes of studying fluid interaction with the gross tank bending and "breathing" modes of vibration. The following development is taken largely from reference 5.9.

The tank walls may be constructed of unstiffened plate, stiffened skin, sandwich structure, or thin skin pressurized for stability. Assuming the stiffness properties to be isotropic with respect to dimensions in the plane of the shell, the following load-strain relations express the rigidity of the shell:

$$N_x = \Lambda(\epsilon_x + \bar{\nu}\epsilon_y) \quad N_{yz} = \beta_z\gamma_{yz}$$

$$N_y = \Lambda(\epsilon_y + \bar{\nu}\epsilon_x) \quad M_{xz} = D_b(w_{xz} + \bar{\nu}'w_{yy})$$

$$N_{xy} = \beta_{xy}\gamma_{xy} \quad M_{yy} = D_b(w_{yy} + \bar{\nu}'w_{xx})$$

$$N_{zz} = \beta_z\gamma_{zz} \quad M_{xy} = Bw_{xy}$$

The notation is illustrated in figures 5.2 and 5.3.

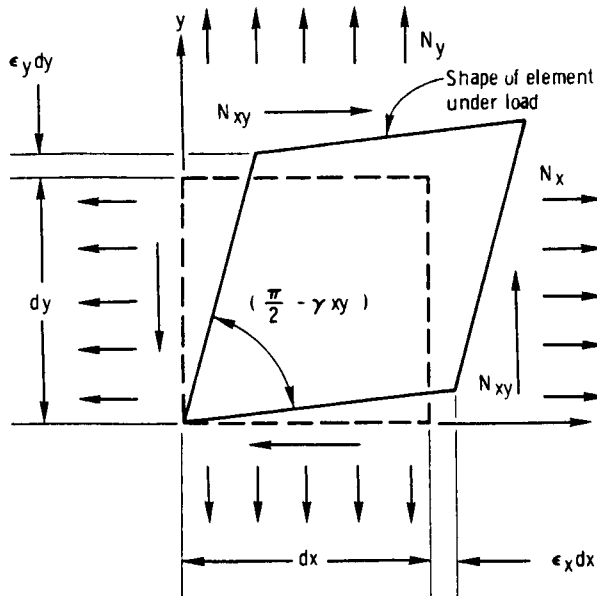


FIGURE 5.2.—In-plane loadings and deformations of shell element: Extension and shear (ref. 5.9).

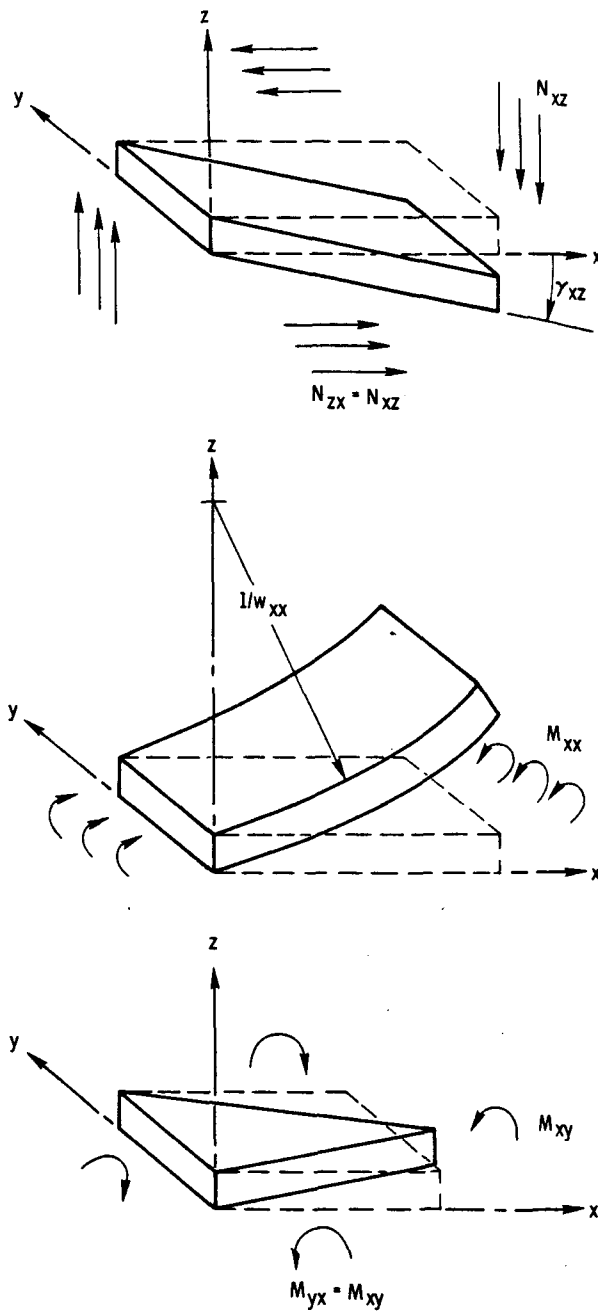


FIGURE 5.3.—Transverse loadings and deformations of shell element: Beam shear, bending, and twisting (ref. 5.9).

$N_z$ =normal force per unit width on edges parallel to  $y$ -axis

$N_{xy}$ =shearing force per unit width, equal on  $x$ - and  $y$ -edges

$M_z$ =bending moment per unit width on edges parallel to  $y$ -axis

$M_{xy}$ =twisting moment per unit width, equal on  $x$ - and  $y$ -edges

$\epsilon_x$ =extensional strain parallel to  $x$ -axis

$\gamma_{xy}$ =in-plane shearing strain; i.e., shear of an element parallel to  $xy$  plane

$\gamma_{xz}$ =transverse shearing strain; i.e., shear of an element parallel to  $xy$  plane

$w$ =transverse displacement of neutral plane of shell wall,  $w(x, y, z)$

$w_{xx}$ =bending curvature of neutral plane about  $y$ -axis,  $\partial^2 w / \partial x^2$

$w_{xy}$ =twisting curvature of neutral plane,  $\partial^2 w / \partial x \partial y$

$\Lambda$ =extensional stiffness, ( $\Lambda = Et / (1 - \bar{\nu}^2)$  for homogeneous plate)

$\beta_{xy}$ =in-plane shearing stiffness, ( $\beta_{xy} = Gt$  for homogeneous plate)

$\beta_z$ =transverse shearing stiffness, ( $\beta_z = Gt$  for homogeneous plate)

$D_b$ =bending stiffness, ( $D_b = Et^3 / 12(1 - \bar{\nu}^2)$  for homogeneous plate)

$B$ =torsional stiffness, ( $B = D_b$  for homogeneous plate)

$\bar{\nu}$ =Poisson's ratio

$\bar{\nu}'$ =Poisson-type elastic constant indicating coupling between moment about one axis and curvature about the other ( $\bar{\nu}' = \bar{\nu}$  for homogeneous plate)

$E$ =elastic (Young's) modulus in extension

$G$ =shear modulus

$t$ =thickness

The stiffnesses ( $\beta_{xy}$ ,  $\beta_z$ ,  $D_b$ , and  $B$ ) can be determined either analytically or experimentally. These relations govern the elastic behavior of isotropic sandwich structure and isotropic symmetrically stiffened sheet, and therefore permit consideration of a wide variation in shell-wall detail to meet overall elastic properties. Orthotropic stiffened skin structure can be handled in the same manner, with additional elastic constants to define anisotropy and cross-coupling of elastic deformation processes.

The advantage of the above representation is that fine detail such as the actual thickness of the wall, dimensions of stiffener detail if a stiffened shell is used, attachments, etc., need not necessarily be duplicated. The overall shell-wall extension and bending are the imme-

diate concern, not extremely local effects such as material rupture or local buckling.

Rupture is a design consideration, however, and, therefore, stress distributions must often be obtained. Stresses, as such, are not recognized as existing in the shell wall in the above load-strain relations which specify only forces  $N$  and moments  $M$ . Similitude is to be preserved with respect to  $N$  and  $M$ , not stress, and to convert from one to the other, the particular section detail (local thickness, etc.) must be used, which will not necessarily be in scale from model to prototype. Similarly, insofar as unit weight is concerned, the significant parameter for the shell wall is  $\rho_s t_w$ , mass per unit of surface area, not of volume, where  $t_w$  is an equivalent distributed thickness measurement for the wall structure.

There may be portions of the tank structure, e.g., baffles, which, in deforming elastically, affect the fluid motion in an important manner, and which cannot be treated as thin plates under plane stress. In such cases it is often possible to express significant deformational characteristics in terms of overall section properties, as is done above for thin plate, and establish similitude requirements for the overall stiffness properties. Thus by introducing an acceptable approximation, the requirement of strict geometric similarity in a small-scale model is avoided. For the present, however, deflections of only the external thin-wall tank structure will be considered.

The significant additional parameters for this model of the tank structure may be summarized as follows:

Quantity	Symbol	Dimension
Load in tank wall.....	$N$	$MT^{-2}$
Moment in tank wall.....	$M$	$MLT^{-2}$
Local displacement, tank wall.....	$x$	$L$
Extensional stiffness.....	$\Lambda$	$MT^{-2}$
In-plane shear stiffness.....	$\beta_{xy}$	$MT^{-2}$
Transverse shear stiffness.....	$\beta_z$	$MT^{-2}$
Bending stiffness.....	$D_b$	$ML^2 T^{-2}$
Torsional stiffness.....	$B$	$ML^2 T^{-2}$
Poisson's ratio.....	$\bar{\nu}$	-----
Bending Poisson-type ratio.....	$\bar{\nu}'$	-----
Density of tank wall.....	$\rho_s t_w$	$ML^{-2}$

The corresponding  $\pi$ -terms are denoted with a prime to denote that they pertain to the above special list. Using the same repeating variables as in previous terms:

$$\left. \begin{aligned} \pi'_{28} &= N/\rho_a D^2 \\ \pi'_{29} &= M/\rho_a D^3 \\ \pi'_{30} &= x/D \\ \pi'_{31} &= \Lambda/\rho_a D^2 \\ \pi'_{32} &= \beta_{xy}/\rho_a D^2 \\ \pi'_{33} &= \beta_z/\rho_a D^2 \\ \pi'_{34} &= D_b/\rho_a D^4 \\ \pi'_{35} &= B/\rho_a D^4 \\ \pi'_{36} &= \bar{\nu} \\ \pi'_{37} &= \bar{\nu}' \\ \pi'_{38} &= \rho_s t_w / \rho D \end{aligned} \right\} \quad (5.45)$$

The first three  $\pi$ -terms of the preceding list are essentially response parameters. Holding the remaining eight parameters the same in model and prototype provides structural similitude insofar as dynamic deflections and frequencies of the tank wall are concerned. As previously noted, stress similarity is not attained, but is assumed to be unimportant with respect to fluid-structure interaction. It does not appear possible to simplify greatly the above parameters for all types of tank-wall construction other than to minimize the appearance of liquid density,  $\rho$ , and tank diameter,  $D$ , in the eight important structural parameters. One result of such a manipulation is as follows (double primes denote results of the manipulation):

$$\left. \begin{aligned} \pi''_{32} &= \pi'_{32}/\pi'_{31} = \beta_{xy}/\Lambda \\ \pi''_{33} &= \pi'_{33}/\pi'_{31} = \beta_z/\Lambda \\ \pi''_{35} &= \pi'_{35}/\pi'_{34} = B/D_b \\ \pi''_{34} &= \pi'_{34}/\pi'_{31} = D_b/\Lambda D^2 \end{aligned} \right\} \quad (5.46)$$

and  $\pi'_{36}$ ,  $\pi'_{37}$ ,  $\pi'_{38}$  are unchanged:

$$\left. \begin{aligned} \pi'_{36} &= \bar{\nu} \\ \pi'_{37} &= \bar{\nu}' \\ \pi'_{38} &= \rho_s t_w / \rho D \\ \pi'_{39} &= \Lambda / \rho a D^2 \end{aligned} \right\} \quad (5.47)$$

This form of the simulation parameters is virtually that arrived at in reference 5.9. These simulation parameters are much simplified in the case that the tank wall in both model and prototype can be represented by an equivalent homogeneous plate.

By substituting the homogeneous plate equivalents for  $\Lambda$ ,  $\beta_{xy}$ ,  $\beta_z$ ,  $D_b$ ,  $B$ , and  $\bar{\nu}'$  into equations (5.46) and (5.47)

$$\left. \begin{array}{l} \pi''_{32} = \pi''_{33} = \frac{1-\bar{\nu}}{2} \\ \pi'_{36} = \pi'_{37} = \bar{\nu} \\ \pi'_{35} = 1 \\ \pi''_{34} = \frac{1}{12} \left( \frac{t_w}{D} \right)^2 \\ \pi'_{31} = E t_w / \rho a D^2 (1 - \bar{\nu}^2) \\ \pi'_{38} = \rho_s t_w / \rho D \end{array} \right\} \quad (5.48)$$

It can be seen that the assumption of homogeneous plate tank walls has the effect of simplifying the form of the results but not helping the simulation problem appreciably. In equation (5.48),  $\pi''_{34}$  requires that the tank walls be scaled down in accordance with the geometric scale ratio,  $D_r$ . If  $\pi''_{34}$  is held the same, then it follows that  $\rho_s/\rho$  must be the same in model and prototype. Additionally, if  $\pi'_{36}$  is the same in model and prototype  $\pi'_{31}$  implies that  $E/\rho a D$  must be the same in model and prototype. Thus, equation (5.48) for homogeneous plate tank walls is exactly the same as the specification for replica modeling shown in equations (5.36), (5.37), (5.28), and (5.19). If the prototype tank wall can be replaced theoretically by an equivalent plate of simpler geometry and greater relative thickness, this approach may be useful. The source of the above difficulty with the homogeneous plate case is in  $\pi''_{34}$  which resulted from the plate bending stiffness parameter,  $D_b$ . If tank-wall bending stiffness can be neglected, considerable simplification of the fabrication may be effected by holding the grouped parameters  $\rho_s t_w / \rho D$ ,  $E t_w / \rho a D^2$ , and  $\bar{\nu}$  the same in model and prototype. Neglect of bending stiffness is roughly equivalent to considering only extensional modes of shell

vibration to be important with respect to fluid interaction and, similarly, buckling not to be a problem.

The foregoing illustrations perhaps point out that simulation of fluid structure interaction requires some very considerable judgment on the part of the designer of the experiment. In general, the replica modeling approach is expensive and suffers from lack of a wide range of suitable materials. The success of the "adequate" structural model approach is highly dependent on a prior understanding of the interaction phenomena being investigated.

### **Dynamic Properties of Fluids: General**

Neglecting interface phenomena and density, which have been considered from the outset, the common dynamic engineering properties of fluids which are of interest may be listed as follows:

For the liquid:

	Symbol	Dimension
Dynamic viscosity	$\mu$	$ML^{-1}T^{-1}$
Vapor pressure	$P_v$	$ML^{-1}T^{-2}$
Bulk modulus	$E_L$	$ML^{-1}T^{-2}$

For the gas:

	Symbol	Dimension
Dynamic viscosity	$\mu_g$	$ML^{-1}T^{-1}$
Bulk modulus	$E_g$	$ML^{-1}T^{-2}$

Five  $\pi$ -terms result when the previously noted repeating variables are used:

$$\left. \begin{array}{l} \pi_{39} = \mu^2 / \rho^2 a D^3 \\ \pi_{40} = \mu_g^2 / \rho^2 a D^3 \\ \pi_{41} = E_L / \rho a D \\ \pi_{42} = E_g / \rho a D \\ \pi_{43} = P_v / \rho a D \end{array} \right\} \quad (5.49)$$

All previous  $\pi$ -terms are assumed to hold, as before.

The parameters  $\pi_{39}$  and  $\pi_{40}$  correspond to the Reynolds number, as can be seen more clearly by performing a replacement operation:

$$\pi'_{39} = \frac{\pi_{12}}{(\pi_{39})^{1/2}} = \frac{\dot{x} D \rho}{\mu} = \frac{\dot{x} D}{\nu} \quad (5.50)$$

where the kinematic viscosity,  $\mu/\rho$ , is signified by  $\nu$ . This form of  $\pi_{39}$  can be immediately recognized as the Reynolds number as used in

fluid flow problems. Sandorff (ref. 5.9) derives a viscosity parameter identical to  $\pi_{39}$ , while in reference 5.10 the form chosen was  $1/\sqrt{\pi_{39}}$ . The characteristic damping of the sloshing of the free surface was correlated with a "damping parameter" equivalent to  $(\pi_{39})^{1/4}$  by Stephens (ref. 5.14). A similar but numerically different "damping parameter" was used by Sumner (ref. 5.15) for correlation and extrapolation of first-mode slosh damping in a roughly ellipsoidal tank. In this case, the "damping parameter" used corresponds to  $(\pi_{39})^{1/2}$ . The material contained in chapter 4 points up the importance of the viscosity parameter to the fuel-sloshing problem. The viscosity parameter for the gas,  $\pi_{40}$ , is most often neglected, indeed it may only have been mentioned once or twice in the sloshing literature (refs. 5.11 and 5.12).

It seems to be generally doubted that any gas properties will have measurable influence on normal lateral sloshing problems because of the much larger relative density of the liquid. In special problems involving liquid surface instability under sudden reversals of an acceleration field normal to the liquid surface, the properties of the gas may be important. Similarly, the properties of the gas may assume greater importance in the low gravity case. The gas viscosity parameter,  $\pi_{40}$ , and the elasticity parameter,  $\pi_{42}$ , will be neglected in the remainder of the present treatment except to comment that  $\pi_{42}$ , the elastic parameter for the gas, may be quite easily transformed into Mach number utilizing  $\pi$ -terms previously determined.

The term  $\pi_{41}$  in equation (5.49) (the form derived in ref. 5.10) may also be transformed into a Mach number for the liquid. (An analogous relationship is used in eq. (9.10) of ch. 9.) Replacing  $\pi_{41}$  as follows, letting  $\sqrt{E_L/\rho} = c_0$

$$\pi'_{41} = \frac{\pi_8}{\sqrt{\pi_{41}}} = \frac{\omega D}{c_0} \quad (5.51)$$

which may be seen to be of the form of  $k$  in equation (9.10), which has to do with coupled pressure resonances in an elastic tank (in that case some of the similarity terms of the preceding sections are also evident).

The last  $\pi$ -term of equation (5.49) to be commented upon is  $\pi_{43}$ , which is a parameter related to cavitation in the liquid. The parameter  $P_v$  is analogous to an ultimate strength. If the pressure at a point in the liquid is

$$P = P_0 + P_a + \rho a h \quad (5.52)$$

where

$P$ =Ambient pressure

$P_0$ =Pressure at free surface (ullage pressure)

$P_a$ =Dynamic pressure in the fluid induced by sloshing

$h$ =Depth from free surface to point in question (measured in the direction of  $a$ )

This pressure must be scaled in accordance with  $\pi_{19}$ , or

$$\frac{P}{\rho a D} = \frac{P_0}{\rho a D} + \frac{P_a}{\rho a D} + \frac{h}{D} \quad (5.53)$$

In order that cavitation occur

$$P - P_v < 0 \quad (5.54)$$

This criterion may be written as the difference of equation (5.53) and  $\pi_{41}$

$$\frac{P_0}{\rho a D} + \frac{P_a}{\rho a D} + \frac{h}{D} - \frac{P_v}{\rho a D} < 0 \quad (5.55)$$

It is to be noted that each term in equation (5.55) has been previously specified as a similarity parameter. The  $h/D$  term is the same in model and prototype if geometrical similarity is maintained, as is the dynamic pressure term (a response) if both geometrical similarity and the time scale implied by equation (5.20) are maintained. If for some reason the ullage pressure must be scaled in accordance with  $P_0/\rho a D$ , then  $\pi_{43}$  fixes the required vapor pressure of the model fluid for similarity of cavitation effects. If strict similarity of the ullage pressure may be neglected, the cavitation effects in the fluid may be considered to be governed by

$$\frac{P_0 - P_v}{\rho a D} = \frac{\Delta P}{\rho a D} \quad (5.56)$$

This parameter may be transformed with the aid of  $\pi_{12}$  into the form of the "cavitation number" usually employed in external flow problems

in high-speed hydrodynamics. Because much of the detail of the basic mechanism of cavitation is imperfectly known, the "cavity pressure" ( $P_c$ , a measurable experimental quantity) is often substituted for the fluid vapor pressure  $P_v$  in such investigations.

Under the assumptions that inertial scaling is required, gas properties and absolute ullage pressure are unimportant, and that the tank is rigid, the three liquid  $\pi$ -terms allow rough simulation charts to be made. Transforming  $\pi_{39}$  and  $\pi_{41}$  and equation (5.56) to ratio notation,

$$\pi_{39}^r = \frac{(\mu_r)^2}{(\rho_r)^2 a_r (D_r)^3} = 1 \quad (5.57a)$$

$$\pi_{41}^r = \frac{(E_L)_r}{\rho_r a_r D_r} = 1 \quad (5.57b)$$

$$\pi_{43}^r = \frac{(\Delta P)_r}{\rho_r a_r D_r} = 1 \quad (5.57c)$$

Rearranging and letting  $\nu$  = the kinematic viscosity  $\mu/\rho$

$$D_r = \frac{(\nu_r)^{2/3}}{a_r^{1/3}} \quad (5.58a)$$

$$D_r = \frac{(E_L)_r}{\rho_r a_r} \quad (5.58b)$$

$$D_r = \frac{(\Delta P)_r}{\rho_r a_r} \quad (5.58c)$$

### Dynamic Properties of Fluids: Viscosity

Equation (5.58a) summarizes the basic problem in simulation of the viscous damping effects discussed in chapter 4. The data on fluid properties presented in the appendix to this monograph allow a rather crude idea of the range of kinematic viscosities to be anticipated for the fluids used as propellants in booster rockets and spacecraft. The situation is summarized in figure 5.4, where a symbolic spec-

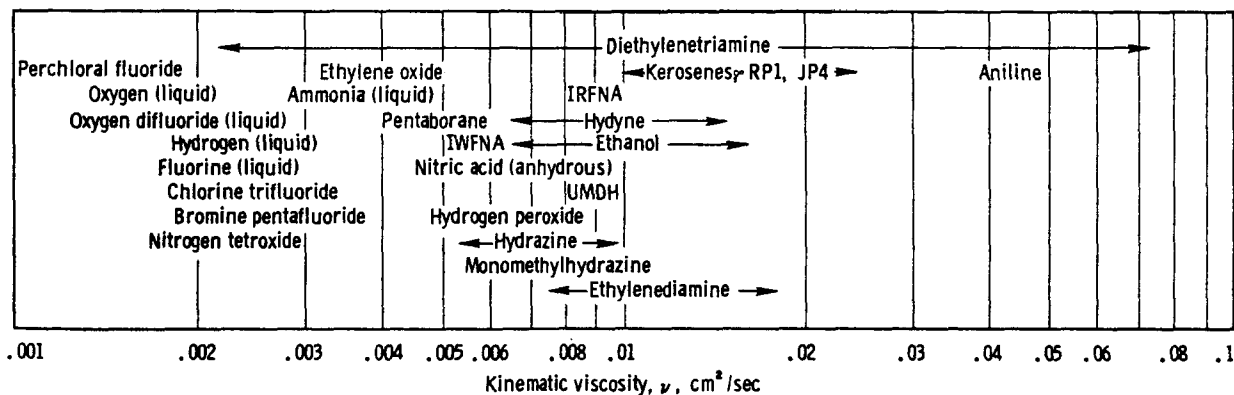


FIGURE 5.4.—Kinematic viscosity: Typical values for fuels and oxidizers.

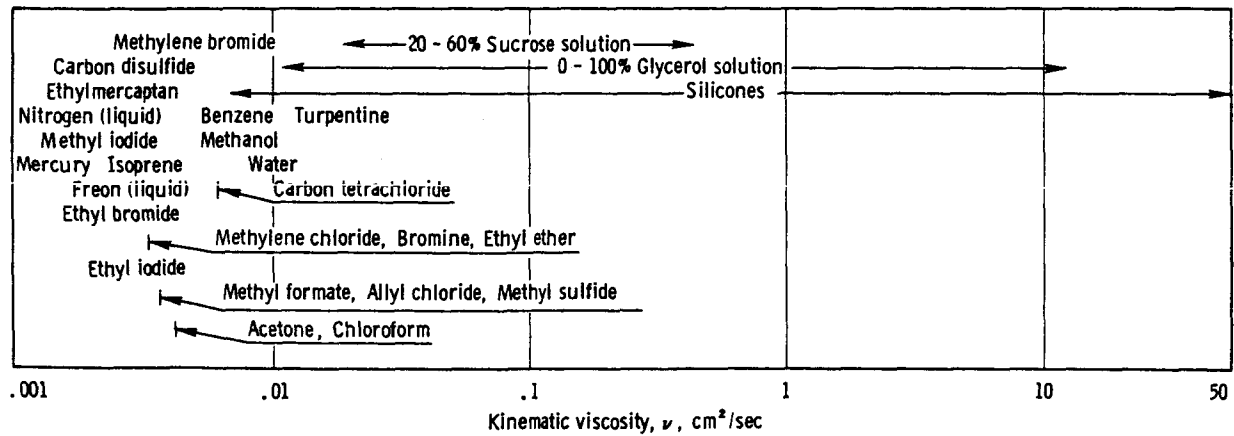


FIGURE 5.5.—Kinematic viscosity: Typical values for various liquids.

trum of propellant kinematic viscosities is displayed. (The kinematic viscosities of all fluids vary considerably over the environmental temperature range possible in space exploration, and the particular points assigned each fluid correspond to the temperatures quoted in the appendix.) For purposes of a general view of what types of inertial-viscous simulation are feasible, it is important to note that the kinematic viscosity range shown in figure 5.4 is nearly covered by the kinematic viscosities of liquid oxygen and kerosene which are at the same time one of the most prevalent oxidizer-fuel combinations.

Figure 5.5 is a similar "spectrum" of kinematic viscosity for a variety of liquids which might serve, or have already served, in sloshing experiments. Some of these would present biological as well as mechanical hazards, as can be easily noted.

The above information on kinematic viscosity, combined with equation (5.58a), allows general remarks on what types of inertial-viscous simulation are possible. Figure 5.6 is a plot of equation (5.58a) for some significant values of  $\nu_r$ . In this plot, the line,  $\nu_r = 1$ , indicates the required relationship between geometric and acceleration scale ratios if model

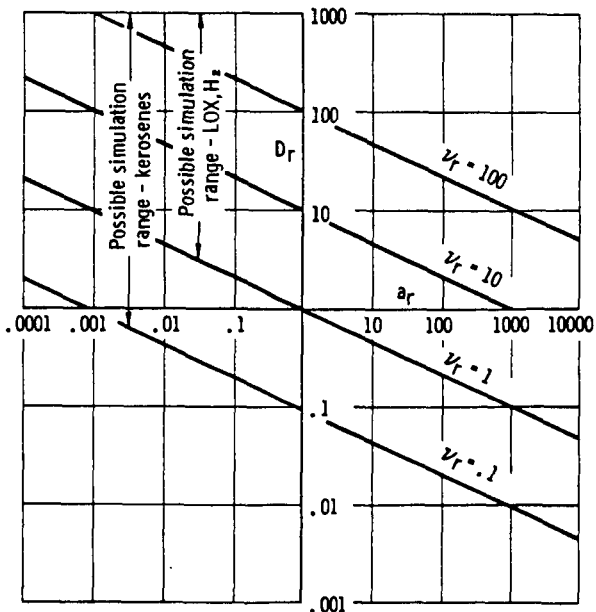


FIGURE 5.6.—Simulation plot: Inertial-viscous scaling, geometrically similar rigid tanks.

and prototype contain the same fluid. If the simulation problem involves a prototype fuel of kerosene, a comparison of figures 5.4 and 5.5 indicates that the smallest ratio of  $\nu_r$ , which may be achieved with the given model fluids is approximately 0.1, and consequently that inertial-viscous simulation of kerosene may be possible anywhere above the line  $\nu_r = 0.1$  on figure 5.6. If liquid oxygen or one of the other cryogenics is involved in the prototype, a comparison of figures 5.4 and 5.5 indicates that the smallest ratio of  $\nu_r$ , which may be achieved is about 1.0, or, in other words, simulation of the cryogenics is possible in principle only near and above the line  $\nu_r = 1$  on figure 5.6. That this situation is unfortunate can be inferred from the following example: Suppose that simulation of a 9-meter-diameter rocket booster tank in a 3-g acceleration field is required, and that models are restricted to be in the laboratory at 1 g. The specified acceleration ratio is (1/3) and consequently from figure 5.6:

(1) If prototype fluid is kerosene, the smallest suitable model tank would be approximately 1.2 meters in diameter.

(2) If the prototype fluid is a cryogenic, the smallest suitable model tank would be approximately 12 meters in diameter (excluding mercury as a practical model fluid).

(3) If the prototype fluid is a cryogenic and the model fluid is water, a suitable model tank diameter would be approximately 40 meters.

The results in the above example are based on the fluid properties outlined in figures 5.4 and 5.5. The problems arise because of the lack of fluids with kinematic viscosities significantly lower than that of liquid oxygen. It might be speculated that simulation of the cryogenic in the above example might be achieved with a 30- or 60-centimeter-diameter tank if liquid helium were the model fluid. However, this might be considered as a highly unlikely possibility because of the unusual properties of liquid helium other than viscosity.

To summarize the general situation with respect to inertial-viscous simulation of fuel sloshing, it must be remarked that simulation in the strict sense with moderate-sized laboratory models can be accomplished in a limited number of cases of interest. Recourse must be

had to the extrapolation methods outlined elsewhere in this monograph.

#### Dynamic Properties of Fluids: Compressibility

To continue the discussion of the simulation equations (5.58), equation (5.58b) allows a summary of what is possible if inertia-compressibility scaling is desired. It is more convenient to alter equation (5.58b) to be a function of sonic velocity ratio. Since

$$\sqrt{\frac{E}{\rho}} = c \quad (\text{the sonic velocity characteristic of the fluid}) \quad (5.59)$$

$$\frac{(E_L)_r}{\rho_r} = c_r^2 \quad (5.60)$$

Thus equation (5.58b) becomes:

$$D_r = \frac{c_r^2}{a_r} \quad (5.61)$$

Though the fluid property data of the appendix are incomplete with respect to sonic velocities, the values shown indicate that sonic velocities for prototype liquids will probably range from 500 to 2000 m/sec, with both liquid oxygen and kerosene having sonic velocities in the vicinity of 1000 m/sec. Almost exactly the same range is shown in the appendix for "modeling" liquids. As a consequence, the probable greatest ratio between model and prototype sonic velocities would be 4 and the smallest 1/4. Thus, a maximum range for  $c_r^2$  may be:

$$0.06 < c_r^2 < 16 \quad (5.62)$$

If kerosene and liquid oxygen are of interest, the probable maximum range of  $c_r^2$  would be

$$0.25 < c_r^2 < 4 \quad (5.63)$$

Equation (5.61) is plotted in figure 5.7 for the above ranges of  $c_r^2$ , with the extreme limits shown. Probably more practical limits are represented by the range between  $c_r^2 = 0.5$  and 2. Sandorff (ref. 5.9) concludes, in effect, that none of the common model fluids is sufficiently compressible to meet LOX-JP-4 simulation needs for geometric-scale ratios of 1/8 and 1/16 and acceleration scale ratios of 0.2 and 2.0.

Figure 5.7 bears out this conclusion, since these combinations of  $D_r$  and  $a_r$  are at or below the line  $c_r^2 = 0.5$ . If compressibility-inertial scaling is required, artificial means of increasing fluid compressibility may be feasible, and Sandorff suggests some possibilities (fig. 5.8).

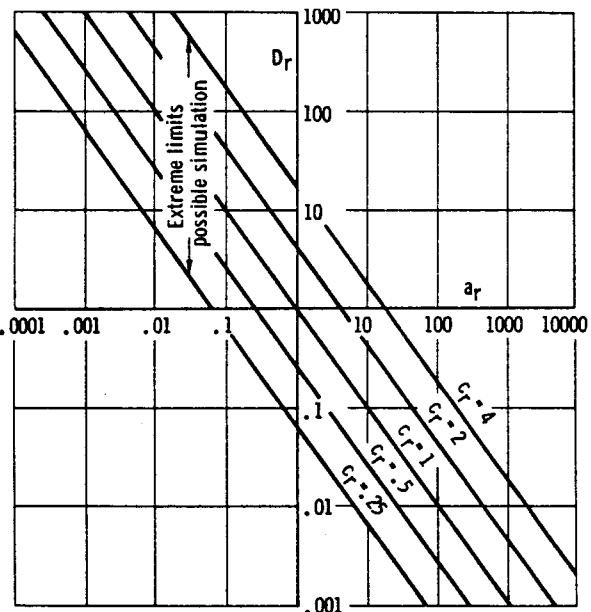


FIGURE 5.7.—Simulation plot: Inertial-compressibility scaling, geometrically similar rigid tanks.

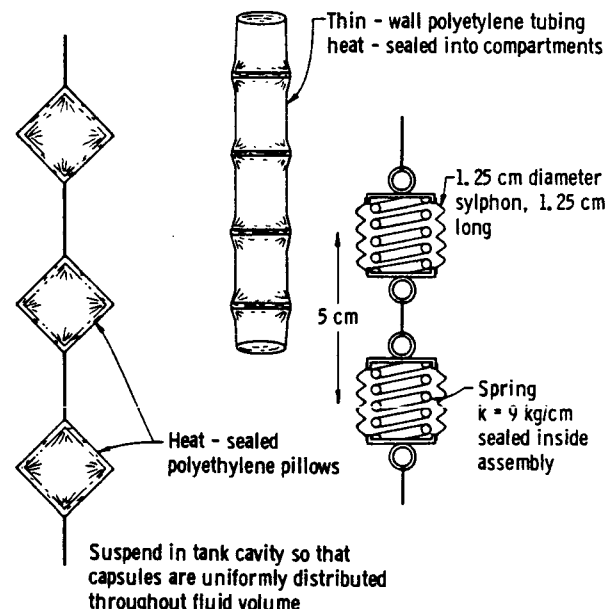


FIGURE 5.8.—Methods of artificially increasing compressibility (ref. 5.9).

### Dynamic Properties of Fluids: Cavitation

The last simulation problem involving fluid properties is equation (5.58c), for cavitation effects:

$$D_r = \frac{(\Delta P)_r}{\rho_r a_r} \quad (5.58c)$$

Since

$$\Delta P = P_0 - P_v$$

where

$P_0$  = gas pressure above the fluid

$P_v$  = fluid vapor pressure

this equation may be satisfied independently of the fluids and scale ratios if the absolute gas pressure is assumed not important to the simulation. The model gas pressure,  $(P_0)_M$ , may be adjusted to achieve the desired ratio,  $\Delta P_r$ , given model and prototype fluids, geometric scale ratio, acceleration scale ratio, and  $(P_0)_F$  the pressure of the prototype gas. Consequently, the simulation possibilities with this particular simulation design philosophy are not limited, in principle. In practice, adjustment of model gas pressure means experimenting within a variable pressure chamber, or designing the model tank structure to withstand possibly much greater pressure differentials than are feasible.

It is instructive to consider the magnitudes of pressure differences  $P_0 - P_v$  which may be encountered in the prototype. For pressure-fed rocket propulsion systems, the gas pressure may be very high, perhaps much greater than 6 atmospheres. For pump-fed propulsion systems, which appear to offer weight advantages over the pressure-fed systems for large booster rockets, a typical minimum gas pressure may be 1.5 atmospheres. Thus a range of  $P_0 - P_v$  for typical booster rocket fuel tanks may be 0.5 to 6 atmospheres, assuming the range of fuel vapor pressures shown in the appendix. Altering equation (5.58c):

$$D_r a_r = \left[ \frac{P_0 - P_v}{\rho} \right]_{model} \left[ \frac{\rho}{P_0 - P_v} \right]_{prototype} \quad (5.64)$$

Again consulting the appendix for typical mass densities  $\rho$  for fuels, an expected typical range for  $(P_0 - P_v)/\rho$  is

$$0.2 < \left[ \frac{P_0 - P_v}{\rho} \right]_{prototype} < 85$$

(the units of the above are atmosphere-cm<sup>3</sup>/gm).

From the point of view of convenience in modeling, it is of interest to see what may be done if  $(P_0)_{model} = 1$  atmosphere and the model fluid is near normal room temperature. Assuming the applicable model fluid vapor pressures and densities given in the appendix:

$$0.6 < \left[ \frac{P_0 - P_v}{\rho} \right]_{model} < 1.4$$

The foregoing ranges allow some very approximate simulation regions to be drawn with equation (5.64), figure 5.9. In this figure, the region below  $(\Delta P)_r/\rho_r = 0.07$  corresponds to situations where the prototype booster fuel tank contains a fluid of very low vapor pressure and may thus indicate a simulation range where cavitation may be quite unimportant. The upper half of the region bounded by  $(\Delta P)_r/\rho_r = 0.07$  and 7 roughly corresponds to the situation where the prototype fluid has a very high vapor pressure, or is a cryogenic, and it can be seen that the model must be bigger than the prototype in this case for the range of acceleration scale ratios important to simulation of rocket booster tanks ( $a_r = 1$  to 0.1). To conclude, it may be remarked that the restrictions placed on model fluids (room temperature) and model gas pressure (atmospheric) severely limit what may be done, and, if cavitation simulation is important, the model designer will very likely be faced with reducing the model gas pressure appreciably.

### Interfacial Effects

In the simulation of fuel sloshing, the primary interest is in the case where a liquid free surface exists. Consequently, three interfaces will exist in most all the problems of interest: liquid-gas, solid-liquid, solid-gas. Molecular attractions between like and dissimilar molecules near the interface give rise to surface effects. The existence of an interface represents the presence of a surface energy which is associated with the work which must

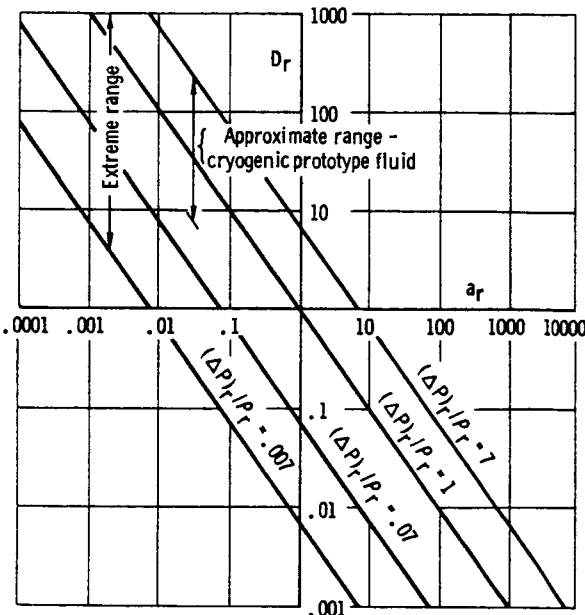


FIGURE 5.9.—Simulation plot: Inertial-cavitation simulation, rigid tank, model fluids at room temperature and ambient pressure of 1 atmosphere.

be done against the mutual attraction of molecules on each side of the interface to effect a separation along that interface. Because the basis of this type of energy is molecular, the magnitude of the surface energy for any particular interface will depend only on the electrochemical composition and thermal state of the matter on either side of the interface and the area of the interface involved. In particular, when chemical compositions are fixed, the surface energy varies directly with interfacial area. Thus when a liquid completely fills a rigid container, the interfacial area is constant, no change in surface energy can be effected by dynamic motions in the fluid, and neglect of surface effects in fluid dynamic modeling is entirely justified. It happens that the energies involved in changing the area of a free liquid surface are small relative to the effects of gravity, viscosity, and so forth, in tanks of greater than 30-cm diameter in acceleration fields of 1 g and greater, and interfacial effects are more often ignored than accounted for.

The surface energy/unit area between a liquid and a gas is customarily called surface tension,  $\sigma$ .

Considerable data on surface tension of various common liquid-gas interfaces are available. Unfortunately, corresponding surface energies/unit area for solid-gas interface,  $\sigma_{SG}$ , and for the solid-liquid interface,  $\sigma_{SL}$ , is almost entirely lacking—at least for fluid dynamic modeling purposes. The problem is that these last quantities are difficult or impossible to measure, and in fact some argument may exist as to the nature of the solid-gas interface in the presence of a liquid, the amount of liquid vapor adsorbed, and the chemical homogeneity of the solid surface control, or at least considerably modify the nature of this interface.

Static relations between surface energy/unit area for the three types of interface are embodied in Young's equation

$$\sigma_{SG} = \sigma_{SL} + \sigma \cos \theta \quad (5.65)$$

where

$\theta$  = the "contact angle" between the liquid-gas interface and the liquid-solid interface at the intersection of the three interfaces.

This equation, in effect, replaces the most difficult surface energy unknowns by a quantity  $\theta$  which is measurable and not dimensional. The dynamic validity of this relation may be in question, but the present state of the art dictates the assumption that it is correct.

In the case of a fuel tank filled with a liquid and a gas, the energy which must be supplied to make a change in the areas of the three interfaces is

$$\Delta E = \sigma_{SG}(\Delta A_{SG}) + \sigma_{SL}(\Delta A_{SL}) + \sigma(\Delta A_{LG}) \quad (5.66)$$

where

$\Delta A_{mn}$  = the total change in the area of the  $(mn)$  interface.

If equation (5.65) is used to eliminate  $\sigma_{SG}$

$$\begin{aligned} \Delta E = & \sigma_{SL}(\Delta A_{SG} + \Delta A_{SL}) \\ & + \sigma(\Delta A_{LG} + \Delta A_{SG} \cos \theta) \end{aligned} \quad (5.67)$$

Since the total area of the tank walls is some fixed constant, an increase in the area of the solid-liquid interface must be accompanied by

an equivalent decrease in the area of the solid-gas interface. Thus

$$\Delta A_{SG} + \Delta A_{SL} = 0 \quad (5.68)$$

and

$$\Delta E = \sigma (\Delta A_{LG}) \left[ 1 - \left( \frac{\Delta A_{SL}}{\Delta A_{LG}} \right) \cos \theta \right] \quad (5.69)$$

Equation (5.69) indicates the several parameters important in simulation of interfacial effects under the assumption that equation (5.65) is dynamically valid, and the similarity analysis can proceed as before:

Parameter	Symbol	Dimension
Change in surface energy---	$\Delta E$	$ML^2 T^{-2}$
Change in interfacial area:		
Liquid-gas-----	$\Delta A_{LG}$	$L^2$
Solid-liquid-----	$\Delta A_{SL}$	$L^2$
Contact angle-----	$\theta$	
Surface tension (liquid-gas)	$\sigma$	$MT^{-2}$

Employing the repeating variables as before

$$\left. \begin{aligned} \pi_{44} &= \Delta E / \rho a D^4 \\ \pi_{45} &= \Delta A_{LG} / D^2 \\ \pi_{46} &= \Delta A_{SL} / D^2 \\ \pi_{47} &= \theta \\ \pi_{48} &= \sigma / \rho a D^2 \end{aligned} \right\} \quad (5.70)$$

The first  $\pi$ -term of equations (5.70) is consistent with the previously noted inertial scaling of forces. Maintenance of the relative magnitudes of  $\Delta E$  and the total energy involved in sloshing in model and prototype is basically what is desired and, if equation (5.69) is valid, will be assured if  $\sigma$  and  $\Delta A_{LG}$  are properly scaled. Consequently  $\pi_{44}$  is a dependent variable, in a sense. Both  $\pi_{45}$  and  $\pi_{46}$  are restatements of  $\pi_3$  for any area. Thus, geometric similarity of the interfaces is implied. The last two terms,  $\pi_{47}$  and  $\pi_{48}$ , are the only new ones introduced in this section.

The first of these two says that the contact angle must be the same in model and prototype. For simulation purposes, this criterion amounts to the proper selection of model tank surface treatment to achieve the proper contact angle.

Since most prototype fluids would be expected to be "wetting" ( $\theta \rightarrow 0^\circ$ ) when in contact with the enclosing tank, "wetting" model fluids are necessary, and most of the model fluids quoted in the appendix are probably wetting with respect to metals. A wetting prototype fluid will probably rule out a liquid metal model fluid such as mercury unless some practical surface treatment can be devised to make mercury "wet" the model tank. In any event, the simulation of contact angle in the model is a subject which has not been extensively treated in the literature and subsidiary experimentation in any given case to see what contact angles can be achieved would be necessary if this parameter is thought of importance. It may not be necessary to achieve exact correspondence of contact angles in model and prototype for wetting or nonwetting fluids ( $\theta = 0^\circ$ , or  $180^\circ$ ), since  $\theta$  appears in equation (5.69) as  $\cos \theta$ , and thus small errors in achieving model contact angles will not greatly affect the ratio between interfacial energy changes in model and prototype.

The last  $\pi$ -term of equations (5.70),  $\pi_{45}$  can be shown to be basically the same result as was found previously (refs. 5.10 through 5.13). Equation (5.71) denotes a replacement operation carried out on  $\pi_{48}$ . The result is the well-known "Weber number" (also written in the squared form, see ch. 11)

$$\pi_{48} = \frac{\pi_{12}}{\sqrt{\pi_{48}}} = \frac{\dot{x}}{\sqrt{\sigma / \rho D}} \quad (5.71)$$

The reciprocal of  $\pi_{48}$  multiplied by  $g/a$ , a variant of  $\pi_{11}$ , and by  $r^2/D^2$ , a variant of  $\pi_1$ , results in the well-known Bond number (see ch. 11)

$$\pi_{48} = \frac{(\pi_1)^2 \pi_{11}}{\pi_{48}} = \frac{\rho g r^2}{\sigma} \quad (5.72)$$

where

$g$ =gravitational acceleration

$r$ =radius of meniscus in an equivalent capillary tube

The Bond number compares the relative magnitudes of gravitational and capillary forces, while the Weber number compares capillary forces to so-called "inertial forces."

For purposes of showing what simulation possibilities are available in a simulation plot, it can be noted that the surface tension,  $\sigma$ , and fluid density,  $\rho$ , always appear as a ratio, and thus a "kinematic surface tension,"  $\phi$ , may be defined

$$\phi = \frac{\sigma}{\rho} \quad (5.73)$$

Substituting in  $\pi_{48}$  and converting to ratio notation

$$1 = \frac{\phi_r}{a_r D_r^2}$$

or

$$D_r = \sqrt{\frac{\phi_r}{a_r}} \quad (5.74)$$

Consulting the appendix for typical values of  $\phi$ , it can be found that prototype liquids at normal operating temperatures have values of  $\phi$  ranging from  $\phi=10$  to  $100$  ( $\text{cm}^3/\text{sec}^2$ ). The model fluids shown have an identical range of values of  $\phi$  for the fluid temperatures shown. Consequently, an outside range of possible variation in  $\phi$  is

$$0.1 < \phi_r < 10$$

If liquid oxygen is the prototype fluid and the model fluids are restricted to the temperatures shown in the appendix

$$1 \leq \phi_r < 10$$

If the prototype fluid is kerosene and the model fluids are restricted as before,

$$0.5 < \phi_r < 4$$

Equation (5.74) is plotted in figure 5.10 for the foregoing ranges of  $\phi_r$ . It is apparent that scaling of surface tension with models significantly smaller than the prototype and acceleration ratios less than 1 is not a very likely proposition. Fortunately, the range  $a_r < 1$  is not too important for surface tension scaling, since the laboratory model at 1-g acceleration implies quite high body forces in the prototype relative to surface tension forces.

The possible simulation ranges on figure 5.10 for  $a_r > 1$  show the possibility of simulation of

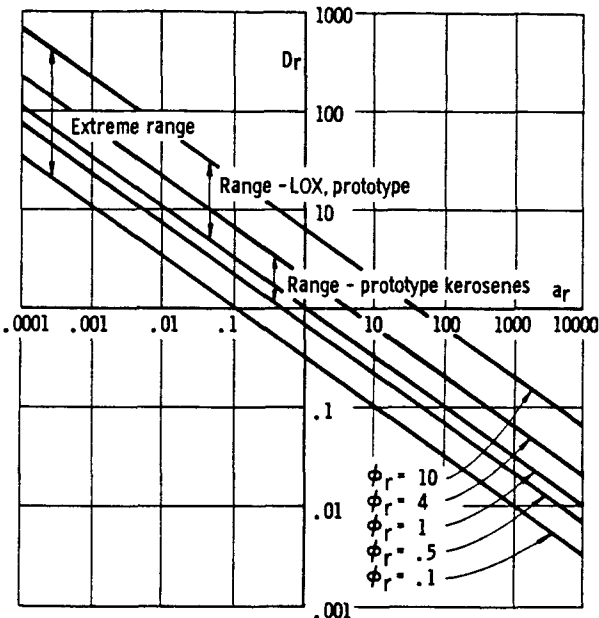


FIGURE 5.10.—Simulation plot: Inertial-surface tension simulation, rigid tank (model fluid temperatures restricted to normal ambient).

relatively low gravity phenomena with small models in a 1-g acceleration field (about which more is said in ch. 11).

Surface tension, as with all model properties, is variable with temperature ( $\sigma \rightarrow 0$  as the fluid temperature approaches the critical temperature), and it is instructive to estimate the order of magnitude of model fluid temperature necessary to result in  $\phi_r$  less than (0.1). Empirically, the variation of  $\sigma$  with temperature is as equation (5.75)

$$\frac{\sigma_{T_1}}{\sigma_{T_2}} \approx \left[ \frac{\rho_{T_1}}{\rho_{T_2}} \right]^{2/3} \left[ \frac{T_c - T_1}{T_c - T_2} \right] \quad (5.75)$$

where

$T_1$ =new temperature

$T_2$ =reference temperature

$T_c$ =critical temperature

Thus

$$\frac{\phi_{T_1}}{\phi_{T_2}} = \left[ \frac{\sigma_{T_1}}{\sigma_{T_2}} \right] \left[ \frac{\rho_{T_1}}{\rho_{T_2}} \right]^{-1} \approx \left[ \frac{\rho_{T_2}}{\rho_{T_1}} \right]^{1/3} \left[ \frac{T_c - T_1}{T_c - T_2} \right] \quad (5.76)$$

Considering model fluids which are liquid at atmospheric pressure and room temperature

( $T_2 \approx 20^\circ \text{ C}$ ), the maximum range of variation in the density ratio factor in equation (5.76) is approximately

$$\left[ \frac{\rho_{T_2}}{\rho_{T_1}} \right]^{1/3} \rightarrow 1.5 \text{ as } T_1 \rightarrow T_c$$

Critical temperatures of the aforementioned model fluids may range from  $180^\circ \text{ C}$  to  $1540^\circ \text{ C}$ . If it is assumed that model fluids at ambient temperatures may be chosen to result in  $[\phi_r]_{T_2} = 0.5$ , then the value of  $\phi_r$  at a new temperature  $T_1$  may be crudely approximated by

$$\begin{aligned} [\phi_r]_{T_1} &= [\phi_r]_{T_2} \left[ \frac{\rho_{T_2}}{\rho_{T_1}} \right]^{1/3} \left[ \frac{T_c - T_1}{T_c - T_2} \right] \\ &\approx (0.5)(1^+) \left[ \frac{1 - (T_1/T_c)}{1 - (T_2/T_c)} \right] \quad (5.77) \end{aligned}$$

It can be seen that the order of magnitude of  $T_1$  must be  $150^\circ \text{ C}$  and more just to change  $\phi_r$  from 0.5 to 0.1. As a consequence, the possibility of achieving  $\phi_r$  less than 0.1 exists, but at the expense of quite extreme model fluid temperatures and pressures.

For the simulation of low gravity in the laboratory ( $a_r >> 1$ ), it can be seen from figure 5.10 that extremely small geometric scale ratios are required for the simulation range shown. Unfortunately, even the liquid metals tend to have kinematic surface tensions not too much greater than that of water ( $\approx 90 \text{ cm}^3/\text{sec}^2$  near the freezing point) because of their higher density; thus, hopes of achieving  $\phi_r > 10$  cannot be placed too high. If simulation of  $10^{-4} \text{ g}$  environment is required, for instance, a geometric scale ratio between 0.003 and 0.03 would be required in the laboratory at 1 g (for a 200-centimeter-diameter prototype tank, model tanks of from 0.6 to 6 centimeters might be required). However, if the "laboratory" acceleration environment can be reduced to  $10^{-2}$  by use of drop towers, and so forth, the required geometric scale ratios would range between 0.3 and 0.03, which would appear to be a practical range.

### 5.5 SIMULTANEOUS SATISFACTION OF ALL SCALING CRITERIA

Because of its importance, inertial scaling is included in all the foregoing discussions pertaining to scaling various dynamic properties of fluids and materials. The approximate simulation ranges,  $D_r$ , versus  $a_r$ , for the following simulations have been discussed:

- (1) Inertial-viscous simulation
- (2) Inertial-compressibility simulation
- (3) Inertial-cavitation simulation
- (4) Inertial-tank elasticity simulation
- (5) Inertial-surface tension simulation

Since in any given real problem more than one of the above combinations may be involved, the possibility of simulation where any two to five of the above simulation criteria are involved is an important consideration. Unfortunately, from the point of view of clarity there are 26 combinations of the above simulations (taken 2, 3, 4, and 5 at a time), and only a few of these can be considered here.

Since many of the most challenging practical fluid dynamic problems of the present and immediate future involve low gravity behavior, some illustrations will follow involving the possibilities of adding to the inertial-surface tension-scaling criteria, the criteria resulting from the consideration of other fluid properties. A simple way of approximating simulation ranges is to superimpose the simulation plots previously exhibited. This procedure is an optimistic one, since fluid properties are not independent of one another, and it may well be that the fluid properties dictating some extreme bound in one type of simulation will not dictate a corresponding bound in another type.

Nevertheless, if figures 5.6 and 5.10 are superimposed, and net simulation ranges are drawn, there results figure 5.11, pertaining to simultaneous simulation of inertial, viscous, and surface tension effects. While the extreme range and the simulation range shown for a kerosene prototype do not differ from the corresponding ranges for surface tension scaling alone, the simulation range for liquid oxygen is truncated at the high acceleration ratio end. Dalzell and Garza (ref. 5.12) give similar plots

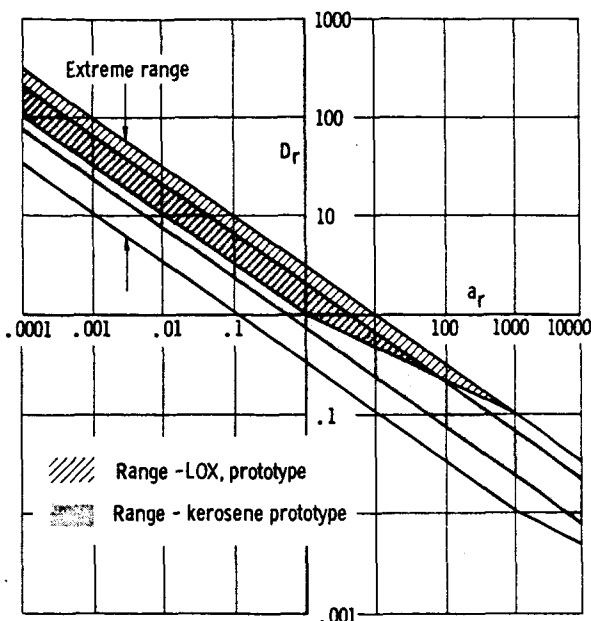


FIGURE 5.11.—Approximate simulation ranges: Inertial-viscous-surface tension scaling (model fluid temperatures restricted to normal ambient).

for inertial surface tension scaling for particular model and prototype fluids. The applicable approximate ranges for liquid oxygen and kerosene prototypes from figure 5.11 have been drawn in on two plots from reference 5.12 and are shown herein as figures 5.12 and 5.13. It can be seen from these figures that the approximate simulation ranges of figure 5.11 are reasonably valid within the assumption of model fluid at ambient temperature which was made in the preparation of figure 5.10 for inertial-surface tension scaling alone. It is also interesting to note from a comparison of figures 5.12, 5.13, and figure 5.11 that even quite fantastic increases in model fluid temperature will apparently not result in simulation points outside the extreme range shown on figure 5.11. Evidently there is hope for inertial-viscous-surface tension scaling of low gravity fluid behavior in the laboratory at 1 g ( $a_r >> 1$ ) if the prototype fluid is relatively viscous. From figures 5.12 and 5.13, and other figures of

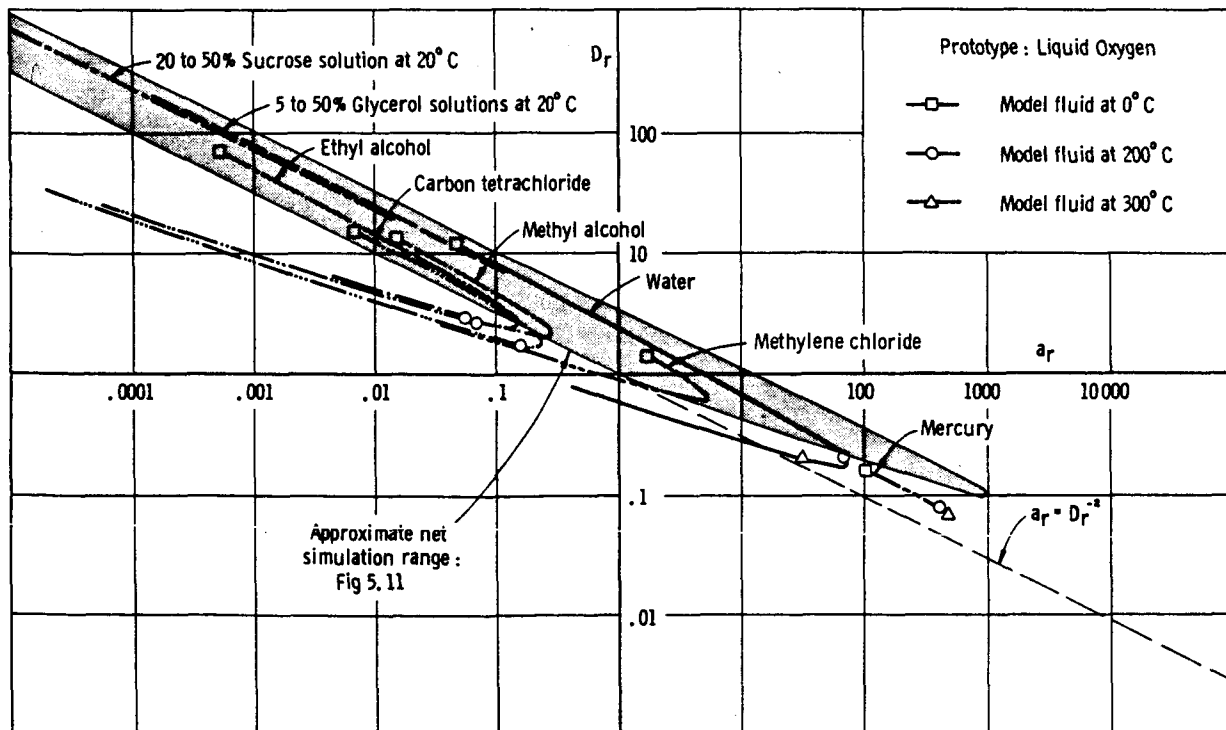


FIGURE 5.12.—Simulation plot: Prototype liquid, liquid oxygen (inertial-viscous-surface tension scaling).

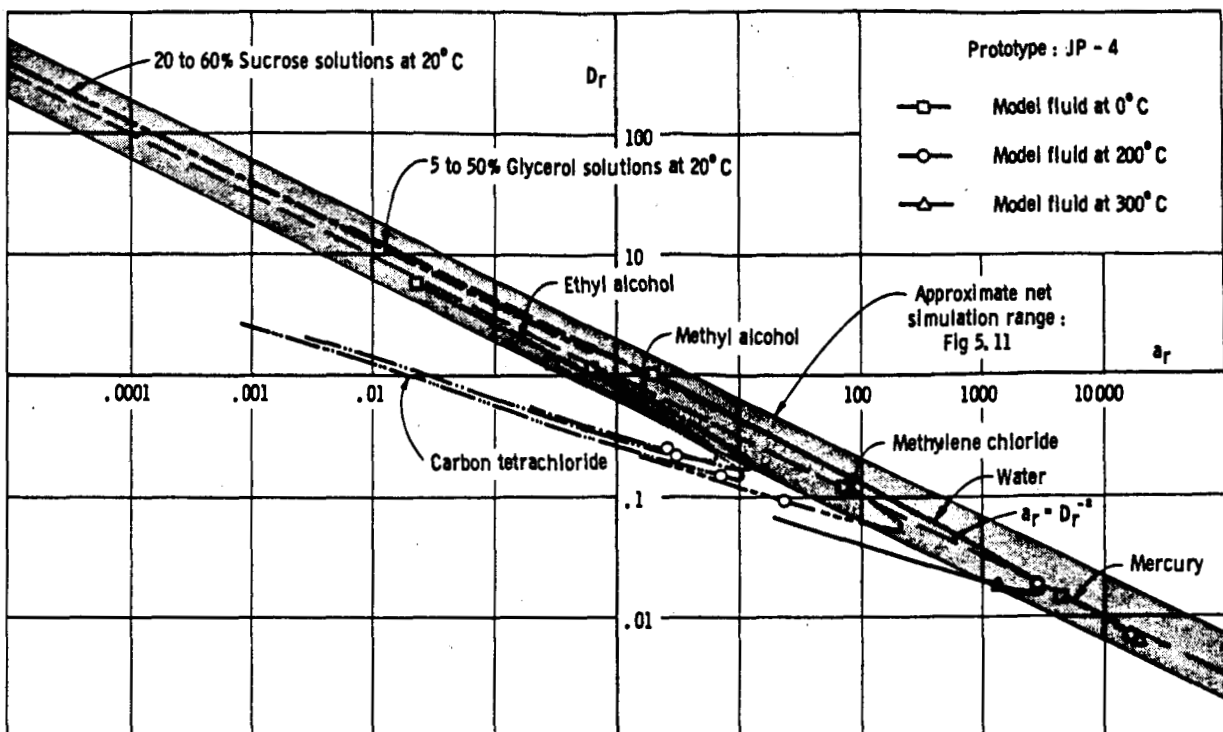


FIGURE 5.13.—Simulation plot: Prototype liquid, JP-4 (inertial-viscous-surface tension scaling).

reference 5.12, it appears that the possibility of a corresponding simulation of liquid oxygen and liquid hydrogen (possibly all the cryogenics also) is rather low.

If figure 5.11 is modified to reflect the cavitation scaling of figure 5.9, there results figure 5.14 which (within the limitations on model fluids noted) pertains to simultaneous inertial, viscous, surface tension, and cavitation scaling. It is evident that the addition of cavitation scaling, where the model fluid is at room temperature and atmospheric pressure, wipes out hopes for low gravity simulation in the laboratory and restricts the simulation range for liquid oxygen for practical purposes to roughly "life size" and "bigger than life" models.

Matters become even worse if all five of the simulation plots are superimposed (fig. 5.15). In this case, the fluid compressibility and tank elasticity criteria combine to decrease both the extreme range of possible simulations and the range for liquid oxygen shown in figure 5.14. It should be remembered that a large number of

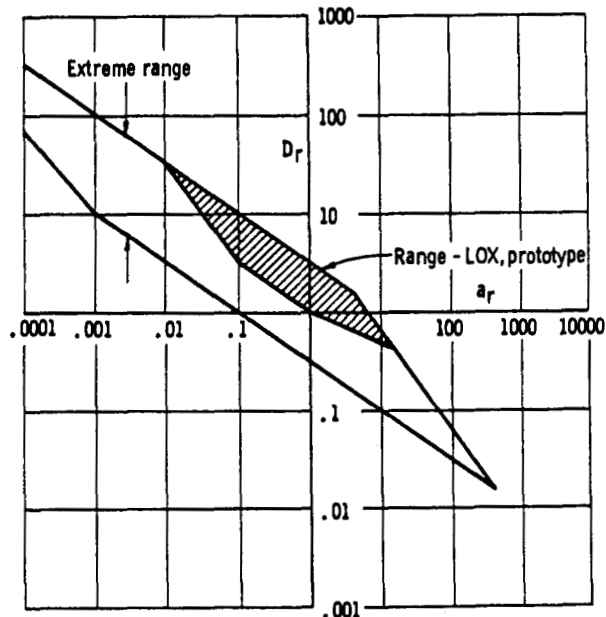


FIGURE 5.14.—Approximate simulation ranges: Inertial-viscous-surface tension-cavitation scaling (model fluid temperatures restricted to room temperature, pressures 1 atmosphere).

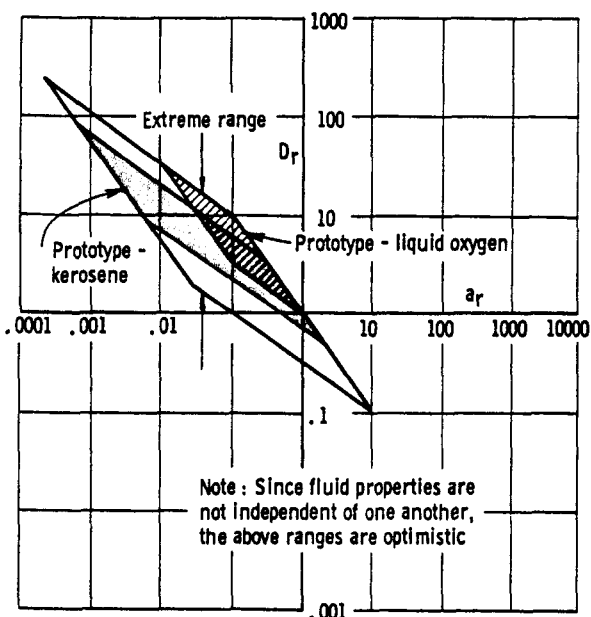


FIGURE 5.15.—Approximate simulation plot: Simultaneous inertial, viscous, cavitation, compressibility, surface tension scaling for scaled elastic replica tank (model fluids restricted to normal laboratory temperatures and pressures).

restrictions were placed on the conditions of the model fluid in the preceding section and that one of the bases for the possible simulation range for tank elasticity in a replica model was that the model structure probably could not be as strong per unit mass as the prototype (these assumptions tend to make the modeling easier). The results shown in figure 5.15 are notable for

their basic lack of coverage of the situation where the model is significantly smaller than the prototype, as well as the situation where the prototype acceleration field is much smaller than 1 g.

### 5.6 CONCLUDING REMARKS ON SIMULATION

The foregoing treatment has been as general as possible in hopes of yielding some perspective on the extent to which fluid dynamic and fluid-structure interaction problems may be simulated. In brief, the prognosis for small-scale direct simulation of every problem in fuel sloshing is not very good, at least not without considerable sophistication of equipment and techniques. However, the general approach to simulation as outlined herein has been of immense practical value and will continue to be, when paralleled with judgment on the part of the experimental designer.

It will continue to be necessary to do experiments aimed at discovering the practical effect of going out of scale with respect to one parameter or another in the problem at hand, if theoretical considerations do not plainly indicate the course to take. There are many instances in the treatment given herein, particularly with respect to surface tension and low-gravity phenomena, where the analysis becomes incomplete through omission of thermodynamic effects. With respect to low gravity phenomena, this situation is corrected to a great extent in chapter 11 of this monograph.

## Part II. Experimental Techniques and Apparatus

*George W. Brooks*

### 5.7 INTRODUCTION

It is generally true in technological developments that adequate understanding of complex physical phenomena is enhanced by, and generally dependent upon, the combined use of experimental and theoretical techniques in support of each other. The complexity of the dynamics of sloshing liquids is well established through the analytical, laboratory, and flight experiences reviewed in other chapters of this monograph, and a review of the literature on the sloshing of liquid propellants in the tanks of launch vehicles clearly shows the eminent role which experimental research has played in both the definition of the problem and in the realization of adequate solutions.

The role of experimental research in propellant sloshing is wide and varied. Its initial function has been, and is, a qualitative one—to show what is happening and why and how. In this phase, it provides the necessary clues to support the selection of theoretical concepts and principles. But of even greater significance is the role which experimental programs must play in providing the quantitative data needed for design. The fact is that current theoretical analyses are limited to treatment of a very few idealized tank configurations which are seldom used in vehicle design, and the theory for even these cases requires restrictive assumptions of fluid idealization and small motions. Thus, experimental programs are necessary to check the validity of the theoretical assumptions and approximations, and to extend the theory for treating configurations representative of many of those selected for flight vehicles on the basis of other design considerations and compromises. Many specialized problems such as dome impact, vortex motions, low gravity effects, and flow in baffled tanks are not currently amenable

to theoretical analysis and, consequently, experimental data provide the only reliable basis for design. This category also includes the essential aspects of the coupled dynamics of the fluid with the motions of the tank and slosh suppression baffles.

The experimental techniques and apparatus developed for research on the dynamics of sloshing propellants reveal many practical, and oftentimes ingenious, approaches, and it is the primary purpose of this section of the monograph to present a review of the literature on the subject. This review is intended to be representative rather than exhaustive, and since experimental techniques for zero-g studies are highly specialized and adequately treated in chapter 11, they will not be included here.

### 5.8 FUNDAMENTAL STUDIES OF LIQUID SLOSHING IN SMALL TANKS

#### Tank Construction Techniques

A brief review of launch vehicle configurations reveals that tanks of varied geometry are the rule rather than the exception. The basic cylindrical section is usually modified by use of conical or elliptical bottoms and tops which may be interior or exterior to the cylinder per se, and by the use of partitions to effectively reduce the free surface area. Other configurations employ variations of oblate spheroids ranging in eccentricity from that of the sphere down to a value of about one-half. Particular configurations, such as the toroid, are also of interest because of their pressure stability and the convenience provided for nesting multiple tanks for minimum overall volume.

Among the various techniques available for the construction of suitable tanks of varied geometry for basic research in propellant sloshing,

the technique of vacuum molding plastics such as Plexiglas or Lucite is perhaps the more versatile. As shown in the sketch of figure 5.16, the technique consists of constructing a female mold of wood, placing a sheet of plastic (heated to permit ready forming to the mold geometry) over the mold cavity, and evacuating the cavity. Two matching half sections are usually made in this manner after which they are trimmed and cemented together to achieve the finished tank. This technique was employed in the construction of the tanks used for the spheroids and toroids of references 5.16 through 5.18 for example.

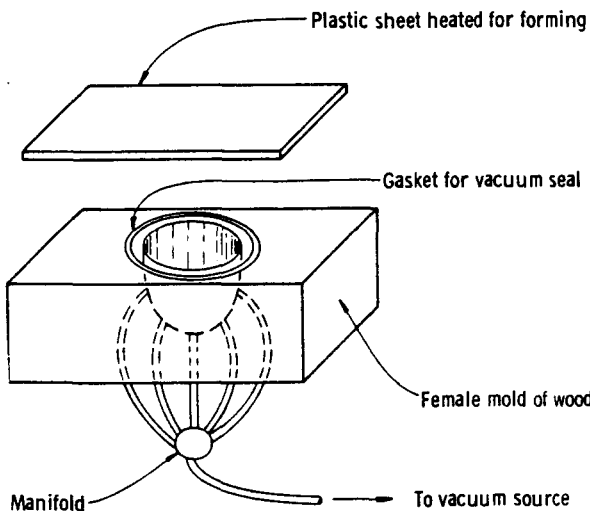


FIGURE 5.16.—Molding technique for model tank construction.

Another method used successfully to construct tanks for small-scale fluid slosh studies (refs. 5.19 through 5.22) is shown in figure 5.17. It involves forming the mating halves of the desired geometrical configurations in Lucite blocks which are subsequently bolted together to form the tank. This technique has the advantage of providing accessibility to the tank interior for installation of baffles, expulsion diaphragms, and so forth, but it has a disadvantage in that the weight of the tank is relatively high and consequently large tare forces make it more difficult to measure accurately the forces imposed on the tank by the contained fluid.

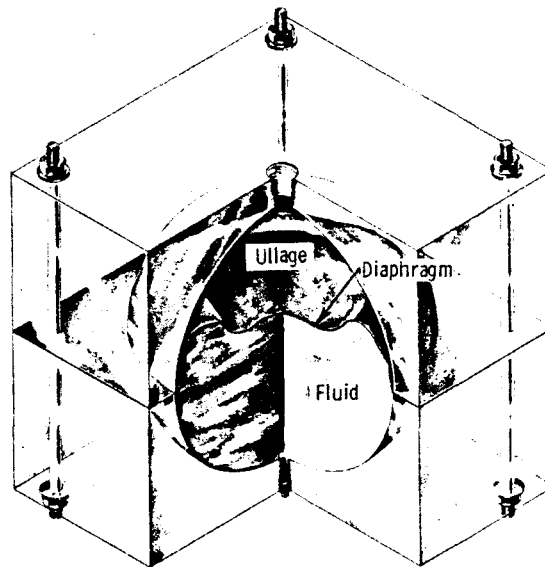


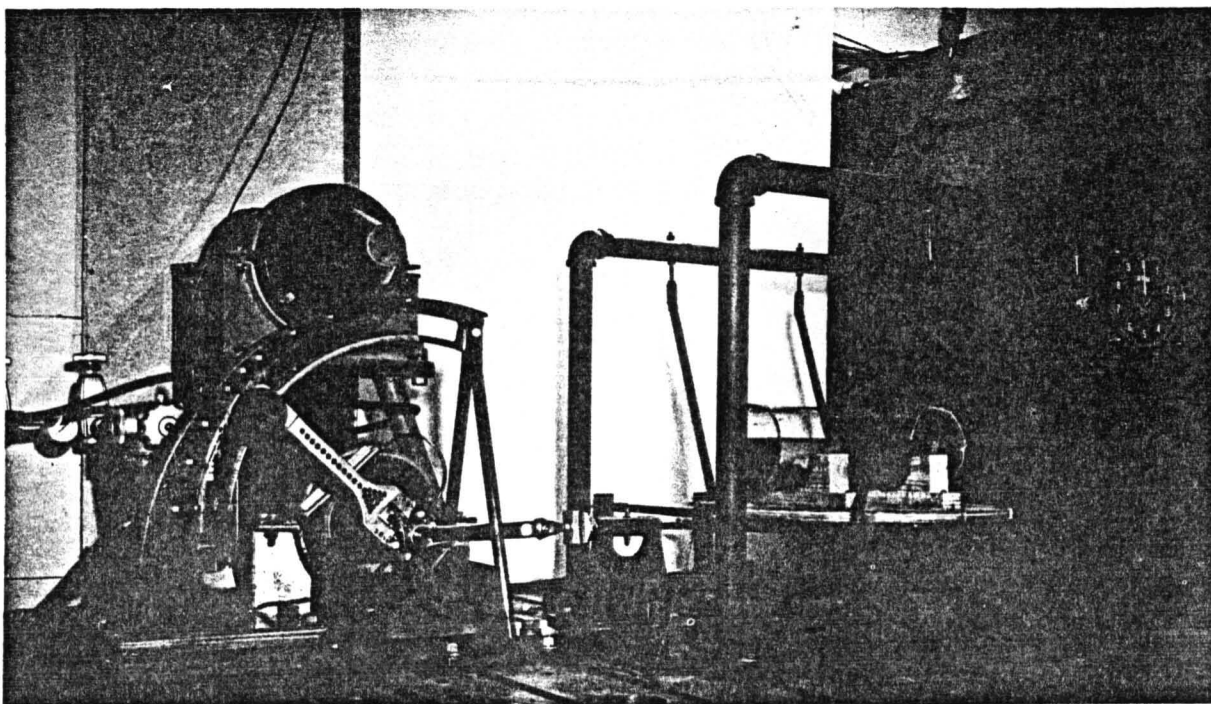
FIGURE 5.17.—Model tank constructed from Lucite blocks having internally formed tank geometry.

In addition to their relative ease and economy of construction, clear plastic tanks also permit visual and photographic observation of the fluid motions—an important feature for documenting unusual or unexpected phenomena.

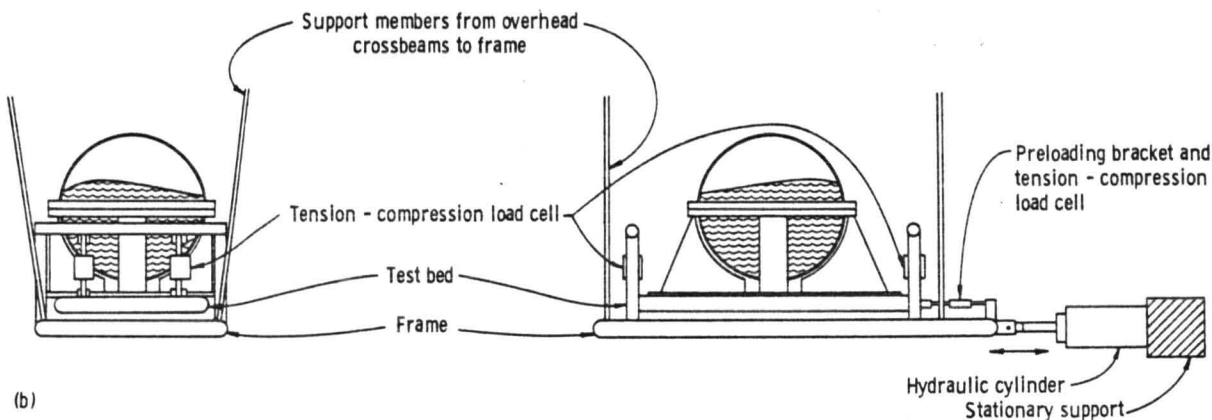
#### Tank Support and Excitation

The problem of supporting and oscillating small tanks to induce fluid-sloshing motions has been treated in many ways. Several variations of the pendular parallelogram (fig. 5.18) have been adapted with general success and used in the studies reported in references 5.15 through 5.18, and 5.23 through 5.26. Another technique widely used is the installation of tanks on rollers or bearings, as indicated by the sketch in figure 5.19. This technique was utilized in the studies reported in references 5.19 through 5.22, and will be referred to in a subsequent section dealing with slosh tests in full-scale tanks.

The excitation technique employed for both the pendular and platform support system is usually a pushrod actuated by an eccentric or cam. The driving mechanism shown in figure 5.18(a) and described in reference 5.27 is unique as a mechanical system in that it permits instantaneous variations in the amplitude of oscil-



(a) NASA, Langley Research Center.



(b) NASA, Lewis Research Center.

FIGURE 5.18.—Test apparatus for mechanically exciting liquid-propellant tank configurations.

lation of the tank and also permits oscillation of the tank at any given frequency without inducing oscillations at other frequencies as in the case of speeding up a motor. Similar conditions of excitation are also feasible through the use of electromagnetic or hydraulic shakers as the driving source.

Two tank-support systems frequently employed (refs. 5.28 and 5.29) for damping studies are shown in figure 5.20. The tripod support legs may be situated near a tank diameter so that the tank can be readily tipped to excite the motions of the fluid, or the motions may be excited by careful manipulations of a paddle.

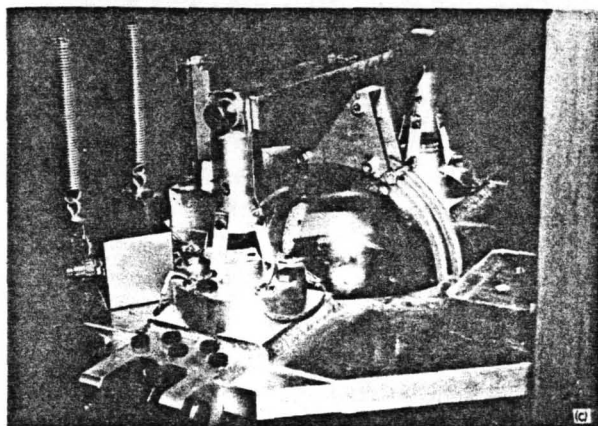
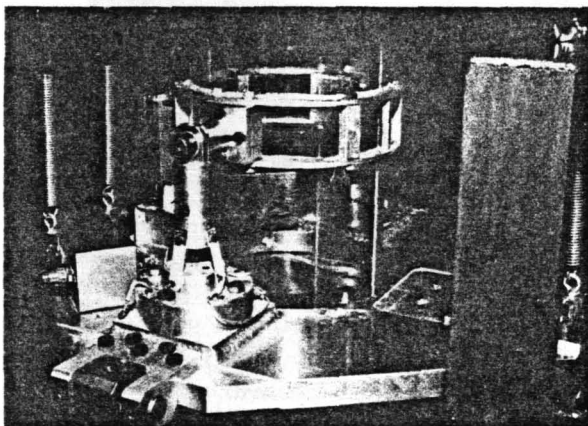
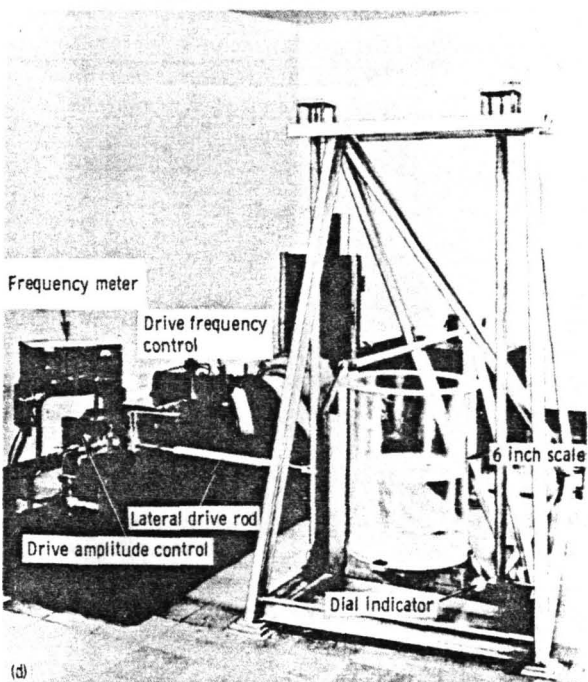


FIGURE 5.18.—Continued. (c) Southwest Research Institute.



(d) Space Technology Laboratories, Inc.

FIGURE 5.18.—Concluded.

The fluid motions may be measured by a strain gage bridge on a torque bar connecting the tank bottom frame to the main frame, as in figure 5.20(a), or by installing a load cell as one of the tripod supports.

#### Natural Frequencies and Mode Shapes

The response of a fluid to the excitation of its container is of prime significance when the

motion of the container is essentially periodic and the period coincides with the first natural frequency of the fluid. Experimental evidence has shown that, though substantial fluid amplitudes may be attained at higher frequency excitations, such as those for the second and higher natural modes, the forces associated with these fluid motions are generally of secondary importance. Thus the fundamental problem in analyzing propellant sloshing in a launch vehicle or spacecraft is the establishment of the characteristics of the first lateral mode, that is, the frequency and mode shape. However, it is generally convenient to use the same apparatus to measure the frequencies and mode shapes for the first two or three modes, and this is usually done as a matter of course.

The references cited present data which document the natural frequencies and mode shapes for the fluid motions in tanks of many of the geometrical configurations of interest. Reference 5.17 treats the case of the circular cylinder and presents frequency data in dimensionless form for transverse and longitudinal modes for the horizontal cylinder and for the transverse modes for the upright cylinder—the configuration of general concern to launch vehicles. Figure 5.21 shows typical mode shapes measured in a tank 30.5 centimeters in diameter and 61 centimeters long.

Experimental data on frequencies and mode shapes for the sphere are given in references

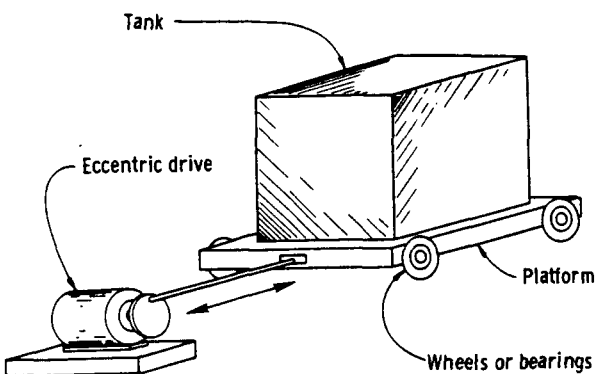


FIGURE 5.19.—Platform-roller tank support and excitation system.

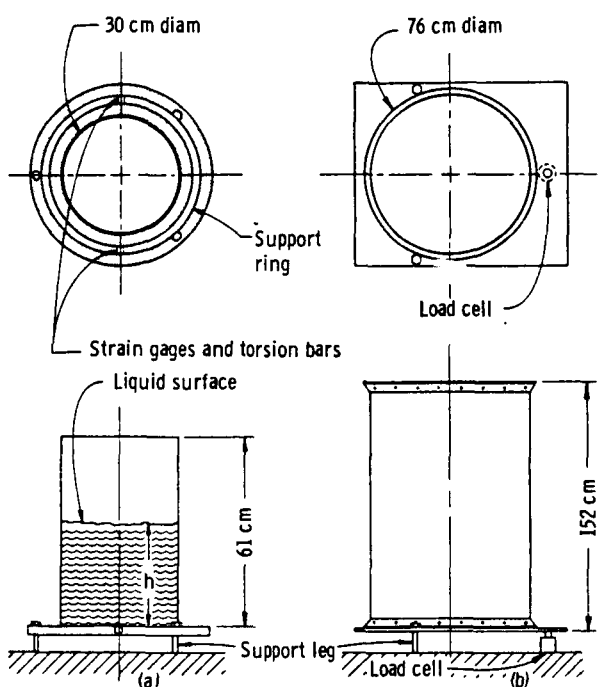


FIGURE 5.20.—Tripod support systems. (a) 30-centimeter-diameter tank; (b) 76-centimeter-diameter tank.

5.17 through 5.19, and 5.25. The first two mode shapes are shown in figure 5.22.

The normal oscillations of fluids in oblate spheroids are presented in reference 5.18, and reference 5.15 presents a study of the Centaur oxygen tank which is a "near" spheroid. Mode shapes for the first three natural modes for fluids in a horizontally oriented spheroid are shown in figure 5.23.

Results of studies on the natural frequencies and mode shapes of toroids are given in refer-

ences 5.16 and 5.21. Figure 5.24 shows the mode shapes measured for the first three modes for a horizontal toroid.

The general technique for measuring the natural frequencies is to oscillate the tank at low amplitudes and record the frequency at which the amplitude of the undistorted wave shape reaches a maximum without rotation. Above the natural frequency, the fluid surface and particles will exhibit a tendency to rotate and, during this rotation, a pronounced increase in wave amplitude is possible. However, the rotary motions are associated with the problem of nonlinear sloshing treated in references 5.25 and 5.26, and summarized in chapter 3.

The photographs presented in figures 5.21 through 5.24 demonstrate the effectiveness of the photographic technique for recording the mode shape and emphasize the convenience of clear plastic tanks for studies of fluid-sloshing characteristics.

#### Damping

The motions of the fluids in launch vehicle tanks, if unchecked, are capable of exerting large upsetting forces and moments on the vehicle. The general procedure for limiting these inputs, and thus minimizing the requirements of the vehicle control system to overcome them, is to install slosh baffles in the tanks. (See ch. 4.) Such baffles are of varied design such as rings, conical frustums, cans, and so forth, but in all cases the weight of the baffles is a burden which reduces payload capability. As a consequence, considerable research has been devoted to evaluating the damping of various types of baffles to maximize their efficiency and minimize their weight. These studies involve the principal geometric tank shapes of interest.

Techniques for measuring the damping supplied by slosh baffles in small research tanks are given in the literature for cylinders (refs. 5.28 and 5.30), spheres (refs. 5.20, and 5.22 through 5.24), and oblate spheroids (refs. 5.15 and 5.29). Two basic techniques are used: the logarithmic decay method or the forced response method.

The logarithmic decay method involves the measurement of the rate of decay of the fluid oscillation in a given mode—invariably the first

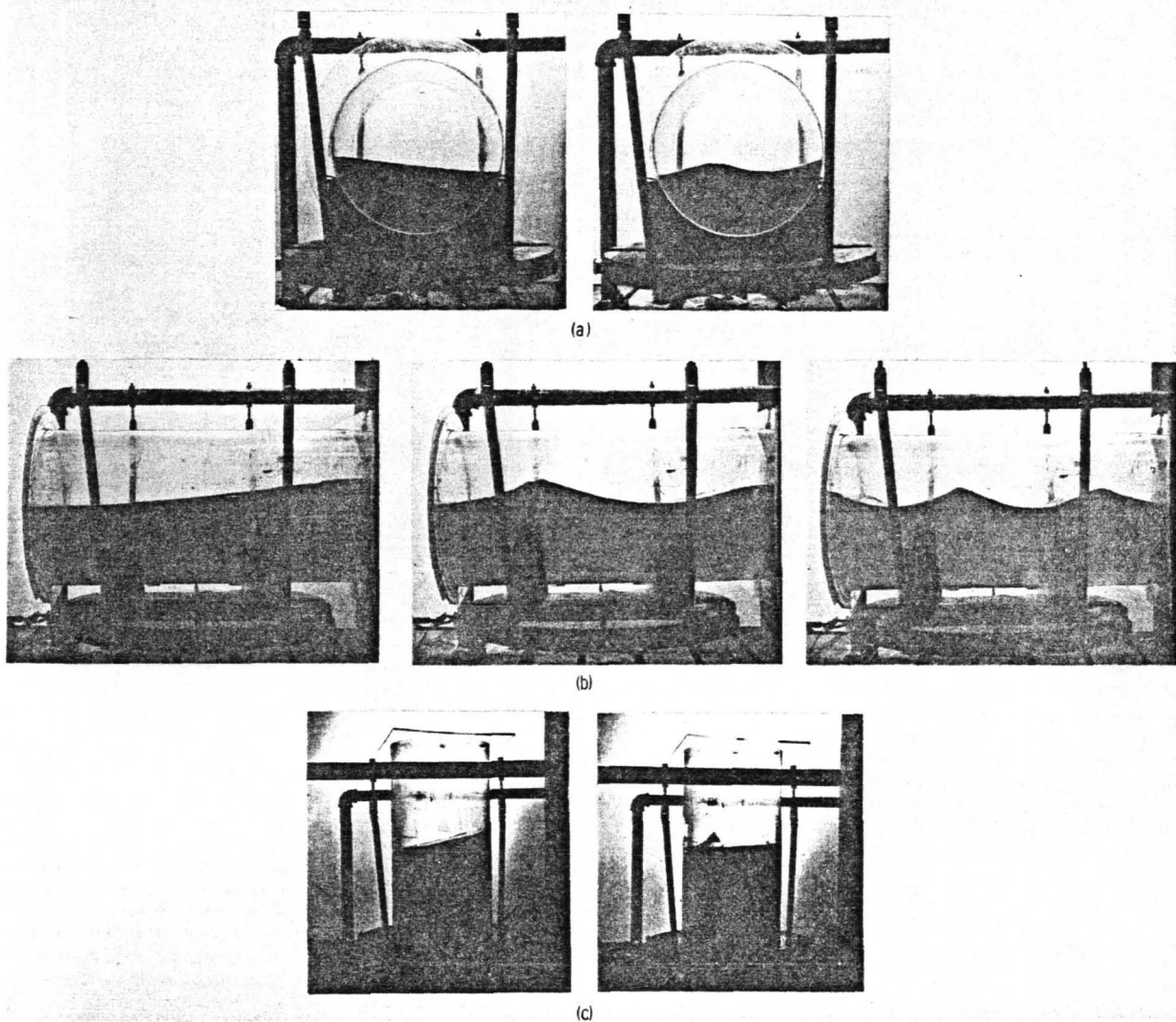


FIGURE 5.21.—Mode shapes for circular cylinder. (a) First two transverse modes for horizontal cylinder; (b) first three longitudinal modes for horizontal cylinder; (c) first two transverse modes for an upright cylinder.

mode, since higher modes are so heavily damped that the oscillations are neither of substantial interest nor amenable to accurate measurement, especially if the tank is fitted with even a minimum of sloshing baffles. The damping may be interpreted in terms of the natural logarithm of the ratio of the forces imposed by the fluid on the tank during consecutive oscillations (e.g., ref. 5.24), or of the ratio of the amplitudes of the fluid motions during consecutive oscillations (e.g., ref. 5.28). In either case, a transducer is used to obtain an effective measure of the magnitude of the

sloshing fluid and the signal is fed into a readout system.

At least four types of transducer systems have been used effectively to measure fuel-sloshing amplitudes. These are sketched in figure 5.25.

The first is a capacitance wire system which consists of two capacitance probes which are mounted parallel to, but offset slightly and insulated from, the walls of the tank at the location of the antinodes of the sloshing fluid. These probes yield electrical outputs proportional to the difference in height of the liquid surface at these points and are self-compensat-

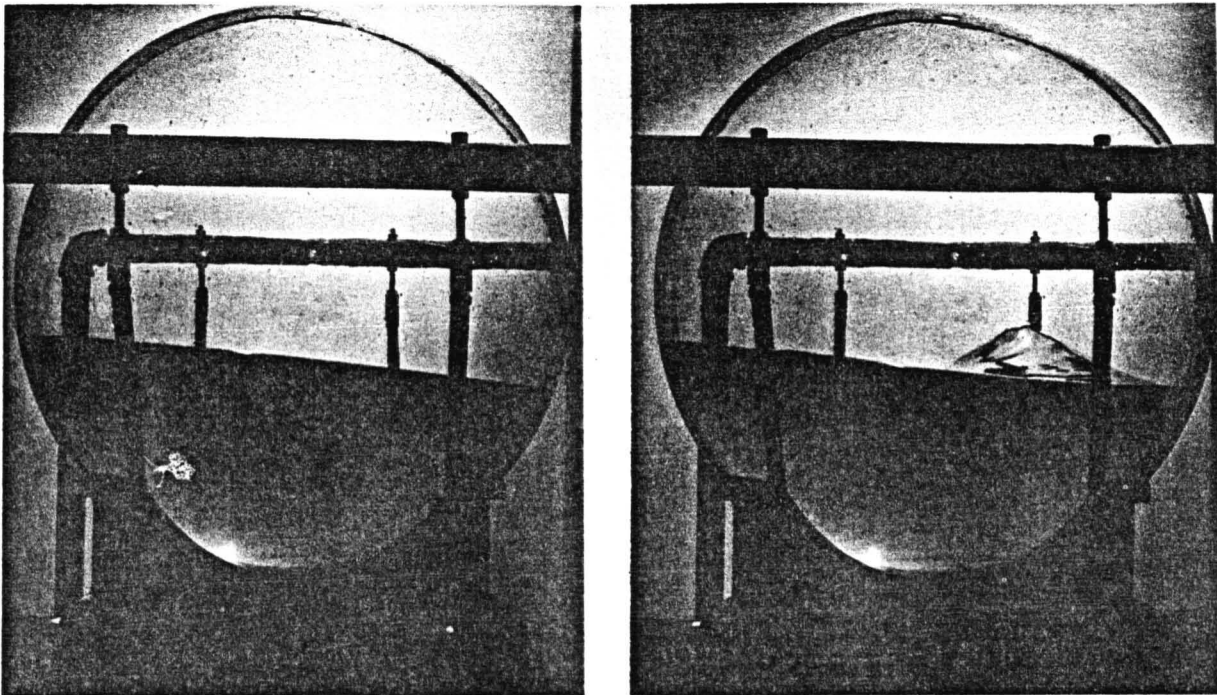


FIGURE 5.22.—First- and second-mode shapes for fluid in a sphere.

ing so as to maintain a constant zero level as the tank is drained. This technique is described in detail in the appendix of reference 5.14.

The second technique, shown by the sketch of figure 5.25(b), involves the use of concentric floats which are positioned in the tanks at desired radial locations by means of wires or cables. Accelerometers or velocity pickups are mounted on the floats and sense the motions of the floats as they rise and fall with the fluid during sloshing.

A third technique utilizes pressure pickups which are mounted in the tank wall or inserted in the fluid to measure the fluid head during sloshing, as shown in figure 5.25(c).

The final, and perhaps most straightforward technique, is to install the tank on some form of load cell arrangement designed to indicate the forces or moments applied to the tank by the sloshing fluid. Load cells used may be of the standard commercial type (ref. 5.29) or may consist of specially designed strain-gage-beam systems. Also, in this category, is the load cell mounted as a series element of the

tank excitation system such as that utilized for the damping studies reported in reference 5.22.

Transducer outputs from any of the aforementioned systems can be readily recorded by an oscillograph to yield a permanent record of the decay of fluid amplitudes and associated damping. However, the Dampometer has proven to be a rapid and very useful device for measuring the damping of single-degree-of-freedom systems such as that associated with the decay of fluid in one of its lower natural modes. The Dampometer is an electronic instrument which converts the frequency and damping characteristics of the analog transducer signal (the input) into a digital count (the output). The input signal is first converted from a damped sinusoid to an Archimedes spiral which is then displayed on two oscilloscopes, one for observation and the second for further reduction of the data. A cover which contains a photocell is placed over the second oscilloscope. In addition, a series of interchangeable calibrated disks are provided with radial slits of different lengths which may be individually placed over the second scope.

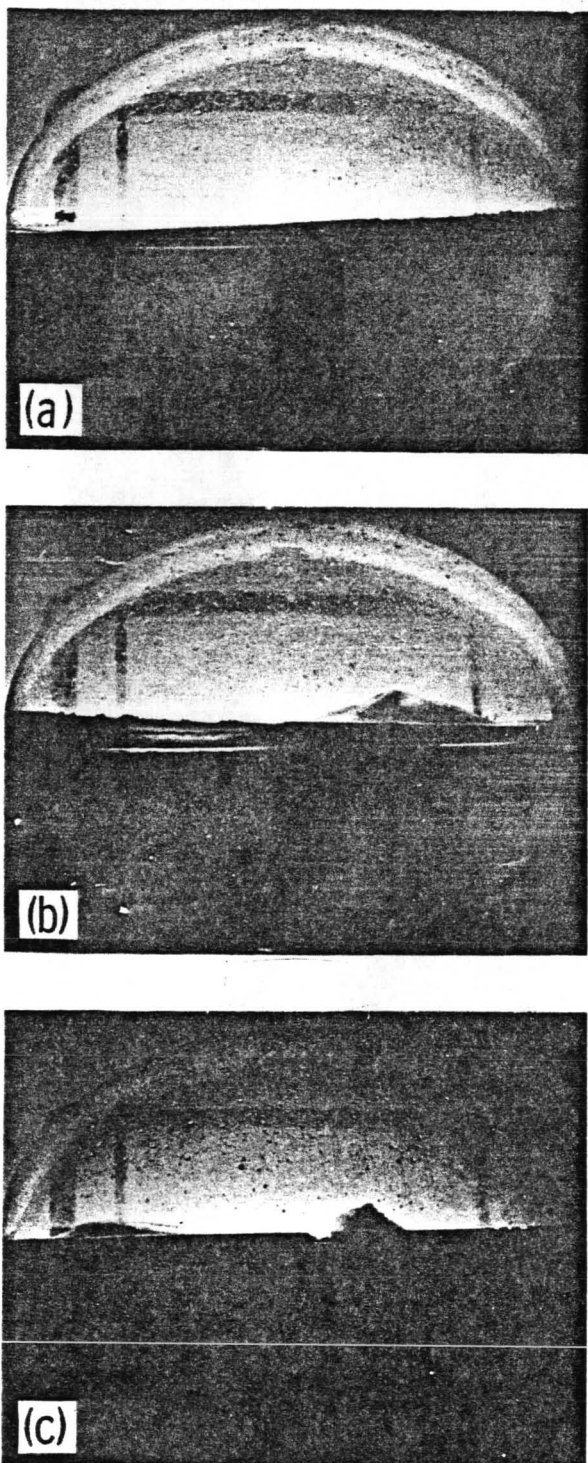


FIGURE 5.23.—Mode shapes for the first three natural modes of liquid in a spheroid. (a) First mode; (b) second mode; (c) third mode.

By proper adjustment of the gain, the spiral generated from the transducer signal appears on the perimeter of the scope and moves toward the center as the magnitude of the fluid motion diminishes and the output spiral decays. As the signal moves across the slits, the photocell detects the intermittent light and provides the input for the counter. By using the number and length of the slits for a given disk, and the counter's reading, the frequency and damping associated with the transducer output are readily obtained from a simple formula. By adjusting the sensitivity of the instrument, the damping is readily obtained for different magnitudes of the sloshing wave.

The measurement of damping by the forced-response method is not as convenient or straightforward as the logarithmic decrement method, but it may be advantageous if the test facility and instrumentation are such that an accurate velocity response curve is available. If such is the case, the damping may be determined by measuring the amplitude of the peak response at the natural frequency or by ratioing the bandwidth at the half-power point to the natural frequency (ref. 5.31).

#### Sloshing Forces

Flight experience with launch vehicles indicates that the principal problem posed by sloshing fluids in launch vehicle tankage is associated with the control system. As the propellants slosh, forces and moments are generated on the vehicle which must be overcome by the control system in order to maintain the vehicle on the programmed flight trajectory. Thus, it is necessary to design the control system to cope with both the frequencies and the amplitudes of the sloshing fluids, and hence it is necessary to know these quantities. Techniques for measuring the frequencies, and for limiting the forces, are discussed in previous sections, but it is essential to know the forces involved even for baffled tanks to assure adequate margins in control system gains and control forces.

Research techniques for measuring the sloshing forces imparted to tanks are cited in the

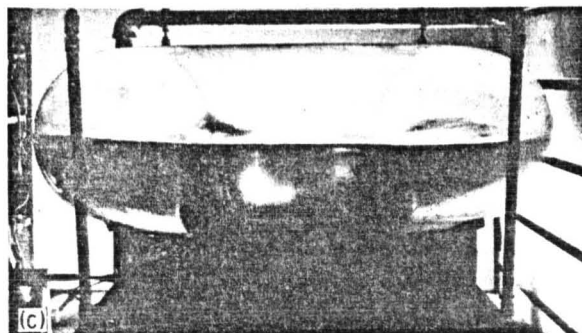
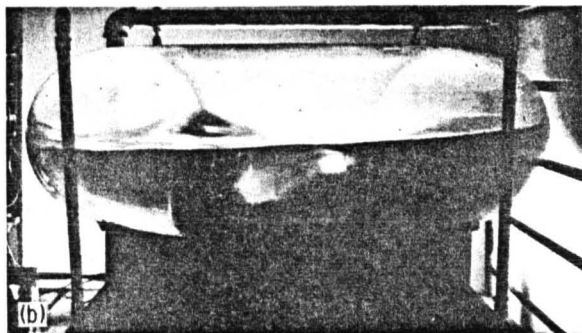
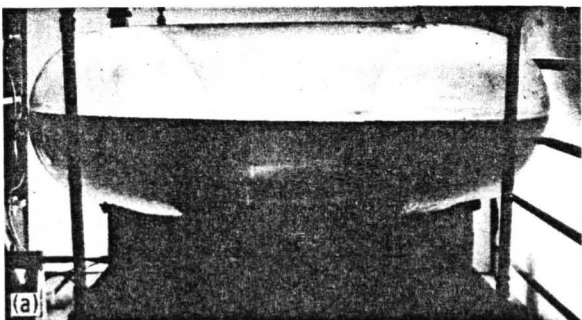


FIGURE 5.24.—Mode shapes for first three natural modes of liquid in a horizontal toroid. (a) First mode; (b) second mode; (c) third mode.

literature. The apparatus shown in figure 5.26 was used to measure the forces on spherical tanks (refs. 5.19, and 5.22 through 5.24) and toroidal tanks (ref. 5.21). The spheroidal tank (ref. 5.15) was investigated with the apparatus shown in figure 5.18(b). The techniques used are typical in that the tank is oscillated at the selected frequency and amplitude to generate the desired fluid motions, is "quick stopped" at a point of zero velocity in the cycle, and the forces imparted by the fluid to the tank during ensuing fluid oscillations measured by installing

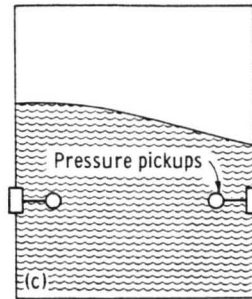
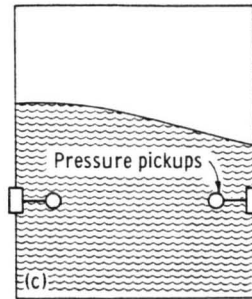
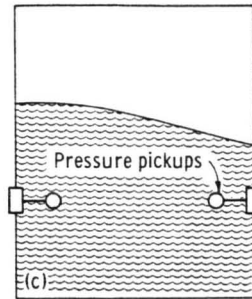
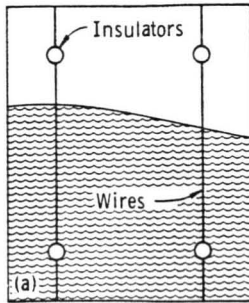


FIGURE 5.25.—Techniques for detecting magnitudes of fluid sloshing. (a) Capacitance wires; (b) floats; (c) pressure pickups; (d) load cells.

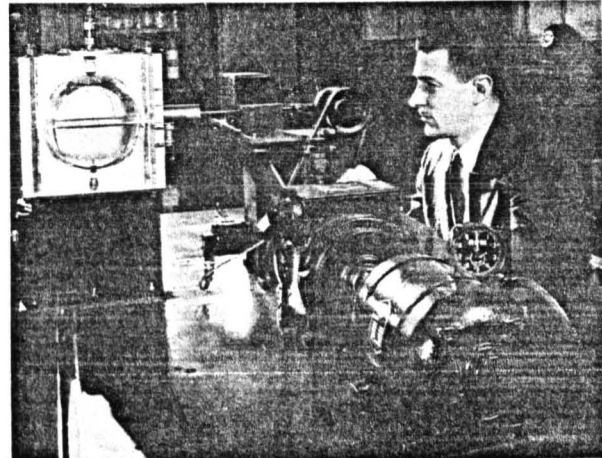


FIGURE 5.26.—Experimental test facility.

a calibrated load cell in the driving link. Typical slosh-force traces are shown in figure 5.27. The measurement of residual forces after bringing the apparatus to rest is preferable to the normally used forced-response technique in that it obviates the need to subtract out the tare

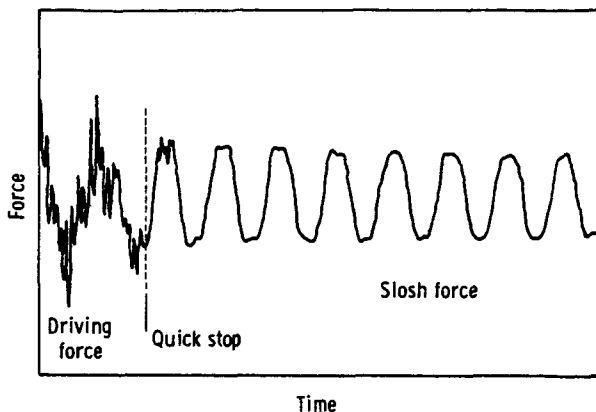


FIGURE 5.27.—Typical slosh-force trace. First mode: liquid-depth ratio,  $h/2R=0.40$ .

forces associated with the tank-support system; however, it does not provide an opportunity to resolve the resultant force into its mass-spring and damping components. Resolution of the forces when utilizing the forced-response technique has been accomplished with the apparatus shown in figure 5.18(a) by feeding the load cell outputs into a resolver system phased with the tank displacements (ref. 5.27).

#### Irregular Fluid Motions—Swirl and Dome-Impact Slosh

When the frequency of excitation of a tank containing a fluid is gradually increased beyond the natural frequency, the fluid wave will begin to swirl. Experimental results show that the swirl is a combination of wave motions and rotary motions—particles in the fluid move up and down and rotate around the tank. As a result of the rotations of the fluid, the amplitude of the wave before the surface breaks may reach amplitudes several times as large as those due to pure sloshing at a natural frequency and, consequently, the fluid forces imparted to the tank may be much higher. Although the swirl is most pronounced for the first sloshing mode, there is experimental evidence that swirling motions are also possible for higher modes. As discussed in chapter 3, this is a nonlinear problem akin to large amplitude motions of a pendulum.

Experimental techniques for evaluation of the forced response during normal sloshing of fluids, such as described in previous sections of this

chapter, have been successfully applied (ref. 5.26) to analysis of fluid swirl and appear to be adequate.

The problem of dome impact arises when the direction of the resultant acceleration of the tank is reversed such as may occur during engine shutdown of a launch vehicle flying through the atmosphere, or if an engine is ignited while the propellant is located in the upper part of a tank. (These problems are discussed in further detail in ch. 10.) The resultant impulsive pressures may be severe and must be considered as a factor in assessing the structural integrity of the tank.

Two experimental techniques have been used to analyze the extent of this problem. References 5.11 and 5.12 describe a technique which utilizes a pressure-activated carriage (shown in fig. 5.28) to accelerate a tank, partially filled with a liquid, downward at accelerations substantially greater than 1 g. The resulting impulsive pressures on the tank dome are measured by an array of pressure cells.

Another technique for investigation of dome-impact fuel slosh is shown in figures 5.29 and 5.30. As shown in figure 5.29, the tank (enclosed in a cage, fig. 5.30) is accelerated upward by a cable attached to a drop weight and passing over a system of pulleys. After the drop weight comes to rest by dropping in a sandpit, the motion of the tank is also brought to rest by the braking force of another cable system. The downward acceleration of the braking force, greater than 1 g, causes the fluid to impact the dome, whereupon both the fluid pressure and the resultant fluid forces are measured. The measurement of the fluid forces is facilitated by supporting the dome from the remainder of the tank by a system of strain gage beams.

#### Coupling of Fluid Motions and Structural Deformations

Although the major problems concerning sloshing propellants involve the uncoupled fundamental lateral sloshing modes of the fluid, experimental evidence indicates that substantial coupling of fluid and tank motions may result in some instances. Reference 5.33, for

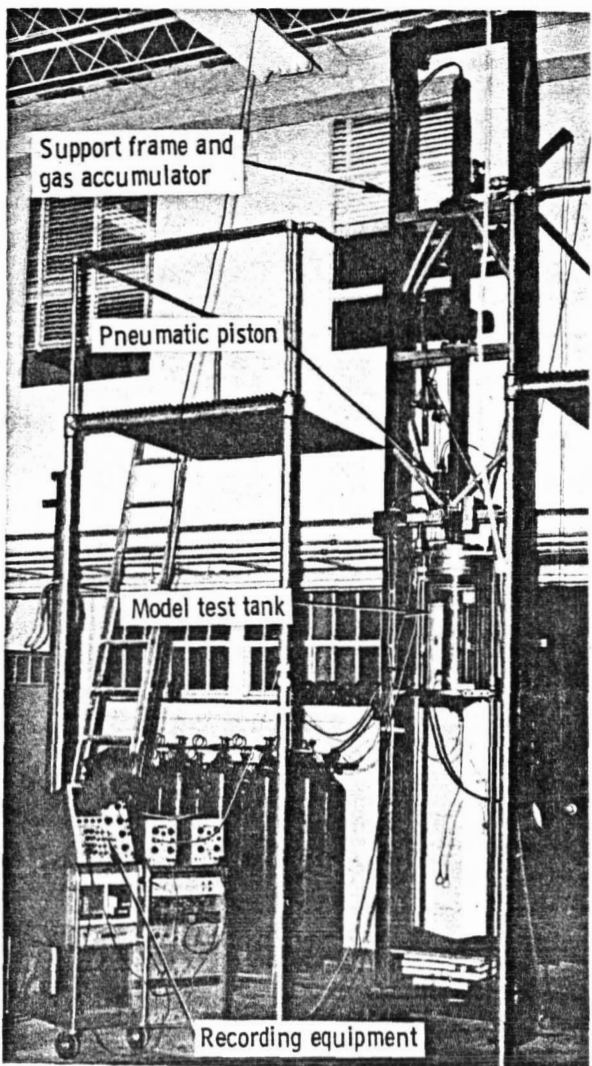


FIGURE 5.28.—Southwest Research Institute apparatus to study dome-impact fuel slosh (refs. 5.11 and 5.12).

example, treats the bending vibrations of a circular cylindrical shell with an internal liquid having a free surface wherein the presence of the free surface liquid was shown to increase the resonant bending frequency of the tank as compared to a similar configuration with the fluid capped. The apparatus used in this study is shown in figure 5.31. The tank, pin ended in this case, is mounted in a stand designed to permit variations in tank-end restraints and equipped with a capping device to restrict the fluid surface for comparison with free surface responses. Vibrations of the tank were excited

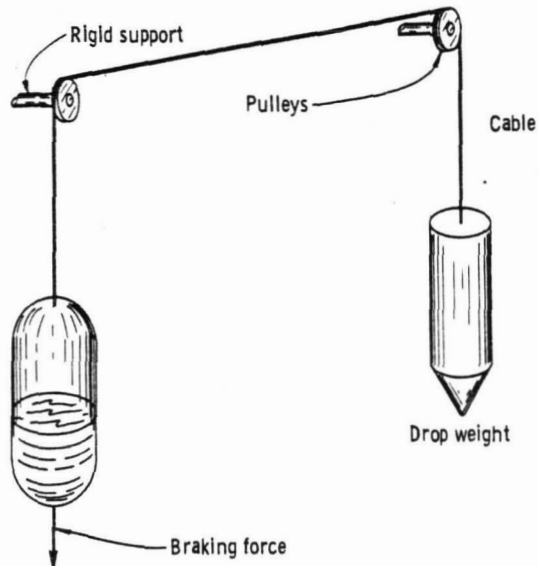


FIGURE 5.29.—Schematic of dome-impact slosh apparatus.

by an electromagnetic coil and measured with inductance pickups.

Another study of interest has been reported (ref. 5.34) which involved the breathing vibrations of a circular cylindrical shell containing a liquid. The technique and apparatus used were similar to those employed for the study of the bending vibrations discussed in the previous paragraph.

#### Coupling of Fluid and Tank Motions

In most of the studies of fluid sloshing, the assumption is generally made that the sloshing phenomena are not appreciably affected by the translatory and pitching motions of the tank, and that sloshing data, generated in rigidly mounted tanks or tanks subjected to small translatory movements such as are necessary to excite the fundamental sloshing modes, are applicable to launch vehicle design. This philosophy was put to the test in a study (ref. 5.35) wherein a tank was mounted in a gimbal supported on long cables so that it could oscillate in both translation and pitch. As shown in figure 5.32, the tank was also fitted with an air jet and control system which permitted close simulation of a launch vehicle under flight. By varying jet pressures, pitching axes, and the spring and damping constants

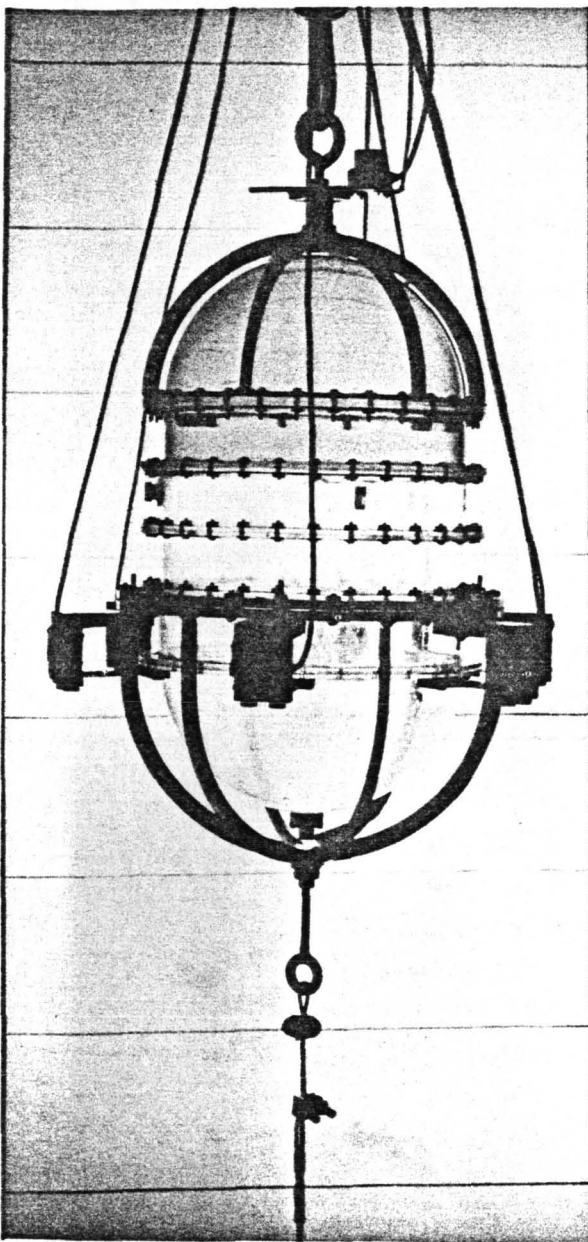


FIGURE 5.30.—Langley Research Center tank and instrumentation for dome-impact slosh studies (ref. 5.32).

of the system, it was possible to study both stable and unstable motions. The results of this study showed that conventional ring baffles immersed in the fluid were substantially more effective in damping pitching motions than lateral motions of the tank, and that by inclusion of the proper damping, the motions and stability of the system could be adequately

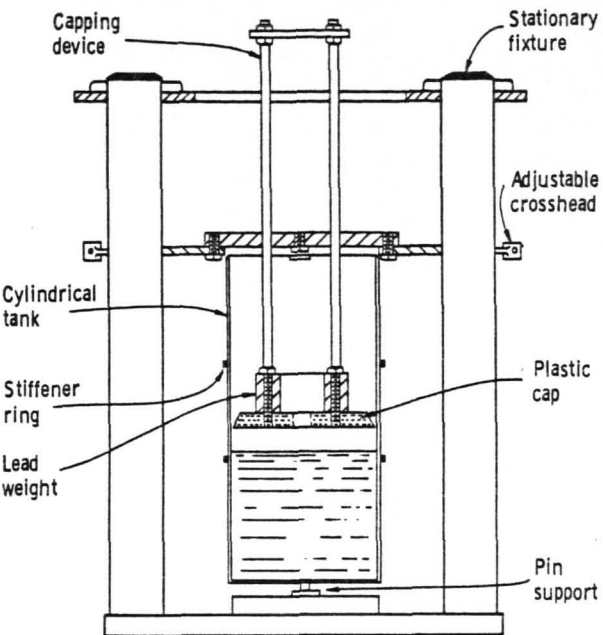


FIGURE 5.31.—Schematic of apparatus showing capping device (ref. 5.33).

predicted by use of data generated during more conventional sloshing studies.

## 5.9 LIQUID MOTIONS IN LARGE TANKS

### Damping in Cylinders

Although most of the research on fluid sloshing has been conducted in small tanks as reviewed in section 5.8, several important investigations have involved experiments with larger tanks. Reference 5.14 presents the results of a study of the effect of time-varying liquid depth on the damping of the fundamental lateral sloshing mode. A Plexiglas tank, 91.5 centimeters in diameter and 183 centimeters high, was partially filled with water, the lateral sloshing mode was excited with a paddle, and the damping was measured with the capacitance wire system shown in figure 5.25(a) as the fluid was drained from the tank at high rates. By comparing the damping at a given fluid level while draining with the damping at the same fluid level without draining, it was shown that the normal rate of efflux of the fluid from a tank has no appreciable effect on the damping of the first lateral sloshing mode.

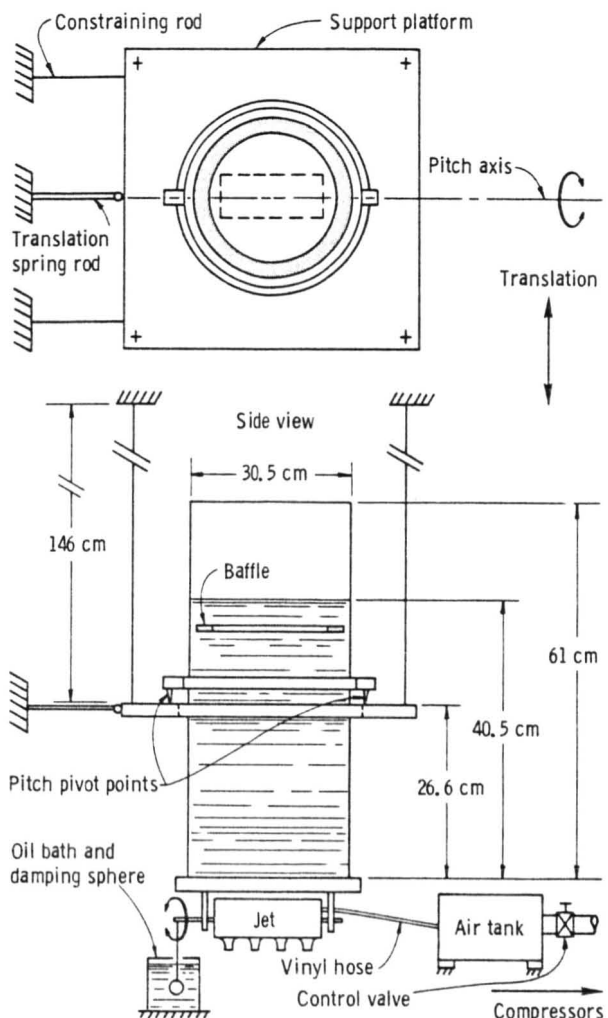


FIGURE 5.32.—Schematic of experimental apparatus (ref. 5.35).

#### Two-Dimensional Damping Effectiveness of Baffles

Reference 5.36 presents a study of the measured two-dimensional damping effectiveness of fuel-sloshing baffles applied to ring baffles in a cylindrical tank. In contrast to the usual approach where a tank of a geometric configuration of interest is fitted with baffles and the damping of the sloshing fluids measured, in this study numerous types of two-dimensional baffle segments were mounted as cantilever elements on a reciprocating blade (fig. 5.33) installed in a two-dimensional tank as shown in figure 5.34. The tank was 30.5 x 152.5 x 152.5 centimeters in size and was filled to a depth of 122 centimeters with water. As shown in

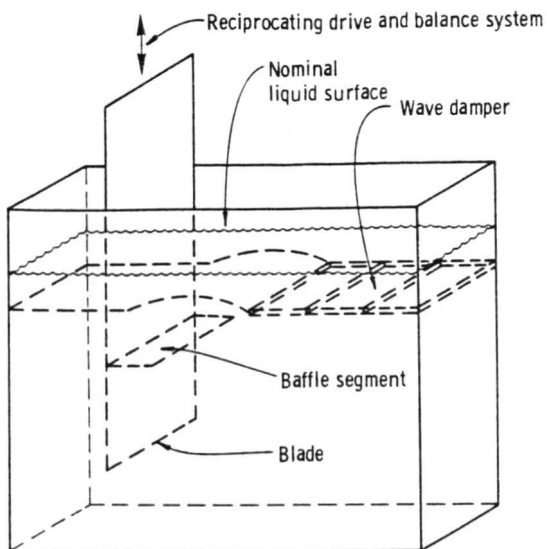


FIGURE 5.33.—Two-dimensional tank.

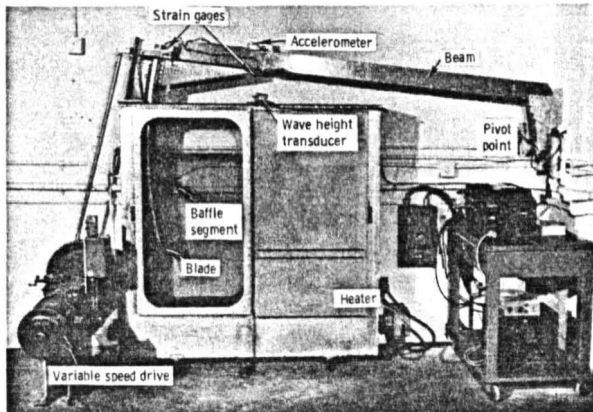


FIGURE 5.34.—Front view of test equipment.

figure 5.34, the blade which supported the baffle segment was mounted to a pivoted beam and instrumented so as to measure the forces imparted by the fluid to the baffle segment as the frequency and amplitude of the support blade vibrations were varied. Data from tests of the two-dimensional plates were utilized in a "strip theory" technique and integrated to obtain the equivalent damping of a circular ring baffle. One of the conclusions of this test was that the damping effectiveness of ring baffles in cylindrical tanks can be adequately predicted from force measurements in a two-dimensional tank, even when surface effects are large. It is

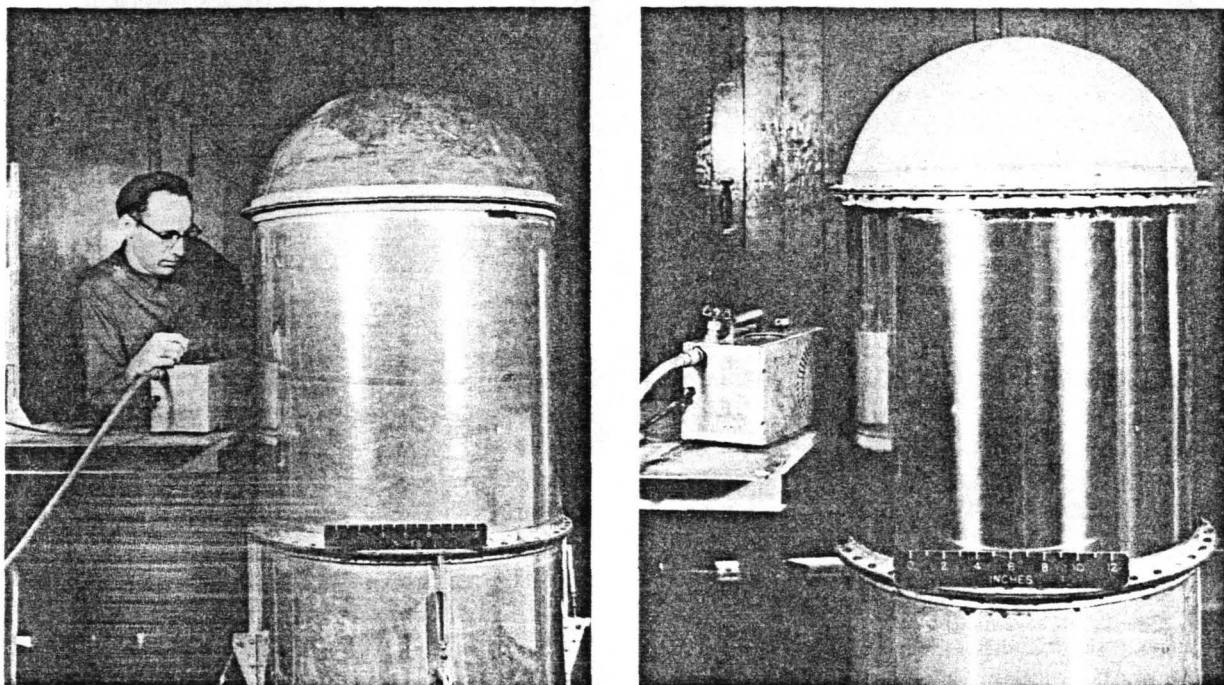


FIGURE 5.35.—View of test cylinders and test setup (ref. 5.39). (a) Cylinder 1; (b) cylinder 2.

pertinent to note here that the quasi-empirical ring damping formula developed by Miles (ref. 5.37) was derived by similar application of two-dimensional data developed by Keulegan and Carpenter (ref. 5.38). As shown in reference 5.28, the damping predicted by Miles' formula is in close agreement with that measured for annular ring baffles in cylindrical tanks (see also ch. 4).

#### Vibration Characteristics of Pressurized Thin-Walled Circular Cylinders Partly Filled With Liquid

The results of a study of the effects of a contained fluid on the vibrations of thin-walled pressurized tanks which simulate launch vehicle applications are presented in reference 5.39. The investigation treats empty, partly filled, and full conditions for two tanks, shown in figure 5.35, having ratios of radius to thickness of 937 and 3000. The cylinders were closed at the top by fiber-glass domes and at the bottom by aluminum cones. The tanks were excited by an air shaker (the rectangular object shown in the figure to the left of the tanks) wherein the applied oscillating force was derived by interrupting a jet of air with the teeth of a rotating

disk. The magnitude of the oscillating force was controlled by varying the air pressure to the jet, and the frequency was controlled by the speed of rotation and the number of teeth on the disk. The principal advantages of this type of shaker are the absence of physical ties or added mass to the structure, and the fine control of the frequency and amplitude.

Using the test setup shown in figure 5.35, the shaker was placed in the position expected to give maximum response of the cylinder in the desired mode, and the frequency was varied until maximum response was obtained. Maximum response was observed by touching the cylinder lightly with the fingertips while varying the frequency of the applied force. The mode was then identified by locating the node lines which represent positions of little or no radial motion. In nearly all cases, an experienced engineer could readily map out the mode shapes using this technique—the only exception being in the case of the very thin tank when unpressurized. In this case, the local imperfections and flexibility necessitated the use of a miniature accelerometer (4 gm) to map out the mode shapes.

Comparison of the experimental and theoretical results for this study showed that the equations derived can be used to adequately predict the characteristics of pressurized cylinders partly filled with a liquid. The results also showed that the damping of tank vibration modes for the water-filled tanks was less than half the damping measured when the tanks were empty—an important consideration relative to the response of the shell modes of a launch vehicle to engine acoustic and atmospheric inputs.

### 5.10 VIBRATION TESTS OF DYNAMIC MODELS

#### General Considerations and Philosophy

The evaluation of mechanical systems is grounded in the mutually supporting developments of theoretical and experimental analysis, and characterized by continued improvements in structural efficiency—the capability of a given weight of material to do a bigger and better job. Improvements in structural efficiency are highlighted in aerospace systems such as the turbojet engine, the airplane, the rocket engine, and the launch vehicle. Rapid improvements in material properties and fabrication techniques make new, high-performance configurations feasible and accentuate the need for adequate methods to predict their behavior.

Prediction of the characteristics (natural frequencies, mode shapes, and response to known loads) of complex, highly efficient structures such as those of launch vehicles is essentially a two-part problem involving development of appropriate equations of motion and assigning correct values to the structural quantities involved. The third part of the problem, that of solving the equations, has been largely overcome through developments in high-speed, high-capacity computers. Comparisons of the predicted and measured characteristics of aerospace structures repeatedly demonstrate the need for experimental tests to generate the data required for refinements of structural inputs, and show that accurate predictions of structural response are difficult to come by except by iterative procedures. Such iterations

involve analysis, experiment, and comparison of results; reexamination of analytical assumptions and concepts, reevaluation of the structural properties, revised calculations and tests, and new comparisons—until the structural properties and structural behavior are predicted within acceptable bounds. Dynamicists have recognized for many years that dynamic models provide efficient, versatile, and economical sources of experimental data necessary for advancement of the state of the art in structural analysis. Applications of dynamic model technology to solution of problems of stability and control, flutter, and forced response of aircraft are well documented in the literature and, more recently, have been applied to launch vehicles and spacecraft as discussed in the following sections.

#### Replica and Dynamically Similar Models

Dynamic models as applied to research in space vehicle technology to date have been of two types: replica and dynamically similar. A replica model is one which involves reproduction of the details of the structure and materials. It is achieved by essential duplication of the prototype on a smaller scale; unless a scale reference is given, the observer could not tell from a picture of the composite vehicle or any of its components whether it be the model or prototype. An exact replica model is very difficult to achieve for obvious practical reasons, but the Saturn V model discussed subsequently is a close approximation. Whereas the design of a replica model is simple (achieved by scaling the numbers on the prototype drawings), its construction may be a very difficult task, necessitating the use of very thin shells and reinforcement structures and new tooling for fabrication. These considerations essentially limit the minimum size of such models.

Dynamically similar models encompass those wherein the important dynamic properties, such as mass and stiffness distributions, are reproduced or simulated either by the use of similar materials and fabrication techniques or by approximations thereto. In essence, a dynamically similar model, usually referred to as a dynamic model, is one which exhibits characteristics which closely represent the

counterparts of the prototype in the areas of importance relative to the phenomena being studied on the prototype. The  $\frac{1}{5}$ -scale Saturn SA-1,  $\frac{1}{5}$ -scale Titan III, and  $\frac{1}{40}$ -scale Saturn V models discussed hereafter are of this type.

#### Propellant Simulation in Large Dynamic Models

As developed in section 5.4, the simulation of fuel sloshing is a most difficult task in any model of a launch vehicle which is adequately scaled and constructed to provide quantitative data of structural dynamics of the prototype. This is true because the natural frequency of a given mode of the structure is inversely proportional to the characteristic length, whereas the natural frequency of any particular mode of the sloshing propellants is inversely proportional to the square root of the characteristic length. For example, on a  $\frac{1}{5}$ -scale replica model, the frequencies of the model structure are nine times as high as those of the prototype, whereas the frequencies of model propellants are only three times as high as the frequencies of the prototype propellants. Thus the structure/propellant frequency ratio, which should be the same on model and prototype for similarity, would differ by a factor of 3. Among the ways of overcoming this problem, such as testing the model in a higher acceleration field (e.g., on the end of a centrifuge) or constructing the model of materials having a lower modulus of elasticity, none have proven very satisfactory. Fortunately, the effects of coupling of the free surface propellant sloshing modes with the structural modes have not proven to be of primary significance, and the general practice to date has been to select model fluids primarily to simulate prototype propellant masses—Freons to simulate liquid oxygen and nitrogen tetroxide, naphthas to simulate hydrazine, polystyrene balls to simulate liquid hydrogen. Frequently water can be used, with appropriate allowances or correction factors, to achieve satisfactory simulation of propellant masses other than for liquid hydrogen. The reader is reminded that impurities associated with all of these fluids may be highly corrosive to aluminum and magnesium alloys, and that the corrosive action is particularly important because of the thin gages of materials used and the fact that the tanks are

pressurized. It has been found necessary to coat the interior of the tanks, to purify Freon, and to deionize and deactivate water with inhibitors such as sodium chromate.

#### Model Support Systems

In essentially all cases of interest, the boundary conditions for launch vehicles are essentially free-free, and an equivalent support system must be used during dynamic model tests to assure that the natural frequencies, mode shapes, structural damping, and dynamic response of the model represent those which occur on the full-scale vehicle under flight conditions. The fundamental criterion is one of frequency separation. If the frequency of the support system can be made sufficiently low compared to the natural frequency of the lowest frequency natural mode of interest, say by a factor of 3 octaves, the effect of the support system on the structural characteristics of the model can usually be neglected. The techniques for supporting various types of dynamic models, and in some cases, full-scale vehicles, are discussed in references 5.40 through 5.42.

If the structure of the vehicle is such that it may be handled as a unit and can be oriented horizontally, the better approach is usually to support it, as shown in figure 5.36. This technique has been used effectively for empty launch vehicle stages up to the size of the Thor. In this type of support system, the effect of the support is secondary, and if, in the excitation of the natural modes of the structure, the supports are located at the nodal points, their effect on the structure is negligible. It is usually desirable to mount the exciter near an antinode to

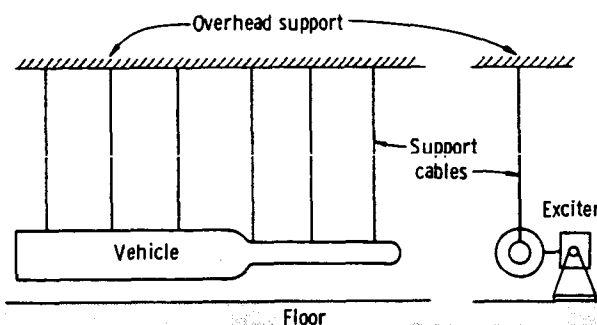


FIGURE 5.36.—Horizontal support systems for launch vehicles.

maximize the response of the structure in the mode of interest. However, if the response of the vehicle indicates coupling of other modes, such coupling can be minimized by mounting the exciter at a node point of the mode producing the undesired coupling effect.

In general, the support cables should be made of elastic shock cord, but the results of many tests of small solid-propellant rocket vehicles at the Langley Research Center indicate that steel cables can be used successfully if properly adjusted. In most cases, a two-point support is adequate for such vehicles, the location of these supports being adjusted to coincide with nodal points of the mode being excited.

In some cases, particularly those involving vehicles containing liquid propellants and thin pressurized shells, it is necessary to orient the vehicle vertically to properly simulate the effects of the earth's gravitational field on the dynamics of the vehicle-propellant system. Herr (ref. 5.41) has studied this problem and has developed two unique and very effective support systems, which are shown in figure 5.37. Both of these systems closely duplicate the free-free boundary conditions for such vehicles.

The first of these vertical support systems is referred to as a high-bay harness. The weight of the vehicle is carried by two support cables which are attached to the bottom of the vehicle and to the overhead support structure. Stability is achieved by two horizontal restraining cables tied between the support cable and the periphery of the vehicle at some point, for example, above the vehicle's center of gravity. This support system has essentially two degrees of freedom in the plane normal to the cables: translation as a pendulum and pitching. In terms of the dimensions shown on the figure, the stiffness, and thus the frequency, of the pitching mode can be controlled by separation of the points where the support cables fasten to the rigid support structure. The vehicle will stand erect if

$$a > f \left( \frac{b}{e_1} - \frac{c}{e} \right) + b$$

and the frequency of the pitching mode will approach zero as

$$a \rightarrow f \left( \frac{b}{e_1} - \frac{c}{e} \right) + b$$

This support system was used successfully on the  $\frac{1}{3}$ -scale SA-1 and the  $\frac{1}{10}$ -scale Saturn V dynamic models studied at the Langley Research Center.

In some instances involving the tests of very large dynamic models or full-scale launch-vehicle structures, it may be difficult to provide an overhead rigid support structure as necessary for the high-bay harness. In such cases, the low-bay harness, though slightly more complicated, is preferable and is being used for the structural dynamics studies of the full-scale Thor-Agena launch vehicle now under study at Langley. As was the case for the high-bay harness, the weight of the vehicle is carried by two support cables. However, in this case, the support cables may be much shorter than the length of the vehicle. The vehicle is held erect by controlling the tensions in the restraining cables by means of turnbuckles, and the condition for neutral stability, and hence, zero frequency in pitch, is (fig. 5.37)

$$T = \frac{Wb}{8 \left( \frac{L^2}{d} - S \right)}$$

Although it is still necessary to have some support structure near the top of the vehicle, this structure can be relatively light, since it need support only a small fraction of the weight of the vehicle.

#### 1/5-Scale Dynamic Model of Saturn SA-1

Because of the complex nature of the clustered structure of the Saturn SA-1, and the urgent need for experimental data to guide the selection of concepts and assumptions for structural analysis, the Langley Research Center constructed and tested a  $\frac{1}{5}$ -scale dynamic model of the SA-1 vehicle (refs. 5.43 through 5.46).

The model, supported in the vibration testing tower, is shown in figure 5.38, and some of the details of construction and test apparatus are shown in figure 5.39. The extent to which the full-scale structure is duplicated in the model is indicated by figure 5.40. The model was tested while supported in both the high-bay

harness (fig. 5.37) and with an eight-cable-support system which simulated the full-scale support system (ref. 5.44). The propellant masses were simulated with water. The experimental vibration characteristics obtained on the model are compared with the results of the full-scale tests, which were conducted at the Marshall Space Flight Center (ref. 5.45). On the basis of this comparison, the authors drew the following conclusions:

(1) The model and full-scale, first-bending-mode frequency parameters are in good agreement (within 6 percent) when the rigid-body, suspension-system rocking frequency parameters are in agreement. The frequency parameters of the model in the first cluster mode, the second cluster mode, and the second bending mode are approximately 10 percent below the corresponding full-scale frequency parameters.

(2) For most of the modes, the damping of the model is of the same order of magnitude as the damping of the full-scale Saturn.

(3) The mode shapes of the model in the first-bending, first-cluster, and second-cluster modes

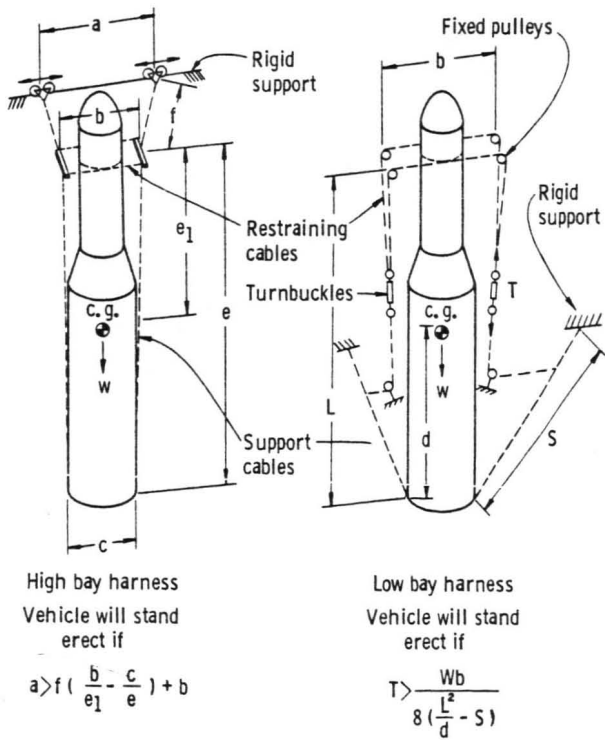


FIGURE 5.37.—Vertical support systems for launch vehicles (ref. 5.41).

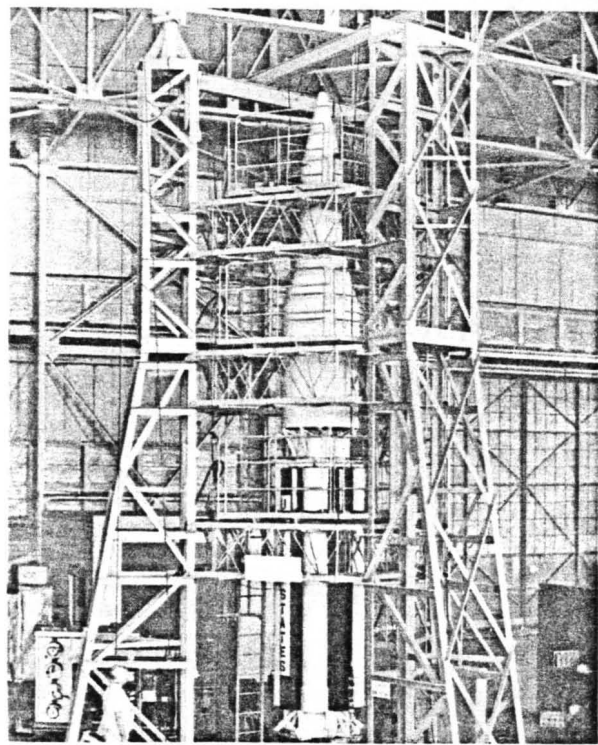


FIGURE 5.38.—1/5-scale dynamic model of Saturn SA-1 suspended in vibration-testing tower.

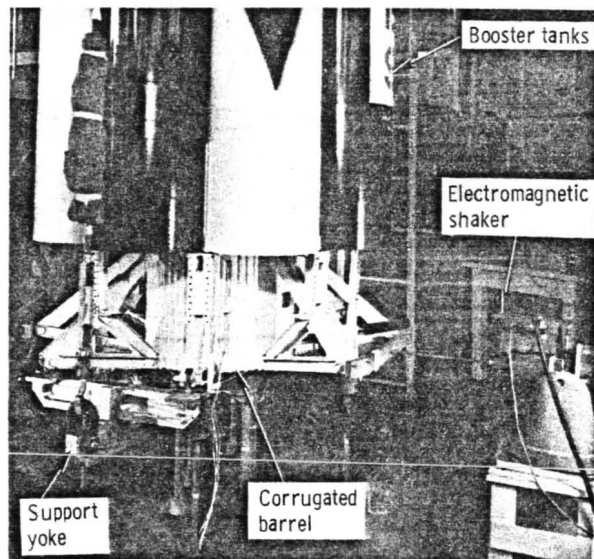


FIGURE 5.39.—Outrigger-barrel area of 1/5-scale dynamic model of Saturn SA-1.

are in agreement with the corresponding full-scale mode shapes. Significant differences between the model and full-scale, second-bending-

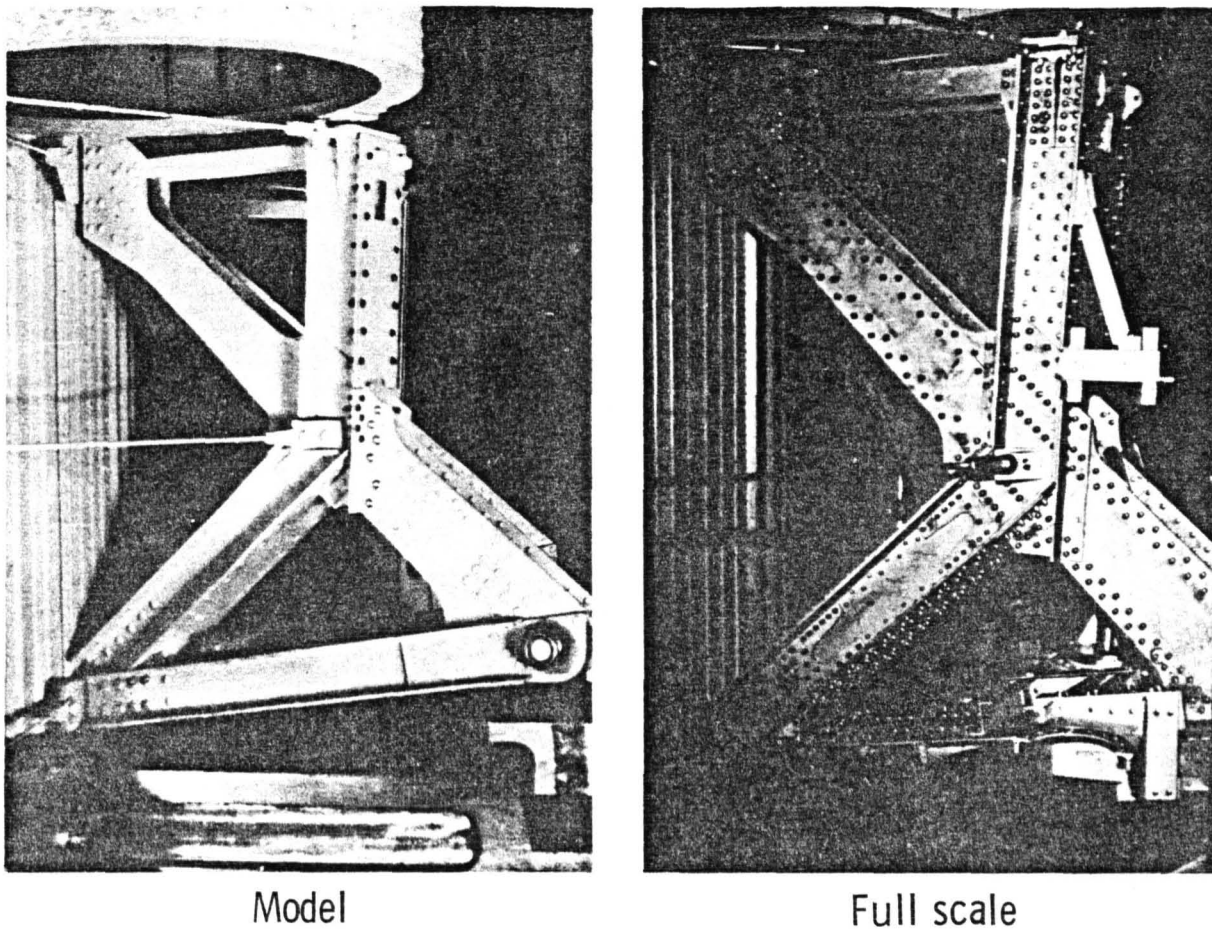


FIGURE 5.40.—Saturn SA-1 structural details.

mode shapes are believed to be caused by a structural simplification made in the second-stage structure of the model.

(4) Both model and full-scale vehicles exhibit a nonlinearity of the first-bending-mode response characterized by a decrease of resonant frequency with increase of vibration amplitude. For the range of amplitudes investigated with the model, the variation of frequency was approximately the same as the variation caused by suspension-system stiffness changes.

#### **1/5-Scale Dynamic Model of Titan III**

Partly as a result of the successful demonstration of the value of a dynamic model in studies of the structural dynamics of the Saturn SA-1 launch vehicle, the Air Force awarded a contract to Martin-Denver to construct and test a  $\frac{1}{5}$ -scale dynamic model of the

Titan III launch vehicle. This contract effort was administered by Aerospace Corp., and the Langley Research Center provided technical support and facilities for the initial model tests. Further and more detailed experimental studies are currently being pursued by NASA at Langley.

Figure 5.41 shows the model of the Titan III installed in the test tower. Some of the details of the bottom of the central core may be seen in figure 5.42 where the model is suspended above a 910-kg electromagnetic shaker for investigation of the longitudinal vibration modes and response.

During the tests, the masses of the hypergolic propellants were simulated by Freon, and a mixture of alcohol and water. The masses of the strap-on solid propellants were simulated with lead weights as shown in figure 5.43.

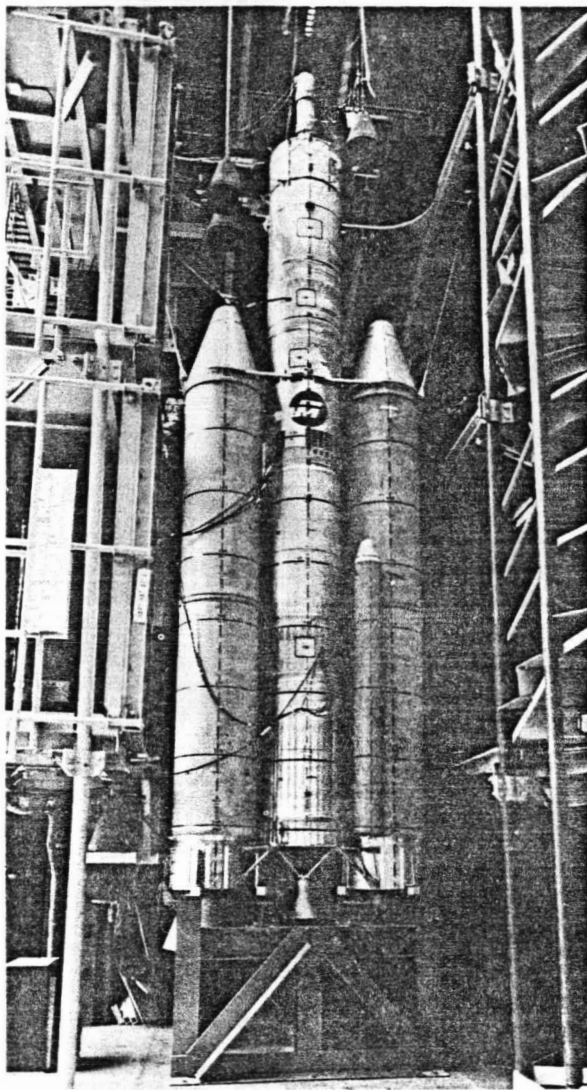


FIGURE 5.41.—1/5-scale dynamic model of Titan III installed in test tower at Langley.

The model test philosophy for the Titan III was somewhat different than for the Saturn SA-1. In this case, the primary purpose of the model tests was to check the adequacy of the theory for prediction of the full-scale Titan III response. Then if the theory, with slight modifications to treat discrepancies between the model and full-scale structures, proved adequate for analyzing the dynamic model, it could be applied with confidence to predict full-scale responses, and the need for structural dynamics testing of the full-scale vehicle would be obviated.

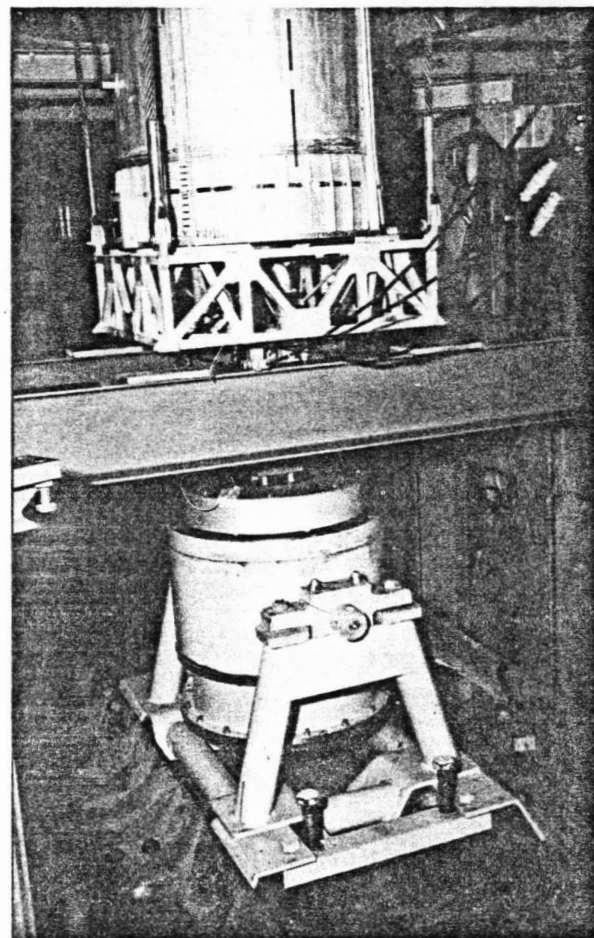


FIGURE 5.42.—Bottom section of Titan III core and vibration exciter.

At the time of writing, comparison between the theory and initial test results from the model indicates that modifications of the theory and future iterations with experiments are necessary and are now in progress. Initial results of the test program and comparison with theory are given in reference 5.47.

#### 1/40-Scale Dynamic Model of Saturn V

The  $\frac{1}{40}$ -scale dynamic model of the Saturn V launch vehicle, the umbilical tower, and the crawler platform are shown in figure 5.44. The components of the model are shown in figure 5.45. This large-scale model is part of the overall Saturn V dynamic model program to advance the technology of dynamic modeling of launch vehicles and to generate data per-

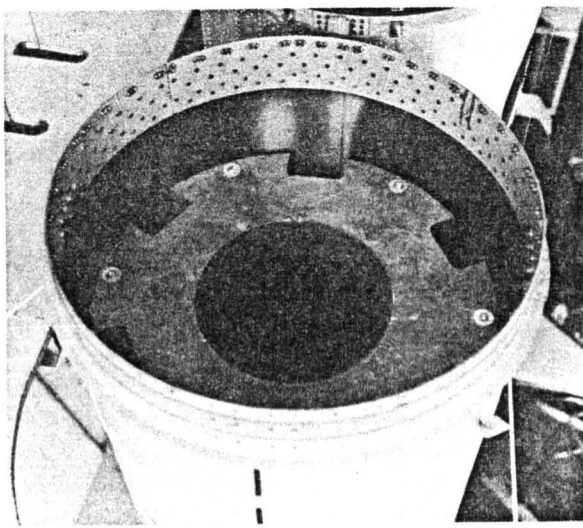


FIGURE 5.43.—Top view of model of Titan III solids showing simulated masses.

tinent to the Saturn V vehicle. Specific objectives of this model were to determine the degree to which the full-scale and  $\frac{1}{10}$ -scale replica model responses could be predicted with an inexpensive and comparatively simple dynamically similar model, to ascertain the effects of fluid propellant coupling with the structure, and to investigate the coupled response of the vehicle and launch umbilical tower.

The model was designed so that the ratios of the fundamental fuel-sloshing frequency (as simulated) to the natural frequencies of the structural bending vibrations of the vehicle could be varied over a range of values which include the full-scale frequency ratios. This was done to facilitate investigation of the effect of coupling of these modes which, as noted previously, is not possible in a replica model. The scaling of the structural aspects can be summarized as follows:

$$\left(\frac{\omega_M}{\omega_F}\right)^2 = \left(\frac{E_M}{E_F}\right) \left(\frac{I_M}{I_F}\right) \left(\frac{m'_F}{m'_M}\right) \left(\frac{l_F^4}{l_M^4}\right)$$

For a replica model

$$\left(\frac{\omega_M}{\omega_F}\right)^2 = (1) \left(\frac{1}{\lambda^4}\right) (\lambda^2) (\lambda^4)$$

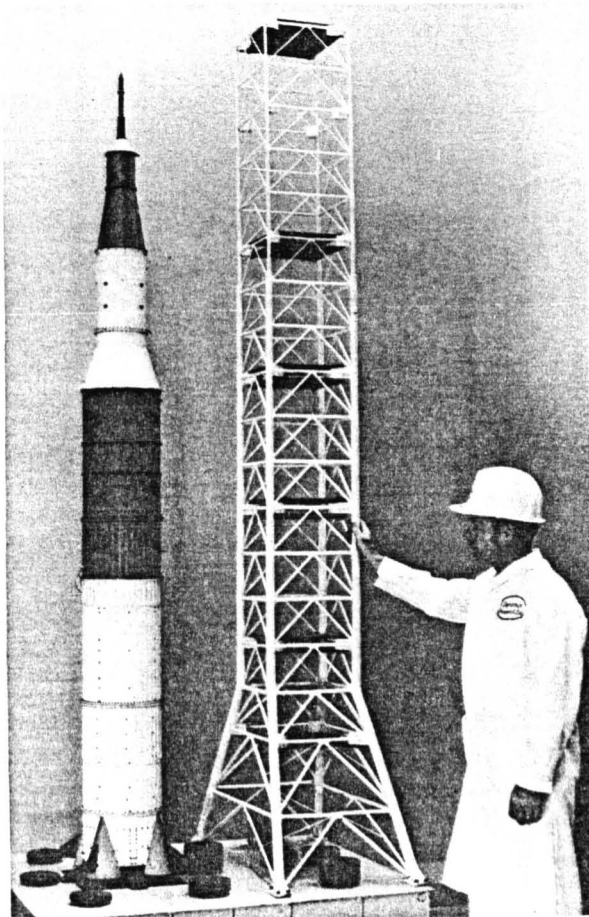


FIGURE 5.44.—1/40-scale dynamic model of Saturn V, umbilical tower and crawler platform.



FIGURE 5.45.—Components of 1/40-scale model of Saturn V.

and for the  $\frac{1}{40}$ -scale Saturn V model

$$\left(\frac{\omega_M}{\omega_F}\right)^2 = \left(\frac{1}{1.5}\right) \left(\frac{4}{\lambda^4}\right) \left(\frac{1.5}{4} \lambda^2\right) \lambda^4$$

where

$\omega$ =structural frequency

$E$ =modulus of elasticity

$I$ =area moment of inertia

$m'$ =mass per unit length

$l$ =length of the structure

$M$ =subscript to denote model

$F$ =subscript to denote full scale

$\lambda$ =characteristic length ratio

The model stiffness was reduced by constructing it of magnesium rather than aluminum, and it was increased by increasing the thickness of the skin relative to that of a  $\frac{1}{40}$ -scale replica model. The model mass distribution was then increased by a factor of (4/1.5) relative to replica values so that the resulting model/prototype frequency ratios of the basic structure would be identical to those of a replica model.

With respect to the simulated propellant frequency ratio

$$\left(\frac{\omega_M}{\omega_F}\right)^2 = \left(\frac{a_M}{a_F}\right) \left(\frac{l_F}{l_M}\right)$$

For a replica model

$$\left(\frac{\omega_M}{\omega_F}\right)^2 = (1) (\lambda)$$

and for  $\frac{1}{40}$ -scale Saturn V model

$$\left(\frac{\omega_M}{\omega_F}\right)^2 = (\lambda) (\lambda)$$

where  $a$  is the acceleration field, and the other symbols and subscripts are as previously defined. The acceleration ratio is effectively increased by a factor  $\lambda$  relative to a replica model by simulating the propellants by means of a spring-mass system. The masses include an alloy which has a low melting temperature placed in containers equipped with electrical heaters so that the alloy can be liquefied to vary the effective inertia of the propellant simulants.

The  $\frac{1}{40}$ -scale model of the launch umbilical tower (LUT) is also a dynamically similar

model where the stiffness, mass, center of gravity, and inertia properties are scaled from full-scale values. This LUT model is used to study coupling between the vehicle and the tower.

Test data from lateral tests obtained at the time of writing indicate good correlation with results from the larger  $\frac{1}{10}$ -scale model and with results from analytical studies of the full-scale vehicle. Both the experimental and the analytical studies are being continued.

### 1/10-Scale Dynamic Model of Saturn V

The  $\frac{1}{10}$ -scale dynamic model of the Saturn V, supported in the high-bay harness suspension system to simulate flight conditions, is shown in figure 5.46. Replica scaling, which necessitated an extension of the state-of-the-art in fabrication, was employed with a resulting 11-meter-tall model that has excellent duplicate representation of full-scale structure from the first-stage-engine gimbals through the Lunar Excursion Module adapter of the payload. Some of the construction details of the first-stage thrust structure are shown in figure 5.47, where the thrust and holdown posts, the reinforced cross-beams, the ring frames, the lower fuel bulkhead, and the actuator support structure are evident. Further indication of the details built into the model are shown on figure 5.48, where the interior of the first-stage fuel tank, prior to completion, can be seen. The complicated bulkhead, LOX suction ducts, slosh baffles, and integrally milled tank skins are visible. As an indication of structural detail, the skin thickness of the skin-stringer forward skirt of the third stage is 0.076 millimeter, while the cover sheets of the honeycomb in the LEM adapter are 0.043 millimeter thick. Extreme full-scale design details, such as bat section stringers spike welded to skins, corrugated intertank sections, and scaled tension strap joint reproduction, have been included in the fabrication of the  $\frac{1}{10}$ -scale model.

Other  $\frac{1}{10}$ -scale model components available for the test program include a multicell first stage, other interstage sections constructed of honeycomb or modified monocoque, and simulated holdown spring restraints.

The LOX and RP-1 propellants are simulated in the  $\frac{1}{10}$ -scale model with deionized

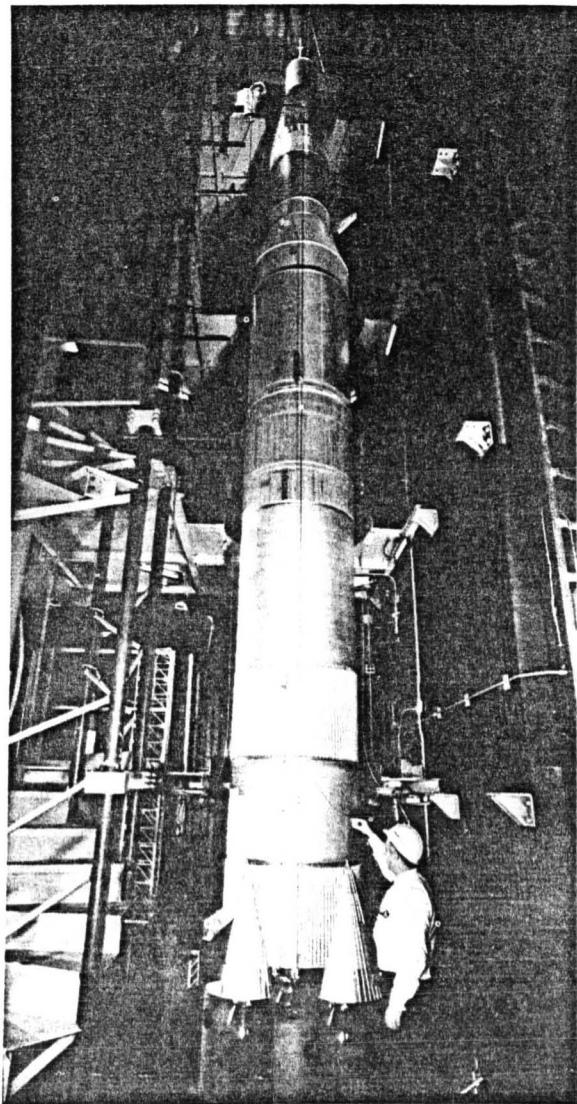


FIGURE 5.46.—1/10-scale dynamic model of Saturn V.

water. The mass distribution of the hydrogen fuel in the second and third stages is simulated with plastic balls possessing the proper specific gravity. A discussion of the early model test results, including comparison with theory, is given in reference 5.48.

#### 5.11 VIBRATION TESTS OF FULL-SCALE THOR-AGENA

The Langley Research Center is also conducting vibration analyses and tests of a full-scale

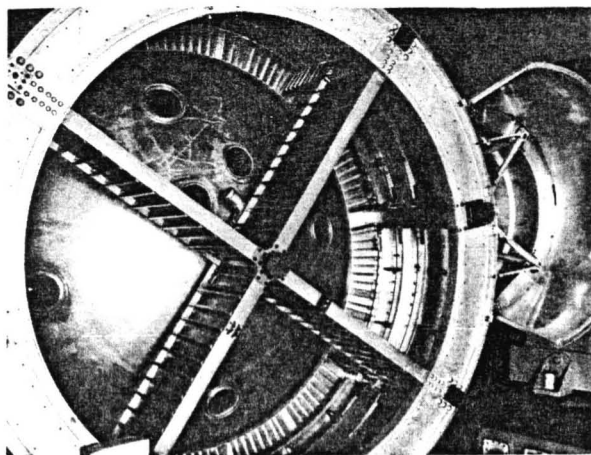


FIGURE 5.47.—First-stage thrust structure details of 1/10-scale model of Saturn V.

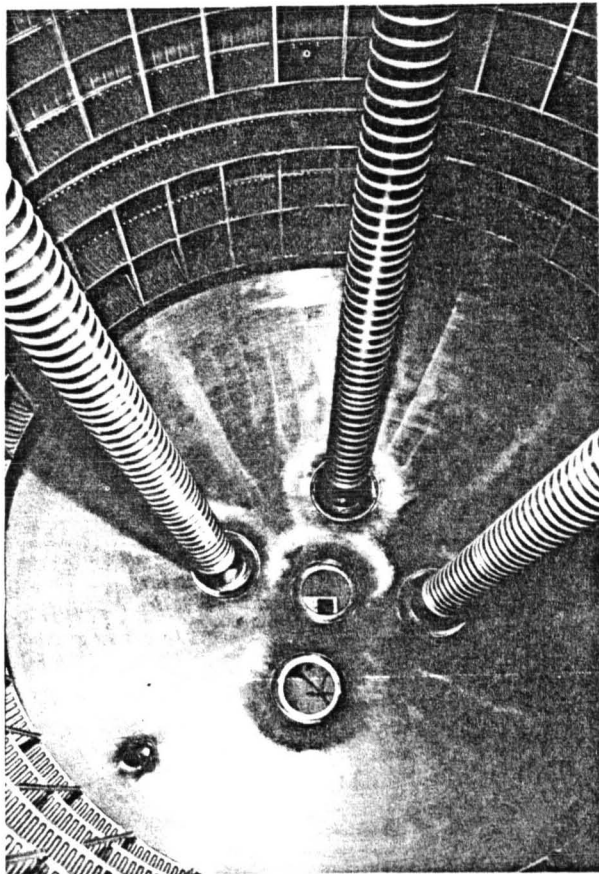


FIGURE 5.48.—Interior view of first-stage fuel tank of 1/10-scale model of Saturn V.

Thor-Agena vehicle to define the structural dynamic characteristics of typical launch ve-

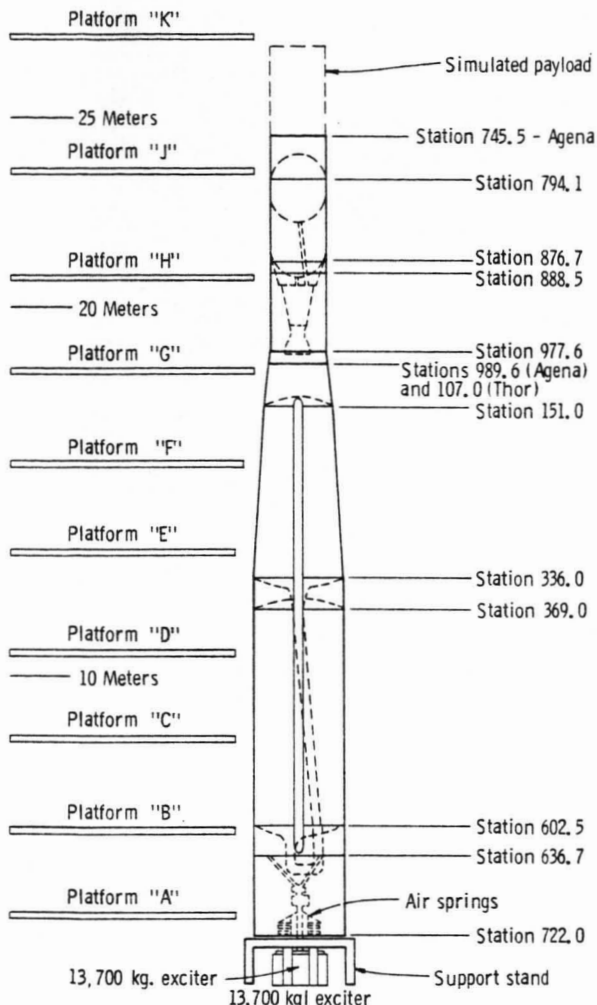


FIGURE 5.49.—Structural components of the Thor-Agena program.

hicle structures. Figure 5.49 shows the components of the various sections of the test setup. Figure 5.50 shows the Thor while being erected in the Langley Research Center's Dynamics Research Laboratory.

A unique air-bellows suspension system was developed to vertically support the vehicle during longitudinal testing. Figure 5.51 is a sketch of the vehicle on the air suspension system with a 13 700-kilogram shaker attached through the gimbal thrust pad. Lateral restraining cables prevent lateral, pitching, or rolling motions of the vehicle while providing minimum restraint to vertical or longitudinal motions. A closeup of the adapter fixture and

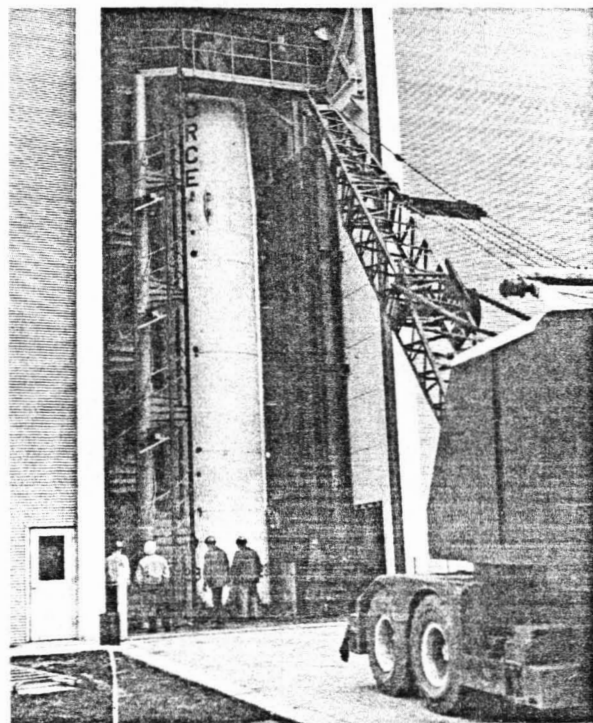


FIGURE 5.50.—Erection of Thor in the Dynamics Research Laboratory.

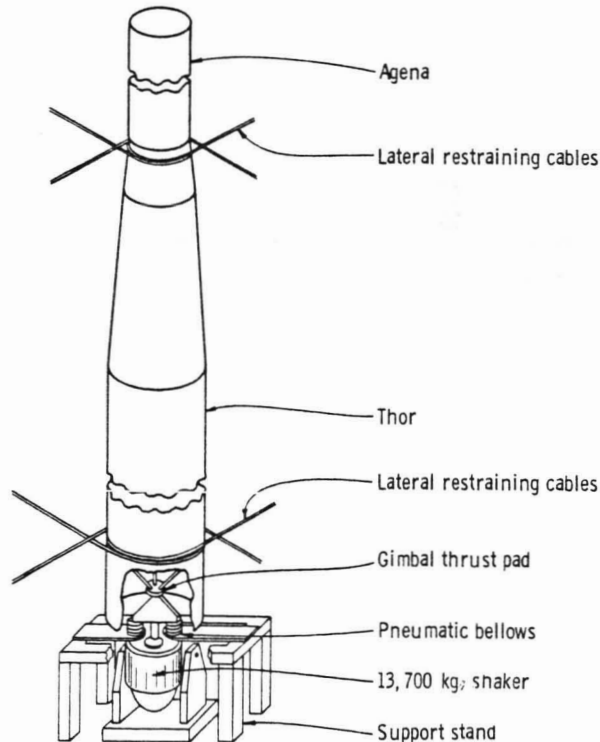


FIGURE 5.51.—Suspension system for the Thor-Agena longitudinal tests.

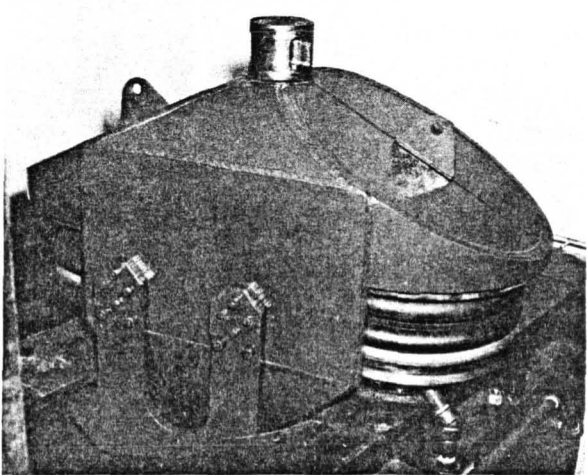


FIGURE 5.52.—Air-bellows fixture for the Thor-Agena longitudinal tests.

air bellows is shown in figure 5.52. Servo control of the bellows pressure maintains the

average elevation of the vehicle essentially fixed for any weight condition, including transient conditions such as associated with high propellant efflux rates. Water will be used to simulate the oxidizer and fuel in the Thor, while Freon and Apcos-467 will be used in the Agena.

The experimental results will yield data on the transmissibility of vibratory forces through the various types of structures used in large launch vehicles. Test objectives include acquisition of impedance data relative to the input forces generated in the engine section and forces transmitted to the payload area, and the effects of propellant flow on the dynamic response of the launch vehicle structures. Experimental data will be compared with current state-of-the-art analytical procedures to assist in determining appropriate parametric values for use in advanced analytical methods.

#### REFERENCES

- 5.1. MURPHY, GLENN: *Similitude in Engineering*. The Ronald Press Co., 1950.
- 5.2. BRIDGMAN, P. W.: *Dimensional Analysis*. Yale Univ. Press, 1931.
- 5.3. DUNCAN, W. J.: *Physical Similarity and Dimensional Analysis*. Edward Arnold & Co., 1955.
- 5.4. ROUSE, HUNTER: *Fluid Mechanics for Hydraulic Engineers*. Dover Publications, Inc., 1961.
- 5.5. ROUSE, HUNTER, ED.: *Advanced Mechanics of Fluids*. John Wiley & Sons, Inc., 1959.
- 5.6. VENNARD, JOHN K.: *Elementary Fluid Mechanics*. Fourth ed., John Wiley & Sons, Inc., 1961.
- 5.7. LORD RAYLEIGH: *Stability of Flow of Fluids and Investigations in Capillarity*. Phil. Mag., vol. 34, no. 59, 1892.
- 5.8. BUCKINGHAM, E.: Model Experiments and the Forms of Empirical Equations. Trans. ASME, vol. 37, 1915, p. 263.
- 5.9. SANDORFF, P. E.: Principles of Design of Dynamically Similar Models for Large Propellant Tanks. NASA TN D-99, 1960.
- 5.10. ABRAMSON, H. N.; AND RANSLEBEN, G. E., JR.: Simulation of Fuel Sloshing Characteristics in Missile Tanks by Use of Small Models. ARS J., vol. 30, July 1960, pp. 603-613.
- 5.11. EPPERSON, T. B.; BROWN, R. B.; AND ABRAMSON, H. N.: Dynamic Loads Resulting From Fuel Motion in Missile Tanks. Proceedings of the Fourth Symposium on Ballistic Missile and Space Technology, vol. II, Pergamon Press, 1961, pp. 313-327.
- 5.12. DALZELL, J. F.; AND GARZA, L. R.: An Exploratory Study of Simulation of Liquid Impact in Space Vehicle and Booster Tanks. Tech. Rept. 9, Contract NAS8-1555, Southwest Research Institute, Sept. 1964.
- 5.13. ABRAMSON, H. N.; AND NEVILL, G. E., JR.: Some Modern Developments in the Application of Scale Models in Dynamic Testing. ASME Colloquium on Use of Models and Scaling in Shock and Vibration, Nov. 1963.
- 5.14. STEPHENS, D. G.; LEONARD, H. W.; AND PERRY, T. W., JR.: Investigation of the Damping of Liquids in Right-Circular Cylindrical Tanks, Including the Effects of a Time-Variant Liquid Depth. NASA TN D-1367, 1962.
- 5.15. SUMNER, I. E.; STOFAN, A. J.; AND SHRAMO, D. J.: Experimental Sloshing Characteristics and a Mechanical Analogy of Liquid Sloshing in a Scale Model Centaur Liquid Oxygen Tank. NASA TM X-999, 1964.
- 5.16. McCARTY, JOHN LOCKE; LEONARD, H. WAYNE; AND WALTON, WILLIAM C., JR.: Experimental Investigation of the Natural Frequencies of Liquids in Toroidal Tanks. NASA TN D-531, 1960.
- 5.17. McCARTY, JOHN LOCKE; AND STEPHENS, DAVID G.: Investigation of the Natural Frequencies of Fluids in Spherical and Cylindrical Tanks. NASA TN D-252, 1960.
- 5.18. LEONARD, H. WAYNE; AND WALTON, WILLIAM C., JR.: An Investigation of the Natural

- Frequencies and Mode Shapes of Liquids in Oblate Spheroidal Tanks. NASA TN D-904, 1961.
- 5.19. STOFAN, ANDREW J.; AND ARMSTEAD, ALFRED L.: Analytical and Experimental Investigation of Forces and Frequencies Resulting From Liquid Sloshing in a Spherical Tank. NASA TN D-1281, 1962.
- 5.20. STOFAN, ANDREW J.; AND PAVLI, ALBERT J.: Experimental Damping of Liquid Oscillations in a Spherical Tank by Positive-Expulsion Bags and Diaphragms. NASA TN D-1311, 1962.
- 5.21. SUMNER, IRVING E.: Preliminary Experimental Investigation of Frequencies and Forces Resulting From Liquid Sloshing in Toroidal Tanks. NASA TN D-1709, 1963.
- 5.22. STOFAN, ANDREW J.; AND SUMNER, IRVING E.: Experimental Investigation of the Slosh-Damping Effectiveness of Positive-Expulsion Bags and Diaphragms in Spherical Tanks. NASA TN D-1712, 1963.
- 5.23. SUMNER, IRVING E.; AND STOFAN, ANDREW J.: An Experimental Investigation of the Viscous Damping of Liquid Sloshing in Spherical Tanks. NASA TN D-1991, 1963.
- 5.24. SUMNER, IRVING E.: Experimental Investigation of Slosh-Suppression Effectiveness of Annular-Ring Baffles in Spherical Tanks. NASA TN D-2519, 1964.
- 5.25. ABRAMSON, H. NORMAN; CHU, WEN-HWA; and KANA, DANIEL D.: Some Studies of Nonlinear Lateral Sloshing in Rigid Containers. *J. Applied Mechanics*, vol. 33, no. 4, Dec. 1966.
- 5.26. HUTTON, R. E.: An Investigation of Resonant, Nonlinear, Nonplanar Free Surface Oscillations of a Fluid. NASA TN D-1870, 1963.
- 5.27. SILVEIRA, MILTON A.; MAGLIERI, DOMENIC J.; AND BROOKS, GEORGE W.: Results of an Experimental Investigation of Small Viscous Dampers. NACA TN 4257, 1958.
- 5.28. SILVEIRA, MILTON A.; STEPHENS, DAVID G.; AND LEONARD, H. WAYNE: An Experimental Investigation of the Damping of Liquid Oscillations in Cylindrical Tanks With Various Baffles. NASA TN D-715, 1961.
- 5.29. STEPHENS, DAVID G.; LEONARD, H. WAYNE; AND SILVEIRA, MILTON A.: An Experimental Investigation of the Damping of Liquid Oscillations in an Oblate Spheroidal Tank With and Without Baffles. NASA TN D-808, 1961.
- 5.30. HOWELL, E.; AND EHLER, F. G.: Experimental Investigation of the Influence of Mechanical Baffles on the Fundamental Sloshing Mode of Water in a Cylindrical Tank. Rept. No. GM-TR-69, Guided Missile Res. Div., The Ramo-Wooldridge Corp., July 6, 1956.
- 5.31. HARRIS, C. M.; AND CREDE, C. E.: Shock and Vibration Handbook. Vol. I, McGraw-Hill Book Co., Inc., 1961, pp. 2-15.
- 5.32. STEPHENS, DAVID G.: Experimental Investigation of Liquid Impact in a Model Propellant Tank. NASA TN D-2913, 1965.
- 5.33. LINDHOLM, ULRIC S.; CHU, WEN-HWA; KANA, DANIEL D.; AND ABRAMSON, H. NORMAN: Bending Vibrations of a Circular Cylindrical Shell With an Internal Liquid Having a Free Surface. *AIAA J.*, vol. 1, no. 9, Sept. 1963, pp. 2092-2099.
- 5.34. LINDHOLM, ULRIC S.; KANA, DANIEL D.; AND ABRAMSON, H. NORMAN: Breathing Vibrations of a Circular Cylindrical Shell With an Internal Liquid. *J. Aerospace Sci.*, vol. 29, no. 9, Sept. 1962, pp. 1052-1059.
- 5.35. STEPHENS, DAVID G.; AND LEONARD, H. WAYNE: The Coupled Dynamic Response of a Tank Partially Filled With a Liquid and Undergoing Free and Forced Planar Oscillations. NASA TN D-1945, 1963.
- 5.36. COLE, HENRY A., JR.; AND GAMBUTTI, BRUNO J.: Measured Two-Dimensional Damping Effectiveness of Fuel-Sloshing Baffles Applied to Ring Baffles in Cylindrical Tanks. NASA TN D-694, 1961.
- 5.37. MILES, J. W.: Ring Damping of Free Surface Oscillations in a Circular Tank. *J. Appl. Mech.*, vol. 25, no. 2, June 1958, pp. 274-276.
- 5.38. KEULEGAN, GARIBIS H.; AND CARPENTER, LLOYD H.: Forces on Cylinders and Plates in an Oscillating Fluid. National Bureau of Standards Report 4821, Sept. 5, 1956.
- 5.39. MIXSON, JOHN S.; AND HERR, ROBERT W.: An Investigation of the Vibration Characteristics of Pressurized Thin-Walled Circular Cylinders Partly Filled With Liquid. NASA TR R-145, 1962.
- 5.40. BROOKS, GEORGE W.: Principles and Practices for Simulation of Structural Dynamics of Space Vehicles. Presented at VPI Conference on the Role of Simulation and Space Technology (Blacksburg, Va.), Aug. 17-21, 1964.
- 5.41. HERR, ROBERT W.; AND CARDEN, HUEY D.: Support Systems and Excitation Techniques for Dynamic Models of Space Vehicle Structures. Proceedings of the Symposium on Aeroelastic and Dynamic Modeling Technology (Dayton, Ohio), Sept. 23-25, 1963.
- 5.42. BROOKS, GEORGE W.: Techniques for Simulation and Analysis of Shock and Vibration Environments of Space Flight Systems. ASME Colloquium on Experimental Techniques in Shock and Vibration, Nov. 1962.
- 5.43. MIXSON, JOHN S.; CATHERINE, JOHN J.; AND ARMAN, ALI: Investigation of the Lateral Vibration Characteristics of a  $\frac{1}{6}$ -Scale Model of Saturn SA-I. NASA TN D-1593, 1963.

- 5.44. MIXSON, JOHN S.; AND CATHERINE, JOHN J.: Experimental Lateral Vibration Characteristics of a  $\frac{1}{2}$ -Scale Model of Saturn SA-I With an Eight-Cable Suspension System. NASA TN D-2214, 1964.
- 5.45. MIXSON, JOHN S.; AND CATHERINE, JOHN J.: Comparison of Experimental Vibration Characteristics Obtained From a  $\frac{1}{6}$ -Scale Model and From a Full-Scale Saturn SA-1. NASA TN D-2215, 1964.
- 5.46. RUNYAN, H. L.; MORGAN, H. G.; AND MIXSON, J. S.: Role of Dynamic Models in Launch Vehicle Development. ASME Colloquium on Experimental Techniques in Shock and Vibration, Nov. 1962.
- 5.47. JASZLICS, IVAN J.; AND MOROSOW, GEORGE: Dynamic Testing of a 20% Scale Model of the Titan III. Proceedings, AIAA Symposium on Structural Dynamics and Aeroelasticity, Boston, 1965, pp. 477-485.
- 5.48. LEADBETTER, S. A.; AND RANEY, J. P.: Some Analytical and Experimental Studies of the Dynamics of Launch Vehicles. Proceedings, AIAA Symposium on Structural Dynamics and Aeroelasticity, Boston, 1965, pp. 523-527.

## PRINCIPAL NOTATIONS

- $A$ =any area  
 $A_2$ =any area moment of inertia  
 $a$ =acceleration (linear)  
 $a_{jk}$ =power of  $j$ th dimension in  $k$ th variable  
 $a_r$ =acceleration scale ratio (model to prototype)  
 $B$ =torsional stiffness  
 $b$ =other linear dimensions of a fuel tank  
 $c, c_0$ =velocity of sound in liquid  
 $c_{pk}$ =function of the  $a_{jk}$   
 $D$ =characteristic tank diameter  
 $D_b$ =bending stiffness  
 $D_j$ =general notation for the  $j$ th fundamental dimension  
 $D_r$ =geometric scale ratio—ratio of characteristic length in the model to that in the prototype  
 $E$ =Young's modulus  
 $E_g$ =bulk modulus, gas  
 $E_L$ =bulk modulus of fluid  
 $F$ =dimension of force (or general force)  
 $F$ =(subscript) denoting prototype value of a parameter  
 $G$ =shear modulus  
 $g$ =gravitational acceleration  
 $H$ =quantity of heat  
 $h$ =depth of liquid in tank  
 $I$ =area moment of inertia (structure)  
 $i, j, k, p$ =indices  
 $L$ =dimension of length  
 $M$ =dimension of mass (or general mass)  
 $M$ =(subscript) denoting model value of a parameter  
 $M$ =a moment  
 $m$ =number of fundamental dimensions  
 $m'$ =mass/unit length, structure  
 $M_x$ =bending moment per unit width, shell element  
 $M_{xy}$ =twisting moment per unit width, shell element  
 $n$ =number of variables  
 $N_z$ =normal force per unit width, shell element  
 $N_{xy}$ =shearing force per unit width, shell element  
 $P$ =pressure  
 $P_c$ ="cavity pressure"  
 $P_d$ =dynamic pressure in liquid  
 $P_0$ =pressure at liquid free surface  
 $P_v$ =vapor pressure  
 $Q$ =charge (electrical)  
 $r$ =radius of meniscus in an equivalent capillary tube  
 $r$ =(subscript) denotes ratio of model value of a parameter to the prototype value of a parameter  
 $T$ =dimension of time  
 $T_c$ =critical temperature of liquid  
 $T_1, T_2$ =temperatures, equation (5.75)  
 $t, t_p$ =plate thickness  
 $t_w$ =equivalent distributed model tank wall thickness  
 $W$ =natural plate vibration frequency  
 $w$ =transverse displacement of neutral plane of shell wall  
 $w_{xz}$ =bending curvature of neutral plane, shell wall  
 $w_{xy}$ =twisting curvature of neutral plane, shell wall

$\dot{x}$ =impressed velocity	$\tilde{\nu}$ =Poisson's ratio
$\ddot{x}$ =impressed acceleration (linear)	$\tilde{\nu}'$ =Poisson-type elastic constant
$x_k$ =general exponent of variable	$\xi, \dot{\xi}, \ddot{\xi}$ =fluid free surface elevations, velocities, accelerations
$x_0$ =tank excitation amplitude	
$\alpha_i$ =general notation $i$ th variable	$\pi_i$ = $i$ th $\pi$ -term
$\beta$ =any angular dimension	$\pi'_i$ =ratio of the value of the $i$ th $\pi$ term for the model to the corresponding value in prototype ( $=1$ for simulation)
$\dot{\beta}$ =angular velocity	
$\ddot{\beta}$ =angular acceleration	
$\beta_{xy}$ =in-plane shearing stiffness	$\rho$ =mass density of liquid
$\beta_z$ =transverse shearing stiffness	$\rho_{\text{gas}}$ =mass density of gas
$\gamma_{zz}$ =transverse shearing strain	$\rho_r$ =mass density scale ratio (model to prototype)
$\gamma_{zy}$ =in-plane shearing strain	$\rho_{\text{solid}}, \rho_s$ =mass density of tank structure
$\Delta A_{so}$	$\sigma$ =surface tension
$\Delta A_{SL}$	$\sigma_{SG}$ =solid-gas interfacial energy/unit area
$\Delta A_{LO}$	$\sigma_{SL}$ =solid-liquid interfacial energy/unit area
$\Delta E$ =total change in interfacial energy	$\sigma_y$ =yield strength of material
$\Delta P=P_0-P$ ,	$\bar{\sigma}$ =stress
$\epsilon$ =strain	$\tau, \tau_t$ =characteristic times
$\epsilon_x$ =extensional strain	$\tau_r$ =time scale ratio (model to prototype)
$\theta$ =temperature	$\phi$ =Kinematic Surface Tension— $\sigma/\rho$
$\theta$ =contact angle	
$\Lambda$ =extensional stiffness	$\omega, \omega_i$ =characteristic frequencies
$\lambda$ =characteristic length ratio	$\nabla$ =any volume
$\mu$ =dynamic viscosity, liquid	$\nabla_2$ =any volume moment of inertia
$\mu_g$ =dynamic viscosity, gas	
$\nu$ =kinematic viscosity	

# Analytical Representation of Lateral Sloshing by Equivalent Mechanical Models

*Franklin T. Dodge*

## 6.1 INTRODUCTION

In the previous chapters, the liquid sloshing caused by lateral motions of the tank has been described analytically and experimentally, and the forces and torques exerted on the tank by the sloshing pressures have also been given. In addition to insuring that the fuel tank structure is strong enough to withstand these loads, the designer must also include the sloshing forces and torques in the stability analysis of the in-flight rocket. For this purpose, it is often advantageous to replace the liquid, conceptually, by an equivalent mechanical system, because the equations of motion for point masses and rigid bodies are usually included more readily in the overall transfer function of the missile than are the equations for a continuously deformable medium such as liquid fuel.

The main point that should be noted about the equivalent mechanical models described in this chapter is that the liquid cannot be completely replaced by a single body of suitable mass and moment of inertia that is rigidly attached to the tank. Instead, a system of spring masses or pendulums must be included. These oscillating masses are necessary to duplicate the oscillating slosh forces arising from the wave action at the free surface. In contrast, where there is no free surface (the liquid completely fills a capped container), Zhukovskii (refs. 6.1 and 6.2) has proved that the liquid can always be replaced by an equivalent rigid body; moreover, the mass and moment of inertia of this equivalent system are independent of both time and the particular type of motion being considered. However, Okhotsimskii (ref. 6.3) has shown that this result is

not true in general for a liquid with a free surface. Although his proof is too long to be considered here, a short heuristic argument following his outline is developed in the next few paragraphs. Besides showing that the equivalent mechanical model must consist of more than merely rigid bodies, except for a few specific types of container motion, the proof also shows how the masses of the free surface motion analogs may be computed.

Consider a cylindrical tank with its axis vertical (the  $z$ -axis of an  $r, \theta, z$  coordinate system fixed in space), and filled to a depth  $h$  with an ideal liquid. Then, as shown in chapter 2, the small linearized liquid motions can be calculated from a velocity potential,  $\Phi$ , which is the solution of Laplace's equation

$$\nabla^2\Phi=0 \quad (6.1)$$

The boundary conditions are

$$\frac{\partial\Phi}{\partial n}=V_n \quad (6.2)$$

at the container walls, where  $V_n$  is the component of the velocity of the tank motion in the direction normal to the wall (the  $n$ -direction); and

$$\ddot{\Phi}+g\frac{\partial\Phi}{\partial z}=0 \quad (6.3)$$

at the free surface.

The potential can be broken down into two parts

$$\Phi=\Phi_1+\Phi_2 \quad (6.4)$$

$\Phi_1$ , which satisfies equations (6.1) and (6.2) but not (6.3), is the potential of a liquid that completely fills a capped container whose height is

equal to twice the actual liquid depth.  $\Phi_2$  is the potential of a liquid in a stationary tank and whose free surface is acted on by the unsteady pressures due to  $\Phi_1$ . That is,  $\Phi_2$  satisfies equation (6.1) and the homogeneous boundary condition

$$\frac{\partial \Phi_2}{\partial n} = 0 \quad (6.5)$$

at the tank walls; it also satisfies the free surface condition, equation (6.3), which now takes the form

$$\ddot{\Phi}_2 + g \frac{\partial \Phi_2}{\partial z} = \ddot{p}(t) = -\ddot{\Phi}_1 - g \frac{\partial \Phi_1}{\partial z} \quad (6.6)$$

The motion of the container can be decomposed in the usual way into a translation and a rotation (the tank is assumed to be a rigid body). Since the problem of calculating the fluid motion is a linear one, the effect of the translation and the rotation can each be treated separately. Thus, only one of the two basic tank motions, say the translation, need be considered.

It is assumed without proof that  $\Phi_1$  can be expressed as

$$\Phi_1(r, \theta, z, t) = \dot{x}_0 \phi_1(r, \theta, z) \quad (6.7)$$

where  $x_0$  is the time-varying tank displacement. In other words, the fluid motion due to  $\Phi_1$  is directly proportional to the tank motion; this is a reasonable result considering the physical definition of  $\Phi_1$ .

The potential,  $\Phi_2$ , can be written as

$$\Phi_2(r, \theta, z, t) = \sum_{m=1}^{\infty} \dot{g}_m(t) \phi_{2,m}(r, \theta, z) \quad (6.8)$$

where  $\phi_{2,m}$  are the ordinary sloshing mode functions, and the  $g_m(t)$  can be calculated with the aid of equation (6.6). After substitution, equation (6.6) can be simplified to give

$$\ddot{g}_m + \omega_m^2 g_m = A_m \ddot{x}_0 \quad (6.9)$$

In equation (6.9) use has been made of the fact that  $\partial \Phi_1 / \partial z = 0$  at the free surface for this type of tank motion.  $\omega_m$  is the natural frequency of the  $m$ th sloshing mode, and  $A_m$  is a constant.

The forces and moments acting on the tank can be computed by integrating the fluid pressures over the walls of the tank. Since the dynamic pressures are proportional to  $\dot{\Phi}$ , i.e., proportional to

$$\ddot{x}_0 \phi_1 + \sum_{m=1}^{\infty} \dot{g}_m \phi_{2,m}$$

it can be seen that the forces and moments are partly due to a rigid body type of liquid motion (the term proportional to  $\ddot{x}_0$ ), and partly due to a more complicated type of motion (the terms proportional to  $\dot{g}_m$ ). Thus, one can conclude that only when every  $\dot{g}_m$  is directly proportional to  $\ddot{x}_0$  can the liquid be replaced entirely by an equivalent rigid body (even in this case the equivalent mass may be a function of parameters such as frequency or amplitude); in general, this is not true. Instead, as can be seen from equation (6.9), a series of spring-mass or pendulum elements must be included in the mechanical model, with the masses and the spring constants (or pendulum lengths) chosen in such a way that equation (6.9) is satisfied.<sup>1</sup>

The inertial parameters of the equivalent mechanical model for sloshing suffer from the disadvantage that they may be functions of the type of tank motion under consideration. However, in addition to easier visualization, the mechanical model has the advantage that the slight damping normally present in sloshing can be treated by adding linear dashpots to the spring-mass or pendulum elements.

It should be emphasized that the above results apply only for rigid containers and linear liquid motions. Very few results are available for mechanical models that include tank elasticity or nonlinear liquid motions.

## 6.2 SIMPLE MECHANICAL MODELS

### Models With One Sloshing Mass

According to the theoretical developments of the preceding section, a complete mechanical analogy for transverse sloshing must include an infinite number of oscillating masses, one for

<sup>1</sup> Equation (6.9) is identical in form, of course, to the equation of forced motion of a spring-mass oscillator or pendulum whose natural frequency is  $\omega_m$ .

each of the infinity of normal sloshing modes. A detailed analysis, such as that to be given in section 6.3, shows that the size of each of these pendulum or spring-mass elements decreases rapidly with increasing mode number. Thus it is generally acceptable to include in the mechanical model only the pendulum or spring mass corresponding to the fundamental mode (at least as long as the exciting frequency is not near the natural frequencies of any of the higher modes). Furthermore, it is nearly impossible to include more than one sloshing mass in those cases for which no analyses exist and for which the inertial parameters of the mechanical model must be determined by a suitable experimental program. Consequently, a number of simple one sloshing mass models are described in this section.

The model parameters may be calculated directly from the sloshing force and moment analysis, if such an analysis is available; several examples of this kind of model are given later. In all cases, the model should be checked with experimental measurements, and, indeed, the model parameters can even be determined from these tests. It appears worthwhile to describe how this may be done, with the development following closely that given in references 6.4 and 6.5.

#### *Experimental Derivation of Model Parameters*

Figure 6.1 shows a typical mechanical model, which in this instance uses a pendulum as the sloshing mass. The pendulum mass,  $m_1$ , is assumed to have no centroidal moment of inertia,<sup>2</sup> but the fixed mass,  $m_0$ , is assumed to have a moment of inertia,  $I_0$ .  $\varphi_0$  is the pitching angle, and  $x_0$  is the translation of the tank.

In order to correlate this model with the results of the experimental sloshing tests, it is necessary to have expressions for the force and moment exerted on the tank. The total lateral force of the mechanical model can be written as

$$F = -m_0\ddot{x}_0 + m_0h_0\ddot{\varphi}_0 - T_1\psi$$

where  $T_1$  is the tension in the pendulum rod. Since only linearized motions are considered,  $\sin \psi$  has been replaced by  $\psi$ . For the same

<sup>2</sup> In other words, the pendulum bob is a point mass, and the pendulum rod is weightless.

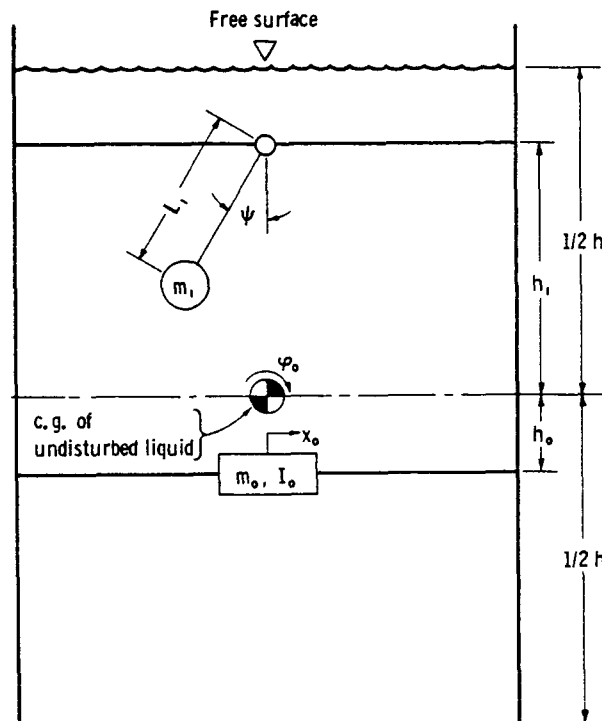


FIGURE 6.1.—Model with one sloshing mass.

reason,  $T_1$  may be replaced by  $m_1g$ , where  $g$  is the longitudinal acceleration of the tank. In other words

$$F = -m_0\ddot{x}_0 + m_0h_0\ddot{\varphi}_0 - m_1g\psi \quad (6.10)$$

The summation of moments about the center of gravity of the liquid is

$$M = -m_0h_0\ddot{x}_0 - (I_0 + m_0h_0^2)\ddot{\varphi}_0 - m_1gh_1\psi \quad (6.11)$$

The pendulum angle,  $\psi$ , can be calculated by writing down the equation of motion for the pendulum (compare this equation with eq. (6.9))

$$\ddot{\psi} + \frac{g}{L_1}\psi = \frac{1}{L_1}\ddot{x}_0 + \frac{h_1}{L_1}\ddot{\varphi}_0 \quad (6.12)$$

Other assumptions are sometimes made; two common ones are that the pendulum is always perpendicular to the liquid surface and that the sum of  $m_0$  and  $m_1$  equals the total liquid mass.<sup>3</sup>

<sup>3</sup> The pendulum angle  $\psi$  can be determined by the use of the first assumption. The last assumption is not strictly true, since the sum of  $m_0$  and the total mass of the infinity of sloshing masses (all but one of which are neglected in this model) should equal the liquid mass.

In one series of tests with the liquid oxygen tank of the Centaur missile (ref. 6.5), the tank was oscillated at a frequency much less than the sloshing natural frequency, and then the tank was quick stopped. Since the tank was not rotated ( $\dot{\phi}_0=0$ ), equations (6.10) and (6.12) can be combined to give

$$m_1 = \frac{F_{\max}}{X_0} \left( \frac{1}{\omega^2} - \frac{L_1}{g} \right) \quad (6.13)$$

where  $F_{\max}$  is the magnitude of the peak sloshing force immediately after quick stopping, and  $X_0$  is the amplitude of the tank motion; that is,  $x_0 = X_0 \sin \omega t$ . From this equation, the pendulum mass,  $m_1$ , may be calculated (since the natural frequency,  $\sqrt{\frac{L_1}{g}}$ , can be measured by noting the excitation frequency for which a sloshing resonance occurs). The reliability of this method is demonstrated in figure 6.2,

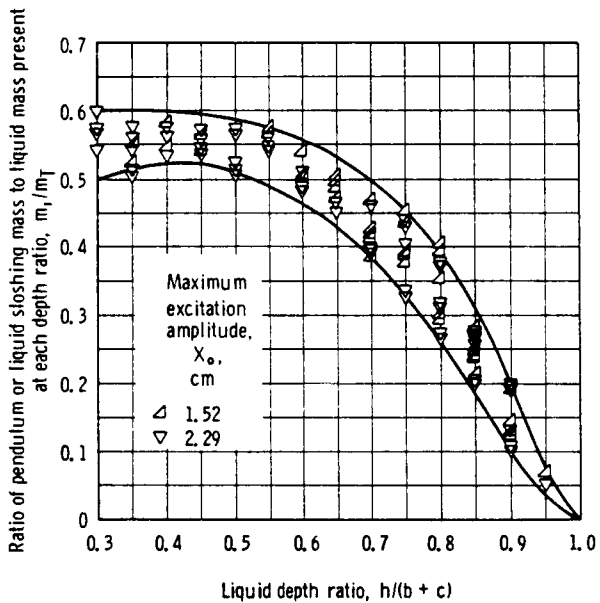


FIGURE 6.2.—Ratio of pendulum mass to liquid mass present at each depth ratio as function of liquid depth ratio (ref. 6.5).

which shows the sloshing mass,  $m_1$ , as a function of liquid depth,  $h$ , and total tank depth,  $b+c$ . (The Centaur liquid oxygen tank is essentially an oblate spheroid with a minor diameter of  $b$ , although the two oblate spheroidal segments are separated by a very small

cylindrical section of height,  $c$ .) The scatter in the experimental data was about  $\pm 5$  percent; for this reason, upper and lower limit curves are drawn on the figure. It can be seen that the sloshing mass is very small when the liquid almost fills the tank, because the free surface area continually decreases as  $h/(b+c)$  is increased above 0.5, until for  $h/(b+c)=1.0$  there is no free surface; that is, there is no wave motion. It should be noted that there was a certain amount of internal hardware in this scale model, such as a thrust barrel, a fill pipe, a vent pipe, and so forth; however, there were no slosh baffles present.

The location of the pendulum hinge point above the center of the tank was determined by quick stopping the tank, as was done in the  $m_1$  measurements, and then the maximum moment and force were recorded. For these conditions, it can be seen from equations (6.10) and (6.11) that  $M_{\max}=h_1 F_{\max}$ , or

$$h_1 = \frac{M_{\max}}{F_{\max}} \quad (6.14)$$

Results of typical measurements for the Centaur tank are shown in figure 6.3. There is a considerable amount of scatter in the data. The abrupt change in the slope of the curves at  $h/(b+c)=0.5$  is probably caused primarily by the fact that the free surface area increases for increasing liquid depths as long as  $h/(b+c)<0.5$ ,

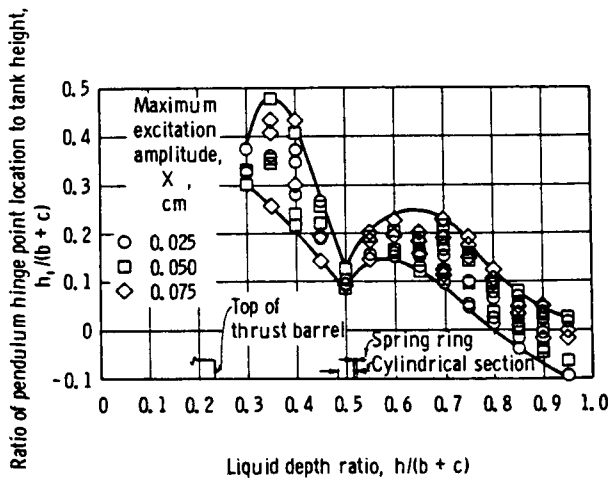


FIGURE 6.3.—Ratio of pendulum hinge point location to tank height as a function of liquid depth ratio (ref. 6.5).

but decreases for increasing liquid depths when  $h/(b+c) > 0.5$ .

The fixed mass,  $m_0$ , can be calculated by the equation

$$m_0 = m_T - m_1 \quad (6.15)$$

where  $m_T$  is the total fluid mass. The location of this mass below the center of gravity of the liquid, and its centroidal moment of inertia, can be determined by pitching the tank ( $\phi_0 \neq 0$ ) and recording the sloshing moment and force. If this is not possible or practical, as was the case in the experiments described in reference 6.5, additional assumptions are necessary. If one assumes that the mechanical model should duplicate the statical properties of the liquid,  $h_0$  can be calculated by requiring that the static moment on the tank, when it is tipped through a small angle, be the same for both the liquid and the mechanical model. In other words

$$h_0 m_0 = (h_1 - L_1) m_1 \quad (6.16)$$

which is identical to requiring that the location of the center of gravity of the mechanical model be the same as that of the liquid. However,  $I_0$  cannot be determined unless it is possible to pitch the tank; if this is done,  $I_0$  can be calculated directly from equations (6.10), (6.11), and (6.12).

The parameters of a mechanical model using a spring-mass element instead of a pendulum can be determined in a similar way.

#### *Analytical Derivation of Model Parameters*

Expressions for the sloshing forces and moments are available for a number of simple tank shapes, and for these the model parameters may be determined without recourse to experiments. Because the theory usually assumes that the liquid is inviscid and the tank is "clean," the inertial parameters are strictly valid only for a tank containing no baffles or other internal hardware; even with baffles, however, the parameters do not change significantly, the main effect being an increase in damping. (However, see discussion following equation (6.51).) Thus, the various masses, pendulum lengths or spring constants, moments of inertia, etc., given in the tables are valid also for tanks which are not perfectly clean.

Simple mechanical models for *cylindrical* tanks are considered first (refs. 6.6 through 6.11). Figure 6.4 shows the two types of models for which analytical models are available, and the equations for calculating the parameters are given in table 6.1. The moment of inertia,  $I_0$ , is the same for both models.

Not all of the models given in the references are identical. In some cases,  $m_0$  is given as the value it would have if all the modal masses were included in the model; thus, since only one of the modal masses is actually included, the total fluid mass is slightly larger than the mass of the mechanical model. Also, the value of  $l_0$  is sometimes given as the value necessary to leave the center of gravity of the fluid unchanged; in table 6.1, the value of  $l_0$  is that which would leave the center of gravity unchanged if all the modal masses were present; thus, the center of gravity of this model is slightly displaced from that of the liquid. Experimental evidence (refs. 6.10 and 6.11) has shown that these discrepancies are very minor.

Figure 6.5 shows an equivalent mechanical model for *rectangular* tanks (refs. 6.12 through 6.14); this model uses a single spring-mass element to represent the liquid sloshing. The motion of the tank is in the plane of the drawing, but a similar model is valid for motions at right angles to this plane. Equivalent models for the sloshing that occurs when the tank is rotated about a vertical axis are available (refs. 6.12 and 6.13), but are not reproduced here since this type of motion is of less interest in space vehicle applications.

Table 6.2 lists the model parameters, which have been developed by neglecting all the terms involving the masses corresponding to high-order modes in the original equations (refs. 6.12 and 6.13).

A series of compound double-pendulum models used to simulate sloshing in long, shallow rectangular tanks, such as the passive antiroll tanks employed in certain ships, have been developed by Dalzell (unpublished notes). In these models, it is necessary to include explicitly the fact that the pivot point of the swinging pendulum is in motion. Figure 6.6 shows two

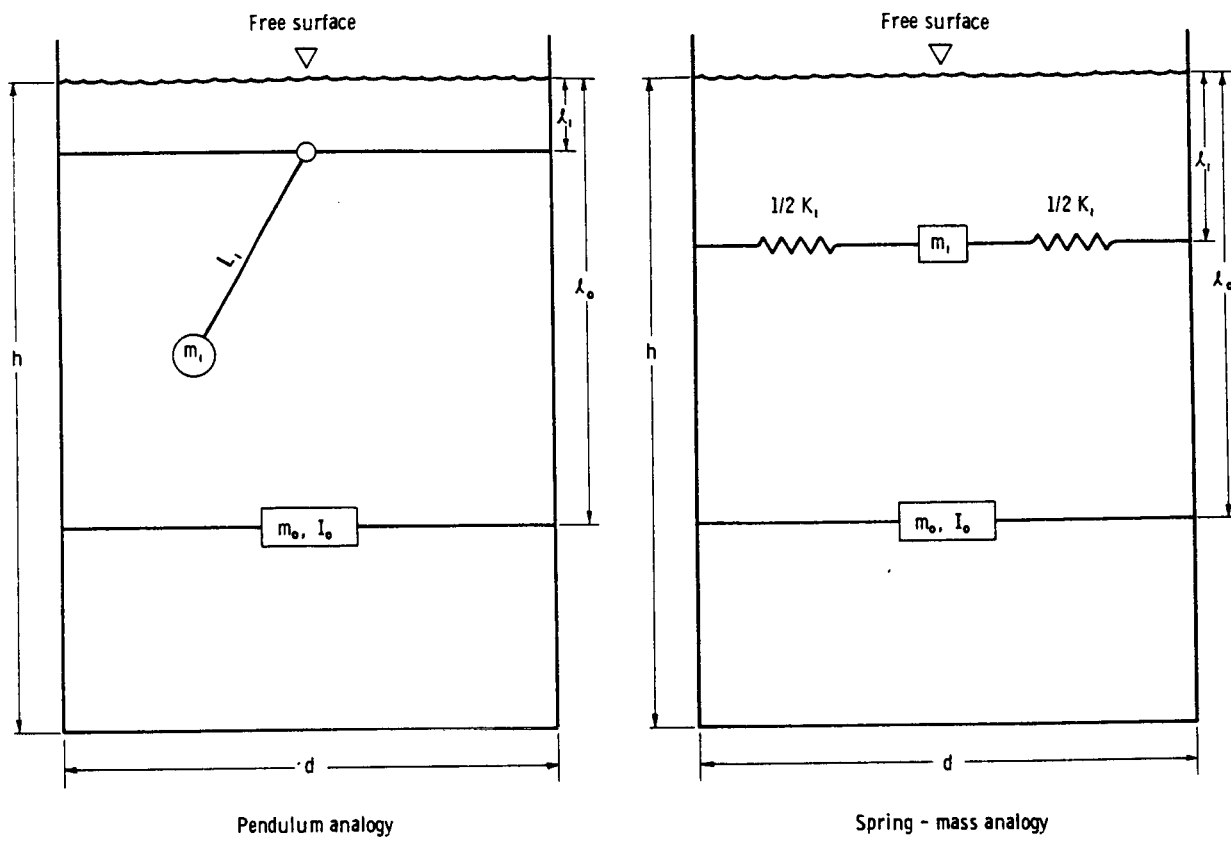


FIGURE 6.4.—Simple mechanical models for cylindrical tanks.

TABLE 6.1.—*Model Parameters for Cylindrical Tank*

$$\left( m_T = \frac{1}{4} \pi \rho d^2 h; l_1 \text{ for spring-mass} = l_1 + L_1 \text{ for pendulum}; N=0 \text{ for spring-mass model}; N=1 \text{ for pendulum model}; I_{\text{rigid}} = m_T d^2 \left[ \frac{1}{12} \left( \frac{h}{d} \right)^2 + \frac{1}{16} \right] \right)$$

Pendulum analogy	Spring-mass analogy
$L_1 = \frac{d}{3.68} \coth 3.68 \frac{h}{d}$	$K_1 = m_T \left( \frac{g}{1.19h} \right) \left( \tanh 3.68 \frac{h}{d} \right)^2$
$m_1 = m_T \left( \frac{d}{4.4h} \right) \tanh 3.68 \frac{h}{d}$	$m_1 = m_T \left( \frac{d}{4.4h} \right) \tanh 3.68 \frac{h}{d}$
$m_0 = m_T - m_1$	$m_0 = m_T - m_1$
$l_1 = -\frac{d}{7.36} \operatorname{esch} 7.36 \frac{h}{d}$	$l_1 = \frac{d}{3.68} \tanh 3.68 \frac{h}{d}$
$l_0 = \frac{m_T}{m_0} \left[ \frac{h}{2} - \frac{d^2}{8h} \right] - (l_1 + L_1) \frac{m_1}{m_0}$	$l_0 = \frac{m_T}{m_0} \left[ \frac{h}{2} - \frac{d^2}{8h} \right] - l_1 \frac{m_1}{m_0}$
$I_0 + m_0 l_0^2 + m_1 (l_1 + N L_1) = I_{\text{rigid}} + m_T \left( \frac{h}{2} \right)^2 - \frac{m_T d^2}{8} \left[ 1.995 - \frac{d}{h} \left( \frac{1.07 \cosh 3.68 \frac{h}{d} - 1.07}{\sinh 3.68 \frac{h}{d}} \right) \right]$	

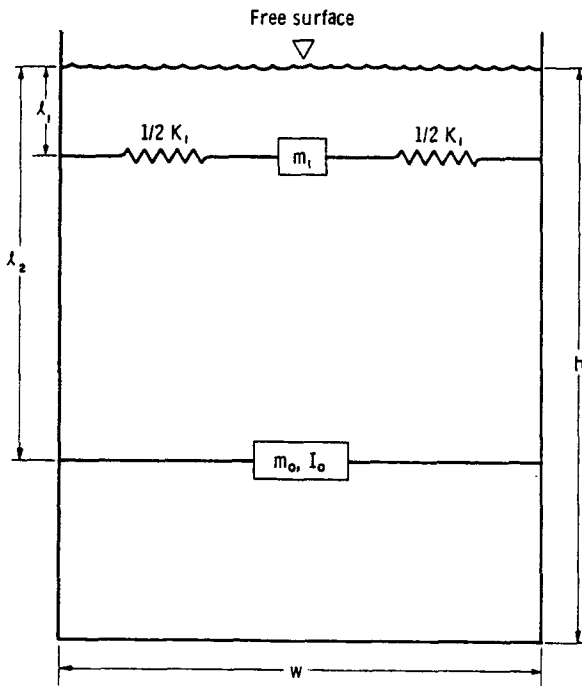


FIGURE 6.5.—Simple mechanical model for rectangular tanks.

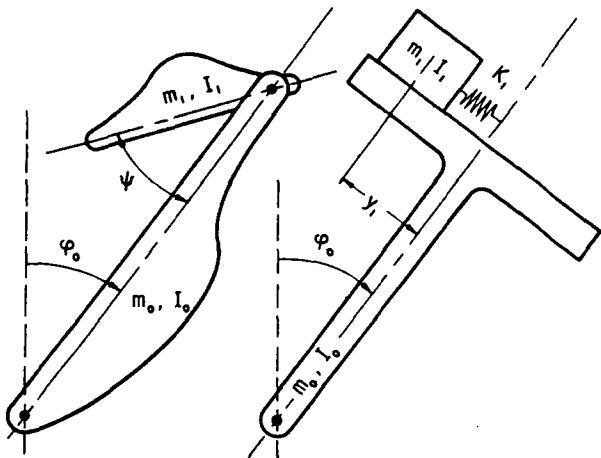


FIGURE 6.6.—Compound double-pendulum mechanical models for long shallow rectangular tanks.

of these models. Since such models are used mostly in connection with waves whose lengths are relatively long in comparison to the liquid depth, they will not be investigated further.

The available analyses for *spherical* tanks (refs. 6.6, and 6.15 through 6.17) are essentially numerical (see ch. 2); hence, the parameters for the mechanical model are presented in the

TABLE 6.2.—Model Parameters for Rectangular Tank

[ $m_T = \rho h w$  = fluid mass per unit width]

$$\begin{aligned}
 K_1 &= m_T \left( \frac{g}{1.23h} \right) \left( \tanh 3.14 \frac{h}{w} \right)^2 \\
 m_1 &= m_T \left( \frac{w}{3.87h} \right) \tanh 3.14 \frac{h}{w} \\
 m_0 &= m_T - m_1 \\
 l_1 &= \frac{w}{1.57} \tanh 1.57 \frac{h}{w} \\
 l_0 &= \frac{h}{2} + \frac{m_1}{m_0} \left( \frac{h}{2} - l_1 \right) \\
 I_0 + m_0 \left( l_0 - \frac{h}{2} \right)^2 + m_1 \left( \frac{h}{2} - l_1 \right)^2 \\
 &= \frac{m_T}{12} (h^2 + w^2) \left[ 1 - \frac{4w^2}{w^2 + h^2} + \frac{2.52w^3}{hw^2 + h^3} \tanh 1.57 \frac{h}{w} \right]
 \end{aligned}$$

form of graphs instead of tables. Figure 6.7 gives the necessary information for a pendulum analogy. The centroidal moment of inertia of the fixed mass is not required in the model since, for an ideal liquid, rotation about an axis through the center of tank does not cause any liquid motion or sloshing forces and moments.

Comparisons of the test results and the predictions of the mechanical model do not agree as well for the spherical tank as they do for cylindrical and rectangular tanks (ref. 6.15). This is because liquid motions in a spherical tank are inherently more nonlinear than in tanks with parallel sides (see ch. 3); thus the results of a linear theory, such as the equivalent mechanical model shown in figure 6.7, cannot be expected to yield results as accurate for spherical tanks as for other configurations.

Experimentally determined parameters for a pendulum model in a spherical tank were compared with analytical values by Sumner (ref. 6.17). While the fundamental frequency parameter agreed well, except for nearly full or nearly empty tanks (where nonlinear effects predominate), the pendulum-sloshing mass ratio did not. The other two parameters, pendulum arm length and hinge-point location, also agreed fairly well.

Equivalent mechanical models for arbitrarily shaped *conical* tanks are not available. How-

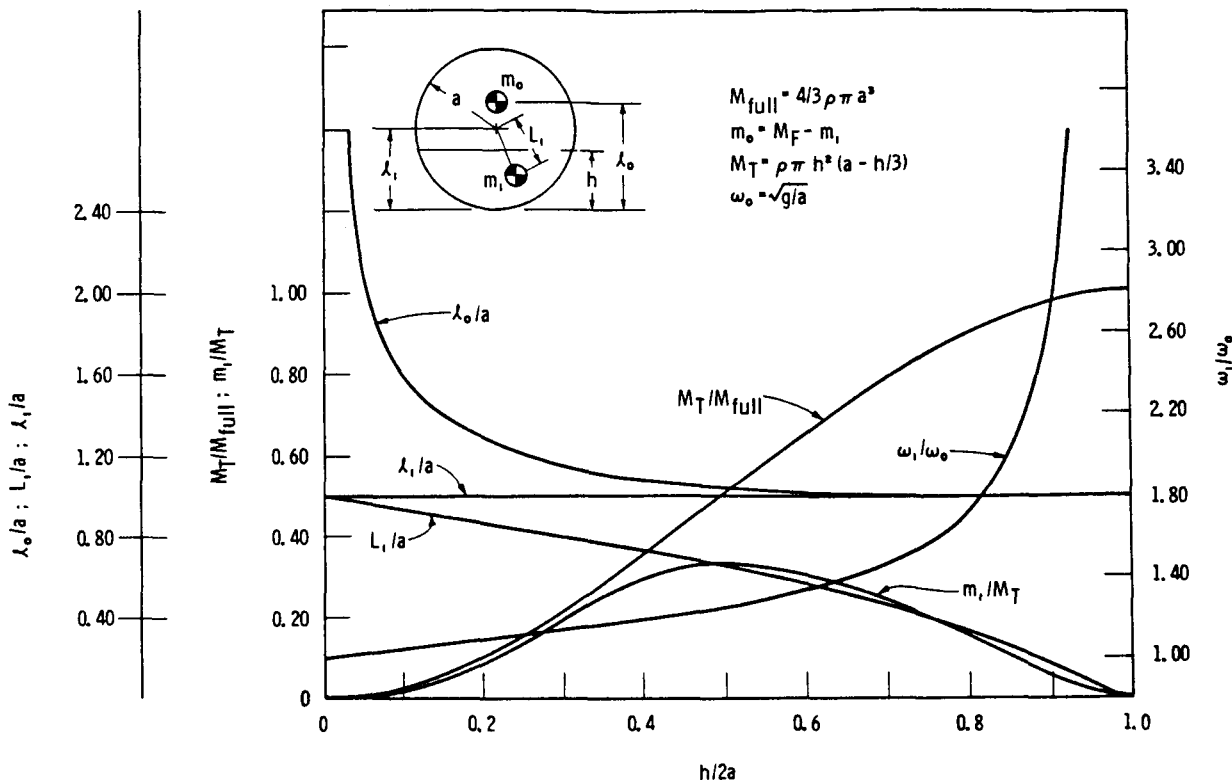


FIGURE 6.7.—Simple-pendulum mechanical model for spherical tanks (ref. 6.6).

ever, a partially complete model for a 45° conical tank (refs. 6.6 and 6.18) is shown in figure 6.8 and table 6.3. The centroidal moment of inertia,  $I_0$ , of the rigid mass,  $m_0$ , is not given in the references; consequently, the mechanical model is valid only for translational motion of the tank, and not for pitching motions.

In most instances, the foregoing models adequately represent the dynamics of liquid sloshing. The two chief restrictions to their use are: (1) the excitation frequency should not be close to the natural frequencies of any of the higher order sloshing modes, and (2) the model is not a valid representation for frequencies in the very near neighborhood of the natural frequency of the fundamental sloshing mode. The first restriction can be lifted by using the more complete mechanical models presented in section 6.3, and the second restriction can be relaxed by including appropriate damping factors in the model, as will be done in section 6.4. In some cases, provision must be made

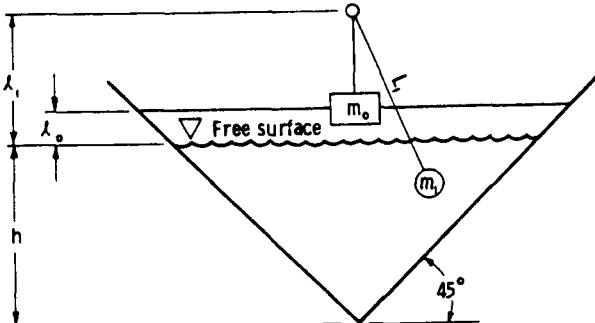


FIGURE 6.8.—Simple mechanical model for 45° conical tanks.

TABLE 6.3.—Model Parameters for 45° Conical Tank

[ $m_T = \frac{1}{3}\rho\pi h^3$ ;  $I_0$  not available]

$$\begin{aligned}L_1 &= h \\m_1 &= 0.75m_T \\m_0 &= 0.25m_T \\l_1 &= 0.6h \\l_0 &= 0.2h\end{aligned}$$

for rotary sloshing. This is discussed in the following paragraphs.

### Pendulum Analogy for Rotary Sloshing

It is an experimental fact that when a cylindrical tank is translated periodically at a frequency very near the natural frequency of sloshing in the fundamental mode, the liquid wave motion ceases to oscillate about a single nodal diameter. Instead, a rotational wave is observed to wash around the tank boundary; that is, the nodal diameter rotates. (This phenomenon is discussed in greater detail in ch. 3.) It is known also that if the point of support of a conical pendulum is oscillated near its natural frequency, the pendulum motion departs from the plane of excitation, and the plane of the to-and-fro motion of the pendulum rotates (refs. 6.19 and 6.20). Since the fluid motion away from resonance is represented adequately by a pendulum, it seems possible, therefore, that the rotary motion of the fluid may also be represented by a pendulum. A model of this type has been analyzed and, indeed, it is a fair representation of the essential characteristics of rotary sloshing (refs. 6.21 and 6.22).

The rotary motion of both the liquid and the pendulum analog are caused by nonlinear effects in which energy is transferred between various modes (or degrees of freedom). An analysis shows that in both cases there are three regimes of motion:

(1) Stable planar motion except in a narrow frequency band centered approximately around the natural frequency.

(2) Stable nonplanar motion in a narrow frequency band immediately above the natural frequency.

(3) Nonstable motion (swirling in which the rotation of the nodal diameter changes constantly) in a narrow frequency band immediately below the frequencies for which motions of type (2) occur.

The proof of these statements follows directly from an analysis of the conical pendulum shown in figure 6.9. The mass of the pendulum bob,  $m_1$ , and the length,  $L_1$ , are the same as for the corresponding mechanical model for ordinary sloshing (fig. 6.4). The equations of

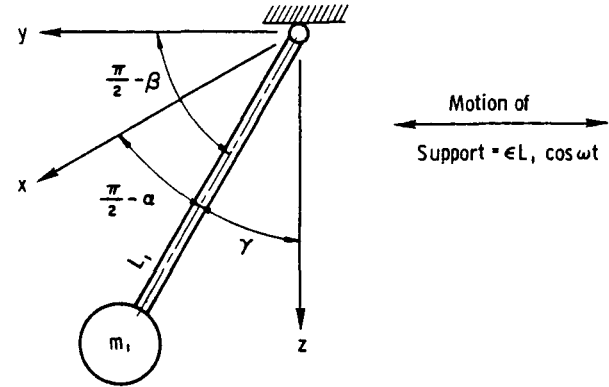


FIGURE 6.9.—Conical-pendulum model for rotary sloshing.

motion for the pendulum, correct to third order in the direction cosines ( $\pi/2-\alpha$ ,  $\pi/2-\beta$ ,  $\gamma$ ), are

$$\begin{aligned} \left[ \frac{d^2}{dt^2} + \frac{g}{L_1} \right] \alpha - \frac{g}{6L_1} \alpha^3 + \frac{1}{2} \alpha \left[ \frac{d^2}{dt^2} + \frac{g}{L_1} \right] \beta^2 &= \epsilon \omega^2 \cos \omega t \\ \left[ \frac{d^2}{dt^2} + \frac{g}{L_1} \right] \beta - \frac{g}{6L_1} \beta^3 + \frac{1}{2} \beta \left[ \frac{d^2}{dt^2} + \frac{g}{L_1} \right] \alpha^2 &= 0 \end{aligned} \quad (6.17)$$

The angle  $\gamma$  has been eliminated in these two equations by the relation  $\sin^2 \gamma = \sin^2 \alpha + \sin^2 \beta$ . The stability of the various types of solution of equations (6.17) has been studied by Freed (ref. 6.19) and Miles (ref. 6.20). The main results are given in terms of a dimensionless frequency,  $\nu$ , defined by  $\nu = \epsilon^{-2/3} \left[ \frac{\omega^2 - \omega_n^2}{\omega_n^2} \right]$  where  $\omega_n^2 = g/L_1$ ; they are:

(1) Simple harmonic, planar motions are stable for  $\nu < -0.945$  or  $\nu > 0.757$ .

(2) Simple harmonic nonplanar motions are stable for  $\nu > 0.154$ .

(3) Simple harmonic motions, either planar or nonplanar, are unstable for  $-0.945 < \nu < 0.154$ .

It can be seen that for  $\nu > 0.757$ , both stable planar and nonplanar motions are possible. Which one is obtained depends on the initial conditions; that is, if there is some initial rotation present, a rotational motion is obtained, but, if not, a nonrotational motion is obtained. The stability properties of the differential equations (6.17) also have been examined with the aid of analog computers, with essentially the same conclusions.

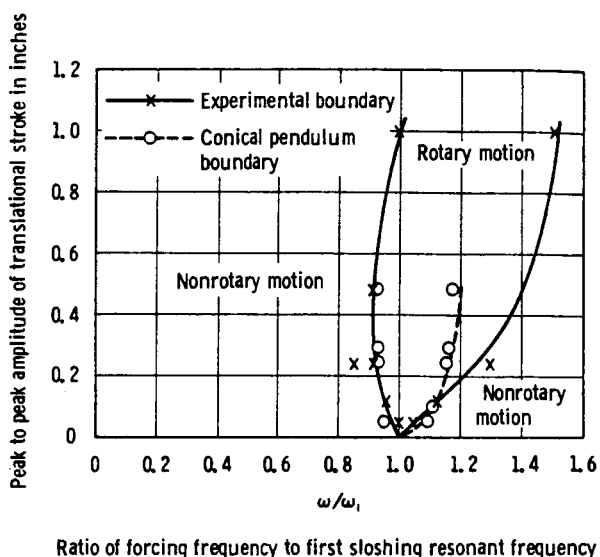


FIGURE 6.10.—Comparisons of experimental and conical-pendulum model regions of rotary sloshing (ref. 6.22).

Figure 6.10 shows a comparison between the stability boundaries of a conical pendulum and those of sloshing in a cylindrical tank. More recent experimental evidence (ref. 6.23) has shown that the right-hand stability boundary for sloshing is a strong function of slight imperfections in the tank geometry or excitation. For more and more exactly lateral translation, roundness of tank, etc., the stability boundaries for sloshing and for the conical pendulum approach each other more and more closely. Thus, a conical pendulum appears to be a good mechanical model for rotary sloshing.

Another formulation of a model that includes pitching as well as translation of the tank has been developed recently by Bauer (ref. 6.24) for this type of sloshing.

### 6.3 COMPLEX MECHANICAL MODELS

As indicated in sections 6.1 and 6.2, a complete mechanical model must include a pendulum or spring mass for each of the infinitely many sloshing modes of the liquid. Physically, each mass in the mechanical system corresponds to the effective mass of liquid that oscillates in each particular slosh mode, and, from its size, it is possible to assess how significant that mode is. The complex mechanical models described

in this section are all derived from analytical results, since it is usually not practical to determine the size of more than one sloshing mass from experimental measurements alone. Although such analytical theories are in general only applicable to clean, unbaffled tanks, it is permissible, in the light of many experimental verifications, to use the same inertial parameters to simulate sloshing in baffled tanks if a dampening mechanism is included in the model.

#### Cylindrical Tanks (refs. 6.25 through 6.33)

The method used to compute the model parameters from analytical results for sloshing will now be described in detail for the case of a rigid circular cylindrical tank, with the analysis following closely that given in references 6.25, 6.29, and 6.30. The mechanical model is shown in figure 6.11; the sloshing action is represented by a set of spring masses, but a similar analysis is valid for a pendulum model.  $\varphi_0$  is the rotation of the tank about an axis through the center of gravity of the liquid;  $y_0$  is the lateral displacement of the tank; and  $y_n$  is the displacement of the mass,  $m_n$ , with respect to the tank walls.

Each of the spring constants,  $K_n$ , are chosen such that their ratio to the oscillating mass is equal to the square of the natural frequency of that mode; that is,

$$\frac{K_n}{m_n} = \omega_n^2 = \frac{2\xi_n g}{d} \tanh \frac{2\xi_n h}{d} \quad (6.18)$$

$\xi_n$  are the zeroes of  $J'_1(\xi_n) = 0$ . In order to preserve the static equilibrium of the liquid, the sum of all the modal masses and the fixed mass must equal the total liquid mass

$$m_0 + \sum_{n=1}^{\infty} m_n = m_T \quad (6.19)$$

To keep the vertical location of the center of gravity unchanged as it should be for small liquid motions,  $h_0$  must satisfy the relation

$$h_0 = \frac{1}{m_0} \sum_{n=1}^{\infty} h_n m_n \quad (6.20)$$

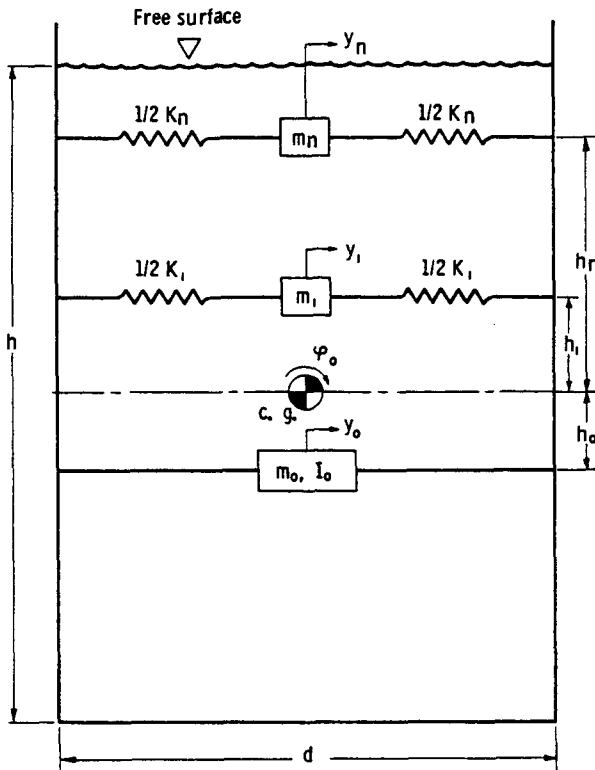


FIGURE 6.11.—Complex mechanical model for cylindrical tanks.

However, a dynamic analysis must be used to calculate the remaining unknown parameters:  $m_n$ ,  $h_n$ , and  $I_0$ . To begin with, the equation of motion for each of the oscillating masses can be written as

$$m_n(\ddot{y}_n + \ddot{h}_n\dot{\varphi}_0) + K_n y_n - m_n g \varphi_0 = 0 \quad (6.21)$$

The reaction force of each of these masses on the tank is simply  $-K_n y_n$ , so that the total force acting on the tank can be expressed as

$$m_0(\ddot{y}_0 - h_0\ddot{\varphi}_0) + \sum_{n=1}^{\infty} m_n(\ddot{y}_n + \ddot{y}_0 + h_n\ddot{\varphi}_0) = -F \quad (6.22)$$

In this equation, the factor  $\sum m_n g \varphi_0$  arising from the sum of equation (6.21) for all modes has been canceled by a factor  $m_0 g \varphi_0$ ; that is, the potential energy change due to gravity alone is zero for a pure pitching motion about the center of gravity.

Equations (6.21) and (6.22) must be put in a form suitable for comparison with the cor-

responding equations for sloshing. For this purpose, it is assumed that the pitching and translational motions are both simple harmonic in time; that is, proportional to, say,  $\cos \omega t$ . Then equation (6.21) can be solved for  $y_n$ ; the results are

$$y_n = -\frac{\ddot{y}_0}{\omega_n^2 - \omega^2} - \left( \frac{h_n + g/\omega^2}{\omega_n^2 - \omega^2} \right) \dot{\varphi}_0 \quad (6.23)$$

and

$$\ddot{y}_n = \frac{\omega^2 \ddot{y}_0}{\omega_n^2 - \omega^2} + \left( \frac{h_n \omega^2 + g}{\omega_n^2 - \omega^2} \right) \ddot{\varphi}_0 \quad (6.24)$$

By using these relations, the total force on the tank can be written as

$$F = -m_T \left\{ 1 + \sum_{n=1}^{\infty} \frac{m_n}{m_T} \left[ \frac{\omega^2 / \omega_n^2}{1 - \omega^2 / \omega_n^2} \right] \right\} \ddot{y}_0 - m_T \ddot{\varphi}_0 \sum_{n=1}^{\infty} \frac{m_n}{m_T} \left[ \frac{h_n \omega^2 / \omega_n^2 + g / \omega_n^2}{1 - \omega^2 / \omega_n^2} \right] \quad (6.25)$$

Now from the results of chapter 2, the actual force due to sloshing is<sup>4</sup>

$$F = -m_T \ddot{y}_0 \left\{ 1 + \sum_{n=1}^{\infty} \frac{(\omega / \omega_n)^2 \tanh 2\xi_n \frac{h}{d}}{\xi_n \frac{h}{d} (\xi_n^2 - 1) [1 - (\omega / \omega_n)^2]} \right\} - m_T \ddot{\varphi}_0 \sum_{n=1}^{\infty} \frac{\tanh 2\xi_n \frac{h}{d}}{\xi_n \frac{h}{d} (\xi_n^2 - 1)} \times \frac{\frac{h}{2} \left( \frac{\omega}{\omega_n} \right)^2 \left[ 1 - \frac{2d}{\xi_n h} \tanh \xi_n \frac{h}{d} \right] + g / \omega_n^2}{1 - \omega^2 / \omega_n^2} \quad (6.26)$$

A direct comparison of equations (6.25) and (6.26) results in the following equations for  $m_n$  and  $h_n$ :

$$\frac{m_n}{m_T} = \frac{\tanh 2\xi_n \frac{h}{d}}{\xi_n \frac{h}{d} (\xi_n^2 - 1)} \quad (6.27)$$

and

$$\frac{h_n}{h} = \left[ \frac{1}{2} - \frac{d}{\xi_n h} \tanh \xi_n \frac{h}{d} \right] \quad (6.28)$$

<sup>4</sup> Terms due to the increase in static fluid pressure with depth have been neglected in the equations developed in this chapter.

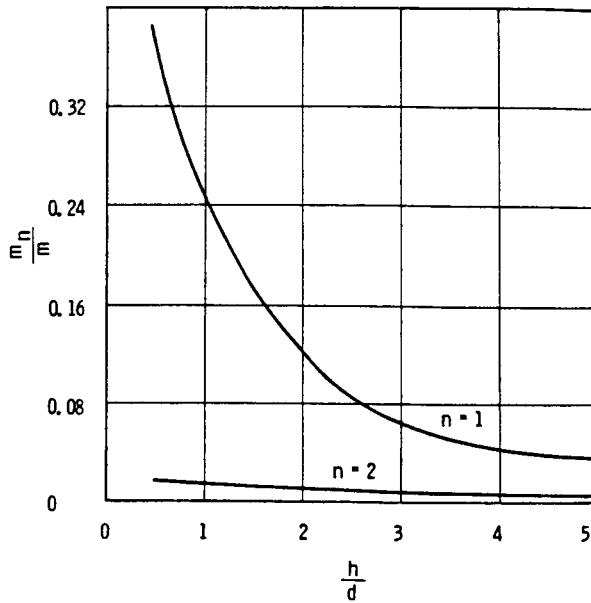


FIGURE 6.12.—Ratio of modal masses to liquid mass for cylindrical tanks (ref. 6.29).

For  $n=1$ , these results are the same as those of the simple model described in section 6.2.

The size of  $m_n$  rapidly decreases for  $n > 1$  because of the term  $\xi_n(\xi_n^2 - 1)$  in the denominator of equation (6.27); this is shown graphically in figure 6.12 which shows  $m_1$  and  $m_2$  in comparison to  $m_T$ , as a function of  $h/d$ . The

value of  $h_n$  for  $n=1$  and 2 is shown in figure 6.13; it can be seen that for small liquid depths, the sloshing mass,  $m_1$ , is below the center of gravity.

The magnitude of  $I_0$  can be determined by writing down the equation for the pitching moment of the mechanical model. It is

$$-M = I_0 \ddot{\varphi}_0 + m_0 h_0^2 \ddot{\varphi}_0 + \sum_{n=1}^{\infty} m_n h_n (\ddot{y}_n + h_n \ddot{\varphi}_0) - g \sum_{n=1}^{\infty} m_n y_n \quad (6.29)$$

The factor  $-g \sum m_n y_n$  arises because of the unbalanced gravity moments when the tank is moved a distance,  $y_0$ , and the masses displaced an additional  $y_n$  at the same time. By substituting equations (6.21) into (6.29), the moment can be expressed as

$$M = -\ddot{\varphi}_0 \left\{ I_0 + m_0 h_0^2 + \sum_{n=1}^{\infty} m_n h_n^2 + m_T \sum_{n=1}^{\infty} \frac{m_n}{m_T} \frac{\frac{2h_n g}{\omega_n^2} + \frac{g^2}{\omega_n^2 \omega_n^2} + h_n^2 \left(\frac{\omega}{\omega_n}\right)^2}{1 - (\omega/\omega_n)^2} - m_T \ddot{y}_0 \sum_{n=1}^{\infty} \frac{m_n}{m_T} \frac{h_n (\omega/\omega_n)^2 + g/\omega_n^2}{1 - (\omega/\omega_n)^2} \right\} \quad (6.30)$$

The actual pitching moment caused by the sloshing (cf. ch. 2) is

$$M = -\ddot{\varphi}_0 \left\{ I_F + m_T \sum_{n=1}^{\infty} \frac{\tanh 2\xi_n \frac{h}{d}}{\xi_n \frac{h}{d} (\xi_n^2 - 1)} \frac{h^2 \omega^2 \left[ 1 - \frac{2d}{\xi_n h} \tanh \xi_n \frac{h}{d} \right]^2}{4\omega_n^2 [1 - (\omega/\omega_n)^2]} + m_T \sum_{n=1}^{\infty} \frac{\tanh 2\xi_n \frac{h}{d}}{\xi_n \frac{h}{d} (\xi_n^2 - 1)} \frac{(g/\omega)^2 + gh \left[ 1 - \frac{2d}{\xi_n h} \tanh \xi_n \frac{h}{d} \right]}{\omega_n^2 [1 - (\omega/\omega_n)^2]} - m_T \ddot{y}_0 \sum_{n=1}^{\infty} \frac{\tanh 2\xi_n \frac{h}{d}}{\xi_n \frac{h}{d} (\xi_n^2 - 1)} \frac{g/\omega_n^2 + \frac{1}{2} h(\omega/\omega_n)^2 \left[ 1 - \frac{2d}{\xi_n h} \tanh \xi_n \frac{h}{d} \right]}{1 - (\omega/\omega_n)^2} \right\} \quad (6.31)$$

where

$$I_F = m_T d^2 \left\{ \frac{1}{12} \left(\frac{h}{d}\right)^2 + \frac{1}{16} - 2 \sum_{n=1}^{\infty} \frac{1 - \frac{d}{\xi_n h} \tanh \xi_n \frac{h}{d}}{\xi_n^2 (\xi_n^2 - 1)} \right\} \quad (6.32)$$

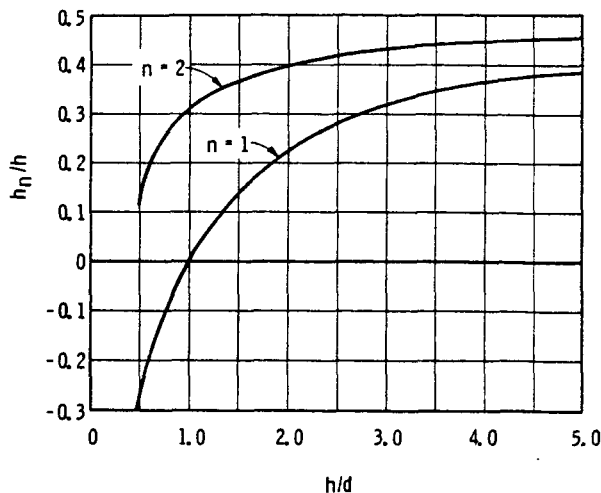


FIGURE 6.13.—Location and magnitude of modal masses for cylindrical tanks (ref. 6.29).

A direct comparison of equations (6.30) and (6.31) gives the same expressions for  $m_n$  and  $h_n$  as before, and in addition it shows that

$$I_0 + m_0 h_0^2 + \sum_{n=1}^{\infty} m_n h_n^2 = I_F \quad (6.33)$$

Now  $m_T d^2 \left[ \frac{1}{12} (h/d)^2 + \frac{1}{16} \right]$  in equation (6.32) is the moment of inertia of a solidified mass of liquid equal in weight to the actual weight of liquid. Hence  $I_F$  is the actual moment of inertia of the inviscid fluid about its center of gravity. A plot of this moment of inertia in terms of the moment of inertia of the solidified liquid is shown in figure 6.14. As can be seen, the moment of inertia of the liquid can be quite small in comparison to  $m_T d^2 \left[ \frac{1}{12} \left( \frac{h}{d} \right)^2 + \frac{1}{16} \right]$ , because not all of the liquid participates in a pitching motion of the tank about the liquid center of gravity; part of it is completely at rest, or nearly so.

The foregoing mechanical model is a nearly exact duplication (it is exact for linear motions of an inviscid fluid) of fuel sloshing in a cylindrical tank as long as the excitation frequency is not almost equal to one of the natural frequencies of sloshing. If this is the case, then damping devices must be added to the model so that the force and moment response do not become infinitely large for  $\omega \rightarrow \omega_n$ . Thus, ex-

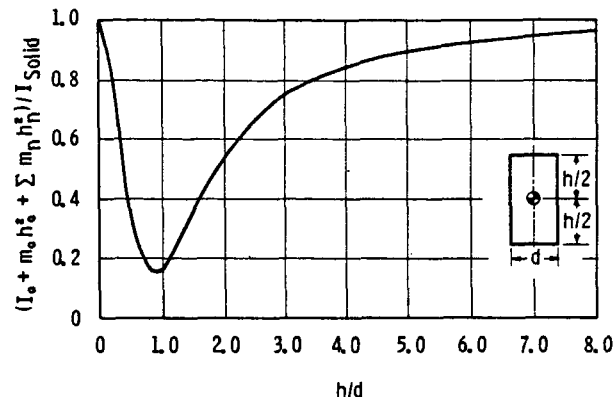


FIGURE 6.14.—Ratio of effective liquid to rigid liquid moment of inertia for cylindrical tanks (ref. 6.26).

perimental proof of the model's validity will necessarily be delayed until section 6.4, when damping is introduced (refs. 6.25, 6.30, and 6.33). For convenience the formulae for the various parameters are collected in table 6.4.

TABLE 6.4.—Model Parameters for Cylindrical Tank

[See ch. 2, table 2.4, for values of  $\xi_n$ ;  $m_T = \frac{1}{4} \pi \rho d^2 h$ ]

$$K_n = m_T \left( \frac{2g}{h(\xi_n^2 - 1)} \right) \left( \tanh 2\xi_n \frac{h}{d} \right)^2$$

$$m_n = m_T \left( \frac{d}{\xi_n h(\xi_n^2 - 1)} \right) \tanh 2\xi_n \frac{h}{d}$$

$$m_0 = m_T - \sum_{n=1}^{\infty} m_n$$

$$h_n = \frac{h}{2} - \frac{d}{\xi_n} \tanh \xi_n \frac{h}{d}$$

$$h_0 = \frac{1}{m_0} \sum_{n=1}^{\infty} m_n h_n$$

$$I_L + m_0 h_0^2 + \sum_{n=1}^{\infty} m_n h_n^2 = \text{fig. 6.14}$$

A limited number of results for other types of cylindrical tanks, such as annular cross-section and quarter-section geometries, are available in scattered references; see especially references 6.27 through 6.32.

#### Rectangular Tank (refs. 6.12 and 6.13)

The parameters of an equivalent mechanical model for fuel sloshing in a rectangular tank

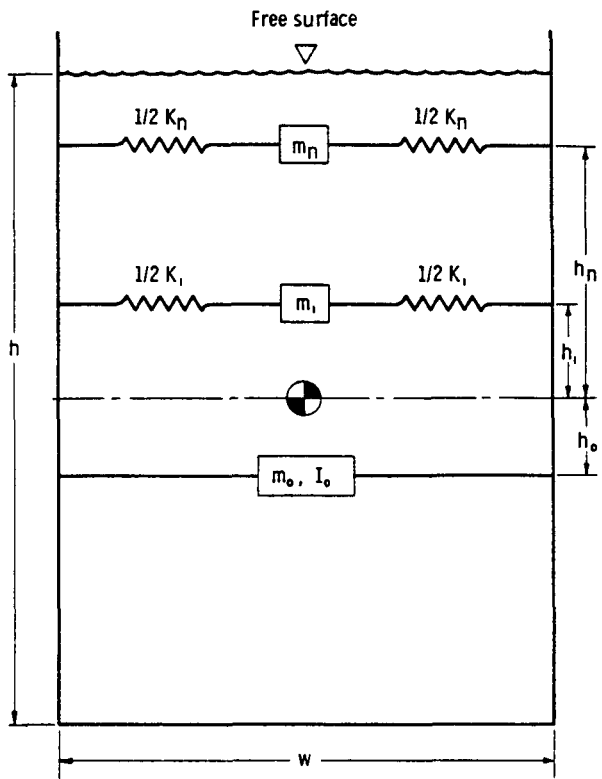


FIGURE 6.15.—Complex mechanical models for rectangular tanks.

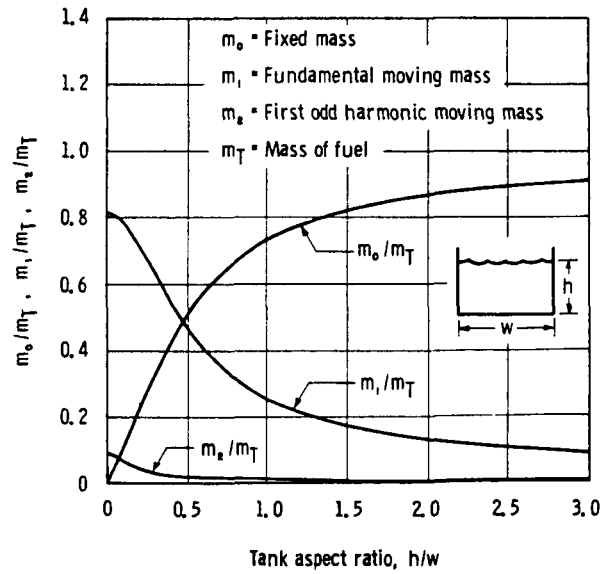


FIGURE 6.16.—Ratio of sloshing masses to fuel mass versus tank aspect ratio for rectangular tanks (ref. 6.13).

may be determined in a manner similar to that used for cylindrical tanks. A model employing spring masses is shown in figure 6.15. The

motion is supposed to be in the plane of the figure, but a similar model is valid for motion at right angles to this plane. The formulae for the various parameters are given in table 6.5 and shown graphically in figures 6.16 through 6.18.

TABLE 6.5.—Model Parameters for Rectangular Tank

[ $m_T = \rho wh$  = fluid mass per unit width]

$$K_n = m_T \left( \frac{4g}{\pi^2 w} \right) \left( \tanh (2n-1)\pi \frac{h}{w} \right)^2$$

$$m_n = m_T \left( \frac{8w}{\pi^2 (2n-1)h} \right) \tanh (2n-1)\pi \frac{h}{w}$$

$$m_0 = m_T - \sum_{n=1}^{\infty} m_n$$

$$h_n = \frac{h}{2} - \frac{2w}{(2n-1)\pi} \tanh (2n-1)\pi \frac{h}{2w}$$

$$h_0 = \frac{1}{m_0} \sum_{n=1}^{\infty} m_n h_n$$

$$I_0 + m_0 h_0^2 + \sum_{n=1}^{\infty} m_n h_n^2 = \text{fig. 6.18}$$

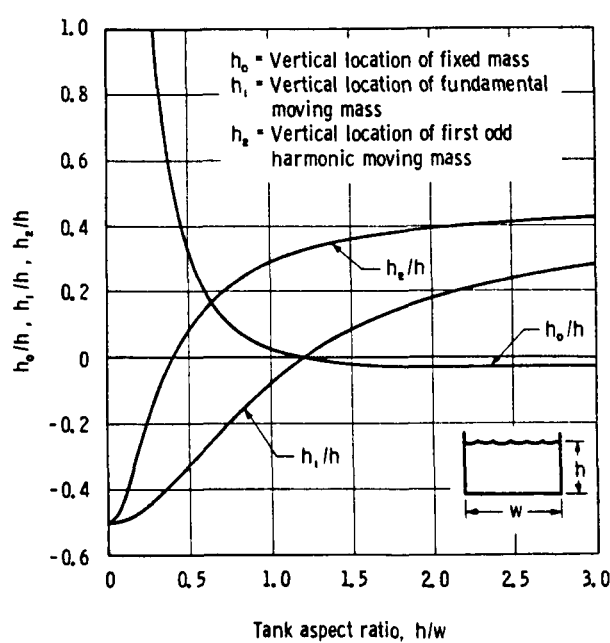


FIGURE 6.17.—Ratios of location of sloshing masses to liquid depth versus tank aspect ratio for rectangular tanks (ref. 6.13).

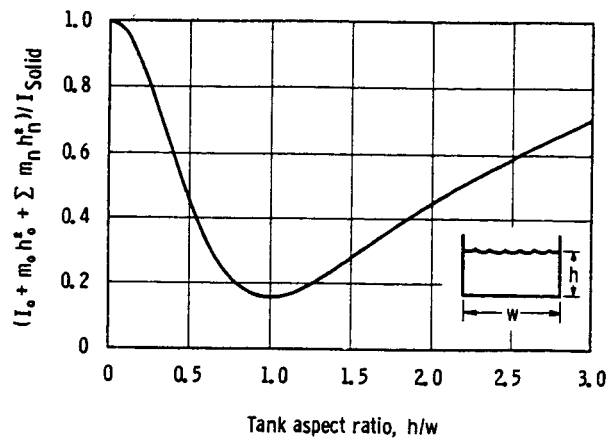


FIGURE 6.18.—Ratio of effective liquid to rigid liquid moment of inertia for rectangular tanks (ref. 6.13).

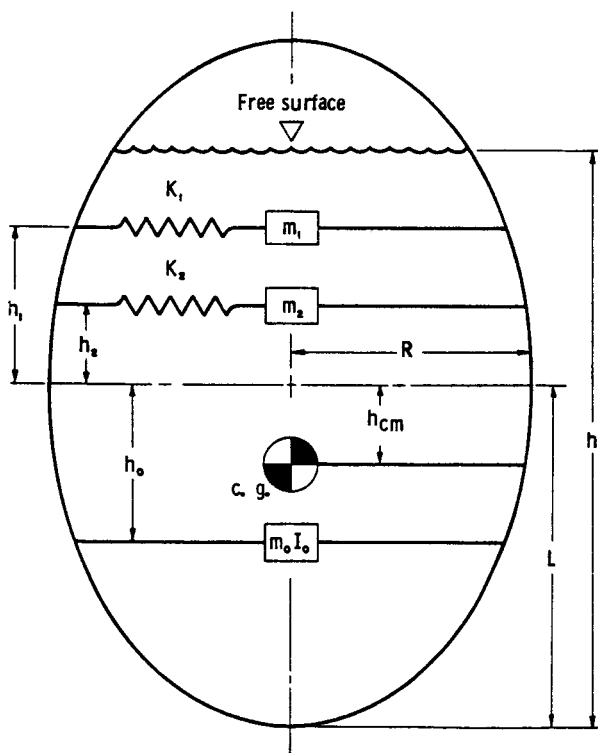


FIGURE 6.19.—Equivalent mechanical model for ellipsoidal tank (ref. 6.34).

#### Axisymmetric Ellipsoidal Tanks (Ref. 6.34)

Sloshing in a rigid axisymmetric ellipsoidal tank is represented by the mechanical model shown in figure 6.19. The magnitudes of the various model parameters were determined by

Rayleigh-Ritz methods. Since some of the resulting equations are too lengthy to be reproduced in a convenient form, these results are given here only graphically; for example, figure 6.20 shows the variation of liquid natural frequency,  $\omega_n$ , in the form of the dimensionless parameter,  $\lambda_n = \omega_n^2 R/g$ , as functions of the liquid depth ratio,  $h/L$ , and height-to-width ratio,  $a = L/R$  ( $a = 1.0$  corresponds to a spherical shape). Likewise, the size of the first two sloshing masses is shown in figure 6.21; the magnitude of the fixed mass is equal to  $m_0 - \sum m_n$ .

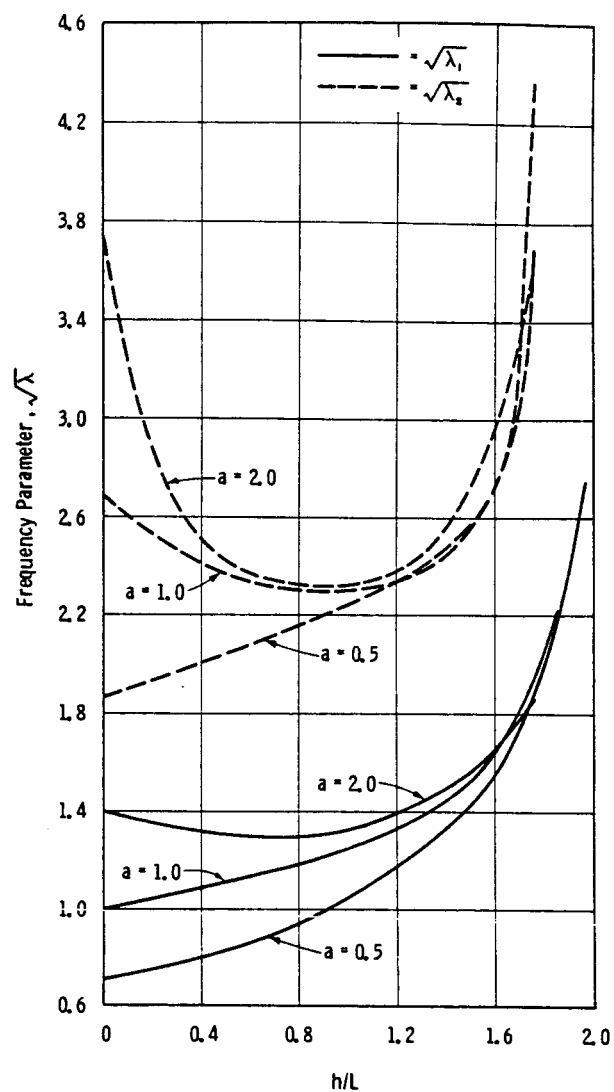


FIGURE 6.20.—Variation of sloshing frequencies with liquid depth for ellipsoidal tanks (ref. 6.34).

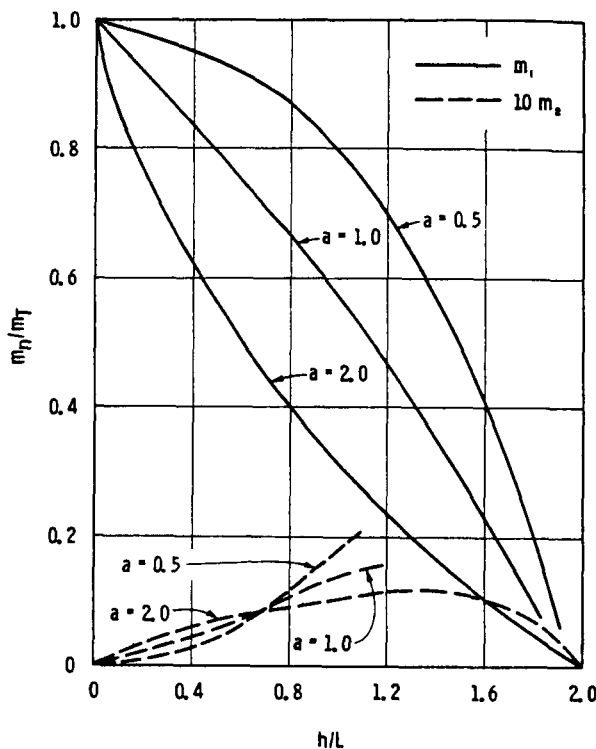


FIGURE 6.21.—Variation of modal masses with liquid depth for ellipsoidal tanks (ref. 6.34).

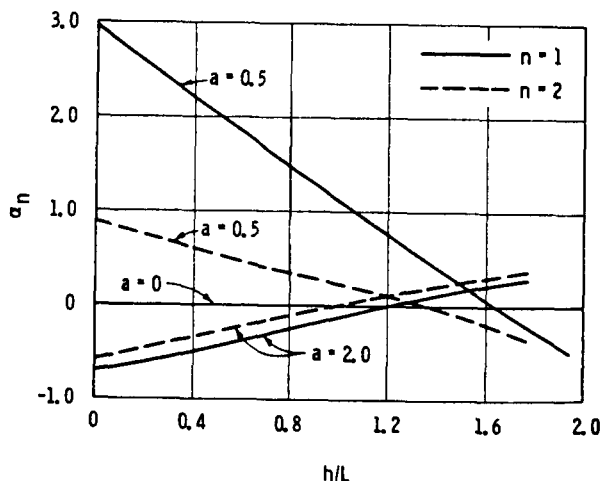


FIGURE 6.22.—Parameter  $\alpha_n$  for slosh mass location versus liquid depth for ellipsoidal tanks (ref. 6.34).

The location of the oscillating masses,  $h_n$ , above the geometric center of the tank, can be obtained from

$$h_n = L\alpha_n - \frac{g}{\omega_n^2} \quad (6.34)$$

where  $\alpha_n$  is given in figure 6.22 for  $n=1$  and 2. The location of the fixed mass may be computed from<sup>5</sup>

$$h_0 = h_{cg} + \frac{1}{m_0} \sum_{n=1}^{\infty} (h_n + h_{cg}) m_n \quad (6.35)$$

where the center of gravity location in reference to the geometric center of the tank is

$$h_{cg} = \frac{3L}{4} \left[ \frac{(2-h/L)^2}{3-h/L} \right] \quad (6.36)$$

Exact methods of calculating the moment of inertia of the liquid are extremely laborious, but an approximate method has been described in reference 6.34. The centroidal moment of inertia of a rigid body having the same shape and mass as the liquid is

$$I_{rigid} = \pi \rho R^4 L \left\{ \frac{h^4}{R^2 L^2} \left[ \frac{5-h/L}{30} - \frac{(4-h/L)^2}{48(3-h/L)} \right] + \frac{h^3}{L^3} \left[ \frac{1}{3} - \frac{h}{4L} + \frac{h^2}{20L^2} \right] \right\} \quad (6.37)$$

Since the fluid is not rigid, equation (6.37) overestimates the moment of inertia of the fluid. The proposed method to obtain the actual moment of inertia is to determine the ratio of the actual liquid to rigid liquid moment of inertia for a cylindrical tank having an identical fluid height and fluid mass, say from figure 6.14. Then this same ratio is assumed to hold for the ellipsoidal tank; that is

$$I_0 + m_0(h_0 - h_{cg})^2 + \sum m_n(h_n + h_{cg})^2 = x I_{rigid} \quad (6.38)$$

where  $x$  is the ratio (a pure number) obtained from figure 6.14. Note that this approximate method introduces an error only in  $I_0$ ; thus, the moment due to pitching will not be greatly influenced by the errors involved in the approximate procedure.

### Spherical Tanks

There are no readily available treatments of complete mechanical models for spherical tanks. The general study of reference 6.15 contains an analysis of such a model, but it contains no

<sup>5</sup> This is not the method proposed in ref. 6.34; however, it is a valid method, since it leaves the center of gravity of the liquid unchanged.

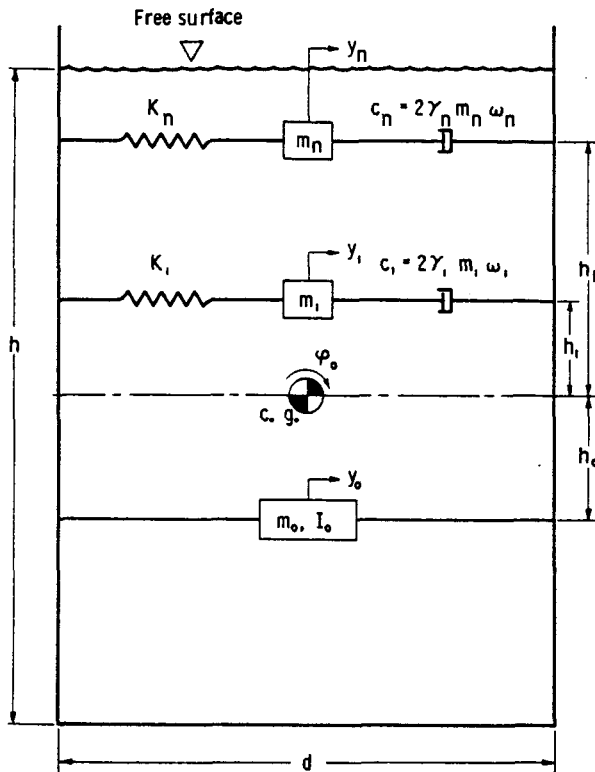


FIGURE 6.23.—Equivalent mechanical model with damping included.

numerical values or charts giving the size of the inertial parameters. Of course, the mechanical model for ellipsoidal tanks (ref. 6.34) for the case of a height-to-width ratio,  $a=1.0$ , corresponds to spherical tanks so these results may be used, provided it is recalled that the total moment of inertia of the model is effectively zero for such a tank.

#### Conical Tanks

There are no analyses of complete models for conical tanks; the only available model is the single sloshing mass model of a  $45^\circ$  conical tank described in section 6.2.

Lomen (ref. 6.35) has presented a generalized analysis in which the equations of motion for a tank of arbitrary shape are developed. The equations include six degrees of freedom, and the parameters from the hydrodynamic solution are matched with the parameters of both an equivalent pendulum system and an equivalent spring-mass system. Digital procedures for evaluating the parameters of the mechanical models are given in reference 6.36.

It should be remembered that all of the preceding models are for ideal liquids with no energy dissipation. The models yield good results as long as the excitation frequency is not too close to any liquid resonance. Near resonance, the sloshing forces and moments are limited solely by the energy dissipation so that damping mechanisms must necessarily be included in a valid model. This subject is treated in the next section.

#### 6.4 INTRODUCTION OF DAMPING EFFECTS

Except for liquid helium at temperatures close to absolute zero, all fluids exhibit a certain amount of resistance to motion; that is, they are viscous. Consequently, because of viscous friction, a small portion of the energy of a sloshing liquid is dissipated during each cycle of the motion, and energy must be supplied to the fluid to maintain a constant slosh amplitude. However, even considering the energy dissipation due to free surface effects, the total dissipation or damping is so small in a clean tank (unbaffled with smooth walls) that practically no limit is placed on the slosh amplitude at resonance. Thus, the damping is usually increased artificially by introducing baffles or other flow obstructions in the tank, as discussed in chapter 3. Although the damping in such cases may still be quite small, an equivalent mechanical model must account for it through some sort of energy dissipation mechanism.

The exact form of the damping of a sloshing liquid in a moving tank is extremely difficult to determine, but, because the damping is small, it seems reasonable to assume that it can be represented adequately by equivalent linear viscous damping. The damping coefficient is then determined experimentally, or obtained from the extensive data presented in chapter 4. Figure 6.23 shows one proposed model for sloshing in a cylindrical tank in which this type of damping has been included (ref. 6.25).

The equation of motion for the  $n$ th sloshing mass is now

$$m_n(\ddot{y}_n + \dot{y}_n + h_n \ddot{\varphi}_0) + 2\gamma_n m_n \omega_n \dot{y}_n + K_n y_n - mg\varphi = 0 \quad (6.39)$$

The force exerted on the tank by the  $n$ th mass is  $-K_n y_n - c_n \dot{y}_n$ , so that the total lateral reaction force can be expressed exactly as before

$$-F = m_0(\ddot{y}_0 - h_0 \ddot{\varphi}_0) + \sum_{n=1}^{\infty} m_n(\ddot{y}_n + \ddot{y}_0 + h_n \varphi_0) \quad (6.40)$$

Then by carrying through the analysis as before, one finds that

$$F = -m_T \ddot{y}_0 \left[ 1 + \sum_{n=1}^{\infty} \frac{m_n}{m_T} \frac{(\omega/\omega_n)^2}{1 - (\omega/\omega_n)^2 + 2i\gamma_n \omega/\omega_n} \right] - m_T \ddot{\varphi}_0 \sum_{n=1}^{\infty} \frac{m_n}{m_T} \frac{h_n(\omega/\omega_n)^2 + g/\omega_n^2}{1 - (\omega/\omega_n)^2 + 2i\gamma_n \omega/\omega_n} \quad (6.41)$$

where  $y_0$  and  $\varphi_0$  are both of the form  $e^{i\omega t}$ . It is now assumed that  $m_n$  and  $h_n$  are the same for the damped liquid as they were for the undamped liquid. This leaves only  $\gamma_n$  to be evaluated, and this must be done experimentally. It should be noted that the same  $\gamma_n$  is used in both the translational part of the force and the pitching part, but this assumption has been verified experimentally (ref. 6.25).

Figure 6.24 shows a typical plot of an experimentally determined damping factor. Using this damping factor, the calculated force using only the first two sloshing masses is shown and compared to actual slosh forces in figure 6.25; the phase angle of the force with respect to the displacement is also shown.

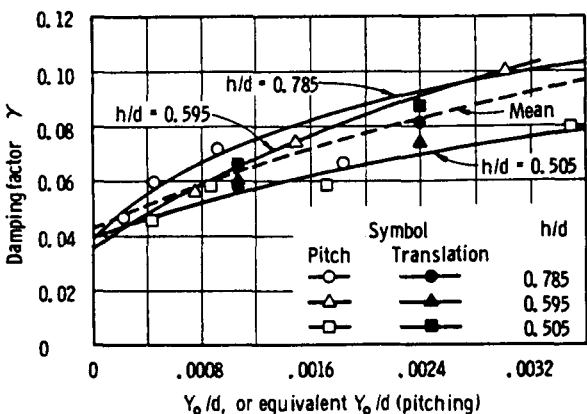


FIGURE 6.24.—Comparison of damping factors in pitching and translation in a cylindrical tank with conical-ring baffles (ref. 6.25).

For these calculations, it was assumed that  $\gamma_1 = \gamma_2 = \gamma$  from figure 6.24. Since the correlation is very good, one can conclude that the mechanical model adequately duplicates the sloshing forces.

It can be seen from equation (6.41) that for very large damping, the slosh force predicted by the model is equal to

$$F = -m_T \ddot{y}_0 \quad (6.42)$$

That is, the free surface motion is damped out entirely, and the fluid behaves as a rigid body; this is the expected result for a very viscous liquid.

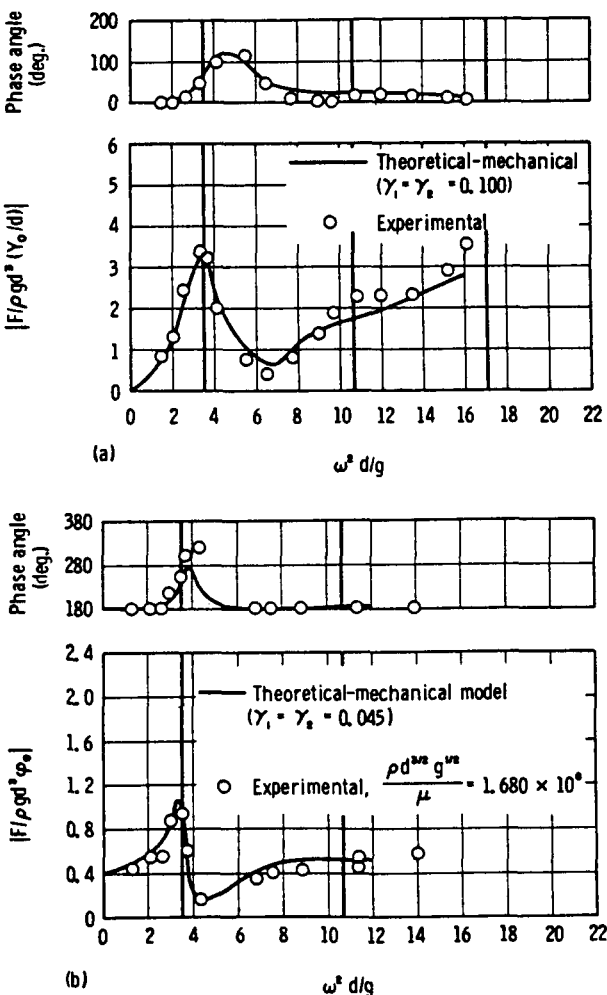


FIGURE 6.25.—Comparison of measured and calculated force response in a cylindrical tank with conical-ring baffles (ref. 6.25). (a) Translation force response; (b) pitching force response.

By following the same procedure as before, the pitching moment can be written for this model as

$$M = -\ddot{\varphi}_0 \left\{ I_0 + m_0 h_0^2 + \sum_{n=1}^{\infty} m_n h_n^2 + m_T \sum_{n=1}^{\infty} \frac{m_n}{m_T} \frac{\left(\frac{h_n \omega}{\omega_n}\right)^2 + \left(\frac{g \omega_n}{\omega}\right)^2 / \omega_n^4 + 2gh_n/\omega_n^2}{1 - (\omega/\omega_n)^2 + 2i\gamma_n \omega/\omega_n} \right\} - m_T \ddot{y}_0 \sum_{n=1}^{\infty} \frac{m_n}{m_T} \frac{h_n (\omega/\omega_n)^2 + g/\omega_n^2}{1 - (\omega/\omega_n)^2 + 2i\gamma_n \omega/\omega_n} \quad (6.43)$$

As  $\gamma_n \rightarrow \infty$  in this equation, the moment reduces to

$$M = -\ddot{\varphi}_0 \left\{ I_0 + m_0 h_0^2 + \sum_{n=1}^{\infty} m_n h_n^2 \right\} \quad (6.44)$$

But from equations (6.31) and (6.33), this is the same as the moment due to an ideal inviscid liquid in a capped container. However, it seems that the moment should be the same as that of an equal mass of rigid fluid, since the fluid's resistance to shearing motion has theoretically approached infinity. In other words,  $I_0$  should be modified somehow to account for the damping. This is a relatively minor point, since the damping is actually quite small (not infinite) and, furthermore, the moment about the center of gravity usually contributes only slightly to the total moment when the center of rotation is more than 1 diameter from the center of gravity of the liquid. But to be complete, the model is now modified so that it approaches the right asymptotic limit.

The proposed modification, shown in figure 6.26, was originally developed by Bauer (refs. 6.29 and 6.30). As before,  $y_0$  is the tank displacement and  $\varphi_0$  the pitching angle about the center of gravity. A weightless disk with moment of inertia  $I_d$  is attached at the center of gravity by means of the dashpot arrangement as shown. The angle of rotation of the disk relative to the tank is  $\psi$ . The force response of this model is the same as that of the one shown in figure 6.23, since the disk is weightless.

It is now specified that the moment of inertia of a rigid body of fluid equal in mass and shape to the actual fluid is<sup>6</sup>

$$I_{\text{rigid}} = I_d + I'_0 + m_0 h_0^2 + \sum_{n=1}^{\infty} m_n h_n^2 \quad (6.45)$$

The pitching moment acting on the tank is now

$$-M = \ddot{\varphi}_0 \left\{ I'_0 + m_0 h_0^2 + \sum_{n=1}^{\infty} m_n h_n^2 \right\} + I_d(\ddot{\varphi}_0 + \ddot{\psi}) + \sum_{n=1}^{\infty} m_n h_n \ddot{y}_n - g \sum_{n=1}^{\infty} m_n y_n \quad (6.46)$$

and the equation of motion of the disk is

$$I_d(\ddot{\varphi}_0 + \ddot{\psi}) + c_d \dot{\psi} = 0 \quad (6.47)$$

Now by assuming  $y_0$ ,  $y_n$ ,  $\varphi_0$ , and  $\psi$  all vary as  $e^{i\omega t}$ , equations (6.39), (6.45), (6.46), and (6.47) can be combined to yield

$$M = -\ddot{\varphi}_0 \left\{ I_{\text{rigid}} - I_d \left( \frac{\omega^2 I_d^2}{\omega^2 I_d^2 + c_d^2} \right) + m_T \sum_{n=1}^{\infty} \frac{\frac{2gh_n}{\omega_n^2} + \left( \frac{g}{\omega/\omega_n} \right)^2 + \left( h_n \frac{\omega}{\omega_n} \right)^2}{1 - (\omega/\omega_n)^2 + 2i\gamma_n \omega/\omega_n} \right\} - c_d \left( \frac{\omega^2 I_d^2}{\omega^2 I_d^2 + c_d^2} \right) \dot{\varphi}_0 - m_T \sum_{n=1}^{\infty} \frac{\left( h_n \frac{\omega}{\omega_n} \right)^2 + g/\omega_n^2}{1 - (\omega/\omega_n)^2 + 2i\gamma_n \omega/\omega_n} \quad (6.48)$$

where  $I_{\text{rigid}}$  is defined in equation (6.45); it is also

$$I_{\text{rigid}} = m_T d^2 \left[ \frac{1}{12} \left( \frac{h}{d} \right)^2 + \frac{1}{16} \right] \quad (6.49)$$

The effective decrease in the moment of inertia because the fluid is not actually rigid is then

$$I_d \left( \frac{\omega^2 I_d^2}{\omega^2 I_d^2 + c_d^2} \right)$$

Thus, as the damping goes to infinity, the moment of inertia of the liquid approaches the

<sup>6</sup>  $I'_0$  is not necessarily equal to the previous  $I_0$ .

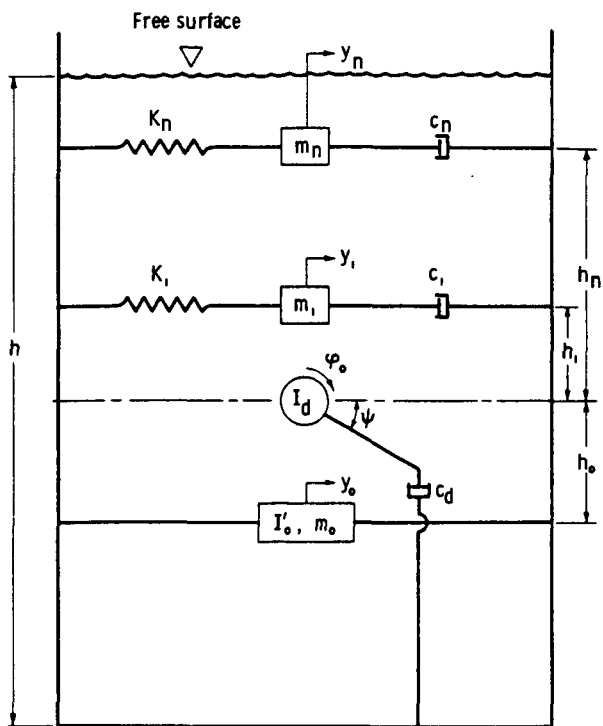


FIGURE 6.26.—Equivalent mechanical model with moment of inertia damping.

value of a similar rigid body, as it should; that is,

$$I_d \left( \frac{\omega^2 I_d^2}{\omega^2 I_d^2 + c_d^2} \right) \rightarrow 0 \text{ as } c_d \rightarrow \infty$$

For zero damping, the moment of inertia of the fluid is

$$I_F = I_{\text{rigid}} - I_d \quad (6.50)$$

and  $I_F$  is given in figure 6.14. Thus, the value of  $I_d$  may be computed. The value of  $c_d$  must be determined experimentally; it is approximately equal to the damping of the liquid when it completely fills a closed tank pitching about the center of gravity of the liquid.  $c_d$  and  $I_d$  have been determined in this way in the tests reported in reference 6.33. The results show that even in a tank with baffles distributed throughout the liquid depth, the coupling of the disk  $I_d$  to the tank is so small as to be negligible (i.e.,  $c_d \approx 0$ ). Thus the inertia of the disk does not enter in any of the calculations. Taking this into account in equations (6.45) and (6.50) shows that

$$I_F = I'_0 + m_0 h_0^2 + \sum_{n=1}^{\infty} m_n h_n^2 \quad (6.51)$$

Consequently, the model shown in figure 6.26 has no real advantage over the one shown in figure 6.23. It should be pointed out, however, that the results given in reference 6.33 show that  $I_F$  for a baffled tank is significantly larger than  $I_F$  in an unbaffled tank; this is caused primarily by the additional liquid motion near the baffles and not by the small increase in damping.

A study of mechanical model representation of force response in a baffled spherical tank has been given in reference 6.15, as indicated previously. (For descriptions and discussions of the baffle configurations, see ch. 4 (fig. 4.17).) Figure 6.27 compares measured and calculated force response curves in a spherical tank with vertical baffles (data are also shown for the horizontal baffle configuration). Two values of damping coefficient (the larger of which corresponds to measured data) were employed in the mechanical model calculations for the half-full tank and one for the three-quarter-full tank. The agreement is not nearly so good as that obtained in the cylindrical tank, no doubt as a result of the strong nonlinear effects present in spherical tanks.

The mechanical models for other types of tanks can be modified in a similar way to include damping. Likewise, the simple, one sloshing mass models presented in section 6.2 may also be modified by including an appropriate damping factor; in this way, they can be made to give a very good approximation to sloshing in the fundamental mode (refs. 6.5, 6.10, and 6.11).

## 6.5 MECHANICAL MODELS FOR TANKS WITH FLEXIBLE WALLS

All of the mechanical models described so far have been for rigid tanks. When tank elasticity is included, the problem of determining an equivalent model is greatly complicated because of the coupling between wall motion and fluid motion. (See ch. 9.) Certain exact solutions to the flexible-wall problem exist in the literature, but their application is by no

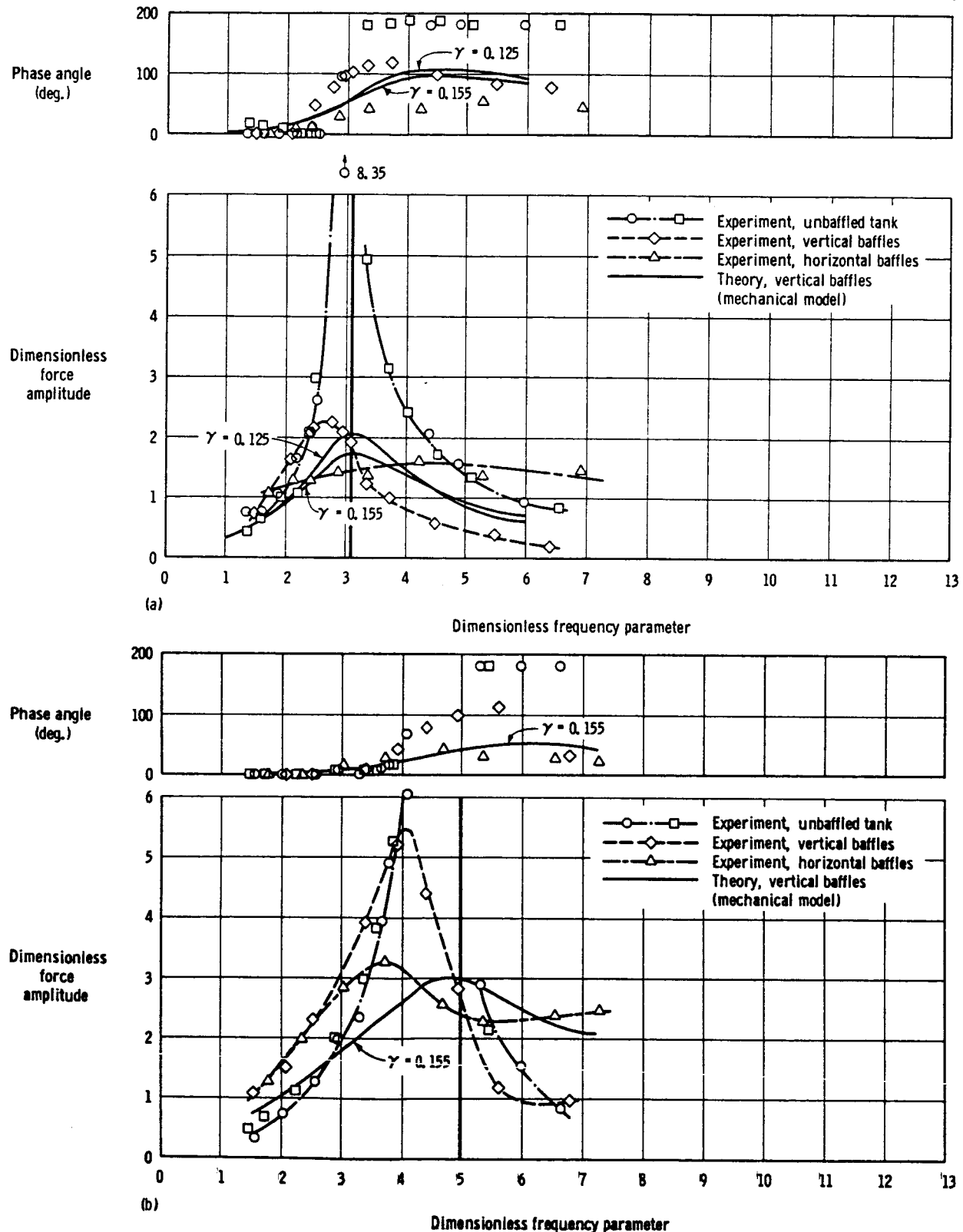


FIGURE 6.27.—Comparison of measured and calculated force response in a spherical tank with vertically oriented baffles (ref. 6.15). (a) Half-full tank; (b) three-quarter-full tank.

means direct. Hence, it appears to be reasonable to try to adapt the rigid-wall models to the flexible-wall problem in an approximate fashion. This can be accomplished by the method outlined by Lukens, Schmitt, and Broucek (ref. 6.4).

At low liquid levels, some of the mechanical elements in the rigid-wall models are located above the liquid surface. (See, for example,  $l_1$  in table 6.1 for small  $h/d$ .) This presents no problem so long as the walls are rigid, but if the force distribution on a flexible wall is to be calculated more accurately, the forces due to the mechanical elements should act at the correct location. In the flexible-wall analogy, the pitching moment caused by the sloshing is broken up into two components: one due to the pressure distribution on the walls and one due to the pressure distribution on the tank bottom. A pure couple is applied at the tank bottom to simulate the pressure distribution on the bottom. Thus, the pitching moment which the mechanical elements actually should simulate is reduced to its correct value, and the spring masses or pendulums and rigid mass are lowered from their rigid wall locations. Such a mechanical model is shown in figure 6.28; only one sloshing mass is shown, but the same method could be used with a complete set of sloshing masses. Furthermore, the damping is not included for reasons of simplicity. The bottom couple,  $M_B$ , acts as shown.

Carrying out the details of the analysis gives the model parameters shown in table 6.6. The bottom couple,  $M_B$ , is specified in terms of the displacement of  $m_1$  relative to the tank walls,  $y_1$ , but since this term usually enters only in a stability analysis, where Laplace transforms are customarily employed anyway, it should present no unusual difficulties. The parameters are also shown graphically in figures 6.29 and 6.30.

By examining the actual sloshing force and moment equations (or experimental results) and breaking the moment into two parts as discussed above, flexible-wall models for other kinds of tanks can be derived. However, such models should be viewed only as first approximations to the actual sloshing in flexible tanks, and not as being exact duplications of these processes.

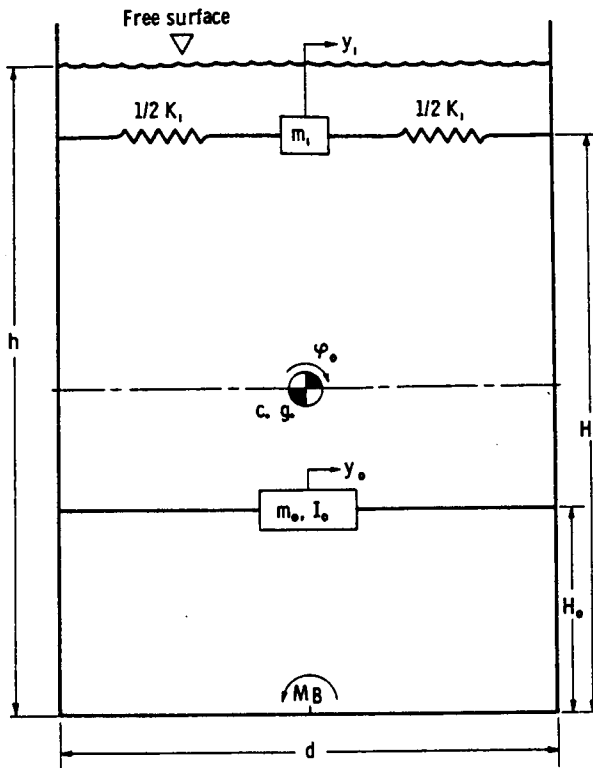


FIGURE 6.28.—Equivalent mechanical model for cylindrical tank with flexible walls.

TABLE 6.6.—*Model Parameters for Flexible-Wall Cylindrical Tank*

$$[m_T = \frac{1}{4}\pi\rho d^2 h]$$

$$K_1 = m_T \left( \frac{g}{1.19h} \right) \left( \tanh 3.68 \frac{h}{d} \right)^2$$

$$m_1 = m_T \left( \frac{d}{4.4h} \right) \tanh 3.68 \frac{h}{d}$$

$$m_0 = m_T - m_1$$

$$H_1 = \frac{d}{3.68} \left[ \frac{1 + 3.68 \frac{h}{d} \sinh 3.68 \frac{h}{d} - \cosh 3.68 \frac{h}{d}}{\sinh 3.68 \frac{h}{d}} \right]$$

$$H_0 = \frac{1}{m_0} \left( \frac{h}{2} m_T - H_1 m_1 \right)$$

$$I_0 = \text{fig. 6.31}$$

$$M_B = m \left[ g y_1 + \frac{1}{12.46} \left( \frac{d^2}{h \cosh 3.68 \frac{h}{d}} \right) \ddot{y}_1 \right]$$

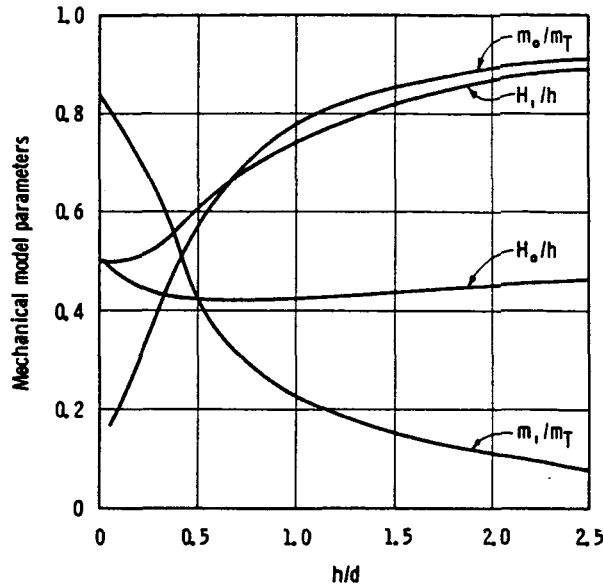


FIGURE 6.29.—Parameters for spring mass elements for flexible tank (ref. 6.4).

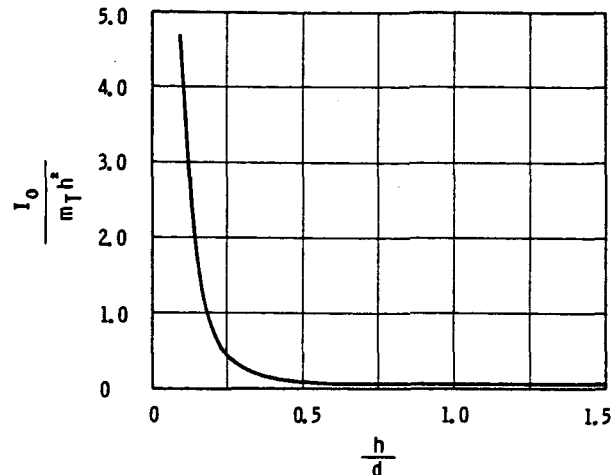


FIGURE 6.30.—Moment of inertia of rigid mass for flexible tank (ref. 6.4).

#### REFERENCES

- 6.1. ZHUKOSKII, N. E.: On the Motion of a Rigid Body Having Cavities Filled With a Homogeneous Liquid. Collected Works (in Russian). Vol. 3. Moscow, 1936.
- 6.2. RUMYANTSEV, V. V.: Stability of Motion of Solid Bodies With Liquid Filled Cavities by Lyapunov's Methods. Advances in Applied Mechanics, vol. 8. Academic Press, 1964.
- 6.3. OKHOTSIMSKII, D. E.: Theory of the Motion of a Body With Cavities Partially Filled With a Liquid. NASA TT F-33, 1960.
- 6.4. LUKENS, D. R.; SCHMITT, A. F.; AND BROUCEK, G. T.: Approximate Transfer Functions for Flexible-Booster-and-Autopilot Analysis. Convair Rept. No. AE 61-0198, Contract No. AF 33(616)-7037, Apr. 1961. (Also issued as WADD TR-61-93.)
- 6.5. SUMNER, I. E.; STOFAN, A. J.; AND SHRAMO, D. J.: Experimental Sloshing Characteristics and a Mechanical Analogy of Liquid Sloshing in a Scale-Model Centaur Liquid Oxygen Tank. NASA TM X-999, 1964.
- 6.6. ARMSTRONG, G. L.; AND KACHIGAN, K.: Propellant Sloshing. Sections 14.14/15, Handbook of Astronautical Engineering (H. H. Koelle, ed.), McGraw-Hill Book Co., 1961.
- 6.7. KACHIGAN, K.: Forced Oscillations of a Fluid in a Cylindrical Tank. Convair Rept. No. ZU-7-046, Oct. 1955.
- 6.8. SCHMITT, A. F.: Forced Oscillations of a Fluid in a Cylindrical Tank Undergoing Both Translation and Rotation. Convair Rept. No. ZU-7-069, Oct. 1956.
- 6.9. SCHMITT, A. F.: Forced Oscillations of a Fluid in a Cylindrical Tank Oscillating in a Carried Acceleration Field—A Correction. Convair Rept. ZU-7-074, Feb. 1957.
- 6.10. WARNER, R. W.; AND CALDWELL, J. T.: Experimental Evaluation of Analytical Models for the Inertia and Natural Frequencies of Fuel Sloshing in Circular Cylindrical Tanks. NASA TN D-856, 1961.
- 6.11. STEPHENS, D. G.; AND LEONARD, H. W.: The Coupled Dynamic Response of a Tank Partially Filled With a Liquid and Undergoing Free and Forced Planar Oscillations. NASA TN D-1945, 1963.
- 6.12. GRAHAM, E. W.; AND RODRIGUEZ, A. M.: The Characteristics of Fuel Motion Which Affect Airplane Dynamics. Douglas Aircraft Co. Rept. No. SM-14212, Nov. 1951.
- 6.13. GRAHAM, E. W.; AND RODRIGUEZ, A. M.: The Characteristics of Fuel Motion Which Affect Airplane Dynamics. Trans. of ASME, Series E, J. Appl. Mech., vol. 19, no. 3, Sept. 1952, pp. 381-388.
- 6.14. HOUSNER, G. W.: Dynamic Pressures on Accelerated Fluid Containers. Bulletin of the Seismological Society of America, vol. 47, Jan. 1957, pp. 15-35.
- 6.15. ABRAMSON, H. N.; CHU, W. H.; AND GARZA, L. R.: Liquid Sloshing in Spherical Tanks. Southwest Research Institute, TR no. 2, Contract no. NAS8-1555, Mar. 1962.

- 6.16. SCHY, A. A.: A Theoretical Analysis of the Effects of Fuel Motion on Airplane Dynamics. NACA TN 2280, 1951.
- 6.17. SUMNER, I. E.: Experimentally Determined Pendulum Analogy of Liquid Sloshing in Spherical and Oblate-Spheroidal Tanks. NASA TN D-2737, 1965.
- 6.18. HARPER, J.: Propellant Sloshing in a Conical Tank Undergoing Arbitrary Forced Translational Motion. Convair Rept. ZU-7-089-TN, Jan. 1958.
- 6.19. FREED, L. E.: Stability of Motion of Conical Pendulums. Ramo-Wooldridge Co. Rept. GM-45, 3-434, Oct. 1957.
- 6.20. MILES, J. W.: Stability of Forced Oscillations of a Spherical Pendulum. Quart. Appl. Math., vol. 20, no. 1, Apr. 1962, pp. 21-32.
- 6.21. HOWELL, J. V.: Motion of Conical Pendulum. Ramo-Wooldridge Co. Rept. GM 42.4-4, Nov. 1957.
- 6.22. BERLOT, R. R.: Production of Rotation in a Confined Liquid Through Translational Motion of the Boundaries. Trans. of the ASME, Series E, J. Appl. Mech., vol. 26, no. 8, Dec. 1959, pp. 513-516.
- 6.23. ABRAMSON, H. N.; CHU, W. H.; AND KANA, D. D.: Some Studies of Nonlinear Lateral Sloshing in Rigid Containers. J. Appl. Mech., vol. 33, no. 4, Dec. 1966.
- 6.24. BAUER, H. F.; CLARK, C. D.; AND WOODWARD, J. H.: Analytical Mechanical Model for the Description of the Rotary Propellant Sloshing Motion. Final Rept., Contract NAS8-11159, Engineering Experiment Station, Georgia Institute of Technology, May 1965.
- 6.25. ABRAMSON, H. N.; CHU, W. H.; AND RANSLEBEN, G. E., JR.: Representation of Fuel Sloshing in Cylindrical Tanks by an Equivalent Mechanical Model. ARS J., vol. 31, Dec. 1961, pp. 1697-1705.
- 6.26. MILES, J. W.: On the Sloshing of Liquid in a Flexible Tank. Ramo-Wooldridge Rept. GM-TR-73, Sept. 1956.
- 6.27. BAUER, H. F.: Fluid Oscillation in a Cylindrical Tank With Damping. Army Ballistic Missile Agency Rept. DA-TR-4-58, Apr. 1958.
- 6.28. BAUER, H. F.: The Moment of Inertia of a Liquid in a Circular Cylindrical Tank. Army Ballistic Missile Agency Rept. DA-TR-5-58, Apr. 1958.
- 6.29. BAUER, H. F.: Mechanical Model of Fluid Oscillations in Cylindrical Tanks and Introducing of Damping. MSFC Rept. MTP-AERO-62-16, Feb. 1962.
- 6.30. BAUER, H. F.: Fluid Oscillations in the Containers of a Space Vehicle and Their Influence Upon Stability. NASA TR-R-187, Feb. 1964.
- 6.31. BAUER, H. F.: Liquid Sloshing in a Cylindrical Quarter Tank. AIAA J., vol. 1, no. 11, Nov. 1963, pp. 2601-2606.
- 6.32. BAUER, H. F.: Liquid Sloshing in a 45° Sector Compartmented Tank. AIAA J., vol. 2, no. 4, Apr. 1964, pp. 768-770.
- 6.33. DODGE, F. T.; AND KANA, D. D.: Moment of Inertia and Damping of Liquids in Baffled Cylindrical Tanks. J. Spacecraft Rockets, vol. 3, no. 1, Jan. 1966, pp. 153-155. Also see discussion, same journal, vol. 3, no. 6, June 1966, pp. 957-959.
- 6.34. RATTAYA, JASTI V.: Sloshing of Liquids in Axisymmetric Ellipsoidal Tanks. AIAA Paper No. 65-114, 2nd Aerospace Sciences Meeting, Jan. 1965.
- 6.35. LOMEN, D. O.: Liquid Propellant Sloshing in Mobile Tanks of Arbitrary Shape. NASA Rept. CR-222, Apr. 1965.
- 6.36. LOMEN, D. O.: Digital Analysis of Liquid Propellant Sloshing in Mobile Tanks With Rotational Symmetry. NASA Rept. CR-230, May 1965.

## PRINCIPAL NOTATIONS

$c_d$ =damping coefficient for disk  $I_d$   
 $c_n$ =damping coefficient for  $n$ th slosh mode  
 $d$ =cylindrical tank diameter  
 $F$ =transverse sloshing force  
 $g$ =acceleration due to gravity, or equivalent longitudinal acceleration  
 $h$ =total liquid depth  
 $h_n$ =location of  $n$ th slosh mass relative to liquid center of gravity, except see equation (6.34)  
 $h_0$ =location of fixed mass relative to liquid center of gravity  
 $I_d$ =moment of inertia of disk, see figure 6.26

$I_f$ =moment of inertia of liquid about transverse axis through center of gravity  
 $I_0$ =moment of inertia of fixed mass  
 $I_{rigid}$ =moment of inertia of solidified liquid about transverse axis through center of gravity  
 $K_n$ =spring constant for  $n$ th spring-mass system of model  
 $l_n$ =location of  $n$ th slosh mass relative to the free surface  
 $l_0$ =location of fixed mass relative to the free surface

$L_n$ =pendulum arm length for $n$ th slosh mode	$\gamma_n$ =damping factor of $n$ th slosh mode
$m_n$ =slosh mass of $n$ th mode	$\nabla^2$ =Laplacian operator
$m_0$ =fixed mass	$\lambda_n$ =dimensionless frequency parameter, see figure 6.20
$m_T$ =total mass of liquid	$\nu$ =dimensionless frequency for rotary sloshing
$M$ =sloshing moment about liquid center of gravity	$\xi_n$ =zeroes of $J'_1(\xi_n)=0$
$t$ =time	$\Phi$ =velocity potential
$x_0, y_0$ =amplitude of lateral excitation	$\varphi_0$ =amplitude of pitching oscillation
$y_n$ =lateral displacement of $n$ th mass relative to tank wall	$\chi$ =see equation (6.38)
$\alpha, \beta, \gamma$ =directional angles for pendulum model of rotary sloshing, see figure 6.9	$\psi$ =pendulum angle, or rotational angle of disk relative to tank
$\alpha_n$ =dimensionless parameter, see equation (6.34)	$\omega$ =frequency of excitation
	$\omega_n$ =natural frequency of $n$ th slosh mode

# Vehicle Stability and Control

*Helmut F. Bauer*

## 7.1 INTRODUCTION

In order to analyze properly the performance of rockets and space vehicles, it is necessary to consider the general problem of dynamics and stability of the vehicle under thrust. Since, with the increasing size of space vehicles and their correspondingly larger tank diameters, the liquid propellant frequencies come closer to the control frequency of the vehicle, therefore the influence of the sloshing propellant can no longer be neglected. Also, with this increase in the diameter of the propellant containers, the amount of propellant participating in sloshing and the corresponding liquid forces become rather pronounced and can influence the stability of the vehicle considerably. Since the largest portion of the total weight of the space vehicle is in form of liquid propellant, the problem of interaction of the sloshing propellant with the motion of the space vehicle remains an important consideration throughout the entire powered flight.

The general problem we are concerned with here is the motion of the center of mass, the vehicle attitude, the motion of the propellants in the tanks, and the lateral bending of the vehicle structure under the action of a control system. For the purpose of the following investigations, the rate of mass, the moment of inertia, and acceleration variations were considered small enough to be negligible.<sup>1</sup>

The questions to be answered therefore are how to decrease the influence of propellant sloshing upon the stability of the vehicle by proper container geometry and location, proper

choice of the control system and its gain values, and how to obtain the requirements for additional baffles to provide damping of the liquid in the containers. To simplify the analysis, aerodynamic effects and the inertia of the swivel engines, as well as their compliances, are neglected. The control moments will be produced by the swivel engines. The main energy is fed into the system by the feedback loops between the structure of the space vehicle and its control system.

The coordinate system has its origin at the center of mass of the undisturbed vehicle. The accelerated coordinate system is substituted by an inertial system such that the space vehicle is subjected to an equivalent field of acceleration (fig. 7.1). Centrifugal and Coriolis forces, which result from a rota-

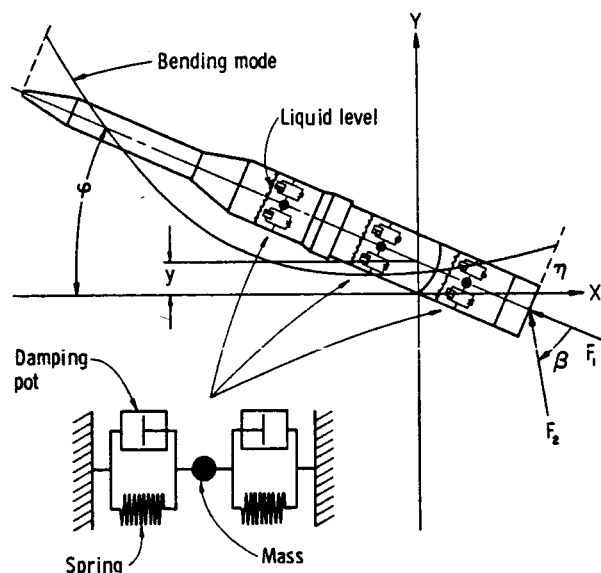


FIGURE 7.1.—Coordinate system of space vehicle.

<sup>1</sup> The equations of motion derived in this chapter are quite simple and are only adequate to illustrate gross effects of the interaction of propellant sloshing, structure, and control.

tion, are considered negligible and the acceleration is in the direction of the trajectory.<sup>2</sup>

## 7.2 SIMPLIFIED EQUATIONS OF MOTION

In order to outline the problem at hand, we will consider the motion of a flexible body in the plane perpendicular to the trajectory. We define a set of body fixed coordinates,  $x$ ,  $y$ ,  $z$ , with the origin coinciding with the center of mass. The translatory motion,  $y$ , of the vehicle, the rotational motion,  $\phi$ , about the center of mass, as well as the propellant motion,  $y_n$ , and the bending vibrations,  $\eta_n$ , are restricted to the  $x$ -,  $y$ -plane. We follow the conventional method of deriving the equations of motion from Lagrange's equation. It is assumed that the motion of the space vehicle can be described by a superposition of a finite number of pre-assigned bending mode shapes with a translatory and rotational motion of the vehicle. The elastic mode shapes are introduced as normal modes of vibration of the vehicle structure.

### Lagrange's Equation

For the derivation of the equations of motion, we employ Lagrange's equation in the form

$$\frac{d}{dt} \left( \frac{\partial T}{\partial \dot{q}_i} \right) + \frac{\partial D}{\partial q_i} + \frac{\partial V}{\partial q_i} = Q_i \quad (7.1)$$

where  $T$  is the kinetic energy of the system,  $D$  the dissipation function, and  $V$  the potential energy. The generalized forces,  $Q_i$ , correspond to those external forces which cannot be derived from a potential. The generalized coordinates,  $q_i$ , are independent of each other and specify the configuration of the system at any time, their number representing the number of degrees of freedom of the system. These coordinates are:

$y$ =the lateral translation of the center of mass, or centerline of the undeformed space vehicle

$\phi$ =the rotational motion of the centerline of the undeformed vehicle about the center of mass, relative to the  $x$ -coordinate

<sup>2</sup> See refs. 7.1 and 7.2. Other papers on the subject of dynamics of missiles are given in refs. 7.3 through 7.6.

$y_n$ =the displacement of the sloshing masses relative to the container wall

$\eta_n$ =the elastic deflection of the normalized bending mode shape

### Kinetic Energy

The kinetic energy is composed of parts arising from motions of the empty structure of the space vehicle and the liquid propellant. The influence of the swivel engines can be neglected. The kinetic energy,  $T_s$ , of the empty structure is obtained by summation of the translational and rotational kinetic energy of each segment. The translational velocity,  $v$ , resulting from translation, rotation and bending displacements and the angular velocity,  $\omega$ , are

$$v = \dot{y} - x\dot{\phi} + \sum_{\nu=1}^{\infty} \dot{\eta}_{\nu} Y_{\nu}, \quad \omega = \dot{\phi} - \sum_{\nu=1}^{\infty} \dot{\eta}_{\nu} Y'_{\nu}$$

where  $x$  is the distance of the considered element from the center of mass of the space vehicle, and  $Y_{\nu}$  is the normalized bending deflection of the  $\nu$ th lateral bending mode. (The dot indicates differentiation with respect to time, while the prime stands for differentiation with respect to  $x$ .) The kinetic energy,  $T_s$ , is then

$$T_s = \frac{1}{2} \int m'_s \left( \dot{y} - x\dot{\phi} + \sum_{\nu=1}^{\infty} \dot{\eta}_{\nu} Y_{\nu} \right)^2 dx + \frac{1}{2} \int I'_s \left( \dot{\phi} - \sum_{\nu=1}^{\infty} \dot{\eta}_{\nu} Y'_{\nu} \right)^2 dx \quad (7.2)$$

Here,  $m'_s$  is the mass of the structure per unit length and  $I'_s$  is the mass moment of inertia per unit length about the center of mass of the elemental segment. The integration is performed over the total vehicle length and the bending mode deflection curves,  $Y_{\nu}$ , are normalized (to unity) at the swivel point of the engines.

The kinetic energy,  $T_p$ , of the liquid propellant can be obtained from an equivalent mechanical model. (See ch. 6.) Such a model describes the linearized liquid motion and may consist of a fixed mass,  $m_0$ , and an infinite set of oscillating masses,  $m_n$ , which are attached to the propellant container wall by means of springs of stiffness  $k_n$ . With this mechanical analogy, the kinetic energy of the propellant can be written as

$$\begin{aligned}
T_p = & \frac{1}{2} \sum_{\lambda=1}^l m_{0\lambda} \left\{ \dot{y} - x_{0\lambda} \dot{\phi} + \sum_{\nu=1}^{\infty} \dot{\eta}_{\nu} Y'_{\nu}(x_{0\lambda}) \right\}^2 \\
& + \frac{1}{2} \sum_{\lambda=1}^l I_{0\lambda} \left\{ \dot{\phi} - \sum_{\nu=1}^{\infty} \dot{\eta}_{\nu} Y'_{\nu}(x_{0\lambda}) \right\}^2 \\
& + \frac{1}{2} \sum_{\lambda=1}^l \sum_{n=1}^{\infty} m_{\lambda n} \left\{ \dot{y} - x_{\lambda n} \dot{\phi} + \sum_{\nu=1}^{\infty} \dot{\eta}_{\nu} Y'_{\nu}(x_{\lambda n}) + \dot{y}_{n\lambda} \right\}^2
\end{aligned} \quad (7.3)$$

where  $l$  indicates the number of propellant containers,  $m_{0\lambda}$  the fixed (nonsloshing) mass in the  $\lambda$ th propellant tank,  $m_{\lambda n}$  the mass of the  $n$ th sloshing mode in the  $\lambda$ th container,  $x_{0\lambda}$  the distance of the nonsloshing mass in the  $\lambda$ th container to the center of mass of the vehicle, and  $x_{\lambda n}$  the distance of the  $n$ th sloshing mass in the  $\lambda$ th container to the center of mass of the vehicle. The value  $I_{0\lambda}$  is the moment of inertia of the nonsloshing mass in the  $\lambda$ th container about its own center of mass. The displacement of the mass of the  $n$ th sloshing mode in the  $\lambda$ th container relative to the tank wall is denoted by  $y_{n\lambda}$ .

#### Potential Energy

The potential energy is also composed of two main parts; namely, that of the structure and that of the propellant. The potential energy of the structure is again made up of two parts, one of which represents the elastic energy of deformation

$$\begin{aligned}
V_{SE} = & \frac{1}{2} \sum_{\nu=1}^{\infty} \eta_{\nu}^2 \left\{ \int \frac{M_{\nu}^2}{EI} dx \right. \\
& \left. + \int \frac{Q_{\nu}^2}{A_s G} dx \right\} = \frac{1}{2} \sum_{\nu=1}^{\infty} \eta_{\nu}^2 V_{\nu}
\end{aligned} \quad (7.4)$$

and the other represents the work performed in raising the center of mass of the empty vehicle in the gravitational field as the result of rotation. This part becomes, in linearized form

$$V_{sg} = m_s g x_s \frac{\phi^2}{2} \quad (7.5)$$

Equation (7.4) can also be expressed as

$$\begin{aligned}
V_{SE} = & \frac{1}{2} \sum_{\nu=1}^{\infty} \omega_{\nu}^2 \eta_{\nu}^2 \left\{ \int m_s' Y_{\nu}^2 dx \right. \\
& \left. + \int I_s' Y_{\nu}'^2 dx \right\} = \frac{1}{2} \sum_{\nu=1}^{\infty} M_{B\nu} \omega_{\nu}^2 \eta_{\nu}^2
\end{aligned} \quad (7.6)$$

Here,  $M_s$  represents the bending moment and  $Q_s$ , the shear force acting on an elemental cross section. The flexural stiffness is  $EI$ ,  $G$  is the shear modulus, and  $A_s$  represents the shear area of the cross section. The bending frequency of the  $\nu$ th lateral bending mode is  $\omega_{\nu}$ , and  $M_{B\nu}$  represents the generalized mass of the space vehicle. It may be mentioned here that the values  $M_{B\nu}$ ,  $Y_{\nu}$ ,  $\omega_{\nu}^2$  are obtained from a lateral bending analysis.

The potential energy of the propellant is obtained also by using the mechanical analogy and is composed of the energy stored in springs and the raising of the model masses in the gravitational field. The complete expression is:

$$\begin{aligned}
V_p = & \frac{1}{2} \sum_{\lambda=1}^l \sum_{n=1}^{\infty} k_{\lambda n} y_{n\lambda}^2 + \frac{1}{2} g \phi^2 \left\{ \sum_{\lambda=1}^l m_{0\lambda} x_{0\lambda} \right. \\
& \left. + \sum_{\lambda=1}^l \sum_{n=1}^{\infty} m_{\lambda n} x_{n\lambda} \right\} - g \sum_{n=1}^{\infty} \sum_{\lambda=1}^l m_{\lambda n} y_{n\lambda} \\
& \times \left\{ \phi - \sum_{\nu=1}^{\infty} \eta_{\nu} Y'_{\nu}(x_{\lambda n}) \right\}
\end{aligned} \quad (7.7)$$

#### Dissipation Function

The dissipation function of the structure arises from its structural damping, which is considered proportional to the amplitude of the elastic system and in phase with its velocity. This, unfortunately, would lead to complex elements which would complicate the analysis considerably. To avoid this computational complication, a dissipation function is employed which is based on an equivalent linear viscous damping. This is justified as long as the damping forces are small and only of importance in the neighborhood of the bending frequencies.

The dissipation function of the structure is therefore given by

$$D_s = \frac{1}{2} \sum_{\nu=1}^{\infty} \omega_{\nu} M_{B\nu} g_s \eta_{\nu}^2 \quad (7.8)$$

where  $g_s$  is the dimensionless structural damping coefficient of the  $\nu$ th lateral bending vibration mode, and ranges in the neighborhood of  $0.001 \leq g_s \leq 0.05$ .

The dissipation function of the liquid propellant arises from the equivalent linear viscous damping as it was introduced by linear dashpots

in the mechanical model. (See ch. 6.) This takes the form, with  $c_{\lambda n} = 2\xi_{n\lambda}\omega_{n\lambda}m_{n\lambda}$

$$D_p = \frac{1}{2} \sum_{\lambda=1}^l \sum_{n=1}^{\infty} c_{n\lambda} \dot{y}_{\lambda n}^2 = \sum_{\lambda=1}^l \sum_{n=1}^{\infty} \xi_{n\lambda} \omega_{n\lambda} m_{n\lambda} \dot{y}_{\lambda n}^2 \quad (7.9)$$

where  $\xi_{n\lambda}$  is the damping factor and  $\omega_{n\lambda}$  is the circular natural frequency of the  $n$ th sloshing mode in the  $\lambda$ th container.

#### Generalized Mass

The equations of motion are to be obtained by performing differentiations for each generalized coordinate in the Lagrange equation, where the following relations have to be observed.

The total mass,  $m$ , of the vehicle is given by (engine mass neglected)

$$m = \int m_s' dx + \sum_{\lambda=1}^l m_{0\lambda} + \sum_{\lambda=1}^l \sum_{n=1}^{\infty} m_{n\lambda} \quad (7.10)$$

The origin of the coordinate system is at the equilibrium position of the center of mass of the total space vehicle, which is expressed by the equation

$$\int m_s' x dx + \sum_{\lambda=1}^l m_{0\lambda} x_{0\lambda} + \sum_{\lambda=1}^l \sum_{n=1}^{\infty} m_{n\lambda} x_{n\lambda} = 0 \quad (7.11)$$

Furthermore, the linear momentum for the normal modes of vibration is conserved and expressed by

$$\int m_s' Y_\nu dx + \sum_{\lambda=1}^l m_{0\lambda} Y_\nu(x_{0\lambda}) + \sum_{\lambda=1}^l \sum_{n=1}^{\infty} m_{n\lambda} Y_\nu(x_{n\lambda}) = 0 \quad (7.12)$$

where the integrations are to be performed along the total vehicle length.

#### Generalized Thrust Forces

Before proceeding to the derivation of the equations of motion, the generalized forces that cannot be represented from a potential are derived. These are obtained by calculating the virtual work done by the external forces through virtual increments,  $\delta q_i$ , of the generalized coordinates,  $q_i$ . Thus,

$$\delta W = \sum Q_i \delta q_i$$

where  $W$  is the work and  $Q_i$  are the generalized forces. Since we neglect aerodynamic forces

and propellant flow forces in the pipelines, the only force we shall be concerned with will be that of the vehicle thrust,  $F$ . If only a part,  $F_2$ , of the thrust  $F = F_1 + F_2$  is employed for control purposes, that is, if only this part of the total thrust can be gimbaled, while the remainder,  $F_1$ , of the thrust is stationary, then the derivation of the generalized forces with respect to the thrust is as follows.

The generalized force of the lateral translation resulting from the thrust vector of the vehicle is given by the thrust component in the  $y$ -direction. The virtual work is (see fig. 7.2)

$$\delta W_y = F \left\{ \phi - \sum_{\nu=1}^{\infty} \eta_\nu Y'_\nu(x_E) \right\} \delta y + F_2 \beta \delta y$$

from which the generalized force,  $Q_y$ , is obtained as

$$Q_y = F \left\{ \phi - \sum_{\nu=1}^{\infty} \eta_\nu Y'_\nu(x_E) \right\} + F_2 \beta \quad (7.13)$$

where  $\beta$  is the engine deflection as measured from the centerline of the vehicle. The generalized force of rotation is presented by the moment of the thrust force about the center of mass of the vehicle, and with

$$\delta W_\phi = F \left\{ x_E \sum_{\nu=1}^{\infty} \eta_\nu Y'_\nu(x_E) - \sum_{\nu=1}^{\infty} \eta_\nu Y_\nu(x_E) \right\} \delta \phi - F_2 x_E \beta \delta \phi$$

gives the expression

$$Q_\phi = F \left\{ x_E \sum_{\nu=1}^{\infty} \eta_\nu Y'_\nu(x_E) - \sum_{\nu=1}^{\infty} \eta_\nu Y_\nu(x_E) \right\} - F_2 x_E \beta \quad (7.14)$$

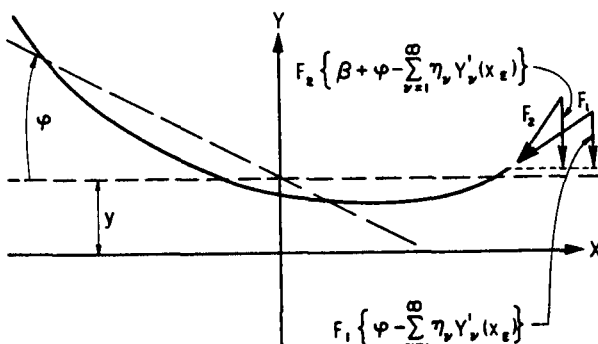


FIGURE 7.2.—Generalized forces resulting from thrust.

Finally, the generalized force of the thrust with respect to the generalized coordinates arising from the lateral bending of the space vehicle are obtained in a similar way by observing that the thrust force is always perpendicular to the lateral bending motion and that the virtual work through a virtual displacement of the generalized coordinate,  $\eta_v$ , is

$$\delta W_{\eta_v} = F_2 \beta Y_v(x_E) \delta \eta_v$$

The generalized force is therefore

$$Q_{\eta_v} = F_2 \beta Y_v(x_E) \quad (7.15)$$

The generalized forces of the thrust with respect to the sloshing displacement are zero; i.e.,  $Q_{\eta_n} = 0$ .

#### Translational Equation of Motion

The equation of motion for translation,  $y$ , of the vehicle is obtained from equation (7.1), with equations (7.2) and (7.3), by employing the results equations (7.10) through (7.13), thus

$$m\ddot{y} + \sum_{\lambda=1}^l \sum_{n=1}^{\infty} m_{n\lambda} \ddot{y}_{n\lambda} = F\phi + F_2 \beta - F \sum_{v=1}^{\infty} \eta_v Y'_v(x_E) \quad (7.16)$$

#### Pitching Equation of Motion

The equation of motion of the vehicle in pitching,  $\phi$ , is obtained from equation (7.1) with  $q_i = \phi$ , and employing equations (7.2) through (7.14), thus

$$I\ddot{\phi} - \sum_{n=1}^{\infty} \sum_{\lambda=1}^l m_{n\lambda} x_{n\lambda} \ddot{y}_{n\lambda} - g \sum_{n=1}^{\infty} \sum_{\lambda=1}^l m_{n\lambda} y_{n\lambda} + F_2 x_E \beta = F \left\{ x_E \sum_{v=1}^{\infty} \eta_v Y'_v(x_E) - \sum_{v=1}^{\infty} \eta_v Y_v(x_E) \right\} \quad (7.17)$$

where the effective moment of inertia of the space vehicle is given by

$$I = mk^2 = \int m'_x dx + \int I'_x dx + \sum_{\lambda=1}^l m_{0\lambda} x_{0\lambda}^2 + \sum_{\lambda=1}^l I_{0\lambda} + \sum_{n=1}^{\infty} \sum_{\lambda=1}^l m_{n\lambda} x_{n\lambda}^2 \quad (7.18)$$

and the equation for the conservation of the angular momentum has been observed as

$$\begin{aligned} & \int m'_x Y_v(x) dx + \int I'_x Y'_v(x) dx + \sum_{\lambda=1}^l m_{0\lambda} x_{0\lambda} Y_v(x_{0\lambda}) \\ & + \sum_{\lambda=1}^l I_{0\lambda} Y'_v(x_{0\lambda}) + \sum_{n=1}^{\infty} \sum_{\lambda=1}^l m_{n\lambda} x_{n\lambda} Y_v(x_{n\lambda}) = 0 \end{aligned} \quad (7.19)$$

The value  $x_E$  is the distance of the swivel point of the engines from the origin and  $k$  is the radius of gyration of the vehicle. The right-hand side of equation (7.17) represents the generalized force of the thrust with respect to lateral bending. The values  $Y_v(x_E)$  and  $Y'_v(x_E)$  are the lateral displacement and slope of the  $v$ th bending mode at the location of the swivel point, respectively.

#### Propellant Equation of Motion

The equation of motion of the moving propellant in the containers of the vehicle is based on the mechanical model and is obtained by applying the Lagrange equation to the generalized coordinate  $y_{n\lambda}$  observing that the generalized force,  $Q_{y_{n\lambda}}$ , vanishes. This yields the equation of the modal sloshing mass (refs. 7.7 and 7.8)

$$\begin{aligned} \ddot{y}_{n\lambda} + 2\xi_{n\lambda} \omega_{n\lambda} \dot{y}_{n\lambda} + \omega_{n\lambda}^2 y_{n\lambda} \\ = - \left\{ \ddot{y} - x_{n\lambda} \ddot{\phi} + \sum_{v=1}^{\infty} \eta_v Y'_v(x_{n\lambda}) \right\} \\ + g \left\{ \phi - \sum_{v=1}^{\infty} \eta_v Y_v(x_{n\lambda}) \right\} \\ \lambda = 1, 2, \dots, l; n = 1, 2, \dots \end{aligned} \quad (7.20)$$

The subscript  $n$  indicates the number of the propellant mode under consideration, while  $\lambda$  indicates the container number.  $\xi_{n\lambda}$  is the damping factor of the propellant and  $\omega_{n\lambda}$  is the undamped circular natural frequency.  $Y_v(x_{n\lambda})$  and  $Y'_v(x_{n\lambda})$  are displacement and slope, respectively, of the  $v$ th lateral bending mode at the location of the  $n$ th sloshing mass in the  $\lambda$ th container.

#### Lateral Bending Equation of Motion

As vehicles increase in size, the lateral fundamental bending frequency approaches more and more closely to the control frequency and

the lower natural frequencies of the propellant. This indicates that in many cases the bending vibrations of the vehicle cannot be neglected in a dynamic analysis of the vehicle that also includes propellant sloshing and the control system. (See ch. 9.)

The equation of motion of the  $\nu$ th bending mode is obtained from equation (7.1) together with equations (7.2) through (7.7) and by noting the results of equations (7.12), (7.19), and the orthogonality relations between normal modes, as expressed by

$$\int m'_s Y_\nu(x) Y_\mu(x) dx + \int I'_s Y'_\nu(x) Y'_\mu(x) dx \\ + \sum_{\lambda=1}^l m_{0\lambda} Y_\nu(x_{0\lambda}) Y_\mu(x_{0\lambda}) + \sum_{\lambda=1}^l I_{0\lambda} Y'_\nu(x_{0\lambda}) Y'_\mu(x_{0\lambda}) \\ + \sum_{n=1}^{\infty} \sum_{\lambda=1}^l m_{n\lambda} Y_\nu(x_{n\lambda}) Y_\mu(x_{n\lambda}) = 0 \quad (7.21)$$

thus

$$\ddot{\eta}_\nu + g_\nu \omega_\nu \dot{\eta}_\nu + \omega_\nu^2 \eta_\nu = \frac{F_2}{M_{B\nu}} Y_\nu(x_E) \beta \\ - \frac{g}{M_{B\nu}} \sum_{n=1}^{\infty} \sum_{\lambda=1}^l m_{n\lambda} y_{n\lambda} Y'_\nu(x_{n\lambda}) \\ - \frac{1}{M_{B\nu}} \sum_{n=1}^{\infty} \sum_{\lambda=1}^l m_{n\lambda} \ddot{y}_{n\lambda} Y_\nu(x_{n\lambda}) \quad (7.22)$$

Here,  $\omega_\nu$  represents the natural circular frequency of the  $\nu$ th lateral bending mode and  $g_\nu$  is the corresponding structural damping. The generalized mass of the  $\nu$ th lateral bending mode,  $M_{B\nu}$ , is given by the expression

$$M_{B\nu} = \int m'_s Y_\nu^2(x) dx + \int I'_s Y'^2_\nu(x) dx \\ + \sum_{\lambda=1}^l m_{0\lambda} Y_\nu^2(x_{0\lambda}) + \sum_{\lambda=1}^l I_{0\lambda} Y'^2_\nu(x_{0\lambda}) \\ + \sum_{n=1}^{\infty} \sum_{\lambda=1}^l m_{n\lambda} Y_\nu^2(x_{n\lambda}) \quad (7.23)$$

The values  $Y_\nu(x_{0\lambda})$  and  $Y'_\nu(x_{0\lambda})$  represent nothing but the displacement and slope of the  $\nu$ th lateral bending mode at the location of the nonsloshing mass in the  $\lambda$ th propellant tank.

### Control System Equation of Motion

Actually, the control equation cannot be expressed as a linear equation; however, translational and rotational motions of the space vehicle usually occur at sufficiently small frequencies so that the control elements can be considered as essentially linear. Nonlinearities usually occur at higher frequencies in the form of saturation of amplifiers, limited output of velocities, and so forth. The control equation is written, therefore, in the form

$$f_1(\beta) = f_2(\phi_i, A_i)$$

where the operators  $f_1$  and  $f_2$  are functions that depend on the character of the system.  $A_i$  is the indicated acceleration, as measured by an accelerometer normal to the longitudinal axis of the vehicle. In linear form one can express this as

$$\sum_\nu p_\nu \frac{d^\nu \beta}{dt^\nu} = \sum_j a_j \frac{d^j \phi_i}{dt^j} + \sum_k g_{k+2} \frac{d^{k+2} A_i}{dt^k} \quad (7.24)$$

Here, the  $p_\nu$  are the so-called phase-lag coefficients, and  $\phi_i$  is the indicated angular deviation from the trajectory as indicated by the gyroscope

$$\phi_i = \phi - \sum_{\nu=1}^{\infty} \eta_\nu Y'_\nu(x_G) \quad (7.25)$$

where  $Y'_\nu(x_G)$  is the derivative of the  $\nu$ th lateral bending mode at the location of the gyroscope. If the fundamental lateral bending frequency is well above the control and propellant sloshing frequencies, of which the corresponding sloshing masses create pronounced dynamic effects, the flexibility of the space vehicle can be neglected and the control equation can be written in the simplified form ( $\nu=0; j=1, 2, k=0$ , and  $p_0=1$ )

$$\beta = a_0 \phi + a_1 \dot{\phi} + g_2 A_i \quad (7.26)$$

Here, time derivatives in  $\beta$ , which produce increasing phase lags with increasing frequency, have been neglected. In order to include the effect of the flexible structure, the phase-lag coefficients are of importance and have to be considered. A still simplified control equation for these cases would be of the form

$$p_2 \ddot{\beta} + p_1 \dot{\beta} + \beta = a_0 \phi_i + a_1 \dot{\phi}_i + g_2 A_i \quad (7.27)$$

which only approximately describes the complexity of an actual control system. By proper choice of the phase-lag coefficients,  $p_1$  and  $p_2$ , and by proper choices of the attitude value,  $a_0$ , and the rate value,  $a_1$ , the control system can be approximated. A simple system is preferred for this type of analysis in order to keep the analysis and the interpretation lucid, and still render good results. If no accelerometer is employed for control purposes, the gain value,  $g_2$ , vanishes. This term,  $g_2$ , is a measure of the strength with which the control accelerometer influences the control of the space vehicle.

The attitude gyroscope is a free gyroscope that measures the position of the vehicle, the main function of the gyroscope being to maintain a space-fixed angular reference. Since we restrict our motion to one plane only (pitching), we consider only the appropriate gyroscope of the stable platform. The essential property of a gyroscope is used, which represents an angular velocity about an orthogonal axis (output axis), if a torque is applied about an input axis. If the platform on which the gyroscope is mounted is perfectly balanced and the bearings are frictionless, no torque will be experienced by the platform, thus maintaining its orientation regardless of the motion of the space vehicle (ref. 7.9). The pickoffs of the gyroscope must be very light in weight and should not introduce any torques; this can be achieved by various forms of capacitive, inductive, or optical pick-offs. Because of unbalances and friction, which cannot be eliminated completely, a disturbance torque is exerted on the stable platform; a servo-system counteracts this disturbing torque and produces essentially a torque-free system. For the purposes of this chapter, we consider a properly designed gyroscope which exhibits a transfer function of unity for a very large bandpass. This means that the indicated attitude angle will be the same as the input angle and is described by equation (7.25).

#### Accelerometer Equation of Motion

A vehicle moving in the pitch plane possesses two rigid body degrees of freedom, one translational degree of freedom in the  $y$ -direction and one rotational degree of freedom denoted by  $\phi$ . While the gyroscope detects rotational motion,

the accelerometer is required to provide a reference for translational motion. An accelerometer and a gyroscope are therefore capable of supplying information about the motion of a rigid space vehicle in the pitch plane ( $x$ ,  $y$  plane). In addition to the gyroscope, an accelerometer provided for control purposes can, by proper choice of the gain value and its vibrational characteristics, also diminish loads and reduce engine angle requirements of the swivel engines. Mounting an accelerometer to the structure of the vehicle such that its sensitive direction is perpendicular to the longitudinal axis of the vehicle, this instrument is then capable of sensing the accelerations due to translation, pitching, and bending motions.

The equation of motion of an accelerometer (shown schematically in fig. 7.3) can be obtained from Lagrange's equation. The kinetic energy is given by

$$T = \frac{m_a}{2} \left\{ \dot{y} - x_a \dot{\phi} + \dot{y}_a + \sum_{v=1}^{\infty} \eta_v Y'_v(x_a) \right\}^2$$

where  $y_a$  is the relative deflection of the accelerometer mass,  $m_a$ , with respect to the space vehicle, and  $(-x_a)$  is the location of the accelerometer measured from the mass center of the vehicle. The dissipation function corresponding to linear damping can be represented by

$$D = \frac{c_a}{2} \dot{y}_a^2$$

where  $c_a$  is the damping coefficient. The potential energy is

$$V = \frac{k_a}{2} y_a^2 - m_a g y_a \left\{ \phi - \sum_{v=1}^{\infty} \eta_v Y'_v(x_a) \right\}$$

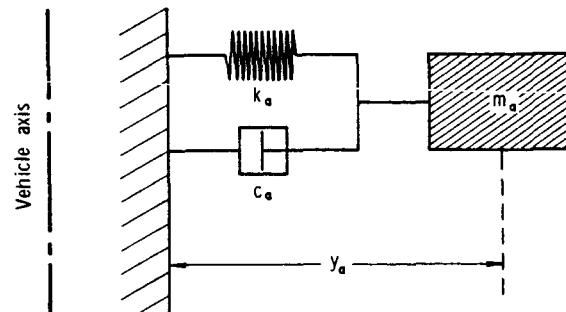


FIGURE 7.3.—Schematic of accelerometer.

The first term is the energy stored in the spring, while the second term is the potential energy decrease resulting from the change of location of the mass,  $m_a$ , in the equivalent acceleration field,  $g$ . With these results, the equation of motion of the accelerometer is obtained by applying Lagrange's equation to yield

$$\begin{aligned} m_a \left\{ \ddot{y} - x_a \ddot{\phi} + \ddot{y}_a + \sum_{v=1}^{\infty} \ddot{\eta}_v Y_v(x_a) \right\} + c_a \dot{y}_a + k_a y_a \\ = m_a g \left\{ \phi - \sum_{v=1}^{\infty} \eta_v Y'_v(x_a) \right\} \end{aligned}$$

With  $k_a/m_a = \omega_a^2$  as the square of the natural circular frequency of the accelerometer, and  $c_a/m_a = 2\xi_a \omega_a$ , one obtains

$$\begin{aligned} \ddot{y}_a + 2\xi_a \omega_a \dot{y}_a + \omega_a^2 y_a = -\ddot{y} + x_a \ddot{\phi} \\ - \sum_{v=1}^{\infty} \ddot{\eta}_v Y_v(x_a) + g \left[ \phi - \sum_{v=1}^{\infty} \eta_v Y'_v(x_a) \right] \end{aligned}$$

where  $\xi_a$  is the damping factor of the accelerometer.

By scaling the output in such a manner that it is equal to the input, for frequencies small in comparison with the natural frequency of the accelerometer, one has to transform with

$$y_a = -\frac{A_i}{\omega_a^2}$$

where  $A_i$  represents the indicated acceleration. The response characteristic of the accelerometer is therefore determined by the differential equation

$$\begin{aligned} \frac{\ddot{A}_i}{\omega_a^2} + \frac{2\xi_a}{\omega_a} \dot{A}_i + A_i = \ddot{y} - x_a \ddot{\phi} - g\phi \\ + \sum_{v=1}^{\infty} \{ \ddot{\eta}_v Y_v(x_a) + g\eta_v Y'_v(x_a) \} \quad (7.28) \end{aligned}$$

### Rate Gyro Equation of Motion

In some space vehicles, the rate of the attitude angle,  $\phi_i$ , in the control equation is not obtained by a differentiating network operating on the angle,  $\phi_i$ , but rather by the output signal of a rate gyroscope. The function of a rate gyroscope is to give an output signal which is proportional to the angular velocity about a perpendicular axis. Figure 7.4 represents the

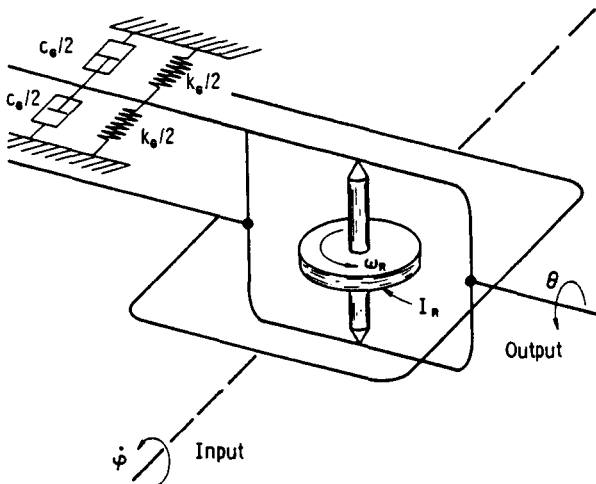


FIGURE 7.4.—Schematic of rate gyroscope mounting.

mounting of such a rate gyroscope. In contrast to the free gyroscope, the outer frame of the rate gyroscope is rigidly fastened to the structure of the vehicle. The inner gimbal support is restrained by a spring and damper which permit a limited rotation about the outer frame. The  $z$ -axis about which the vehicle turns is called the input axis, and the axis of rotation of the inner gimbal frame is called the output axis. Any rotation of the vehicle frame at a rate  $\dot{\phi}_{IR}$  will act as a forced precession of the spin axis and will induce a gyroscopic reaction torque. This torque is given by

$$M_R = I_R \omega_R \dot{\phi}_R$$

where  $I_R$  is the moment of inertia of the rotor and  $\omega_R$  its angular velocity.  $\dot{\phi}_R$  represents the angular velocity of the structure of the vehicle at the location of the rate gyroscope. The torque,  $M_R$ , is balanced by the inertial, damping, and restoring moments of the gyroscope about its output axis. Damping has been introduced to prevent the undesirable condition of excessive overshoot and oscillations about the steady-state angle. The behavior of the rate gyroscope can therefore be established from the differential equation

$$I_G \ddot{\theta} + c_G \dot{\theta} + K_G \theta = I_R \omega_R \dot{\phi}_R$$

where  $I_G$  represents the moment of inertia of

the rotor and the inner gimbal frame with respect to the output axis.  $c_G$  is the coefficient of viscous damping and  $K_G$  is the restoring moment per unit angle. By defining

$$\theta = I_R \omega_R \theta_i / I_G \omega_G^2$$

the angle  $\theta$  is scaled in such a fashion that the indicated value,  $\theta_i$ , for frequencies small in comparison with the natural frequency,  $\omega_G$ , of the rate gyroscope ( $\omega_G^2 = K_G/I_G$ ), represents the angular velocity of the vehicle at the location of the gyroscope. The response characteristic of a rate gyroscope of natural circular frequency,  $\omega_G$ , a damping factor,  $\zeta_G$ , and an angular velocity,  $\omega_R$ , of the rotor is therefore described by the differential equation

$$\frac{\ddot{\theta}_i}{\omega_G^2} + \frac{2\zeta_G}{\omega_G} \dot{\theta}_i + \theta_i = \dot{\phi}_R = \dot{\phi} - \sum_{r=1}^{\infty} \dot{\eta}_r Y'_r(x_R) \quad (7.29)$$

where  $\theta_i$  represents the indicated angular velocity of the airframe of the vehicle at the location of the rate gyroscope. The control equation, in which the rate is governed by the output of a rate gyroscope, and with additional accelerometer control, is then (see eq. (7.27))

$$p_2 \ddot{\beta} + p_1 \dot{\beta} + \beta = a_0 \phi_i + a_1 \theta_i + g_2 A_i \quad (7.30)$$

where

$$\phi_i = \phi - \sum_{r=1}^{\infty} \eta_r Y'_r(x_G) \quad (7.31)$$

### 7.3 INFLUENCE OF PROPELLANT LATERAL SLOSHING

The dynamics of space vehicles are best described by the two essential investigations of stability and response. Stability expresses the ability of a system to achieve a state of motion and how rapidly this can be done. In the analysis of space vehicle performance, one usually is satisfied to determine just the roots (boundaries) of stability, rather than solving the total system of equations. The shifting of roots to more optimal positions, if possible, is a major part of the analysis. If this is accomplished, however, the response of the vehicle is then required to determine whether or not the design of the system is appropriate for certain given inputs. In a space vehicle, these design values are the available engine deflection,

its rate, maximum bending moments, wave height of the oscillating propellants, etc., as a consequence of a given wind increase and gust through which the vehicle may have to pass during the ascent phase of its flight. The dynamic characteristics of the vehicle differ in complexity depending, of course, upon the complexity of the system itself; they are reduced here to a less complex system by truncating the equations of motion in such a fashion that a more lucid presentation can be provided without loss of the more general features of the system.

### Stability Techniques and Stability Boundaries

Since the response of a system depends on its stability, the roots of the system are the most basic parameters of the system dynamics. These describe the response resulting from any excitation and depend only on the physical parameters of the system. We shall therefore discuss, in this section, the basic techniques for obtaining the characteristic roots of a dynamic system and shall study the variation of these stability roots with changes in the physical characteristics of the vehicle.

The optimization of the response behavior of the vehicle is based upon the possibility of shifting the stability roots of the system. (See fig. 7.5.) This means that if the location of the roots can be changed in the complex plane (root locus plane) (fig. 7.5) in such a fashion that they exhibit a larger negative real

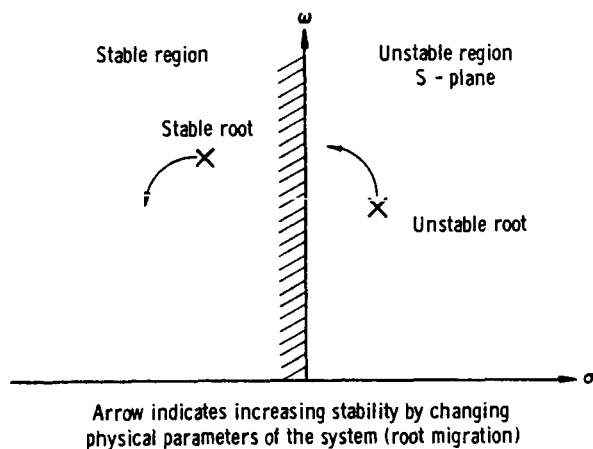


FIGURE 7.5.—Root locus plane.

part, by changing the physical properties of the system, the system will show enhanced stability and will more efficiently achieve a steady-state condition and absorb a disturbance more rapidly. A very convenient way to study the migration of stability roots is by plotting them as continuous functions in the complex plane; this is called a root locus plot and represents a curve of all (or those which we are most interested in) root locations in the complex plane ( $\sigma + i\omega$ ) corresponding to the change of some of the physical parameters of the space vehicle. The effect of the change of any other parameter can also be obtained. One can therefore investigate the necessary changes that should be introduced into the system to yield enhanced stability and response features.

In space vehicles, the characteristic equation is of higher order and a direct analytical solution is laborious and sometimes even unnecessary for design purposes. Although the solution of such a polynomial can be performed by the method of Sturm and Graeffe (ref. 7.10), or its modification by Brodetsky and Smeal (ref. 7.11) without any difficulties, in many cases it is sufficient to know whether or not the real parts of the roots are negative, thus indicating a decaying motion with increasing time (stable motion) or whether they are positive and represent an unstable motion with increasing amplitude as time increases. When a design parameter is to be considered as a variable, it is especially important to have available criteria for the stability in terms of the roots. Criteria of this type are given by Routh (ref. 7.12) and Hurwitz (ref. 7.13). Another method for the determination of the location of the roots is the root locus method by Nyquist (ref. 7.14). In the following, we shall use only the Hurwitz criteria.

A necessary and sufficient condition that the equation

$$\sum_{\lambda=0}^n a_\lambda s^\lambda = 0 \quad (7.32)$$

with real and positive coefficients,  $a_n$ , have only roots with negative real parts, is that the  $a_\lambda$  and the values of the determinants,  $H_r$ , all be positive. The determinant  $H_r$  is of the form:

$$H_r = \begin{vmatrix} a_1 & a_3 & a_5 & a_7 & \dots \\ a_0 & a_2 & a_4 & a_6 & \dots \\ 0 & a_1 & a_3 & a_5 & \dots \\ 0 & a_0 & a_2 & a_4 & \dots \\ \dots & \dots & \dots & \dots & \dots \\ 0 & \dots & \dots & \dots & \dots \end{vmatrix} \quad (7.33)$$

or

$$H_1 = a_1; H_2 = \begin{vmatrix} a_1 & a_3 \\ a_0 & a_2 \end{vmatrix}; \quad H_3 = \begin{vmatrix} a_1 & a_3 & a_5 \\ a_0 & a_2 & a_4 \\ 0 & a_1 & a_3 \end{vmatrix} \quad (7.34)$$

and

$$H_n = a_n H_{n-1} = \begin{vmatrix} a_1 & a_3 & a_5 & \dots \\ a_0 & a_2 & a_4 & \dots \\ 0 & a_1 & a_3 & \dots \\ 0 & a_0 & a_2 & \dots \\ \dots & \dots & \dots & \dots \end{vmatrix}$$

For a quadratic equation in  $s$ , these conditions are satisfied if the coefficients  $a_0$ ,  $a_1$ , and  $a_2$  are positive. For a cubic equation, the Hurwitz conditions are

$$H_1 = a_1 > 0, H_2 = \begin{vmatrix} a_1 & a_3 \\ a_0 & a_2 \end{vmatrix} > 0,$$

and

$$H_3 = \begin{vmatrix} a_1 & a_3 & 0 \\ a_0 & a_2 & a_4 \\ 0 & a_1 & a_3 \end{vmatrix} > 0 \quad (7.35)$$

To obtain some insight into the degree of stability, that is, the rapidity of decay of the motion, it is sometimes of interest to determine

the magnitude of the smallest negative real part. For this reason, one shifts the imaginary axis toward the left by

$$s = \bar{s} - \bar{\sigma}$$

where  $\bar{\sigma} > 0$  and real. If the transformed polynomial is just still stable, that is, the smallest root is very close to the shifted imaginary axis, we obtain a measure of the magnitude of stability.

The stability boundaries are characterized by the roots, of which at least one has a zero real part while the others are stable roots. For an  $n$ th-degree polynomial the stability boundaries are presented by

$$a_n = 0 \text{ and } H_{n-1} = 0$$

To determine which side of the stability boundary represents the stable region, one point (not located on the boundary) is chosen, and its stability is investigated with the previous Hurwitz determinants,  $H_r > 0$  (eq. (7.35)). For a quadratic equation, the stability boundaries are given by  $a_2 = 0$  and  $a_1 = 0$ . For a cubic equation, the conditions are

$$a_3 = 0 \text{ and } H_2 = a_1 a_2 - a_0 a_3 = 0$$

and for a quartic equation they are

$$a_4 = 0 \text{ and } H_3 = 0, \text{ i.e., } a_1 a_2 a_3 = a_1^2 a_4 + a_0 a_3^2$$

Another method for determining the stability would be that of the locus curve. The polynomial of the complex variable,  $s$ , represents a complex value,  $w$

$$w = P(s)$$

If all roots,  $s$ , are stable roots, they must be located in the left half plane of  $s$ , that is, the imaginary axis,  $s = i\omega$ , separates the left stable from the right unstable region of the  $s = \sigma + i\omega$ -plane. Introducing  $s = i\omega$  into the polynomial  $w = P(s)$  and investigating the mapping of this imaginary axis in the  $w$ -plane should yield some criteria for the stability of the roots of the polynomial. With

$$s = i\omega$$

and

$$P(s) = \sum_{\lambda=0}^n a_\lambda s^\lambda$$

we have

$$w = P(i\omega) = \sum_{\lambda=0}^{[n/2]} (-1)^\lambda a_{2\lambda} \omega^{2\lambda}$$

$$+ i \sum_{\lambda=0}^{[n/2]} (-1)^\lambda a_{2\lambda+1} \omega^{2\lambda+1} = X(\omega) + i Y(\omega)$$

where  $[n/2]$  means the smaller integer closest to  $n/2$ , or equal  $n/2$ , if  $n$  is even. This indicates that for even  $n$  the expression  $X(\omega)$  will be an even polynomial of  $n$ th degree while  $Y(\omega)$  is an odd polynomial of  $(n-1)$ st degree. For an odd value  $n$ , the  $X(\omega)$  is an even function of  $(n-1)$ st degree and  $Y(\omega)$  is an odd polynomial of  $n$ th degree. Therefore,  $X(\omega) = X(-\omega)$  and  $Y(\omega) = -Y(-\omega)$ . The function  $w(\omega)$  is represented in the  $w$ -plane locus curve as  $\omega$  assumes the values from  $-\infty$  to  $+\infty$ . All roots of the polynomial  $w = P(s) = 0$  are mapped into the origin  $w = 0$  of the  $w$ -plane. The location of this point, therefore, with respect to the locus curve will be characteristic for the root,  $s_v$ , with respect to the imaginary axis. The fact that  $X(\omega)$  is even and  $Y(\omega)$  is odd reveals that only  $\omega \geq 0$  has to be considered. The locus curve starts out for  $\omega = 0$  on the  $X$ -axis and the  $w$ -plane at  $w = a_0$  and represents, with  $\omega \rightarrow \infty$ , a curve such as shown in figure 7.6. In order to answer now the question of stability of the roots,  $s_v$ , we imagine a point,  $s = i\omega$ , on the imaginary axis of the  $s$ -plane and consider the connecting lines of the  $v$ th roots,  $s_v$ , to

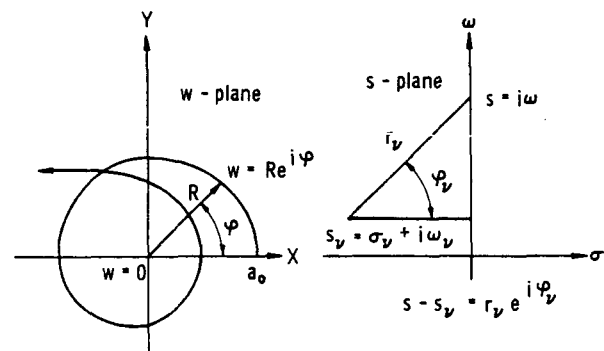


FIGURE 7.6.—Locus-curve method.

that point. This is, however, a factor of the product representation of the polynomial

$$w = P(s) = a_n \prod_{v=1}^n (s - s_v) = a_n \left( \prod_{v=1}^n r_v \right) e^{i \sum_{v=1}^n \phi_v} = R e^{i\phi}$$

where

$$w = X + iY$$

$$X = R \cos \phi$$

$$Y = R \sin \phi$$

From this, one obtains

$$R = a_n \prod_{v=1}^n r_v$$

$$\phi = \sum_{v=1}^n \phi_v$$

If none of the roots,  $s_v$ , is located on the imaginary axis, i.e.,  $r_v \neq 0$ , and if  $a_n > 0$ , it follows that  $R > 0$ , which means that  $X$  and  $Y$  have the same zeros as  $\cos \phi$  and  $\sin \phi$ , respectively. If all roots,  $s_v$ , are in the left-hand plane (stable roots), then  $\phi_v$  can cover only the angular region from  $-\pi/2$  to  $+\pi/2$  for  $s = i\omega$  moving on the imaginary axis. The angle,  $\phi$ , therefore, can only cover the angular region  $-n\pi/2$  to  $+n\pi/2$ ; or, for  $\omega = 0$  to  $\infty$ , it will cover the angular region 0 to  $n\pi/2$ . The angle,  $\phi$ , is the angle of the complex value  $w = R e^{i\phi}$  of the locus curve, and one now obtains the criterion:

The equation  $P(s) = 0$  has only roots with negative real part, if the locus curve  $w = P(s) = w(\omega)$  (for  $s = i\omega$ ) circles the origin  $w = 0$  in such a fashion, that the angle,  $\phi$ , covers the angular region from 0 to  $n\pi/2$  as  $\omega$  changes from 0 to  $\infty$  (counting positive toward the left).

If one root is in the positive half plane, say on the real axis, then the angle covers the region from  $\pi$  to  $\pi/2$ , in rotating by  $\pi/2$  in the negative sense. For  $\lambda$  stable and  $\mu$  unstable roots, the angle,  $\phi$ , yields a rotation of  $(\lambda - \mu)\pi/2 = m\pi/2$  in the positive sense, if  $\omega$  ranges from 0 to  $\infty$ . With  $n$  as the total number of roots

$$\lambda + \mu = n$$

$$\lambda - \mu = m$$

one concludes:

The polynomial of  $n$ th degree  $P(s) = 0$  has

$$\lambda = \frac{n+m}{2} \text{ stable roots}$$

and

$$\mu = \frac{n-m}{2} \text{ unstable roots}$$

if the locus curve for  $\omega = 0$  to  $\infty$  covers the angular region from 0 to  $(\lambda - \mu)\pi/2$  in the positive sense.

This method is particularly useful for investigating the effects of changes in physical parameters on the behavior of a dynamic system, especially if high-speed computing machines are available.

### General Criteria for Stability of Vehicle With No Propellant Sloshing

After the equations of motion have been formulated, as indicated in the preceding sections, a dynamic analysis of the vehicle in flight must be performed. The interaction of the bending of the flexible vehicle with the rigid body motion, the sloshing of the propellants, the reaction of the swivel engines and their compliance, the excitations provided by aerodynamic forces and wind gusts, and the coupling of the control system providing the stability of the space vehicle, must all be taken into account. The equations of motion have been linearized and can be solved on a high-speed computer. It is evident that a detailed formulation and dynamic analysis is beyond the scope of this monograph; however, it is possible to discuss more or less simplified sets of equations of motion which shall serve to illustrate gross effects and yet be of fundamental importance in the preliminary design of a space vehicle.

In order to maintain stable conditions throughout powered flight, it is necessary to avoid adverse feedback conditions arising from inherent phase lags of the sensing element and erroneous signals from bending vibrations. Especially for aerodynamically unstable vehicles, which are particularly sensitive to atmospheric disturbances, artificial stabilization through the control system (with accelerometer)

can alleviate the required control deflections of the gimbal engines, and reduce the loads which can be a potential hazard to the flight performance of the vehicle. We will consider here the problem of rigid and flexible vehicles, where the propellant is treated as rigid mass, and determine some of the basic requirements for the location of the sensors and their vibrational characteristics. Some criteria can be developed which yield enhanced stability of the vehicle without resorting to electrical filter networks, as is performed in a complete root locus analysis of the dynamic system. The sensors treated here comprise accelerometers and rate gyroscopes. With these assumptions, the equations of motion, considering only one bending mode, reduce to the following form:

*Translational motion:* Equation (7.16)

$$m\ddot{y} = F\phi + F_2\beta - F\eta Y'(x_E) \quad (7.36)$$

where  $Y$  is the first bending mode.

*Pitching motion:* Equation (7.17)

$$I\ddot{\phi} + F_2x_E\beta = F\{x_E\eta Y'(x_E) - \eta Y(x_E)\} \quad (7.37)$$

*Lateral bending vibration:* Equation (7.22)

$$\ddot{\eta} + g_B\omega_B\dot{\eta} + \omega_B^2\eta = \frac{F_2}{M_B} Y(x_E)\beta \quad (7.38)$$

The dynamic characteristics of the control sensors are represented by the following equations:

*Accelerometer:* Equation (7.28)

$$\frac{\ddot{A}_t}{\omega_a^2} + \frac{2\xi_a}{\omega_a} \dot{A}_t + A_t = \ddot{y} - \dot{x}_a\ddot{\phi} - g\phi + \ddot{\eta}Y(x_a) + \eta gY'(x_a) \quad (7.39)$$

*Rate gyro:* Equation (7.29)

$$\frac{\ddot{\theta}_t}{\omega_G^2} + \frac{2\xi_G}{\omega_G} \dot{\theta}_t + \theta_t = \ddot{\phi} - \ddot{\eta}Y'(x_R) \quad (7.40)$$

The control equation is used in its simplified form

$$p_2\ddot{\beta} + p_1\dot{\beta} + \beta = a_0\phi_t + a_1 \begin{Bmatrix} \dot{\phi}_t \\ \theta_t \end{Bmatrix} + g_2A_t \quad (7.41)$$

For a given configuration, the control requirements are strongly dependent on the mutual settings of the control system.

In the following discussion, numerical results have been presented for a Saturn I-type vehicle for which half of the thrust is available for control purposes (refs. 7.9 and 7.15).

#### Criteria for Position Gyroscope

This investigation presents the stability boundaries in the  $(Y'_G, g_B)$  plane, indicating at what location a gyroscope should be mounted to maintain stability for a certain structural damping  $g_B$  and for various gain values and lag coefficients.

The control equation, equation (7.27), was employed with an accelerometer gain value of  $g_2=0$ , that is, no additional accelerometer control. Neglecting the effect of translational motion and combining the equations for pitching motion, equation (7.37), and bending oscillations, equation (7.38), with the control equation, equation (7.41), leads to the condition that for this system of three homogeneous algebraic equations the coefficient determinant

$$\begin{vmatrix} Is^2\omega_c^2 & Fx_E & FY(x_E) - Fx_EY'(x_E) \\ 0 & -\frac{F_2Y(x_E)}{M_B} & s^2\omega_c^2 + g_Bs\omega_c\omega_B + \omega_B^2 \\ -(a_0 + a_1s\omega_c) & p_2s^2\omega_c^2 + p_1s\omega_c + 1 & (a_0 + a_1s\omega_c)Y'(x_G) \end{vmatrix} = 0$$

must vanish. The stability polynomial is of sixth degree. For  $p_2=0.0084$  and  $p_1=0.05$ , it was found that for a gyroscope location close to the antinode, the degree of structural

damping usually provided is sufficient to maintain stability. For low bending frequencies the location behind the antinode seems reasonable, but for larger bending frequencies

a location in front of the antinode also yields stability; this is due to the lag terms in the control equation.

If only the bending equation, equation (7.38), is combined with the simple control equation

$$\beta = a_0 \phi_i + a_1 \dot{\phi}_i$$

where

$$\phi_i = -\eta Y'(x_G)$$

the stability polynomial is of second order and exhibits stability if the coefficients are positive, and is of the form

$$s^2 \omega_c^2 + s \omega_c \left[ g_B \omega_B + \frac{F_2 Y(x_E) Y'(x_G)}{M_B} a_1 \right] + \left[ \omega_B^2 + \frac{F_2 Y(x_E) Y'(x_G)}{M_B} a_0 \right] = 0$$

Since all of the values in these coefficients are positive by their very nature except for  $Y'(x_G)$ , which can be either positive or negative, the system definitely exhibits stability for  $Y'(x_G) > 0$ , that is, for a positive bending mode slope at the location of the gyroscope. This means that the gyroscope should be located behind the antinode in the aft section of the vehicle. The stability boundary is at

$$Y'(x_G) = -\frac{M_B g_B \omega_B}{F_2 Y(x_E) a_1}$$

that is, slightly forward of the antinode.

#### Criteria for Rate Gyroscopic

We shall consider the stability criteria for a rate gyroscope by dividing our investigation into two parts: one in which the vehicle is considered as a rigid body, and the other in which the flexibility of the vehicle is described by the fundamental bending mode.

#### Rigid Body Stability

Treating the equation for pitching motion, equation (7.37), together with the rate gyroscope equation, equation (7.40), together with the simple control equation in its ideal form

$$\beta = a_0 \phi_i + a_1 \theta_i$$

and assuming again time dependency of the form  $e^{s\omega_c t}$ , the stability polynomial is obtained

by setting the coefficient determinant equal to zero. Thus

$$\begin{vmatrix} I s^2 \omega_c^2 & 0 & F_2 x_E \\ -s \omega_c & \frac{s^2 \omega_c^2}{\omega_G^2} + \frac{2 \zeta_G \omega_c}{\omega_G} s + 1 & 0 \\ -a_0 & -a_1 & 1 \end{vmatrix} = 0$$

which yields a fourth-order stability polynomial:

$$\sum_{\lambda=0} B_\lambda s^\lambda = 0$$

with the coefficients

$$B_4 = 1, B_2 = \frac{\omega_c^2}{\omega_G^2} + \frac{a_0 F_2 x_E}{I \omega_c^2}, B_0 = \frac{a_0 F_2 x_E \omega_G^2}{I \omega_c^4},$$

$$B_3 = \frac{2 \zeta_G \omega_G}{\omega_c}, B_1 = \frac{F_2 x_E a_1 \omega_G^2}{I \omega_c^3} + \frac{2 \zeta_G \omega_G a_0 x_E F_2}{I \omega_c^3}$$

with

$$\omega_c^2 = \frac{g x_E \epsilon a_0}{k^2}$$

and

$$\frac{g x_E a_1 \epsilon}{k^2} = 2 \zeta_G \omega_c$$

where

$$\epsilon g = \frac{F_2}{m}, g = \frac{F}{m}$$

is the longitudinal acceleration of the vehicle and  $k^2 = I/m$  is the square of the radius of gyration. This yields

$$B_4 = 1, B_2 = 1 + \frac{\omega_c^2}{\omega_G^2}, B_0 = \frac{\omega_G^2}{\omega_c^2},$$

$$B_3 = \frac{2 \zeta_G \omega_G}{\omega_c}, B_1 = 2 \frac{\omega_G}{\omega_c} \left[ \zeta_G \frac{\omega_G}{\omega_c} + \zeta_G \right]$$

The stability boundary is obtained by setting  $B_1 B_2 B_3 = B_0 B_3^2 + B_4 B_1^2$  which leads to

$$\left( \frac{\omega_c}{\omega_G} \right)^2 + \left( \frac{\zeta_G}{\omega_G} \right) \left( \frac{\omega_c}{\omega_G} \right) - 1 = 0$$

representing a hyperbola in the  $\left[ \left( \frac{\omega_c}{\omega_G} \right), \left( \frac{\zeta_G}{\omega_G} \right) \right]$ -plane.

Only the branch in the first quadrant of the coordinate system is of physical significance and is shown in figure 7.7. The cross-hatched area represents the stable area. From

this we can conclude that rigid body stability can be accomplished by choosing the natural frequency of the rate gyroscope larger than the control frequency and adjust its damping factor to an appropriate value. For a ratio of the damping factors of unity, a frequency ratio range of  $0 \leq \frac{\omega_c}{\omega_G} < \left(\frac{\sqrt{5}-1}{2}\right)$  would maintain stability of the rigid vehicle.

#### Bending Mode Stability

Taking, in this case, the bending equation, equation (7.38), and rate gyroscope equation, equation (7.40), together with the control equation, equation (7.41), while omitting all terms corresponding to rigid body motion, yields the coefficient determinant

$$\begin{vmatrix} s^2\omega_c^2 + g_B s\omega_c \omega_B + \omega_B^2 & -\frac{F_2}{M_B} Y(x_E) & 0 \\ s\omega_c Y'(x_R) & 0 & \frac{s^2\omega_c^2 + 2\xi_G \omega_c s}{\omega_G^2} + 1 \\ a_0 Y'(x_G) & p_2 s^2 \omega_c^2 + p_1 s \omega_c + 1 & -a_1 \end{vmatrix} = 0$$

The stability polynomial, which is of sixth degree, is reduced to a quartic by setting the phase through making the coefficients  $p_2 = p_1 = 0$ , which yields finally the stability boundary

$$\epsilon'_R = 0$$

and

$$\epsilon'_G + \left(\frac{\xi_G}{\omega_G}\right) \left(\frac{\omega_c}{\omega_G}\right) \epsilon'_R - \left(\frac{\omega_G}{\omega_c}\right)^2 \left[1 - \left(\frac{\omega_B}{\omega_G}\right)^2\right] = 0$$

where

$$\epsilon'_G = \frac{Y(x_E) Y'(x_R)}{M_B} |x_{cIR}|$$

and

$$\epsilon'_R = \frac{Y(x_E) Y'(x_R)}{M_B} |x_{cIR}|$$

The value  $|x_{cIR}|$  represents the distance between the center of instantaneous rotation and the mass center of the vehicle.

In the  $(\epsilon'_R, \epsilon'_G)$ -plane, as shown in figure

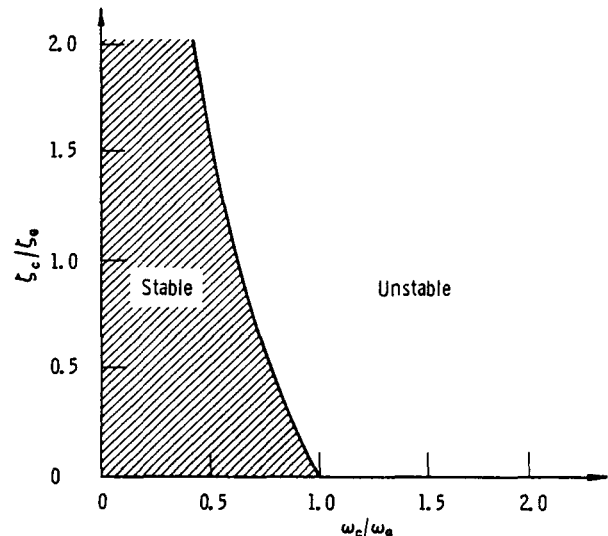


FIGURE 7.7.—Stability boundary for rigid vehicle with rate gyroscope.

7.8, this represents a family of straight lines. The distance of the intersection point with the axis from the origin is decreased by increasing the frequency ratio ( $\omega_B/\omega_G$ ), that is, by decreasing the rate gyroscope frequency toward the bending frequency. The slope of the stability boundary line decreases with decreasing damping ratio ( $\xi_G/\omega_G$ ) and increasing frequency ratio ( $\omega_c/\omega_G$ ). Since the frequency ratio is limited to a small value because of the rigid body stability, the slope is most effectively changed by the damping ratio. This indicates that a supercritical damping of the rate gyroscope is desirable. A further conclusion that can be drawn from figure 7.8 with regard to the proper location of the rate gyroscope is that positive slope  $Y'(x_R)$  minimizes stability.

Therefore, it can be concluded that the natural frequency for the rate gyroscope should be quite large compared with the control frequency and the highest to-be-controlled bending frequency under consideration. The

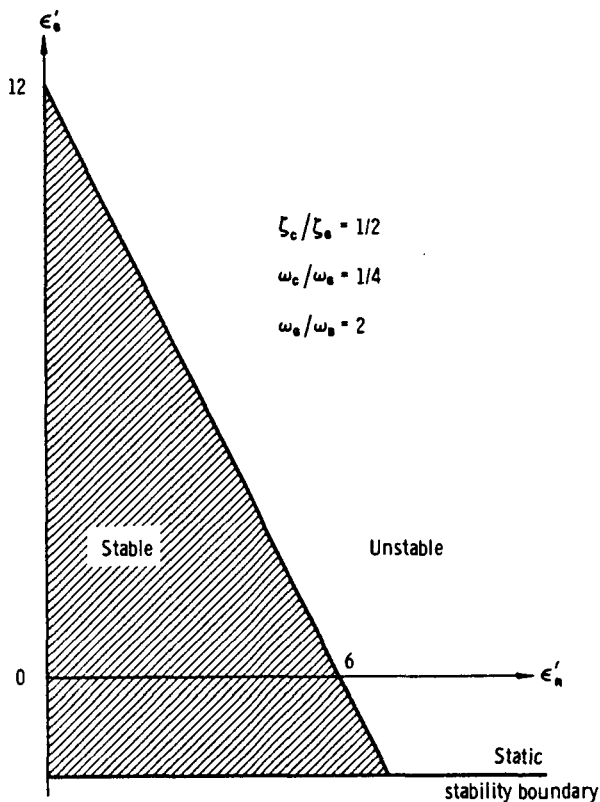


FIGURE 7.8.—Stability boundary for flexible vehicle with rate gyroscope.

damping should preferably be supercritical, or large in comparison with the control damping. Furthermore, the rate gyroscope should

be located behind the last antinode of the to-be-controlled bending modes.

#### Criteria for Accelerometer

In many vehicles, an accelerometer is used as an additional control element. By proper choice of its gain value in the control equation and its vibrational characteristics, such an element can help to diminish loads on the space vehicle and to reduce deflection requirements of the swivel engines. In this section, therefore, we shall investigate the effect of the vibrational characteristics and the gain value  $g_2$  of an accelerometer and shall try to determine simple criteria for the preliminary determination of those values (ref. 7.16).

#### Rigid Body Stability

Since the translational motion of the vehicle is sensed by an accelerometer, this has to be considered in a simplified stability analysis. Therefore, for rigid body stability, we treat the translational motion, equation (7.36), together with the pitching motion, equation (7.37), the accelerometer equation, equation (7.39), and the control equation, equation (7.41), together with the usual assumption  $e^{i\omega t}$  for the solution. The coefficient determinant that has to vanish yields, with  $\eta=0$ ,  $\phi_i=\phi$  and the phase coefficients  $p_1=p_2=0$ , the expression

$$\begin{vmatrix} m s^2 \omega_c^2 & -F \\ 0 & I s^2 \omega_c^2 \\ -s^2 \omega_c^2 & (x_a s^2 \omega_c^2 + g) \\ 0 & -(a_0 + s \omega_c a_1) \end{vmatrix} = 0$$

The stability condition, with  $B_1 B_2 B_3 \geq B_0 B_3^2 + B_4 B_1^2$  and  $|x_{c1R}| = k^2/x_E$ , is then given by

$$\begin{aligned} & \left( \frac{\zeta_c}{\zeta_a} \right) \left( \frac{\omega_c}{\omega_a} \right)^4 + 4 \zeta_c^2 \left( \frac{\omega_c}{\omega_a} \right)^3 + \left( \frac{\omega_c}{\omega_a} \right)^2 \left\{ 4 \zeta_c^2 \left( \frac{\zeta_c}{\zeta_a} \right) \right. \\ & \quad \left. + 4 \zeta_a \zeta_c - 2 \left( \frac{\zeta_c}{\zeta_a} \right) - \epsilon g g_2 (1+\alpha) \left( \frac{\zeta_c}{\zeta_a} \right) \right\} \\ & \quad + \left( \frac{\omega_c}{\omega_a} \right) \left\{ 4 \zeta_c^2 - \epsilon g g_2 (1+\alpha) \left[ 1 + \left( \frac{\zeta_c}{\zeta_a} \right)^2 \right] \right\} \\ & \quad + \left( \frac{\zeta_c}{\zeta_a} \right) [1 - \epsilon g g_2 (1+\alpha)] \geq 0 \end{aligned}$$

This is a polynomial of fourth degree in  $\omega_c/\omega_a$ .

The stability polynomial is of fourth degree with the coefficients

$$\begin{aligned} B_4 &= 1 \\ B_3 &= 2 \left\{ \zeta_a \frac{\omega_a}{\omega_c} + \zeta_c \right\} \\ B_2 &= 1 + \frac{\omega_a^2}{\omega_c^2} + 4 \zeta_a \zeta_c \frac{\omega_a}{\omega_c} - \epsilon g g_2 \frac{\omega_a^2}{\omega_c^2} \left[ 1 + \frac{x_a x_E}{k^2} \right] \\ B_1 &= 2 \frac{\omega_a}{\omega_c} \left[ \zeta_a + \zeta_c \frac{\omega_a}{\omega_c} \right] \\ B_0 &= \frac{\omega_a^2}{\omega_c^2} \end{aligned}$$

A case of special interest is the ideal accelerometer for which  $\omega_a \gg \omega_c$ . With  $\alpha \equiv x_a/|x_{cIR}|$ , the result of the above equation with  $\epsilon gg_2 = \lambda$ , yields the simple expression ( $|x_{cIR}|$  is the distance of the center of instantaneous rotation from the mass center)

$$\lambda = \frac{1}{1+\alpha}$$

which is shown in figure 7.9. From this it can be concluded that an accelerometer should be located forward of the center of instantaneous rotation to allow all possible gain values  $\lambda (> 0)$ . With decreasing gain values  $\lambda$ , the location of the accelerometer becomes less important for rigid body stability. Figures 7.10 and 7.11 show the influence of the natural frequency,  $\omega_a$ , of the accelerometer and of the damping factor,  $\zeta_a$ . The influence of the change of these parameters is not very pronounced and does not exhibit a large difference from the results for an ideal accelerometer. If the natural frequency of the accelerometer, however, is small (which should be avoided in many respects), the stability boundary curves spread a little more. One can conclude from the above results that a location forward of the mass center will insure stability of the rigid body. With decreasing gain values, the location of the accelerometer becomes less impor-

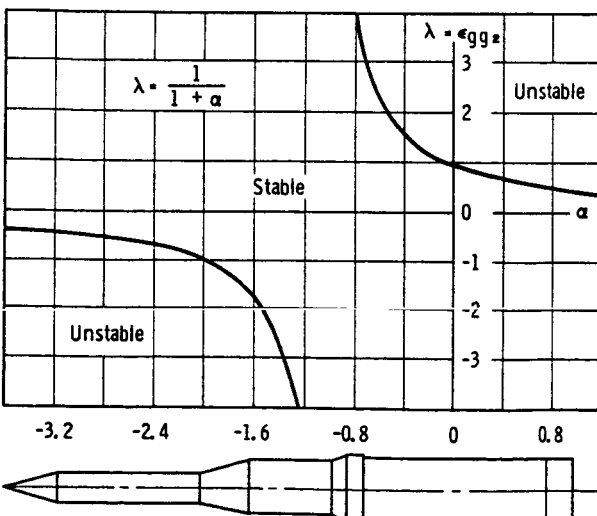


FIGURE 7.9.—Stability boundary for rigid vehicle with ideal accelerometer control.

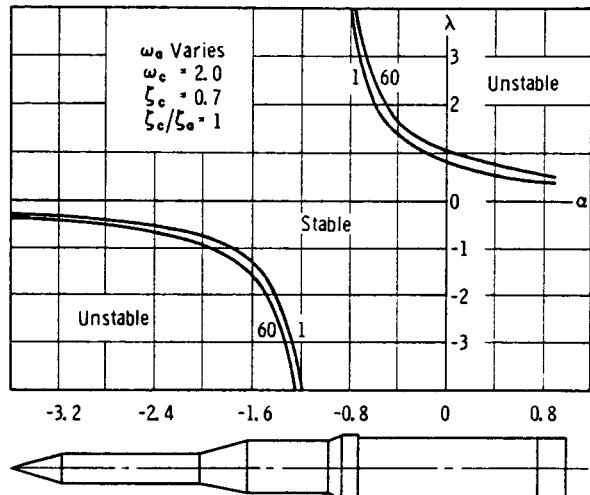


FIGURE 7.10.—Stability boundaries for rigid vehicle with accelerometer control of various natural frequency.

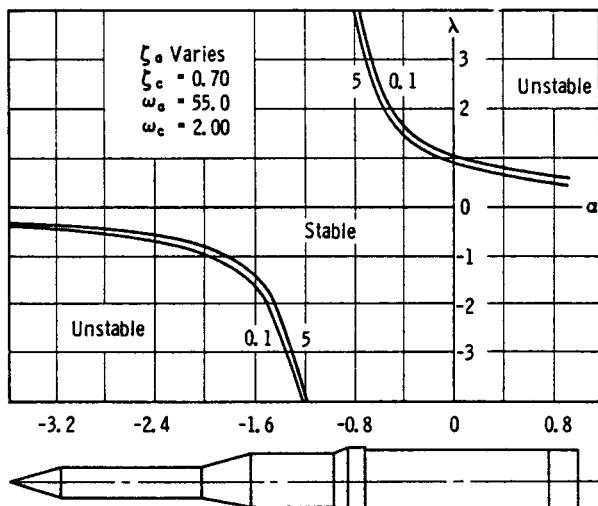


FIGURE 7.11.—Stability boundaries for rigid vehicle with accelerometer control of various damping factor,  $\zeta_a$ .

tant, indicating that a location aft of the mass center also becomes permissible.

It should be mentioned that the expression

$$\omega_c^2 = \frac{\epsilon g x_B a_0}{k^2}$$

represents the undamped natural frequency of the rigid body (referred to as the control frequency) without accelerometer control. The actual control frequency with accelerometer control depends upon the gain value and loca-

tion of the accelerometer and is given by the expression

$$\omega_{ca}^2 = \frac{\epsilon g x_E a_0}{k^2(1-\lambda-\lambda\alpha)}$$

From this it can be seen that a location,  $x_a$ , of the accelerometer near the center of instantaneous rotation, that is,  $\alpha=-1$ , makes the control frequency nearly independent of the gain value,  $\lambda$ . For this value,  $\lambda\alpha$ , failure of the

control accelerometer would therefore not result in an abrupt change of the control frequency and would not drastically influence the stability behavior of the vehicle.

#### Bending Mode Stability

Considering only the vehicle, equation (7.38), and its interaction with the accelerometer, equation (7.39), and the control equation, equation (7.41), yields the stability determinant

$$\begin{vmatrix} s^2\omega_c^2 + g_B\omega_B s\omega_c + \omega_B^2 & -\frac{F_2}{M_B} Y(x_E) & 0 \\ -[s^2\omega_c^2 Y(x_a) + g Y'(x_a)] & 0 & \frac{s^2\omega_c^2}{\omega_a^2} + \frac{2\zeta_a\omega_c s}{\omega_a} + 1 \\ (a_0 + a_1 s\omega_c) Y'(x_G) & p_2\omega_c^2 s^2 + p_1\omega_c s + 1 & -g_2 \end{vmatrix} = 0$$

The stability polynomial is of sixth degree. Assuming, for reasons of simplification as before, that the phase-lag coefficients vanish, that is,  $p_1=p_2=0$ , the stability polynomial reduces to one of fourth degree. The coefficients are given by

$$\begin{aligned} B_4 &= 1 \\ B_3 &= 2\zeta_a \frac{\omega_a}{\omega_c} + 2\epsilon'_G \zeta_c \\ B_2 &= \frac{\omega_B^2 + \omega_a^2}{\omega_c^2} - \lambda\epsilon_a \frac{\omega_a^2}{\omega_c^2} + \epsilon'_G \left( 1 + 4\zeta_c \zeta_a \frac{\omega_a}{\omega_c} \right) \\ B_1 &= 2\zeta_a \frac{\omega_a}{\omega_c} \left[ \frac{\omega_B^2}{\omega_c^2} + \epsilon'_G \right] + 2\zeta_c \epsilon'_G \frac{\omega_a^2}{\omega_c^2} \\ B_0 &= \frac{\omega_B^2 \omega_a^2}{\omega_c^4} - \epsilon'_a \lambda \frac{\omega_a^2}{\omega_c^2 a_0 \epsilon} + \epsilon'_G \frac{\omega_a^2}{\omega_c^2} \end{aligned}$$

where

$$\epsilon_a = \frac{Y(x_E)Y(x_a)}{\frac{M_B}{m}}$$

and

$$\epsilon'_a = \frac{Y(x_E)Y'(x_a)}{\frac{M_B}{m}} |x_{cIR}|$$

For an even more simple criterion, let us assume that the position gyroscope is mounted at the antinode of the bending mode, that is, at the location where the slope of the bending mode vanishes ( $\epsilon'_G=0$ ). With this assumption, the coefficients of the stability polynomial yield

$$\begin{aligned} B_4 &= 1 \\ B_3 &= 2\zeta_a \frac{\omega_a}{\omega_c} \\ B_2 &= \frac{\omega_B^2 + \omega_a^2}{\omega_c^2} - \lambda\epsilon_a \frac{\omega_a^2}{\omega_c^2} \\ B_1 &= 2\zeta_a \frac{\omega_B^2 \omega_a}{\omega_c^2} \\ B_0 &= \frac{\omega_B^2 \omega_a^2}{\omega_c^4} - \frac{\lambda\epsilon'_a \omega_a^2}{a_0 \epsilon} \end{aligned}$$

The static stability limit is established from the coefficient  $B_0$ , which yields

$$\epsilon'_a \leq \frac{\omega_B^2 a_0 \epsilon}{\omega_c^2 \lambda}$$

where the equal sign expresses the boundary. In the  $(\epsilon_a, \epsilon'_a)$ -plane, this represents a line parallel to the  $\epsilon_a$ -axis and with a distance from the  $\epsilon_a$ -axis which increases with the increase of the frequency ratio  $\omega_B/\omega_c$ , the bending frequency over the control frequency (without accelerometer). With increasing attitude gain value,  $a_0$ , this boundary shifts farther away from the  $\epsilon_a$ -axis. Increasing the accelerometer gain, that is, providing more influence of the accelerometer on the control of the vehicle, decreases the distance of the static stability boundary from the  $\epsilon_a$ -axis. The dynamic stability is expressed by

$$\epsilon'_a \geq a_0 \epsilon \left( \frac{\omega_B}{\omega_c} \right)^2 \epsilon_a$$

where the equal sign represents the stability boundary (fig. 7.12). In the  $(\epsilon_a - \epsilon'_a)$ -plane the stability boundary represents a straight line of slope  $a_0 \epsilon \left( \frac{\omega_B}{\omega_c} \right)^2$  through the origin. Stability is therefore provided below the parallel line to the  $\epsilon_a$ -axis (static stability boundary) and to the left of the straight line (dynamic stability boundary). With increasing attitude control gain,  $a_0$ , the dynamic stability boundary rotates toward the  $\epsilon'_a$ -axis, providing a large part of the left half plane for stability; in addition, the static stability boundary moves upward. This expresses that a limited range for the location along the vehicle can be provided for the mounting of a control accelerometer. If  $\epsilon_a$  is negative, that is, the accelerometer is mounted at a location where the bending mode exhibits negative values (vehicle normalized to unity at the gimbal station  $x_E$ ), then positive and negative values for the slope of the bending mode are available for the location of the accelerometer. With increasing frequency ratio of bending to control frequency, the same trend occurs. For an increase of the availability of thrust for control purposes, the static stability boundary remains at its position, while the dynamic stability boundary rotates again toward the vertical. For increasing accelerometer gain,  $\lambda$ , the static stability boundary moves toward the  $\epsilon_a$ -axis while the dynamic stability boundary remains fixed, which indicates that a more restricted range of locations for the mounting of a control accelerometer is available.

### Propellant Sloshing in One Container of a Vehicle With Simple Control System

In order to obtain some of the basic effects of the influence of propellant sloshing upon vehicle stability without expending any great numerical effort, the equations of motion of the vehicle will be treated with the propellant as free to oscillate in one container only. The vehicle will be considered as rigid ( $\eta_r = 0$ ) and only the most pronounced modal sloshing mass (see ch. 6) will be retained in the analysis; that is,  $\lambda = 1$  and  $n = 1$ . Introducing  $\eta_r = 0$  and  $n = \lambda = 1$  into equations (7.16), (7.17), (7.20), (7.26), and (7.28), one obtains the equations of motion for the rigid vehicle with propellant sloshing in one container and additional accelerometer control (refs. 7.17 and 7.18).

$$\dot{m}\ddot{y} + m_{11}\ddot{y}_{11} - F\phi - F_2\beta = 0 \quad (7.42)$$

$$\ddot{I}\phi - m_{11}x_{11}\ddot{y}_{11} - gm_{11}\ddot{y}_{11} + F_2x_E\beta = 0 \quad (7.43)$$

$$\ddot{y}_{11} + 2\xi_{11}\omega_{11}y_{11} + \omega_{11}^2y_{11} + \ddot{y} - x_{11}\ddot{\phi} - g\phi = 0 \quad (7.44)$$

$$\beta - a_0\phi - a_1\dot{\phi} - g_2A_i = 0 \quad (7.45)$$

$$\frac{\ddot{A}_i}{\omega_a^2} + \frac{2\xi_a}{\omega_a} \dot{A}_i + A_i - \ddot{y} + x_a\ddot{\phi} + g\phi = 0 \quad (7.46)$$

The first equation represents translational motions and the second one represents pitching motion of the vehicle. Equation (7.44) is the sloshing equation describing the motion of the first modal sloshing mass. The fourth equation represents the control, which indicates that a position gyroscope and additional accelerometer are employed for the control of the vehicle. Finally, the last equation represents the dynamics of the control accelerometer. If an ideal accelerometer were employed, that is,  $\omega_a \gg \omega_c$ , the first and second terms of equation (7.46) would be neglected. A control system employing no accelerometer control would lead to the omission of the last equation and a vanishing gain value  $g_2$  in equation (7.45). The stability of the solutions of such a system is again obtained by assuming a solution of the

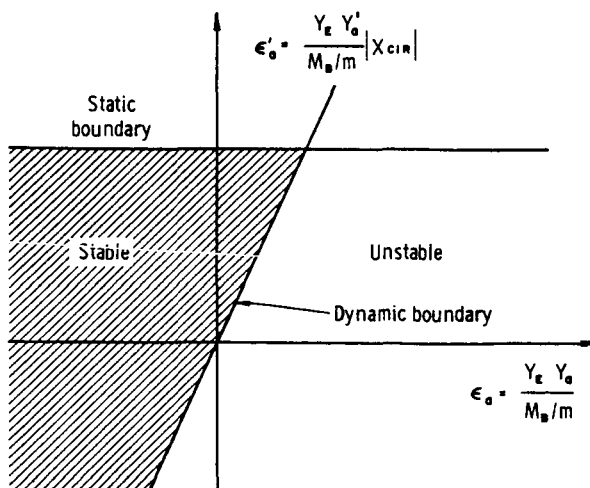


FIGURE 7.12.—Stability boundaries for flexible vehicle with accelerometer control.

form  $e^{s\omega_c t}$ , where  $s$  is the complex frequency,  $s=\sigma+i\omega$ . This assumption for the solution transforms the differential equations into a homogeneous algebraic system, which exhibits nontrivial solutions only if the determinants of

$$\begin{array}{cc|cc} (y) & (\phi) & (y_{11}) & (A_t) \\ \hline s^2\omega_c^2 & -g(1+\epsilon a_0+a_1\epsilon\omega_c s) & \mu_{11}s^2\omega_c^2 & -\lambda\epsilon \\ 0 & s^2\omega_c^2 + \frac{\epsilon g x_E}{k^2} (a_0+a_1 s \omega_c) & -\frac{\mu_{11}}{k^2} (x_{11}\omega_c^2 s^2 + g) & \frac{\lambda x_E \epsilon}{k^2} \\ s^2\omega_c^2 & -(x_{11}\omega_c^2 s^2 + g) & \omega_c^2 s^2 + 2\omega_c \omega_{11} \xi_{11} s + \omega_{11}^2 & 0 \\ -s^2\omega_c^2 & (x_a \omega_c^2 s^2 + g) & 0 & \frac{s^2\omega_c^2}{\omega_a^2} + \frac{2\xi_a \omega_c s}{\omega_a} + 1 \end{array} = 0 \quad (7.47)$$

Here,  $\lambda=gg_2$  and  $\mu_{11}=m_{11}/m$  is the ratio of the sloshing mass in the container to the total mass of the vehicle. The coefficient determinant yields then the characteristic polynomial in  $s$

$$\sum_{i=0}^6 B_i s^i = 0$$

where the coefficients,  $B_i$ , are represented as polynomials of  $\xi_s$  and  $\gamma_s$ ,

$$\begin{aligned} B_6 &= k_{17} + k_{18}\xi_s^2 \\ B_5 &= k_{13} + 2k_{14}\gamma_s + k_{15}\xi_s + k_{16}\xi_s^2 \\ B_4 &= k_9 + 2k_{10}\gamma_s + k_{11}\xi_s + k_{12}\xi_s^2 \\ B_3 &= k_6 + 2k_7\gamma_s + k_8\xi_s \\ B_2 &= k_3 + 2k_4\gamma_s + k_5\xi_s \\ B_1 &= k_1 + 2k_2\gamma_s \\ B_0 &= k_0 \end{aligned} \quad (7.48)$$

The location of the modal mass,  $\xi_{11}=x_{11}/k\equiv\xi_s$  (with respect to the mass center), and the damping factor,  $\xi_{11}\equiv\gamma_s$ , are extracted, since they are the ones by which the stability of the vehicle can be influenced most readily; the representation of the stability boundaries will be in these coordinates. This therefore yields not only the magnitude of the damping required in the tanks but also its location. The abbreviations  $k_j$  ( $j=0, 1, 2, \dots, 18$ ) depend on the frequency and damping factors, and the gain values of the control system, as well as

coefficients vanish. With only the part  $F_2=\epsilon F$  available for control purposes,  $F_1=(1-\epsilon)F$  and the longitudinal acceleration of the vehicle is  $g=F/m$ . The coefficient determinant is therefore

on the mass ratio,  $\mu_{11}\equiv\mu$ , and the vibrational characteristics of the accelerometer. With the notations  $\xi_c$  as the damping factor of the control system,  $\omega_c$  as the circular frequency of the control system,  $\omega_c^2=\omega_{c0}^2/(1-\lambda\epsilon-\lambda x_E x_a \epsilon/k^2)$  and  $\omega_{c0}$  as the circular frequency of the control system without accelerometer ( $\omega_{c0}^2=gx_E \epsilon a_0/k^2$ ), and  $\xi_E=x_E/k$ ,  $\xi_a=x_a/k$  as the distance with respect to the radius of gyration, and  $\nu_s=\omega_s/\omega_c$ ,  $\nu_a=\omega_a/\omega_c$  as the ratios of the eigenfrequencies of sloshing and accelerometer ( $\omega_{11}\equiv\omega_s$ ) as well as the value  $\Lambda=1-\epsilon\lambda(1+\xi_E \xi_a)$ , and with

$$a_1 = \frac{2\xi_c a_0}{\omega_c}; \quad \frac{gx_E a_1 \epsilon}{k^2} = 2\xi_c \omega_c (1-\lambda\epsilon-\lambda x_E x_a)$$

the coefficients  $k_j$  are given by the expressions:

$$\begin{aligned} k_0 &= \Lambda \left[ \nu_s^2 + \frac{\mu\Lambda}{a_0 \xi_E \epsilon} \right] \\ k_1 &= 2\Lambda \left( \xi_c + \frac{\xi_a}{\nu_a} \right) \left[ \frac{\mu\Lambda}{a_0 \xi_E^2 \epsilon} + \nu_s^2 \right]; \quad k_2 = \Lambda \nu_s \\ k_3 &= \Lambda \left\{ \frac{1}{\nu_a} \left( \frac{1}{\nu_a} + 4\xi_c \xi_a \right) \left( \frac{\mu\Lambda}{a_0 \xi_E^2 \epsilon} + 1 \right) \right. \\ &\quad \left. + 1 - \mu + \nu_s^2 - \frac{\mu\Lambda \xi_a}{a_0 \xi_E} \right\} \\ k_4 &= 2\nu_s \Lambda \left( \xi_c + \frac{\xi_a}{\nu_a} \right); \quad k_5 = \frac{\mu\Lambda}{a_0 \xi_E \epsilon} (a_0 \epsilon - 1 + \lambda\epsilon) \\ k_6 &= 2\xi_a \frac{\nu_s^2}{\nu_a} + \Lambda \left\{ \frac{2\mu \xi_c \Lambda}{a_0 \xi_E^2 \nu_a^2 \epsilon} + 2(1-\mu) \frac{\xi_a}{\nu_a} \right. \\ &\quad \left. + 2\xi_c \left( 1 - \mu - \frac{\nu_s^2}{\nu_a^2} \right) \right\} \end{aligned}$$

$$\begin{aligned}
 k_7 &= \Lambda \left\{ \nu_s + 4\xi_a \xi_c \frac{\nu_s}{\nu_a} + \frac{\nu_s}{\nu_a^2} \right\} \\
 k_8 &= \frac{2\mu\Lambda}{\nu_a \xi_E} \left\{ \xi_c \nu_a + \xi_a - \frac{\xi_a}{a_0 \epsilon} \right\} \\
 k_9 &= \frac{\nu_s^2}{\nu_a^2} - \epsilon \mu \lambda + \frac{\Lambda(1-\mu)}{\nu_a^2} [1 + 4\xi_c \xi_a \nu_a + \nu_a^2] \\
 k_{10} &= \frac{2\nu_s}{\nu_a^2} [\xi_c \Lambda + \xi_a \nu_a] \\
 k_{11} &= \frac{\Lambda \mu}{\xi_E a_0 \nu_a^2 \epsilon} [a_0 \epsilon + 4\xi_c \xi_a a_0 \nu_a \epsilon - 1] - \mu \lambda \epsilon (\xi_E + \xi_a) \\
 k_{12} &= \mu(\lambda \epsilon - 1); k_{13} = \frac{2(1-\mu)}{\nu_a^2} [\xi_a \nu_a + \xi_c \Lambda]; k_{14} = \frac{\nu_s}{\nu_a^2} \\
 k_{15} &= \frac{2\mu\Lambda\xi_c}{\xi_a \nu_a^2}; k_{16} = -\frac{2\mu\xi_a}{\nu_a}; k_{17} = \frac{1-\mu}{\nu_a^2}; k_{18} = -\frac{\mu}{\nu_a^2}
 \end{aligned}$$

The various parameters are as follows:

$\mu = m_s/m$  = ratio of modal mass of liquid to total mass of space vehicles

$\xi_c$  = control damping factor

$\nu_s = \omega_s/\omega_c$  = frequency ratio of undamped propellant frequency to undamped control frequency

$\gamma_s$  = damping factor of propellant  
 $\nu_a = \omega_a/\omega_c$  = frequency ratio of undamped accelerometer frequency to undamped control frequency  
 $\xi_a$  = damping factor of the accelerometer  
 $\lambda = gg_2$  = product of longitudinal acceleration of the vehicle and gain value of the accelerometer  
 $\xi_s = x_s/k$  = ratio of the coordinate of the accelerometer location to radius of gyration of the space vehicle  
 $\xi_s = x_s/k$  = ratio of the coordinate of the location of the modal mass of the propellant to radius of gyration of the space vehicle  
 $a_0$  = gain value of the attitude control system

The stability boundaries are characterized by the roots,  $s$ , one of which at least will have a zero real part, while the others are stable roots. The theorem of Hurwitz for a stability polynomial of the  $n$ th degree (ref. 7.13)

$$B_n = 0, \quad H_{n-1} = 0$$

where  $H_{n-1}$  represents the Hurwitz determinant of the form

$$H_{n-1} = \begin{vmatrix} B_1 & B_3 & B_5 & \dots \\ B_0 & B_2 & B_4 & \dots \\ 0 & B_1 & B_3 & \dots \\ 0 & B_0 & B_2 & \dots \\ \dots & \dots & \dots & \dots \end{vmatrix} \quad (n-1) \text{ lines and columns}$$

Representing the stability boundaries in the  $(\xi_s, \gamma_s)$ -plane, the Hurwitz determinant  $H_s = 0$  results in a polynomial

$$\sum_{j=0}^5 C_j(\xi_s) \gamma_s^j = 0$$

where the functions  $C_j(\xi_s)$  are polynomials in  $\xi_s$ . The stability boundary for the undamped liquid is  $C_0(\xi_s) = 0$ , and represents the intersection points with the  $\xi_s$ -axis. For all points  $(\xi_s, \gamma_s)$  above the stability boundary, one obtains stability. Because of  $B_n = 0$ , the stability is interrupted at the left and at the

right so that only within these boundaries is stability guaranteed. The stability boundaries of  $B_n = 0$  to the right and left are given in the form of straight lines perpendicular to the  $\xi_s$ -axis as

$$\xi_s = \pm \sqrt{\frac{k_{17}}{k_{18}}} = \pm \frac{\sqrt{1-\mu}}{\mu}$$

For most vehicles, however, these boundaries play no practical role. Substitution of  $\xi_s = \gamma_s = 0$  into the Hurwitz determinants determines whether the origin is in the stable or unstable region. A necessary and sufficient condition for stability is (ref. 7.19)

(1) The coefficients:

$$B_n, B_{n-1}, B_{n-3} \dots > 0$$

$$B_1, B_0 > 0 \text{ for even } n$$

$$B_0 > 0 \text{ for odd } n$$

(2) The Hurwitz determinants:

$$H_{n-1}, H_{n-3} \dots > 0$$

$$H_3 > 0 \text{ if } n \text{ is even}$$

$$H_2 > 0 \text{ if } n \text{ is odd}$$

#### Rigid Space Vehicle Without Accelerometer Control

Using a simple control system without an accelerometer ( $\lambda=0$ ) results in a stability polynomial of fourth degree. The coefficients  $B_i$  would be obtained from equations (7.48) and (7.49) if one introduces  $\omega_a=\infty$  and  $\lambda=0$ , which yields  $B_6=B_5=0$ . The stability boundaries due to  $B_n=0$  are again straight lines given by  $\xi_s = \pm \frac{\sqrt{(1-\mu)}}{\mu}$ . The stability boundary, from the Hurwitz determinant  $H_{n-1}=0$  (here  $H_3=0$  or  $B_1B_2B_3=B_0B_3^2+B_1^2B_4$ ), is then given by the expression

$$(K_1 + K_2\xi_s + K_3\xi_s^2) + 2\gamma_s(K_4 + K_5\xi_s + K_6\xi_s^2) + 4\gamma_s^2(K_7 + K_8\xi_s + K_9\xi_s^2) + 8\gamma_s^3 = 0$$

where

$$K_1 = k_1k_3k_6 - k_1^2k_9 - k_0k_6^2$$

$$K_2 = k_1k_5k_6 + k_1k_3k_8 - 2k_0k_6k_8 - k_1^2k_{10}$$

$$K_3 = k_1k_5k_8 - k_0k_8^2 - k_2^2k_{11}$$

$$K_4 = k_1k_4k_6 + k_2k_3k_6 + k_1k_3k_9 - 2k_0k_6k_7 - 2k_1k_2k_9$$

$$K_5 = k_2k_5k_6 + k_1k_5k_7 + k_1k_4k_8 + k_2k_3k_8 - 2k_0k_1k_8 - 2k_1k_2k_{10}$$

$$K_6 = k_2k_5k_8 - 2k_1k_2k_{11}$$

$$K_7 = k_2k_4k_6 + k_1k_4k_7 + k_2k_3k_7 - k_0k_7^2 - k_2^2k_9$$

$$K_8 = k_2k_5k_7 + k_2k_4k_8 - k_2^2k_{10}$$

$$K_9 = k_2^2k_{11}$$

$$K_{10} = k_2k_4k_{11}$$

The points of intersection of this stability boundary with the  $\xi_s$ -axis are obtained by setting  $\gamma_s=0$  and solving the quadratic equation

$$K_1 + K_2\xi_s + K_3\xi_s^2 = 0$$

The roots of this quadratic equation yield

$$\xi_1 = -|\xi_d|$$

$$\xi_2 = |\xi_d|(1-\mu)/a_0\nu_s^2$$

and give a first estimate for the critical area. The value  $1/a_0\nu_s^2$  has been considered to be of small magnitude. This assumption is satisfied in some cases if the control frequency is far enough away from the first natural frequency of the liquid. Therefore, the result expresses that the stability boundary for small values of  $1/a_0\nu_s^2$  intersects the  $\xi_s$ -axis in the vicinity of the center of mass (origin) and the instantaneous center of rotation  $\xi_d = x_d/k$ .

One can see that the second point of intersection,  $\xi_2$ , becomes sensitive to changes of  $1/a_0\nu_s^2$ , which indicates that for decreasing gain values,  $a_0$ , the intersection point shifts toward the tail of the vehicle. The same behavior occurs if  $\nu_s = \omega_s/\omega_c$  decreases. This means that, for a decreasing eigenfrequency of the liquid (or increasing control frequency), damping of the propellant must be provided in a container in the aft section of the vehicle in order to maintain stability. Figure 7.13 indicates that the danger zone for instability of the vehicle is located approximately between the center of gravity and the center of instantaneous rotation. In this zone, the propellant must be more or less damped, depending on the magnitude of the modal mass of the liquid. For

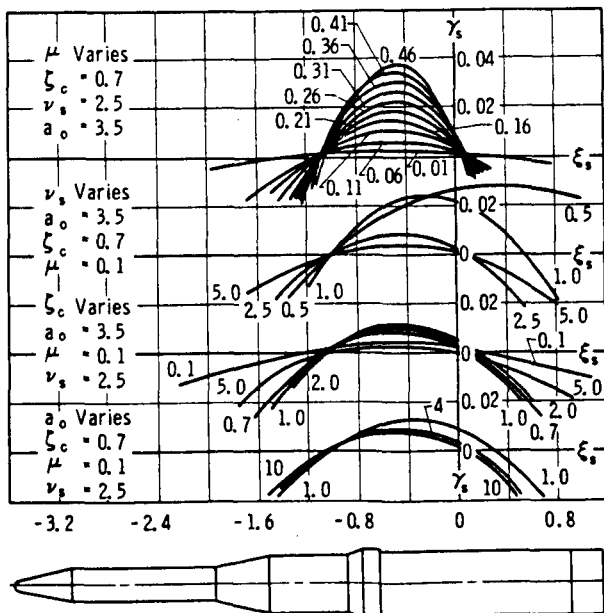


FIGURE 7.13.—Stability boundaries of rigid vehicle with simple control system.

increasing modal mass, more damping is needed in the danger zone. This is most unfavorable if the control frequency is below the natural frequency of the propellant; that is, if  $\nu_s < 1.0$ . For  $\nu_s > 2$ , the wall friction ( $\gamma_s = 0.01$ ) alone is sufficient to guarantee stability.

The change of the control damping,  $\xi_c$ , indicates that, for increasing subcritical damping,  $\xi_c < 1$ , the stability in the danger zone will be diminished while, for increased supercritical damping,  $\xi_c > 1$ , the stability is enhanced. This means that less damping is necessary in the container to maintain stability in the case  $\xi_c > 1$ . No additional baffles are required in the danger zone if (for a mass ratio  $\mu = 0.1$ ) the control damping  $\xi_c \leq 0.5$ , or  $\xi_c \geq 2.0$ . This indicates that, for these values and the parameters  $\nu_s = 2.5$  and  $a_0 = 3.5$ , the wall friction in the container is sufficient to maintain stability.

Another important question in the design of a large space vehicle is the choice of the form of the propellant containers. We observed in chapter 2 that tank geometry plays an important role in governing the modal masses and the natural frequencies of the propellant. Containers with large diameters exhibit small natural frequencies, which often are too close to the control frequency. Of course, the magnitude of the modal mass considerably emphasizes this unfavorable effect upon the stability. Clustering of numerous smaller containers not only increases the natural frequencies of the propellant (because of the smaller diameters) but also reduces the modal masses, which is a much more important effect. In addition to weight saving and the slight increase of the natural frequencies, subdivision

of tanks by sector walls has the advantage of distributing the modal masses to different vibration modes of the liquid. To summarize then, we note that with increasing mass, the stability naturally decreases. The influence of the eigenfrequency change of the propellant with fixed modal mass is such that a decrease of the natural frequency increases the danger zone toward the end of the vehicle and requires more local damping in the propellant. With increasing natural frequency of the liquid, the influence of the propellant sloshing on the stability of the vehicle diminishes more and more. Wall friction alone is then already sufficient to maintain stability.

The gain value,  $a_0$ , of the attitude control system shows, for decreasing magnitude, a decrease of stability in addition to a small enlargement of the danger zone toward the end of the vehicle.

For these numerical results, a Saturn I-type space vehicle of a length of about 170 feet was employed, as before.

#### *Rigid Space Vehicle With Ideal Accelerometer Control (ref. 7.16)*

By introducing an additional control element into the control system in the form of an ideal accelerometer ( $\omega_a \gg \omega_c$ ), and properly choosing the gain value,  $g_2$ , which determines the influence of the accelerometer in the control system, the danger zone can be minimized considerably. Because of  $\nu_a \gg 1$ , the coefficients of the stability polynomial are  $B_6 = B_5 = 0$ , and one obtains again a stability polynomial of fourth degree. The same formulas as in the previous case are valid, except that in the values  $k$ , the appropriate terms with  $\lambda$  have to be considered. The boundaries  $B_4 = 0$  are again straight lines, given by the equation

$$\xi_s = \frac{\frac{1}{4\mu(\epsilon\lambda - 1)} \{2\mu\lambda\epsilon(\xi_B + \xi_a) \pm \sqrt{4\mu^2\lambda^2\epsilon^2(\xi_B + \xi_a)^2 - 16\mu(\lambda\epsilon - 1)[1 - \mu - \lambda\epsilon - \lambda\epsilon(1 - \mu)\xi_B\xi_a]}\}}{\sqrt{1 - \frac{1}{16\mu^2(\epsilon\lambda - 1)^2} \{2\mu\lambda\epsilon(\xi_B + \xi_a) \pm \sqrt{4\mu^2\lambda^2\epsilon^2(\xi_B + \xi_a)^2 - 16\mu(\lambda\epsilon - 1)[1 - \mu - \lambda\epsilon - \lambda\epsilon(1 - \mu)\xi_B\xi_a]\}}^2}}$$

and are parallel to the  $\gamma_s$ -axis. For values of  $\lambda = gg_2 < 1$ , the danger zone is located approximately behind the center of instantaneous rotation and shifts with decreasing gain value  $g_2$  toward a zone between the mass center and

the center of instantaneous rotation. The stability decreases, which means more damping in the tank is necessary for increasing  $\lambda > 1$ . This indicates that, for a greater influence of the accelerometer in the control system, the

danger zone shifts forward of the center of instantaneous rotation and increases with increasing gain value toward the nose of the vehicle (fig. 7.14). For propellant containers in this location, strong damping must be employed to obtain stability. For values of  $\lambda=1.5$ , the vehicle is unstable if the tank, even with only a 10-percent slosh mass, is located in front of the center of instantaneous rotation, unless additional baffles are provided. For containers behind the center of instantaneous rotation, the vehicle is stable. Furthermore, one recognizes that  $\lambda \approx 1.0$  represents the most favorable gain value. In this case, the danger zone shrinks to a small region around the center of instantaneous rotation, in which case the wall friction of the propellant is usually sufficient to provide a stable flight situation.

Changes in the other parameters, such as the slosh mass ratio,  $\mu$ , the frequency ratio,  $\nu_s = \omega_s/\omega_c$ , the control system damping,  $\zeta_c$ , as well as the gain value,  $a_0$ , of the attitude system, exhibit the same influences as in the previous case. An enlargement of the danger zone toward the end of the vehicle occurs for large control frequencies and also for small propellant frequencies ( $\nu_s < 1$ ), even in the most favorable case in which  $\lambda=1.0$ .

The addition of an accelerometer introduces another important parameter: its location  $\xi_a$ . For  $\lambda=1$ , the most favorable case for an ideal accelerometer, the influence of its location upon stability of the vehicle is unimportant. For other values of  $g_2$ , the location of the accelerometer has considerable influence upon stability. A stronger effect of the accelerometer (say  $\lambda >$

1.5) in the control system and a location in front of the center of mass yields large instability if the container is located behind the center of instantaneous rotation with the accelerometer being in front of the center of mass. Propellant sloshing in those tanks located forward of the center of instantaneous rotation will make the vehicle unstable if the accelerometer is forward of the center of mass. For decreasing values  $g_2 < 1/g$ , the stability behavior of the vehicle approaches that of a rigid vehicle without additional accelerometer control. It should, however, be mentioned here that these results are too optimistic, since every accelerometer has its own vibrational characteristics which must be considered.

#### Rigid Space Vehicle With Accelerometer Control of Nonideal Characteristic

The dynamic behavior of an accelerometer, its natural frequency,  $\omega_a$ , and damping factor,  $\zeta_a$ , have a nonnegligible influence upon the overall stability of the vehicle. From the results of equations (7.47), (7.48), and (7.49), it is recognized that the stability polynomial is of sixth degree; therefore, the stability boundaries are given by  $H_s=0$ , and  $B_s=0$ .

The main influence arises from the natural frequency of the accelerometer. In the numerical evaluation, two circular frequencies ( $\omega_a=55$  and 12 rad/sec) were considered for the accelerometer. For decreasing accelerometer frequency, with a damping factor,  $\zeta_a=\sqrt{2}/2$ , the danger zone increases from the center of instantaneous rotation toward the end of the vehicle (fig. 7.15). The influence of increasing liquid mass has the same effect as previously, with the exception that it is very much amplified for small eigenfrequencies of the accelerometer; a large amount of damping is required in the container in order to obtain stability of the vehicle. For a natural frequency of the accelerometer of  $\omega_a=55$  rad/sec, wall friction is in most cases sufficient to maintain stability. For small natural frequencies of the accelerometer, propellant sloshing is excited. This indicates that the situation is more unfavorable with a "bad" accelerometer than in the case without one. The damping required in such a

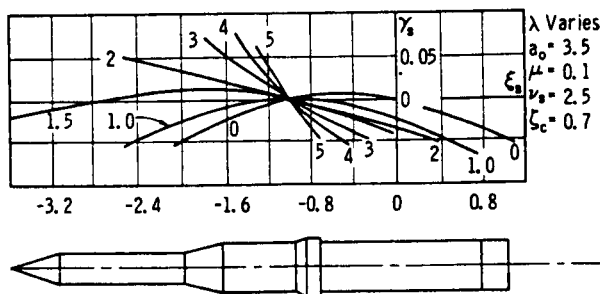


FIGURE 7.14.—Stability boundaries of rigid vehicle with additional ideal accelerometer control (influence of gain value of the accelerometer).

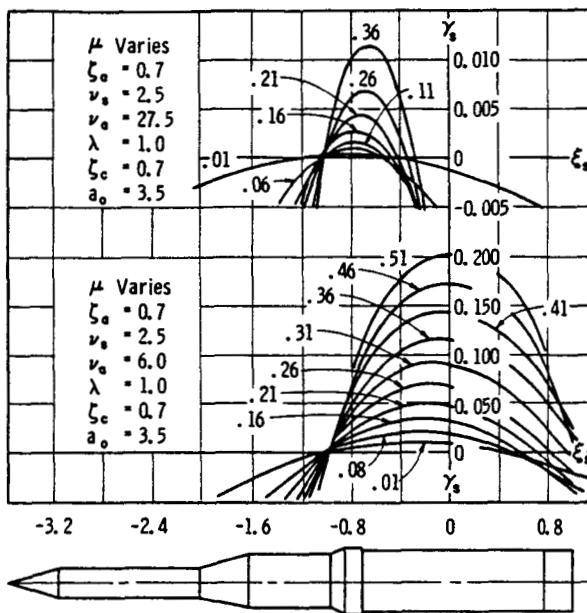


FIGURE 7.15.—Stability boundaries of rigid vehicle with additional accelerometer control of various eigenfrequencies.

case would be about three to four times as much as in the case without additional accelerometer control. The results of the preceding section, and those presented here, indicate that the natural frequency of the accelerometer should be chosen as large as possible. In order to emphasize the influence of the accelerometer characteristics, we consider the effect of the changes of the undamped natural frequency,  $\omega_a$ , the damping factor,  $\xi_a$ , and the coordinate of location,  $x_a$ , upon the stability of the vehicle. For increasing natural frequency of the accelerometer  $\omega_a < \omega_s$ , an increase of the danger zone is obtained, and more damping is required in the container to maintain stability. Above the natural frequency of the propellant, a decrease of the danger zone and enhanced stability can be observed. This means that less damping is required to maintain stability. The larger the frequency ratio  $\nu_a/\nu_s = \omega_a/\omega_s$ , the less damping is required in the then continuously decreasing danger zone. The influence of the frequency,  $\omega_a$ , and the damping factor,  $\xi_a$ , of the accelerometer is exhibited in figure 7.16. The increase of  $\xi_a$  enlarges the danger zone and requires more

damping in the propellant container. This effect is more pronounced the smaller the eigenfrequency of the accelerometer. From a damping factor,  $\xi_a$ , which is about twice the critical damping or larger, one recognizes, in the case  $\omega_a = 12$  rad/sec, that a further increase of the damping factor decreases the danger zone slightly from the back and only slightly enhances the stability. A very important parameter in the design of a control system of a space vehicle is the location,  $\xi_a$ , of an accelerometer for control purposes. The influence of this value can be seen in figure 7.17. An accelerometer location aft of the center of gravity of the vehicle must be avoided; shifting the accelerometer toward the nose of the vehicle enhances the stability. An increase in the control frequency,  $\omega_c$  (fig. 7.18), below the natural frequency of the propellant ( $\nu_s > 1$ ) increases the danger zone toward the tail of the vehicle. For  $\omega_a = 55$  rad/sec (the larger natural frequency of the accelerometer), the required damping in the liquid for maintaining stability of the vehicle is relatively small ( $\gamma_s = 0.005$  and less). The influence of the control damping,  $\xi_c$ , is given by

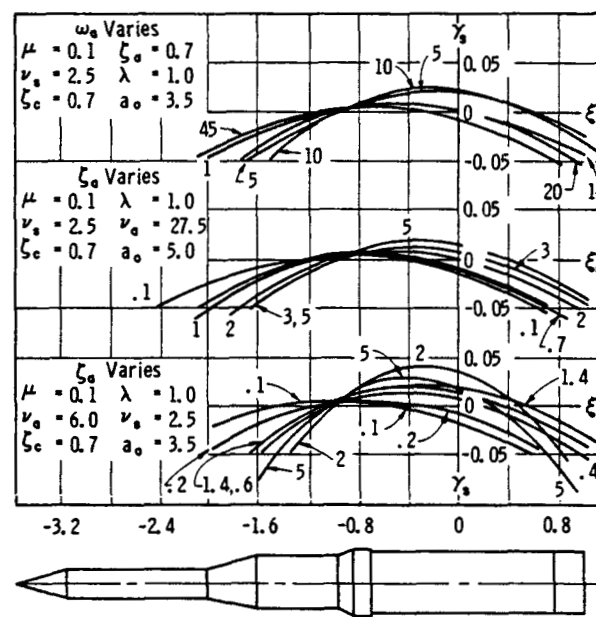


FIGURE 7.16.—Stability boundaries of a rigid vehicle with additional accelerometer control of various vibrational characteristics.

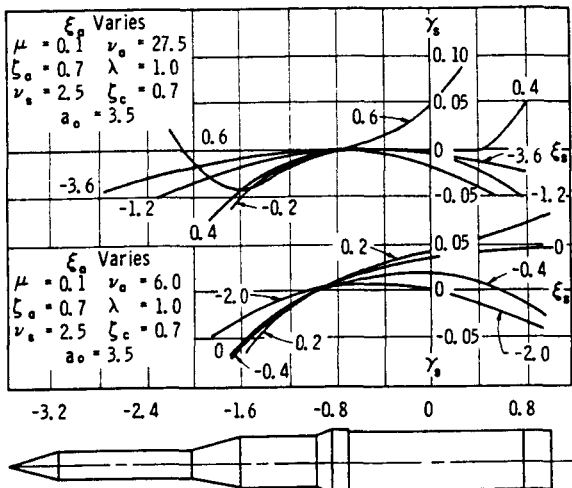


FIGURE 7.17.—Stability boundaries of a rigid vehicle with additional accelerometer control (influence of the location of the accelerometer).

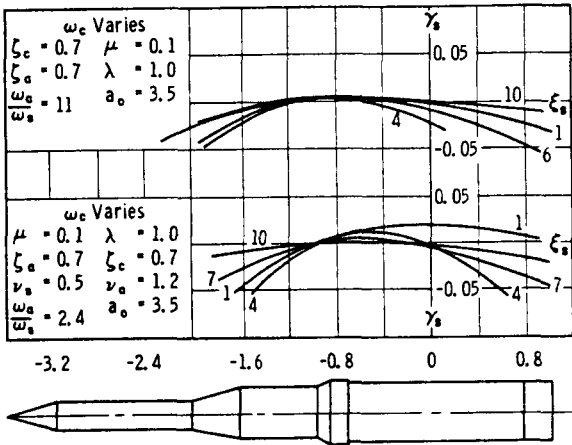


FIGURE 7.18.—Stability boundaries of a rigid vehicle with additional accelerometer control (influence of the control frequency).

the fact that, for increasing subcritical control damping,  $\xi_c < 1$ , the danger zone decreases and the stability increases, while for supercritical damping,  $\xi_c > 1$ , the stability becomes more unfavorable (fig. 7.19). The influence of the propellant frequency being below the control frequency indicates again the enlarged danger zone which stretches nearly from the center of instantaneous rotation toward the end of the vehicle. Increasing propellant frequency leads

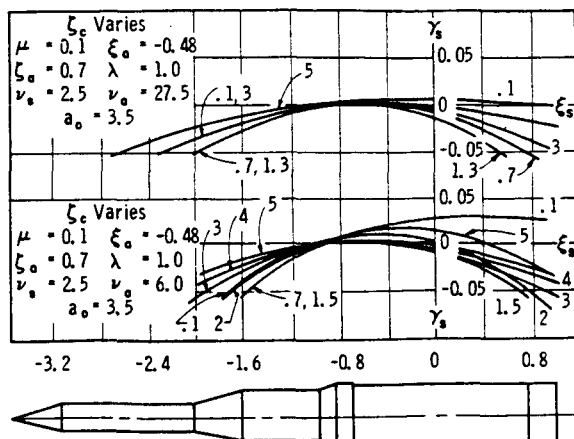


FIGURE 7.19.—Stability boundaries of a rigid vehicle with additional accelerometer control (influence of the control damping).

to a decreasing danger zone and less required damping. Approaching the natural frequency,  $\omega_a$ , of the accelerometer makes the vehicle more unstable and increases the danger zone toward the end of the vehicle. The gain value,  $a_0$ , has only a small influence on the stability; its gain growth increases stability slightly and somewhat decreases the danger zone. Of important influence upon stability is the gain value  $g_2$  of the accelerometer because it presents the strength of the accelerometer in the control system. Figure 7.20 exhibits this influence for

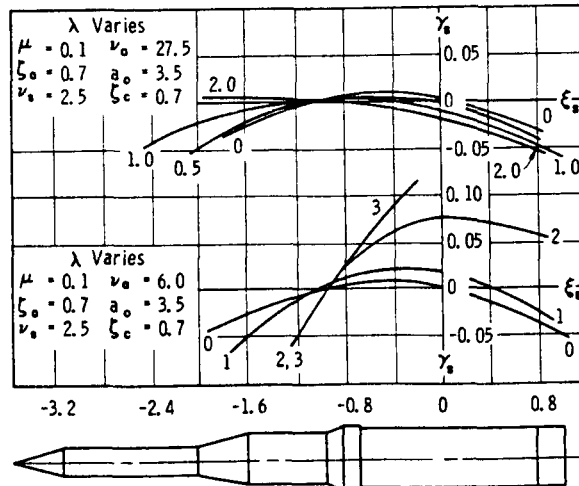


FIGURE 7.20.—Stability boundaries of a rigid vehicle with additional accelerometer control (influence of the gain value of the accelerometer).

two accelerometer frequencies. For an eigenfrequency of the accelerometer of  $\omega_a = 55$  rad/sec, one recognized similar behavior as in the case of the ideal accelerometer case, for a value of  $\lambda \approx 1.5$ . An increase of  $\lambda = gg_2$  exhibits an increase in stability and a decrease of the danger zone between the center of instantaneous rotation and the center of mass of the vehicle. For further increase of  $\lambda$ , the danger zone shifts forward of the center of instantaneous rotation. With increasing  $\lambda$ , more damping is required in the propellant container in this zone to maintain stability. For an accelerometer with a small eigenfrequency, the situation is quite different. For increasing gain value  $g_2$ , the stability constantly decreases. Here, the influence of the accelerometer favors instability; it not only increases the danger zone toward the end of the vehicle but it also requires considerably more damping in the propellant tank. It even requires more damping than in the case without accelerometer control ( $\lambda = 0$ ). From this, one can again conclude that large accelerometer frequency is required to stabilize the vehicle with respect to propellant sloshing.

In conclusion, one can state that the danger zone is located between the center of instantaneous rotation and the center of mass, and that it can be diminished by an additional control element in the form of an accelerometer, recognizing that the natural frequency and location have to be properly chosen. These results are valid only for a rigid vehicle in which the sloshing propellant mass in one container is much larger than those in the other tanks. Furthermore, it has to be mentioned that the bending vibration of the vehicle has an effect on the propellant sloshing as well as on the choice of the accelerometer characteristics and its location. If the control frequency and the first bending frequency are sufficiently separated from each other, then the location of an accelerometer requires negative displacement of the bending modes (if the bending modes are normalized at the tail of the vehicle). This indicates that, for the control of the first two bending modes, an approximate location of the accelerometer forward of the center of gravity

is appropriate. This location would also be favorable from the standpoint of propellant sloshing.

### Effects of Container Geometry and Tank Arrangements

A question of great importance in the design of a large space vehicle is the choice of the form of the propellant containers. As was shown in chapter 2, tank geometry establishes the modal masses and the natural frequencies of the propellant. Containers with large diameters exhibit small natural frequencies that in many cases are too close to the control frequency. The magnitude of the modal mass considerably emphasizes this unfavorable effect upon the stability. Clustering of numerous smaller containers not only increases the natural frequencies of the propellant (because of the smaller diameters) but also reduces the modal masses, of which the latter is a much more important effect on the overall dynamics of the vehicle. In addition to the weight saving and the slight increase of the natural frequencies, subdivision of tanks by sector wall has the advantage of distributing the modal masses to different vibration modes of the liquid.

To summarize the previous results, with increasing mass the stability decreases and the influence of the eigenfrequency change of the propellant of fixed modal mass is such that a decrease of the natural frequency increases the danger zone toward the end of the vehicle and requires more local damping in the propellant. With increasing natural frequency of the liquid, the influence of the propellant sloshing on the stability of the vehicle diminishes more and more. Wall friction is in many cases sufficient to maintain stability.

#### *Clustered Containers*

In the case of a cluster of tanks with smaller diameters, the results are very similar. The natural frequency is increased because of the smaller diameters. The natural frequency ratio of the propellants in a single circular cylindrical

tank of radius  $a$ , and  $p$  identical circular cylindrical tanks of the same total volume, is

$$\frac{f_n^{(1)}}{f_n^{(p)}} = \frac{1}{(p)^{1/4}} \left\{ \frac{\tanh \frac{\epsilon_n h}{a}}{\tanh \epsilon_n (p)^{1/2} \frac{h}{a}} \right\}^{1/2}$$

This shows that the frequency increase is proportional only to the slowly increasing value  $(p)^{-1/4}$ . The total sloshing mass, however, decreases more rapidly with the inverse value of the square root of the number of containers. The ratio of the total sloshing mass of  $p$  tanks and the sloshing mass of the single container is

$$\frac{m_s^{(p)}}{m_s^{(1)}} = \frac{1}{p^{1/2}} \frac{\tanh \epsilon_n (p)^{1/2} \frac{h}{a}}{\tanh \frac{\epsilon_n h}{a}}$$

This is of great advantage for the dynamics, but, from the design and overall performance standpoint, the clustering of tanks has structural and weight disadvantages.

The slosh damping required for  $p$  clustered tanks is therefore approximately that of a

$s^2 \omega_c^2$	$-g(1 + \epsilon a_0 + \epsilon a_1 s \omega_c)$	$\mu_1 s^2 \omega_c^2$	$\mu_2 s^2 \omega_c^2$	$\mu_3 s^2 \omega_c^2$	= 0
0	$s^2 \omega_c^2 + \frac{\epsilon g x_E}{k^2} (a_0 + s \omega_c a_1)$	$\frac{\mu_1}{k^2} (x_1 \omega_c^2 s^2 + g)$	$-\frac{\mu_2}{k^2} (x_2 \omega_c^2 s^2 + g)$	$-\frac{\mu_3}{k^2} (x_3 \omega_c^2 s^2 + g)$	
$s^2 \omega_c^2$	$-(x_1 \omega_c^2 s^2 + g)$	$s^2 \omega_c^2 + 2\gamma_1 \omega_1 \omega_c s + \omega_1^2$	0	0	
$s^2 \omega_c^2$	$-(x_2 \omega_c^2 s^2 + g)$	0	$s^2 \omega_c^2 + 2\gamma_2 \omega_2 \omega_c s + \omega_2^2$	0	
$s^2 \omega_c^2$	$-(x_3 \omega_c^2 s^2 + g)$	0	$s^2 \omega_c^2 + 2\gamma_3 \omega_3 \omega_c s + \omega_3^2$		

(7.50)

Here,  $\mu_v = m_v/m$  is the ratio of the sloshing mass in the  $v$ th container to the total mass of the vehicle. For nontrivial solutions, the coefficient determinant, equation (7.50), must vanish, from which one obtains the characteristic polynomial in  $s$

$$\sum_{i=0}^8 B_i s^i = 0$$

and for which the coefficients  $B_i$  depend on the previously mentioned parameters. A similar result is obtained for two containers by remov-

sloshing mass that is reduced by  $1/p^{1/2}$ . There is, of course, also a small stability enhancing effect because of the increase of the natural frequency.

#### Rigid Vehicle With Propellant Sloshing in Two and Three Tanks

In some cases the influence of the propellant in other tanks cannot be neglected, making the determination of stability boundaries for vehicles with more sloshing masses mandatory (ref. 7.17). The equations of motion are obtained by treating equations (7.20), (7.42), (7.43), and (7.45) with  $\eta_v = 0$ ,  $\lambda = 1, 2, 3$  and/or  $n = 1, 2$ . The propellant will be treated as being free to oscillate in three tanks. This seems to be sufficient, since usually, even in large vehicles, only three of the tanks will exhibit large sloshing masses. The sloshing propellant masses of tanks with light propellants and tanks of smaller diameter can be neglected. With the usual assumption regarding solutions of the form  $e^{s \omega_c t}$ , where  $s$  is the complex frequency,  $s = \sigma + i\omega$ , the differential equations are transformed into homogeneous algebraic equations, with the characteristic determinant

$s^2 \omega_c^2$	$-g(1 + \epsilon a_0 + \epsilon a_1 s \omega_c)$	$\mu_1 s^2 \omega_c^2$	$\mu_2 s^2 \omega_c^2$	$\mu_3 s^2 \omega_c^2$	= 0
0	$s^2 \omega_c^2 + \frac{\epsilon g x_E}{k^2} (a_0 + s \omega_c a_1)$	$\frac{\mu_1}{k^2} (x_1 \omega_c^2 s^2 + g)$	$-\frac{\mu_2}{k^2} (x_2 \omega_c^2 s^2 + g)$	$-\frac{\mu_3}{k^2} (x_3 \omega_c^2 s^2 + g)$	
$s^2 \omega_c^2$	$-(x_1 \omega_c^2 s^2 + g)$	$s^2 \omega_c^2 + 2\gamma_1 \omega_1 \omega_c s + \omega_1^2$	0	0	
$s^2 \omega_c^2$	$-(x_2 \omega_c^2 s^2 + g)$	0	$s^2 \omega_c^2 + 2\gamma_2 \omega_2 \omega_c s + \omega_2^2$	0	
$s^2 \omega_c^2$	$-(x_3 \omega_c^2 s^2 + g)$	0	$s^2 \omega_c^2 + 2\gamma_3 \omega_3 \omega_c s + \omega_3^2$		

(7.50)

ing the last column and line from the above determinant, equation (7.50).

The stability boundaries for four important propellant tank configurations are discussed below:

(1) *Two concentric containers.*—It may be possible to remedy the influence of propellant sloshing by choosing a concentric tank arrangement consisting of an inner tank with circular cross section (radius  $r=b$ ) and an outer tank of annular cross section with an outer radius  $r=a$ . By proper choice of the diameter ratio

$k=b/a$ , the liquid masses in the inside container and outside container can be brought into such a phase relation that the forces and moments of these individual tanks cancel each other. Figures 7.21, 7.22, and 7.23 show the results of this study for diameter ratios  $k=b/a=0.3$ , 0.5, and 0.7. The results are very similar to those of the case of a single container, since the difference in the location of the sloshing

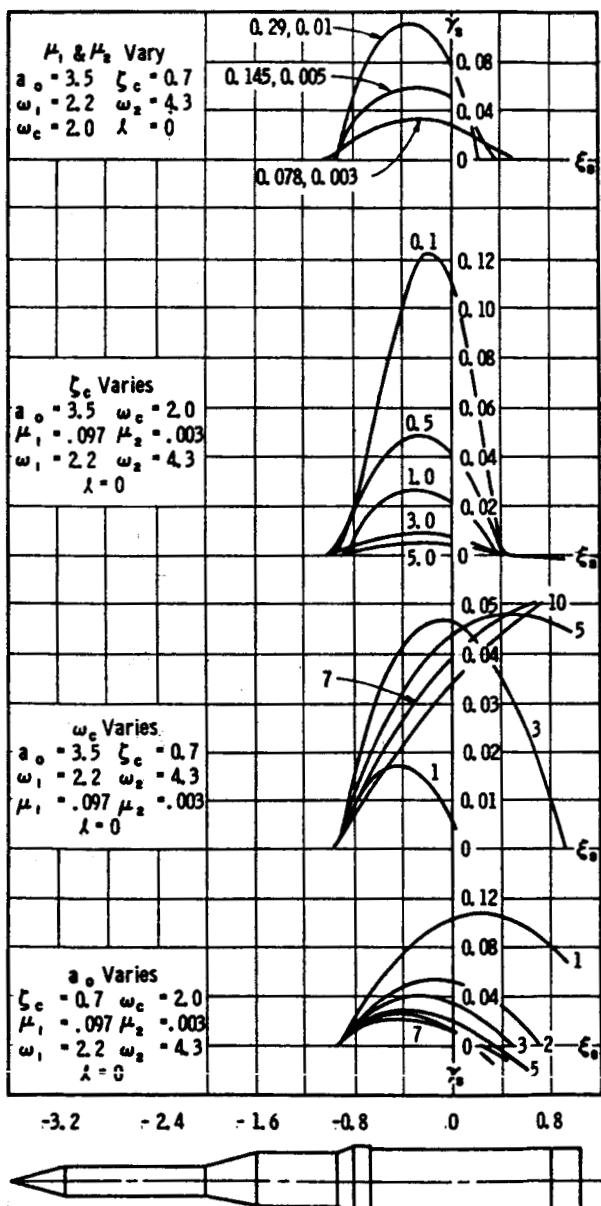


FIGURE 7.21.—Stability boundaries for sloshing in concentric tanks ( $k=0.3$ ).

masses is very small. The danger zone is increased somewhat toward the rear of the vehicle. For increasing control damping,  $\xi_c$ , the stability is decreased. A decrease in the control frequency enhances the stability, as in the preceding section. For a sloshing frequency of the center tank below the control frequency, more baffling has to be employed over the enlarged danger zone. For increasing sloshing

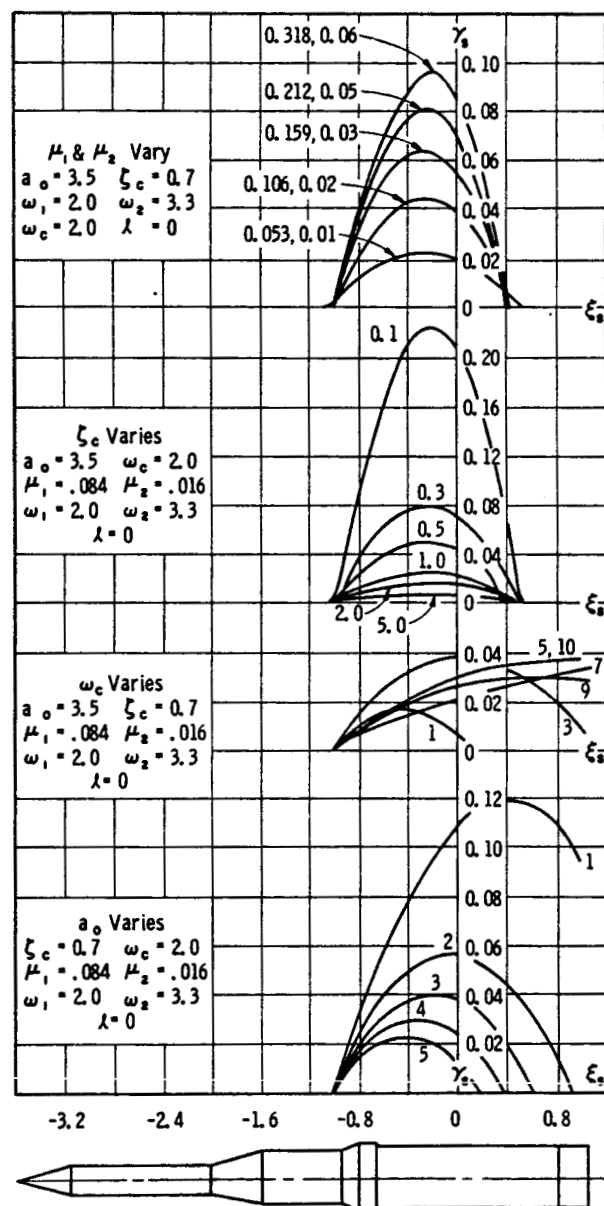


FIGURE 7.22.—Stability boundaries for sloshing in concentric tanks ( $k=0.5$ ).

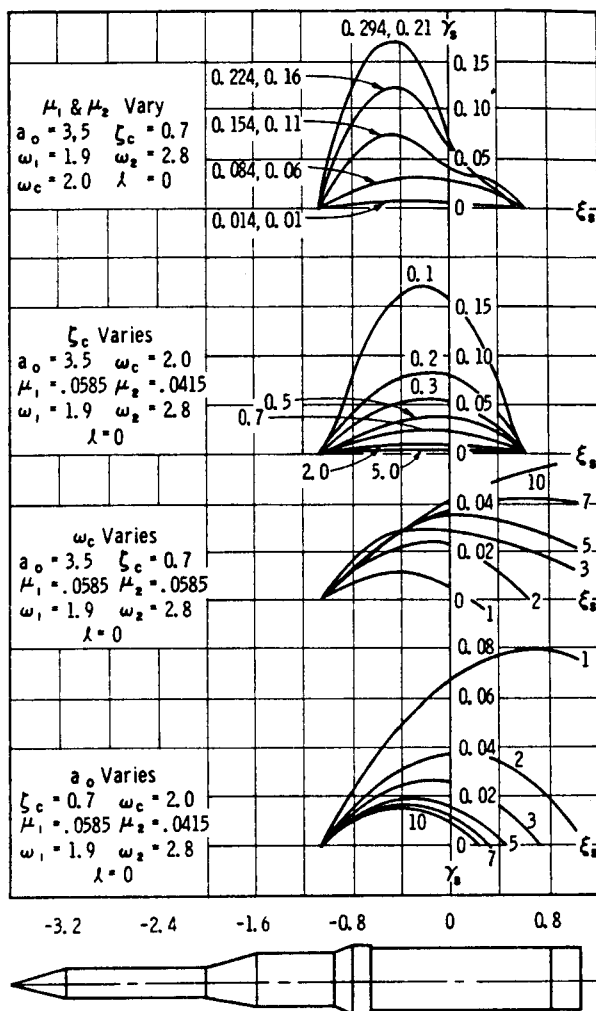


FIGURE 7.23.—Stability boundaries for sloshing in concentric tanks ( $k=0.7$ ).

frequency, the stability increases. To obtain maximum cancellation effects, the sloshing masses of the center and outer container should be equal and should oscillate in antiphase. Equal sloshing masses can be obtained for a diameter ratio of about  $k=0.77$  for which, unfortunately, the phases are not favorable. If the phases are chosen favorably, as in the case of a diameter ratio  $k=0.5$ , the sloshing masses exhibit a ratio of 1:5. This shows that no pronounced benefit can be obtained by a concentric tank arrangement. For the diameter ratios  $k=0.3, 0.5$ , and  $0.7$ , the damping required for stability in the container is in the ratio 12:9:8.

(2) *Sector tank arrangement.*—As shown in reference 7.7, compartmentation of containers by radial walls exhibits considerably decreased sloshing masses. In the case of a quarter-tank arrangement, the first modal mass is only about a third of the value of a cylindrical container with circular cross section. But other vibration modes are still important, such as the succeeding sloshing mode of which the mass still represents 43 percent of that of the first one. This indicates that, in stability investigations, this second mode can no longer be neglected. This tank arrangement has, in addition to the reduced modal mass, the advantage that the fundamental frequency is slightly larger than that of a container of circular cross section. (See ch. 2.) Also, the total sloshing mass is distributed to various modes; thus, it is not all excited at the same frequency as in clustered tanks.

Two slosh masses are again considered in the equations of motion, representing the first and second sloshing mode of the quarter-tank arrangement; the results are very similar to the previous ones. Again, the danger zone is located between the center of instantaneous rotation and the center of mass. The increase of the control damping,  $\zeta_c$ , in the subcritical region decreases the stability, while an increase in the supercritical region increases the stability region. For increasing control frequency, the danger zone is enlarged toward the base of the vehicle and requires larger damping in the tank in order to maintain stability. The influence of the simultaneous change of the sloshing frequencies shows that for sloshing frequencies below the control frequency, more baffling in an enlarged danger zone (toward the rear) is required. Increasing sloshing frequencies result in a decrease of the danger zone toward the one between the center of mass and the center of instantaneous rotation and requires less damping in the tanks to maintain stability of the vehicle. Low gain values ( $a_0=1$ ) require more baffling along a larger danger zone, while an increase of the gain,  $a_0$ , reduces the danger zone and the requirement of damping in the tanks (fig. 7.24).

(3) *Tandem arrangement of two tanks.*—For a tandem-tank arrangement, the results can

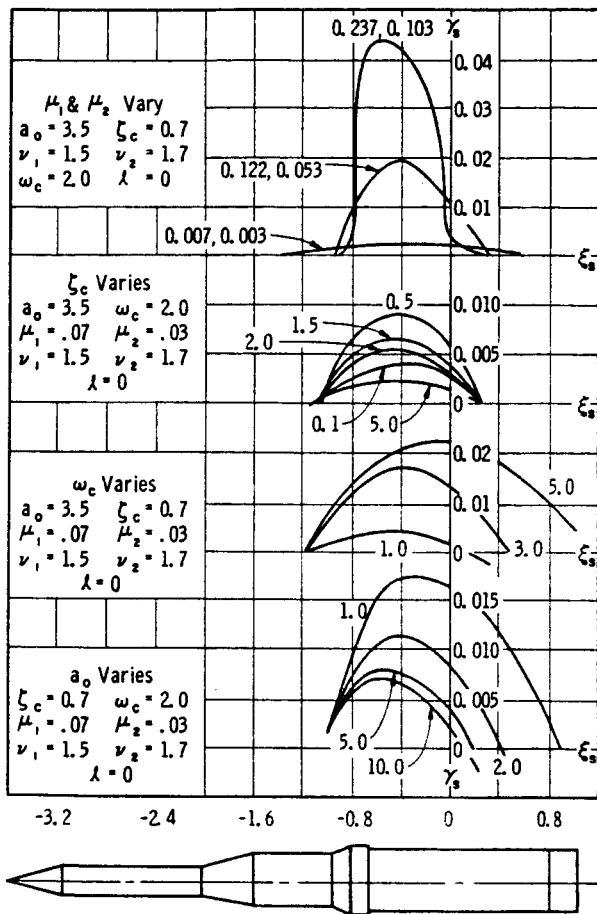


FIGURE 7.24.—Stability boundaries for sloshing in quarter-tank arrangement.

be seen in figure 7.25. Tank No. 1 is designated as the rear tank, and No. 2 is the forward tank. The distance between the two sloshing masses is called  $l(\xi_s = l/k)$ . The sloshing frequency of the liquid in these two tanks is the same. In the numerical evaluation, the diameter was taken to be approximately 100 meters (256 inches). It can be seen that for increasing sloshing mass, a loss in stability region is encountered; furthermore, the danger zone is shifted slightly toward the rear of the vehicle. Increasing control damping,  $\xi_c$ , increases the stability area. An increase of the control frequency,  $\omega_c$ , results in an increased baffling requirement over an enlarged danger zone toward the aft of the space vehicle.

For sloshing frequencies below the control frequency, a large amount of damping is

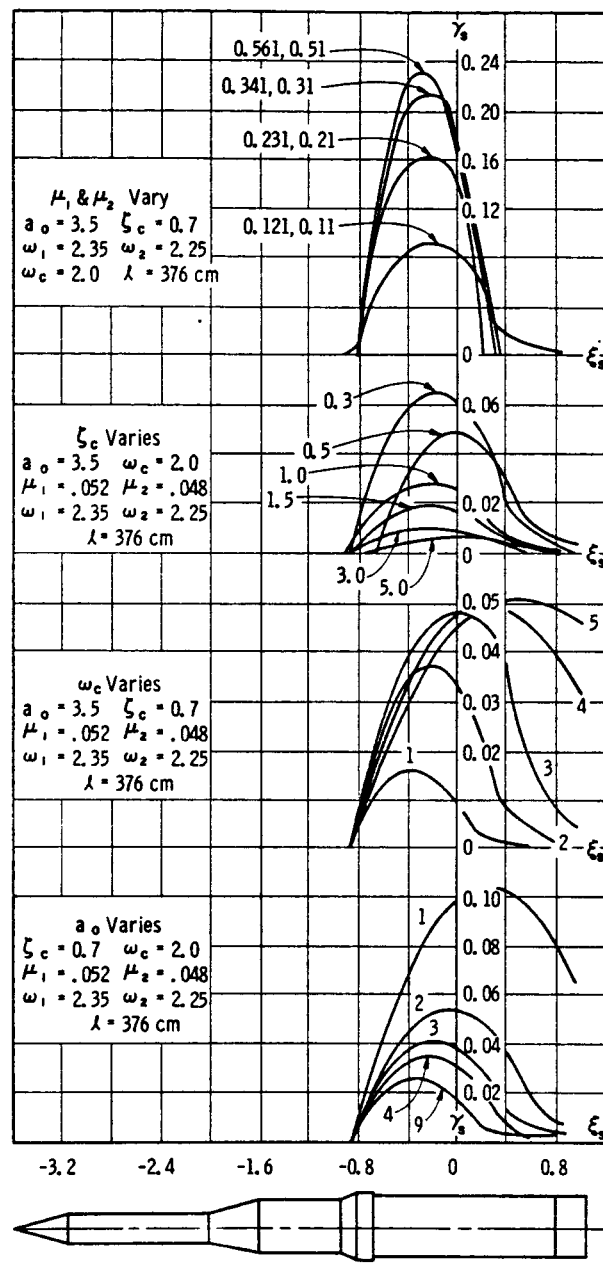


FIGURE 7.25.—Stability boundaries for sloshing in two tanks in tandem arrangement.

required in the enlarged danger zone in order to maintain stability. Increasing the sloshing frequency decreases the danger zone and the amount of damping required.

Changing the gain value,  $a_0$ , has an effect similar to that for a single tank. Small gain values require strong baffling over an enlarged danger zone. An increase in the gain value

enlarges the stability region and shifts the danger zone slightly toward the center of instantaneous rotation.

The influence of the difference,  $\xi_e = l/k$ , in the tank location exhibits, for increasing distance between tanks, a shifting of the danger zone aft on the vehicle, with slightly less damping requirements. This indicates that, in a vehicle in which one sloshing mass is stationary during flight and in which the other liquid mass shifts aft on the vehicle, the entire rear part of the vehicle has to be provided with appropriate damping to maintain stability (fig. 7.26).

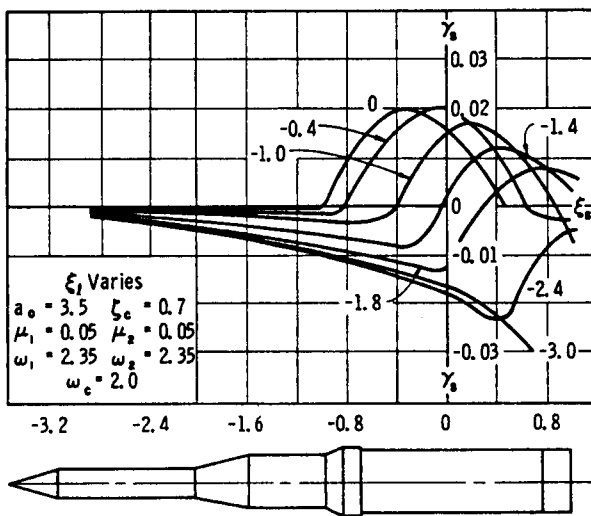


FIGURE 7.26.—Stability boundaries for rigid vehicle with simple control system and two tandem tanks (distance between tanks varying).

(4) *Tandem arrangement of three tanks.*—In almost all space vehicles, the consideration of sloshing in three propellant containers is sufficient for simplified stability boundary determinations. The liquid propellants in any remaining tanks exhibit either small sloshing masses (because of their low density or different tank geometry) or larger natural frequencies of the propellants. For this case the total determinant, equation (7.50), must be treated. The results are similar as in the tandem arrangement of two tanks. Figure 7.27 exhibits the shifting ( $\xi_s$ ) of the two booster slosh masses toward the rear of the space vehicle (as it takes place during the draining of the first-

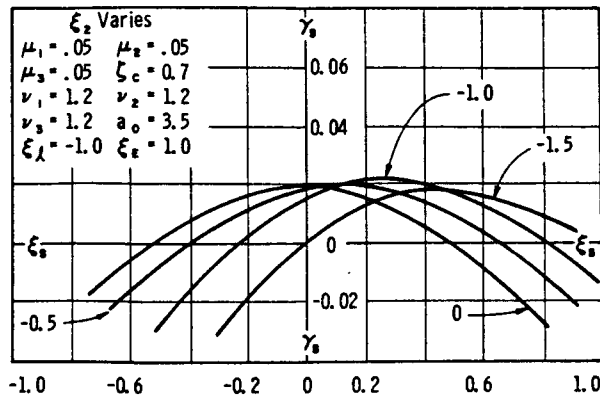


FIGURE 7.27.—Stability boundaries for sloshing in three tanks in tandem arrangement.

stage containers during first-stage flight). The danger zone shifts aft on the vehicle with increasing slosh mass difference; this again indicates that the booster must be provided with appropriate baffles to maintain stability.

For elastic vehicles, the situation changes more or less, depending on the elastic properties of the vehicle (refs. 7.20 and 7.21). This will be discussed further in chapter 9.

#### 7.4 RESPONSE OF A VEHICLE TO ATMOSPHERIC DISTURBANCES

For satisfactory flight performance of a space vehicle, its stability is essential. This is usually obtained by proper design of the vehicle and proper choice of the control system by which the thrust vector will be controlled. In addition to the stability, the response of the system to winds must be well within the limits of the control deflections, gimbal rates, and maximum permissible structural loads on the airframe. It is therefore essential to investigate the response of the space vehicle to atmospheric disturbances. The reduction of these responses can be accomplished by proper airframe design, such that the structure can withstand the loads, and by designing the shape of the vehicle in such a fashion that aerodynamic forces and moments are minimized, as well as by a properly selected control system.

Wind buildup and gusts may require large engine deflections and engine rates, and may

induce bending vibrations and propellant sloshing. In order to study the response of a vehicle, we limit ourselves again to investigations in only one plane. This does not seem to be a significant restriction, since the interactions between pitch, yaw, and roll motions are very small for this type of vehicle. The equations of motion have been linearized and can be solved for variable coefficients by use of the Runge-Kutta method (ref. 7.22).

In the following, the numerical results are presented for a particularly large space vehicle. The complexity of the problem does not allow a detailed analytical evaluation of the equations of motion. The presentation of the results for this particular vehicle, however, should exhibit the basic idea and the valuable conclusions that can be drawn from such an investigation.

### Stability

Before one can talk about the response of a vehicle, the stability of such a system has to be established. For this reason, a root locus phase study of the vehicle, with the inclusion of two bending modes and three sloshing masses (one for each of the heavy propellant tanks) is first performed. For control damping, a rate gyroscope at the engine gimbal station (a very favorable position) with a damping factor,  $\zeta_a = 0.7$ , and a natural frequency,  $f_a = 16$  cps, is employed. The control frequency is considered to be 0.2 cps and the structural damping is chosen to be 1 percent. It can be shown that with a (conservative) 5-percent damping for the sloshing propellant, the vehicle is stable with respect to the propellant motion. With the bending frequencies during flight time varying from 0.8 to 1.2 cps in the first bending mode and from 1.9 to 2.5 cps in the second bending mode, the system was found to be stable. In this particular case, the second of the bending modes exhibited the smallest stability.

### Wind Response

After the stability of all generalized coordinates has been established, the response of the space vehicle resulting from some atmospheric disturbance can be investigated. In order to determine the influence of the vehicle flexibility

and propellant sloshing in the tanks, four different cases are studied:

(1) Rigid vehicle with no sloshing in the propellant tanks.

(2) Rigid vehicle with propellant sloshing in the three heavy tanks (No. 1: LOX tank of the booster stage; No. 2: Fuel tank of the booster stage; No. 3: LOX tank of the second stage).

(3) Elastic vehicle with no sloshing in the propellant tanks.

(4) Elastic vehicle with propellant sloshing in the three heavy tanks.

The input used is a 95-percent probability wind building up in about 11½ seconds to a value of 75 m/sec. To this wind, starting at 58.5-seconds flight time, a 9-m/sec gust is added which starts at 70-seconds flight time, remains at 84 m/sec for about 1 second (an altitude band of about 250 meters) and then drops down to 75 m/sec (fig. 7.28). This occurs at a flight time of 70 seconds where the product of angle of attack and dynamic pressure assumes its maximum value. At that flight time, the sloshing frequencies in the tanks were:

Fundamental sloshing frequency in tank 1:

$$f_1 = 0.44 \text{ cps}$$

Fundamental sloshing frequency in tank 2:

$$f_2 = 0.445 \text{ cps}$$

Fundamental sloshing frequency in tank 3:

$$f_3 = 0.45 \text{ cps}$$

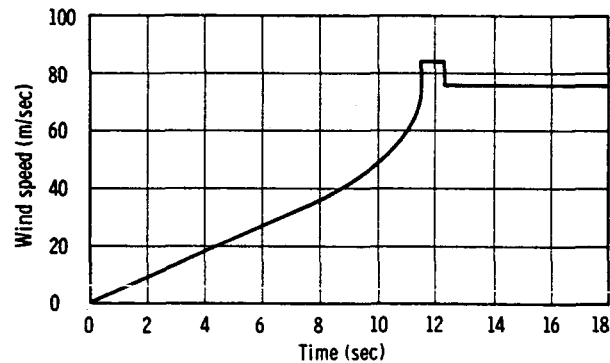


FIGURE 7.28.—Wind buildup and gust.

The bending frequencies were:

$$\text{First bending: } f_{1B} = 1.15 \text{ cps}$$

$$\text{Second bending: } f_{2B} = 1.92 \text{ cps}$$

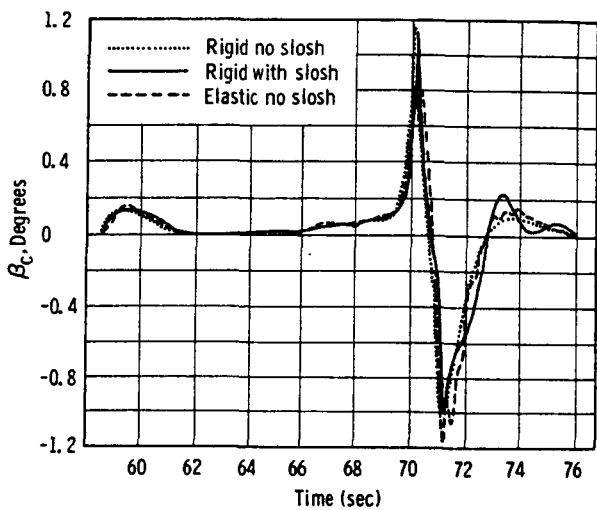


FIGURE 7.29.—Response analysis: Engine command signal.

In figures 7.29 through 7.40, the response of each of the various generalized coordinates is compared to that of the rigid vehicle without and with liquid sloshing and the elastic vehicle without sloshing. Here, the influence of sloshing in a rigid vehicle as well as the elastic influence can be obtained. Figure 7.29 shows the engine deflection  $\beta_c$ , reaching an angle of about  $1.2^\circ$  after the gust hits the vehicle. The value for a rigid vehicle without sloshing exhibits a slightly larger magnitude. After the gust has been applied, the sloshing liquid requires a little more than  $0.1^\circ$  engine deflection; the engine follows the propellant motion with a frequency of about 0.45 cps. This oscillation exhibits a damping value of about 6 percent. The elastic vehicle shows a slightly smaller maximum peak value; it requires, however, a little larger engine deflection in the transient than does the rigid vehicle. The oscillation of the engine deflection is at a frequency of about 2 cps and has an amplitude of about  $0.015^\circ$ , showing that the less stable second mode has been excited.

A similar behavior can be detected in figure 7.30 for the rate of the engine deflection, with the exception that  $\dot{\beta}_c$  reaches its stop of  $5^\circ/\text{sec}$ . The three cases show no appreciable difference in the attitude angle (fig. 7.31). It reaches its peak of about  $4^\circ$  shortly after the gust has disappeared. The elasticity of the vehicle increases the angle slightly by a value of about

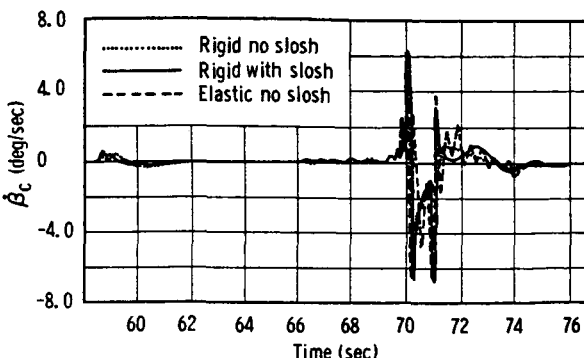


FIGURE 7.30.—Response analysis: Engine command rate.

$0.1^\circ$ . Figure 7.32 shows the result for  $\phi$  in deg/sec<sup>2</sup>. The angle of attack,  $\alpha$ , is exhibited in figure 7.33 and presents a maximum value of about  $10^\circ$  at the time the gust is applied. Sloshing and elasticity of the vehicle result only in very small differences compared with the rigid vehicle. The same is true for the translational displacement,  $y$ , of the vehicle (fig. 7.34). The translational acceleration of the vehicle exhibits the fact that translational sloshing results in a larger disturbance than does sloshing resulting from pitching (fig. 7.35). The vehicle performs translational oscillations with a frequency of 0.45 cps as a result of the propellant oscillations in the tanks. Elastic oscillations have only a minor effect. After the gust has hit the rigid vehicle, the propellant in the first tank (LOX tank of the booster stage) reaches a maximum amplitude of 21 centimeters and performs a damped oscillation

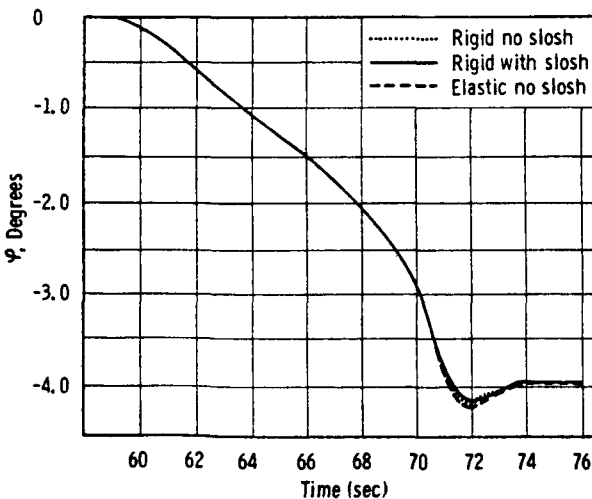


FIGURE 7.31.—Vehicle rotation.

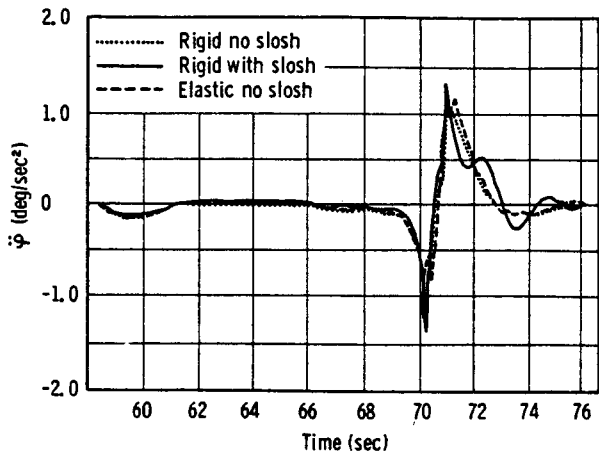


FIGURE 7.32.—Vehicle angular acceleration.

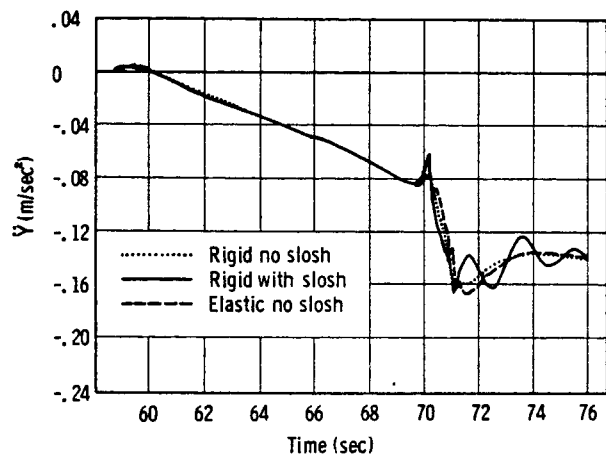


FIGURE 7.35.—Vehicle translatory acceleration.

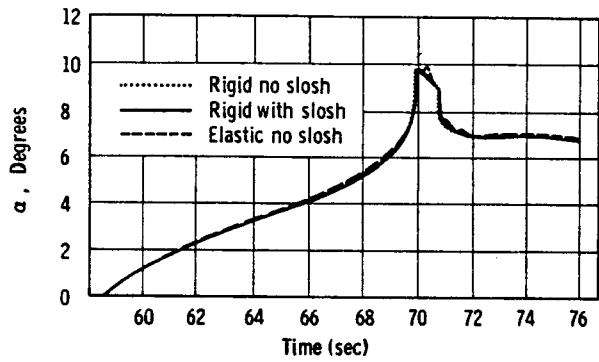


FIGURE 7.33.—Angle of attack.

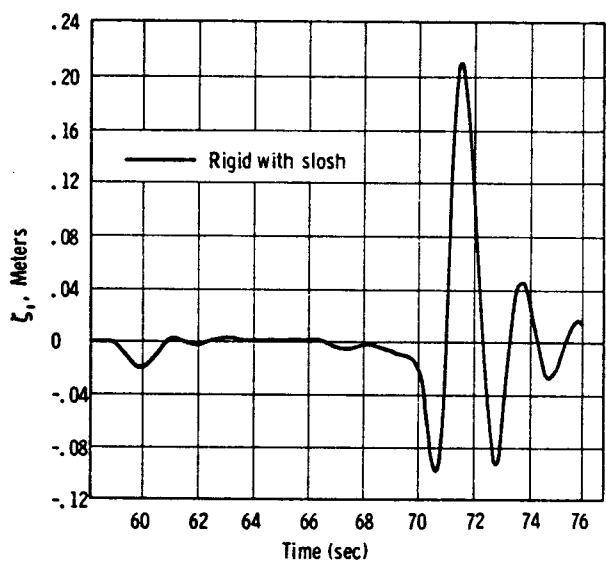


FIGURE 7.36.—First-slosh amplitude.

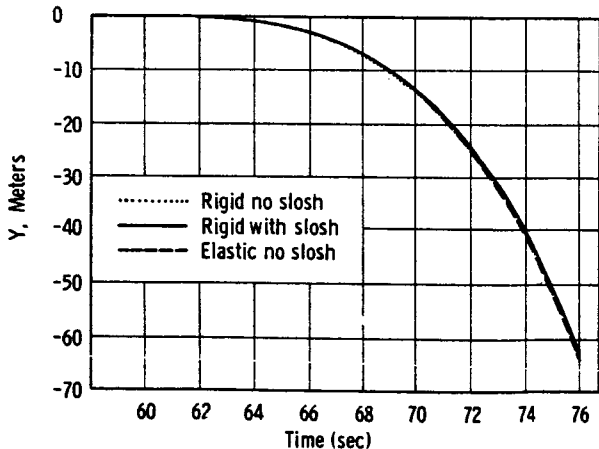


FIGURE 7.34.—Vehicle translation.

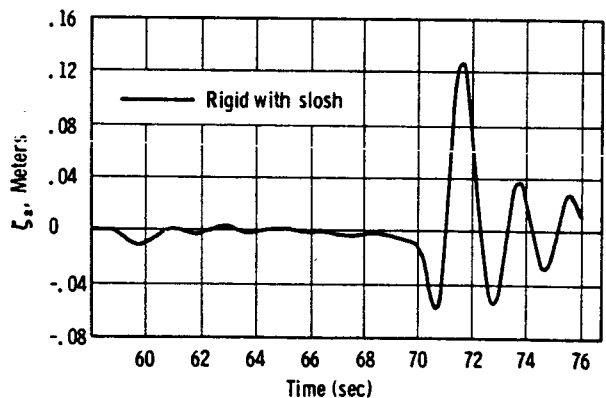


FIGURE 7.37.—Second-slosh amplitude.

with about 5 percent damping (fig. 7.36). The propellant in the second tank (fuel tank of the booster stage) reaches a maximum of 13 centimeters (fig. 7.37). The amplitude of the pro-

pellant in the third tank (LOX tank of the S-II stage) is 4 centimeters (fig. 7.38), and remains constant for a larger time period. For the elastic vehicle without propellant sloshing, the first bending mode has a maximum displacement of the generalized coordinate,  $\eta_1$ , of 1.7 centimeters right after the gust has hit the vehicle (fig. 7.39). The second mode exhibits only  $4\frac{1}{2}$  millimeters, but shows sustained vibrations of one-tenth of a millimeter in the transient, indicating that this has a frequency content to which the second bending mode is susceptible (fig. 7.40).

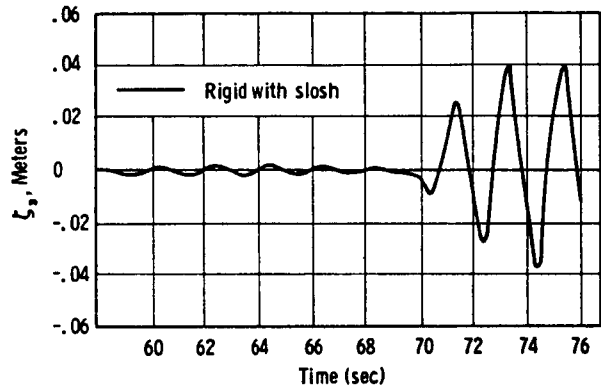


FIGURE 7.38.—Third-slosh amplitude.

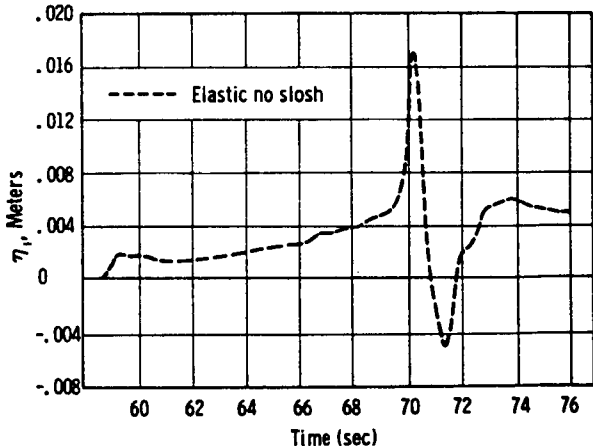


FIGURE 7.39.—First bending deflection.

Figures 7.41 through 7.52 compare the response of the elastic vehicle with propellant sloshing in its tanks with that of the elastic vehicle without sloshing and with that of the rigid vehicle with sloshing. In figure 7.41, it can be seen that the engine deflection at about

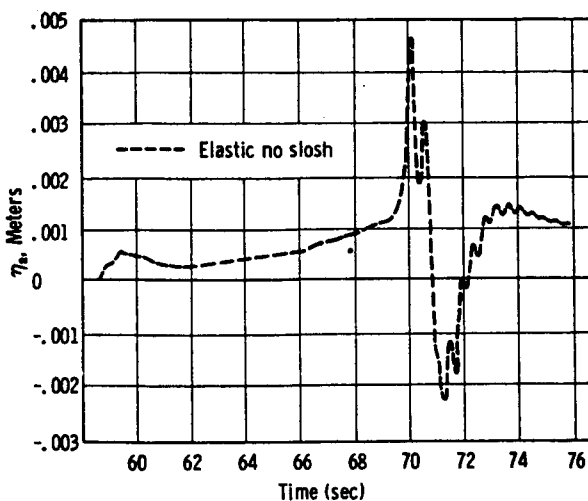


FIGURE 7.40.—Second bending deflection.

the time the gust is applied is about  $1.2^\circ$  and slightly less for the elastic vehicle. Then the engine performs a damped oscillation which is always forced to react to the sloshing of the propellant and exhibits a slightly larger value for the elastic vehicle. If propellant sloshing is suppressed, the engine performs small oscillations at the frequency of the second bending mode. As can be seen in figure 7.42, the stop of  $5^\circ/\text{sec}$  for  $\dot{\beta}_c$  has again been reached. There is not much difference indicated in the attitude angle,  $\phi (\approx 4^\circ)$ , as shown in figure 7.43. Figure 7.44 shows  $\dot{\phi}$ . The angle of attack,  $\alpha$ , reaches a maximum of  $10^\circ$ , but the difference between the rigid and elastic vehicle is only minor

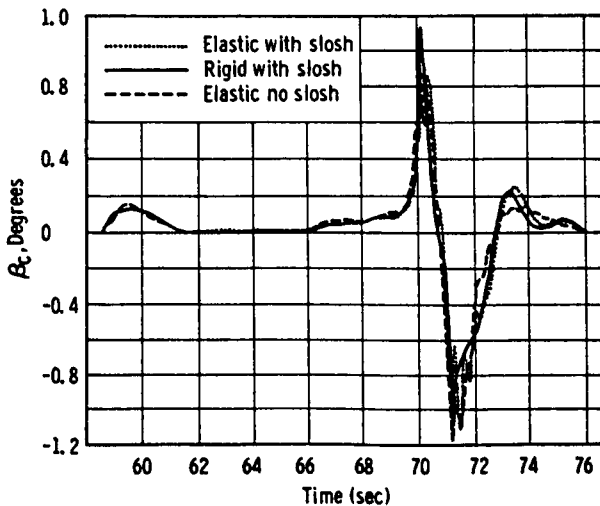


FIGURE 7.41.—Engine command signal.

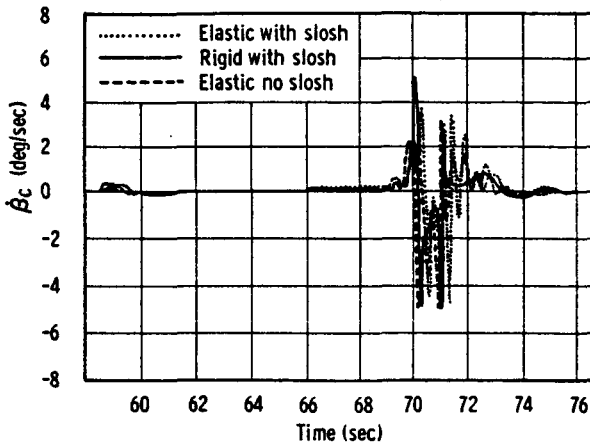


FIGURE 7.42.—Engine command rate.

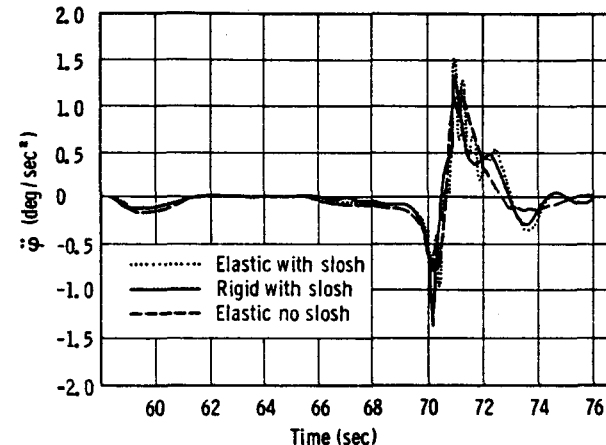


FIGURE 7.44.—Vehicle angular acceleration.

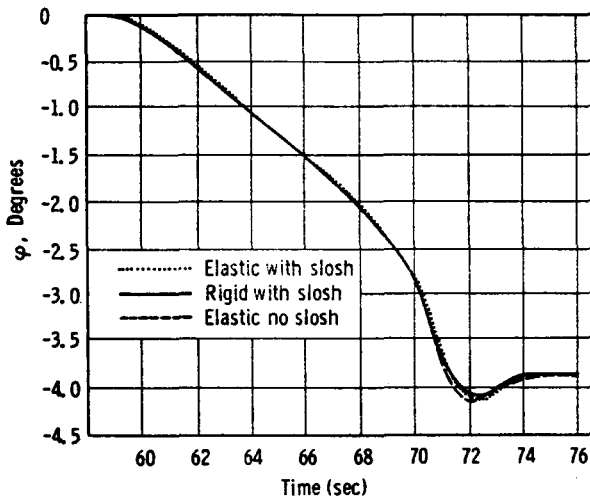


FIGURE 7.43.—Vehicle rotation.

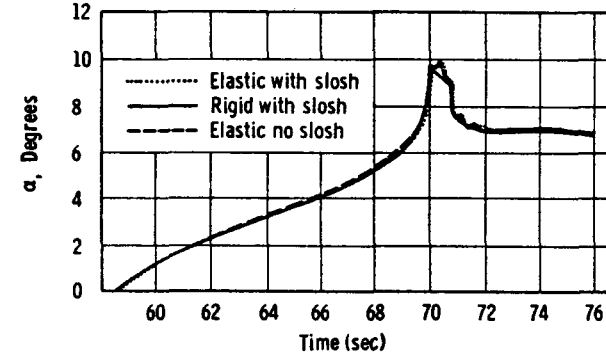


FIGURE 7.45.—Angle of attack.

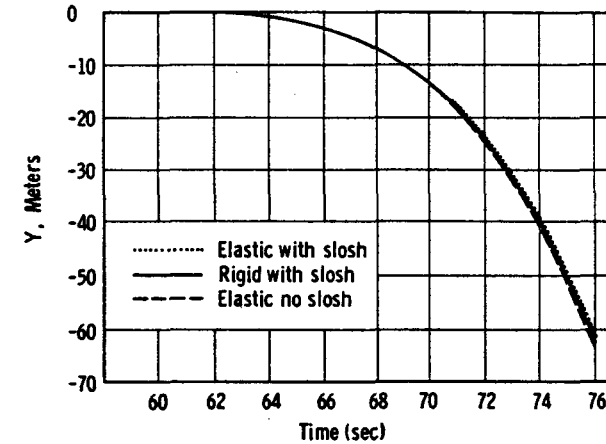


FIGURE 7.46.—Vehicle translation.

(fig. 7.45). The translation of the vehicle is given in figure 7.46 and exhibits only very slight differences between the various cases. The translational acceleration, however, indicates immediately the effect of propellant sloshing. The maximum acceleration is 17 cm/sec<sup>2</sup> (fig. 7.47). The propellant exhibits a maximum amplitude of 21 centimeters in container No. 1. Elastic and rigid vehicles show nearly the same value, except that in the elastic case the peaks come at a slightly later flight time (fig. 7.48). In the second tank (fig. 7.49), the maximum is 13 centimeters for a rigid vehicle and about 1½ centimeters higher for the elastic vehicle. This is because the bending mode at this tank location exhibits a larger

deflection. This effect is increased for the third tank, which is even closer to the antinode of the bending mode and is also located in the danger zone between center of mass and the center of instantaneou s rotation where more baffling is

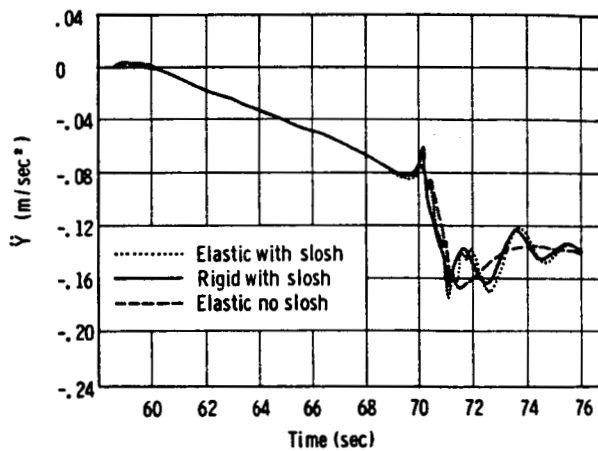


FIGURE 7.47.—Vehicle translatory acceleration.

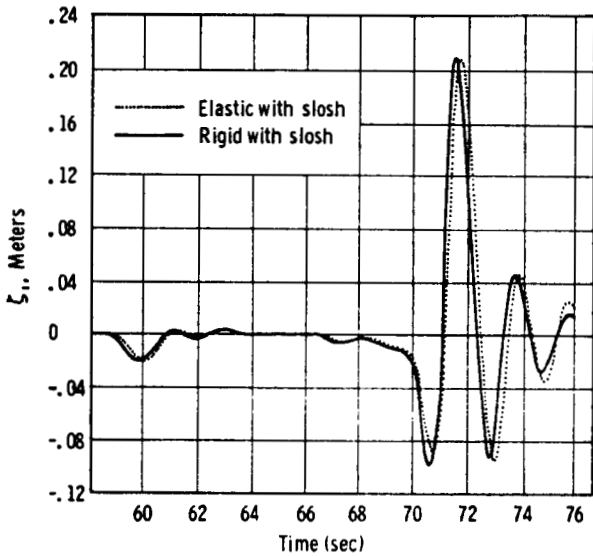


FIGURE 7.48.—First-slosh amplitude.

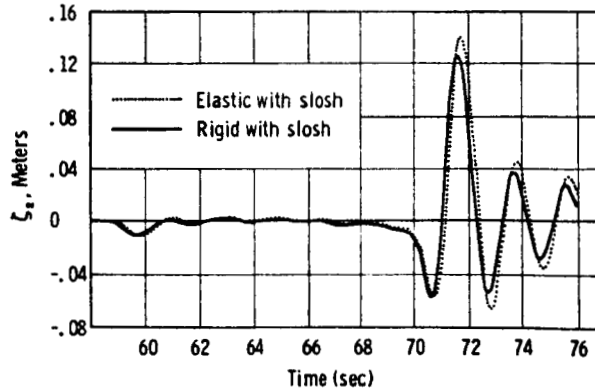


FIGURE 7.49.—Second-slosh amplitude.

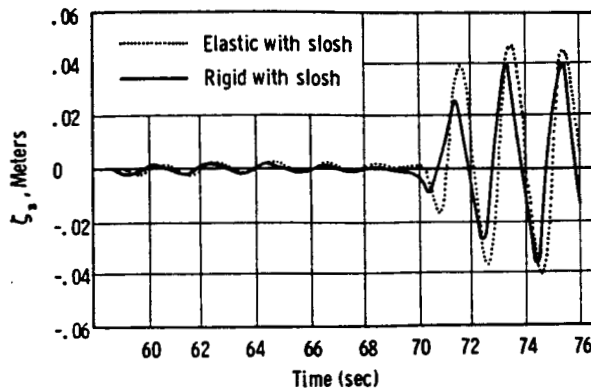


FIGURE 7.50.—Third-slosh amplitude.

required. In figure 7.50, the maximum sloshing amplitude of a rigid vehicle is 4 centimeters, while for an elastic vehicle the amplitude reaches 5 centimeters. The propellant motion exhibits very little damping. The first bending mode is represented in figure 7.51, and reaches its peak of 1.7 centimeters right after the gust has hit the vehicle (the sloshing influences the transient). The second bending mode, shown in figure 7.52, has a maximum value of 4.5 mm and exhibits larger but (because of the low frequency sloshing) smoother values in the transient. In both bending modes, the presence of sloshing propellant influences the decay of the bending motion of the space vehicle.

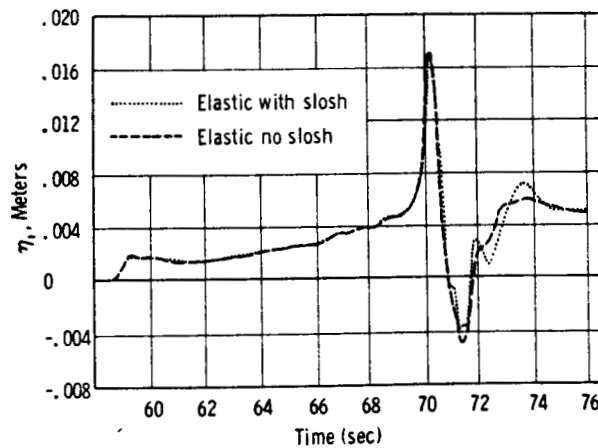


FIGURE 7.51.—First bending deflection.

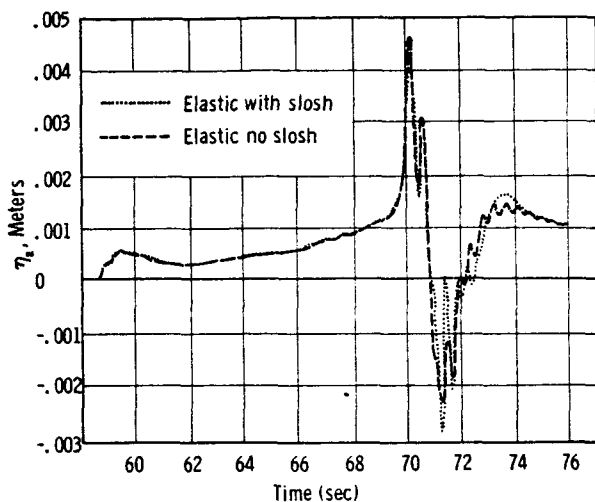


FIGURE 7.52.—Second bending deflection.

### 7.5 EXAMPLE

The following is a simple example which employs the previous results. A Saturn I-type vehicle for which half of the thrust ( $\epsilon = \frac{1}{2}$ ) is available for control purposes is used. The Saturn I booster is powered by a cluster of eight engines, each of which will produce 188000 pounds of thrust to give a total of 1.5 million pounds. The booster is about 6.55 meters in diameter and 25 meters in length. The total length of the vehicle is about 51.8 meters. The eight engines are arranged in two square patterns, of which the inner ones are rigidly attached, while the outer engines are mounted on gimbals which permit them to be turned through angles of about  $10^\circ$  to provide control of the vehicle during first-stage powered flight. Nine separate tanks feed the eight engines. Clustered in a circle about a center tank of 267 centimeters in diameter are eight small tanks of 178 centimeters each in diameter. The center tank (noted as tank No. 1) and four outer containers (noted as tank No. 2) contain liquid oxygen, while the remaining four outer containers (noted as No. 3) contain fuel (RP-1). The S-IV, which is the second stage, is powered by six 15,000-pound-thrust liquid hydrogen/liquid oxygen engines. This stage has a diameter of about 5.5 meters and is about 12.2 meters long. A look at the frequency spectrum versus flight time (fig. 7.53) reveals that the

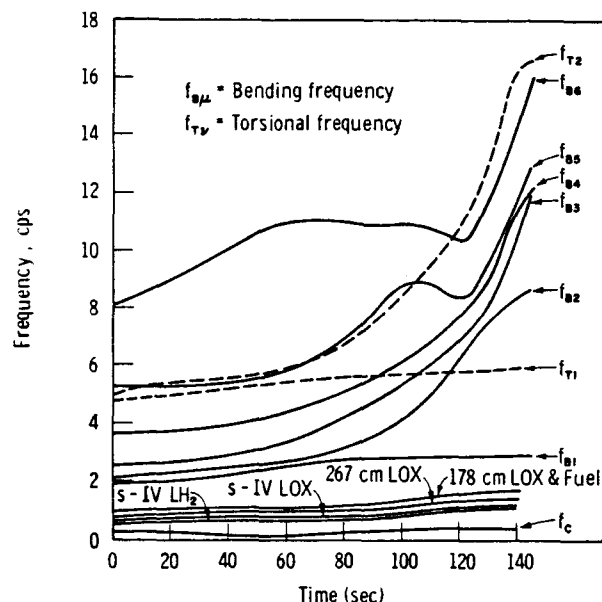


FIGURE 7.53.—Frequency spectrum versus flight time.

control feedback stability problem is a quite involved one. The purpose of such an exercise is to decide early enough in the planning stage as to how the vehicle should be efficiently designed.

The sloshing frequencies range from about 0.5 cps to 1.5 cps. At 140-seconds flight time, the four inboard engines are shut down, which decreases the longitudinal accelerations and is exhibited in the graph by the abrupt drop of the propellant frequencies. The smaller natural frequencies in the 267-centimeter-diameter containers compared to the 178-centimeter container are the result of its larger tank diameter. The same effect, and the smaller liquid height, contributes to the small sloshing frequency in the S-IV LOX tank. The control frequency is in the neighborhood of 0.2–0.3 cps, while the first lateral bending frequency ranges from about 2 to 2.4 cps during booster flight. The location of the mass center and the center of instantaneous rotation of the vehicle, as well as the location of the sloshing masses, for booster flight is shown in figure 7.54. Since the sloshing propellant masses are of great importance upon the dynamics of the vehicle, their magnitude is presented in figure 7.55 as the ratio of the mass of the sloshing propellant in a container

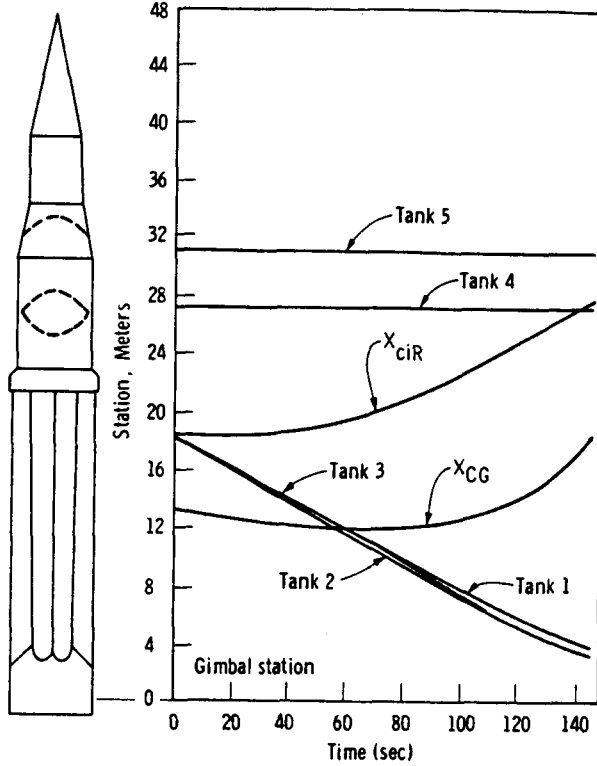


FIGURE 7.54.—Slosh mass location versus booster flight time.

to the total vehicle mass, versus booster flight time. Immediately, it can be seen that the LOX tank of the S-IV stage which exhibits (because of the mass change of the vehicle with booster flight time) large values will have a very pronounced effect upon the stability of the vehicle.

In the following, we shall apply the results of this chapter. The frequency ratios,  $\nu_s = \omega_s / \omega_c$ , are always larger than unity, thus indicating a favorable situation. The gain value is  $a_0 = 1.5$  and changes, at a flight time of 110 seconds, to the magnitude  $a_0 = 1$ . If only one mass were sloshing, say that of the S-IV LOX container, the conclusions we could draw at a flight time of 70 seconds, where  $\mu = 0.03$ ,  $\xi_c = 0.7$ ,  $\nu_s \approx 3$ , and  $\xi_s \approx -1.2$ , from figure 7.13 would be the following: for this flight time no damping would be needed in this container since it is located outside the danger zone, i.e., outside the zone between center of mass and center of instantaneous rotation; at a flight time of 140 seconds, where

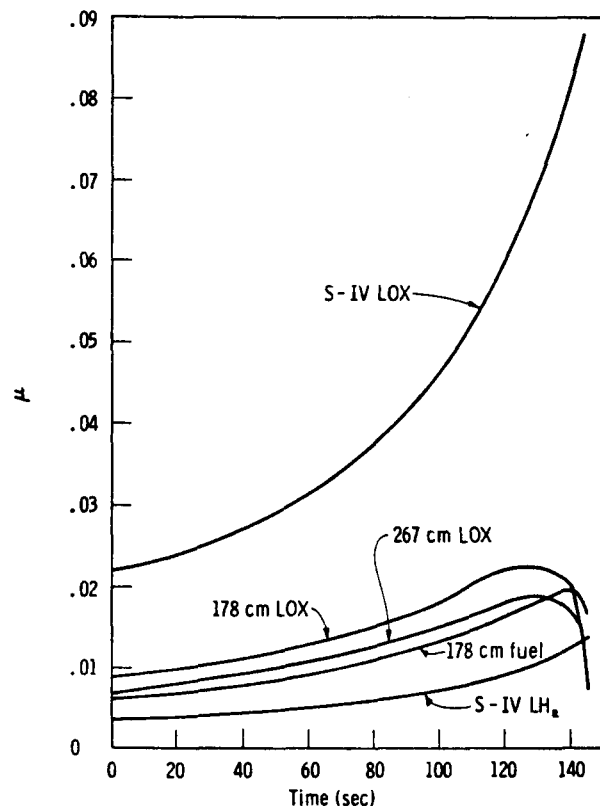


FIGURE 7.55.—Slosh mass ratio for SA-I booster flight.

$\mu = 0.09$ ,  $\nu_s = 4$ , and  $\xi_s \approx -0.9$ , a little damping in the amount of about  $\gamma_s \approx 0.005$  would be needed to maintain stability.

Combining all sloshing masses of the booster in one mass and considering the effect of the S-IV stage sloshing masses as negligible yields the following: first of all, at a flight time of 70 seconds, the combined slosh mass ratio  $\mu$  would be of the magnitude of about  $\mu = 0.09$ ; the frequency ratio,  $\nu_s$ , is about  $\nu_s \approx 3$ , and the location  $\xi_s \approx 0$ . For this particular case, a damping of about 1 percent should be provided. At a flight time of 140 seconds,  $\mu = 0.18$ ,  $\nu_s = 4$ , and  $\xi_s = 0.8$ , no damping is needed since the sloshing mass is located outside of the danger zone. From this simple consideration, one can conclude that a stationary baffle arrangement in the upper part of the booster tanks is sufficient to maintain flight stability during the boost phase.

To obtain, however, a more realistic requirement, we have to look at the sloshing in several containers. Considering the S-IV LOX slosh-

ing mass together with the combined booster sloshing mass, one can use the results presented in figures 7.25 and 7.26. At 70-seconds flight time, the sloshing masses are given by  $\mu_1=0.09$  and  $\mu_2=0.03$ , while  $\nu_1=\nu_2\approx 3$ . The distance  $l$  of the combined booster sloshing mass,  $\mu_1$ , to the fixed sloshing mass,  $\mu_2$ , of the second stage is  $l\approx -16.25$  meters; that is,  $\xi_1\approx -1.3$ . The value  $\xi_2\approx 0$ , and we conclude that a damping of  $\gamma_s\approx 0.013$  is needed to have a stable flight condition. At a flight time of 140 seconds,  $\mu_1=0.18$ ,  $\mu_2=0.09$ ,  $\nu_1\approx\nu_2\approx 4$ ,  $\xi_1=0.8$ , and  $\xi_2\approx -1.8$ , and a damping of about 1 percent is needed. It furthermore can be seen that damping is needed in the lower part of the booster containers. Since the fundamental bending frequency is close to the sloshing frequencies,

the effects of vehicle elasticity (ch. 9) must also be considered. Furthermore, some wind response studies will show the adequacy of the baffles. (See sec. 7.4.)

The actual feedback analysis of the flexible vehicle with all its slosh masses included indicated that with smooth container walls a slight instability occurred in the 178-centimeter containers between 40- and 60-seconds flight time, and in the 267-centimeter-diameter container an instability occurs between 60- and 90-seconds flight time (ref. 7.23). By employing proper baffles, these instabilities could be removed. The same procedure can now be performed for the second-stage flight, but has been omitted here for reasons of limited space.

## REFERENCES

- 7.1. BAUER, H. F.; AND RHEINFURTH, M. H.: Flutter and Stability Analysis. Army Ballistic Missile Agency, Redstone Arsenal, Ala., DA-TM-4-60, 1960.
- 7.2. RHEINFURTH, M. H.: Control Feedback Stability Analysis. Army Ballistic Missile Agency, Redstone Arsenal, Ala., DA-TR-2-60, 1960.
- 7.3. THORP, F. A.; AND HUTCHINSON, R. C.: The Dynamics of Rocket-Powered Vehicles. Massachusetts Institute of Technology, Rept. R-208, Feb. 1959.
- 7.4. LUKENS, D. R.; SCHMITT, A. F.; AND BROUCEK, G. T.: Approximate Transfer Function for Flexible-Booster-and-Auto-Pilot Analysis. WADD-TR-61-93, 1961.
- 7.5. BARTON, M.: Generalized Missile Dynamics Analysis. Ramo-Wooldridge Corp., 1958.
- 7.6. HEIST, E. K.: Equations of Motion of Missile With Sloshing. Guided Missile Research Division, Ramo-Wooldridge Corp. Rept. No. GM-TM-146, 1956.
- 7.7. BAUER, H. F.: Fluid Oscillations in the Container of a Space Vehicle and Their Influence Upon Stability. NASA-TR R-187, 1964.
- 7.8. BAUER, H. F.: Dynamics of Liquid Propellant Vehicles. Proceedings of the ONR/AIA Symposium on Structures and Dynamics of High Speed Flight, ONR/AIA Symposium, 1961.
- 7.9. BAUER, H. F.: The Effects of Interaction of Structure, Control and Propellant Sloshing Upon the Stability of Large Space Vehicles. Marshall Space Flight Center, NASA, MTP-AERO-61-83, 1961.
- 7.10. ZURMÜHL, R.: Praktische Mathematik für Ingenieure und Physiker. Springer-Verlag, Berlin, 1953.
- 7.11. BRODETSKY, S.; AND SMEAL, G.: On Graeffe's Method for Complex Roots of Algebraic Equations. Proc. Cambridge Phil. Soc., vol. 22, 1924, pp. 83-87.
- 7.12. ROUTH, E. J.: A Treatise on the Stability of a Given Motion. Macmillan, London, 1877, pp. 74-81.
- 7.13. HURWITZ, A.: Über die Bedingungen unter welchen eine Gleichung nur Wurzeln mit negativen reellen Theilen besitzt. Mathematische Annalen, vol. 46, 1895, pp. 273-284.
- 7.14. NYQUIST, H.: Regeneration Theory. Bell System Technical Journal, vol. 11, 1932, 126-147.
- 7.15. RHEINFURTH, M. H.: The Influence of Control Sensors on the Stability of Space Vehicles. Marshall Space Flight Center, NASA, MTP-61-65, 1961.
- 7.16. BAUER, H. F.: The Effects of Propellant Sloshing on the Stability of an Accelerometer Controlled Rigid Space Vehicle. NASA TN D-1831, 1963.
- 7.17. BAUER, H. F.: Stability Boundaries of Liquid Propelled Space Vehicles With Sloshing. AIAA J., vol. 1, no. 7, 1963.
- 7.18. HEINRICH, K.; AND KAUFMAN, F. H.: Sloshing Stability Criteria for Vehicles With One Free Fluid. Ramo-Wooldridge Memo GM-45.3-45, 1956.
- 7.19. FULLER, A. T.: Stability Criteria for Linear Systems and Reliability Criteria for RC Networks. Proc. Cambridge Phil. Soc., vol. 53, 1957, pp. 878-896.
- 7.20. GEISSLER, E. D.: Problems in Attitude Stabilization of Large Guided Missiles. Aero-Space Engineering, Oct. 1960, pp. 24-29.

- 7.21. BAUER, H. F.: Parametric Study of the Influence of Propellant Sloshing on the Stability of Space Crafts. J. Aerospace Sci., Oct. 1961, pp. 819-820.
- 7.22. BAUER, H. F.: Wind Response of the Saturn

- LOR Vehicle. Marshall Space Flight Center, NASA, MTP-AERO-63-19, 1963.
- 7.23. HAYS, P. J., AND SUMRALL, J. P.: Stability Analysis of Saturn SA-5 With Live S-IV Stage. NASA TM-X-53017, 1964.

## PRINCIPAL NOTATIONS

$a_0$ =gain factor of attitude channel  
 $a_1$ =coefficient of control damping  
 $A_t$ =output signal of accelerometer  
 $A_s$ =shear area of airframe cross section  
 $c_a$ =damping coefficient of accelerometer  
 $c_g$ =damping coefficient of rate gyroscope  
 $c_{n\lambda}$ =damping coefficient of  $n$ th sloshing mode in  $\lambda$ th propellant container  
 $D$ =dissipation function  
 $D_p$ =dissipation function of propellant  
 $D_s$ =dissipation function of vehicle structure  
 $EI$ =flexural stiffness of airframe  
 $F=F_1+F_2$ =thrust  
 $F_1$ =stationary thrust  
 $F_2$ =gimbal thrust  
 $g=\frac{F}{m}$ =longitudinal vehicle acceleration  
 $g_1$ =structural damping factor of the  $v$ th bending mode  
 $g_2$ =gain factor of accelerometer channel  
 $G$ =shear modulus  
 $H_r$ =Hurwitz determinant  
 $I$ =mass moment of inertia of total vehicle about mass center of vehicle  
 $I_c$ =moment of inertia of rate gyroscope about its output axis  
 $I_{0\lambda}$ =moment of inertia of nonsloshing liquid mass in  $\lambda$ th propellant container (about its center of mass)  
 $I_R$ =moment of inertia of rotor of rate gyroscope about spin axis  
 $I'_s$ =moment of inertia of structure per unit length  
 $k$ =radius of gyration of vehicle about its mass center  
 $k_a$ =spring constant of accelerometer

$k_x$ =spring constant of swivel compliance  
 $k_{n\lambda}$ =spring constant of  $n$ th mode of slosh model in  $\lambda$ th tank  
 $K_G$ =restoring moment of rate gyroscope per unit angle  
 $m$ =mass of vehicle  
 $m_a$ =mass of accelerometer  
 $m_{n\lambda}(m_s)$ =mass of  $n$ th sloshing mode in  $\lambda$ th tank  
 $m_{0\lambda}$ =mass of nonsloshing liquid in  $\lambda$ th tank  
 $m'$ =mass of structure per unit length  
 $M_B$ =generalized mass of  $v$ th bending mode  
 $M_R$ =gyroscopic reaction torque of rate gyroscope  
 $M_v$ =bending moment of  $v$ th bending mode  
 $p_{1,p}$ =phase-lag coefficients of control system  
 $q_i$ =generalized coordinates  
 $Q_i$ =generalized forces  
 $Q_v$ =shear force of  $v$ th bending mode  
 $s=\sigma+i\omega$ =complex frequency  
 $t$ =time  
 $T$ =kinetic energy  
 $T_p$ =kinetic energy of propellant  
 $T_s$ =kinetic energy of structure  
 $v$ =cross-velocity  
 $V$ =potential energy of vehicle  
 $V_p$ =potential energy of propellant  
 $V_{sx}$ =potential energy of elastic deformation of structure  
 $V_{sg}$ =potential energy of raising center of mass in equivalent gravitational field  
 $V_v$ =potential energy of bending vibration  
 $x$ =abscissa, distance from mass center  
 $x_a$ =coordinate of accelerometer  
 $|x_{cIR}|$ =distance of center of instantaneous rotation to mass center of vehicle

$x_g$ =coordinate of swivel point  
 $x_g$ =coordinate of gyroscope  
 $x_{n\lambda}(x_s)$ =coordinate of sloshing mass of  $n$ th mode in  $\lambda$ th tank  
 $x_{0\lambda}$ =coordinate of nonsloshing mass in  $\lambda$ th tank  
 $x_R$ =coordinate of rate gyroscope  
 $y$ =lateral translation of rigid vehicle  
 $y_a$ =displacement of accelerometer mass relative to vehicle  
 $y_{n\lambda}$ =displacement of  $n$ th sloshing mass in  $\lambda$ th container relative to vehicle  
 $Y_v$ =normalized bending deflection curve of  $v$ th bending mode  
 $\alpha = \frac{x_a}{|x_{e(R)}|}$ =location parameter of accelerometer  
 $\beta$ =engine deflection angle against vehicle center axis  
 $\beta_c$ =control deflection  
 $\gamma_s$ =slosh damping factor  
 $\epsilon = \frac{F_2}{F}$ =ratio of thrust available for control purpose to total thrust of vehicle  
 $\epsilon_a$ =abbreviation for accelerometer defined on page 242  
 $\epsilon'_a$ =abbreviation for accelerometer defined on page 242  
 $\epsilon'_g$ =abbreviation for gyroscope defined on page 239  
 $\epsilon'_R$ =abbreviation for rate gyroscope defined on page 239  
 $\zeta_a$ =damping factor of accelerometer  
 $\zeta_c$ =damping factor of control system  
 $\zeta_g$ =damping factor of rate gyroscope  
 $\zeta_{n\lambda}$ =damping factor of  $n$ th sloshing mode in  $\lambda$ th tank  
 $\eta_v$ =generalized coordinate of  $v$ th bending mode

$\theta_i$ =indicated angular velocity of airframe at the location of the rate gyroscope  
 $\lambda = \epsilon gg_2$  "gain parameter" of accelerometer  
 $\lambda = gg_2$   
 $\mu_{n\lambda} = \frac{m_{n\lambda}}{m}$ =slosh mass ratio of  $n$ th sloshing mode in  $\lambda$ th container to total vehicle mass  
 $\nu_a = \omega_a/\omega_c$ =frequency ratio of accelerometer to control frequency  
 $\nu_s = \omega_s/\omega_c$ =frequency ratio of propellant to control frequency  
 $\xi_a = \frac{x_a}{k}$   
 $\xi_d = \frac{x_d}{k}$   
 $\xi_E = \frac{x_E}{k}$   
 $\xi_i = \frac{x_i}{k}$   
 $\xi_s = \frac{x_s}{k}$   
 $\phi$ =rotation angle of rigid vehicle relative to space  
 $\phi_i$ =output signal of attitude gyroscope  
 $\dot{\phi}_R$ =angular velocity of airframe at the location of the rate gyroscope  
 $\omega_a$ =natural circular frequency of accelerometer  
 $\omega_c$ =natural circular control frequency  
 $\omega_g$ =natural circular frequency of rate gyroscope  
 $\omega_{n\lambda}(\omega_s)$ =natural circular frequency of  $n$ th propellant mode in  $\lambda$ th container  
 $\omega_R$ =angular velocity of rotor in rate gyroscope  
 $\omega_v$ =natural circular frequency of  $v$ th bending mode

## **Vertical Excitation of Propellant Tanks**

*Franklin T. Dodge*

### **8.1 INTRODUCTION**

The dynamic response of liquids is discussed in this chapter for the case when the containing tank is vibrated vertically. Vertical and longitudinal vibrations in actual rockets can arise from several sources. One cause of such vibrations is a dynamic coupling between the rocket structure and engine thrust during flight. Several large liquid fuel boosters, including Thor-Agena, Atlas-Agena, Titan I, and Titan II, have been subject to this kind of vibration, with the frequency usually corresponding to the first longitudinal structural mode, typical values being between 10 and 30 cps. Another type of longitudinal vibration, apparently originating through a coupling of the vehicle structure and the pneumatic tank pressure regulation system, also has been observed during the early part of the flight of some missiles; as one example, the frequency of such vibrations is about 5 cps for Atlas-D boosters. Some of these types of longitudinal vibrations encountered in flight have been called "pogo oscillations," and are discussed more fully in chapter 10.

Vertical vibrations may also occur during the time preceding actual launch when the vehicle is held down and its engines brought up to full thrust, which, for large boosters, may be on the order of several seconds. The vibrations occurring then are very complex because of such factors as the rough burning of the fuel, the interaction of the exhaust and the exhaust deflection structure, etc.

A complete analysis of the origin of the various types of vertical vibration is beyond the scope of this chapter; however, regardless of the origin, the effect of the vibration on the liquid fuel depends primarily on its frequency

and amplitude. At low frequencies<sup>1</sup> the liquid surface may respond in a large amplitude standing wave; as an example, the first symmetrical mode in a 14.5-centimeter-diameter tank model, for an excitation of approximately 7.5 cps, is shown in figure 8.1. The wave motion frequency for a response of this type is exactly one-half that of the excitation; consequently, such motions are called one-half subharmonic responses.

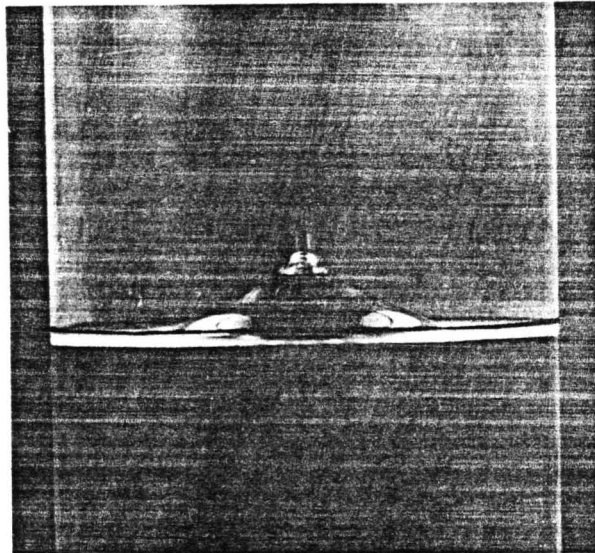


FIGURE 8.1.—Typical liquid motion for  $m=0, n=1$  mode  $\frac{1}{2}$ -subharmonic (ref. 8.20).

At higher frequencies, the amplitude of the liquid motion is usually quite small. But for certain combinations of excitation frequency and amplitude, these small capillary waves may disintegrate, form a dense spray, and

<sup>1</sup> Precisely what is meant by "high" and "low" frequencies will be clarified in later sections of this chapter.

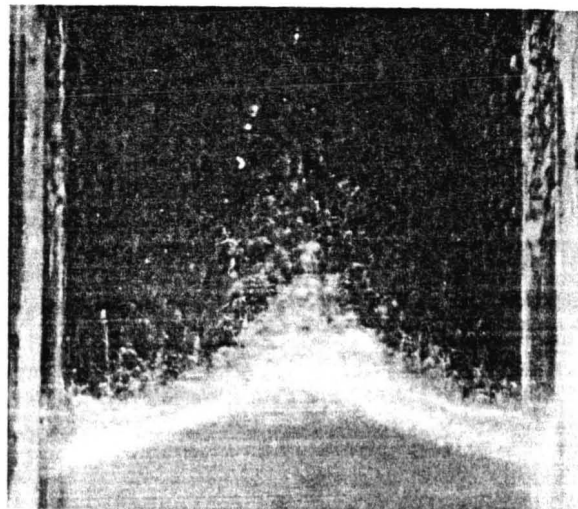


FIGURE 8.2.—Second-mode surface wave maintained by spray (ref. 8.18).

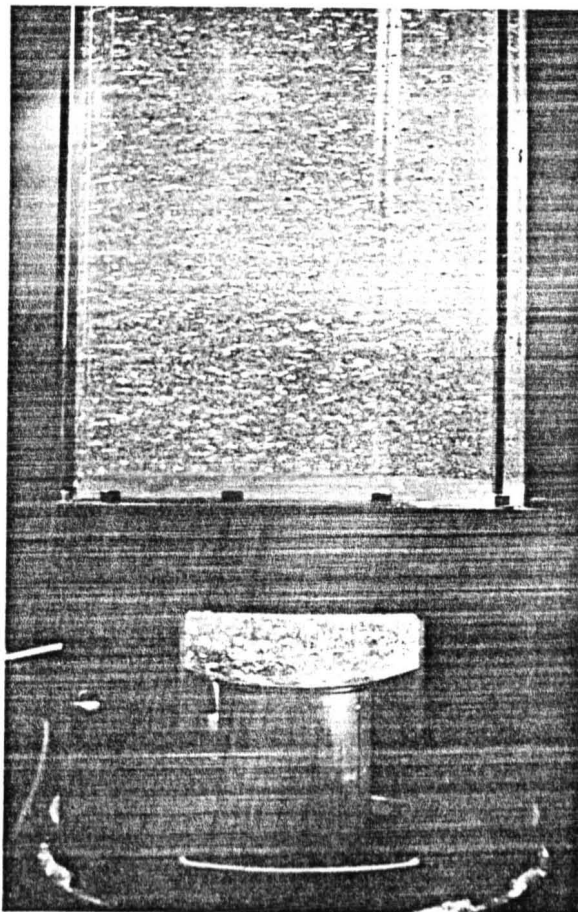


FIGURE 8.3.—Bubbles entering drain line in vertically excited tank (ref. 8.35).

thereby generate a large amplitude, much lower frequency standing wave. This phenomenon is illustrated in figure 8.2, which shows a typical spray-formed wave in a small rectangular test tank.

The free surface motion sometimes becomes very violent at larger input levels of vibration, and small vapor bubbles are entrained in the liquid. The bubbles can become negatively buoyant and thus sink to the tank bottom; such bubble motions are, of course, contrary to the usual state of affairs. Once these sinking bubbles reach the tank bottom they can either form a large aggregate bubble, or, as in the model tank shown in figure 8.3, they can surge continuously into the drain pipe. Both of these situations may pose serious problems for liquid fuel rockets, although it must be emphasized that such occurrences have not yet been evidenced in any way other than in laboratory experiments.

All of the foregoing types of liquid responses will be examined in greater detail in the following sections.

## 8.2 LIQUID SURFACE RESPONSE TO LOW-FREQUENCY EXCITATION

### Historical Survey

When a tank containing a heavy liquid is forced to vibrate vertically, at a frequency not too large in comparison with one of the first few natural frequencies of free sloshing discussed in chapter 2, a pattern of standing waves can be observed on the free surface. Contrary to one's intuition, it has been observed that the wave frequency, that is, the frequency of the surface oscillations, usually occurs at exactly one-half that of the container motion, although in some cases the liquid frequency is equal to the forcing frequency, and in other cases, greater. The frequency of the free surface vibrations for transverse excitation, of course, corresponds precisely to the forcing frequency, as discussed in chapter 2.

This apparently anomalous behavior for vertical excitation was first noticed by Faraday during a series of investigations of vibrating plates covered by a thin layer of water (ref. 8.1).

In his experiments, it appeared that the free surface waves vibrated with a frequency which was only half that of the plate. About 40 years later, a similar series of tests was conducted by Mathiessen (refs. 8.2 and 8.3), and on one very important point he recorded an opinion in opposition to that of Faraday: in his experiments, Mathiessen found that the liquid vibrations were synchronous. Since the theory of gravity waves had not been developed to a point at which this contradiction could be resolved analytically, Lord Rayleigh repeated Faraday's original experiments with improved equipment. Rayleigh observed, in support of Faraday's view, that the liquid oscillations were a one-half subharmonic of the forcing motion; that is, they occurred at a frequency equal to half that of the excitation (ref. 8.4). In addition, by generalizing his theory of forced vibrations which he had originally restricted to systems having only one degree of freedom, he developed a tentative theory to explain the liquid oscillations (refs. 8.5 and 8.6). His analysis led to a single Mathieu equation; using this analysis, Rayleigh was able to show the existence of subharmonic surface waves.

It is now known, as will be shown in the following sections, that vertical vibration causes a quiescent liquid free surface to become unstable for much the same reasons as those discussed by Taylor (ref. 8.7) in his treatment of the well-known Rayleigh-Taylor instabilities. The theory of such liquid motions leads to a system of Mathieu equations. Because of the more complete development of the theory of Mathieu functions since Rayleigh's time, it is now possible to show that Faraday, Mathiessen, and Rayleigh might all have been correct; also, the actual dynamics of the liquid motion, which are important in missile stability analyses, may now be calculated.

#### Linearized Theory

As in most dynamical systems, the equations of motion for the liquid contained in a vertically vibrating tank can be developed either from an integral equation (energy) approach, or from a differential equation approach. The energy method, which is especially suitable for approximate calculations or for tank shapes which do

not correspond to any standard coordinate system, has been developed extensively by Moiseyev (refs. 8.8 and 8.9) and Bolotin (ref. 8.10). However, the more elementary differential equation approach is sufficient for a large number of practical cases, and it is the method employed in this chapter.

The linearized theory developed here follows closely the analysis of Benjamin and Ursell (ref. 8.11) and is given with as much generality as possible. The results are then specialized in later sections when particular examples are discussed. In nearly all of this section, the elasticity of the liquid container is neglected; this subject is discussed in detail in chapter 9.

Suppose that a rigid cylindrical tank of arbitrary cross section, but having a flat bottom, is filled to a depth,  $h$ , with an incompressible, inviscid liquid. The tank is vibrated vertically with an amplitude,  $x_0$ , and a frequency,  $N\omega$ , where  $N$  is a positive number. The frequency of the liquid motion is assumed to be  $\omega$ , so that specifying  $N$  determines, in effect, whether the liquid response is subharmonic, harmonic, or superharmonic.

Cartesian axes ( $x$ ,  $y$ ,  $z$ ) are fixed to the tank, with the  $z$ -axis pointing upward along the tank axis. The undisturbed free surface corresponds to  $z=0$  and the tank bottom to  $z=-h$ . Thus, the axes move with a vertical acceleration  $N^2\omega^2x_0 \cos N\omega t$ , and the motion relative to these axes is the same as if the tank were at rest and the gravitational acceleration were  $g - N^2\omega^2x_0 \cos N\omega t$ . The fluid velocity relative to the moving axes may be derived from a potential,  $\Phi$ , that satisfies Laplace's equation

$$\frac{\partial^2 \Phi}{\partial x^2} + \frac{\partial^2 \Phi}{\partial y^2} + \frac{\partial^2 \Phi}{\partial z^2} = 0 \quad (8.1)$$

The Eulerian equations of motion can be integrated by using  $\Phi$  to yield the unsteady form of Bernoulli's equation

$$-\frac{p}{\rho} + \frac{\partial \Phi}{\partial t} - \frac{1}{2} \left[ \left( \frac{\partial \Phi}{\partial x} \right)^2 + \left( \frac{\partial \Phi}{\partial y} \right)^2 + \left( \frac{\partial \Phi}{\partial z} \right)^2 \right] - (g - N^2\omega^2x_0 \cos N\omega t)z = 0$$

where  $p$  is the fluid pressure measured relative to the ullage pressure and  $\rho$  the fluid density.

At the free surface there is an additional pressure restriction of the form

$$p = \nu \left( \frac{1}{R_1} + \frac{1}{R_2} \right)$$

where  $\nu$  is the surface tension, and  $R_1, R_2$  the principal radii of curvature of the surface. It is acceptable to consider only small motions and displacements in a linearized theory, so that

$$\frac{1}{R_1} + \frac{1}{R_2} \approx \frac{\partial^2 \eta}{\partial x^2} + \frac{\partial^2 \eta}{\partial y^2}$$

where  $z = \eta(x, y, t)$  is the equation of the free surface. Consequently, the linearized form of Bernoulli's equation that must be satisfied at the free surface is<sup>2</sup>

$$\left[ -\frac{\nu}{\rho} \left( \frac{\partial^2 \eta}{\partial x^2} + \frac{\partial^2 \eta}{\partial y^2} \right) + \frac{\partial \Phi}{\partial t} - (g - N^2 \omega^2 x_0 \cos N\omega t) \eta \right]_{z=0} = 0 \quad (8.2)$$

It must also be required that the velocity of the free surface normal to itself must equal the fluid velocity normal to the surface. When linearized, as shown in chapter 2, this requirement takes the form

$$\left[ \frac{\partial \eta}{\partial t} = -\frac{\partial \Phi}{\partial z} \right]_{z=0} \quad (8.3)$$

The remaining boundary conditions are that the perpendicular velocities at the walls and bottom must be zero; that is

$$\frac{\partial \Phi}{\partial n} = 0 \quad (8.4)$$

at the walls, and

$$\frac{\partial \Phi}{\partial z} = 0 \quad (8.5)$$

at the bottom,  $z = -h$ .

By combining equations (8.3) and (8.4) it can be seen that  $\partial \eta / \partial n = 0$  on the curve bounding the free surface; hence, from equation (8.2) one can show that

<sup>2</sup> This equation is strictly valid only if the liquid contact angle at the tank walls is 90°.

$$\frac{\partial}{\partial n} \left[ \frac{\partial^2 \eta}{\partial x^2} + \frac{\partial^2 \eta}{\partial y^2} \right] = 0$$

on the same bounding curve. These conditions are typical of an eigenvalue problem, and consequently they show that  $\Phi$  and  $\eta$  can each be expanded in terms of a complete orthogonal set of functions  $S_m(x, y)$ . Hence, from equation (8.1) it can be seen that

$$\left( \frac{\partial^2}{\partial x^2} + \frac{\partial^2}{\partial y^2} + \tilde{\lambda}_m^2 \right) S_m = 0 \quad (8.6)$$

in the fluid interior, and

$$\frac{\partial S_m}{\partial n} = 0$$

on the bounding curves or surfaces.  $\tilde{\lambda}_m$  are the eigenvalues. It then follows (ref. 8.11) that the required expansions are

$$\begin{aligned} \eta(x, y, t) &= \sum_{m=0}^{\infty} a_m(t) S_m(x, y) \\ \frac{\partial^2 \eta}{\partial x^2} + \frac{\partial^2 \eta}{\partial y^2} &= - \sum_{m=0}^{\infty} \tilde{\lambda}_m^2 a_m(t) S_m(x, y) \\ \Phi(x, y, z, t) &= - \sum_{m=0}^{\infty} \dot{a}_m(t) \frac{\cosh \tilde{\lambda}_m(z+h)}{\tilde{\lambda}_m \sinh \tilde{\lambda}_m h} S_m(x, y) \end{aligned} \quad (8.7)$$

Substituting equations (8.7) into equation (8.2) shows that

$$\ddot{a}_m + \tilde{\lambda}_m \tanh \tilde{\lambda}_m h \left( \frac{\tilde{\lambda}_m^2 \nu}{\rho} + g - N^2 \omega^2 x_0 \cos N\omega t \right) a_m = 0 \quad (8.8)$$

for  $m = 0, 1, 2, \dots$ , and, of course,  $m$  specifies the particular mode under consideration. Using this equation, the unknown time varying liquid sloshing amplitude can be determined.

It may be seen immediately that one solution of equation (8.8) is  $a_m = 0$ , identically. This solution corresponds to no sloshing motion at all; i.e., the liquid column acts as a rigid body and vibrates up and down as a slug. Under ideal conditions such a response may be possible, but if the free surface is disturbed in any way, one should expect that the disturbance would tend to grow into some more sizable liquid

motion. Consequently, the problem at hand is one of the stability of a quiescent free surface, and equation (8.8) actually determines the kinds of excitation for which the free surface is unstable; that is, it determines the conditions for which disturbances tend to grow. In order to find these conditions as simply as possible, it is best to let the frequency of the liquid motion be variable and the excitation frequency be fixed at  $\omega$ , instead of, as heretofore assumed, letting the liquid frequency be fixed and the excitation frequency vary through the parameter  $N$ . (It will soon be seen that the original formulation, however, is more convenient in a nonlinear analysis.) So, letting  $N=1$ , and introducing the parameters

$$p_m = \frac{4\tilde{\lambda}_m \tanh \tilde{\lambda}_m h}{\omega} \left( g + \frac{\tilde{\lambda}_m^2 \nu}{\rho} \right)$$

$$q_m = 2\tilde{\lambda}_m x_0 \tanh \tilde{\lambda}_m h$$

$$T = \frac{1}{2} \omega t$$

allows equation (8.8) to be written more simply as

$$\frac{d^2 a_m}{dT^2} + (p_m - 2q_m \cos 2T) a_m = 0 \quad (8.9)$$

which may be recognized as the standard form of Mathieu's equation.

In the usual treatises on Mathieu functions it is shown that equation (8.9) can have stable or unstable solutions, depending on the values of  $p_m$  and  $q_m$ . The regimes of stability and instability are usually shown in a plot such as figure 8.4. The shaded areas in this figure correspond to unstable solutions of equation (8.9), the solutions for which  $a_m \rightarrow \infty$  as  $T \rightarrow \infty$ . Only the first three unstable regions are shown, and the predominant frequency of the liquid motion for each area is indicated on the plot. The unshaded regions correspond to stable solutions of equation (8.9).

When  $x_0$  and  $\omega$  are given, a point on the stability chart may be determined for each of the sequence of eigenvalues  $\tilde{\lambda}_m$ . To determine whether or not the free surface is unstable,  $p_m$  and  $q_m$  must be calculated for each mode and their position on the stability chart observed.

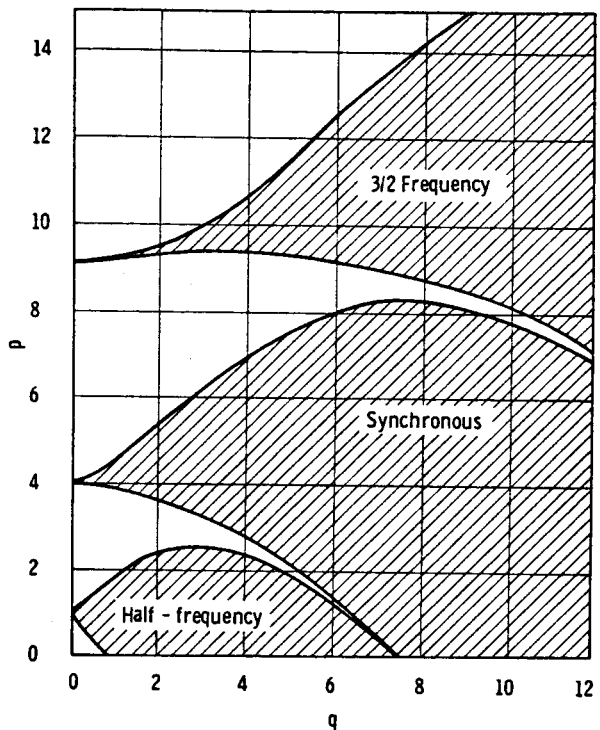


FIGURE 8.4.—Stability chart for the solutions of Mathieu's equation.

It can be argued that at least one of the points  $(p_m, q_m)$  for some mode lies in an unstable region, whatever  $x_0$  and  $\omega$ . In practical cases, however, where the system is slightly dissipative, the higher order modes tend to be suppressed, and an appreciable disturbance of the free surface occurs only when one of the lower order modes is excited.

A good deal more information about possible types of unstable liquid motion can be obtained by replotted figure 8.4 with dimensional parameters. Figure 8.5 illustrates such a stability diagram for a 14.5-centimeter-diameter circular cylindrical tank model, with a liquid depth equal to the tank diameter; this tank is essentially rigid for the low frequency excitation considered here and, thus, the preceding results are applicable. Only a few of the unstable and stable regions corresponding to the mode of lowest natural frequency (smallest  $\tilde{\lambda}_m$ ) are shown. One obvious point of difference between figures 8.4 and 8.5 is that the instability regions are much narrower when plotted dimensionally. Since the effect of damping is to

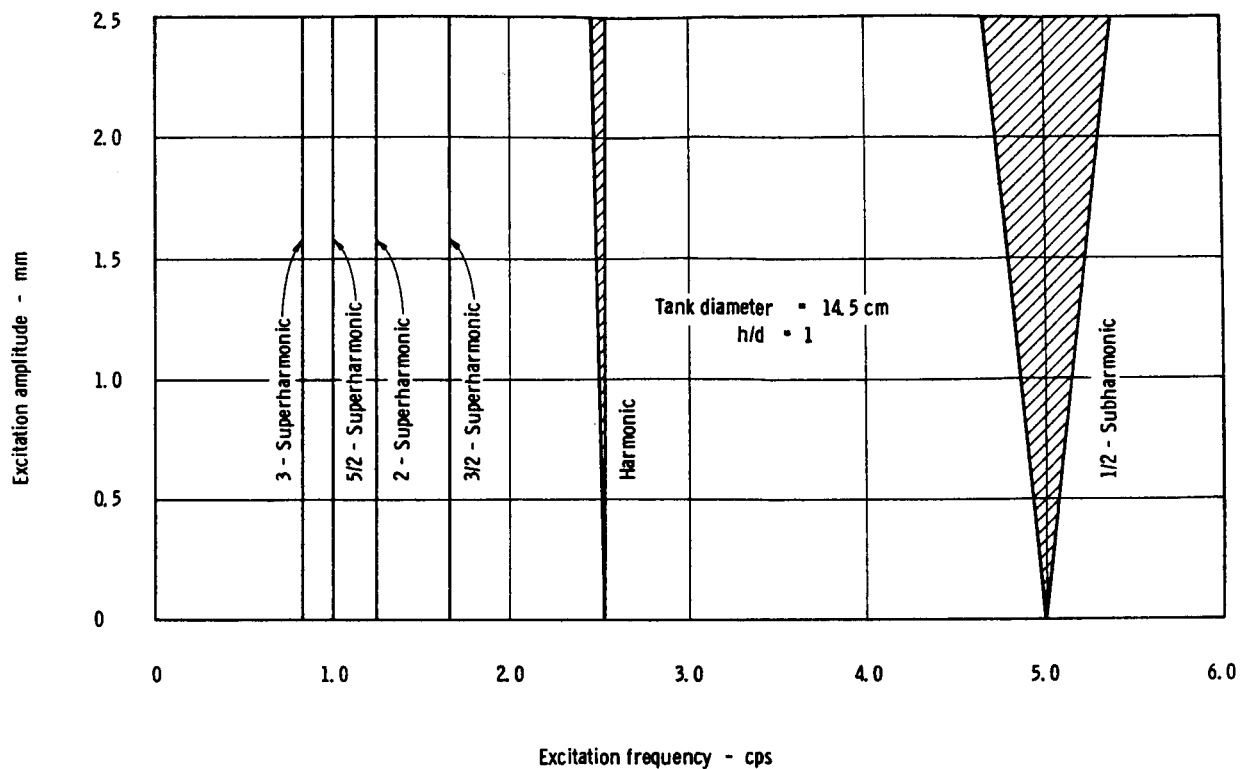


FIGURE 8.5.—Partial Mathieu stability chart for  $m=1$ ,  $n=1$  mode.

make these regions even narrower, one can see that the one-half subharmonic would probably be the only large amplitude wave motion observed in experiments.

In any given tank there are a large number of modes, each having its own stability diagram. Figure 8.6 shows some of the one-half subharmonic instability regions, and the location of several harmonic modes, for the same tank model as figure 8.5. From this chart, one can see that the unstable regions for various sloshing modes overlap one another; for example, the first symmetrical mode ( $m=0$ ,  $n=1$ , in this chart) and the second and third antisymmetrical modes ( $m=2$ ,  $n=1$ , and  $m=3$ ,  $n=1$ ) overlap considerably. In fact, for almost any combination of excitation frequency and amplitude, there is some overlapping of unstable regions, and it is apparent that this overlapping is even more congested at higher frequencies. The low-order modes can be fairly well isolated, however, so that they are con-

venient modes to study both experimentally and analytically. These modes are also the most important in practical applications.

#### Large Amplitude Subharmonic Motion

As mentioned previously, the only sizable liquid motion that is usually observed in a vertically vibrated tank is the  $\frac{1}{2}$ -subharmonic response. In order to investigate this response more thoroughly, it is now assumed that the time dependence of the  $m$ th sloshing mode is adequately represented by

$$a_m = A \sin \omega t + B \cos \omega t$$

If  $N=2$  in equation (8.8), then the steady-state motion given by this equation does indeed represent a  $\frac{1}{2}$ -subharmonic response.

By substituting the above equation into equation (8.8), setting  $N=2$ , and collecting terms, one finds that

$$\left[ -\omega^2 + \tilde{\lambda}_m \tanh \tilde{\lambda}_m h \left( \frac{\tilde{\lambda}_m^2 \nu}{\rho} + g + 2\omega^2 x_0 \right) \right] A \sin \omega t \\ + [\dots] \sin 3\omega t + \left[ -\omega^2 + \tilde{\lambda}_m \tanh \tilde{\lambda}_m h \left( \frac{\tilde{\lambda}_m^2 \nu}{\rho} + g - 2\omega^2 x_0 \right) \right] B \cos \omega t + [\dots] \cos 3\omega t = 0$$

Hence, to the first approximation either  $B=0$  and  $A \neq 0$ , with the additional requirement that

$$\omega^2 (1 - 2x_0 \tilde{\lambda}_m \tanh \tilde{\lambda}_m h) = \tilde{\lambda}_m \tanh \tilde{\lambda}_m h \left( \frac{\tilde{\lambda}_m^2 \nu}{\rho} + g \right)$$

or else  $A=0$ ,  $B \neq 0$ , and

$$\omega^2 (1 + 2x_0 \tilde{\lambda}_m \tanh \tilde{\lambda}_m h) = \tilde{\lambda}_m \tanh \tilde{\lambda}_m h \left( \frac{\tilde{\lambda}_m^2 \nu}{\rho} + g \right)$$

These two relations can be combined into a more convenient form by introducing the natural frequency of the  $m$ th mode, which is given by

$$\omega_m^2 = \tilde{\lambda}_m \tanh \tilde{\lambda}_m h \left( \frac{\tilde{\lambda}_m^2 \nu}{\rho} + g \right)$$

and by letting  $\epsilon = x_0 \tilde{\lambda}_m \tanh \tilde{\lambda}_m h$  be a dimensionless excitation amplitude. Then according to the general theory of Mathieu's equation, small liquid motions will tend to increase without limit in the frequency range given by <sup>3</sup>

$$\frac{1}{1+2\epsilon} \leq \left( \frac{\omega}{\omega_m} \right)^2 \leq \frac{1}{1-2\epsilon} \quad (8.10)$$

Equation (8.10) is valid only for the first few modes (small values of  $m$ ) because the higher order modes are damped quite severely.

Figure 8.7 shows an experimentally determined stability boundary for the first antisymmetrical sloshing mode in a 14.5-centimeter-diameter, rigid cylindrical tank. As can be seen from this figure, the theoretical predictions of equation (8.10) and experimental results are correlated very well except for a slight decrease in the width of the experimental boundary which is probably caused by viscous effects.

<sup>3</sup> It should be recalled that the excitation frequency is  $2\omega$ .

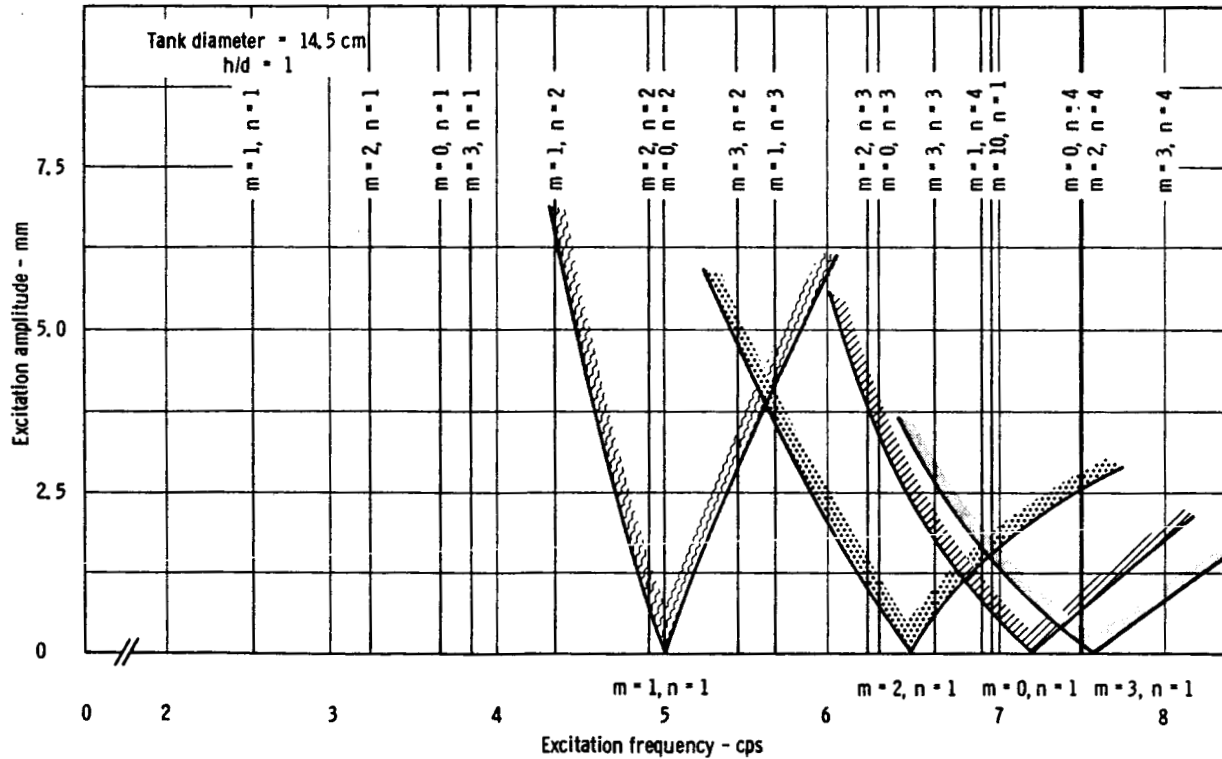


FIGURE 8.6.—General liquid behavior at low frequencies.

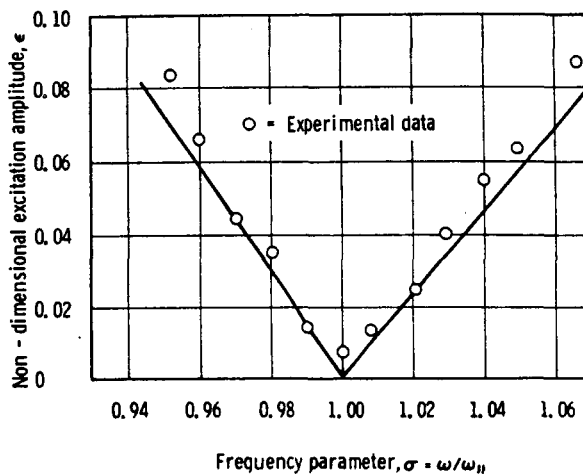


FIGURE 8.7.—Theoretical correlation for  $m=1, n=1$  mode 1/2-subharmonic stability boundary (ref. 8.20).

Although the linearized theory predicts an infinitely large sloshing amplitude in the unstable region, experience has shown that even in this range, only a finite amplitude is obtained, and if it or the fluid pressure is to be determined, a nonlinear analysis must be employed. Since the only mathematical source of nonlinearity for an inviscid liquid in a rigid container is in the free surface boundary conditions, equations (8.2) and (8.3) should not be linearized entirely.

As mentioned previously, the theory developed in this section can be justified only for the lower order sloshing modes. Thus, the effect of surface tension may be neglected for the relatively long wavelengths under consideration here.<sup>4</sup> The pressure boundary conditions may now be written as

$$\left\{ \frac{\partial \Phi}{\partial t} - \frac{1}{2} \left[ \left( \frac{\partial \Phi}{\partial x} \right)^2 + \left( \frac{\partial \Phi}{\partial y} \right)^2 + \left( \frac{\partial \Phi}{\partial z} \right)^2 \right] - (g - 4\omega^2 x_0 \cos 2\omega t) z \right\}_{z=\eta} = 0 \quad (8.11)$$

It should be noted that equation (8.11) is evaluated at  $z=\eta$  instead of at  $z=0$ , the position of the undisturbed free surface.

By resolving the fluid velocity into components normal to the free surface, the kinematic boundary condition may be written as

<sup>4</sup> This conclusion is true only so long as  $g$ , or an equivalent steady longitudinal acceleration of the tank, is not too small. If  $g=0$ , the surface tension forces become predominant, as discussed in ch. 11.

$$\left[ \frac{\partial \eta}{\partial t} = - \frac{\partial \Phi}{\partial z} + \frac{\partial \Phi}{\partial x} \frac{\partial \eta}{\partial x} + \frac{\partial \Phi}{\partial y} \frac{\partial \eta}{\partial y} \right]_{z=\eta}, \quad (8.12)$$

Even with these nonlinear boundary conditions, the potential,  $\Phi$ , can still be expanded in a series of orthogonal eigenfunctions of equation (8.1); that is

$$\Phi = \sum_0^{\infty} a_m \frac{\cosh \tilde{\lambda}_m (h+z)}{\tilde{\lambda}_m \sinh \tilde{\lambda}_m h} S_m(x, y) \quad (8.13)$$

is still valid and still satisfies the boundary conditions (eqs. (8.4) and (8.5)), which, of course, always remain true as long as the tank flexibility is neglected. However, it is no longer legitimate to write  $\eta = \sum a_m S_m(x, y)$ . Instead, the unknown  $a_m$ 's in equation (8.13) must be determined somehow from the boundary conditions (eqs. (8.11) and (8.12)), and calculating these coefficients is the central problem in most of the remaining discussion. There are several methods that might be used to do this; one way would be to eliminate  $\eta$  from equations (8.11) and (8.12), thus getting one equation in  $\Phi$  only; another way is to extend the linear analysis by assuming

$$\eta = \sum_0^{\infty} b_m S_m(x, y) \quad (8.14)$$

and then determining the  $a_m$ 's and  $b_m$ 's simultaneously.<sup>5</sup> The latter method is convenient, and it is the method used here.

The general way of attacking the solution is: Substitute the expansions, equations (8.13) and (8.14), into the boundary conditions, equations (8.11) and (8.12). Consider the resulting two equations as functions of  $x$  and  $y$ , and expand them in a series of the orthogonal eigenfunctions  $S_m(x, y)$ . In this way, two equations of the form

$$\sum_{m=0}^{\infty} F_m S_m(x, y) = 0 \quad (8.15)$$

are obtained, where  $F_m$  are, in general, functions of all the  $a_m$  and  $b_m$ . Since the  $S_m(x, y)$  are orthogonal, one can readily see that each  $F_m = 0$  separately. Consequently, the problem

<sup>5</sup> The dot over  $a_m$  indicating time differentiation has been dropped in eq. (8.13), since  $\dot{a}_m$  is not *a priori* equal to  $b_m$ , as was the case in eq. (8.7).

of solving equations (8.11) and (8.12) has been reduced to the problem of solving a set of equations  $F_m=0$ ,  $m=0, 1, 2, \dots$ , which involve only  $a_m$  and  $b_m$ . Now assume that the  $n$ th sloshing mode is the dominant one, so that  $a_n$  and  $b_n$  are much larger than the other  $a_m$  and  $b_m$ . By inspecting the equations, the orders of magnitude of all  $a_m$  and  $b_m$  can be determined in terms of  $a_n$  and  $b_n$ . The equations are then solved for  $a_m$  and  $b_m$  to any degree of approximation by neglecting all terms above the specified degree.

This procedure is well illustrated by the example of two-dimensional waves. Two-dimensional finite amplitude standing waves were considered first by Penney and Price (ref. 8.12) during a study designed to assist in the engineering design of the Mulberry harbors for the Normandy invasion of World War II. They worked out the wave form to the fifth power in the dominant amplitude. Among their results was the fact that the frequency of finite amplitude standing waves in deep water was always less than that of an infinitesimal wave, and that the maximum possible amplitude wave made a sharp corner at its crest and enclosed an angle of  $90^\circ$  at that point. Taylor (ref. 8.13) later made an experimental study of standing waves, and confirmed Penney and Price's main conclusions. In particular, he found that the wave of maximum amplitude did come to a sharp point, as shown in figure 8.8. He also showed that the response curve was slightly nonlinear softening, which is a consequence of the decrease in fre-

quency with amplitude. As might be expected, the maximum amplitude waves tended to be unstable and break at the crest. Later, Tadjbaksh and Keller (ref. 8.14) carried out an analysis of standing waves in water of finite depth by a method entirely different from Penney and Price's. They showed that for liquid depths less than about 0.17 times the wavelength, the frequency increases with amplitude; for greater depths, the frequency decreases, as Penney and Price predicted. This has been confirmed experimentally by Fultz (ref. 8.15). Three-dimensional standing waves also have been analyzed (refs. 8.16 and 8.17); in particular, Mack (ref. 8.17) has shown that the maximum amplitude axisymmetric wave has a crest enclosing an angle of approximately  $109.5^\circ$ .

#### Rectangular Tank

Penney and Price's general method was adopted by Yarymovych and Skalak (refs. 8.18 and 8.19) to study two-dimensional waves in a vertically vibrated tank. The salient points of the nonlinear analysis are easily identified in this, the simplest of all physically significant vertical sloshing problems, and for this reason their theory is given here even though there are very little experimental data available for comparison. Only the first symmetrical mode is considered in detail, although it is possible to produce antisymmetrical sloshing even in such a seemingly symmetrical situation as vertical vibration, since in reality neither the tank nor the vibration are perfectly vertical

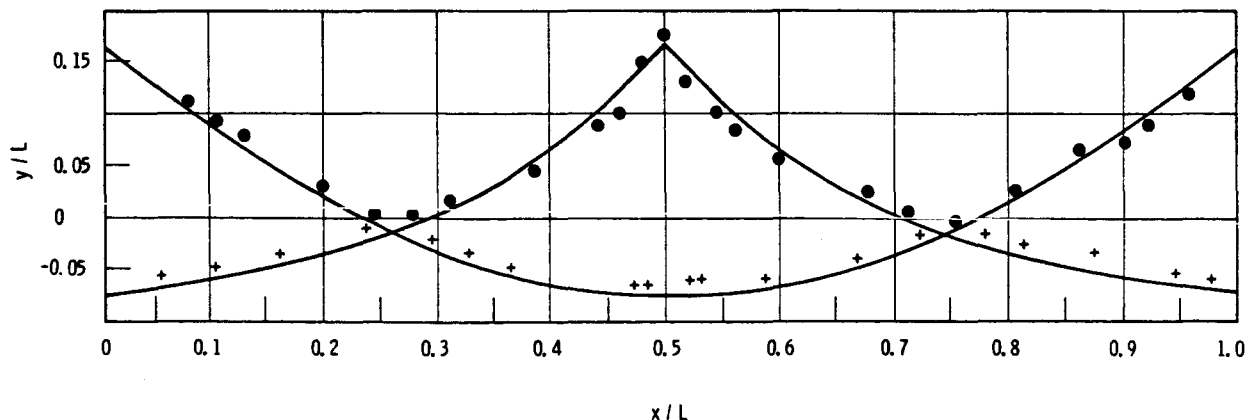


FIGURE 8.8.—Form of largest amplitude standing wave (ref. 8.13).

and symmetrical. Symmetrical sloshing does not cause any unbalanced forces or moments on the tank structures directly, as does anti-symmetrical sloshing, but it does influence the pressure at the tank bottom, and thereby could influence the pressure in the combustion chamber and the total rocket thrust.

For a two-dimensional wave in an infinitely deep, thin rectangular tank described by  $-\frac{L}{2} \leq x \leq \frac{L}{2}$ ,  $h=\infty$ , the appropriate velocity potential for a wave composed only of symmetric modes is

$$\Phi = a_0 + \sum_{m=1}^{\infty} a_m e^{+\frac{2\pi m}{L} z} \cos \frac{2\pi m}{L} x \quad (8.16)$$

This can be derived from equation (8.14) by noting that  $S_m(x, y) = \cos \tilde{\lambda}_m x$  with  $\tilde{\lambda}_m = 2\pi m/L$ , by letting  $h \rightarrow \infty$ , and by absorbing  $1/\tilde{\lambda}_m$  into the coefficient  $a_m$ .

In line with the general theory outlined previously, it is assumed that the equation of the free surface can be written in the form

$$\eta = \sum_{m=1}^{\infty} b_m \cos \frac{2\pi m}{L} x \quad (8.17)$$

The constant term  $b_0$  is necessarily zero, since the plane  $\eta=0$  locates the mean position of the surface.

Before substituting equations (8.16) and (8.17) into (8.11) and (8.12), it is much more convenient to cast all the parameters into dimensionless form. Because the first mode is assumed to be predominant, the appropriate length for use in nondimensionalizing is  $L/2\pi$  and the appropriate time is  $(L/2\pi g)^{1/2}$ . (Compare this with the nondimensionalizing of eq. (8.11).) Let  $\phi$  be the nondimensional form of  $\Phi$ ,  $\xi$  the nondimensional form of  $\eta$ ,  $\alpha_m$  the nondimensional form of  $a_m$ ,  $\beta_m$  the nondimensional form of  $b_m$ ,  $\tau$  the nondimensional form of  $t$ , and  $\epsilon$  the nondimensional form of  $x_0$ . The nondimensional form of the variables  $x$  and  $z$  will still be  $x$  and  $z$ , but the tank dimensions are now  $-\pi \leq x \leq \pi$ . The nondimensional surface wave frequency is denoted by  $\sigma = \omega/(2\pi g/L)^{1/2}$ , where  $(2\pi g/L)^{1/2}$  is the natural frequency of free small amplitude waves.

The series expansion of the velocity potential becomes

$$\phi = a_0 + \sum_{m=1}^{\infty} \alpha_m e^{+mx} \cos mx \quad (8.18)$$

and the surface displacement is

$$\xi = \sum_{m=1}^{\infty} \beta_m \cos mx \quad (8.19)$$

After substitution, equation (8.11) may be written as

$$(1 - 4\sigma^2 \epsilon \cos 2\sigma\tau) \xi - \sum_{m=0}^{\infty} \dot{\alpha}_m e^{+mx} \cos mx + \frac{1}{2} \sum_{m=1}^{\infty} \sum_{n=1}^{\infty} mn \alpha_m \alpha_n e^{+(m+n)x} \cos (n-m)x = 0 \quad (8.20)$$

and equation (8.12) as

$$\sum_{m=1}^{\infty} (\dot{\beta}_m + \alpha_m e^{+mx}) \cos mx = \sum_{m=1}^{\infty} \sum_{n=1}^{\infty} mn \beta_m \alpha_n e^{+nx} \sin mx \sin nx \quad (8.21)$$

Equations (8.20) and (8.21) can be solved by the method outlined previously (eq. (8.15) and the accompanying text). Penney and Price (ref. 8.12) used this method to solve a set of equations very similar to equations (8.20) and (8.21); details of their analysis are given in chapter 3. By using the same procedure here, and then examining the resulting equations to determine the orders of magnitude of the various terms, it follows that  $\alpha_n$  or  $\beta_n$  are of the order of magnitude  $(\alpha_1)^n$  or  $(\beta_1)^n$ ; that is,  $\alpha_2$  and  $\beta_2$  are second-order terms in comparison to  $\alpha_1$  and  $\beta_1$ ;  $\alpha_3$  and  $\beta_3$  are third-order terms in comparison to  $\alpha_1$  and  $\beta_1$ , and so on. Consequently, it is relatively straightforward to write down the governing equations to any order of approximation. However, only a third-order theory is given here because the algebraic work becomes extremely laborious for higher order approximations. But as will be seen, it is necessary to retain at least third-order terms, since a lower order approximation does not yield any quantitative information about the sloshing amplitude.

Because the amplitude of the free surface motion, and not the velocity potential, is more easily correlated with experimental data, the  $\alpha_m$  are eliminated from the approximate equations. Hence, by modifying equations (3.58) and (3.59) of chapter 3 to conform to the

nomenclature of this chapter and by including the changes necessitated by the factor  $(1 - 4\sigma^2\epsilon \cos 2\sigma\tau)$ , the first-order linear approximation to the sloshing amplitude is found to be

$$\ddot{\beta}_1 + (1 - 4\sigma^2\epsilon \cos 2\sigma\tau)\beta_1 = 0 \quad (8.22)$$

The second-order approximation is found to be

$$\begin{aligned} \ddot{\beta}_1 + (1 - 4\sigma^2\epsilon \cos 2\sigma\tau)\beta_1 &= 0 \\ \ddot{\beta}_2 + 2(1 - 4\sigma^2\epsilon \cos 2\sigma\tau)\beta_2 &= \dot{\beta}_1^2 \end{aligned} \quad (8.23)$$

The third-order approximation is

$$\begin{aligned} \ddot{\beta}_1 + (1 - 4\sigma^2\epsilon \cos 2\sigma\tau)\beta_1 &\left( 1 - 2\beta_2 - \frac{3}{4}\beta_1^2 \right) \\ &= \frac{1}{2}\beta_1^2\dot{\beta}_1 + \beta_1 \left( \frac{1}{2}\dot{\beta}_2 - \frac{3}{4}\dot{\beta}_1^2 \right) - \dot{\beta}_1\dot{\beta}_2 \\ \ddot{\beta}_2 + 2(1 - 4\sigma^2\epsilon \cos 2\sigma\tau)\beta_2 &= \dot{\beta}_1^2 \\ \ddot{\beta}_3 + 3(1 - 4\sigma^2\epsilon \cos 2\sigma\tau)\beta_3 &= 3\dot{\beta}_1\dot{\beta}_2 - \frac{3}{4}\beta_1\dot{\beta}_1^2 \end{aligned} \quad (8.24)$$

The first-order equation is a Mathieu equation, and is simply the nondimensional form of equation (8.8) for  $m=1$  and  $N=2$ . The second-order set consists of a Mathieu equation for  $\beta_1$  and an equation for  $\beta_2$  which contains the solution of the first equation as a parameter. This set does not result in any improvement of the frequency-amplitude relation but only refines the surface wave shape. The third-order equations are nonlinear and describe large amplitude waves to a better approximation than the lower order equations. Furthermore,

it is the lowest order approximation that predicts the sloshing amplitude as a function of frequency.

It is now assumed that the solution of equations (8.24) can be written in the form of a Fourier series, either as

$$\beta_1 = \sum_{n=1}^{\infty} A_n \sin n\sigma\tau \quad (8.25)$$

or as

$$\beta_1 = \sum_{n=1}^{\infty} B_n \cos n\sigma\tau \quad (8.26)$$

These two steady-state solutions have been chosen by analogy with the linear solutions described previously. It is found that retaining only the first term in the series equations (8.25) or (8.26) gives satisfactory results. By assuming that the time variation of  $\beta_n$  is of the form  $[\beta_1(t)]^n$ , the third-order approximate solution corresponding to equation (8.25) may be written down as

$$\begin{aligned} \beta_1 &= A \sin \sigma\tau \\ \beta_2 &= A_{20}^2 - A_{22}^2 \cos 2\sigma\tau \\ \beta_3 &= A_{31}^3 \sin \sigma\tau - A_{33}^3 \sin 3\sigma\tau \end{aligned} \quad (8.27)$$

where  $A_i$  is of order  $A$ . A similar set of equations may be written for the solution (8.26).

By substituting equations (8.27) into equations (8.24) and collecting coefficients of  $\sin \sigma\tau$ ,  $\sin 3\sigma\tau$ ,  $\cos 2\sigma\tau$ , and constants, the  $A_i$  may be determined. The results are

$$\begin{aligned} (A)^2 &= \frac{1+2\sigma^4-3\sigma^2+8\epsilon^2(1-2\epsilon)\sigma^6-4\epsilon(1+2\epsilon)\sigma^4-2\epsilon\sigma^2}{\frac{9}{16}-\left(\frac{5}{16}-\frac{3}{2}\epsilon\right)\sigma^2-\frac{1}{2}\sigma^4-2\epsilon^2\sigma^6} \\ A_{20}^2 &= \frac{(1-2\sigma^2+2\sigma^2\epsilon)}{4(1-2\sigma^2-8\sigma^4\epsilon^2)} \sigma^2 A^2 = C_{20}^2 A^2 \\ A_{22}^2 &= -\frac{(1+4\sigma^2\epsilon)}{4(1-2\sigma^2-8\sigma^4\epsilon^2)} \sigma^2 A^2 = C_{22}^2 A^2 \\ A_{31}^3 &= -\frac{(1-3\sigma^2+2\sigma^2\epsilon)\left(\frac{1}{16}-C_{22}^2\right)}{\left(1-\frac{1}{3}\sigma^2+2\sigma^2\epsilon\right)(1-3\sigma^2)-4\sigma^2\epsilon^2} \sigma^2 A^3 = C_{31}^3 A^3 \\ A_{33}^3 &= \frac{\left(1-\frac{1}{3}\sigma^2+4\sigma^2\epsilon\right)\left(\frac{1}{16}-C_{22}^2\right)}{\left(1-\frac{1}{3}\sigma^2+2\sigma^2\epsilon\right)(1-3\sigma^2)-4\sigma^2\epsilon^2} \sigma^2 A^3 = C_{33}^3 A^3 \end{aligned} \quad (8.28)$$

The coefficients  $C_{ij}$  are the combinations of  $\sigma$  and  $\epsilon$  as indicated. Once these  $\beta_m$  coefficients have been computed, the nondimensional surface displacement may be calculated to the third order in  $A$

$$\begin{aligned}\xi(x, t) = & A \sin \sigma t \cos x \\ & + (C_{20}^2 - C_{22}^2 \cos 2\sigma t) A^2 \cos 2x \\ & + (C_{31}^3 \sin \sigma t - C_{33}^3 \sin 3\sigma t) A^3 \cos 3x\end{aligned}$$

In this equation,  $A$  is calculated as a function of the frequency and amplitude of excitation from the first of equations (8.28).

The maximum vertical distance from crest to trough,  $y_0$ , may be determined from the previous equation as

$$\begin{aligned}y_0 = & \xi(x=0, \sigma t=\frac{\pi}{2}) - \xi(x=0, \sigma t=\frac{3\pi}{2}) \\ = & 2(1 + C_{31}^3 A^2 + C_{33}^3 A^2) A\end{aligned}\quad (8.29)$$

This equation is shown in figure 8.9 for the case  $\epsilon=0.05$ . A few experimental points are also shown. It may be seen that the agreement between theory and experiment is fairly good.

The amplitude-frequency relation corresponding to the assumed solution equation (8.26) has been shown (ref. 8.18) to correspond to an unstable steady state so that the steady-state solution equation (8.26) will never be observed in actual experiments; however, the theoretical calculations for this solution are shown in figure 8.9 as the slightly curved vertical line originating at  $\sigma=0.95$ .

#### Cylindrical Tank

Although the two-dimensional theory outlined above is relatively straightforward, considerably more experimental and theoretical work has been done for the more practical case of waves in a circular cylindrical tank (refs. 8.20 through 8.24). For that reason, a brief sketch of the main results is given here.

For this situation, the tank geometry is described by  $0 \leq r \leq R$ ,  $0 \leq \theta \leq 2\pi$ , and the water depth is again given by  $z=-h$ . The appropriate velocity potential is

$$\Phi = a_0 + \sum_{m=0}^{\infty} \sum_{n=1}^{\infty} a_{mn} J_m(\tilde{\lambda}_{mn} r) \cos m\theta \frac{\cosh \tilde{\lambda}_{mn}(z+h)}{\cosh \tilde{\lambda}_{mn} h} \quad (8.30)$$

$J_m(\tilde{\lambda}_{mn} r)$  is the  $m$ th order Bessel function of the first kind, and the eigenvalues,  $\tilde{\lambda}_{mn}$ , are determined by the transcendental equation

$$J'_m(\tilde{\lambda}_{mn} R) = 0$$

The corresponding free surface displacement is given by

$$\eta = \sum_{m=0}^{\infty} \sum_{n=1}^{\infty} b_{mn} J_m(\tilde{\lambda}_{mn} r) \cos m\theta \quad (8.31)$$

The first case considered here is the lowest frequency antisymmetrical ( $\cos \theta$ ) sloshing mode, so that  $a_{11}$  and  $b_{11}$  are the predominant amplitudes in the expansions (8.30) and (8.31). The appropriate length for nondimensional purposes is  $(\tilde{\lambda}_{11} \tanh \tilde{\lambda}_{11} h)^{-1}$  and the appropriate time is  $(\tilde{\lambda}_{11} g \tanh \tilde{\lambda}_{11} h)^{-1/2}$ .

By substituting the dimensionless forms of equations (8.30) and (8.31) into the nonlinear boundary conditions, and then keeping terms up through the third order in  $a_{11}$  and  $b_{11}$ , as before,

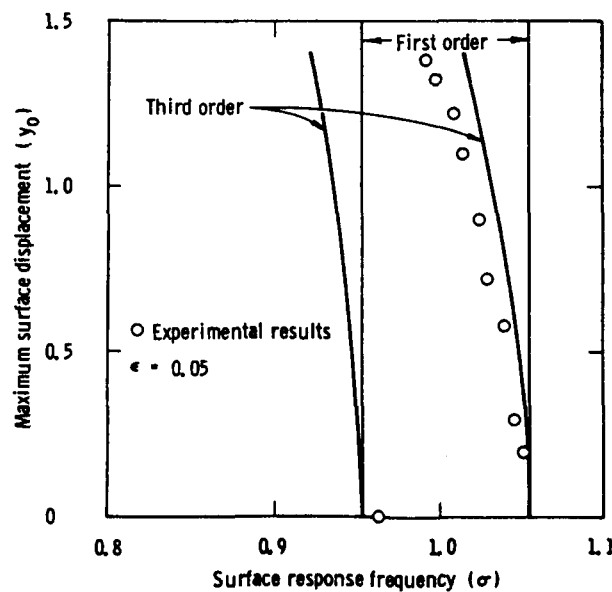


FIGURE 8.9.—Comparison of theory and experiment for 1/2-subharmonic response (ref. 8.18).

it can be shown (ref. 8.20) that  $\beta_{11}$ , the non-dimensional equivalent of  $b_{11}$ , is determined by

$$\begin{aligned} \ddot{\beta}_{11} + (1 - 4\sigma^2 \epsilon \cos 2\sigma\tau) \beta_{11} (1 + K_{11} \beta_{11}^2) \\ + K_{01} \beta_{01} - K_{21} \beta_{21}) + 0.034780 \lambda_{11}^2 \dot{\beta}_{11} \ddot{\beta}_{11}^2 \\ + k_{11} \dot{\beta}_{11}^2 \beta_{11} + 0.165118 \ddot{\beta}_{01} \beta_{11} - 0.198686 \ddot{\beta}_{21} \beta_{11} \\ + k_{01} \dot{\beta}_{01} \dot{\beta}_{11} - k_{21} \dot{\beta}_{21} \dot{\beta}_{11} = 0 \quad (8.32) \end{aligned}$$

The rather lengthy constants  $K_{ij}$  and  $k_{ij}$  are given in the appendix to this chapter.

The second-order terms are  $\beta_{01}$  and  $\beta_{21}$ , and they correspond to the first symmetric mode and the first  $\cos 2\theta$  mode. They may be calculated from the following equations, both correct to the third order

$$\begin{aligned} \ddot{\beta}_{01} + \lambda_{01} \tanh \lambda_{01} b (1 - 4\sigma^2 \epsilon \cos 2\sigma\tau) \beta_{01} \\ - \ddot{\beta}_{11} \beta_{11} (0.12148^2 \lambda_{01} \tanh \lambda_{01} b - 0.263074 \lambda_{11}^2) \\ + \dot{\beta}_{11}^2 [\lambda_{01} \tanh \lambda_{01} b (0.070796 \lambda_{11}^2 - 0.060741) \\ + 0.263074 \lambda_{11}^2] = 0 \quad (8.33) \end{aligned}$$

and

$$\begin{aligned} \ddot{\beta}_{21} + \lambda_{21} \tanh \lambda_{21} b (1 - 4\sigma^2 \epsilon \cos 2\sigma\tau) \beta_{21} \\ + \dot{\beta}_{11} \beta_{11} (0.350807 \lambda_{21} \tanh \lambda_{21} b - 0.482670 \lambda_{11}^2) \\ + \dot{\beta}_{11}^2 [\lambda_{21} \tanh \lambda_{21} b (0.175403 - 0.065931 \lambda_{11}^2) \\ - 0.482670 \lambda_{11}^2] = 0 \quad (8.34) \end{aligned}$$

A complete third-order theory would include a few other  $\beta_{mn}$  which are about of the magnitude of  $\beta_{11}^3$ . However, these  $\beta_{mn}$  are not needed to calculate any of  $\beta_{11}$ ,  $\beta_{01}$ , or  $\beta_{21}$  and hence are not given here.

The assumed solution to equations (8.32), (8.33), and (8.34) is <sup>6</sup>

$$\begin{aligned} \beta_{11} &= A \sin \sigma\tau \\ \beta_{01} &= A_{00}^2 - A_{02}^2 \cos 2\sigma\tau \\ \beta_{21} &= A_{20}^2 - A_{22}^2 \cos 2\sigma\tau \quad (8.35) \end{aligned}$$

The  $A_{ij}$  may be calculated as before by substituting equations (8.35) into equations (8.32), (8.33), and (8.34), and collecting the coefficients of the various sines and cosines. The dimen-

<sup>6</sup> The other possible solution,  $\beta_{11} = B \cos \sigma\tau, \dots$ , can be shown to be an unstable steady state and consequently is not observed in practice (ref. 8.20).

sionless sloshing amplitude can then be written as

$$\begin{aligned} \xi(r, \theta, \tau) &= A \sin \sigma\tau \cos \theta J_1(\tilde{\lambda}_{11} r) \\ &+ (A_{20}^2 - A_{22}^2 \cos 2\sigma\tau) \cos 2\theta J_2(\tilde{\lambda}_{21} r) \\ &+ (A_{00}^2 - A_{02}^2 \cos 2\sigma\tau) J_0(\tilde{\lambda}_{01} r) \end{aligned}$$

The average wave amplitude

$$Y_0 = \frac{1}{2} \left[ \xi \left( \frac{r}{R} = 0.837, \theta = 0, \sigma\tau = \frac{\pi}{2} \right) \right. \\ \left. - \xi \left( \frac{r}{R} = 0.837, \theta = 0, \sigma\tau = \frac{3\pi}{2} \right) \right]$$

is shown plotted in figure 8.10, for  $h/d = 1$ .<sup>7</sup> As can be seen, theory and experiment compare fairly well for the smaller values of  $Y_0$ , but at larger amplitudes they deviate severely. Some idea of the reason for this can be obtained from figure 8.11, which shows the experimental liquid response over a wide frequency range in a 14.5-centimeter-diameter, rigid cylindrical tank. As the forcing frequency is gradually decreased from a point slightly to the right of the stability boundary (see fig. 8.7), the liquid amplitude continually increases as the unstable region is traversed. After a steady state is reached, the forcing frequency can be further decreased, even to points considerably to the left of the left-hand stability boundary, that is, into the stable region for small motions, and the steady-state amplitude increases still more. However, a point is finally reached at which the liquid motion quickly decays to zero, as indicated by the downward pointing dashed arrow for  $x_0 = 0.65$ . On the other hand, if the frequency is gradually increased from a point to the left of the unstable region, the liquid remains quiescent until the stability boundary is reached. At this point, the liquid amplitude quickly increases to a sizable magnitude, as indicated in the figure by the upward-pointing dashed arrow. Both of these types of response are similar to the well-known "jumps" in other nonlinear systems. A photograph of the large amplitude motion is shown in figure 8.12; it is quite complex, as can be seen, with breaking

<sup>7</sup> Neither the calculations nor the experimental measurements were taken exactly at the wall,  $r/R = 1.0$ , in order to minimize viscous and wall effects.

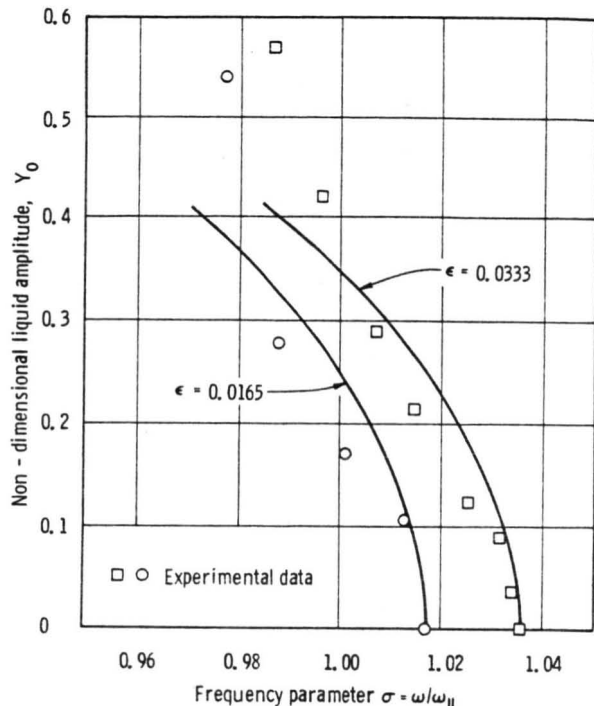


FIGURE 8.10.—Comparison of theory and experiment for  $m=1, n=1$  mode 1/2-subharmonic response (ref. 8.20).

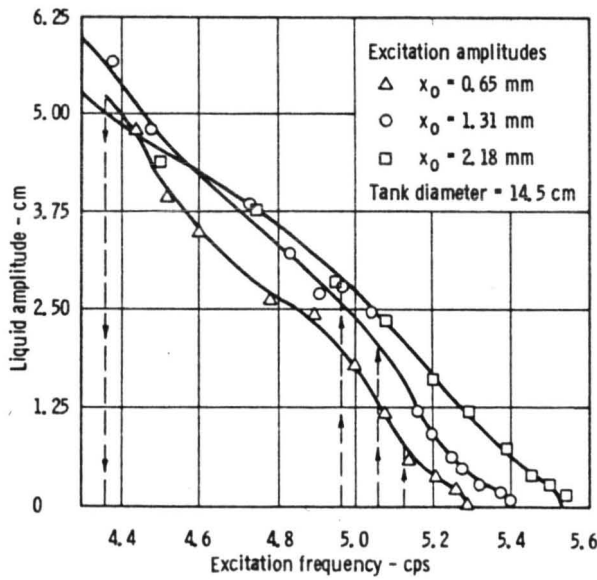


FIGURE 8.11.—Experimentally determined liquid response for  $m=1, n=1$  mode 1/2-subharmonic response for various excitation amplitudes (ref. 8.20).

waves being present. Of course, the idealized theory presented here does not take into account such phenomena as these. Neither does the

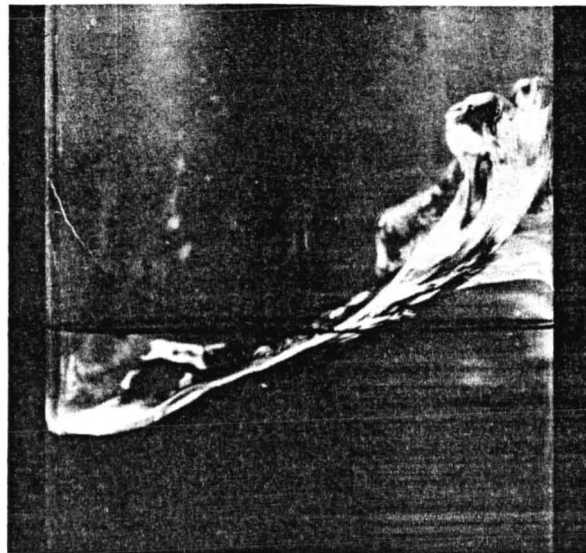


FIGURE 8.12.—Large amplitude breaking wave (ref. 8.20).

theory predict the point at which the liquid “jumps down” from a large to a practically zero amplitude; in order to do this, a dissipation mechanism would need to be included. (The upward jump is predicted, however.) Hence, it should not be expected that the theory would remain valid for very large amplitude liquid motions.

Symmetrical sloshing in a cylindrical tank can be studied by the same methods (ref. 8.20). For example, one finds that for  $h/R \geq 2$ , the predominant dimensionless amplitude  $\beta_{01}$  for the first symmetric mode is given by

$$\begin{aligned}
 \ddot{\beta}_{01} + (1 - 4\sigma^2\epsilon \cos 2\sigma\tau)\beta_{01}(1 + 0.352202\beta_{01} \\
 + 0.169000\beta_{01}^2 + 0.359844\beta_{02}) \\
 + 0.528303\beta_{01}\dot{\beta}_{01} + 0.338000\beta_{01}\dot{\beta}_{01}^2 \\
 + 0.266000\ddot{\beta}_{01}\beta_{02} + 0.119922\beta_{01}\dot{\beta}_{02}^2 \\
 + 0.088051\dot{\beta}_{01}^2 - 0.022490\beta_{01}\ddot{\beta}_{02} \\
 - 0.086164\dot{\beta}_{01}\dot{\beta}_{02} = 0 \quad (8.36)
 \end{aligned}$$

It should be noted that equation (8.36) contains second-order terms, in contrast to the previous analyses. Even so, the second-order terms alone do not predict the size of  $\beta_{01}$ , and the third-order terms must be retained.

The second-order term,  $\beta_{02}$ , i.e., the amplitude of the second-order symmetrical sloshing mode, is calculated from

$$\begin{aligned}\beta_{02} + 1.830937(1 - 4\sigma^2\epsilon \cos 2\sigma\tau)\beta_{02} \\ - 0.074207\dot{\beta}_{01}\beta_{01} - 0.661359\dot{\beta}_{01}^2 = 0 \quad (8.37)\end{aligned}$$

The solution of equations (8.36) and (8.37), correct to the third order, is

$$\begin{aligned}\beta_{01} &= A \sin \sigma\tau + A_{10}^2 - A_{12}^2 \cos 2\sigma\tau \\ \beta_{02} &= A_{20}^2 - A_{22}^2 \cos 2\sigma\tau\end{aligned}$$

with the  $A_{ij}$  calculated as before. The approximate sloshing amplitude may then be written as

$$\xi = (A \sin \sigma\tau + A_{10}^2 - A_{12}^2 \cos 2\sigma\tau)J_0(\tilde{\lambda}_{01}r) + (A_{20}^2 - A_{22}^2 \cos 2\sigma\tau)J_0(\tilde{\lambda}_{02}r)$$

By using this equation the wave form at any time may be calculated. A typical shape, normalized so that the maximum amplitude is unity, is shown in figure 8.13. Theory and experiment agree very well in this case; however, as before, the actual liquid response amplitude and the theoretically calculated

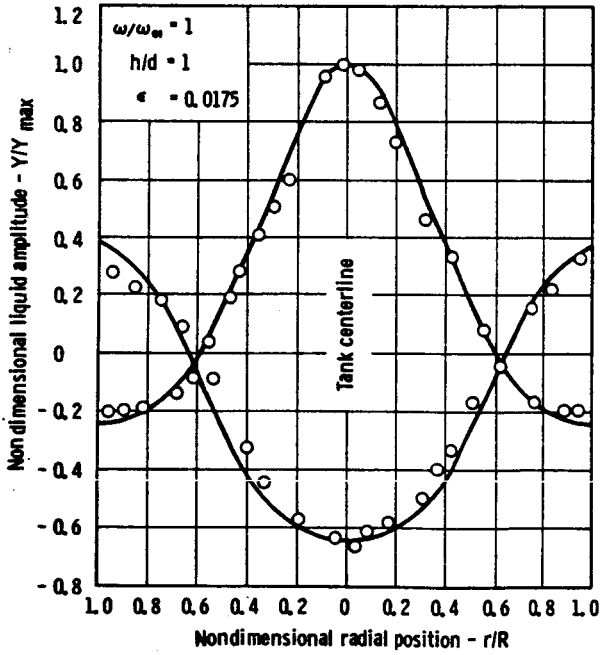


FIGURE 8.13.—Comparison of theoretical and experimental wave shape for  $m=0$ ,  $n=1$  mode 1/2-subharmonic (ref. 8.20).

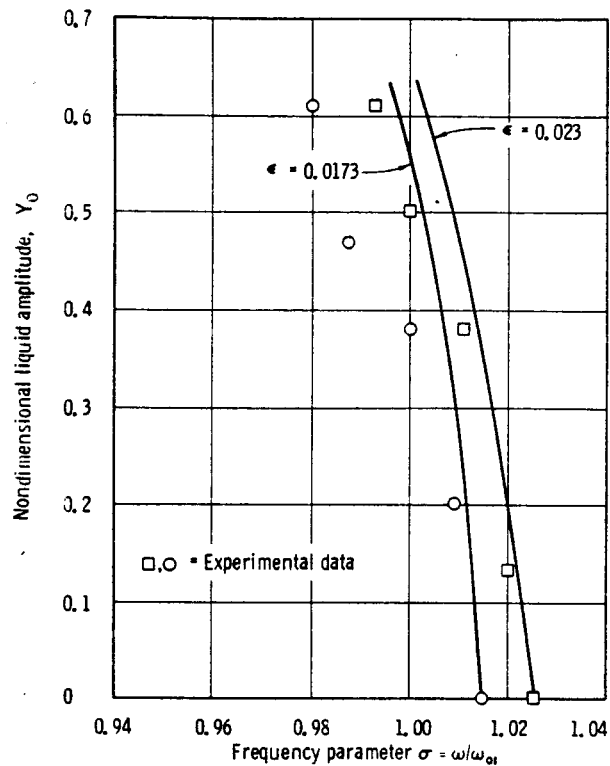


FIGURE 8.14.—Comparison of theory and experiment for  $m=0$ ,  $n=1$  mode 1/2-subharmonic response (ref. 8.20).

response do not agree quantitatively at large amplitudes, as shown in figure 8.14. The reasons for this disagreement are similar to the ones pointed out previously for anti-symmetrical sloshing.

#### 90° Sector Cylindrical Tank

Such tanks are of much practical interest, as has been discussed in earlier chapters, and therefore experimental studies of liquid surface subharmonic motion have been undertaken by Kana (ref. 8.25). The frequency of the fundamental subharmonic mode corresponds to the sector 2-4 mode for lateral translation. (See ch. 3.) However, in this case, the liquid in every sector executes the same sort of free surface motion, although the phasing of the liquid motion relative to the excitation may vary from sector to sector. The second-mode frequency corresponds to the frequency of the fundamental axisymmetrical mode in a circular cylindrical tank, which is sector 1-3 resonance for lateral excitation. The response

curves for both modes are quite similar in appearance to figure 8.11.

#### Spherical Tank

The behavior of liquids in spherical tanks under vertical excitation has also been investigated by Kana (refs. 8.25 and 8.26). Again, the liquid surface modes appear predominantly as one-half subharmonics of the excitation frequency and are qualitatively similar in shape to those occurring in a cylindrical tank. Of course, there is a variation of the liquid resonant frequencies with depth, but no new aspects of the subharmonic liquid response seem to arise.

#### Summary of Subharmonic Results

The types of subharmonic sloshing discussed in this section are the only ones for which any substantial amount of laboratory data are available. Even in these cases, there are no data reported on fluid pressures and forces.

The available theories,<sup>8</sup> while probably not accurate enough to calculate large amplitude sloshing and fluid pressures, are sufficient to determine the frequency range for which large amplitude motions should be expected; in some instances this information is all that is required. As an additional note, one should recall that the method of solving nonlinear problems outlined earlier is not the only feasible one. For example, one might attempt an expansion in powers of  $\epsilon$ , the nondimensional forcing amplitude, instead of an expansion in powers of  $\beta_1$  (or  $\beta_{11}$  or  $\beta_{01}$  as the case may be). Or one might employ the method developed by Hutton (ref. 8.28) in which the two nonlinear boundary conditions are combined to give one equation involving only  $\Phi$ . Even with this procedure, however, the resulting equation is correct only to a certain preassigned degree in the velocity potential. The essential points of this analysis, and other possibly fruitful approaches, are given in chapter 3.

<sup>8</sup> Only for rectangular or cylindrical tanks; no analysis has yet been completed for either the 90° sector compartmented cylindrical tank or for the spherical tank. A general theory for tanks of arbitrary geometry has been formulated (ref. 8.27), but no computations have been made.

#### Large Amplitude Harmonic and Superharmonic Motions

Up to this point, the only liquid motion that has been discussed in detail is the large amplitude subharmonic response, chiefly because it is this response that would probably prove to be the most troublesome and the easiest to excite in actual tanks. However, other types of responses are possible since, according to figure 8.4 or 8.5, harmonic and superharmonic motions may be excited for certain forcing frequency-amplitude combinations. In contrast to the subharmonic motions, however, there appear to be two entirely different types of harmonic and superharmonic responses: small amplitude motions which seem to correspond to stable responses, and large amplitude motions which correspond to unstable solutions of equation (8.8). Although the excitation frequency for these responses is higher than for subharmonic motion, it is still sufficiently low that the tank elasticity may be neglected.

As mentioned previously, the widths of the unstable regions of the Mathieu stability chart for harmonic and superharmonic responses are quite narrow, even for no damping. With damping, a rather severe amplitude cutoff exists; that is, the unstable regions do not extend completely to the line  $x_0=0$  in figure 8.5. This amplitude cutoff may be circumvented, however, by using a small enough tank or a large enough excitation; the reason for this is that the width of the unstable regions increases with the nondimensional excitation amplitude approximately as  $\epsilon^{2/N}$ , where  $N$  is, as before, the ratio of the forcing frequency to the dominant liquid frequency. But  $\epsilon$  is proportional to  $x_0/d$ , where  $d$  is the significant tank dimension.<sup>9</sup> Consequently, the width of the unstable subharmonic region varies as  $x_0/d$ , the width of unstable harmonic region varies as  $(x_0/d)^2$ , the width of the 3/2-superharmonic region varies as

<sup>9</sup> For a circular cylindrical tank,  $d$  is the tank diameter; for a thin rectangular tank,  $d$  is the tank length. Also, it should be mentioned that "amplitude cutoff" does not imply here that a certain minimum *response* amplitude is required for the assumed motions to exist, as it does in some other kinds of nonlinear damped systems. Instead, once the required minimum *excitation* amplitude is obtained, the response amplitude can be arbitrarily near to zero.

$(x_0/d)^3$ , and so on. Hence, by increasing  $x_0$  or decreasing  $d$ , any of the unstable motions may eventually be obtained.

Harmonic and 3/2-superharmonic responses were observed by Dodge, Kana, and Abramson (ref. 8.20) in laboratory tests conducted in a small cylindrical tank. The theory of these motions was not reported in detail, but it can be developed using the methods given earlier in this section by letting  $N$  assume appropriate values. For example, the results for harmonic motion in the  $m=1$ ,  $n=1$  mode, which are analogous to equations (8.32), (8.33), and (8.34), are

$$\begin{aligned} \ddot{\beta}_{11} + (1 - \sigma^2 \epsilon \cos \sigma \tau) \beta_{11} (1 + K_{11} \beta_{11}^2 + K_{01} \beta_{01} \\ - K_{21} \beta_{21}) + 0.034780 \lambda_{11}^2 \dot{\beta}_{11} \beta_{11}^2 + k_{11} \dot{\beta}_{11}^2 \beta_{11} \\ + 0.165118 \ddot{\beta}_{01} \beta_{11} - 0.198686 \ddot{\beta}_{21} \beta_{11} \\ + k_{01} \dot{\beta}_{01} \dot{\beta}_{11} - k_{21} \dot{\beta}_{21} \dot{\beta}_{11} = 0 \quad (8.38) \end{aligned}$$

$$\begin{aligned} \ddot{\beta}_{01} + \lambda_{01} \tanh \lambda_{01} d (1 - \sigma^2 \epsilon \cos \sigma \tau) \beta_{01} \\ - \ddot{\beta}_{11} \beta_{11} (0.121482 \lambda_{01} \tanh \lambda_{01} b \\ - 0.263074 \lambda_{11}^2) \\ + \dot{\beta}_{11}^2 [\lambda_{01} \tanh \lambda_{01} b (0.070796 \lambda_{11}^2 \\ - 0.060741) + 0.263074 \lambda_{11}^2] = 0 \quad (8.39) \end{aligned}$$

$$\begin{aligned} \ddot{\beta}_{21} + \lambda_{21} \tanh \lambda_{21} b (1 - \sigma^2 \epsilon \cos \sigma \tau) \beta_{21} \\ + \ddot{\beta}_{11} \beta_{11} (0.350807 \lambda_{21} \tanh \lambda_{21} b \\ - 0.482670 \lambda_{11}^2) \\ + \dot{\beta}_{11}^2 [\lambda_{21} \tanh \lambda_{21} b (0.175403 \\ - 0.065931 \lambda_{11}^2) - 0.482670 \lambda_{11}^2] = 0 \quad (8.40) \end{aligned}$$

The approximate third-order solution to these equations is of the same form as equation (8.35); but, of course, in this case all of the  $A_{ij}$  (and  $A$ ) have numerical values different from before.

The other harmonic modes and the superharmonic motions may be analyzed in a similar fashion. Very little experimental data exist for comparison purposes, probably because motions of this type are not nearly so predominant in large tanks as would be the  $\frac{3}{2}$ -subharmonic response.

#### Small Amplitude, Stable Harmonic, and Superharmonic Motions

It has been observed (ref. 8.20) that even in relatively large laboratory tanks, small ampli-

tude harmonic and superharmonic responses are possible for excitation frequency-amplitude combinations that lie completely outside any of the unstable regions shown in figure 8.4. These motions do not seem to be at all the same type as the responses discussed previously.

Figure 8.15 shows an experimental curve for the  $m=1$ ,  $n=1$  harmonic mode in a 14.5-centimeter-diameter cylindrical tank. This curve should be compared with the  $1/2$ -subharmonic response curve for the same mode given in figure 8.11. The amplitude of the subharmonic response is much larger, but even so, the harmonic response is large enough to be easily observed visually. The main point of difference, however, is that the harmonic response (fig. 8.15) gives the appearance of the harmonic response of a slightly nonlinear, damped system in the vicinity of a resonance, while the  $1/2$ -subharmonic response (fig. 8.11) does not. In fact, the phase angle of the harmonic response relative to the tank motion shifts slowly from zero, for frequencies less than peak response, to  $90^\circ$  at peak response, to essentially  $180^\circ$  for excitation frequencies greater than peak response, exactly as would a simple spring-mass system.

This kind of harmonic response occurs in the vicinity of what is normally an unstable region for harmonic motions (if the forcing amplitude is sufficiently large), but actually it is not an unstable motion; that is, the amplitude does not

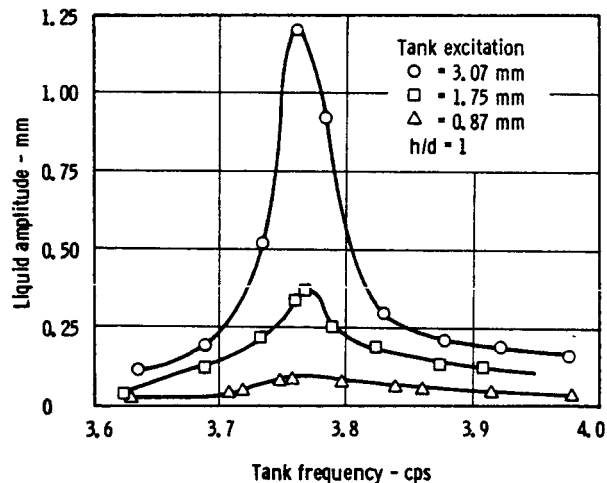


FIGURE 8.15.—Experimental response for  $m=1$ ,  $n=1$  mode harmonic (ref. 8.20).

exhibit a sudden increase when the frequency is changed slightly. Consequently, this response does not correspond to an unstable solution of Mathieu's equation. On the other hand, it does not correspond to a stable solution, either, since the theoretical period of any possible stable solution is not exactly equal to the period of the forcing motion except for a few discrete values of  $\sigma$  and  $\epsilon$ . Small amplitude responses, however, have been partially analyzed by Bhuta and Yeh (ref. 8.21) in their treatment of tanks with a vibrating bottom. The essential difference between their analysis and the one presented in the preceding sections of this chapter is that they satisfied the boundary conditions on the undisturbed positions of the boundaries in a fixed frame of reference. That is, their boundary conditions for a cylindrical tank are

$$\begin{aligned}\frac{\partial \Phi}{\partial t} - g\eta &= 0 \\ \frac{\partial \eta}{\partial t} - \frac{\partial \Phi}{\partial z} &= 0\end{aligned}\quad (8.41)$$

at the free surface,  $z=0$ ;

$$\frac{\partial \Phi}{\partial r} = 0 \quad (8.42)$$

at  $r=R$ ; and

$$\frac{\partial \Phi}{\partial z} = x_0 \omega \sin \omega t \quad (8.43)$$

at the tank bottom,  $z=-h$ . Hence, this is a linearized theory, but even if it were not, their results are valid only for small motions in an absolute sense (because of equation (8.43)), whereas in the moving coordinate system employed in the linearized subharmonic analysis presented previously, the motion of the tank itself can be finite as long as the relative motion of the liquid is small.

The details of the analysis presented in reference 8.21 are lengthy and so are not given here, but the main result is that the wave height relative to the tank bottom is

$$\eta(r, t) = x_0 \cos \omega t \sum_{n=1}^{\infty} \frac{a_n}{\omega^2 - \omega_{0n}^2} J_0(\tilde{\lambda}_{0n} r) \quad (8.44)$$

where  $\omega_{0n}$  is the natural frequency of the  $n$ th symmetrical mode, the only type of sloshing

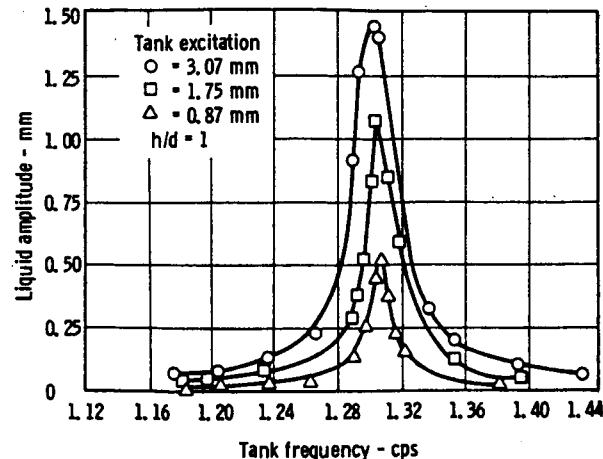


FIGURE 8.16.—Experimental response for  $m=1, n=1$  mode 2-superharmonic (ref. 8.20).

considered. Equation (8.44) is of the correct form to predict the observed harmonic response, but the method of calculating  $a_n$ , according to reference 8.21, seems to depend upon specific initial conditions and not upon the excitation. Thus, it is difficult to compare equation (8.44) directly with experimental results.

Bhuta and Koval (refs. 8.23 and 8.24) have shown analytically the existence of harmonic liquid responses in a series of papers concerned with tanks having an elastic bottom (but rigid sides). This kind of vibration, of course, excites the liquid in a vertical direction. They have found that the natural frequencies of the free surface motions are slightly different from the case of a rigid bottom. Some details of their analyses are given in this monograph in chapter 9, where the interaction of the liquid with the elastic tank is considered more fully.

In addition to harmonic responses, small amplitude superharmonic responses also have been observed in laboratory experiments (ref. 8.20). In figure 8.16, a response curve for the  $m=1, n=1$  double-superharmonic mode in a 14.5-centimeter-diameter cylindrical tank is illustrated. The peak response for this case is considerably sharper than the harmonic response curve shown in figure 8.15. Once again, this response is not an unstable motion, nor does it correspond to a stable solution of Mathieu's equation—as a point of fact, no suitable analysis of this sort of superharmonic motion has yet been discovered. It appears

that considerably more theoretical work is needed to put the small amplitude harmonic and superharmonic responses into a satisfactory state of agreement with experiments, and to determine their significance in possible applications.

### Mechanical Model for Vertical Vibrations

As a complement to the equivalent mechanical model analogies given in chapter 6, it would be convenient in missile stability analyses to have a similar type of mechanical model for vertical sloshing. Developing an equivalent model for vertical excitation, however, is considerably more difficult than for transverse excitation because of the tremendous number of possible liquid motions; e.g., subharmonic, stable and unstable harmonic, stable and unstable superharmonic. But the 1/2-subharmonic response would probably be the most important in applications, so that any equivalent model should be directed primarily toward duplicating this kind of response.

Even for the limited problem of subharmonic response, there are no available analyses of

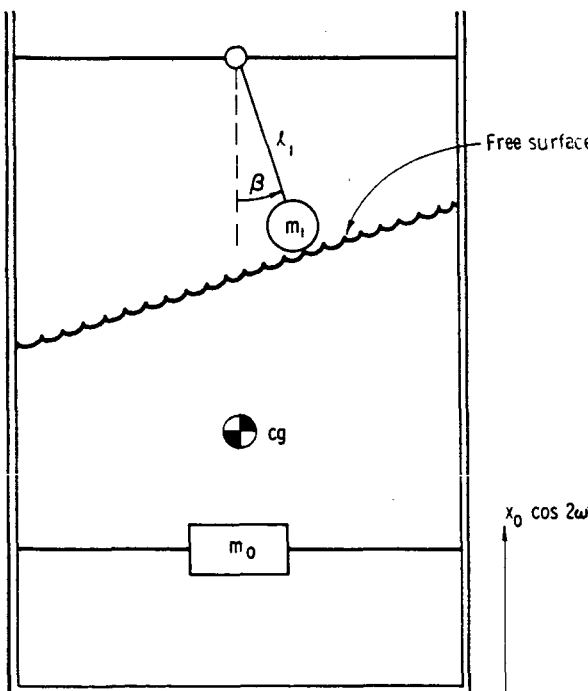


FIGURE 8.17.—Equivalent mechanical model for antisymmetric vertical sloshing.

mechanical models for vertical excitation. A hypothetical model for the first antisymmetric mode, however, is shown in figure 8.17. The fixed mass,  $m_0$ , is supposed to duplicate the inertia effects of the more or less rigid body portion of the fluid motion, and the pendulum mass,  $m_1$ , is supposed to duplicate the sloshing mass of the liquid. The equation of motion for the pendulum, correct to the third order in the pendulum amplitude,  $\beta$ , is

$$l_1 \ddot{\beta} + (g - 4\omega^2 x_0 \cos 2\omega t) \beta \left( 1 - \frac{1}{6} \beta^2 \right) = 0 \quad (8.45)$$

This equation is approximately of the same form as the nonlinear equation specifying the dominant amplitude for antisymmetrical vertical sloshing. In fact, it has the same region of unstable motion, and, consequently, the model should duplicate fairly well the actual liquid dynamics, especially if the parameters such as  $l_1$ ,  $m_1$ , and  $m_0$  are derived from experimental results. However, the problem of determining the plane of the pendulum's motion remains to be solved. That is, the line  $\theta=0$  in, say, equation (8.30) is dependent upon slight imperfections in the symmetry of any actual system; thus, it is not prescribed by the idealized theory given in the preceding sections. Instead, it must be determined experimentally for each particular case.

It should be emphasized that the model shown in figure 8.17 will not give a good analog for symmetric sloshing, although the pendulum parameters could probably be adjusted to duplicate the stability properties of the liquid free surface for this type of sloshing. The problem is that the equivalent sloshing mass,  $m_1$ , inherently gives forces of the same form as antisymmetrical sloshing. Some sort of pendulum which vibrates up and down, rather than to and fro, would be needed to duplicate symmetrical sloshing forces, but it is not clear how this could be arranged and still retain the stability properties of the free surface.

The problems associated with equivalent models for subharmonic vertical sloshing can be summarized, then, as: What kind of pendulum or spring mass has the same sort of stability

as the liquid free surface, and, at the same time, is able to duplicate the sloshing forces? At the present time this question has not been answered satisfactorily. Furthermore, the next few sections show that for higher excitation frequencies, the free surface responds in ways that are entirely different from the responses considered up to now. Other kinds of mechanical models would be needed to simulate these responses.

### 8.3 LIQUID SURFACE RESPONSE TO HIGH-FREQUENCY EXCITATION

While performing experiments at relatively high excitation frequencies, Yarymovych (ref. 8.18) observed large amplitude surface waves whose frequencies were of the order 1/25 to 1/50 of the excitation; a typical wave is shown in figure 8.2. (Similar observations have been made by Kana in tanks of various geometries (refs. 8.25, 8.26, and 8.29).) Such low subharmonic responses cannot be explained on the basis of any of the large amplitude wave theories discussed in previous sections, and so Yarymovych advanced the hypothesis that these waves are generated by a complex interaction of the free surface and the spray droplets formed by the high-frequency free surface motion. It is also apparent that for such high-frequency excitation, tank flexibility may play an important role.

The free surface waves that first form when the excitation is of high frequency and low amplitude are short-wavelength capillary waves. Even though surface tension has a dominant influence on these waves, their frequency is still exactly one-half that of the excitation, as discussed previously. The amplitudes of these capillary waves build up until the waves become unstable, and then they disintegrate by forming droplets that separate from the surface; with increasing excitation amplitude, the droplets describe higher trajectories. A dense spray is thus created, since each of the multitude of the original waves releases a droplet. For certain excitation conditions, a first, second, or higher order low-frequency wave is formed, with the formation usually requiring a considerable period of time.

No satisfactory theory for this sort of surface motion exists at the present time. An exact quantitative analysis of the origin and perpetuation of the low-frequency waves is a formidable task because of the statistical nature of the response; that is, there are many different spray particles thrown off at different instants and with different masses and different initial velocities. Also, the transition from high-frequency, short-wavelength ripples to low-frequency, long-wavelength sloshing is probably caused by some kind of low-order instability, as evidenced by the relatively long period needed to accomplish the transition. Such instabilities are generally difficult to predict analytically. However, the steady-state motion which eventually occurs should be easier to analyze if one accepts Yarymovych's hypothesis that the impacts of the spray droplets on the free surface are the primary agents in sustaining the low-frequency sloshing.

It has been observed that the portion of the wave near its peak produces a higher and denser spray than the depressed positions. There is also a periodic spray-density distribution with respect to the time of the cycle when the droplets are released. In order to produce such forcing as to help maintain an existing wave, rather than retarding it, the droplets must return to the wave surface when it is moving downward. Only droplets having certain trajectory times and released during certain intervals will produce positive forcing.

A crude attempt to translate the foregoing observations into a quantitative theory is given in the following paragraphs. In the first place, the spray action is much more important over certain critical areas of the surface than it is over the rest. (See fig. 8.18.) If the wave crests are excited properly, the rest of the surface will naturally follow with the proper frequency and wave shape. In the second place, the accelerations, and the velocities, of every part of these critical portions of the free surface are nearly equal at every instant; thus, the spray droplets in the critical areas are released at practically the same time and with practically the same initial velocities. If the trajectory time of these droplets is about equal to one-half the period of the low-frequency

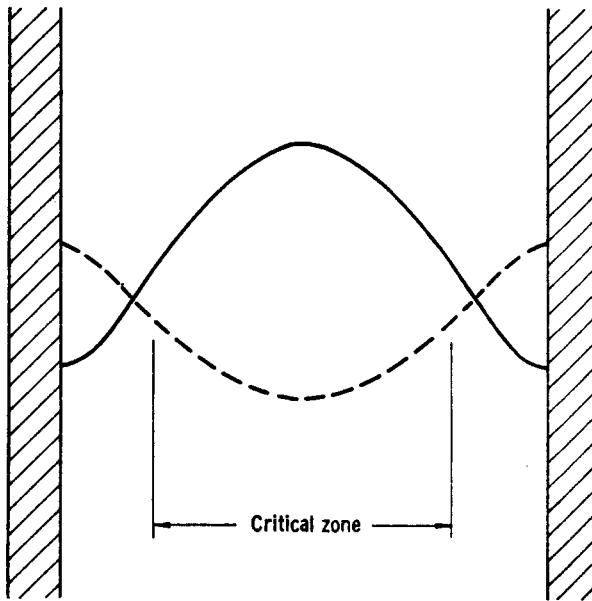


FIGURE 8.18.—"Critical area" for symmetrical surface wave.

motion, the droplets will impact when the wave crest is moving downward, and the low-frequency motion will be reinforced.

In analytical terms, the total displacement of the free surface is approximately

$$a_m S_m(x, y) \cos(\frac{1}{2} \omega t + \phi_m) + a_n S_n(x, y) \cos(\omega_n t + \phi_n) + x_0 \cos \omega t$$

$S_m(x, y)$  is the normalized mode shape (eigenfunction), with  $m$  a large integer, and  $a_m$  the corresponding amplitude of the higher frequency ripples (the frequency of these capillary waves is one-half that of the excitation);  $S_n(x, y)$  is the mode shape of the low-frequency wave ( $n$  a small integer),  $a_n$  its amplitude, and  $\omega_n$  its natural frequency;  $\phi_m$  and  $\phi_n$  are phase angles; and  $x_0 \cos \omega t$  is the forcing motion. Now,  $a_m$  may be determined from known results which give the amplitude of a capillary wave just as it becomes unstable and begins to disintegrate (refs. 8.12 and 8.17); however,  $a_n$  cannot, in general, be calculated using the crude theory outlined here, except for the case of the maximum amplitude wave when  $a_n$  is also determinate.

The spray droplets are released whenever the surface acceleration is a little greater than

$1 g$  downward, which, because  $x_0 \omega^2$  is large, is just after  $\cos \omega t$  passes through zero and then increases. Because  $\cos(\frac{1}{2} \omega t + \phi_m)$  and  $\cos(\omega_n t + \phi_n)$  both vary much more slowly than  $\cos \omega t$ , the phase angles may be neglected, so that

$$\sin \omega t = \sin \frac{1}{2} \omega t = \sin \omega_n t = 1$$

at the critical time when the drops are released. This is tantamount to assuming that the drops are released at the instant when the total velocity of the surface is a maximum. Thus, the initial velocity of the drops released near the wave crest is

$$V_d \approx x_0 \omega + \frac{1}{2} a_m \omega + a_n \omega_n$$

In terms of the drop velocity, the trajectory time is  $2V_d/g$ . Since for positive forcing this time must be approximately  $\pi/\omega_n$ , the final result is

$$x_0 \omega = \frac{\pi g}{2\omega_n} - \frac{1}{2} a_m \omega - a_n \omega_n$$

This equation includes, in a general way, most of the phenomena observed in experiments.

Analysis of certain preliminary data indicates that a satisfactory correlation for the first symmetrical mode in a circular cylindrical tank may be obtained from

$$x_0 \omega = \left( \frac{g}{\omega^2 d} \right)^{0.414} [0.0453 \omega d + 0.0942 a_n \omega]$$

where  $d$  is the tank diameter. By a liberal interpretation, it can be seen that this empirical equation and the previous theoretical equation are approximately of the same form. Consequently, although there are obvious differences between the two equations, it appears that the theoretical approach taken above is probably fundamentally sound.

While it is obvious that more experimental and theoretical development work need to be done in this area, especially as concerns the effect of tank elasticity on the liquid motions, the significance of the spray-formed waves in actual applications remains to be determined.

#### 8.4 BUBBLE BEHAVIOR AND CAVITATION

##### Bubble Motion in Vertically Vibrated Liquids

The possible generation of bubbles with an apparent negative buoyancy was mentioned briefly in section 8.1. Such sinking bubbles have been observed in a number of experimental programs, and, in fact, chemical engineers have long been interested in the effect of vertical vibration on heat and mass transfer and the role of bubble dynamics in improving such mixing and transfer (refs. 8.30 and 8.31). Other investigations have centered around the effects of bubble vibration in cavitation and sound propagation. In more recent years, determination of the motion of vapor bubbles in vibrating fuel tanks of large missiles has assumed an added importance, since clusters of sinking or stationary bubbles could seriously affect the fuel flow through the tank and pumping systems (refs. 8.32 through 8.35). In addition, a ready supply of bubbles is available here because of the near-boiling condition of cryogenic fuels. Nonetheless, one should note with care that while such difficulties *could* occur in actual vehicles, seemingly none have yet materialized.

In order to set the stage for the following analysis of bubble dynamics in vibrated tanks, the results of a typical series of tests (ref. 8.35) in a simulated rocket fuel tank, using water as the test fuel, are summarized in the next few paragraphs. In these experiments, the bubbles were formed by free surface sloshing, since the water temperature was far too low to form vapor bubbles; however, the results appear to be independent of the method of bubble formation as long as the bubbles somehow reach the interior of the liquid.

The entire process begins by exciting the tank at a relatively high frequency with a total input vibrational acceleration of about 7 g's.<sup>10</sup> At first, the violent surface agitation (shown in fig. 8.19) entrains air bubbles at various depths

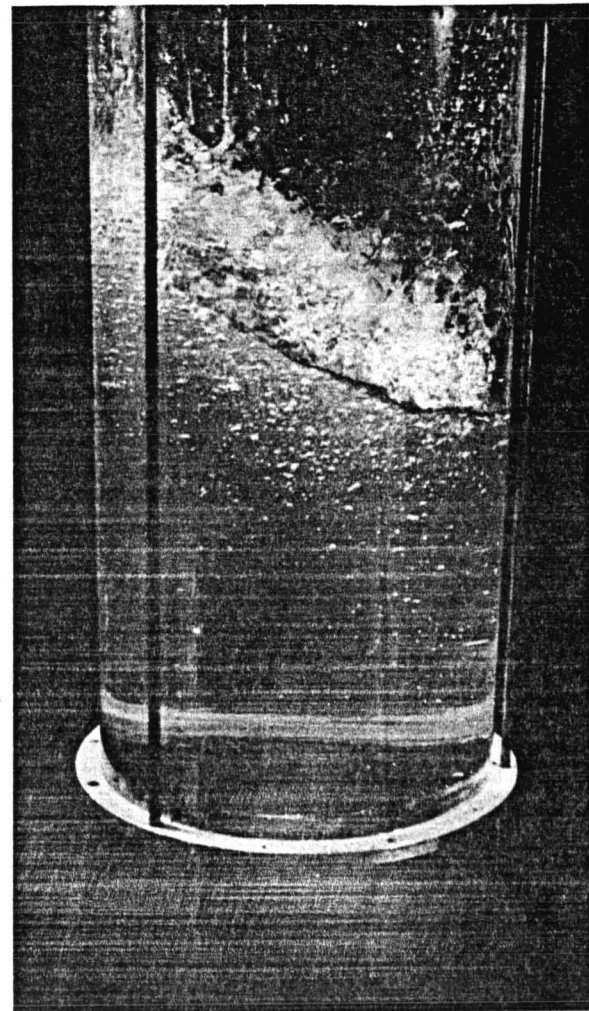


FIGURE 8.19.—Generation of bubbles by violent surface motion (ref. 8.35).

in the liquid. These bubbles do not return to the liquid surface, but, instead, they stream downward to the bottom of the tank. The deeper the bubbles initially are thrown from the surface, the more easily they sink.

As they reach the bottom, the bubbles begin to coalesce into a cluster that continually grows as time goes on; this is illustrated in figure 8.20. Stroboscopic observation reveals that the cluster as a whole pulsates at the same frequency as the container, and, as the cluster grows, the phase of its vibration begins to lag more and more behind that of the container. In addition, the amplitude of the cluster vibration, and the fluid pressure in the tank,

<sup>10</sup> The resulting bubble motion seems to be practically independent of the actual vibration frequency, and, therefore, the resulting sequence of events might be caused by a random input. The particular acceleration levels given here refer, of course, to small laboratory models and may not be applicable to actual vehicles.



FIGURE 8.20.—Bubble cluster growing at tank bottom (ref. 8.35).

continually increases. Suddenly, the cluster motion becomes extremely violent, as shown in figure 8.21. Bubbles rapidly shoot downward from the intensely agitated free surface. Fluid pressures are very high at this time.

After a relatively short period of violent motion, the bubble cluster leaves the tank bottom and rises to a new position in the body of the liquid, as shown in figure 8.22. The exact level at which the cluster then settles appears to vary with the amount of air originally entrained in the cluster, but as long as the vibrational input is not changed and as long as no more air bubbles are entrained, the cluster remains at this level indefinitely. The liquid free surface, at this time, is undergoing very large antisymmetric sloshing motions. Increasing the level of vibrational acceleration now causes the cluster to rise, and lowering it causes the bubble to sink. If the input acceleration is decreased too much, however, the cluster no longer remains submerged but, instead, rises to the surface and vents. This final phase of the cluster motion seems to be dependent upon the elasticity of the tank

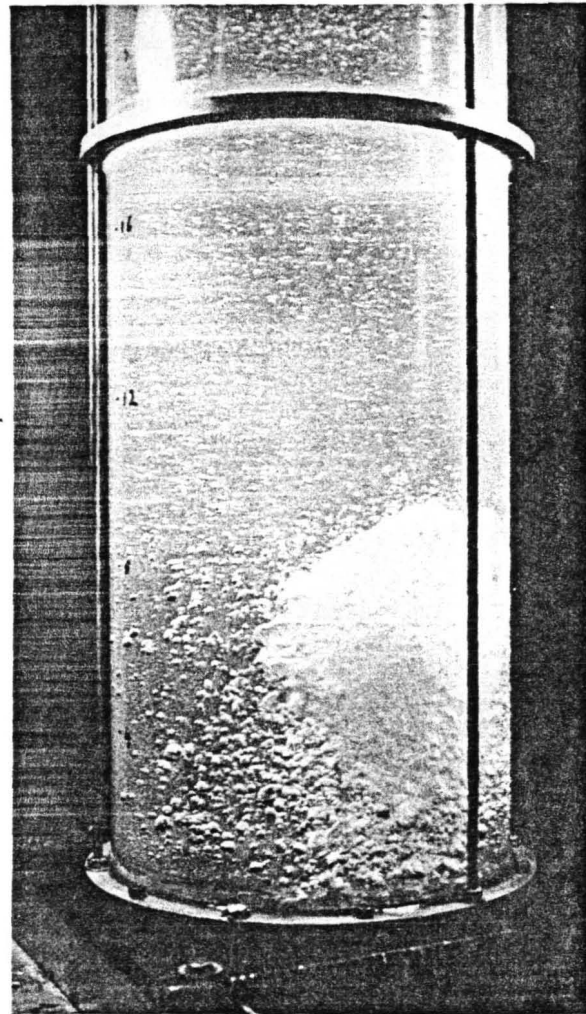


FIGURE 8.21.—Bubble cluster during most violent phase (ref. 8.35).

because, in another series of experiments with a more rigid tank (ref. 8.31), the cluster always vented, and the entire process then began anew, even with no change in the input.

Motion pictures have been taken which depict very vividly all of these aspects of the bubble motions. It should be mentioned, again, that the pressures in the fluid caused by the pulsating cluster are quite large.

#### Theory of Bubble Vibration

The first step in understanding the startling bubble motions outlined in the preceding section is to realize that bubble and liquid together represent an elastic system that possesses a definite natural frequency. Ap-

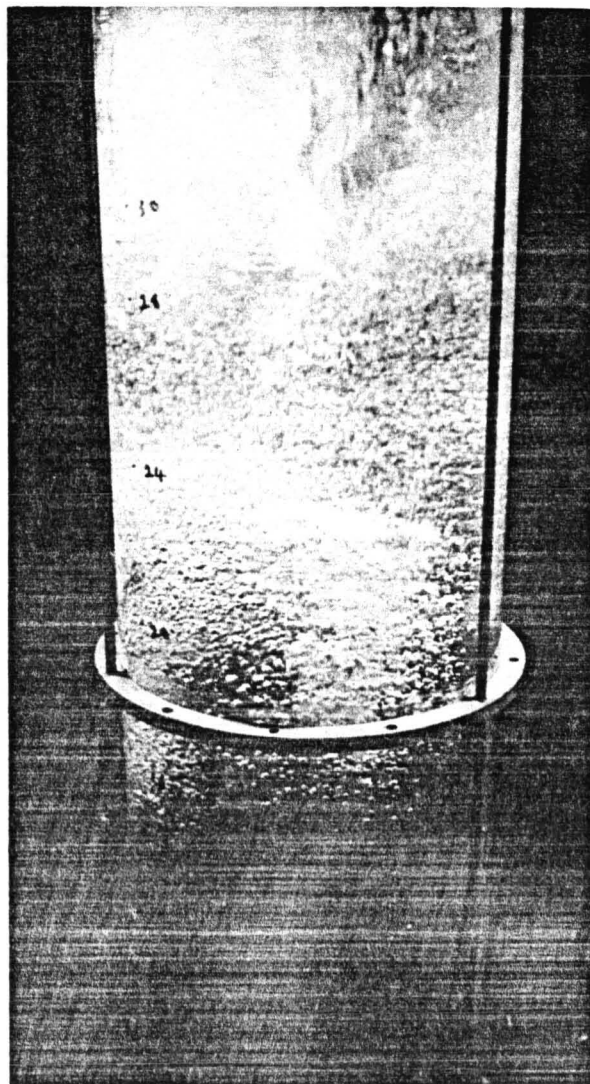


FIGURE 8.22.—Bubble cluster after most violent phase (ref. 8.35).

parently, this was first noticed by Minnaert (ref. 8.36) in his study of the origin of the "burbling" sounds of running water.

Suppose that a bubble with average radius,  $a$ , is completely immersed in an infinite space of incompressible liquid. The bubble is assumed to execute spherically symmetric pulsations, so that the bubble radius is  $a + \Delta(t)$ , as a function of time. As the bubble volume changes, the pressure inside the bubble follows the polytropic law:  $p_1 a^{3\gamma} = p(a + \Delta)^{3\gamma}$ , where  $p_1$  is the fluid pressure in the vicinity of the bubble (surface tension forces are neglected).

Thus, the work done in compressing the bubble from pressure  $p_1$  to  $p$  is

$$\frac{4\pi a^3}{3} p_1 \left\{ \frac{1}{\gamma-1} \left[ \left(1 + \frac{\Delta}{a}\right)^{3-\gamma} - 1 \right] + \left(1 + \frac{\Delta}{a}\right)^3 - 1 \right\} \quad (8.46)$$

By assuming that  $\Delta/a \ll 1$ , the work done, that is, the potential energy of the bubble, turns out to be

$$P.E. = 6\pi a \gamma p_1 \Delta^2 \quad (8.47)$$

The kinetic energy of the fluid, when the bubble radius is changing at a rate  $\dot{\Delta}$ , is

$$K.E. = 2\pi \rho (a + \Delta)^3 \dot{\Delta}^2 \approx 2\pi \rho a^3 \dot{\Delta}^2 \quad (8.48)$$

According to the law of conservation of energy, the sum of equations (8.47) and (8.48) must be constant; consequently

$$\frac{d}{dt} \{ 2\pi \rho a^3 \dot{\Delta}^2 + 6\pi a \gamma p_1 \Delta^2 \} = 0$$

or

$$\ddot{\Delta} + \frac{3\gamma p_1}{\rho a^2} \Delta = 0 \quad (8.49)$$

Thus, the natural frequency of the bubble-liquid combination is

$$\Omega = \sqrt{\frac{3\gamma p_1}{\rho a^2}} \quad (8.50)$$

The exact value of  $\gamma$  in equation (8.50) appears to vary from about 1.4 (adiabatic pulsations) to nearly 1.0 (isothermal pulsations), depending on the experimental conditions and the bubble size.

Although equation (8.50) is not sufficient to predict sinking bubbles, it does help explain the formation of the large clusters shown in figure 8.20. According to the theory of vibrations, a harmonic oscillator (in this case, the bubble) will vibrate in phase with an exciting motion if the exciting frequency is less than the oscillator's natural frequency, but otherwise it will oscillate out of phase. (If there is damping, the change in phase occurs over a band of frequencies instead of instantaneously.) Thus, bubbles smaller than the resonant size will all be in phase with each other and in phase with

the exciting motion; the small bubbles shown in figures 8.19 through 8.22 are all smaller than the resonant size for the excitation frequency used in the reported experiments. But if two nearby bubbles oscillate in phase with one another, the motion of the fluid around them is such that an attractive force is set up between them, and consequently they tend to coalesce or orbit about a common center (ref. 8.32).

The mechanical strain of the fluid in the vicinity of a pulsating bubble can be increased as much as 10 000 times over that caused solely by the exciting pressure. In support of this observation, Kana (ref. 8.29) noted that the wall motion of an elastic tank underwent large erratic vibrations whenever a bubble was trapped in the vertically vibrating fluid.

### Dynamics of Bubble Motion

The cause of stationary and sinking bubbles is a coupling between the bubble's pulsations, which are described above, and its overall motion through the body of the vibrating fluid. This has been shown by Bleich (refs. 8.33 and 8.34), Buchanan et al. (ref. 8.31), Baird (ref. 8.30), and Kana and Dodge (ref. 8.35). The theory given here is due to Bleich (ref. 8.33), as modified in reference 8.35.

Although the mathematical details of bubble motion tend to be complicated, it is fairly easy to describe the physical processes that occur. When the tank is vibrated up and down, the effect on the liquid is the same as if gravity were varying. For the moment, only the changes in the fluid pressure caused by this varying gravity need be considered. During the upward acceleration, the pressure increases over its static value, and, consequently, the volume of the bubble is smaller than for static conditions. The pressure gradient at this time creates a net positive change in buoyancy, and the bubble gains a certain amount of upward momentum. During the downward acceleration, the pressure change is negative, and the bubble volume increases. A net negative buoyancy is created, and the bubble gains a certain amount of downward momentum. But the downward momentum is larger than the upward momentum; that is, the bubble volume (and the

buoyant force) is larger during the downward acceleration part of the cycle. If the difference of these buoyancies is great enough, the static buoyancy caused by gravity may be exceeded, and thus the bubble will sink.

In order to make numerical calculations, a more explicit formulation of the theory than is given in the preceding paragraph is needed. For simplicity, the necessary theory is worked out for a rigid tank; in most practical cases, however, the tank is sufficiently elastic at the forcing frequencies used in experiments that some account must be taken of its flexibility; hence, the theory will be modified immediately to include tank elasticity in an approximate fashion.

The most significant part of bubble behavior observed in experiments is that part in which an individual bubble initially begins to sink. Once this occurs, all of the rest of the phenomena described earlier naturally follow. Thus, it is this situation for which the theory is developed, but even here there may be other bubbles present in the liquid, and their effect on the fluid compressibility must be included.

To obtain the equations of motion for the bubble-tank-liquid system shown in figure 8.23, it is convenient to use Lagrange's method.

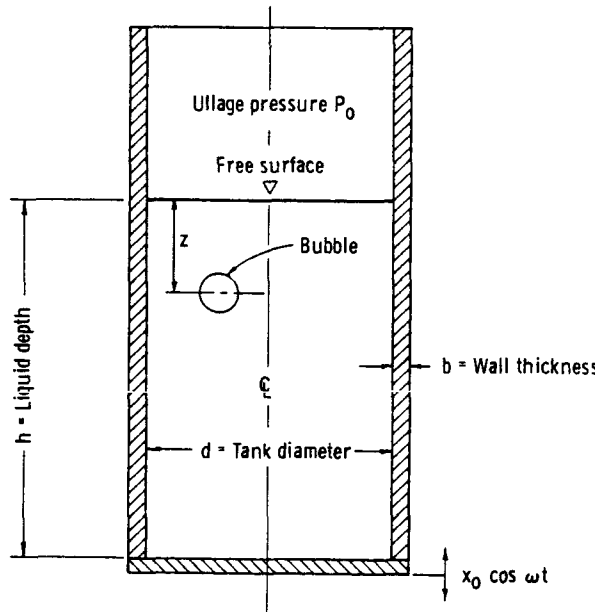


FIGURE 8.23.—Bubble-tank-liquid dynamic system.

The bubble is assumed to be very small compared to the tank and located far from any surface. The fluid velocity at any point is

$$\vec{u} = \vec{u}_x + \vec{u}_\Delta + \vec{u}_z$$

where  $\vec{u}_x = \dot{x} - x_0 \omega \sin \omega t$  is the velocity due to the overall tank motion,  $\vec{u}_\Delta$  is the velocity due to the bubble's expansion, and  $\vec{u}_z$  is the velocity due to the bubble's vertical motion. If  $dV$  is the element of volume, the kinetic energy of the fluid is

$$\begin{aligned} \text{K.E.} &= \frac{1}{2} \rho \int \vec{u} \cdot \vec{u} dV = \frac{1}{2} \rho \dot{x}^2 \int dV + \frac{1}{2} \rho \int \vec{u}_\Delta \cdot \vec{u}_\Delta dV + \frac{1}{2} \int \vec{u}_z \cdot \vec{u}_z dV + \rho \dot{x} \int (w_\Delta + w_z) dV \end{aligned} \quad (8.51)$$

where  $w_\Delta$  and  $w_z$  are the vertical components of  $\vec{u}_\Delta$  and  $\vec{u}_z$ . There are no contributions such as  $\rho \int \vec{u}_\Delta \cdot \vec{u}_z dV$  because of the assumed symmetry.

The first integral in equation (8.51) is simply  $M\dot{x}^2/2$ , where  $M$  is the total mass of fluid. The second integral is the same as the nonlinearized form of equation (8.48). The third term can be shown to equal  $\pi\rho(a+\Delta)^3 z^2/3$ , where  $z$  is the vertical velocity of the bubble. The fourth integral is  $-4\pi \frac{\partial}{\partial t} [(a+\Delta)^3 z]/3$ , according to reference 8.33. Hence, the total kinetic energy is

$$\begin{aligned} \text{K.E.} &= \frac{1}{2} M\dot{x}^2 + 2\pi\rho(a+\Delta)^3 \dot{z}^2 + \frac{1}{3} \pi\rho(a+\Delta)^3 z^2 \\ &\quad - \frac{4\pi}{3} \rho \dot{x} \frac{\partial}{\partial t} [(a+\Delta)^3 z] \end{aligned} \quad (8.52)$$

The contribution to the kinetic energy due to free surface sloshing has been neglected in equation (8.52).

The potential energy consists of three parts. The potential of the gravity field is

$$-gMx + \frac{4\pi}{3} \rho g (a+\Delta)^3 z$$

The potential of the ullage gas above the surface is

$$\frac{4\pi}{3} p_0 [(a+\Delta)^3 - a^3]$$

The potential of the compressed gas bubble is

$$\frac{4\pi}{3} p_1 \left\{ \frac{a^{3\gamma}}{\gamma-1} [(a+\Delta)^{3-\gamma} - a^{3-\gamma}] + (a+\Delta)^3 - a^3 \right\}$$

Collecting all the terms gives

$$\begin{aligned} \text{P.E.} &= -gMx + \frac{4\pi}{3} \rho g (a+\Delta)^3 z \\ &\quad + \frac{4\pi}{3} p_0 [(a+\Delta)^3 - a^3] + \frac{4\pi}{3} p_1 \left\{ \frac{a^{3\gamma}}{\gamma-1} [(a+\Delta)^{3-\gamma} - a^{3-\gamma}] \right. \\ &\quad \left. + (a+\Delta)^3 - a^3 \right\} \end{aligned} \quad (8.53)$$

The two pertinent forms of Lagrange's equations are

$$\frac{d}{dt} \frac{\partial L}{\partial \dot{z}} - \frac{\partial L}{\partial z} = 0 \quad \frac{d}{dt} \frac{\partial L}{\partial \Delta} - \frac{\partial L}{\partial \Delta} = 0 \quad (8.54)$$

where  $L = \text{K.E.} - \text{P.E.}$ . When equations (8.52) and (8.53) are substituted into equations (8.54), the results are

$$\frac{d}{dt} [(a+\Delta)^3 \dot{z}] = 2(a+\Delta)^3 (\ddot{x} - g) \quad (8.55)$$

and

$$\begin{aligned} \ddot{\Delta} + \frac{3\dot{\Delta}^2}{2(a+\Delta)} - \frac{p_1}{\rho(a+\Delta)} \left[ \frac{a^{3\gamma}}{(a+\Delta)^{3\gamma}} - 1 \right] \\ + \frac{(g-\ddot{x})z}{a+\Delta} - \frac{z^2}{4(a+\Delta)} = -\frac{p_0}{\rho(a+\Delta)} \end{aligned} \quad (8.56)$$

Equations (8.55) and (8.56) may now be solved simultaneously to yield the necessary conditions for sinking bubbles. However, Bleich (ref. 8.33) showed that this was equivalent to solving a much simpler problem: find the conditions for which a bubble will undergo a small periodic vertical motion about some level,  $l$ . The level,  $l$ , can be shown to separate the regions for which bubbles sink and the regions for which they rise.

It is convenient to replace the coordinate  $z$  by  $\lambda = z - l$ . Then, because  $|\lambda/l| \ll 1$  (since the bubble is assumed to vibrate near the level  $l$ ) and  $|\Delta/a| \ll 1$ , equations (8.55) and (8.56) can be partially linearized to yield

$$\frac{d}{dt} [(a+3\Delta)\dot{\lambda}] = 2(a+3\Delta)(\ddot{x}-g)$$

$$\ddot{\Delta} + \frac{3\gamma p_1}{\rho a^2} \Delta = \frac{l}{a} \ddot{x} \quad (8.57)$$

in which use has been made of the relation  $p_1 = p_0 + \rho g l$ .

Instead of investigating the solution of equations (8.57), the same problem for a non-rigid tank is examined, since the rigid tank solution is merely a special case of this. The necessary modifications can be performed readily if it is noted that in equations (8.57) the dynamic pressure  $\bar{p}$  is  $-\rho \ddot{x}$  and the pressure gradient is  $\frac{\partial \bar{p}}{\partial z} = -\rho \ddot{x}$ . Hence, by analogy, the equations for a nonrigid tank can be written down immediately

$$\frac{d}{dt} [(a+3\Delta)\dot{\lambda}] = -2(a+3\Delta) \left( \frac{1}{\rho} \frac{\partial \bar{p}}{\partial z} + g \right)$$

$$\ddot{\Delta} + \frac{3\gamma p_1}{\rho a^2} \Delta = -\frac{\bar{p}}{a\rho} \quad (8.58)$$

The dynamic pressure  $\bar{p}$  must be calculated before the location of stationary bubbles can be found from equations (8.58). Since equations (8.58) are themselves somewhat approximate, a really complete pressure analysis is not warranted. A relatively simple approach, very similar to that used in an ordinary water-hammer pressure analysis, is found to be satisfactory. That is, the pressure is assumed to be uniform across any horizontal section through the tank, the deflection of the tank wall is assumed to be the same as its static deflection caused by the same instantaneous pressure, and longitudinal and bending deflections are neglected.

First, the water-hammer wave velocity must be calculated; to do this the density of the fluid and the compressibility of the system must be determined. The equivalent density of the liquid-gas mixture is simply

$$\rho = (1-s)\rho_l + s\rho_g$$

where  $s$  is the gas to total volume ratio,  $\rho_l$  is the liquid density, and  $\rho_g$  the gas density. Also, the effective compressibility of the gas-liquid-

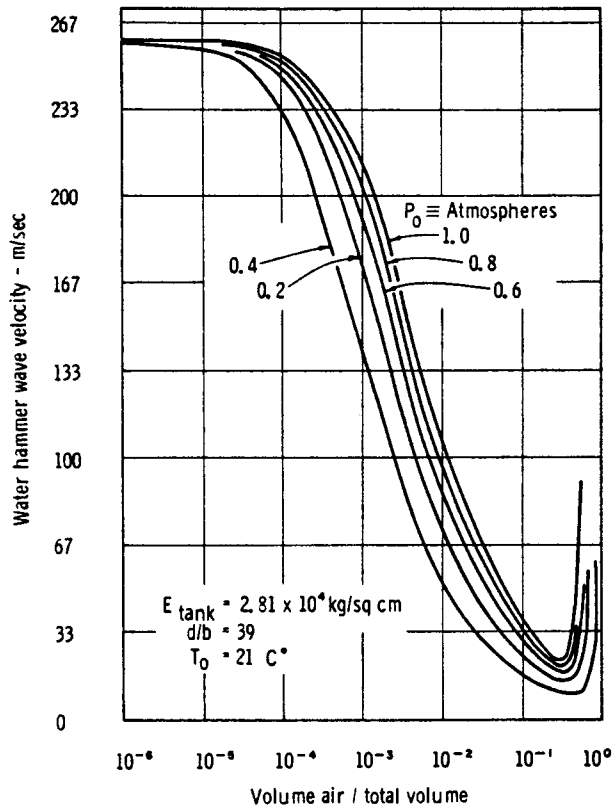


FIGURE 8.24.—Water-hammer wave velocity in a liquid-air mixture.

tank system is the sum of the three individual compressibilities

$$K = (1-s)K_l + sK_g + K_t$$

$K_l$  is the reciprocal of the liquid's bulk modulus;  $K_g = (\gamma p)^{-1}$  is the compressibility of an ideal gas;  $K_t = d/bE$  is the compressibility of the tank, where  $E$  is the modulus of elasticity of the tank material. By definition, the wave velocity is  $c = (\rho K)^{-1/2}$  so that

$$c = \left\{ [(1-s)\rho_l + s\rho_g] \left[ (1-s)K_l + \frac{s}{\gamma p_0} + \frac{d}{bE} \right] \right\}^{-1/2} \quad (8.59)$$

This equation is shown graphically in figure 8.24 for various values of  $p_0$  and a typical value of  $d/b=39$  for a small plastic test tank.<sup>11</sup>

<sup>11</sup> The compressibility of the gas,  $K_g$ , varies throughout the liquid, but it is sufficient here to evaluate it for the ullage gas and neglect any variation caused by depth of submersion of the gas bubbles.

Equation (8.59) gives only a correct order of magnitude value of the wave velocity, chiefly because the compressibility  $K$ , is overestimated. Furthermore, the exact quantity of gas is difficult to measure, and it is not homogeneously distributed throughout the liquid as assumed implicitly in equation (8.59); hence, an experimentally determined value of  $c$  should be used in numerical calculations. But, equation (8.59) does give a correct qualitative picture, and rather small values of the speed of sound,  $c$ , should be expected.

The fluid pressure is now determined by treating the pressure wave as a one-dimensional acoustic wave. Thus, if  $\xi(z, t)$  are the fluid particle displacements measured from their equilibrium positions, then

$$\frac{\partial^2 \xi}{\partial z^2} = \frac{1}{c^2} \frac{\partial^2 \xi}{\partial t^2}$$

The boundary conditions require that  $\xi(h, t) = x_0 \cos \omega t$  and  $\partial \xi / \partial z(0, t) = 0$ ; the bottom of the tank is  $z=h$ , the free surface is  $z=0$ . An appropriate form for  $\xi(z, t)$  is

$$\xi(z, t) = x_0 \frac{\cos \frac{\omega}{c} z}{\cos \frac{\omega}{c} h} \cos \omega t$$

Since the pressure is  $\bar{p} = \rho c^2 \partial \xi / \partial z$ , it can be seen that

$$\bar{p} = -\rho c \omega x_0 \frac{\sin \frac{\omega}{c} z}{\cos \frac{\omega}{c} h} \cos \omega t \quad (8.60)$$

The second of equations (8.58) can now be solved for  $\Delta$  by using equation (8.60), with the result that

$$\Delta = \frac{\omega x_0 c}{a \Omega^2} \left[ \frac{\sin \frac{\omega}{c} z}{\cos \frac{\omega}{c} h} \right] \left[ \frac{\cos \omega t}{1 - \omega^2 / \Omega^2} \right]$$

where  $\Omega^2 = 3\gamma p_1 / a^2 \rho$  is the square of the natural frequency of bubble pulsations. Since  $\Omega$  is generally very large, the ratio  $\omega^2 / \Omega^2$  can be neglected in comparison to unity.

The critical value of  $l$ , that is, the depth for which the bubble will remain stationary, can be found from the first of equations (8.58) by requiring that the average buoyancy over one cycle of motion be zero. That is

$$\text{Average of } (a + 3\Delta) \left( \frac{1}{\rho} \frac{\partial \bar{p}}{\partial z} + g \right) = 0$$

which reduces to

$$ag + \text{Average of } \left[ \frac{3\Delta_c}{\rho} \cdot \frac{\partial \bar{p}}{\partial z} \right] = 0$$

where  $\Delta_c$  is the value of  $\Delta$  corresponding to the critical value of  $z=l$ . Consequently, the critical bubble depth  $l$  can be calculated from

$$\frac{\omega^2 x_0}{g} \left[ \frac{\sin \frac{2\omega l}{c}}{\frac{\omega l}{c} \left( 1 + \cos \frac{2\omega h}{c} \right)} \right]^{1/2} = \left[ 2\gamma \left( 1 + \frac{p_0}{\rho g l} \right) \right]^{1/2}$$

This equation can be further simplified by using the nondimensional variables  $\psi = 2\omega h/c$  and  $\alpha = l/h$ . The final result is

$$\frac{\omega^2 x_0}{g} \left[ \frac{2 \sin \alpha \psi}{\alpha \psi (1 + \cos \psi)} \right]^{1/2} = \left[ 2\gamma \left( 1 + \frac{p_0}{\rho g l} \right) \right]^{1/2} \quad (8.61)$$

(Eq. (61) can be specialized to the case of a rigid tank and incompressible liquid-air mixture by setting the bracketed term on the left-hand side equal to one; that is, by letting  $c \rightarrow \infty$  or  $\psi \rightarrow 0$ .)

Actual test results (ref. 8.35) are compared with equation (8.61) in figure 8.25. As can be seen, the correlation is very good, although an experimental value for  $c$  was employed. It may be noted that  $\psi = \pi$  corresponds to a first-mode resonance. For values of  $\psi$  greater or even slightly less than  $\pi$ , bubbles do not sink completely to the bottom no matter how large the input vibration is, but, instead, they collect at some lower depth. Bubbles inserted below this depth will rise to this level, as is indicated in the figure by the fact that for some values of  $\psi$  there exist two critical values of  $l$  for a given  $\omega^2 x_0 / g$ . As a specific example, consider the  $\psi = 4.0$  curve with 6 g's acceleration. Bubbles above a depth ratio  $\alpha = 0.16$  return to the free

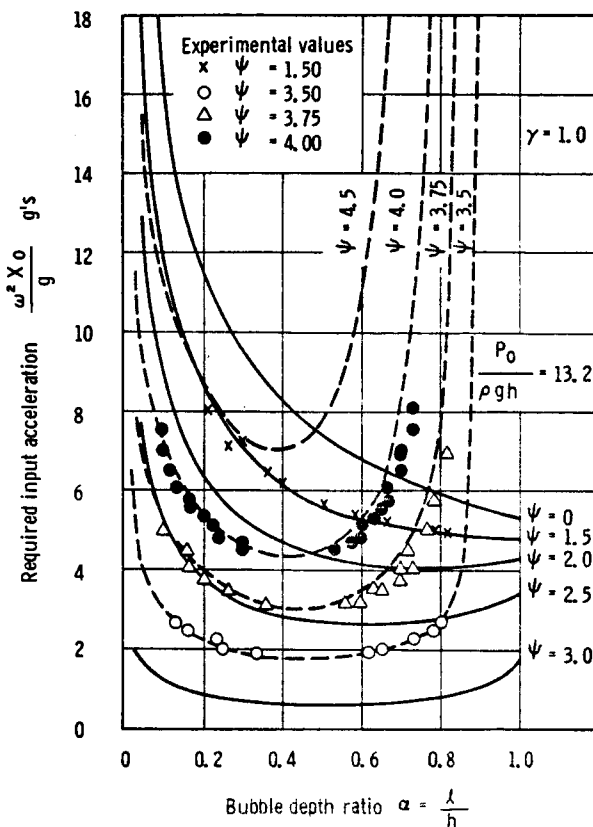


FIGURE 8.25.—Variation of required input acceleration with depth ratio (ref. 8.35).

surface, while bubbles below this depth collect at a depth  $\alpha=0.64$ .

For values of  $\psi$  less than about  $\pi$ , the bubbles always sink completely to the tank bottom if  $\omega^2 x_0/g$  is large enough. For  $\psi > \pi$ , the bubble behavior becomes increasingly complex since, for these values of  $\psi$ , equation (8.61) has increasingly more values of  $l$  as roots. This is illustrated in figure 8.26 for a relatively large value of  $\phi$ . Several bubble equilibrium planes (critical values of  $l$ ) are shown, with the upper one being unstable (bubbles move away from it when they are slightly displaced), the second level stable, the third unstable, and so on. Bubble migration directions are indicated by the arrows.

A slightly different theory for sinking bubbles was proposed by Buchanan et al. (ref. 8.31). The essential result is that

$$\omega^2 x_0 = C \left[ g + \sqrt{3g^2 + \frac{2gp_0}{\rho l}} \right] \quad (8.62)$$

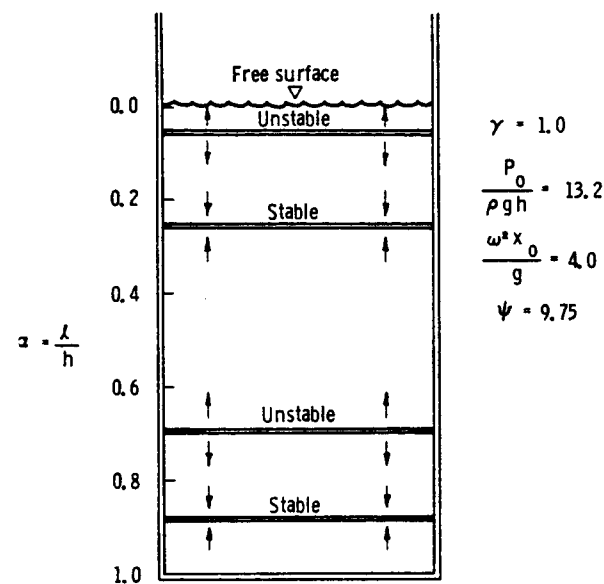


FIGURE 8.26.—Bubble pattern at higher frequency.

where  $C$  is an experimentally determined constant. This equation is compared to test results in figure 8.27, with correlation being fairly good for  $C=1$ . However, equation (8.62) is not as general as the preceding equation (8.61).

#### Explanation of Overall Bubble Behavior

With the aid of the preceding analysis, it is possible to explain completely the bubble behavior described in figures 8.19 through 8.22.

At the start of the process, air bubbles are thrown into the body of the liquid by the free surface sloshing motions. The bubbles that sink at least to a depth  $l$  (the root of eq. (8.61) for the given input vibration conditions) will continue to sink to the tank bottom. As more and more air bubbles are entrained and then sink, the wave velocity decreases (see fig. 8.24), so that  $\psi$ , which was initially considerably less than  $\pi$ , increases continually. Eventually, a value of  $\psi$  equal to  $\pi$  is obtained, a resonance occurs, and the cluster motion is very violent. As a result of the large quantity of air that is entrained during resonance, a value of  $\psi > \pi$  ultimately results. Then, according to figure 8.25, bubbles (or clusters of bubbles) no longer can remain on the bottom, and the cluster rises to an appropriate  $\alpha$ . At this level, the cluster

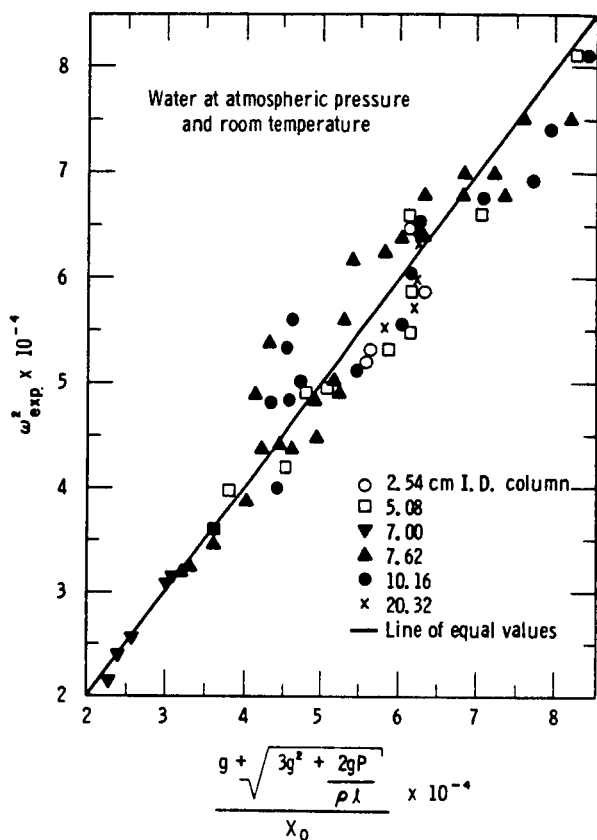


FIGURE 8.27.—Theoretical and experimental values of vibrational acceleration required for bubble stabilization (ref. 8.31).

is in stable equilibrium so long as  $\psi$  does not change further.

Quantitative prediction of the large-scale cluster motion obviously cannot be obtained with the simple theory outlined above, although Bleich indicates (ref. 8.34) that a somewhat similar theory would probably be applicable. However, the simple theory is sufficient to predict the point at which the process begins, and to give an overall qualitative picture.

Although the preceding discussion applies strictly only to simple harmonic excitation,

Fritz et al. (ref. 8.37) have shown experimentally that the same sort of behavior occurs when the excitation is random if the input acceleration is large enough. Their experiments demonstrate, in addition, that the large bubble cluster will eventually vent after a sufficiently long time; the entire sequence of events then begins again.

### Cavitation

The processes of cavitation and bubble formation are not well understood at the present time. Existing theories tend to support the belief that small nucleation sites, such as microscopic gas bubbles, must exist before a bubble may form in a fluid. The forces required to form a bubble nucleus solely from rupturing a totally degassed fluid by low pressure (or high temperature) are so large that theories which do not presuppose nucleation sites are generally not applicable. However, in most practical cases, including cryogenic fuels, there is a sufficient amount of dissolved gas or vapor to insure the formation of bubbles whenever the local fluid pressure is significantly below the vapor pressure.

No systematic investigation of bubble motion in a vertically vibrating, boiling (or near boiling) liquid seems to have been reported, although a review of the work that is available has been given (ref. 8.32). For the purposes of this chapter, however, it is sufficient to realize that in a near-boiling fluid, bubbles will always be present whenever the instantaneous pressure drops below the vapor pressure, provided that the bubbles formed in this way grow to a sufficient size so that they do not collapse during the succeeding, positive part of the pressure cycle. Once the bubbles are formed it is apparent that the vibration of the fluid will have the same effect as that discussed in the preceding sections. In other words, the bubble motion is more or less independent of their formation.

### REFERENCES

- 8.1. FARADAY, MICHAEL: On the Forms and States Assumed by Fluids in Contact With Vibrating Elastic Surfaces. Phil. Trans. Roy. Soc. (London), vol. 121, 1831, pp. 319-340.
- 8.2. MATHIESSEN, L.: Akustische Versuche, die Kleinsten Transversalwellen der Flüssigkeiten betreffend. Annalen der Physik, vol. 134, 1868, pp. 107-117.

- 8.3. MATHIESSEN, L.: Über die Transversalschwingungen tönender tropfhaerer und elastischer Flüssigkeiten. *Annalen der Physik*, vol. 141, 1870, pp. 375-393.
- 8.4. LORD RAYLEIGH: On the Crispations of Fluid Resting Upon a Vibrating Support. *Phil. Mag.*, vol. 16, 1883, pp. 50-58.
- 8.5. LORD RAYLEIGH: On Maintained Vibrations. *Phil. Mag.*, vol. 15, Apr. 1883, pp. 229-235.
- 8.6. LORD RAYLEIGH: On the Maintenance of Vibrations by Forces of Double Frequency, and on the Propagation of Waves Through a Medium Endowed With a Periodic Structure. *Phil. Mag.*, vol. 24, Aug. 1887, pp. 145-159.
- 8.7. TAYLOR, SIR G. I.: The Instability of Liquid Surfaces When Accelerated in a Direction Perpendicular to Their Planes, Part I. *Proc. Roy. Soc. (London)*, A201, 1950, pp. 192-196.
- 8.8. MOISEYEV, N. N.: The Problem of the Motion of a Rigid Body Containing Liquid Masses With Free Surfaces. *Matem. Sbornik (Math. Review)*, vol. 32, no. 1, 1953, p. 32.
- 8.9. MOISEYEV, N. N.: Introduction to the Theory of Oscillation of Liquid Containing Bodies. *Advances in Applied Mechanics*, vol. 8, Academic Press, 1964.
- 8.10. BOLOTIN, V. V.: On Liquid Motion in a Vibrating Container. *Prikladnaia Matematika in Mekhanika*, vol. 20, no. 2, 1956, pp. 293-294.
- 8.11. BENJAMIN, T. BROOKE; AND URSELL, F.: The Stability of a Plane Free Surface of a Liquid in Vertical Periodic Motion. *Proc. Roy. Soc. (London)*, A225, 1954, pp. 505-515.
- 8.12. PENNEY, W. G.; AND PRICE, A. T.: Finite Periodic Stationary Gravity Waves in a Perfect Liquid, Part II. *Phil. Trans. Roy. Soc. (London)*, A244, 1952, pp. 254-284.
- 8.13. TAYLOR, SIR G. I.: An Experimental Study of Standing Waves. *Proc. Roy. Soc. (London)*, A218, 1954, pp. 44-59.
- 8.14. TADJBAKSH, I.; AND KELLER, J. B.: Standing Surface Waves of Finite Amplitude. *J. Fluid Mech.*, vol. 8, no. 3, July 1960, pp. 442-451.
- 8.15. FULTZ, D.: An Experimental Note on Finite-Amplitude Standing Gravity Waves. *J. Fluid Mech.*, vol. 13, no. 2, June 1962, pp. 193-212.
- 8.16. VERMA, G. R.; AND KELLER, J. B.: Three-Dimensional Standing Surface Waves of Finite Amplitude. *Phys. Fluids*, vol. 5, no. 1, Jan. 1962, pp. 52-56.
- 8.17. MACK, L. R.: Periodic, Finite-Amplitude, Axisymmetric Gravity Waves. *J. Geophys. Res.*, vol. 67, no. 2, Feb. 1962, pp. 829-843.
- 8.18. YARYMOVICH, M. I.: Forced Large Amplitude Surface Waves. *D. Eng. Sci. thesis*, Columbia University, Dec. 1959.
- 8.19. SKALAK, R.; AND YARYMOVICH, M.: Forced Large Amplitude Surface Waves. *Proceedings of the Fourth U.S. National Congress of Applied Mechanics*, 1962, pp. 1411-1418.
- 8.20. DODGE, F. T.; KANA, D. D.; AND ABRAMSON, H. N.: Liquid Surface Oscillations in Longitudinally Excited Rigid Cylindrical Containers. *AIAA J.*, vol. 3, no. 4, Apr. 1965, pp. 685-695.
- 8.21. BHUTA, P. G.; AND YEH, G. C. K.: Liquid Sloshing Due to a Time Dependent Discontinuous Boundary. *Int. J. Mech. Sci.*, vol. 7, July 1965, pp. 475-488.
- 8.22. BLEICH, H. H.: Longitudinal Forced Vibrations of Cylindrical Fuel Tanks. *Jet Propulsion*, vol. 26, 1956, pp. 109-111.
- 8.23. BHUTA, P. G.; AND KOVAL, L. R.: Coupled Oscillations of a Liquid With a Free Surface in a Tank Having a Free Bottom. *Zeitschrift für angewandte Mathematik und Physik*, vol. 15, 1964, pp. 466-480.
- 8.24. BHUTA, P. G.; AND KOVAL, L. R.: Hydroelastic Solution of the Sloshing of a Liquid in a Cylindrical Tank. *J. Acoust. Soc. Am.*, vol. 36, no. 11, 1964, pp. 2071-2079.
- 8.25. KANA, D. D.: Vertical Oscillation of Partially Full Spherical Tanks. Contract NASw-146, Southwest Research Institute, Apr. 1963.
- 8.26. KANA, D. D.: An Experimental Study of Liquid Surface Oscillations in Longitudinally Excited Compartmented Cylindrical and Spherical Tanks. NASA CR-545, 1966.
- 8.27. CHU, W. H.: Subharmonic Oscillations in an Arbitrary Axisymmetric Tank Resulting From Axial Excitations. Tech. Rept. No. 5, Contract No. NAS8-11045, Southwest Research Institute, Sept. 1965.
- 8.28. HUTTON, R. E.: An Investigation of Resonant, Nonlinear, Nonplanar Free-Surface Oscillations of a Fluid. NASA TN D-1870, 1963.
- 8.29. KANA, D. D.: Longitudinal Forced Vibration of Partially Filled Tanks. Tech. Rept. No. 6, Contract No. NASw-146, Southwest Research Institute, 1963.
- 8.30. BAIRD, M. H. I.: Resonant Bubbles in a Vertically Vibrating Liquid Column. *Canadian Journal of Chemical Engineering*, vol. 41, Apr. 1963, pp. 52-55.
- 8.31. BUCHANAN, R. H.; JAMESON, G.; AND OEDJOE, D.: Cyclic Migration of Bubbles in Vertically Vibrating Liquid Columns. *Industrial and Engineering Chemistry Fundamentals*, vol. 1, no. 2, 1962, pp. 82-86.
- 8.32. DODGE, F. T.: A Review of Research Studies on Bubble Motion in Liquids Contained in Vertically Vibrating Tanks. Tech. Rept. No. 1, Contract No. NAS8-11045, Southwest Research Institute, Dec. 1963.
- 8.33. BLEICH, H. H.: Effect of Vibrations on the Motion of Small Gas Bubbles in a Liquid. *Jet Propulsion*, vol. 26, 1956, pp. 958-978.
- 8.34. BLEICH, H. H.: Motions of Clusters of Gas Bubbles in Vibrated Vessels. Rept. No. GM-TR-27, Contract No. AF(600)-1190, Ramo-Wooldridge Corp., 1956.

- 8.35. KANA, D. D.; AND DODGE, F. T.: Bubble Behavior in Liquids Contained in Vertically Vibrated Tanks. *J. Spacecraft Rockets*, vol. 3, no. 5, May 1966, pp. 760-763.
- 8.36. MINNAERT, M.: On Musical Air Bubbles and the Sounds of Running Water. *Phil. Mag.*, ser. 7, vol. 16, no. 104, Aug. 1933, pp. 235-248.
- 8.37. FRITZ, C. G.; PONDER, C. A., JR.; AND BLOUNT, D. H.: Bubble Coalescence in a Longitudinally Vibrated Liquid Column. *Proc. of the ASME Symposium on Cavitation in Fluid Machinery, 1965 ASME Winter Annual Meeting, Nov. 7-11, 1965.*

## PRINCIPAL NOTATIONS

*Symbols in parentheses are the nondimensional equivalents of the preceding quantity*

$a$ =average bubble radius	$s$ =ratio of gas volume to total mixture volume
$a_{mn}(\alpha_{mn})$ =expansion coefficient of $m, n$ th component of velocity potential	$S_m$ = $m$ th eigenfunction of $\nabla^2\Phi=0$
$b$ =tank wall thickness	$t(\tau)$ =time
$b_{mn}(\beta_{mn})$ =expansion coefficient of $m, n$ th component of free surface mode	$x_0(\epsilon)$ =excitation amplitude
$c$ =water-hammer wave velocity	$x, y, z$ =tank-fixed Cartesian axes
$d$ =cylindrical tank diameter	$r, \theta, z$
$E$ =modulus of elasticity	$\alpha$ =critical depth ratio, $l/h$
$g$ =acceleration due to gravity, or equivalent acceleration	$\gamma$ =polytropic constant
$h(H)$ =fluid depth	$\Delta$ =time varying part of bubble radius
$J_m$ = $m$ th-order Bessel function of first kind	$\zeta$ =fluid particle displacements
$K$ =compressibility of gas-liquid-tank system	$\eta(\xi)$ =free surface displacement
$l$ =critical depth for sinking bubbles	$\lambda_m$ = $m$ th eigenvalue
$L$ =rectangular tank length	$\nu$ =surface tension
$N\omega$ =excitation frequency ( $N$ is a positive number)	$\rho$ =fluid density
$p$ =fluid pressure	$\sigma$ =frequency parameter, $\omega/\omega_{mn}$
	$\Phi(\phi)$ =fluid velocity potential
	$\psi$ =dimensionless wavelength, $2\omega h/c$
	$\omega_{mn}$ =natural frequency of $m, n$ th free surface mode
	$\Omega$ =bubble pulsation natural frequency

## APPENDIX

The constants in equation (8.37) are

$$K_{11} = 0.122515 - \frac{0.045199 - 0.043438\lambda_{01}}{\tanh \lambda_{01}H} + \frac{0.010759\lambda_{11} + 0.09500\lambda_{21}}{\tanh \lambda_{21}H} - \frac{0.149793\lambda_{11}^3}{\lambda_{21} \tanh \lambda_{21}H}$$

$$K_{01} = 0.343624\lambda_{01}\lambda_{11}$$

$$K_{21} = 0.620686\lambda_{11}^2 - 0.044582\lambda_{11}\lambda_{21}$$

$$k_{11} = \frac{0.045199\lambda_{11}^3}{\tanh \lambda_{01}H} + \frac{0.149793\lambda_{11}^4}{\lambda_{21} \tanh \lambda_{21}H} - \frac{0.010759\lambda_{11}^3}{\tanh \lambda_{21}H}$$

$$k_{01} = 0.165118 + \frac{0.171812\lambda_{11}}{\tanh \lambda_{01}H}$$

$$k_{21} = 0.198686 + \frac{0.310343\lambda_{11}^2}{\lambda_{21} \tanh \lambda_{21}H} - \frac{0.022291\lambda_{11}}{\tanh \lambda_{21}H}$$

$H$  is the nondimensional liquid depth; that is,  $H = h\tilde{\lambda}_{11} \tanh \tilde{\lambda}_{11}h$ ;  $\tilde{\lambda}_{11}$  is the first root of  $J'_1(\tilde{\lambda}_{11}R) = 0$ ; and terms  $\lambda_{ki}$  ( $k=0, 1, 2$ ) are defined by  $\lambda_{ki} = \frac{\tilde{\lambda}_{ki}}{\tilde{\lambda}_{11} \tanh \tilde{\lambda}_{11}h}$ .

# Interaction Between Liquid Propellants and the Elastic Structure

*Daniel D. Kana*

## 9.1 GENERAL DISCUSSION OF COUPLED PROBLEM

The previous chapters have dealt primarily with a description of the variety and complexity of liquid behavior that can be encountered in a rigid container in motion. The tanks and entire structure of liquid-fueled space vehicles are, however, by no means rigid; hence, the coupling of the various possible liquid responses with elastic deformations of the tanks and vehicle structure must be considered in the overall analysis of vehicle dynamics. The internal pressurized liquid and gas column, together with the shell-like tank of a space vehicle, represents a system which, in addition to liquid surface motions, can experience bending and breathing motions of the tank walls, breathing of the tank bottom, and pressure oscillations in the liquid column, while all of these motions can couple with the motions of the rest of the structure and vehicle control system. Considering the complexities of the rigid tank liquid behavior that have already been described, along with the complexities in analyzing elastic responses of shell-like structures, it is obvious that the combined problem is one of extreme difficulty.

Recognizing this complexity of the coupled system, it becomes apparent that some simplifications must be assumed in the overall problem, so that at least solutions for restricted ranges of input conditions are obtained. For this reason, this chapter has been outlined into sections which discuss the analysis of various individual aspects of the overall coupled problem. Further, it will be seen that within each section, further simplifications of the problem have been assumed, particularly in

the investigations of the influence of the liquid on breathing vibrations of the tank walls. The solutions of these simplified problems still give valuable information that contributes to the description of the overall behavior. As methods and ideas progress, in time, all of the solutions of the individual problems will be consolidated into the general description of the coupled liquid-elastic structure system. This cannot necessarily be accomplished by a simple superposition of what is already available because of nonlinearities present. In other words, the development scheme is an example of progressing from the comparatively simple to the more complex.

The solutions of what have been described here as individual simplified problems appear, in many cases, to give a very good description of the responses of the actual overall system for a limited range of input conditions. By and large, for a given liquid in a tank of given size and geometry, the various forms of liquid-elastic tank behavior that arise are a function of the type of excitation. For forced oscillation, in other words, the responses of the various coupled natural modes of the system depend on whether the input (lateral or longitudinal translation and pitching) forms a generalized force capable of exciting a given natural mode. It may happen that liquid surface modes are excited for a limited range of excitation parameters, but significant elastic tank modes are not; as a result, for that limited range, the analysis of the liquid in a rigid tank provides a good description of the overall behavior. On the other hand, if for some ranges of frequencies, significant liquid

surface motion does not occur, while elastic action of the tank wall does occur, then the presence of the liquid simply causes the addition of a distributed mass on the tank walls, as well as allows longitudinal pressure modes, and an analysis neglecting the liquid surface condition would provide an adequate description of the overall behavior in that limited frequency range.

For linear responses, in many cases, coupling of liquid and elastic container modes may become significant because of close proximity of their respective uncoupled natural frequencies. For example, coupling of low-frequency liquid surface modes with low-frequency bending modes of the vehicle may be a distinct possibility. This follows from the fact that in the uncoupled cases, that is with sloshing modes in a rigid tank, or with bending modes in a liquid-filled tank having a capped surface, the respective motions occur at frequencies relatively near to each other. For the two cases occurring simultaneously, it is obvious that strong coupling might result, so that each respective coupled mode would occur at a frequency different from the respective uncoupled cases. On the other hand, "breathing" or "shell modes" of the walls of a tank containing a capped liquid may occur at somewhat higher frequencies than the significant bending modes in a space vehicle, depending on the type of stiffeners used on the tank walls. As a result, one might anticipate only weak coupling with the low-frequency liquid surface modes, but might expect strong coupling with higher frequency spray phenomena. It must be emphasized that the above type of reasoning is valid only for linear behavior. When significant nonlinearities are present, coupling can occur between individual responses even though they may be considered remote in frequency. This type of coupling can, in fact, occur for the above-mentioned high-frequency breathing tank and low-frequency liquid surface modes. Both linear and nonlinear coupling of liquid and elastic tank motion will be discussed in this chapter.

Finally, the interaction of the elastic structure, fluid systems, and the control system must be considered. Vehicle flexing and propellant

sloshing have become critical factors in the overall stability of large space vehicles, especially since the fundamental lateral bending frequency of vehicles with large-diameter propellant containers is very low, and often near the propellant and control frequencies. As in chapter 7, stability boundaries shall be presented which exhibit the influence of the various propellant parameters, such as sloshing mass, propellant frequency, container location, gain values of the control system, gyro location, and phase-lag coefficients, as well as the influence of elastic parameters, such as bending frequency, generalized bending mass, and structural damping.

## 9.2 COUPLING OF PROPELLANT MOTIONS WITH ELASTIC TANK BENDING VIBRATIONS

### General Discussion

The significant bending modes of large rockets and space vehicles usually occur at relatively low frequencies (i.e., less than 5 cps). As has already been pointed out, the most important liquid surface modes in cylindrical tanks of typical geometries also occur at low frequencies; therefore, mutual interaction between the two motions might be anticipated. Nevertheless, comparatively few investigations have been attempted in this area of the overall coupled problem, and virtually all of the work is restricted to cylindrical tanks.

Bauer has analyzed the behavior of an incompressible, ideal liquid of arbitrary depth in a circular cylindrical tank (refs. 9.1 and 9.2) and in a sectorized cylindrical tank (ref. 9.3) that is subjected to a specified bending oscillation. In other words, attention is focused on the liquid behavior in a container whose walls are forced to oscillate with a prescribed bending shape. Bauer's analysis is one step beyond that of the study of liquid behavior due to translation or pitching in a rigid tank; however, it does not allow for complete elastic coupling with the tank walls. In effect, this work is a study of the influence of forced tank bending on the liquid behavior, with no allowance for complete interaction between liquid and tank bending

motion. (The results of these analyses are included in ch. 2.)

More general analyses of the complete coupled bending-liquid sloshing problem have been given by Rabinovich (ref. 9.4) and Miles (ref. 9.5). Both assume the existence of potential flow, so that a velocity potential may be determined in the bending cylindrical tank. Rabinovich uses an integro-differential approach to the partially filled tank problem. The liquid potential function is derived using a Lagrange-Cauchy integral, from which expressions for the hydrodynamic and hydrostatic forces acting on the tank walls are obtained. These expressions are then introduced into the differential equations for the oscillations of a thin-walled elastic bar. Characteristic frequencies of the resulting integro-differential equation can then be solved by Galerkin's method. No numerical examples or results are given for this analysis.

Miles' analysis (ref. 9.5) of the coupled problem involves the use of the Lagrangian procedure for potential sloshing in a bending cylindrical tank, and includes numerical examples and results which fairly readily can be applied to a tank of given boundary conditions. Since this work appears to be the most readily applicable for a given specific tank, it will be summarized in this chapter in some detail. In addition, experiments (ref. 9.6) that have been correlated with this analysis will also be described.

### Lagrangian Analysis

In Miles' analysis (ref. 9.5) of the coupled liquid-bending tank system, the equations of motion for the circular cylindrical tank are determined by a Lagrangian formulation, taking the kinetic energy in the form  $T = \frac{1}{2} \sum_i \sum_j m_{ij} q_i \dot{q}_j$  and the potential energy as  $V = \frac{1}{2} \sum_i \sum_j k_{ij} q_i q_j$ , where the  $q_i$  are generalized coordinates corresponding to translation, rotation, bending, and sloshing motion of the coupled system. For the purposes of this discussion, only bending motions of the tank will be discussed, so that the coordinates that are of concern are shown in figure 9.1. In effect,  $f(z)$  is the mode shape

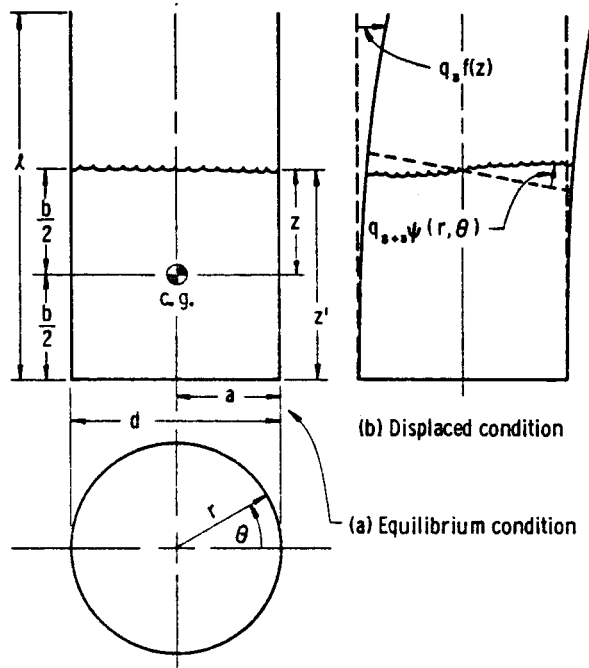


FIGURE 9.1.—Coordinate system for bending tank containing a liquid.

of the bending wall, and  $\psi(r, \theta)$  is the shape of the liquid free surface in some mode. Details of the derivation of the kinetic and potential energy coefficients,  $m_{ij}$  and  $k_{ij}$ , may be obtained directly from reference 9.5; but, in essence, they are determined by assuming the existence of potential fluid flow, and simple inextensional beamlike bending of the cylindrical tank walls, and solving the appropriate potential equation consistent with the boundary conditions of the partially full bending tank. The resulting coefficients appropriate for coupled bending oscillations are summarized in the appendix to this chapter, and examples for a cantilever tank are given.

Having determined the kinetic and potential energy expressions, these are then substituted into Lagrange's equations so that, for bending and liquid free surface motion only, the following equations are obtained:

$$(\bar{m}_e + \bar{m}_{3,3})\ddot{q}_3 + \sum_1^{\infty} \bar{m}_{3,s+3}\ddot{q}_{s+3} + (\bar{m}_e \omega_e^2 + \bar{k}_{3,3})q_3 + \sum_1^{\infty} \bar{k}_{3,s+3}q_{s+3} = 0 \quad (9.1a)$$

$$\begin{aligned} & \bar{m}_{3,s+3}\ddot{q}_3 + \bar{m}_{s+3,s+3}\ddot{q}_{s+3} + \bar{k}_{3,s+3}q_3 \\ & + \bar{k}_{s+3,s+3}q_{s+3} = 0 \quad s=1, 2, 3, \dots \end{aligned} \quad (9.1b)$$

The frequency equation obtained from equations (9.1), by assuming periodic motion, is

$$\omega^2 - \omega_e^2 - \sum_{s=1}^{\infty} \alpha_{3s} \frac{(\omega^2 - \Omega_{3s})^2}{\omega^2 - \omega_{s+3}^2} = 0 \quad (9.2)$$

The subscripts 3 and  $s+3$  correspond to the generalized displacements,  $q_s(t)f(z)$  denoting bending displacement and  $q_{s+3}(t)\psi(r, \theta)$  denoting displacement in the  $s$ th sloshing mode of the liquid free surface from a plane normal to the generator of the cylinder. (See fig. 9.1.) In equations (9.1) and (9.2), the following notation is used:

$$\omega_3 = \sqrt{\frac{\bar{m}_e \omega_e^2 + \bar{k}_{3,3}}{\bar{m}_e + \bar{m}_{3,3}}} \quad \text{uncoupled bending frequency}$$

$$\omega_{s+3} = \sqrt{\frac{\bar{k}_{s+3,s+3}}{\bar{m}_{s+3,s+3}}} \quad \text{uncoupled sloshing frequencies}$$

$$\Omega_{3s} = \frac{\bar{k}_{3,s+3}}{\bar{m}_{3,s+3}} \quad \text{coupling coefficients}$$

$$\alpha_{3s} = \frac{\bar{m}_{3,s+3}^2}{\bar{m}_{s+3,s+3}(\bar{m}_e + \bar{m}_{3,3})}$$

$\bar{m}_e$  and  $\omega_e$  are the effective empty tank mass and resonant bending frequency, respectively. The bars over the coefficients indicate normalization by the total liquid mass.

The frequency equation, equation (9.2), has an infinite number of roots  $\omega = \omega_n$ , the coupled tank bending, liquid sloshing frequencies. As has been mentioned, for an actual vehicle the lowest coupled bending frequencies (i.e.,  $\omega_1$  and  $\omega_2$ , corresponding to the first two roots of equation (9.2)) occur in the neighborhood of some of the uncoupled sloshing modes  $\omega_{s+3}$ , which display significant response amplitudes. As a result, in a specific case, equation (9.2) must be solved, using some judgment as to what terms of the series may be neglected as insignificant, and at best only numerical solutions to the resulting equation can be obtained.

In general, it may be anticipated that a coupled frequency (root of equation (9.2)) will occur for each uncoupled bending and liquid sloshing mode included, and the coupled frequencies will be different from those of the corresponding uncoupled modes. Further discussion of this equation will be deferred momentarily.

An approximate solution to equation (9.2) has been investigated in reference 9.6, for the case of small, thin circular cylindrical shells, both with simply supported and cantilever boundary conditions. For the case of the small uniform cylindrical shell, the liquid frequencies are still comparatively low, while the coupled bending frequency is high; therefore, a considerably simplified expression for equation (9.2) may be obtained. Having  $\omega_{s+3}$  and  $\Omega_{3s}$  small compared to  $\omega$ , they may be neglected, and equation (9.2) reduces to

$$\omega^2 = \omega_e^2 \left[ 1 - \sum_{s=1}^{\infty} \alpha_{3s} \right]^{-1} \quad (9.3)$$

For this case, the difference between the coupled and uncoupled bending frequencies is thus determined by the coefficient  $\alpha_{3s}$ . The uncoupled inertia coefficients,  $\bar{m}_{3,3}$ ,  $\bar{m}_{s+3,s+3}$ , and  $\bar{m}_e$  are always positive. The inertia coupling coefficient  $\bar{m}_{3,s+3}$  may be either positive, negative, or zero, depending upon the ratio  $b/a$ . When  $m_{3,s+3}=0$ , it follows that  $\alpha_{3s}=0$ , causing a sharp minimum in coupling for certain tank configurations (the coupling need not actually become zero because of the summation over  $s$  and the presence of the small potential coupling  $\bar{k}_{3,s+3}$ ). This minimum in coupling is particularly noted in the results for the cantilever tank near  $b/a=2$ . This situation is analogous to the inertially coupled bending and torsional vibrations of a beam, in which case the uncoupling occurs when the shear center of the beam coincides with the centroid. For  $\bar{m}_{3,s+3} \neq 0$ , the factor  $[1 - \sum \alpha_{3s}]^{-1}$  is always greater than unity, thus yielding an increase in the coupled bending frequency due to the liquid sloshing.

Equation (9.3) is solved for the particular cases of a cantilever and pin-ended tank for the liquid at varying partial depths  $b/l$ . Figures 9.2 and 9.3 show the results for these two types

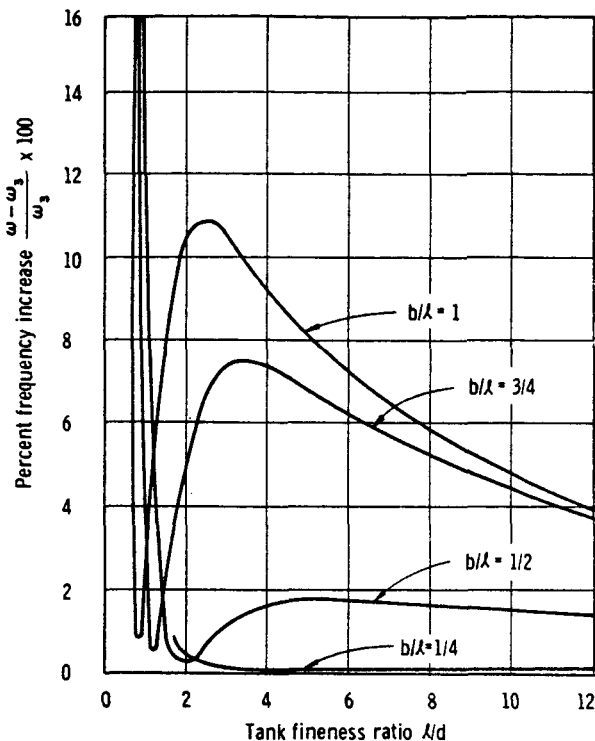


FIGURE 9.2.—Theoretical percent increase in resonant bending frequency due to free surface effects in cantilever tanks (ref. 9.6).

of tanks, plotted as the percent increase in bending frequency due to coupling ( $\omega - \omega_3$ )  $\omega_3 \times 100$  versus tank fineness ratio  $\lambda/d$  for varying partial depths  $b/l$ . These curves may be appreciably affected by the assumed bending mode shape, which in these analyses involved a parabolic mode shape for the cantilever tank and sinusoidal for the pin-ended tank.

We now return to the discussion of equation (9.2), the more exact frequency equation. The curves of figures 9.2 and 9.3 are for the special case of a uniform shell where  $\omega_3 \gg \omega_{s+3}$ . In order to determine the effect of coupling on the resonant frequencies of the system when  $\omega_3$  and  $\omega_{s+3}$  are of the same order of magnitude, the exact frequency equation, equation (9.2), was solved for a cantilever tank with a tip mass added in order to lower the bending resonance. Analytically, this involved only a slight modification of the empty tank inertia coefficient,  $\bar{m}_e$ , but required considerably more effort in solving for the eigenvalues of the frequency determinant

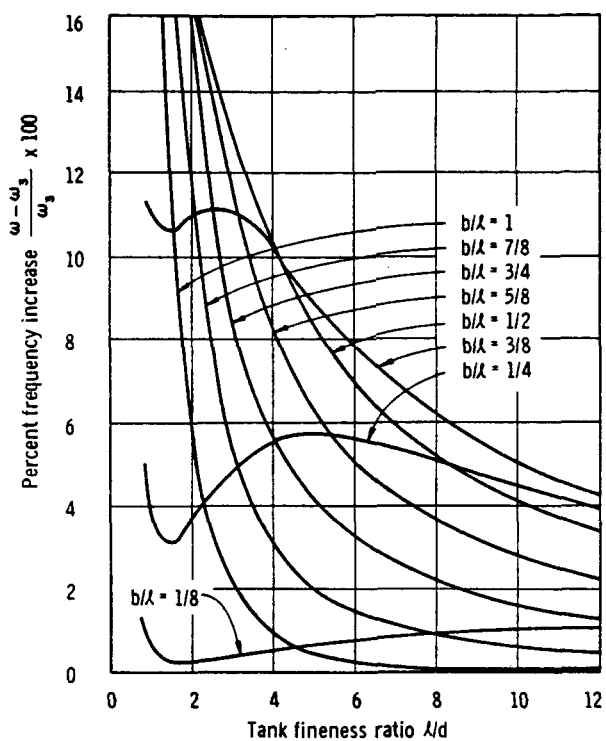


FIGURE 9.3.—Theoretical percent increase in resonant bending frequency due to free surface effects in simply supported tanks (ref. 9.6).

of the set of equations (9.1a) and (9.1b). In the analysis, six modes (one bending and five sloshing) were used.

The results of this analysis showed that the addition of mass to the vibrating system, although lowering the resonant bending frequency, also reduced the effect of the sloshing mass on the response of the entire system. For the cantilever tank, the addition of a tip mass of 10 times the empty tank mass reduced the maximum frequency increase of approximately 11 percent, as shown in figure 9.2, to less than 1.5 percent. Further increases in tip mass reduce the influence of the free surface on resonant bending frequency still further. It would appear, therefore, that consideration of the free surface boundary condition will only be significant in those cases where the sloshing mass is an appreciable portion of the total vibrating mass, as in the bending of relatively low fineness ratio, uniform shells. For large missile structures where the total bending mass

is large, the liquid-sloshing mass can probably be neglected in the calculation of overall bending resonant frequencies without significant error. The solution for all six roots of the coupled frequency equations also showed that the coupled sloshing frequencies did not change appreciably from their uncoupled values. Thus, rigid-tank-sloshing frequencies appear to be adequate for use in analyzing the bending tank in a space vehicle.

#### Experimental Verification of Lagrangian Analysis

In order to correlate with the results predicted by the simplified frequency equation, as given in the preceding section, experiments were conducted by Lindholm et al. (ref. 9.6) in which the coupling effect on the bending frequency was measured for thin cylindrical shells with cantilever and simply supported ends. Bending frequencies of several shells containing water at various depths were measured, both

with a free liquid surface and a capped liquid surface.

Data were obtained for two cantilever tanks having  $l/d$  (length to diameter) ratios of 2.76 and 5.03. Figure 9.4 shows the experimental and theoretical capped liquid surface (uncoupled) bending frequencies for the tanks as a function of the fractional depth of the liquid. The influence of the mode shape on the theoretical curves is readily apparent by the difference in the two curves representing a linear mode shape and parabolic mode shape. It can be seen that the actual data fell somewhere in between for both tanks tested. This is readily explained from the fact that the actual mode shapes, which were obtained by measurements on both tanks, also fell between a linear and parabolic shape.

The difference in capped and uncapped resonant frequencies for the same two cantilever tanks is plotted in figure 9.5 as the percentage frequency increase against fractional depth. Here again, the data fell between that for the two assumed mode shapes. It is obvious that

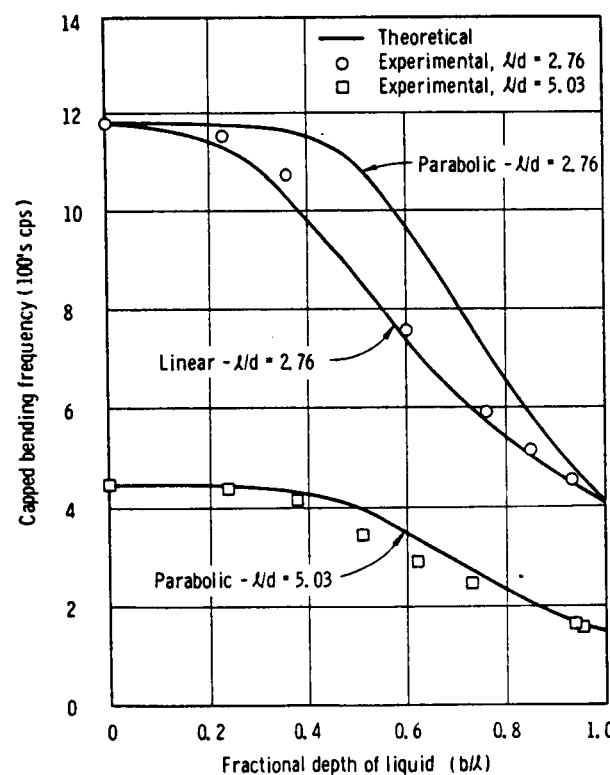


FIGURE 9.4.—Theoretical and experimental capped resonant bending frequency variation with liquid depth for cantilever tanks (ref. 9.6).

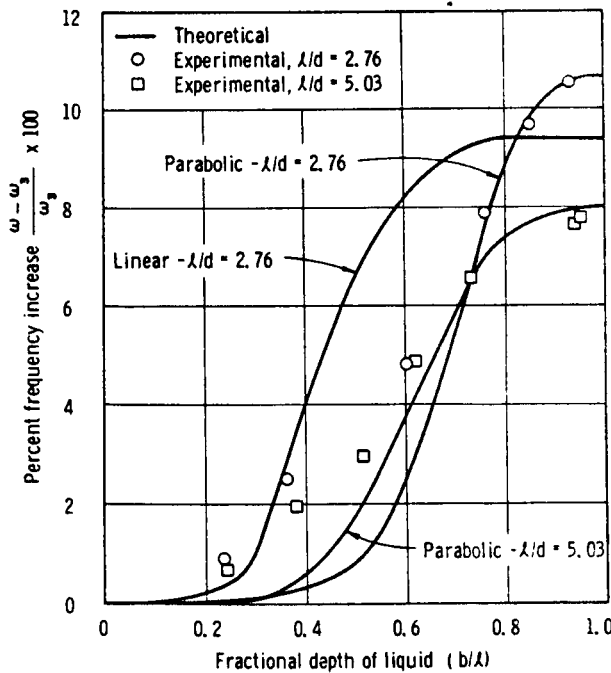


FIGURE 9.5.—Theoretical and experimental percent increase in resonant bending frequency versus liquid depth in cantilever tanks (ref. 9.6).

the extreme sensitivity of the theory to mode shape requires the substitution of the actual mode shape into the theory in order to get the best possible prediction of coupled frequency and percent frequency change.

Similar experiments were also performed on circular cylindrical, simply supported tanks, the results of which are shown in figures 9.6 and 9.7. It can be seen that the agreement between theory and experiment was not as good as with the cantilever tanks. The deviation was explained as probably resulting from a lack of proper satisfaction of the boundary condition at the tank bottom, and a considerable distortion in mode shape which occurs at partially full liquid depths. The theoretical curves were based on a half-sine wave, but measurements indicated that this shape approximated the actual shape only for a completely full or empty tank.

In general, it was concluded that for the cases studied, Miles' theory appeared to give an adequate prediction of the influence of the liquid motion on the elastic bending frequency, but its use is complicated because of the strong

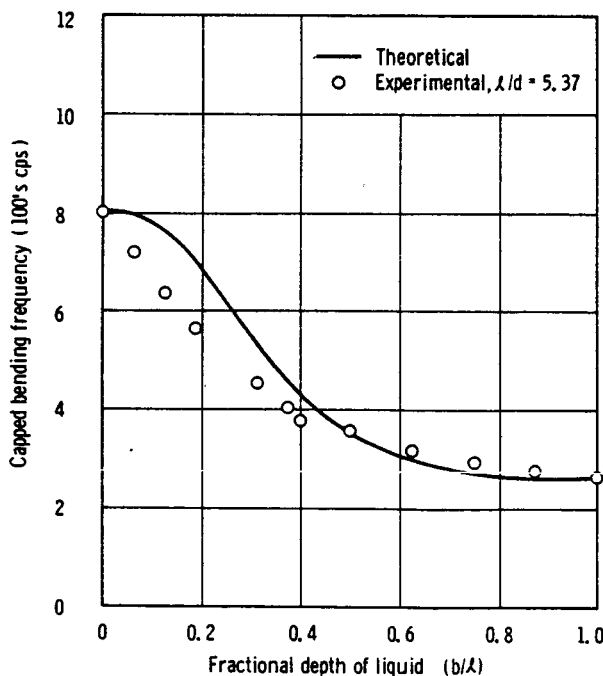


FIGURE 9.6.—Theoretical and experimental capped resonant bending frequency variation with liquid depth for simply supported tanks (ref. 9.6).

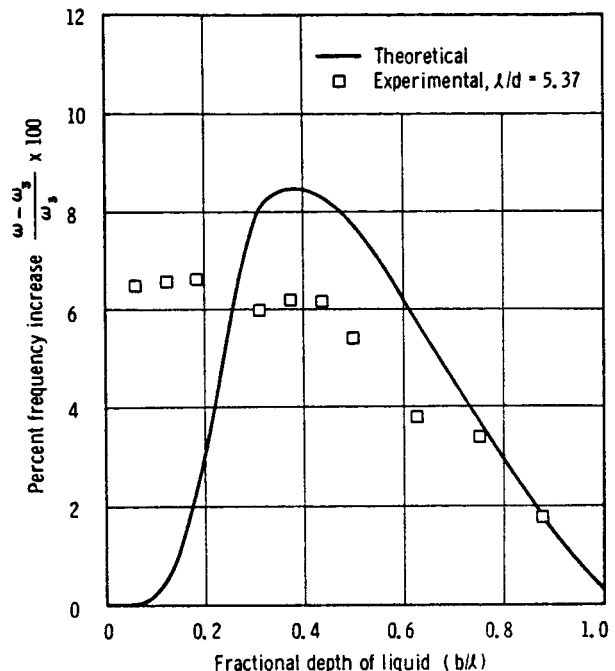


FIGURE 9.7.—Theoretical and experimental percent increase in resonant bending frequency versus liquid depth in simply supported tanks (ref. 9.6).

dependence on actual mode shape, thereby indicating the necessity for a numerical formulation of a specific problem.

### 9.3 COUPLING OF PROPELLANT MOTIONS WITH ELASTIC TANK BREATHING VIBRATIONS

#### General Discussion

Vibrations of vehicle tanks in which the wall motions are predominantly radial, such that both flexure and stretching of the wall occurs while the longitudinal axis of the tank remains straight, are often referred to as breathing vibrations. For the purposes of this chapter, the term "breathing vibrations" will include shell modes that display both circumferential and axial wave patterns for rotationally symmetric tanks, with the axially symmetric circumferential modes being included as one case. It is recognized that this type of vibration can be very important in shell-like structures where the walls are thin compared to other dimensions. Although most space ve-

hicle tanks are not simple shells, since they usually have internal stiffeners or other structural components of various designs, it is highly desirable to attempt to predict their breathing vibrational behavior on the basis of simple shell theory as an approximation to the actual tanks, since analytical predictions are otherwise virtually impossible. Of course, the accuracy of the predicted behavior depends on how well the actual tank conforms to such a representation.

The purpose of this section is to discuss breathing vibrations of thin shells, as they apply to rocket vehicle tanks, and to consider the influence of the liquid propellant and pressurization on this type of vibration of the tank wall. Virtually all of the work in this area to date has been concentrated on the circular cylindrical tank, obviously because of its wide use in the main stages of current vehicles; therefore, the present emphasis will also be on that geometry, although it must be admitted that breathing vibrations in shells of other geometry can be equally as important. The intent here is to give, first, a rather general discussion of shell vibration, and to describe in some detail the behavior of empty circular cylindrical shells to have some measure of understanding of this type of vibration in purely shell-like structures. Then the variations in this behavior caused by internal pressurization and the presence of fluids will be considered.

#### Breathing Vibrations of Empty Shells

A review of the work done to date on the vibration of empty shells of various geometries, including a general discussion of assumptions often used in simplifying the analysis of the problem, together with an extensive reference list, has been presented by Hu (ref. 9.7). Only a few comments from this review will be repeated here to introduce our discussion of empty shell vibrations, and the results of only a few of the more fundamental analyses will be mentioned. It is pointed out that, because of the complexity of the problem, the analytical as well as the experimental results accumulated in the technical literature do not present an entirely clear picture of shell vibrations, even

for the simplest shell geometries. The main difficulty lies not in the formulation of a set of equations describing the shell vibrations, but rather in the simplification and solution of these equations. As a result, various approximate theories are introduced to solve certain classes of shell vibration problems.

Rayleigh's theory of inextensional vibrations assumes that for the fundamental modes, the middle surface (an imaginary surface situated at midthickness of the shell wall) of a vibrating shell remains unstretched. The displacement functions of the middle surface can be determined with this condition, and the fundamental frequencies are then found from the potential and kinetic energies corresponding to these displacements. On the other hand, Rayleigh's theory of extensional vibrations, which would be more appropriate for certain modes, assumes that the shell deformation consists mainly of stretching in the middle surface.

Considering the strain energy that is periodically stored in the shell wall during vibration, the two approximate theories appear to be on opposite extremes. In the theory of inextensional vibrations, the strain energy is assumed to be associated with bending stresses only, and no membrane stresses exist, since the displacements are determined by the inextension condition. But, when membrane theory is used to study extensional vibrations of a shell, the strain energy is assumed to be solely associated with membrane stresses and that associated with bending is neglected. These two approximations do not contradict each other, but are complementary for the purpose of determining various vibrational modes. The tendency is to classify shell modes into these two distinct groups.

In addition to the above two general approximate theories, there are other approaches proposed for certain specific shell configurations. The Donnell equations for circular cylindrical shells and the Reissner equations for shallow shells are examples (a shallow shell is one in which the ratio of rise to span is much less than 1, say one-eighth). In these theories, the governing differential equations are simplified by neglecting what are considered to be the

unimportant terms, based on geometric arguments for the specific case or on an order of magnitude analysis. The accuracy of the results obtained from any of the approximate theories depends entirely on how well the basic assumptions are satisfied in a given case. In addition, it must be pointed out that virtually all of the existing theories predict the *free natural* vibrational modes of a shell; therefore, how well these conform to those encountered for *forced* vibration again depends on the specific case investigated.

Numerous investigations of circular cylindrical shell vibration have been conducted, one of the most significant being that of Arnold and Warburton (ref. 9.8). In this work, the emphasis is on vibration of shells with freely supported ends (simply supported ends), whereby the ends of the cylinder are held circular but are not held by restraining moments. Under these conditions, the mode shapes of vibration assume patterns like those illustrated in figure 9.8. For such vibrational forms, a given mode is completely specified by two integer parameters:  $n$ , the number of circumferential stationary waves, and  $m$ , the number of axial stationary half waves. Although not shown in the figure, it is understood that the  $n=0, m$  arbitrary (axially symmetric circumferential pattern) modes are included in the present consideration, while  $n=1$  is not, since it corresponds to a bending motion, already discussed in the previous section of this chapter. Theoretically, an infinite number of such modes is possible in a given shell. It is recognized that in a space vehicle tank, simply supported end conditions may not be exactly duplicated, and the effects of varying end conditions will be discussed later.

Considering vibration in the above modes, neither Rayleigh's inextensional nor extensional assumptions are correct over a wide range of the integers  $m$  and  $n$ , and, therefore, those approximations cannot be used in this case. For modes of vibration in which both circumferential and axial modes exist, both bending and stretching of the shell wall must be considered. Under these conditions, a method of deriving a frequency equation given in reference 9.8 can be summarized as follows: First, obtain

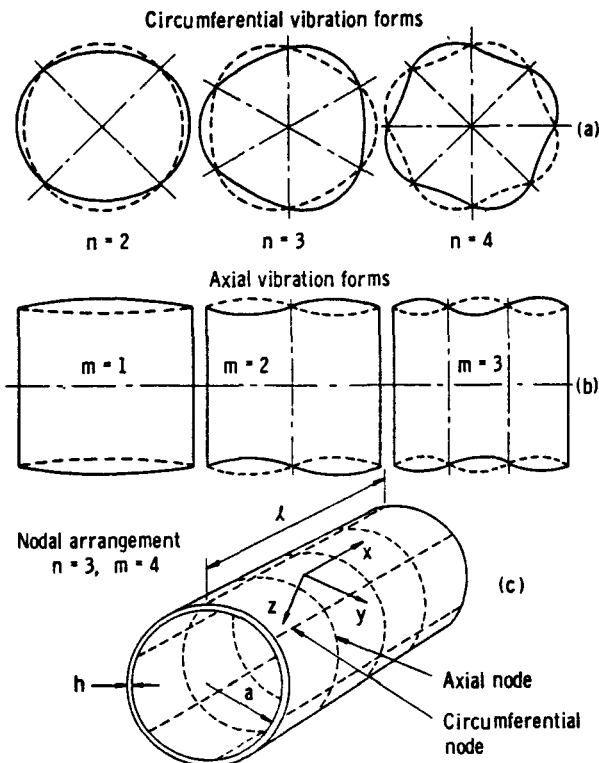


FIGURE 9.8.—Forms of vibration of thin cylinders with freely supported ends (ref. 9.8).

equations relating the three component displacements  $u$ ,  $v$ , and  $w$  in the directions  $x$ ,  $y$ ,  $z$  (fig. 9.8), of a point in the middle surface of the shell. In the present case, this is most readily accomplished by assuming a vibration form compatible with the end conditions; i.e.

$$\begin{aligned} u &= A \cos \frac{m\pi x}{l} \cos n\theta \cos \omega t \\ v &= B \sin \frac{m\pi x}{l} \sin n\theta \cos \omega t \\ w &= C \sin \frac{m\pi x}{l} \cos n\theta \cos \omega t \end{aligned} \quad (9.4)$$

where  $\theta$  defines the angular position in a cross section;  $n$  and  $m/2$  are, respectively, the number of circumferential and axial wavelengths; and  $A$ ,  $B$ , and  $C$  are constants. Then, using these forms, the strain energy is expressed in terms of the displacements and the kinetic energy in terms of the time rate of change of the displacements. Further, both strain energy and kinetic energy are functions of the three dis-

placement variables  $u$ ,  $v$ , and  $w$ , and the Lagrange equations are utilized to form three equations relating the displacements. A frequency equation is then formulated from these three displacement equations.

Some results obtained from the method described above are shown in figure 9.9, in which frequency is given in the nondimensional form

$$\sqrt{\Delta} = f_{mn} \sqrt{\frac{4\pi^2 a^2 \rho_s (1 - \nu^2)}{Eg}}$$

where  $f_{mn}$  is the natural frequency of the  $m$ ,  $n$ th mode. In the axial wave length factor  $\lambda_m$ , the  $l$  is the shell length, and  $\alpha$  is the ratio of shell thickness  $h$  to mean radius  $a$ . It might be pointed out that these results represent only one of three natural frequencies that exist for each nodal pattern, all of which can be obtained from the above theory. However, these are the lowest of the three frequencies, and are therefore considered the most significant. From figure 9.9, progressing from figures 9.9(a) to 9.9(d),

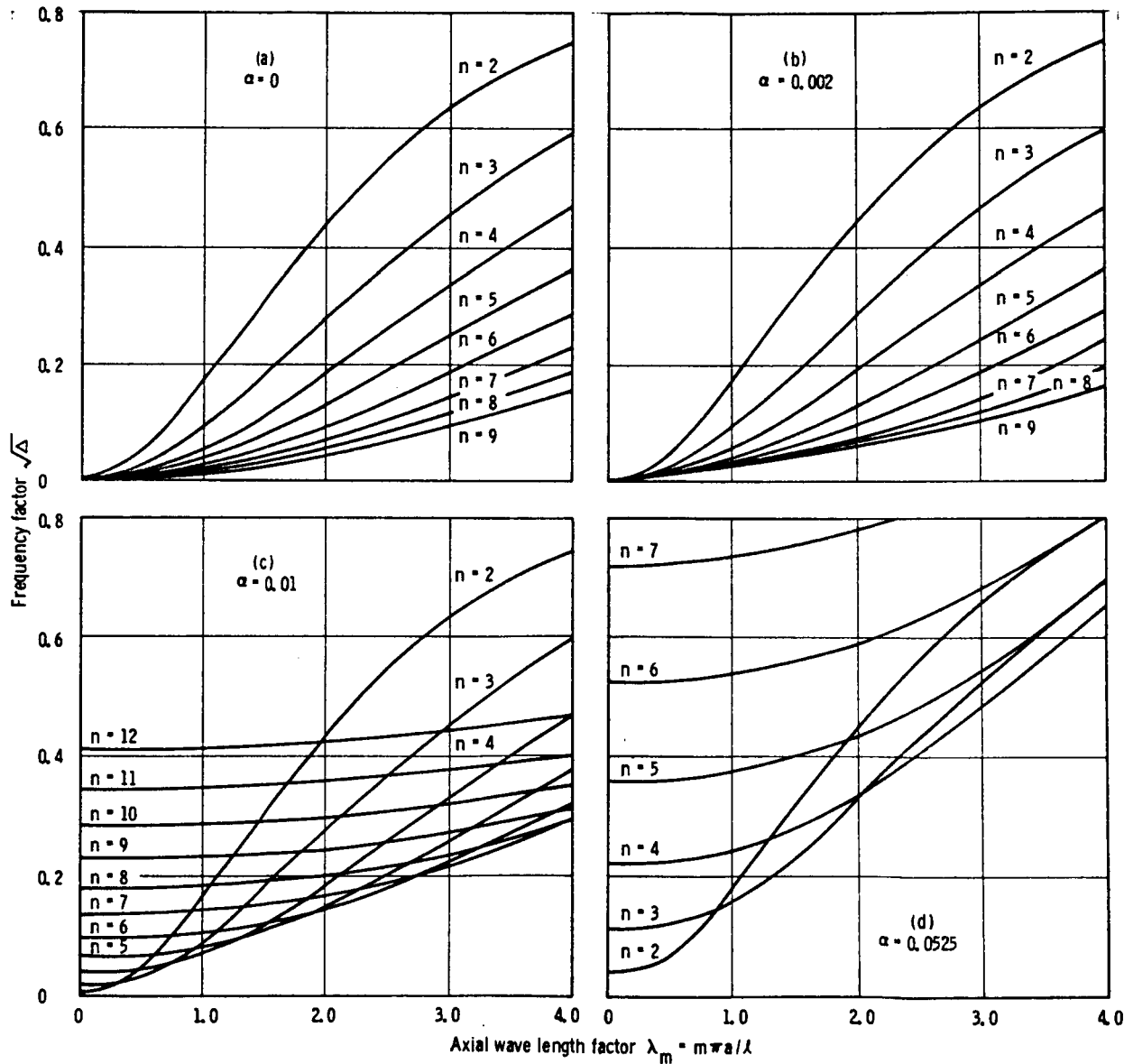


FIGURE 9.9.—Theoretical frequency curves for cylinders with freely supported ends (ref. 9.8).

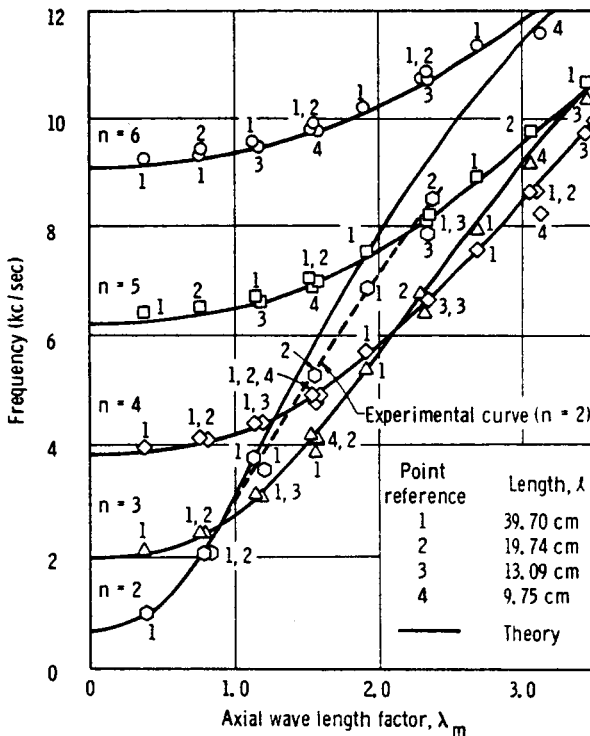


FIGURE 9.10.—Natural frequencies of empty cylinders (ref. 9.8).

the effect of wall thickness on the frequency is readily apparent. An experimental correlation with figure 9.9(d), also taken from reference 9.8, is shown in figure 9.10, where the agreement is seen to be very good.

Figure 9.11, obtained by Lindholm et al. (ref. 9.9), is given for comparison with the above work of Arnold and Warburton. The theoretical curves in this plot also are for freely supported circular cylinders, but are based on the shallow shell theory of Reissner. Here the ordinate scale is plotted to a slightly different nondimensional frequency parameter. The nondimensional form of all the above results lends itself well to use in design approximations.

A very interesting observation can be made from figures 9.9 through 9.11. That is, for a given tank and  $m$ -pattern (fixed  $\lambda_m$ ), the lowest natural frequency does not necessarily have the simplest circumferential pattern. Arnold and Warburton (ref. 9.8) have shown that this behavior results from the partitioning of strain energy between bending energy and stretching

energy in the vibrating shell. This is shown qualitatively in figure 9.12 where a strain energy factor as a function of circumferential wave pattern is shown at a constant value of  $\lambda_m = 3.81$ , and  $\alpha = 0.01$ . Note that this curve corresponds to the frequencies of a vertical cross-plot of figure 9.9c at a constant value of  $\lambda_m = 3.81$ . It is now apparent that Rayleigh's purely extensional vibration theory is a good approximation only for small values of  $n$  (depending on the value of  $\lambda_m$ ), the inextensional theory is good only for larger values of  $n$ , and neither is accurate over intermediate values of  $n$ . Fung et al. (ref. 9.10) have shown that in the empty cylindrical shell the minimum frequency is approximately given by

$$\rho_s \frac{\omega^2 a^2}{E} \approx \left( \frac{h}{a} \right) \left[ \lambda_m^2 / \sqrt{3(1-\nu^2)} \right]$$

and has a nodal pattern of the nearest integer to

$$n' \approx \sqrt{2\lambda_m} \left( \frac{a}{h} \right)^{1/4}$$

As long as

$$\lambda_m \ll \sqrt{a/h}$$

Considering that in space vehicles (particularly in the first stages where cylindrical tanks are used) the tank walls are usually integral with the shell of the entire structure, the assumption of freely supported ends may not be a good approximation to the actual tank end conditions. An approximate method of estimating the effects of restraining moments applied at the ends has been presented by Arnold and Warburton (ref. 9.11). The increase in frequency for a given mode as a result of fixing the ends perfectly can be estimated by applying an appropriate correction factor to the results presented in figures 9.9 through 9.11, and then an estimate of the actual increase can be made by selecting some intermediate frequency. This procedure is illustrated in figure 9.13.

Having selected the curve for a particular mode from figures 9.9 through 9.11, say an  $m=3$  and  $n=\text{arbitrary}$  curve, it would appear as shown in figure 9.13, and would represent an axial mode pattern as shown in figure 9.13(a).

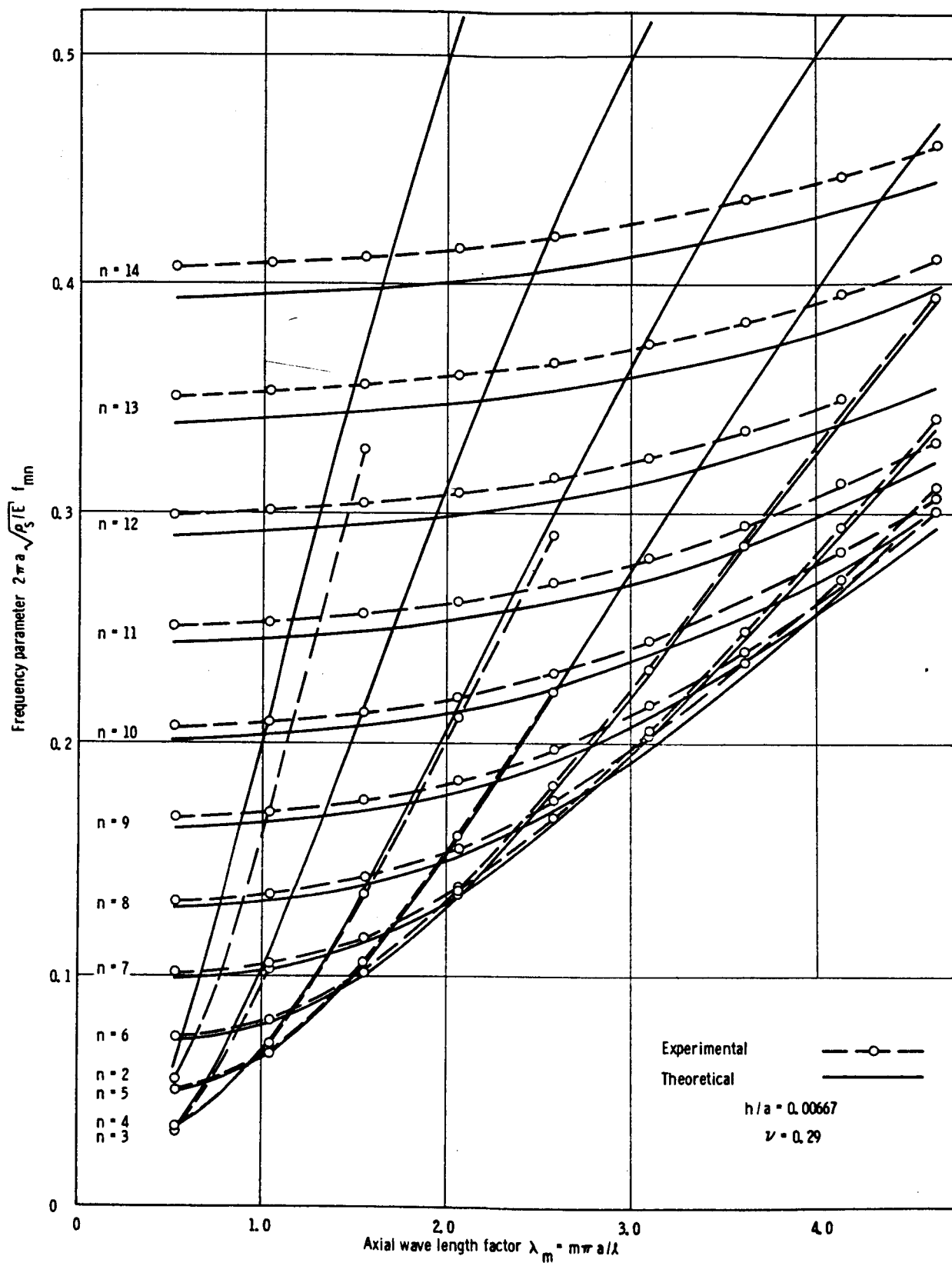


FIGURE 9.11.—Theoretical and experimental natural frequencies of empty cylinders (ref. 9.9).

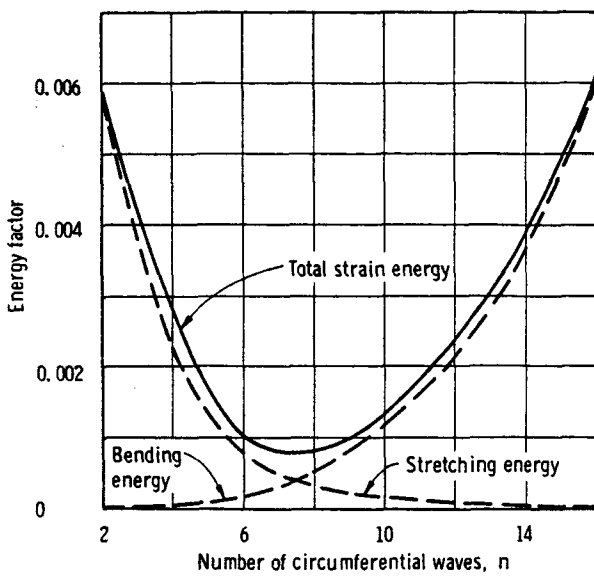


FIGURE 9.12.—Strain energy due to bending and stretching (ref. 9.8).

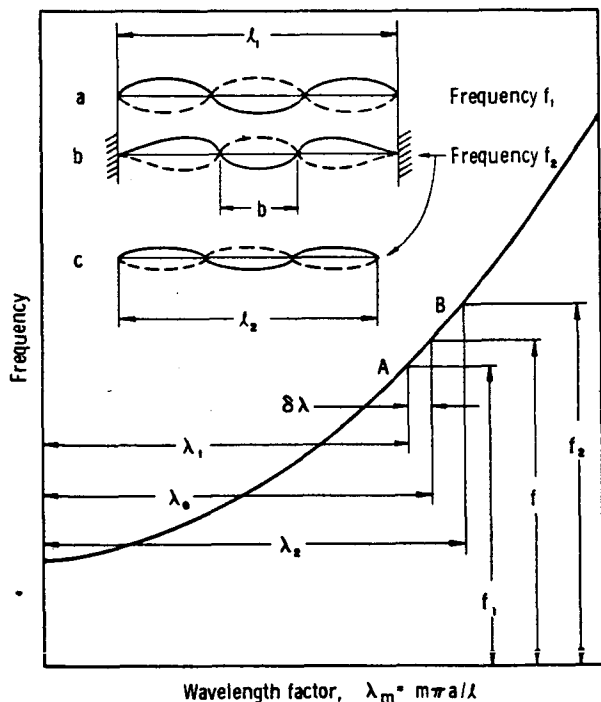


FIGURE 9.13.—Effects of end conditions on breathing frequencies of empty shells (ref. 9.11).

For a given tank with *freely* supported ends, corresponding to a given  $\lambda_1$ , one would obtain a given frequency  $f_1$  at  $\lambda_1$ . However, for a tank of the same geometry but with perfectly *fixed* ends, the mode pattern would appear

as in figure 9.13(b). The frequency  $f_2$  for this condition may be obtained from the curve at an equivalent wavelength factor given by

$$\lambda_2 = (m + c_e) \frac{\pi a}{l}$$

where  $c_e \approx 0.3$ . The frequency  $f_2$  is then an estimated upper limit, and the actual frequency would fall somewhere between  $f_1$  and  $f_2$ . Details of this approximation are given in reference 9.11.

#### Breathing Vibrations of Shells Containing Fluids

Having described in some detail the general aspects of breathing vibrations of empty circular cylindrical shells, we now turn to the effects of including multiple, immiscible, heavy and light fluids inside the shell. For the present case of space vehicle applications, we consider a cylindrical shell partially filled with a heavy fluid (liquid) to some arbitrary depth, such that the liquid has a free surface, and is topped by a light fluid (gas) at some arbitrary pressure. Among various properties that can be significant in the problem at hand, both fluids possess relatively small viscosity, and both possess finite compressibility and density, although these properties are drastically different for the liquid and the gas. During different parts of the flight, the relative amount of liquid and gas inside the tank changes as fuel is expended. In view of this rather brief statement of the problem, this section is devoted to a general discussion of the influence that the multiple fluid column exerts on the vibrating tank, and the methods of analyzing that influence.

Considering the typical fluids, pressures, and geometries used in current vehicle tanks, it appears that a number of the known effects of the internal fluid column on the breathing vibrations of the tank can be summarized in terms of several basic categories, most of which depend on the relative heights of the liquid and gas in the multiple fluid column. These categories are:

- (1) The viscosity of typical rocket propellants is small; therefore, inviscid flow theory is usually used in analyses of the problem.

(2) Internal static pressurization causes a stiffening effect in the shell; it adds potential energy to the system.

(3) The multiple-fluid column possesses both compressibility and inertia; therefore, it can sustain pressure modes of oscillation at various frequencies, even in a rigid tank. In the flexible tank, this adds additional degrees of freedom, and linear coupling of these modes with the breathing modes of the tank is expected. Further, the possibility of the existence of high pressures at some point in the tank, due to a resonance in such a pressure mode, can be very important in itself. Thus, the system can sustain coupled pressure modes as well as coupled wall breathing modes.

(4) The inertia of the fluid column causes a hydrodynamic loading on the shell wall which, in effect, results in a nonuniformly distributed apparent mass being added to the wall, so that the inertia of the breathing tank is considerably increased. This effect results predominantly from the liquid part of the fluid column, because of its greater density.

(5) The liquid free surface phenomena add additional degrees of freedom to the breathing fluid-tank system, so that linear coupling of this motion must be considered.

(6) It has been found that, under certain conditions, the free surface motion can cause the tank breathing vibration to become strongly nonlinear, giving rise to various nonlinear coupling effects.

The above listing of the influence of the fluid on the breathing tank is given more or less in the order of increasing complexity of analysis. Two basic methods of approach have been used to analyze the fluid behavior—compressible flow theory, and incompressible flow theory, but neither alone is capable of predicting all effects. The behavior is spread over a wide frequency range and, by and large, each analysis is restricted to some part of this frequency range.

Inviscid compressible fluid theory, along with some set of shell equations, has been used to investigate effects mentioned in paragraphs (2), (3), and (4) above. The wave equation is used as the governing differential equation for the fluid, and the interaction with the tank wall is specified by equating the normal accelerations

of the fluid and the shell at the shell wall, along with equating the fluid pressure and hydrodynamic loading at the same point. This type of analysis is particularly useful for determining the coupling effects of pressure modes in the fluid column, and can be used to predict the hydrodynamic inertia effects of both the liquid and the gas, but is not normally used to predict liquid free surface effects.

Inviscid incompressible fluid theory, along with some set of shell equations, has been used to predict effects indicated in paragraphs (4) and (5), and even those of paragraph (3). That is, this type of analysis is useful for predicting liquid apparent mass, and free surface effects, and can further be used to predict coupled axisymmetric, longitudinal pressure modes, for it is found that these modes coincide with the corresponding axisymmetric ( $n=0$ ) shell breathing modes, for the case of a relatively incompressible fluid in a flexible tank. A number of the available analyses consider only the hydrodynamic loading effects of the liquid, neglecting the free surface effects, while some consider both. The degree to which free surface effects are neglected, in the former case, varies in the different studies that have been performed. All of the analyses assume potential flow so that Laplace's equation is assumed to be the governing differential equation for the liquid; the boundary conditions at the shell wall require that the liquid normal acceleration be equal to that of the tank and that the liquid pressure equal the hydrodynamic loading of the tank wall in all cases, but different solutions result from the imposition of different boundary conditions at the liquid free surface.

It has been pointed out in chapter 2 that the basic linearized free surface conditions for free surface oscillations are the following: At the free surface we must have

$$\frac{\partial \Phi}{\partial t} = g\xi \quad (9.5)$$

and

$$\frac{\partial \xi}{\partial t} = -\frac{\partial \Phi}{\partial Z} \quad (9.6)$$

where  $\xi$  is the elevation of the free surface above the undisturbed surface level, and is a

function  $\zeta = \zeta(r, \theta)$  in cylindrical coordinates, and  $\Phi$  is the velocity potential. Equation (9.5), called the dynamic condition, requires that the dynamic pressure at the free surface be constant (i.e., the ullage pressure), while equation (9.6), called the kinematic condition, requires that no fluid mass cross the free surface boundary. It has further been pointed out that both conditions can be combined to give

$$\frac{\partial^2 \Phi}{\partial t^2} + g \frac{\partial \Phi}{\partial Z} = 0 \quad (9.7)$$

on the free surface. Just how these conditions are imposed at the free surface is what determines whether the free surface coupling is included in these analyses using incompressible flow theory.

Nonlinear coupling of free surface motions and tank breathing vibrations has been investigated experimentally, and analytical investigations are in progress, but no specific results have yet been reported.

Each of the following portions of this section is devoted to a discussion of various analyses and investigations of the above-mentioned liquid effects on breathing vibrations of shells. Virtually all of the work has concentrated on circular cylindrical shells having freely supported ends and rigid bottoms. Some of the analyses investigate more than one of the indicated effects, but none is capable of predicting all effects.

### Light Compressible Fluids

Fung et al. (ref. 9.10) have investigated both analytically and experimentally the effects of internal pressurization on the breathing modes of freely supported cylindrical shells, for the case where only a gas is present in the fluid column. The pressurizing gas is considered to have no mass; as a result, it adds potential energy to the overall system, but the inertia of the system is the same as that of an empty tank. Strictly speaking, this is a limiting case application of compressible flow theory, since the inertia of the gas is neglected and, as a result, the wave velocity becomes large. The analysis is applicable to the actual case only for vibrational frequencies well below the

coupled pressure resonances in the compressed fluid column.

In contrast with the method of deriving a shell frequency used by Arnold and Warburton, here the Timoshenko shell equations (ref. 9.12), written in terms of the displacements  $u, v, w$ , are utilized, and the loading terms are comprised of the static internal pressurization and dynamic tank inertia terms. Inertia of the internal fluid is neglected. Displacements of the type in equations (9.4) are assumed and a rather complex frequency equation results. For comparison, a simplified frequency equation is further derived using Reissner's shallow shell theory (ref. 9.13), with the longitudinal and tangential shell inertia terms neglected in the governing differential equations. This results in the equation

$$\rho_s \frac{\omega^2 a^2}{E} = \frac{\lambda_m^4}{(n^2 + \lambda_m^2)^2} + \frac{(h/a)^2}{12(1-\nu^2)} (n^2 + \lambda_m^2)^2 + \bar{n}_x \lambda_m^2 + \bar{n}_\theta n^2 \quad (9.8)$$

where

$$\bar{n}_\theta = \frac{p_0 a}{E h}, \quad \bar{n}_x = \frac{p_0 a}{2 E h}$$

$p_0$  being the static internal pressure in the cylinder. It must be emphasized that this expression is most accurate in general for larger values of  $n$  (i.e., say  $n > 2$ ), where shallow shell theory applies, and no coupling with fluid pressure resonances is allowed. The existence of this trend was determined by comparing the results of this frequency equation with the results of the previously mentioned, more exact frequency equation. Equation (9.8) is, of course, also suitable for the empty tank for  $p_0 = 0$ . Results for this case are shown to be similar to figures 9.9 through 9.11 of the previous section.

Results calculated from equation (9.8) when the internal pressurization is not zero are shown in figures 9.14 through 9.16. The lowest natural frequency and its associated mode shape for a given empty shell were discussed in the previous section. From figure 9.14, it can be seen that pressurization alters the mode shape of the lowest mode to a lower order pattern, while, at the same time, all natural frequencies

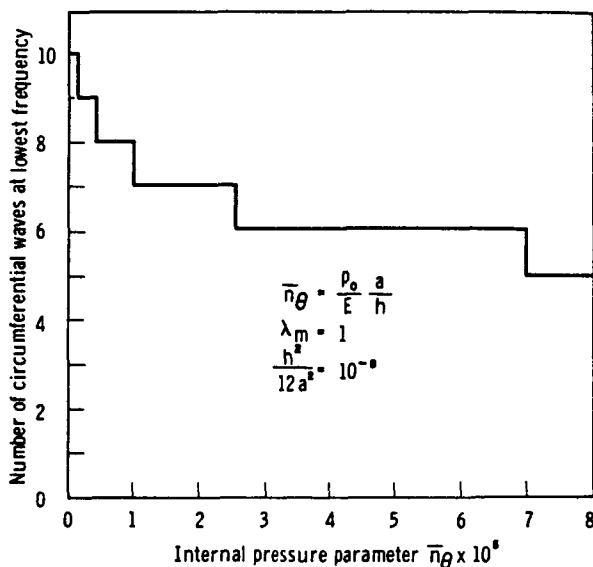


FIGURE 9.14.—Number of circumferential waves at the lowest frequency versus internal pressure (ref. 9.10).

are increased. This is shown in figures 9.15 and 9.16, along with experimental correlation with equation (9.8).

It is further pointed out (ref. 9.10) that for a given forced input to a cylindrical shell, the amplitude of the response of the various modes at resonance is very erratic, and larger responses are by no means confined to the lowest modes. Therefore, where breathing responses in shell-like structures are anticipated, a large range of frequencies must be examined.

#### Compressible Fluids With Inertia

To study pressure resonance coupling over a wide range of parameters in a breathing shell, along with the hydrodynamic loading of the shell wall, it is necessary to include both the compressibility and inertia of the fluid column, whether it contains only pressurized gas or liquid, or both pressurized gas and liquid. Such analyses are applicable at frequencies, where the compressibility effects are important, but are not readily capable of including the liquid free surface effects.

Berry and Reissner (ref. 9.14) have investigated the effects of pressurization with fluids of significant mass, where only one fluid completely fills the tank. Using shallow shell

equations for the circular cylinder, with loading terms composed of internal static pressure, shell inertia due to radial motion only, and fluid inertia from the apparent mass of the pressurizing fluid, the following frequency equation is formulated for the coupled breathing modes

$$(\rho_s h + m_f) \omega^2 = \frac{Eh}{a^2} \left[ \frac{\left(\frac{\pi}{l}\right)^4}{\left(\frac{\pi}{l}\right)^2 + \left(\frac{n}{a}\right)^2} + D \left[ \left(\frac{\pi}{l}\right)^2 + \left(\frac{n}{a}\right)^2 \right] \right] + p_0 a \left[ \frac{1}{2} \left(\frac{\pi}{l}\right)^2 + \left(\frac{n}{a}\right)^2 \right] \quad (9.9)$$

which is most accurate for circumferential values  $n \geq 2$ . In this equation,

$$D = Eh^3 / 12(1 - \nu^2)$$

and  $m_f$  is the apparent mass of the internal fluid. The fluid apparent mass is derived assuming small motions of an inviscid, compressible fluid; hence the wave equation is solved with boundary conditions such that the unsteady fluid pressure at the cylinder wall represents the fluid loading on the tank, and the normal velocity of the fluid at the tank wall is the same as the wall velocity. Solutions for this pressure distribution are taken in the form

$$q = e^{i\omega t} \cos n\theta \sin \frac{\pi x}{l} Q(r)$$

As a result, the following apparent mass is obtained:

$$m_f = \rho_0 a \left[ \frac{I_n(\sqrt{\lambda_1^2 - k_c^2})}{\sqrt{\lambda_1^2 - k_c^2} I'_n(\sqrt{\lambda_1^2 - k_c^2})} \right] \quad \text{for } k_c < \lambda_1 \quad (9.10a)$$

$$m_f = \rho_0 a \left[ \frac{J_n(\sqrt{k_c^2 - \lambda_1^2})}{\sqrt{k_c^2 - \lambda_1^2} J'_n(\sqrt{k_c^2 - \lambda_1^2})} \right] \quad \text{for } k_c > \lambda_1 \quad (9.10b)$$

where  $\rho_0$  is the reference static fluid density,  $\lambda_1 = \frac{\pi a}{l}$ ,  $k_c = \frac{\omega a}{c_0}$ ,  $c_0$  being the velocity of sound in the fluid at the reference pressure, and  $J_n$  and  $I_n$  are the ordinary and modified  $n$ th-order Bessel functions, respectively.

It can be seen that the solution for the frequency,  $\omega$ , from equations (9.9) and (9.10), is a difficult task. Tables of solutions are

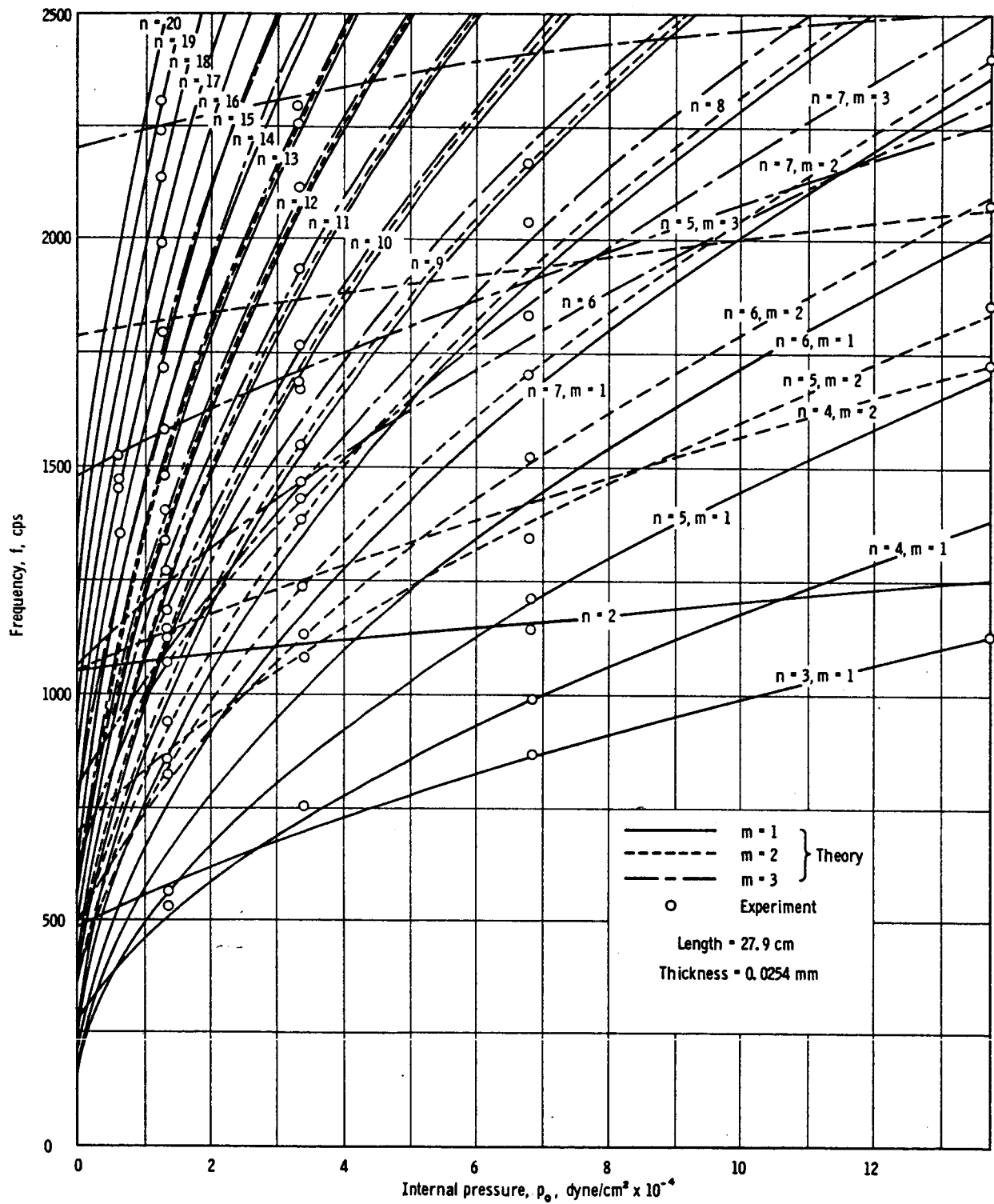


FIGURE 9.15.—Theoretical and experimental natural frequencies versus internal pressure (ref. 9.10).

given in reference 9.14 for some limited values of the parameters involved. In general, it is concluded that the effect of including inertia and compressibility of the internal fluid column is to lower the natural frequencies of the breathing vibrations of the shell in comparison with

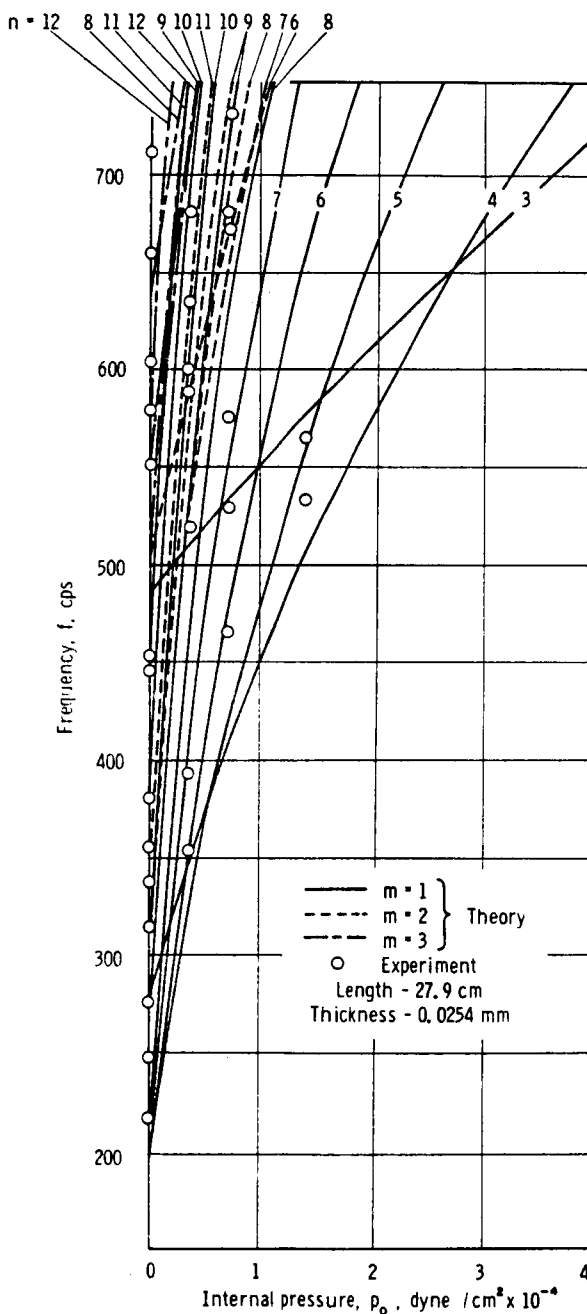


FIGURE 9.16.—Theoretical and experimental natural frequencies versus internal pressure (ref. 9.10).

their values (i.e., those predicted by eq. (9.8) or for  $m_f=0$  in eq. (9.9)) when the inertia and compressibility of the internal fluid are absent.

In addition to the coupled shell breathing mode frequencies given by equation (9.9), there also occur higher natural frequencies, each of which is associated with a particular number of pressure nodal circles in the oscillating fluid column. That is, the assumed form of pressure distribution allows for a multiple pressure wave pattern to be established in the fluid, in the radial direction. For heavy liquids, it is estimated that the frequencies of these coupled pressure modes are nearly equal to those of a free boundary column of liquid. In other words, the presence of the liquid in the shell has a significant effect whereby it lowers the tank breathing modes, while the flexible tank wall has a less significant effect on the frequencies of the assumed form of pressure resonances in the free column of liquid.

Saleme and Liber (ref. 9.15) have investigated the effects of a compressible fluid column on the breathing shell, both for the case of the shell completely filled with one fluid, and also for the case of the shell filled with two separate, immiscible fluids. Their approach to the tank filled with one fluid is essentially the same as that of Berry and Reissner (ref. 9.14), just discussed, except that tangential inertia terms are kept in the shell equations, so that two additional sets of natural frequencies result for each modal pattern of the shell. The lower set of these natural frequencies correspond to those obtained by Berry and Reissner, using equation (9.10b) for the apparent mass factor; lower frequency resonances corresponding to those obtained for the case for which equation (9.10a) applies were not discussed. For multiple, immiscible fluids, a method of superposition is indicated for the solution of certain modes; however, no appreciable numerical calculations have been completed.

Finally, a few comments must be added with regard to the fluid pressure modes considered in the previous two analyses. Only longitudinal oscillational pressure distributions of the type

$$q = Q(r, \theta, t) \sin \frac{m\pi x}{l}$$

were considered, in which all multiple pressure wave patterns have zero amplitudes at both ends of the liquid column. It must be emphasized that other coupled pressure modes, particularly *axisymmetric* modes which result in a *maximum* pressure amplitude at the tank bottom (as occur for longitudinal tank excitation), can be excited in the compressible fluid-elastic tank combination (or even in an incompressible fluid-elastic tank system). Such axisymmetric pressure modes can occur within the same frequency range as the nonsymmetric coupled tank breathing modes of the form shown above, depending on the shell geometry and the properties of the fluid. Pressure modes of this type in a longitudinally excited cylindrical shell filled with a compressible fluid have been studied by Reissner (ref. 9.16). The shell is considered strictly to be a circumferential membrane, and a prescribed excitational pressure is assumed to act at the bottom of the fluid column. This analysis shows that pressures at the tank bottom become very large at a coupled longitudinal resonance of the fluid column.

The very similar, and more practical, case of a prescribed oscillatory acceleration at the bottom of an elastic cylindrical tank containing a liquid has already been discussed in chapter 8. Longitudinal pressure responses, of the type to which we are now referring, can be approximated by equation (8.60) in chapter 8, and the frequencies at which the resonances occur are those values where this equation predicts infinite pressure. Thus, for a liquid in an elastic tank, the lowest set of the axisymmetric, longitudinal pressure modes, in which the radial pressure distribution is essentially plane, can be approximated by water-hammer theory, as shown in chapter 8. This approximate analysis is a special case of that of Reissner's, mentioned above, and it becomes less accurate at lower liquid levels. More accurate analyses of these coupled longitudinal modes have become available only recently, and will be discussed briefly at the end of the next two sections.

#### Incompressible Fluids (Free Surface Effects Neglected)

The hydrodynamic loading inertia and pressurization effects of fluids on the breathing

shell can readily be analyzed using incompressible fluid theory, while neglecting the free surface effects by some suitable assumption. In this section, we discuss several methods by which this has been done, along with experimental confirmation of the analyses.

Based on ideas presented by Reissner (ref. 9.16), and Berry and Reissner (ref. 9.14), which have been discussed in the preceding section, Lindholm et al. (ref. 9.9) developed a frequency equation for the completely liquid filled tank, similar to equation (9.9), using incompressible theory for the fluid, in an unpressurized circular cylindrical shell. The method is essentially the same as that of Berry and Reissner (ref. 9.14), except that the Laplace equation is taken as the governing equation for the liquid, and the radial deflection is taken with  $m \geq 1$ :

$$w = A_{mn} \sin \frac{m\pi x}{l} \cos n\theta \cos \omega t$$

and the pressure distribution is taken as

$$q = C_{mn} I_n \left( \frac{m\pi r}{l} \right) \sin \frac{m\pi x}{l} \cos n\theta \cos \omega t$$

It may be noted that this form of pressure distribution requires that the free surface remain essentially plane; hence, the free surface effects are neglected. The liquid apparent mass is

$$m_f = a\rho_L [I_n(\lambda_m)/\lambda_m I'_n(\lambda_m)] \quad (9.11)$$

in which  $\lambda_m = m\pi a/l$ . It may be noted that this expression is the same as equation (9.10a) when  $k_c \rightarrow 0$  (or when  $c_0 \rightarrow \infty$ ), a result anticipated in reference 9.14 for heavy fluids. In this case, equation (9.9) becomes

$$(\rho_s h + m_f) \omega_{mn}^2 = \frac{D}{a^4} (\lambda_m^2 + n^2)^2 + \frac{Eh}{a^2} \left[ \frac{\lambda_m^4}{(\lambda_m^2 + n^2)^2} \right] \quad (9.12)$$

Results predicted by this equation for a thin shell filled with water, along with experimental correlation, are shown in figure 9.17. For comparison purposes, it may be noted that these results were obtained from the same cylinder as that used for the empty shell data shown in figure 9.11. The theoretical curves in figure

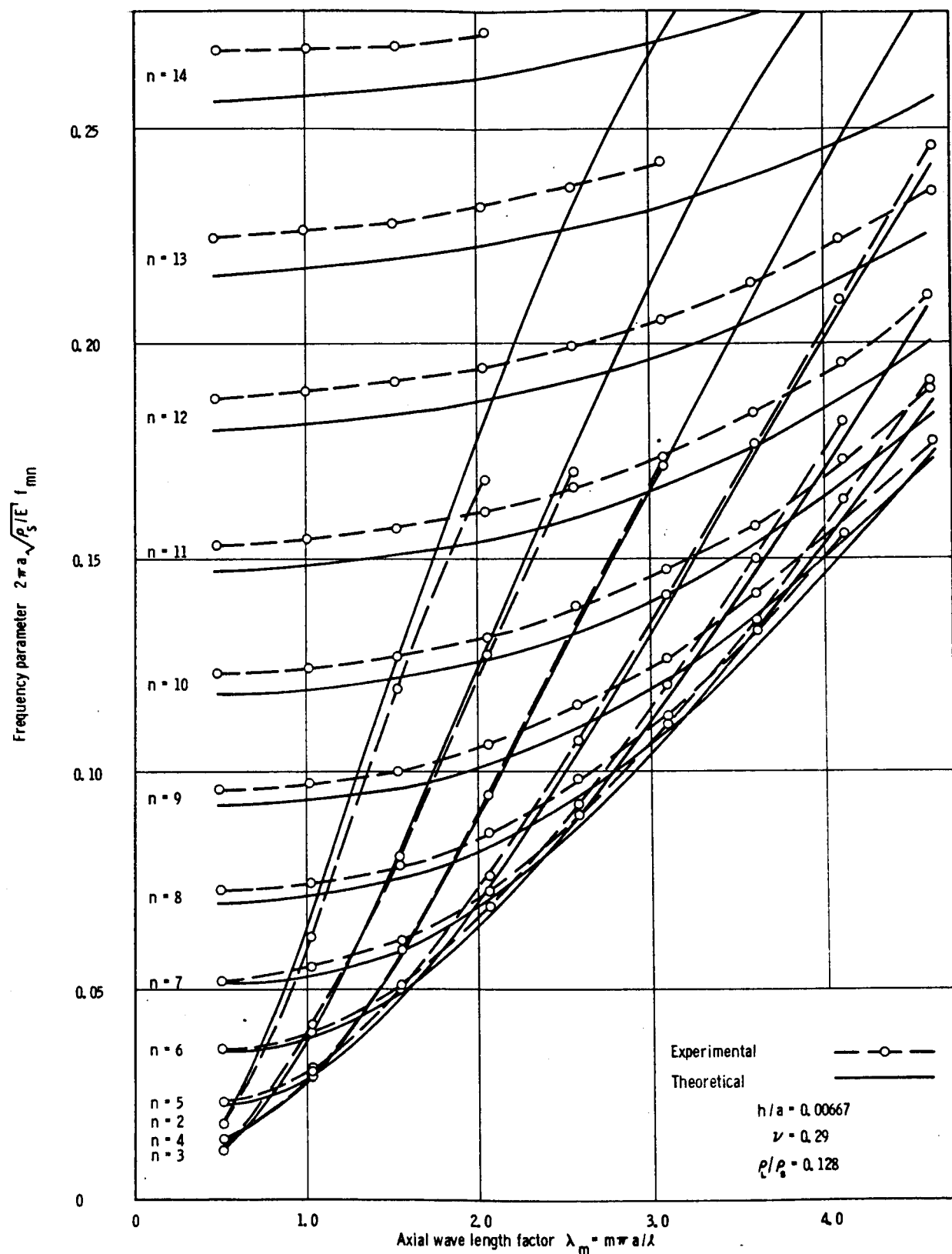


FIGURE 9.17.—Theoretical and experimental natural frequencies of liquid-filled cylinder in breathing vibration (ref. 9.9).

9.11 were obtained from equation (9.12) with  $m_f=0$ .

Further experimental work was performed in reference 9.9 to determine the liquid effects on frequency at partial liquid depths, as shown in figure 9.18. The data are for water in a freely supported steel cylinder with  $a=3.77$  centimeters,  $h=0.229$  millimeter, and  $l=23.4$  centimeters. Further, figures 9.19 and 9.20 show experimental data showing the effect of liquid depth on axial mode pattern for two different modes. Distortion of the axial pattern from a sine wave is especially apparent at liquid depths other than empty or full.

Keeping in mind the above-indicated distortion of axial mode pattern, Leroy (ref. 9.17) has presented an analysis for natural frequencies of a partially liquid filled, unpressurized, cylindrical shell. The displacements of the distorted pattern are assumed to be representable as linear combinations of all the natural modes for the empty cylinder:

$$\left. \begin{aligned} u &= \cos n\theta \sum_m^{\infty} A_m \cos \frac{m\pi x}{l} \\ v &= \sin n\theta \sum_m^{\infty} B_m \sin \frac{m\pi x}{l} \\ w &= \cos n\theta \sum_m^{\infty} C_m \sin \frac{m\pi x}{l} \end{aligned} \right\} \quad (9.13)$$

Similar to Lindholm et al. (ref. 9.9), the liquid free surface is assumed to remain essentially plane, but an expression for the composite hydrodynamic pressure loading of the shell wall is determined, having components in each mode of the linear combinations (eq. (9.13)), and an arbitrary partial depth is allowed. Substituting these expressions into a suitable set of cylindrical shell equations, an infinite order frequency determinant results. The natural frequencies can then be approximated numerically by assuming a limited number of modes in the composition of the actual distorted modal patterns. Figure 9.21 shows a comparison of some calculated results of this theory with the experimental results shown in figure 9.18 for two different modes.

One of the most complete investigations of the effects of both pressurization and liquids

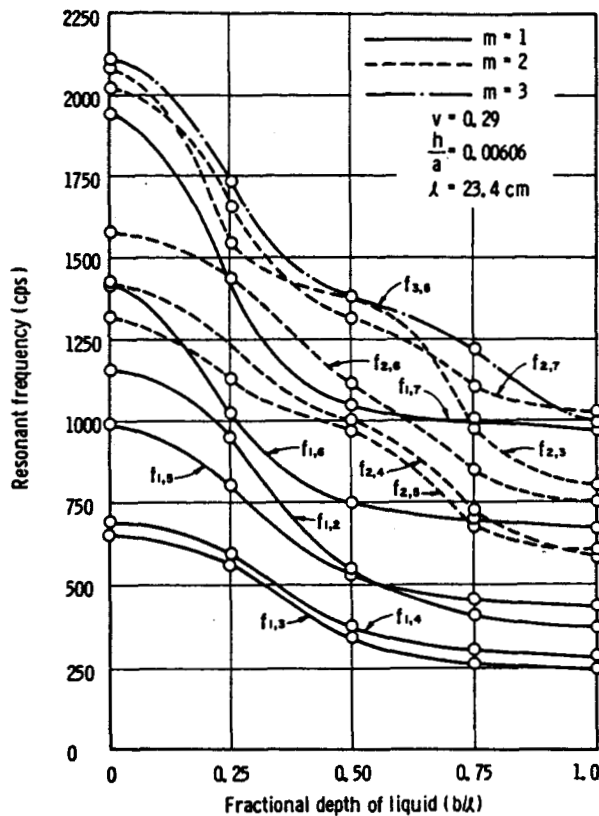
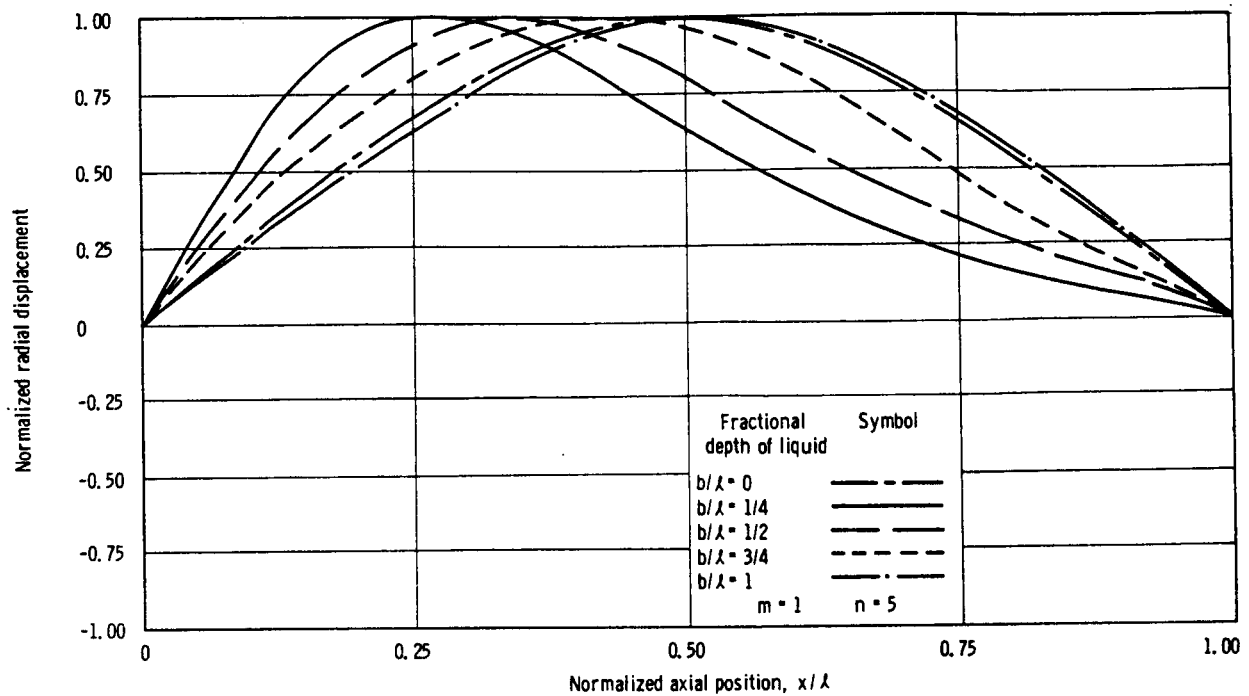
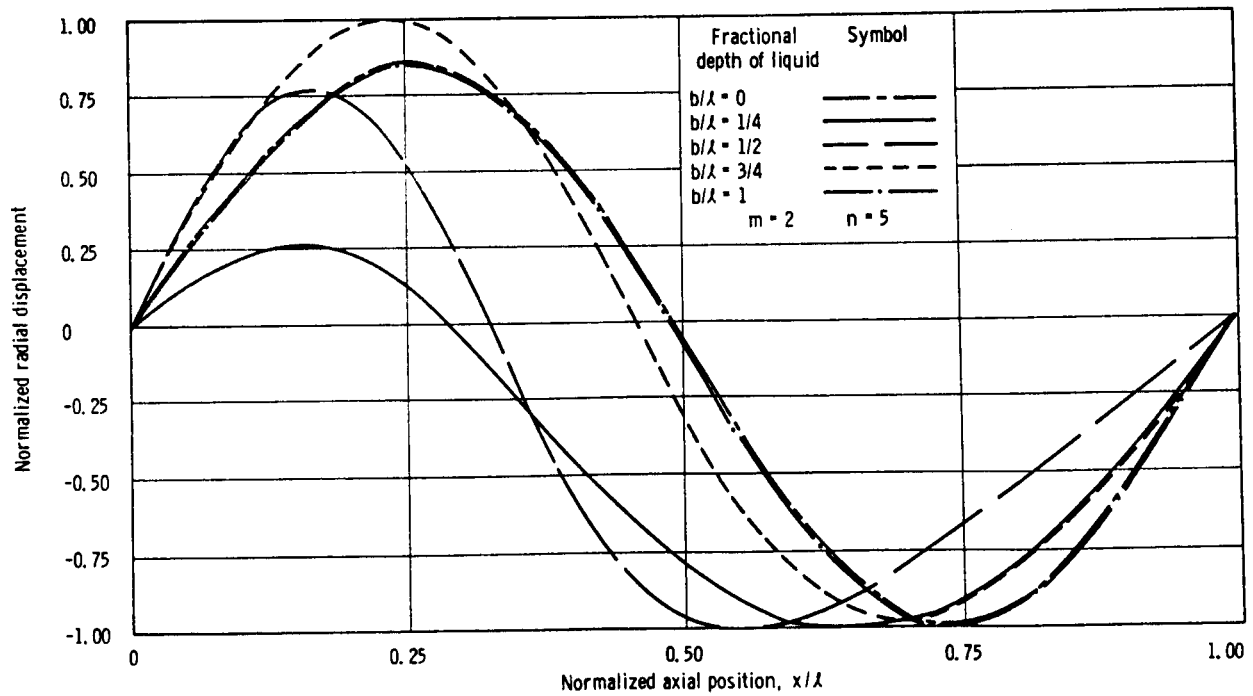


FIGURE 9.18.—Experimental variation of natural breathing frequencies with liquid depth (ref. 9.9).

at partial depths in breathing cylindrical shells with freely supported ends has been performed by Mixson and Herr (ref. 9.18). An analysis was carried out, combining a number of the methods already here discussed with that given by Baron and Bleich (ref. 9.19) for partially filled cantilever shells, and then compared with experimental results. Basically, Lagrange's equations are utilized to obtain the equations of motion of the coupled system. For this approach, of course, the kinetic and potential energy of the combined system must be determined. The potential and kinetic energy of the shell is expressed in terms of displacements using a method similar to that used by Arnold and Warburton (ref. 9.8), except that additional terms are included to allow for internal pressurization. Only radial inertia terms for the cylinder are included, so that only the lowest set of natural frequencies is determined, and inertia for the pressurizing gas is neglected.

FIGURE 9.19.—Axial mode shape distortion for  $m=1$ ,  $n=5$  mode versus fractional depth of liquid (ref. 9.9).FIGURE 9.20.—Axial mode shape distortion for  $m=2$ ,  $n=5$  mode versus fractional depth of liquid (ref. 9.9).

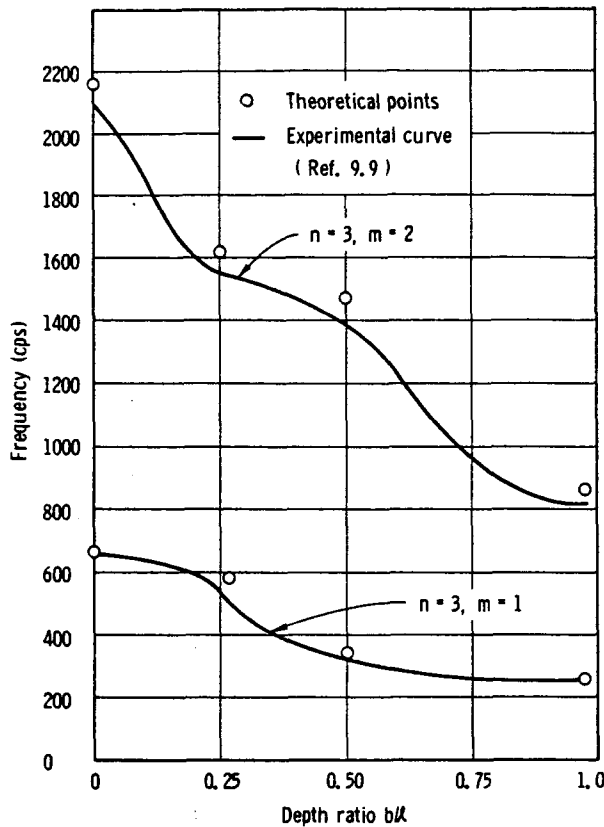


FIGURE 9.21.—Comparison of Leroy theory with experiments for breathing modes (ref. 9.17).

The kinetic and potential energies for the arbitrary depth column of liquid are determined using incompressible potential flow theory, employing the boundary conditions at the shell wall, as have already been discussed, but the free surface effects are neglected in a different manner than that of Lindholm et al. (ref. 9.9). Here the boundary condition at the free surface employs equation (9.5), but  $g=0$  is set into this equation. As in reference 9.19, it is argued that the significant liquid free surface modes occur at very low frequencies compared to those of the breathing tank. Therefore, their effects can be neglected so that the free surface is allowed to oscillate, but it is assumed that the potential energy associated with the free surface motion is negligible. In this case, the kinematic equation, equation (9.6), is still valid, but it is not necessary in order to determine the velocity potential,  $\Phi$ , in the problem.

Anticipating axial mode shape distortions at partial depths, the shell displacement functions are chosen as linear combinations of a finite number of the modes of the empty shell in the following form:

$$\left. \begin{aligned} u &= \cos n\theta \sum_{s=0}^N U_s(t) \cos \frac{\lambda_s x}{a} \\ v &= \sin n\theta \sum_{s=0}^N V_s(t) \sin \frac{\lambda_s x}{a} \\ w &= \cos n\theta \sum_{s=0}^N W_s(t) \sin \frac{\lambda_s x}{a} \end{aligned} \right\} \quad (9.14)$$

For empty or completely full shells only, where little distortion occurs, the first term of each expansion is satisfactory. Using Lagrange's method, the equations of motion for the coupled system are determined, and after the assumption of simple harmonic motion, a  $3(N+1)$  order frequency determinant is obtained. This frequency determinant, similar to that of Leroy (ref. 9.17), can then be solved numerically for any value of  $N$ , depending on the accuracy desired. (Because of the complexity of the frequency determinant that results from the above procedure, the details will not be given here, but the original report (ref. 9.18) should be consulted.)

Numerical computations were performed to predict a number of natural frequencies for two different cylinders subjected to various conditions, and the results were compared with experimental values. Detailed characteristics of the two cylinders are summarized in table 9.1, p. 330. For the simple case of a tank pressurized with a light gas and  $N=0$  (one-term approximation of the displacements), the resulting frequency equation is identical to equation (9.8), and the experimental results obtained were similar to that shown in figures 9.15 and 9.16. For a pressurized liquid filled tank and  $N=0$ , the resulting frequency equation is similar to equations (9.9) and (9.10) for the case of  $k_c=0$ , except that additional terms are included which account for the effects of hydrostatic pressure of the liquid and finite cylinder length. Correlation of predicted results with experiments for this case is shown in figure 9.22. (The upper figure is for cylinder 1, and the lower figure is for cylinder 2.) For partial liquid depths,

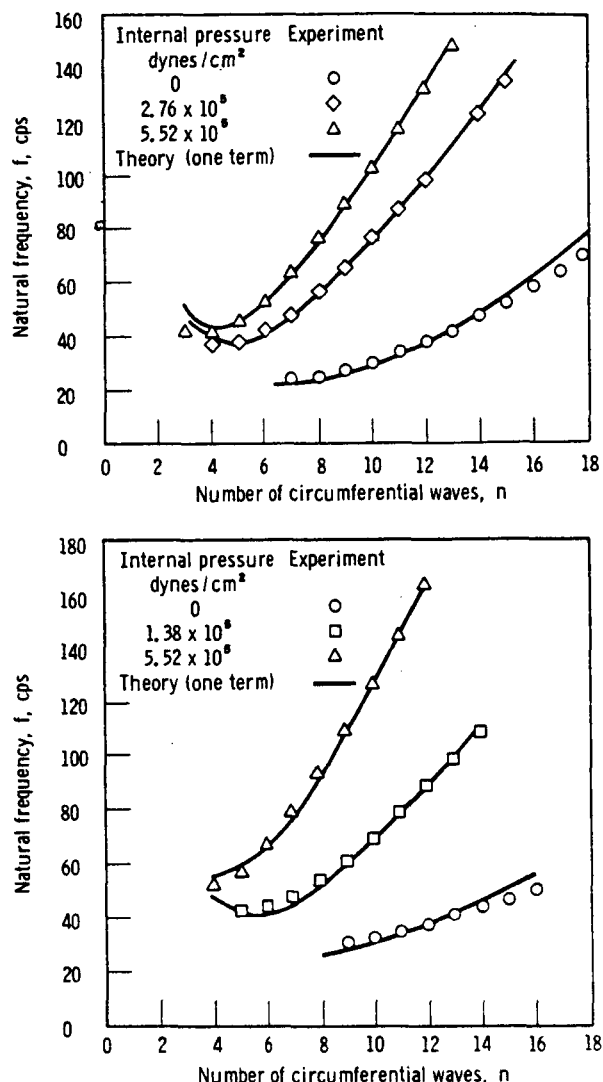


FIGURE 9.22.—Theoretical and experimental natural frequencies for pressurized, water-filled cylinders (ref. 9.18).

for both the cases of  $N=0$  and of  $N=1$  (one- and two-term approximation to the displacements), calculations also were performed and compared to experimental results. For convenience, some of the compared results are shown in figures 9.23a through 9.23c. (All data are for cylinder 2, and  $m=1$  modes.) Theoretical curves are shown both for the exact theory and for a simplified approximation of the liquid apparent mass. The experimental results were obtained from cylinders having fixed ends, but are compared to theoretical results for freely supported ends by using the

method outlined in the section on breathing vibrations of empty shells to make the end conditions equivalent to freely supported ends. Only  $m=1$  modes were investigated; however, the analysis is applicable to higher modes as well, as long as  $N$  is chosen to give sufficient accuracy.

An analysis for partially liquid filled cantilever cylindrical shells has been given by Baron and Skalak (ref. 9.20), which is based on similar work of Baron and Bleich in references 9.19 and 9.21. Although these analyses are for liquids in cylindrical shells simply supported at the bottom and free at the top, the methods of approach can readily be modified and used with boundary conditions more applicable to space vehicle tanks, as has been done by Mixson and Herr, previously described.

The case of longitudinal forced vibration of a cylindrical tank filled with an incompressible fluid has been investigated by Bleich (ref. 9.22), using an approximate analysis. The emphasis is on the axisymmetric, longitudinal pressure distribution in the fluid column, and the effects of the wall elasticity are approximated by considering the tank to be a series of rings, rather than using a complete shell analysis. Free surface effects are neglected. The results are comparable to the findings of Reissner (ref. 9.16), mentioned in the preceding section, as well as the water-hammer analysis given in chapter 8. That is, for a relatively incompressible liquid in a flexible cylinder, one can neglect the compressibility of the liquid; for this case the analysis of Reissner (ref. 9.16), and the water-hammer analysis of chapter 8, essentially reduce to the analysis of Bleich (ref. 9.22). Although the liquid is considered incompressible, a longitudinal axisymmetric pressure mode, having a maximum at the tank bottom, still occurs in a system in which the inertia is assumed to lie solely in the liquid, and the effective compressibility to be solely in the tank wall. In effect, the resulting modes represent  $n=0$  shell displacement modes which can be approximated by

$$w = W(t) \cos \lambda_b x$$

where  $\lambda_b$  is determined by the liquid depth  $b$ ,

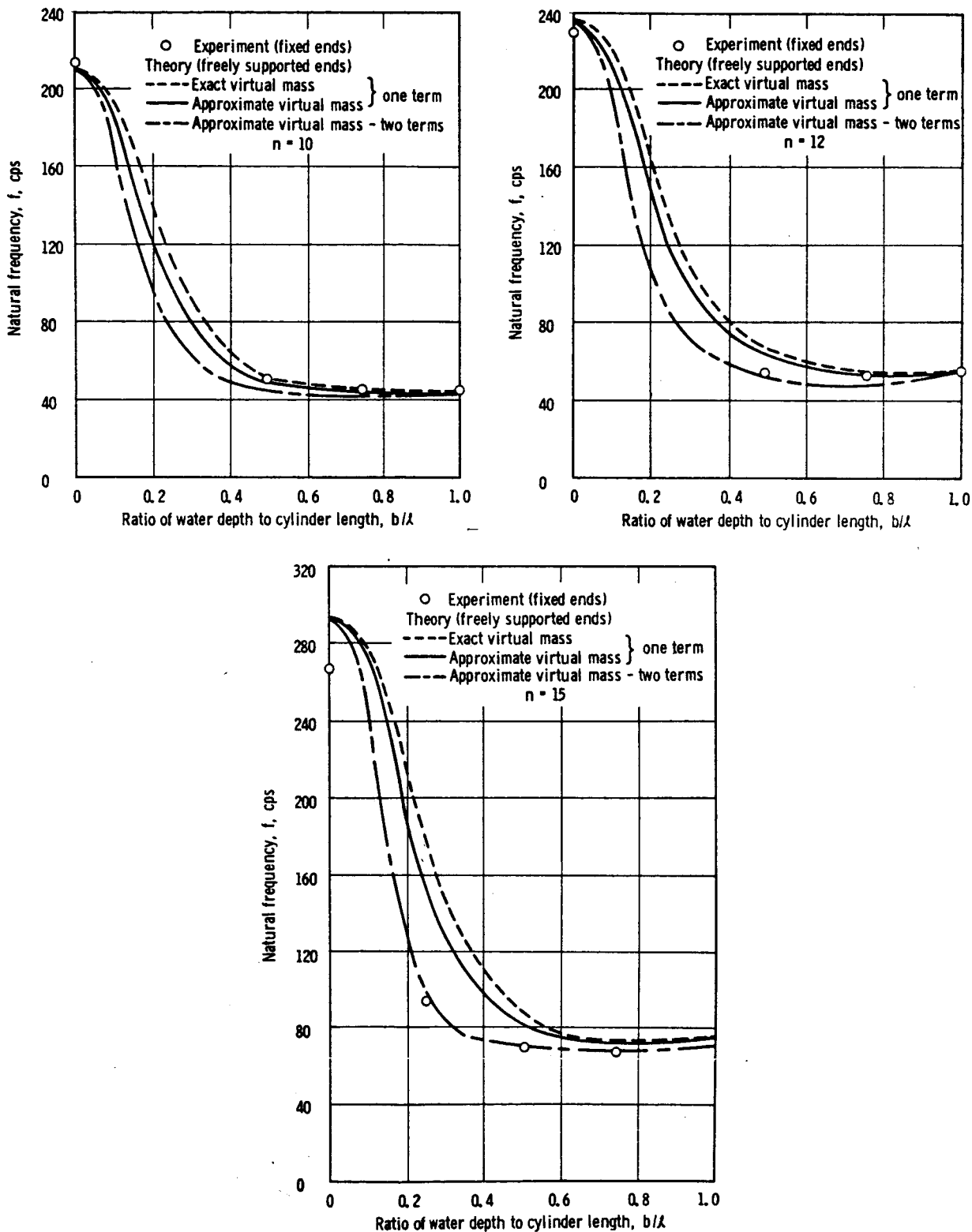


FIGURE 9.23a.—Theoretical and experimental variation of natural frequency of a pressurized cylinder with water depth (ref. 9.18).  $p_0 = 3.45 \times 10^4$  dyne/cm<sup>2</sup>.

229-648 O-67—22

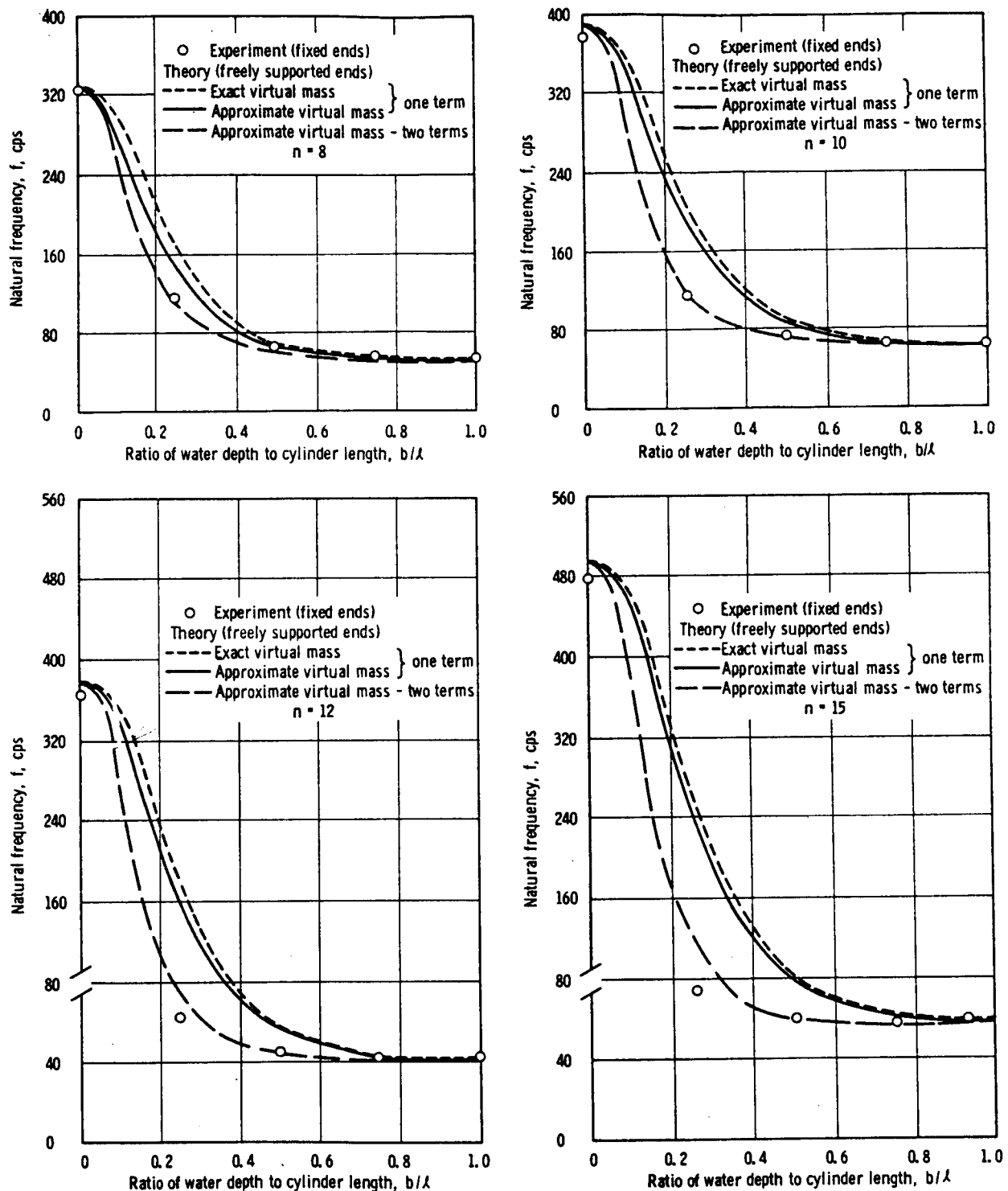


FIGURE 9.23b.—Theoretical and experimental variation of natural frequency of a pressurized cylinder with water depth (ref. 9.18).  $p_0 = 1.38 \times 10^6$  dyne/cm<sup>2</sup>.

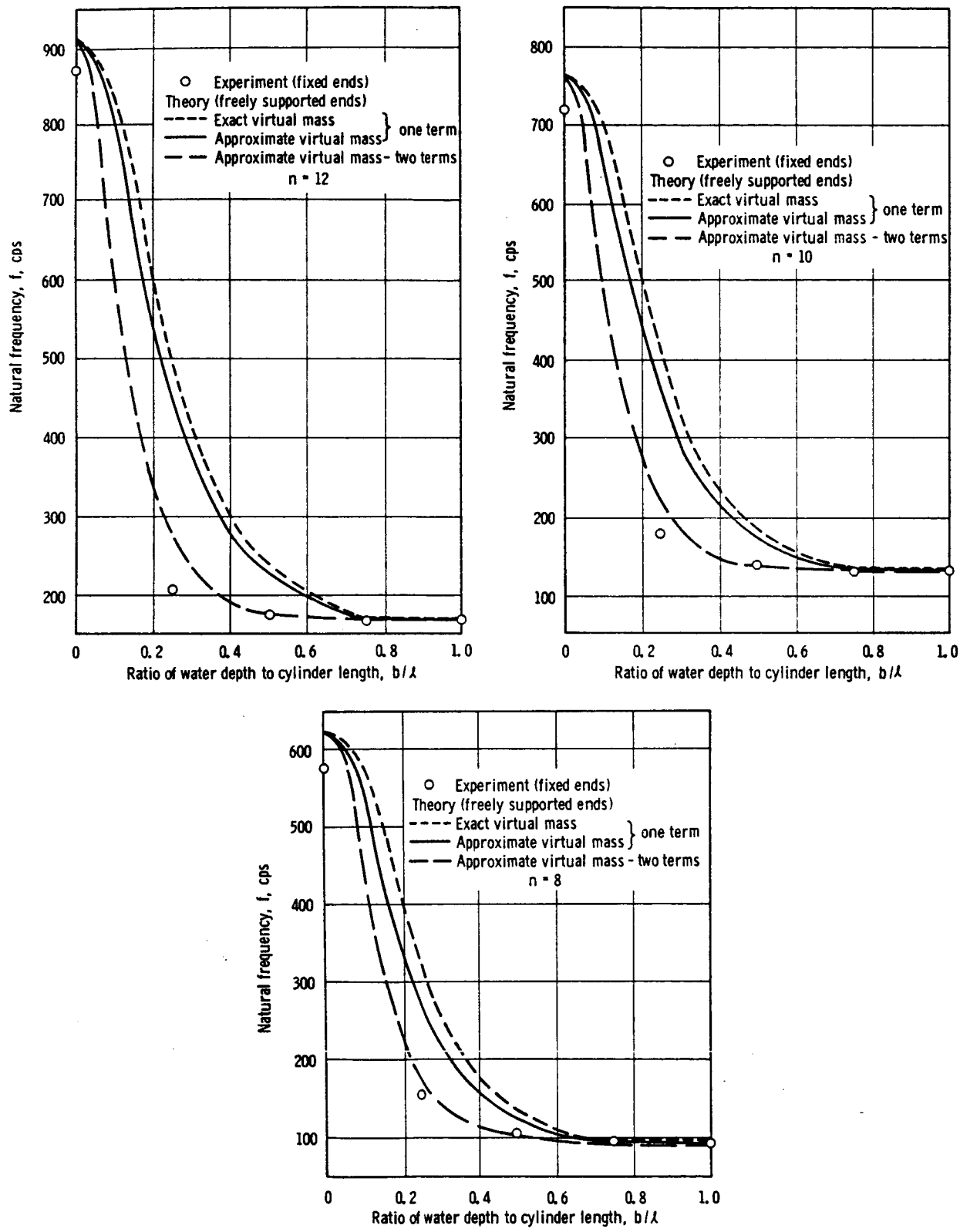


FIGURE 9.23c.—Theoretical and experimental variation of natural frequency of a pressurized cylinder with water depth (ref. 9.18).  $p_0 = 5.51 \times 10^5$  dyne/cm<sup>2</sup>.

TABLE 9.1.—*Details of Experimental Cylinders*

[Ref. 9.18]

Parameter	Cylinder 1	Cylinder 2
Material	Aluminum (2014-T6)	Steel (stainless)
Mass density, gram/cc	2.77	7.75
Young's modulus, $E$ , dyne/cm <sup>2</sup>	$6.89 \times 10^{11}$	$2.07 \times 10^{12}$
Poisson's ratio, $\nu$	0.33	0.30
Length, $l$ , cm	72.7	55.9
Mean radius, $a$ , cm	38.1	30.5
Skin thickness, $h$ , mm	0.406	0.1015
Radius-thickness ratio, $a/h$	937	3000
Radius-length ratio, $a/l$	0.525	0.546

rather than the tank length  $l$ . Obviously this simplified assumption of displacement violates the zero-displacement boundary condition at the tank bottom, and a series is required for exact satisfaction of that boundary condition.

A more detailed numerical analysis of the above type of longitudinal modes has been performed by Palmer and Asher (ref. 9.23), and verified experimentally. This work became available only shortly before the final printing of this monograph so that the details could not be included here. However, the existence of the  $n=0$  bulging modes described above is verified, and it is found that these modes are intermixed frequencywise, with the nonaxisymmetric breathing modes ( $n \geq 2$ ), described in the previous sections of this chapter. This reference should be consulted for the details of such modes. One more recent investigation of these modes is discussed at the end of the next section.

#### Incompressible Fluids (Free Surface Effects Included)

Breathing vibrations of partially liquid filled shells, with the free surface effects neglected, were considered in the preceding section. It was pointed out by Baron and Bleich (ref. 9.19), however, that for the case of partially full cylindrical shells simply supported at the bottom and free at the top, with free surface effects included, the coupled breathing modes were still very nearly the same as if free surface effects had not been included, while additional resonances corresponding to coupled fuel sloshing modes occurred at very low frequencies, near

the values they would have in a rigid container. In this present section, similar results will be found for a freely supported cylindrical shell.

Chu (ref. 9.24), and Chu and Gonzales (ref. 9.25), have investigated breathing vibrations, including free surface effects, for a partially liquid filled, freely supported cylindrical shell. Displacement functions of the form for a completely empty shell as in equations (9.4) are assumed in the computations for the partially full tank, allowing no distortion of the mode shape. The dynamic shell equations of Yu (ref. 9.26) are used, except that tangential and longitudinal inertia for the shell is neglected. The hydrodynamic loading of the shell wall is determined, allowing for both inertia of the liquid and free surface effects. Potential fluid flow is utilized, as has been described previously, except that here the free surface boundary condition is given by equation (9.7). It is found that, in the hydrodynamic loading, the additional terms due to the free surface effects are very small unless the excitation is in the vicinity of a frequency corresponding to a natural liquid mode for a similar rigid cylindrical container. Since in practical cases small damping is always present, it is concluded that these effects are negligible except for the very lowest liquid modes. Hence, for a shell frequency higher than those of the first several uncoupled sloshing modes, it appears that the liquid free surface effects on the shell breathing motion are negligible.

Computations were performed for the  $m=1$ ,  $n=4$ , and  $m=2$ ,  $n=4$  modes for a shell with

$h/a = 0.00606$ , and  $a/l = 0.1609$ , for several liquid depths, and compared in reference 9.24 with experimental results from figure 9.18. The results are shown in figures 9.24 through 9.26, along with the results of additional computations performed in reference 9.25, in which distortion of the mode shape was accounted for. For these cases, the terms due to free surface effects were negligible.

The ratio of natural frequency for partial liquid depth to empty tank frequency agrees well with experimental data only for the  $m=1$ ,  $n=4$  mode when using the undistorted mode shape approximation. The results from reference 9.25 were obtained by including mode shape distortion, using a Galerkin procedure ( $10 \times 10$  matrix), and it was found that the second-mode results then agreed better than the first-mode results, as can be seen in figures 9.24 and 9.25. Since the empty tank frequency was a critical factor in the frequency ratio as given, the absolute frequencies were compared in figure 9.26. It can be seen that the agreement between theory and experiment is good except for the empty tank frequencies. It was suspected that this discrepancy was the result of nonuniformities in the shell.

It must be emphasized that the above results indicate that the effects of the free surface are

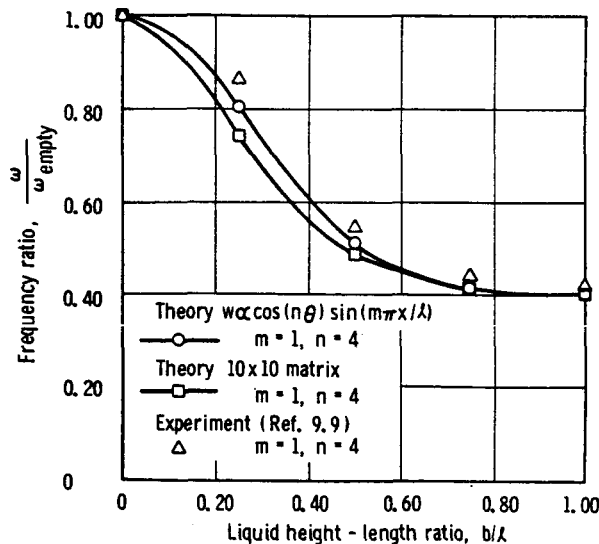


FIGURE 9.24.—Comparison of calculated and measured natural frequency ratio versus liquid depth,  $m=1$ ,  $n=4$  (ref. 9.25).

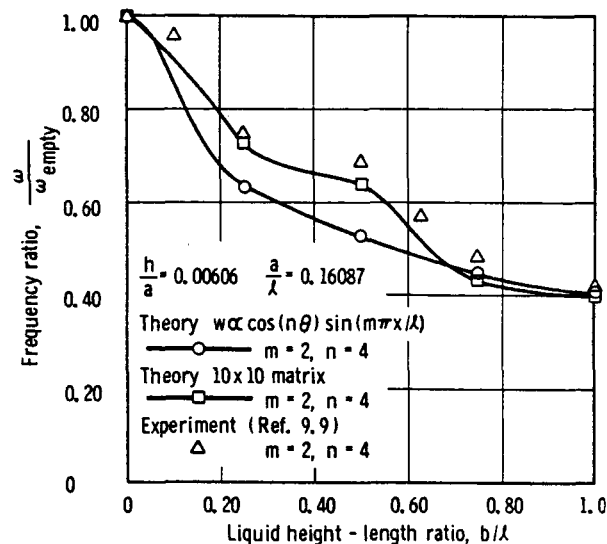


FIGURE 9.25.—Comparison of calculated and measured natural frequency ratio versus liquid depth,  $m=2$ ,  $n=4$  (ref. 9.25).

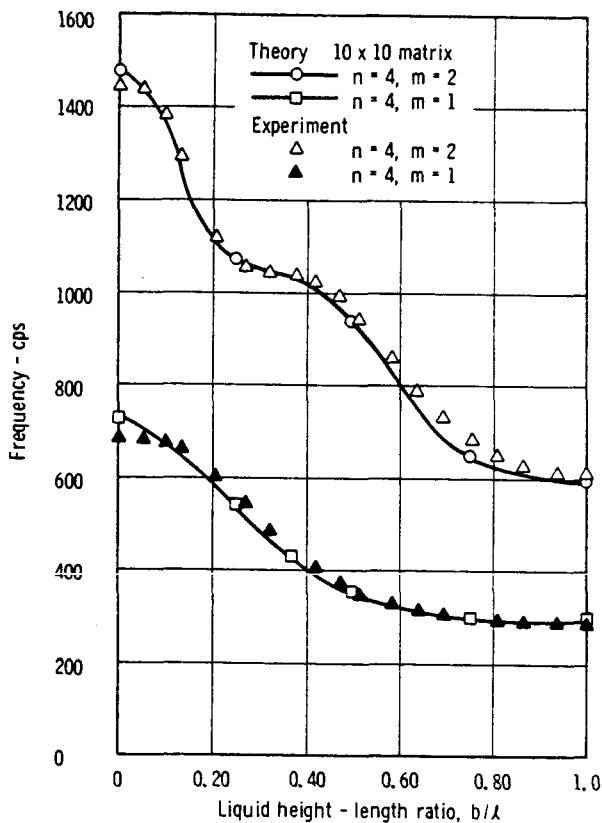


FIGURE 9.26.—Comparison of calculated and measured natural frequency versus liquid depth (ref. 9.25).

negligible only for the case where the shell frequency is higher than the first several uncoupled liquid surface frequencies. No investigation was made to determine the effects for a case where these conditions did not hold, although it appears that the computations could be based on the analytical results of reference 9.24, assuming that it is physically possible to have a cylindrical shell of some geometry that possessed breathing frequencies in a low range near the corresponding sloshing frequencies for that geometry.

Breathing vibrations, of a shell with free surface effects included, have been analyzed by several additional investigators; however, only a brief comment on these studies will be included here.

Fontenot and Lianis (ref. 9.27) have investigated the case of a full, pressurized cylindrical shell using a perturbation technique. Rabinovich (ref. 9.28) has analyzed the partially full cylindrical shell, using the Vlasov shell equations and a Lagrange-Cauchy integral to determine the hydrodynamic pressure on the shell. The natural frequencies and natural modes of the shell are obtained by expressing the modes as linear combinations of the empty tank modes, similar to the methods used in several of the articles previously described. Computed results for a full tank compare well with experimental data of Lindholm et al. (ref. 9.9). Natushkin and Rakhimov (ref. 9.29) have investigated the partially filled cylindrical tank with arbitrary end conditions, while Samoilov and Pavlov (ref. 9.30) have investigated a liquid-filled hemispherical shell. This liquid-filled shell configuration has also been investigated by Hwang (ref. 9.31). It was found that only very weak coupling exists between liquid surface and shell breathing modes, similar to the findings for the case of a cylindrical tank. Shmakov (ref. 9.32) has investigated axially symmetric vibrations of a cylindrical shell containing liquid, including free surface effects. Again, these modes correspond to breathing modes, such that the tank radial displacement is independent of the angular position at all levels ( $n=0$ ). As has already been mentioned, these modes are of most concern for longitudinal excitation. It is found

that the lowest shell mode suffers axial distortion for various partial liquid depths, similar to that observed for the regular breathing modes of the partially filled shell, already described.

One final reference should be included in this discussion of cylindrical shell breathing vibrations including free surface effects. Beal et al. (ref. 9.33), utilizing a numerical analysis, also have investigated the coupled tank bulging ( $n=0$ )—liquid pressure modes. This analysis became available only shortly before this monograph was printed. It was found that the coupled modes separated into two groups: the coupled liquid surface modes and the coupled bulging or pressure modes. For practical ranges of tank parameters, the liquid surface modes were found to be essentially at the same frequency as in a rigid tank. Further, the symmetric bulging tank modes occur primarily as an exchange of kinetic energy of the fluid (i.e., all the inertia of the system is in the fluid), and the strain energy of the shell (i.e., all the elasticity of the system is in the shell). The influence of shell bending stiffness was found to be negligible, and that of shell inertia secondary, in tanks of engineering interest.

### Nonlinear Effects

#### General

The preceding sections of this chapter have been devoted to a discussion of various linear effects of fluids on the breathing vibrations of cylindrical shells. Most of the analyses are concerned with the natural free vibrational frequencies of the shell and liquid, and small vibration theory is assumed throughout, for liquid free surface oscillations, pressure oscillations, and shell wall oscillations. It follows, then, to question at what physical amplitudes, if any, of the various oscillations in the liquid-shell system, does the linear theory fail to describe adequately the overall behavior of the system? Further, are the frequencies influenced by the excitation in the case of forced vibration? An experimental investigation along these lines has been performed, and some of the results are summarized in this section.

Kana et al. (refs. 9.34 and 9.35) have experimentally investigated some of the nonlinear breathing behavior of several elastic shells containing liquids with free surfaces under forced vibrational excitation. Cylindrical shells of about 0.254-millimeter wall thickness, 22.9-centimeter length, and about 3.81-centimeter mean radius were used with water for most of the investigations. In particular, liquid surface responses and shell wall responses were observed for both simply supported and cantilever shells subjected to lateral or longitudinal excitation. Responses were studied for various liquid depths.

Generally, it was concluded that laterally excited empty shells display an essentially linear response during breathing vibration up to amplitudes as large as one-half the wall thickness for the shells investigated. A typical empty cylindrical shell response is shown in figure 9.27. Full, simply supported shells also display a response that is linear, for the

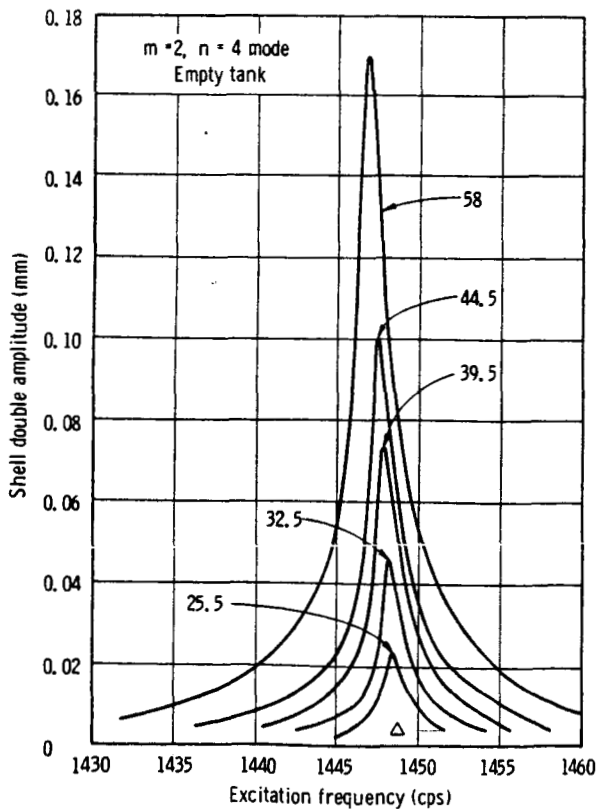


FIGURE 9.27.—Experimental forced response of empty simply supported shell (ref. 9.34).

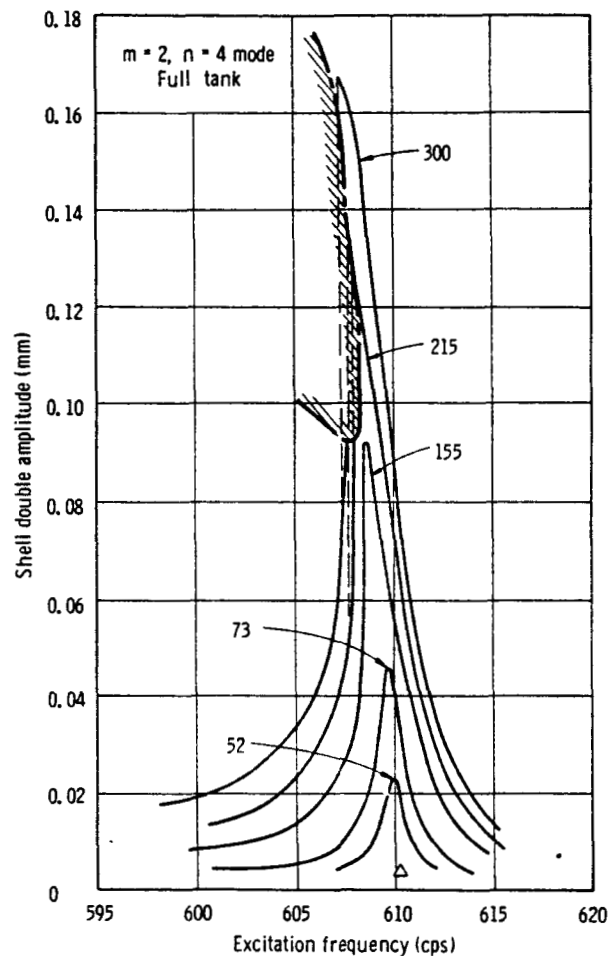


FIGURE 9.28.—Experimental forced response of full simply supported shell (ref. 9.34).

most part, up to the same amplitude limit, as can be seen from figure 9.28 for the same tank and mode. Some slight nonlinear softening is apparent at the larger amplitudes; a similar result occurs for a partial liquid depth where the liquid surface is in the vicinity of an axial node in the modal pattern of the breathing shell.

If the liquid surface is not in the vicinity of an axial node, and particularly if it is in the vicinity of an axial antinode of the shell motion, then a marked nonlinear softening response occurs for the shell, as can be seen from figure 9.29. Here, the response is linear up to only about one-tenth the wall thickness, and is strongly nonlinear softening for larger amplitudes. The region marked "I" on the figure

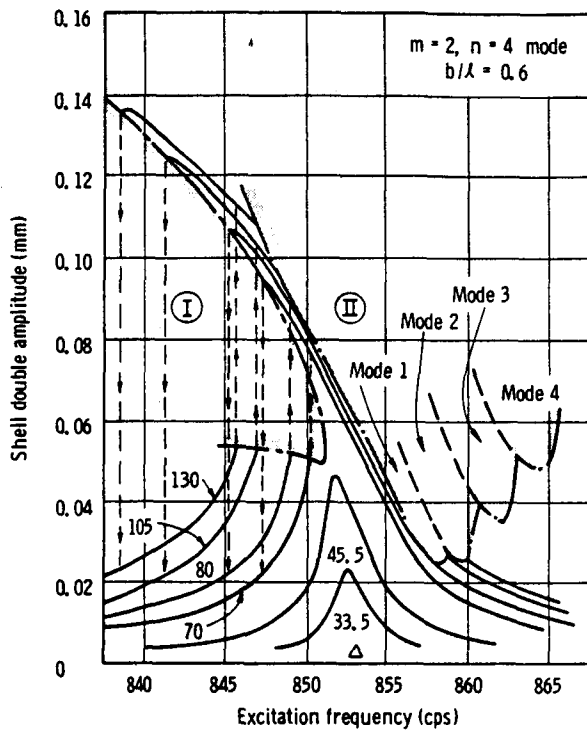


FIGURE 9.29.—Measured forced response of partially full simply supported shell (ref. 9.34).

is the region of instability of a typical nonlinear softening response, where jump phenomena occur, as indicated by the dashed lines. Region II is a second region of instability that occurs in this case, and is not at all typical of a nonlinear softening response. The behavior of the system in this region will be discussed subsequently. It is obvious that "small" vibration for the partially full tank in this case refers to amplitudes of less than at most one-tenth wall thickness. Experimental natural frequency data for partial liquid depths, discussed earlier and shown in figure 9.18, were taken at such small shell amplitudes. The numbers on each of the response curves in figures 9.27 through 9.29 give only a qualitative indication of the relative forcing amplitude for that respective curve.

Liquid free surface response in the form of high-frequency ripples is most pronounced for the case where the mean surface level is at an antinode of the shell motion. In fact, the excitation of the high-frequency free surface motion may be the source of the nonlinearity

of the shell response. The liquid has a tendency to pile up at the shell wall in the vicinity of the antinodes of the shell motion. For very low shell amplitudes, with the liquid surface near an axial antinode, or for even larger shell amplitudes, with the liquid surface near an axial node, very little free surface motion is apparent. It appears, then, that the wall motion at the liquid surface is most important in determining the free surface motion.

Similar responses were observed for cantilever shells subjected to either lateral or longitudinal excitation at various liquid levels. However, for longitudinal excitation, an additional peculiarity in the breathing vibration was observed. It was found that the longitudinally excited cylindrical shell with liquid would readily respond in breathing modes at frequencies that were subharmonic to the excitation, as well as at frequencies the same as that of the excitation. These subharmonic responses have yet to be explained, although they are obviously the result of some unknown nonlinearity. (The subharmonic response of liquids in *rigid* tanks undergoing vertical excitation was discussed in detail in ch. 8.)

#### *Nonlinear Coupling*

It has been pointed out earlier that when tank breathing resonances occur at frequencies considerably higher than those of the significant liquid-sloshing modes, one would not normally consider interaction between the two motions to be very probable. However, where nonlinearity exists, experimental studies (refs. 9.34 and 9.35) have shown that this reasoning does not prove to be correct.

We pointed out in the paragraphs just preceding that a nonlinear shell response occurs for the forced vibration of a cylindrical shell containing a liquid to such a depth that the free surface is near an axial antinode of the shell modal pattern, and some measured response data for this case were shown in figure 9.29. This type of response is typical for virtually all breathing modes, as long as the liquid depth is within the proper range, corresponding to the shell mode being investigated. Within the region indicated "II" in figure 9.29, a most peculiar coupling occurs between the

high-frequency shell motion, and low-frequency liquid surface motion.

As indicated in figure 9.29, region II is composed of a number of subregions, within each of which some symmetric liquid free surface mode, at its respective low frequency, can be excited by the high-frequency breathing motion of the shell. The form of the first three symmetric liquid modes is shown in figure 9.30, and is based on experimental measurements.

As an example, within the region marked "mode 1," in the cylindrical shell described in the previous section, the first symmetric liquid surface mode is excited at about 5.1 cps by the shell breathing motion occurring at, say, 856 cps (for excitation frequency at 856 cps), and about 0.025-millimeter shell amplitude. The liquid surface motion was observed in some cases to be as large as 1.5-centimeter amplitude. Simultaneously, the high-frequency shell motion exhibits an amplitude modulation at 5.1 cps. Once this type of coupling starts, it appears to stabilize at some amplitude combination for the liquid and shell, and continues indefinitely as long as the excitation conditions are unaltered. The coupling can be excited by either transverse or longitudinal excitation of the shell.

Further experimental data for this behavior are shown in figure 9.31, where oscilloscope photographs of the shell wall and liquid surface responses are compared for three different excitational conditions and three different liquid modes. Only the envelope of the

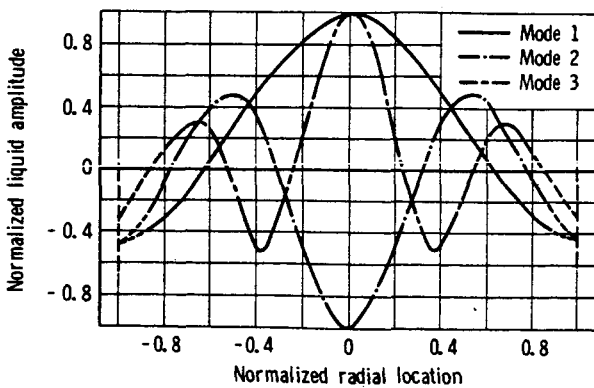


FIGURE 9.30.—Experimental symmetric surface modes generated by breathing vibration (ref. 9.34).

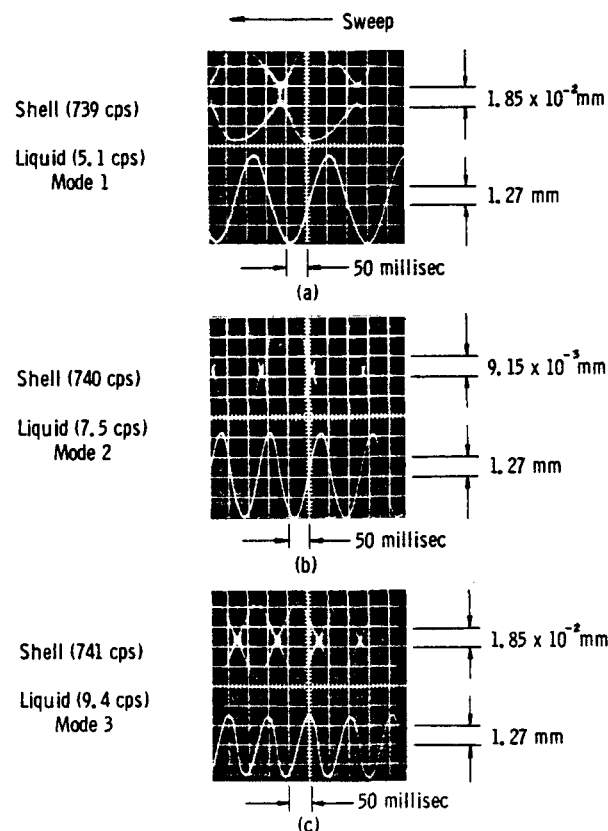


FIGURE 9.31.—Phase of tank and liquid motions for coupled vibration (ref. 9.34).

modulated high-frequency shell motion can be seen, and the liquid surface response represents the liquid motion at the center of the tank. These photographs correspond to response data obtained near the  $m=2, n=5$  mode in a cantilever shell about three-fourths full of liquid, conditions different from that represented by the response curve of figure 9.29. However, the response photographs are typical of the coupling behavior, regardless of which shell mode is excited, and for both cantilever and freely supported ends. The liquid mode excited depends on the excitational and, therefore, shell response conditions, as indicated by the four subregions corresponding to the first four symmetric liquid modes. In the 7.62-centimeter-diameter cylinder studied, these modes occurred with largest liquid response at 5.1, 7.5, 9.4, and 11.7 cps, respectively.

A theoretical analysis of the nonlinear coupling described above has recently been

completed by Chu and Kana (ref. 9.36). This report was only being written during the final preparation of this monograph; therefore, the details could not be presented here. Also, a somewhat similar coupling of liquid surface motions with a vibrating rectangular tank has been described in section 8.3 of chapter 8.

#### 9.4 COUPLING OF PROPELLANT MOTION AND ELASTIC TANK BOTTOM

##### General Discussion

In many respects, it appears plausible that the interaction between propellants and elastic bottom motion should display the same general characteristics as that between the propellants and the breathing vibrations of the tank walls. In fact, vibrations of the elastic bottom correspond to breathing vibrations of the tank. Hence, it might be conjectured that all of the general discussion of section 9.3 concerning the interactions of the propellants and the elastic walls also apply to interactions of the propellant with an elastic bottom. Of course, the geometry of the bottom, as well as the presence of drain lines and manifolds attached to an actual vehicle bottom, would considerably complicate the analysis of the coupled bottom vibrations.

Apparently, only few investigations of elastic bottom behavior have been performed, and even those are rather simple in nature, in that they consider only a flat bottom in an otherwise rigid tank. However, the results of these studies still give valuable qualitative indications of what behavior might be expected for the more practical, more complicated geometric shapes and, therefore, we shall summarize them briefly here.

##### Coupling With Free Surface

Bhuta and Koval have investigated the interaction between the liquid surface oscillations in a rigid cylindrical tank having a thin, flat membrane bottom (ref. 9.37), and having a thin, flat plate bottom (ref. 9.38). The two analyses are virtually identical except, of course, that the thin circular membrane equation governs the bottom motion in the first case, while the thin

circular plate equation governs the bottom motion in the second.

The fluid is considered incompressible and ideal so that it is governed by Laplace's equation, while the boundary conditions at the tank walls are the same as for a completely rigid tank. At the fluid surface, the boundary condition is equation (9.7), while at the tank bottom the normal velocity of the liquid must equal that of the vibrating bottom. In either the case of the thin membrane bottom or the thin flat plate bottom, the solution for the natural vibrational frequencies of the coupled boundary value problem results in an infinite order determinant for the coupled natural frequencies.

For the membrane bottom (ref. 9.37), numerical solutions were obtained for the first several symmetric coupled frequencies by truncating the determinant at the eighth order. The resulting modes might be called the first several coupled liquid surface modes. Depending on the value of the membrane tension, the coupled membrane modes would occur at higher frequencies and could not normally be obtained from only an eighth-order truncation of the frequency determinant. Figure 9.32 shows the general behavior that is predicted by the numerical results for the first two symmetrical sloshing modes of the liquid surface at a rather shallow liquid depth. The examples are for

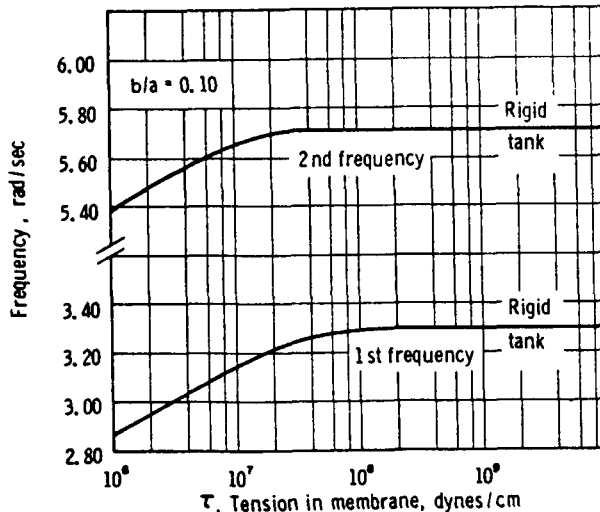


FIGURE 9.32.—Influence of bottom elasticity on surface modes (ref. 9.37).

water in a 2.54-meter-diameter tank. Additional numerical results are shown in tables 9.2 and 9.3 in which the natural frequencies in radians per second are given for the first several symmetric modes, and comparison with several experimental values for water in a 7.62-centimeter-diameter tank is given in table 9.4.

From the numerical examples for this case, it can be concluded that the bottom elasticity tends to lower the liquid surface natural frequencies below their respective values in a

rigid tank, but the effect is rather small. It can further be seen that the coupling effect diminishes for increasing liquid depth, and becomes negligible for  $b/d > \frac{1}{2}$ . Finally, it may be noted that an increase in liquid density tends to raise the coupled sloshing frequencies very slightly. It must be remembered that in a rigid tank the sloshing frequencies are independent of the liquid density. Similar conclusions are found for the case of the thin, flat plate bottom in reference 9.38.

TABLE 9.2.—Natural Frequencies in a Rigid Tank With an Elastic Membrane Bottom

[Ref. 9.37]

$\{\rho_L = 1.00 \text{ gm/cc}\}$

(a)  $b/a = 0.10$

Mode number	Natural frequency, rad/sec, for $\tau$ , dyne/cm—						
	$1.75 \times 10^6$	$8.75 \times 10^6$	$1.75 \times 10^7$	$4.37 \times 10^7$	$8.75 \times 10^7$	$1.75 \times 10^8$	Rigid tank
1-----	2.938	3.140	3.207	3.254	3.271	3.279	3.288
2-----	5.443	5.658	5.693	5.713	5.717	5.718	5.726
3-----	7.632	7.743	7.757	7.764	7.768	7.771	7.770

(b)  $b/a = 0.25$

(c)  $b/a = 0.50$

TABLE 9.3.—*Natural Frequencies in a Rigid Tank With Elastic Membrane Bottom for Different Liquid Densities (Ref. 9.37)*

[ $\tau = 4.37 \times 10^4$  dyne/cm;  $b/a = 0.50$ ]

Mode number	Natural frequency, rad/sec	
	$\rho_L = 0.0378$ gram/cc	$\rho_L = 0.505$ gram/cc
1-----	5. 237	5. 321
2-----	7. 352	7. 353
3-----	8. 862	8. 862
4-----	10. 142	10. 142

The influence of the liquid on the coupled bottom breathing modes was not discussed in reference 9.37 or 9.38, perhaps because these modes would occur at higher frequencies depending on the bottom flexibility, and a higher order frequency determinant would be necessary to predict them. However, judging by the influence of only the apparent mass effects of the liquid on a breathing shell, it is anticipated that the coupled bottom breathing modes would occur at considerably lower frequencies than their respective empty tank values. Such modes would have a very important effect on the pressure distribution in the tank.

A formulation of the problem of forced longitudinal vibration of liquid in a rigid tank with a thin membrane bottom has been performed by Tong and Fung (ref. 9.39). This problem differs from those above in that the stability of small motions of the liquid surface must be considered, and any practical fuel sloshing that results will be  $\frac{1}{2}$ -subharmonic in nature. The analysis, in effect, investigates how bottom elasticity affects the onset of the  $\frac{1}{2}$ -subharmonic sloshing that has been discussed in chapter 8. Since solutions and numerical computations are not yet available from this analysis, no further discussion can be presented. An approximate analysis of forced longitudinal vibrations of liquid in a flexible tank, including the effects of a flexible bottom, has been carried out by Bleich (ref.

9.22). The effect on pressure distribution was obtained by considering the volume changes of the flexible bottom, but the free surface kinematic condition was neglected. The obtained approximate results are valid only for frequencies well below the resonance of the tank bottom. Finally, the effects of a flexible bottom have been included in the investigation of Palmer and Asher (ref. 9.23).

## 9.5 EFFECTS OF THE ELASTIC STRUCTURE ON VEHICLE STABILITY AND CONTROL<sup>1</sup>

### General Discussion

With the increasing length of space vehicles, the significant fundamental bending frequencies of the structure continually become lower. The close grouping of control, propellant, and bending frequencies creates acute problems because of the interaction of these various modes with propellant sloshing. This indicates that an additional danger of instability resulting from propellant sloshing due to the elastic behavior of the vehicle is present, which, of course, becomes more critical because of the low bending frequencies and the overall low structural damping. It is possible to reduce these interactions by various techniques (refs. 9.40 and 9.41), as follows:

(1) Proper location of the sensors, which minimizes the amplitude of the input signal. This means that an attitude gyroscope should be located at an antinode; however, this can be accomplished for only one bending mode, and even then, is not exactly possible because of the tankage of the vehicle, and the varying frequencies and mode shapes during flight. Generally, the fundamental bending mode is the most critical mode and is usually phase stabilized, while higher modes are strongly attenuated.

(2) The input from the sensors to the control system should have small gains at the natural frequencies. This can be accomplished by filters and shaping networks, if the frequencies

<sup>1</sup> This section was written by Helmut F. Bauer.

TABLE 9.4.—*Comparison of the Fundamental Theoretical and Experimental Frequencies for Rigid Bottom and Flexible Bottom Tanks (Ref. 9.37)*  
 [ $\rho_L = 1.00$  gram/cc;  $\tau = 6.58 \times 10^4$  dyne/cm]

$b/a$	Natural frequency, rad/sec				Percent change in frequency	
	Rigid tank		Flexible bottom tank			
	Theory	Experiment	Theory	Experiment	Theory	Experiment
0.50-----	4.93	5.27	4.90	5.23	0.61	0.75
1.00-----	5.00	5.43	4.98	5.40	.40	.55

are not too close to the control frequency. At the present time, the most important point is the provision of appropriate filters.

(3) Proper location of heavy propellants, tank geometry, proper gain settings, and baffles.

As has been seen in chapter 7, the stability characteristics of the vehicle with respect to propellant sloshing is influenced by the tank geometry, which determines the amount of sloshing propellant, its location in the tank, and its natural frequencies. Subdivision of tanks into small compartments by radial walls offers great advantage in the reduction of sloshing masses, as has been discussed in chapter 2; furthermore, this increases the eigenfrequency of the propellant slightly, thus shifting it away from the control frequency but, unfortunately, a little closer to the elastic frequencies. Although the latter effect makes the situation with respect to frequency slightly less favorable, the main dynamic result is governed by the considerably reduced sloshing mass.

Stability is also strongly influenced by the tank location; that is, the slosh mass location with respect to the vehicle center of mass. Proper gain settings and filters in the control system providing appropriate phases also exhibit a tremendous influence upon the stability. A parametric study is usually made to investigate the possibility of eliminating instabilities resulting from propellant sloshing and indicates the amount of damping necessary in the tanks

to maintain overall vehicle stability. This is achieved by determining stability boundaries in terms of the amount of damping of the propellant required in the tank for various locations along the vehicle. We shall present an example of such an analysis.

For simplification in the treatment of the equations of motion of a space vehicle, an equivalent (analytical) mechanical model describing the motion of the propellant in the tank is used. (See ch. 6.) Only the first bending mode will be considered and propellant sloshing in only one tank is to be included. All effects due to aerodynamics, inertia, and compliance of the swivel engine are neglected. It is furthermore assumed that only the amount  $F_2$  of the total thrust  $F = F_1 + F_2$  is available for control purposes. Previous investigations of a rigid space vehicle with a simple attitude control, as described in chapter 7, showed the possibility of a significant danger zone where instability can occur if the tank is not properly baffled. This danger zone is essentially between the center of gravity and the center of instantaneous rotation. This approximation is only valid for values  $1/a_0\nu_s^2 < 1$ , where  $\nu_s = \omega_s/\omega_c$  is the ratio of sloshing to the control frequency. For most practical cases, the center of instantaneous rotation for a rigid vehicle marks approximately the location where the danger zone starts. The other intersection point of the stability boundary with the  $\xi$ -axis, however, is more critical to changes in the parameters. If the slosh frequency is below the

control frequency (natural frequency of pitch mode), the danger zone increases aft of the center of gravity, and more effective baffling is required for stability. Control damping increase in the subcritical region requires increased baffling, while control damping increase in the supercritical region requires less baffling.

Decreasing the gain value,  $a_0$ , at constant control frequency, increases the danger zone slightly to the aft of the vehicle and requires more effective baffling. A decrease in the baffling requirement can be obtained by increasing the slosh frequency by a change of tank geometry, as discussed previously. Here, it can already be seen that the difficulty in providing control of forces resulting from propellant sloshing in the tank of a rigid space vehicle can be reduced not only by baffling but also by the proper choice of the tank form, and by proper selection of the control system. This, of course, is even more so if the influence of the elastic behavior of the space vehicle is considered. All the large space vehicles exhibit very low bending frequencies, which makes the inclusion of at least the first bending mode necessary.

#### **Equations of Motion and Control Equation**

To obtain some general knowledge of the influence of the various parameters and to determine the amount of damping in the propellant tank necessary to obtain stability, the interaction of translation, pitching, and bending motions and propellant sloshing was investigated (ref. 40). Only the first sloshing mode is considered in the analysis because the effect of higher modes is generally negligible for circular cylindrical tanks.<sup>2</sup>

---

<sup>2</sup> The sloshing mass of the second mode is less than 3 percent of the sloshing mass of the first mode for a liquid in a cylindrical tank with circular cross section. In a quarter-sector tank arrangement, however, the next pronounced sloshing mode exhibits a mass of about 43 percent of that of the lowest one. (See ch. 2.)

The coordinate system (fig. 7.1) has its origin in the center of gravity of the undisturbed space vehicle; that is, when all generalized coordinates are zero. The accelerated coordinate system is replaced by an inertial system such that the vehicle is considered in an equivalent gravitational field. The  $x$ -coordinate of this inertial coordinate system is tangent to the standard flight path. Furthermore, acceleration in the direction of the trajectory, mass, moment of inertia, etc., are considered constant.

The equations of motion have already been presented in chapter 7. Considering translatory motion, equation (7.16); pitching motion, equation (7.17); the first mode of the propellant motion in three containers, equation (7.20), for  $\lambda=1, 2, 3$ ;  $n=1$ ; one bending mode, equation (7.22), for  $v=1$ ; and a simplified control equation of the form

$$p_2 \ddot{\beta} + p_1 \dot{\beta} + \beta = a_0 \phi_i + a_1 \dot{\phi}_i \quad (9.15)$$

one obtains (with the usual assumption for solution of the form  $e^{s\omega_c t}$ , where  $s\omega_c$  is the complex frequency,  $s\omega_c = \sigma + i\omega$ ) homogeneous algebraic equations of which the coefficient determinant must vanish in order that a nontrivial solution exists.

#### **Stability Boundaries**

The main results of the influence of the interaction of propellant sloshing, bending vibrations, and the control system upon the stability of the space vehicle can be obtained if we treat the equations of motion and the propellant as being free to oscillate in three tanks. This seems to be sufficient since, usually, even in large space vehicles, only three of the tanks will exhibit large sloshing masses. The sloshing propellant masses of tanks with light propellants and tanks of smaller diameter can be neglected. The characteristic polynomial in  $s$  is

$$\sum_{j=0}^{12} B_j s^j = 0 \quad (9.16)$$

and the coefficient determinant is

$$\begin{vmatrix} \omega_c^2 s^2 & -g & \mu_1 s^2 \omega_c^2 & \mu_2 s^2 \omega_c^2 & \mu_3 s^2 \omega_c^2 & g Y'_E & -\lambda g \\ 0 & s^2 \omega_c^2 & -\frac{\mu_1}{k_r^2} (x_1 s^2 \omega_c^2 + g) & -\frac{\mu_2}{k_r^2} (x_2 s^2 \omega_c^2 + g) & -\frac{\mu_3}{k_r^2} (x_3 s^2 \omega_c^2 + g) & -\frac{g}{k_r^2} (x_E Y'_E - Y_E) & \frac{\lambda x_E g}{k_r^2} \\ \omega_c^2 s^2 - (x_1 s^2 \omega_c^2 + g) & s^2 \omega_c^2 + 2\gamma_1 \omega_1 \omega_c s + \omega_1^2 & 0 & 0 & 0 & (s^2 \omega_c^2 Y_1 + g Y'_1) & 0 \\ \omega_c^2 s^2 - (x_2 s^2 \omega_c^2 + g) & 0 & s^2 \omega_c^2 + 2\gamma_2 \omega_2 \omega_c s + \omega_2^2 & 0 & 0 & (s^2 \omega_c^2 Y_2 + g Y'_2) & 0 \\ \omega_c^2 s^2 - (x_3 s^2 \omega_c^2 + g) & 0 & 0 & s^2 \omega_c^2 + 2\gamma_3 \omega_3 \omega_c s + \omega_3^2 & (s^2 \omega_c^2 Y_3 + g Y'_3) & 0 & 0 \\ 0 & 0 & \frac{\mu_1}{M_B/m_0} (Y_1 s^2 \omega_c^2 + g Y'_1) & \frac{\mu_2}{M_B/m_0} (Y_2 s^2 \omega_c^2 + g Y'_2) & \frac{\mu_3}{M_B/m_0} (Y_3 s^2 \omega_c^2 + g Y'_3) & s^2 \omega_c^2 + \omega_B \omega_c g_B s + \omega_B^2 & -\frac{\lambda g Y_E}{M_B/m_0} \\ 0 & -(a_0 + a_1 s \omega_c) & 0 & 0 & 0 & Y'_G (a_0 + a_1 s \omega_c) & s^2 \omega_c^2 p_2 + s \omega_c p_1 + 1 \end{vmatrix} = 0 \quad (9.17)$$

The coefficients  $B_i$  depend on the parameters:

$\mu_i = m_i/m_0$ =ratios of modal mass of liquid over total mass of space vehicle

$\xi_c$ =control damping

$\nu_s = \omega_s/\omega_c$ =frequency ratio of undamped propellant frequency to undamped control frequency

$\gamma_s$ =damping factor of propellant

$\xi_s = x_s/k_r$ =ratio of the coordinate at the location of the modal mass of the propellant to the radius of gyration of the space vehicle

$Y, Y'$ =displacement and slope at the first bending mode. (Subscript 1, 2, 3 means at location of sloshing masses, subscript  $G$  means at location of gyroscope, and subscript  $E$  means at swivel point of the engines.)

$M_B/m_0$ =generalized mass ratio

$\xi_E = x_E/k_r$ =ratio of distance of swivel point of engines from center of gravity to radius of gyration

$\xi_1, \xi_2$ =distance between rear tank and upper tanks, respectively

$a_0$ =gain value of attitude control system  
 $g_B$ =structural damping

$p_1, p_2$ =phase-lag coefficients

The stability boundaries are characterized by the roots, one of which, the real part, will be zero, while the others are stable roots. With the Hurwitz theorem for a stability polynomial of  $n$ th degree (ref. 9.42), this is

$$B_n = 0 \text{ and } H_{n-1} = 0$$

where  $H_{n-1}$  represents the Hurwitz determinant of the form

$$H_{n-1} = \begin{vmatrix} B_1 & B_3 & B_5 & \dots \\ B_0 & B_2 & B_4 & \dots \\ 0 & B_1 & B_3 & \dots \\ 0 & B_0 & B_2 & \dots \\ \dots & \dots & \dots & \dots \end{vmatrix} \quad (n-1) \text{ lines and columns}$$

Representing the stability boundaries in the  $(\xi_s, \gamma_s)$ -plane, the Hurwitz determinant  $H_{11}=0$  results in

$$\sum_{j=0}^{11} C_j(\xi_s) \gamma_s^j = 0$$

where the functions  $C_j(\xi_s)$  are polynomials in  $\xi_s$ . The stability boundary for the undamped liquid is  $C_0(\xi_s)=0$ , representing intersection

points with the  $\xi_s$ -axis. For all points  $(\xi_s, \gamma_s)$  above the stability boundary, the system is stable. Because  $B_n=0$ , the stability boundary is limited both at the left and at the right. From  $B_{12}=0$ , it is recognized that the corresponding stability boundaries to the right and left are given in the form of straight lines perpendicular to the  $\xi_s$ -axis. These boundaries, however, play no practical role. Substitution

of  $\xi_s = \gamma_s = 0$  into the Hurwitz determinants determines whether the origin is in the stable or unstable region.

A necessary and sufficient condition for stability is that (ref. 9.43)

(1) The coefficients  $B_n, B_{n-1}, B_{n-2}, \dots > 0$

$$\begin{cases} B_1, B_0 > 0 & \text{if } n \text{ is even} \\ B_0 > 0 & \text{if } n \text{ is odd} \end{cases}$$

(2) The Hurwitz determinants  $H_{n-1}, H_{n-2}, \dots > 0$

$$\begin{cases} H_3 > 0 & \text{if } n \text{ is even} \\ H_2 > 0 & \text{if } n \text{ is odd} \end{cases}$$

To obtain the basic results of the influence of the propellant sloshing on the stability of the flexible vehicle, the propellant is considered free to oscillate in only one container. This is done by removing the fourth and fifth lines and column from determinant equation (9.17). This yields the characteristic polynomial in  $s$

$$\sum_{j=0}^8 B_j s^j = 0$$

### Numerical Results

In the numerical evaluation, the distance of the swivel point from the center of gravity was chosen as  $x_B = 12.5$  meters and the radius of gyration as  $k_s = 12.5$  meters. The total length of the vehicle is 57.5 meters. Furthermore, half of the thrust has been considered available for control purposes.

For an elastic vehicle without propellant sloshing, it can easily be shown that for a gyroscope location exhibiting positive bending mode slope, the vehicle is essentially stable, if proper structural damping is present and the phase-lag coefficient  $p_2$  is smaller than 0.025. The various parameters have essentially the following effects. Increasing the control frequency enhances the stability in the domain of positive bending mode slope at the gyroscope location, and enlarges the instability in the unstable area; i.e., for a gyro location exhibiting negative slope of the bending mode. This means that more structural damping would be necessary if the gyroscope is situated at a location on the vehicle exhibiting negative bending mode slope.

A similar result is obtained for increasing control system damping. An increase in the generalized mass and bending frequency shows the opposite effect. The larger the bending frequency, the more the system becomes independent of the location of the position gyroscope and structural damping. A strong effect is experienced by changing the phase-lag coefficients  $p_1$  and  $p_2$ . In the unstable area, an increase in  $p_1$  yields an increase in stability. For positive bending slope, the usual structural damping is sufficient to guarantee stability in the practical range of  $0 < p_1 < 0.2$ . The situation is quite different with regard to the phase-lag coefficient  $p_2$ , increase of which exhibits decreasing stability and limited possibilities for improvements in the location of the gyro. For certain values, the gyro can only be located within a short range of small positive bending slope. For  $p_2 > 0.006$ , no gyroscope location can be found that will yield stability within the practical range of structural damping of the space vehicle.

For an elastic space vehicle with a simple control system having no phase-lag coefficients (eq. (7.26) with  $g_2 = 0$  and  $p_1 = p_2 = 0$ ), it can be seen that the danger zone for instability of the vehicle is (compared to a rigid vehicle) enlarged to both sides of the center of gravity, and the center of instantaneous rotation. This requires locally more (about three times more) damping than for a rigid space vehicle (ref. 9.44). For increasing modal mass,  $\mu$ , more damping is needed in the danger zone to guarantee stability of the vehicle, as can be seen from figure 9.33. The vehicle is stable if a container of large modal sloshing mass is located outside the danger zone. The influence of decreasing frequency ratios,  $\nu_s$ , of the propellant natural frequency,  $\omega_s$ , to the control frequency,  $\omega_c$ , is also exhibited in figure 9.33. For  $\nu_s > 1$  and increasing, the stability in a decreasing danger zone is enhanced. The approach of the control frequency toward the propellant frequency, or vice versa, not only increases the danger zone but also requires more damping to maintain stability. For  $\nu_s > 5$ , the wall friction ( $\gamma_s = 0.01$ ) is already sufficient to prevent instability.

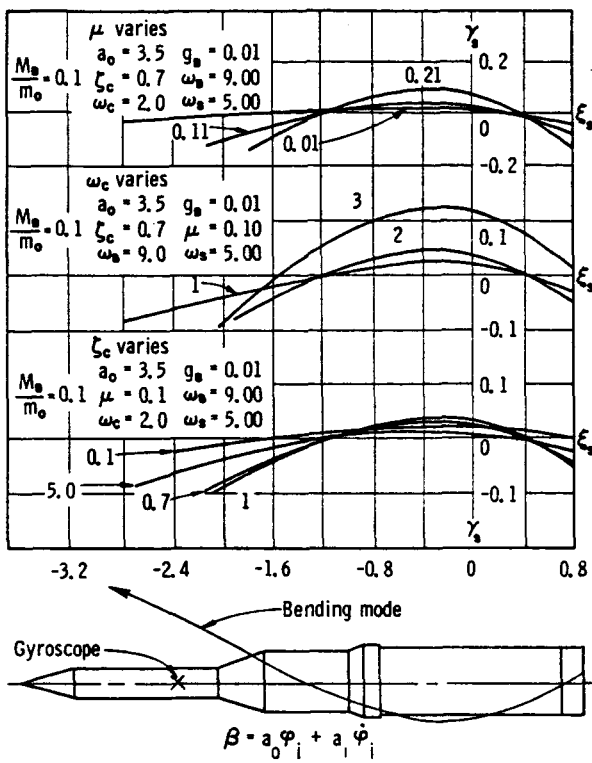


FIGURE 9.33.—Stability boundaries for an elastic vehicle with a simple control system, varying modal mass, control frequency, and control damping.

The change of the control damping,  $\zeta_c$ , indicates that, for increasing subcritical damping,  $\zeta_c < 1$ , the stability in the danger zone will be diminished, whereas, for increased supercritical damping,  $\zeta_c > 1$ , the stability is enhanced. Furthermore, the danger zone decreases for increasing damping.

The influence of the control factor,  $a_0$ , of the attitude control system is considerably more pronounced than in the case of a rigid vehicle. With decreasing gain values, the danger zone increases tremendously over almost the complete vehicle length and demands considerable damping in the tanks to maintain stability (fig. 9.34).

The generalized mass of the space vehicle also has some influence, as shown in figure 9.34. For increasing generalized mass, the trend exhibits increased stability. This means that uniform vehicles ( $M_B/m_0 = 0.25$ ) are more stable than nonuniform ones; it furthermore indicates that when the propellant is nearly exhausted, stability will be enhanced since a

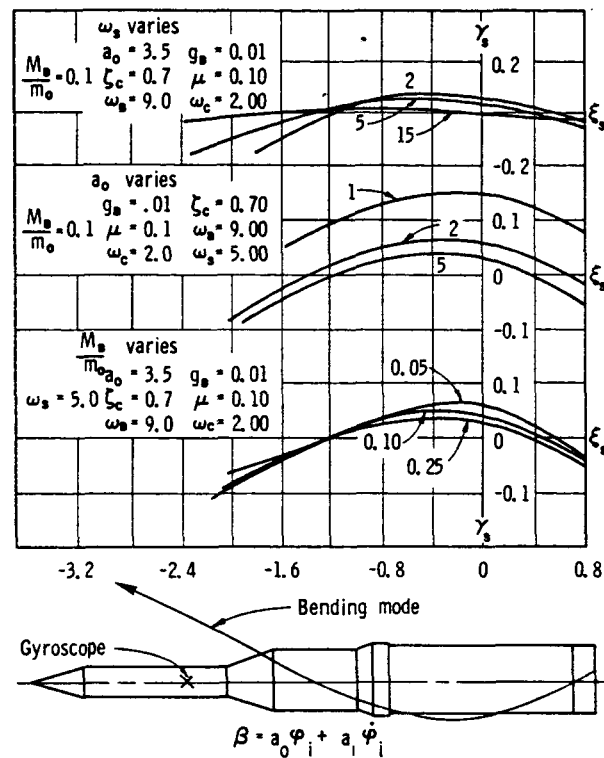


FIGURE 9.34.—Stability boundaries for an elastic vehicle with a simple control system, varying slosh frequency, gain factor, and generalized mass ratio.

nonuniform vehicle approaches more and more the state of a uniform beam as flight time continues.

One major factor in the stability of elastic space vehicles is the influence of the bending frequency. For large bending frequencies, of course, the stability is enhanced and approaches the values for a rigid vehicle. With decreasing bending frequency, the stability decreases and additional baffling is required (fig. 9.35).

The slope of the bending mode at the location of the position gyroscope should preferably be chosen as positive, that is, the gyro is located aft of the bending loop; however, this is practically impossible. Usually, the gyroscope is located in front of the bending loop, and the slope at its location is negative. It can be seen that, for increasing negative slope of the bending mode at the gyro location, the danger zone is increased and the stability is decreased. The further the position gyro is moved from the bending loop toward the nose of the vehicle, the more damping is required, and

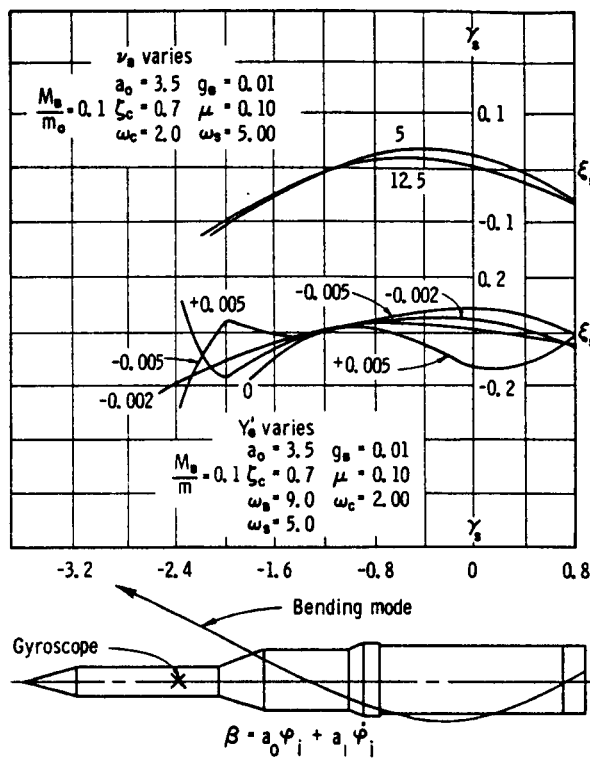


FIGURE 9.35.—Stability boundaries for an elastic vehicle with a simple control system, varying bending frequency, and mode shape.

the larger the area becomes where baffles have to be introduced to maintain stability.

With twice the bending displacement, the stability decreases, the danger zone increases, and a little more than twice the amount of baffling is required to obtain stability.

For an elastic space vehicle having a simple control system with phase-lag coefficients  $p_1$  and  $p_2$ , the situation with respect to propellant sloshing is quite enhanced for proper control gains.<sup>3</sup>

The phase-lag coefficients have been chosen for this example to be  $p_1=0.05$  second and

<sup>3</sup> It may be noted that the simple control system treated here is by no means close to those customarily employed in actual vehicles, but was selected for reasons of simplicity in this treatment. Yet, even such a simple system already exhibits a tremendous improvement for the idealized vehicle having no engine compliances, etc. The proper description of the real control system, taking into account lead network, filters, and actuator system, would be of much higher order and would make the numerical evaluation very unwieldy.

$p_2=0.00084$  second squared. Two main cases have been investigated. The first one considers the position gyroscope in a location where the bending mode exhibits positive slope, which would be a favorable location for stability. In the second case, the gyroscope is located (as is in most space vehicles) in the forward part of the vehicle, an unfavorable location by necessity where the bending mode slope is negative.

Figures 9.36 through 9.38 show the results for the first case of gyro location at positive bending mode slope. The danger zone is considerably decreased, and in most cases shifted toward the vicinity of the center of instantaneous rotation. With increasing sloshing mass, the zone increases slightly, shifts slowly farther toward the nose of the space vehicle, and requires more damping.

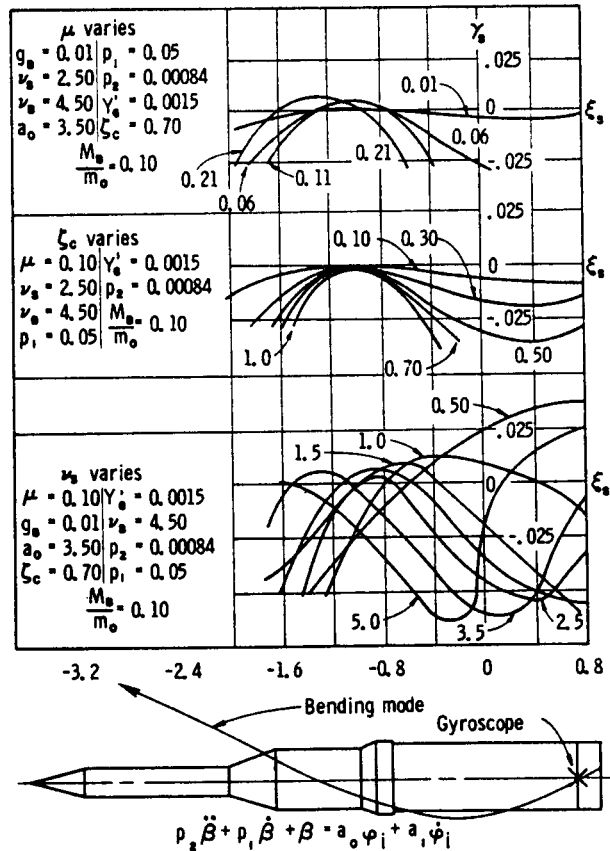


FIGURE 9.36.—Stability boundaries for an elastic vehicle with an idealized control system (positive bending slope), varying modal mass, control damping, and slosh frequency.

The change of the control damping,  $\zeta_c$ , indicates that for increasing subcritical damping,  $\zeta_c < 1$ , the danger zone decreases and the stability in it is intensified. The influence of decreasing the frequency ratio,  $\nu_s$ , exhibits the following behavior: if the two frequencies approach each other, the danger zone increases toward the end of the vehicle and requires more local damping; as the sloshing frequency approaches the bending frequency, the danger zone appears at the tail of the vehicle and requires more baffling to maintain stability. The result can be summarized by stating that increasing control frequency increases the danger zone, which when near the bending frequency will cover the entire vehicle.

Increasing slosh frequency,  $\omega_s < \omega_B$ , first decreases the danger zone to a small region about the center of instantaneous rotation, and then creates a new danger zone at the tail of the

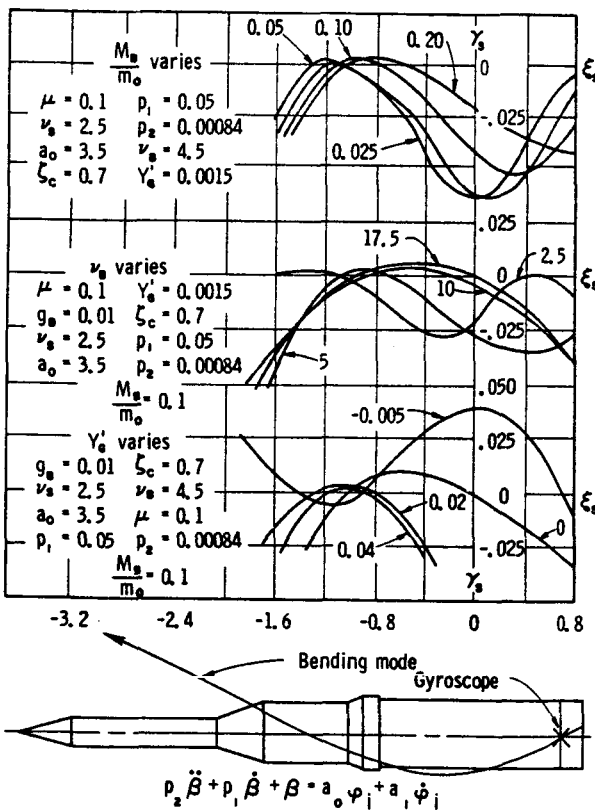


FIGURE 9.37.—Stability boundaries for an elastic vehicle with an idealized control system (positive bending slope), varying generalized mass ratio, bending frequency, and mode shape.

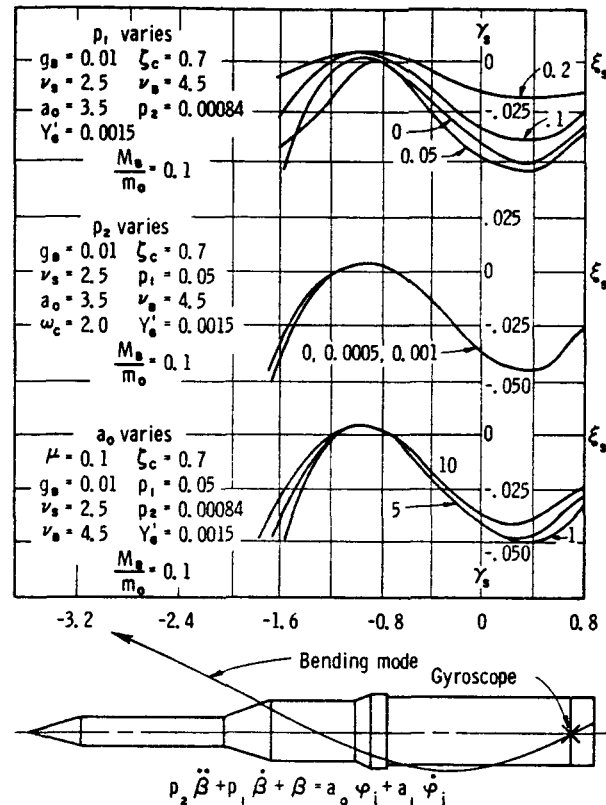


FIGURE 9.38.—Stability boundaries for an elastic vehicle with an idealized control system (positive bending), varying control system gain, and lag factor.

vehicle as soon as it approaches the bending frequency. The change of the gain value,  $a_0$ , of the attitude control system exhibits hardly any influence. Increasing bending frequency,  $\omega_B$ , shifts the danger zone from the front part of the vehicle toward a location between the center of gravity and the center of instantaneous rotation, which is the danger zone of a rigid vehicle (fig. 9.37).

A very important influence upon the stability of a space vehicle is exerted by the location of the position gyro. (See fig. 9.38.) Shifting the gyro from the tail of the vehicle toward the nose shows a continuous decrease in stability and requires increasing baffling to maintain stability. The danger zone shifts with increasing magnitude toward the rear of the vehicle. Location of the gyroscope in the region of positive bending mode slope is therefore desirable; however, because of the unavailability of a location and the gyro's use for many stages,

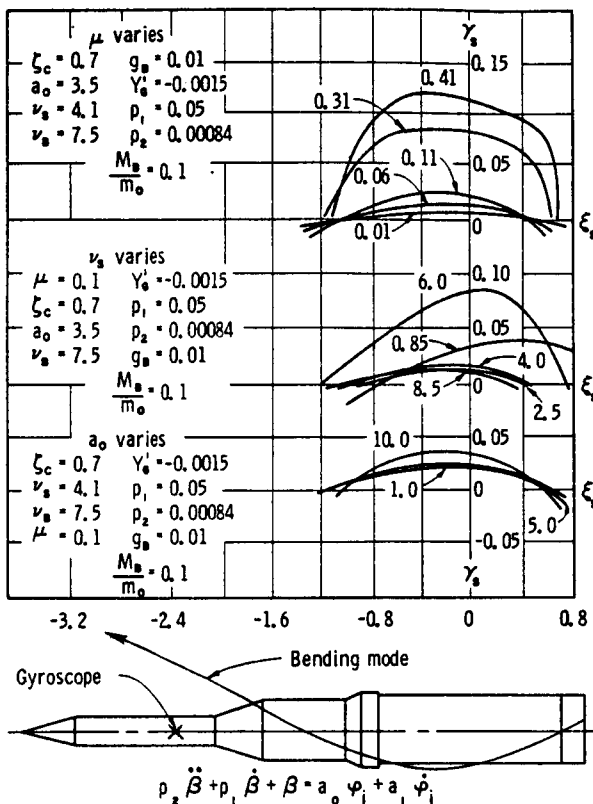


FIGURE 9.39.—Stability boundaries for an elastic vehicle with an idealized control system (negative bending slope), varying mass ratio, slosh frequency, and gain factor.

this cannot be accomplished, so that filters and phase-shaping networks have to provide the necessary lags. The change of the phase-lag coefficient  $p_1$  for decreasing magnitude shows a decrease in the danger zone and an enhanced stability. A small change of the phase-lag coefficient  $p_2$  (for a gyroscope location in the rear of the vehicle) does not exhibit any appreciable influence.

The results of the second case of a gyro location at a negative bending mode slope is exhibited in figures 9.39 through 9.41. The danger zone is considerably larger than in the case of a gyroscope location at positive slope of the bending mode. It is even larger than in the rigid body case. The danger zone is located aft of the center of instantaneous rotation and extends nearly to the end of the vehicle. With increasing sloshing mass, more damping is re-

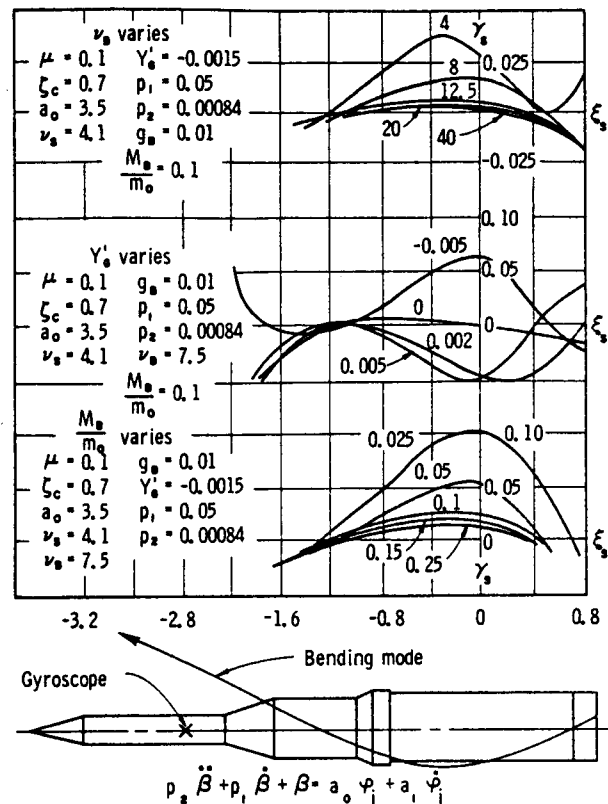


FIGURE 9.40.—Stability boundaries for an elastic vehicle with an idealized control system (negative bending slope), varying bending frequency, mode shape, and generalized mass ratio.

quired in this zone; for smaller sloshing masses, it also extends toward the nose of the space vehicle.

The change of the frequency ratio,  $\nu_s$ , exhibits the following behavior: if the control and sloshing frequencies approach each other, the danger zone increases toward the end of the vehicle and requires more local damping; further increase of the sloshing frequency (or decrease of the control frequency) enhances stability, and thus decreases the danger zone and locally required damping in the propellant container; approaching the vehicle bending frequency exhibits a strong increase in the requirement of damping which, for a further increase of  $\nu_s$ , is again considerably reduced for  $\nu_s > 8.5$ , and a reduction of the danger zone is also noticed. Maintaining control, sloshing, and bending frequencies well separated yields

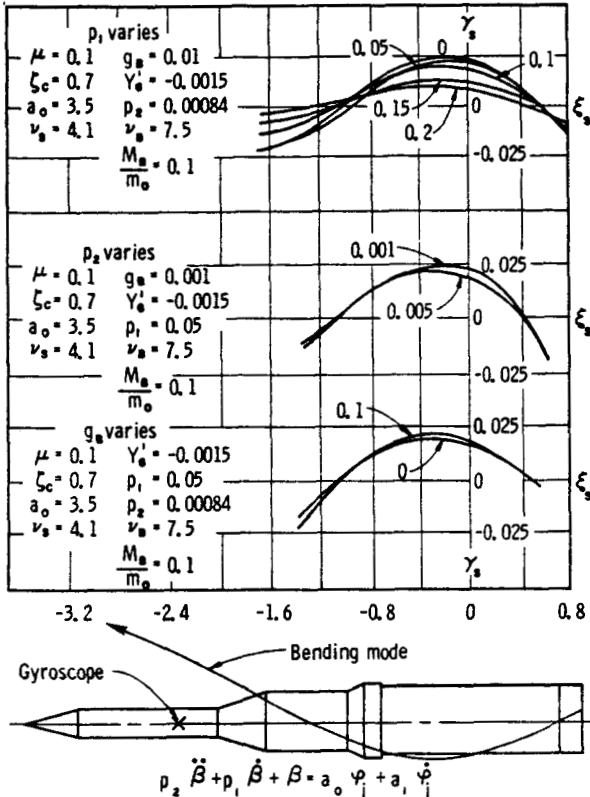


FIGURE 9.41.—Stability boundaries for an elastic vehicle with an idealized control system (negative bending slope), varying control system parameter, and structural damping.

a small baffling requirement to maintain vehicle stability. The change of the gain value,  $a_0$ , of the attitude control system exhibits no change of the danger zone and only a slight increase of local damping requirements for increasing magnitude.

Figure 9.40 shows the influence of increasing bending frequency. For low bending frequency, of course, the danger zone is large and

nearly covers the vehicle, past the center of instantaneous rotation, with large local damping requirements. With increasing bending frequency the danger zone reduces to that of the rigid body case and diminishes the local baffling requirements by a factor of about 7.

The influence of the location of the position gyroscope is again shown and exhibits essentially the same character as in the previous case. Positive slope of the bending mode at the location of the position gyro is very favorable for the stability of the vehicle. There is only a very small danger zone around the center of instantaneous rotation where the wall friction of the propellant in the container is already sufficient to maintain stability of the vehicle. For a gyro location exhibiting zero slope of the bending mode, the baffling requirements are about the same as those of the rigid body case, while for a location of the gyro on the vehicle with negative bending mode slope, the danger zone is enlarged from the center of instantaneous rotation toward the rear of the vehicle. There is also an additional danger zone in front of the center of instantaneous rotation. Both zones require large local damping. For increasing magnitude, the change of the generalized mass ratio,  $M_B/m_0$ , shows a slowly decreasing danger zone and decreasing local baffle requirements.

Figure 9.41 shows the effects of change of the phase-lag coefficients. The increase of  $p_1$  at first shows a slight decrease in stability but improves stability at a further increase. The slight variation of the phase-lag coefficient  $p_2$  does not exhibit much change in stability. Finally, the increase of structural damping,  $g_B$ , slightly improves the stability of the space vehicle with respect to propellant sloshing.

## APPENDIX

The kinetic and potential energy coefficients,  $m_{it}$ , and  $k_{it}$ , for the tank, subject to coupled bending and liquid oscillations as shown in figure 9.1, are given below. These are essentially the same as those given by Miles (ref. 9.5). Following Miles,  $i=3$  corresponds to a

bending displacement along  $\theta=0$  and  $i=s+3$  corresponds to a displacement of the free liquid surface from a plane normal to the axis of the tank. The bars over the coefficients indicate normalization by the total liquid mass,  $M=\pi a^2 b \rho_L$ :

$$\begin{aligned}
\bar{m}_{3,3} &= F_0^2 + \frac{1}{2} \sum_{s=1}^{\infty} \psi_s F_s^2 + \frac{2a^2}{b} \sum_{s=1}^{\infty} \frac{f'(-\frac{b}{2}) x_s(-\frac{b}{2}) - f'(\frac{b}{2}) x_s(\frac{b}{2})}{\beta_s^2 - 1} \\
&\quad + \frac{1}{8} \frac{2a^2}{b} \left[ f'(-\frac{b}{2}) - f'(\frac{b}{2}) \right] F_0 + \frac{b}{\pi^2} \sum_{s=1}^{\infty} \frac{1-\psi_s}{s^2} \left[ (-1)^{s+1} f'(\frac{b}{2}) + f'(-\frac{b}{2}) \right] F_s \\
&\quad + \frac{2a^3}{b} \sum_{s=1}^{\infty} \frac{\operatorname{csch}(\frac{\beta_s b}{a})}{\beta_s^3 (\beta_s^2 - 1)} \left\{ \left[ f'^2(\frac{b}{2}) + f'^2(-\frac{b}{2}) \right] \cosh(\frac{\beta_s b}{a}) - 2f'(\frac{b}{2}) f'(-\frac{b}{2}) \right\} \\
\bar{m}_{3,s+3} &= \frac{a}{b} x_s(\frac{b}{2}) - \frac{a^2}{b \beta_s^3} \operatorname{csch}(\frac{\beta_s b}{a}) \left[ f'(\frac{b}{2}) \cosh(\frac{\beta_s b}{a}) - f'(-\frac{b}{2}) \right] \\
\bar{m}_{s+3,s+3} &= \frac{a}{2b} \frac{\beta_s^2 - 1}{\beta_s^3} \coth(\frac{\beta_s b}{a}) \\
\bar{m}_s &= \frac{M_s}{M} \left[ \bar{f}^2(z') + \frac{a^2}{2} \bar{f}'^2(z') \right]^* \\
\bar{f}^2(z') &= \frac{1}{l} \int_0^l \bar{f}^2(z') dz' \\
\bar{k}_{3,3} &= g \left\{ \frac{a^2}{4b} \left[ f'^2(\frac{b}{2}) - f'^2(-\frac{b}{2}) \right] + \frac{1}{b} \int_{-b/2}^{b/2} z f'^2(z) dz - \frac{1}{2} \int_{z_0}^{b/2} f'^2(z) dz + \frac{1}{2} \int_{-b/2}^{z_0} f'^2(z) dz \right\} \\
\bar{k}_{3,s+3} &= -\frac{ga}{b \beta_s^2} f'(\frac{b}{2})
\end{aligned}$$

The following notation has been used:

$$\begin{aligned}
F_0 &= \frac{1}{b} \int_{-b/2}^{b/2} f(z) dz \\
F_s &= \frac{2}{b} \int_{-b/2}^{b/2} f(z) \cos \left[ \frac{s\pi(z+\frac{b}{2})}{b} \right] dz, \quad s \geq 1 \\
\psi_s &= \frac{I_1(\frac{s\pi a}{b})}{\frac{s\pi a}{b} I_0(\frac{s\pi a}{b}) - I_1(\frac{s\pi a}{b})} \\
x_s(\frac{b}{2}) &= \frac{\operatorname{csch}(\frac{\beta_s b}{a})}{\beta_s a} \int_{-b/2}^{b/2} f(z) \cosh \left[ \frac{\beta_s(z+\frac{b}{2})}{a} \right] dz \\
J'_1(\beta_s) &= 0
\end{aligned}$$

The  $m_{ij}$ ,  $k_{ij}$ , and assumed bending mode shapes for the cantilever tank are given as follows.

\*The second term in the brackets includes the effect of rotary inertia of the tank walls not included in ref. 9.5.  $M$  is the total tank mass.

---

**Cantilever Tank**

$$\begin{aligned}
f(z) &= \left( \frac{z+\frac{b}{2}}{l} \right)^2 = \left( \frac{z'}{l} \right)^2 \\
\bar{m}_{3,3} &= \left( \frac{b}{l} \right)^4 \left[ \frac{1}{45} - \frac{1}{6} \left( \frac{2a}{b} \right)^2 - \frac{7}{384} \left( \frac{2a}{b} \right)^4 \right. \\
&\quad \left. + \frac{16}{\pi^4} \sum_{s=1}^{\infty} \frac{\psi_s}{s^4} + 2 \left( \frac{2a}{b} \right)^3 \sum_{s=1}^{\infty} \frac{\coth(\frac{\beta_s b}{a})}{\beta_s^3 (\beta_s^2 - 1)} \right] \\
\bar{m}_{3,s+3} &= \left( \frac{b}{l} \right)^2 \left[ \frac{1}{2\beta_s^2} \left( \frac{2a}{b} \right) \right. \\
&\quad \left. - \left( \frac{2a}{b} \right)^2 \frac{\coth(\frac{\beta_s b}{a})}{\beta_s^3} + \frac{1}{4\beta_s^4} \left( \frac{2a}{b} \right)^3 \right]
\end{aligned}$$

$$\bar{m}_{s+3,s+3} = \frac{1}{4} \left( \frac{2a}{b} \right) \frac{(\beta_s^2 - 1)}{\beta_s^3} \coth \left( \frac{\beta_s b}{a} \right)$$

$$\bar{m}_s = \frac{2h\rho_s}{b\rho_L} \left[ \frac{1}{5} \left( \frac{l}{b} \right) \left( \frac{b}{a} \right) + \frac{2}{3} \left( \frac{a}{b} \right) \left( \frac{b}{l} \right) \right]$$

$$\bar{k}_{3,3} = \frac{2g}{l} \left[ \left( \frac{b}{2l} \right) \left( \frac{a}{l} \right)^2 - \frac{4}{3} \left( \frac{b}{2l} \right)^3 \right]$$

$$\bar{k}_{3,4+3} = -\frac{2g}{l\beta_s^2} \left( \frac{a}{l} \right)$$

## REFERENCES

- 9.1. BAUER, H. F.: Fluid Oscillations in a Circular Cylindrical Tank Due to Bending of the Tank Wall. Rept. No. DA-TR-3-58, ABMA, Redstone Arsenal, Apr. 1958.
- 9.2. BAUER, H. F.: Damped Fluid Oscillations in a Circular Cylindrical Tank Due to Bending of the Tank Wall. Rept. No. DA-TR-9-58, ABMA, Redstone Arsenal, May 1958.
- 9.3. BAUER, H. F.: Theory of Liquid Sloshing in Compartmented Cylindrical Tanks Due to Bending Excitation. AIAA J., vol. 1, no. 7, July 1963, pp. 1590-1596.
- 9.4. RABINOVICH, F. I.: Concerning the Equations of Elastic Oscillations of Thin-Walled Bars Filled With a Liquid Having a Free Surface. Space Technology Lab, Translation STL-T-RV-19 from Akad. Nauk. SSSR Izvestija O.T.N. Meckhanika i Machinostrojenie, no. 4, 1959.
- 9.5. MILES, J. W.: On the Sloshing of Liquid in a Flexible Tank. J. Appl. Mech. June 1958, pp. 277-283.
- 9.6. LINDHOLM, U. S.; CHU, W. H.; KANA, D. D.; AND ABRAMSON, H. N.: Bending Vibrations of a Circular Cylindrical Shell Containing an Internal Liquid With a Free Surface. AIAA J., vol. 1, no. 9, Sept. 1963, pp. 2092-2099.
- 9.7. HU, W. C. L.: A Survey of the Literature on the Vibrations of Thin Shells. Technical Rept. No. 1, Contract No. NASR-94(06), Southwest Research Institute, June 30, 1964.
- 9.8. ARNOLD, R. N.; AND WARBURTON, G. B.: Flexural Vibrations of the Walls of Thin Cylindrical Shells Having Freely Supported Ends. Proc. Roy. Soc. (London), Ser. A, vol. 197, 1949, p. 238.
- 9.9. LINDHOLM, U. S.; KANA, D. D.; AND ABRAMSON, H. N.: Breathing Vibrations of a Circular Cylindrical Shell With an Internal Liquid. J. Aerospace Sci., vol. 29, no. 9, Sept. 1962, pp. 1052-1059.
- 9.10. FUNG, Y. C.; SECHLER, E. E.; AND KAPLAN, A.: On the Vibration of Thin Cylindrical Shells Under Internal Pressure. J. Aeron. Sci., vol. 24, no. 9, Sept. 1957, pp. 650-660.
- 9.11. ARNOLD, R. N.; AND WARBURTON, G. B.: The Flexural Vibrations of Thin Cylinders. J. Proc. Inst. Mech. Eng. (London), vol. 167, 1953, pp. 62-74.
- 9.12. TIMOSHENKO, S.: Theory of Plates and Shells. McGraw-Hill Book Co., Inc., 1940.
- 9.13. REISSNER, E.: On Transverse Vibrations of Thin Shallow Elastic Shells. Quart. Appl. Math., vol. 13, no. 2, July 1955, pp. 169-176.
- 9.14. BERRY, J. G.; AND REISSNER, E.: The Effect of an Internal Compressible Fluid Column on the Breathing Vibrations of a Thin Pressurized Cylindrical Shell. J. Aerospace Sci., vol. 25, 1958, pp. 288-294.
- 9.15. SALEME, E.; AND LIBER, T.: Breathing Vibrations of Pressurized Partially Filled Tanks. AIAA J., vol. 3, no. 1, Jan. 1965, pp. 132-136.
- 9.16. REISSNER, E.: Notes on Forced and Free Vibrations of Pressurized Cylindrical Shells Which Contain a Heavy Liquid With a Free Surface. Rept. No. GM-TR-87, AM No. 6-15, Contract No. AF 18-(600)-1190, Guided Missile Division, TRW Space Technology Laboratories, Nov. 1956.
- 9.17. LEROY, JEAN: On Breathing Vibrations of Thin Cylinders Partially Full of Liquid (in French). Comptes Rendus, vol. 257, no. 18, Oct. 1963, pp. 2607-2609.
- 9.18. MIXSON, J. S.; AND HERR, R. W.: An Investigation of the Vibration Characteristics of Pressurized Thin-Walled Circular Cylinders Partially Filled With Liquid. NASA TR R-145, 1962.
- 9.19. BARON, M. L.; AND BLEICH, H. H.: The Dynamic Analysis of Empty and Partially Full Cylindrical Tanks, Part I—Frequencies and Modes of Free Vibration and Transient Response by Mode Analysis. DASA No. 1123A (Contract DA-29-044-X2-557), Defense Atomic Support Agency (available from ASTIA), May 1959.
- 9.20. BARON, M. L.; AND SKALAK, R.: Free Vibrations of Fluid Filled Cylindrical Shells. J. of Engr. Mech., ASCE, vol. 88, no. EM3, part I, June 1962.
- 9.21. BARON, M. L.; AND BLEICH, H. H.: The Dynamic Analysis of Empty and Partially Full Cylindrical Tanks, Part II—Analysis of Uplift and Structural Damage. DASA No. 1123B, Defense Atomic Support Agency, Sept. 1959.
- 9.22. BLEICH, H. H.: Longitudinal Forced Vibrations of Cylindrical Fuel Tanks. Jet Propulsion, vol. 26, no. 2, Feb. 1956, pp. 109-111.
- 9.23. PALMER, J. H.; AND ASHER, G. W.: Calculation of Axisymmetric Longitudinal Modes for Fluid-Elastic Tank-Ullage Gas System and Comparison With Model Test Results. Proc.

- AIAA Symposium on Structural Dynamics and Aeroelasticity, Boston, 1965, pp. 189-193.
- 9.24. CHU, W. H.: Breathing Vibrations of a Partially Filled Cylindrical Tank—Linear Theory. *J. Appl. Mech.*, vol. 30, no. 4, Dec. 1963, pp. 532-536.
- 9.25. CHU, W. H.; AND GONZALES, R.: Supplement to Breathing Vibrations of a Partially Filled Cylindrical Tank—Linear Theory. *J. Appl. Mech.*, vol. 34, no. 4, Dec. 1964, pp. 722-723.
- 9.26. YU, Y. Y.: Free Vibration of Thin Cylindrical Shells. *J. Appl. Mech.*, vol. 22; *Trans. ASME*, vol. 77, 1955, pp. 547-552.
- 9.27. FONTENOT, L. L.; AND LIANIS, G.: The Free Vibrations of Thin Elastic Pressurized Cylindrical Shells Filled With a Perfect and Incompressible Liquid Having a Free Surface. International Symposium on Space Technology and Science (Tokyo, Japan), Sept. 1963.
- 9.28. RABINOVICH, B. I.: The Equations of the Transverse Vibrations of Liquid-Filled Shells (Eng. trans.). NASA TT F-216, 1964.
- 9.29. NATUSHKIN, V. F.; AND RAKHIMOV, I. S.: Oscillations of a Cylindrical Shell Partially Filled With a Fluid (in Russian). *Aviatsionnaia Tekhnika*, vol. 17, no. 3, 1964, pp. 75-78. (IAA A64-28276)
- 9.30. SAMOILOV, E. A.; AND PAVLOV, B. S.: Oscillations of a Hemispherical Shell Filled With a Fluid (in Russian). *Aviatsionnaia Tekhnika*, vol. 7, no. 3, 1964, pp. 79-86. (IAA A64-28277)
- 9.31. HWANG, CHINTSUN: Longitudinal Sloshing of Liquid in a Flexible Hemispherical Tank. Paper No. 65-APM-14, Applied Mechanics/Fluids Engineering Conference, ASME (Washington, D.C.), June 7-9, 1965.
- 9.32. SHMAKOV, V. P.: The Equations of the Axially Symmetric Vibrations of a Liquid-Filled Cylindrical Shell. NASA TT F-219, July 1964.
- 9.33. BEAL, T. R.; COALE, C. W.; AND NAGANO, M.: Influence of Shell Inertia and Bending Stiffness on the Axisymmetric Modes of a Partially Filled Cylindrical Tank. AIAA Paper No. 65-412, AIAA Annual Meeting, July 1965.
- 9.34. KANA, D. D.; LINDHOLM, U. S.; AND ABRAMSON, H. N.: An Experimental Study of Liquid Instability in a Vibrating Elastic Tank. *J. Spacecraft Rockets*, vol. 3, no. 8, Aug. 1966, pp. 1183-1188.
- 9.35. KANA, D. D.: Longitudinal Forced Vibration of Partially Filled Tanks. Tech. Rept. No. 6, Contract No. NASW-146, Southwest Research Institute, Feb. 1963.
- 9.36. CHU, W. H.; AND KANA, D. D.: A Theory for Nonlinear Transverse Vibrations of a Partially Filled Elastic Tank. Final Rept. Part I, Project 02-1748, Southwest Research Institute, Mar. 1966.
- 9.37. BHUTA, P. G.; AND KOVAL, L. R.: Coupled Oscillations of a Liquid With a Free Surface in a Tank Having a Flexible Bottom. *J. Appl. Math. and Phys.*, vol. 15, no. 5, 1964.
- 9.38. BHUTA, P. G.; AND KOVAL, L. R.: Hydroelastic Solution of the Sloshing of a Liquid in a Cylindrical Tank. *J. Acoust. Soc. Am.*, vol. 36, no. 11, Nov. 1964, pp. 2071-2079.
- 9.39. TONG, P.; AND FUNG, Y. C.: The Effect of Wall Elasticity and Surface Tension on the Forced Oscillations of a Liquid in a Cylindrical Container (Part I: Analysis). SM-64-40, Grad. Aero. Labs., Cal. Inst. of Tech., Oct. 1964.
- 9.40. BAUER, H. F.: Effects of Interaction of Structure, Control, and Propellant Sloshing Upon the Stability of Large Space Vehicles. MTP-AERO-61-89, Marshall Space Flight Center, NASA, 1961.
- 9.41. GEISSLER, E. D.: Problems of Attitude Stabilization of Large Guided Missiles. *Aerospace Eng.*, vol. 19, Oct. 1960, pp. 24-29, 68-71.
- 9.42. HURWITZ, A.: Über die Bedingungen, unter welchen eine Gleichung nur Wurzeln mit negativen reellen Theilen besitzt. *Mathematische Annalen*, vol. 46, 1895, pp. 273-284.
- 9.43. FULLER, A. T.: Stability Criteria for Linear Systems and Reliability Criteria for RC Networks. *Proc. Cambridge Phil. Soc.*, vol. 53, 1957, pp. 878-896.
- 9.44. BAUER, H. F.: Stability Boundaries of Liquid-Propellant Elastic Vehicles With Sloshing. *J. Spacecraft Rockets*, vol. 3, no. 2, Feb. 1966, pp. 240-246.

## PRINCIPAL NOTATIONS

*A, B, C*=displacement constant coefficients  
*a*=tank radius  
*a<sub>0</sub>, a<sub>1</sub>*=gain value of attitude control system  
*b*=liquid depth  
*c<sub>e</sub>*=0.3=equivalent wavelength factor constant

*c<sub>0</sub>*=velocity of sound in fluid at reference static pressure  
 $D = \frac{Eh^3}{12(1-\nu^2)}$ =stiffness coefficient  
*d*=tank diameter  
*E*=modulus of elasticity  
*f*=frequency (cps)

$f_{mn}$ =natural frequency of $m, n$ th breathing mode of a circular cylindrical shell (cps)	$u, v, w$ =axial, tangential, and radial displacement of middle surface of a circular cylindrical shell
$f(z)$ =mode shape function for bending tank	$V$ =potential energy
$g$ =acceleration of gravity	$x, y, z$ =cylindrical shell coordinates (fig. 9.8)
$g_B$ =structural damping	$Y, Y'$ =displacement and slope at the first bending mode. (Subscripts 1, 2, 3 mean at locations of sloshing masses, subscript $G$ means at location of gyroscope, and subscript $E$ means at swivel point of the engines.)
$h$ =shell wall thickness	$z$ =axial coordinate from liquid center of gravity (fig. 9.1)
$h_B$ =bottom thickness	$\alpha=h/a$ =shell thickness factor for breathing tank
$J_n, I_n$ =ordinary and modified $n$ th-order Bessel functions	$\gamma_s$ =damping factor of propellant
$k_c = \frac{\omega_a}{c_0}$ =compressibility factor of fluid in a breathing tank	$\sqrt{\Delta} = f_{mn} \left[ \frac{4\pi^2 a^2 \rho_s (1 - \nu^2)}{Eg} \right]^{1/2}$ =non-dimensional frequency parameter for a breathing tank
$k_i$ , $=$ generalized stiffness coefficient	$\xi$ =liquid surface displacement above undisturbed level
$k_r$ =radius of gyration of space vehicle about the mass center	$\xi_c$ =control damping
$l$ =tank length	$\lambda_m = \frac{m\pi a}{l}$ =shell wavelength factor for breathing tank
$M_B/m_0$ =generalized mass ratio	$\mu_s = m_s/m_0$ =ratios of modal mass of liquid over total mass of space vehicle
$m$ =axial wave number for breathing cylindrical tank	$\nu$ =Poisson's ratio
$\bar{m}_s$ =empty tank mass	$\nu_s = \omega_s/\omega_c$ =frequency ratio of undamped propellant frequency to undamped control frequency
$m_f$ =fluid apparent mass	$\xi_1, \xi_2$ =distance between rear tank and upper tanks, respectively
$\bar{m}_{s,i}$ =generalized mass coefficient	$\xi_E = x_E/k_r$ =ratio of distance of swivel point of engines from center of gravity to radius of gyration
$n$ =circumferential wave number for breathing tank	
$\bar{n}_x = \frac{p_0 a}{2Eh}$ =axial internal static pressure parameter	
$\bar{n}_\theta = \frac{p_0 a}{Eh}$ =tangential internal static pressure parameter	
$p_0$ =internal static pressure	
$p_1, p_2$ =phase-lag coefficients	
$Q(r)$ =unsteady pressure radial mode function	
$q$ =unsteady internal pressure	
$q_i$ =generalized coordinate	
$r, \theta, Z$ =cylindrical coordinates (fig. 9.1)	
$T$ =kinetic energy	
$t$ =time	
$U_s(t), V_s(t), W_s(t)$ =axial, tangential, and radial displacement of middle surface of breathing shell as functions of time	

$\xi_s = x_s/k_r$  = ratio of the coordinate at the location of the modal mass of the propellant to the radius of gyration of the space vehicle

$\rho_L$  = liquid mass density

$\rho_0$  = fluid mass density at reference static pressure

$\rho_s$  = shell mass density

$\tau$  = bottom membrane tension

$\Phi$  = liquid velocity potential

$\psi(r, \theta)$  = liquid surface mode shape function

$\Omega_{ij}, \alpha_{ij}$  = coupling coefficients for sloshing in bending tank

$\omega$  = circular frequency

$\omega_e$  = empty tank resonant bending frequency

$\omega_i$  = resonant frequency for  $i$ th coordinate,  $i=1, 2, 3 \dots$

$\omega_{s+3}$  = uncoupled liquid sloshing frequencies

## *Chapter 10*

# **Special Topics**

## **Part I. Liquid Impact on Tank Bulkheads**

***John F. Dalzell***

### **10.1 INTRODUCTORY REMARKS ON DOME IMPACT**

There are a number of possible operational situations where a sudden thrust reversal on the rocket or spacecraft may produce a sudden alteration in the apparent relative gravitational field of the fluid in the various propellant tanks, and thus cause or tend to cause the fluid to reorient itself at the opposite end of the tank with such rapidity as to produce impact-type loading on the far bulkhead. These situations may be divided, for present purposes, into two general types:

- (1) Maneuvering or docking of spacecraft in an essentially low gravity environment.
- (2) Thrust termination in the atmosphere.

The impulsive accelerations imposed upon a space vehicle during docking are very much a function of the operational procedures and latching and shock-absorbing systems involved for the particular vehicle. Typical studies of the first-generation docking program (ref. 10.1) neglect the fluid dynamics of contained fluids. As of this writing, quantitative estimates of the effect of motions of contained liquids on the motions of spacecraft seem to be confined to the admittedly preliminary analysis of reference 10.2. Methods for estimating the possibility of fluid impact in this case, and of the pressures involved, seem not readily available, though the entire field of low-gravity fluid mechanics is under intensive study at the present time. The extent of practical estimation procedures

is summarized in chapter 11, section 11.5, to which the reader is referred.

The second general situation mentioned above, thrust termination or alteration in the atmosphere, has been of some concern up to the present and it will be the purpose in the remainder of this section to review what work has been accomplished in this area.

Thrust termination in the atmosphere before virtually all of the propellants have been used can be intentional (mission abort, or perhaps associated with short-range ballistic missile flights) or unintentional (engine failure or premature ignition during staging). In either event, the possible rupture of a tank bulkhead could result in a structural breakup or, in the case of hypergolic fuels, could result in a fireball. In the cases of interest to manned space flight, either the intentional or unintentional thrust termination case will probably spoil the mission and indirectly destroy the booster rocket (at least until such time as practical booster recovery techniques are perfected). As far as current practice is concerned, whether or not the upper bulkhead (or dome) of a booster ruptures will be of no consequence to the ultimate disposition of the booster; however, it is necessary during an abort to separate the man-carrying upper stages and anything else recoverable and to insure that this equipment and the men aboard are a safe distance from the booster before it breaks up or a fireball is formed. Hence, the possibility of rupturing tank bulkheads by fluid impact during an abort

or engine malfunction may be an important safety consideration.

Experimental investigations of dome-impact phenomena are limited in number. Chronologically, the first of three such studies was carried out in 1957 at Southwest Research Institute (ref. 10.3), later published in condensed form (ref. 10.4). The second and third studies (refs. 10.5 and 10.6) were carried out almost simultaneously 7 years later at NASA Langley and Southwest Research Institute. Owing to the difficulty in documenting the importance of this problem from operational failures, and to the great diversity of rocket attitudes, accelerations, etc., which are possible when thrust is terminated, the overall problem is not presently well set from the fluid dynamicist's point of view, either experimentally or theoretically. As a consequence, much of the experimental work to be reviewed is exploratory in nature, and an adequate theoretical treatment has yet to be developed. Engineering analyses are of the "order of magnitude" variety, impact pressures estimated being very much a function of initial assumptions regarding fluid behavior (refs. 10.7 and 10.8).

#### 10.2 SOME ESTIMATES OF THE CONDITIONS IMPOSED ON THE TANK FLUID BY THRUST TERMINATION

As mentioned previously, the diversity of possible rocket attitudes, accelerations, and operational situations when thrust is unexpectedly terminated is so great that simple generalizations covering all possibilities are not feasible. It must be assumed that the data will be at hand to estimate the drag deceleration and subsequent behavior of the vehicle for thrust termination or for loss of attitude control during any portion of the flight. With such estimates, the possibilities of fluid impact on the dome can be assessed and the boundary conditions for the fluid dynamic problem set.

However, it is not possible for interpretative reasons to sidestep this question altogether in the present treatment, and some crude estimates of conditions which may be expected are necessary. For simplicity, it will be assumed that initially a rocket vehicle is proceeding on some assigned trajectory under power and con-

trol in the Earth's atmosphere when engine failure or intentional shutdown occurs. It is further assumed that staging does not also occur, and that any portions of the vehicle which are separated after thrust termination are of negligible mass relative to the original vehicle assembly. The wealth of data contained in reference 10.9 allows some estimates of this situation to be made which may serve present purposes.

For a gross treatment of the accelerations imposed on the vehicle, it will be assumed that the vehicle is a material point located at the vehicle center of gravity. Simplified two-dimensional trajectory equations are derived in reference 10.9, section 6.22, in tangential (direction of velocity vector) and normal coordinates, neglecting Earth rotation. Figure 10.1 indicates the forces on the rocket as a point mass (from ref. 10.9). In this figure

$$W = mg$$

$$m = \text{rocket mass}$$

$$g = \text{local gravity}$$

$$L = \text{lift force}$$

$$D = \text{drag force}$$

$$T = \text{engine thrust}$$

$$u, v = \text{normal and tangential velocities}$$

$$\alpha = \text{angle of attack}$$

$$\nu = \text{flight path angle}$$

$$r_0 = \text{Earth radius}$$

The corresponding differential equations for trajectory analysis are given in reference 10.9 as

$$\left. \begin{aligned} \dot{v} &= \frac{T \cos \alpha}{m} - \frac{D}{m} - g \cos \nu \\ \dot{\nu} &= \frac{T \sin \alpha}{mv} + \frac{L}{mv} + \left( \frac{g}{v} - \frac{v}{r} \right) \sin \nu \end{aligned} \right\} \quad (10.1)$$

Integration of these coupled equations gives velocity,  $v$ , and flight path angle,  $\nu$ , as functions of time. For present purposes, it is convenient to rewrite the equations for an approximation to tangential and normal accelerations ( $\dot{v}$ ,  $\dot{\nu}$ )

$$\left. \begin{aligned} \dot{v} &= \frac{T \cos \alpha}{m} - \frac{D}{m} - g \cos \nu \\ \dot{\nu} &= \frac{T \sin \alpha}{m} + \frac{L}{m} + g \sin \nu \end{aligned} \right\} \quad (10.2)$$

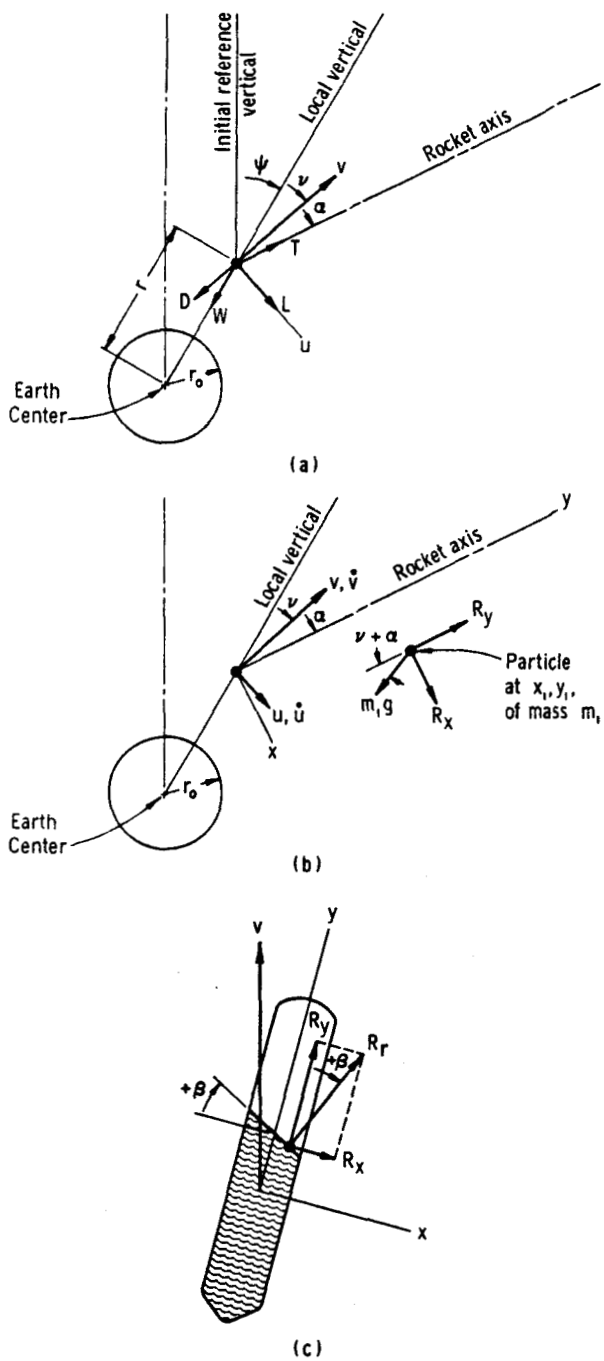


FIGURE 10.1.—Coordinate systems.

In a similar way, crude equations of motion of a single small particle of fluid in one of the rocket tanks can be written. Taking a moving coordinate system, origin at the material point of figure 10.1(a), with  $y$ -axis alined with the rocket longitudinal axis, a fluid particle of mass,

$m_1$ , is assumed acted upon by forces,  $R_y$  and  $R_z$ , as shown in figure 10.1(b). Conceptually, these forces are exerted on the particle by the tank; aerodynamic forces and thrust do not act directly on the particle, which is assumed to be of a much smaller order of magnitude than, and contained, in the "material point" of figure 10.1(a). Rotation of the material point (rocket) is also neglected. From figure 10.1(b), the equations of motion are

$$\left. \begin{aligned} \ddot{y}_1 + \dot{v} \cos \alpha + \dot{u} \sin \alpha &= \frac{R_y}{m_1} - g \cos (\nu + \alpha) \\ \ddot{x}_1 - \dot{v} \sin \alpha + \dot{u} \cos \alpha &= \frac{R_z}{m_1} + g \sin (\nu + \alpha) \end{aligned} \right\} \quad (10.3)$$

(Magnitudes of  $y_1$  and  $x_1$  are grossly distorted in figure 10.1(b) relative to  $r$ ; the particle weight vector ( $m_1 \vec{g}$ ) is sensibly parallel to local vertical.)

Substitution of the accelerations of the origin of the moving coordinate system, equation (10.2) into equation (10.3) yields

$$\left. \begin{aligned} \ddot{y}_1 &= \frac{R_y}{m_1} + \frac{D \cos \alpha - L \sin \alpha - T}{m} \\ \ddot{x}_1 &= \frac{R_z}{m_1} - \frac{D \sin \alpha + L \cos \alpha}{m} \end{aligned} \right\} \quad (10.4)$$

In effect, this result illustrates the point that both the fluid and the tank are in free fall. Consequently, the relative acceleration between fluid and tank is independent of the flight path angle,  $\nu$ , and of local gravity,  $g$ .

The axial aerodynamic force on the rocket,  $F_y$ , and the normal aerodynamic force,  $F_z$ , are

$$\left. \begin{aligned} F_y &= L \sin \alpha - D \cos \alpha \\ F_z &= L \cos \alpha + D \sin \alpha \end{aligned} \right\} \quad (10.5)$$

Substituting in equation (10.4) gives

$$\left. \begin{aligned} \ddot{y}_1 &= \frac{R_y}{m_1} - \frac{T + F_y}{m} \\ \ddot{x}_1 &= \frac{R_z}{m_1} - \frac{F_z}{m} \end{aligned} \right\} \quad (10.6)$$

It appears from reference 10.9 that angles of attack,  $\alpha$ , of  $10^\circ$  or less are generally desirable from structural considerations. Consequently, the angle of attack might be assumed small for

present purposes, since the present example assumes a controlled vehicle up to the point of thrust termination. (The perturbations in direction of thrust were also neglected as small deviations in the above analysis.) For small angles of attack the aerodynamic lift,  $L$ , on an unfinned body of revolution might be expected to be (from ref. 10.9, sec. 5.2)

$$L \approx q[2(k_2 - k_1)S_b\alpha + \eta C_{DC}A_p\alpha^2]$$

and the increment of drag due to lift

$$\Delta D \approx q[(k_2 - k_1)S_b\alpha^2 + \eta C_{DC}A_p\alpha^3]$$

where

$q$  = dynamic pressure

$S_b$  = area of base of rocket

$(k_2 - k_1)$  = inertia coefficients

$\eta C_{DC}$  = adjusted crossflow drag coefficient

$A_p$  = projected lateral area

The above approximations should be representative for transonic velocity as well as subsonic, according to reference 10.9. Thus, the increment to axial force due to lift will be (linearized)

$$\Delta F_y \approx L\alpha - \Delta D$$

$$\approx q[(k_2 - k_1)S_b\alpha^2]$$

and the increment to normal force due to lift will be

$$\Delta F_x \approx L + \Delta D \cdot \alpha$$

$$\approx q[(k_2 - k_1)S_b(2\alpha + \alpha^3) + \eta C_{DC}A_p(\alpha^2 + \alpha^4)]$$

Manipulating

$$\frac{\Delta F_y}{qS_b} \approx (k_2 - k_1)\alpha^2$$

$$\frac{\Delta F_x}{qS_b} \approx (k_2 - k_1)(2\alpha + \alpha^3) + \eta C_{DC} \frac{A_p}{S_b} [\alpha^2 + \alpha^4]$$

$$\approx (k_2 - k_1)(2\alpha) + \eta C_{DC} \frac{A_p}{S_b} \alpha^2$$

(The omitted powers of  $\alpha$  introduce only a small percentage error for  $\alpha \leq 10^\circ$ .)

For orders of magnitude for most vehicles

$$A_p \approx ldk_p, S_b \approx \frac{\pi d^2}{4}$$

where

$k_p$  varies from 0.6 to 0.9

$l$  = overall vehicle length

$d$  = base diameter

Thus

$$\frac{A_p}{S_b} \approx \frac{\pi k_p}{4} \left( \frac{l}{d} \right)$$

From reference 10.9, section 5.2, both  $(k_2 - k_1)$  and  $\eta$  are functions of  $(l/d)$ . Again, very crudely, between  $l/d = 5$  and 20

$$\eta \approx (0.57) + (0.01)(l/d)$$

The crossflow drag coefficient  $C_{DC}$  is a function of Mach number and angle of attack, but its total variation is between 1.2 and 1.8, approximately. Thus,

$$\eta C_{DC} \frac{A_p}{S_b} \approx \frac{\pi k_p}{4} \left( \frac{l}{d} \right) (C_{DC}) \left[ (0.57) + (0.01) \left( \frac{l}{d} \right) \right] \\ \approx k^1$$

where  $k^1$  might range from 2 to 20 for vehicles with  $l/d$  from 5 to 20. Similarly from reference 10.9

$$0.8 < (k_2 - k_1) < 1 \text{ for } 5 < l/d < 20$$

Thus, for orders of magnitude

$$\frac{\Delta F_x}{qS_b} \approx k^2 \alpha + k^1 \alpha^2$$

$$\frac{\Delta F_y}{qS_b} \approx k^3 \alpha^2$$

where

$$2.0 \leq k^1 \leq 20$$

$$1.6 \leq k^2 \leq 2.0$$

$$0.8 \leq k^3 \leq 1.0$$

The basic drag at zero angle of attack for cone cylinders without fins in the transonic range seems to be made up of friction, base and wave drag, and it might be assumed that these components of drag will not be greatly changed for small deviations in angle of attack. Consequently, it will be assumed that the drag force at zero angle of attack is the remaining part of  $F_y$ .

$$\Delta_2 F_y \approx -D_{(\alpha=0)} \approx -q S_b C_{D_{\alpha=0}}$$

where, for orders of magnitude,  $C_{D_{\alpha=0}}$  varies between 0.15 and 0.8. Combining all the above results gives

$$\begin{aligned} \frac{F_x}{q S_b} &\approx \frac{\Delta F_x}{q S_b} \approx [k^2 \alpha + k^1 \alpha^2] \\ \frac{F_y}{q S_b} &\approx \frac{\Delta F_y + \Delta_2 F_y}{q S_b} \approx [k^3 \alpha^2 - C_{D_{\alpha=0}}] \end{aligned}$$

where the coefficients have the ranges previously cited. Substituting the above approximations into equations (10.6) then leads to

$$\left. \begin{aligned} \ddot{y}_1 &\approx \frac{R_y}{m_1} \frac{T + q S_b [k^3 \alpha^2 - C_{D_{\alpha=0}}]}{m} \\ \ddot{x}_1 &\approx \frac{R_x}{m_1} \frac{q S_b [k^2 \alpha + k^1 \alpha^2]}{m} \end{aligned} \right\} \quad (10.7)$$

where

$$0.15 \leq C_{D_{\alpha=0}} \leq 0.8$$

$$2 \leq k^1 \leq 20$$

$$1.6 \leq k^2 \leq 2$$

$$0.8 \leq k^3 \leq 1$$

If the fluid in the tanks is not moving prior to thrust termination and has no relative velocity or acceleration,  $\ddot{x}$  and  $\ddot{y}$  for each particle is zero and the forces exerted on each particle are

$$\begin{aligned} R_y &= m_1 \frac{T + q S_b [k^3 \alpha^2 - C_{D_{\alpha=0}}]}{m} \\ R_x &= m_1 \frac{q S_b [k^2 \alpha + k^1 \alpha^2]}{m} \end{aligned} \quad (10.8)$$

The sketch given in figure 10.1(c) indicates the positive directions of  $R_x$  and  $R_y$ . The quiescent fluid free surface will be approximately normal to the resultant,  $R$ , of  $R_x$  and  $R_y$ , as shown. Then, the angle the free surface makes with the normal to the tank axis is

$$\begin{aligned} \beta &\approx \tan^{-1} \left( \frac{R_x}{R_y} \right) \\ &\approx \tan^{-1} \left\{ \frac{k^2 \alpha + k^1 \alpha^2}{(C_{D_{\alpha=0}} - k^3 \alpha^2) \left[ \frac{T}{q S_b (C_{D_{\alpha=0}} - k^3 \alpha^2)} - 1 \right]} \right\} \end{aligned} \quad (10.9)$$

For angles of attack of  $10^\circ$  or less, the denominator in the expression above is insensitive to  $\alpha$ . Depending on rocket velocity and altitude, the magnitude of rocket thrust,  $T$ , can be very much larger than the drag [ $q S_b (C_{D_{\alpha=0}} - k^3 \alpha^2)$ ] with the result that the denominator in equation (10.9) can be very large. During flight through the atmosphere, the dynamic pressure,  $q$ , is generally a maximum somewhere. If this occurs at the transonic peak in the drag coefficient ( $C_{D_{\alpha=0}} \approx 0.8$ ), the denominator in equation (10.9) is approximately minimized with respect to drag variation and is approximately equal to

$$\left( \frac{T}{q S_b} - 0.8 \right)$$

From reference 10.9, the practical variation in the quantity,  $T/S_b$ , for multistage rockets built or projected as of the date of that reference, appears to lie between 1.0 and  $2.5 \text{ kg/cm}^2$ , for the first stages of multistage vehicles having thrusts varying from 13,000 to 4 million kg, with values of 2 to  $2.5 \text{ kg/cm}^2$  for man-carrying vehicles. If maximum  $q$  is assumed to be 1 or  $1.5 \text{ kg/cm}^2$ , then a plausible lower limit on the denominator of equation (10.9) is approximately unity for the maximum  $q$  condition for man-carrying vehicles. These considerations imply a plausible range for  $\tan \beta$  of

$$0 \leq \tan \beta \leq (2\alpha + 20\alpha^2)$$

The lower limit corresponds to  $\alpha = 0$  or very low  $q$ ; the upper end of the range to maximum  $q$ . Evaluation of this upper range indicates that between angles of attack of 0 and  $10^\circ$ , the angle  $\beta$  varies between 0 and 2 to  $4\frac{1}{2}$  times  $\alpha$  for large booster vehicles in normal flight (before thrust termination).

If the thrust,  $T$ , should terminate, and the angle of attack and velocity does not change while the fluid is reorienting itself, the final angle,  $\beta$ , is approximated by

$$\tan \beta \approx - \left( \frac{k^2 \alpha + k^1 \alpha^2}{C_{D_{\alpha=0}} - k^3 \alpha^2} \right) \quad (10.10)$$

The right-hand side of equation (10.10) is essentially the ratio between the normal and

axial aerodynamic force coefficients. In addition to the condition ( $\alpha=0$ ), which means  $\beta=180^\circ$  in this case (since the fluid must end up in the opposite end of the tank), an upper and lower bound can be put on  $\beta$  as a function of  $\alpha$  by inserting the previously cited ranges of  $k^1$ ,  $k^2$ ,  $k^3$ , and  $C_{D_{\alpha=0}}$  into equation (10.10). One "bound" is found for the "high lift," subsonic velocity case ( $C_{D_{\alpha=0}} \approx 0.15$ ) and another for the "low lift," sonic velocity case. Both are plotted in figure 10.2 along with the range on  $\beta$  found previously for the case before thrust termination, and some sketches indicating the range of quiescent fluid surface positions for  $\alpha=5^\circ$ .

The results for  $\beta$  before thrust termination indicate a possible range of initial conditions for the fluid. Normal sloshing can easily be visualized superimposed on the initial fluid angle. Even in a vehicle under control to within  $\pm 3^\circ$  angle of attack, the initial fluid angle may approach  $10^\circ$  from the tank axis normal. The estimates for the final angle of  $\beta$  after thrust termination presuppose that rocket velocity, angle of attack, and so forth, do not

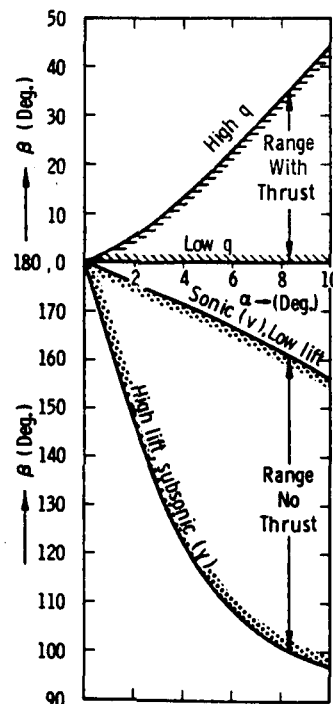
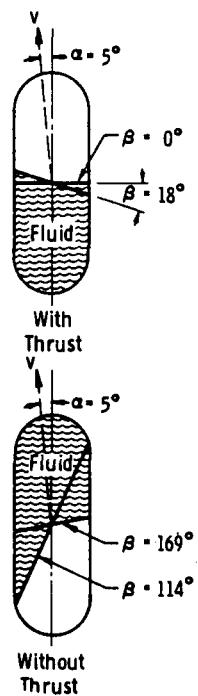


FIGURE 10.2.—Variation of liquid free surface orientation with respect to tank axis.

change for the time required for the fluid to come to rest. This assumption is, of course, incorrect and the meaning of these final angles is subject to further considerations on the dynamics of the vehicle.

When thrust is terminated at  $t=0$ , the second of equations (10.6) for the hypothetical particle is unchanged. The first of equations (10.6) becomes

$$\ddot{y}_1 = \frac{R_y}{m_1} - \frac{F_y}{m} = \frac{R_y}{m_1} + \frac{D \cos \alpha - L \sin \alpha}{m} \quad (10.11)$$

Since  $(D \cos \alpha)$  predominates over  $(L \sin \alpha)$ , the particle is accelerated upward. If  $R_y$  is also assumed zero at  $t=0$

$$\ddot{y}_1 = \frac{(-F_y)}{m} \quad (10.12)$$

and the distance through which the particle travels toward the upper bulkhead,  $\bar{y}$ , in time,  $t$ , becomes

$$\bar{y} = \frac{-F_y t^2}{m} \frac{t^2}{2} = \frac{F_{y_0} t^2}{m} \frac{t^2}{2}$$

assuming  $F_y$  is constant during time  $t$ , ( $F_y = -F_{y_0}$ ) and that the particle was initially at rest. If  $b$  denotes the distance of the free liquid surface from the upper bulkhead, the minimum time required for a particle on the free surface to reach the bulkhead will be approximately

$$t_{\min}^b = \sqrt{\frac{2b}{(F_{y_0}/m)}} \quad (10.13)$$

The minimum time required for a particle on the bottom of the tank to reach the position of the hypothetical ultimate free surface (fig. 10.2) will be about the same. Since the fluid particles react with one another and there will be a resistance to flow, the first of the fluid should reach the upper bulkhead slightly later than  $t_{\min}^b$ , and the time required for the fluid to move to an even approximately final position may be several times equation (10.13). As the tank empties,  $b \rightarrow h$  thus raising the time to impact. Equation (10.13) suggests a nondimensional representation for time in the form

$$\left. \begin{array}{l} \tau = \frac{t}{t_{\min}^*} \\ t = \tau \sqrt{\frac{2bm}{F_{v_0}}} \end{array} \right\} \quad (10.14)$$

As mentioned in a previous paragraph, the question of how long the relative acceleration of particle and tank persists is of considerable importance. After  $t=0$ , and assuming no interaction between fluid particles, from equations (10.6) and (10.12)

$$\left. \begin{array}{l} \ddot{y}_1 = -\frac{F_y}{m} \\ \ddot{x}_1 = -\frac{F_x}{m} \end{array} \right\} \quad (10.15)$$

What is sought, consequently, is the variation with time of the aerodynamic forces which are explicit functions of rocket velocity and angle of attack and, thus, indirectly functions of flight path angle. This amounts to a general integration of the nonlinear trajectory equations (10.1) and is not feasible, in general. Some rough magnitudes may be found from special cases. If angle of attack,  $\alpha$ , and flight path angle,  $\nu$ , are zero, and thrust,  $T$ , is zero at  $t=0$ , and gravity is negligible, equations (10.1) become

$$\left. \begin{array}{l} \dot{v} = -\frac{D_{\alpha=0}}{m} \\ \dot{\nu} = 0 \end{array} \right\} \quad (10.16)$$

If it is assumed that the drag can be linearized as

$$D = D_0 + D'_0(v - v_0)$$

where

$D_0$  = drag at  $t=0, v=v_0, \alpha=0$

$$D'_0 = \left. \frac{\partial D}{\partial v} \right|_{v=v_0}$$

then

$$\dot{v} + \frac{D'_0}{m}(v) = \frac{D'_0}{m}v_0 - \frac{D_0}{m} \quad (10.17)$$

From equation (10.17), the rocket velocity might behave for short ranges of velocity as

$$v = v_0 - \frac{D_0}{D'_0} \left( 1 - e^{-\frac{D'_0}{m}v} \right) \quad (10.18)$$

Substituting equation (10.18) in the drag force approximation then gives

$$D \approx D_0 e^{-\frac{D'_0}{m}v} \quad (10.19)$$

Assuming that axial aerodynamic force,  $F_v$ , is largely drag, the first of equations (10.15) becomes

$$\ddot{y}_1 \approx \frac{F_{v_0}}{m} e^{-\frac{D'_0}{m}v}$$

or

$$\frac{\ddot{y}_1}{(\ddot{y}_1)_0} \approx e^{-\frac{D'_0}{m}v} \quad (10.20)$$

where  $(\ddot{y}_1)_0$  = relative acceleration at  $t=0$ . Non-dimensionalizing time with equations (10.14) gives

$$\frac{\ddot{y}_1}{(\ddot{y}_1)_0} \approx e^{-\left[ \frac{2b(D'_0)^2}{mD_0} \right]^{1/2} v}, \quad (10.21)$$

with respect to the quantity  $(D'_0)^2/D_0$  in equation (10.21)

$$\begin{aligned} \frac{(D'_0)^2}{D_0} &= \frac{\left( \frac{\partial D}{\partial v} \Big|_{v=v_0} \right)^2}{D_0} \\ &= \frac{\left[ \rho S_b v_0 C_D \Big|_{v=v_0} + \frac{\rho}{2} S_b v_0^2 \left( \frac{\partial C_D}{\partial v} \right) \Big|_{v=v_0} \right]^2}{\frac{1}{2} \rho S_b v_0^2 C_D \Big|_{v=v_0}} \\ &= 2\rho S_b C_D \Big|_{v=v_0} \left[ 1 + \frac{v_0}{2C_D \Big|_{v=v_0}} \left( \frac{\partial C_D}{\partial v} \right) \Big|_{v=v_0} \right]^2 \end{aligned} \quad (10.22)$$

Substitution of the standard analytic forms for  $C_D$  as functions of velocity into the bracketed portion of equation (10.22) indicates that the value of the expression in brackets does not vary greatly with velocity and has a maximum of unity. Consequently

$$\frac{(D'_0)^2}{D_0} \approx 2\rho S_b C_D \Big|_{v=v_0}$$

For orders of magnitude  $(C_D)_{\max} \approx 1$  and

$$\frac{(D'_0)^2}{D_0} > 2\rho S_b$$

Substituting in equation (10.21)

$$\frac{\ddot{y}_1}{(\dot{y}_1)_0} < e^{-\left[\frac{4b}{l} \frac{\rho S_b l}{m}\right]^{1/2} \tau} \quad (10.23)$$

The quantity  $\left(\frac{\rho S_b l}{m}\right)$  represents the mass of displaced air over rocket mass and could easily have a maximum of only 0.001 for typical booster vehicles. Since  $b$  is by definition at most the length of the tank, a plausible upper limit on  $\left(\frac{4b}{l}\right)$  is 2.0, assuming at least two tanks in the vehicle. These considerations lead to

$$1 \gtrsim \frac{\ddot{y}_1}{(\dot{y}_1)_0} \gtrsim e^{-\frac{\tau}{20}} \quad (10.24)$$

or

$$1 \gtrsim \frac{\ddot{y}_1}{(\dot{y}_1)_0} \geq 0.6$$

(At the end of a time interval 10 times as long as the time required for the first particle to impact the upper bulkhead.)

Most of the assumptions above are fairly conservative, and it seems plausible to assume that the relative axial acceleration of equation (10.15) changes quite slowly with respect to the time required for initial portions of the fluid impact. Equation (10.22) for  $[(D'_0)^2/D_0]$  and the subsequent orders of magnitude also imply that the velocity,  $v$ , varies slowly. This indicates that the flight path angle,  $\nu$ , of the rocket having zero angle of attack during and after thrust termination will be very little different than that of the free particle in the tank "falling" toward the upper bulkhead, or at least the period of negligible change will not be much shorter than that for relative axial acceleration.

The normal relative acceleration of the fluid,  $\ddot{x}_1$  (eq. (10.15)), is angle of attack,  $\alpha$ , sensitive. Given thrust and control termination at some angle of attack,  $\alpha_0$ , the lateral forces,  $F_z$ , will tend to zero for the aerodynamically stable vehicle, and tend to increase for the unstable vehicle. In terms of large launch vehicles, the aerodynamically unstable case is the more pertinent.

Writing a grossly simplified equation of motion for the vehicle, after thrust and control termination

$$I\ddot{\alpha} \approx M_\alpha \cdot \alpha \quad (10.25)$$

(Moments are taken about the vehicle center of gravity.)

where

$I$ =mass moment of inertia of the vehicle

$$M_\alpha = \frac{\partial M}{\partial \alpha} \Big|_{\alpha=0}$$

$M$ =aerodynamic moment

$\alpha_0$ =angle of attack at  $t=0$

from which the angle of attack,  $\alpha$ , would be expected to diverge as (ref. 10.9)

$$\frac{\alpha}{\alpha_0} \approx \cosh \sqrt{\frac{M_\alpha}{I}} \cdot t$$

Substituting equation (10.14)

$$\frac{\alpha}{\alpha_0} \approx \cosh \left( \sqrt{\frac{2b m M_\alpha}{I F_{v_0}}} \cdot \tau \right) \quad (10.26)$$

Assuming, as before, that

$$F_z \approx q S_b k^2 \alpha \text{ (for small } \alpha)$$

$$\frac{F_z}{F_{z_0}} \approx \left( \frac{v}{v_0} \right)^2 \frac{\alpha}{\alpha_0}$$

( $F_{z_0}$ =normal force at thrust termination)

and then using equation (10.15)

$$\frac{\ddot{x}_1}{(\ddot{x}_1)_0} \approx \left( \frac{v}{v_0} \right)^2 \cosh \left( \sqrt{\frac{2b m M_\alpha}{I F_{v_0}}} \cdot \tau \right) \quad (10.27)$$

The order of magnitude of the radical of equation (10.27) is of interest

$$M_\alpha = \frac{\partial F_z}{\partial \alpha} \Big|_{\alpha=\alpha_0} \cdot \bar{Z}$$

where

$\bar{Z}$ =distance of "center of pressure" forward of the center of gravity

Using previously estimated expressions for  $F_z$  and  $F_y$ ,

$$\frac{1}{F_{v_0}} \cdot \frac{\partial F_z}{\partial \alpha} \Big|_{\alpha=\alpha_0} = \frac{qS_b(k^2 + 2k^1\alpha_0)}{qS_b(C_{D_{\alpha=0}} - k^3\alpha_0^2)}$$

$$\approx \frac{k^2 + 2k^1\alpha_0}{C_{D_{\alpha=0}}} \text{ (for } \alpha_0 < 10^\circ \text{)}$$

or (using previously estimated coefficients)

$$2 \leq \frac{1}{F_{v_0}} \frac{\partial F_z}{\partial \alpha} \leq 20$$

where the low end roughly corresponds to very low angle of attack, transonic velocity, and the upper end roughly corresponds to subsonic velocity and  $\alpha_0 \approx 1.5^\circ$ .

For the aerodynamically unstable vehicle, a minimum for  $\bar{Z}$  would be near zero and a maximum perhaps,  $0.4l$ . Under these assumptions

$$0 < \frac{M_\alpha}{F_{v_0}} < Nl$$

where

$$N = \begin{cases} 0.8 & \text{for low } \alpha, \text{ transonic velocity} \\ 8.0 & \text{for subsonic velocity, } \alpha_0 = 1.5^\circ \end{cases}$$

The moment of inertia of a slender vehicle may be approximately

$$I \approx m \left( \frac{l}{4} \right)^2$$

Consequently

$$\frac{2m}{I} \approx \frac{32}{l^2}$$

The preceding approximations lead to

$$\frac{\ddot{x}_1}{(\ddot{x}_1)_0} \approx \left( \frac{v}{v_0} \right)^2 \cosh \left( \sqrt{\frac{b}{l}} \cdot J \cdot \tau \right)$$

where

$$\begin{cases} 0 < J < 5 & \text{for low } \alpha, \text{ transonic velocity} \\ 0 < J < 16 & \text{for } \alpha = 1.5^\circ, \text{ subsonic velocity} \end{cases}$$

If  $(v/v_0)^2$  is constant, the time,  $\tau$ , for the relative normal acceleration to double will be

$$\tau \approx \frac{1.32}{J} \sqrt{\frac{l}{b}}$$

Assuming  $l/b = 4$ , the relative normal acceleration could double in one-half the time required for a particle at the initial free surface to "fall" to the upper bulkhead under the influence of a constant initial relative axial acceleration of  $(\dot{y}_1)_0$ . It seems possible that the normal relative acceleration can appreciably increase during time intervals of the same magnitude as those required for initial portions of impact, indeed under the worst of circumstances a free particle starting to "fall" from one side of the tank may tend to "fall" across the tank rather than along the tank axis.

In general, then, the "final" fluid angles shown in figure 10.2 could only occur for a neutrally stable vehicle.

The treatment above excludes the possibility of upper stage exhaust-gas impingement on a separated lower stage during premature staging. This was considered for some special cases in reference 10.7 and, as far as the present treatment is concerned, can very appreciably increase the relative axial acceleration of the fluid for a time which is of the same magnitude as the time required for initial portions of impact. Consequently, while the crude analysis preceding implies a suddenly applied  $\frac{1}{2}$ - to 2-g relative axial acceleration which decays very slowly, exhaust-gas impingement may produce a relative acceleration pulse. Both types of axial acceleration time histories have been used in simulation.

From the simulation viewpoint, the relative normal acceleration is the most difficult to rationalize. If the fluid has an initial quiescent inclination when thrust is terminated, it is probably the result of vehicle angle of attack, and in all cases (except the unlikely one of neutral aerodynamic stability) this angle of attack may change quite rapidly with a consequent rapid variation of normal relative acceleration with time. In the aerodynamically stable vehicle, this normal acceleration may decay rapidly enough to zero that the effect of normal acceleration on the impact problem may only be to bias the motion of the fluid toward one side of the tank or the other. In the aerodynamically unstable case, the very presence of an appreciably inclined initial fluid free surface implies an appreciable angle of attack which, in

turn (depending on the degree of instability), practically guarantees a radical increase in normal relative acceleration during times of the same magnitude required for the fluid to "fall" from one position in the tank to another. This situation also indicates that the probable mode of motion of the fluid will be to run "up" one side of the tank toward the upper bulkhead.

It should also be noted that the fluid can have initial motion in the form of normal lateral sloshing and that this may appreciably affect the behavior of the fluid after thrust termination. This has been verified experimentally.

Since all practical tanks are elastic, the relative acceleration conditions before thrust termination may influence the impact indirectly by deforming the lower bulkhead under the inertial loads of the liquid. Upon thrust termination, the lower bulkhead could impart additional relative acceleration to the fluid, thus having the effect of shortening time to impact and probably accentuating impact pressures. This point has not, to date, been investigated thoroughly.

### 10.3 REVIEW OF EXPERIMENTAL WORK

#### Early Experiments at Southwest Research Institute (refs. 10.3 and 10.4)

The objective of this first study was to determine the pressures resulting from the impact of fuel on the head of a fuel tank in a particular suddenly decelerated guided missile. Though the initial prototype acceleration before thrust termination was not specified, a change in acceleration of up to 0.6 g was specified for a 1.8-meter-diameter fuel tank containing kerosene and a helium pressurant at 3 atmospheres. A similarity analysis was performed, assuming that the parameters of importance were:

- (1) Characteristic linear dimensions
- (2) Acceleration change
- (3) Time
- (4) Liquid impact pressures
- (5) Surface tension of liquid
- (6) Density of liquid
- (7) Density of pressurant
- (8) Viscosity of liquid
- (9) Viscosity of gas

Similitude requirements were found to be quite closely satisfied by a 14.3-centimeter-diameter tank containing carbon tetrachloride as the liquid and  $\beta$ -butylene at 1½ atmospheres as the pressurant. The associated model to prototype time ratio was 0.031, the model to prototype pressure ratio was 12.4, and the model to prototype acceleration ratio was 82.5. Implicit in the modeling assumption was that the acceleration field immediately prior to the acceleration change would have no effect on impact forces; i.e., no lower bulkhead spring back effect.

The apparatus used (pictured in ch. 5, fig. 5.28) was a pneumatically driven device which was capable of accelerating a small model toward the Earth over a distance of about 60 centimeters at up to 50 g's. This apparatus is shown schematically in figure 10.3. Since it was desired to explore the effects of normal relative acceleration, it was possible to incline the apparatus to the vertical by the angle  $\theta$ , as shown. The tank is supported on a piston rod which is constrained to move axially. Just before firing, the accelerating force is balanced by a restraining force,  $F_r$ , applied through a mechanical latch. Fixing a

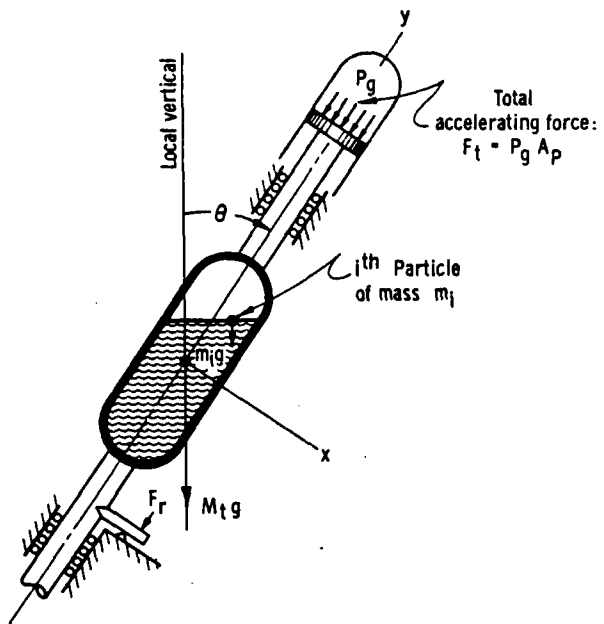


FIGURE 10.3.—Schematic of liquid impact test facility  
(ref. 10.4).

coordinate system at the tank position before release, the equations of motion for the tank assembly after release are

$$\begin{aligned} M_t \ddot{y}_t &= -F_t - M_t g \cos \theta \\ \ddot{x}_t &= 0 \end{aligned}$$

An isolated particle  $m_i$ , in the absence of reaction with other particles or the tank, has equations of motion

$$\begin{aligned} m_i \ddot{y}_i &= -m_i g \cos \theta \\ m_i \ddot{x}_i &= -m_i g \sin \theta \end{aligned}$$

Thus, the relative accelerations between a hypothetical free-falling particle and the tank are

$$\left. \begin{aligned} \ddot{Y} = \ddot{y}_i - \ddot{y}_t &= \frac{F_t}{M_t} = g \cdot n(t) \\ \ddot{X} = \ddot{x}_i - \ddot{x}_t &= -g \sin \theta \end{aligned} \right\} \quad (10.28)$$

The quantity  $g \cdot n(t)$  is proportional to the change in signal from an accelerometer mounted with sensitive axis parallel to the tank axis. The time history of the acceleration pulse had a roughly trapezoidal shape, as shown in figure 10.4. It is the character of the apparatus that the duration of the acceleration stroke is quite sharply defined, thus making it possible to compute an acceleration index,  $n_s$ , which is the uniform acceleration necessary for the tank to travel the constant stroke of the apparatus,  $S$ , in the observed time,  $T_s$ . Thus

$$n_s = \frac{2S}{gT_s^2} \quad (10.29)$$

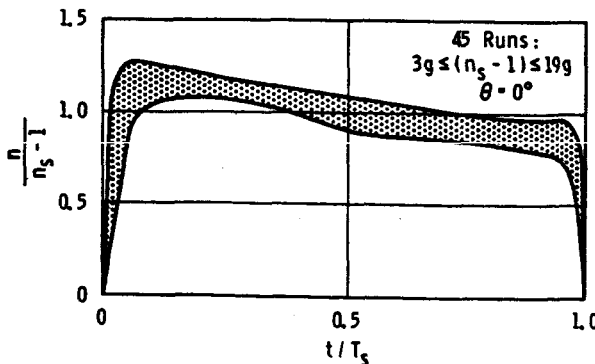


FIGURE 10.4.—Normalized acceleration pulses obtained in test facility (ref. 10.6).

The quantity  $(g \cdot n_s)$  is inclusive of  $(g \cos \theta)$ , and, therefore, the relative acceleration of the fluid in the tank can be normalized by the quantity  $[g(n_s - \cos \theta)]$ , as shown in figure 10.4 (for  $\theta = 0$ ). The shaded band in figure 10.4 denotes the range of values of normalized relative acceleration pulse obtained in a series of vertical firings.

It can be noted from equation (10.28) that the relative acceleration normal to the tank axis is always constant. Strictly, then, the relative acceleration conditions imposed on the fluid in this apparatus are what might be expected in the initial stages of thrust termination on a vehicle having neutral aerodynamic stability. In light of the possible radical variation of normal relative acceleration during the time of interest, this inherent constancy of normal acceleration is an experimental deficiency. However, in light of what is practical in an exploratory investigation, it comes to rationalizing this deficiency or doing nothing about the problem. The results from this apparatus remain the only available approximations to what may happen when relative normal accelerations are appreciable.

Some additional characteristics of the apparatus may be approximated. Figure 10.4 justifies an assumption of roughly constant acceleration over a length of time,  $T_s$ , or

$$n(t) \approx n_s - \cos \theta \quad (10.30)$$

Integrating the first of equation (10.28) twice, under the assumptions that

$n(t) = \bar{n} = \text{constant from } t=0 \text{ to } t=t_a$  (average relative acceleration)

$t_a = \text{minimum time for a particle initially on the fluid surface to impact the upper bulkhead}$

$$\ddot{y}_i = 0 \text{ at } t=0$$

$$\dot{y}_i = 0 \text{ at } t=0$$

we have

$$b = y_i - (y_i)_{t=0} = (n_s - \cos \theta) \frac{gt_a^2}{2} \quad (10.31)$$

where

$b = \text{shortest axial distance from initial free liquid surface to the upper bulkhead.}$

Combining equations (10.29) through (10.31)

$$\frac{t_a}{T_s} = \sqrt{\frac{b}{S} \left(1 + \frac{\cos \theta}{\bar{n}}\right)} \quad (10.32)$$

Equation (10.32) relates the duration of the experiment with the approximate minimum time required for the first particles of fluid to "fall" to the upper bulkhead in the absence of any interaction with other particles or the tank, and it is important to note that  $(t_a/T_s)$  is relatively insensitive to acceleration levels,  $\bar{n}$ , greater than 3 or 4 g's.

The test program, proper, in references 10.3 and 10.4, involved two 14.3-centimeter-diameter tanks, one having a conical upper bulkhead and one having an upper bulkhead in the shape of a spherical segment, as shown in figure 10.5. Quantitative data were obtained by means of pressure taps on the upper bulkheads. An extensive experimental program included tests with each head configuration, with and without ring frames added per figure 10.5 for  $\frac{1}{4}$ - and  $\frac{1}{2}$ -full tank conditions. In each of these cases, the acceleration level,  $\bar{n}$ , was varied between 10 and 50 g's for each of three angles of inclination ( $0^\circ$ ,  $25^\circ$ , and  $50^\circ$ ), requiring approximately 90 tests to cover the parameter range. Additionally, many of these tests were repeated in order to obtain high-speed motion picture coverage.

A typical oscillograph record of pressure and accelerations obtained during a test of a smooth walled tank, one-quarter full with spherical head and inclined at  $50^\circ$  to the vertical is shown in figure 10.6. Worthy of note is that pressures reached a definite maximum during the acceleration stroke of the apparatus and that the pressure rise starts at about the midpoint of the stroke in time. This last roughly checks with equation (10.32) since, in the case of figure 10.7,  $b$  was about 20 centimeters and the stroke of the apparatus is about 71 centimeters [ $t_a \approx 0.53 T_s$  from equation (10.32)]. Figure 10.7 is typical of the many results obtained under this program. Immediately notable is the great difference in head pressures between vertical and inclined firings. The conclusions from references 10.3 and 10.4 were as follows:

(1) The pattern of motion of the fuel is

relatively independent of the magnitude of the acceleration, but is quite sensitive to angle of inclination and head shape.

(2) In the vertical configuration, the fuel breaks away from the surface, first as an outer ring followed by a progressive breaking away of droplets toward the center, forming a hollow truncated cone shape. This is in turn followed by a general formation of streamers or

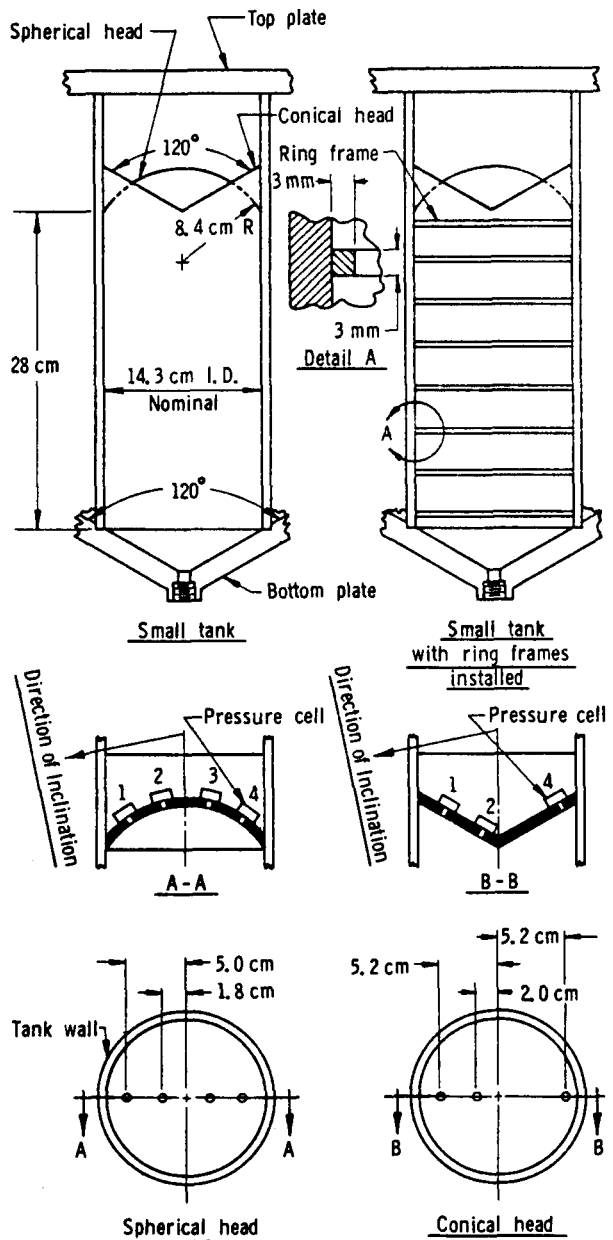


FIGURE 10.5.—Model tank geometries (ref. 10.4).

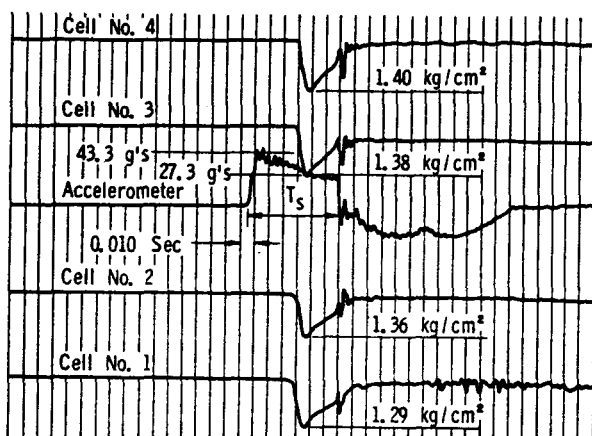


FIGURE 10.6.—Typical test record (ref. 10.4).

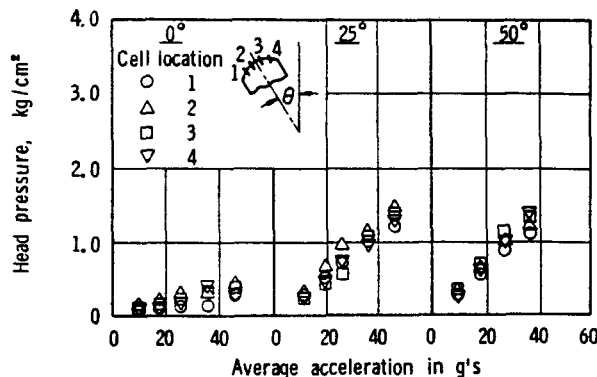


FIGURE 10.7.—Spherical bulkhead pressure data in a 1/2-full tank as a function of acceleration and for three angles of inclination (ref. 10.4).

columns over the entire surface which move up and impinge on the head. A large increase in viscosity tends to exaggerate the ring-cone effect and results in the formation of a single center column of fuel. An increase in gas pressure tends to delay the formation of the outer ring.

(3) In the inclined positions with a spherical tank head, a relatively smooth circulatory motion is set up, with the fuel moving up the far wall, around the head and down the near wall.

(4) In the inclined positions with a conical tank head, the fuel splits, flowing around the two sides of the cone, converging in an arrow-head shape and rebounding toward the tank bottom.

(5) There is little difference in the flow

pattern between the 25° configuration and the 50° configuration.

(6) Head pressures corresponding to the 50° angle of inclination are from 5 to 15 times greater than the corresponding pressures with the tank oriented vertically. Pressures corresponding to the 25° configuration are generally lower than those corresponding to the 50° configuration.

(7) For a given configuration, the variation in pressure over the head is not great and in many cases appears to be nearly constant.

(8) For a given configuration, the pressure at a point on the head is approximately proportional to acceleration and can be expressed in kg/cm² by multiplying the acceleration in g by a constant which varies from 0.22 to 0.42, depending upon the particular configuration.

(9) Pressures for the quarter-full conditions are from 5 to 10 percent higher than corresponding pressures for the half-full conditions. An exception to this is the smooth-wall tank with spherical head in which case the pressures are practically identical for both full conditions.

(10) Pressures on the conical head are approximately 60 percent higher than the corresponding pressures on the spherical head.

(11) The addition of ring frames causes a significant decrease in head pressures, the decrease being on the order of 25 percent.

(12) The average time of prototype pressure buildup is of the order of 0.3 second and the average time of duration is of the order of 1.6 seconds.

(13) The maximum pressure in a prototype with conical head, at 50° inclination, quarter full, decelerated at the rate of 0.6 g, is estimated to be 0.25 kg/cm², with peak developed in 0.13 second and lasting for 1.3 seconds.

#### Later Experiments at Southwest Research Institute (ref. 10.6)

The objective of this program was to assess possible scale effects due to fluid viscosity and surface tension, since it was found that extension of the almost perfect prototype scaling of reference 10.3 to larger prototypes or fluids less viscous than kerosene was not possible. Toward this end, a 28-centimeter-diam-

eter tank with an ellipsoidal head was fitted on the same apparatus used in reference 10.3 and a series of vertical firings was carried out with three different test liquids. The upper bulkhead in this tank was instrumented to indicate total force rather than pressures.

Insofar as data of direct use in design are concerned, these experiments were of little value. By virtue of equation (10.32), and the fixed stroke of the apparatus, it was necessary to fill the tank to 78 percent full in order to make the impact forces begin to build up soon enough during the stroke. It was found, even so, that no definite maximum on total force was reached prior to the end of the acceleration stroke. The initial portions of the force records were correlated, however, with the following results:

- (1) The beginning of the force pulse for vertical firings is only very slightly later than predicted by equation (10.31).
- (2) The magnitudes of the initial portions of the force time histories are nearly proportional to relative acceleration,  $\bar{n}$ .
- (3) An indication was found that viscous scale effects would complicate the extrapolation of data.

#### Experiments at NASA Langley (ref. 10.5)

The experimental apparatus used in these experiments has been described in chapter 5 (see figs. 5.29 and 5.30). Basically, the tank is attached to a drop weight by a cable passing through a system of pulleys. Upon release of the weight, the tank is accelerated upward to a desired velocity (depending upon the release height of the weight), whereupon the drop weight is arrested. The tank continues upward and is decelerated by gravity and an elastic cable (which remains slack until the drop weight is stopped). The deceleration time history of the tank produced by this apparatus is shown schematically in figure 10.8. The period of time denoted by  $T_s$  in figure 10.8 is the experiment duration. For the tank and drop weights used, the absolute deceleration of the tank during the experiment could be accurately described by

$$\ddot{y} = -g - n_0 g \sin\left(\pi \frac{t}{T_s}\right)$$

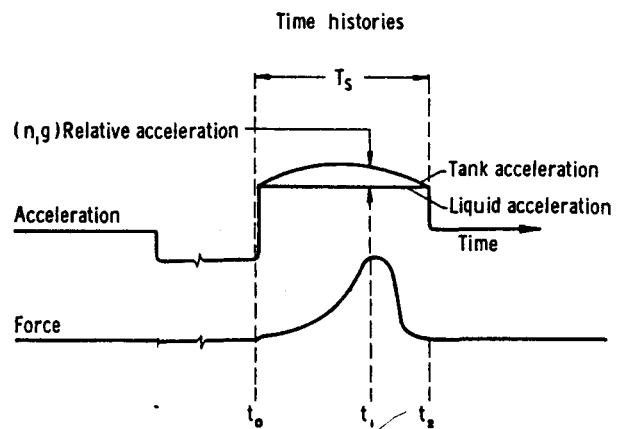


FIGURE 10.8.—Force and acceleration characteristics of test facility (ref. 10.5).

where time is reckoned from  $t_0$  in figure 10.8. Since a particle in the tank would be in free fall after the drop weight is stopped, the relative acceleration between tank and fluid is

$$\dot{Y} = n_0 g \sin\left(\pi \frac{t}{T_s}\right)$$

The authors (ref. 10.5) chose to correlate their results with the relative acceleration,  $n_0 g$ , shown in figure 10.8, which is the acceleration at the time of maximum measured impact force. Total durations of the experiment,  $T_s$ ; times of initial contact,  $t_c$ ; and maximum relative acceleration data,  $n_0$ , are not available and, therefore, it is not possible to construct the general capabilities of the apparatus as in the previous discussion; in fact, much of the behavior of this apparatus depends on the size of the tank.

In these experiments (ref. 10.5), a 22-centimeter-diameter cylindrical tank having hemispherical ends was utilized (fig. 10.9). One hemispherical bulkhead was attached to the remainder of the tank through a balance system so that total force could be measured, and a pressure cell was also fitted in the center of this bulkhead. Geometric variations in this tank included Z-ring baffles and "screen" baffles as indicated in figure 10.9. The tank was filled 28 percent by volume in all tests.

With this particular tank, relative acceleration amplitudes,  $n_0 g$ , up to about 3.5 g were achieved and data were displayed with asso-

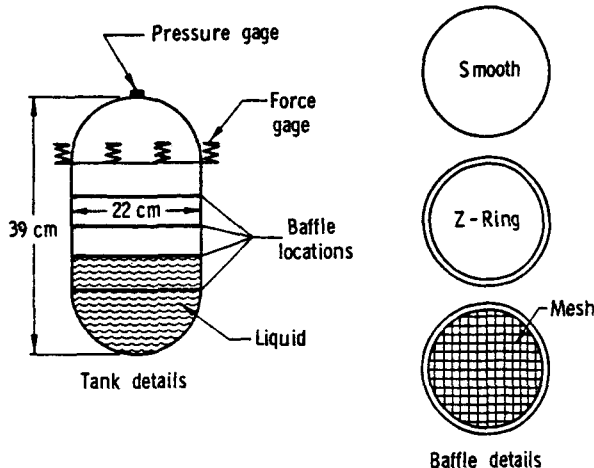


FIGURE 10.9.—Model tank geometries (ref. 10.5).

ciated accelerations at time of maximum force,  $n_1 g$ , as low as 0.5 g. The sample force and pressure time histories shown in reference 10.5 imply that the total duration of the deceleration pulse,  $T_s$ , ranged between 1<sup>+</sup> and 3 times the time necessary for the first portions of the fluid to contact the dome.

The effect of a first-mode lateral slosh existing at the beginning of deceleration was investigated, and this was found to affect significantly the mode of fluid motion. When the initial fluid surface was quiescent, the fluid behaved in the same way as in reference 10.3. Depending on the portion of the lateral sloshing cycle at which the deceleration started, the fluid tends to travel up one side of the tank, around the bulkhead, and down as illustrated in figure 10.10. This is virtually the same behavior as shown in the experiments of reference 10.3 when the apparatus was inclined. Maximum pressure data obtained are reproduced here as figure 10.11. Though no appreciable alteration in total dome impact force was found by the addition of Z-ring baffles, the "screen" baffles made a visible reduction (fig. 10.12).

A scale effect study was also made by varying the temperature of the fluid in the tank to alter vapor pressure and viscosity, and by adding a detergent to reduce surface tension.

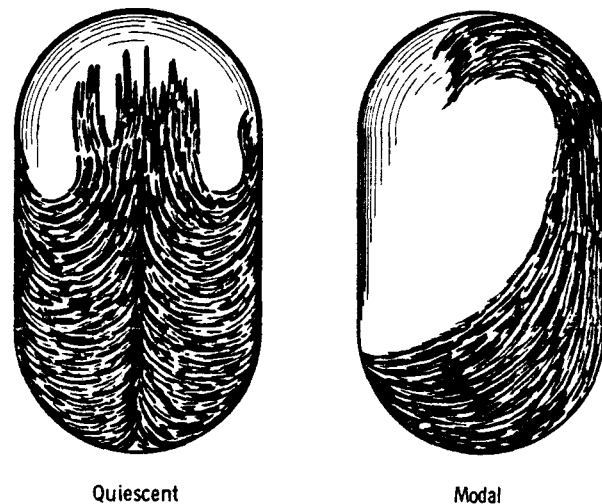


FIGURE 10.10.—Representation of liquid motions (ref. 10.5).

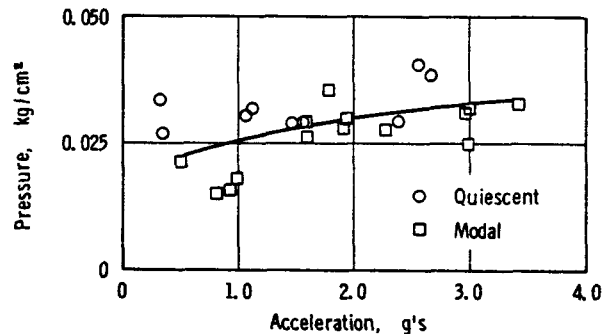


FIGURE 10.11.—Pressure versus acceleration in smooth wall tank (ref. 10.5).

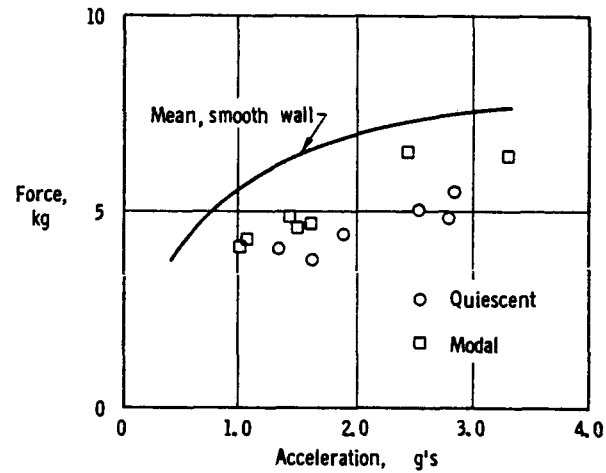


FIGURE 10.12.—Force versus acceleration with and without screen baffle (ref. 10.5).

This program led to the following tentative conclusions:

(1) The liquid exhibits one of two flow patterns depending upon the condition of the surface prior to arrest: i.e., (a) if the liquid surface is undisturbed or quiescent, it travels in a series of streamers; (b) if the surface is oscillating in its fundamental antisymmetric mode, a portion of the liquid travels up one side of the tank, around the dome, and down the opposite side.

(2) The impact force appears to be dependent upon the relative acceleration of the tank at the time of impact.

(3) For a given acceleration level, there appears to be no significant difference in the magnitude of the modal and quiescent impact force.

(4) The pressure in the center of the dome is about twice as high as the value obtained by dividing the average force by the projected area.

(5) The force level was not significantly altered by the inclusion of ring baffles; however, a reduction in force of approximately 30 percent was observed with the inclusion of the  $\frac{1}{4}$ -inch screen baffles.

(6) For the range covered in this investigation, no dependency of the force or pressure on the vapor pressure, surface tension, or viscosity was observed.

#### 10.4 SUMMARY OF LIQUID IMPACT STUDIES

From the point of view of practical design, the results obtained in the studies reviewed in the previous sections do not permit every question to be disposed of with great confidence; however, a review of some of the divergent conclusions arrived at and a gross comparison of results will be attempted in the paragraphs to follow.

##### Fluid Scale Effects

The previously cited references have considered the following fluid properties to be of possible importance:

- (1) Viscosity,  $\mu$
- (2) Surface tension,  $\sigma$

- (3) Fluid vapor pressure,  $p_v$
- (4) Mass density,  $\rho$

The nature of the problem is such as to make a relative deceleration of importance. The various similitude analyses result in scaling parameters analogous to the Euler, Reynolds, Weber, and cavitation numbers; a set of these sufficient for present purposes may be written as

$$\left. \begin{aligned} \text{Pressure coefficient} &= p/\rho_f \bar{n} g d_t \\ \text{Viscosity parameter} &= \bar{n} g d_t^3 / \nu_f^2 \\ \text{Surface tension parameter} &= \rho_f \bar{n} g d_t^2 / \sigma \\ \text{Cavitation index} &= (p_a - p_v) / \rho_f \bar{n} g d_t \end{aligned} \right\} \quad (10.33)$$

In effect, scaling of pressures by the first relation is correct if the remaining three parameters are satisfied or are not important. Satisfaction of these is not possible for every conceivable case. Figure 10.13 indicates the ranges of viscosity parameter and surface tension parameter which have been attained in references 10.3, 10.5, and 10.6, compared with an outside prototype range. The prototype range spans conditions from a 2-meter-diameter tank containing kerosene to a 9-meter-diameter tank

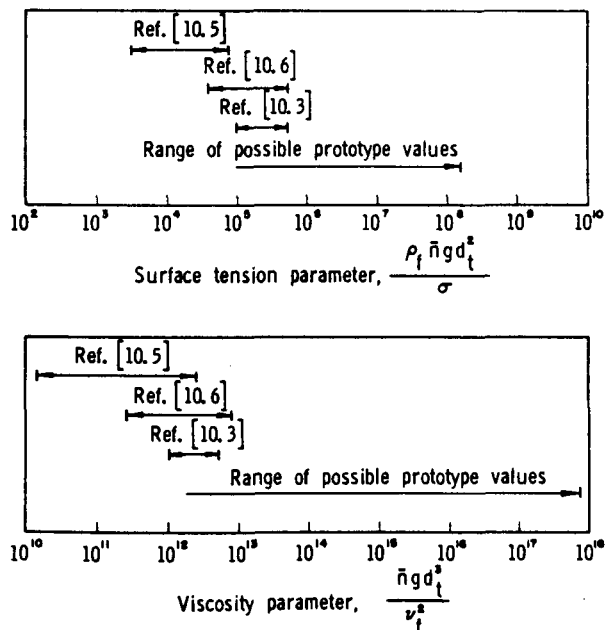


FIGURE 10.13.—Approximate ranges of viscosity and surface tension parameters.

containing liquid oxygen and subject to a 2-g deceleration. While reference 10.6 indicates the possibility of a viscous scale effect, this is based on analysis of initial portions of the total dome force records and thus can serve only as a warning, not as a source of quantitative design data. On the other hand, no scale effects were found in the study of reference 10.5; however, this conclusion is a qualified one, and it may be seen by examining the evidence presented in substantiation in reference 10.5 that, indeed, no systematic differences in impact force were obtained which were substantial enough to overcome the normal scatter of data. These experiments are difficult, and it appears in both references 10.5 and 10.6 that unexplained data scatter can range to  $\pm 20$  percent. It would seem possible, then, that at most a 20-percent change in force from one end to the other of the viscosity range covered in references 10.5 and 10.6 might be present. If so, straight-line extrapolation on a logarithmic plot of viscosity parameter (fig. 10.13) would indicate that pressures estimated at a viscosity parameter of  $10^{12}$  and extrapolated to the end of the prototype range using the pressure coefficient approach, equation (10.33) could be as much as 40 percent in error. Exactly the same argument and result applies to possible surface tension scale effects.

The scale effect work in reference 10.5 covered a cavitation index range of

$$6 < \text{cavitation index} < 100$$

The lower end of this range is important from the cavitation standpoint. Cryogenic fuels in a 9-meter tank with a pressurant of 2 atmospheres may have a cavitation index corresponding to the above of unity, and it may be that the experiments of reference 10.5 have covered most of the practical range of cavitation index without enormous scale effect.

#### Impact Pressure Distributions

The data of reference 10.3 imply a relatively constant pressure distribution over the upper bulkhead, while those of reference 10.5 indicate a distribution with maximum at the center. This is an apparent disagreement only. When

the pressure data for vertical firings with hemispherical head of reference 10.3 are examined alone, it appears that pressures near the edges of the dome average about half of those near the top. This is the only comparable case with the data of reference 10.5. The data for vertical firings from reference 10.3 are subject to considerable scatter, and while all of the pieces of data from Cell No. 1 (fig. 10.5, hemispherical head) follow this trend, 3 out of 10 of the datum from Cell No. 4 do not. The pressure data in reference 10.3 for vertical firings for the conical bulkhead display no consistent trend. Indicated maximum pressures from the cells at the sides (Cells Nos. 1 and 4, fig. 10.5) range from half to twice those measured near the center (Cell No. 2), with no preponderance of either trend. The conclusion in reference 10.3 of a "not great" pressure variation over the head is apparently based on the preponderance of data which are from the inclined firings. In all the inclined cases, variation in maximum pressures appears generally to be  $\pm 25$  percent.

#### Duration of Experiments

Since equation (10.24) implies that significant axial deceleration resulting from rocket drag will persist for many times the minimum time required for a free particle to arrive at the upper bulkhead,  $t_a$ , an assessment of the cited experimental work in this light is in order. The tank sizes used in reference 10.3 indicate experiment duration times of two to three times  $t_a$ . The work in reference 10.6 indicates that actual first-arrival times roughly correspond to  $t_a$  for vertical firings. Since the vertical firing case of references 10.3 and 10.6 is analogous to the situation in the apparatus of reference 10.5, it would seem that the experiments of reference 10.5 also had durations of  $3t_a$  at most. If impact forces reach a definite maximum in this interval and seem unaffected by the premature end of the experimental deceleration, then this experimental compromise with what may happen in reality is not important.

In the experiments of reference 10.3, a maximum, unaffected by the shortness of the experiment, was apparently experienced for inclined firings. The experiments of reference

10.6 (vertical firings) resulted in force maxima so obviously dictated by the end of the deceleration pulse that the maxima of the data were not considered of general use. It is not clear from reference 10.3 that a definite maximum is reached for vertical firings before the end of the deceleration pulse. Review of the motion pictures produced at the time indicated that the fluid breaks away from the initial quiescent free surface in a large number of streamers slightly after a relatively thin annular ring of fluid moves up the walls of the tank. This annular ring of fluid is believed to be an effect produced by surface tension. Thus, the first fluid reaching the dome is thought to be composed of a very thin sheet of fluid moving up the sides, plus a "cloud" of droplets. The breaking away of the fluid from the main body at the bottom of the tank apparently proceeds at a rate depending on the properties of the fluid and the acceleration. The motion pictures show most of the fluid in transit or remaining at the upper bulkhead at the end of the stroke, for the  $\frac{1}{4}$ -full case. For the  $\frac{1}{2}$ -full case, however, about half the original amount of fluid remains at the bottom of the tank, while the amount in transit and the mode of transit appears similar to the  $\frac{1}{4}$ -full case.

These observations lead to the hypothesis that when the deceleration is directed perpendicular to the free surface, the initial fluid impact on the upper bulkhead is similar to that of a hard rain on an empty bowl; high pressures can be generated, but average pressures over reasonable areas are small. As the deceleration continues, "rain" is generated continuously from the main body of fluid, and builds up against the upper bulkhead, slowly increasing an essentially fluid-static pressure until all the fluid is in contact. If this be the case for the vertical firings of reference 10.3, the maximum pressures measured were not the maximum which would have been attained had the deceleration continued for twice or three times the attained interval.

Judging from the sample force and pressure time histories in reference 10.5, the maximum force or pressure was reached at about three-fourths of the total duration of the half-sine relative acceleration pulse. This point in time is about where the acceleration pulse may be

thought to be beginning the most rapid half of its decay from maximum to zero. Whether the observed forces or pressures in reference 10.5 may be expected to hold for longer deceleration pulses of the same magnitude is perhaps an open question.

In summary, the question of the duration of the experiments relative to possible prototype durations has been consistently omitted from the cited references, but is a consideration in the problem.

#### Variation of Impact Pressures With Acceleration

The conclusions of reference 10.3 recommended, for design purposes, that a design impact pressure could be taken as a constant times the deceleration. This approach is consistent with the pressure coefficient approach noted in equation (10.33). Reference 10.5, on the other hand, noted that maximum pressures and forces are dependent on acceleration, and the force and pressure results of that reference do not appear to be proportional to acceleration. The comparative situation is summarized in figure 10.14. This figure was prepared from all the pressure data contained in references 10.3 and 10.5 (which together may very well contain all existing pressure data) as follows:

The pressure data of figure 10.11 were converted to pressure coefficient form using the indicated accelerations of that figure. (These accelerations are those derived for the moment of maximum pressure.) Both the "quiescent" and "modal" data are shown, and the pressure coefficients are plotted against indicated relative acceleration in the left-hand portion of figure 10.14.

The pressure data of reference 10.3 are too voluminous to fit on a single plot with clarity if the results of all pressure cells are included. Consequently, the highest maximum pressure,  $P_{max}$ , measured on any cell during a single firing was arbitrarily chosen as indicative and this pressure was nondimensionalized by the average acceleration measured during that firing. The results are plotted against average acceleration on the right-hand side of figure 10.14. Each series of connected solid or dashed line segments connect the test points obtained in a series of firings at different accelerations with the same inclination, head geometry, baffling, and amount of fluid.

It appears that the results of the two references are not consistent. The pressure coefficients derived from the data of reference 10.3 appear to be relatively independent of

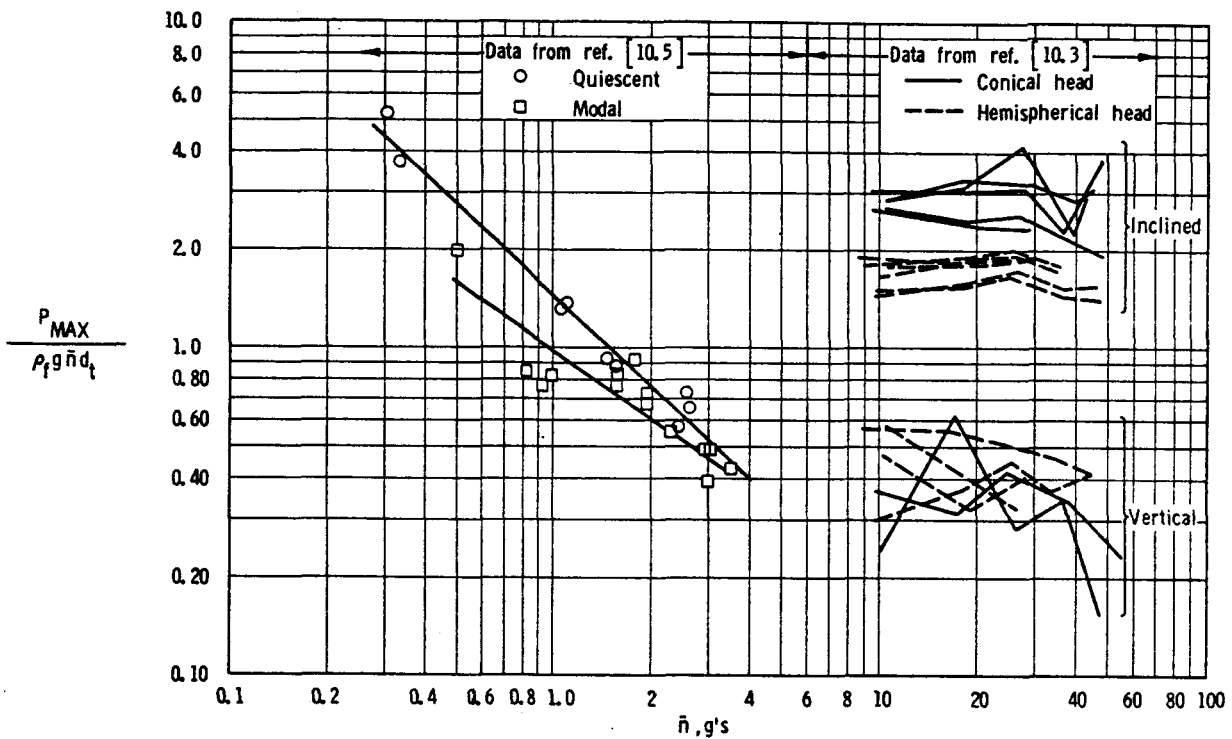


FIGURE 10.14.—Maximum pressure coefficient versus acceleration.

acceleration within attainable experimental accuracy, which is as it should be if this extrapolation approach is valid. The trend of the pressure coefficients from reference 10.5 indicate just the opposite; in fact, to the same accuracy that the data of reference 10.3 indicate proportionality of pressure and acceleration, the data of reference 10.5 indicate virtual independence of pressure and acceleration.

#### Effect of Lateral Sloshing and Lateral Acceleration

Figure 10.14 illustrates the differences of pressures between the rotational and "modal" mode of fluid motion. The data of reference 10.5 quite plainly indicate that about the same pressures are induced by the modal and the "quiescent" mode. In the results of reference 10.3, even though the fluid behaves in a manner similar to the "modal" of reference 10.5 for inclined firings, the pressures induced are several times higher than those from vertical firings. The obvious difference is that the first-mode lateral sloshing of reference 10.5 dictates initial conditions, while the constant

lateral acceleration of reference 10.3 acts continuously on the fluid.

From the point of view of the estimates of section 10.2, the variation of impact pressures with relative normal acceleration is of greater interest than the variation with the inclination of apparatus in the laboratory. Accordingly, the maximum pressure coefficients from reference 10.3 are shown in figure 10.15 as a function of the ratio of relative normal to axial acceleration ( $\bar{x}/\bar{n}$ ). The data points have been segregated according to initial angle of inclination of the free surface and according to head shape. Included, but not denoted by special symbols, are both the cases of one-fourth and one-half full and the cases where ring frames were installed. Quantitative data for an apparatus inclination of  $12.5^\circ$  were obtained from the authors of reference 10.3 and are included. As in the preceding paragraph, each point reflects the highest pressure recorded on any of the pressure taps during a test firing.

Figure 10.15 shows that, within the limits dictated by the appreciable data scatter, the

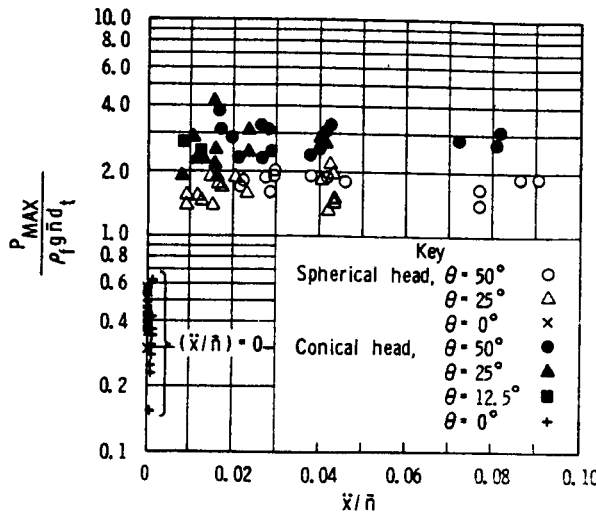


FIGURE 10.15.—Maximum pressure coefficient versus lateral acceleration ratio.

pressures are not appreciably influenced by the magnitude of lateral acceleration until the lateral acceleration ratio falls somewhere below 0.008. The transition in pressures between  $(\ddot{x}/\bar{n})$  of 0.008 and 0.0 is unfortunately not covered by the data. That a value of  $\ddot{x}/\bar{n}$  of 0.01

is a practical value may be seen by noting, in accordance with section 10.2, that  $\ddot{x}/\bar{n}$  is roughly equivalent to rocket lift to drag ratio, and that this value of lift to drag might be achieved with a rocket angle of attack between  $4^\circ$  and  $2\frac{3}{4}^\circ$ . According to figure 10.2, an initial fluid angle of  $6^\circ$  or  $8^\circ$  is possible for an angle of attack of  $2\frac{3}{4}^\circ$ .

By noting that the pressures for the differing initial fluid angles are the same within data scatter, the hypothesis that impact pressures are not influenced by the magnitudes of either initial fluid angle or lateral acceleration may be approximately true. Perhaps all that is important is to have an initial angle and a slight lateral acceleration to set the mode of motion of the free surface.

Small relative normal accelerations and first-mode sloshing are both to be expected in a booster vehicle in the atmosphere and, in the absence of better data, it must probably be assumed that the pressures measured in the inclined firings of reference 10.3 are indicative of practical possibilities.

## Part II. Liquid Rotation and Vortexing During Draining

*Franklin T. Dodge*

### 10.5 INTRODUCTORY REMARKS ON ROTATIONAL LIQUID MOTIONS

Of the various types of liquid motion that may occur in rocket fuel tanks, those that involve rotational liquid motions are of special interest for several reasons. As one example, unexpected behavior during the flight of Transit 2-A has been tentatively explained by postulating that rotational sloshing (see ch. 3) occurred in the fuel tank (unbaffled); the sloshing produced a certain amount of fluid angular momentum, which in turn caused a roll torque of about 3 kilogram-meters to be exerted on the missile (ref. 10.10). Furthermore, if a considerable amount of liquid angular momentum exists, it is relatively easy for a large vortex to form during draining; this can result in a hollow core over the drain (see fig. 10.16) and a consequent decrease in the fuel flow rate.

### 10.6 RECENT RESEARCH TRENDS

Problems of liquid rotation and vortexing are intrinsically very complex. Sufficiently accurate and detailed experimental data to give real insight into the actual physical processes are extremely difficult to obtain, and theoretical analyses are hindered by this same lack of understanding. Available theories and experimental results are reviewed in this section; however, as will be seen, they leave considerable room for improvement.

The central subject of this section is the vortex that forms whenever a tank drains through a small orifice; however, in order to carry out a reasonable discussion of this problem, it is also necessary to discuss liquid rotation, since by its very nature a vortex is accompanied by a substantial amount of swirling liquid motion. In this context, "rotation" implies only that a certain amount of liquid angular momentum exists about some axis (usually the vortex core);

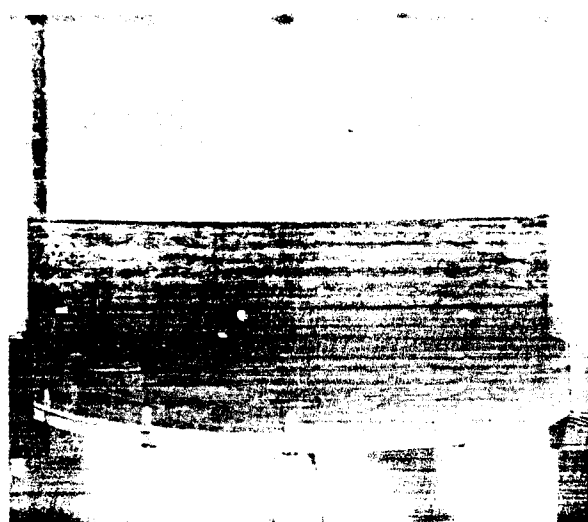


FIGURE 10.16.—Vortex formed during steady gravity draining from a cylindrical tank (ref. 10.11).

it does not necessarily mean that the smallest liquid particles rotate about their own axes, which is the more common definition of liquid rotational motions.

As anyone who has ever seen a draining vortex has noted, the centrifugal forces in the rotating liquid are sometimes large enough to form a hollow core over the drain. This causes a decrease in the draining rate for two reasons: the effective area of the drain is decreased by the air core, and the liquid potential head is partially converted into rotational velocity instead of axial (drain) velocity. A physical picture of these phenomena can be constructed in a relatively simple way. To start with, a free vortex in an ideal liquid carries along with it a rotational or swirling fluid velocity of magnitude

$$V_r = \frac{\Gamma}{2\pi r} \quad (10.34)$$

where  $\Gamma$  is the circulation and  $r$  is the distance from the vortex.  $\Gamma$  measures the vortex strength; its exact value may be computed by taking the line integral of the velocity around any curve enclosing the vortex, since the integral is equal to  $\Gamma$ . It is clear from equation (10.34) that the vortex flow field possesses a definite amount of angular momentum (the momentum is theoretically infinitely large if the field extends to  $r = \infty$ ); however, no physical significance can be attached to this flow field near  $r = 0$ , since infinite velocities are predicted here. For this reason, Rankine hypothesized that a line vortex must consist of a filament of finite radius,  $a$ , and constant vorticity,  $\omega$ , surrounded by an irrotational vortex field of the same circulation,  $\Gamma = \pi \omega a^2$ , as the periphery of the filament.<sup>1</sup> The liquid velocity at  $r = a$ , from equation (10.34), is equal to  $\pi \omega a^2 / 2\pi a = \frac{1}{2}\omega a$ . Hence, since the velocity varies linearly with radius in the forced vortex, the flow field of Rankine's combined free and forced vortex is

$$\begin{aligned} V_\theta &= \frac{1}{2} \omega r \text{ for } 0 \leq r \leq a \\ V_\theta &= \frac{\omega a^2}{2r} \text{ for } r \geq a \end{aligned} \quad (10.35)$$

The free surface shape can be computed from Euler's equation by inserting in it the velocity profiles of equation (10.35). Typical results are shown in figure 10.17 for two different values of the filament radius,  $a$ . It can be seen that increasing the vorticity,  $\omega$ , or decreasing the filament size,  $a$ , increases the depth of the depression at the center; ultimately an air core will form. (Fig. 10.12 and most of the preceding discussion are taken from an informative article by Rouse (ref. 10.12). A rather complete bibliography is included in this article; more recent developments are reported in ref. 10.13.)

The preceding explanation of vortexing is by no means complete, since, in fact, radial and axial (drain) velocities also exist; moreover, the size of the core and the assumed vorticity

<sup>1</sup> The flow field of equation (10.34) is irrotational except at the origin. This can be seen by computing the actual particle rotation, which is

$$\omega_{\text{part}} = \frac{1}{2} \left( \frac{\partial V_\theta}{\partial r} + \frac{V_\theta}{r} \right) = \frac{1}{2} \left( -\frac{\Gamma}{2\pi r^2} + \frac{\Gamma}{2\pi r^2} \right) = 0$$

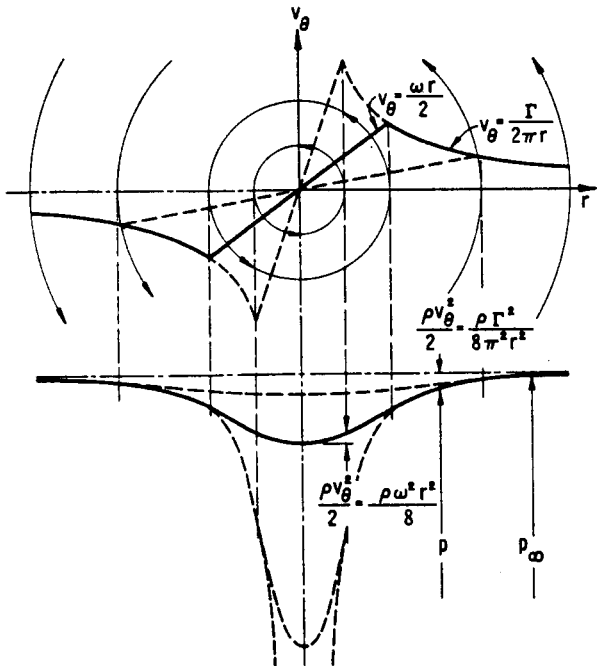


FIGURE 10.17.—Characteristics of the Rankine combined vortex (ref. 10.12).

distribution within it are only approximations. However, more serious questions than these arise. Motions of the type described by equation (10.34) or (10.35) cannot arise in a perfect fluid, which at some instant was free of vortices, unless at least a part of the forces acting on the liquid are not conservative; that is, unless they are not derivable from a scalar potential. In fact, according to Prandtl (ref. 10.14), application of the principle of angular momentum to an inviscid fluid leads to the conclusion that in all cases the moving fluid must previously have possessed circulation. Consequently, one may ask: How does the angular momentum (or the vortex) come into being? One answer is that when the flow field exists on a large-enough scale, such as in hurricanes or tornadoes, the radial velocity toward the center can generate a rotational flow field through the Coriolis effect of the Earth's rotation. But Coriolis forces are not sufficient to explain the vortices of even sizable drains (ref. 10.12), so that other effects are primarily responsible here.

Dergarabedian (ref. 10.15) has given an approximate theory of vortex formation during

tank draining. According to his discussion, the core formation is a consequence of the unsteady free surface boundary conditions. He has shown that during draining, any small initial swirling velocity increases in magnitude with time and asymptotically approaches the distribution given by equation (10.34), except near the center  $r=0$ . However, his analysis is not completely satisfactory because it is necessary to assume an initial rotational flow field, even though the velocity of this field may be indefinitely small. A recent series of experiments (ref. 10.16) have shown that under some conditions the combination of a rectilinear boundary layer flow with a symmetrical sink flow is unstable in the sense that amplifications of perturbations of the secondary vorticity associated with the curved streamline pattern lead to the creation of circulation around the sink outlet. These observations suggest that the circulation in a "bathtub vortex" might be created in a similar manner.

To circumvent the foregoing difficulties, it is customary in both theoretical and experimental investigations of draining vortices to produce initially a large swirling motion by artificial means. Typical results of these investigations have been presented by Binnie and his co-workers (refs. 10.17 and 10.18). Kamel has verified part of these results in his experiments (ref. 10.19). Figure 10.18 shows his results for the discharge coefficient,  $K$ , of a number of different orifices located at the bottom of a 27-centimeter-long, 10-centimeter-diameter tank, as a function of the initial swirl,  $X$ .

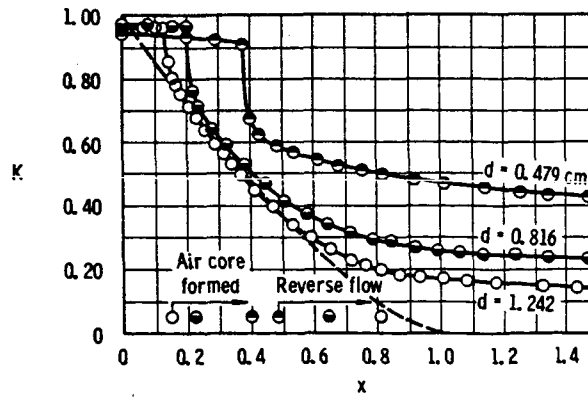


FIGURE 10.18.—Nozzle discharge coefficients (ref. 10.17).

229-648 O-67—25

In terms of the draining flow rate,  $Q$ , the total liquid head,  $H$ , and the orifice diameter,  $d_0$ ,  $K$  and  $X$  are defined as

$$K = \frac{4Q}{\pi d_0^2 (2gH)^{1/2}} \quad (10.36)$$

and

$$X = \frac{2\Omega}{d_0(2gH)^{1/2}} \quad (10.37)$$

where  $\Omega$  is the product of the swirling (tangential) velocity near the inner surface of the tank and the tank radius. For  $X=1.0$ , the theoretical discharge coefficient should fall to zero; this implies that the available liquid head has been completely converted into swirling motion. Experimentally, a nonzero value of  $K$  was reported for all values of  $X$ ; however,  $K$  does fall off significantly from its no-swirl value as  $X$  increases from zero. Moreover, an air core was observed in the large orifices. Reversal of the axial velocity close to the air core was also observed, but this is a consequence of the flow through the boundary layer on the bottom plate exceeding the discharge capacity of the outlet.

In a draining fuel tank, rotary sloshing is a readily available mechanism for producing swirling motion. (See ch. 3.) Thus, it is possible for effects such as those illustrated in figure 10.18 to occur naturally when sloshing and draining occur simultaneously. In order to compute the magnitude of the swirling motion due to sloshing, Hutton (ref. 10.20) has computed the transport velocity of the fluid particles during rotary sloshing. It was necessary to include nonlinear terms in the analysis, which is based on the inviscid flow assumption of irrotationality, because the average particle displacement in a linear wave theory is zero. He found that the maximum angular momentum of the fluid was about  $0.32(\eta/d_t)^2$  of the angular momentum if the fluid moved as a rigid body at the same rate as the free surface waves ( $\eta$  is the peak wave height, and  $d_t$  is the tank diameter). Thus, the angular momentum of rotary sloshing, while small, is probably sufficient to initiate the vortex formation, according to Dergarabedian's theory.

Another consequence of this angular momentum is that a roll torque will be exerted on the tank walls by the swirling motion. (See also the discussion of ch. 1 with regard to flight tests of the Saturn vehicle.) In a series of full-scale and model tests designed to test this conclusion (ref. 10.10), it was found that negligibly small torques (less than 0.15 kilogram-meter) were produced by rotary sloshing in an *unbaffled* tank. These findings appear to disagree with the data from the Transit 2-A flight test mentioned previously; however, the tank motion during flight was considerably more severe than in the full-scale ground tests. Also, during flight the drain rate of the fuel was approximately 14 kilograms per second, while, in the ground tests, it was zero; thus any torque produced by the simultaneous sloshing and draining would be absent in the ground tests. According to the previous paragraphs, draining tends to increase any rotational motions present, so the above conclusions are probably reasonable.

As an interesting sidelight, the roll torque produced in the *baffled* tank was as large as 3 kilogram-meters in some cases. This, of course, is in disagreement with the common assumption that an increase in damping decreases the sloshing forces and torques.

A series of qualitative experiments of draining and sloshing are reported in reference 10.11. The model tank employed in these experiments was 28 centimeters in diameter, with a 2.9-centimeter-diameter drain hole at the bottom. The tank was drained both by gravity and by pumping, with and without initial liquid rotation. Some of the observations were made with a cross-type baffle over the drain, as shown in figure 10.19. The results of numerous tests can be summarized as follows:

(1) Tank filled and draining initiated immediately. No baffle. Vortex appeared when the fluid level dropped to approximately 2 centimeters from bottom. Drain time, 24.0 seconds.

(2) Tank filled and draining initiated after substantial time delay. No baffle. Small vortex appeared when fluid level dropped to

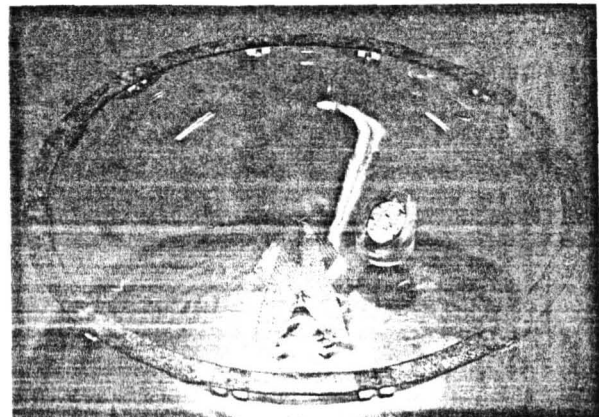


FIGURE 10.19.—Cruciform vortex baffle.

approximately 2 centimeters from bottom. Drain time, 23.0 seconds.

(3) Tank filled and draining initiated immediately. Cross-type baffle above drain. No vortex. Drain time, 22.5 seconds.

(4) Tank filled and strong initial liquid rotation introduced artificially. No baffle. Vortex appeared when fluid level dropped to approximately 9 centimeters from bottom. Drain time, 40 seconds.

(5) Tank filled and strong initial liquid rotation introduced artificially. Cross-type baffle. No vortex. Drain time, 23.0 seconds.

(6) Draining while undergoing normal sloshing. Similar to (1) above.

(7) Draining while undergoing rotary sloshing. Similar to (4) above. Draining time was very long.

(8) Draining while undergoing normal sloshing. Cross-type baffle. Similar to (3) above, except drain time for last 2 centimeters of fluid was considerably longer.

From these results it may be concluded that a small amount of liquid rotation appears to have a negligible effect on vortex formation. Moreover, sloshing tends to break up a vortex as soon as it is formed, except that rotary sloshing produces a strong vortex. This is in agreement with the other results mentioned previously.

The flow of liquid from tanks in a *low-gravity* field can lead to considerable surface distortion and gas ingestion in the outlet line, even when

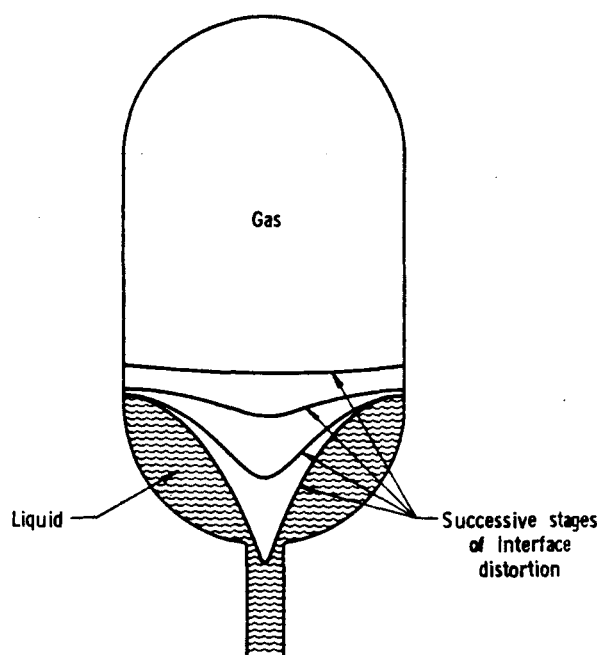


FIGURE 10.20.—Gas ingestion during low-gravity draining  
(ref. 10.21).

the vorticity is negligible. (See fig. 10.20.) This is caused primarily by the reduced body forces acting in combination with the non-uniform flow velocity across the tank cross section (ref. 10.21).

As a conclusion to this brief section, it appears that no existing theory completely explains vortex formation and liquid rotation during draining. In some cases, such as when rotary sloshing and draining occur simultaneously, large roll torques can be exerted on the tank, and the draining flow rate may be substantially decreased. Fortunately, it appears that adequate baffling can be provided on an empirical basis to ameliorate this situation. Such suppressors are almost invariably provided to control normal sloshing, so vortexing and rotational motions should be adequately controlled in normal cases. Thus, these types of liquid motion, while of considerable interest from a fluid mechanic viewpoint, are probably of less importance in practice.

## Part III. Longitudinal Oscillations of Flight Vehicles

Daniel D. Kana

### 10.7 POGO PHENOMENA

Longitudinal structural oscillations at low frequencies (5 to 25 cps), superimposed on the usual steady accelerating motion, have been observed on a number of rockets and launch vehicles during flight. The basic structural oscillation occurs in the fundamental longitudinal free-free mode, so that the vehicle experiences an accordion-like motion, with the ends of the vehicle moving out of phase with respect to each other; hence, the behavior has been nicknamed "pogo" oscillation.

A general description of this type of behavior is shown in figure 10.21, which is taken from the report of Rubin (ref. 10.22). At some time during the steady rising trajectory of the vehicle, an unstable coupling between some vehicle subsystem and the structure occurs, so that an oscillation at the structural frequency builds up, levels off, and then subsequently decays after enough change has occurred for the coupling to become stable again. The time of flight at the onset of the oscillations, as well as the frequency, severity, and duration of the phenomena, depends on the particular vehicle in which this type of behavior has occurred. However, in all cases, it appears that the frequency of the oscillations tracks the changing

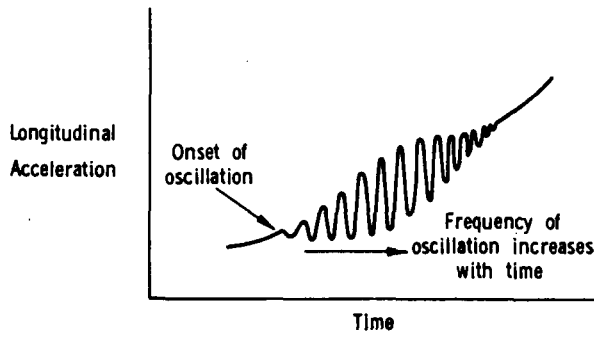


FIGURE 10.21.—Pogo oscillation superimposed on rising trajectory acceleration (ref. 10.22).

structural resonant frequency during the entire period of the behavior.

Thor-Agena and Titan II have experienced particularly severe oscillations (typically 0.5 to 3 g at the payload) toward the end of first-stage burnout. The frequency variations are about 16.5 to 21 cps for Thor-Agena and 10 to 13.5 cps for Titan II, with the most severe oscillations occurring at 20 cps and 11 cps, respectively, for the two vehicles. Characteristically, they have been referred to as the 20-cps problem and the 11-cps problem. Associated with the behavior of these vehicles are strong pressure fluctuations in various parts of the propellant feed system, and at the combustion chamber. Analyses have revealed that this behavior of these vehicles results from a closed-loop instability resulting from propulsion feedback with the fundamental longitudinal structural mode.

A somewhat different type of instability has occurred on most Atlas flights, although the results are essentially the same. Here the oscillations occur near 5 cps, with a duration of about 20 to 30 seconds immediately following liftoff. A dynamic analysis of this vehicle has revealed that the instability results from the coupling of the pneumatic regulation system for the ullage pressure and the longitudinal structural mode. The engine system is apparently not involved to any extent.

Several other vehicles have experienced similar oscillations at various times, but not with the severity of the cases mentioned above. It is obvious that such oscillations at low levels are at best undesirable, and at severe levels approach destruction of the vehicle. Elimination of pogo oscillations is particularly important in the case of launch vehicles used for manned flights because of possible adverse effects on astronaut's vision and manual reac-

tions. The use of the Titan II as the launch vehicle for the Gemini spacecraft prompted an extensive program to determine the causes of pogo oscillations in the various existing vehicles, as well as to develop fixes for these systems. Sufficient knowledge has now been gained so that the behavior has been explained qualitatively, and simplified models have been developed to study some of the systems over a wide range of parameters. Much of the present effort is being expended in refining the details of these models, so that they will provide a better quantitative prediction of pogo behavior. Further, the knowledge gained has indicated the requirement for dynamic analyses of all future systems during the design stage to detect potential pogo behavior.

Considering the current state of investigation of pogo behavior, as well as the variety of vehicles in which it has occurred to one degree or another, the present discussion will be limited to only a qualitative description of the two types of coupling mentioned above, along with a brief description of several of the devices employed as fixes for the system described. It must also be emphasized that the intent here is to recognize the overall role of the liquid fuel systems in the occurrence of this behavior, rather than to give a complete description of pogo behavior in any specific vehicle.

#### 10.8 ENGINE-STRUCTURE COUPLING

##### Simple Model

It has been mentioned that the study of pogo oscillations has developed to the point at which simplified models, including the appropriate mathematical transfer functions of the subsystems involved, can be formulated for the various vehicles to assist in the study of their behavior over wide ranges of parameters. The results of studies of engine-structural coupling using such models are given in references 10.22 through 10.25. Relatively simple models can be used to explain the behavior qualitatively, but more complex approximations are necessary to correlate quantitatively with the actual vehicle performance. A simple block diagram of a model will be used to describe the behavior in the present case.

The comparatively severe oscillations experienced by Thor-Agena and Titan II near the end of first-stage burning have been found to be the result of an instability in a closed loop comprised of the propellant system, engine, and structure. In the closed-loop system shown in figure 10.22, an oscillating thrust disturbance causes a longitudinal acceleration response in the first axial mode; the acceleration in turn acts on the mass of propellants in the tanks and feed lines, causing pressure fluctuations at the inlet to the propellant pumps; this causes corresponding perturbations in the pump flow rate, and thus an oscillatory engine thrust, which closes the loop. When the closed-loop gain is sufficiently large, and the total phase angle is such as to allow positive feedback, the acceleration response will be larger than the acceleration input disturbance; that is, an unstable situation exists, and the amplitude of all variables involved will tend to grow without

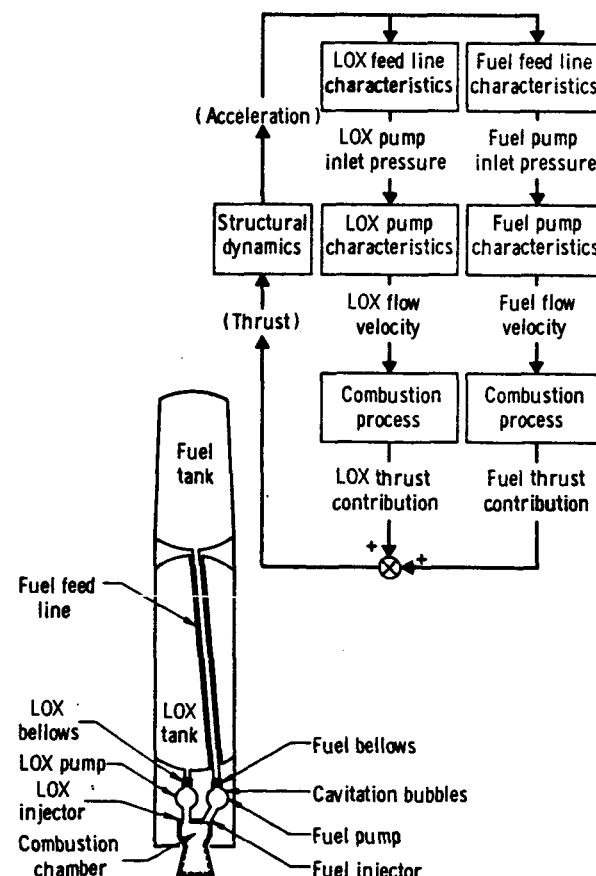


FIGURE 10.22.—Propellant transfer functions for simple vehicle representation (ref. 10.23).

limit. The actual limiting and subsequent restabilizing will occur as a result of changes in the system.

The entire sequence of pogo behavior for engine-structural coupling can be described by means of figures 10.23 and 10.24. For simplicity, only two subsystems in the loop are used: the structural system, whose resonant frequency,  $\omega_s$ , increases with burning time, and the propellant feed line, whose frequency,  $\omega_p$ , remains constant. The feed line frequency,  $\omega_p$ , is the resonant frequency for pressure oscillations in that subsystem and, hence, depends on the propellant compressibility characteristics, including effects due to gas bubbles from pump

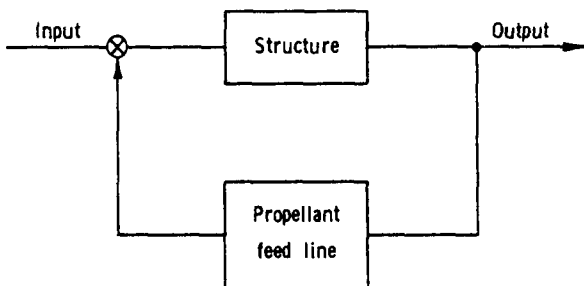


FIGURE 10.23.—Closed-loop positive feedback system (ref. 10.23).

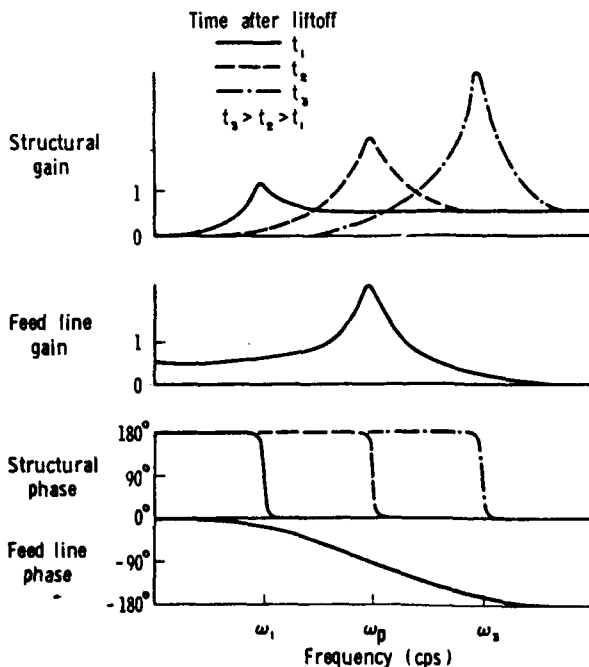


FIGURE 10.24.—Frequency response for sample subsystem (ref. 10.23).

cavitation or otherwise, and apparent compressibility effects as a result of the flexibility of the lines themselves. The resonances for both these systems are lightly damped. Pogo behavior results from the interaction of the two resonances as the changing structural frequency,  $\omega_s$ , sweeps past the propellant feed line frequency,  $\omega_p$ .

The interaction of the two resonances can be seen more in detail from figure 10.24. Here the changing structural gain (acceleration response per unit force input) and phase are shown at three different times, and can be compared to the constant propellant feed line gain (pressure response to unit pressure input) and phase. The structural gain and resonant frequency both increase with time, due to the decreasing propellant mass in the vehicle. Damping in the feed line is somewhat greater than that of the structure, so that its phase changes more gradually with frequency than does the structural phase. It may be noted that the structural phase is 180° leading (180° lagging) below resonance, passes through 90° leading (270° lagging) at resonance, and becomes zero (360° lagging) above resonance. This is because the observation point is at the engine section in the lower end of the structure, and the accordion-like motion results in such a phase response. The feed line inlet, also near the engine section, has the customary phase response of 0° below resonance, 90° lag at resonance, and 180° lag above resonance.

The net loop gain for the two systems is the product of the individual gains, and the net phase is the sum of the two individual phase angles. Instability will occur when the net gain is greater than unity, and the net phase angle is zero. At  $t=t_1$ ,  $\omega_s$  is at  $\omega_1$ , which is below  $\omega_p$ , and the net gain is less than unity. This corresponds to a stable condition early in flight. At a later time  $t=t_2$ ,  $\omega_s$  and  $\omega_p$  coincide, and the structural gain has increased to where the net gain is greater than unity, and the net phase is zero; hence, instability results and the oscillations grow. At a still later time,  $t=t_3$ , the structural gain has further increased so that the net gain is high, but the net phase angle has become negative so that the system is again stable.

### More Complete Model

The above explanation of pogo oscillations for engine-structural coupling has been based on only two subsystems: the structure and the propellant feed system. In the complete system, other subsystems, such as those shown in figure 10.22, influence the basic behavior to some extent. Therefore, in order to make quantitative predictions from a model, all of the significant subsystems shown must be represented. In fact, an even more complete system is shown in figure 10.25. This block diagram represents a simplified layout of the model used to study engine-structural coupling in Titan II and Thor-Agena. The complexity of the interaction of the various subsystems can readily be realized. An important feature in this schematic is that the net thrust is composed of the vector addition of engine thrust as well as apparent thrust felt by the engine from the (inlet pressure)  $\times$  (feed line area), from both the oxidizer and fuel lines.

Although the system, as depicted in figure 10.25, is considerably more complicated than

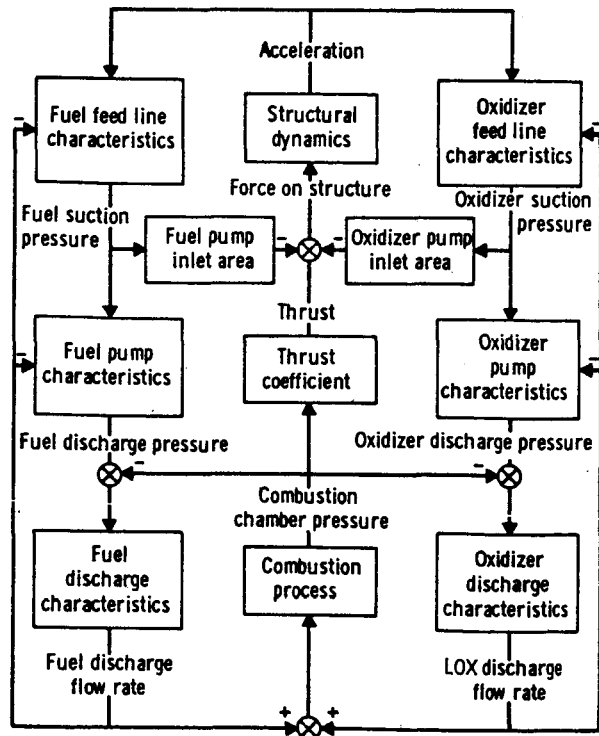


FIGURE 10.25.—Block diagram for complex vehicle representation (ref. 10.23).

as it is shown in figure 10.23, the occurrence of the pogo instability results from the same basic behavior: the sweeping of the structural resonant frequency through the constant propellant feed line resonant frequency, at a time during flight when the structural gain is high. As far as is known, resonance does not occur in any of the other subsystems in present vehicles; these subsystems simply alter the net loop gain and phase. Their presence is, of course, very important, because they can either deter or promote the instability, depending on their contribution to the total loop gain and phase. It must also be emphasized that the entire closed-loop system is composed of the oxidizer and fuel loops in parallel, and a pressure resonance occurring in either loop can cause the engine-structural instability.

### Fixes for Engine-Structure Coupling

Several devices have been proposed as fixes for engine-structural coupling, two of which have been used successfully on Titan II. Three such devices are shown in figure 10.26. Basically, all of these devices have but one purpose: to alter the propellant feed line pressure characteristics so that the changing structural frequency,  $\omega_s$ , can never coincide with the feed line frequency,  $\omega_p$ , or at least so that the coincidence will occur at such a time during flight that the net gain and phase will not result in an unstable system.

Additional compliance is added to the propellant feed system by means of a mechanical piston and spring in the accumulator (fig. 10.26(a)), by means of a gas bubble in the standpipe (fig. 10.26(b)), and by means of the bellows in the bellows device (fig. 10.26(c)). The accumulator has been used on the fuel system and the standpipe on the oxidizer system in Titan II. The result of incorporating these devices is to cause the propellant feed system frequency,  $\omega_p$ , to occur at a considerably lower frequency. Then, even if it is still above the structural frequency,  $\omega_s$ , at liftoff, as the two frequencies coincide early in flight, the structural gain is so low because of the nearly full fuel load, that the net gain never becomes greater than unity until after the net phase becomes negative. The use of such devices might be avoided

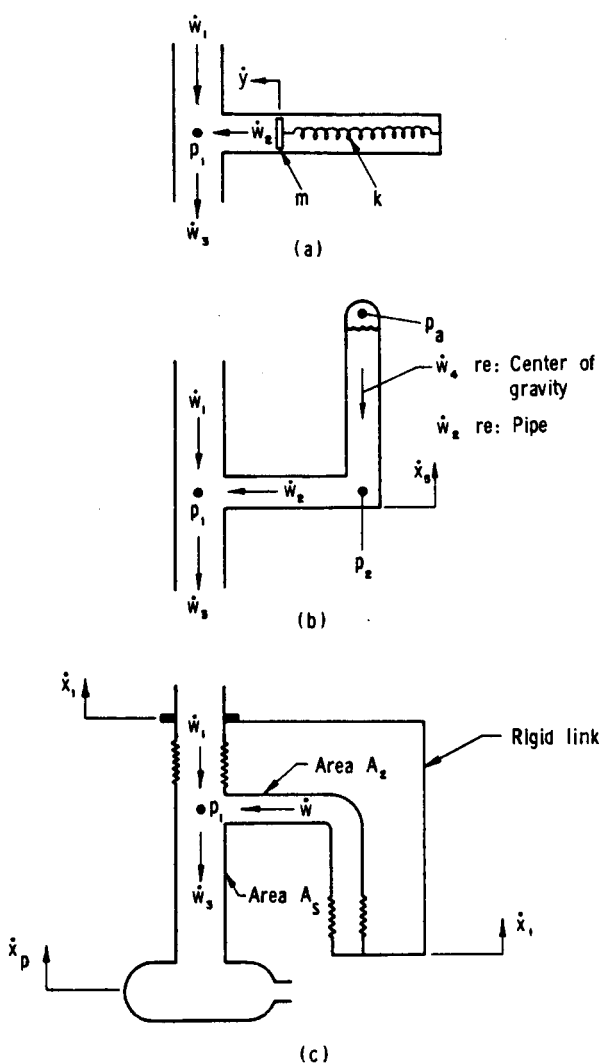


FIGURE 10.26.—Schematics of mechanical devices employed as pogo fixes (ref. 10.22).

if the proposed system can be analyzed sufficiently accurately for potential pogo behavior during the design stage of newly proposed vehicles.

#### 10.9 PRESSURE REGULATOR-STRUCTURE COUPLING

Analyses of pogo-type phenomena in the Atlas vehicle have been reported by Rose and Harris (refs. 10.26 and 10.27). In this vehicle, the oscillations occur for a duration of about 20 to 30 seconds immediately after liftoff, and at the longitudinal structural frequency of

approximately 5 cps. The analyses indicate that the engine does not play a significant role in this case, the unstable coupling occurring through the pressure regulation system for both the fuel and oxidizer tank ullage pressure.

Figure 10.27 shows a schematic of the pressure regulation system for either the fuel or oxidizer tank, the only difference being that a mixture of helium and oxygen is used for the oxidizer tank, while only helium is used for the fuel tank ullage. This system maintains a constant gage pressure in the tank ullage as the tank is drained. A pressure-sensing line transmits the ullage pressure to a pneumatic regulator, which in turn adjusts the flow rate of helium gas through a supply duct into the tank ullage.

At liftoff the transient engine thrust and launch forces excite the longitudinal modes of the vehicle, and a corresponding oscillation occurs in the tank ullage volume and pressure. This pressure oscillation results both from the

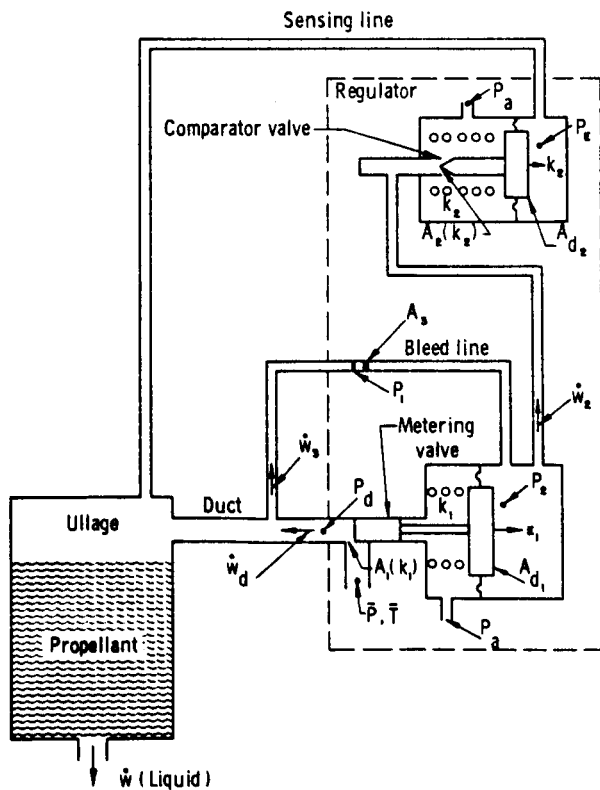


FIGURE 10.27.—Schematic of Atlas pressure regulation system (ref. 10.26).

variation in tank volume and a variation in the quantity of ullage gas present, resulting from the regulator responding to the ullage pressure oscillation. This oscillating pressure acts as an effective axial force on the vehicle structure. Analyses of suitable models of the system have indicated that the closed-loop system can be unstable for a period of time when the ullage volume is small, immediately

after liftoff. Subsequently, the gains and phases of the various subsystems change so that the net gain and phase no longer allow an unstable system. It must be emphasized that this type of coupling is entirely different from the previously described engine-structure coupling, but the net result is the same although the oscillations occur early in flight rather than near burnout.

## REFERENCES

- 10.1. NOLTING, R. K.: Simulation of Orbital Mooring of Gemini and Agena Vehicles by Means of Dynamically Scaled Models. Proceedings of Symposium on Aeroelastic and Dynamic Modeling Technology, U.S. Air Force, RTD-TDR-63-4197, 1964.
- 10.2. EIDE, DONALD G.: Preliminary Analysis of Variation of Pitch Motion of a Vehicle in a Space Environment Due to Fuel Sloshing in a Rectangular Tank. NASA TN D-2336, 1964.
- 10.3. EPPERSON, THOMAS B.; AND BROWN, ROBINSON: Dynamic Loads Due to Fuel Motion in Fuel Tanks of Missiles. Final Rept., Contract No. DA-23-072-ORD-1062, Southwest Research Institute, June 1957.
- 10.4. EPPERSON, T. B.; BROWN, R. B.; AND ABRAMSON, H. N.: Dynamic Loads Resulting From Fuel Motion in Missile Tanks. Proceedings of the Fourth Symposium on Ballistic Missile and Space Technology, vol. II, pp. 313-327, Pergamon Press, 1961.
- 10.5. STEPHENS, D. G.: Experimental Investigations of Liquid Impact in a Model Propellant Tank. NASA TN D-2913, 1965.
- 10.6. DALZELL, JOHN F.; AND GARZA, LUIS R.: An Exploratory Study of Simulation of Liquid Impact in Space Vehicle and Booster Tanks. Tech. Rept. No. 9, Contract No. NAS8-1555, Southwest Research Institute, Sept. 1964.
- 10.7. COKONIS, T. J.; TOMASSONI, J. E.; AND SEIFERTH, R. W.: Dome Impact Analysis—An Approximate Solution. Martin Co. Rept., TN LV 211, May 1963.
- 10.8. PINSON, L. D.: Propellant-Dome Impact Analysis. NASA Internal Memorandum, Nov. 1963.
- 10.9. Handbook of Astronautical Engineering. First edition, McGraw-Hill Book Co., Inc., 1961.
- 10.10. BRADY, W. F.; POPE, M. D.; AND PODÉ, L.: Ablestar Experimental Studies. Rept. SGC 32R-19, Space-General Corp., Aug. 1962.
- 10.11. ABRAMSON, H. N.; CHU, W. H.; GARZA, L. R.; AND RANSLEBEN, G. E., JR.: Some Studies of Liquid Rotation and Vortexing in Rocket Propellant Tanks. NASA TN D-1212, Jan. 1962.
- 10.12. ROUSE, H.: On the Role of Eddies in Fluid Motion. American Scientist, vol. 51, no. 3, Sept. 1963, pp. 285-314.
- 10.13. KÜCHEMANN, D.: Report on the I.U.T.A.M. Symposium on Concentrated Vortex Motions in Fluids. J. Fluid Mech., vol. 21, pt. I, Jan. 1965, pp. 1-20.
- 10.14. PRANDTL, L.: Essentials of Fluid Dynamics. Hafner, New York, 1949.
- 10.15. DERGARABEDIAN, P.: The Behavior of Vortex Motion in an Emptying Container. Proc. of the 13th Heat Transfer and Fluid Mechanics Institute, Stanford University, June 1960, pp. 47-61.
- 10.16. WESKE, J. R.: On the Origin and Mechanism of Vortex Motion at the Inlet of Intakes Placed Near a Flat Surface. Univ. of Maryland Tech. Note BN-152, AFOSR TN-58 863, 1958.
- 10.17. BINNIE, A. M.; AND HARRIS, D. P.: The Application of Boundary-Layer Theory to Swirling Liquid Flow Through a Nozzle. Quart. J. Mech. Appl. Math., vol. 3, pt. 1, 1950, pp. 89-106.
- 10.18. BINNIE, A. M.; HOOKINGS, G. A.; AND KAMEL, M. Y. M.: The Flow of Swirling Water Through a Convergent-Divergent Nozzle. J. Fluid Mech., vol. 3, 1957, pp. 261-274.
- 10.19. KAMEL, M. Y. M.: The Effect of Swirl on the Flow of Liquids Through Bottom Outlets. ASME Paper 64-WA/FE-37, ASME Winter Annual Meeting, New York, Dec. 1964.
- 10.20. HUTTON, R. E.: Fluid Particle Motion During Rotary Sloshing. J. Appl. Mech., Trans. ASME, Series E, vol. 31, Mar. 1964, pp. 123-130.
- 10.21. GLUCK, D. F.; AND GILLE, J. P.: Fluid Mechanics of Zero-G Propellant Transfer in Spacecraft Propulsion Systems. J. Eng. for Industry, Trans. ASME, Series B, vol. 87, Feb. 1965, pp. 1-8.
- 10.22. RUBIN, S.: Instability Model of Missile Longitudinal Oscillation Due to Propulsion Feedback. Rept. No. TOR-269(4126)-28, Contract No. AF04(695)-269, Aerospace Corp., Sept. 21, 1964.

- 10.23. DAVIS, W. F.; LYNCH, T. F.; AND MURRAY, T. R.: Thor 20-Cycle Longitudinal Oscillation Study. The Shock and Vibration Bulletin, no. 34, pt. 2, Dec. 1964, pp. 177-196.
- 10.24. MCKENNA, K. J.; WALKER, J. H.; AND WINJE, R. A.: Engine-Airframe Coupling in Liquid Rocket Systems. AIAA J. Spacecraft Rockets, vol. 2, no. 2, Mar.-Apr. 1965, pp. 254-256.
- 10.25. RADOVICH, N. A.: Analytical Model for Missile Axial Oscillation Induced by Engine-Structure Coupling. Proc. of AIAA Unmanned Spacecraft Meeting, Mar. 1965.
- 10.26. ROSE, R. G.; AND HARRIS, R.: Dynamic Analysis of a Coupled Structural/Pneumatic System Longitudinal Oscillation for Atlas Vehicles. Paper No. 64-483, Annual AIAA Meeting, Washington, D.C., June 1964.
- 10.27. ROSE, R. G.: Dynamics of the Atlas—5 cps Longitudinal Oscillation Following Launch as Related to the Tank Pressure Regulation System. Vol. 1, Longitudinal Model Development, General Dynamics/Astronautics, Dec. 31, 1963.

## PRINCIPAL NOTATIONS

- $A_p$ =projected lateral area  
 $a$ =radius of line vortex  
 $b$ =distance between initial position of a particle and the upper tank bulkhead  
 $C_{D_{\alpha=0}}$ =drag coefficient at zero angle of attack  
 $D$ =drag force  
 $D_0$ =drag at  $t=0$ ,  $v=v_0$ ,  $\alpha=0$   
 $D' = \frac{\partial D}{\partial v} \Big|_{v=0}$   
 $d$ =base diameter  
 $d_0$ =orifice diameter  
 $d_t$ =tank diameter  
 $F_i$ =acceleration force of apparatus (ref. 10.3)  
 $F_z$ =normal aerodynamic force  
 $F_y$ =axial aerodynamic force  
 $F_{x_0}$ =initial normal aerodynamic force  
 $F_{y_0}$ =initial axial aerodynamic force  
 $g$ =local gravitational acceleration  
 $H$ =total head  
 $h$ =tank depth  
 $I$ =mass moment of inertia of vehicle  
 $K$ =discharge coefficient  
 $(k_1 - k_2)$ =inertia coefficients  
 $k_p$ ,  $k^1$ ,  $k^2$ ,  $k^3$ =coefficients  
 $L$ =lift force  
 $l$ =overall vehicle length  
 $M$ =aerodynamic moment  
 $M_i$ =mass of apparatus (ref. 10.3)  
 $M_a = \frac{\partial M}{\partial \alpha}$   
 $m$ =vehicle mass  
 $m_i$ =mass of a particle of fluid  
 $m_r$ =mass of a particle of fluid in experimental apparatus
- $n$ =acceleration index (ref. 10.3)  
 $n_0$ =amplitude of half-sine relative acceleration pulse  
 $n_i$ =relative acceleration at maximum indicated impact force  
 $\bar{n}$ =average relative acceleration  
 $n(t)$ =acceleration pulse  
 $P_{max}$ =maximum impact pressure  
 $p$ =pressure  
 $p_a$ =ambient tank pressure  
 $p_v$ =fluid vapor pressure  
 $Q$ =draining flow rate  
 $q$ =dynamic pressure  
 $R_x$ ,  $R_y$ =forces acting on an isolated particle  
 $r$ =radius  
 $r_0$ =Earth radius  
 $S$ =stroke of apparatus (ref. 10.3)  
 $S_b$ =base area of booster  
 $T$ =engine thrust  
 $T_i$ =duration of experiment  
 $t$ =time  
 $t_a$ =minimum time for a particle to impact dome, experimental apparatus (ref. 10.3)  
 $t_c$ =time of initial contact  
 $t_{min}^b$ =minimum time required for a given fluid particle to reach the tank bulkhead  
 $u$ =normal velocity  
 $V$ =fluid velocity  
 $V_s$ =swirling velocity of fluid  
 $v$ =tangential velocity  
 $v_0$ =initial velocity  
 $W=mg$   
 $X$ =initial swirl  
 $x, y$ =moving coordinates

$x_1, x_t, y_1, y_t$ =coordinates of a particle

$x, y$ =coordinates

$\bar{y}$ =distance through which a particle travels in time  $t$

$(\ddot{y}_1)_0$ =relative particle acceleration at  $t=0$

$\bar{Z}$ =distance of center of pressure forward of vehicle center of gravity

$\alpha$ =vehicle angle of attack

$\alpha_0$ =vehicle angle of attack at  $t=0$

$\beta$ =angle of the quiescent fluid free surface with the normal to the tank axis

$\Gamma$ =circulation

$\eta$ =peak wave height

$\eta C_{Dc}$ =adjusted cross-flow drag coefficient.

$\theta$ =inclination of apparatus

$\mu$ =dynamic viscosity

$\nu$ =flight path angle

$\nu_f$ =kinematic viscosity of fluid

$\rho$ =mass density of air (local)

$\rho_f$ =mass density of fluid

$\sigma$ =surface tension

$\tau$ =nondimensional time

$\Omega$ =product of tangential velocity and tank radius

$\omega$ =vorticity

$\omega_p$ =propellant feed line frequency

$\omega_r$ =rocket structure resonant frequencies

## Liquid Propellant Behavior at Low and Zero g

*William C. Reynolds and Hugh M. Satterlee*

### 11.1 HYDROSTATICS AND HYDRODYNAMICS AT LOW g

#### Introduction

A full range of problems associated with the sloshing motions of liquids have been considered in previous chapters. The sloshing was presumed to arise as a result of a body force (gravitational or equivalent accelerational) acting on the liquid as a whole. When the magnitude of this body force becomes very small, other forces come into play and these must be considered in analyses of the sloshing motions. In this chapter, we shall consider the influence of the most important of these additional forces, capillary forces, on the sloshing motions and associated phenomena.

The term "zero g" is a misnomer. Even in the most advanced solar system mission one can contemplate, gravitational forces are never absent. In fact, the strength of the Earth's gravitational field 1000 miles from its surface is about 64 percent of the ground-level value. When we refer to a low-gravity environment we really mean that the statics or dynamics of a system relative to its traveling vehicle can be treated as though it were in fact in a low-gravity field. To illustrate this point, consider Newton's law as applied to a particle moving with acceleration  $a$  in some inertial frame:

$$F_{\text{rel}} + W = ma \quad (11.1)$$

$F_{\text{rel}}$  denotes the forces which the vehicle exerts on the particle, and  $W$  is the force exerted by the gravitational field. The acceleration may be represented as the sum of the vehicle acceleration,  $a_v$ , plus the particle acceleration relative to the vehicle,  $a_{\text{rel}}$ . The weight is

given by  $W = mg_L$ , where  $g_L$  is the local acceleration of a free particle in the gravitational field. Equation (11.1) then becomes

$$F_{\text{rel}} + m(g_L - a_v) = ma_{\text{rel}} \quad (11.2)$$

which may be written

$$F_{\text{rel}} + mg_{\text{rel}} = ma_{\text{rel}} \quad (11.3)$$

Under the special condition where the vehicle is accelerating at the exact acceleration that the particle would experience if it were free in the gravitational field; that is, when  $g_L = a_v$ , the dynamical equation for the particle relative to the vehicle would be identical with the equation for the particle in a truly zero-g environment. This condition is very nearly met in a freely falling vehicle, be it falling toward the Earth, around the Earth, or around the Sun.

The condition  $g_L = a_v$  is met exactly only if there is no external drag on the vehicle, and then only if the particle is exactly at the center of gravity of the vehicle. Orbital systems experience drag decelerations of the order of  $10^{-7} g_0$ .<sup>1</sup> Aerodynamic drag is less significant in deeper space, but the existence of a gradient in the gravitational field means that the acceleration of a free particle at one point in the vehicle differs from that of a free particle elsewhere in the vehicle. Near Earth the gravity gradient is of the order of  $10^{-9} g_0/\text{cm}$ . It would seem, then, that in the missions of most immediate concern, the effective residual gravity will never be much smaller than  $10^{-7}$ – $10^{-8} g_0$ .

The term "zero g" must be interpreted as meaning that the difference  $g_L - a_v$  is sufficiently small that the effective body forces

---

<sup>1</sup>  $g_0$  is here used throughout to denote 980 cm/sec<sup>2</sup>.

seen by an observer moving in the reference frame of the vehicle are very small compared to other forces, and consequently do not influence the behavior of fluid particles. In this chapter, we are concerned primarily with the relative importance of body forces and capillary forces, and with the dynamics of liquid motion under the combined influence of both kinds of forces.

### Hydrostatic Regimes: The Bond Number

We can make some simple estimates of the condition under which capillary and body forces are important. Consider the rise of a liquid in a tube as shown in figure 11.1. The height,  $h$ , of the liquid may be estimated from a force balance on the column of liquid between points 1 and 2, which gives

$$P_2 - P_1 = \rho gh \quad (11.4)$$

Assuming that the liquid wets the wall completely, a force balance on the meniscus gives (see eq. (11.12))

$$P_\infty - P_1 = 2\sigma/r \quad (11.5)$$

Assuming that  $P_2 = P_\infty$ , we combine the equations above, and express our estimate of  $h$  nondimensionally as

$$\frac{h}{r} \approx 2 \frac{\sigma}{\rho gr^2} \quad (11.6)$$

The dimensionless grouping,  $Bo = \rho gr^2/\sigma$ , is called the *Bond number*,<sup>2</sup> it compares the relative magnitudes of gravitational and capillary forces, and is the pertinent parameter delineating capillary-dominated and gravity-dominated hydrostatics. For values of  $Bo >> 1$ , the gravi-

<sup>2</sup> The dimensionless number,  $Bo = \rho g L^2/\sigma$ , has come to be known in the current literature as the Bond number (refs. 11.1, 11.2, and 11.3). Reference 11.3 is the earliest work known to the authors in which the group  $Bo$  is specifically called the Bond number after W. N. Bond's employment of the parameter to indicate the importance of surface tension in the correlation of the rise rate of bubbles in liquids (ref. 11.4). The parameter appears in different forms perhaps in the literature at a much earlier date, however; e.g., refs. 11.5 and 11.6.

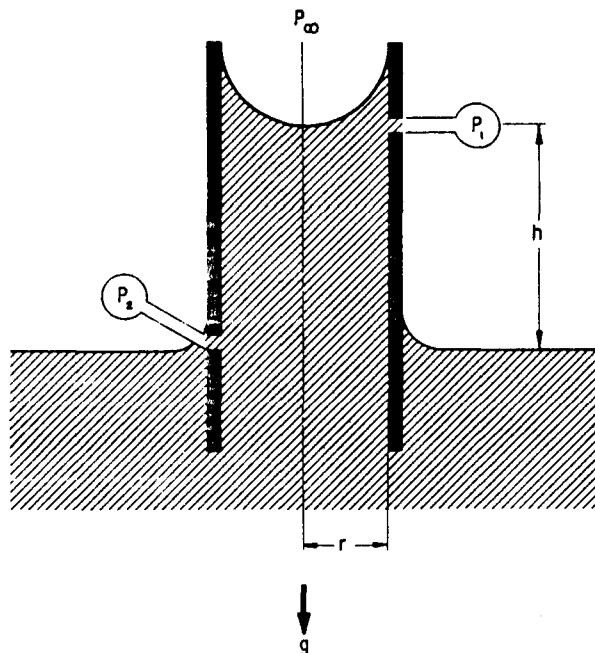


FIGURE 11.1.—Capillary action in a tube.

tational force predominates, and the column of liquid would barely rise up the tube. For values of  $Bo << 1$ , capillary forces predominate, and the liquid would rise high in the tube. We can apply this criterion to the case of liquid in a partially filled container. At very high values of the Bond number, gravity dominates, and we would expect that the interface would be nearly horizontal. Conversely, at very low Bond numbers the capillary forces predominate, and the hydrostatic configuration of the contained liquid would involve a strongly curved interface (meniscus). This behavior is in fact observed, as anyone who has ever compared the behavior of mercury in a manometer to that in a thermometer can testify.

Regimes of hydrostatic behavior are qualitatively separated by the condition  $Bo = 1$ . These regimes are indicated for a number of liquids in figure 11.2. The straight lines correspond to constant values of the physical property "kinematic surface tension,"  $\beta = \sigma/\rho$ , which is the relevant property in capillary fluid mechanics. Values for typical liquids are indicated in figure 11.2. In the region above the line for the pertinent  $\beta$ , the body forces dominate; this is the gravity-dominated regime,

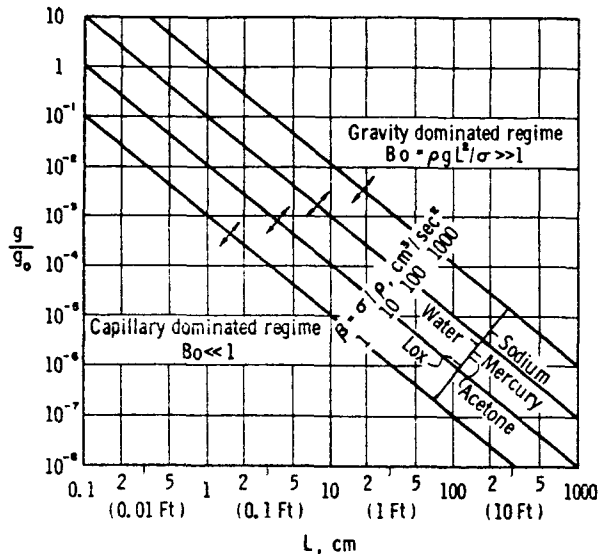


FIGURE 11.2.—Hydrostatic regimes for typical liquids.

the subject of the previous chapters of this monograph. Below the line, capillary forces dominate; this is the "zero g" regime. In the region near the line, both capillary and body forces must be considered, and this is seen to be the case for many situations of practical interest. It should be understood that the regime division is only qualitative, and that only for Bond numbers much greater than unity can one be sure that capillary forces are negligible. Similarly, only for very small Bond numbers is gravity effectively zero. Note that gravity effects can be important in large systems, even though the magnitude of  $g$  might be quite small.

Some feeling for the Bond number influence can be obtained from the photographs of methyl-alcohol menisci (under air) in Lucite tubes, shown in figure 11.3. There is some optical distortion, but the Bond number effect should be evident.

Again we see some difficulty in the meaning of "zero g." Henceforth, by *zero-g hydrostatics* we shall mean situations with very *low Bond numbers*, such that body forces do not affect the fluid statics appreciably. In small-enough systems, "zero g" can be effectively obtained at  $1 g_0$  (as in the mercury thermometer). In larger systems, even  $10^{-7} g_0$  cannot properly be considered as zero g. To emphasize further the importance of body forces in large booster

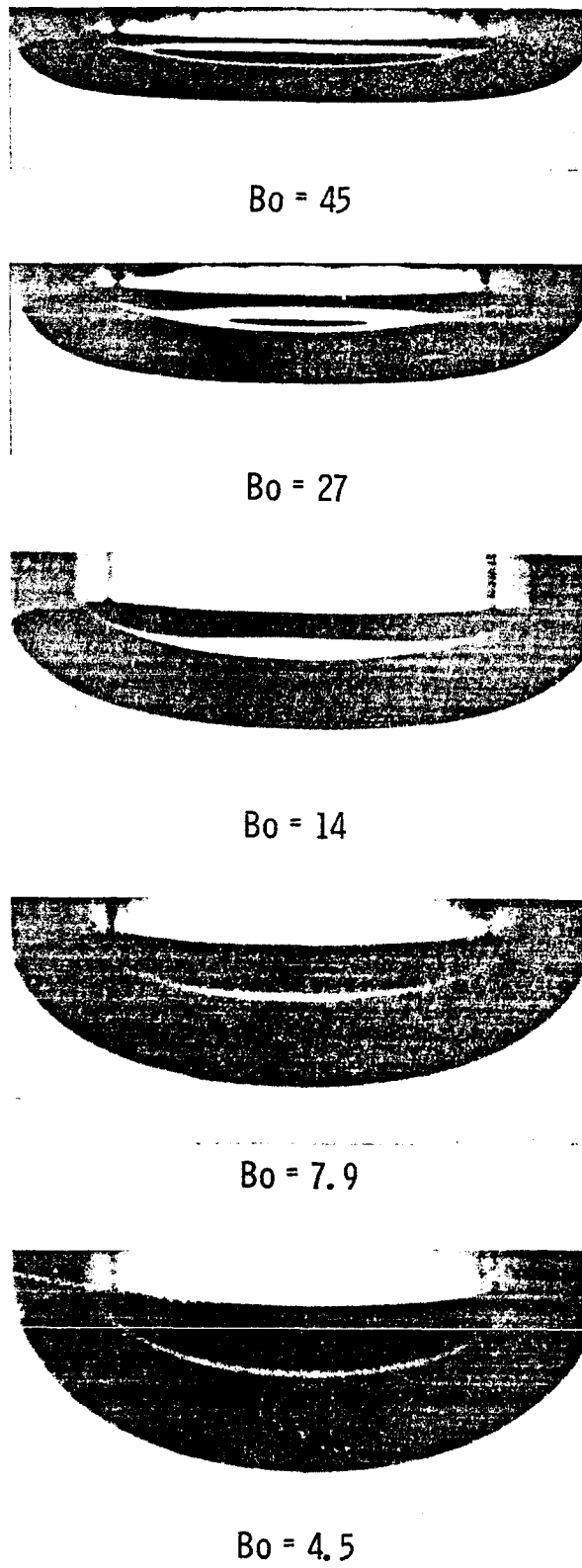


FIGURE 11.3.—Methyl-alcohol menisci (under air).

systems, the Bond numbers associated with the liquid in cylindrical tanks approximately 1.5, 3, and 9 meters in diameter have been calculated for effective body forces arising as a result of aerodynamic drag, the gravitational field gradient, and rotational motion required for geocentric orientation. The results are shown in figure 11.4, which also portrays the parameters of the calculation. These calculations show clearly the importance of considering both body and capillary forces in many liquid-propellant-handling problems, and the danger of oversimplifying an analysis by the idealization of "zero g."

### Hydrodynamic Regimes

The dynamic motion of a liquid-gas system may be influenced by capillary forces, body forces, and viscous forces. In many instances, all but one of these forces can be neglected, and the analysis of the motion or correlation of experimental data is thereby considerably simplified. A number of dimensionless parameters can be defined, and these serve to divide the hydrodynamic behavior into regimes.

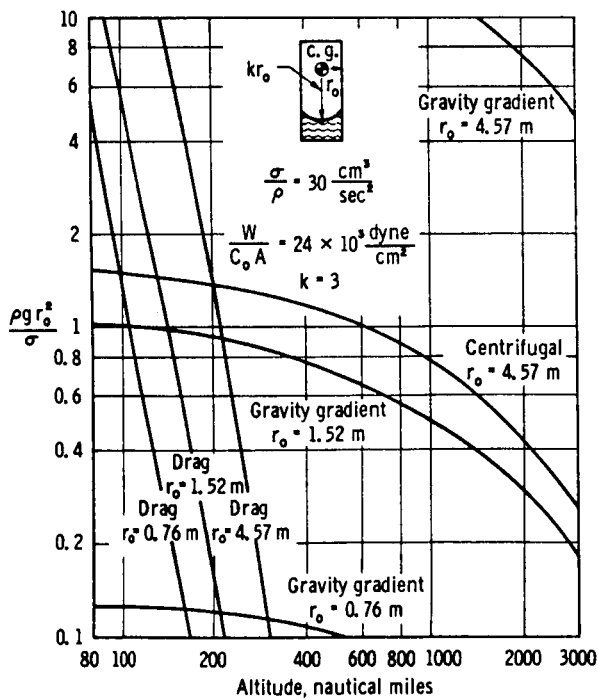


FIGURE 11.4.—Bond number for atmospheric drag, centrifugal, and gravity gradient accelerations.

### The Weber number

$$We = \rho V^2 L / \sigma \quad (11.7)$$

provides an estimate of the ratio of "inertial forces" to capillary forces. Here  $L$  is a "characteristic length" of the system. For  $We \gg 1$ , capillary forces influence the dynamic behavior only slightly, while for  $We \ll 1$  they play a dominant role in determining the motion. The Froude number<sup>3</sup>

$$Fr = V^2 / gL \quad (11.8)$$

provides an estimate of the ratio of inertial force to body forces. For  $Fr \gg 1$ , the body forces are sufficiently weak that they cannot be expected to play an important role in the fluid dynamics, while for  $Fr \ll 1$  they must certainly be considered. The Bond number is seen to be simply the ratio of the Weber and Froude numbers

$$Bo = We / Fr \quad (11.9)$$

The regimes of flow as determined by these three parameters are shown in figure 11.5. In each case, viscous effects may or may not be important, and this question must be decided separately.

This monograph deals primarily with problems associated with sloshing; for gravity-dominated sloshing, the natural sloshing frequency,  $\omega$ , is correlated by the dimensionless group ( $r_0$  is a characteristic system dimension)

$$\bar{\Omega}^2 = r_0 \omega^2 / g \quad (11.10a)$$

Under capillary-dominated conditions, it is more convenient to use the kinematic surface tension in the normalization, and hence to work with the dimensionless frequency

$$\Omega^2 = r_0^3 \omega^2 \rho / \sigma \quad (11.10b)$$

Note that

$$\bar{\Omega}^2 = \Omega^2 / Bo \quad (11.10c)$$

When we extend the inviscid, irrotational analyses of the earlier chapters to include the effects of capillary forces, we will find that

<sup>3</sup> Sometimes the Froude number is defined as  $V / \sqrt{gL}$ .

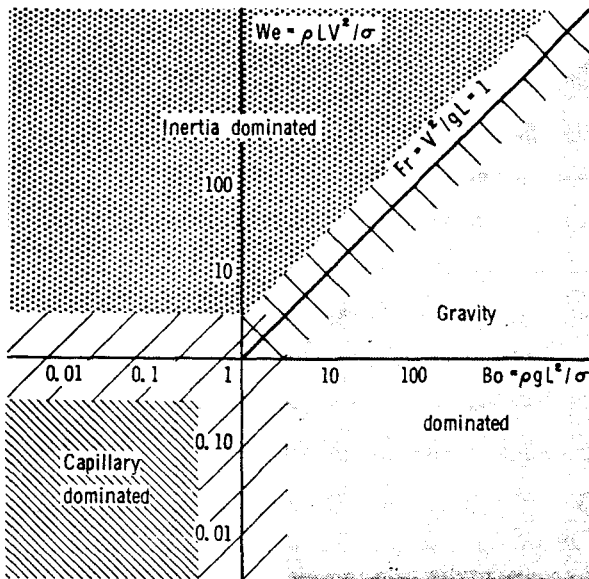


FIGURE 11.5.—Hydrodynamic regimes.

$\Omega^2$  can be expressed as a function of the Bond number for any particular configuration; for low Bond numbers  $\Omega^2$  will approach a constant, while for high Bond numbers  $\Omega^2$  will approach the constant values given earlier. The importance of the Bond number as a parameter in low-g sloshing should now be evident.

#### Response Time Estimates

In section 11.4, we will discuss the natural frequency of liquid sloshing motions, from which characteristic times for capillary-dominated and gravity-dominated motions will emerge. These characteristic times are found to be

$$T = \sqrt{L/g} \text{ for the gravity-dominated regime} \quad (11.11a)$$

$$T = \sqrt{\rho L^3 / \sigma} \text{ for the capillary-dominated regime} \quad (11.11b)$$

These expressions provide order-of-magnitude estimates for the time required for reorientation of liquid to take place following the transition from one hydrostatic regime to another. These estimates are shown quantitatively for typical systems in figure 11.6. Note that

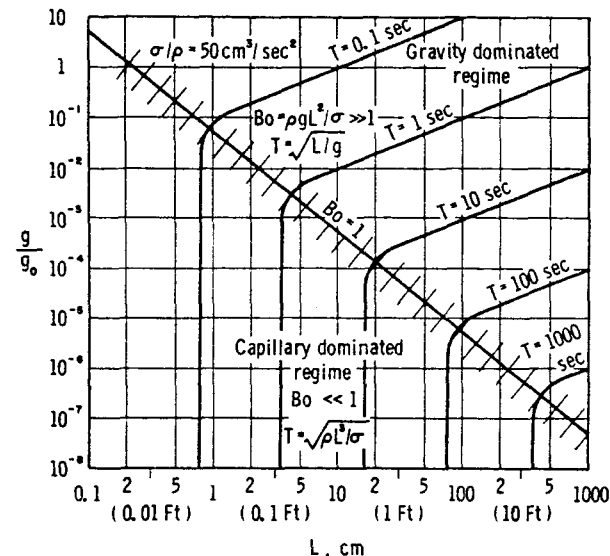


FIGURE 11.6.—Hydrostatic regimes and characteristic response times.

the reorientation period at low  $g$  can be several minutes in a large tank.

#### 11.2 THE MECHANICS AND THERMODYNAMICS OF CAPILLARY SYSTEMS

##### Introduction

Capillarity has been a subject of considerable interest to surface chemists for several decades, and there is a vast body of related literature confronting the engineer concerned with low-g sloshing. It is known that capillary<sup>4</sup> effects arise as a result of rather short-range molecular interactions, and there are various theories for predicting the surface tension. For a comprehensive summary, see reference 11.7. A presentation more oriented to the temperament of an engineer is given by Bikerman (ref. 11.8).

Although the microscopic interpretations and analyses are interesting and important, for engineering purposes macroscopic representations are much more suitable. In this section, we shall review the key ideas of the macroscopic approach to capillarity, emphasizing in partic-

<sup>4</sup> Historically, a "capillary" tube was so small that it could only admit a hair (capella). For an interesting historical review, see Maxwell (ref. 11.6).

ular those aspects which are relevant to the low- $g$  sloshing problem. Other treatment of capillary hydrostatics and hydrodynamics is given in references 11.9, 11.10, and 11.11. To the novice to this field, we strongly recommend the educational motion picture of Trefethen (ref. 11.12).

### Surface Tension and Contact Angle

It has been found that liquids behave as if they were covered by a contractile membrane in uniform tension. This tension acts along the surface and tends to make its surface as small as possible. The force-per-unit length acting normal to any line drawn in the surface is defined as the *interfacial* or *surface tension*.

Consider a spherical bubble of gas embedded in a liquid, as shown in figure 11.7. If we denote the surface tension by  $\sigma$ , then the tensile force acting along a great circle is  $F_s = \sigma\pi D$ . For static equilibrium, this must be balanced by the pressure force,  $F_p = (\pi D^2/4)(P_i - P_o)$ , where  $P_i$  and  $P_o$  represent the pressures inside and outside of the bubble. The pressure difference is therefore given by

$$P_i - P_o = \frac{4\sigma}{D} = \frac{2\sigma}{r} \quad (11.12)$$

and is known as the capillary pressure.

If the interface is not spherical, the capillary pressure difference across the interface at any point is given by (refs. 11.8 and 11.9)

$$\Delta P = \sigma \left( \frac{1}{r_1} + \frac{1}{r_2} \right) \quad (11.13)$$

where  $r_1$  and  $r_2$  are the principal radii of curvature at that point. This relation forms the basis for the analysis of every hydrostatic

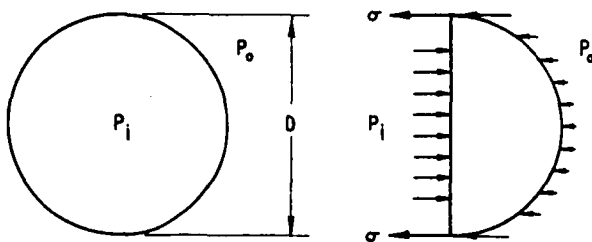


FIGURE 11.7.—Spherical gas bubble embedded in a liquid.

interface in which capillary phenomena are important, and is often called *Laplace's law*.

The surface tension is generally considered to be a thermodynamic property of the interface and is a function mainly of temperature for a given interface. However, during and shortly after the formation or destruction of new surface, the apparent surface tension may differ somewhat from its equilibrium value. This modified surface tension is called the *dynamic surface tension* (ref. 11.13). Fortunately, these dynamic effects may be neglected in many engineering analyses, in particular for the ones at hand, and we shall not consider them further.

The surface tension is a monotonically decreasing function of temperature, and vanishes at the critical point. Values of the surface tension of several important liquids are given in the appendix.

When a liquid drop comes in contact with a solid surface, three angles are formed in a plane perpendicular to the three-phase line in the solid surface. For drops on flat surfaces, the solid phase occupies  $180^\circ$ , while both the gaseous and liquid phases occupy the remaining  $180^\circ$ . The angle measured within the liquid between the solid and the tangent to the liquid-gas interface at the three-phase line is called the *contact angle* (fig. 11.8(a)).

The value of the contact angle is related to the relative magnitudes of the microscopic adhesive and cohesive forces (ref. 11.8). If the contact angle is less than  $90^\circ$ , the liquid is said to "wet" the solid; if the contact angle is greater than  $90^\circ$ , the liquid is said to be "non-wetting" (fig. 11.8(b)). Both wetting and nonwetting liquids will adhere to solid surfaces.

Consider now a cylindrical droplet of liquid resting on the surface of another liquid, both under a third liquid (or gas), as shown in figure 11.8(c). If we define the individual surface tensions of the three interfaces as before, then equilibrium of the contact line requires that

$$\sigma_{23} = \sigma_{13} \cos \theta + \sigma_{12} \cos \phi \quad (11.14a)$$

$$\sigma_{13} \sin \theta = \sigma_{12} \sin \phi \quad (11.14b)$$

The above relations have been reasonably well substantiated by independent measurements of the three interfacial tensions and contact angles.

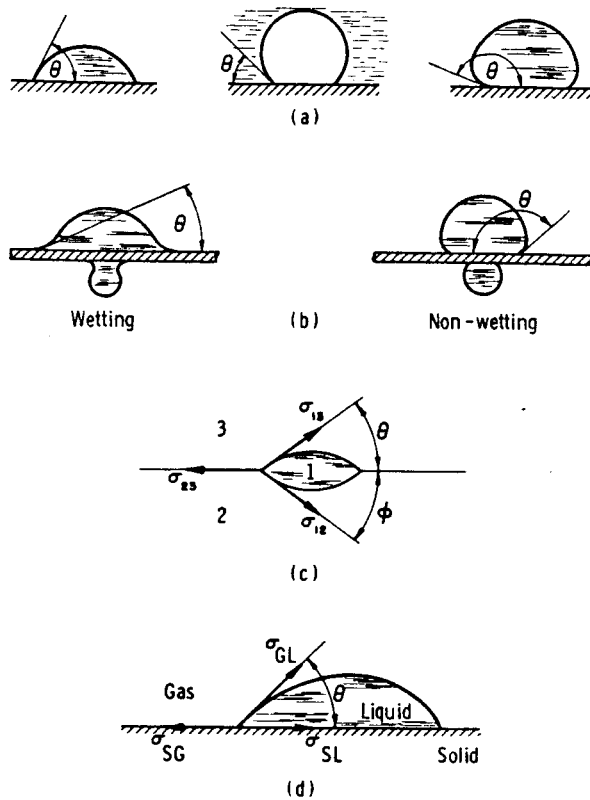


FIGURE 11.8.—Contact angles.

Consider next the three cylindrical interfaces formed by a solid, a liquid, and a gas, as shown in figure 11.8(d). The condition of horizontal equilibrium can be satisfied if

$$\sigma_{SG} = \sigma_{GL} \cos \theta + \sigma_{SL} \quad (11.15)$$

However, the condition of vertical equilibrium cannot be satisfied. Nevertheless, this picture of the interfacial force "triangle" is commonly employed and justified on the basis of its analogy to equation (11.14a). Equation (11.15) is often called *Young's equation*.

Although surface tension and contact angle are manifestations of microscopic forces, there is a great deal of evidence which indicates that together they define an appropriate macroscopic representation of capillary phenomena. For example, the height to which liquid will rise in a capillary tube can be predicted in terms of the surface tension and contact angle, both independently measurable, and these predictions

are confirmed experimentally. The shapes of liquid drops on a surface can be computed in terms of the contact angle and surface tension, and these computations are in agreement with measurements. Henceforth, we will consider that contact angle and surface tension do indeed allow capillary phenomena to be treated macroscopically.

Although the surface tension is a relatively invariant property of the interface, the contact angle is not, and hysteresis is common. If a little liquid is added to a drop, it is observed that the base does not change, but that the drop merely changes its shape, and consequently the contact angle changes. After a period of growth, the base will suddenly expand in a jerky manner, and the contact angle will again be reduced. The greatest angle obtained on growth is termed the *advancing contact angle*, and the smallest angle on removal is the *receding contact angle*. A similar effect is observed when a drop is placed on a plate which is subsequently tilted. The advancing and receding of the contact angle, characteristic of the hysteresis process, have been measured for mercury on a tilted glass plate. Figure 11.9 presents some quantitative data for this case. This hysteresis seems to depend somewhat upon the drop size and orientation in the gravity field. Hysteresis is also observed with a moving interface. The angular amount of hysteresis is not excessive, but its existence is perhaps the most disconcerting factor in the contact angle-surface tension representation of capillary phenomena. An exception is found for pure fluids on clean

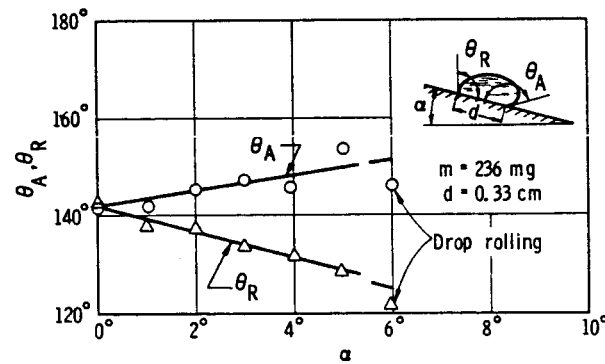


FIGURE 11.9.—Contact angle variation with inclination for mercury on glass.

surfaces, where no hysteresis is observed (ref. 11.14).

Both the contact angle and the surface tension are dependent on the condition of the interfaces. Contamination by foreign material influences the value of the surface tension somewhat, and alters the contact angle even more. Sensitivity to surface and environmental conditions makes reproducible measurements of the contact angle difficult. This partial uncertainty in contact angle is a key factor which often makes predictions of capillary phenomena subject to uncertainty. The difficulties are the greatest when the contact angle is near 90°, for slight changes in this range can change a wetting fluid very rapidly into a nonwetter.

### Capillary Thermodynamics

The thermodynamics of a capillary system are useful in formulating the conditions of equilibrium and stability. To determine the energy change associated with a change of state in a capillary system, consider the two cones with a cylindrical mass of liquid stretched between, as shown in figure 11.10(a). The dotted lines denote the boundaries of a system of fixed mass, and we imagine that these boundaries are free to move in a manner which keeps the system volume constant. The shape of the cones is adjusted so that the liquid retains its cylindrical shape, even if the contact angle changes.

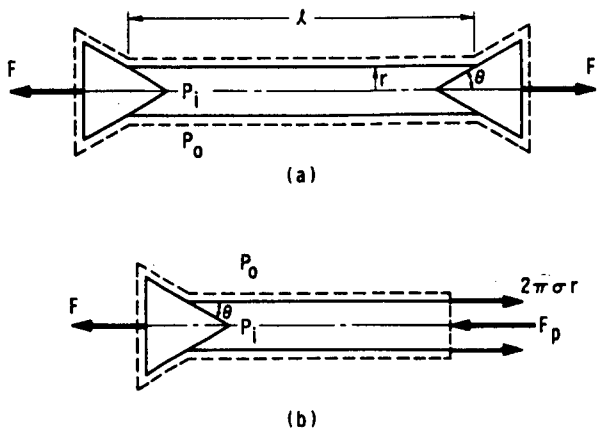


FIGURE 11.10.—Computing the energy change in a capillary system.

When the separation between the cones is increased by an infinitesimal amount  $dx$ , the work done on this system ( $PdV$  work is zero for this constant volume system) will be  $dW = Fdx$ . The instantaneous force,  $F$ , may be determined by a force balance on a second system, defined in figure 11.10(b). The pressure difference across the interface is  $P_i - P_0 = \sigma/r$ , so the force  $F_p$  is  $\pi r \sigma$ . The surface tension force on the system is  $2\pi r \sigma$ , and, therefore, the force balance indicates that the cone force,  $F$ , is  $2\pi r \sigma - \pi r \sigma = \pi r \sigma$ . The work done is therefore

$$dW = \pi r \sigma dx \quad (11.16)$$

The radius may be expressed as a function of the volume using the constraint that the liquid volume remain fixed. We find

$$dV = 2\pi r l dr - \pi r^2 dl + 2\pi \frac{r^2 dr}{\tan \theta} = 0 \quad (11.17)$$

The length change  $dl$  is related to  $dx$  and  $dr$  by

$$dl = dx + 2dr/\tan \theta \quad (11.18)$$

Combining equations (11.16) and (11.17), one finds

$$dW = \sigma \pi r (dl - 2dr/\tan \theta) \quad (11.19)$$

This can be put in a more convenient form by observing that the incremental change in the interface area is  $dA = 2\pi r dl - 2\pi l dr$ , and the incremental change in the wetted area is  $dA_w = 4\pi r dr / \sin \theta$ . Combining equations (11.17) and (11.19), we can obtain

$$dW = \sigma (dA - \cos \theta dA_w) \quad (11.20)$$

The case of constant  $\theta$  is of particular interest. For this case, we define the *capillary area*,  $A_c$ , by

$$A_c = A - \cos \theta A_w \quad (11.21)$$

The work is then related to the capillary area by

$$dW = \sigma dA_c \quad (11.22)$$

Consider now a reversible change of state for which the entropy change is related to the energy transfer as heat to the capillary system by

$$dS = dQ/T \quad (11.23)$$

An energy balance on the system gives

$$dU = dQ + dW \quad (11.24)$$

where  $U$  is the system internal energy. Combining these two equations, we obtain the Gibbs equation of the capillary system (ref. 11.15)

$$dS = \frac{1}{T} dU - \frac{\sigma}{T} dA_c \quad (11.25)$$

We next differentiate the functional relationship  $U(T, A_c)$

$$dU = \left(\frac{\partial U}{\partial T}\right)_{A_c} dT + \left(\frac{\partial U}{\partial A_c}\right)_T dA_c \quad (11.26)$$

Substituting into equation (11.25), we obtain

$$dS = \frac{1}{T} \left(\frac{\partial U}{\partial T}\right)_{A_c} dT + \left[\frac{1}{T} \left(\frac{\partial U}{\partial A_c}\right)_T - \frac{\sigma}{T}\right] dA_c \quad (11.27)$$

From which it follows that

$$\left(\frac{\partial S}{\partial A_c}\right)_T = \frac{1}{T} \left(\frac{\partial U}{\partial A_c}\right)_T - \frac{\sigma}{T} \quad (11.28)$$

Now, consider the Helmholtz free energy,  $F = U - TS$ . Differentiating,

$$dF = dU - T dS - S dT \quad (11.29)$$

Upon combination with equation (11.25), we find

$$dF = \sigma dA_c - S dT \quad (11.30)$$

Since  $dF$  is exact, we have the Maxwell relation

$$\left(\frac{\partial S}{\partial A_c}\right)_T = -\left(\frac{\partial \sigma}{\partial T}\right)_{A_c} \quad (11.31)$$

so that equation (11.28) becomes

$$\left(\frac{\partial U}{\partial A_c}\right)_T = \sigma - T \left(\frac{\partial \sigma}{\partial T}\right)_{A_c} \quad (11.32)$$

Measurements indicate that the surface tension is a function only of temperature, and henceforth we consider this to be the case. Integrating equation (11.32) at fixed  $T$ , we have

$$U = \left(\sigma - T \frac{d\sigma}{dT}\right) A_c + U_0(T) \quad (11.33)$$

where  $U_0$  represents the system energy when  $A_c = 0$ , that is, the internal energy of the

liquid, and is a function only of temperature (ref. 11.16). The term

$$U_c = \left(\sigma - T \frac{d\sigma}{dT}\right) A_c \quad (11.34)$$

represents the energy associated with the capillary forces. Note that the capillary energy per unit of capillary area is also a function only of temperature.

Integrating equation (11.31), at constant  $T$ , we find

$$S = \left(-\frac{d\sigma}{dT}\right) A_c + S_0(T) \quad (11.35)$$

where  $S_0$  represents the entropy of the liquid phase (ref. 11.16).  $-(d\sigma/dT)$ , the capillary entropy per unit of capillary area, is also a function solely of temperature. Since  $d\sigma/dT$  is negative, the entropy increases during an isothermal stretching.

The Helmholtz free energy is then

$$F = \sigma A_c + F_0 \quad (11.36)$$

where  $F_0 = U_0 - TS_0$ . We see that the surface tension may be interpreted as the capillary Helmholtz free energy per unit of capillary area; this is sometimes used as a basic definition of  $\sigma$ .

Now, let us consider a capillary system which reaches equilibrium irreversibly without a work interaction with its environment, such as the reorientation of propellant in a system transitioning from a high-g to a zero-g state. The first law is then simply

$$dU = dQ \quad (11.37)$$

and the second law gives

$$TdS - dQ \geq 0 \quad (11.38)$$

The change in entropy is related to the instantaneous state ( $U$  and  $A_c$ ) of the system through the Gibbs equation, equation (11.25). Combining with the two equations above, we find

$$dU - \sigma dA_c - dU \geq 0 \quad (11.39)$$

which tells us that, during the irreversible approach to equilibrium,

$$dA_c \leq 0 \quad (11.40)$$

Since the capillary area continually decreases during the process, the final equilibrium state is a configuration of *minimum capillary area*.

A similar result is obtained for an isothermal capillary system when the gravitational force is not zero. The work done on a capillary system by external force when its center of mass is lifted an amount  $dh$  is

$$dW_s = Mg dh \quad (11.41)$$

where  $M$  is the liquid mass, and  $g$  is the local gravitational acceleration.

The total work done on a capillary system is then

$$dW = \sigma dA_c + Mg dh \quad (11.42)$$

Applying the first law of thermodynamics

$$dU = dW + dQ \quad (11.43)$$

The energy transfer as heat and the entropy change must be such that the second law of thermodynamics for a reversible process is satisfied; that is,

$$TdS = dQ_{rev} \quad (11.44)$$

For this system the Gibbs equation, describing changes of state, is obtained by combination of the first and second laws, and is

$$dS = \frac{1}{T} dU - \frac{\sigma}{T} dA_c - \frac{Mg}{T} dh \quad (11.45)$$

Upon differentiating the functional relationship  $U(T, A_c, h)$ , and following the steps leading to equation (11.28), one finds that equation (11.28) holds for this system also, provided that the derivatives are taken at constant  $T$  and  $h$ . Similarly, the Maxwell relations, equations (11.31) and (11.32), both hold if  $h$  is held constant in forming the partial derivatives. Then, integrating equation (11.32), one has

$$U = \left( \sigma - T \frac{d\sigma}{dT} \right) A_c + f(h) + U_0 \quad (11.46)$$

The function  $f(h)$  is determined by considering a reversible isothermal elevation at constant  $A_c$ , and is simply  $f(h) = Mgh$ . The entropy is also given by equation (11.35).

Now, consider a capillary system which is allowed to approach equilibrium without any

work interaction with its environment, such as the propellant reorientation from one g loading to another. An energy balance for an elemental step in this process then gives

$$dU = dQ \quad (11.47)$$

and the second law for the irreversible process is

$$TdS - dQ \geq 0 \quad (11.48)$$

The change in entropy is related to the change in state ( $U$ ,  $A_c$ , and  $h$ ) through the Gibbs equation, equation (11.45). Combining with the two equations above, we learn that the changes in state which occur during the irreversible process must be such that

$$\sigma dA_c + Mg dh \leq 0 \quad (11.49)$$

The term  $Mgh$  is the *gravitational potential energy* of the system; sometimes the term  $\sigma A_c$  is called the *capillary potential energy*. The stable equilibrium state is then the state of *minimum total potential energy*, where

$$PE = \sigma A_c + Mgh \quad (11.50)$$

This is an extremely important result, for it provides the basis for the determination of stable equilibrium configurations in capillary systems. We shall use it frequently in the following section.

### 11.3 CAPILLARY HYDROSTATICS

#### Preferred Configurations in Zero g

The thermodynamic analysis in section 11.2 indicated that the stable equilibrium state of a capillary system in an isothermal zero-g environment is the state where the potential energy,  $PE = \sigma A_c$ , has the least value. There may be several states for which small perturbations in configuration result in an increase in  $PE$ ; all of these states, except for the one of lowest  $PE$ , are metastable, for with a sufficiently large disturbance the system will pass to the stable state. This behavior is indicated in figure 11.11. We can use this idea to determine where liquid is most likely to be found in a container. Since the surface tension depends

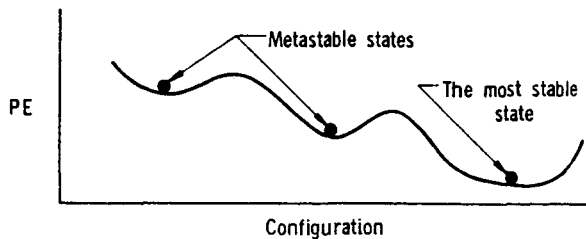


FIGURE 11.11.—Stable states.

only on temperature, it is constant in an isothermal system, and we need only to investigate the capillary area  $A_c$ . Thus the calculation is entirely geometrical.

It is important to realize that one cannot be sure from these considerations that the system will indeed be in this stable state; it may be "trapped" in a metastable state. The analysis merely indicates what is most likely, which often is too weak a prediction for purposes of conservative design.

Consider first a collection of liquid drops away from interaction with walls. Suppose the drops are floating aimlessly about, and we seek to learn if there will be any tendency for them to merge upon contact with one another. Let us take the simple case where all  $N$  drops have the same diameter,  $D$ . If  $V$  represents the total liquid volume, then

$$V = C_1 N D^3 \quad (11.51)$$

The capillary area of each will be proportional to  $D^2$ , and the total capillary area is therefore

$$A_c = C_2 N D^2 \quad (11.52)$$

Since  $V$  is fixed, we conclude that the capillary area is of the form

$$A_c = C_3 V^{1/3} \quad (11.53)$$

The capillary area will therefore be least when the drops are merged into one. The general proof of this is a classic problem in the calculus of variations, where one finds that the shape of smallest surface area for given volume is a single sphere. We conclude therefore that the drops will tend to coalesce to form a single large sphere.

By similar arguments, it is easily demonstrated that small free bubbles will tend to join,

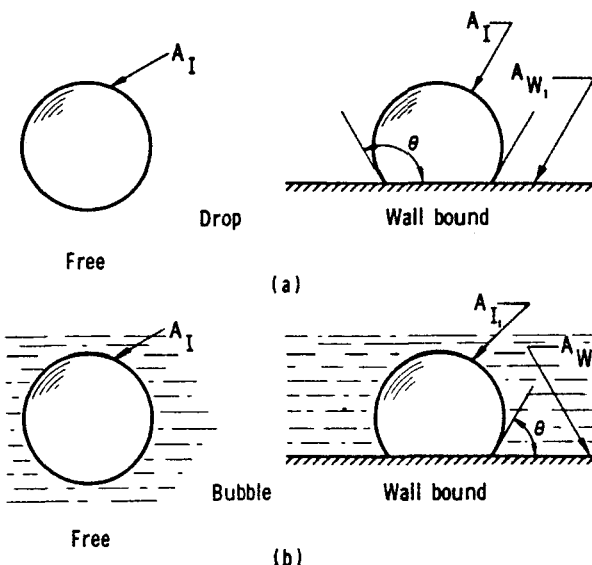


FIGURE 11.12.—Capillary areas for wall-bound and free drops and bubbles.

forming one large bubble. These trends are in fact observed experimentally.

Let us next ask if a drop prefers to be floating free of the surface or if it has lower potential energy in a "wall-bound" state. A bit of geometrical calculation (fig. 11.12) leads to a relationship between the capillary areas for wall-bound and free drops (or bubbles) of identical volume on a plane surface.<sup>5</sup>

$$\frac{A_{c \text{ bound}}}{A_{c \text{ free}}} = \left[ \frac{1}{4} (2 - 3 \cos \theta + \cos^3 \theta) \right]^{1/3} \text{ (drops)} \quad (11.54a)$$

$$\frac{A_{c \text{ bound}}}{A_{c \text{ free}}} = \left[ \frac{1}{4} (2 + 3 \cos \theta - \cos^3 \theta) \right]^{1/3} \text{ (bubbles)} \quad (11.54b)$$

These ratios are less than 1 for all  $\theta$ . Consequently, we conclude that the wall-bound configurations are more stable. If a free-floating drop (or bubble) collides with a wall not too violently, it will stick. In zero g, drops or bubbles prefer to be wall bound.

Similar geometrical calculations have been made for the case of liquid in a spherical tank, and the results are summarized in figure

<sup>5</sup> For bubbles  $A_c = A_I + \cos \theta A_{NW}$ , where  $A_{NW}$  is the nonwetted area.

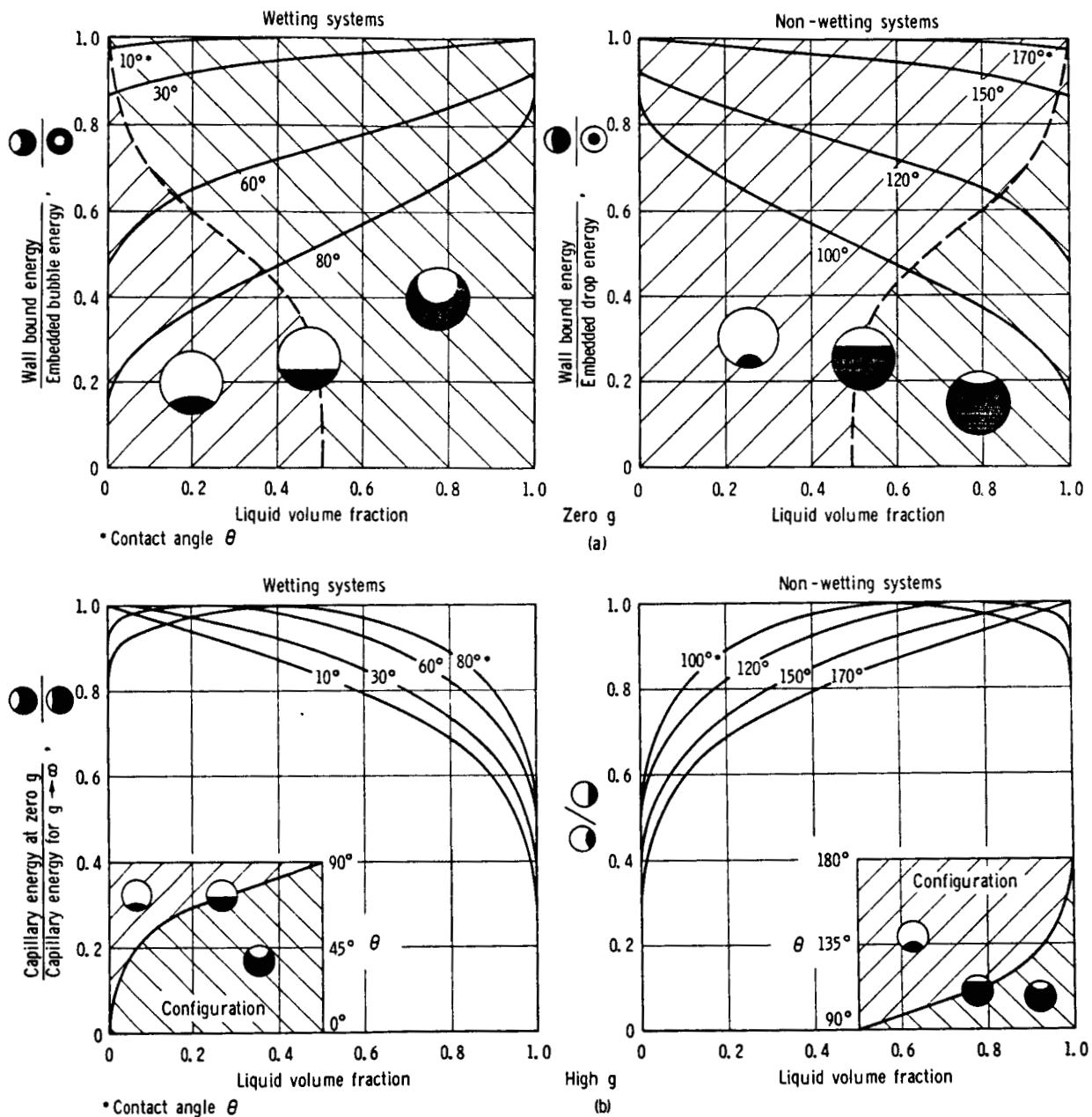


FIGURE 11.13.—Comparison of capillary energies of possible configurations in a spherical tank.

11.13(a). The ratio of the capillary areas for the wall-bound and free-floating configurations are plotted versus the liquid volume percentage for several wetting and nonwetting contact angles. The conclusion is as stated previously, that in every case both the liquid and gas bubbles are wall bound in the preferred configuration. The ratios of the high-g capillary areas (assuming a flat interface) to the wall-

bound zero-g capillary areas are shown in figure 11.13(b). Note that the capillary area would indeed decrease as the fluid passes from an initial high-g state to a zero-g state after the removal of the body force field. An exception is observed for the particular situation where the liquid meets the wall at the contact angle, in which case no motion would ensue following removal of the body force.

These predictions have been qualitatively observed in free-fall experiments. However, with wetting liquids in large quantity, the ullage bubble sometimes becomes embedded. This is attributed to inertial effects and it is felt that after an extended period of very small g, the bubble would drift toward the wall and eventually become wall bound.

In the foregoing discussions, we tacitly assumed that the interface was a spherical sector. In a zero-g hydrostatic system, the pressures on either side of the interface will be uniform, and equation (11.13) then requires that the sum of the reciprocals of the principal radii

of curvature be constant. Thus, an axisymmetric meniscus in zero g will take the shape of a spherical sector, provided it extends to  $r=0$ ; an annular meniscus does not meet this requirement. If the Bond number is not too great, it is a fair approximation that the meniscus is spherical, and this idealization can be used in estimating the configuration of many capillary systems. Clodfelter (ref. 11.17) used the spherical sector model to determine the position of the meniscus in a spherical tank under zero g, and design graphs adapted from his report are shown in figure 11.14.

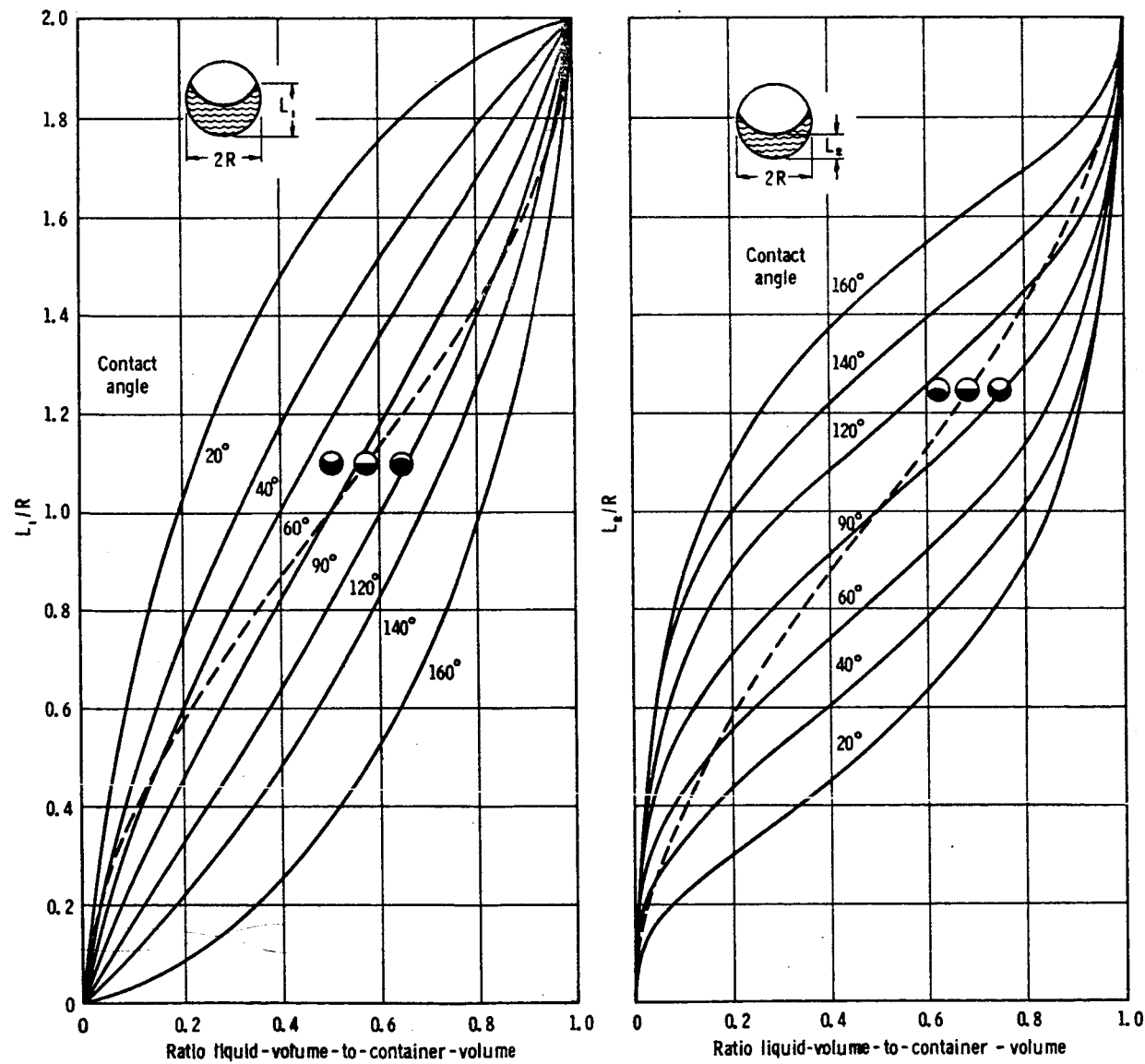


FIGURE 11.14.—Meniscus configuration in a spherical tank at zero g.

### Parallel Meniscus Systems in Zero g

Parallel meniscus systems are of considerable interest in a variety of space systems. Their preferred zero-g configurations may be determined using the minimum capillary area ideas, and sometimes alternatively by force balance considerations. For example, consider the two menisci formed by two concentric tubes, as shown in figure 11.15(a). This parallel meniscus system has application under certain conditions in large booster fuel tanks as a propellant positioning device, for, if the radii are properly chosen, the liquid will flow into the inner tube as the vehicle enters zero g. We can make a simple analysis for the preferred configuration. Neglecting the thickness of the inner tube, and assuming perfect wetting, the following pressure differences can be derived directly from the differential equations for the shapes of the inner and outer menisci, or from simple force balances.

$$P_{\infty} - P_b = \frac{2\sigma}{r_i} \quad (11.55a)$$

$$P_{\infty} - P_a = \frac{2\sigma}{r_o - r_i} \quad (11.55b)$$

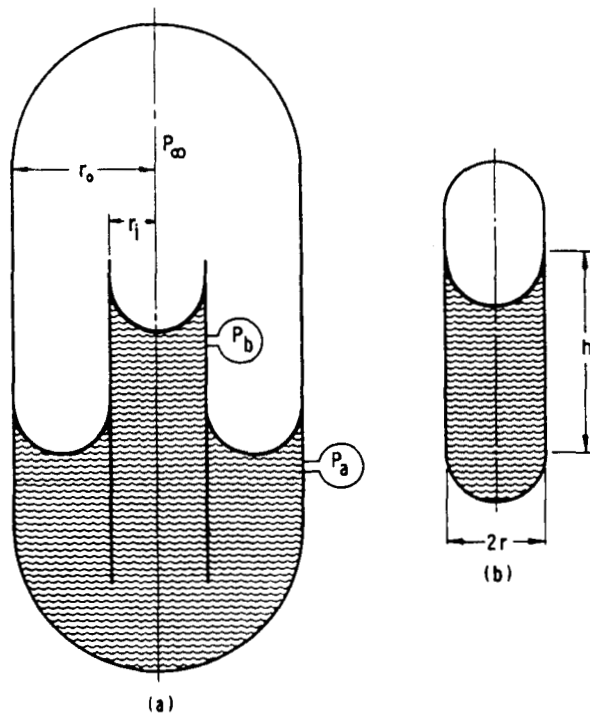


FIGURE 11.15.—Menisci in typical tanks.

Now, if  $P_b$  is less than  $P_a$ , the liquid will flow to the inner tube. Hence

$$\left. \begin{array}{l} (1) \text{ if } \frac{1}{r_i} < \frac{1}{r_o - r_i} \\ \qquad \qquad \qquad \text{liquid moves up the annulus} \\ (2) \text{ if } \frac{1}{r_i} = \frac{1}{r_o - r_i} \\ \qquad \qquad \qquad \text{liquid remains in any position} \\ (3) \text{ if } \frac{1}{r_i} > \frac{1}{r_o - r_i} \\ \qquad \qquad \qquad \text{liquid moves up the center tube} \end{array} \right\} \quad (11.56)$$

Thus, if the inner radius is smaller than half of the outer radius, the liquid will flow to the center. This prediction was substantiated in the experiments of Pettrash and Otto (ref. 11.18).

It must be emphasized that the tendencies previously indicated may be overridden by dynamic effects. For example, if the liquid were suddenly drawn up through the inner tube, following the removal of the body force, its momentum may carry it out of the inner tube into the top end of the tank; this possibility should be guarded against in any design utilizing this sort of standpipe.<sup>6</sup> An analysis of the minimum-capillary-energy type, which is relevant to this problem, involves the determination of the container geometry in which a liquid of fixed volume can be contained with the least capillary energy. Consider a family of cylindrical tanks with hemispherical ends, as shown in figure 11.15(b). Assuming full wetting, the liquid volume is

$$V = \pi r^2 h \quad (11.57a)$$

The capillary area is

$$A_c = 2\pi r^2 - [2\pi rh + 2\pi r^2] = -2\pi rh \quad (11.57b)$$

Combining, one finds that the least potential energy for fixed  $V$  is obtained with the largest radius. Hence, should the liquid squirt up to the top end of the tank of figure 11.15(a), it

<sup>6</sup> This has been demonstrated in small-scale experiments carried out by Siegel (ref. 11.19).

may well stay there in the absence of any restoring body forces.

The foregoing example serves to illustrate the dangers of relying on the predictions of this type of zero-g analysis, and the need for careful consideration of dynamic effects, either by analysis or by properly scaled model experiments. Both of these topics will be discussed in subsequent sections.

We have seen how the spherical segment model can be used in zero-g meniscus configuration analyses. To make accurate design calculations at nonzero Bond numbers, one must use a more accurate meniscus-shape equation. In many systems, the meniscus is axisymmetric, and a very large class of configurations can be handled when the characteristics of such a meniscus are known. We shall now consider a general treatment for axisymmetric menisci, the results of which can be used in design problems.

### Shape of Axisymmetric Menisci

Consider the infinitesimal annular ring cut from the meniscus (fig. 11.16). A force balance in the vertical direction provides the differential equation for the static interface

$$\sigma \frac{d}{ds} \left( r \frac{dh}{ds} \right) = r \frac{dr}{ds} (P_g - P_l) \quad (11.58)$$

The pressure is assumed to have a hydrostatic distribution<sup>7</sup>

$$P_l = P_{l_0} - \rho gh \quad (11.59)$$

where  $P_l$  is the pressure in the liquid just beneath the interface, and  $P_{l_0}$  is the liquid pressure at the bottom of the meniscus.

Introducing the dimensionless quantities

$$R = r/r_c; H = h/r_c; S = s/r_c; B = \rho g r_c^2 / \sigma \quad (11.60)$$

where

$$r_c = \sigma / (P_g - P_{l_0})$$

and combining equations (11.58) and (11.59), one finds

<sup>7</sup> The gas density is neglected. To consider it, replace  $\rho$  by  $\rho_l - \rho_g$  in the analysis.

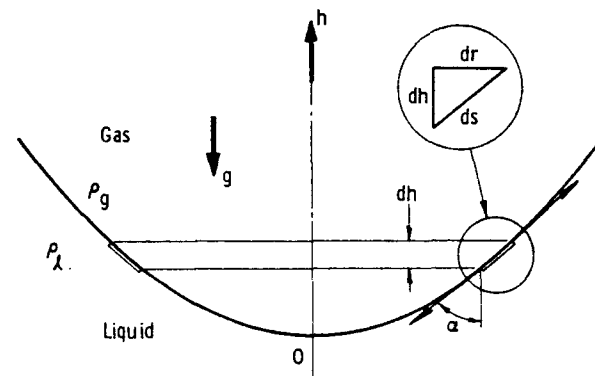


FIGURE 11.16.—Force balance for axisymmetric menisci.

$$\frac{d}{ds} \left( R \frac{dH}{ds} \right) = R \frac{dR}{ds} (1 + BH) \quad (11.61)$$

A second differential equation is obtained from the geometric condition

$$\left( \frac{dh}{ds} \right)^2 + \left( \frac{dr}{ds} \right)^2 = 1 \quad (11.62)$$

which, when differentiated and normalized, gives

$$\frac{dH}{ds} \frac{d^2H}{ds^2} + \frac{dR}{ds} \frac{d^2R}{ds^2} = 0 \quad (11.63)$$

Equations (11.61) and (11.63) form a pair which may be solved numerically. The problem may be treated as an initial value problem, in which we prescribe

$$\left. \begin{aligned} R(0) &= H(0) = H'(0) = 0 \\ R'(0) &= 1 \end{aligned} \right\} \quad (11.64)$$

Calculations of this type have been carried out at fixed  $B$ , yielding values of  $\alpha$  along the way. These results were then cross-plotted for selected values of  $\alpha$  to obtain the curves of figure 11.17. In these figures,  $V$  represents the volume of revolution bounded by the meniscus and the plane of the contact line. These curves may be used in design calculations involving any axisymmetric meniscus, which must extend to  $r=0$ .

To illustrate the usefulness of these curves, suppose we wish to calculate the general configuration of a meniscus in a spherical tank as

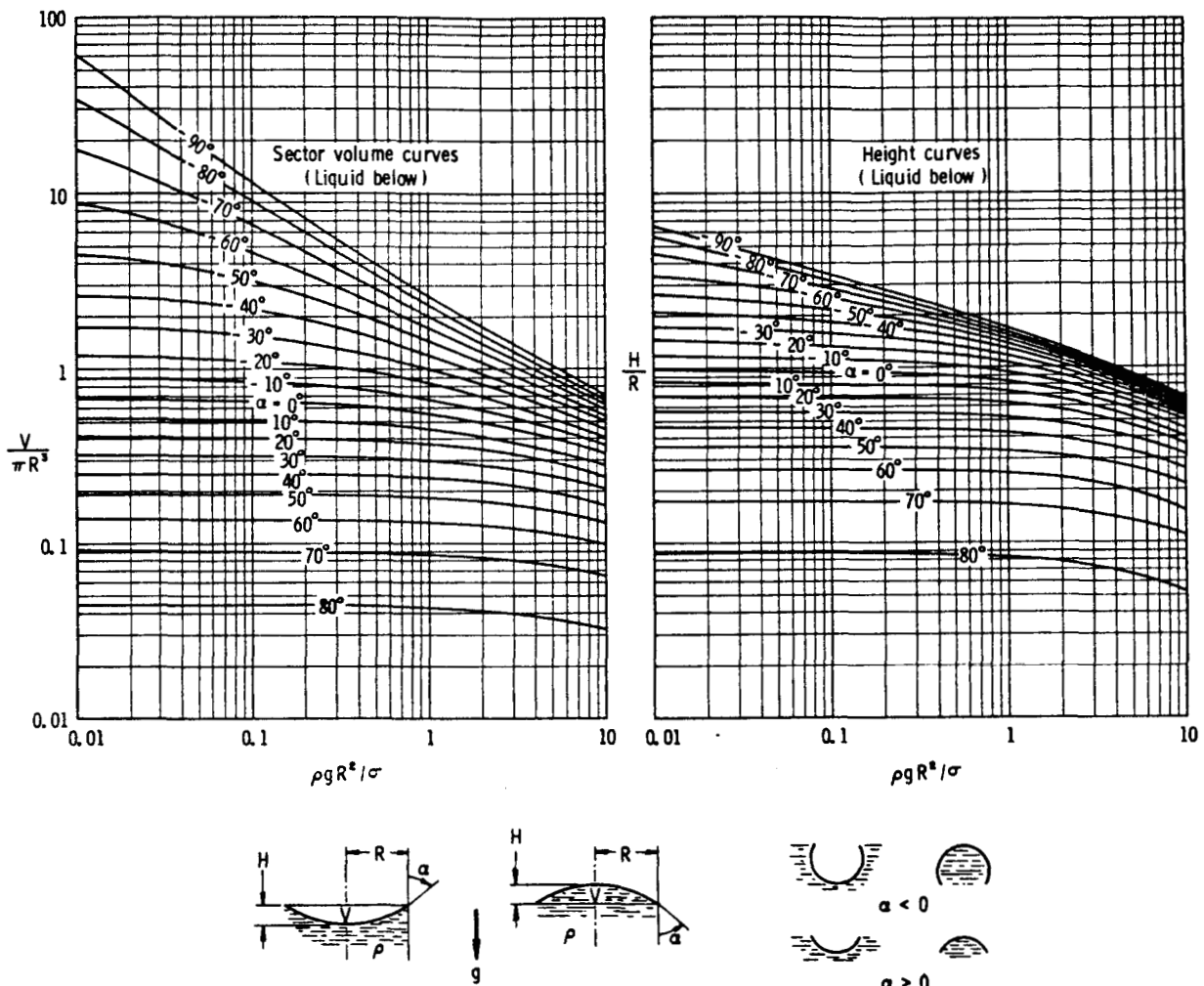


FIGURE 11.17.—Configuration parameters for axisymmetric menisci.

a function of the percent volume loading, to develop a curve similar to those in figure 11.14. It is a simple matter to read the required values from figure 11.17, and the calculation method is outlined in table 11.1. Figure 11.18 shows the results of this calculation for a particular case of moderate Bond number. Note that the depth of the meniscus is less than predicted by the simple zero-g (circular segment) model of figure 11.14. This points up the fact that the zero-g analysis, though in error, may often provide a simple conservative estimate of the meniscus extension. When more accurate results are desired, the curves of figure 11.17 can be used.

Approximate calculations for configurations not covered by the curves discussed above can be made using some assumed shape for the meniscus. For example, Satterlee and Chin (ref. 11.20) have found that an ellipsoidal approximation gave quite adequate results for axisymmetric menisci at low Bond numbers.

#### Stability of Axisymmetric Menisci

In a zero-g environment, a meniscus will hold its position and shape as the container is slowly inverted. At sufficiently low g, the inversion may also be made and the liquid left "hanging" at the top of the container. There are important situations in which one would like to

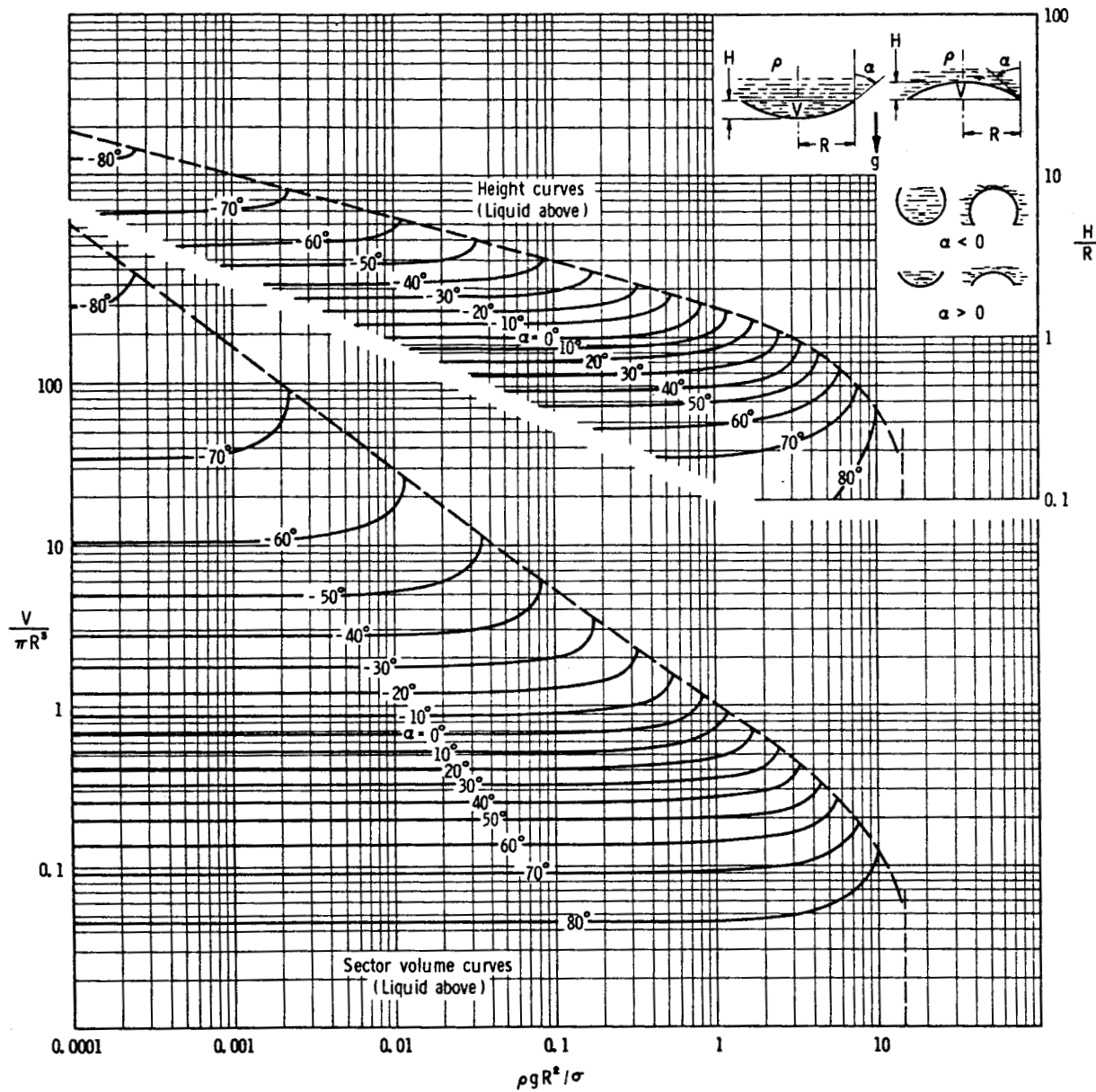


FIGURE 11.17.—Concluded.

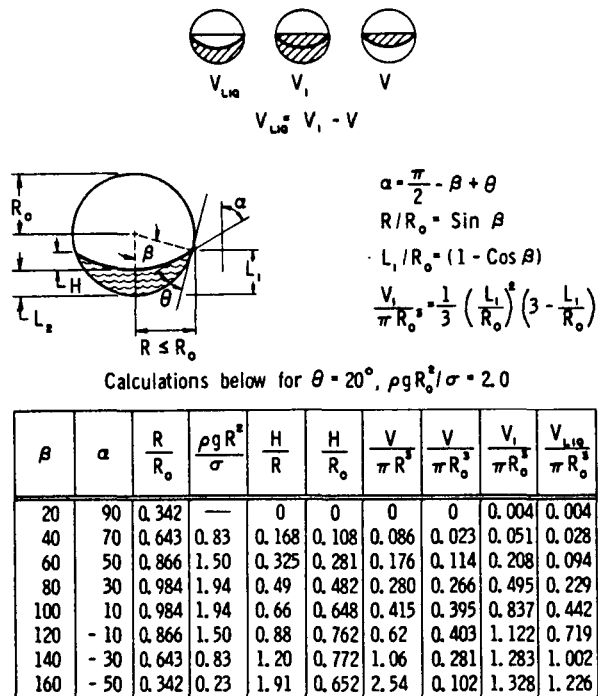
design the container such as to maintain the inverted meniscus, and other instances where it is important that the liquid not remain in the inverted position. In these engineering problems, knowledge of the stability of the meniscus, with respect to a destabilizing body force field, is of considerable utility, and we now will take up this important question.

The concept of interface stability can be introduced by drawing on common experience.

Consider a mercury-in-glass thermometer. Held in any position at normal  $g$ , the interface is stable, and the mercury does not run down the tube. In fact, it is possible to perform the same experiment with a tube 0.2 centimeter in diameter. However, if one attempts to invert a column of similar length in a 3.0-centimeter-diameter tube, the mercury invariably falls down and out of the tube. We therefore expect that there is a critical radius below which the

interface is stable, and above which it is unstable. The determination of this radius and the associated critical Bond number will be considered momentarily.

TABLE 11.1.—Method of Determining the Meniscus Configuration as a Function of Liquid Volume for a Spherical Tank



A first thought might be to attribute the support of the heavy liquid at the top of the tube to capillary forces. However, one finds that wetting fluids can also be suspended at the top of a glass tube, as in the alcohol-in-glass thermometer. In fact, by being careful in the inversion process, water can be suspended in a 0.6-centimeter-diameter tube. For wetting liquids, the surface tension forces tend to assist gravity in pulling the liquid down. In non-wetting liquids, some slight assisting support is given by surface tension, but the liquid is basically supported by pressure. Atmospheric pressure acts on the interface, and a reduced pressure acts at the top end of the tube (fig. 11.19(a)).

Since the ratio of weight to pressure force is independent of diameter, it is possible to support fluid in any diameter tube, provided, of course,

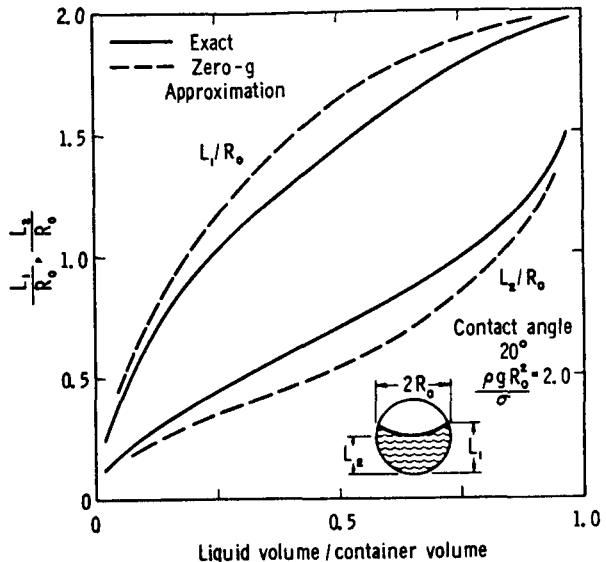


FIGURE 11.18.—Menisci in a spherical tank.

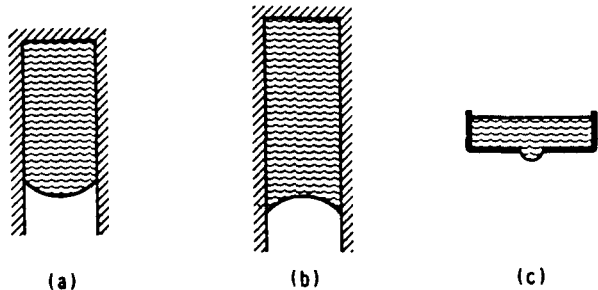


FIGURE 11.19.—Menisci in inverted tubes.

that the length is small enough so that a positive absolute pressure results at the top of the tube. But we observe instability of the column in large tubes, while in the smaller tubes the interface is stabilized by surface tension.

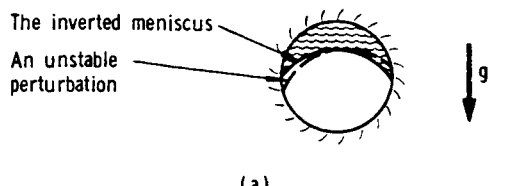
What would happen if we opened the top end of the tube, equalizing the pressures? Of course the liquid would fall down. This would not be considered an instability because the suspended configuration is impossible in itself, and one can only sensibly discuss stability when the static configuration could in principle occur. But suppose we restricted the bottom end of the tube, causing an interface of different curvature to be formed, as shown in figure 11.19(c). Suppose the interface curvature is such as to produce a pressure in the liquid at the hole which is higher than atmos-

pheric, perhaps even high enough to support the liquid column. The tallest column will be possible when the radius of curvature of the protruding interface is least, for this yields the greatest "capillary pressure." Here we see an example of a system in which capillary forces simultaneously provide both support and stability.

The stability of a meniscus may be analyzed in a number of ways. One can do a dynamic analysis of the liquid motion, and then look for normal modes of vibration which grow in amplitude with increasing time. This is a difficult computational task, for although the problem may be linearized in a study of small disturbances, the domain in which the solution must be obtained is not simple. It is possible to show that the eigenvalue equation giving the stability limit obtained from an inviscid theory of this type is exactly as would be obtained simply by invoking the thermodynamic criterion of marginal stability; that is, that variations in the meniscus shape produce no variations in the total potential energy (refs. 11.21 and 11.22). This condition marks the boundary between states of minimum free energy (stable states) and maximum free energy (unstable states). We will use the latter method, and in section 11.4 will demonstrate for a simple case that the dynamic stability analysis indeed yields the same critical Bond number.

According to our thermodynamic criteria, for a meniscus shape to be stable there must be no small perturbation of its shape which can lead to a reduction in the total potential energy. For example, consider the meniscus formed by the liquid at the top of a spherical container, as shown in figure 11.20(a). Suppose the meniscus somehow finds itself with exactly the same shape, but with its position rotated slightly about the center of the sphere. The capillary potential energy would be unchanged, but the gravitational potential energy would be decreased, and hence the total potential energy would be reduced. Consequently, the meniscus in an "inverted" spherical tank is always unstable. This fact has important application in propellant tank design.

All "inverted" menisci become unstable at sufficiently high g's. The limit of stability is



(a)

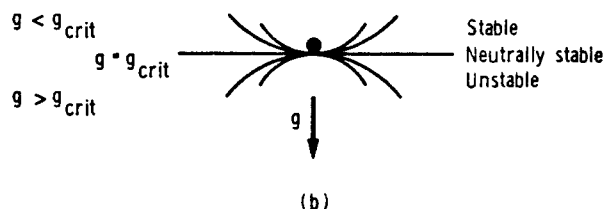


FIGURE 11.20.—Stability of menisci.

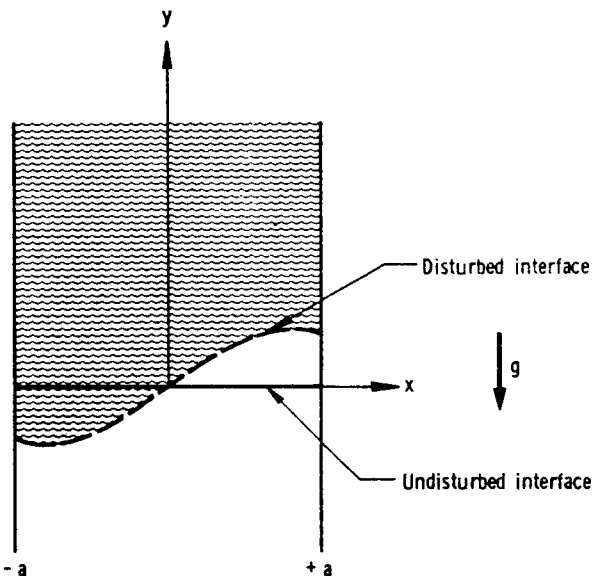


FIGURE 11.21.—Liquid in an inverted channel.

given by the point at which the total potential energy of the capillary system ceases to be a minimum, and starts becoming a maximum. A simple analogy helpful in grasping this concept is given in figure 11.20(b).

To illustrate the methods, we will now carry out the stability analysis for a simple case. Consider the liquid having  $\theta=90^\circ$  in an inverted two-dimensional channel, as shown in figure 11.21. The capillary potential energy per unit of channel length is, for a two-dimensional disturbance,

$$PE_c = \int_{-a}^{+a} \sigma \sqrt{1 + \left(\frac{dy}{dx}\right)^2} dx \quad (11.65a)$$

Hence, for small perturbations  $y(x)$ , the variation in capillary energy is, to first order

$$\delta PE_c \approx \sigma \int_{-a}^{+a} \frac{1}{2} \left(\frac{dy}{dx}\right)^2 dx \quad (11.65b)$$

The variation in gravitational potential energy per unit of length from the equilibrium (flat interface) value is

$$\delta PE_g = - \int_{-a}^{+a} \rho g \frac{y^2}{2} dx \quad (11.66)$$

Denoting  $Y = y/a$ ,  $X = x/a$ ,  $Bo = \rho g a^2 / \sigma$ , the total variation in potential energy may be expressed nondimensionally as

$$\delta PE = \frac{1}{2} \int_{-1}^{+1} \left(\frac{dY}{dX}\right)^2 dX - \frac{Bo}{2} \int_{-1}^{+1} Y^2 dX \quad (11.67)$$

For stability,  $\delta PE = 0$  for any small virtual variation  $Y(X)$ . The neutrally stable case occurs when  $\delta PE$  vanishes. Hence, in a stable state

$$Bo = \int_{-1}^{+1} (Y')^2 dX / \int_{-1}^{+1} Y^2 dX = I_1/I_2 \quad (11.68)$$

To find the critical Bond number, we should seek the shape perturbation  $Y(X)$  which minimizes the ratio  $I_1/I_2$  above. This leads us to an isoperimetric problem in the calculus of variations (ref. 11.23); the solution which maintains the contact angle fixed is

$$Y = A \sin \frac{\pi}{2} X \quad (11.69)$$

Then, substituting back into equation (11.68), we find

$$Bo_{\text{crit}} = \pi^2/4 = 2.46 \quad (11.70)$$

This is identical with the result obtained as a byproduct of the sloshing analysis. In the sloshing analysis, one considers the normal-mode oscillations, each of which yields a periodic interface perturbation  $Y_n(X)$ . If the Bond number is such that one of these normal modes grows in time, rather than oscillating, the system is unstable. The critical Bond

number marks the onset of this instability. Now, the stability criteria obtained from the potential energy considerations admit any  $Y(X)$  which satisfies the proper contact conditions. Hence, if instability occurs for a normal-mode perturbation, both methods will yield identical values for the critical Bond number.

Concus (ref. 11.21) has used this approach to treat the instability in the two-dimensional channel for contact angles other than  $90^\circ$ . He found that the  $90^\circ$  case was the most stable, and that the critical Bond number for fully wetting or nonwetting liquids was only about 0.72 (compared to 2.46 for  $\theta = 90^\circ$ ). This same trend is found in axisymmetric menisci, which are of more practical interest. However, an important result of a later study by Concus (ref. 11.22) indicated that any meniscus for which the curvature changes sign was unstable. While this was shown only for a two-dimensional meniscus, it might be speculated that it would be true for any meniscus, when applied to the total meniscus curvature. These criteria might provide a good way of estimating critical Bond numbers for menisci of irregular shape.

The extension of the stability analysis to generalized axisymmetric menisci is considerably more complicated; the details differ somewhat from the previous analysis, but they are the same in concept. A summary of the analysis is given in reference 11.1, and we shall simply present the results here.

The critical Bond number may be related to the radius of curvature ( $r_w$ ) of the bounding walls at the contact point in a plane containing the axis, to the contact angle, and to the angle  $\alpha$  which the meniscus makes with the axis. This relationship may be expressed nondimensionally in the form

$$B_{\text{crit}} = f\left(\frac{r}{r_w \sin \theta}, \alpha\right) \quad (11.71)$$

This relationship was determined by numerical solution and is shown graphically in figure 11.22. The meanings of the symbols are given on that figure.

The curves of figure 11.22 can be used to examine the stability of practically any axisym-

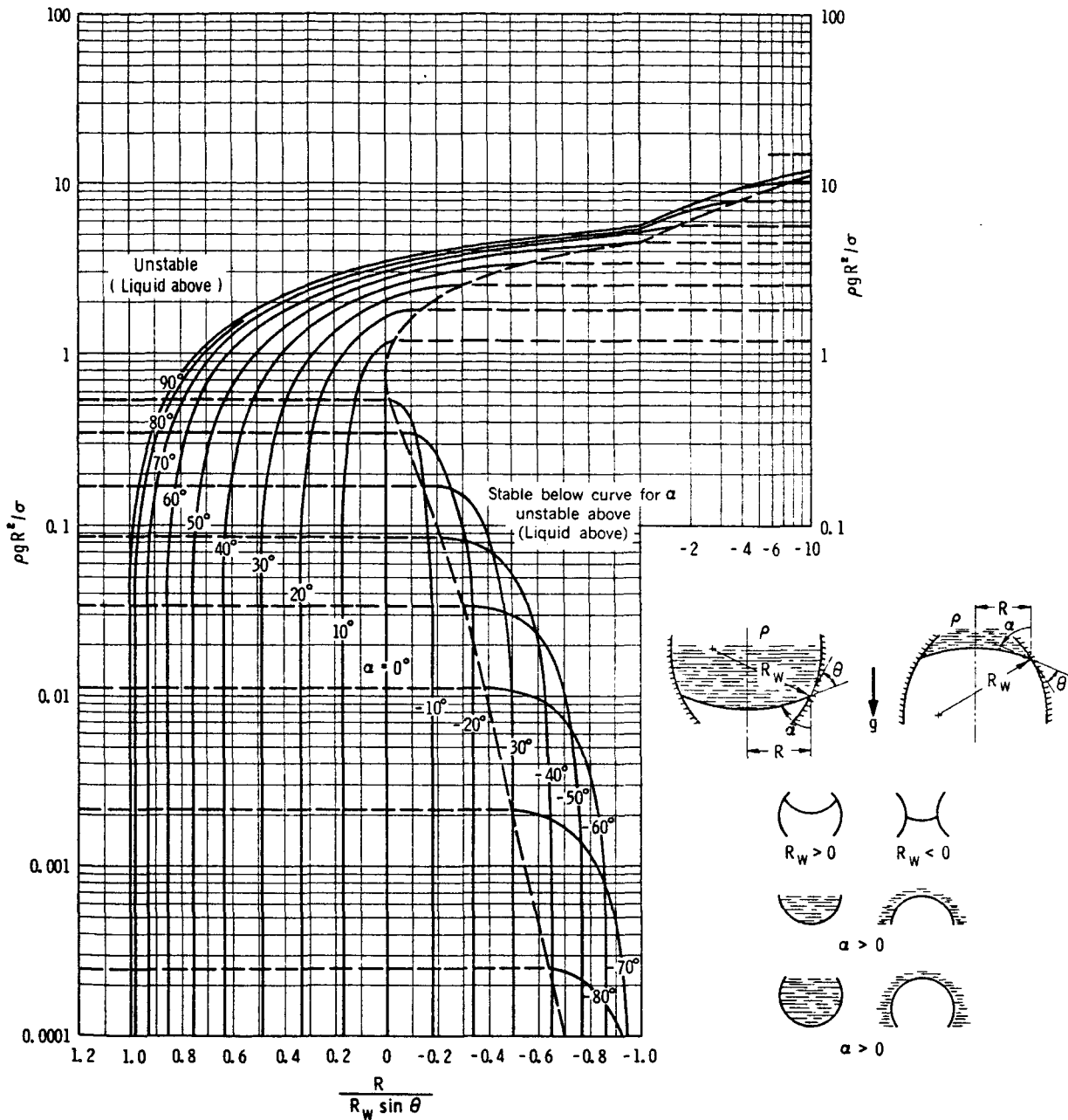


FIGURE 11.22.—Neutral stability curves for axisymmetric menisci.

metric meniscus. Several important general conclusions may be drawn from them directly:

(1) An "inverted meniscus" is unstable at all Bond numbers for positive wall curvature (concave with respect to the meniscus) such that the parameter  $r/(r_w \sin \theta)$  is greater than +1. This includes the spherical tank case previously discussed.

(2) The critical Bond number for zero wall curvature ( $r_w = \infty$ ) depends only upon the angle which the meniscus makes with respect to the axis, and is otherwise independent of the contact angle. This allows the stability criteria for conical capillaries to be represented in the manner of figure 11.23.

(3) The critical Bond number for wall-bound

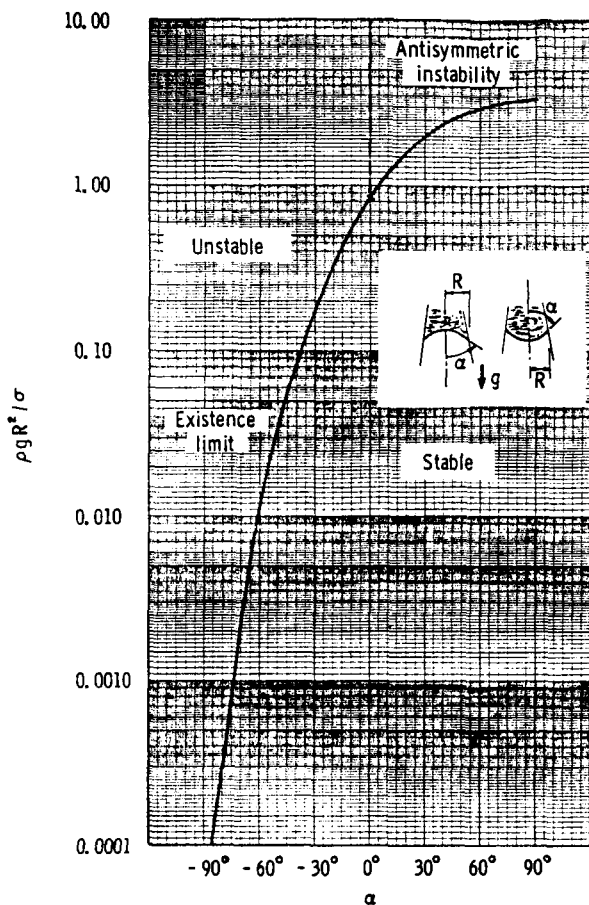


FIGURE 11.23.—Critical Bond number for axisymmetric menisci in a conical tank.

drops and bubbles may be determined from figure 11.22, and expressed in terms of a critical volume. The result is shown in figure 11.24.

(4) The maximum destabilizing  $g$  loading can be sustained when the interface is flat ( $\alpha=90^\circ$ ).

What experimental data are available seem to confirm the instability theory. Satterlee and Reynolds (ref. 11.24) performed extensive experiments in a slightly tapered tube, and these data are in very good agreement with figure 11.22 over the range of  $0^\circ < \alpha < 90^\circ$ . Similar data of Masica et al. (ref. 11.25) also support these predictions. Jakob (ref. 11.26) discusses the wall-bound bubble case in his nucleate boiling chapter, and shows a variety of data which are in very good agreement with figure 11.23 over the range  $-90^\circ < \alpha < 0^\circ$ . The case of very small negative radius of

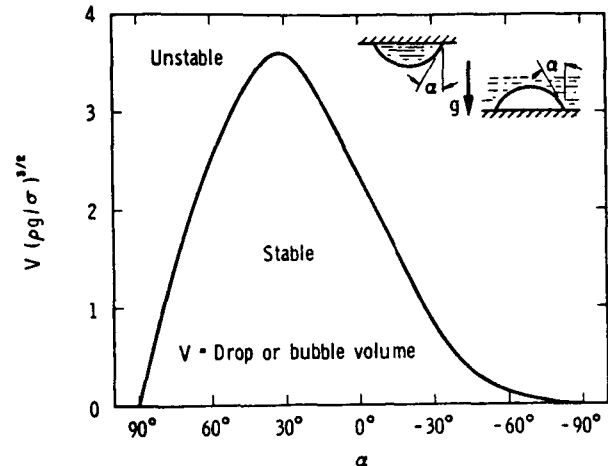
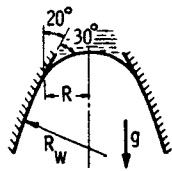


FIGURE 11.24.—Stability of wall-bound drops and bubbles.

curvature occurs at the bottom edge of a vertical tube, or in a horizontal orifice; if the meniscus is flat, the critical Bond number is 14.6. Experiments of Duprez (ref. 11.27) support this prediction. The case  $\alpha=0^\circ$  gives the maximum size of a long bubble which can persist in a straight vertical tube, and is in agreement with the theory and experiments reported by Bretherton (ref. 11.28). Two examples illustrating the use of these curves in axisymmetric meniscus stability analysis are given in figure 11.25.

There are a number of important applications of these results in the design of liquid storage systems for use in space. If it is desirable that the liquid not remain in the inverted position, that is, that it fall to the "bottom" of the tank, a spherical design should be used. Then, with any slightly destabilizing orientation of the body force, the liquid will migrate to the bottom of the tank. On the other hand, if it is desired that the liquid should remain "above" the gas, then one would try to design the vessel so as to achieve a flat meniscus. This might be accomplished by placing thin rings around the walls, as shown in figure 11.26(a). The meniscus would become attached to one of these rings, and an optimally stable flat interface thereby obtained. If the  $g$ -loading is more than the critical value for stability, the tank can be partitioned to break up the meniscus into smaller stable menisci, as indicated in figure

Example 1



Suppose

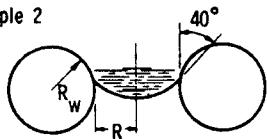
$$\begin{aligned} \alpha &= 50^\circ \\ \theta &= 30^\circ \\ R_w/R &= 3 \end{aligned}$$

$$\phi = \frac{R}{R_w \sin \theta} = \frac{1}{3 \times 0.5} = 0.667$$

For  $\alpha = 50^\circ$ ,  $\phi = 0.667$ , read on Fig. 11.22

$$(\rho g R^2/\sigma)_{\text{crit}} = 0.36$$

Example 2



Suppose

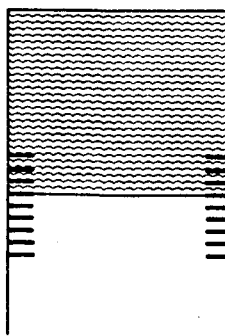
$$\begin{aligned} \theta &= 135^\circ \\ \alpha &= 40^\circ \\ R_w/R &= -1 \end{aligned}$$

$$\phi = \frac{R}{R_w \sin \theta} = \frac{1}{-1 \times 0.707} = -1.41$$

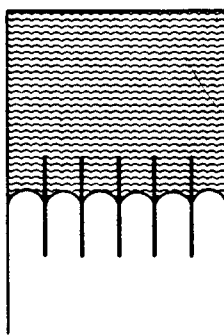
For  $\alpha = 40^\circ$ ,  $\phi = -1.41$ , read on Fig. 11.22

$$(\rho g R^2/\sigma)_{\text{crit}} = 3.3$$

FIGURE 11.25.—Two examples of axisymmetric meniscus stability calculations.



(a)



(b)

FIGURE 11.26.—Two methods for improving stability.

11.26(b). Screens can be used effectively for this purpose.

A recent study by Anliker and Pi (ref. 11.29) involved calculation of interface instability by the dynamic method described in section 11.4. However, they used an inverse

procedure, in which the interface shape was first specified and the container shape then calculated. In order to maintain the assumed meniscus shape, a nonuniform pressure must be impressed on the outside of the meniscus. Anliker and Pi state that the shape of the container bottom is very important in determining the stability criteria. The present work would suggest that it is only the container shape at the contact point which is important, and it is believed that the stability limits given by the Anliker-Pi scheme for realistic meniscus shapes would be in full agreement with the curves of figure 11.22.

### Flat Annular Meniscus

The stability of a flat meniscus in an annular tank has been analyzed by these same methods. The eigenvalue problem for a flat meniscus is relatively simple, and the solution is given in reference 11.1.<sup>8</sup> The results of this stability analysis are presented here in figure 11.27.

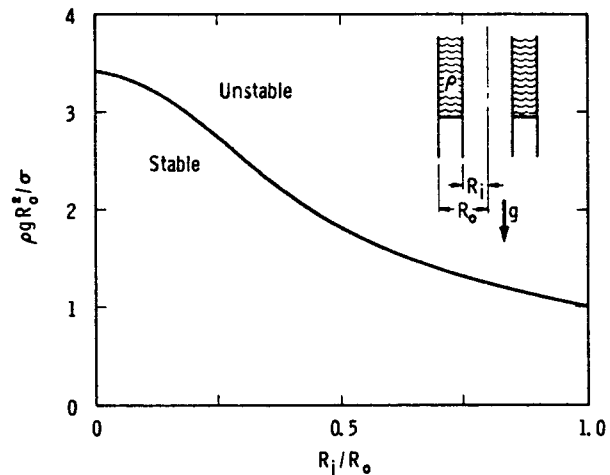


FIGURE 11.27.—Stability of a flat annular meniscus.

Note that the critical Bond number for the case of  $r_i/r_o = 0$ , corresponding to a thin wire in the center of a tube, is 3.39, the same value as obtained without the wire. This suggests

<sup>8</sup> In ref. 11.1, the ordinate of the illustration corresponding to fig. 11.27 is incorrectly labeled. The right-hand side of the first equation on p. 85 of ref. 11.1 should be multiplied by  $R$ . Eqs. (11.61) and (11.64) have been corrected for typographical errors that were present in ref. 11.1.

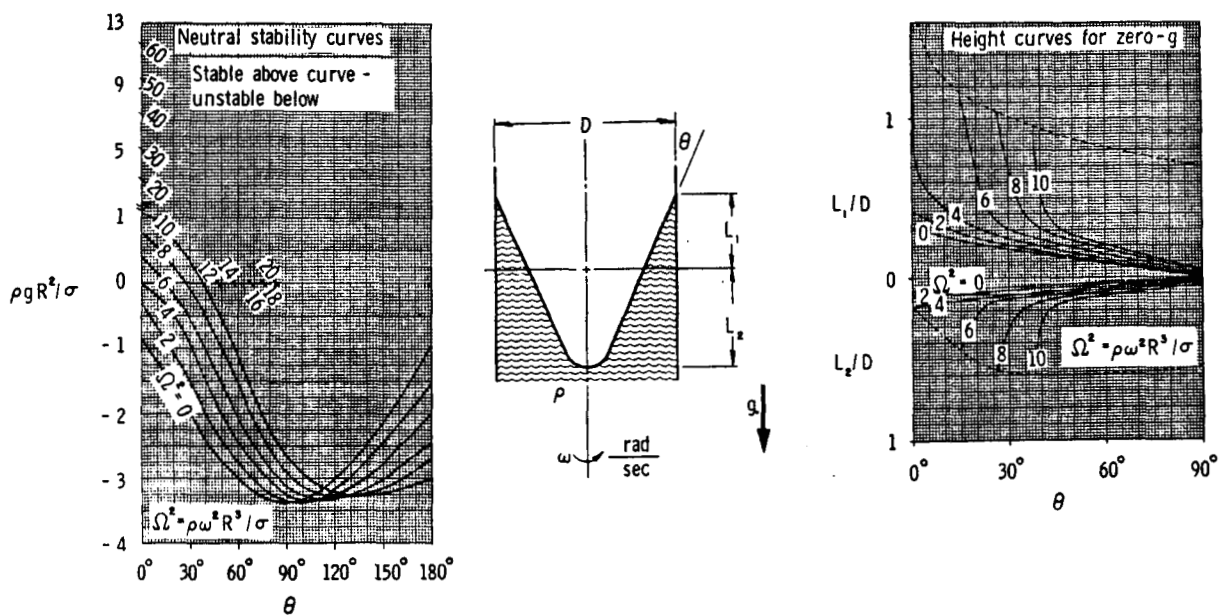


FIGURE 11.28.—Shape and stability of a rotating meniscus in a cylindrical tank.

that the presence of a small standpipe in the center of a large tank would have little effect on the critical Bond number.

It should be noted that the two-dimensional channel, with a two-dimensional disturbance, does not form the limiting case as  $r_i/r_0 \rightarrow 1$ . This is because of the azimuthal variation permitted in the annular tank.<sup>9</sup> However, the numerical calculations are checked by the observation that a disturbance with no radial variation which wiggles once and meets itself in going around the circumference is equivalent to the two-dimensional problem, with  $a$  replaced by one-fourth the circumference, or  $\pi r/2$ . Then, using equation (11.70), we would predict  $\rho g r^2/\sigma = 1$ , which agrees with figure 11.27.

#### Shape and Stability of a Rotation Axisymmetric Meniscus

Seibold and Reynolds (refs. 11.30 and 11.31) have made similar calculations for a rotating meniscus in a cylindrical tank, assuming that

<sup>9</sup> It is important to appreciate that the two-dimensional channel idealization, while simplifying the analysis, does not lead to meaningful results in the stability problem; for this reason the results of Concus' pioneering study (refs. 11.21 and 11.22), which set the method for the stability analysis, have not been included herein.

the liquid is in a state of solid body rotation. Some of their results are given in figure 11.28. It is interesting to note that a rotating meniscus may be unstable even at zero  $g$ , enabling the liquid to move entirely to the outer perimeter. This has important applications in liquid-vapor separation.

For the special case of zero contact angle and zero Bond number, Seibold and Reynolds (ref. 11.30) obtained a simplified stability criteria for the rotating meniscus in an annular tank. Their results may be written as

$$\Omega^2 = \rho r_0^3 \omega^2 / \sigma < \frac{4}{(1 - r_i/r_0)^2} \quad (11.72a)$$

Here  $r_i$  and  $r_0$  are the inner and outer radii of the tank,  $\omega$  is the angular frequency (rad/sec), and  $\Omega^2$  is the rotational Weber number. If  $\Omega^2$  exceeds this critical value, or if the meniscus contacts the bottom of the tank, the liquid moves rapidly to the outer wall.

This theory indicates that even very slow rotations will produce full liquid separation in large tanks. For example, in a 3-meter-diameter tank, a rotation of the order of two revolutions per hour is sufficient to cause separation, once the state of solid body rotation has been achieved. Seibold and Reynolds present a

number of other data pertinent to the design of rotating tanks for low g. In particular, the reference includes a more complete description of a calculation method for axisymmetric menisci, and a detailed discussion and analysis of the stability problem.

The experiments of Seibold and Reynolds indicate that figure 11.28 provides a conservative estimate of the critical rotation parameter. Separation was usually obtained at somewhat lower Bond and Weber numbers, primarily due to "dynamic overshoot" in the reorientation period.

Blackshear and Eide (ref. 11.32) have examined the meniscus in a tank whirling about an axis perpendicular to the tank axis. This motion produces an effective body force gradient, but the shape and stability can be determined essentially by the value of the body force at the meniscus surface. Hence the stability criteria, estimated using a critical equivalent Bond number of 0.84 (for fully wetting liquids), would be

$$L\omega^2 r^2 / \sigma \leq 0.84 \quad (11.72b)$$

Here  $L$  is the distance from the whirl axis to the meniscus, and  $\omega$  is the whirling angular frequency.

#### Condition for Sufficient Supporting Pressure

Throughout the previous three sections we tacitly assumed that the pressure forces in the gas are sufficient to support the meniscus in an inverted position. This must be examined in each application. The pressure at the uppermost point in the fluid will be less than that at the lowermost point by an amount (see fig. 11.29)

$$P_2 - P_1 = \rho gh \quad (11.73)$$

where  $h$  is the distance between these two points. The pressure at  $P_1$  must not be lower than the saturation pressure of the liquid at the particular temperature involved, or else vaporization is likely to occur at the top of the tank. The maximum liquid height which can be supported is therefore

$$h_{\max} = \frac{(P - P_{\text{sat}})}{\rho g} \quad (11.74)$$

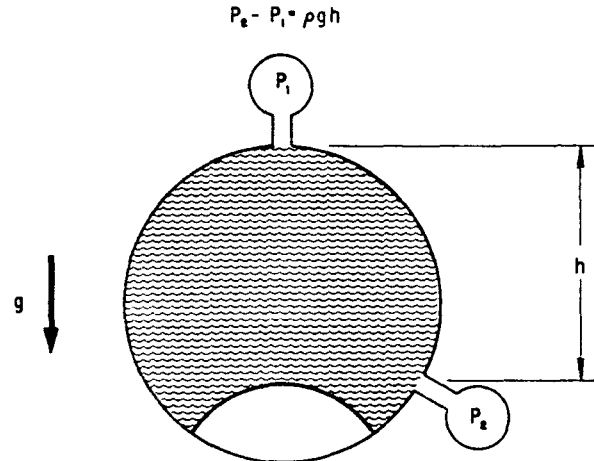


FIGURE 11.29.—Supporting pressure.

This length must not be exceeded if the meniscus is to be supported, and such considerations should be made if the liquid is in a nearly saturated state. If the liquid is saturated, no inverted meniscus can be supported. This fact must be considered in the design of cryogenic liquid storage systems.

#### Stability in Capillary-Supported Systems

The menisci discussed in previous sections are supported in an inverted position by pressure forces. In contrast, consider the capillary-supported systems of figure 11.30. This system can also be analyzed by the minimum potential energy method. However, instabilities generally occur at very low values of the Bond number, based on the radius of the supporting menisci, and hence the simpler force-balance methods, utilizing the idealization that the meniscus is spherical, are usually quite adequate. For example, equating the total pressure variation along the axis of figure 11.30(a) to zero, one finds

$$\frac{2\sigma}{r_1} = \rho gh \quad (11.75)$$

Since  $r_1 > r$ , a stable system is possible only if

$$\rho hr/\sigma \leq 2 \quad (11.76)$$

Similar analyses yield the results shown for figure 11.30(b).

In a series of experiments on a system such as figure 11.30(c)-(e), Hollister (ref. 11.33)

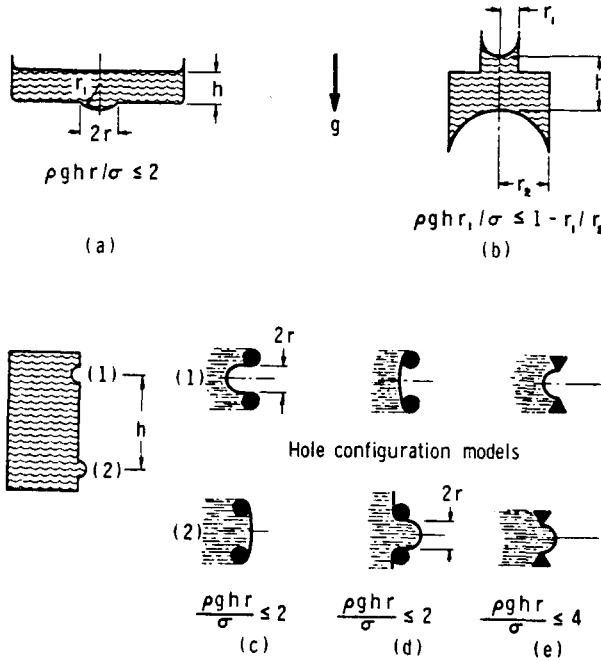


FIGURE 11.30.—Stability of some capillary-supported systems.

found that the maximum values of  $\rho g h r / \sigma$  ranged from 1.5 to 3.5. Highest values were obtained with a water-Teflon system, which is probably most closely modeled by figure 11.30(e). These experiments prove that simple analyses of this type can yield stability criteria sufficiently accurate for many engineering design purposes.

#### Instabilities in Other Capillary Systems

Lamb (ref. 11.34) presents analysis which shows that a cylinder of liquid is unstable under the action of surface tension in zero g. The column of liquid tends to pinch together and form drops of liquid. If  $D_0$  is the cylinder diameter, the most amplified disturbance is found to have an axial wavelength of

$$\lambda \approx 4.5D_0 \quad (11.77a)$$

The implication of the linearized theory is that the drops formed on breakup of the cylinder will have a diameter of approximately

$$D \approx 1.5D_0 \quad (11.77b)$$

The inverse problem of a gas column in a liquid under zero g was studied by Rayleigh (ref. 11.35). He showed that the cylindrical interface is unstable, and tends to pinch off, forming bubbles. The most rapidly amplified disturbance has an axial wavelength of

$$\lambda \approx 6.48D_0 \quad (11.78a)$$

from which we estimate the pinched-off bubble diameter as

$$D \approx 1.7D_0 \quad (11.78b)$$

These predictions have been confirmed experimentally and are beautifully demonstrated in the motion picture of Trefethen (ref. 11.12).

Anliker and Beam (ref. 11.36) studied the stability of uniform liquid layers spread over cylinders and spheres and found that the film on a fully covered sphere or cylinder is always unstable. This contradicts the simplified analysis of Lee (ref. 11.37) which dealt primarily with longitudinal wave instabilities. With water, Lee always observed instability, but with oil he did not. It might be thought that this was a viscous effect, but the analysis of Bellman and Pennington (ref. 11.38) indicates that viscosity does not alter the critical Bond number. The surface tension value for oil used by Lee seems high, and hence his oil experiments are questionable.

Otto (ref. 11.39) reports experiments on the stability of a meniscus in a horizontal tube. The critical Bond numbers, based on tube radius, ranged from about 1 to about 2.5; this was not attributed by Otto to contact angle variations, but may well have been due to differences in contact angle or to contact angle hysteresis, which Satterlee and Reynolds (ref. 11.24) found to be important in their sloshing studies.

#### 11.4 LOW-g SLOSHING AND SOME RELATED PROBLEMS

##### Introduction

The sloshing analyses presented in previous chapters apply whenever the Bond number is substantially greater than unity. At low g

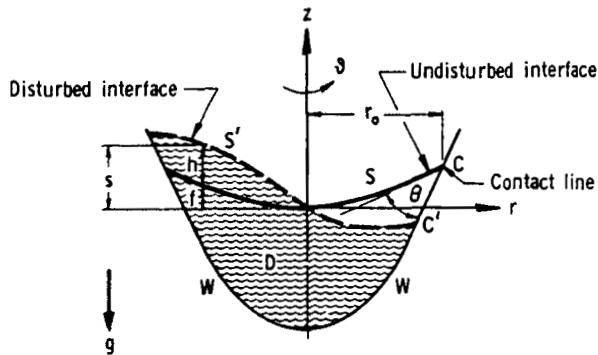


FIGURE 11.31.—Definitions for axisymmetric meniscus sloshing analysis.

these analyses must be modified to account for the distortion of the undisturbed interface shape and the added interface pressure difference caused by capillarity. While these new factors make the mathematics considerably more complicated, the general approach remains unchanged. In this section, we will formulate the sloshing analysis for axisymmetric menisci and present the results for the particularly useful case of a cylindrical tank with an axial body force. For more details of the treatment, see reference 11.24.

#### General Formulation for Low-g Sloshing

We presume that the essential features of sloshing motions will be revealed by an inviscid, incompressible flow theory. Consider the liquid in the axisymmetric tank of figure 11.31. The bounding walls are denoted by  $W$ , the undisturbed interface by  $S$ , the disturbed interface by  $S'$ . The domain occupied by the liquid in the undisturbed and disturbed configurations are  $D$  and  $D'$ , respectively. We denote the velocity components in the  $r$ ,  $\theta$ , and  $z$  directions by  $u$ ,  $v$ , and  $w$ , respectively. The fluid meets the wall at contact angle,  $\theta$ , measured in a plane perpendicular to the contact line,  $C$ . Assuming the motion to be inviscid, incompressible, and irrotational, the equation of continuity may be expressed in terms of the velocity potential,  $\phi$ , as

$$\nabla^2 \phi = 0 \text{ in } D' \quad (11.79)$$

Here the velocity potential is defined by

$$\begin{aligned} u &= -\phi_r \\ v &= -\frac{1}{r} \phi_\theta \\ w &= -\phi_z \end{aligned} \quad (11.80)$$

Subscript notation is used to denote partial differentiation with respect to the subscripted variable. The boundary condition appropriate for the inviscid problem at the solid walls is

$$\frac{\partial \phi}{\partial n} = 0 \text{ on } W \quad (11.81)$$

Since the motion is irrotational, Bernoulli's equation is satisfied throughout the liquid domain, and in particular at the free surface. The unsteady form of Bernoulli's equation applied at the perturbed surface is

$$\frac{P}{\rho} + \frac{V^2}{2} + gs = \phi_t + \psi(t), \text{ on } S' \quad (11.82)$$

where  $\psi(t)$  is an arbitrary function of time. Here  $P$  is the pressure just inside of the interface and  $V$  is the total fluid velocity. It should be pointed out that the only point at which dynamics enters the analysis is through equation (11.82).

$P$  is related to the pressure just outside of the liquid,  $P_s$ , by

$$P_s - P = \sigma K \quad (11.83)$$

where the total interface curvature,  $K$ , is given by (ref. 11.24)

$$\begin{aligned} K = \frac{1}{r} \frac{\partial}{\partial r} \left[ \frac{rs_r}{\sqrt{1+s_r^2 + \frac{1}{r^2}s_\theta^2}} \right] \\ + \frac{1}{r^2} \frac{\partial}{\partial \theta} \left[ \frac{s_\theta}{\sqrt{1+s_r^2 + \frac{1}{r^2}s_\theta^2}} \right] \end{aligned} \quad (11.84)$$

A kinematic relation between the velocity field and the interface motion is essential to this analysis. This kinematic relation is (ref. 11.24)

$$s_t = -\phi_z + \phi_r s_r + \frac{1}{r^2} \phi_\theta s_\theta \quad (11.85)$$

If the meniscus is flat, or nearly so, only the first term on the right in equation (11.85) need be retained, as was the case in earlier chapters. However, with the strongly curved meniscus, the second term will also contribute to a linearized analysis, and all three terms would have to be used in a proper nonlinear treatment.

For convenience, the arbitrary function of time in equation (11.82) may be set equal to the equilibrium liquid pressure at the vertex of the equilibrium free surface shape, divided by the liquid density. Then, using the kinematic condition, the free surface condition reduces to

$$\frac{P_s - P_0}{\rho} - \frac{\sigma}{\rho} K + \frac{1}{2} \left( \phi_r^2 + \frac{1}{r^2} \phi_\vartheta^2 + \phi_z^2 \right) + g s - \phi_t = 0 \text{ on } S' \quad (11.86)$$

Equation (11.79) is the equation which must be solved, and the boundary conditions which must be imposed are equations (11.81) and (11.86), plus a contact angle condition. The kinematic connection between the shape of the free surface and the velocity potential is equation (11.85). Obviously, the nonlinear problem is quite difficult, and in the interests of obtaining a useful approximate method, we will now linearize the problem by idealizing that the perturbations are small.

### The Linearized Problem

We assume that  $\phi$  is of the order  $\epsilon$ , where  $\epsilon$  is a small parameter, and express the interface as

$$s(r, \vartheta, t) = f(r) + \epsilon h(r, \vartheta, t) \quad (11.87)$$

The values of  $\phi$  and its derivatives on the disturbed surface are expressed as a Taylor's series expansion about their values on the undisturbed meniscus. This in effect allows the single boundary condition to be "transferred" from  $S'$  to  $S$ . The linearized problem then becomes (to order  $\epsilon$ ):

*Differential equation:*

$$\nabla^2 \phi = 0 \text{ in } D \quad (11.88a)$$

*Surface boundary condition:*

$$\begin{aligned} \frac{\sigma}{\rho} \left\{ \frac{1}{r} \frac{\partial}{\partial r} \left[ \frac{rh_r}{\sqrt{1+f_r^2}} \right] + \frac{1}{r^2} \frac{\partial}{\partial \vartheta} \left[ \frac{h_\vartheta}{\sqrt{1+f_r^2}} \right] \right\} \\ - gh + \phi_t = 0 \text{ on } S \end{aligned} \quad (11.88b)$$

*Wall boundary condition:*

$$\frac{\partial \phi}{\partial n} = 0 \text{ on } W \quad (11.88c)$$

*Kinematic condition at the surface:*

$$h_t = -\phi_z + f_r \phi_r \text{ on } S \quad (11.88d)$$

In addition, we require a contact point condition. We assume that the perturbation in the slope  $h$ , at the contact point is given, to order  $\epsilon$ , by

$$h_r = \gamma h \text{ on } C \quad (11.88e)$$

The parameter  $\gamma$  provides a macroscopic way for including the effects of contact angle hysteresis (ref. 11.24). In walls with curvature in an axial plane,  $\gamma$  also includes the curvature effects.

Now that the problem has been linearized, we can reduce it to the familiar sort of eigenvalue problem for the natural sloshing modes. We put

$$\left. \begin{aligned} R &= r/r_0 & Z &= z/z_0 & F &= f/r_0 \\ \phi &= \sqrt{gr_0^3} \Phi(R, \vartheta, Z) \sin \omega t \\ h &= \sqrt{\frac{r_0 g}{\omega}} H(R, \vartheta) \cos \omega t \\ Bo &= \rho g r_0^2 / \sigma & \Omega^2 &= \rho r_0^3 \omega^2 / \sigma & \Gamma &= r_0 \gamma \end{aligned} \right\} \quad (11.89)$$

and obtain the dimensionless eigenvalue problem for  $\Phi$ ,  $H$ , and  $\Omega$ :

*Differential equation:*

$$\nabla^2 \Phi = 0 \text{ in } D \quad (11.90a)$$

*Wall boundary condition:*

$$\Phi_N = 0 \text{ on } W \quad (11.90b)$$

*Surface boundary condition:*

$$\frac{1}{R} \frac{\partial}{\partial R} \left[ \frac{RH_R}{\sqrt{1+F_R^2}} \right] + \frac{1}{R^2} \frac{\partial}{\partial \vartheta} \left[ \frac{H_\vartheta}{\sqrt{1+F_R^2}} \right] - BoH + \Omega^2 \Phi = 0 \text{ on } S \quad (11.90c)$$

*Kinematic condition:*

$$H = \Phi_z - F_R \Phi_R \text{ on } S \quad (11.90d)$$

*Contact angle condition:*

$$H_R = \Gamma H \text{ on } C \quad (11.90e)$$

In spite of the linearization, we still are faced with a formidable problem; except for very simple cases, the domain  $D$  is not well suited for solution of equation (11.90a), for the meniscus shape  $F(R)$  is known only numerically. We will now obtain a solution for the special case of a cylindrical tank with a flat bottom and a flat interface, and subsequently formulate and use a variational scheme for analysis of more realistic situations.

### Solution for a Special Case

For the special case indicated by figure 11.32, solutions satisfying equation (11.90a) in  $D$  are

$$\Phi = J_m(k_{m,n}R) \cos m\vartheta \cdot \cosh [k_{m,n}(L+Z)] \quad (11.91)$$

where  $J_m(x)$  is the Bessel function of order  $m$ . Note that  $m=0$  corresponds to the first symmetric perturbation, while  $m=1$  gives the first antisymmetric (lateral sloshing) mode. The eigenvalues  $k_{m,n}$  are determined from equation (11.90b), which gives

$$J'_m(k_{m,n}) = 0 \quad (11.92)$$

Note that equation (11.90d) is satisfied by equation (11.91). Using the kinematic condition, the surface boundary condition becomes

$$\frac{1}{R} \frac{\partial}{\partial R} (R\Phi_{zR}) + \frac{1}{R^2} \Phi_{z\vartheta\vartheta} - Bo\Phi_z + \Omega^2 \Phi = 0 \text{ on } S \quad (11.93)$$

This will be satisfied by solutions of the form of equation (11.91) only for particular values of  $\Omega$ , namely

$$\Omega_{m,n}^2 = \tanh (k_{m,n}L) [m^2 k_{m,n}^3 + Bo k_{m,n}] \quad (11.94)$$

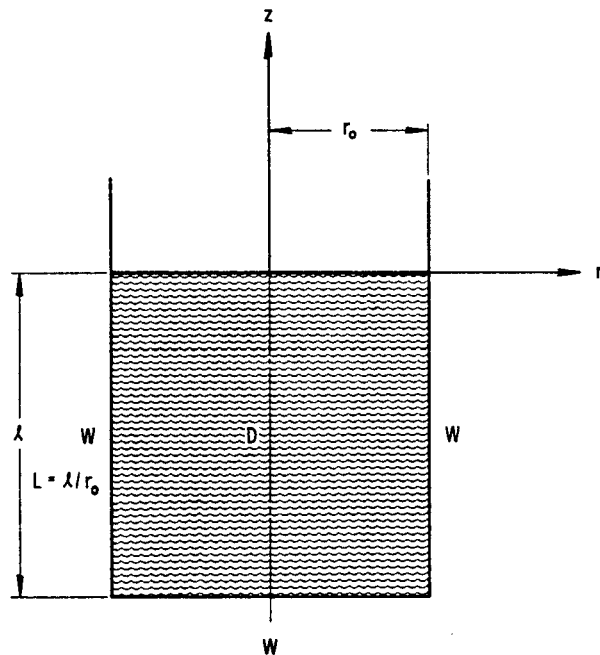


FIGURE 11.32.—Geometry for a special case.

Note that we were unable to enforce any contact point condition. However, it may easily be shown that the contact angle is unchanged for this solution, which therefore corresponds to  $\Gamma=0$ . The lowest sloshing frequency (the fundamental) is obtained for  $m=n=1$ , and is

$$\Omega^2 = \tanh(1.841L)[6.255 + 1.841Bo] \quad (11.95)$$

Note that for very large Bond numbers, equation (11.95) gives

$$\Omega^2/Bo = \bar{\Omega}^2 = \omega^2 r_0/g = 1.841 \tanh(1.841L) \quad (11.96)$$

which is the result obtained when surface tension is neglected.

As long as  $Bo > -3.39$ ,  $\Omega^2$  will be positive and hence the motion oscillatory. But for  $Bo < -3.39$   $\Omega^2$  is imaginary, corresponding to a growing disturbance. The neutral stability point is therefore  $Bo = -3.39$ , which agrees exactly with the value obtained from the simpler potential energy considerations. (Note that the sign difference is due to the different direction for positive  $g$ . Note also that the critical value is independent of depth, which is also in agreement with our earlier discussions.)

### A Variational Formulation

In general, exact solution of the eigenvalue problem, equation (11.90), is not possible, and approximate methods are preferable. In particular, a variational formulation can be made (ref. 11.24). Following the usual formalisms of the calculus of variations, one can show that,<sup>10</sup> when  $\Phi$  and its  $H$  are eigenfunctions satisfying equation (11.90), associated with eigenvalue  $\Omega^2$ , the function

$$\begin{aligned} I = & \frac{\Omega^2}{2} \iiint_D \left[ \Phi_R^2 + \frac{1}{R^2} \Phi_\vartheta^2 + \Phi_z^2 \right] R dR d\vartheta dZ \\ & + \frac{1}{2} \iint_s \left\{ \frac{H_R^2}{\sqrt{1+F_R^2}} + \frac{1}{R^2} \frac{H_\vartheta^2}{\sqrt{1+F_R^2}} \right. \\ & \left. + Bo H^2 - 2\Omega^2 \Phi H \right\} R dR d\vartheta \\ & - \frac{\Gamma}{2} \int_c \frac{H^2}{\sqrt{1+F_R^2}} d\vartheta \quad (11.97a) \end{aligned}$$

is stationary with respect to arbitrary small variations in  $\Phi$  and  $H$  satisfying

$$\Phi_N = 0 \text{ on } W \quad (11.97b)$$

$$H = \Phi_z - F_R \Phi_R \text{ on } S \quad (11.97c)$$

$$H_R = \Gamma H \text{ on } C \quad (11.97d)$$

The variational problem, equation (11.97), can be attacked directly by the Rayleigh-Ritz method. We assume a solution of the form

$$\Phi = \sum_{i=1}^N a_i \psi^{(i)}(R, \vartheta, Z) \quad (11.98)$$

The functions  $\psi^{(i)}$  must be chosen so as to satisfy equations (11.97b) through (11.97d). The expression for  $I$  then becomes of the form

$$I = \sum_{i=1}^N \sum_{j=1}^N (A_{ij} + B_{ij} \Omega^2) a_i a_j \quad (11.99)$$

where the  $A_{ij}$  and  $B_{ij}$  are numbers which can be calculated by integration. The requirement that  $I$  be stationary then produces a characteristic determinant, from which  $\Omega^2$  must be evaluated,

<sup>10</sup> This may be derived physically from Hamilton's principle (ref. 11.24).

$$\text{Det } (A_{ij} + \Omega^2 B_{ij}) = 0 \quad (11.100)$$

The roots of this expression provide the approximation to the eigenvalues.

Some considerable reduction in the amount of numerical work can be obtained if the wall geometry is such that each member of the approximating functions  $\psi^{(i)}$  can be chosen so as to satisfy  $\nabla^2 \Phi = 0$  in  $D$ . Satterlee and Reynolds (ref. 11.24) show that when  $\Phi$  and  $H$  are eigenfunctions satisfying equation (11.90), the function

$$\begin{aligned} \bar{I} = & \iint_s \left[ \frac{H_R^2}{\sqrt{1+F_R^2}} + \frac{1}{R^2} \frac{H_\vartheta^2}{\sqrt{1+F_R^2}} \right. \\ & \left. + Bo H^2 - \Omega^2 H \Phi \right] R dR d\vartheta - \Gamma \int_c \frac{H^2}{\sqrt{1+F_R^2}} d\vartheta \quad (11.101a) \end{aligned}$$

is stationary with respect to arbitrary variations satisfying

$$\nabla^2 \Phi = 0 \text{ in } D \quad (11.101b)$$

$$\Phi_N = 0 \text{ on } W \quad (11.101c)$$

$$H = \Phi_z - F_R \Phi_R \text{ on } S \quad (11.101d)$$

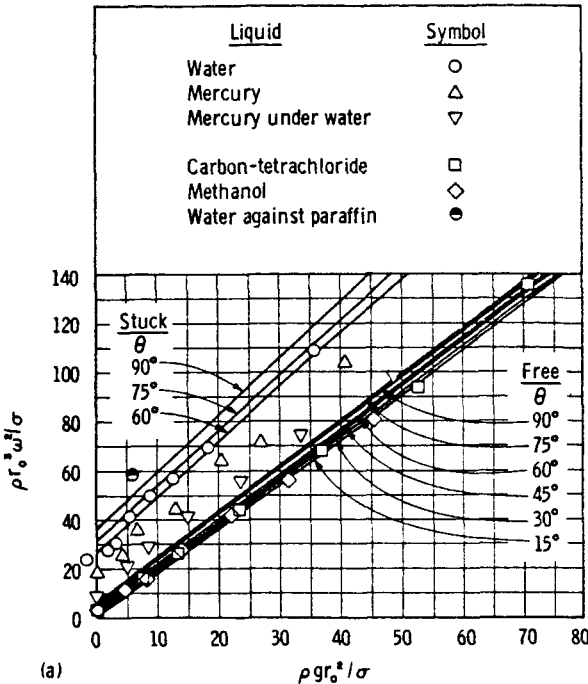
$$H_R = \Gamma H \text{ on } C \quad (11.101e)$$

Now, if we look for eigenfunctions associated with a particular azimuthal mode, we can use

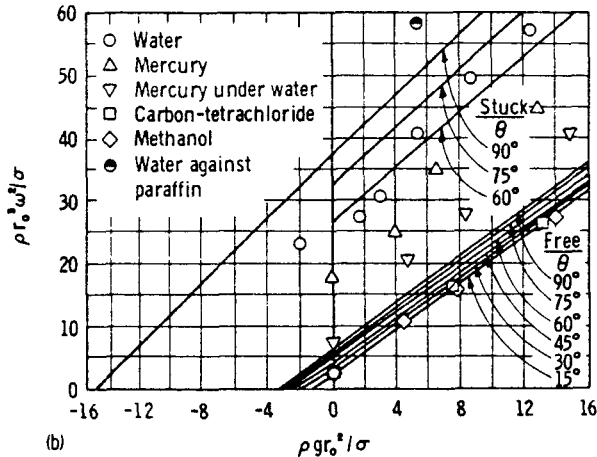
$$\Phi = \sum_{i=1}^N a_i \cos m\vartheta \cdot \Psi^{(i)}(R, Z) \quad (11.102)$$

and the required numerical integrations are purely one-dimensional. The functions  $\Psi^{(i)}(R, Z) \cos m\vartheta$  can be taken as the normal modes for the high g (flat interface) problem, if these are known in a convenient analytical form.

Satterlee and Reynolds (ref. 11.24) have applied this idea in the analysis of the fundamental sloshing mode for a liquid in a cylindrical tank with a flat bottom. Convergence difficulties were encountered with nonwetting contact angles, but the method proved quite effective for wetting liquids. Figure 11.33 shows the results of these predictions and some measurements obtained in a companion experi-



(a)



(b)

FIGURE 11.33.—Lateral sloshing in a cylinder of infinite depth.

ment. The lines denote the theory; "free" refers to a calculation with  $\Gamma=0$ ; and "stuck" denotes  $\Gamma=-\infty$ , for which the contact line remains fixed. Note that the effect of meniscus curvatures becomes increasingly important at low and negative Bond numbers. For example, the natural frequency for a highly wetting liquid is more than two times less than that predicted earlier for a flat interface, while nonwetting liquids slosh much more rapidly than wetting liquids at zero g.

Figure 11.34 shows the predictions and experiments for zero g. The solid line represents the theory in the range where the convergence of the variational calculation was considered adequate, and the dotted line our present best estimates, based on the theory. An approximate equation, based on an empirical fit to the theory for the fundamental (lateral) mode (free-interface case), is

$$\rho r_0^3 \omega^2 / \sigma \approx \tanh(1.84L)[6.26 + 1.84Bo - 4.76 \cos \theta] \quad (11.103)$$

where  $\theta$  is the contact angle. This approximation will be suitable for most design estimates.

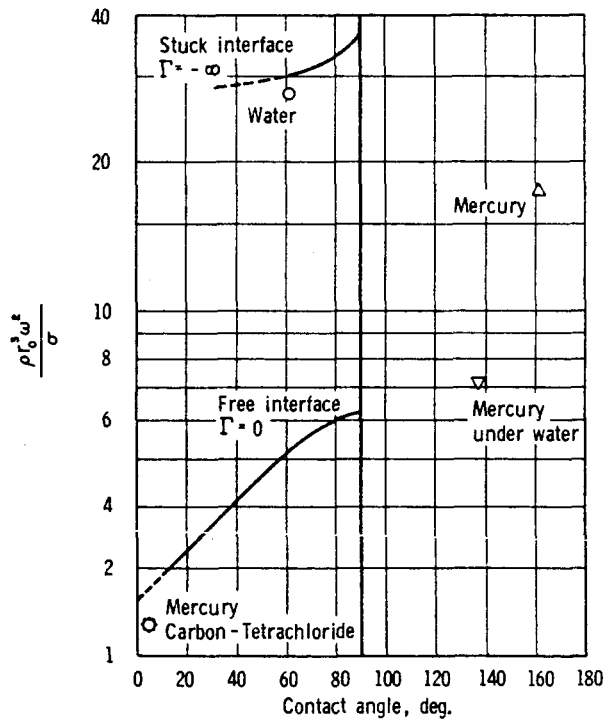


FIGURE 11.34.—Zero-g lateral sloshing in a cylinder of infinite depth.

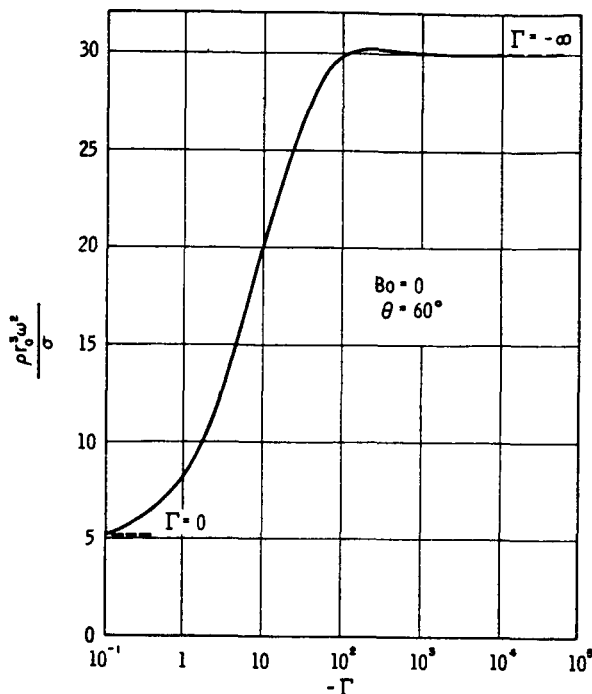


FIGURE 11.35.—Effect of contact angle hysteresis on zero-g lateral sloshing in a cylinder of infinite depth.

The experiments of reference 11.24 showed that for some liquid-container combinations the surface forces are so strong that the interface becomes "stuck" along the contact lines. The theoretical prediction for  $\Omega^2$ , including hysteresis, is shown in figure 11.35. Note that this effect is quite pronounced at zero g. In making a sloshing frequency prediction for zero g, it is consequently quite important to learn whether the liquid will move freely up and down the container surface, or whether it is so tenacious as to become stuck. Experience to date seems to suggest that the free-interface model is most approximate for typical propellant systems.

#### An Estimating Method

At this writing, a large body of zero-g sloshing analyses are noticeably lacking. The designer, faced with problems of estimation, is therefore forced to make educated extrapolations. Based on the results at hand, we suggest the following scheme:

- (1) Determine the high-g sloshing frequency

$$\bar{\Omega}^2 = \omega^2 r_0/g$$

(2) Determine the critical Bond number in the manner described in the previous section (note that there is a sign change due to the definition of g).

(3) The  $\Omega^2 - Bo$  curves seem to be straight lines, so put

$$\Omega^2 = \rho r_0^3 \omega^2 / \sigma = a + b Bo \quad (11.104a)$$

The information in (1) and (2) above suffice to determine the constants  $a$  and  $b$

$$b = \bar{\Omega}^2 \quad (11.104b)$$

$$a = |Bo_{crit}|/b \quad (11.104c)$$

This should provide a reasonable estimate for the natural frequency of low-g sloshing.

#### Elastic Interactions

Smith (ref. 11.40) has studied the effect of elastic interactions with the container on sloshing frequencies and meniscus instability in a two-dimensional channel where the contact angle is  $90^\circ$ . He finds that the critical Bond number for antisymmetric disturbances is unaffected by the elasticity of the wall, but a surprising result was found when symmetric disturbances were considered. When the wall is elastic, one possible mode of vibration has the meniscus (which is flat in his model) moving up and down, without changing its shape. In such a situation, surface tension cannot exert a restoring influence, and hence Smith predicts that the critical Bond number will be zero if the tank is elastic. As yet, this surprising prediction has not been confirmed experimentally, nor is it expected to hold for realistic containers and contact angles. Although Smith's work suggests that elastic effects are very important at low Bond numbers, in practical situations the elastic frequencies are much greater than the sloshing frequencies, and hence the interactions are relatively weak. Hence it is suggested that the rigid-wall model will be entirely adequate for consideration of the meniscus stability in a realistic system.

Tong and Fung (ref. 11.41) have studied the elastic interaction effects in a cylindrical container, and find that the increased system flexibility tends to reduce the natural frequency, as expected.

It is interesting to note that the pertinent elastic parameter is a "Bond number" where the equivalent membrane-force-per-unit length replaces the surface tension (ref. 11.40). Hence, when the membrane Bond number is large compared to the surface tension Bond number, elastic effects will be important.

## Reorientation Time Estimates

A problem related closely to low-g sloshing is that of determining the time required for a meniscus to form its zero-g shape following the removal of a strong body force. Siegert, Petrash, and Otto (refs. 11.42 and 11.43) have made an experimental study of this problem, correlating their results in the form

$$t = K D^{3/2} / \sqrt{\sigma/\rho} \quad (11.105)$$

as suggested by dimensional arguments. With wetting liquids, the constant  $K$  was found to have the following values:

Cylindrical tank	0.15
Spherical tank, 50 percent full	0.16
Annular tanks:	
$r_i/r_0 = \frac{1}{4}$	0.15
* $r_i/r_0 = \frac{1}{2}$	0.10
* $r_i/r_0 = \frac{3}{4}$	0.042

\*With  $D$  replaced by the gap width in equation (11.105).

When the body force field is suddenly removed, the capillary energy is considerably in excess of its equilibrium value. If there were damping, when the interface reached its equilibrium configuration the liquid would possess this extra energy in the form of kinetic energy. Paynter (ref. 11.44) has used this idea to estimate the velocity of the meniscus and hence the time required to reach the equilibrium configuration. His analysis is perhaps oversimplified, but does seem to represent the data of Petrash, Zappa, and Otto (ref. 11.45) rather well.

Unless the energy released is quickly damped, the liquid will tend to oscillate about the zero-g equilibrium shape. A linearized analysis of this oscillation has been given by Fung (ref. 11.46), which seems to check experiments

reasonably well. In this case, it is the first symmetric mode which is predominantly excited, whereas the first antisymmetric mode is normally the fundamental sloshing frequency. For a cylindrical tank, Fung finds that the frequency of the resulting oscillation, as given by the first symmetric mode, is about 2.5 times the fundamental frequency (first antisymmetric mode).

Oscillations on a mercury droplet have been studied in a similar manner by Shuleikin (ref. 11.47).

Petrash and Nelson (ref. 11.48) have studied capillary rise rates in tanks of the form of figure 11.15(a), and find that reasonable prediction of these rates can be made using conventional momentum analyses.

## Oscillation of Drops and Bubbles in Zero g

Lamb (ref. 11.34) shows that drops and bubbles of fixed size are stable configurations in zero g. On the basis of an inviscid analysis, the fundamental frequencies of oscillation and their corresponding periods are found to be—

(1) for the drop in an infinite void

$$\omega = \sqrt{\frac{8\sigma}{\rho r^3}}, \quad T = 2.22\sqrt{\rho r^3/\sigma} \quad (11.106a)$$

(2) for a bubble in an infinite liquid

$$\omega = \sqrt{\frac{8\sigma}{\rho r^3}}, \quad T = 2.22 \sqrt{\rho r^3 / \sigma} \quad (11.106b)$$

Reid (ref. 11.49) studied the effect of viscous damping on the oscillations of a liquid sphere. He showed that—

(1) if  $\frac{\sigma r}{\rho v^2} > 1.7$  damped oscillations occur

(2) if  $\frac{\sigma r}{\rho \nu^2} < 1.7$  the motion is critically damped  
(11.107b)

For water, the radius below which the motions are critically damped is 0.23 millimeter. Hence, slowly decaying oscillations are expected in

drops or bubbles of larger size, as are usually found in zero-g systems.

### Draining

There is at present a considerable need for knowledge of and prediction methods for the draining of liquid from a tank under low g. Saad and Oliver (ref. 11.50) have made a linearized analysis of the sloshing problem during draining for nearly flat interfaces. Their results indicate a slight reduction in the critical Bond number for draining of an "inverted" tank.

A visual study by Nussel, Derdul, and Pettrash (ref. 11.51) indicates a marked dip occurs in the interface as the liquid is forced out by a pressurizing gas. Blowthrough occurs if the draining velocity is too great. It is evident that considerable precaution is necessary in the design of a liquid-venting system for zero-g operation, and that model tests are definitely in order in the present absence of reliable design criteria. We will add to the engineering side of these comments in section 11.5.

### Forced Oscillations

At this writing, very little is known about the peculiarities of forced oscillations at low g. Tong and Fung (ref. 11.41) studied the motion in an elastic tank subjected to periodic axial oscillations using a variational method. They found that surface tension becomes very important at low Bond numbers, and that the stability limits and frequencies can be shifted considerably by surface tension. Eide (ref. 11.52) has examined the motion of a space vehicle brought about by sloshing in a rectangular tank. His analysis shows that thrusting impulses can be properly phased so as to minimize the effects of sloshing on the vehicle attitude, and to control the amplitude of slosh within a maneuvering vehicle.

Although the published work on forced low-g sloshing is limited, the methods of analysis presented throughout this monograph may be readily applied to treat particular cases of interest in design.

## 11.5 FLUID-HANDLING PROBLEMS AT LOW g

### Propellant Positioning and Control at Low g

The positioning of liquids in large rocket tanks is not a straightforward task under conditions met in space vehicle operation. During prelaunch and ascent conditions, liquid location is determined by the direction of the acceleration-induced body forces. If the behavior of liquids in a spacecraft were clearly dominated by surface forces, the matter would be simple. Calculation of the Bond number for a typical large space vehicle using an acceleration of  $10^{-6} g_0$  ( $Bo = 37$  for the Saturn S-IV) indicates that the liquid will be dominated by adversely directed acceleration-induced body forces under practically any conceivable mission (ref. 11.53). With this in mind, means must be found to effect control over the location of the liquid in spite of significant extraneous forces acting on the space vehicle. (For recent summaries of zero-g propellant-handling problems, see refs. 11.54 and 11.55.)

One method of positioning liquids in tanks is to provide strategically located surfaces for the liquid to wet (since all propellants now in use wet most practical tank materials). Under low-g conditions, wetting liquids will tend to wet more solid surfaces. An example of this system is the central standpipe liquid positioner tested by the Lewis Research Center on the Mercury MA-7 spacecraft (ref. 11.56). This device is shown schematically in figure 11.36.

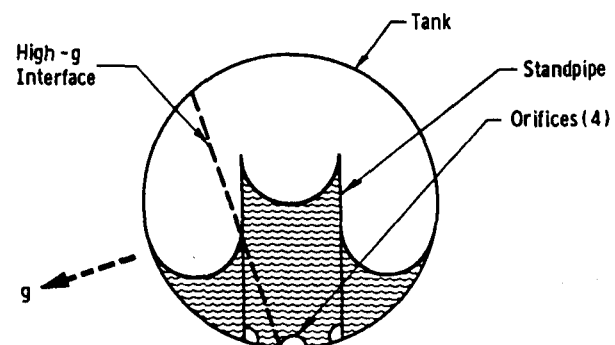


FIGURE 11.36.—Mercury MA-7 liquid positioning experiment.

The device tested consisted essentially of an 8.9-centimeter ID plastic sphere with a 2.79-centimeter-diameter standpipe fixed to one end as shown. The lower edge of the standpipe was penetrated by four 0.79-centimeter-radius semi-circular holes to provide communication between the central standpipe and the tank. Body force direction during ascent is indicated by the arrow  $g$  and the resultant liquid level is shown by the dotted line.

Using the Bond number as a modeling basis, the data from reference 11.56 indicate that the maximum transverse  $g$  loading for which such a system can retain control of the liquid is approximately

$$g_{\max} \approx 67 \frac{\sigma/\rho}{D^2} \quad (11.108a)$$

where  $D$  is the baffle diameter. An estimate of the time required for a baffle of this sort to gain control of the liquid, based on the data of reference 11.56 and equation (11.11b), is <sup>11</sup>

$$t \approx 15 \sqrt{\frac{D^3}{\sigma/\rho}} \quad (11.108b)$$

When body forces are directed parallel to the axis of the tank and toward the end in which the baffle is located, the height of capillary rise can be estimated using the theory developed in the previous sections.

The use of perforated materials, such as screening, in small model tests has been reported (ref. 11.17). This sort of material affords useful weight saving, since the liquid wets it almost as readily as if it were solid sheet metal.

Siegel (ref. 11.19) reports the results of an analysis and experiments which allow time estimates to be made for the filling rate of large capillary tubes under very low-g conditions. His method of analysis is given in sufficient detail to be used as a guide in calculating the rate at which a capillary tube type of locator baffle in a propellant tank will fill when the body forces acting on the liquid are suddenly reduced to very low levels.

<sup>11</sup> For this particular geometry, pressure drop through the semicircular orifices probably plays an important role in determining the time to reach equilibrium.

An important use of the stability ideas is the enhancement of meniscus stability with screens. A typical application is the placement of a plane screen mesh or perforated sheet metal baffle across the tank, as shown in figure 11.37. If the liquid in the tank is subjected to body forces tending to make the liquid run in the  $z$ -direction, the liquid forward of the baffle will do so, provided meniscus  $A$  is unstable. The liquid behind the screen mesh can be stabilized by the capillary surfaces in the screen mesh. If the liquid in the tank is subjected to a transverse body force, the liquid will be kept from running out through the screen by the capillary pressure across the liquid-gas interfaces in the screen mesh. This method is being applied to current liquid rocket systems. The newest model of the Agena upper stage vehicle, for example, has been redesigned incorporating a containment sump system (fig. 11.38). This containment sump is separated from the main propellant tank by a conical screen mesh of approximately 30 holes per centimeter and a porosity of about 50 percent. This assures the

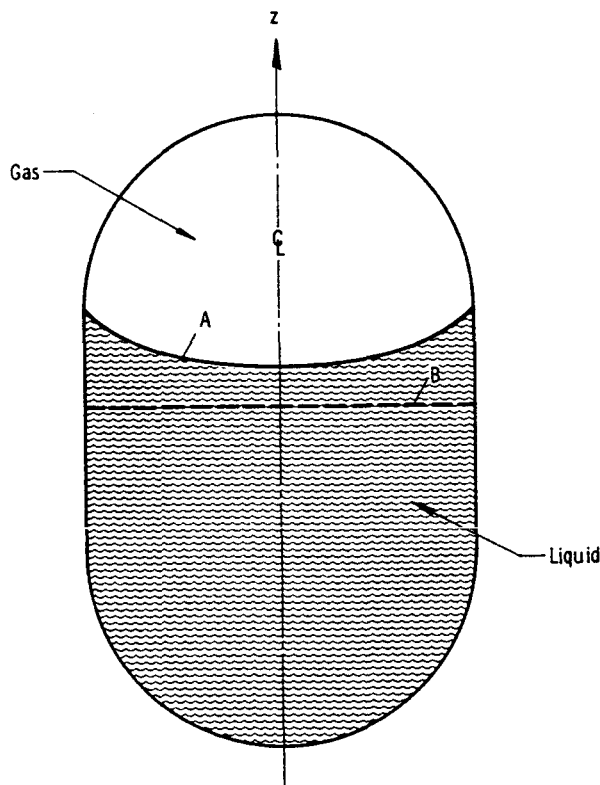


FIGURE 11.37.—Screen baffle for liquid control.

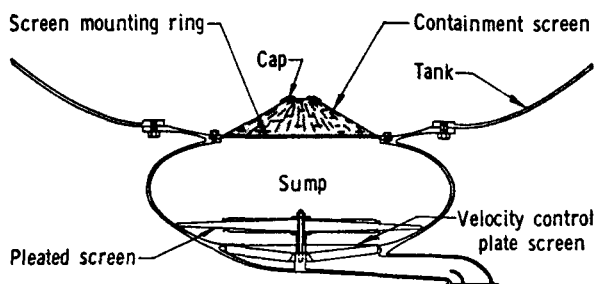


FIGURE 11.38.—Agena containment sump.

presence of liquid at the tank outlet when the engine is restarted, and thus eliminates the need for auxiliary rocket motors. The conical screen separating the sump from the tank will retain sufficient liquid in the sump ready for use by the engine. After restart, the main body of liquid is carried to and through the screen by the thrusting forces, refilling the sump for a subsequent engine operation.

The two propellant-positioning methods just described are best suited for propellants stored in a single phase (the so-called storable propellants). The unavoidable heat transfer to cryogenic tanks may cause local boiling of the propellant within the region of the screen baffle, thus forcing liquid out and destroying the baffle effectiveness.

### Capillary Pumping

The pressure differences across liquid-gas interfaces of different curvature can be used to pump liquids from one place to another. The pressure differences are extremely small, so the expected pumping rates are very small. This use of capillary forces therefore has limited application. Consider the tanks shown in figure 11.39. The pressure difference across the liquid-gas interface in the larger tank will be less than that across the interface in the smaller tank because the curvature of the surface in the larger tank is smaller. Thus,  $P_1 > P_2$ , and the liquid will move toward the smaller tank. It is a straightforward manner to develop a single relationship to express the flow rate in terms of the geometry of the system (assuming laminar flow and no losses due to bends or enlargements and contractions and that the transfer line and pressure communication line have the same diameter). When

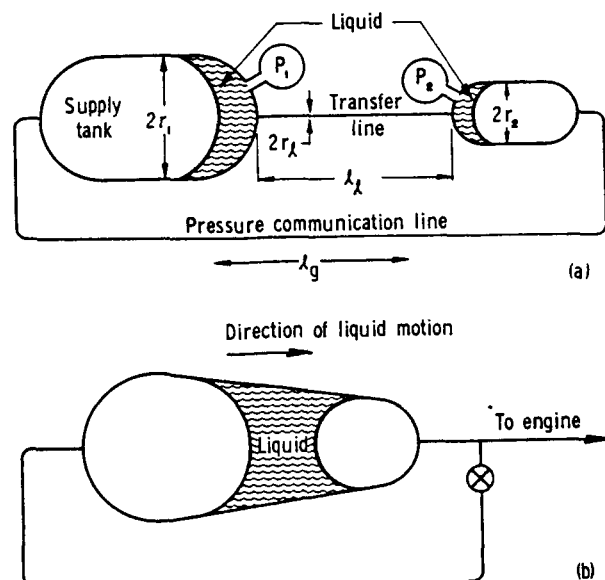


FIGURE 11.39.—Capillary pumping systems.

typical values ( $r_1 = 4.57$  m,  $r_2 = 1.52$  m,  $r_0 = 0.152$  m) of tank, and transfer and communication line radii and lengths are introduced, the expected flow rate is very small, on the order of  $0.5 \times 10^{-3}$  kg/hr for liquid hydrogen. This rate could be increased considerably by baffling the smaller tank, creating more highly curved menisci.

Pettrash and Otto (ref. 11.57) have suggested a similar scheme for orienting liquid within a single tank in a desired location. The tank is tapered as shown in figure 11.39(b). The drain end of the tank is connected temporarily to the far end of the tank by a pressure communicating line. Under zero-g conditions, the pressure equalization in the gas afforded through the line will cause the liquid in the tank to move toward the smaller end of the tank. The process will continue until the liquid has filled the pressure equalization line such that its interface spreads out on the inside of the tank opposite the drain end.

Application of systems of this type will be very limited in larger systems. First, the time required to transfer the large quantities of liquids from one tank to another or from one end of the tank to the other will be too great for operational convenience. Second, the pumping action will occur only so long as no adverse forces act on the tanks. Forces of any

size at all would probably stop the pumping action.

Capillary pumping on a small scale has been proposed as a means for providing small quantities of liquid needed to feed certain devices. For example, McGinnes (ref. 11.58) experimented with a capillary pumping system in which liquid is first evaporated at one temperature; the vapor then flows through some device requiring a very small gas flow rate (such as a gas bearing for a gyro) and is condensed at lower temperature. The liquid is then returned to the point of evaporation by capillary action. In the experiments, capillary pumping pressures on the order of 0.011 kilogram (force) per square centimeter were developed across the wick material, resulting in flow rates on the order of  $0.11 \times 10^{-5}$  kilograms per second.

#### Problems and Methods of Liquid Expulsion at Low g

There is growing interest in problems of liquid expulsion from a container at low g, both for feeding of rocket engines and transfer of propellants from one vehicle to another. What limited information is presently available suggests that draining rates will have to be considerably less than at  $1 g_0$ . Nussel, Derdul, and Petrasch (ref. 11.51) report a visual study of draining at zero g which clearly illuminates the problems. In draining to a center hole, one invariably finds a "dip" in the interface, produced by the lower central pressure resulting from the inward acceleration. Body forces act to smooth this dip out at  $1 g_0$ , but under zero g only the relatively weak surface tension forces remain to prevent the liquid from being removed in a central core. (See, for example, the analysis of Bhuta and Koval (ref. 11.59).) A schematic representation of draining at the identical rate at low and high g is shown in figure 11.40. It is evident that a considerable amount of liquid may be retained at low g if adequate precautions are not taken. If the draining rate is sufficiently slow, the meniscus will retain essentially its initial shape and the maximum amount of liquid will be withdrawn. An estimate for this maximum draining rate is quite vital.

It is, of course, entirely possible to formulate a mathematical model of the problem; an

inviscid irrotational treatment is reasonable, but the large changes in surface shape mean that the nonlinear effects must be considered; as yet, there has been no really satisfactory computation method for this problem. (See the recent calculation scheme of Concus, Crane, and Perko (ref. 11.60), however.)

We can, however, make some estimates as to the maximum draining rate for which the meniscus will retain its initial shape, using the reorientation-time correlation as a basis. For the draining rate to be sufficiently slow that the meniscus has time to adjust, the reorientation period must be shorter than the time required for the meniscus to travel its length. Using equation (11.105) for the response time and setting the time for the meniscus to travel its depth as

$$\frac{D/2}{[V(d/D)^2]}$$

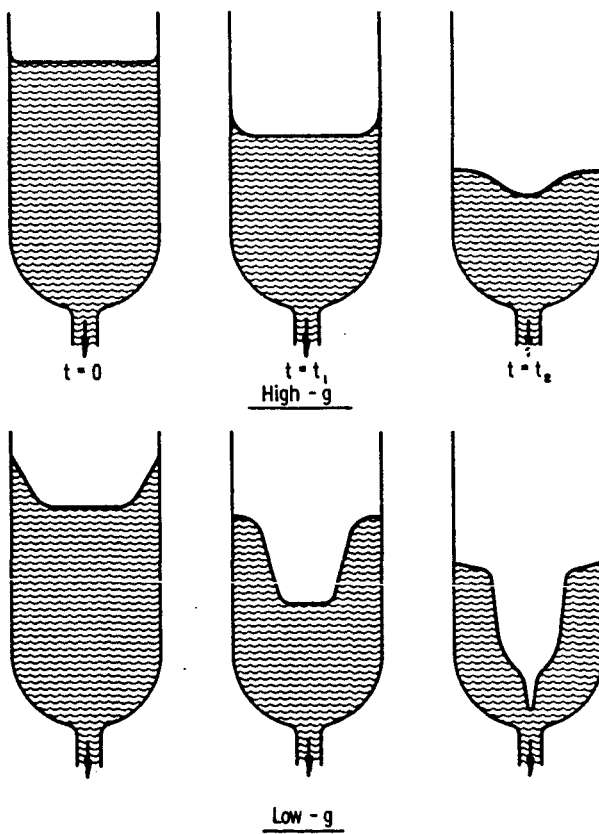


FIGURE 11.40.—Interface configuration during draining at low and high g.

where  $V$  is the velocity in the drain,  $D$  is the tank diameter, and  $d$  the drain diameter, we obtain the maximum drain-rate criteria

$$We_{\max} \approx \left( \frac{DV^2\rho}{\sigma} \right)_{\max} \approx 10 \left( \frac{D}{d} \right)^4 \quad (11.109)$$

Thus, if  $We < We_{\max}$ , the meniscus should retain its general shape during draining. Nussel et al. (ref. 11.51) experimented with a system having  $d/D = 0.1$  (for which  $We_{\max} \approx 10^6$ ), at Weber numbers of approximately  $1.2 \times 10^4$  and  $2.7 \times 10^5$ . In the first case, the meniscus did indeed retain its shape and in the second it did not. Hence, the estimate of equation (11.109) has at least some experimental support.

When the tank Weber number exceeds the critical value estimated from equation (11.109), the diameter of the meniscus can be estimated under the assumption that the Weber number based on meniscus diameter is equal to the critical value. This is equivalent to assuming that the meniscus diameter gets as large as possible in the period of time which it has to adjust to changes in its position. Hence, we estimate

$$D_m V^2 \rho / \sigma \approx 10 \left( \frac{D}{d} \right)^4 \quad (11.110a)$$

Equation (11.110a) can be used to estimate  $D_m/D$ . Then, the amount of retained liquid is estimated as

$$\frac{\pi}{4} (D^2 - D_m^2) H + \frac{1}{24} \pi D_m^3$$

Here  $H$  is the initial mean depth of the liquid. This volume is based on leaving an annulus of liquid on the wall, and the volume beneath the spherical meniscus of diameter,  $D_m$ , when its nose just reaches the drain. The fraction of liquid retained is therefore estimated as

$$f = \left[ 1 - \left( \frac{D_m}{D} \right)^2 \right] + \frac{1}{8} \frac{D_m}{H} \quad (11.110b)$$

When we apply equation (11.110b) to the experiments of reference 11.51, with  $H/D = 1.5$ ,  $We = 2.7 \times 10^5$ ,  $d/D = 0.10$ , we find  $f \approx 0.88$ . For the corresponding experiment, Nussel et al. measured  $f \approx 0.76$ .

At very low discharge rates, where the meniscus spans the tank, the volume of liquid beneath the meniscus when it reaches the drain will inevitably be trapped. In the simple model presented above, this fraction is  $\frac{1}{8} D/H$ .

More accurate calculations can be made using the curves of figure 11.17.

Further experiments using baffles at the outlet and at the gas inlet indicated that such devices could be used to allow substantial increase in the drain-flow rate of liquid from the tank with little increase in the trapped fraction. The use of a plane baffle over the tank drain at high-flow rates resulted in some reduction of the trapped quantity at fixed-flow rate, probably because the central vortex is eliminated. Use of a baffle at the gas inlet greatly reduced the trapped residuals at a given flow.

It is evident from this work that draining of tanks in low-g conditions will likely result in high trapped residuals, and therefore some mechanical means of flattening the meniscus inside the tank is highly desirable.

When the Bond number is sufficiently great, an entirely different type of retention mechanism will become important. Suppose a pump is sucking liquid from a tank, as shown in figure 11.41. The pumping demand must be less than the critical flow rate for the drain, which

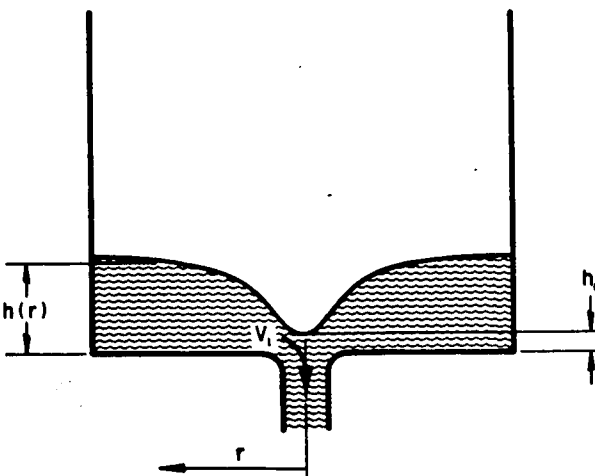


FIGURE 11.41.—Simple model for estimate of drain choking.

will be determined approximately by the condition at which the flow over the lip of the drain becomes critical (Froude number unity). The maximum flow rate is therefore estimated as

$$w_{\max} \approx \rho h_0 \pi d \sqrt{gh_0} \leq w_{\text{pump}} \quad (11.111a)$$

When the liquid depth at the lip ( $h_0$ ) has fallen below the level implied by equation (11.111a), the required flow cannot be delivered, and to all intents and purposes the draining is finished. At reduced  $g$ , the critical depth,  $h_0$ , can be surprisingly large, and hence the choking problem should be thoughtfully considered.

Assuming that the rate at which the liquid level is falling is slow compared to the liquid velocity over the drain, a quasi-steady estimate of  $h$  may be made, using one-dimensional theory. This gives

$$\sqrt{2g(h-h_0)} = V_1 = \sqrt{gh_0} \quad (11.111b)$$

The volume of trapped liquid can then be estimated as

$$\begin{aligned} \frac{\pi}{4} (D^2 - d^2) h &= \frac{\pi}{4} (D^2 - d^2) \frac{3}{2} h_0 \\ &= \frac{\pi}{4} (D^2 - d^2) \frac{3}{2} \left( \frac{w_{\text{pump}}}{\pi d \rho \sqrt{g}} \right)^{2/3} \end{aligned} \quad (11.111c)$$

The Bond number involved in the draining of a large booster tank under a low- $g$  condition may well be considerably greater than unity, in which case model experiments at 1  $g$  on smaller tanks can give insight into the draining problems. An experimental study of draining of cylindrical tanks with flat bottoms in the Bond number range 100–1000 has been reported by Gluck, Gille, Simkin, and Zukoski (ref. 11.61). This range may be considered high-Bond number, and the surface tension effects may be expected to be minor. This was indeed the case, for these authors found that the point at which gas ingestion occurred depended only on the Froude number in the drain. The height,  $h$ , from the drain at which ingestion occurred was correlated quite well by

$$\frac{h}{D} = 0.43 \tanh \left[ 1.3 \left( \frac{V^2}{gd} \right)^{0.29} \right] \quad \begin{aligned} 0.05 < Fr < 100 \\ 3 < D/d < 20 \end{aligned} \quad (11.111d)$$

Note that at very high rates of draining ingestion occurred when the height at the wall was  $0.43D$ .

Another aspect of the flow of liquids from propellant tanks which will have to be carefully watched by the propulsion system designer is the formation of vortex flow. Since axial body forces do not enter the equations for angular momentum, the formation of vortex flow can be expected to develop at the same rate under low- $g$  conditions as under high- $g$  conditions. When the vortex does occur, though, the result will be very much more pronounced under low- $g$  conditions, with the vortex funnel penetrating much thicker layers of liquid at low  $g$ .

In the event more positive control over the liquid during expulsion is desired, one must use some sort of flexible containment device, such as a bladder. Such techniques are discussed at length elsewhere (ref. 11.62), and will not be treated here.

### Problems and Methods of Vapor Expulsion at Low $g$

The operation of a rocket propulsion system often requires that gas be allowed to escape from a tank without expelling liquid at the same time. For instance, in storable propellant tanks used with pressure-fed engines, it may be necessary to effect a pressure reduction in one of the tanks prior to restarting the engine. The use of cryogenic propellants is accompanied by the urgent need periodically to relieve pressure buildup due to heating. The venting of pressurization gas and propellant vapors presents no difficulty at all under high- $g$  conditions when the location of the liquid in the tanks is well defined. Under low- $g$  operating conditions, however, the liquids may be located in a variety of places in the tank, depending on the level of and the direction of body forces acting on the liquids and, in part, on the flight history. Some effort is therefore necessary to assure that when the tank vents are opened, only gas will be expelled, and not precious liquid propellants.

If the flight history is well known, it may be possible to use the passive methods described earlier to hold the liquid away from the vent. When this is not possible, some active means for removing the liquid from the vent must be

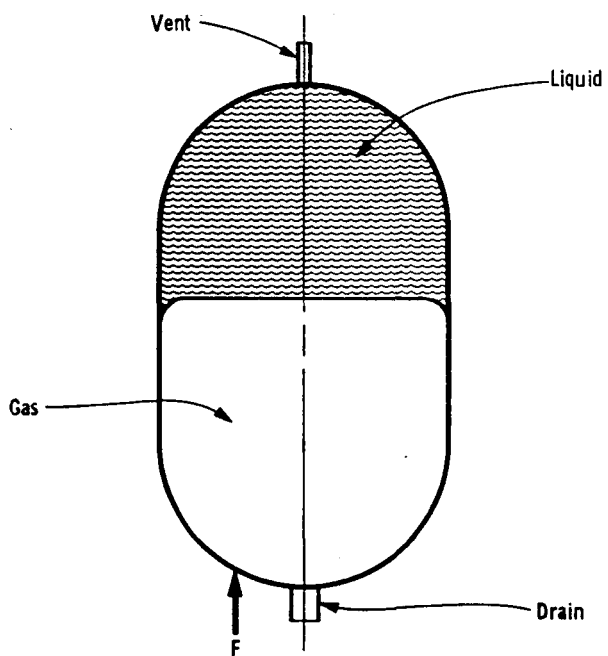


FIGURE 11.42.—Vent clearing by a temporary thrust.

employed. Consider the propellant tank of figure 11.42. The vent at the top of the tank is temporarily covered by liquid which flowed there under the action of extraneous force encountered by the vehicle during a prior phase of the mission. Application of a thrust in the direction of  $F$  will cause the liquid in the tank to move toward the bottom end of the tank, clearing the vent. For proper design, we need to know both the minimum force required to bring this change about and the time required for the liquid transfer.

The acceleration produced by  $F$  must be sufficient to destabilize the meniscus, and the required magnitudes can be estimated, using the analyses and results of section 11.3. Good design would normally use several times the theoretical minimum acceleration, which may be a small thrust, especially for a very large system.

Care must be taken not to use too much acceleration, however, lest the liquid cause damage in impacting against the bottom of the tank. It is quite important, therefore, to have a rather good estimate of the rundown time and the velocity of the liquid mass on impact. Unfortunately, methods for making these

calculations really accurately are not presently available, and the designer must rely on educated guesses and model experiments.

We can, however, estimate the minimum time and maximum impact velocity simply by assuming the liquid falls freely. This gives

$$t_{\min} = \sqrt{2L/g} \quad (11.112a)$$

$$V_{\max} = \sqrt{2gL} \quad (11.112b)$$

With drag, the actual impact velocity may be considerably less. In studies of the motion of bubbles in tubes, which closely resembles this phenomenon, velocities of the order of one-third that given by equation (11.112b) are found (ref. 11.11). Thus, a conservative design procedure would be to use a reorientation acceleration something in excess of the critical value determined from the stability analysis, and design the structure to take the impact velocity of equation (11.112b). Then, allow 5 to 10 times the reorientation time from equation (11.112a) for the liquid to clear the vent.

The flow behavior during reorientation has been studied experimentally by Hollister and Satterlee (ref. 11.63). As the acceleration is applied, liquid begins to flow down the wall in a relatively thin sheet of liquid. If the Bond number,  $\rho g r_0^2 / \sigma$ , is of the order 10 or less, a large central bubble forms along the axis of the cylinder; but if the Bond number is of order 150 or greater, the formation of the wall sheet is accompanied by the delayed formation of a central plateau of liquid which grows down the axis of the cylinder, narrowing as it falls. The time trajectory of the wall sheets in these cases is given approximately by (for  $d/r_0 < 1.2$ )

$$d/r_0 = 0.69\tau + 0.41\tau^2 \quad 3.5 < Bo < 10 \quad (11.113a)$$

$$d/r_0 = 0.65\tau^2 \quad Bo \approx 150 \quad (11.113b)$$

where

$$\tau = t\sqrt{g/(2r_0)} \quad (11.113c)$$

and  $d$  is the fall distance.

In the lower  $Bo$  case, the large central bubble slows down as it approaches the top of the

tank; consequently, a slight projection of the vent pipe into the tank will help insure that no liquid is removed.

Hollister and Satterlee (ref. 11.63) have made a simple shallow-water analysis, which seems to predict the velocity of the bubble in the region near the top of a hemispherical tank rather well. They suggest use of the velocity of rise of bubbles in tubes, which is approximately (ref. 11.11) <sup>12</sup>

$$V = 0.46\sqrt{gr_0} \quad (11.113d)$$

until the bubble nose has risen to  $0.23r_0$  of the top of the tank. At this point they patch to the shallow-water analysis, which indicated that

$$V = 2 \frac{h}{r_0} \sqrt{gr_0} \quad (11.113e)$$

where  $h$  is the distance of the bubble nose from the end of the tank. This procedure provides a reasonable estimate for the time required for the bubble to reach the projected vent pipe.

An interesting approach to noncondensable gas bubbles is being explored by Funk and Welch (ref. 11.65). They consider a system which suddenly passes from a high-g state to zero g, and look for the statistical distribution of bubble sizes that exists when the bubbles are first formed. While this work is still in a preliminary stage, it does indicate that certain aspects of statistical mechanics are applicable to bubble distributions; in fact, a Maxwellian distribution of bubble sizes seems to be found.

The use of nonwetting screens for passive separation of small amounts of liquid from a vapor stream has been successfully employed by Smith, Cima, and Li (ref. 11.66). Using water-air mixtures, containing of the order of 0.8 percent by mass of water, separation efficiencies of the order of 95 percent were achieved in small-scale bench tests.

### Dielectrophoresis

One of the methods presently being considered as a means of locating liquid propellants in

<sup>12</sup> For  $\rho gr_0^2/\sigma > 5$ . The rise velocity is considerably slower at lower Bond numbers, and is zero at the critical Bond number. See, for instance, ref. 11.64.

rocket tanks involves the use of electrically induced body forces in dielectric materials. The term which has been applied to this is "dielectrophoresis." A theoretical explanation for this can be obtained using electric field theory, that is, Landau and Lifschitz (ref. 11.67). This theory has been specialized to the study of the behavior of fluid surfaces in electric and magnetic fields by Melcher (ref. 11.68). The theory as applied to a dielectric liquid with uniform dielectric constant and with no free charge indicates that a surface <sup>13</sup> force is exerted directed away from the liquid at the liquid-gas interface (where a change in the dielectric constant occurs). Consider, for example, the force on a cylindrical body of liquid partially filling the annular space between a pair of concentric cylindrical electrodes. If the liquid is concentric with the electrodes, the theory tells us that there is no net force exerted on the liquid. If, however, the liquid mass is perturbed to a nonconcentric position, the surface force exerted on the liquid farthest from the central electrode will decrease and that on the liquid surface closer in will increase. In effect, there is a net force acting to reduce the displacement of the liquid. Hence, the liquid will be stabilized around the central electrode where the electric field intensity is greatest for this electrode geometry.

The theory explaining dielectrophoresis indicates that the surface force acting on the liquid is proportional to  $E^2$ ,  $E$  being the electric field intensity. This means that the polarity of the electrode system does not affect the direction in which the net restoring force acts. In fact, alternating voltages can be used. The surface force will be periodic but will always act in the same direction.

A difficulty arises in practice with the use of direct currents. No liquid is a perfect dielectric. A finite current will be conducted in even the most nonconductive material. Such a current eventually results in the accumulation of an electric charge of one polarity on the free surface of the liquid. This charge

<sup>13</sup> Some reports have erroneously held that the electric force is a body force.

distributed on the free surface is, of course, mutually repulsive. Its effect is just the opposite of that of the surface tension of the liquid. Where surface tension causes liquid masses to form into shapes with minimum capillary area, the accumulated charge will cause the liquid mass to be unstable and to break up with the attendant formation of more surface area rather than less. If, instead, alternating currents are used, the accumulation of a net charge on the free surface of the liquid can be kept to low-enough levels that the instability just described is eliminated. This effect has been described recently by J. M. Reynolds (ref. 11.69).

Depending on the electrode geometry considered, there are a number of regimes of liquid behavior which may be described. Consider again, for example, the concentric cylindrical geometry used previously:

(1) When no potential is applied between the electrodes, the liquid will tend to break up into a series of discrete spherical drops much like a string of beads. This instability is caused by the action of surface tension and can be explained by the tendency toward shapes with minimum capillary area. (See sec. 11.3.)

(2) The application of a constant potential between the electrodes will result first in the stabilization of the liquid into a cylindrical mass centered around the inner electrode. However, when the surface charge has built up sufficiently, the liquid cylinder will again become unstable and will break up.

(3) Application of an alternating potential between the electrodes will result in the formation of a stable cylinder of liquid about the inner electrode.

(4) If the frequency of the current is too high, higher order instabilities are observed. Further, as a practical matter, the reactive current, which flows because of the fact that the electrode system acts as a huge capacitor, becomes excessive.

(5) High voltages are required in application to rocket propellant tanks to produce reasonable body forces. However, potential gradients must be kept below breakdown quantities. Otherwise arcing will occur which could be

disastrous, particularly in oxidizer tanks. This requires that voltages be limited or that staging of the electrodes be employed.

This thumbnail sketch of the phenomenon of dielectrophoresis indicates how it works. A number of applications have been considered for this technique of liquid positioning. First, liquids can be held in the drain end of a tank ready for withdrawal to a using system such as a rocket engine. This, of course, requires the proper choice of electrode geometry. Second, the tank vent can be located in the vapor space away from the liquid. This also requires proper choice of electrode geometry. Third, bubbles formed as a result of nucleate boiling, as in cryogenic rocket tanks, can be forced out of the liquid mass and combined with the gases in the ullage space. A fourth application envisions reducing possible trapped residual propellant quantities occurring with the rapid draining of a propellant tank under reduced gravitational conditions.

Cryogenics appear to be the best application for dielectrophoresis because they generally exhibit high dielectric constant properties and consequently high specific electrical resistivity. This results in modest and quite feasible power requirements. Storable liquids ordinarily have much lower dielectric constants and specific resistivity properties. The high potential required, coupled with relatively high current flows, render the use of dielectrophoresis infeasible for room temperature liquids.

Application of a force of a different type than the normally experienced unidirectional gravitational body force actually removes the low-g character of the behavior of tanked liquids. A new set of liquid equilibrium shapes will occur in response to the shapes of this new force, and the behavior of the liquid may no longer be dominated by capillary forces.

#### 11.6 HEAT TRANSFER TO CONTAINED LIQUIDS AT LOW $g$

##### Introduction

One of the major reasons for studying the mechanics of liquids at low  $g$  is to determine the nature of convection heat transfer under

these conditions. Knowledge of important heat transfer modes is important in controlling liquid temperatures and resultant vapor pressures. It may be expected that natural convection, the prime mechanism for heat transfer to or from a propellant, will be much reduced at low g. Consequently, diffusion of both energy and mass will be more important than under normal conditions. One must be particularly careful in analysis to assess the importance of each energy transport mechanism before discarding any. In this section, we shall describe some of the work in the study of energy transport under low-g conditions. We shall consider, in order, storable liquids, cryogenic liquids, and low-g boiling heat transfer.

#### Temperature Control in Storable Propellant Tanks

There are several reasons for temperature control for storable propellants. For example, in pump-fed engines, the success of the combustion control depends in large measure on precise flow-rate control, which in turn means that the liquid viscosity must be held near some preset value.

Temperatures and temperature variations depend on many complicated factors, including system geometry and flight program. When the tanks are embedded within the vehicle, little difficulty in maintaining uniform and constant temperatures is expected; but when the tanks are part of the external vehicle structure, large temperature differences can be expected, and propellant temperature within any one tank can vary considerably. The energy input is a strong function of the flight program. For example, a geocentrically oriented satellite in a twilight orbit intercepts about three times the direct solar energy as one in a noon orbit. The seriousness of the possible temperature nonuniformity is clear if one calculates the temperature variation around a thin-walled cylinder exposed to solar radiation on one side. With typical emissivity values and wall thickness, temperature differences of the order of 200° F are found (ref. 11.70). Acting to smooth out these large temperature variations are diffusion and convection, which we shall now consider.

Temperature nonuniformity in the liquid results in differences in vapor pressure. These differences in vapor concentration set up a diffusive flow of the propellant vapor in the gas phase from regions of higher concentration to regions of lower concentration. Propellant will be evaporated from the free surface in regions of higher temperature and condensed on cooler portions of the surface. This mechanism is quite important, particularly at zero g. At sufficiently high g these diffusive processes will be enhanced by convective motions, particularly if the hot portion of the system is "below" the liquid in the (effective) g field. The dimensionless parameter, which is important in determining the onset and strength of convective processes, is the Rayleigh number

$$Ra = \beta g \rho^2 L^3 \Delta t C_p / (\mu k)$$

where  $\beta$  is the coefficient of thermal expansion (at constant pressure) and  $L$  is a characteristic length in the direction of the temperature gradient. If the fluid is heated from above, it is stable and convection is suppressed. However, if it is heated from below, it becomes unstable at Rayleigh numbers of the order of 1000–2000 (ref. 11.71). Under typical orbital conditions, the Rayleigh number for the gas phase will be rather small, and hence only diffusive mechanisms are expected to operate. Within the liquid, however, large Rayleigh numbers are expected, especially in big booster tanks, and, if the g field is properly oriented with respect to the temperature field, an efficient natural convection process will evolve. Weinbaum (ref. 11.72) has studied the natural convection within a horizontal cylindrical tube, completely filled with liquid, and subjected to a circumferential wall temperature distribution. His generalized treatment is particularly useful for purposes of estimating the smoothing effects of conduction and laminar natural convection on the temperature profile. Convection is suppressed when the Rayleigh number, based on the cylinder radius and the maximum wall temperature variation, is about 1200.

In the gas phase, where the diffusive mechanisms are controlling, theoretical formulation

is not difficult, though solution is another story. The basic equation governing diffusion of two ideal-gas species may be written as (in one-dimension)<sup>14</sup>

$$J_{M_1} = -D_{11} \frac{dc_1}{dx} - D_{12} \frac{dc_2}{dx} - D_{1t} \frac{dt}{dx} \quad (11.114a)$$

$$J_{M_2} = -D_{21} \frac{dc_1}{dx} - D_{22} \frac{dc_2}{dx} - D_{2t} \frac{dt}{dx} \quad (11.114b)$$

$$J_E = -k_{11} \frac{dc_1}{dx} - k_{12} \frac{dc_2}{dx} - k \frac{dt}{dx} \quad (11.114c)$$

Here  $c_i$  is the local modal concentration of species  $i$ ,  $J_{M_i}$  is the local mass flux of species  $i$ , which is produced by gradients in its concentration, gradients in the concentration of other species, and temperature gradients, and  $J_E$  is the energy flux. Note that there can be a gradient in the inert gas concentration of a particular species, even though it is not flowing, produced by gradients in temperature or in the concentration of the other species.

These equations, plus the conservation equations for energy and mass, provide the basis for analysis of simultaneous diffusion of mass and energy. Wang (ref. 11.73) has solved a rather simplified model problem based on approximations to the equations. Even with these approximations, his results are indicative of the order of magnitude of the effects. In particular, he finds that in a typical situation, where UDMH vapor diffuses through helium along a 1.5-meter path, the contribution of the first and second and third terms of equation (11.114c) is significantly larger than the "heat" conduction term ( $-k dt/dx$ ). The relative importance of these energy transport mechanisms is strongly influenced by the ratio of the average partial pressure of the diffusing vapor to the total pressure. In the case studied, the ratio of the diffusive energy transfer to the conduction energy transport is 0.233 and 0.037 for pressure ratios of 0.40 and 0.175, respectively. Thus, at high partial pressure fractions, the

<sup>14</sup> Here  $D_{ij}$  denotes the coefficient in the linear diffusion equation for species  $i$  due to a gradient in concentration of species  $j$ . This is somewhat at odds with older literature.

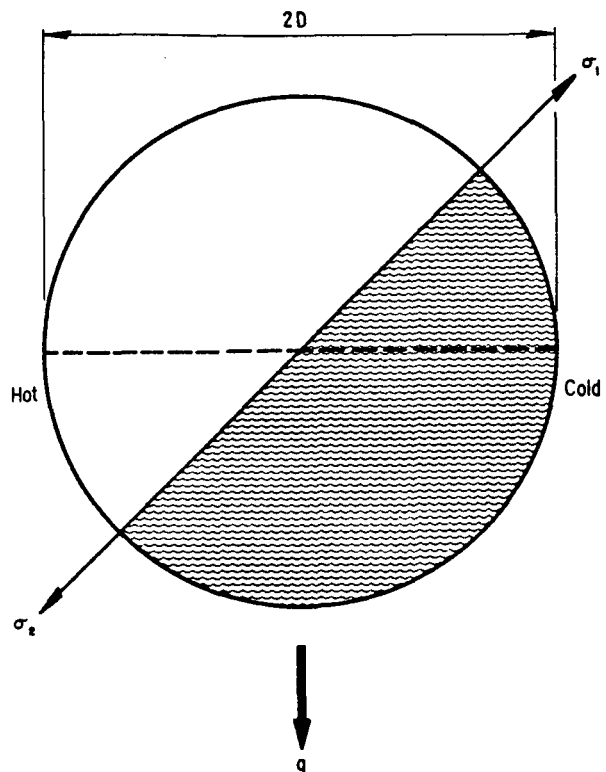


FIGURE 11.43.—Estimating temperature effects at low g.

diffusive transport may well be the controlling process. This points up the importance of considering coupled diffusive mass and energy transfer, and particularly the importance of considering them properly.

Temperature differences within a tank result in differences in temperature of the free surface of the liquid. The surface tension decreases with increasing temperature, and the resulting gradient in surface tension acts to pull molecules in the interface toward regions of colder temperature. Surface-tension-driven motions are probably very important in low-g environments; they are beautifully illustrated on a laboratory scale in reference 11.12. As yet, these effects have not been examined in sufficient detail, but we can make a rather simple estimate of the conditions under which they are important. Using dimensional arguments, we find that the pertinent dimensionless parameter relevant to the thermally induced distortion of the meniscus of figure 11.43 is

$$\frac{\Delta t \frac{d\sigma}{dT}}{\rho g r^3}$$

So, if

$$\left| \frac{\Delta t \left( \frac{d\sigma}{dT} \right)}{\rho g r^2} \right| << 1 \quad \text{The effects are small} \quad (11.115a)$$

$$\left| \frac{\Delta t \left( \frac{d\sigma}{dT} \right)}{\rho g r^2} \right| >> 1 \quad \text{The effects are large} \quad (11.115b)$$

Note that at very low  $g$ , the effects are most pronounced. At zero  $g$ , the interface would swing to the cold side of the tank.

Surface tension gradients can also give rise to cellular convection patterns. Consider, for example, the two-dimensional channel of figure 11.44. The surface tension gradient would set up interface motion, which in turn would augment the heat transfer within the liquid. This interesting kind of "natural" convection recently was reviewed at length by Scriven and Sternling (ref. 11.74).

#### Heat Transfer in Cryogenic Tanks

The analysis of heat transfer between a cryogenic tank and its surroundings and within the tank itself is quite different than in the case of the storables propellant tank. While the mean temperature of the surface surrounding the storables propellant tank can be controlled within the temperature range in which the propellant must be used, tank outer surface temperatures are at least 100° F above the use

temperature of even the warmest cryogen. This means that if pressure rise rates within the tanks are to be held to acceptable limits, the tank must be well insulated. It also means that heat transfer is always to the fluid, unlike the usual circumstance with storables propellants. Because of the insulation, the heat transfer to the liquid is quite uniform over the wetted area and relatively constant throughout the flight.

It is important to know the details of the mechanisms of energy transport within a cryogenic tank. On the basis of a first examination, it might be considered that a certain amount of heat will flow into the liquid through the insulation and that this energy rate will result in liquid boiloff, thus causing the pressure in the tank to rise at a certain rate which is easily calculated. This is not the case, however; it is found that the pressure rise is considerably less than would be predicted by an analysis which assumed equilibrium between the liquid and vapor phases. Consequently, it is necessary to know something of the details of the energy transport mechanisms within the tank so that an accurate estimate of the temperature distribution inside the tank can be made.

Levy et al. (ref. 11.75) have used an integral-boundary layer analysis to study the stratification problem. Since their methodology would seem to be generally applicable, it will be outlined here. Consider liquid in the cylindrical tank of figure 11.45. For simplicity, let us assume that the free surface is plane and that the only heating occurs on the cylindrical walls. Energy entering the tank wall forms a buoyant boundary layer adjacent to the wall, which rises toward the free surface. We assume that all the energy entrained in the boundary layer enters and remains in a stratified region at the top, where the liquid temperature is greater than that in the central core.

The general method of analysis is to write an expression for the rate of mass transfer to the stratified region. This will be of the form

$$w = f(H - \Delta) \quad (11.118)$$

where  $H - \Delta$  is the working height of the natural convection boundary layer. This expression

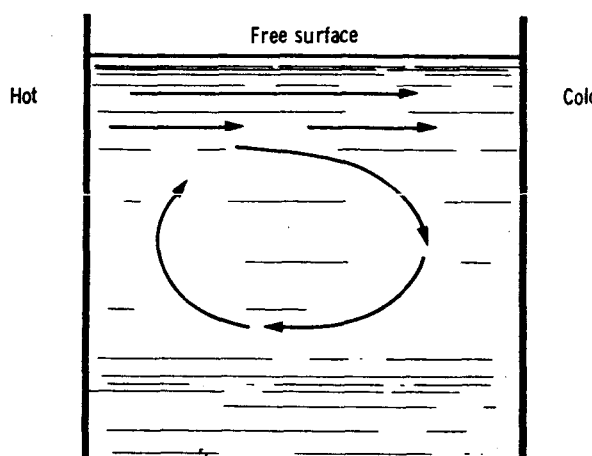


FIGURE 11.44.—Surface-tension-driven convection in zero g.

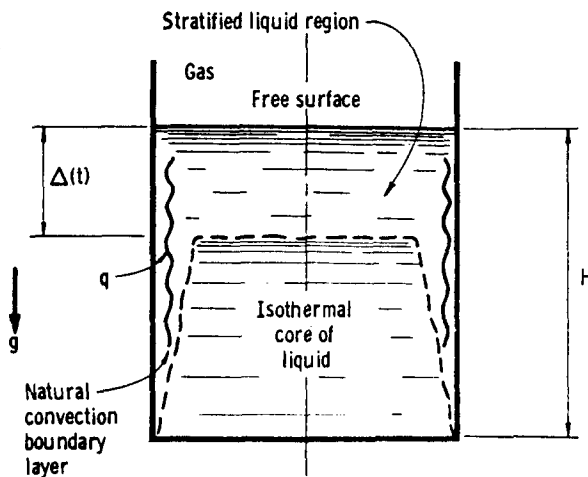


FIGURE 11.45.—Liquid stratification.

would be determined from established theory and correlations for natural convection from vertical surfaces with specified heat flux, and it allows one to determine the rate of growth of the stratified layer. An energy balance, plus some assumption about the internal temperature distribution in the stratified layer, then suffices to fix the interface temperature.

The idealizations employed in writing the energy balance on the stratified layer will depend on the composition of the ullage gas. If inert gas pressurization is used, the liquid will be strongly subcooled below the total pressure, and the only place where evaporation will occur is at the upper surface. One could assume that the ullage gas is saturated with propellant vapor but, in many cases, satisfactory results may be obtained by neglecting any energy or mass transfer from the interface. Bailey et al. (ref. 11.76) did this, and further assumed that the temperature was uniform throughout the stratified region. Levy et al. (ref. 11.75) also neglected ullage interaction, but assumed that the temperature profile in the stratified region maintained a similar shape during the heating period. Using established results for laminar natural convection boundary layers, they predicted that the thickness of the stratified region would be<sup>15</sup>

<sup>15</sup> Here  $\beta$  is the coefficient of thermal expansion of the liquid phase,  $q$  the heat flux, and  $\mu$ ,  $c_p$ ,  $\nu$ , and  $k$  the fluid properties of the liquid phase.

$$\frac{\Delta(t)}{H} = 1 - \left[ 1 - 0.62 \left( \frac{H}{r_0} \right) \left( \frac{\nu t}{H^2} \right) \frac{(Gr^*)^{1/5}}{Pr^{0.388}} \right]^{+5} \quad 1 < Pr < 30 \quad \Delta(t) \leq H \quad (11.117a)$$

where

$$Gr^* = g\beta r_0^4 q / (k\nu^2) \quad (11.117b)$$

$$Pr = \mu c_p / k \quad (11.117c)$$

A corresponding analysis for turbulent convection boundary layers gave

$$\frac{\Delta(t)}{H} = 1 - \left[ 1 + 0.092 \frac{H}{r_0} \left( \frac{\nu t}{H^2} \right) \frac{1}{Pr^{2/3}} \times \left( \frac{Gr^*}{1 + 0.443 Pr^{2/3}} \right)^{2/7} \right]^{-7} \quad (11.118)$$

The turbulent relation is recommended for  $Gr^* Pr > 10^{11}$ , which will normally be the case in large booster tanks.

Levy et al. (ref. 11.75) also report some experiments, from which some idea for the assumed temperature profile can be obtained.

Clark and Barakat (ref. 11.77) have examined the transient heating of a liquid partly filling a two-dimensional channel in an exact numerical solution of a model problem. They assumed that the liquid motion is laminar, its density is a linear function of temperature, and it is at rest with a uniform temperature at time zero. The mathematical treatment of this problem is as a boundary-initial value problem. The non-steady-state energy, continuity, and momentum equations, written in terms of the stream function, were reduced to difference equations and solved numerically. The interface was assumed to be a surface of zero shear. Upper and lower surfaces of the tank were considered to be: (1) insulated, (2) subject to a uniform heat flux, or (3) kept at a constant temperature. Tank side walls were: (1) subject to constant heat flux, or (2) kept at constant temperature. Results of their calculations for liquid nitrogen standing approximately 30 centimeters deep in a 15-centimeter-wide tank show that temperature is uniform across the tanks except near the tank wall. Irregular wavelike streamline motion near the intersection of the free surface and the

tank wall was also predicted, and this has been noted in some experimental flow visualization work.

Although in principle the method used by Clark and Barakat is fundamentally the soundest for laminar flow, it cannot be used for turbulent flow, which seems to be of primary interest in large tanks. Moreover, even the simple model problems require a large amount of computer time. Nevertheless, the "exact" solutions do provide a valuable basis for comparison with the approximate methods.

It appears that the most interesting heat transfer problems in propellant tanks may well involve transient natural convection. A recent study by Schwartz and Adelberg (ref. 11.78) showed that a very long time is required to obtain a steady-state natural convection boundary layer in a typical large tank. The Schwartz-Adelberg survey is recommended as a starting point for any designer faced with making a propellant heat transfer estimate.

### **Boiling Under Low-g Conditions**

There are a number of important boiling heat-transfer problems encountered in low-g environments. A direct problem related to propellants is that boiling may cause the liquid to be displaced from known or preferred locations by the attendant phase change. Fortunately, burnout is not a problem in propellant tanks, since the heat transfer rates encountered are very modest.

A number of workers have investigated the various forces acting on bubbles as they form and grow in a nucleate pool boiling condition. Adelberg (ref. 11.79) has presented one of the more recent and comprehensive studies of this sort. He made an order-of-magnitude estimate of the various forces based on data of Ellion (ref. 11.80) for experiments using a water-aerosol solution. Not surprisingly, this indicates that inertial and surface forces control the early stages of bubble growth. Buoyant and drag forces are shown to be approximately two orders smaller.

Adelberg also estimated the forces as a function of  $\Delta t = t_{\text{wall}} - t_{\text{sat}}$ . He found that at high  $\Delta t$ 's the bubbles are removed from nucleation sites by dynamic effects, while at lower  $\Delta t$ 's buoyant forces take this role. This suggests

that at low  $\Delta t$ 's the g level will affect the character of nucleate pool boiling, while at higher  $\Delta t$ 's it should not.

Keshock and Siegel (ref. 11.81) present a similar order-of-magnitude analysis, based on their own data. Their experiments were carried out at  $g_0$  and at reduced g conditions. The liquids used on these experiments were distilled water and a 60-percent water-sucrose solution. The authors indicate that when bubble growth rate is large, nucleate boiling is essentially independent of g level. In this case, bubble departure was governed by inertial and surface tension forces. For more slowly growing bubbles, departure was governed by buoyant forces and surface tension forces. Viscous forces were indicated to be of little importance.

Merte and Clark (ref. 11.82), Sherley (ref. 11.83), Steinle (ref. 11.84), and Usiskin and Siegel (ref. 11.85) have carried out nucleate boiling experimental studies under near-weightless conditions. Different liquids were used by these investigators, and hence it is difficult to relate their results. However, at high heat transfer rates, the first two studies indicate that heat flux is essentially the same function of  $t_w - t_{\text{sat}}$ , in near weightlessness as under standard gravitational conditions, which agrees with the qualitative arguments just presented. However, the quantitative effect of low g on nucleate boiling under conditions of low heat fluxes is not established. Since this is the most important region for boiling in propellant tanks, experiments in this range are badly needed.

Burnout heat transfer rates are indicated by most investigators to be significantly reduced by reduction in acceleration level. Merte and Clark (ref. 11.82) tentatively give the zero-g to 1-g burnout heat flux ratio as 0.41. It should be noted that this was for a spherical heater on which a stable film can be sustained under zero g. However, on cylinders the film tends to be unstable, even at zero g, due to the surface tension effects and, hence, less drastic reductions in burnout heat flux are expected.

Rex and Knight (ref. 11.86) report an experimental study to propane in a spherical tank under nearly zero g. The nucleate boiling heat transfer rate for fixed  $\Delta t$  was approximately 30 percent of the value at 1  $g_0$ .

There is a rather large body of literature dealing with condensing in zero g. However, as this work is aimed primarily at tube condensers, and is therefore not particularly related to propellant problems, we will omit its discussion here.

### 11.7 EXPERIMENTAL SIMULATION OF LOW-g ENVIRONMENTS

#### Simulation Requirements

Before we investigate the various means which one can use to simulate low gravity environments, let us examine the conditions which one would like to simulate.

We first consider hydrostatic configurations. The Bond number,  $Bo = \rho g L^2 / \sigma$ , is the pertinent dimensionless parameter characterizing hydrostatics. In addition, the contact angle must be maintained for proper modeling. The simplest means for maintaining contact angle is to use the same fluids and surfaces in the test which would normally be employed in the space system. Then, in order to model environmental conditions of a prototype with a scale model, the  $g$  imposed on the model would have to be selected to maintain the proper value of the Bond number. If the same fluid is used for both model and prototype, a  $\frac{1}{10}$ -scale model of a system designed to operate in  $10^{-5} g_0$  should therefore be tested in a  $10^{-3} g_0$  environment. Modeling of the Bond number is not so important if its value is significantly less than unity (i.e., in the range of "zero-g hydrostatics"). For example, if the prototype will operate with the Bond number equal to 0.001 and at  $10^{-7} g_0$ , testing the  $\frac{1}{10}$ -scale model at  $10^{-4} g_0$  ( $Bo \approx 0.01$ ) would likely provide adequate modeling. However, if the Bond number of the prototype will be of order unity, modeling of the Bond number is essential.

The relative time response for the model will be determined by the length and gravity scaling. In the gravity dominated regime ( $Bo \gg 1$ ), the time constant varies as  $\sqrt{L/g}$  (see eq. (11.11a)). If the same fluid is employed, and if  $g$  will have to appropriately be increased to maintain the model  $Bo$ , the response times of the prototype and model will be related by

$$\frac{T_m}{T_p} = \sqrt{\frac{L_m}{L_p} \frac{g_p}{g_m}} = \left( \frac{L_m}{L_p} \right)^{3/2} \quad (11.119)$$

A  $\frac{1}{10}$ -scale model would therefore have a time constant of the order of  $\frac{1}{10}$  of the prototype's.

In the capillary-dominated regime ( $Bo \ll 1$ ), the time constant varies as  $L^{3/2}$  for a given fluid. Therefore, in this regime the model and prototype time constants would also be related by equation (11.119). These arguments suggest that, in the region  $Bo \approx 1$ , where both capillary and gravity forces are important, the time constant should also scale like  $L^{3/2}$  for a given fluid. This provides a strong motivation for using the design fluid in any model tests.

The desirability of visual observation in the model tests may well exclude the use of solid surfaces. In the event that transparent containers are used in the tests, the fluid should be selected to provide the proper contact angle. The appropriate dimensionless parameters would then have to be employed to determine the proper scaling.

In hydrodynamic situations, the Weber number, Reynolds number, and Bond number should be maintained to provide accurate scaling. While scaling of the Bond number can be accomplished by proper selection of  $g$  for the model test, the Reynolds and Weber numbers cannot both be maintained if the design fluid is employed, since velocity and characteristic length appear in different ways in the dimensionless group. In situations where interface stability is of prime concern, it would appear best to forego maintenance of the Reynolds number and keep the proper Weber number. This should be reasonable as long as the resulting Reynolds number is such that the model and prototype operate in the same flow regime (i.e., laminar or turbulent).

We shall now discuss some experimental techniques currently used to investigate hydrostatics and hydrodynamics at low  $g$ .

#### Bench Testing

It may seem strange to suggest testing a space system on a bench at  $1 g_0$ . However, in large vehicles subjected to very small loadings, the Bond number may be sufficiently high that

a bench test on a small-scale model will give a realistic appraisal of the prototype performance. For example, suppose we are interested in knowing the sloshing frequencies of the propellant in a large tank of peculiar configuration at  $10^{-4} g_0$ . Neglecting viscous effects, the dimensionless frequency,  $\Omega^2 = \rho L^3 \omega^2 / \sigma$ , is a function only of the Bond number. The Bond number will be maintained in a bench test on a  $\frac{1}{100}$ th-scale model. If the general size of the prototype is of the order of 10 meters, the model size is sufficiently large so as to be manageable.

Hydrostatic configurations at low and zero g can be bench tested, using a second liquid in place of the gas. In hydrostatics, the density difference is really what appears in the Bond number, and this difference can be adjusted so as to give the proper modeling. However, the technique should not be used for dynamic modeling, for the greater inertia of the second liquid will not properly model the behavior of a light gas.

Bench testing is by far the easiest and cheapest means for simulating a low-g environment, and should be considered whenever feasible.

#### Free-Fall Simulation

Free-fall capsules provide the simplest means for simulating low-g environments. The time available for a zero-g experiment is approximately given by

$$t = \frac{1}{2.2} \sqrt{h} \text{ seconds} \quad (11.120)$$

where  $h$  is the height in meters. A 5-meter drop therefore allows roughly 1 second. A drop of 20 meters is required to double the test time to 2 seconds. With greater falling distances, air resistance becomes a severe problem. A double-capsule system, in which the outer capsule acts as a drag shield, is preferable even for short-fall systems. With the long drop come severe arresting problems and longer setup time.

With a drag shield and a partially evacuated carrier capsule, environments of the order  $10^{-7} g_0$  can be simulated. The addition of

counterweights can provide simulation in the range  $0.02$ – $1 g_0$ . The difficult range to obtain in a controlled way is  $10^{-2}$ – $10^{-7} g_0$ . The counterweight system is awkward because the effective mass of even a rising cable is appreciable. If the inner capsule must be secured to the drag shield to get the counterweight effect, then the velocity-dependent drag forces will cause the effective g to vary during the drop. Very weak springs attached between the capsules offer an interesting possibility for getting into the moderately low-g range. We used thin rubberbands for this purpose in some early experiments.

The designer of simulation experiments using free fall in a drop tower should make sure that the response time of the phenomena in the model is less than the drop time. The data given earlier should be useful in making these estimates.

With free-fall times of the order of 1 second, the experiments must necessarily be of small scale if meaningful low-g results are to be obtained. Referring to figure 11.6, we see that characteristic lengths of the order of 1 or 2 centimeters would be required for a fluid having a kinematic surface tension of the order of  $50 \text{ cm}^3/\text{sec}^2$ . Since, for a given response time the characteristic length varies as only the one-third power of the kinematic surface tension, we can estimate that for most fluids 1-centimeter experiments would be practicable. This limitation on the permissible size in free-fall experiments is the chief drawback of this relatively inexpensive low-g simulation technique.

#### Aircraft Simulation

A variety of low-g experiments have been performed in aircraft executing a Keplerian trajectory. Approximately 32 seconds of near-zero g can be obtained with a jet transport. Free-floating capsules are used to isolate the experiment from the airframe.

Although experiments of larger scale than in free-fall towers are possible, and the simulation time is longer, the aircraft experimentation has some serious drawbacks. It is difficult for the pilot to accurately maneuver the aircraft

around the floating capsule, and collisions between the experiment and the padded walls of the aircraft are frequent. Stress loadings on the aircraft are high, resulting in limited lifetime and therefore high cost per flight. Initial roll imparted to the experiment upon release of the capsule from the airframe is maintained during the floating period, and is difficult to control. Nevertheless, aircraft experiments have provided much valuable information on system performance during brief periods of low gravity.

### Orbital and Suborbital Systems

The use of suborbital systems further increases the experimentation time to the order

of several minutes. Drawbacks are the large expense involved, the high launch acceleration, and the need to either recover the capsule or telemeter the data. The experiments are subject to the motions of the vehicle, and control of the effective g is virtually impossible to obtain. The utility of such testing would seem to be limited to prototype hardware which is to be tested for operation during launch, coast, and reentry. The usefulness of such systems in basic research seems limited.

With the coming of the manned orbital laboratory, one has the possibility of performing extended zero-g experiments; though not everyone will have this opportunity, a significant amount of basic research data will doubtlessly be obtained in this manner.

### REFERENCES

- 11.1. REYNOLDS, W. C.; SAAD, M. A.; AND SATTERLEE, H. M.: Capillary Hydrostatics and Hydrodynamics at Low-g. Tech. Rept. No. LG-3, Dept. of Mech. Eng., Stanford Univ., Sept. 1, 1964.
- 11.2. UNTERBERG, W.; AND CONGELIERE, J.: Zero Gravity Problems in Space Powerplants; A Status Survey. Am. Rocket Soc. J., vol. 32, no. 6, June 1962, pp. 862-872.
- 11.3. HERMANS, J. J.: Flow Properties of Disperse Systems. Interscience, New York, 1953, p. 286.
- 11.4. BOND, W. N.; AND NEWTON, D. A.: Bubbles, Drops, and Stokes Law. Phil. Mag., vol. 5, 1928, pp. 794-800.
- 11.5. RAYLEIGH, LORD: On the Theory of the Capillary Tube. Scientific Papers. Vol. VI. Cambridge Univ. Press, 1920, p. 355.
- 11.6. MAXWELL, J. C.: Capillary Action. The Scientific Papers of James Clerk Maxwell. Vol. 1. Cambridge Univ. Press, 1890, p. 586.
- 11.7. FLÜGGE, S., ED.: Handbuch der Physik. Vol. X. Springer-Verlag, Berlin, 1960.
- 11.8. BIKERMAN, J. J.: Surface Chemistry. Academic Press, 1958.
- 11.9. MILNE-THOMPSON, L. M.: Theoretical Hydrodynamics. Macmillan Co., 1960.
- 11.10. LEVICH, V. G.: Physicochemical Hydrodynamics (Eng. trans.). Prentice Hall, 1962.
- 11.11. LANE, W. R.; AND GREEN, H. L.: The Mechanics of Drops and Bubbles. G. I. Taylor 70th Ann. Vol., Cambridge Univ. Press, 1956, pp. 162-215.
- 11.12. TREFETHEN, L.: Surface Tension in Fluid Mechanics. (Color-sound educational motion picture, available for loan or purchase.) Educational Services, Inc., Watertown, Mass.
- 11.13. SCRIVEN, L. E.: Dynamics of a Fluid Interface. Chem. Eng. Sci., vol. 12, 1960, pp. 98-108.
- 11.14. MICHAELS, A. S.; AND DEAN, S. W.: Contact Angle Relationships of Silica Aquagel Surfaces. Dept. of Chem. Eng., M.I.T., Cambridge, Mass., 1961.
- 11.15. REYNOLDS, W. C.: Thermodynamics. McGraw-Hill Book Co., 1965, p. 218.
- 11.16. REYNOLDS, W. C.: Thermodynamics. McGraw-Hill Book Co., 1965, p. 394.
- 11.17. CLODFELTER, R. G.: Fluid Mechanics and Tankage Design for Low Gravity Environments. ASD-TDR-63-506, Wright-Patterson AFB, Ohio, Sept. 1963.
- 11.18. PETRASH, D. A.; AND OTTO, E. W.: Controlling the Liquid-Vapor Interface Under Weightlessness. Astronaut. & Aeron., vol. 2, no. 3, Mar. 1964, p. 56.
- 11.19. SIEGEL, R.: Transient Capillary Rise in Reduced and Zero Gravity Fields. J. Appl. Mech., ser. E, vol. 28, no. 2, 1961, p. 165.
- 11.20. SATTERLEE, H. M.; AND CHIN, J. L.: Meniscus Shape Under Reduced-Gravity Conditions. Symposium on Fluid Mechanics and Heat Transfer Under Low Gravitational Conditions, Lockheed Missiles & Space Co., June 24-25, 1965.
- 11.21. CONCUS, P.: Capillary Stability in an Inverted Rectangular Tank. Symposium on Physical and Biological Phenomena in a Weightless State. Vol. 14 (E. T. Benedikt and R. W. Halliburton, eds.). American Astronautical Soc., 1963.

- 11.22. CONCUS, P.: Capillary Stability in an Inverted Rectangular Channel for Free Surfaces With Curvature of Changing Sign. *AIAA J.*, vol. 2, no. 12, Dec. 1964, p. 2229.
- 11.23. WEINSTOCK, R.: *Calculus of Variations*. McGraw-Hill, 1952.
- 11.24. SATTERLEE, H. M.; AND REYNOLDS, W. C.: The Dynamics of the Free Liquid Surface in Cylindrical Containers Under Strong Capillary and Weak Gravity Conditions. Tech. Rept. No. LG-2, Dept. of Mech. Eng., Stanford Univ., May 1, 1964.
- 11.25. MASICA, J. W.; PETRASH, D. S.; AND OTTO, E. W.: Hydrostatic Instability of the Liquid-Vapor Interface in a Gravitational Field. NASA TN D-2267, 1964.
- 11.26. JAKOB, M.: *Heat Transfer*. Vol. 1, ch. 29. John Wiley & Sons, 1949.
- 11.27. DUPREZ, F.: Sur un Cas Particuler de L'équilibre de Liquides. *Memoirs de l'Academie Royale de Sciences, de Lettres, et des Beau-Arts de Belgique*. Vol. 26, 1851, and vol. 28, 1854.
- 11.28. BRETHERTON, F. P.: The Motion of Long Bubbles in Tubes. *J. Fluid Mech.*, vol. 10, pt. 2, 1961, p. 166.
- 11.29. ANLIKER, M.; AND PI, W. S.: Effects of Geometry and Unidirectional Body Forces on the Stability of Liquid Layers. SUDAER Rept. No. 150, Dept. of Aero. and Astro., Stanford Univ., Mar. 1963.
- 11.30. SEEBOULD, J. G.; AND REYNOLDS, W. C.: Configuration and Stability of a Rotating Axisymmetric Meniscus at Low g. Tech. Rept. LG-4, Dept. of Mech. Eng., Stanford Univ., Mar. 1965.
- 11.31. SEEBOULD, J. G.; AND REYNOLDS, W. C.: Shape and Stability of the Liquid-Gas Interface in a Rotating Cylindrical Tank at Low-g. Symposium on Fluid Mechanics and Heat Transfer Under Low Gravitational Conditions, Lockheed Missiles & Space Co., June 24-25, 1965.
- 11.32. BLACKSHEAR, W. T.; AND EIDE, D. G.: The Equilibrium Free Surface of a Contained Liquid Under Low Gravity and Centrifugal Forces. NASA TN D-2471, Oct. 1964.
- 11.33. HOLLISTER, M. P.: Propellant Containment Utilizing Screen Mesh and Perforated Plate Surfaces. Lockheed Missiles & Space Co., Rept. No. LMSC/A665481, Dec. 1964.
- 11.34. LAMB, H.: *Hydrodynamics*. Dover Publ., 1945.
- 11.35. RAYLEIGH, LORD: On the Instability of Cylindrical Fluid Surfaces. *Papers*. Vol. 3, Cambridge Univ. Press, 1892, p. 594.
- 11.36. ANLIKER, M.; AND BEAM, R. M.: On the Stability of Liquid Layers Spread Over Simple Curved Bodies. *J. Aerospace Sci.*, vol. 29, 1962, p. 1196.
- 11.37. LEE, S-L.: Taylor Instability of a Liquid Film Around a Long, Horizontal, Circular Cylindrical Body in Still Air. *J. Appl. Mech.*, ser. E, vol. 30, Sept. 1963, pp. 443-447.
- 11.38. BELLMAN, R.; AND PENNINGTON, R. H.: Effects of Surface Tension and Viscosity on Taylor Instability. *Quart. J. Mech. Appl. Math.*, vol. 12, no. 2, July 1954, p. 151.
- 11.39. OTTO, E. W.: Static and Dynamic Behavior of the Liquid-Vapor Interface During Weightlessness. NASA TM-X-52016, Technical Preprints for Fluid Dynamics Panel Specialists' Meeting (AGARD), Marseille, France, Apr. 20-24, 1964.
- 11.40. SMITH, R. D.: Interfacial Stability of Liquid Layers on Elastic Surfaces. Symposium on Fluid Mechanics and Heat Transfer Under Low Gravitational Conditions, Lockheed Missiles & Space Co., June 24-25, 1965.
- 11.41. TONG, P.; AND FUNG, Y. C.: The Effect of Wall Elasticity and Surface Tension on the Forced Oscillations of a Liquid in a Cylindrical Container. Symposium on Fluid Mechanics and Heat Transfer Under Low Gravitational Conditions, Lockheed Missiles & Space Co., June 24-25, 1965.
- 11.42. SIEGERT, C. E.; PETRASH, D. A.; AND OTTO, E. W.: Time Response of Liquid-Vapor Interface After Entering Weightlessness. NASA TN D-2458, 1964.
- 11.43. SIEGERT, C. E.; PETRASH, D. A.; AND OTTO, E. W.: Behavior of Liquid-Vapor Interface of Cryogenic Liquids during Weightlessness. NASA TN D-2658, 1965.
- 11.44. PAYNTER, H. L.: Time for a Totally Wetting Liquid to Deform From a Gravity-Dominated to a Nulled-Gravity Equilibrium State. *AIAA J.*, vol. 2, no. 9, Dec. 1964, p. 1627.
- 11.45. PETRASH, D. A.; ZAPPA, R. F.; and OTTO, E. W.: Experimental Study of the Effects of Weightlessness on the Configuration of Mercury and Alcohol in Spherical Tanks. NASA TN D-1197, 1962.
- 11.46. FUNG, F. W.: Dynamic Response of Liquids in Partially-Filled Containers Suddenly Experiencing Weightlessness. Symposium on Fluid Mechanics and Heat Transfer Under Low Gravitational Conditions, Lockheed Missiles & Space Co., June 24-25, 1965.
- 11.47. SHULEIKIN, V. V.: Second Series of Ground-Level Experiments With Weightless Fluids (Eng. trans.). *Soviet Physics-Doklady*, vol. 8, no. 12, June 1964, p. 1221.
- 11.48. PETRASH, D. A.; AND NELSON, T. M.: Effect of Surface Energy on the Liquid Vapor Interface During Weightlessness. NASA TN D-1582, 1963.
- 11.49. REID, W. H.: Oscillations of a Viscous Liquid Drop. Tech. Rept. no. 32, Div. of Appl. Mech., Brown Univ., 1960.

- 11.50. SAAD, M. A.; AND OLIVER, D. A.: Linearized Time-Dependent Free-Surface Flow in Rectangular and Cylindrical Tanks. 1964 Heat Transfer and Fluid Mechanics Institute, Stanford Univ. Press, 1964.
- 11.51. NUSSEL, R. C.; DERDUL, J. D.; AND PETRASH, D. J.: Photographic Study of Propellant Outflow From a Cylindrical Tank During Weightlessness. NASA TN D-2572, 1965.
- 11.52. EIDE, D. G.: Preliminary Analysis of Variation of Pitch Motion of a Vehicle in a Space Environment Due to Fuel Sloshing in a Rectangular Tank. NASA TN D-2336, 1964.
- 11.53. SWALLEY, F. E.; PLATT, G. K.; AND HASTINGS, L. J.: Saturn V Low-Gravity Fluid Mechanics Problems and Their Investigation by Full-Scale Orbital Experiment. Symposium on Fluid Mechanics and Heat Transfer Under Low Gravitational Conditions, Lockheed Missiles & Space Co., June 24-25, 1965.
- 11.54. PAYNTER, H. L.: Special Zero-Gravity Fluid Problems. Rocket Propellant and Pressurization Systems (E. Ring, ed.). Prentice-Hall, 1964.
- 11.55. GLUCK, D. F.; AND GILLE, J. P.: Fluid Mechanics of Zero-g Propellant Transfer in Spacecraft Propulsion Systems. Trans. ASME, Ser. B, vol. 87, no. 1, Feb. 1965, p. 1.
- 11.56. PETRASH, D. A.; NUSSEL, R. C.; AND OTTO, E. W.: Effect of the Acceleration Disturbances Encountered in the MA-7 Spacecraft on the Liquid-Vapor Interface in a Baffled Tank During Weightlessness. NASA TN D-1577, 1963.
- 11.57. PETRASH, D. A.; AND OTTO, E. W.: Studies of the Liquid-Vapor Interface Configuration in Weightlessness. ARS Space Power Systems Conf., Sept. 25-28, 1962.
- 11.58. MCGINNES, H. D.: Capillary Pumping for Closed-Cycle Gas Systems. Research Summary no. 36-10, vol. 1, Jet Propulsion Lab., Sept. 1961.
- 11.59. BHUTA, P. G.; AND KOVAL, L. R.: Sloshing of a Liquid in a Draining or Filling Tank Under Variable G Conditions. Symposium on Fluid Mechanics and Heat Transfer Under Low Gravitational Conditions, Lockheed Missiles & Space Co., June 24-25, 1965.
- 11.60. CONCUS, P.; CRANE, G. E.; AND PERKO, L. M.: Inviscid Fluid Flow in an Accelerating Axisymmetric Container. Symposium on Fluid Mechanics and Heat Transfer Under Low Gravitational Conditions, Lockheed Missiles & Space Co., June 24-25, 1965.
- 11.61. GLUCK, D. F.; GILLE, J. P.; SIMKIN, D. J.; AND ZUKOSKI, E. E.: Distortion of the Liquid Surface During Tank Discharge Under Low G Conditions. AIChE National Meeting, Houston, Tex., Feb. 7-11, 1965.
- 11.62. PORTER, R. N.; AND STANFORD, H. B.: Positive Expulsion Devices Assure Smooth, Reliable Starts for Spacecraft in Zero-g Space. J. SAE, Aug. 1965, pp. 70-77.
- 11.63. HOLLISTER, M. P.; AND SATTERLEE, H. M.: Low Gravity Liquid Reorientation. Symposium on Fluid Mechanics and Heat Transfer Under Low Gravitational Conditions, Lockheed Missiles & Space Co., June 24-25, 1965.
- 11.64. MASICA, W. J.; AND SALZMAN, J. A.: An Experimental Investigation of the Dynamic Behavior of the Liquid-Vapor Interface Under Adverse Low-Gravitational Conditions. Symposium on Fluid Mechanics and Heat Transfer Under Low Gravitational Conditions, Lockheed Missiles & Space Co., June 24-25, 1965.
- 11.65. FUNK, E.; AND WELCH, N. E.: Distributions of Noncondensable Gases in Liquids Under Low-g Conditions. Symposium on Fluid Mechanics and Heat Transfer Under Low Gravitational Conditions, Lockheed Missiles & Space Co., June 24-25, 1965.
- 11.66. SMITH, J. M.; CIMA, R. M.; AND LI, Y.-S.: The Application of Hydrophilic and Hydrophobic Surfaces for Phase Separation in a Low-g Environment. Symposium on Fluid Mechanics and Heat Transfer Under Low Gravitational Conditions, Lockheed Missiles & Space Co., June 24-25, 1965.
- 11.67. LANDAU, L. D.; AND LIFSHITZ, E. M.: Electrodynamics of Continuous Media. Pergamon Press, 1960, pp. 64 ff.
- 11.68. MELCHER, J. R.: Field Coupled Surface Waves. MIT Press, Cambridge, Mass., ch. 2, 1963.
- 11.69. REYNOLDS, J. M.: Stability of an Electrically Supported Fluid Column. Phys. of Fluids, vol. 8, no. 1, Jan. 1965, pp. 61-70.
- 11.70. HRYCAK, P.; AND HELGANS, R. E., JR.: Equilibrium Temperature of Long Thin-Walled Cylinders in Space. AIChE preprint no. 17, Seventh National Heat Transfer Conference, AIChE-ASME, Cleveland, Ohio, Aug. 19-22, 1964.
- 11.71. CHANDRASEKHAR, S.: Hydrodynamic and Hydromagnetic Stability. Clarendon Press, Oxford, 1961.
- 11.72. WEINBAUM, S.: Natural Convection in a Horizontal Circular Cylinder. J. Fluid Mech., vol. 18, Mar. 1964, p. 409.
- 11.73. WANG, N. P.: Study of Forces on Propellants Due to Heat Transfer Influencing Propellant Temperatures in a Recovery-Type Vehicle. Dynamic Science Corp., Rept. No. 2, Subcontract 28-2524, Aug. 30, 1962.

- 11.74. SCRIVEN, L. E.; AND STERNLING, C. V.: On Cellular Convection Driven by Surface Tension Gradients: Effects of Mean Surface Tension and Surface Viscosity. *J. Fluid Mech.*, vol. 19, pt. 3, 1964, p. 321.
- 11.75. LEVY, A. M.; CHIN, J. H.; DONALDSON, J. O.; GALLAGHER, L. W.; HARPER, E. Y.; HURD, S. E.; AND SATTERLEE, H. M.: Analytical and Experimental Study of Liquid Orientation and Stratification in Standard and Reduced Gravity Fields. *Lockheed Missiles & Space Co., Rept. 2-05-64-1*, July 1964.
- 11.76. BAILEY, T.; VANDEKOPPEL, R.; SKARTVEDT, G.; AND JEFFERSON, J.: Cryogenic Propellant Stratification Analysis and Test Data Correlation. *AIAA J.*, vol. 1, 1963, p. 1657.
- 11.77. CLARK, J. A.; AND BARAKAT, H. Z.: Transient, Laminar, Free-Convection Heat and Mass Transfer in Closed, Partially Filled, Liquid Containers. *Univ. of Mich. Dept. of Mech. Eng. Tech. Rept., Contract NAS8-825*, Jan. 1964.
- 11.78. SCHWARTZ, S. H.; AND ADELBERG, M.: Some Thermal Aspects of a Contained Fluid in a Reduced-Gravity Environment. *Symposium on Fluid Mechanics and Heat Transfer Under Low Gravitational Conditions*, Lockheed Missiles & Space Co., June 24-25, 1965.
- 11.79. ADELBERG, M.: Boiling, Condensation and Convection in a Gravitational Field. *AIChE National Meeting*, Feb. 10, 1965.
- 11.80. ELLION, M. E.: A Study of the Mechanism of Boiling Heat Transfer. *Jet Propulsion Lab. Memorandum No. 20-88*, Calif. Inst. of Tech., Mar. 1, 1954.
- 11.81. KESHOCK, E. G.; AND SIEGEL, R.: Forces Acting on Bubbles in Nucleate Boiling Under Normal and Reduced Gravity Conditions. *NASA TN D-2299*, 1964.
- 11.82. MERTE, H.; AND CLARK, J. A.: Boiling Heat Transfer Data for Liquid Nitrogen at Standard and Zero Gravity. *Advances in Cryogenic Engineering*, vol. 7 (K. D. Timmerhaus, ed.). Plenum Press, New York, 1962.
- 11.83. SHERLEY, J. E.: Nucleate Boiling Heat Transfer Data for Liquid Hydrogen at Standard and Zero Gravity. *Advances in Cryogenic Engineering*, vol. 8 (K. D. Timmerhaus, ed.). Plenum Press, New York, 1963.
- 11.84. STEINLE, H. F.: An Experimental Study of Transition From Nucleate to Film Boiling Under Zero-Gravity Conditions. *Proc. Heat Transfer and Fluid Mechanics Institute, Stanford Univ.*, Stanford Univ. Press, 1960.
- 11.85. USISKIN, C. M.; AND SIEGEL, R.: An Experimental Study of Boiling in Reduced and Zero Gravity Fields. *J. of Heat Transfer, Trans. ASME, ser. C*, vol. 83, Aug. 1961, pp. 243-251.
- 11.86. REX, J.; AND KNIGHT, B. A.: An Experimental Assessment of the Heat Transfer Properties of Propane in a Near-Zero Gravity Environment. *Tech. Note Space 39*, Ministry of Aviation, Aug. 1964, ARC Document 26368 (UK).

## PRINCIPAL NOTATIONS

$A_c$ =capillary area  
 $Bo$ =Bond number  
 $D$ =tank diameter  
 $d$ =tank drain diameter  
 $Fr$ =Froude number  
 $g$ =local acceleration  
 $g_0=980 \text{ cm/sec}^2$   
 $L$ =characteristic length  
 $r$ =radial distance or coordinate  
 $r_0$ =tank radius  
 $T$ =characteristic time

$t$ =time  
 $We$ =Weber number  
 $\beta$ =kinematic surface tension,  $\sigma/\rho$   
 $\Gamma$ =contact angle hysteresis parameter  
 $\theta$ =contact angle  
 $\rho$ =liquid density  
 $\sigma$ =surface tension  
 $\Omega^2$ =low-g sloshing frequency parameter,  
 $\rho r_0^3 \omega^2 / \sigma$   
 $\tilde{\Omega}^2$ =high sloshing frequency parameter,  $r_0 \omega^2 / g$   
 $\omega$ =sloshing or rotational frequency, rad/sec

## **APPENDIX**

Preceding page blank 440 441

## **Physical Properties of Selected Liquids<sup>1</sup>**

Included in this appendix are tables of typical physical properties of various rocket propellants and various fluids which have been or might be used in model studies. The values in these tables should be interpreted as "typical" since in many cases disagreements of various orders of magnitude were observed among the various references. It should also be noted that many of the fluids are toxic and/or dangerous to handle. For this reason, references 15 through 22 are appended to the list of references since they present data on the properties of dangerous materials and laboratory equipment necessary to handle these materials.

---

<sup>1</sup> The information contained in this appendix was compiled by John F. Dalzell, with the assistance of Sandor Silverman.

**TABLE A-I**  
*Typical Mechanical Properties of Various Rocket Propellants*

No.	Name (chemical symbol)	Freezing point, °C	Boiling Point, °C	Specific gravity at 20° C and 71.1° C, referred to water at 4°C	Dynamic viscosity, $\mu$ , at $T$ , poises	Kinematic viscosity, $\eta$ , at $T$ , $\text{cm}^2/\text{sec}$	Velocity of sound, $C$ , at $T$ , °C, m/sec	Vapor pressure, $P$ , at $T$ , °C, atmospheres	Surface tension, $\sigma$ , at $T$ , °C, dynes/cm	Contact angle, $\theta$ , at room temperature, deg	In
1	Hydrogen (H <sub>2</sub> )	-260	-253	*(0.071)	0.00014	-253	0.00197	-253	1.9	-253	
2	Diborane (B <sub>2</sub> H <sub>6</sub> )	-166	-92	*(.43)	.0026	-33	.0038	-33	.53	-100	13.7
3	Ammonia (NH <sub>3</sub> )	-78	-33	*(.68)	.00317	20	.00545	=1400	=1.0	-34	34.2
4	Pentaborane (B <sub>5</sub> H <sub>9</sub> )	-47	60	.627	.0125	20	.0158	20	.22	20	21.4
5	Ethanol (CH <sub>3</sub> OH)	-114	78	.79	.74	.00483	71.1	.0065	1127	.058	20
6	Unsym-dimethylhydrazine, UMDH [(CH <sub>3</sub> ) <sub>2</sub> NNH <sub>2</sub> ]	-57	64	.793	.751	.0055	20	.00695	30	.162	20
7	Kerosene, RP-1 (CH <sub>3</sub> CH <sub>2</sub> O)	-44	162-268	.806	.767	.0186	20	.0231	20	.0014	20
8	JP-4			.78		.0088	71.1	.0115	71.1	.0014	20
9	Monomethylhydrazine (CH <sub>3</sub> NHNH <sub>2</sub> )	-52	87	.82		.0083	20	.01	20	1237	20
10	Hydne (90% UMDH, 40% DETA)	<-84	65	.859	.809	.0046	71.1	.0055	20	.048	20
11	Ethylene oxide [(CH <sub>2</sub> ) <sub>2</sub> O]	-110	11	(0.887 at $T$ , °C)	.00513	71.1	.0063	71.1	.180	20	28
12	Ethylene diamine [NH <sub>2</sub> (CH <sub>2</sub> ) <sub>2</sub> NH <sub>2</sub> ]	11	117	.898	.850	.0057	-50	=.004	0	=1.0	10
13	Diethylene triamine {[NH <sub>2</sub> (CH <sub>2</sub> ) <sub>2</sub> NH <sub>2</sub> ]} <sub>3</sub>	-39	208	.952	.910	.0160	20	.0178	20	.014	20
14	Hydrazine (N <sub>2</sub> H <sub>4</sub> )	2	113	1.008	.964	.0097	20	.0097	20	.0027	20
15	Aniline (C <sub>6</sub> H <sub>5</sub> NH <sub>2</sub> )	-6	185	1.022		.0051	20	.0053	71.1	.0136	20
16	n-propyl nitrate (C <sub>3</sub> H <sub>7</sub> NO <sub>2</sub> )	110	1.058		.0044	20	.0043	20	.00034	20	63.2-74.8
17	Oxygen (O <sub>2</sub> )	-219	-184	*1.14	.0019	-189	=.0017	-185	.98	.0136	20
18	Perchloryl fluoride (ClO <sub>3</sub> F)	-147	-47	1.434	1.15	.0018	20	.00125	20	.0022	20
19	Nitrogen tetroxide (N <sub>2</sub> O <sub>4</sub> )	-11	21	1.447	1.313	.0013	71.1	.0013	71.1	.017	21.3
20	Hydrogen peroxide (H <sub>2</sub> O <sub>2</sub> )	-1	150	1.448	1.359	.0126	20	.0087	20	<.007	20
21	Fluorine (F <sub>2</sub> )	-220	-189	*1.51		.0035-	-189	.0023	-188	.34	20
22	Inhibited white fuming nitric acid (IWFA)			1.51		.0086	20	.0057	20	.063	20

23	Inhibited red fuming nitric acid (IRFNA)		1.56	.014	20	.0090	20		.140	20
24	Nitric acid (anhydrous) (HNO <sub>3</sub> )	-42	85	1.513	.0095	20	.0063	20	.41.2	20
25	Oxygen difluoride (OF <sub>2</sub> )	-225	-145	*1.53	.00280	-145	.00183	-145	.527	-147
26	Chlorine trifluoride (ClF <sub>3</sub> )	-76	11.8	1.682	.00433	20	.00236	20	=1.0	12
27	Bromine difluoride (BrF <sub>2</sub> )	-62	40	2.48	2.30	.00635	20	.00264	.43	20
28	Aerodine - 50 (51% hydrazine +46.9% UTMH +2% impurities) (percent by weight).	7	70	.904	.857	.0091	25	.0101	.161	20 (†)
									.651	.68

\*At normal boiling point.

In table I of ref. 12, it may be seen that the advancing and receding contact angles for this liquid in contact with the following surfaces and its vapor lie within the range 0°-2°, pyrex glass, polished and satinized 6061 T6 aluminum, polished and satinized ASTM B348-59T Grade 6 titanium alloy, and polished and satinized Type 301 stainless steel.

## APPENDIX

TABLE A-II  
*Typical Mechanical Properties of Various Model Fluids*

24	Carbon tetrachloride ( $\text{CCl}_4$ ).	-14	76	1.60	20	.00699	20	.00605	20	.905	30	.12	20	26.8	Air	20	0	Glass - Air.	
25	Ethyliodide ( $\text{CH}_3\text{ICH}_2\text{I}$ )	-100	72	1.93	20	.00578	20	.00298	20	≈850	10	.14	20	29.9	Air	16			
26	Methyl iodide ( $\text{CH}_3\text{I}$ )	-60	42	2.28	20	.0050	20	.00220	20			.53	26	26.5	Air	20			
27	Methylene bromide ( $\text{CH}_2\text{Br}_2$ ).	-65	98	2.46	20	.0123	20	.0030	20			.053	23						
28	Bromine ( $\text{Br}_2$ )	-7	57	3.12	20	.00905	20	.00319	20			.131	9	41.5	Air or vapor.	20			
29	Mercury (Hg)	-38	357	13.55	20	.016	20	.00117	20	1451	20	.000016	20	476.1	Air	20	130	Glass - Air.	
30	Olive oil.			.914	18	.632	18	1.02	18					33.1		18	0		
31	Zinc (Zn)		880	6.51	360	.0142	360	.00218	360					877		360			
32	n-Heptane ( $\text{C}_7\text{H}_{16}$ )		98	.985	20	.00400	20	.00697	20							20.26			
33	Toluene ( $\text{C}_7\text{H}_8$ )		110	.868	20	.00500	20	.0068	20							28.55			
34	Lithium (Li)		1372	.536	181	.00452	181	.00396	181			1	1372	394		181			
35	Cesium ( $\text{Cs}$ )		*28	1.88	20	.00686	28	.00365	28					39.4		28			
36	Bismuth (Bi)		*271	10.0	271	.0185	271	.00185	271					377		356			
37	Lead (Pb)		*327	10.61	327	.0212	320	.00220	320					442		350			
38	Tetrabromomethane (Br $\text{CH}_3\text{CBr}_3$ ).		151	2.97	20	.0638	20	.0333	20					49.67	Air	20			
39	Trifluorotrihydroethane			1.58	20										18.6	0	Air		
40	Syn. tetrabromoethane			2.965	20										49.67	20	0	Air	

\*This is the melting point temperature.

TABLE A-III  
*Contact Angle Values\**

Solid	Phase 1	Phase 2	Contact angle, deg	Type of measurement
Glass	Air	Water	0	
		Benzene	0	
		Mercury	128-148	
Silica	Air	Water	0	
		Acetone	0	
		Benzene	0	
Mercury	Air	Water	0	
Anatase ( $TiO_2$ )	Air	Water	0	
Barium sulfate	Air	Water	0	
Tin dioxide ( $SnO_2$ )	Air	Water	0	
Graphite	Air	Water	80	(Tilting slide.)
		Water	60	(Sessile drop.)
		Benzene	0	
Paraffin	Air	Water	106	Tilting slide.
		Water	105	Tilting slide.
Carbon	Air	Water	40	Porous plug.
Stibnite ( $Sb_2S_3$ )	$\alpha$ -Bromonaphthalene	Water	145	Porous plug.
		Water	84	Tilting slide.
Talc	Air	Water	0-38	Porous plug, solid given various heat treatments.
		Benzene	130	Porous plug.
		$\alpha$ -Bromonaphthalene	133	Porous plug.
Steel	Air	Water	88	Tilting slide.
		$CH_2I_2$	52	Sessile bubble or drop.
		Water	53	Sessile drop.
Aluminum oxide ( $Al_2O_3$ )	Benzene	Water	22	Various surface treatments; sessile drop.
Hexadecyl alcohol	Air	Water	50-72	Porous plug.
Octadecylanine	Air	Water	45	Tilting slide.
Gel 4.0% $SiO_2$ (pure)	Air	Paraffin	$50.5 \pm 0.5$ , adv	Sessile drop.
Gel (impure)	Air	Paraffin	$49.5 \pm 0.5$ , rec	Captive bubble.
		MeI <sub>2</sub>	$51.3 \pm 0.5$ , adv	Captive bubble.
		MeI <sub>2</sub>	$51.3 \pm 0.5$ , rec	Sessile drop.
Glass	Water	Paraffin	$52.2 \pm 0.4$ , adv	Sessile drop.
		Oleic acid	$52.0 \pm 0.7$ , rec	Sessile drop.
Mica	Water	Paraffin	$32.5 \pm 2.5$ , adv	Sessile drop.
		Mercury	0, rec	Sessile drop.
		Mercury	55, water rec	
Talc	Water	Benzene	80, water adv	
		Benzene	41, water rec	
		Benzene	0, water rec	
Aluminum (Agena tank material)	Water	Benzyl alcohol	135, water rec	
		Ethylene dibromide	122, water rec	
		Nitric acid (IRFNA)	145, water rec	
	He	Unsymmetrical dimethylhydrazine (UDMH)	$3^\circ-15'$ at $76^\circ F$ , 5 psia	Tilting plate method.
			$3^\circ-10'$ at $76^\circ F$ , 15 psia	Tilting plate method.
			$15^\circ-20'$ at $76^\circ F$ , 25 psia	
			$0^\circ-45'$ at $76^\circ F$ , 5, 15, and 25 psia	Tilting plate method.

\*This table is taken from ref. 10.

## REFERENCES

1. STEINLE, HANS F.: An Experimental Study of the Transition From Nucleate to Film Boiling Under Zero-Gravity Conditions. 13th Heat Transfer and Fluid Mechanics Institute, Stanford University, June 1960.
2. SUMNER, IRVING E.: Preliminary Experimental Investigation of Frequencies and Forces Resulting From Liquid Sloshing in Toroidal Tanks. NASA TN D-1709, 1963.
3. SEVERNS, WILLIAM H.; AND FELLOWS, JULIAN R.: Air Conditioning and Refrigeration. John Wiley & Sons, Inc., 1958.
4. SCOTT, RUSSELL B.: Cryogenic Engineering. D. Van Nostrand Co., Inc., 1959.
5. SILVERMAN, J.; ET AL.: Liquid Propellants. Section 20.2. In *Handbook of Astronautical Engineering* (H. H. Koelle, editor-in-chief), McGraw-Hill Book Co., 1961.
6. ANON.: Physical Properties and Thermodynamic Functions of Fuels, Oxidizers, and Products of Combustion. Parts I, II, III. Reports R-127, R-129, R-196, Battelle Memorial Inst., 1949. (U.S. Air Force Project Rand.)
7. ANON.: Nitrogen Tetroxide. Allied Chemical Product Bulletin, Nitrogen Div., 40 Rector St., New York.
8. ANON.: Storable Liquid Propellants, Nitrogen Tetroxide/Aerozine-50. Report No. LRP 198 (Special) Revision C. Aerojet-General Corp., June 1961. (Copies may be obtained from: Manager, Customer Relations, Liquid Rocket Plant, Aerojet-General Corp., PO Box 1947, Sacramento, Calif.)
9. SATTERLEE, H. M.; AND REYNOLDS, W. C.: The Dynamics of the Free Liquid Surface in Cylindrical Containers Under Strong Capillary and Weak Gravity Conditions. Tech. Rept. No. LG-2, Thermosciences Div., Dept. of Mechanical Engineering, Stanford University, May 1, 1964.
10. REYNOLDS, W. C.; SAAD, M. A.; AND SATTERLEE, H. M.: Capillary Hydrostatics and Hydrodynamics at Low g. Tech. Rept. No. LG-3, Thermosciences Div., Dept. of Mechanical Engineering, Stanford University, Sept. 1964.
11. MASICA, WILLIAM J.; PETRASH, DONALD A.; AND OTTO, EDWARD W.: Hydrostatic Stability of the Liquid-Vapor Interface in a Gravitational Field. NASA TN D-2267, 1964.
12. LYERLY, GEORGE A.; AND PEPER, HENRY: Summary Report—Studies of Interfacial Surface Energies. NASA CR-54175, 1964.
13. SANDORFF, PAUL E.: Principles of Design of Dynamically Similar Models for Large Propellant Tanks. NASA TN D-99, 1960.
14. ANON.: Handbook of Chemistry and Physics. 42nd ed., Chemical Rubber Pub. Co., 1960.
15. FAIRHALL, L. T.: Industrial Toxicology. 2nd edition, The Williams & Wilkins Co. (Baltimore), 1957.
16. ELKINS, H. B.: The Chemistry of Industrial Toxicology. 2nd edition, John Wiley & Sons, 1959.
17. JACOBS, M. B.: The Analytical Chemistry of Industrial Poisons, Hazards, and Solvents. 2nd edition, Interscience Pub., Inc., 1949.
18. BAMFORD, F.: Poisons, Their Isolation and Identification. 2nd edition, revised by C. P. Stewart, J. & A. Churchill (London), 1947.
19. BROOKS, V. J.; AND JACOBS, M. B.: Poisons, Properties, Chemical Identification, Symptoms and Emergency Treatment. 2nd edition, D. Van Nostrand Co., Inc., 1958.
20. SAX, N. I.: Dangerous Properties of Industrial Materials. 2nd edition, Reinhold Publishing Corp., 1963.
21. ARMAND, H., ED.: Best's Safety and Maintenance Directory of Safety, Maintenance, Fire Control, Hygiene, and First Aid Products and Equipment. Alfred M. Best Co., Inc. (New York), 1954.
22. ANON.: Catalog of Industrial Safety Equipment. Mine Safety Appliances Co., Pittsburgh, Pennsylvania, 3rd edition, Catalog 7-B, 1957.

## AUTHOR INDEX

Numbers in parentheses refer to pages on which the references are listed.

### A

- ABRAMSON, H. N., 1, (10), (11), 50, 58, (65), (66), (67), 79, (101), (102), 105, 114, 115, 124, 132, (141), (142), (194), (195), (221), (222), 285, (299), (349), (350), (383)  
ADELBERG, M., 433, (439)  
ANLIKER, M., 409, 412, (437)  
ARMAN, A., (195)  
ARMAND, H., (appendix)  
ARMSTEAD, A. L., 49, (67), (142), (195)  
ARMSTRONG, G. L., (66), 127, (142), (221)  
ARNOLD, R. N., 311, 313, 317, 323, (349)  
ASHER, G. W., 330, 338, (349)  
AYRE, R. S., (11)

### B

- BAILEY, T., 432, (439)  
BAIRD, M. H. I., 293, (299)  
BAMFORD, F., (appendix)  
BARAKAT, H. Z., 432, 433, (439)  
BARON, M. L., (11), 323, 326, 330, (349)  
BARTON, M., (265)  
BAUER, H. F., 13, 26, 29, 30, 47, (65), (66), (67), 93, (102), 121, 122, 124, (141), (142), 208, 217, (222), 225, (265), 304, 338, (349), (350)  
BEAL, T. R., (350)  
BEAM, R. M., 412, (437)  
BELLMAN, R., 412, (437)  
BENEDIKT, E. T., (436), (438)  
BENJAMIN, T. B., 271, (299)  
BERLOT, R. R., (102), (222)  
BERRY, J. G., 318, 320, 321, (349)  
BHUTA, P. G., 286, (299), 336, (350), 423, (438)  
BIKERMAN, J. J., 391, (436)  
BINNIE, A. M., 375, (383)  
BISHOP, R. E. D., (141)  
BISPLINGHOFF, R. L., (11)  
BLACKMON, J. B., (438)  
BLACKSHEAR, W. T., 411, (437)  
BLAGOVESHCHENSKY, S. N., (11)  
BLEICH, H. H., (11), 293, 294, 298, (299), 323, 326, 330, 338, (349)  
BLOUNT, D. H., (300)  
BOLOTIN, V. V., 271, (299)  
BOND, W. N., 388, (436)  
BRADY, W. F., (383)  
BRETHERTON, F. P., 408, (437)  
BRIDGMAN, P. W., (194)  
BRODETSKY, S., 234, (265)  
BROOKS, G. W., 170, (195)  
BROOKS, V. J., (appendix)  
BROUCEK, G. T., 220, (221), (265)  
BROWN, R. B., 149, (194), (383)

- BUCHANAN, R. H., 293, (299)  
BUCKINGHAM, E., 146, (194)  
BUDIANSKY, B., 14, 49, (66)

### C

- CALDWELL, J. T., (221)  
CARDEN, H. D., (195)  
CARPENTER, L. H., (142), 183, (195)  
CARR, J. H., (10)  
CASE, K. M., (141)  
CATHERINE, J. J., (195), (196)  
CHANDRASEKHAR, S., (438)  
CHIN, J. H., (439)  
CHIN, J. L., 402, (436)  
CHU, W.-H., 47, 50, 53, (66), (67), 79, (101), (102), (142), (195), (221), (222), (299), 330, 336, (349), (350), (383)  
CIMA, R. M., 427, (438)  
CLARK, C. D., (222)  
CLARK, J. A., 432, (439)  
CLODFELTER, R. G., 399, (436)  
CLOUGH, R. W., (11)  
COALE, C. W., (350)  
COKONIS, T. J., (383)  
COLE, H. A., (142), (195)  
CONCUS, P., 406, 410, 423, (436), (437), (438)  
CONGELIERE, J., (436)  
COOPER, R. M., 6, (10), (65)  
CRANE, G. E., 423, (438)  
CREDE, C. E., (195)

### D

- DALZELL, J. F., (101), 145, 166, (194), 203, 353, (383)  
DAVIS, W. F., (384)  
DEAN, S. W., (436)  
DERDUL, J. D., 420, 423, (438)  
DERGAREBEDIAN, P., 374, 375, (383)  
DODGE, F. T., 79, 199, (222), 269, 285, 293, (299), (300), 373  
DOKUCHAEV, L. V., (66)  
DONALDSON, J. O., (439)  
DOROZHINKIN, N. Y., (67), (141)  
DUNCAN, W. J., (194)  
DUPREZ, F., 408, (437)

### E

- EHLER, F. G., (141), (195)  
EHRLICH, L. W., 14, (66)  
EIDE, D. G., 18, (66), (383), 411, 420, (437), (438)  
ELKINS, H. B., (appendix)  
ELLION, M. E., (439)  
EPPERSON, T. B., 149, (194), (383)  
EULITZ, W. R., 14, (66), 115, (142)

## F

- FAIRHALL, L. T., (appendix)  
 FARADAY, M., 270, 271, (298)  
 FELLOWS, J. R., (appendix)  
 FLÜGGE, S., (436)  
 FONTENOT, L. L., 332, (350)  
 FREED, L. E., 207, (222)  
 FRITZ, C. G., 298, (300)  
 FULLER, A. T., (265), (350)  
 FULTZ, D., 93, (102), (299)  
 FUNG, F. W., 419, (437)  
 FUNG, Y. C., 317, (349), (350), 418, 420, (437)  
 FUNK, E., 427 (438)

## G

- GAILLARD, P., (102)  
 GALLAGHER, L. W., (439)  
 GAMBUCCI, B. J., (141), (142), (195)  
 GARZA, L. R., (65), (66), (67), (101), (102), 120, 125,  
 130, (141), (142), 166, (194), (221), (383)  
 GAUZY, H., (141)  
 GEISSLER, E. D., (11), (265), (350)  
 GIDDINGS, A. J., (11)  
 GILLE, J. P., (11), (383), 425, 436, (438)  
 GLADWELL, G. M. L., (141)  
 GLUCK, D. F., (11), (383), 425, (438)  
 GOLDSBOROUGH, G. R., (10)  
 GONZALES, R., 330, (350)  
 GRAEFFE, 234  
 GRAHAM, E. W., (11), (66), (221)  
 GREEN, H. L., (436)

## H

- HALLIBURTON, R. W., (436)  
 HARPER, E. Y., (439)  
 HARPER, J., (222)  
 HARRIS, C. M., (195)  
 HARRIS, D. P., (383)  
 HARRIS, R. G., 382, (384)  
 HASTINGS, L. J., (438)  
 HAYS, P. J., (266)  
 HEINRICH, K., (265)  
 HEIST, E. K., (265)  
 HELGANS, R. E., Jr., (438)  
 HERMANS, J. J., (436)  
 HERR, R. W., (195), 323, 326, (349)  
 HOLLISTER, M. P., 411, 426, 427, (437), (438)  
 HOOKINGS, G. A., (383)  
 Housner, G. W., (11), (221)  
 HOWELL, E., (141), (195)  
 HOWELL, J. V., (222)  
 HRYCAK, P., (438)  
 HU, W. C. L., 310, (349)  
 HURD, S. E., (439)  
 HURWITZ, A., 234, 245, (265), 341, 342, (350)  
 HUTCHINSON, R. C., (265)  
 HUTTON, R. E., 93, 95, 96, 97, 100, (102), (195), 284,  
 (299), 375, (383)  
 HWANG, C., 332, (350)

## J

- JACOBS, M. B., (appendix)  
 JACOBSEN, L. S., (10), (11)  
 JAKOB, M., 408, (437)  
 JAMESON, G., (299)  
 JASZLICS, I. J., (196)  
 JEFFERSON, J., (439)

## K

- KACHIGAN, K., 47, (66), 127, (142), (221)  
 KAMEL, M. Y. M., 375, (383)  
 KANA, D. D., (65), (67), (101), (142), (195), (222), 283,  
 284, 285, 288, 293, (299), (300), 303, 333, 336, (349),  
 (350), 378  
 KAPLAN, A., (349)  
 KAUFMAN, F. H., (265)  
 KELLER, J. B., 93, (102), 277, (299)  
 KESHOCK, E. G., 433, (439)  
 KEULEGAN, G. H., (142), 183, (195)  
 KNIGHT, B. A., 433, (439)  
 KOELLE, H. H., (67), (221), (appendix)  
 KOVAL, L. R., 286, (299), 336, (350), 423, (438)  
 KÜCHEMANN, D., (383)

## L

- LAMB, H., (10), 14, 17, 20, (66), 412, 419, (437)  
 LANE, W. R., (436)  
 LANGER, RUDOLPH E., (66)  
 LAWRENCE, H. R., 14, 57, (66)  
 LEADBETTER, S. A., (196)  
 LEE, S.-L., 412, (437)  
 LEONARD, H. W., (67), (141), (142), (194), (195), (221)  
 LEROY, J., 323, 325, (349)  
 LEVICH, V. G., (436)  
 LEVIN, E., (67)  
 LEVY, A. M., 431, 432, (439)  
 LI, Y.-S., 427, (438)  
 LIANIS, G., (350)  
 LIBER, T., 320, (349)  
 LINDHOLM, U. S., (142), (195), 313, 321, 323, 325,  
 (349), (350)  
 LIU, F. C., 130, (142)  
 LOMEN, D. O., (67), 215, (222)  
 LUKENS, D. R., 220, (221), (265)  
 LYERLY, G. A., (appendix)  
 LYNCH, T. F., (384)

## M

- MCCARTY, J. L., 49, (67), (194)  
 McGINNES, H. D., 423, (438)  
 MCKENNA, K. J., (384)  
 MACK, L. R., 277, (299)  
 MAGLIERI, D. J., (195)  
 MASICA, W. J., 408, (437), (438), (appendix)  
 MATHIESSEN, L., 271, (298), (299)  
 MAXWELL, J. C., 391, (436)  
 MERTE, H., 433, (439)

MICHAELS, A. S., (436)

MICHEL, D., (11)

MIKISHEV, G. N., (67), (141)

MILES, J. W., (11), 47, (67), (102), 106, 107, 111, 121, 122, 124, (141), 183, (195), 207, (222), 299, (349)

MILNE-THOMPSON, L. M., (436)

MINNAERT, M., 292, (300)

MIXSON, J. S., (195), (196), 323, 326, (349)

MODISSETTE, J. E., (101)

MOISEYEV, N. N., (11), 83, 85, 86, 87, (101), 271, (299)

MOONEY, J., (66)

MORGAN, H. G., (196)

MOROSOW, G., (196)

MURPHY, G., (194)

MURRAY, T. R., (384)

MYSHKIS, A. D., (11)

### N

NAGANO, M., (350)

NARIMANOV, G. S., (101)

NATUSHKIN, V. F., 332, (350)

NELSON, R. H., Jr., (141)

NELSON, T. M., 419, (437)

NEVILL, G. E., Jr., (194)

NEWTON, D. A., (436)

NOLTING, R. K., (383)

NUSSEL, R. C., 420, 423, (438)

NYQUIST, H., 234, (265)

### O

OEDJOU, D., (299)

OKHOTSIMSKII, D. E., (66), 199, (221)

OLIVER, D. A., 420, (438)

O'NEIL, J. P., 122, 124, (141)

OTTO, E. W., 400, 412, 419, 422, (436), (437), (438), (appendix)

### P

PALMER, J. H., 330, 338, (349)

PARKINSON, W. C., (141)

PAVLI, A. J., (141), (195)

PAVLOV, B. S., 332, (350)

PAYNTER, H. L., 419, (437), (438)

PENNEY, W. G., 10, 87, 90, 92, 93, (102), 277, 278, (299)

PENNINGTON, R. H., 412, (437)

PEPER, H., (appendix)

PERKO, L. M., 423, (438)

PERRY, T. W., (141), (194)

PETRASH, D. A., 400, 419, 420, 422, 423, (436), (437), (438), (appendix)

PETROV, A. A., (11)

PI, W. S., 409, (437)

PINSON, L. D., (383)

PLATT, G. K., (438)

PODE, L., (383)

PONDER, C. A., Jr., (300)

POPE, M. D., (383)

PORTER, R. N., (438)

PRANDTL, L., 374, (383)

PRICE, A. T., (10), 87, 90, 92, 93, (102), 277, 278, (299)

### R

RABINOVICH, F. I., 305, 332, (349), (350)

RADOVICH, N. A., (384)

RAKHIMOV, I. S., 332, (350)

RANEY, J. P., (196)

RANSLEBEN, G. E., Jr., 58, (66), (67), (102), 114, 115, (141), (194), (222), (383)

RATTAYYA, J. V., 51, (66), (222)

RAYLEIGH, J. W. S., (66), 146, (194), 271, (299), 310, 311, 313, 412, (436), (437)

REDDY, R. B., 14, (66)

REID, W. H., (437)

REISSNER, E., 313, 317, 318, 320, 321, 326, (349)

REYNOLDS, J. M., 427, (428)

REYNOLDS, W. C., 387, 408, 410, 411, 412, 416 (436), (437), (appendix)

REX, J., 433, (439)

RHEINFURTH, M. H., (265)

RILEY, J. D., 49, (66)

RING, E., (438)

RODRIGUEZ, A. M., (11), (66), (221)

ROGGE, T. R., 96, (102)

ROSE, R. G., 382, (384)

ROSENBAUM, R., (141)

ROUSE, H., (194), 374, (383)

ROUTH, E. J., 234, (265)

RUBIN, S., 378, (383)

RUMYANTSEV, V. V., (221)

RUNYAN, H. L., (196)

RYAN, J., (66)

### S

SAAD, M. A., 420, (436), (438), (appendix)

SALEME, E., 320, (349)

SALZMAN, J. A., (438)

SANDORFF, P. E., 149, 152, 154, 158, 161, (194), (appendix)

SAMOILOV, E. A., 332, (350)

SATTERLEE, H. M., 387, 402, 408, 412, 416, 426, 427, (436), (437), (438), (439), (appendix)

SAX, N. I., (appendix)

SCANLAN, R. H., (141)

SCHMITT, A. F., 47, (66), 220, (221), (265)

SCHWARTZ, S. H., 433, (439)

SCHY, A. A., (222)

SCOTT, R. B., (appendix)

SCOTT, W. E., (11)

SCRIVEN, L. E., (436), (439)

SECHLER, E. E., (349)

SEEBOLD, J. G., 410, 411, (437)

SEIFERTH, R. W., (383)

SEVERN, W. H., (appendix)

SEWALL, J. L., (11)

SHERLEY, J. E., 433, (439)

SHMAKOV, V. P., 332, (350)

SHRAMO, D. J., (194), (221)

SHULEIKIN, V. V., (437)

SIEGEL, R., 421, 433, (436), (439)

SIEGERT, C. E., 419, (437)

- SILVEIRA, M. A., (141), (142), (195)  
 SILVERMAN, J., 105, (appendix)  
 SIMKIN, D. J., 425, (438)  
 SKALAK, R. 277, (299), 326, (349)  
 SKARTVEDT, G., (439)  
 SLOANE, M. N., (10)  
 SMEAL, G., 234, (265)  
 SMITH, J. M., 427, (438)  
 SMITH, R. D., 418, (437)  
 STANFORD, H. B., (438)  
 STEINLE, H. F., 433, (439), (appendix)  
 STEPHENS, D. G., 49, (67), 110, 136, (141), (142), 158, (194), (195), (221), (383)  
 STERLING, C. V., (439)  
 STEWARTSON, K., (11)  
 STILLWELL, J. J., (11)  
 STOFAN, A. J., 49, 53, (67), 115, (141), (142), (194), (195), (221)  
 STOKER, J. J., (66), (101)  
 STRANGE, W. G., (66)  
 STURM, 234  
 SUMNER, I. E., 53, (67), 132, (141), (142), 158, (194), (195), 205, (221), (222), (appendix)  
 SUMRALL, J. P., (266)  
 SUNDQUIST, K. J., (10)  
 SWALLEY, F. E., (438)
- T
- TADJBAKHSH, I., 93, (102), 277, (299)  
 TAPLIN, A., (11)  
 TAYLOR, G. I., (102), 271, 277, (299), (436)  
 THORP, F. A., (265)  
 TIMMERHAUS, K. D., (439)  
 TIMOSHENKO, S., 317, (349)  
 TOMASSONI, J. E., (383)  
 TONG, P., (350), 418, 420, (437)  
 TREFETHEN, L., 392, 412, (436)  
 TREMBATH, N. W., 49, (66)  
 TROESCH, B. A., 14, (66)

- U
- UNTERBERG, W., (436)  
 URSELL, F., 271, (299)  
 USISKIN, C. M., 433, (439)
- V
- VANDEKOPPEL, R., (439)  
 VANONI, V. A., (10)  
 VASTA, J., (11)  
 VENNARD, J. K., (194)  
 VERMA, G. R., 93, (102), (299)
- W
- WALKER, J. H., (384)  
 WALLS, J., (66)  
 WALTON, W. C., Jr., (67), (194)  
 WANG, C. J., 14, (66)  
 WANG, N. P., 430, (438)  
 WARBURTON, G. B., 311, 313, 317, 323, (349)  
 WARNER, R. W., (221)  
 WEINBAUM, S. 429, (438)  
 WEINSTOCK, R., (437)  
 WEISS, H. J., 96, (102)  
 WELCH, N. E., 427, (438)  
 WERNER, P. W., (10)  
 WESKE, J. R., (383)  
 WESTERGAARD, H. M., (10)  
 WINCH, D. M., (11)  
 WINJE, R. A., (384)  
 WOODWARD, J. H., (222)
- Y
- YARYMOVYCH, M. I., 277, 288, (299)  
 YEH, G. C. K., 286, (299)  
 YU, Y. Y., 330, (350)
- Z
- ZAPPA, R. F., 419, (437)  
 ZHUKOSKII, N. E., 199, (221), 425  
 ZUHOSKI, E. E., (438)  
 ZURMÜHL, R., (265)

## SUBJECT INDEX

### A

Accelerating vehicle  
coordinates for, 16  
pitching motions of, 16  
Acceleration pulse, from exhaust-gas impingement, 361  
Accelerometer  
criteria for, 240  
equation of motion, 231  
gain value, 250  
influence on vehicle stability, 249  
for vehicle stability  
ideal, 247  
nonideal, 248  
Aerodynamic drag, 387  
body forces from, 390  
Agena, 193; *see also* Thor-Agena  
containment sump, 422  
Air resistance during free fall, 435  
Air shaker, 183  
Amplitude; *see* finite amplitude and liquid amplitude  
Amplitude of excitation  
effect  
on damping, 125  
of liquid frequency, 32, 79  
of slosh force in spherical tank, 53  
Analogy, mechanical; *see* mechanical model  
Angle of contact; *see* contact angle  
Annular meniscus, stability of, 409  
Annular tank; *see* cylindrical tank with ring cross section  
Antiroll tank, mechanical model, 203  
Arbitrary cross section, of cylindrical tank, 47  
Arbitrary motions, of circular cylindrical tank, 47  
Asymmetrical plate segment baffles, 120  
Atlas, pogo-type phenomena, 382  
Atmospheric disturbances, vehicle response to, 256

### B

Baffles; *see also* damping and experimental investigation  
asymmetric plate segment, 108, 120  
asymmetric type, 182  
configurations of, 122  
conical section perforated ring, 126  
cross type; *see* cruciform below  
cruciform, 108, 116, 376  
for damping, 108  
effect on  
    liquid frequency, 117, 125, 130  
    liquid impact, 368  
fixed nonring type, 116  
flexible, 134  
floating cans, 115  
floating or movable lid, 107, 117  
for liquid control, 421  
loads on, 107, 125, 130  
partition, 108  
perforated, 130

Baffles—Continued  
screen type, 368, 421  
    for liquid control, 421  
theory for loads on ring, 127  
truncated cone type, 6  
Bandwidth technique, 106  
    for measuring damping, 177  
Beating, during rotary slosh, 99  
Bending vibrations of shell coupled with liquid motions;  
    *see* coupling and cylindrical shell of circular cross  
    section  
Bernoulli's law, 15  
Blast effects; *see* impulsive motion  
Body force; *see also* force  
    from aerodynamic drag, gravitational field gra-  
    dient, and rotational motion, 390  
    electrically induced, 427  
Boiling  
    under low-g conditions, 433  
    nucleate, 428  
Bond number, 388  
    critical, 406  
    for menisci of irregular shape, 406  
    modeling, 434  
Bottoms, of various geometry; *see* cylindrical tank of  
    circular cross section  
Boundaries, for stability; *see* stability boundary  
Boundary conditions  
    linearized, 16  
    for model support systems, 185  
Breaking waves in spherical tank, 97  
Breathing of shell; *see* cylindrical shell of circular cross  
    section  
Bubble(s)  
    behavior and cavitation for longitudinal excitation,  
        290  
    behavior for random longitudinal excitation, 298  
    cluster, 291  
    effect of tank elasticity on cluster, 291  
    entrainment, 270  
    experiments in dynamics of, 290  
    explanation of behavior, 297  
    free, 397  
    motions, 270  
    from nucleate boiling, 428  
    oscillations in zero g, 419  
    pulsations, 292  
    stabilization of, 298  
    surge of, 270  
    theory of vibration, 291  
    velocity of rise in tube, 427  
Buckingham  $\pi$ -theorem, 146  
Bulging modes; *see* cylindrical shell of circular cross  
    section  
Bulkhead of tank; *see* liquid impact, and particular  
    bulkhead geometry  
Buoyancy of bubbles, negative, 290

## C

- Cables for support of model, 186  
 Canal  
   circular, 48  
   conical, 14  
   elliptical, 14  
 Capacitance wire system for measurement of liquid displacement, 175  
 Capillary; *see also* capillary system  
   area defined, 394  
   energies for spherical tank, 398  
   forces, 387  
   hydrostatics, 396  
   phenomena, Laplace's law for, 392  
   potential energy, 396  
   pumping, 422  
   rise rates, 419  
   stability of conical, 407  
   systems supported by, 411  
   thermodynamics, 394  
   waves, 269, 288  
 Capillary system; *see also* capillary  
   Gibbs equation for, 395  
   Helmholtz free energy for, 395  
   instabilities, 412  
   Laplace's law for, 392  
   Maxwell relation for, 395  
   mechanics and thermodynamics of, 391  
   metastable states of, 396  
 Capped liquid in shell  
   comparison of model and full-scale results, 180  
   equivalent rigid body, 199  
 Cavitation  
   of liquid for longitudinal excitation, 290  
   simulation of, 162  
 Cavitation index for  
   cryogenic fuels, 369  
   liquid impact experiments, 369  
 Centaur missile sloshing in liquid oxygen tank, 201  
 Characteristic equation  
   analytical solution, 234  
   techniques for obtaining roots, 233  
 Choked flow at low g, 425  
 Circular canal, 48  
 Circular free surface cross section, 47  
 Circulation, as a measure of vortex strength, 374  
 Closed-loop positive feedback system, 380  
 Cluster of bubbles, 290  
 Clustered tanks  
   damping required, 252  
   effect on stability, 251  
 Compartmentation of tank; *see* cylindrical tank  
 Compressibility of fluid  
   effect of shell vibrations; *see* coupling and cylindrical shell of circular cross section  
   simulation of, 1962  
 Complex mechanical model; *see* mechanical model  
 Complex plane; *see* root locus plane  
 Concentric tanks, stability boundaries for vehicle with, 252  
 Condensing in zero g, 434  
 Conical bottom, in cylindrical tank, 47, 58  
 Conical bulkhead, liquid impact on, 364, 365  
 Conical canal, 14  
 Conical capillaries, stability of, 407  
 Conical pendulum for rotary slosh, 99, 207  
 Conical-section baffles, 126  
 Conical tank, 14, 57  
   mechanical model, 205, 215  
   viscous damping in, 113  
 Contact angle, 392  
   advancing defined, 393  
   hysteresis effect on zero-g lateral sloshing, 418  
   hysteresis of, 393  
   values for, appendix  
 Container; *see also* vehicle, canal, and particular container configuration  
   flexible, 107, 115, 425  
 Container geometry; *see also* vehicle, canal and particular container configuration  
   effect on stability, 251  
 Control and positioning of liquid at low g, 420; *see also* expulsion  
 Control and stability of vehicle; *see* stability and control  
 Control system; *see also* stability and control  
   control factor for, 343  
   damping, 247, 343  
   effect on mass center, 225  
   equation of motion, 230, 232, 340  
   lateral bending, 225  
   liquid motion, 223  
   phase lag coefficients, 230  
   vehicle attitude, 225  
 Conversion factors, viii  
 Convection in propellant tanks, 433  
 Convection patterns from surface tension at zero g, 431  
 Convective processes, onset and strength of, 429  
 Coordinate  
   generalized, 229  
   for linear theory, 15  
 Coriolis force, effect on vortex formation, 374  
 Coupled liquid pressure modes, 321  
 Coupled response of vehicle umbilical tower, 190  
 Coupling; *see also* cylindrical shell of circular cross section and nonlinear  
   of compressible fluid motion with shell breathing vibrations, 318  
   between engine and structure, 379  
   fixed for, 381  
   of incompressible liquid motion with shell breathing vibrations, 321, 330  
   of light compressible fluid with breathing vibrations, 317  
   of liquid and elastic shell, model study, 190  
   between liquid and elastic structure, 179, 180, 303, 309, 316, 321, 334, 336, 418

- Coupling—Continued**
- of liquid motion and elastic tank bottom, 336
  - of liquid and rigid tank motions, 180
  - of liquid and shell motions, inertial coupling coefficient, 306
  - of liquid and shell motions nonlinear effects, 332 at low g, 418
  - mechanical model for engine-structure, 379, 381 between structure and pneumatic tank pressure regulation system, 269, 378, 382
- Criteria for vehicle stability**, 236; *see also* stability
- Critical damping**, 106
- Crossflow drag coefficient**, 356
- Cryogenic fuels**, cavitation index for, 369; *see also* appendix for fuel properties
- Cryogenic tanks**, heat transfer in, 431
- Cylinder**, covered by liquid film at zero g, 412
- Cylindrical shell of circular cross section**; *see also* liquid impact, experimental investigation, damping, coupling and longitudinal excitation
  - breathing vibrations
  - coupled with
    - compressible fluid motions, 318
    - incompressible fluid motions, 321, 330
    - light compressible fluid motions, 317
  - effect of
    - liquid inertia and compressible, 180, 315, 320
    - pressurization and liquid on, 323
  - of empty shell, 309, 310
  - subharmonic response of shell, 333, 334
- bulging modes**, 330
- containing liquid and longitudinally excited**, 280, 285, 326, 334
- containing liquid and unpressurized**, frequencies for, 323
- Donnell equations** for, 310
- with elastic bottom**, 286, 336
- mechanical model** for, 220
- nonlinear liquid-shell coupling**, 306, 333, 334
- pressurized**, 317, 318, 323
- Cylindrical tank**; *see also* liquid impact, experimental investigation, damping, coupling, and longitudinal excitation
  - with annular cross section: *see* ring cross section, below
  - arbitrary cross section, 47
  - of circular cross section
    - arbitrary rigid body motions of, 47
    - effects of ellipticity of the cross section, 14, 47
    - equivalent flat bottom for, 14, 47
    - floating devices for damping, 107
    - free surface modes of, 7
    - harmonic and superharmonic liquid response to longitudinal excitation, 284, 285
    - with hemispherical ends, 47, 110, 332, 366, 400
    - jump phenomena in, 97
    - liquid stability diagram for longitudinal excitation, 273
- Cylindrical tank—Continued**
- of circular cross section—Continued
    - mass moment of inertia of fluid, 211
    - mechanical model for, 203, 208, 220
    - nonlinear effects in, 97
      - compartmented, 79, 80
    - nonlinear liquid motions from lateral excitation, 93
    - reorientation time estimates, 419
    - ring damping theory, 122
    - with spherical bottom, 47, 110
    - with splitter plate, 96
    - subharmonic liquid response to longitudinal excitation, 269, 270, 274, 280, 281, 283
    - with conical bottom, 47, 58
    - with elliptical cross section, 14, 47
    - with 45° sector cross section, 29
    - liquid response to longitudinal excitation, 271
    - with 90° sector cross section, 30, 211, 283
    - with perforated compartments, equivalent Reynolds number for, 80
    - with quarter sector cross section, mechanical model for, 211
    - with ring cross section, 33, 36, 38, 41, 43, 419
      - mechanical model for, 211
      - reorientation time estimates, 419
    - with ring sector cross section, 20–23, 26
    - of sector cross section, 20, 29, 34
    - with 60° sector cross section, 32

**D****Damping**

- of accelerometer, 231
- by baffles
  - asymmetrical plate segment, 120
  - cruciform, 116
  - fixed nonring, 116
  - fixed ring, 107, 121, 127, 183
  - flexible, 107, 115, 134
  - movable or liquid surface devices, 107, 114, 115, 117
  - partition, 108
  - perforated, 130
  - two-dimensional (asymmetric), 182
- calculated by
  - bandwidth technique, 177
  - the forced response method, 177
  - Miles' theory, 183
- in circular cylindrical tank with spherical bottom, 110
- comparison of model and full-scale results, 187; *see also* experimental investigation
- in conical tank, 113
- of control systems, 247, 343
- critical, 106
- in cylindrical tank, 109, 110
  - theory, 122
  - by dampometer, 176

- Damping—Continued  
 dependence on  
     excitation amplitude, 125  
     liquid amplitude, 106, 110, 113  
     effect of efflux rate draining, 111, 181  
 effect on  
     liquid mass moment of inertia, 217  
     liquid stability boundaries, 273, 284  
     surface tension, 110  
     equivalent viscous, 106  
     experimental techniques, for determination of, 106  
     general discussion, 105  
     introduction into  
         mechanical model, 200, 215  
         vehicle equations of motion, 105, 227  
 in oblate spheroidal tank, 111, 130, 131  
 of pitching motion, 181  
 required  
     clustered tanks, 252  
     to predict "jump down," 283  
     for vehicle stability and control, chapter 7, 339  
 in sector cylindrical tank, 117  
 significant variables, 107  
 in spherical tank, 110, 111, 115, 131, 132  
 in spheroidal tank, 111, 130, 131  
 strip theory for, 182  
 structural, for vehicle stability and control, 342  
 subcritical, 342  
 supercritical, 343  
 theory, for ring, 107, 122, 183  
 in toroidal tank, 114  
 of vehicle, 227  
 viscous  
     in circular cylindrical tank, 109  
     in conical tank, 113  
     effect on oscillations of a liquid sphere, 419  
     equivalent, 106, 227  
     by flexible bags and diaphragms, 107, 115  
     for spherical tank, 111, 112  
     in toroidal tank, 114
- Dampometer for measuring damping, 176  
 Dangerous liquids, handling of, appendix  
 Density requirements for simulation, 151  
 Determinant, positive roots of, 22  
 Decrement; *see* logarithmic  
 Diaphragms for damping, 107, 115  
 Dielectrophoresis, 427  
 Diffusion of two ideal-gas species, governing equation for, 430  
 Dimensional analysis, 145; *see also* simulation  
     applied to simulation, 148  
 Displacements of liquid; *see* text in chapter 2 under particular tank configuration and excitation of interest  
 Dissimilar structural material modeling, 153  
 Dissipation function; *see* damping  
 Docking impact, 6, 353; *see also* liquid impact  
 Dome impact, 6, 353; *see also* liquid impact  
     experimental techniques to measure, 179  
     pressure measurements, 170, 179
- Donnell equations for circular cylindrical shell, 310  
 Drag  
     aerodynamic, 387, 390  
     coefficient for crossflow, 356  
     decelerations, 387  
     shield for free fall experiments, 435
- Draining  
     effect of damping, 111, 181  
     gas ingestion while, 377  
     liquid rotation and vortexing while, 9, 373  
     at low g, 420
- Drain-rate criteria, maximum, 424
- Droplets, 288
- Drop oscillations in zero g, 419
- Duration of experiment for liquid impact, 370
- Dynamically similar model, testing of, 184; *see also* simulation
- Dynamic  
     model study of propellant coupling with structure, 190  
     stability; *see* stability  
     surface tension, 392
- Dynamics of bubble motion, 293
- E**
- Efflux rate; *see* draining
- Eigenvalue; *see* characteristic equation
- Elastic bottom, response of liquid in tank with, 286, 336
- Elastic shell; *see* cylindrical shell of circular cross section, coupling, and stability
- Elastic structure; *see* cylindrical shell of circular cross section, coupling, and stability
- Elastic vehicle; *see* cylindrical shell of circular cross section, coupling, and stability
- Elastic vibrations; *see* cylindrical shell of circular cross section, coupling, and stability
- Elasticity of shells; *see* cylindrical shell of circular cross section, coupling, and stability
- Electrically induced body forces for liquid control, 427
- Ellipsoidal bulkhead, liquid impact on, 366
- Ellipsoidal tank, mechanical model, 213
- Elliptic cross section  
     cylindrical tank with, 14, 47  
     of free surface, 47, 61
- Elliptical canal, 14
- Energy dissipation; *see* damping
- Energy transport  
     within a cryogenic tank, 431  
     at low g, 429  
     mechanism for, 430
- Engine-structure coupling; *see* coupling
- Entrained vapor in liquid, 270
- Equations  
     empirical for frequency  
         in spherical tank, 51  
         in spheroidal tank, 61  
     governing diffusion of gases, 430

- Equations—Continued  
 of motion for  
     accelerometer, 231  
     bending, 229  
     control system, 230  
     control; *see* equations of motion for vehicle  
     elastic body, 226  
     liquid, 229  
     pitching vehicle, 229  
     rate gyroscope, 232  
     vehicle, 105, 227, 232, 243, 340  
 for trajectory analysis, 354  
 for vehicle stability, 243
- Equivalent flat bottom, circular cylindrical tank with, 14, 47
- Equivalent linear conical pendulum, 99
- Equivalent mechanical model; *see* mechanical model
- Equivalent rigid body, replacement of liquid by, 199
- Equivalent Reynolds number for  
     conical-section perforated ring baffles, 127  
     perforated sector cylindrical tank, 80, 117
- Euler constant, 26
- Excitation amplitude; *see* amplitude of excitation
- Excitation frequency; *see* longitudinal excitation
- Exhaust-gas impingement, simulation of, 361
- Experimental derivation of mechanical model parameters, 201
- Experimental investigation  
     baffle loads, 130  
     bubble dynamics, 290  
     bubble stabilization, 298  
     canal, circular, 47, 48  
     circular cylindrical tank  
         bending, comparison of model and full scale, 187  
         breathing vibrations, 322, 326, 331, 333  
         bubble behavior, 290, 298  
         compartmented, 30, 79, 117  
         with conical bottom, 47  
         coupled liquid-shell bending, 308  
         clamping, 107, 110, 124; *see also* damping  
         with elastic bottom, 339  
         frequencies for empty shell, 314  
         liquid stability boundaries, 275  
         with perforated sector compartments, 117  
         pressurized and liquid filled, 319, 325, 326, 327, 331, 333  
         with ring baffles, 107, 108, 124, 126  
         shell bending  
             comparison of model and full scale, 187  
             frequency for capped liquid, 308, 309  
         with spherical bottom, 47  
         subharmonic liquid response to longitudinal excitation, 275, 280–282, 285, 286, 288  
         superharmonic liquid response to longitudinal excitation, 286  
     conical tank, 47, 57, 113, 364  
     cruciform baffle over drain, 376  
     cylindrical tank of 90° sector, 283
- Experimental investigation—Continued  
 damping  
     by asymmetric plate segment baffles, 120  
     by cruciform baffles, 116  
     by expulsion bags and diaphragms, 115  
     by flexible baffles, 136  
     by floating  
         cans, 115  
         lids, 114  
     by perforated sector compartments, 117  
     by ring baffles, 107, 108, 124, 126, 130, 131, 136  
     viscous, 110, 113, 114  
 flexible baffles, 136  
 frequency reversal, 93  
 liquid impact  
     on conical bulkhead, 364  
     on ellipsoidal bulkhead, 366  
     pressures, 365, 369  
     on spherical bulkhead, 364  
     time duration, 369  
 liquid positioning in Mercury MA-1, 420
- nonlinear  
     coupling between liquid and shell, 335  
     liquid motion in spherical tank, 97  
     nucleate boiling at zero g, 433  
     planar and nonplanar liquid motion, 100  
     rectangular tank, 89, 92  
     reorientation time, 419  
     review of work related to liquid impact, 362  
     spherical tank, 47, 50, 53, 82, 97, 110, 116, 131, 136, 173, 284, 364, 433  
     swirl motion, 101  
     tank draining, 376  
         at high bond number, 425  
     toroidal tank, 54, 114, 174  
     zero-g liquid sloshing, 417
- Experimental techniques  
     apparatus for simulation, 170  
     to determine damping, 106  
     harness for model experiments, 186  
     for low-g simulation, 434  
     to measure  
         dome impact pressures, 179  
         forces during swirl, 179  
         liquid displacements by  
             capacitance wire system, 175  
             concentric float, 176  
             load cell, 173, 176  
             pressure pickup, 176  
             strain gauge bridge, 173  
             torque bar, 173  
             visual and photographic means, 171  
     of tank  
         construction, 170  
         support and excitation, 171
- Explosion, effects on liquid-filled tanks, 2, 13
- Expulsion bags for damping, 107, 115, 425

Expulsion of  
liquids at low g, 423  
vapor at low g, 425

Extensional vibrations, Rayleigh's theory, 310

## F

Feedback conditions, adverse, 236

Feedback loops, 380

between structure and control system, 225

Finite amplitude; *see also* longitudinal excitation  
harmonic and superharmonic liquid response, 284,  
285

stable wave, theory for rectangular tank, 87

standing wave, 270, 277

stationary oscillations in

axisymmetric tank, 353

rectangular tank, 87

Finite differences applied to spherical tank, 49

Fireball resulting from bulkhead impact, 353

Flexible baffles, 134

Flexible containment device, 107, 115

for positive expulsion, 425

Flexible shell; *see* coupling, cylindrical shell of circular cross section and stability

Flexible vehicle; *see* coupling, cylindrical shell of circular cross section and stability

Floating cans, lids or mats for damping, 107, 115

Force; *see also* liquid force and pressure

from atmospheric disturbances, 256

body, 390, 427

on bulkhead from liquid impact, 367, 368

electrically induced, 427

from engine thrust, 228

on ring baffles; *see* baffles

simulation of; *see* simulation

virtual work by, 228

Young's equation for interface, 393

Force response method of measuring damping, 174

Forced oscillations at low g, 420

Forming techniques for tank construction, 171

Free-fall simulation, 435

Free surface

coupling with shell bottom, 336

devices for damping, 114

displacements; *see* text in chapter 2 under particular

tank configuration and excitation of interest

effects on coupled liquid-shell motions; *see* coupling

and cylindrical shell of circular cross section

with elliptical planform, 14, 47, 61

equation of, 16

response to longitudinal excitation; *see* longitudinal excitation

stability; *see* stability

Frequency; *see also* liquid frequency and cylindrical shell of circular cross section

reversal, experimental verification of, 93

of shell with free and capped liquid surfaces, 180

variation with flight time, 5

Froude number, 390

Fuel; *see* liquid

## G

Gain values of accelerometer, 250

Gamma function, 26

Gas

diffusion, 430

ingestion, 377

simulation of impingement, 361

Generalized coordinate, 229

Gibbs equation for capillary system, 395

Gravitational field gradient, body forces resulting from, 390

Gravitational potential energy of capillary system, 396

Gravity

low; *see* low g

simulation of earth's, 186

zero; *see* zero g

Gravity draining, vortex during, 9

Gust loads, vehicle response to, 256

Gyroscope

criteria for position of, 237

equation of rotation, 232

preferable position for, 343

transfer function for, 231

use in control system equations, 230

## H

Handling liquid at low g, 420

Hardware, effect on model parameters, 203

Harness for model experiments, 186

Heat transfer

by convection in tanks, 433

in cryogenic tanks, 431

to liquids at low g, 428

Helmholtz free energy, for capillary system, 395

Hemispherical; *see* spherical bulkhead and spherical tank

Hurwitz

criteria for stability, 234

determinant, 341

stability polynomial, 341

Hydrodynamic loading on shell, 316

Hydrodynamics at low g, 387

Hydrostatics at low g, 386, 387

Hyperboloidal tank, 14

Hysteresis of contact angle, 393

effect on zero-g lateral sloshing, 418

## I

Ingestion of gas during draining, 377

Impact, 353; *see also* liquid impact

Impingement of exhaust gas, 361

Impulsive motion, tank subjected to, 2, 13

Incompressible liquid motions coupled with tank breathing vibrations, 321, 330; *see also* cylindrical shell of circular cross section and coupling

- Inertia coupling coefficient for coupled liquid-shell motions, 306
- I**
- Inertia
- of fluid, effect on tank breathing vibrations, 316, 320; *see also* coupling of liquid, effect of damping on, 217
  - moment of; *see* moment of inertia of liquid simulation; *see* simulation
- Inertial parameters of equivalent mechanical model, 200
- Inextensional vibrations, Rayleigh's theory, 310
- Instability; *see also* stability
- in capillary-supported systems, 411, 412
  - criterion for large amplitude stationary waves in rectangular tank, 92
  - of liquid
    - during dielectrophoresis, 428
    - for longitudinal excitation; *see* longitudinal excitation
    - Rayleigh-Taylor type, 271
  - in liquid response, 334
  - regions, subharmonic; *see* longitudinal excitation
  - Saturn I, 2, 4
- Interaction; *see* coupling and cylindrical shell of circular cross section
- Interface stability, 403
- Interfacial effects, simulation of, 162
- Interfacial force, Young's equation for, 393
- Interfacial (surface) tension, 392
- Internal hardware, effect on model parameters, 203
- Internal pressure, comparison of theoretical and experimental frequencies of shells with, 316-319; *see also* cylindrical shell of circular cross sections, and coupling
- Inverted meniscus, 407
- J**
- Jump phenomenon in circular cylindrical tank, 96
- K**
- Kinetic energy of
- empty structure, 226, 347
  - liquid, 226, 347
- L**
- Large amplitude; *see* finite amplitude
- Laplace
- constant, 388
  - equation, in rectangular coordinates, 15
  - law for capillary phenomena, 392
- Liquid(s)
- behavior
    - at low g and zero g; *see* low g and zero g during reorientation, 426
  - displacement measurement techniques; *see* experimental techniques
  - draining; *see* draining
- Liquid(s)—Continued
- effect on
    - damping of amplitude
    - shell vibrations; *see* cylindrical shell of circular cross section and coupling
    - equation of motion, 229
    - equivalent rigid body for, 199
    - expulsion; *see* expulsion
    - film on sphere and cylindrical at zero g, 412
    - force; *see also* text in chapter 2 under particular tank configuration and excitation of interest; force
      - for nonlinear liquid rotational motion, 95
      - measurement of, 178
      - on shell, 316; *see also* coupling and cylindrical shell of circular cross section
    - free surface; *see* free surface
  - frequency; *see also* text in chapter 2 under particular tank configuration
    - dependence on excitation amplitude, 32, 79
    - sensitivity of, 14
    - variation
      - with baffle location, 125, 134
      - in circular cylindrical tank, 125
      - with depth in cylindrical tank, 13
      - in perforated sector compartmented cylindrical tank, 117
  - impact, 353, 368, 426
    - on conical bulkhead, 364, 365
    - duration of experiments, 369
    - effect of
      - baffles on, 368
      - lateral sloshing and lateral acceleration, 371
    - on ellipsoidal bulkhead, 366
  - experimental
    - techniques, 179
    - work, 362
  - fireball resulting from, 353
  - force on bulkhead, 367, 368
  - pressures
    - resulting from, 362-366
    - variation with acceleration, 370
  - resulting from
    - docking, 6, 353
    - thrust termination, 353
    - simulation of, 362, 368, 369
    - on spherical bulkhead, 364, 366
    - structural breakup from, 363
    - summary, 368
  - inertia and compressibility, effect on shell vibrations; *see* coupling and cylindrical shell of circular cross section
  - instability; *see* instability and stability
  - kinematic viscosity
    - effect on force in spherical tank, 53
    - simulation of, 162
    - values for typical model fluids and propellants, appendix

- Liquid(s)—Continued  
 location by dielectrophoresis, 427  
 mass moment of inertia for cylindrical tank, 211  
 oxygen (LOX), 191  
 pressure; *see also* force  
   distribution; *see* text in chapter 2 under particular tank configuration and excitation of interest  
   modes, 320, 321; *see also* cylindrical shell of circular cross section  
 properties; *see* particular property and appendix for numerical values  
 response to longitudinal excitation: *see* longitudinal excitation  
 rotary slosh  
   bearing during, 99  
   pendulum analogy, 207  
   swirl motion, 97  
 rotation  
   during draining; *see* draining  
   roll torque from 373, 376  
 safety with, appendix  
 separation by nonwetting screens, 427  
 simulation; *see* simulation  
 sloshing  
   defined, 6  
   influenced on vehicle; *see* stability and control  
   simulation of; *see* simulation  
   at zero g; *see* zero g  
 stability; *see* stability  
 subharmonic response to longitudinal excitation; *see* longitudinal excitation  
 swirl; *see* swirl  
 vortexing; *see* simulation  
 Literature  
   other than English language, 8  
   on safety, appendix  
 Load cell to measure liquid motion, 173, 176  
 Loads; *see* force  
 Locus-curve method of determining stability, 235  
 Logarithmic decrement  
   defined, 105  
   to measure damping, 174  
   for viscous damping in circular cylindrical tank, 109  
 Longitudinal excitation; *see also* coupling, cylindrical tank of circular cross section, cylindrical shell of circular cross section, and stability  
   bubble behavior; *see* bubbles  
   cavitation of liquid, 290  
   of circular cylindrical tank, 269, 270, 274, 280, 281, 283, 285, 326, 334  
   at high frequency, 288  
   linearized theory, 269, 271  
   liquid response to, 269, 274, 280, 284, 285, 286, 288  
   Mathieu equation for, 271  
   mechanical model for, 287  
   of 90° sector cylindrical tank, 283  
   pogo phenomena, 269, 378, 382  
   random, 298  
   of rectangular tank, 278
- Longitudinal excitation—Continued  
 of spherical tank, 284  
 stability chart, 273  
 summary, 284  
 superharmonic response, 285  
 Loops; *see* feedback loops  
 Low g; *see also* zero g  
   behavior of liquid at, 387  
   boiling at, 433  
   draining at, 420  
   expulsion of vapor and liquid, 423, 425  
   forced oscillations at, 420  
   free fall simulation, 435  
   gas ingestion, 377  
   heat transfer to liquid, 428  
   hydrodynamics and hydrostatics, 386, 387  
 liquid  
   configuration, 396  
   energy transfer, 429  
   handling, 420  
   positioning and control, 420, 421  
   temperature control, 429  
 maximum  
   acceleration for liquid control, 421  
   flow rate, 425  
 orbital and suborbital systems to obtain, 436  
 phenomena, 6  
 positive expulsion devices, 425  
 response time estimates, 391  
 rotating tanks in, 411  
 simulation of, 434, 435  
 sloshing, 412  
   elastic tank interactions, 418  
   estimating methods, 418  
   general formulation for, 413  
   solution for a special case, 415  
   the linearized problem, 414  
   time required to gain control of liquid, 421  
   a variation formulation, 416  
   Weber number modeling, 434  
 LOX (liquid oxygen), 191  
 Lunar excursion module (LEM), 191  
 LUT (launch umbilical tower), 191
- M**
- Magnification factors for liquid force and moment; *see* text in chapter 2 under particular tank configuration and excitation of interest  
 Mass; *see also* liquid mass  
   conservation law, 15  
   density requirements for simulation, 151  
 Material properties, simulation of, 153  
 Mathieu equation for longitudinal excitation, 271  
 Maxwell relation for capillary system, 395  
 Measurement of; *see also* experimental techniques  
   damping with a Dampometer, 176  
   dome impact pressures, 170, 179  
   liquid forces, apparatus for, 178

- Measurements of—Continued  
 liquid motion, 171, 173, 176  
     types of transducers used, 175  
     with strain gauge bridge, 173  
 swirl forces, experimental techniques, 179
- Mechanical model  
 annular cylindrical tank, 211  
 antiroll tank, 203  
 calculation of parameters, 201  
 circular cylindrical  
     shell, 220  
     tank, 203, 208, 220  
 conical tank, 205, 215  
 effect of internal hardware, 203  
 elastic shell, 218  
 ellipsoidal tank, 213  
 engine-structure coupling, 379, 381  
 experimental derivation of parameters, 201  
 inertial parameters of, 200  
 introduction  
     of damping, 200, 215  
     into vehicle equations of motion, 339  
 lateral sloshing, 199  
 longitudinal excitation, 287  
 with moment of inertia damping, 218  
 nonlinear, 207, 214  
 oblate spheroidal tank, 202, 213  
 pendulum type, 201  
 rectangular tank, 203  
 representation of sloshing, 199  
 restrictions to their use, 206  
 spherical tank, 205, 214, 218  
 spheroidal tank, 202, 213
- Mechanics of capillary system, 391
- Membrane, bottom of rigid tank, 336
- Meniscus, 388  
 bond number for, 406  
 in capillary-supported systems, 411  
 differential equation for, 401  
 inverted, 407  
 in inverted tube, 404  
 reorientation time estimates, 419  
 rotating, 410  
 shape and stability of axisymmetric, 401, 402, 410  
 in spherical tank at zero g, 399, 404, 405  
 stability of, 402, 405  
     flat annular, 409  
 support pressures required, 411  
 system in zero g, parallel, 400
- Mercury MA-7, liquid positioning experiment, 420
- Mesh, conical screen type, 421
- Metastable states of capillary system, 396
- Model; *see also* simulation and mechanical model  
 dynamically similar, 184, 191  
 harness for, 186  
 mechanical; *see* mechanical model  
 propellants, 185, appendix  
 replica, 153  
 support systems, 185  
 vibration testing of, 184
- Modeling; *see* simulation
- Moment; *see* liquid moment
- Moment of inertia of liquid; *see also* inertia  
 in cylindrical tank, 211  
 effect of damping on, 217, 218
- Motions, arbitrary, 47
- Mulberry harbors, 1
- N**
- Negative buoyancy of bubbles, 290
- New mode of oscillation in oblate spheroidal tank, 61
- Newton's second law, 15
- Nonlinear  
 coupling between liquid and shell, 325, 333–336;  
     *see also* coupling and cylindrical shell of circular  
     cross section  
 effects, 97  
     arising from large amplitude liquid motions, 82  
     from compartmentation, 80  
     from excitation amplitude, 79  
     in rectangular tank, 82  
     in spherical tank, 82  
     from tank geometry, 79  
 liquid motions in circular cylindrical tank, 79, 80,  
     93, 97; *see also* coupling and cylindrical tank of  
     circular cross section  
 mechanical model, 207, 214  
 rotary motion, 100  
 softening in circular cylindrical tank, 96
- Nonwetting liquid, defined, 392
- Nucleate boiling, 428, 433
- O**
- Oblate spheroidal tank, 47, 58, 60, 174  
 damping in, 111  
 mechanical model, 202, 213  
 new mode of liquid oscillation, 61
- Oscillations; *see also* liquid, force, and cylindrical shell  
 of circular cross section  
 finite; *see* finite amplitude  
 free; *see* text in chapter 2 under particular tank  
 configuration; *see also* liquid frequencies
- P**
- Parabolic tank, 14
- Passive antiroll tank, mechanical model, 203
- Partition baffles, 108
- Pendulum  
 analogy for  
     rotary sloshing, 207  
     spherical tank, 205  
 equivalent linear conical, 99  
 type mechanical model, 201
- Pendular tank support, 171
- Perforated  
 material for liquid wetting, 421  
 partitioned cylindrical tank, equivalent Reynolds  
     number for, 117  
 sector cylindrical tank, 80

- Phase-lag coefficient, 342  
for control system, 230
- Pitching motion  
of an accelerating vehicle, 16  
damping of, 181  
equations of motion of vehicle with, 229
- $\pi$ -theorem, 146
- Planar motion, 100
- Plate  
bottom of rigid tank, 336  
segment baffles asymmetric, 120
- Pneumatic regulation system, coupling with longitudinal structure oscillations, 378, 382  
vehicle structure, 269
- Pogo phenomena, 269, 378, 382
- Poisson equation, 17
- Polynomial, stability type, 237
- Positive expulsion devices at low g, 425
- Potential, velocity, 15, 16
- Potential energy of  
liquid, 227, 347  
structure, 227, 347
- Pressure; *see also* force  
on conical bulkhead during impact, 365  
distribution during lateral sloshing, 14  
forces required for meniscus support, 411  
measurement of during dome impact, 170, 179  
resulting from liquid impact, 362  
simulation of, 152
- Pressure modes of oscillation in circular cylindrical tank, 316, 320; *see also* cylindrical shell of circular cross section
- Pressure pickups for measurement of liquid displacements, 176
- Pressure regulator-structure coupling, 382
- Pressurization, of shell; *see* cylindrical shell of circular cross section
- Projectile, spin-stabilized, 2
- Propellant; *see also* appendix for typical properties and liquid  
model study of coupling with structure, 190  
simulation in dynamic models, 185
- Properties of liquid, appendix
- Pulsations, of bubble, 292
- Q**
- Quarter-tank; *see* cylindrical tank with 90° sector
- R**
- Random longitudinal acceleration of tank, bubble behavior for, 298
- Rate gyroscope; *see* gyroscope
- Rayleigh number, 429
- Rayleigh's theory for extensional and inextensional vibrations, 310
- Rectangular tank  
for antroll, 203  
finite stationary oscillations in, 87
- Rectangular tank—Continued  
instability criterion, 92  
lateral excitation, 17, 18  
longitudinal excitation, 278  
low gravity in, 18  
mechanical model, 203, 211  
nonlinear response characteristics, 82  
wave frequency as a function of wave amplitude, 87
- Reissner's shallow shell theory, 310, 317
- Reorientation  
liquid behavior during, 426  
time estimates, 419
- Replica and dynamically similar models, 153; *see also* simulation testing of, 184
- Reversal of frequency, experimental verification of, 93
- Reynolds number  
equivalent for  
conical section perforated ring baffles, 127  
45°, 60°, and 90° perforated compartmented cylindrical tanks, 80, 117  
modeling at low g, 434
- Rigid body, equivalent for capped liquid, 199
- Rigid body stability; *see* stability
- Rigid vehicle; *see* stability
- Ring baffles; *see* baffles
- Ring damping; *see* damping
- Ring tank; *see* cylindrical tank with ring cross section
- Rocket; *see* vehicle and particular vehicle geometry
- Roll torque resulting from liquid rotation, 373, 376
- Root  
of determinant, 22  
stability, 233
- Root locus plane, 233
- Rotary slosh; *see* liquid rotary slosh
- Rotating tank at low g, 411
- Rotational motion  
body forces resulting from, 390  
instantaneous center of, 339
- S**
- Safety with liquid, appendix
- Saturn I  
example problem of vehicle stability and control, 263  
flight instability, 2, 4
- Saturn V  
 $\frac{1}{10}$ -scale dynamic model of, 191  
 $\frac{1}{4}$ -scale model, 186, 189, 190  
support system for  $\frac{1}{4}$ -scale model of, 187
- Saturn SA-1  
model and full-scale test comparison, 187  
 $\frac{1}{8}$ -scale dynamic model, 186  
support system for  $\frac{1}{8}$ -scale model, 187
- Scaling; *see* simulation
- Scalloped tanks, 4
- Screen baffle  
effect on liquid impact force, 368  
for liquid control, 421
- Screens, nonwetting for liquid separation, 427

- Sector tank; *see* cylindrical tank  
 Shaker, air, 183  
 Shell; *see also* particular shell configuration, coupling, and vehicle  
     shallow, Reissner equations for, 310, 317  
 Ship stabilization in roll, 2, 203  
 Simulation; *see also* model  
     of bond number, 434  
     of cavitation, 162  
     of dependent variables, forces, pressures, and response parameters, 152  
     dimensional analyses applied to, 148  
     with dissimilar structural materials, 153  
     of dynamic properties of liquids, 157  
     of earth's gravitational field, 186  
     of exhaust-gas impingement, 361  
     experimental techniques and apparatus, 170;  
         *see also* experimental techniques  
     geometrical consideration, 150  
     of interfacial effects, 162  
     of liquid  
         compressibility, 161  
         kinematic viscosity, 159  
         impact, 361, 362, 368, 369  
         interfacial effects, 162  
         sloshing, 145, 149  
         surface tension, 163  
     liquids for, 185, appendix  
     of low-g environments, 434  
     mass density requirements, 151  
     models for; *see* model  
     of prototype propellant, 185  
     with replica models, 153  
     of scaling effects for liquid impact, 369  
     simultaneous satisfaction of scaling criteria, 166  
     of structural material properties, 153  
     summary of inertial and mechanical scaling, 152  
     using free fall techniques, 435  
     of Weber number, 434  
 Sinking bubbles for longitudinal excitation; *see* longitudinal excitation  
 Sloshing; *see* liquid sloshing  
 Small amplitude liquid motions for longitudinal excitation, 285, 286; *see also* longitudinal excitation  
 Softening in circular cylindrical tank nonlinear, 96  
 Sphere  
     covered by liquid film at zero g, 412  
     of liquid, effect of viscous damping on, 419  
     for low-g wetting experiments, 421  
 Spherical bulkhead; *see also* spherical tank  
     in circular cylindrical tank, 47, 110, 332, 366, 400  
     liquid impact on, 364, 366  
 Spherical tank, 49; *see also* spherical bulkhead and experimental investigation  
     breaking waves in, 97  
     capillary energies, 398  
     damping by  
         expulsion bags and diaphragms, 115  
         ring baffles, 131, 132  
     free surface modes of, 7  
 Spherical tank—Continued  
     measurement of liquid force, 53, 178  
     mechanical model, 205, 214, 218  
     meniscus configuration at zero g, 399, 404, 405  
     modal parameters for, 53  
     nonlinear effects in, 82  
     reorientation time estimates, 419  
     with splitter plate, 96, 97  
     subharmonic response of liquid to longitudinal excitation, 284  
     viscous, 110, 111  
 Spheroidal tank; *see also* oblate spheroidal tank  
     damping in, 111, 130, 131  
     measurement of liquid force, 178  
     mechanical model, 202, 213  
 Splitter plate in  
     circular cylindrical tank, 96  
     spherical tank, 96, 97  
 Spray formation from high frequency excitation, 288  
 Spray-formed wave, 270  
 Spray surface, 6, 9, 288  
 Stable harmonic liquid motion for longitudinal excitation, 285; *see also* longitudinal excitation  
 Stable nonlinear (rotary) motion, 100  
 Stability; *see also* instability and stability and control  
     aerodynamic, 361  
     of axisymmetric meniscus, 402, 410, 450  
     boundary for liquid  
         effect of damping, 273, 284  
         experimentally determined, 275  
     boundary for vehicle; *see* stability of vehicle  
     of conical capillary, 407  
     of flat annular meniscus, 409  
     interfacial, 403  
     of liquid  
         film on sphere and cylinder at zero g, 412  
         free surface, 6, 95, 97, 100; *also see* longitudinal excitation  
     by locus-curve method, 235  
     polynomial, 237  
     of rigid vehicle; *see also* stability of vehicle  
         without accelerometer control, 246  
         with ideal accelerometer, 247  
         with nonideal accelerometer control, 248  
     root, 233  
     of vehicle, 233, 235, 240, 252, 340; *see also* stability of rigid vehicle  
         bending mode, 239, 242  
         effect of tank geometry and location, 251, 252  
         general criteria, 236  
         with liquid sloshing, 243, 252  
         with quarter tank, 254  
         with sector tank, 254  
         subjected to wind loads, 257  
         with tandem tank arrangement, 254, 256  
 Stability and control; *see also* control system and stability  
     control factor for attitude control, 343  
     damping required for; *see* chapter 7  
     effects of elastic structure on, 338

- Stability and control—Continued  
     example problem, 263  
     of vehicle, 225, 233, 252, 340
- Stabilization  
     of bubbles, 298; *see also* bubbles  
     of ships in roll, 2, 203  
     of vehicle; *see* stability
- Standing wave of finite amplitude, 270, 277
- Stationary oscillations; *see* finite amplitude
- Strain energy due to bending and stretching of shell, 315
- Strain gage bridge to measure liquid motion, 173
- Strip theory applied to damping, 182
- Structural damping; *see* damping
- Structural deformation coupled with liquid motions;  
     *see also* coupling and cylindrical shell of circular cross section
- Structural material modeling with dissimilar material, 153
- Structural oscillations; *see also* coupling and cylindrical shell of circular cross section  
     coupling with  
         engine, 379, 381  
         pneumatic regulation system, 269, 378, 382  
         pressure regulator, 382
- Subharmonic liquid response; *see* longitudinal excitation
- Subharmonic shell response, 333, 334; *see also* cylindrical shell of circular cross section
- Support system; *see also* experimental techniques  
     for 1/5-scale model of Saturn SA-1, 187  
     for 1/40-scale model of Saturn V, 187  
     pendular type, 171  
     for models, 185
- Support cables, types for model experimentation, 186
- Surface response; *see* free surface
- Surface spray formation, 288
- Surface tension, 392  
     effect on convection at zero g, 431  
     effect on damping, 110  
     effect of temperature on, 430  
     gradients, 431  
     kinematic, 388  
     simulation of, 162  
     values for typical model fluids and propellants,  
         appendix
- Surge of bubbles, 270
- Swirl; *see also* stability  
     experimental techniques of measuring forces during,  
         179  
     unstable liquid free surface motion, 6, 95, 97, 100,  
         373
- T**
- Tandem arrangement of  
     three tanks, stability of vehicle with, 256  
     two tanks, stability of vehicle with, 254
- Tank; *see also* vehicle, and particular tank configuration and coupling  
     clustered, 251  
     convection in, 433  
     longitudinal excitation; *see* longitudinal excitation  
     scalloped, 4
- Tank bottom motion coupled with liquid motion, 336
- Tank bulkhead; *see* liquid impact and particular bulkhead geometry
- Tank construction techniques, 170
- Tank draining; *see* draining
- Tank elasticity; *see also* cylindrical shell of circular cross section, coupling and stability  
     effect on  
         bubble behavior, 293  
         bubble cluster motion, 291  
         low g sloshing, 418  
         mechanical model, 218
- Tank geometry, nonlinear effects from 79; *see also* nonlinear
- Tank location, effect on vehicle stability, 251; *see also* stability
- Tank motion  
     coupled with liquid motion; *see* coupling  
     excitation with air shaker, 183  
     experimental techniques for excitation, 171  
     impulsive, 2, 13  
     velocity potential for, 16
- Tank pressure regulation system, coupling with vehicle structure, 269, 378, 382
- Tank pressurization with fluids possessing inertia; *see* coupling
- Tank support; *see also* experimental techniques  
     for models, 185  
     platform for, 171  
     tripod type, 172
- Temperature  
     control in storable tanks, 429  
     effect on surface tension 430  
     effect at low g, 430  
     nonuniformity in liquid, 429
- Theory  
     for axisymmetric tank, stable waves of large amplitude, 83  
     of bubble vibration, 291  
     extended Hutton's for nonlinear liquid motions in circular cylindrical tank, 93  
     linear, 14  
     liquid sloshing at low g, 413, 414, 416  
     longitudinal excitation, 269, 271  
     Miles' for ring damping, 107, 183  
     Moiseyev's for large waves in axisymmetric tank, 83
- Thermodynamics of capillary systems, 391
- Thin-walled; *see* tank elasticity
- Thor-Agena  
     full-scale dynamics studies, 186  
     pogo oscillations of, 378, 379, 381  
     vibration tests of, 192
- Thrust forces, 228  
     for vent clearing, 426
- Thrust termination, bulkhead impact resulting from, 353
- Tidal oscillations, 1
- Time, estimates for reorientation of meniscus, 419

Timoshenko shell equations, 317  
 Titan II, pogo oscillations of, 378, 379, 381  
 Titan III,  $\frac{1}{3}$ -scale model, 188, 189  
 Toroidal tank, 54  
     liquid mode shapes, 174  
     viscous damping in, 114  
 Torque, resulting from liquid rotation, 373, 376  
 Torque bar to measure liquid motion, 173  
 Tower, launch umbilical, 191  
 Toxic liquids, appendix  
 Trajectory analysis, differential equations for, 354  
 Transducer system, types of used, 175  
 Transfer of liquid; *see* liquid transfer  
 Transverse excitation of shells, nonlinear coupling between liquid and shell, 335; *see also* coupling and particular shell configuration  
 Tripod tank support, 172

**U**

Umbilical tower, dynamically similar model of, 191  
 Unstable; *see* stability  
 Unstable liquid free surface (swirl) motion, 6, 95, 97, 100; *see also* stability

**V**

Vapor bubbles entrained in the liquid, 270  
 Vehicle; *see also* coupling, particular vehicle configurations, and stability  
     characteristics of launch, 3  
     configuration of launch, 3  
     configurations of space, 6  
 Vehicle bending frequency, effect of liquid, 307  
 Vehicle control; *see also* control system  
     equations for, 340  
     during lateral sloshing, 233  
 Vehicle coupling; *see* coupling  
 Vehicle dissipation function; *see* damping  
 Vehicle propellants, appendix  
 Vehicle response to  
     atmospheric disturbances, 256  
     wind load, 257  
 Vehicle stability; *see* stability  
 Vehicle stability and control; *see* stability and control  
 Vehicle umbilical tower response, 190  
 Velocity potential, 15  
     for tank motion, 16

Vent clearing by temporary thrust, 426  
 Vertical excitation; *see* longitudinal excitation  
 Vibration tests, of dynamic models, 184  
 Virtual displacement of the generalized coordinate, 229  
 Virtual work done by the external forces, 228  
 Viscosity; *see* liquid kinematic viscosity  
 Viscous damping; *see* damping  
 Vortex formation, 6  
     effect of  
         Coriolis force, 374  
         liquid rotation on, 376  
 Vortex strength, determined from circulation, 374  
 Vortexing during draining, 9, 373

**W**

Wall-pressure distributions, 14  
 Water hammer  
     analysis, 295  
     theory, 321  
 Waves; *see also* free surface and finite amplitude  
     breaking, in spherical tank, 97  
     capillary, 269, 288  
     spray-formed, 289  
 Weber number, 390  
     modeling at low g, 434  
 Wetting  
     defined, 392  
     experiments, 421  
     of wall by liquid, 388  
 Wind disturbance, vehicle response to, 256

**Y**

Young's equation, for interfacial force, 393

**Z**

Zero g; *see also* experimental investigation and low g  
 condensing in, 434  
 convective patterns, 431  
 drop and bubble oscillations in, 419  
 effect of contact angle hysteresis on lateral sloshing, 418  
 meniscus configuration in spherical tank, 399, 404, 405  
 parallel meniscus systems in, 400  
 stability of liquid film on sphere and cylinder, 412  
 Zero gravity; *see* zero g